

Selected Papers from the
Proceedings of Geo-Chicago 2016

GSP 270



Geo-Chicago 2016: Geotechnics for Sustainable Energy

ASCE

EDITED BY Arvin Farid, Ph.D., P.E.;
Anirban De, Ph.D., P.E.; Krishna R. Reddy,
Ph.D., P.E., D.GE; Nazli Yesiller, Ph.D.; and
Dimitrios Zekkos, Ph.D., P.E.



**GEO-
INSTITUTE**

GEOTECHNICAL SPECIAL PUBLICATION NO. 270

GEO-CHICAGO 2016

GEOTECHNICS FOR SUSTAINABLE ENERGY

SELECTED PAPERS FROM SESSIONS OF
GEO-CHICAGO 2016

August 14–18, 2016
Chicago, Illinois

SPONSORED BY

Geo-Institute of the American Society of Civil Engineers

EDITED BY

Arvin Farid, Ph.D., P.E.

Anirban De, Ph.D., P.E.

Krishna R. Reddy, Ph.D., P.E., D.GE

Nazli Yesiller, Ph.D.

Dimitrios Zekkos, Ph.D., P.E.



Published by the American Society of Civil Engineers

Published by American Society of Civil Engineers
1801 Alexander Bell Drive
Reston, Virginia, 20191-4382
www.asce.org/publications | ascelibrary.org

Any statements expressed in these materials are those of the individual authors and do not necessarily represent the views of ASCE, which takes no responsibility for any statement made herein. No reference made in this publication to any specific method, product, process, or service constitutes or implies an endorsement, recommendation, or warranty thereof by ASCE. The materials are for general information only and do not represent a standard of ASCE, nor are they intended as a reference in purchase specifications, contracts, regulations, statutes, or any other legal document. ASCE makes no representation or warranty of any kind, whether express or implied, concerning the accuracy, completeness, suitability, or utility of any information, apparatus, product, or process discussed in this publication, and assumes no liability therefor. The information contained in these materials should not be used without first securing competent advice with respect to its suitability for any general or specific application. Anyone utilizing such information assumes all liability arising from such use, including but not limited to infringement of any patent or patents.

ASCE and American Society of Civil Engineers—Registered in U.S. Patent and Trademark Office.

Photocopies and permissions. Permission to photocopy or reproduce material from ASCE publications can be requested by sending an e-mail to permissions@asce.org or by locating a title in ASCE's Civil Engineering Database (<http://cedb.asce.org>) or ASCE Library (<http://ascelibrary.org>) and using the “Permissions” link.

Errata: Errata, if any, can be found at <http://dx.doi.org/10.1061/9780784480137>

Copyright © 2016 by the American Society of Civil Engineers.
All Rights Reserved.
ISBN 978-0-7844-8013-7 (PDF)
Manufactured in the United States of America.

Preface

Geo-engineers and geo-scientists have been playing a major role in providing, protecting, and preserving infrastructure and the environment. Many innovative technologies and practices are constantly being developed and implemented. Evolving global climate change and exploding world population are leading to major concerns such as extreme geohazards, increased environmental pollution, and rapid depletion of natural resources. These new challenges can be addressed with new and innovative concepts, materials, energy sources, technologies, and practices. Sustainability and resiliency have become essential in the development of new materials and infrastructure systems. *Geo-Chicago 2016: Sustainability, Energy, and the Environment* held in Chicago August 14-18, 2016, provided a unique opportunity to highlight recent advances, new directions, and opportunities for sustainable and resilient approaches to design and protect infrastructure and the environment.

The Geo-Chicago 2016 Conference attracted a significant amount of interest and in the end more than 350 papers were accepted for publication. The papers are divided into five Geotechnical Special Publications (GSPs) that capture the multidisciplinary aspects and challenges of sustainability and resiliency, energy and the geoenvironment.

The first GSP, *Sustainability and Resiliency in Geotechnical Engineering*, addresses major broad issues related to sustainability and resilience in geotechnical and geoenvironmental engineering, including carbon sequestration as well as characterization, analysis, monitoring, and response to geohazards and natural disasters, including earthquakes and landslides. Advances in emerging technologies and materials such as bio-mediated soils and nanomaterials are also presented.

The second GSP, *Geotechnics for Sustainable Energy*, tackles the new and innovative ways of storing and extracting energy in and from geotechnical media and structures such as shallow and deep ground, piles and foundations, and landfills. The second GSP also presents the challenges of the energy storage and extraction at the field and lab scales as well as its numerical and experimental modeling.

The third GSP, *Sustainable Geoenvironmental Systems*, addresses recent advances in landfill engineering and geosynthetics used for geoenvironmental systems, as well as advances in sustainable barrier materials and systems. The third GSP also presents studies into slopes, dikes, and embankment, the application of ground improvement in geoenvironmental applications, and the geoengineering of mine wastes and industrial byproducts.

The fourth GSP, *Sustainable Materials and Resource Conservation*, describes the properties and applications of new, recycled, and residual materials, detailed/improved characterization of soils with laboratory and field testing methods, and effects of chemicals and other environmental factors on properties and behavior of soils. The fourth GSP also presents the approaches and use of modeling and simulations in geoenvironmental engineering.

The fifth GSP, *Sustainable Waste Management and Remediation*, addresses various aspects of remediation, contaminated materials, containment, policy, and education. In addition, international perspectives are included to provide further context on challenges and innovations in geoenvironmental engineering on a global scale.

Following standards of practice of the Geo-Institute of the American Society of Civil Engineers, each paper published in these Geotechnical Special Publication (GSPs) was peer reviewed by at least two anonymous, qualified, technical reviewers (and in some cases three or four reviewers) and selected for publication by the proceedings editors. An advanced document management service was utilized in order to assure anonymity and maintain uniformity of standards. As such, the papers contained in these proceedings are eligible for discussion in the ASCE Journal of Geotechnical and Geoenvironmental Engineering and for ASCE awards.

The Editors

Nazli Yesiller, Ph.D., A.M.ASCE, Global Waste Research Institute / California Polytechnic State University, San Luis Obispo
Dimitrios Zekkos, Ph.D., P.E., M.ASCE, University of Michigan
Arvin Farid, Ph.D., P.E., M.ASCE, Boise State University
Anirban De, Ph.D., P.E., M.ASCE, Manhattan College
Krishna R. Reddy, Ph.D., P.E., D.GE, F.ASCE, University of Illinois at Chicago

Acknowledgments

The success of Geo-Chicago 2016 is credited to the session chairs and authors of the technical papers and also plenary session presenters for their valuable contributions to the geotechnical literature. The commendable quality of the Conference's technical content and these proceedings are also the result of the efforts of the hundreds of reviewers. We thank the session chairs, authors and reviewers for generously contributing their valuable time and expertise, in many cases, under time pressure and demanding deadlines.

The following individuals served as the conference program committee. They deserve special acknowledgment and recognition for their extraordinary efforts in making this Conference a reality and a resounding success:

- Conference Chair – Krishna R. Reddy, University of Illinois at Chicago
- Conference Co-Chair/Workshops Co-Chair – Nazli Yesiller, Global Waste Research Institute / California Polytechnic State University, San Luis Obispo
- Technical Program Chairs – Dimitrios Zekkos, University of Michigan; Arvin Farid, Boise State University and Anirban De, Manhattan College
- Short Courses Chair – Michael A. Malusis, Bucknell University
- Workshops Chair – James L. Hanson, California Polytechnic State University, San Luis Obispo
- Technical Tours/Social Program Co-Chairs – Doug Hermann, Independent Consultant; and Dhooli Raj, Collins Engineers, Inc.
- Sponsorships and Exhibits Co-Chairs – Carsten H. Floess, AECOM and Charles Wilk, ALLU Group, Inc.
- G-I TCC Liaison – Susan E. Burns, Georgia Institute of Technology

The Editors sincerely appreciate the help and patience of Ms. Helen Cook and Mr. Brad Keelor of Geo-Institute of the ASCE for their help in managing the paper submissions and organization of the conference.

We hope that these GSPs will serve as valuable references to all working in geoen지니어ing.

The Editors

Nazli Yesiller, Ph.D., A.M.ASCE, Global Waste Research Institute / California Polytechnic State University, San Luis Obispo

Dimitrios Zekkos, Ph.D., P.E., M.ASCE, University of Michigan

Arvin Farid, Ph.D., P.E., M.ASCE, Boise State University

Anirban De, Ph.D., P.E., M.ASCE, Manhattan College

Krishna R. Reddy, Ph.D., P.E., D.GE, F.ASCE, University of Illinois at Chicago

LIST OF SESSION CHAIRS

Michel Aubertin	Enad Mahmoud	Marcelo Sanchez
Susan E. Burns	John McCartney	Nina Stark
Halil Ceylan	Debakanta Mishra	Xinbao Yu
Fleur Loveridge	Guillermo Narsilio	Xiong (Bill) Yu
Melissa E. Landon	Cassandra J.	
Joan M. Larrahondo	Rutherford	

LIST OF REVIEWERS

Sherif Abdelaziz	Carlos Guzman	Amir Rahim
Martin Achmus	Chanjuan Hanson	Jorge Rodriguez
Charles Aubeny	Jim Hanson	Cassandra Rutherford
Michel Aubertin	Edward Hoppe	Rajni Saggi
Maria Claudia Barbosa	Zahid Hossain	Marcelo Sanchez
Ivana Barisic	Isaac Howard	James Schneider
Luis Leguizamón Barreto	Jie Huang	Daniel Spikula
Tugce Baser	Andre Huepers	Nina Stark
Prasenjit Basu	Sihyun Kim	Robert Stevenson
Michelle Bernhardt	Sunghwan Kim	Atsushi Takai
Jonathan Black	Stefan Kreiter	Xiaochao Tang
Aaron Bradshaw	Melissa Landon	Junliang Tao
Susan Burns	Thomas Langford	Marco Terzariol
Byron Byrne	Joan Larrahondo - Cruz	James Tinjum
Bora Cetin	Barry Lehane	Shun Uchida
Halil Ceylan	Anthony Leung	Pavana Vennapusa
Shengli Chen	Zhen Liy	Quan Wang
Shiao Huey Chow	Fleur Loveridge	David White
Ed Clukey	Huan-Lin Luo	Xinbao Yu
Diego Cobos	Enad Mahmoud	Martins Zauamanis
Charles Coccia	Ross McAdams	Katerina Ziotopoulou
Julio Colemenares	John McCartney	
Sheng Dai	Mohamed Mekkway	
Vishal Dantal	Debakanta Mishra	
Maria Diaz	Cristopher Moen	
Brian Diefenderfer	Guillermo Narsilio	
Shaoyang Dong	Majidreza Nazem	
Yi Dong	Kam Ng	
Tuncer Edil	Manuel Ocampo	
Hossein Eslami	Tolga Ozudogru	
Ismaail Ghaaowd	Angelica Palomino	
Omid Ghasemi-Fare	Tongyan Pan	
Malay Ghose Harja	Eun Park	
Bob Gilbert	Cesar Pasten	
Kasthurirangan	Ryan Phillips	
Gopalakrishnan	Yinghong Qin	

Contents

Thermal Geotechnics

Dynamic Calibration of a Fiber-Optic Distributed Temperature Sensing Network at a District-Scale Geothermal Exchange Borefield	1
Adam McDaniel, Matthew Harper, Dante Fratta, James M. Tinjum, Christopher Y. Choi, and David J. Hart	
Electro-Osmosis and Heating in HVDC Grounding Systems.....	12
Maria Claudia Barbosa, Antonio C. S. Lima, Iara F. Rezende, and Joaquim S. Lima Neto	
Hydro-Thermo-Mechanical Behavior of Granular Material near a Wellbore.....	22
Ingrid Tomac	
Impact of Drainage Conditions on the Thermal Volume Change of Soft Clay	32
Atsushi Takai, Ismaail Ghaaowd, John S. McCartney, and Takeshi Katsumi	
Impact of Long-Term Temperature Cycling on the Thermo-Hydro-Mechanical Behavior of Unsaturated Soils Surrounding an Energy Pile	42
Charles J. R. Coccia and John S. McCartney	
Impact of the Seasonal Variations in Ground Temperature on Thermal Response Test Results.....	52
Linden Jensen-Page, Guillermo A. Narsilio, Asal Bidarmaghz, and Ian W. Johnston	
Impact of Temperature Variations on the Hydro-Mechanical Parameters of a Sensitive Soil.....	62
Hossein Eslami, Sandrine Rosin, Adel Abdallah, and Farimah Masrouri	
Large-Scale Thermo-Hydrodynamic Modeling of a Flooded Underground Mine for Geothermal Applications	72
Ting Bao and Zhen (Leo) Liu	
Thermal Protection Analyses of Underground Steam Pipes	84
Chanjuan Han and Xiong (Bill) Yu	

The Use of Recycled Materials as Thermal Insulation in Underground Construction.....	94
James L. Hanson, Kevin B. Kopp, Nazli Yesiller, Craig M. Cooledge, and Emily Klee	

Geoenergy

A Sustainable Perspective for the Long-Term Behavior of Energy Pile Groups	104
Sherif L. Abdelaziz	

Fully Instrumented Life-Cycle Analyses for a Residential Geo-Exchange System	114
Eleanor F. Bloom and James M. Tinjum	

Impact of a Thermo-Hydraulic Insulation Layer on the Long-Term Response of Soil-Borehole Thermal Energy Storage Systems.....	125
Tugce Baser, John S. McCartney, Ali Moradi, Kathleen Smits, and Ning Lu	

Mechanical Behavior of a Pile Used for Small-Scale Compressed Air Energy Storage.....	135
Sihyun Kim, Seunghee Kim, Hoyoung Seo, and Jongwon Jung	

Settlement Response of a Geothermal Energy Pile Group in Sand	144
Rajni Saggu and Tanusree Chakraborty	

Temperature-Induced Alterations of the Shaft and Base Resistances of a Model Geothermal Pile in Dry Sand	155
Amir Ahmadipur and Prasenjit Basu	

The Average Temperature of Energy Piles	166
Fleur A. Loveridge and William Powrie	

Thermally-Induced Pore Pressure Fluctuations around a Geothermal Pile in Sand.....	176
Omid Ghasemi-Fare and Prasenjit Basu	

Energy Geotechnics

A New Model Concrete for Reduced-Scale Model Tests of Energy Geo-Structures	185
Davide Vitali, Anthony K. Leung, Andrew Minto, and Jonathan A. Knappett	

Consideration of the Cyclic Degradation of Cohesive Soils in Pile Foundation Design for Onshore Wind Turbines.....	195
Hao Yu, Carlos Guzman, and Eric Ntambakwa	

Deep Foundations under Wind Turbines—A Case Study	207
Önder Akçakal, Ertun Sözen, Turhan Karadayılar, Selim İkiz, and H. Turan Durgunoğlu	
Design and Analysis of Foundations for Onshore Tall Wind Turbines	217
Shweta Shrestha and Nadarajah Ravichandran	
Micromechanical Modeling of Proppants for Hydraulic Fracturing	227
Mehmet B. Cil and Giuseppe Buscarera	
Thermo-Hydro-Chemo-Mechanical Formulation for CH₄-CO₂ Hydrate Conversion Based on Hydrate Formation and Dissociation in Hydrate-Bearing Sediments	235
Shun Uchida, Christian Deusner, Assaf Klar, and Matthias Haeckel	
<i>Mining Wastes</i>	
Centrifuge Modeling of Mine Tailings and Waste Rock Co-Disposal, Consolidation, and Dynamic Loading	245
Nonika Antonaki, Tarek Abdoun, and Inthuorn Sasanakul	
Compressibility Behavior of Synthetic Mine Tailings Amended with Fly Ash	255
Mohammad H. Gorakhki and Christopher A. Bareither	
Design, Construction, and Preliminary Results of Two Insulation Covers at the Meadowbank Mine	267
Sylvette A. Awoh, Bruno Bussière, Charles Batzenschlager, Vincent Boulanger-Martel, Thomas Lepine, and Erika Voyer	
Estimating the Cyclic and Post-Earthquake Behavior of Coal Mine Tailings at a Site in Eastern Kentucky	279
M. E. Kalinski and A. Salehian	
Field Experiments to Test the Elevated Water Table Concept Combined with a Desulfurized Tailings Cover Layer	289
Nicolas J. Rey, Isabelle Demers, Bruno Bussière, Mamert Mbonimpa, and Sylvain Lortie	
Geotechnical Characterization of Compacted Bauxite Residue for Use in Levees	299
Matthew S. Gore, Robert B. Gilbert, Ian McMillan, and Shannon L. Isovitsch Parks	
Heat Extraction from Mining Waste Piles	311
Nazli Yeşiller, James L. Hanson, Emma H. Yee, and Kevin B. Kopp	

Modeling the Effect of Flocculation and Desiccation on Oil Sands Tailings.....	321
Nicholas A. Beier, Louis K. Kabwe, J. Don Scott, Nam H. Pham, and G. W. Wilson	
Pore Water Pressure Variations in Cemented Paste Backfilled Stopes	331
Mohammad Shahsavari and Murray Grabinsky	
Review of the Reclamation Techniques for Acid-Generating Mine Wastes upon Closure of Disposal Sites.....	343
Michel Aubertin, Bruno Bussière, Thomas Pabst, Michael James, and Mamert Mbonimpa	
Tailings Disposal Challenges and Prospects for Oil Sands Mining Operations	359
Michel Aubertin and Gord McKenna	
Vulnerability Assessment of Underground Mine Stopes Filled with Granular Backfills	372
P. Rajeev and N. Sivakugan	
<i>Offshore Energy Geotechnics</i>	
A Novel Mixed-in-Place Pile System for Offshore Platforms	382
Giovanni Spagnoli, Paul Scheller, and Paul Doherty	
Design Charts for Laterally-Loaded Rigid Monopiles in Multilayered Elastic Soil	393
Bipin K. Gupta and Dipanjan Basu	
Effect of Climate Change on the Reliability of Offshore Wind Turbine Foundations	407
Sumanta Halder and Dipanjan Basu	
Evaluating the $p - y$ Curve Method of Analysis for Large-Diameter Monopiles Using Centrifuge Modelling	418
Steven M. Bayton and Jonathan A. Black	
In Situ Geotechnical Early Site Assessment of a Proposed Wave Energy Converter Site in Yakutat, Alaska, Using a Portable Free-Fall Penetrometer	429
Ali Albatal and Nina Stark	
Installation Torque Measurements of Helical Piles in Dry Sand for Offshore Foundation Systems.....	439
Giovanni Spagnoli, Soroosh Jalilvand, and Kenneth Gavin	

Lateral Performance of Helical Piles as Foundations for Offshore Wind Farms	449
Sherif A. Y. Akl, Omar M. Elhami, and Mustafa A. Abu-keifa	
Preliminary Development of a New Concept to Improve the Sustainability of Offshore Foundations	459
Hande Gerkus, Joseph R. Giampa, Asitha I. Senanayake, Ying Lai, Yunhan Huang, Jose Eugenio Iturriaga Flores, Nikolaus B. Breithaupt, Sven Sivarajah, Aaron S. Bradshaw, and Robert B. Gilbert	
Rotational Behavior of Squat Monopiles in Soft Clay from Centrifuge Experiments.....	470
Ryan D. Beemer, Madhuri Murali, Giovanna Biscontin, and Charles Aubeny	
Shear Behavior of Methane Hydrate Bearing Sands during Gas Production	481
Masayuki Hyodo, Shintaro Kajiyama, and Koji Nakashima	
Suction Caissons in Soft Clay for Tidal Current Turbine Applications.....	492
Jeff F. Wallace and Cassandra J. Rutherford	
Towards the Anchoring of Marine Hydrokinetic Energy Devices: Three-Dimensional Discrete Element Method Simulations of Interface Shear	503
Nan Zhang and T. Matthew Evans	
<i>Renewable Energy and Sustainable Pavement Solutions</i>	
Airport Apron Heated Pavement System Operations: Analysis of Energy Consumption, Greenhouse Gas Emissions, and Operating Costs.....	513
Weibin Shen, Kasthurirangan Gopalakrishnan, Sunghwan Kim, and Halil Ceylan	
Characterization of Cement Treated Base Course Using Reclaimed Asphalt Pavement, Aggregate By-Products, and Macro-Synthetic Fibers.....	523
Jeffrey R. LaHucik, Scott R. Schmidt, Erol Tutumluer, and Jeffery R. Roesler	
Demonstrating the Worth of Recycled Aggregates—A Case Study from Qatar	534
J. Murray Reid, Khaled E. Hassan, Okan Sirin, and Ramzi A. Taha	
Durability Studies on Fly Ash Stabilized Reclaimed Asphalt Pavement Materials.....	546
Deepti Avirneni and Sireesh Saride	

Energy Harvesting from Pavement via PVDF: Hybrid Piezo-Pyroelectric Effects.....	556
Jie Hu and Junliang Tao	
Evaluating the Performance of Cementitious Treated/Stabilized Very Weak and Wet Subgrade Soils for Sustainable Pavement	567
Allam Ardah, Murad Abu-Farsakh, and Qiming Chen	
Feasibility of the Discrete Element Method to Simulate RAP Asphalt Mixtures' Fracture Behavior	577
Enad M. Mahmoud, Shadi M. Saadeh, and Roberto R. Yanez	
Feasibility Study on Harvesting Energy from Roadway Infrastructure	588
H. Roshani, S. Dessouky, A. T. Papagiannakis, A. Montoya, and J. Helffrich	
Geothermal Energy for Bridge Deck and Pavement Deicing—A Brief Review	598
Xinbao Yu, Nan Zhang, Asheesh Pradhan, and Anand J. Puppala	
Gradation Effects on the Strength Properties of Cement and Fly Ash Stabilized Quarry By-Products	610
Issam Qamhia, Joshua Cheung, Wenting Hou, Vincent Mwumvaneza, Hasan Ozer, and Erol Tutumluer	
Ground Granulated Blast Furnace Slag (GGBS) and Rice Husk Ash (RHA) Uses in the Production of Geopolymer Concrete.....	621
Sundeep Inti, Megha Sharma, and Vivek Tandon	
Heat Exchangers for Pavement Surface De-Icing	633
Soji Pallathu Abraham, Sherif L. Abdelaziz, and Jon Longtin	
Laboratory Evaluation of Mixtures Incorporating GTR and RAP.....	644
Md. Tanvir Iqbal, Munir D. Nazzal, Sang Soo Kim, Ala Abbas, Md. Tanvir Quasema, and Walaa Mogawer	
Performance of Aggregate Subgrade Layers in Low-Volume Roads Constructed with Unconventional Recycled Aggregates	654
Hasan Kazmee, Erol Tutumluer, and Debakanta Mishra	
Rejuvenators for Asphalt Binders Using Oil Extracted from Spent Coffee Grounds	666
Rita Jalkh, Mohamad Abiad, and Ghassan R. Chehab	
Resilient Modulus of a Blended Mixture of Recycled Asphalt Pavement and Natural Aggregate as Road Pavement Base Material	677
Prabir K. Kolay and Pralendra Singh	

Sustainability Evaluation of Geosynthetic Stabilized Soft Subgrade Soil in Unpaved Test Sections.....	687
Murad Abu-Farsakh, Shadi Hanandeh, Xiaochao Tang, and Qiming Chen	
The Effect of Rejuvenators on RAP Mixtures: A Study Based on Multiple Scale Laboratory Test Results.....	697
H. F. Haghshenas, H. Nabizadeh, and Y.-R. Kim	
Variability Associated with the Resilient Modulus of Reclaimed Asphalt Pavements.....	708
Pranav R. T. Peddinti, Sireesh Saride, and B. Munwar Basha	

Dynamic Calibration of a Fiber-Optic Distributed Temperature Sensing Network at a District-Scale Geothermal Exchange Borefield

Adam McDaniel¹; Matthew Harper²; Dante Fratta, Ph.D., P.E., M.ASCE³; James M. Tinjum, Ph.D., P.E., M.ASCE⁴; Christopher Y. Choi, Ph.D., P.E.⁵; and David J. Hart, Ph.D.⁶

¹Graduate Student, Geological Engineering, Univ. of Wisconsin-Madison, 1415 Engineering Dr., Madison, WI 53706. E-mail: almcdaniel@wisc.edu

²Graduate Student, Biological Systems Engineering, Univ. of Wisconsin-Madison, 460 Henry Mall, Madison, WI 53706. E-mail: mharper2@wisc.edu

³Associate Professor, Geological Engineering, Univ. of Wisconsin-Madison, 1415 Engineering Dr., Madison, WI 53706. E-mail: fratta@wisc.edu

⁴Associate Professor, Engineering Professional Development, Geological Engineering, Univ. of Wisconsin-Madison, 1415 Engineering Dr., Madison, WI 53706. E-mail: jmtinjum@wisc.edu

⁵Professor, Biological Systems Engineering, Univ. of Wisconsin-Madison, 460 Henry Mall, Madison, WI 53706. E-mail: cchoi22@wisc.edu

⁶Professor, Univ. of Wisconsin-Extension, 3817 Mineral Point Rd., Madison, WI 53705. E-mail: djhart@wisc.edu

Abstract: Subsurface heat exchange research in a low-temperature district-scale geothermal borefield is a demanding application for fiber-optic distributed temperature sensing (DTS). While DTS systems do provide internal calibration routines, external calibration schemes are often needed to achieve desired accuracy and precision. This study systematically documents a set of tests aimed at evaluating the efficacy of both internal and external calibration routines and selects the most appropriate external calibration technique for a geothermal borefield monitoring study. The selection of this calibration scheme is based on the inability of static DTS calibration to prevent measurement drift and the physical requirement of sophisticated cable networks and splices at the district-scale field site. A double-ended and dynamic calibration with centralized and remotely accessible data collection and processing is developed to prevent measurement drift and to solve differential attenuation challenges. The calibration is primarily achieved by two long-term calibration baths that keep reference sections of each fiber-optic cable at continuously known temperatures. After calibration, temperature profiles from fiber-optic cables placed within ground heat exchangers (GHX) and sentry boreholes provide valuable knowledge of subsurface heat flow which assists in detection of borefield overheating, comparison of individual GHX performance, and design optimization of future borefields.

INTRODUCTION

Ground source heat pump (GSHP) systems are designed to match anticipated heating and cooling loads with system capacity. Due to high installation cost, an

appropriately sized and efficient system is vital to achieving optimal payback periods (Nagano et al. 2006). Historically, lifetime heating and cooling performance has been difficult to predict and systems have repeatedly deviated from expected design performance (Kara 2007, Magraner et al. 2010, Knudson 2013). Uncertain heat exchange performance can be attributed to the complex interplay between groundwater flow, thermal properties of surrounding lithology, cyclical changes to the bulk temperature of the field, and imbalances in heating/cooling demands of the facilities (Florides and Kalogirou 2007). At district-scale borefields, uncertain performance magnifies investment risk and may discourage potential users from choosing to supply HVAC needs with GSHP systems. However, with quantification and proper application of the subsurface heat exchange mechanisms and variables, predictions of long-term ground heat exchanger (GHX) performance can be made with greater confidence (Walker et al. 2015). A common experimental GHX performance metric involves calculating the energy exchange accomplished in the subsurface by measuring the flow rate and change in entering and exiting fluid temperatures (Puttagunta et al. 2010; Luo et al. 2015). While this method is useful to provide a basic energy balance, it fails to deliver insight into specific locations that advantageous heat transfer occurs. Since vertical GHX can extend 150 m into the subsurface, the $\Delta T > 2.0$ °C often accomplished may have occurred anywhere along a 300-m data gap between the inlet and outlet temperature. Questions of where and how the energy was exchanged are left unanswered.

Advances in numerical modelling have provided insight into the mechanisms of ground heat exchange (Florides and Kalogirou 2007). GHX modeling has progressed from one-dimensional pipe flow (Tzaferis et al. 1992) to complex finite element models of time-varying heat flow throughout the entire system (Ozdoğan-Dölçek 2015). However, the need remains for experimental data collection to provide model validation and refinement. Through its ability to provide continuous temperature profiles over long distances, fiber-optic distributed temperature sensing (DTS), can provide experimental data over the entire length of GHX systems. Fujii et al. (2009) utilized fiber-optic temperature sensors within two U-bend GHX to validate numerical modelling data as part of a thermal response test. Acuna and Palm (2010) performed a similar experiment using fiber-optic temperature data every 10 m along two GHX to compare the heat exchange performance of one coaxial and one standard U-bend configuration. DTS technology has advanced significantly in the past three decades to allow for the application of studying temperature perturbations within GHX at meaningful temporal and spatial resolutions. The capabilities of DTS arrays are helping researchers both hypothesize and validate the interaction of geology, hydrogeology, and technological development to improve the design and sustainability of geothermal fields. This manuscript aims at documenting the development needed for calibrated data collection using a DTS network.

DTS MEASUREMENTS

DTS was first developed in the early 1980's (Hartog 1983) and the oil industry was the first to take advantage. Companies installed cables both within and surrounding oil and gas pipelines as a means of leak and fire detection (Kersey 2000). In this early

application, the temperature and spatial resolutions were poor; however, oil companies only needed to detect large spikes in temperature over broad areas. As the advantages of temperature sensor networks became evident, effort was spent on technological advancement to improve instrument accuracy and resolution. By the early-2000s, a robust calibration could achieve temperature and spatial resolutions of 0.01 °C and 1 m (Henninges et al 2003). With this upgraded resolution researchers have been able to implement the technology into ever-expanding applications.

For example, fiber-optic cables buried in stream beds have provided insight into groundwater and stream interaction by sensing lower temperature melt water leaving the stream, or by quantifying higher temperature groundwater encroaching on the stream (Selker et al. 2006b). Bahr et al. (2011) buried fiber-optic cables in underground trenches beside a heat source and monitored how quickly heat dissipated with DTS temperature profiles to estimate soil moisture content. DTS networks have been utilized to monitor the Antarctic ice sheet for melting potential with semi-permanently installed fiber-optics within and beneath the ice sheet (Tyler et al. 2013). A distributed borehole flowmeter was created by Read et al. (2014) with armored fiber optic cables, and the knowledge that within a flowing fluid, the temperature difference between a heated and unheated cable is a function of fluid velocity. The driving force behind each of these applications is the inherent advantage of continuous temperature profiles in time and space despite harsh environmental conditions, the same advantage that inspired the use of DTS to monitor heat flow in a district-scale GHX borefield.

DTS technology utilizes the scattering of laser light to create temperature profiles along the fiber-optic cables through which the light passes. When a light pulse propagates through a fiber, it interacts with the constituent molecules of that medium. If the photon/constituent molecule collision does not occur at a wavelength near medium resonance, a scattering event forms. There are three predictable scattering events: Rayleigh, Brillouin, and Raman (Bao and Chen 2012 – Fig. 1). Rayleigh scattering is a linear and elastic scattering process that returns light of similar wavelength and intensity of the incident light pulse. This elastic scattering occurs when the kinetic energy of the protons are conserved through the collision (Suárez et al. 2011). Brillouin scattering is an inelastic scattering event that creates two pulse events of unique wavelengths above and below the wavelength of the incident light (Hausner 2010 - Fig. 1). Raman scattering is also an inelastic event that occurs when a portion of incident light is adsorbed and reemitted at alternate wavelengths due to

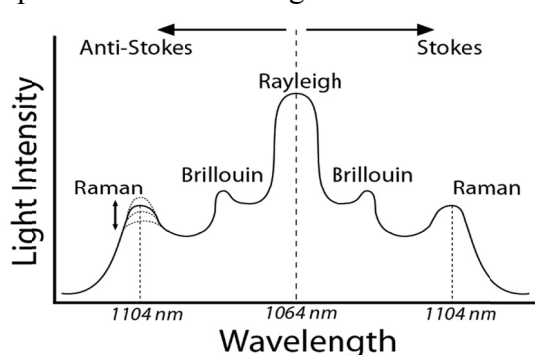


FIG. 1: Schematic of wavelength spectrum after a wave scattering event.

the loss/gain of energy with the electrons in the fiber molecules. Stokes light is created when a photon excites a molecule at its base vibrational state and bumps the molecule to the next highest vibrational state by the addition of energy. Anti-Stokes light is the result of a constituent molecule receiving energy from the photon and releasing it at a lower vibrational and energy state (Suárez et al. 2011). The ratio of photons

in the Anti-Stokes and Stokes states is a function of the temperature at which the scattering event occurred (Smith and Dent 2005).

DTS uses Raman spectra scattering within fiber-optics to create temperature profiles along the length of the fiber-optic cable. Interrogators generate pulses of light for typically 10 to 20 ns at a known wavelength that propagate down the cable (Suárez et al. 2011). A fiber-optic cable consists of a glass core encapsulated by glass cladding with a higher index of refraction to allow for total internal reflection. Typical multimode DTS cables have a 50 μm diameter core and a 125 μm diameter cladding. In all fiber-optic cables light encounters inconsistencies in the core's crystal structure and molecular inclusions (commonly GeO_2) to create scattering events (Selker et al. 2006a). At these backscatter events, a fraction of the incident light propagates back to the interrogator. The interrogator is equipped with a high-precision photodiode that will measure only the amplitudes of the Stokes and Anti-Stokes Raman backscatter. Because of the differential temperature dependence of the ratio of these intensities, this 'raw' light data can be used to calculate temperature data. The distance along the fiber to which the temperature data belongs is calculated by time-domain reflectometry using the known speed of light within the glass fiber which varies between $1.7 \cdot 10^8$ and $2.0 \cdot 10^8$ m/s (Suárez et al. 2011). Assuming a light speed of $2.0 \cdot 10^8$ m/s and a sampling interval of 20 ns, the spatial resolution obtained is 2 m until the end of the fiber or until light intensity attenuates.

Additionally, the fiber and interrogator may be set up for a single- or double-ended measurement. In the single-ended setting, light pulsates from one end of a fiber-optic cable for the prescribed duration, creating one profile before moving to the next fiber. In the double-ended setting, each fiber-optic cable is looped back and reattached to the interrogator so that both ends of the fiber will propagate light sequentially. In this way, the interrogator can receive two sets of intensity data for the same stretch of fiber, providing a buffer against the effects of differential attenuation. Either by an internal calibration routine, or a manual calibration procedure, the light intensity ratios may be decoded to provide continuous strings of temperature data. The parameters that describe the relationship between the Stokes/Anti-Stokes ratio and temperature are prone to vary with the operating temperature of the interrogator, the quality and consistency of the power supply, mechanical variance within the equipment, and localized strain in the fiber (Hausner et al. 2011). In some applications, the internal calibration routine can provide acceptable accuracy of these parameters, while in other applications a manual calibration scheme is needed.

MANUAL CALIBRATION

Manual calibration requires that the DTS user create an experimental setup in which multiple sections of each fiber-optic cable are at a known temperature. Eq. 1 governs the relationship between the ratio of light intensities, temperature, and the calibration parameters (Hausner et al. 2011):

$$T(z) = \frac{\gamma}{\frac{P_s(z)}{P_{as}(z)} + C - \Delta\alpha} \quad (1)$$

where γ , C , and $\Delta\alpha$ are the calibration parameters that represent a physical constant, the change in internal mechanics of the interrogator, and differential attenuation of light along the cable lengths, respectively. $P_s(z)/P_{as}(z)$ is the ratio of the Stokes intensity to the anti-Stokes intensity at a given point along the fiber z , and $T(z)$ is the temperature at that point. The calibration process requires determination of the three unknown variables C , γ , and $\Delta\alpha$. The most straightforward way to accomplish this is by knowing three different temperatures at three different positions along the fiber-optic cable. Under these conditions, three values of $T(z)$ are known from the external temperature measurement, and three values for $P_s(z)/P_{as}(z)$ are known from the DTS outputs. Eq. 1 may then be thrice restated with the known values specified to provide a system of three equations with three unknowns. The calibration variables are then calculated using linear regression techniques. Once the calibration parameters are specified, the light intensity ratios provided by the interrogator for the remainder of the cable length can be converted to temperature.

Single-ended calibration techniques are only able to calculate one value of $\Delta\alpha$ for a fiber. In contrast, by utilizing double-ended calibration, a unique $\Delta\alpha$ can be calculated at each data acquisition point z independently of temperature references (van de Giesen et al. 2012). This procedure allows for correction of step losses incurred by splicing and different $\Delta\alpha$ values of different fiber sections. Additionally, a double-ended configuration requires only two unique temperature reference sections of each fiber-optic run to solve for the calibration variables.

METHODS AND MATERIALS

A geothermal borefield located in Southern Wisconsin was used in this study. This borefield consists of nearly twenty-five hundred 150-m-deep GHX (Fig. 2). To assess the effect of ground water on subsurface heat exchange, external sentry wells equipped with fiber-optics and piezometers provide ground water flow and temperature measurements. Internal sentry wells contain fiber-optics grouted in contact with the lithology to provide a three-dimensional grid of ground temperature. One coaxial and one U-bend GHX in the southeast corner of the borefield contain fiber-optic cables to compare their individual heat exchange performance. The Sensornet Sentinel DTS-LR

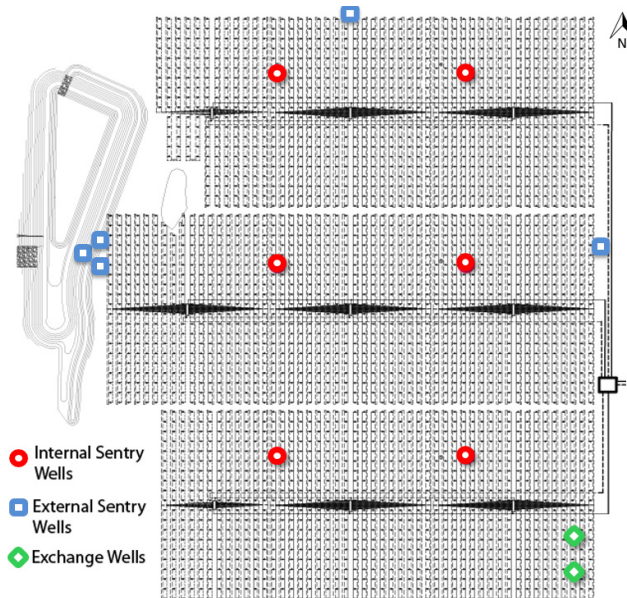


FIG. 2: District-scale GHX borefield equipped with DTS to monitor heat exchange.

interrogator with a 16-channel multiplexer is located in an underground vault that

serves as a central hub for borefield hydraulics. The fiber-optic cables loop through subterranean trenches to their respective wells and return back to the interrogator. A single loop that reaches two internal sentry wells includes nine fusion splices. The large amount of splices presents concerns for localized step-losses in light intensity and differential attenuation within different runs of cable (Hausner et al. 2011).

CALIBRATION STUDIES

Default calibration temperature data from the heavily-spliced internal sentry well loop was observed to contain data bias. Before any heat exchange had occurred within the ground, the two southern-most internal sentry wells should have provided nearly identical temperature profiles. However, there is a 0.5 °C shift in temperature profiles from one well to the next (Fig. 3). Additionally, the absolute ground temperature presented by the default calibration did not align well with 9 °C to 11 °C temperature range measured at nearby borefields. The temperature shifts

shown in the data provided strong evidence that the default calibration was unable to correctly capture the system temperatures. On a cold day, a gas heater raised the temperature of the underground vault that houses the interrogator. The internal temperature of the interrogator elevated from 10 °C to 25 °C between 8am and 10am.

Fig. 4 shows the resulting failure of the default calibration to accurately handle the change in air temperature that was created. Both data sets measured the same environment inside of the GHX, and should nearly overlap. However, a shift of nearly -6 °C is observed. While this is an extreme example, Fig. 5 shows the same interrogator temperature

fluctuations occur on a smaller scale from diurnal temperature swings and weather patterns. A server box with a temperature set-point controlled fan was installed around the interrogator to counteract the mechanical heating from sustained use.

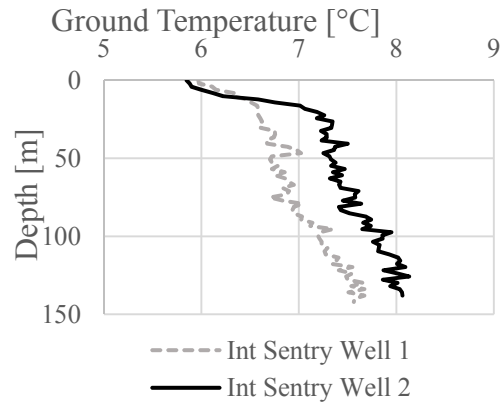


FIG. 3: Temperature profiles from sentry wells of the geothermal gradient within the borefield.

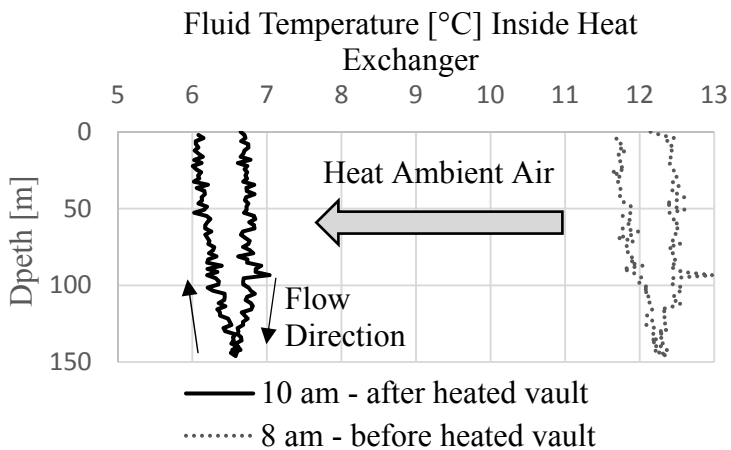


FIG. 4: Two U-Bend fluid temperature profiles from fiber-optic cables. Notice that heating the ambient air caused a -6 °C shift in data.

Although the diurnal temperature swings are muffled by the server box to less than 0.5 °C, these temperature swings still create appreciable biases in the default calibration output. In addition, this experiment revealed that, despite its subterranean installation, the interrogator temperature mimicked the trend of the general ambient air temperatures. The DTS interrogator cyclically responds to seasonal temperature patterns, which could be expected to proliferate this data bias.

Experimental results exposed the default calibration as insufficient for the needs of a studying a district-scale GHX borefield. Temperature shifts caused by ambient temperature swings existed and were unable to be sufficiently controlled for. Taking into account lessons learned from the weaknesses of the default calibration, a manual calibration scheme was designed.

Within a manual calibration scheme, it is necessary to understand if static calibration would provide accurate results as time passes, or if a dynamic calculation of the calibration parameters is necessary. To answer this question, four water calibration baths were placed on-site and equipped with fiber-optic coils as well as independent temperature measurement to provide a pre-calibrated measurement of the water temperature. Two subsurface vaults (denoted by dashed and solid lines in Fig. 6) each housed one cold (initially 3 °C) and one warm (initially 25 °C) calibration bath. Using these four baths, calibration parameters were statically calculated at the beginning of the experiment and then applied to the raw light intensity data for five subsequent days.

The statically calibrated temperatures were compared to temperatures recorded by Solinst Leveloggers, which are pre-calibrated and claim temperature accuracy of +/- 0.05 °C (Solinst, 2016). Fig. 6 plots the difference between levelogger and DTS temperature readings (ΔT) for each of the four baths. Over the course of just one week, instrument drift was observed in all four measurement points at unacceptable levels. As it is an experimental impracticality to statically calibrate the system on a weekly basis, a dynamic calibration was needed that would recalibrate the machine each iteration of new light intensity data.

Two calibration baths of unique, steady, and uniformly known temperatures were

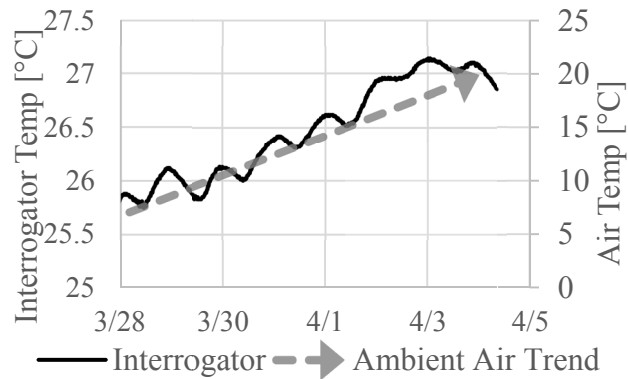


FIG 5: Temperature inside the DTS interrogator mirrors the air temperature at a muffled scale.

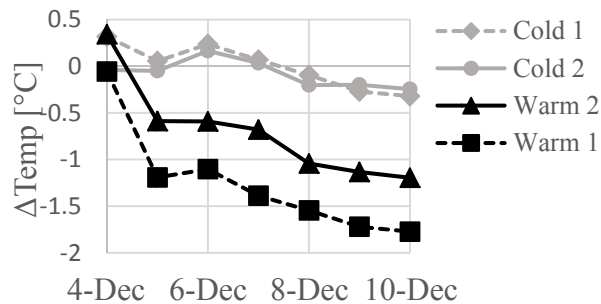


FIG. 6: The difference in levelogger and statically calibrated DTS temperatures. Note the clear instrument drift over a 7 day period.

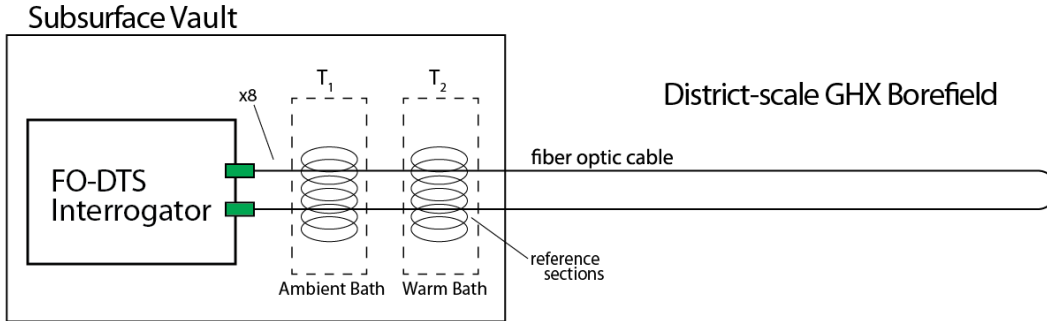


FIG. 7: Double ended, dynamic, remotely accessible, and centralized calibration design at a district-scale bore field.

designed for the double-ended and dynamic calibration. Two insulated chest coolers filled with 0.05 m³ of deionized water and 10 m of reference cable from each side of each loop serve as the dynamic calibration baths (Fig. 7). Literature suggests reference sections at least ten times greater than spatial resolution (1 m at this installation) to provide assurance that the true bath temperature is reached and recorded (Selker et al. 2006a). The first of the calibration baths lacks heating or cooling so that it may settle at the ambient temperature of the underground vault (5 °C to 25 °C, seasonally dependent). The second calibration bath was equipped with an electric-resistance heating and recirculation unit with an adjustable set point to control the temperature of the bath. One platinum thermistor is placed in each bath among the calibration coils to record true bath temperatures and transmit that data back into the interrogator unit. Each loop of fiber is prepared with a ten meter coil in each bath before the fiber run leaves the vault, and an analogous coil in each bath upon returning from the borefield creating useful redundancy in calibration calculations.

Dynamic calibration is achieved by continuously running a script on a server that has access to the interrogator’s data storage. As each subsequent file with the calibration bath temperature and light intensity data is created by the interrogator, the script calibrates for that instance and exports the calibrated temperature data in real time. The script uses light intensity data points taken from within the calibration baths and true temperatures from the thermistors as inputs to solve for calibration parameters of Eq. 1. With C and γ for

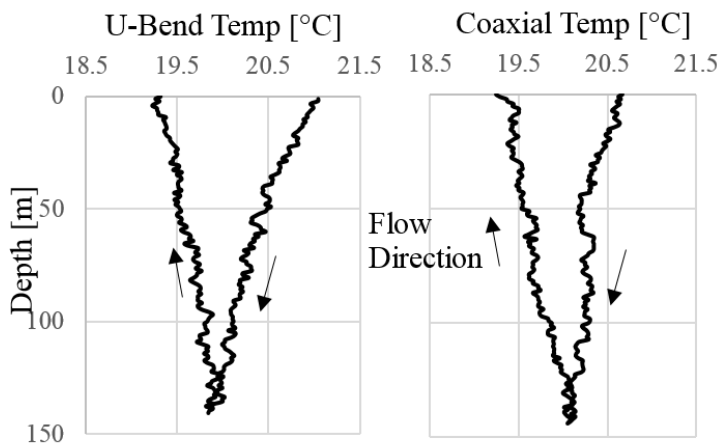


FIG. 8: Temperature profiles inside of the U-bend (left) and coaxial (right) GHX provided by the default DTS interrogator calibration.

that instance of data along that specific fiber loop and $\Delta\alpha$ for each data point along that fiber, the remainder of the data on that cable is calibrated to true temperatures. This process repeats itself indefinitely for each output file the interrogator produces representing one temperature profile along one fiber-optic loop. Initial down-well fiber-optic temperature data from the two GHX configurations is collected and used as a check of calibration accuracy (Fig. 8). Independent of the fiber optic data, in-pipe thermocouples provide inlet and outlet temperatures for both the coaxial and the U-Bend GHX.

The calibration method will be conducted as described utilizing the calibration baths in the vault. However, the entering and exiting water temperatures provide additional reference temperatures near the midpoints of the loops with which to ensure accuracy of the calibration. The temperature profiles shown in Fig. 8 are provided by the default calibration, and provide inlet and outlet temperatures 1 °C to 3°C higher than the in-pipe thermocouples. The same comparison with dynamically calibrated data will ensure a useful check for post-calibration spatially and temporally accurate temperature profiles.

CONCLUSIONS

In place of the default calibration, a double-ended and dynamic calibration with centralized and remotely accessible data collection and processing was developed. The double-ended configuration was chosen over single-ended in response to the installation of a district-scale fiber-optic network that required as many as nine fusion splices and seven different sections of cable in a single loop. The complexity of the fiber-optic network meant that differential attenuation of light was a primary concern, and had experimentally shown inaccuracies in the data. A double-ended configuration is the best remedy for this concern. Dynamic calibration was chosen to correct for the time-variable nature of the outdoor installation and clear instrument drift observed over a single week from a static calibration. An added advantage of combining dynamic and double-ended calibration was the need for only two independent calibration baths. Dynamic calibration requires baths of uniform, relatively constant, and unique temperatures over the entire period of data collection. The logistics of maintaining two such baths rather than three simplify the necessary preparations for calibration.

ACKNOWLEDGEMENTS

This research was funded in part by NSF grants EEC-1156674 and CMMI-1317315.

REFERENCES

- Acuna, J., and Palm, B. (2010). "A novel coaxial borehole heat exchanger: description and first distributed thermal response test measurements." *Proceedings of the World Geothermal Congress, 2010*.
- Bahr, J., Hart, D., and Leaf, A. (2011). "Distributed temperature sensing (DTS) as a hydrostratigraphic characterisation tool." *Completion Report to the Wisconsin Department of Natural Resources*.

- Bao, X., and Chen, L. (2012). "Recent process in distributed fiber optic sensors." *Sensors*, 12 (2012). Elsevier, Amsterdam, NL: 8601-8639.
- Florides, G., and Kalogirou, S. (2007). "Ground heat exchangers – a review of systems, models, and applications" *Renewable Energy*, 32 (2007). Elsevier, Amsterdam, NL: 2461-2478.
- Fujii, H., Okubo, H., Nishi, K., Itoi, R., Ohyama, K., and Shibata, K. (2009) "An improved thermal response test for U-tube ground heat exchanger based on optical fiber thermometers." *Geothermics*, 38 (2009). Elsevier, Amsterdam, NL: 399-406.
- Hartog, A. (1983). "A distributed temperature sensor based on liquid-core optical fibers." *Journal of Lightwave Technology*, 1 (3): 498-509.
- Hausner, M. (2010). "Estimating in situ integrated soil moisture content using fiber-optic distributed temperature sensing (DTS) measurements in the field." Master's thesis, Dept. of Hydrologic Sciences, University of Nevada, Reno.
- Hausner, M., Suárez, F., Glander, K., van de Giesen, N., Selker, J., and Tyler, S. (2011). "Calibrating single-ended fiber-optic raman spectra distributed temperature sensing data." *Sensors*, 2011 (11), Elsevier, Amsterdam, NL: 10859-10879.
- Henniges, J., Zimmermann, G., Buttner, G., Schrotter, J., Erbas, K., and Huenges, E. (2003). "Fiber-optic temperature measurements in boreholes." Presented at the 7th FKPE-Workshop: "Bohrlochgeophysik und Gesteinsphysik". GeoZentrum Hannover, Germany.
- Kara, Y.A. (2007). "Experimental performance evaluation of a closed-loop vertical ground source heat pump in the heating mode using energy analysis method." *Int. J. Energy Res.*, 2007 (31), John Wiley & Sons, Ltd., Hoboken, N.J.: 1504-1516.
- Kersey, A. (2000). "Optical Fiber Sensors for Permanent Downwell Monitoring Applications in the Oil and Gas Industry." *IEICE Trans. Electron.*, Vol. E83-C (3).
- Knudson, R. (2013). "Energy monitoring and verification of ground-coupled heat pumps: utilizing live building control data for the wisconsin institutes for discovery." Master's thesis, Dept. of Mechanical Engineering, University of Wisconsin-Madison.
- Luo, J., Rohn, J., Bayer, M., Priess, A., Wilkman, L., and Xiang, W. (2015). "Heating and cooling performance analysis of a ground source heat pump system in southern germany." *Geothermics*, 53 (2015). Elsevier, Amsterdam, NL: 57-66.
- Magraner, T., Montero, À., Quilis, S., Urchuequia, J.F. (2010). "Comparison between design and actual energy performance of a HVAC-ground coupled heat pump system in cooling and heating operation." *Energy and Buildings*, 42 (2010). Elsevier, Amsterdam, NL: 1394-1401.
- Nagano, K., Katsura, T., Takeda, S. (2006). "Development of a design and performance prediction tool for the ground source heat pump system." *Applied Thermal Engineering*, 26 (2006). Elsevier, Amsterdam, NL: 1578-1592.
- Özdoğan-Dölçek, A. (2015). "Numerical modeling of heat transport for ground-coupled heat pump (GCHP) systems and associated life cycle assessments." PhD. Dissertation, Dept. of Civil and Environmental Engineering, University of Wisconsin-Madison.

- Puttagunta, S., Aldrich, R.A., Owens, D., Mantha, P., (2010). "Residential ground-source heat pumps: in-field system performance and energy modeling." *GRC Transactions*, 34 (2010). Steven Winter Associates, Inc., Norwalk, CT: 941-948.
- Read, T., Bour, O., Selker, J.S., Bense, V.F., Le Borgne, T., Hochreutener, R., Lavenant, N. (2014). "Active-distributed temperature sensing to continuously quantify vertical flow in boreholes." *Water Resour. Res.*, 50 (2014). AGU Publications: 3706-3713.
- Selker, J., Thévenaz, L., Huwalk, H., Mallet, A., Luxemburg, W., van de Giesen, N., Stejskal, M., Zeman, J., Westhoff, M., and Parlange, M.B. (2006a). "Distributed fiber-optic temperature sensing for hydrologic systems." *Water Resour. Res.*, 42 (2006) W12202.
- Selker, J., van de Giesen, N., Westhoff, M., Luxemburg, W., and Parlange, M.B. (2006b). "Fiber optics opens window on stream dynamics." *Geophys. Res. Lett.*, 33, L24401.
- Smith, E., Dent, G. (2005). "Modern raman spectroscopy, a practical approach. Chapter three: the theory of raman spectroscopy." John Wiley & Sons, Ltd., Hoboken, N.J.
- Solinst Levellogger Series. Model 3001 Data Sheet. Levellogger Gold. <<http://www.solinst.com/products/data/3001gold.pdf>> Accessed January 19, 2016.
- Suárez, F., Hausner, M. B., Dozier, J., Selker, J., Tyler, S. (2011). "Heat transfer in the environment: development and use of fiber-optic distributed temperature sensing." *Developments in Heat Transfer*, 31 (2011): 611-636.
- Tyler, S.W., Holland, D.M., Zagorodnov, V., Stern, A.A., Sladek, C., Kobs, S., White, S., Suárez, F., Bryenton, J., (2013). "Using distributed temperature sensors to monitor an antarctic ice shelf and sub-ice-shelf cavity." *J. of Glaciology*, 59 (215): 583-591.
- Tzaferis, A., Liparakis, D., Santamouris, M., Argiriou, A., (1992). "Analysis of the accuracy and sensitivity of eight models to predict the performance of earth-to-air heat exchangers." *Energy and Buildings*, 18 (1992): 35-43.
- van de Giesen, N., Steele-Dunn, S., Jansen, J., Hoes, O., Hausner, M., Tyler, S., Selker, J. (2012). "Double-ended calibration of fiber-optic raman spectra distributed temperature sensing data." *Sensors*, 12(5), 5471–5485.
- Walker, M., Meyer, L., Tinjum, J., Hart, D., (2015). "Thermal property measurements of stratigraphic units with modeled implications for expected performance of vertical ground source heat pumps." *Geotech. Geol. Eng.*, 33 (2015): 223-238.

Electro-Osmosis and Heating in HVDC Grounding Systems

Maria Claudia Barbosa¹; Antonio C. S. Lima²; Iara F. Rezende³; and Joaquim S. Lima Neto⁴

¹D.Sc., Associate Professor, Program of Civil Engineering, Federal Univ. of Rio de Janeiro, COPPE/UFRJ, Rio de Janeiro, RJ, Brazil. E-mail: mclaudia@coc.ufrj.br

²D.Sc., Associate Professor, Program of Electrical Engineering, Federal Univ. of Rio de Janeiro, COPPE/UFRJ, Rio de Janeiro, RJ, Brazil. E-mail: acsl@dee.ufrj.br

³M.Sc., Civil Engineer, Program of Civil Engineering, Federal Univ. of Rio de Janeiro, COPPE/UFRJ, Rio de Janeiro, RJ, Brazil. E-mail: iaferreiraderezende@gmail.com

⁴P.E., Electrical Engineer, Graduate Student, Program of Electrical Engineering, Federal Univ. of Rio de Janeiro, COPPE/UFRJ, Rio de Janeiro, RJ, Brazil. E-mail: netowaters@hotmail.com

Abstract: This work aims to contribute to an accurate theoretical model for the risk assessment of soil drying in the vicinity of ground electrodes of an HVDC (high voltage direct current) system due to electro-osmosis flow and temperature rising. Electro-osmosis might occur due to the interaction of the electric field with surrounding media, i.e., ground due to the high current injection. There may be cases where this current injection might reach 10 kA, which may cause soil drying. This also leads to an increase in the soil temperature that can lead to the loss of the whole grounding system. One key aspect is the area under the influence of these two phenomena, namely, electro-osmosis flow and temperature rising. There were some simplified hypothesis adopted such as neglected the electro-osmosis consolidation and the groundwater flow. These were assumed to be negligible when compared with the effects associated to the electrical field. The combined models consider the overall process for each electrode installed below the water table. The results indicate the relative importance of both phenomena for a dryness risk assessment using hydraulic, electrical and electrokinetic parameters for a given soil with estimated thermal data.

INTRODUCTION

The bulk power transmission may occur in AC or DC. For the latter, the HVDC (high voltage direct current) system is a possible solution for power transmission over long distances or to connect systems with distinct operating frequencies. An HVDC is typically comprised of two converters stations, namely a rectifier station connected to the energy production source and an inverter one at the energy distribution end, and a bipolar transmission line between them, as represented on Figure 1. During maintenance or in case of outages, a single-pole operation might occur which leads to a direct involvement with the ground return. It is a system used to connect system between Canada and the US, the north to the south islands of Japan. More recently, countries such as those in the so-called BRICS (Brazil, Russia, India, China and

South Africa) are facing challenges for power transmission that may be over 2000 km. Needless to say, for such systems reliability is a premium and an adequate design is of the outmost importance. Therefore, a detailed knowledge of the system characteristics and behavior is very important.

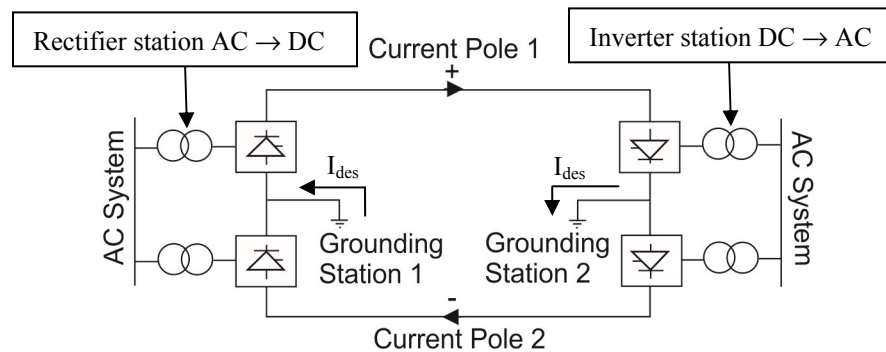


FIG. 1. Schematic bipolar HVDC transmission line (I_{des} is the disequilibrium current).

At normal operation conditions, the current injected through the grounding systems (disequilibrium current) is around 1 to 3% of the current in the corresponding pole. At outages events, such as the loss of one pole, high currents can be injected into the soil, which can reach thousands of Ampères. In such events that can last for hours or even days, there is a risk of drying out the soil around the electrodes and, consequently, of losing the whole grounding system.

The soil can dry out for a combination of processes, and the most relevant is the heating generated by Joule effect of the electric current injected into the soil mass. For the magnitude of the electric currents involved, the high temperatures developed may vaporize the soil water in the vicinity of the grounding electrodes. It is therefore crucial for the project of HVDC grounding systems to predict the temperature increase distribution within the soil mass related to the electric field caused in such events. The grounding system is designed to distribute the total current among a number of electrodes, in order to decrease the magnitude of the individual currents injected and, therefore, the corresponding heating and dryness effect in the soil. A typical arrangement is represented on Figure 2, where the HVDC electrode consists of a toroidal configuration of individual cylindrical vertical electrodes installed below the water table for additional protection.

Greiss et al (1990) present the numerical modeling of the heating problem for a toroidal electrode installed 3 m below surface, for homogeneous and heterogeneous soil profiles. They used a 3D coordinate system and finite difference method to solve the mathematical problem, not taking into account the water level directly neither representing the water and vapor fluxes related to the temperature increase. Mitani and Takahashi (2000) present a theoretical analysis of the electric potential and temperature distributions around a single cylindrical electrode vertically positioned. They considered a stratified soil profile and different depths of burial. As in Greiss et al (1990), the water table position was not considered explicitly, neither the water and vapor fluxes. In both cases the water table could be represented as a frontier between two soil layers, the unsaturated upper layer and the saturated soil layer, with corresponding different electric and thermal properties.

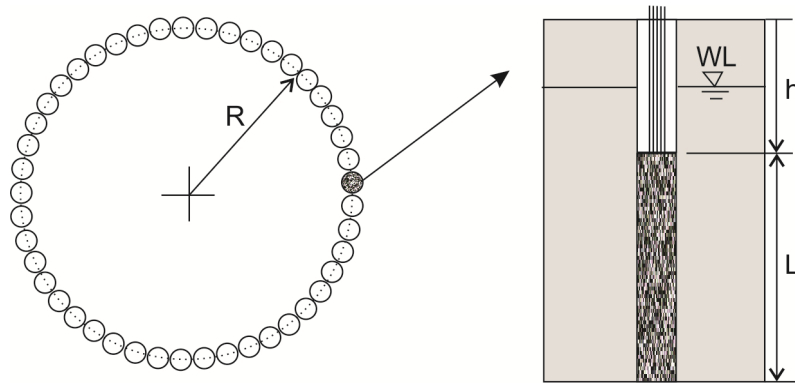


FIG. 2. Scheme of a toroidal HVDC grounding electrode (WL – water level; R – radius of the grounding system; L – length of the electrodes; h – depth of burial of the electrodes).

The other processes involved are the water and vapor flows related to the soil heating, the changes imposed to the soils hydraulic, electric and thermal properties upon drying, and electroosmosis. Villas and Portela (2003) addressed these phenomena in a 3D numerical model of the problem, considering a toroidal electrode close to the surface (1 m below surface), for homogeneous and stratified soil profiles. The variation of each soil layer properties was considered in an iterative processing scheme, based on empirical correlations obtained in the literature at the time. As in the aforementioned models, the water level influence was not considered explicitly.

The present paper discusses the relative influence of electroosmosis and heating effects in the overall process, for a single cylindrical electrode vertically buried below the water table. This condition was established to represent the practical design assumptions and criteria, which are based on a single electrode behavior and the surrounding soils properties. With the maximum permissible value of current density for each individual electrode, engineers define the number of electrodes necessary for distribution of the total expected electric current to be injected. In the present work, an uncoupled analysis is realized, separating the analytical modeling of potential and temperature distribution and the corresponding electroosmosis flow around the electrode, of the numerical simulation of the water and vapor flows and the corresponding changes in soil properties related to a fixed temperature source at the same position of the electrode.

METHODOLOGY

The analysis was performed for a set of usual data and parameters adopted in the practical design of HVDC grounding systems. The mathematical modeling was realized using Mathematica 10.0 software, and the numerical simulations were performed with Hydrus2D/3D software. The results are compared and discussed.

Electroosmosis and temperature distribution analysis

Conceptual model

Figure 3 presents the geometry of the model for a single electrode with diameter d , length L and buried below the water table at depth h . The cylindrical coordinate system adopted (r, θ, z) has the origin at the soil surface and the electrode vertical axis (Fig. 3b). The analysis was realized for a homogeneous soil profile with horizontal surface and axisymmetric condition.

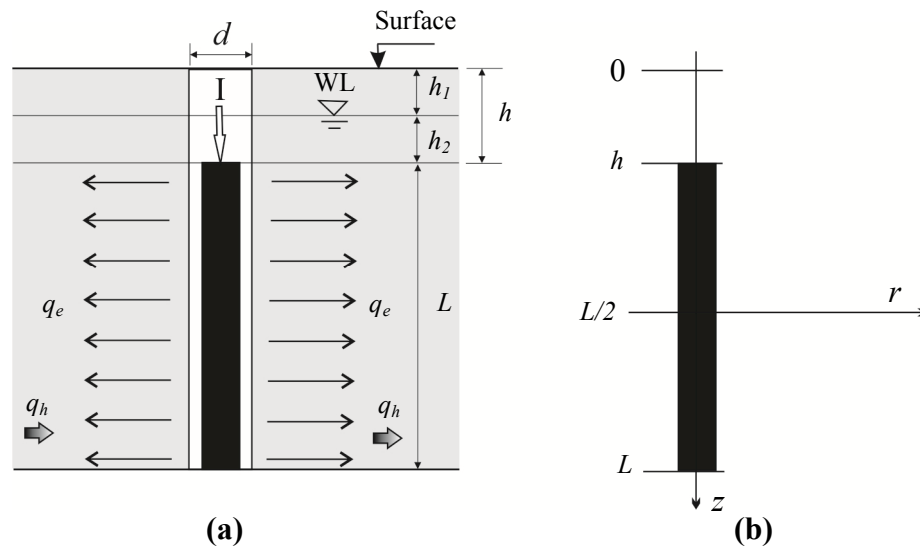


FIG. 3. Geometry of the single electrode model and coordinate system.

Simplifying assumptions:

1. Soil homogeneous and isotropic
2. Horizontal surface
3. Soil incompressible
4. Electrode inside the aquifer only
5. Steady state electric field
6. Electrode works as anode in electroosmosis
7. The natural thermal gradients are negligible as compared to the thermal effects of the electric field induced
8. Groundwater flow velocity is too small as compared to the electroosmosis flow ($q_h \ll q_e \Rightarrow q_h \cong 0$)
9. The soil beneath the electrode is kept saturated over time
10. The soil hydraulic, electric and thermal properties are constant

Some of the assumptions correspond to the normal operation conditions (4, 5, 6), while others were adopted to simplify the mathematical formulation at this point and will be reviewed in the future (particularly 1, 7, 8 and 10). The assumption of an incompressible medium can be a limitation, but this particular hypothesis may be acceptable if the electrode is installed in rigid layers of the aquifer at greater depths.

The assumption of permanent saturated condition beneath the electrode is also reasonable because the surrounding water mass of the aquifer will probably be able to compensate the water loss in that region. The same is not true for the soil layers above the electrode, closer to the vadose zone and to the atmosphere.

Mathematical formulation

The electric potential distribution was calculated by Mitani and Takahashi (2000) equation in cylindrical coordinates as in Fig. 3b:

$$V(r,z) = \frac{\rho I}{4\pi L} \left(\ln \left[\frac{L+h-z+\sqrt{r^2+(L+h-z)^2}}{h-z+\sqrt{r^2+(h-z)^2}} \right] + \ln \left[\frac{L+h+z+\sqrt{r^2+(L+h+z)^2}}{h+z+\sqrt{r^2+(h+z)^2}} \right] \right) \quad (1)$$

In eq. (1) the parameter I is the current injected (Ampères), and ρ is the surrounding soil electric resistivity (Ωm). Because of the axisymmetric condition the potential V (Volts) is independent of the coordinate θ ($\partial V / \partial \theta = 0$).

Equation (2) represents the electric field E (V/m) obtained as the vector summation of the electric potential partial derivatives in r and z , and eq. (3) the calculation of the corresponding current density J (A/m^2).

$$E_{(r,z)} = \sqrt{\left(\frac{-\partial V_{(r,z)}}{\partial r} \right)^2 + \left(\frac{-\partial V_{(r,z)}}{\partial z} \right)^2} \quad (2)$$

$$J_{(r,z)} = \frac{E_{(r,z)}}{\rho} \quad (3)$$

The electroosmotic flow is the net water mass flow ($\text{kg}/\text{m}^2.\text{s}$) through the soil under an electric field (V/m), related to water molecules dragged by the hydrated moving ions. Because soil particles surfaces are generally charged, there is no equilibrium and a net flux is produced. It is calculated by equation (4), where $\rho_w = 1000 \text{ kg}/\text{m}^3$ is the water density and k_e ($\text{m}^2/\text{V}.\text{s}$) is the electroosmotic permeability of the soil.

$$q_e(r,z) = \rho_w k_e \frac{\partial V(r,z)}{\partial r} \quad (4)$$

The temperature increase distribution because of the Joule effect is calculated by eq. (5), where k_t is the soil thermal conductivity ($\text{W}/^\circ\text{C}.\text{m}^2$) and α the soil thermal diffusivity (m^2/s). This temperature increase is time dependent, even if assumed constant soil properties.

$$\nabla^2 T_{(t,r,z)} + \frac{\rho J_{(r,z)}^2}{k_t} = \frac{1}{\alpha} \left(\frac{\partial T_{(t,r,z)}}{\partial t} \right) \quad (5)$$

The model domain was 100m vertical x 200m radial: $r_o \leq r \leq r_f$ where $r_o = -100$ m and $r_f = 100$ m; and $z_o \leq z \leq z_f$ where $z_o = 0$ m and $z_f = 100$ m.

Operational conditions adopted were: water table 1.0 m below surface; an electrode 3 m long (L); diameter $d = 0.05$ m; buried at 1.0 m below the water table; and an injected current of 30 A.

Boundary conditions assumed:

- Electric current uniform and constant along the electrode:
 $I = \text{constant}$ for $L \rightarrow 2 \leq z \leq 5$ m and $-0,025 \leq r \leq 0,025$ m
- Heat exchange between soil and atmosphere at the surface as in eq. (6):

$$\frac{\partial T_{(t,r,z_o)}}{\partial z} = \frac{h_c}{k_t} (T_{(t,r,z_o)} - T_{ar}) \quad \text{for } z = z_o, \forall r \text{ and } \forall t \quad (6)$$

Where h_c is the air convection coefficient, assumed as $1 \text{ W/}^\circ\text{C.m}^2$

- Null electric potential far away from the electrode:
 $V(r,z) = 0$ for $r = r_o$ and $r = r_f, \forall z$ and $\forall t$
- Constant temperatures at long distances from the electrode in both directions r and z :
 $T = T_o$ for $z = z_f, \forall r$ and $\forall t$
 $T = T_o$ for $r = r_o$ and $r = r_f, \forall z$ and $\forall t$

The initial condition was $T = 20^\circ\text{C}$ in soil and atmosphere, uniform. The soil parameters were a combination of physical, electric and electroosmotic parameters measured in a natural soil of one HVDC project in Brazil (Barbosa et al, 2012), and thermal parameters as in Villas and Portela (2003).

Analysis of the effects of a heat source at the electrode position

The HVDC grounding systems are usually designed for a maximum current density of 1 A/m^2 to achieve a maximum temperature in the electrodes in the range $75^\circ - 95^\circ\text{C}$. Since the modeling of the coupled phenomena is very complex, it was decided to first investigate the magnitude of soil drying effects of the heat source represented by the electrode, considering the average temperature adopted as design criteria (80°C). To perform this analysis it was employed the program Hydrus2D/3D (Simunek et al, 2012), developed for water, heat and solute fluxes in saturated and unsaturated soils. This code presents some limitations to the analysis intended, but is very powerful in the representation of the hydraulic flows in soils at both saturated and unsaturated conditions. A great advantage is that it allows modeling the variation in soil hydraulic and thermal properties with changes in the degree of saturation. The limitations are related to the representation of the heat source, since the code does not include the process of heating by Joule effect (and the soil electric properties). It was thus necessary to adopt a fixed steady state temperature source of planar geometry (a 2D plan configuration instead of a 3D axisymmetric source). Another limitation is

that it is not possible to enter the soil thermal properties as input data. The code calculates the necessary thermal properties based on soil composition (percentages of minerals, organic matter, water and air).

Conceptual model

The configuration was similar to the model represented in Fig. 3, but with a more restricted domain of 7 m in the vertical direction and 4 m in horizontal direction with the origin at the electrode vertical axis (half space). Besides, the code works with elevation z instead of depth. The limits were therefore: $0 \leq z \leq 7$ m from bottom to the surface, and $0 \leq x \leq 4$ m from the electrode vertical axis to the external boundary. The water level was represented at elevation $z = 6$ m. The geometry was the same as in Fig. 3a, with a different coordinate system.

The electrode was represented as a vertical plate at 80°C in the same position, that is, between $2 \leq z \leq 5$ m ($L = 3$ m), and the soil mass and atmosphere at 20°C as initial condition.

The soil was represented as “silty clay” in the program library but using the same physical characteristics as the reference natural soil (dry density, porosity and saturated hydraulic conductivity). The program library assumed a corresponding set of soil water retention curve and hydraulic conductivity function for variable degree of saturation, and the thermal properties. The adopted boundary conditions are summarized in Table 1.

Table 1. Boundary conditions in the Hydrus2D/3D simulations

Boundary	Water Flow	Heat Flow
Surface: ($z = 7$ m, $\forall x$)	Atmospheric condition	Third type condition
Bottom: ($z = 0$, $\forall x$)	No flux	No flux
Vertical external border: ($x = 4$ m, $\forall z$)	No flux	No flux
Electrode: ($x = 0$ and 2 m $\leq z \leq 5$ m)	Constant head ($h = h_o$)	Constant temperature (80°C)
Vertical border above: ($x = 0$ and 5 m $< z < 7$ m)	No flux	No flux
Vertical border below: ($x = 0$ and $0 < z < 2$ m)	No flux	No flux

Mathematical modeling in Hydrus

The Hydrus2D/3D code uses Richards equation for the water flux in variably saturated porous media, and heat transport by conduction and convection with the moving water. The code has a library with a set of theoretical models to represent the soil water retention behavior (volumetric water content versus matric suction) and hydraulic conductivity function (k_h versus matric suction). The user can select a theoretical model and enter experimental data, or select a type of soil in the code

library, and the code adjusts an existing function from its dataset. For the equations and functions available, see Simunek et al (2012).

RESULTS AND DISCUSSION

Soil properties

Table 2 summarizes the parameters adopted for the analytical modeling. The thermal parameters were assumed based on Villas and Portela (2003), because there was no data measured for the soil of interest. But the remaining physical properties were measured in the laboratory on a natural undisturbed soil sample (Barbosa et al, 2012).

Table 2. Soil properties used in the analytical model

n	γ_d (kN/m³)	k_h (m/s)	k_e (m²/Vs)	ρ (Ωm)	α (m²/s)	k_t (W/°Cm)
0.40	16.0	6.8×10^{-8}	4.12×10^{-9}	100	7.74×10^{-7}	2.6

Electric potential distribution

Figure 4 presents the electric potential distribution around the electrode. Fig. 4a is a 2D representation at small distances from the electrode ($r \leq 1$ m). The electric potential close to the electrode surface is higher than 600 Volts, but has a sharp decrease with distance. This pattern becomes more evident in the graph of Fig. 4b that goes up to radial distances of 20 meters from the electrode. Around 5 m the electric potential gets approximately uniform in the surrounding soil mass with values below 80 Volts. At 20 m the potential is slightly above 25 V and independent of vertical position. The soil surface ($z = 0$) becomes electrically charged all along.

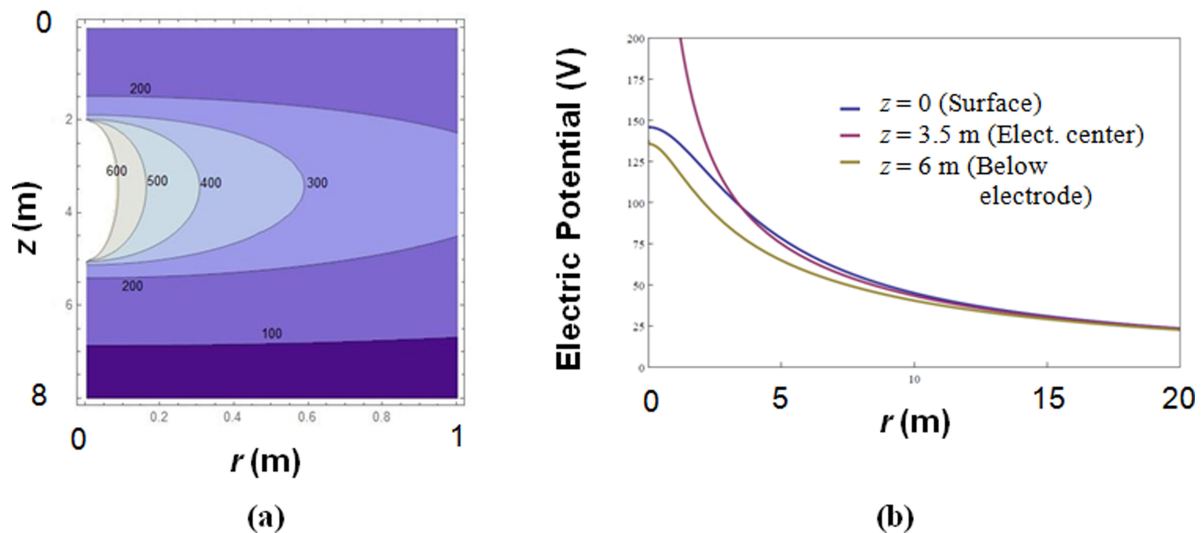


FIG. 4. Electric potential distribution around a single electrode for an injected current of 30 Ampères and soil electric resistivity of 100 Ω m.

Electroosmosis flow

Figure 5 presents the corresponding electroosmotic flow predicted at a certain distance from the electrode in Fig. 5a and at a certain depth in Fig. 5b. Electroosmosis is negligible at depths above and below the electrode, and decreases sharply with electric potential. But since the modeling represents a steady state electric field condition, the soil water is being drained constantly, and if the electrode keeps working for a long time, the risk of drying the soil mass around is real.

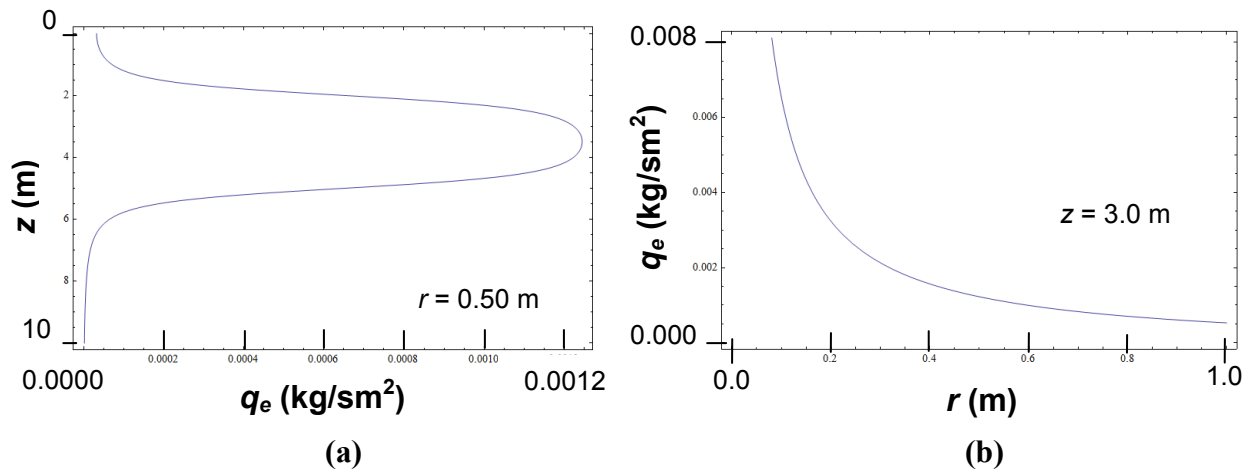


FIG. 5. Electroosmotic flow distribution around a single electrode for an injected current of 30 Ampères and soil electric resistivity of 100 Ωm.

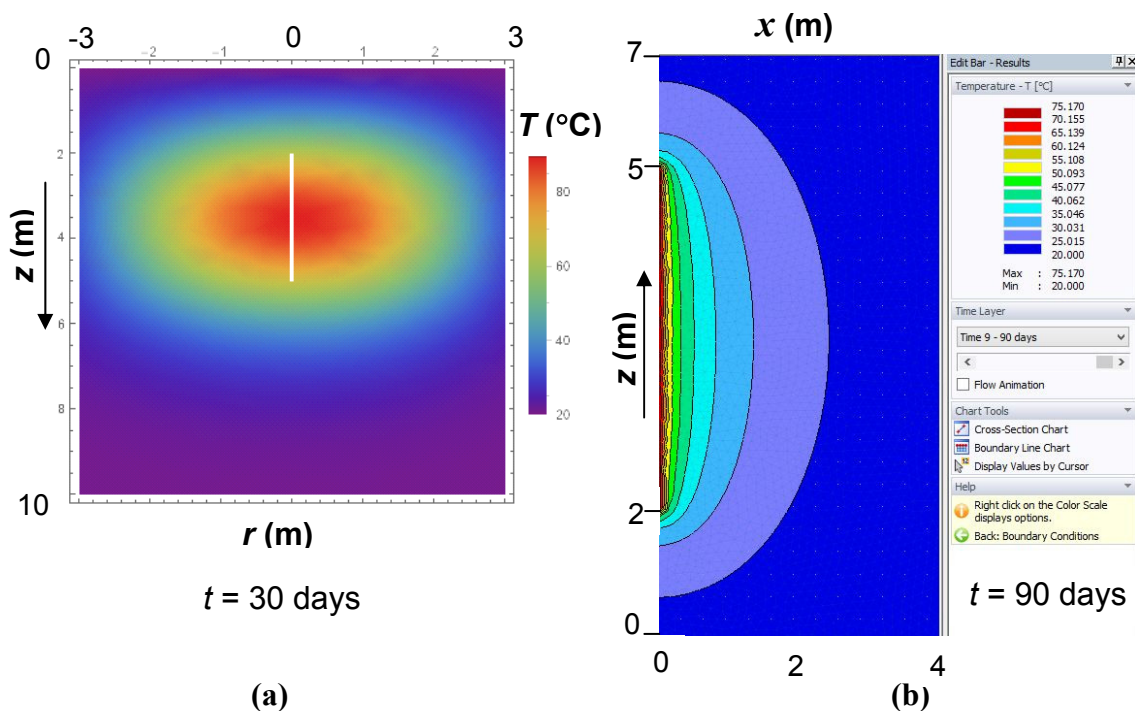


FIG. 6. Temperature distribution around the electrode for: (a) injected current of 30 A and soil electric resistivity of 100 Ωm, (b) constant heat source at 80°C.

Temperature distribution and analysis of possible effects

The temperature distribution after 1 month of operation is represented in Figure 6a for a soil with thermal conductivity of 2.6 W/°Cm. For the conditions tested, temperatures around the central portion of the electrode rise to 80°C for $r \leq 1$ m, in the range acceptable for design. Figure 6b shows the temperature distribution in the soil for a fixed 80°C heat source as predicted by Hydrus2D/3D for 90 days of operation. In such condition, where heat is transmitted by conduction, temperature only rises significantly very close to the heat source, at distances of a few centimeters, even after 90 days. But in the region with temperatures above 50°C, approximately, water flow is observed and soil drying is initiated (Rezende, 2015), although much less significant than electroosmosis for this particular set of soil parameters.

CONCLUSIONS

Theoretical analysis demonstrates that the risk of drying the soil mass around a grounding electrode is real, but the risk is limited to a distance of a few meters from the electrode surface. For a soil electric resistivity of 100Ωm and the operational conditions adopted, electroosmotic flow seems more important than temperature effects up to 1 m from the electrode. More resistive soils can be a challenge.

ACKNOWLEDGMENTS

To the Brazilian agencies CNPq and Capes for the graduate students scholarships.

REFERENCES

- Barbosa, M.C. et al (2012). Determinação dos fatores de filtração e de eletro-osmose de solos para projeto dos eletrodos de aterramento. Final Report. Project PEC15195. COPPETEC Foundation, UFRJ, Rio de Janeiro, 98p.
- Greiss, H., Mukhedkar, D. and Lagace, P.J. (1990). Heat dissipation computations of a HVDC ground electrode using a supercomputer. *IEEE Transactions on Power Delivery* 5 (4): 1802-1810.
- Mitani, M. and Takahashi, T. (2000). Theoretical analysis of grounding resistance for the rod buried into the multi-layered earth. *Proc. Power Eng. Soc. Summer Meeting IEEE*, Vol.1, Seattle: 145-150.
- Rezende, I.F. (2015). Modeling of water flows by thermal gradient and electro-osmosis related to grounding electrodes. *MSc. Dissertation*. Program of Civil Engineering, COPPE-UFRJ, Rio de Janeiro, RJ, Brazil, 160p.
- Simunek, J., van Genuchten, M.Th. and Sejna, M. (2012). The HYDRUS Software Package for Simulating the Two- and Three-Dimensional Movement of Water, Heat, and Multiple Solutes in Variably-Saturated Porous Media. *Technical Manual, Version 2.0*. PC-Progress, Prague, 260p. (digital)
- Villas, J.E.T. and Portela, C.M. (2003). Soil heating around the ground electrode of an HVDC system by interaction of electrical, thermal, and electroosmotic phenomena. *IEEE Transactions on Power Delivery* 18(3): 874-881.

Hydro-Thermo-Mechanical Behavior of Granular Material near a Wellbore

Ingrid Tomac, Ph.D., A.M.ASCE

Assistant Research Scientist, Dept. of Structural Engineering, Univ. of California San Diego, 9500 Gilman Dr., La Jolla, CA 92093-0085. E-mail: itomac@ucsd.edu

Abstract: This paper investigates hydro-thermo-mechanical behavior of weakly-bonded granular sandstone material in the vicinity of the wellbore. The study uses discrete element modeling (DEM) for micro-crack development due to stress changes caused by fluid flow and heat flow and transport. A network of fluid channels and reservoirs is used to discretize fluid flow through a weakly-cemented materials. The heat flow and transport through a DEM model accounts for both conduction and convection. The convective flow of fluid and heat is especially important for infiltration of fluid into newly formed cracks modeled as a transient problem. Parallel plate flow is used on a local scale for modeling flow in channel formed between two DEM particles, while a fluid reservoir is used to locally store fluid over a time-stepping procedure for mass conservation. The conclusions give a better understanding of the transient thermal micro-cracking evolution around the non-cased wellbore under influence of pressurized compressible water, whose temperature is different from the surrounding material, with respect to the geo-material strength and stiffness parameters and temperature difference.

INTRODUCTION

Heat flow and transport in weakly bonded permeable synthetic rock is studied in this paper using the newly implemented thermal conduction-convection coupled Discrete Element Method (DEM) (Tomac and Gutierrez, 2015). Particularly, a close up region of the hot rock around the wellbore in geothermal reservoir is modeled in order to better understand the effects of cold fracturing fluid pressurization on the wellbore wall for geothermal heat exchangers. In spite of the fact that the hydro-thermo-mechanical coupling effects in rock were investigated by many researchers, the full understanding of dynamics of pressure and temperature influence of cold water injection in the near wellbore area of porous rock has not yet been achieved. Some examples of published numerical work include, but are not limited to, the use of the finite element method (FEM), integral methods, boundary element methods, hybrid continuum methods combined with fluid flow solved over discrete fractures, and discrete element method (DEM) (Bower and Zyvoloski, 1997; Geiger and Emmanuel, 2010; Ghassemi, 2012; Ghassemi et al., 2008; Ghassemi et al., 2005; Kolditz and Clauser, 1998; McDermott et al., 2009; Tomac and Gutierrez, 2014a, b; Wang and Dusseault, 2003). Experimental and field data were used to support modeling efforts (Koh et al., 2011; Rutqvist et al., 2008; Yong and Wang, 1980).

METHODOLOGY

Hydro-thermo-mechanical coupling between DEM particles and fluid is obtained using the DEM heat flow and transport model, which is implemented in PFC2D. The spatial discretization that is unique for DEM method enables simulations of arbitrary oriented single and interconnected fluid channels through the solid. The evolution of fluid paths with time follows the redistribution of thermal and mechanical stress fields. The heat flow and transport model aims for capturing the complete thermal energy migration (without radiation) through fractured and porous solid filled with flowing fluid with initially non-uniform thermal distribution. Local thermal equilibrium between fluid and rock is assumed during the simulation, which is reasonable given the very small element sizes used to discretize the geometries. Buoyancy is neglected in this simulation because the model represents a horizontal cross-section across the wellbore in two dimensions. Heat conduction for a continuum follows Fourier's law that describes the relation between the heat-flux vector q_i and the temperature gradient as:

$$q_i = -k_{i,j} \frac{\partial T}{\partial x_j} \quad (1)$$

where $k_{i,j}$ is the thermal conductivity tensor [W/m°C]. The transient heat conduction equation for a continuum assuming that strain changes play a negligible role in influencing the temperature:

$$-\frac{\partial q_i}{\partial x_i} + q_v = \rho C_v \frac{\partial T}{\partial t} \quad (2)$$

where $\partial q_i / \partial x_i$ represents the heat-flux gradient, q_v is the volumetric heat source/sink intensity or power density [W/m²], ρ is the mass density, C_v is the specific heat at constant volume [J/kg°C], T is the temperature [°C] and t is time. Fig. 1 shows the thermal DEM discretization with a network of "heat reservoirs" at center of particles mass interconnected with "thermal pipes" passing via contacts between particles. Heat flow occurs via conduction in the active thermal pipes which connect the heat reservoirs. The thermal pipe activation criteria is user-prescribed and checked at the beginning of each time-step, usually being an active contact or bond between DEM particles at the previous time-step.

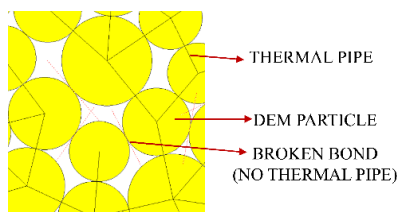


FIG. 1. System of thermal pipes for conductive heat flow in Bonded Particle Model (BPM)

Parameters for the conductive heat flow equation related to each thermal reservoir are the temperature T , mass m , the volume V , the specific heat at the constant volume C_v , and the coefficient of linear thermal expansion, α_t . Associated with each thermal pipe

are the heat energy Q and the thermal resistance η . Details of the implementation, numerical stability and convergence of the conductive heat flow and transport in PFC2D can be found in the PFC2D Manual (Itasca, 2004) and therefore will not be repeated here. The stress tensor of the DEM assembly spatially evolves during the time stepping procedure. Stress changes consist of mechanical and thermal components. The thermal stress component is a consequence of temperature-induced strains in DEM, which arise due to thermal volumetric deformation of particles and contact bonds. The temperature-induced particle radius change is:

$$\Delta R = \alpha R \Delta T \quad (3)$$

where R is the particle radius, α is the particle coefficient of linear thermal expansion and ΔT is the temperature change. If parallel bond is present at the particle contact associated with a pipe, then the thermal volumetric deformation of the bond material is accounted for by assuming that only the normal component of the force vector carried by the bond will be affected by the temperature change. The bond length changes with the normal component of the bond force vector:

$$\Delta F^n = \bar{k}^n A \Delta U^n = \bar{k}^n A (\bar{\alpha} L \Delta T) \quad (4)$$

where \bar{k}^n is the bond normal stiffness, A is the area of the bond cross section, $\bar{\alpha}$ is the expansion coefficient of the bond material, and ΔT is the temperature increment (equal to the average temperature change of the two particles at the ends of the pipe associated with the bond). Fluid flows through a system of interconnected channels of coherent particle assembly with a strong pressure gradients, where the fluid and the heat convective flow are implemented in PFC2D using PFC's built-in FISH programming language. The fluid flow scheme has a limitation to model only the solid or quasi-solid materials where particles do not significantly spatially rearrange during the calculation. Fluid reservoirs are introduced for transient fluid flow modeling and the conservation of mass. The aperture of a fluid channel is proportional to the normal displacement at corresponding contact, and the fluid reservoir volumes that are related to the sizes of surrounding channels. Pressures are stored in fluid reservoirs and are updated during the fluid calculation, and act on the surrounding particles as equivalent body forces. The micro-permeability of the DEM specimen is obtained by performing tests which ensure that the sample matches the required permeability of the realistic material. In the numerical sense, the fluid flow through a network of channels and reservoirs is superimposed to the DEM particle assembly finite difference scheme. The fluid flow rate, q , in a fluid channel is calculated using the parallel plate flow solution of Navier-Stokes equation for incompressible Newtonian fluid and laminar flow:

$$q = \frac{d^3 \Delta P}{12 \mu L} \quad (5)$$

where d is the channel aperture, ΔP is the pressure difference of the reservoirs at two ends of the channel, μ is dynamic fluid viscosity and L is the fluid channel length. It is assumed that each contact has residual initial fluid channel aperture, d_0 , when the normal contact force is at its prescribed residual value. The increase in normal load decreases the apparent fluid channel aperture in the case of compressive normal contact force:

$$d = \frac{d_0 F_0}{F + F_0} \quad (6)$$

where F is the value of normal contact force and F_0 is its residual value at d_0 . For the case of tensile normal contact force:

$$d = d_0 + wa \quad (7)$$

where w is arbitrary chosen dimensionless multiplier which can be set different from unity for calibration purposes, and a is the physical distance between two particle contacts. The increase in fluid pressure in a fluid reservoir is:

$$\Delta P = \frac{K_f}{V_d} (\Sigma q \Delta t - \Delta V_d) \quad (8)$$

where K_f is the fluid bulk modulus, V_d is the apparent volume of the fluid, q is the fluid flow rate and Δt is the time step. Finally, it is assumed that the fluid flow through a fluid channel is localized at the corresponding contact, and the pressure region of the fluid reservoir is uniform, leading to tractions that are independent of the path around the fluid reservoir. For the polygonal path that joins the contacts surrounding the fluid reservoir, the force vector F_i on a particle is:

$$F_i = P n_i s \quad (9)$$

where n_i is the unit normal vector of the line joining the two contact points on the particle and s is the length of the line.

Heat exchange between solid phase and fluid in channels occurs simultaneously with fluid flow driven by pressure gradients in fluid channels which exist between particles. Parallel plate flow solution is introduced in the numerical scheme for fluid and heat flow at fluid channel. Eq. 11 below gives the heat convection approximation for the laminar fluid flow in a channel between two parallel plates. Eq. 11 assumes conductive heat flow from the channel boundary into the fluid and vice versa, while conductive heat flow in the fluid along the channel lengths is neglected (i.e., heat convection is one-dimensional along the lengths of the channels only). The relative significance of convective and conductive transfers can be estimated by checking the value of the Peclet number, Pe :

$$Pe = \frac{\rho_f v C_p L}{\lambda_f} \quad (10)$$

where ρ_f is the fluid density, v is the fluid velocity, C_p is the fluid specific heat at a constant pressure, L is the length of the channel and λ_f is the fluid thermal conductivity. For $Pe > 1$ fluid convection dominates over conduction, and for $Pe \gg 1$ the conduction parallel to the fluid flow can be neglected (Yang et al., 2010). Potential and kinetic energy changes are negligible, and the fluid and particle specific heat capacities do not change. The amount of heat transferred from the host material to the fluid and vice versa over a given time step equals to the amount of heat extracted from the particle at the end of the time step. Because two particles adjacent to the fluid channel change temperature due to both convection and conduction through the granular assembly, a thermal input parameter Q_v associated with the particles represents a new boundary condition for each conductive thermal time-step. Mean fluid velocity and temperature parameters are introduced for the flow between two parallel plates:

$$\frac{\partial}{\partial x} \left[\frac{T_s(x) - T(r, x)}{T_s(x) - T_m(x)} \right]_{fd,t} = 0 \tag{11}$$

where x is the axial channel dimension, $T_s(x)$ is the channel surface temperature at a position x , $T_m(x)$ is the mean fluid temperature at a position x , and $T(r, x)$ is the fluid temperature at a position x and distance r from the center of the channel in y direction perpendicular to x . Fig. 2 shows the mean temperature and surface temperature with advection along the channel of length L .

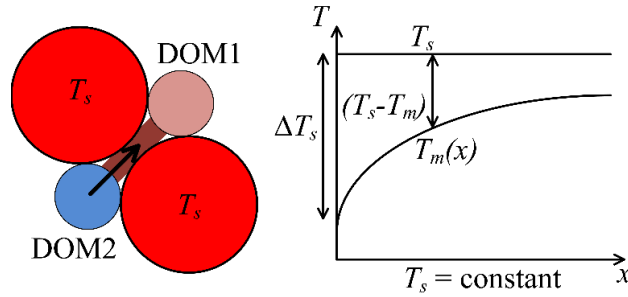


FIG. 2. Advection solution for parallel plate fluid and heat flow implemented in DEM

The expression for the mean temperature variation along the channel for a mean temperature $T_{m,out}$ in the case of constant channel surface T_s temperature, is derived from the energy balance for a control volume:

$$\frac{T_s - T_m(x)}{T_s - T_{m,i}} = \exp\left(-\frac{D_H x}{dm/dt} \bar{h}\right) \tag{12}$$

where T_s is the channel surface temperature, $T_{m,i}$ is the mean fluid temperature at the channel entrance, $T_m(x)$ is the mean channel temperature at a position x , D_H is the channel hydraulic diameter ($D_H=4A/P$ where A is the channel cross-sectional area and P is the wetted perimeter), dm/dt is the fluid mass flow rate through the channel cross-section at position x and \bar{h} is the average channel heat convection coefficient. The fluid mass flow rate is obtained from the pressure difference in the fluid channel. The average heat convection coefficient can be determined using the Nusselt number for a laminar flow for the parallel plate geometry ($Nu_D=hD/k_f=3.66$ for constant T_s) (Nguyen et al., 2012). A special case can occur when there is no local fluid flow through the fluid channel but fluid has different temperature than adjacent particle. The change of average particle i temperature with time is:

$$\frac{T_s - T_m(x)}{T_s - T_{m,i}} = e^{\left(\frac{-dt}{\tau_t}\right)} \tag{13}$$

where T_∞ is the fluid temperature, $T_{i,0}$ is the particle temperature at the beginning of the time step, T_i is the particle temperature at the end of the time step, dt is the time step and τ_t is the thermal time constant:

$$\tau_t = \frac{\rho V c_p}{h A_s} \tag{14}$$

where ρ is the particle density, V is the particle volume, C_p is the particle material (rock) specific heat at a constant pressure, A_s is the surface of the contact and L is the

length of the channel. The value of the thermal time constant is a measure of how fast the temperature of the object reacts to its thermal environment.

Eq. 12 is used to write a FISH function in PFC2D for approximating the fluid temperature at the channel between two particles of each time step. If transient fluid flow is considered, some amount of energy storage will be included at each time t in the control volume of the fluid:

$$\frac{dQ_{st}}{dt} = \frac{d}{dt}(\rho V c_v T) \quad (15)$$

At each fluid domain, a control change in volume is assigned through the fluid flow FISH function. Accordingly, the conservation of energy can be written for a domain. The change in the domain thermal energy storage is equal to the heat flow rate from the adjacent channels minus the thermal energy of the domain at the beginning of the time step:

$$\Delta Q_{dom} = Q_t - Q_{dom} \quad (16)$$

where Q_{dom} is the domain thermal energy, and Q_t is the convective heat transferred from the adjacent fluid channels. The new particle temperature is imposed as a thermal boundary condition on enclosing particles for the next thermal time step:

$$\Delta T = -\frac{dQ_{conv}}{c_{v,p} \rho_p V_p} \quad (17)$$

where ΔT is the particle temperature change, $dQ_{t,conv}$ is the amount of heat transferred from the particle to the fluid in the previous mechanical time step, $c_{v,p}$ is the particle specific heat at constant volume, ρ_p is the particle density, and V_p is the particle volume. An additional consideration is given to the case when fluid is present but there is not flow in a fluid channel during the time-step and fluid has different temperature from the adjacent DEM particles, which is modeled with a lump capacitance method for determining the average particle and stagnant fluid heat.

RESULTS

Convective-conductive heat flow and transport in the vicinity of the wellbore in highly permeable sandstone is analyzed with the DEM. BPM which incorporates the novel coupled rock-fluid convection-conduction formulation is used for investigation of heat exchange between cold fluid and hot surrounding rock. Micro-cracking of the material around the wellbore is observed in addition to the heat flow and transport, in a specimen with and without far-field compressive confinement stresses. The model size is $0.1 \times 0.1 \text{ m}^2$, with the boundary and initial conditions shown in the Table 1. Wellbore is pressurized with the cold fluid at $50 \text{ }^\circ\text{C}$ while the synthetic rock sample boundaries have a constant temperature of $200 \text{ }^\circ\text{C}$. The initial temperature is also $200 \text{ }^\circ\text{C}$. Table 2 shows the micro-mechanical parameters of the synthetic sandstone in DEM, where R_{min} = minimum particle radius; R_{max} = maximum particle radius; fi = particle friction coefficient; P_{b_kn} = parallel bond normal stiffness; P_{b_ks} = parallel bond shear stiffness; P_{b_sstr} = parallel bond shear strength; P_{b_nstr} = parallel bond normal strength; and w_0 = initial fluid channel aperture. Table 3 shows the macro-mechanical parameters of the synthetic sandstone BPM. Macro-mechanical parameters are obtained in DEM by simulating standard rock laboratory tests (Direct Tension Test and Unconfined Compression Test).

Table 1. Boundary conditions of the model

Parameter	Magnitude	Parameter	Magnitude
$\sigma_{min,x}$	14,0 MPa	$T_{ini,rock}$	200 °C
$\sigma_{max,z}$	26,0 MPa	$T_{ini,fluid}$	50 °C

Table 2. Micro-mechanical properties of BPM

Parameter	Value	Parameter	Value
R_{min} (mm)	0.3	$P_{b\ ks}$ (GPa)	4.25
ρ (kg/m ³)	2500	$P_{b\ sstr}$ (MPa)	21.4
R_{max}/R_{min} (-)	1.66	$P_{b\ nstr}$ (MPa)	4.9
f_i (-)	0.5	w_0 (m)	$5 \cdot 10^{-4}$
$P_{b\ kn}$ (GPa)	17.0		

Table 3. Macro-mechanical properties of BPM of synthetic sandstone.

	Tensile Strength	Young's Modulus	Poisson's Ratio	Hydraulic Permeability
Synthetic sandstonePFC2D	σ_t (MPa)	E (GPa)	ν (-)	k (m ²)
	2.2	10.0	0.22	$9.6 \cdot 10^{-4}$

Fig. 3 shows the two snapshots from the time stepping procedure in DEM, after $t=1.4 \cdot 10^{-3}$ s and $t=2.1 \cdot 10^{-3}$ s. Fluid is introduced into wellbore with a constant flow rate, which has a consequence of rising wellbore pressures, P_b . Fluid also infiltrates synthetic sandstone pores, as it can be seen on the second snapshot in Fig. 3.

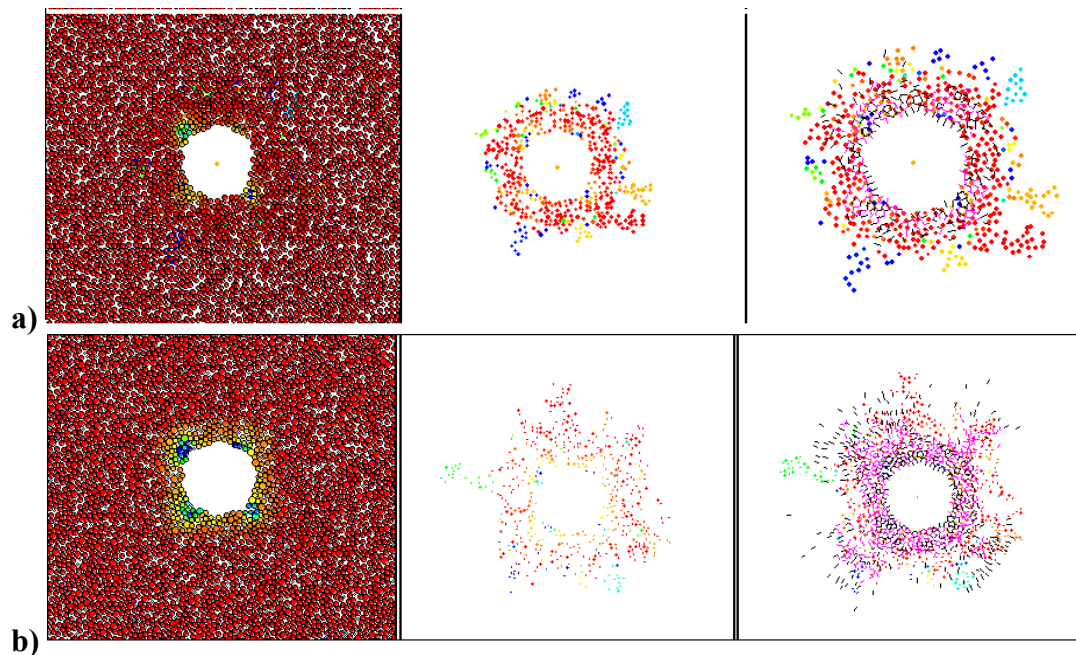


FIG. 3. Unconfined sample and the wellbore, a) $t=1.4 \cdot 10^{-3}$ s; $P_b=0.14$ kN and b) $t=2.1 \cdot 10^{-3}$ s; $P_b=0.23$ kN

Different colors represent fluid and particle temperatures across the spectrum, where red is hot 200 °C and blue is cold 50 °C. Heat flow and transport can be observed as the particles around the wellbore cool down while the fluids heat up. Fluid flow is in a star-like formation from the wellbore, which indicates some preferential fluid paths. The preferential fluid paths are however not exceeding far from the overall thermally altered zone. Third plot in Fig.3 shows tensile and shear parallel bond breakage, which did not exist in the beginning of the simulation. Parallel bond breaks and crack occurs when local stress field exceeds the strength of the bond. Black lines are tensile cracks and magenta lines are shear cracks. Tensile micro cracks are concentrated near the wellbore wall, while shear micro cracks seem to extend further to the synthetic sandstone, and some of the shear micro cracks are grouped along the preferential fluid flow paths. Fig. 4 shows a snapshot from the time stepping procedure in DEM, after $t=1.17 \cdot 10^{-3}$ s in confined sample. Vertical confinement stress is larger than horizontal (Table 1). Fluid is also introduced into wellbore with a constant flow rate, same as for simulation in Fig. 3, which has a consequence of rising wellbore pressures, P_b . Fluid also infiltrates synthetic sandstone pores, as it can be seen on the second snapshot in Fig. 4. Different colors represent fluid and particle temperatures across the spectrum, where red is hot 200 °C and blue is cold 50 °C. Heat flow and transport can be observed as the particles around the wellbore cool down while the fluids heat up. Fluid flow is in a star-like form from the wellbore, similar like in Fig. 3 but more constrained towards minimum confinement stress direction. Third plot in Fig. 4 shows development of tensile (black) and shear (magenta) micro cracks. Here, it is very pronounced that development of micro cracks follows the fluid flow, which is at an angle with minimum confinement stress direction. The predominant direction of micro cracks suggests that the synthetic sandstone does not behave like a quasi-brittle material, and a dominant hydraulic fracture was not observed. In quasi-brittle rocks, hydraulic fracture initiates and propagates from the pressurized wellbore in the direction perpendicular to the minimum confinement stress direction.

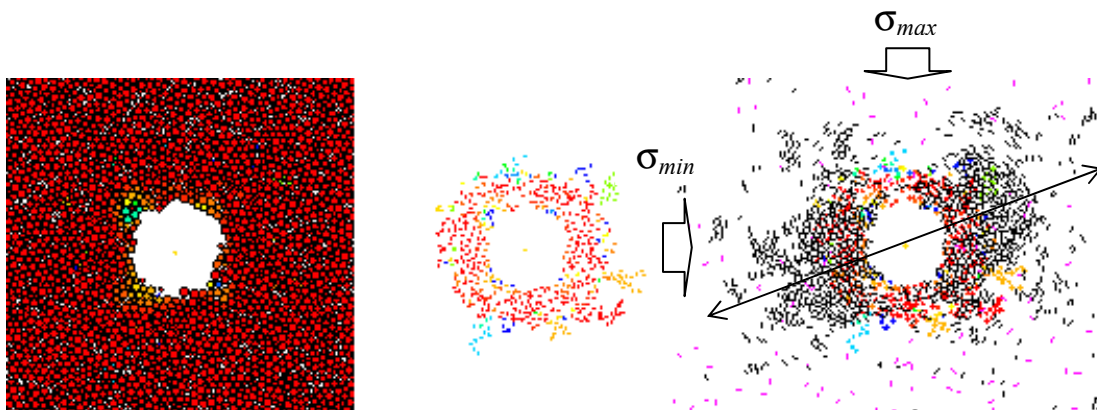


FIG. 4. Confined sample and the wellbore $t=1.17 \cdot 10^{-3}$ s $P_b=0.16$ kN

CONCLUSIONS

Convective-conductive heat flow and transport in the vicinity of a wellbore in highly permeable sandstone was analyzed with the Discrete Element Method using

commercially available Particle Flow Code (PFC) in two dimensions. The Bonded Particle Model (BPM) for modeling solids with bonded DEM particles, also incorporated the novel coupled rock-fluid convection-conduction formulation and it was used for investigation of heat exchange between cold fluid and hot surrounding weakly bonded and highly permeable sandstone. Micro-cracking of the material around the wellbore was observed in addition to the heat flow and transport, in a specimen with and without far-field compressive confinement stresses. A wellbore in the middle of a quadratic specimen was pressurized with the cold fluid at 50 °C while the synthetic rock sample boundaries had a constant temperature of 200 °C. The initial sandstone temperature was also 200 °C. The unconfined sample showed different results from the unconfined sample, and mechanisms which govern evolution of micro cracking were better understood. In the unconfined sample, parallel bond broke and crack occurred when local stress field exceeded the strength of the bond. Tensile micro cracks were concentrated near the wellbore wall, while shear micro cracks seemed to extend further to the synthetic sandstone, and some of the shear micro cracks were grouped along the preferential fluid flow paths. The presence of temperature difference between pressurized fluid in the wellbore and initial sandstone temperature induced thermal stresses to the area around the wellbore, in addition to the pressurization stresses. Formation of preferential fluid paths in a star-like composition around the wellbore was accompanied with shear micro cracks. On the contrary, in the biaxially confined specimen, a very pronounced that development of micro cracks also followed the fluid flow, which was at an angle with minimum confinement stress direction. The predominant direction of micro cracks suggested that the synthetic sandstone does not behave like a quasi-brittle material, and a dominant hydraulic fracture was not observed. In quasi-brittle rocks, hydraulic fracture initiates and propagates from the pressurized wellbore in the direction perpendicular to the minimum confinement stress direction. Further studies will be dedicated to better understanding how the difference between quasi-brittle rocks and ductile rocks behave in the scenarios where hydro-thermo-mechanically dominated stress fields around the wellbore.

ACKNOWLEDGMENTS

Financial support provided by University of California San Diego is gratefully acknowledged. The opinions expressed in this paper are those of the authors and not the DOE.

REFERENCES

- Bower, K. and Zyvoloski G. (1997). "A numerical model for thermo-hydro-mechanical coupling in fractured rock." *International Journal of Rock Mechanics and Mining Sciences*, V. 34: 1201-1211.
- Geiger, S. and Emmanuel S. (2010) "Non-Fourier thermal transport in fractured geological media." *Water Resources Research*. V. 46.
- Ghassemi, A. (2012) "A review of some rock mechanics issues in geothermal reservoir development." *Geotechnical and Geological Engineering*. V. 30: 647-664.
- Ghassemi, A., Nygren A. and Cheng A. (2008) "Effects of heat extraction on fracture aperture, a poro-thermoelastic analysis." *Geothermics*. V. 37: 525-539.

- Ghassemi, A., Tarasovs S. and Cheng A.D. (2005) "Integral equation solution of heat extraction-induced thermal stress in enhanced geothermal reservoirs." *International journal for numerical and analytical methods in geomechanics*. V. 29: 829-844.
- Itasca (2004) "PFC user manual". *Minneapolis: Itasca Consulting Group Inc.*
- Koh, J., Roshan H. and Rahman S.S. (2011) "A numerical study on the long term thermo-poroelastic effects of cold water injection into naturally fractured geothermal reservoirs." *Computers and Geotechnics*. V. 38: 669-682.
- Kolditz, O. and Clauser C. (1998) "Numerical simulation of flow and heat transfer in fractured crystalline rocks: application to the hot dry rock site in Rosemanowes (UK)." *Geothermics*. V. 27: 1-23.
- McDermott C.I., Walsh R., Mettier R., Kosakowski G. and Kolditz O. (2009) "Hybrid analytical and finite element numerical modeling of mass and heat transport in fractured rocks with matrix diffusion." *Computational Geosciences*. V. 13: 349-361.
- Nguyen, V.D., Benhabib K., Marie C. and Coorevits P. (2012) "Heat Transfer in a Granular Media Modeled by a Coupled DEM-Finite Difference Method, Application to Fluidized Bed Processes" *Procedia Engineering*. V. 42: 824-832.
- Rutqvist, J., Freifeld B., Min K.B., Elsworth D. and Tsang Y. (2008) "Analysis of thermally induced changes in fractured rock permeability during 8 years of heating and cooling at the Yucca Mountain Drift Scale Test." *International Journal of Rock Mechanics and Mining Sciences*. V. 45: 1373-1389.
- Tomac, I. and Gutierrez M. (2014a) "Coupled hydro-thermo-mechanical modeling of hydraulic fracturing in quasi-brittle rocks using DEM". *Digital Humanitarians: How Big Data Is Changing the Face of Humanitarian Response*: 423.
- Tomac, I. and Gutierrez M. (2014b) "Micro-Mechanics of Hydro-Thermo-Mechanical Fracture Propagation in Granite". *48th US Rock Mechanics/Geomechanics Symposium*.
- Tomac, I. and M. Gutierrez (2015) "Formulation and implementation of coupled forced heat convection and heat conduction in DEM." *Acta Geotechnica*. V. 10: 421-433.
- Wang, Y. and Dusseault M.B. (2003) "A coupled conductive-convective thermo-poroelastic solution and implications for wellbore stability." *Journal of Petroleum Science and Engineering*. V. 38: 187-198.
- Yang, J., Wang Q., Zeng M. and Nakayama A. (2010) "Computational study of forced convective heat transfer in structured packed beds with spherical or ellipsoidal particles." *Chemical Engineering Science*. V. 65: 726-738.
- Yong, C. and Wang C.Y., (1980) "Thermally induced acoustic emission in Westerly granite." *Geophysical research letters*. V. 7: 1089-1092.

Impact of Drainage Conditions on the Thermal Volume Change of Soft Clay

Atsushi Takai¹; Ismaail Ghaaowd²; John S. McCartney³; and Takeshi Katsumi⁴

¹Assistant Professor, Kyoto Univ., Yoshida-Honmachi, Sakyo, Kyoto 6068501.

²Doctoral Student, Univ. of California San Diego, 9500 Gilman Dr., La Jolla, CA 92093-0085.

³Associate Professor, Univ. of California San Diego, 9500 Gilman Dr., La Jolla, CA 92093-0085.

⁴Professor, Kyoto Univ., Yoshida-Honmachi, Sakyo, Kyoto 6068501.

Abstract: This study focuses on an evaluation of the thermal volume change of normally-consolidated Kaolinite clay under both undrained and drained conditions. For the tests under either condition, clay specimens were heated in a modified triaxial test setup from room temperature (23°C) to approximately 60°C then subsequently cooled. In both tests, the thermal volume change of the clay specimen was inferred using image analysis. During heating, elastic expansion was observed for the undrained specimen while plastic contraction was observed for the drained specimen. The thermally-induced excess pore water pressures measured in the undrained specimen compared well with predicted values from a mechanistic model. However, the thermal volume change of the drained specimen predicted using the pore water pressures measured in the undrained specimen indicated an under-prediction, possibly due to the particular parameters used in the analysis as well as the possibility that thermally-accelerated creep may be superimposed atop thermal consolidation.

INTRODUCTION

A clear understanding for the thermal behavior of soil is needed in many geotechnical engineering applications, such as design of deep repositories of radioactive waste (Gens et al. 2010), energy piles (Brandl 2006; Laloui et al. 2006; Murphy and McCartney 2015), thermal ground improvement (Abuel-Naga et al. 2006) and thermally-active geotechnical systems (Coccia and McCartney 2013; Stewart et al. 2014). These applications have led to increasing considerations of the temperature effects on the engineering properties of soils and have made the thermo-mechanical behavior of soils as one of the major issues in latest geotechnical engineering.

The aim of this research is to study the thermo-mechanical behavior of normally-consolidated Kaolinite clay under temperatures up to approximately 60 °C

under different drainage conditions. A laboratory testing program using a modified triaxial test was formulated to evaluate the effect of temperature on the thermally induced pore water pressure generation in undrained conditions and thermally induced volume change in drained conditions. The results from the laboratory tests under different drainage conditions were compared to evaluate whether the drainage of thermally-induced pore water pressure is the main mechanism of thermal volumetric contraction observed in soils (Campanella and Mitchell 1968; Hueckel and Baldi 1990). The volume change during tests with different drainage conditions was also compared with the isotropic compression curve measured for the saturated clay.

PREDICTION OF THERMALLY-INDUCED EXCESS PORE WATER PRESSURE IN SATURATED SOILS

Campanella and Mitchell (1968) developed a theoretical approach to estimate the excess pore water pressure generation in a specimen of saturated soil during undrained heating using the concepts of thermo-elasticity and linear elasticity. Specifically, to ensure compatibility of strains during undrained heating, the sum of the changes in volume of the soil constituents due to changes in both temperature and pressure must equal the sum of the volume changes of the total soil mass during changes in temperature ΔT and pore water pressure Δu . The excess pore water pressure generated by a change in temperature during undrained conditions can be expressed as follows:

$$\Delta u = \frac{n\Delta T(\alpha_s - \alpha_w) + \alpha_{st}\Delta T}{m_v} \quad (1)$$

where n is the porosity of a saturated soil, α_w is the cubical coefficient of thermal expansion of the pore water (equal to $0.00017 \text{ 1/}^\circ\text{C}$), α_s is the cubical coefficient of thermal expansion of the mineral solids, ΔT is the change in temperature of the soil, Δu is the change in pore water pressure, α_{st} is the physico-chemical coefficient of structural volume change, and m_v is the coefficient of volume compressibility. The value of α_s does not vary significantly for the tests on different clay minerals reported in the literature, so the value used by Campanella and Mitchell (1968) of $0.000035/^\circ\text{C}$ can be used to analyze the results from other clays. The value of α_w is an order of magnitude greater than α_s , which is one of the primary reasons for the pore water pressure change observed during undrained heating of saturated clays. Regarding the estimation of the value of m_v , Campanella and Mitchell (1968) and Uchaipichat and Khalili (2009) observed that a saturated soil expands along the recompression line during undrained heating. On this basis, the value of m_v can be determined from the isotropic recompression curve $(m_v)_r$ at a given value of mean effective stress, as follows:

$$(m_v)_r = \frac{1}{1 + e_0} \frac{\kappa}{p'} \quad (2)$$

where κ is the slope of the isotropic recompression line, e_0 is the initial void ratio, and p' is the mean effective stress.

The physico-chemical coefficient of soil structural volume change, α_{st} , represents the tendency for thermal volume change of soils due to the soil structure and physico-chemical effects, and depends primarily on the soil mineralogy for normally-consolidated clays. Ghaaowd et al. (2015) proposed an empirical relationship between the physico-chemical coefficient of structural volume change and the plasticity index, PI , based on the thermally induced pore water pressures measured in 13 normally-consolidated soil specimens from different studies, as follows:

$$\alpha_{st} = 1.0 \times 10^{-4} \cdot e^{-0.014PI} \quad (3)$$

MATERIALS AND SPECIMEN PREPARATION

In this study, commercial Kaolinite clay from M&M Clays Inc., of McIntyre, Georgia was used for the experiment. The geotechnical properties of the clay are summarized in Table 1. As the clay has a liquid limit of 47% and a plasticity index of 19, the clay is classified as CL according to the Unified Soil Classification Scheme (USCS). The clay has a specific gravity of 2.6. The isotropic compression curve is shown in Figure 1. The slopes of the normal compression line (λ) and the recompression line (κ) are equal to 0.1 and 0.016, respectively.

Table 1. Properties of the Kaolinite clay and initial conditions of the specimen used in this study.

Liquid limit	47%
Plastic limit	28%
Plasticity index	19
Specific gravity	2.6
Initial gravimetric water content	31%
Initial void ratio	0.90
Initial porosity	0.47

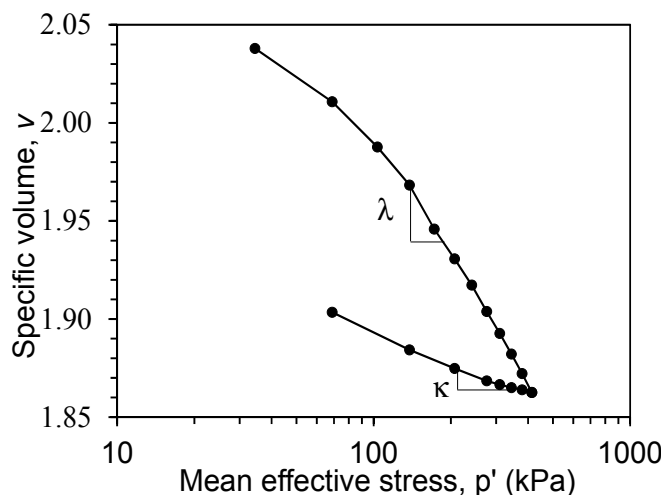


FIG1. Isotropic compression curve for Kaolinite clay.

EXPERIMENTAL METHODOLOGIES

Equipment and procedures

The test was performed by using a modified triaxial system originally developed by Alsherif and McCartney (2013, 2015). A schematic of the system is shown in Figure 2. The cell is comprised of a Pyrex pressure vessel that has the advantage of having low thermal creep behavior while still remaining transparent after repeated heating and cooling cycles. The temperature within the cell is controlled by circulating heated water from a heated water bath through a stainless steel pipe bent into a “U” shape over the specimen. A solar pump is used to circulate the cell water to ensure that it is uniformly mixed, and a thermocouple is used to monitor the cell temperature changes. A pore water pressure transducer is used to monitor the pore water pressure during undrained heating. The cell fluid temperature was monitored using a thermocouple and temperature recorder having a precision of 0.5 °C. The cell pressure and backpressure were controlled using a pressure panel.

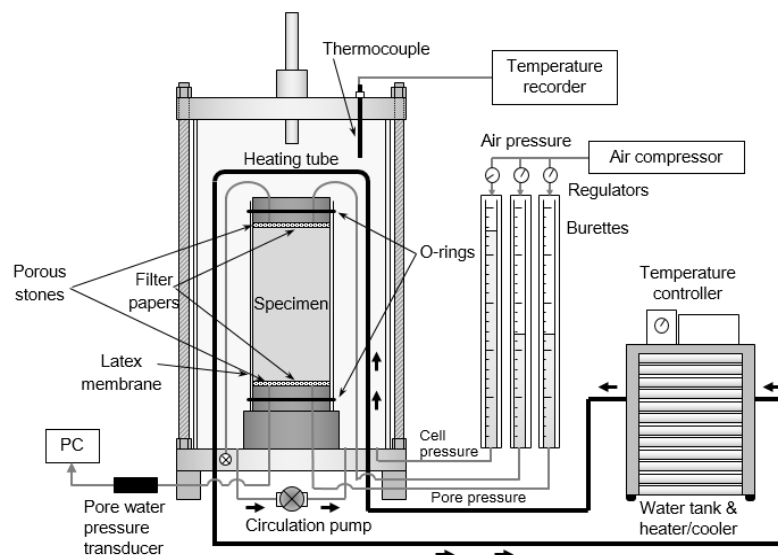


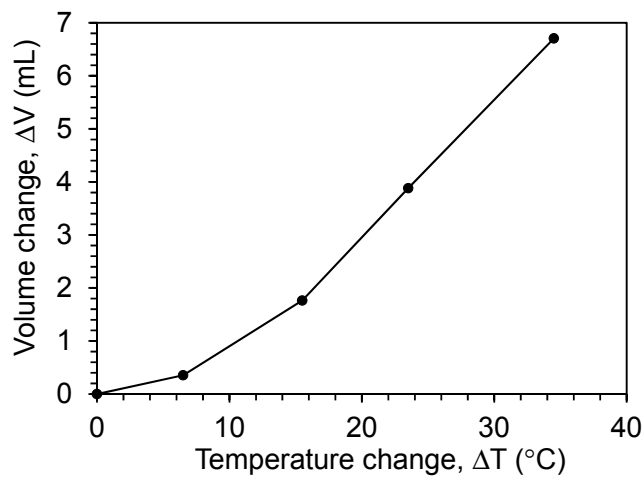
FIG 2. Schematic view of the thermal triaxial system.

The testing procedure first involved back-pressure saturation of the specimen, which was performed by applying the cell pressure and backpressure in stages until reaching a value of Skempton's pore water pressure parameter B of 0.95 while maintaining a constant seating mean effective stress of 21 kPa, then the specimen was consolidated isotropically to a mean effective stress of 276 kPa. During the drained heating test, the drainage valves at the top and bottom of the specimen were kept open, while during the undrained heating test they were all maintained closed except the one leading to the pore water pressure transducer. In both the tests with undrained and drained conditions, the specimens were heated from 23 °C to approximately 60 °C in 5 to 10 °C increments, and each increment was maintained until the pore water pressure or volume change stabilized. Also, during the drained heating test the outflow drainage was also recorded. Images of the specimens were taken using a high resolution camera (model D610 from Nikon) during both the tests to measure changes in volume of the specimen.

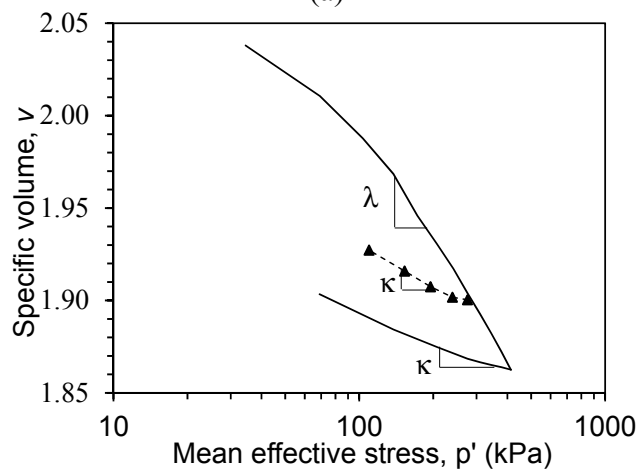
RESULTS AND DISCUSSION

Volume change during undrained heating

The thermal volume change of the specimen during undrained heating is shown in Figure 3(a). Despite some nonlinearity in the first stage, the trend between the thermally induced pore water pressure and the temperature is relatively linear. The specific volume of the specimen is shown as a function of the mean effective stress during heating in Figure 3(b). The mean effective stress during heating was calculated as the difference between the initial mean effective stress and the thermally-induced change in pore water pressure. Figure 3(b) also includes the normal compression and recompression curves from Figure 1 for reference. During undrained heating, the specific volume increases with temperature following the elastic recompression curve. These results verify that the value of κ from the recompression curve ($\kappa = 0.02$) matches well with the data from the undrained heating test. This confirms the choice of κ in the definition of the physico-chemical coefficient of structural volume change.



(a)

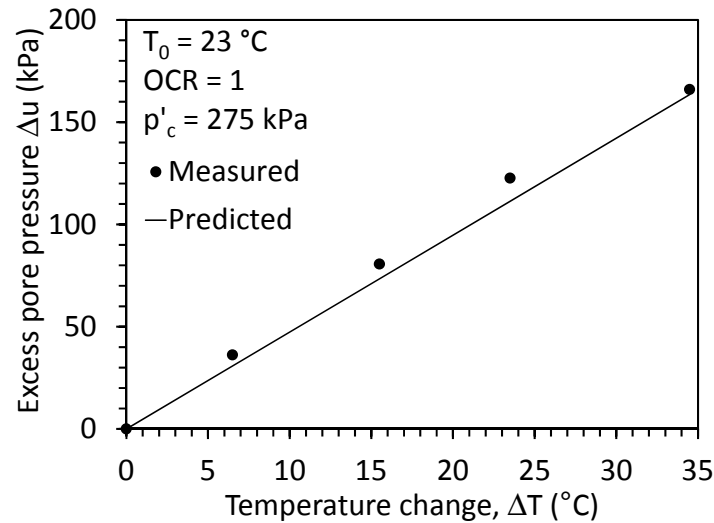


(b)

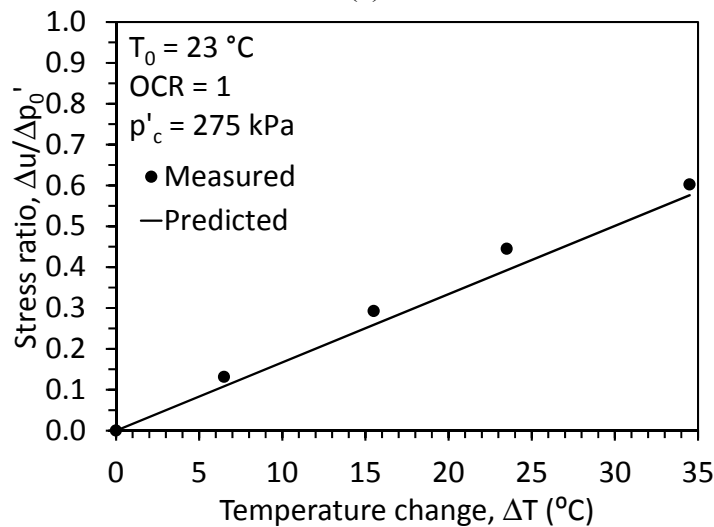
FIG. 3. (a) Volume change versus temperature; (b) Specific volume vs. mean effective stress during undrained heating with comparison to the isotropic compression curve.

Excess pore water pressure generation during undrained heating

The change in pore water pressure as a function of the change in temperature is shown in Figure 4(a). The same data normalized by the initial mean effective stress is shown in Figure 4(b). The thermally induced excess pore water pressure was observed to increase linearly with the change in temperature for the normally consolidated Kaolinite clay.



(a)



(b)

FIG 4. Effect of temperature change on the change in pore water pressure for Kaolinite clay along with the predicted trend from Eq. 1: (a) Pore water pressure; (b) Pore water pressure normalized by the initial mean effective stress

The physico-chemical coefficient ($\alpha_{st} = 7.7 \times 10^{-5} \text{ 1/}^\circ\text{C}$) was calculated using Equation 3 using the PI of the Kaolinite clay reported in Table 1, which was then used to predict the pore water pressure as a function of temperature using Equation 1. The predicted thermally induced pore water pressures are shown together with the measured values in Figure 4. Good correspondence between the experimental and

predicted pore water pressures for the normally-consolidated Kaolinite clay is observed. This observation confirms that the empirical equation of Ghaaowd et al. (2015) can be used to predict soil behavior from index properties, and that the generation of pore water pressure during heating can be estimated from basic properties of the soil constituents and knowledge of the current stress condition. This is useful as it permits the thermally induced excess pore water pressures in undrained conditions to be estimated without having to perform complex experiments.

Volume Change during Drained Heating

The measured volumetric strain of a second specimen of Kaolinite clay during drained heating is shown in Figure 5. The specimen was observed to contract nonlinearly during heating by approximately 1.1%. During cooling, the specimen was observed to partially recover the contraction, indicating that all of the contraction may not have been permanent. This behavior during cooling has been observed in some studies (e.g., Coccia and McCartney 2012), while others have observed additional thermal contraction during cooling (e.g., Uchaipichat and Khalili 2009).

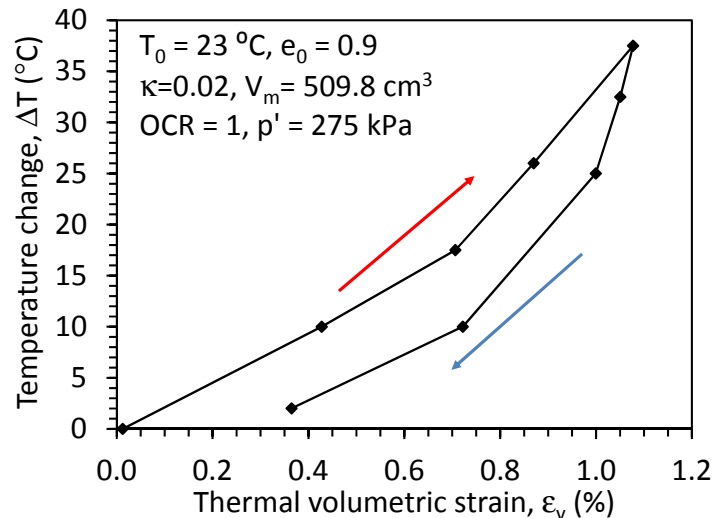


Fig. 5. Volumetric strain under drained heating/cooling cycle of normally consolidated Kaolinite clay.

The volume of water drained from the specimen due to the temperature change $(\Delta V_{DR})_{\Delta T}$ can be predicted from the measured value of pore water pressure during the undrained test using the following equation developed by Campanella and Mitchell (1968) as shown Figure 5. Even though the drainage is allowed during the drained heating, due to the low permeability of the clay, thermal excess pore water pressure will be generated. This will lead to the decrease in the effective stress, and the volume will not decrease. At the moment the thermal excess pore pressure will dissipate, the effective stress will be recovered, and cause a decrease in volume. The volume change during drainage of these pore water pressures is expected to follow the recompression line, which can be expressed as follows:

$$(\Delta V_{DR})_{\Delta T} = (m_v)_r V_m \Delta p' \quad (4)$$

where V_m is the initial total volume of the specimen (509.87 mL) and $\Delta\pi'$ can be assumed to equal the change in mean effective stress due to the thermally-induced excess pore water pressure Δu . The value of Δu can be estimated as the value measured from an undrained heating test or predicted using the approaches of Campanella and Mitchell (1968) or Ghaaowd et al. (2015). Accordingly, Equation 4 can be rewritten into the form of the isotropic recompression curve as follows:

$$(\Delta V_{DR})_{\Delta T} = -\frac{1}{1+e_0} \frac{\kappa}{p'} V_m \Delta u \tag{5}$$

This equation signifies the change in volume due to the thermally induced flow of water from the soil, and is expected to be equal to the volume of water flowing out of the specimen during drained heating. In addition to the overall volume change shown in Figure 5, the water drained from the specimen was also measured during the heating process. The measured and predicted volumes of water outflow are shown in Figure 6. The parameters used in the prediction are summarized in the figure. More outflow of water was observed than that predicted using Equation 5. This may indicate that the simple effective stress volume change analysis in Equation 5 may not be sufficient to capture the thermal volume change of saturated soils, and that an analysis that considers thermal creep may be necessary.

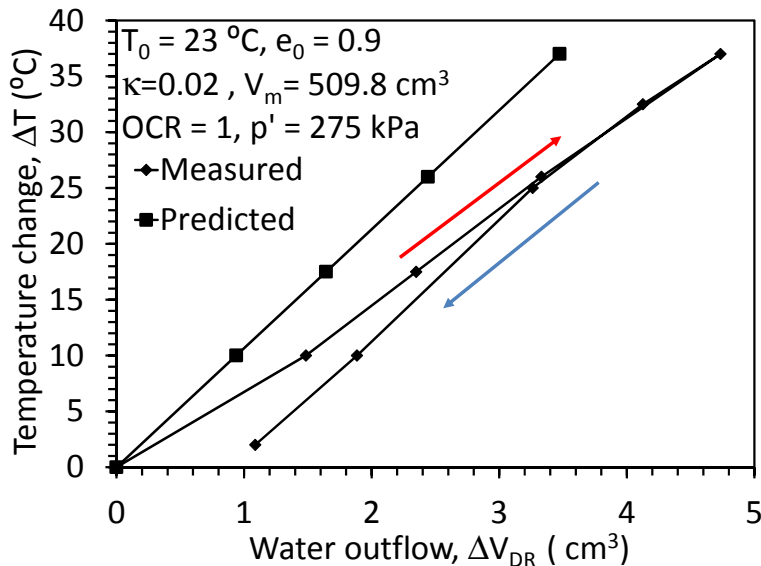


FIG.6. Measured and predicted drained water volume during drained heating.

The overall change in volume of the soil specimen $(\Delta V_m)_{\Delta T}$ due to a change in temperature depends both on the volumetric contraction calculated using Equation 6-b which is rearrange of the change in volume of water drained equation as well as the expansion of the different phases, as follows (Campanella and Mitchell 1968):

$$(\Delta V_{DR})_{\Delta T} = \alpha_w V_w \Delta T + \alpha_s V_s \Delta T - (\Delta V_m)_{\Delta T} \tag{6-a}$$

$$(\Delta V_m)_{\Delta T} = \alpha_w V_w \Delta T + \alpha_s V_s \Delta T - (\Delta V_{DR})_{\Delta T} \quad (6-b)$$

where V_w is the initial volume of pore water before heating (241.5 mL for the test with OCR = 1), and V_s is the volume of mineral solids (268.3 mL for the test with OCR = 1). A comparison between the measured volume change of the specimen and the prediction using Equation 6-b is shown in Figure 7. As the temperature is increased, the soil constituents will expand by different values and cause thermal excess pore water pressure generation followed by water drainage, moving and reorientation of the solid particles, and contraction in the soil specimen. The difference between the predicted data and the recorded data could be due to the thermal creep which happened after the primary thermal consolidation, or the use of particular parameters in the prediction such as the slope of the recompression line, and cubical coefficient of thermal expansion of the mineral solids.

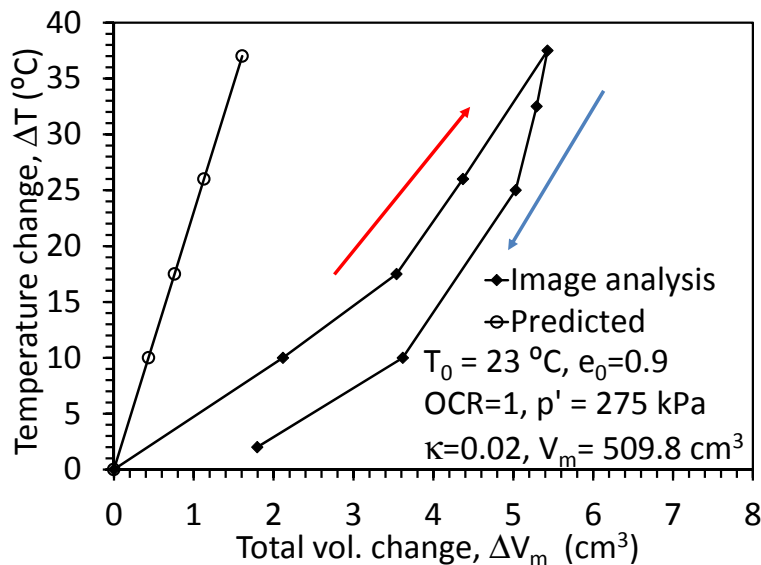


FIG.7. Measured and predicted volume changes for drained heating.

CONCLUSIONS

Drained and undrained heating triaxial tests were performed to evaluate the impact of the drainage on the volume change during the specimen temperature change. The thermally-induced pore water pressures measured during the undrained heating test were found to correspond well with the results from a mechanistic model. The thermally-induced volume expansion during the drained heating test was found to be partially recoverable. When the pore water pressures from the undrained heating test were used to predict the thermally-induced volumetric contraction observed in the drained heating test, an under-prediction was observed. This is possibly due to the particular parameters used in the analysis such as slope of the recompression line, and cubical coefficient of thermal expansion of the mineral solids, but could also be due to thermal creep which could have happened right after the thermal consolidation.

ACKNOWLEDGMENTS

The authors would like to acknowledge financial support from the University of California San Diego and the Program for Advancing Strategic International Networks of the Japan Society for the Promotion of Science.

REFERENCES

- Alsherif, N.A. and McCartney, J.S. (2013). "Triaxial cell for nonisothermal shear strength of compacted silt under high suction magnitudes." *Proceedings of the 1st Pan-American Conference on Unsaturated Soils*, Feb. 20-22. Cartagena de Indias. Taylor and Francis Group, London. 147–152.
- Alsherif, N.A. and McCartney, J.S. (2015). "Nonisothermal behavior of compacted silt at low degrees of saturation." *Géotechnique*. 65(9), 703-716.
- Abuel-Naga, H.M., Bergado, D.T., and Chaiprakaikeow, S. (2006). "Innovative thermal technique for enhancing the performance of prefabricated vertical drain during the preloading process." *Geotextiles and Geomembranes*, 24, 359–370.
- Brandl, H. (2006). "Energy foundations and other thermo-active ground structures." *Géotechnique*. 56(2): 81-122.
- Campanella, R.G., and Mitchell, J.K. (1968). "Influence of temperature variations on soil behavior." *J. of the Soil Mechanics and Foundation Div.* 94(SM3), 709–734.
- Coccia, C.J.R. and McCartney, J.S. (2012). "A thermo-hydro-mechanical true triaxial cell for evaluation of the impact of anisotropy on thermally-induced volume changes in soils." *ASTM Geotechnical Testing Journal*. 35(2), 227-237.
- Coccia, C.J.R., and McCartney, J.S. (2013). "Impact of heat exchange on the thermo-hydro-mechanical response of reinforced embankments." *Proc. GeoCongress 2013*. ASCE. pp. 343-352.
- Hueckel, T. and Baldi, M. (1990). "Thermoplasticity of saturated clays: Experimental constitutive study." *Journal of Geotechnical Engineering*, 116(12): 1778–1796.
- Gens, A., Guimaraes, L. do N., Olivella, S., and Sanchez, M. (2010). "Modelling thermo-hydro-mechano-chemical interactions for nuclear waste disposal." *Journal of Rock Mechanics and Geotechnical Engineering*, 2(2), 97–102.
- Ghaawd, I., Takai, A., Katsumi, T. and McCartney, J.S. (2016). "Pore water pressure prediction for undrained heating of soils." *Environmental Geotechnics*. 1-9. 10.1680/jenge.15.00041.
- Laloui, L., Nuth, M. and Vulliet, L. (2006). "Experimental and numerical investigations of the behaviour of a heat exchanger pile." *IJNAMG*. 30: 763–781.
- Murphy, K.D. and McCartney, J.S. (2015). "Seasonal response of energy foundations during building operation." *Geotechnical and Geological Engineering*. 33(2), 343-356.
- Stewart, M.A., Coccia, C.J.R., and McCartney, J.S. (2014). "Issues in the implementation of sustainable heat exchange technologies in reinforced, unsaturated soil structures." *Proc. GeoCongress 2014*. ASCE. pp. 4066-4075.
- Uchaipichat, A. and Khalili, N. (2009). "Experimental investigation of thermo-hydro-mechanical behaviour of an unsaturated silt." *Géotechnique*. 59(4), 339–353.

Impact of Long-Term Temperature Cycling on the Thermo-Hydro-Mechanical Behavior of Unsaturated Soils Surrounding an Energy Pile

Charles J. R. Coccia, Ph.D., S.M.ASCE¹; and
John S. McCartney, Ph.D., P.E., M.ASCE²

¹Graduate Research Associate, Dept. of Civil, Environmental and Architectural Engineering, Univ. of Colorado Boulder, UCB 428, Boulder, CO 80309. E-mail: coccia@colorado.edu

²Associate Professor, Dept. of Structural Engineering, Univ. of California San Diego, 9500 Gilman Dr., La Jolla, CA 92093-0085. E-mail: mccartney@ucsd.edu

Abstract: This paper describes a numerical investigation into the thermo-hydro-mechanical response of unsaturated soil surrounding an example energy pile subjected to two different seasonal temperature fluctuations over five years. Long-term temperature cycling was observed to lead to a progressive zone of drying around the energy foundation and a corresponding decrease in hydraulic and thermal conductivity values. A larger decrease in degree of saturation was observed for temperature fluctuations from 0 to 45°C than for temperature fluctuations from 5 to 25°C. Further, a larger decrease in degree of saturation was found for soils with lower initial degree of saturation. In the example evaluated in this study, the decrease in degree of saturation was relatively small, but is still associated with a decrease in long term heat exchange efficiency as well as increased effective stress in the soil, which may affect the intended performance of the energy pile. The example presented in this study may help guide site-specific evaluations to evaluate this behavior.

1. INTRODUCTION

Energy piles are a well-established technology to exchange heat with the subsurface (Brandl 2006; Laloui et al. 2006). There have been several recent studies on their thermal properties measured using thermal response tests, and thermo-mechanical behavior under different boundary restraints and cyclic heating and cooling. However, there have not been many studies on their long-term performance under seasonal temperature fluctuations, which in the continental U.S. typically range from approximately 5 to 35 °C (Murphy and McCartney 2015). Wider temperature ranges may be encountered in more extreme climate settings or in settings dominated by

heating or cooling. This study is focused on the observations from the numerical simulation of the behavior of energy piles in unsaturated soil layers. The reason for the focus on this particular soil setting is that changes in the long-term thermo-hydro-mechanical behavior of unsaturated soils may be expected during heating and cooling cycles. It is well known water will flow away from an available heat source if subjected to a thermal gradient (Philip and de Vries 1957; Milly 1982; Thomas and Sansom 1995). Further, changes in degree of saturation will lead to a decrease in the thermal conductivity (Lu et al. 2010a; Smits et al. 2013), a decrease in the hydraulic conductivity (van Genuchten 1980), and an increase in the effective stress (Lu et al. 2010b) of unsaturated soils. Due to these coupled thermo-hydro-mechanical behaviors, a progressive zone of drying and densification may occur around the energy pile that may need to be considered in their design.

2. BACKGROUND

In the presence of a temperature gradient, water will move from regions of high temperature to regions of low temperature in both liquid and vapor phases. Vapor transport is primarily a diffusive process resulting from the development of a vapor pressure gradient in response to a thermal gradient. Liquid water is observed to flow from areas of warm to cold due to the presence of a surface tension gradient, as the surface tension of water in contact with air increases with decreasing temperature. As the matric suction, ψ , also increases with decreasing temperature, a suction gradient within the soil may also contribute to thermally-induced liquid water flow (Cary 1966). Previous studies have defined the coupled governing equations for coupled flow of liquid water, water vapor, and heat (Philip and de Vries 1957) as well as the analytical and numerical solutions to these equations (Milly 1982; Thomas and Sansom 1995). These solutions have also been extended to incorporate the volume change response of a deformable soil to the coupled flow of heat and water (Thomas and He 1995). McCartney (2012) described experimental evaluations of thermally induced water flow in sand and clay, and noted that the zone of influence for thermally induced water flow is a function of initial saturation, hydraulic conductivity, thermal conductivity, and porosity, a greater zone of influence is expected for silts or clays of low plasticity with a higher initial degree of saturation.

The hydraulic conductivity of unsaturated soils will vary as a function of the soil solid pore network (i.e., porosity or void ratio), the properties of the pore fluid (viscosity) and the amount of pore fluid within the system (i.e., the degree of saturation or water content). The hydraulic conductivity of unsaturated soil will decrease with decreasing saturation due to a reduction in the water pathways required for water to flow out of the soil. The effective degree of saturation S_e (i.e., the degree of saturation normalized by the residual degree of saturation) is related to the matric suction via a soil specific relationship referred to as the soil water retention curve (SWRC). van Genuchten (1980) developed a smooth hyperbolic function for the SWRC that can be fitted to experimental ψ - S_e data points, along with an approach to estimate the hydraulic conductivity as a function of the effective saturation for an unsaturated soil from the fitting parameters of the SWRC (van Genuchten 1980).

The effective stress in unsaturated soils is closely linked with the hydraulic behavior of the soil. Bishop (1959) defined the effective stress of unsaturated soils as:

$$\sigma' = (\sigma - u_a) + \chi(u_a - u_w) = \sigma_n + \chi\psi \quad (1)$$

where $\sigma_n = (\sigma - u_a)$ is the net stress, $\psi = (u_a - u_w)$ is the matric suction equal to the difference in pore air and water pressures, and χ is an effective stress parameter. The effective stress approach relies heavily on the definition of χ , which is related to the soil's structure and degree of saturation. Lu et al. (2010b) proposed that the value of χ is equal to S_e , which permits the van Genuchten (1980) SWRC specific to a given soil to be incorporated into the definition of the effective stress. In this case, changes in ψ or S_e lead to changes in effective stress in the soil, which may result in changes in volume or shear strength.

3. MODELING OF THERMALLY-INDUCED WATER FLOW

Vadose/W[©] 2007 was used to model the thermally induced water flow as a result of the long-term thermal cycling of a hypothetical energy foundation. Wilson et al. (1994) provides a detailed discussion on the theory utilized by the software; however, a brief summary is described herein. The water and heat mass transfer equations utilized in Vadose/W[©] 2007 are derived from the one-dimensional Richards' equation for transient flow in unsaturated soils with adaptations for vapor flow added by Wilson (1990). The partial differential equation for this case is given as follows:

$$\frac{1}{\rho} \frac{\partial}{\partial z} \left(D_v \frac{\partial P_v}{\partial z} \right) + \frac{\partial}{\partial z} \left(k_z \frac{\partial (P/\rho g + z)}{\partial z} \right) + Q = \left(C_s + L \frac{\partial \theta}{\partial T} \right) \frac{\partial P}{\partial t} \quad (2)$$

where P is the absolute water pressure, P_v is the vapor pressure, k_z is the hydraulic conductivity of the unsaturated soil in the z -direction obtained from the hydraulic conductivity function, Q is a boundary flux, D_v is the vapor diffusion coefficient, z is the elevation head, ρ is the density of water at a temperature (T), g is the acceleration due to gravity, C_s is the volumetric heat capacity of unsaturated soil obtained from a volumetric heat capacity function, L is the latent heat of vaporization of water, θ is the volumetric water content, and t is time. The partial differential equation governing one-dimensional heat flow in unsaturated soils is given as follows:

$$L \frac{\partial}{\partial z} \left(D_v \frac{\partial P_v}{\partial z} \right) + \frac{\partial}{\partial z} \left(k_{tz} \frac{\partial T}{\partial z} \right) + \rho_c v_z \frac{\partial T}{\partial z} + Q_t = \left(C_s + L \frac{\partial \theta}{\partial T} \right) \frac{\partial T}{\partial t} \quad (3)$$

where ρ_c is the volumetric specific heat value, k_{tz} is the thermal conductivity of the unsaturated soil in the z -direction obtained from a thermal conductivity function, v_z is the Darcy velocity of water in the z -direction, and Q_t is the thermal boundary flux.

Considering that the governing equations for heat and water flow contain three unknown variables: P , T , and P_v , Vadose/W incorporates the following relationship between absolute pressure and the vapor pressure, as follows:

$$P_v = P_{vs} \cdot e^{\frac{-P \cdot w}{\rho \cdot R \cdot T}} \quad (4)$$

where P_{vs} is the saturated vapor pressure of pure free water, w is the molecular mass of water vapor, and R is the universal gas constant. Use of this equation permits the two coupled governing equations to be solved simultaneously.

For this paper, the properties of Bonny silt were chosen to highlight the impact of long-term temperature cycling on the thermo-hydro-mechanical response of an unsaturated soil surrounding an energy pile. For a “Full Thermal” analysis, Vadose/W[©] requires the SWRC, a hydraulic conductivity function (HCF), a thermal conductivity function (TCF), and a volumetric heat capacity function (VHCF) for the soil modeled. The SWRC was represented using the model of van Genuchten (1980), which was fitted to experimental data obtained by Khosravi and McCartney (2012). The hydraulic conductivity, thermal conductivity, and volumetric heat capacity functions were defined using the models of van Genuchten (1980), Johansen (1975), and Johnston et al. (1981), respectively, which are implemented through sub-modules provided within the program. Table 1 summarizes the key properties of Bonny silt required for these models for a dry density of 1.5 Mg/m³ and a porosity of 0.41.

Table 1: Properties of Bonny silt used in the VADOSE/W analysis

van Genuchten (1980) SWRC Model Parameters	a	28.571	kPa	Specific gravity	G_s	2.54	-
	n	1.77	-	Thermal Strain Rate	ϵ_{Tz}	0.0015	%/°C
	θ_s	0.41	-	Cohesion	c'	0	kPa
	θ_r	0.04	-	Friction Angle	ϕ'	32.4	°
Thermal Conductivity of Soil	k_{tz}	121.8	kJ/(day·m·°C)	Thermal Conductivity of Water	k_w	52.27	kJ/(day·m·°C)
Vol. Heat Capacity of Soil	C_s	1840	kJ/(m ³ ·°C)	Vol. Heat Capacity of Water	C_w	4187	kJ/(m ³ ·°C)
Sat. Hydraulic Conductivity	k_s	8.64×10 ⁻³	m/day	Latent Heat of Water	L	2260	kJ/kg

The influence of long-term temperature cycling on the surrounding soil of a 1-m diameter, 25-m deep energy pile shown in Fig. 1(a) was analyzed in this study. The particular dimensions are typical of energy piles encountered in the field (Brandl 2006; Laloui et al. 2006; Murphy and McCartney 2015). The groundwater table was selected to be located at the toe of the energy pile and the unsaturated zone above the groundwater table is assumed to satisfy initially hydrostatic conditions. Axisymmetric models are the best choice for modeling the behavior of a cylindrical deep foundation, but this option is not available in Vadose/W[©] 2007. Accordingly, the energy pile was modeled as a 2-dimensional half space as shown in Fig. 1(b). Despite this modeling simplification, the flow processes in the soil are still approximately representative of that surrounding an energy pile. The 25 m energy pile is underlain by 5 m of silt with 10 m of silt set to the right side. Preliminary analysis indicated this range to be large enough to avoid any undesired boundary effects while maintaining reasonable program run times during analysis. Furthermore, infinite elements were included at the right of the problem geometry to simulate a “far field” boundary as indicated in Fig. 1(a) by a green boundary. Inclusion of the infinite elements helps simulate an infinite boundary to the right of the hypothetical energy pile to avoid any influence of the model boundary.

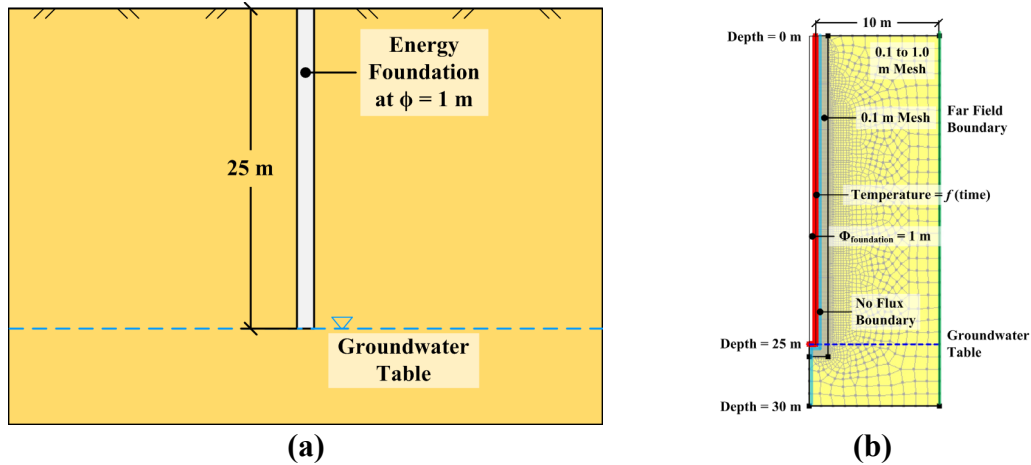


Fig. 1. (a) Schematic of Problem Geometry; (b) Schematic of Mesh, Initial Conditions, and Boundary Conditions for Energy Pile Model

The immediate 1 m zone surrounding the energy pile was meshed with a combined quadrilateral-triangular grid at a maximum size of 0.1 m. Outside the finely meshed region, a 0.1 to 1.0 m gradient quadrilateral-triangular mesh is applied. This meshing regiment allowed Vadose/W[©] 2007 to model the thermally induced water flow immediately surrounding the foundation without loss of detail. An initially constant earth subsurface temperature of 15 °C was selected which reflects the conditions of most non-tropical climates (Brandl 2006). Two sinusoidal energy pile temperature fluctuations were considered in this study, shown in Figs. 2(a) and 2(b). Case 1 involves a temperature range of 5-25 °C typical of an energy pile in a temperate climate, while Case 2 involves a temperature range of 0-45 °C for extreme conditions. Case 2 was used investigate the influence of heightened thermal swings on the thermo-hydro-mechanical response of the soil in comparison with that from Case 1. Application of these thermal cycles were applied at the boundary of the energy pile as indicated in Fig. 2(b) by the red line. Finally, a “no flux” hydraulic boundary condition, indicated by a blue line in Fig. 1(a), was applied along the energy foundation so that no water flow could occur into the energy pile during analysis.

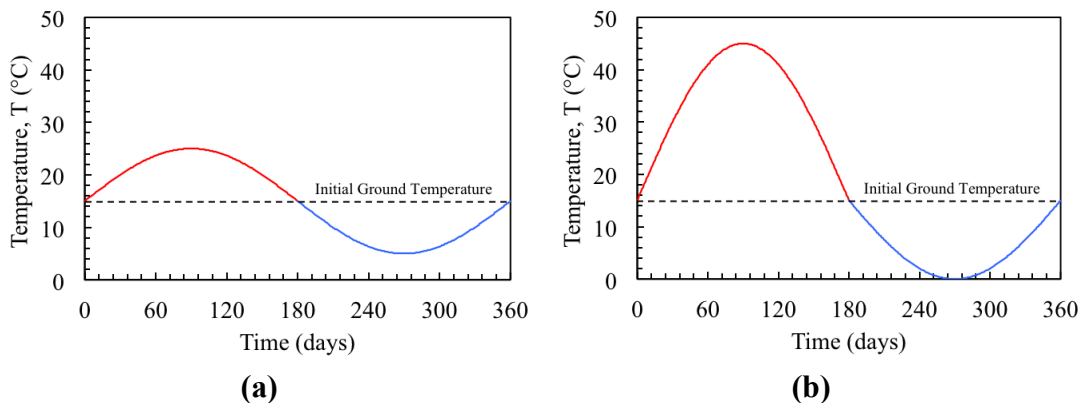


Fig. 2. Energy Pile Yearly Temperature Cycles: (a) Case 1; (b) Case 2

Prior to application of any thermal cycles, the 30 m soil profile was allowed to reach hydrostatic conditions based on a groundwater table located at a depth of 25 m. The resulting initial saturation and matric suction profile is shown in Fig. 3. Based on the groundwater location at a depth of 25 m, degrees of saturation along the soil-structure interface ranged from 1 to nearly 0.25. After hydrostatic conditions were reached, thermal cycles were applied at the boundary of the energy pile for 1800 days at time increment of 18 days. No infiltration of water occurs during the heating period, which is representative of energy piles covered by an impermeable slab.

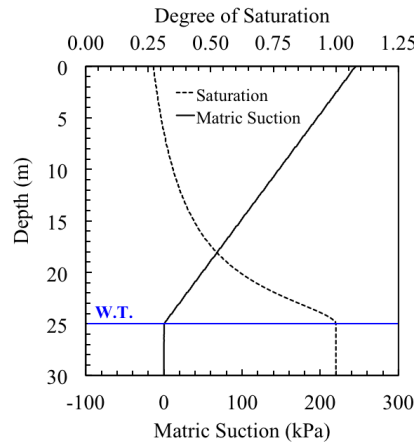


Fig. 3. Initial Profiles of Degree of Saturation and Matric Suction

4. SIMULATION RESULTS

The temperature distribution within the 2-dimensional model space at various times for Case 1 is shown in Fig. 4. The temperature distribution for Case 2 is similar, albeit with greater magnitudes, so it is not shown here. On day 90, the soil was subjected to a maximum temperature of 25 °C from an initial temperature of 15 °C (initial), resulting in a fairly linear temperature distribution away from the energy pile. Continuing onto Day 180, the temperature of the foundation begins to decrease back to 15 °C. During cooling from Day 90 to 180, the initial temperature of the silt is not recovered, leaving a region of warmer soil bounded by colder temperatures. The reverse phenomenon is observed during temperature reversal.

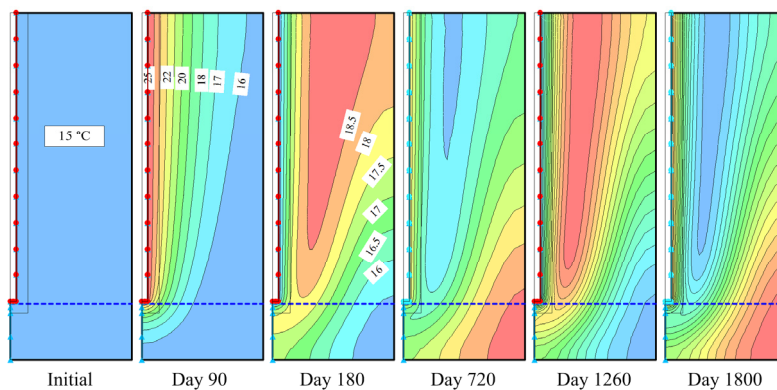


Fig. 4. Temperature Contours Around the Energy Pile (Case 1)

Variations in the thermal gradient with time due to thermal cycling of the energy pile will impact the movement of water within the soil profile during heating and cooling. This behavior is observed in Fig. 5 for Cases 1 and 2 where the resulting changes in saturation along the length of the energy pile is presented during the peaks of summer (25 or 45 °C applied) and winter (5 or 0 °C applied). Progressive drying is observed around the energy pile in both cases. This indicates that soils with lower initial degrees of saturation at the beginning of a temperature cycle will show greater decreases in degree of saturation due to thermally induced water flow. Comparison of the results for the two Cases indicates that nearly 10 times more drying was observed for the pile Case 2, which experienced a 20 °C greater temperature in the summer.

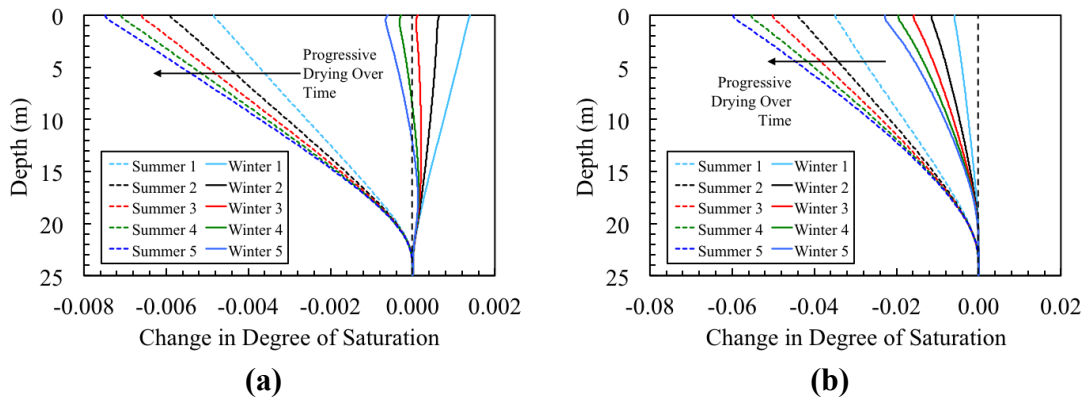


Fig. 5. Changes in Degree of Saturation with Depth: (a) Case 1; (b) Case 2

The variation in saturation at a depth of 4.8 m (corresponding to an initial degree of saturation of 0.3) with time from the start of heating is shown in Fig. 6 for Cases 1 and 2. A downward trend is observed in the degree of saturation superimposed atop the temperature cycles. The magnitude of the variation of degree of saturation appears to be greater for the exaggerated thermal cycle for Case 2. This may be due to the coupled influences of changing saturation, hydraulic conductivity, and thermal conductivity. A final decrease in degree of saturation, after 1800 days, of about 0.002 was observed for Case 1, while a decrease in degree of saturation of about 0.015 was observed for Case 2, though larger decreases are observed following summer cooling.

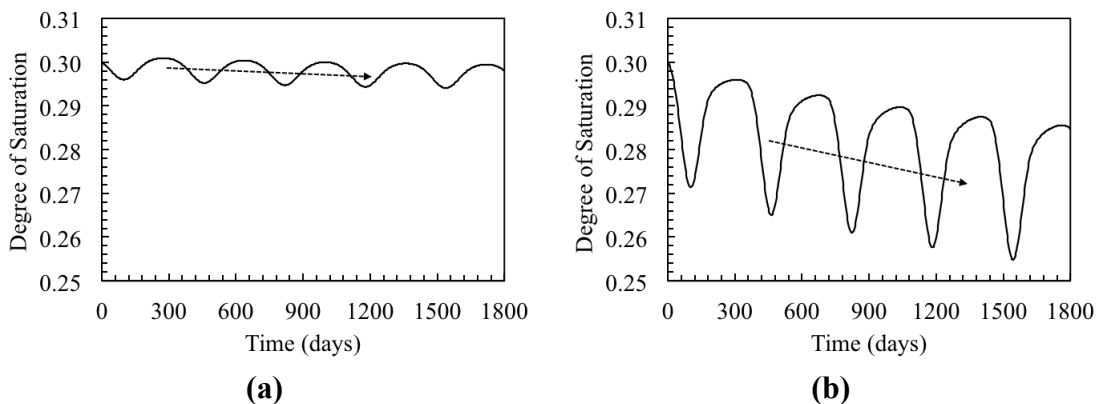


Fig. 6. Variation in Saturation at a Depth of 4.8 m: (a) Case 1; (b) Case 2

For the temperature fluctuations applied, the decreases in degree of saturation were smaller than those observed by Coccia and McCartney (2013), which were as high as 0.2 for a sustained temperature boundary condition over the course of 50 days. The difference is a result of the transient change in the temperature boundary condition applied by the energy pile. The gradual temperature fluctuation will result in a small thermal gradient which may not activate a substantial flow of pore water away from the zone of highest temperature. As the degree of saturation decreases, it is expected that the values of hydraulic conductivity and thermal conductivity will also decrease. The changes in hydraulic conductivity and thermal conductivity with time at a depth of 4.8 m for Case 1 are shown in Figs. 7(a) and 7(b), respectively, and for Case 2 in Figs. 7(c) and 7(d), respectively. Differing trends for Case 1 and 2 are due to the nonlinear relationships in the SWRC, HCF and TCF. As the seasons continue to transition from summer to winter, the thermal gradient reverses, causing pore water to return to the foundation. However, due to the decreased hydraulic conductivity from the previous summer heating regiment, the initial saturation of the soil will not be fully recovered. As the unsaturated soil nearest the energy pile undergoes further temperature cycling, the process will amplify, resulting in the continuous drying trend observed in Fig. 6.

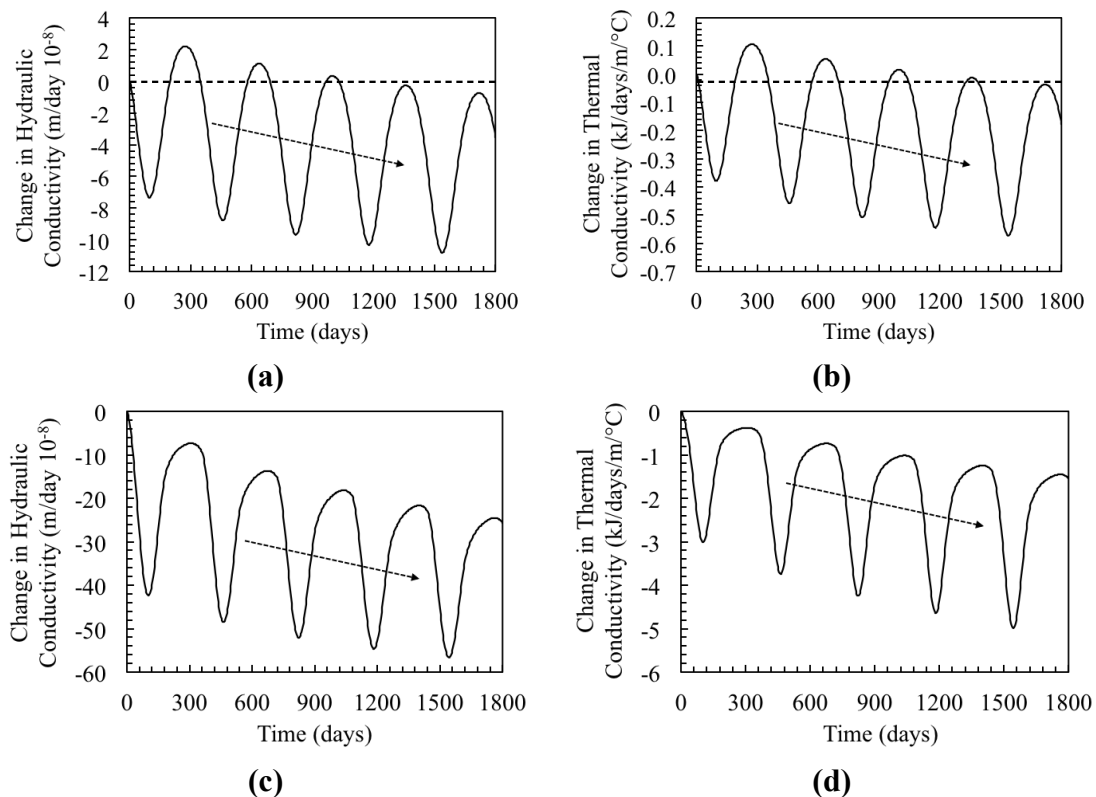


Fig. 7. Variations in Soil Properties at a Depth of 4.8 m: (a) Hydraulic Conductivity for Case 1; (b) Thermal Conductivity for Case 1; (c) Hydraulic Conductivity of Case 2; (d) Thermal Conductivity for Case 2

Decreases in the degree of saturation (and increases in matric suction) will also result in increased effective stress surrounding the energy pile accordingly the Eq. (1). The change in effective stress during the peak summer and winter seasons along the depth of the foundation is shown in Fig. 8 for Cases 1 and 2. The temperature fluctuations in Case 2 led to an increase in effective stress at the head of the foundation that was nearly 10 times greater than that in Case 1. As the water table is fixed at the base, no change in effective stress was observed at this level. Increased effective stresses may result in increased skin friction, resulting in a greater ultimate load capacity with increased temperature. This may explain the increased capacity of energy piles in unsaturated silt observed by Goode and McCartney (2015), but not for energy piles in dry sand. Increases in effective stress may also cause additional settlement, leading to dragdown effects and increased axial stresses in energy piles.

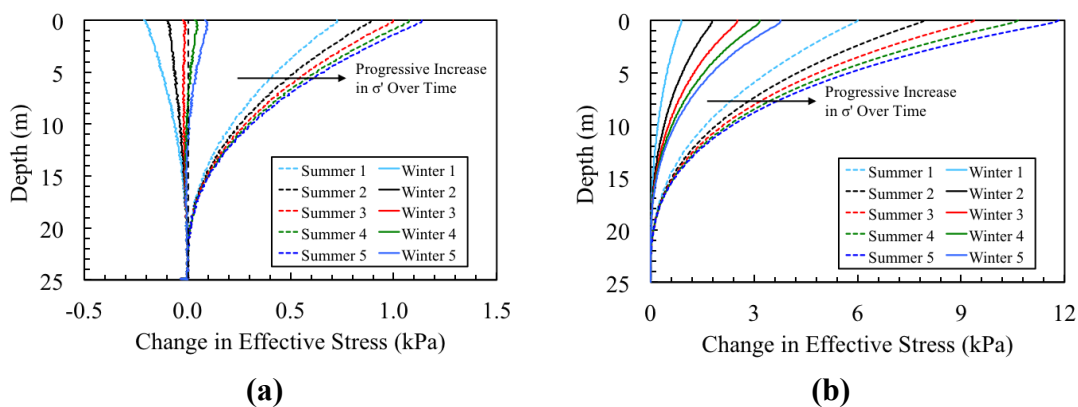


Fig. 8. Changes in Effective Stress with Depth: (a) Case 1; (b) Case 2

5. CONCLUSION

As temperature cycles are applied to energy piles in unsaturated soil layers, a gradual irreversible movement of water may occur away from the energy pile. This irreversible decrease in saturation is attributed to the coupled influences of changes in saturation, hydraulic conductivity, and thermal conductivity, which is exaggerated for higher temperature changes. For an initial degree of saturation of 0.3, the thermal conductivity of the surrounding soil decreased by 0.18 kJ/day/m/°C for Case 1 but decreased by -1.53 kJ/day/m/°C for Case 2. Soils having lower initial degrees of saturation were found to show greater drying and larger changes in hydraulic and thermal conductivity. The effective stresses in the soil around the energy pile will increase with time due to drying, which may be either beneficial or detrimental to the pile depending on the loading conditions. Nonetheless, the changes in soil behavior due to cyclic heating were not significant but be relevant in some situations.

REFERENCES

- Bishop, A.W. (1959). "The Principle of Effective Stress." *Tek. Uke.* 106: 859-863.
 Brandl, H. (2006). "Energy Foundations and other Thermo-Active Ground Structures." *Géotechnique.* 56(2): 81-122.

- Cary, J.W. (1966). "Soil Moisture Transport due to Thermal Gradients: Practical Aspects." *SSSA Journal*. 30(4): 428-433.
- Coccia, C.J.R. and McCartney, J.S. (2013). "Impact of Heat Exchange on the Thermo-hydro-mechanical Response of Reinforced Embankments." *Proc. GeoCongress 2013*. ASCE. San Diego, CA. Mar. 3-5. 343-352.
- Demars, K.R. and Charles, R.D. (1982). "Soil Volume Changes Induced by Temperature Cycling." *Canadian Geotechnical Journal*. 19: 188-194.
- Goode, J.C., III and McCartney, J.S. (2015). "Centrifuge Modeling of Boundary Restraint Effects in Energy Foundations." *Journal of Geotechnical and Geoenvironmental Engineering*. 141(8), 04015034-1-13.
- Johnston, G.H., Ladanyi, B., Morgenstern, N.R. and Penner, E. (1981). "Engineering Characteristics of Frozen and Thawing Soils." *Permafrost Engineering Design and Construction*. John Wiley & Sons. New York, USA. 73-147.
- Khosravi, A. and McCartney, J.S. (2012). "Impact of Hydraulic Hysteresis on the Small-strain Shear modulus of Unsaturated Soils." *JGGE*. 138(11), 1326-1333.
- Laloui, L., Nuth, M. and Vulliet, L. (2006). "Experimental and Numerical Investigations of the Behaviour of a Heat Exchanger Pile." *IJNAMG* 30: 763-781.
- Lu, Y., Wu, X. and Cui, Y. (2010a). "On the Thermo-Mechanical Properties of Unsaturated Soils." *J. of Rock Mech. and Geotech. Eng.* 2(2): 143-148.
- Lu, N., Godt, J. and Wu, D. (2010b). "A Closed-Form Equation for Effective Stress in Unsaturated Soil." *Water Res. Res.* 46, 1-14.
- McCartney, J.S. (2012). "Issues involved in using temperature to improve the mechanical behavior of unsaturated soils." *Proc. 5th Asia-Pacific Unsaturated Soils Conference*. Pattaya, Thailand. 509-514.
- Murphy, K.D. and McCartney, J.S. (2015). "Seasonal response of energy foundations during building operation." *Geotechnical and Geological Eng.* 33(2), 343-356.
- Milly, P.C.D. (1982). "Effects of Thermal Vapor Diffusion on Seasonal Dynamics of Water in the Unsaturated Zone." *Water Res. Res.* 32(3): 509-518.
- Philip, J.R. and de Vries, D.A. (1957). "Moisture Movement in Porous Materials under Temperature Gradients." *Trans. of the Am. Geophys. U.* 38(2): 222-232.
- Smits, K., Sakaki, S.T., Howington, S.E., Peters, J.F., and Illangasekare, T.H. (2013). "Temperature dependence of thermal properties of sands across a wide range of temperatures (30-70 °C)." *Vadose Zone Journal*, doi: 10.2136/vzj2012.0033.
- Thomas, H.R. and He, Y. (1995). "Analysis of Coupled Heat, Moisture, and Air Transfer in a Deformable Unsaturated Soil." *Géotechnique*. 45(4): 677-689.
- Thomas, H.R. and Sansom, M.R. (1995). "Fully Coupled Heat, Moisture, and Air Transfer in an Unsaturated Soil." *Journal of Engineering Mech.* 12(3): 392-405.
- van Genuchten, M.T. (1980). "A Closed Form Equation for Predicting the Hydraulic Conductivity of Unsaturated Soils." *SSSA Journal*. 44: 892-898.
- Wilson, G.W. (1990). *Soil Evaporative Fluxes for Geotechnical Engineering Problems*. Ph.D. Thesis. Dept. of Civil Engineering. University of Saskatchewan.
- Wilson, G.W., Fredlund, D.G. and Barbour, S.L. (1994). "Coupled Soil-Atmosphere Modeling for Soil Evaporation." *Canadian Geotechnical Journal*. 31: 151-161.

Impact of the Seasonal Variations in Ground Temperature on Thermal Response Test Results

Linden Jensen-Page; Guillermo A. Narsilio; Asal Bidarmaghz; and Ian W. Johnston

Infrastructure Engineering, Univ. of Melbourne, VIC 3010, Australia.

Abstract: Due to the prevalent use of the thermal response test (TRT) for estimating the key design parameters of Ground Source Heat Pump systems, it is important to understand how external factors may impact on their accuracy. The infinite line source model (ILSM) is typically used to interpret TRT data, relying on many simplifying assumptions, which when violated may lead to errors in the results. Seasonal variation causes the ground temperature profile to vary significantly at the surface, with decreasing effect at increasing depth, while the ILSM assumes this profile is constant. A numerical study of ILSM performance under different seasonal conditions using a state-of-the-art FE model is presented. The study aims to determine if TRT interpretation may become misleading when tests are conducted at different times of the year. Results suggest there is little variability in effective thermal conductivity, but up to ~50% in GHE thermal resistance, and as much as ~9°C in mean fluid temperature.

INTRODUCTION

As the need to curtail greenhouse gas (GHG) emissions becomes more pressing and energy prices increase, the market for small-scale renewable energy technologies has grown. One such technology is Direct Geothermal, which can provide low GHG emission, energy efficient heating and cooling for buildings (Colls, Johnston & Narsillo 2012). It works by exchanging heat between the air inside a building and water flowing through pipes embedded in trenches, boreholes or foundations (Ground Heat Exchanger, GHE), via a heat pump. This technology presents an efficient and environmentally friendly solution for space conditioning (Lund, Sanner, Rybach, Curtis & Hellstrom 2004).

For larger projects, an in situ Thermal Response Test (TRT) is often conducted. TRT rigs inject heated (or cooled) water at a constant heating rate into a test GHE, while recording the inlet and outlet water temperature response. Analysis of TRT data can lead to estimates of soil thermal conductivity and GHE thermal resistance, usually referred to as borehole resistance, which are then used for designing the remaining unconstructed GHEs. Accurate measurements allow for economical design of GHE length and number (Sanner et al. 2013), as GHE construction encompasses a significant proportion of the cost and complexity of Direct Geothermal projects. It is therefore imperative to understand the shortfalls associated with the interpretation of TRT data.

TRT Data Analysis

One of the most common approaches to TRT data analysis is to implement the Infinite Line Source Model (ILSM), either by linear regression or parameter estimation

through curve fitting (Zhang et al. 2014). The ILSM is based on Kelvin's heat transfer equation and was tailored to model heat transfer in a GHE by Ingersoll & Plass (1948), with Mogensen (1983) first applying it to the problem of back-calculating thermal conductivity from TRT data. This method was shown to be acceptably accurate when all simplifying assumptions are approximately true (Signorelli et al. 2007). Those assumptions are: the surrounding medium is homogenous and isotropic, the line source is infinite and has a constant heat flux per unit length, heat transfer from the source is radial and purely conductive, the initial ground temperature is uniform, and the temperature at an infinite radial distance from the source remains constant (Raymond et al. 2011).

Issues arise when these assumptions are no longer valid, such as in the presence of groundwater flow, a large geothermal gradient, different soil types, or fluctuations in heating rate, easily leading to errors greater than 10% (Signorelli et al. 2007; Wagner et al. 2012; Raymond et al. 2011). More advanced analytical and numerical models exist for approximating GHE behaviour, but the simplicity and generally acceptable performance of the ILSM maintains its popularity and use.

Error in ILSM estimates can come from environmental factors or model error. Environmental factors include measurement error, changes in ambient air temperatures, and fluctuations in the power supply causing variation in the flow rate and heating rate (Witte et al. 2002). Model error is due to violations of the simplifying assumptions listed above or due to processes not described by the model. The consequences of these errors can be significant. Kavanaugh (2000) suggests a 10% error in thermal conductivity estimates can lead to a 5% change in GHE length, while Marcotte & Pasquier (2008) show a 50% overestimation of GHE resistance can lead to a 17% increase in length. Recent numerical analyses suggest inclusion of the ground temperature profile in design of GHEs can lead to a 5% to 10% decrease in length when considering long term (20-30 years) operation (Bidarmaghz et al. 2015, 2016; Kurevija et al. 2011). For large borehole fields, these differences translate into either cost overruns or under/over design.

Therefore, studies addressing the impact of using models whose assumptions deviate from reality on TRT interpretation are still important. This paper will address the violation of the uniform initial temperature assumption due to seasonally forced time and depth fluctuations in ground temperatures.

Ground Temperature Profile: Seasonally Forced Fluctuations

The undisturbed ground temperature ($T_{farfield}$) is a key parameter in most methods used to analyse TRT data. Accurate measurement is crucial for realistic calculation of soil and GHE thermal properties (Gehlin & Nordell, 2003). Even though the ILSM assumes a constant $T_{farfield}$, in reality the ground temperature profile can vary significantly along the length of a GHE. There are three mechanisms for this variation: high local geothermal gradient ($>50^{\circ}\text{C}/\text{km}$), deviation from this due to groundwater flow, and shallow variation due to climate.

While groundwater flow (Wang et al. 2009) and a large geothermal gradient can alter the ground temperature profile leading to overestimation of thermal parameters (Signorelli et al. 2007; Wagner et al. 2012); the authors believe that the impact of the preceding two mechanisms is fairly constant once the GHE is built (i.e. does not change significantly over short to medium time scales). In comparison, the error in effective

thermal properties calculated with the ILSM due to seasonal fluctuations changes cyclically over the year. Geothermal system designs based on values measured in winter may not be suited to how the GHE responds in summer. FIG. 1 exemplifies the fluctuations in the ground temperature profile with season. It shows data gathered at The University of Melbourne (Colls et al. 2012) superimposed with a local predictive model developed by Baggs (1983), which will be used in this paper as a boundary condition to a numerically modelled GHE.

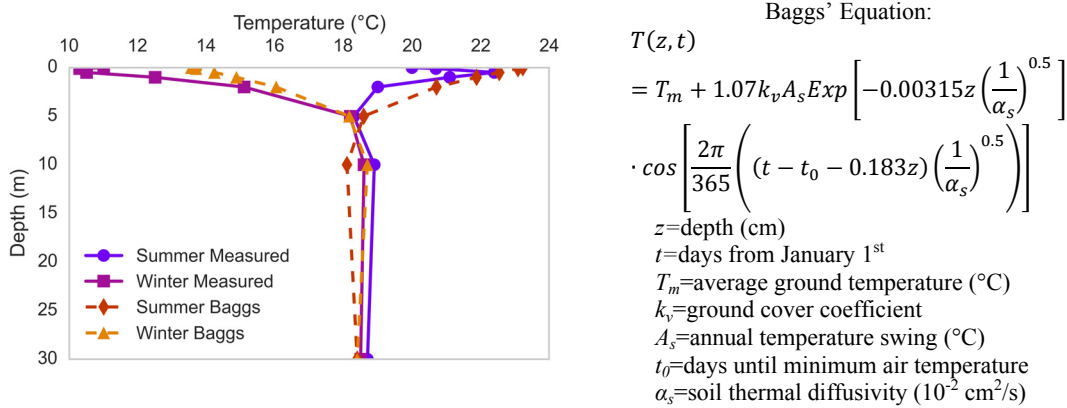


FIG. 1: Measured temperature profiles compared to Baggs’ equation, data from the Beaurepaire Centre, The University of Melbourne (Colls et al. 2012).

METHODOLOGY

To investigate the impact of seasonal variation, several TRT datasets were generated using a detailed 3D numerical GHE model with fully coupled 1D fluid flow built in the Finite Element package COMSOL (a detailed description of the model can be found in Bidarmaghz, 2014). The datasets were then analysed using the ILSM.

Numerical Model

Simulated TRTs were carried out on a grout filled single U-loop GHE of length H placed in a homogenous soil profile. The extents of the soil are defined as far enough from the side and bottom of the GHE ensuring no artificial boundary effects occur, mimicking the conditions required by the ILSM (FIG. 2). The GHE was treated as being at equilibrium with its surroundings. A zero heat flux Neumann boundary was defined at the top and bottom of the model. A constant heating rate of $q = 72 \text{ W/m}$ was applied to the GHE. A varying ground temperature profile was applied as an initial condition (T_i) throughout the model and as a boundary condition ($T_{farfield}$) along the sides of the soil medium, defined by Baggs’ Equation (Baggs 1983). FIG. 2 shows a schematic representation of the numerical model.

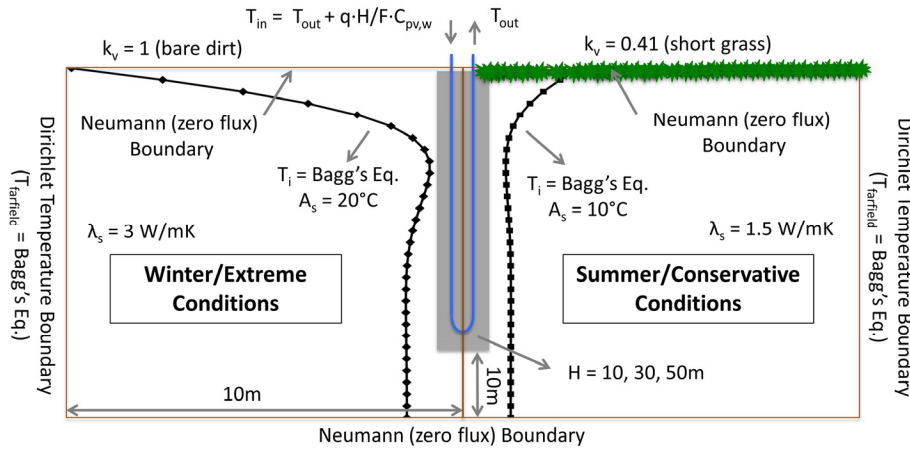


FIG. 2: Schematic of seasonal variation and ground conditions used in the numerical model (not to scale)

Sensitivity Study

In order to define the shape and extent of the variations in ground temperature between seasons, four key parameters were chosen: GHE length (H), soil thermal conductivity (λ_s , which is directly related to α_s in Baggs’ equation), the amplitude of the annual air temperature swing (A_s), and the ground cover coefficient (k_v). Two values were then chosen for each parameter making a **conservative** (con) and **extreme** (ext) set of test conditions. For each set, a summer and winter test was conducted. The starting day of each test was determined by the two measured datasets shown in FIG. 1, with summer starting on day 9 and winter on day 194. A **baseline** test dataset was generated in some cases to show the thermal behaviour of the GHE without the seasonally varying boundary condition (i.e., $T_i = T_{farfield} = \text{constant} = 18.4^\circ\text{C}$).

TABLE No. 1: “Constant” numerical model input parameters and their values

Material	λ W/(mK)	C_p J/(kgK)	ρ kg/m ³	$T_{farfield}$ °C	Diameter m
Soil	1.5; 3	850	2350	18.4 or $T(z,t)$	-
Grout (borehole*)	1.1	1190	2,200	-	0.125
HDPE (pipe ⁺)	0.4	-	-	-	0.02
Water	0.582	4,180	1,000	-	-

λ =thermal conductivity; C_p =heat capacity; ρ =density; *geometry: radius $r_b=0.125\text{m}/2$; pipe spacing=0.04m; borehole length $H=10, 30, 50\text{m}$; ⁺inner diameter=0.017m, wall thickness $t_p=0.0015\text{m}$; average water velocity in the pipe $u_{ave}=0.78 \text{ m/s}$.

An extreme value of $\lambda_s = 3 \text{ W/mK}$ was chosen as it is the upper bound of realistic thermal conductivities of soils and rocks, and $\lambda_s = 1.5 \text{ W/mK}$ is conservative. The amplitude of the annual soil temperature swing is a characteristic of climate at the GHE location. $A_s = 10^\circ\text{C}$ could be considered a temperate climate such as Melbourne, Australia, whereas $A_s = 20^\circ\text{C}$ a cold inland climate. The ground cover coefficient accounts for different surfaces above the GHE. Baggs (1983) considers $k_v = 1$ as bare dirt and $k_v = 0.41$ short grass. GHE lengths of 30m and 50m, while quite short by

international standards, are common in Australia, and 10m was chosen as being an extreme case opposing the ILSM infinite length assumption. The “constant” and variable input parameters for each test can be seen in TABLE No. 1 & TABLE No. 2.

TABLE No. 2: Numerical model parameter values for all testing conditions. Summer and winter tests were conducted for each test condition shown

Test Name	H (m)	λ_s (W/m.K)	A_s (°C)	k_v (-)
baseline	30	3	-	-
con	30	1.5	10	0.41
con $\lambda_s 3$ (Melbourne)	30	3	10	0.41
con kv1	30	1.5	10	1
con As20	30	1.5	20	0.41
con H50	50	1.5	10	0.41
con H10	10	1.5	10	0.41
ext	30	3	20	1
ext $\lambda_s 1.5$	30	1.5	20	1
ext kv0.41	30	3	20	0.41
ext As10	30	3	10	1
ext H50	50	3	20	1
ext H10	10	3	20	1

Analytical Analysis Using the Infinite Line Source Method

Once test data was numerically generated, the ILSM was applied using linear regression to calculate values of thermal conductivity (λ_s) and GHE resistance (R_b). The average of flow and return temperatures T_{mean} was used as the temperature response curve. Linear regression was then applied, from which λ_s is directly calculated from the slope m of the line of best fit (LOBF) to the steady state (late time) region of the T_{mean} curve on a semi-log plot (i.e., T_{mean} vs $\ln(time)$) as $\lambda_s = q/(4\pi m)$ (Beier and Smith 2002). To find R_b , one may evaluate the steady state LOBF of the TRT curve at $T(t_{1hr})$, which is conveniently the intercept in ln-space (Beier and Smith 2002):

$$R_b = \frac{1}{4\pi\lambda_s} \left[\frac{T(t_{1hr}) - T_0}{m} - \ln\left(\frac{4\alpha_s t_{1hr}}{1.78r_b^2}\right) \right] \quad (1)$$

RESULTS

The first step in this investigation was to simulate the GHE discussed in FIG. 1 under winter and summer conditions. This set of parameters is named ‘con $\lambda_s 3$ ’ for its conservative climate conditions but high ground thermal conductivity (TABLE No. 2), which is similar to the conditions encountered in the Silurian mudstone at the University of the Melbourne. The results are shown in FIG. 3.

Each point indicates the value of λ_s and R_b calculated from ILSM linear regressions over a given region on the T_{mean} curve, beginning at the start time shown and ending at the last time point in the dataset (70 hrs). Thus, many regressions were fitted to each

TRT curve over a series of regions with increasing start time, allowing a distribution of possible thermal conductivity and GHE resistance values to be estimated. It is immediately clear that there is little difference in temperature response or soil thermal conductivity, and only a ~3.5% variation in GHE resistance. This is less than previously quoted as being of concern, therefore under these conditions it seems that seasonal variation in ground temperature does not impact on the TRT analysis.

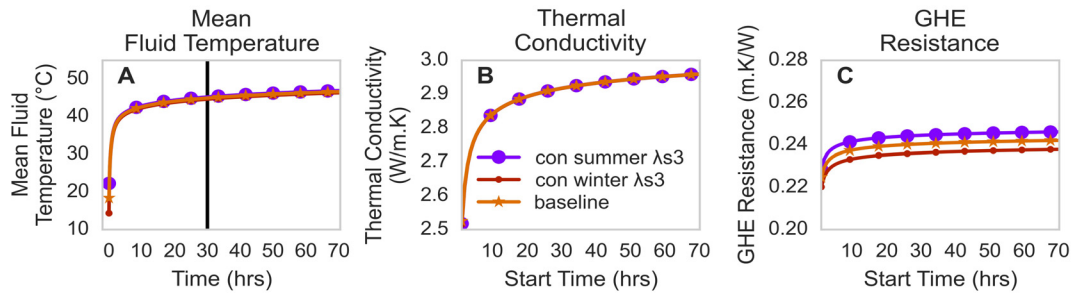


FIG. 3: Results of TRT analysis, con λ_s3 model (Melbourne conditions)

However, the question remains as to when this effect might be large enough to have an impact on GHE design length, leading to the formation of the ‘extreme’ set of test parameters (‘ext’ in TABLE No 1). Results for the ‘extreme’ test on a 30m deep GHE are shown in FIG. 4. Again, there is almost no difference in λ_s , but a greater increase in fluid temperature in summer, and a much higher value of R_b in summer compared to winter of nearly 17%.

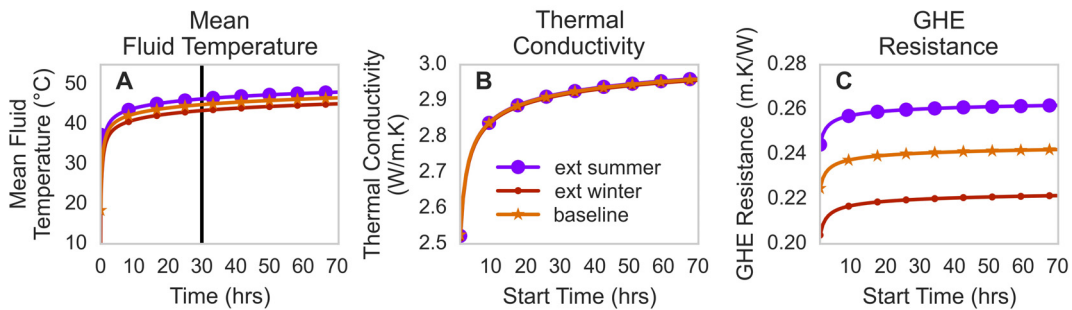


FIG. 4: Results of TRT analysis, ext (H=30m) model

This analysis process was repeated for all tests (TABLE No. 2) with the relative difference in T_{mean} and R_b between summer and winter summarised in FIG. 5. These single value results were calculated from fitting m starting at 30 hours (solid vertical line on FIG. 3A when steady state seems fully reached). The 10m long GHE model shows an increase of nearly 55% in summer compared to winter, which could lead to significant over design of GHE length. However, a 10m GHE is a short, special case, so this result should not be generalised. The difference for the 50m model is a reduced 10% compared to the 10m and 30m models, suggesting that the impact of seasonal variation in ground temperatures decreases with increasing GHE length.

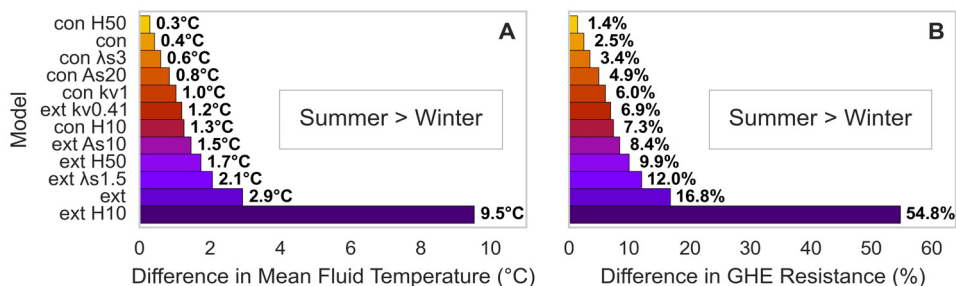


FIG. 5: Difference in T_{mean} (A) and R_b (B) between summer and winter for each set of test conditions.

A comment should also be made on the appropriateness of analysing simulated TRTs with the ILSM. The thermal conductivity curves in FIG. 3B and FIG. 4B show that the starting time used to define the regression region clearly causes variation in ILSM regression results, even in the absence of noisy data. Additionally, the maximum value estimated is less than the 3 W/mK set for the soil thermal conductivity in the COMSOL numerical model. This inaccuracy has been attributed to ILSM model error (Signorelli et al. 2007), where complex effects such as fluid thermal storage and pipe-to-pipe short-circuiting fail to be captured. Therefore, differences in R_b as estimated by the ILSM may include additional variance, and are not necessarily solely due to seasonal variation. This may be especially true for the 10m, where there is likely increased error due to a short GHE length.

Regarding the sensitivity analysis, the difference between seasons for each winter and summer test pair indicates the relative importance of each parameter, with FIG. 5 showing a clear ranking. GHE length is the most important factor, followed by the surface covering above the GHE (k_p). The amplitude of the change in ground temperatures between seasons (A_s) is next, and then finally, the soil thermal conductivity (λ_s) value itself seems to have the smallest impact.

DISCUSSION

The difference in GHE thermal resistance seems to be due to the difference in mean fluid temperature between seasons, as FIG. 5 shows the relative magnitude of T_{mean} and R_b to be the same. This relates to the way in which R_b is calculated with (1), which uses the y-intercept value of T_{mean} when $\ln(\text{time}) = 0$. As the temperature curve moves up the y-axis, the intercept value gets larger, thus giving rise to higher values of GHE thermal resistance.

In terms of the heat transfer mechanisms occurring within the GHE-soil system, higher values of temperature reached during summer tests and corresponding larger thermal resistances are due to decreased thermal gradient between the undisturbed ground temperature profile and fluid temperature. FIG. 6 shows that in winter conditions, the ground temperature close to the surface is much lower than the fluid temperature, resulting in a region of higher thermal gradient and thus heat transfer. In summer, it is the opposite, even to the extent that the initial ground temperature is similar to the fluid temperature in the first 20 minutes of the test, reducing initial heat transfer. This most likely explains the difference in temperature response and GHE thermal resistance between seasons.

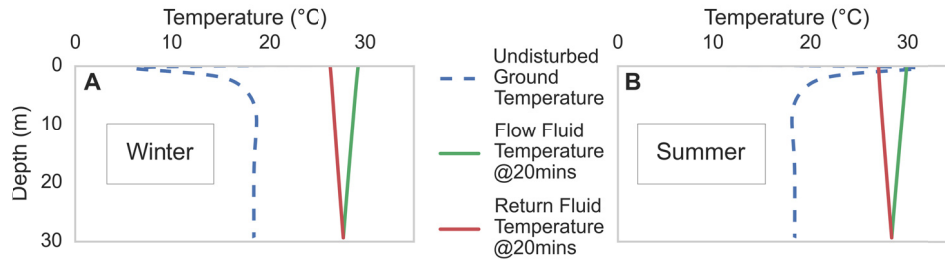


FIG. 6: Ground and fluid temperature profiles with depth for ‘con λ_s3 ’ model (Melbourne Conditions).

The outcome of these observed seasonal differences is that heat transfer conditions in winter are more favourable than in summer. Thus, TRT results collected at the height of winter and used in design could overestimate the thermal efficiency of the GHE, leading to shorter lengths than are required, and an under-performing system. The opposite could occur if the test was carried out in summer, leading to system over-design and unnecessary costs. However, the numerically simulated nature of these data coupled with short GHE lengths and artificially extreme seasonal and soil conditions suggest that, in most cases, the above-described impact on TRT results is unlikely to have a detrimental impact on design.

CONCLUSION

In this paper, the impact of seasonal variation in the ground temperature profile on TRT results analysed with the ILSM has been assessed. Almost no difference in effective thermal conductivity between seasons is observed. However, the difference in mean fluid temperature response seems to give rise to a difference in GHE thermal resistance, but only under extreme conditions.

Higher fluid temperatures are seen in summer compared to winter, which results in larger values of effective GHE thermal resistance in summer conditions of up to 55% for a 10m GHE. This difference decreases with increasing GHE length down to 17% for a 30m GHE and only 10% for 50 metres. This means that winter has more favourable heat transfer conditions, potentially leading to under sized GHEs if those TRT results are used in design. Conversely, designs based on summer results may cause additional cost due to over-sized GHEs. The impact on the design process is unique compared to error caused by other ‘constant’ environmental effects, such as groundwater flow or a large overall geothermal gradient.

However, due to the artificially extreme conditions used to produce these results, in most cases the seasonal influence on TRT analysis using the ILSM would be minimal and no cause for concern. Only when conditions are extreme enough, or there exists multiple sources of error, would such an effect have the potential to cause significant inaccuracies. Nevertheless, to reduce the effects of seasonal fluctuations it is recommended to conduct TRTs in autumn or spring.

ACKNOWLEDGMENTS

The authors appreciate the support of the Australian Research Council (FT140100227), The Victorian Government (DEDJTR, SEPD program) and The University of Melbourne.

REFERENCES

- Baggs, S. (1983). "Remote prediction of ground temperature in Australian soils and mapping its distribution." *Solar Energy*, 30(4), 351–366.
- Beier, R. A., and Smith, M. D. (2002). "Borehole thermal resistance from line-source model of in-situ tests." *ASHRAE Transactions*, American Society of Heating, Refrigeration and Air Conditioning Engineers, Inc., 108(2), 212–219.
- Bidarmaghz, A. (2014). "3D numerical modelling of vertical ground heat exchangers." PhD Thesis. The University of Melbourne.
- Bidarmaghz, A., Narsilio, G. A., and Johnston, I. W. (2013). "Numerical Modelling of Ground Heat Exchangers with Different Ground Loop Configurations for Direct Geothermal Applications." *Aust Geomechanics*, 47(4), 15–20.
- Bidarmaghz, A., Narsilio, G. A., and Johnston, I. W. (2015). "Effects of Surface Air Temperature on Thermal Performance of Vertical Ground Heat Exchangers." *Proceedings of the 1st International Symposium on Energy Geotechnics - SEG2015*, M. Sanchez, E. Romero, A. Gens, and S. Olivella, eds., Barcelona, Spain, 2-4 June 2015.
- Bidarmaghz, A., Narsilio, G. A., Johnston, I. W., and Colls, S. (2016). "The Importance of Surface Air Temperature Fluctuations on Long-term Performance of Vertical Ground Heat Exchangers." *Geomechanics for Energy and the Environment*, Under Review.
- Colls, S., Johnston, I., and Narsilio, G. (2012). "Experimental study of ground energy systems in Melbourne, Australia." *Aust Geomechanics*, 47(4), 15–20.
- Gehlin, S. E. A., and Nordell, B. (2003). "Determining undisturbed ground temperature for thermal response test." *Transactions-American society of heating refrigerating and air conditioning engineers*, ASHRAE; 1999, 109(1), 151–156.
- Ingersoll, L. R., and Plass, H. J. (1948). "Theory of the ground pipe heat source for the heat pump." *ASHVE Transactions*, 47(7), 339–348.
- Kavanaugh, S. P. (2000). "Field tests for ground thermal properties - methods and impact on ground-source heat pump design." *ASHRAE Transactions*, ASHREA, 106.
- Kurevija, T., Vulin, D., and Krapec, V. (2011). "Influence of undisturbed ground temperature and geothermal gradient on the sizing of borehole heat exchangers." *Proceedings of World Renewable Energy Congress, Linköping, Sweden*, 8–13.
- Lund, J., Sanner, B., Rybach, L., Curtis, R., and Hellström, G. (2004). "Geothermal (Ground-Source) Heat Pumps: A World Overview." *GHC Bulletin*, 1–10.
- Marcotte, D., and Pasquier, P. (2008). "On the estimation of thermal resistance in borehole thermal conductivity test." *Renewable Energy*, 33(11), 2407–2415.
- Mogensen, P. (1983). "Fluid to Duct Wall Heat Transfer in Duct System Heat Storage." *Proc. Int. Conf. On Subsurface Heat Storage in Theory and Practice*, Swedish Council for Building Research, 652–657.

- Raymond, J., Therrien, R., Gosselin, L., and Lefebvre, R. (2011). "Numerical analysis of thermal response tests with a groundwater flow and heat transfer model." *Renewable Energy*, Elsevier Ltd, 36(1), 315–324.
- Sanner, B., Hellström, G., Spitler, J., and Gehlin, S. (2013). "More than 15 years of mobile Thermal Response Test—a summary of experiences and prospects." *Proc European Geothermal Congress, Pisa, Italy, 3rd-7th June*.
- Signorelli, S., Bassetti, S., Pahud, D., and Kohl, T. (2007). "Numerical evaluation of thermal response tests." *Geothermics*, 36(2), 141–166.
- Wagner, V., Bayer, P., Kübert, M., and Blum, P. (2012). "Numerical sensitivity study of thermal response tests." *Renewable Energy*, Elsevier Ltd, 41, 245–253.
- Wang, H., Qi, C., Du, H., and Gu, J. (2009). "Thermal performance of borehole heat exchanger under groundwater flow: A case study from Baoding." *Energy and Buildings*, 41(12), 1368–1373.
- Witte, H. J. L., Van Gelder, G. J., and Spitler, J. D. (2002). "In situ measurement of ground thermal conductivity: a Dutch perspective." *Ashrae Transactions*, 108(1), 263–272.
- Zhang, C., Guo, Z., Liu, Y., Cong, X., and Peng, D. (2014). "A review on thermal response test of ground-coupled heat pump systems." *Renewable and Sustainable Energy Reviews*, 40, 851–867.

Impact of Temperature Variations on the Hydro-Mechanical Parameters of a Sensitive Soil

Hossein Eslami^{1,2}; Sandrine Rosin¹; Adel Abdallah¹; and Farimah Masrouri¹

¹LEMETA (CNRS, UMR 7563), Université de Lorraine, Vandœuvre-lès-Nancy, France.

²ESITC de Metz, Metz, France.

Abstract: The incorporation of heat exchangers in geostructures produces a cyclic variation of the temperature in the adjacent soil. Therefore, there are important questions about the effect of temperature variations on hydro-mechanical soil parameters. In this study, mini-pressuremeter tests were conducted in laboratory on a homogeneous material submitted to different thermal loading (1 to 40°C). The tested material, an illitic soil, is compacted in a thermo-regulated container with 0.6 m diameter and 0.8 m height, at optimal water content (31.3%) and 90% of maximum dry density (1.29 Mg/m³). Only six tests are performed in each container to prevent edge effects and the influence between the tests. The impact of temperature variation on creep pressure (p_f), limit pressure (p_l) and pressuremeter modulus (E_p) were determined. A decrease in creep pressure and limit pressure with increasing temperature was observed, while the variation of pressuremeter modulus was less pronounced. The first cycle induced more important parameter variations than the subsequent cycles.

INTRODUCTION

The incorporation of heat exchangers in geostructures leads to a temperature variation in the adjacent soil over a range from 4 to 30 °C (Knellwolf et al., 2011). Consequently, there are important questions about the effect of temperature variations on hydro-mechanical soil properties and load transfer in the pile.

In the case of energy piles, on one hand, the thermal expansion or contraction causes additional thermal stresses in the pile, which can influence the skin friction and end bearing and consequently the load transfer (Bourne-Webb et al., 2013; Olgun et al., 2015). On the other hand, the cyclic thermal variation of the soil may affect its hydro-mechanical properties. Thus, the behavior of an energy pile is directly related to the coupling of thermal, hydraulic and mechanical phenomena.

Various studies on the behavior of energy piles and their thermo-mechanical response have been conducted in-situ (Laloui et al., 2003; Bourne-Webb et al., 2009; Akrouch et al., 2014; Murphy and McCartney, 2015) and in the laboratory (Stewart and McCartney, 2013; Tang et al., 2013). All these studies have focused on pile behaviour. The effect of temperature variations on the soil parameters has been neglected despite the potentially important effect of cyclic temperature variations on shear strength, yielding and critical-state soil properties. In particular, the contraction of the elastic domain (i.e., the yield locus) with increasing temperature has been demonstrated for various clay materials (Hueckel and Baldi 1990; Tanaka et al., 1997; Graham et al., 2001; Cekerevac and Laloui 2004; Marques et al., 2004; Uchaipichat and Khalili 2009). The calculation of the bearing capacity of deep foundations is actually based on pressuremeter or/and penetrometer test results (AFNOR, 2012). Eslami et al. (2015) studied the effect of temperature variation on penetration test parameters in two compacted soils. However, no data are available on the effect of temperature on pressuremeter parameters. In this study, the mini-pressuremeter tests were conducted in laboratory on a soil submitted to different thermal loading (1 to 40 °C) to quantify the temperature effect on the mechanical behavior of the soil.

In the following sections, the material and the developed experimental device are first described. Then, the results are detailed and the impact of thermal variations on the pressuremeter parameters is discussed.

MATERIAL AND METHOD

In this part, the studied material is first presented, then experimental device is described and finally the mini-pressuremeter tests are detailed.

Basic characterization of the material

The tested material is an illitic soil named Arginotech® that contains 77% illite, 10% kaolinite, 12% calcite and traces of quartz and feldspar according to the furnisher. Mini-penetration tests, conducted on this soil by Eslami et al. (2015) showed the sensitivity of this material to temperature variations.

The particle-size distribution of the soil was determined using a laser Malvern Mastersizer 2000® device (Figure 1a). Almost 85% of the particles of the illitic material are smaller than 0.002 mm (clay particles). The liquid limit (LL), plastic limit (PL) and plasticity index (PI) are 65%, 34%, and 31% respectively (AFNOR, 1993). A optimum water content of 31.3% and a maximum dry density of 1.43 Mg/m³ are obtained from the standard Proctor curve for the material (AFNOR, 1999) (Figure 1b).

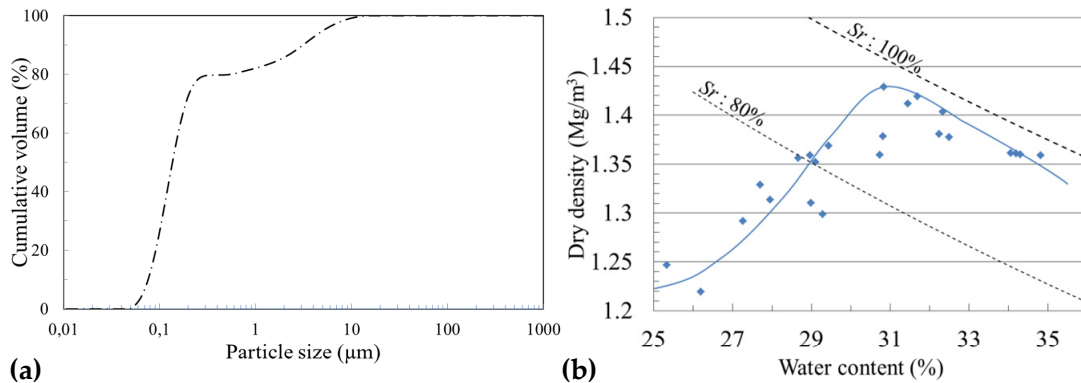


FIG. 1. Characteristic of the studied illitic soil: a) particle size distribution and b) Compaction curve, S_r : The degree of saturation.

Experimental device and methods

To perform mini-pressurimeter tests under controlled temperature, a homogeneous massif with a large volume is required as well as an experimental device to impose thermal variations to the massif. In this part, the developed methodology to obtain a meter-scale sample with homogeneous properties (temperature, water content and dry density) is described.

First, the required amount of water was added to the material ($w_{initial} \approx 17\%$) in a large capacity fixed-speed (38 rpm) mixer (MIX120®) to reach the target water content: $w_{OPN} = 31.3\%$. The wet material is stored in 8 plastic drums for a minimum of 5 days to ensure good homogenization. A pneumatic compactor is used to compact the material in a cylindrical stainless steel container of 800 mm in height and 600 mm in diameter (Figure 2a). The compactor applied dynamic forces on a metallic plate of 4 mm in thick and 600 mm in diameter to facilitate a homogeneous compaction of the soil. The results of the preliminary series lead to the choice of a compaction in 11 70-mm-thick layers.

A stainless steel tube welded to the outside of the container was connected to a Vulcatherm® thermoregulator to facilitate the circulation of an ethylene glycol-water solution at the target temperature (-20 to 90 °C) in the tube. Thus, the soil compacted in the container is heated or cooled by the container's outer lateral surface. Insulating sleeves were placed around the tube to reduce the heat exchange with the surrounding atmosphere. The top of the massif was insulated with a plastic film to preserve the initial water content. Finally, the entire device was placed in a box constructed of 40-mm-thick extruded polystyrene plates to reinforce the insulation. Figure 2b shows the total parts of the developed experimental device in order to perform the mini-pressurimeter tests.

Seven thermal sensors PT100 are positioned within the massif at various depths and various distances from the wall of the container. The sensors are plugged to a data logger in order to monitor the temperature evolution inside the compacted soil during the temperature variations.

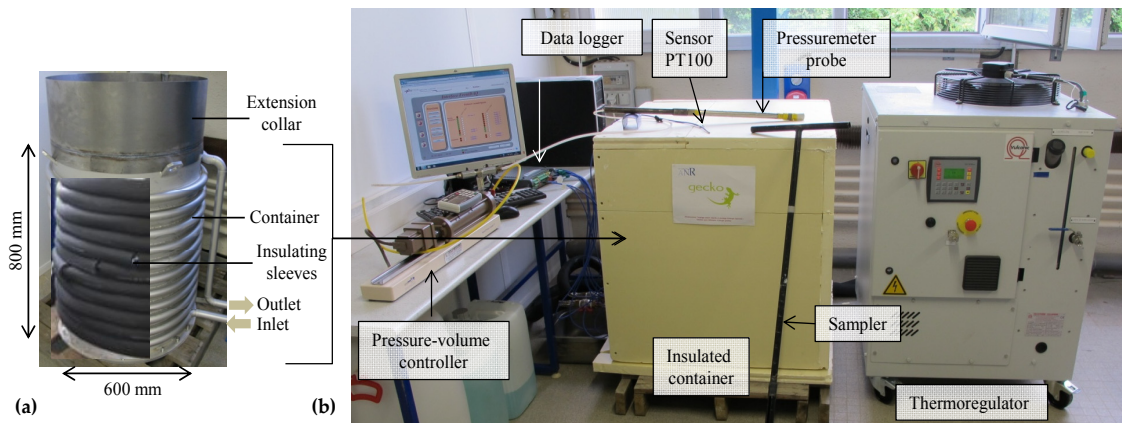


FIG. 2. (a) Thermo-regulated metric scale container; (b) Total parts of developed experimental device.

Mini-pressuremeter tests

The principle of a pressuremeter test is to introduce a cylindrical probe with a flexible cover membrane which can expand radially in a hole (AFNOR, 2000; ASTM, 2007). The pressuremeter test is realized in 3 steps: (i) the probe inflates to obtain the contact with the wall of the hole, (ii) the volume increases linearly with the increasing pressure allowing the calculation of the pressuremeter modulus E_M (the soil pseudo-elastic reaction versus the probe pressure) and (iii) the large displacements take place and the soil becomes plastic. The creep pressure, p_f is the boundary between the second and the third steps of the test. The limit pressure p_l is the measured pressure when the injected volume reaches twice the original volume of the cavity.

Only six mini-pressuremeter tests were performed in each massif to prevent edge effects and cross-influence between the tests. The test points were positioned on a concentric circle with a diameter half that of the container (Figure 3). All the test points were located at the same radial position to allow a comparison of the results. The pressuremeter tests were conducted with an APAGEO® mini-pressuremeter probe of 380 mm in height and 28 mm in diameter. Before each pressuremeter test, a core with a diameter equal to that of the mini-pressuremeter probe was extracted using a core sampler. The 630-mm-length core was divided into small pieces to measure the water content and density of the material as a function of depth. The center of the probe was positioned halfway along the height of the compacted soil (385 mm). The probe was connected to a GDS® pressure-volume controller. The pressure controlled test consisted in applying increasing pressure with equal increments of 25 kPa for at least one minute per step. The equilibrium volume was measured for each increment and the volume was plotted as a function of pressure. The test was stopped when the injected volume (i.e., the volume variation limit of the probe) reached 140,000 mm³. Immediately after the pressuremeter test at a given temperature, the borehole was filled with the same material, at the same water content, to avoid influencing the later tests. The effect of temperature variations on the resistance of the mini-pressuremeter membrane was measured by

placing the probe in a climatic chamber at a given temperature during the calibration test of the membrane resistance.

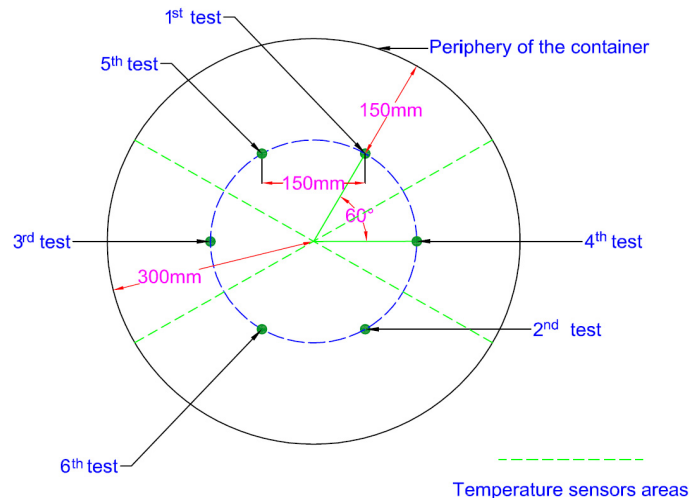


FIG. 3. Positions of the test points.

RESULTS

In the framework of this study, a preliminary series and four test series, with six mini-pressurimeter tests for each series, were conducted. In this paper only the two last test series, which aimed to quantify the effect of a cyclic thermal variation on the pressurimeter parameters, are presented. The tests performed on each sample were numbered as “Xx”, where X is the massif temperature used in the test (i.e., 1, 20 or 40 °C) and x is a letter indexing the test that increments for each new test conducted at the same temperature.

The results of the preliminary test series indicated that the tests had good repeatability and facilitated the estimation of the uncertainty of each parameter according to the Student's t-distribution (because of the limited number of measurements) for a 90% confidence interval: $E_p: \pm 10\%$, $p_f: \pm 5\%$, $p_i: \pm 5\%$.

The selected test series, named series I and series II, consisted in tests at 20, 1 and 40 °C. The initial temperature of the massif was 20 °C and the massif was successively brought to 1 and 40 °C, each step lasted at least 70 hours (Figure 4 and Figure 5). The thermal equilibrium was reached for each step before performing the mini-pressurimeter test.

Table 1 and Table 2 present all the obtained parameters and properties. The average water content and the average dry density variations according to the temperature change were lower than 1%: the massifs were homogeneous.

The mini-pressurimeter tests were conducted at the end of the selected steps as shown in the Figure 4 and Figure 5. The pressurimeter curves (Figure 6) were consistent with the classical pressurimeter results. Considering the length of the 2nd step of the pressurimeter curve, one can conclude that a softening occurred upon heating to 40 °C and a hardening was observed upon cooling to 1 °C, regardless of testing order.

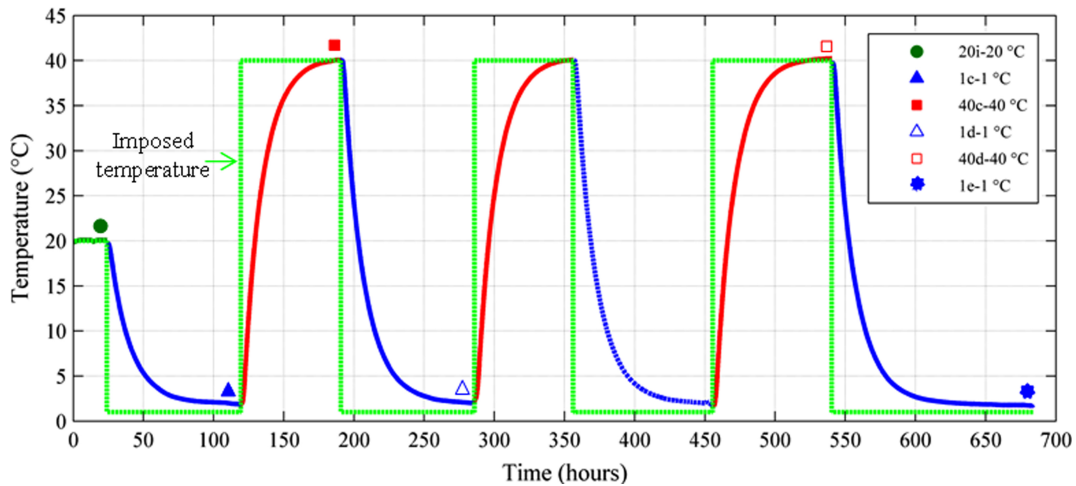


FIG. 4. Temperature variation at 150 mm from the edge of the massif (lines) and the chronology of the pressuremeter tests (points) for series I.

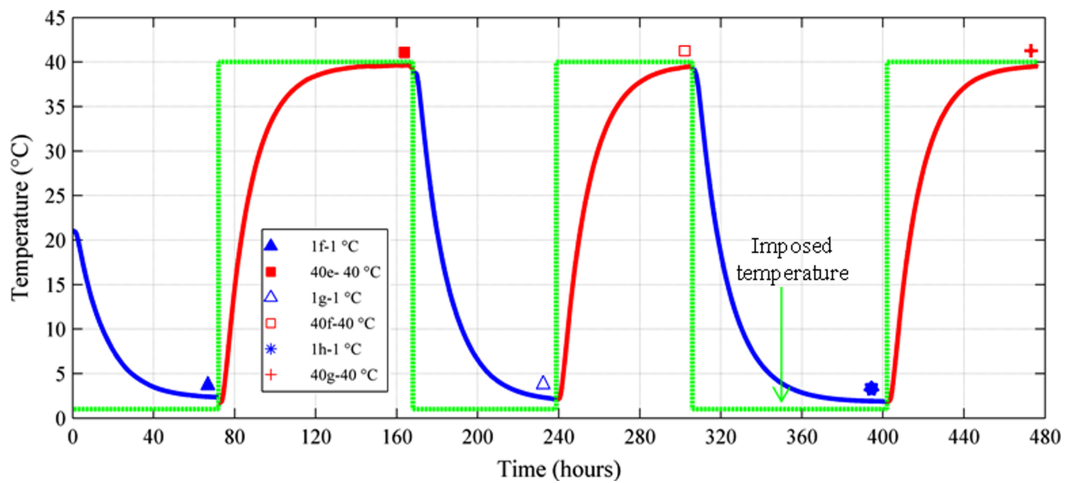


FIG. 5. Temperature variation at 150 mm from the edge of the massif and the chronology of the pressuremeter tests (points) for series II.

Table 1. Pressuremeter parameters for the series I: temperature cycling (20-1-40-1-40-1-40-1 °C).

Test	Temperature (°C)	w (%)	ρ_d (Mg/m ³)	p_f (kPa)	p_l (kPa)	E_p (MPa)
20i	20	31.4	1.25	103	240	5.51
1c	1	31.4	1.26	124	303	5.73
40c	40	32.1	1.25	125	236	7.68
1d	1	31.7	1.25	123	337	4.16
40d	40	31.5	1.28	143	270	6.85
1e	1	31.6	1.24	133	310	5.66

Table 2. Pressuremeter parameters for the series II: temperature cycling (20-1-40-1-40-1-40 °C).

Test	Temperature (°C)	w (%)	ρ_d (Mg/m ³)	p_f (kPa)	p_l (kPa)	E_p (MPa)
40e	40	31.2	1.30	174	305	6.24
1g	1	31.5	1.24	170	357	6.97
40f	40	31.2	1.28	170	307	6.18
1h	1	31.0	1.24	160	344	6.16
40g	40	31.1	1.25	153	276	5.76

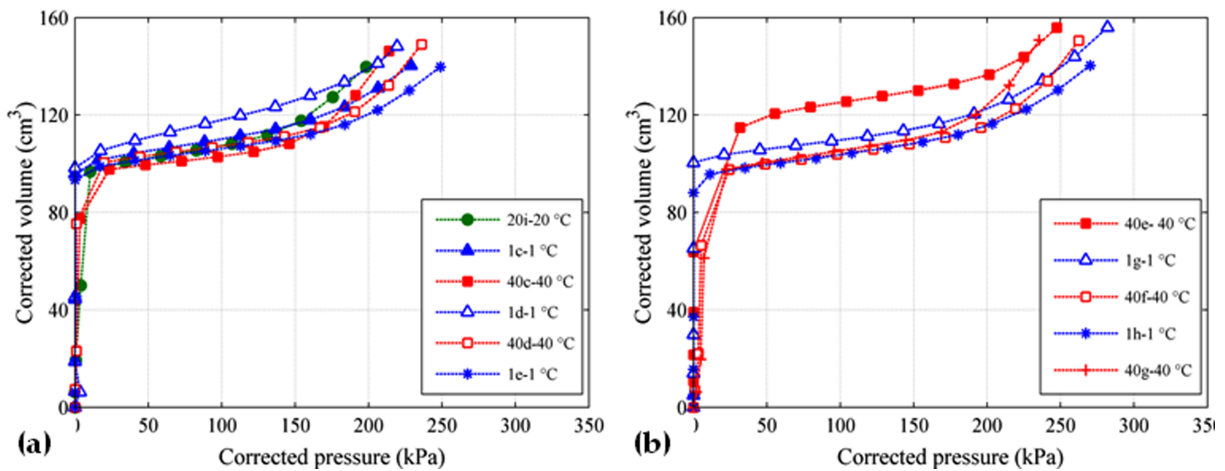


FIG. 6. Pressuremeter curves: (a) series I; (b) series II.

The pressuremeter parameters were calculated for each step of each series and presented in Figure 7. In series I, p_f increased slightly with cooling the massif from 20 to 1 °C, The value of p_f then remained nearly constant over the subsequent heating/cooling cycles (1-40-1 °C). The p_l values increased with heating and decreased with cooling. In series II, the first value at 20 °C was invalid; in Figure 7, the corresponding values were estimated by assuming similarity between series I and series II.

The parameters evolutions from these two series are comparable. After the first thermal cycle, the variation of p_f with temperature decreased within the parameter uncertainty domain, and this parameter reached a stable value (Figure 7a, b). Meanwhile, the evolution of p_l differed from that of p_f . The temperature impact remained measurable as well as completely reversible. Its change rate could be estimated at 1.5 kPa/°C in the studied temperature range (1-40 °C) (Figure 7c, d). These results are consistent with the contraction of the elastic domain (yield locus) with increasing temperature shown in the literature with oedometer or triaxial tests for various clay materials (Hueckel and Baldi 1990; Tanaka et al., 1997; Graham et al., 2001; Cekerevac and Laloui 2004; Marques et al., 2004; Uchaipichat and Khalili 2009).

The variation of E_p with temperature was lower than the other pressuremeter parameters (Figure 7e, f). The E_p evolution for series I was erratic. In contrast, a slight E_p decrease, which was consistent with the previous tests, was measured when the massif was heated.

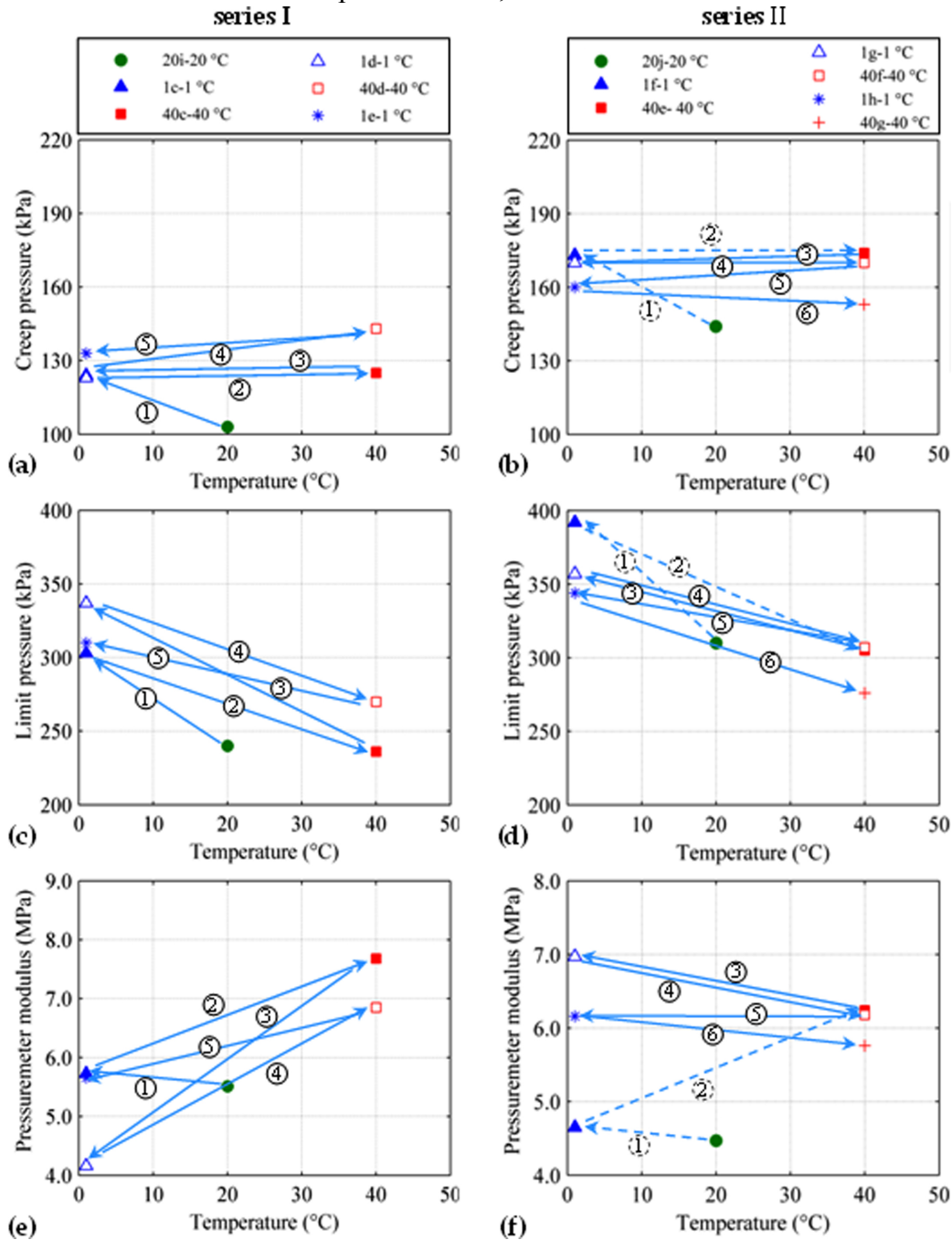


Figure 7. Variation of creep pressure (p_f) (a-b), limit pressure (p_l) (c-d) and pressuremeter modulus (E_p) (e-f) with temperature for series I and II. Dotted lines correspond to estimated parameters.

CONCLUSIONS

The objective of this paper was to quantify the effect of cyclic temperature variations on parameters linked to the pile design. A protocol allowing the realization of mini-pressuremeter test in laboratory conditions was developed. The evolution of the pressuremeter modulus (E_p), the creep pressure (p_f) and the limit pressure (p_l) was measured under imposed thermal conditions on a clayey compacted soil selected for its high sensitivity to temperature variations.

The results of the mini-pressuremeter tests on the compacted illitic soil showed a decrease in the creep pressure and the limit pressure as temperature increased (thermal softening), while the variation of the pressuremeter modulus was less significant, possibly due to the variability of this parameter, which is known to be high. For the following cycles, the effect of the temperature variation was lower. After more than one cycle, p_f seemed to reach an equilibrium value independent of the temperature. The p_l kept its temperature dependence beyond the 1st cycle but its evolution was reversible and the evolution rate was 1.5 kPa/°C in the studied temperature range (1- 40 °C).

The limit pressure is the key parameter in the calculation of the ultimate load of piles. Therefore, the variation of the limit pressure with temperature should be considered when estimating the bearing capacity of geothermal piles, particularly when constructed in temperature-sensitive soils.

ACKNOWLEDGEMENTS

This study was part of the GECKO research program funded by ANR.

REFERENCES

- AFNOR, NF P94-051 (1993). "Soil : investigation and testing. Determination of Atterberg's limits. Liquid limit test using cassagrande apparatus. Plastic limit test on rolled thread." Paris, France: Association Française de Normalisation, p. 15.
- AFNOR, NF P94-093 (1999). "Soils : investigation and testing - Determination of the compaction reference values of a soil type - Standard proctor test - Modified proctor test." Paris, France: Association Française de Normalisation, p. 18.
- AFNOR, NF P94-110-1 (2000). "Soil : investigation and testing - Menard pressure meter test - Part 1 : test without unload-reload cycle." Paris, France: Association Française de Normalisation, p. 42.
- AFNOR, NF P94-262 (2012). "Justification of geotechnical work – National application standards for the implementation of Eurocode 7 – Deep foundations." Paris, France: Association Française de Normalisation, p. 206.
- ASTM D4719-07 (2007). "Standard Test Methods for Prebored Pressuremeter Testing in Soils." ASTM International, West Conshohocken, PA www.ASTM.org, p. 10.
- Akrouch, G. A., Sánchez, M., and Briaud, J. L. (2014). "Thermo-mechanical behavior of energy piles in high plasticity clays." *Acta Geotechnica*, Vol. 9(3): 399–412.

- Bourne-Webb, P. J., Amatya, B., Soga, K., Amis, T., Davidson, C., and Payne, P. (2009). "Energy pile test at Lambeth College, London: geotechnical and thermodynamic aspects of pile response to heat cycles." *Géotechnique*, Vol. 59 (3): 237–248.
- Bourne-Webb, P. J., Soga K., and Amatya, B. (2013). "A framework for understanding energy pile behaviour." *Geotech. Eng.*, Vol. 166 (2): 170–177.
- Cekerevac, C., and Laloui, L. (2004). "Experimental study of thermal effects on the mechanical behaviour of a clay." *Int. J. Numer. Anal. Methods Geomech.*, Vol. 28(3): 209–228.
- Eslami, H., Rosin-Paumier, S., Abdallah, A., and Masrouri, F. (2015). "Impact of temperature variation on penetration test parameters in compacted soils." *Eur. J. Environ. Civ. Eng.*, Vol. 19(5): 628-648.
- Graham, J., Tanaka, N., Crilly, T., and Alfaro, M. (2001). "Modified Cam-Clay modelling of temperature effects in clays." *Can. Geotech. J.*, Vol. 38(3): 608–621.
- Hueckel, T., and Baldi, G. (1990). "Thermoplasticity of saturated clays: experimental constitutive study." *J. Geotech. Eng.*, Vol. 116(12): 1778–1796.
- Knellwolf, C., Peron, H. and Laloui, L. (2011). "Geotechnical Analysis of Heat Exchanger Piles." *J. Geotech. & Geoenv. Eng.*, Vol 137(10): 890-902
- Laloui, L., Moreni, M., and Vulliet, L. (2003). "Comportement d'un pieu bi-fonction, fondation et échangeur de chaleur." *Can. Geotech. J.*, Vol. 40(2): 388–402.
- Marques, M. E. S., Leroueil, S., and Soares de Almeida, M. D. S. (2004). "Viscous behaviour of St-Roch-de-l'Achigan clay, Quebec." *Can. Geotech. J.*, Vol. 41(1): 25–38.
- Murphy, K. D., McCartney, J. S. (2015). "Seasonal response of energy foundations during building operation." *Geotech Geol Eng.* Vol 33: 343–356.
- Olgun, C. G., Ozudogru, T. Y., and Arson, C. F. (2014). "Thermo-mechanical radial expansion of heat exchanger piles and possible effects on contact pressures at pile-soil interface" *Geotech. Lett.*, Vol. 4: 170-178.
- Stewart, M.A., and McCartney, J.S. (2013). "Centrifuge Modeling of Soil-Structure Interaction in Energy Foundations." *J. Geotech. & Geoenv. Eng.*, Vol 140(4).
- Tanaka, N., Graham, J., and Crilly, T. (1997). "Stress-strain behaviour of reconstituted illitic clay at different temperatures." *Eng. Geol.*, Vol. 47(4): 339–350.
- Tang, A. M., Pereira, J. M., Hassen, G., and Yavari, N. (2013). "Behavior of Heat-Exchanger Piles from Physical Modeling." *Energy Geostructures*, 79–97.
- Uchaipichat, A., and Khalili, N. (2009). "Experimental investigation of thermo-hydro-mechanical behaviour of an unsaturated silt." *Géotechnique*, vol. 59(4): 339–353.

Large-Scale Thermo-Hydrodynamic Modeling of a Flooded Underground Mine for Geothermal Applications

Ting Bao¹ and Zhen (Leo) Liu²

¹Graduate Assistant, Dept. of Civil and Environmental Engineering, Michigan Technological Univ., 1400 Townsend Dr., Dow 854, Houghton, MI 49931. E-mail: tbao@mtu.edu

²Assistant Professor, Dept. of Civil and Environmental Engineering, Michigan Technological Univ., 1400 Townsend Dr., Dillman 201F, Houghton, MI 49931 (corresponding author). E-mail: zhenl@mtu.edu

Abstract: The concept of recovering geothermal energy from water in abandoned underground mines has been gaining momentum worldwide in recent years. This is possibly because mine water and surrounding geologic formations can be used for a higher-grade geothermal reservoir than other low-enthalpy geothermal applications. However, the scientific understanding of this application is still in a preliminary stage, leading to a limited number of detailed numerical simulations involving both hydrodynamics and physical process in porous materials. This paper pioneers large-scale hydrodynamics modeling of mine water coupled with heat transfer between mine water and surrounding geologic formations for geothermal applications. For this purpose, a numerical model was implemented and validated against documented experiments. Based on that, a representative case was simulated to shed light on the question regarding how the buoyancy-driven flow is triggered and maintained by the temperature difference that results from the geothermal gradient.

INTRODUCTION

Geothermal energy is one of the alternative energy sources, which provides green and relatively renewable energy for human demands to make the world towards global energy sustainability (Rybach 2003; Lund et al. 2005). One of the attractive applications using geothermal energy is electric power generation considering its advantages such as environment-friendliness and cost-competitiveness over conventional sources of energy (Milora and Tester 1977). Exploring geothermal for the electric power generation needs specific qualifications such as a very high enthalpy fluid or vapor; as a result, only a few countries (24 more or less) can generate electricity by employing geothermal resources (Bertani 2012). Another direct use of geothermal is to heat or cool buildings using geothermal heat pumps (Self et al. 2013). Such apparatus can transfer heat from a low enthalpy source to a high enthalpy fluid via the fluid circulation in heat pumps to boost efficiency for heating /cooling buildings. This type of geothermal application has to drill to access a location of heat stored in the geothermal fields, which is only capable of implementing the extraction of energy from specific areas of the Earth due to economic and technical concerns.

Underground mining is activated in almost every country and a great number of underground mines in numerous counties were closed and abandoned in the past years, many of which were flooded with water after closure (Ramos et al. 2015). Due to this reason, an interesting and valuable question has been proposed that “Can we take the heat

from those abandoned and flooded mines for human demands?" Mine water heated by the Earth's geothermal energy can run through a heat exchanger for humanity's energy needs, which could be an economical, reliable, and environmental option for exploring geothermal energy. Practical attempts have been made to answer this question. A realistic case of using mine water as a large reservoir of heat in Canada was evaluated, and the results of this study confirmed that extraction of energy from mine water in underground mines beneath the community was not only feasible to heat or cool commercial buildings, but also environmental for atmosphere due to a reduction in carbon dioxide emissions (Jessop 1995; Allen et al. 2000). Observations from more investigations also proved that water in closed mines contains a great reserve of geothermal energy (10-50°C) such as in Poland (Malolepszy 2003), Netherlands (Bazargan et al. 2008), Germany (Wieber and Pohl 2008), and Spain (Loredo et al. 2011). Additional efforts have been made on the estimate of thermal output and mine water temperature recovery (Wieber and Pohl 2008), a typical investment and corresponding economic paybacks (Raymond et al. 2008), effective and suitable geothermal energy recovery systems (Hall et al. 2011), effective velocities of mine water (Hasche-Berger 2013), possible environmental impacts (Preene and Younger 2014), and a methodology for implementing mine water-based geothermal heat recovery (Ramos et al. 2015).

The scientific understanding of this topic far lags behind its implementation. Though not extensively, numerical simulations have been adopted to understand the underlying mechanisms. Hamm and Sabet (2010) modeled the hydraulic behavior of the mine reservoir and mine water temperature in a production shaft and revealed the impact of natural convection, the production flow rate, and the permeability of the surrounding rocks on the geothermal potential for exploitations. More efforts are made with the emphasis on critical issues, including the state-of-art challenges of numerical modeling of mine water for geothermal applications (Renz et al. 2009), the locality for extracting the mine water at a required temperature without causing a decrease in the potential of the discharge (Streb and Wieber 2011), and the lifespan of the required temperature supply from mine water (Arias et al. 2014). However, it is still a great challenge to model a flooded underground mine for geothermal energy recovery because of the multiphysical phenomena involved in the process, more specifically, a thermo-hydro-diffuso-chemico-mechanical problem (Liu et al. 2015). This study pioneers a fully coupled 3D model based upon the Finite Volume Element (FVM) to numerically solve the coupled multiphysical processes in the mine water-surrounding geologic formations system, with an aim at understanding natural convection in mine water. The FVM model was validated against documented experiments. Thermo-hydrodynamic modeling of a typical inclined and flooded underground mine shaft in the Upper Peninsula (U.P.) in Michigan was developed to shed light on the primary physical mechanisms underneath the geothermal application using mine water.

3D MODEL DEVELOPMENT

The governing equations of the system involving a multiphysical process are presented in this section. The thermo-hydrodynamic system includes transient natural convective motion of water and heat transfer in the system to describe this multiphysical process. For the natural convective motion of a fluid, the mass of a moving fluid element is conserved by applying the constitutive equation to this element:

$$\frac{\partial \rho}{\partial t} + \nabla \cdot (\rho \mathbf{U}) = 0 \quad (1)$$

where ρ is the fluid density and \mathbf{U} is the velocity. The momentum equation corresponding to the Navier-Stokes equations ensures the conservation of momentum for a fluid element and is described as:

$$\frac{\partial(\rho \mathbf{U})}{\partial t} + \nabla \cdot (\rho \mathbf{U} \mathbf{U}) - \nabla \cdot [\mu_{\text{eff}} (\nabla \mathbf{U} + \nabla \mathbf{U}^T) - \frac{2}{3} \mu_{\text{eff}} (\nabla \cdot \mathbf{U}) \mathbf{I}] = -\nabla p_d - \rho_{\text{eff}} \mathbf{g} h_e \quad (2)$$

where μ_{eff} is the effective viscosity and described by $\mu_{\text{eff}} = \mu_{\text{laminar}} + \mu_{\text{turbulent}}$; μ_{laminar} and $\mu_{\text{turbulent}}$ are the laminar dynamic viscosity and turbulent viscosity, respectively; \mathbf{I} is the identity matrix; h_e is the elevation. p_d is the dynamic pressure, which is corrected by the following equation:

$$p_d = p - \rho \mathbf{g} h_e \quad (3)$$

where p is the total pressure; the absolute value of $\rho \mathbf{g} h_e$ is the static pressure. ρ_{eff} in Eq. 2 is the effective density, which can be represented using the classical Boussinesq approximation in which the relationship between the fluid density and the corresponding temperature is assumed to be linear associated with the coefficient of thermal expansion β :

$$\rho_{\text{eff}} = \rho_{\text{ref}} [1 - \beta(T - T_{\text{ref}})] \quad (4)$$

where ρ_{ref} is the reference density, and T_{ref} is the reference temperature. The energy within the moving fluid element is also conserved and can be written as in terms of enthalpy:

$$\frac{\partial(\rho h)}{\partial t} + \nabla \cdot (\rho \mathbf{U} h) - \nabla \cdot (\alpha_{\text{eff}} \nabla h) = \frac{\partial p}{\partial t} + \mathbf{U} \cdot \nabla p \quad (5)$$

where α_{eff} is the thermal diffusivity which is given by $\alpha_{\text{eff}} = \alpha_{\text{laminar}} + \alpha_{\text{turbulent}}$. h is the specific total enthalpy, which is equal to $h = h_0 + \frac{1}{2} |\mathbf{U}|^2$, where h_0 is the specific enthalpy.

As heat transfer in the surrounding solid regions is coupled, thermal conduction in the solid regions is governed by the equation:

$$\rho_s c_p \frac{\partial T}{\partial t} = \nabla \cdot (k \nabla T) \quad (6)$$

where ρ_s is the solid density, c_p is the specific heat of the solid, k is the thermal conductivity of the solid, and T is the temperature. It is noted that the surrounding solid regions were assumed as solid rocks (non-porous materials) for simplicity and the effect of temperature on the thermal properties of water was neglected in this study.

The governing equations presented above are solved using an open source FVM platform, OpenFoam. Since there is one more variable which is coupled with other variables as shown in Eqs 1 to 6, the efficient way to address such a problem is to solve the

governing equations separately in different regions. The final results then can be obtained via combining results from each part. The details regarding discretization of the governing equations can be found in Ferziger and Peric (2012). The PISO algorithm was used in this study to solve the iteration of the system (J. Oliveira 2001; Ferziger and Peric 2012), which applies very few corrector steps to obtain a desired accuracy of the pressure and velocity. The difference in temperature is relatively small so that the correction of temperature is achieved at each time step by employing the Boussinesq approximation (J. Oliveira 2001). The heat transfer between fluids and surrounding solids is coupled using “baffles” that can emulate transfer thermal energy between both sides of the baffle.

SIMULATION RESULTS AND MODEL VALIDATION

The validation of the developed model in the above section against a documented experiment is presented in this section. Braga and Viskanta (1992) conducted an experiment to investigate transient natural convective heat transfer in water (near its maximum density) in a rectangular cavity with inside dimensions of 150 mm in height, 300 mm in length, and 75 mm in depth. The experiment consisted of three major parts as shown in Fig. 1, i.e., a cold wall in which the temperature was maintained at 273.15 K, a hot wall (opposite to the cold wall) in which the temperature was maintained at 281.15 K, and water between the two walls in which there was a small gap (3 mm) between the top insulation and water to produce a free water surface. The walls around water were insulated and several thermocouples were inserted into the top, middle and bottom of the water body to measure temperature variations with respect to time at these points.

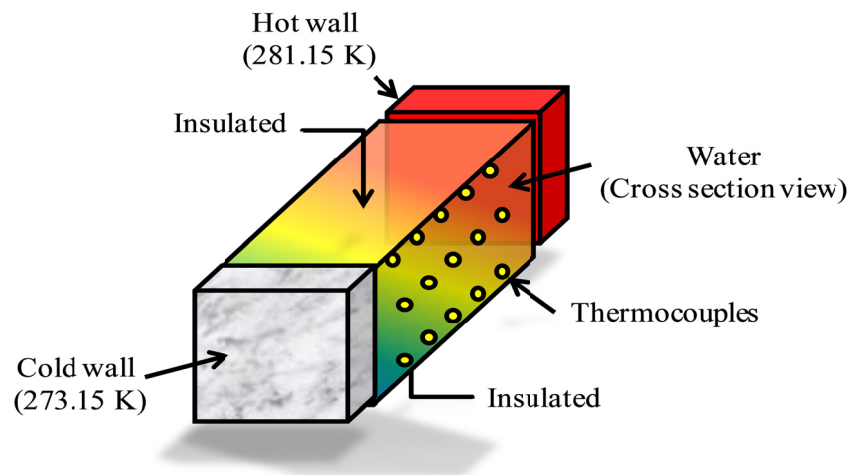


FIG.1. Schematic cross section view of the experiment conducted by Braga and Viskanta (1992).

This experiment was performed to investigate heat transfer and water movement triggered by temperature differences. To visualize the flow patterns, the water was mixed with an amount of neutrally buoyant particles (Braga and Viskanta 1992), which was scanned by the laser beam so that the flow patterns can be visualized through the front and back insulations. The Boussinesq approximation in Eq. 4 is valid in most cases to simulate natural convection as the density of fluids decreases linearly with increasing temperature.

However, this approximation is invalid for this experiment due to the effect of density inversion. To be more special, the maximum density of water appears at 277.13 K so that the density fails to linearly vary with temperature, which significantly affects the natural convective motion at locations near to the density extremum (Braga and Viskanta 1992). In order to accurately simulate this experiment, the relationship between the fluid density and the corresponding temperature was corrected using Eq. 7 (McDonough and Faghri 1994):

$$\left\{ \begin{array}{l} \rho_{\text{eff}} = \rho_{\text{ref}} [1 + \beta_1 T + \beta_2 T^2 + \beta_3 T^3 + \beta_4 T^4]^{-1} \\ \rho_{\text{ref}} = 999.972 (\text{kg} / \text{m}^{-3}) \\ \beta_1 = -0.67896452 \times 10^{-4} (\text{°C}^{-1}) \\ \beta_2 = 0.907294338 \times 10^{-5} (\text{°C}^{-1}) \\ \beta_3 = -0.964568125 \times 10^{-7} (\text{°C}^{-1}) \\ \beta_4 = 0.873702983 \times 10^{-9} (\text{°C}^{-1}) \end{array} \right. \quad (7)$$

The initial and boundary conditions in the current simulation were set up according to the real conditions. An initial temperature of 281.15 K was uniformly distributed within the water body. Non-slip was used on all boundaries between the water and walls. For the boundary conditions of flow on the free surface, the velocity normal to the surface was set up zero while zero gradients were defined for velocities in the other directions. Due to the negligible dimensions in the surrounding solids, heat transfer in the solids was not considered in this case. The parameters regarding thermal and transport properties used in the model were adopted from Braga and Viskanta (1992). 78,120 volume cells were generated for the water body and 0.1 s was selected as the time step. Such a mesh and time step were tested and a good accuracy and computing cost were obtained with them.

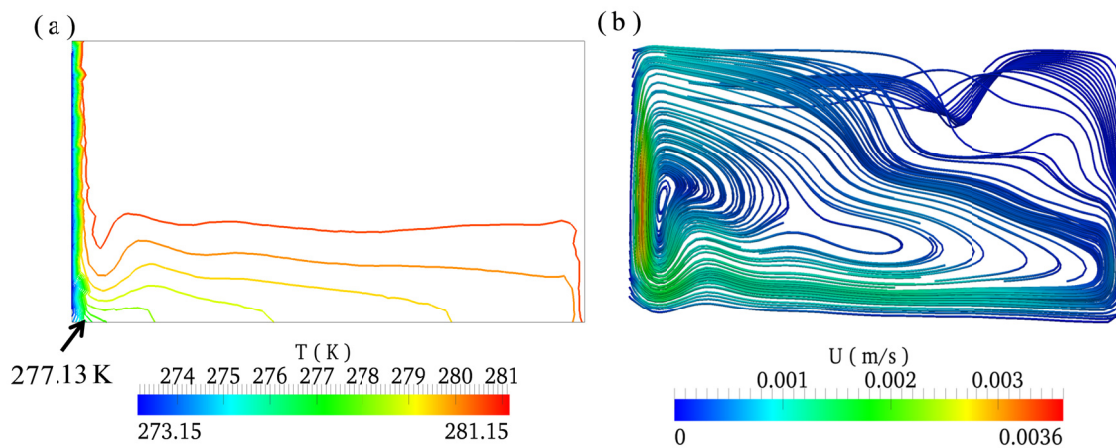


FIG.2. Numerical simulation results on a cross section of height at $t=5$ min: (a) temperature distribution and (b) streamlines.

The water density distribution with temperature in the cavity has been presented in Fig. 2a based upon transient isotherms. The maximum density appears at the 277.13 K isotherm at a location close to the corner, which separates the water body into two parts with

different flow patterns. But during this period, heat conduction was predominant within the water body in the process. Therefore, these two separate parts with different flow patterns in the cavity is not explicit. This result also can be validated by the corresponding transient streamlines presented in Fig. 2b. It can be clearly seen that the flow circulates anticlockwise from the hot wall to the cold wall, which verifies that heat conduction was dominant and convection was initiated during this period. Unfortunately, no results regarding flow patterns were obtained in the experiments during this period.

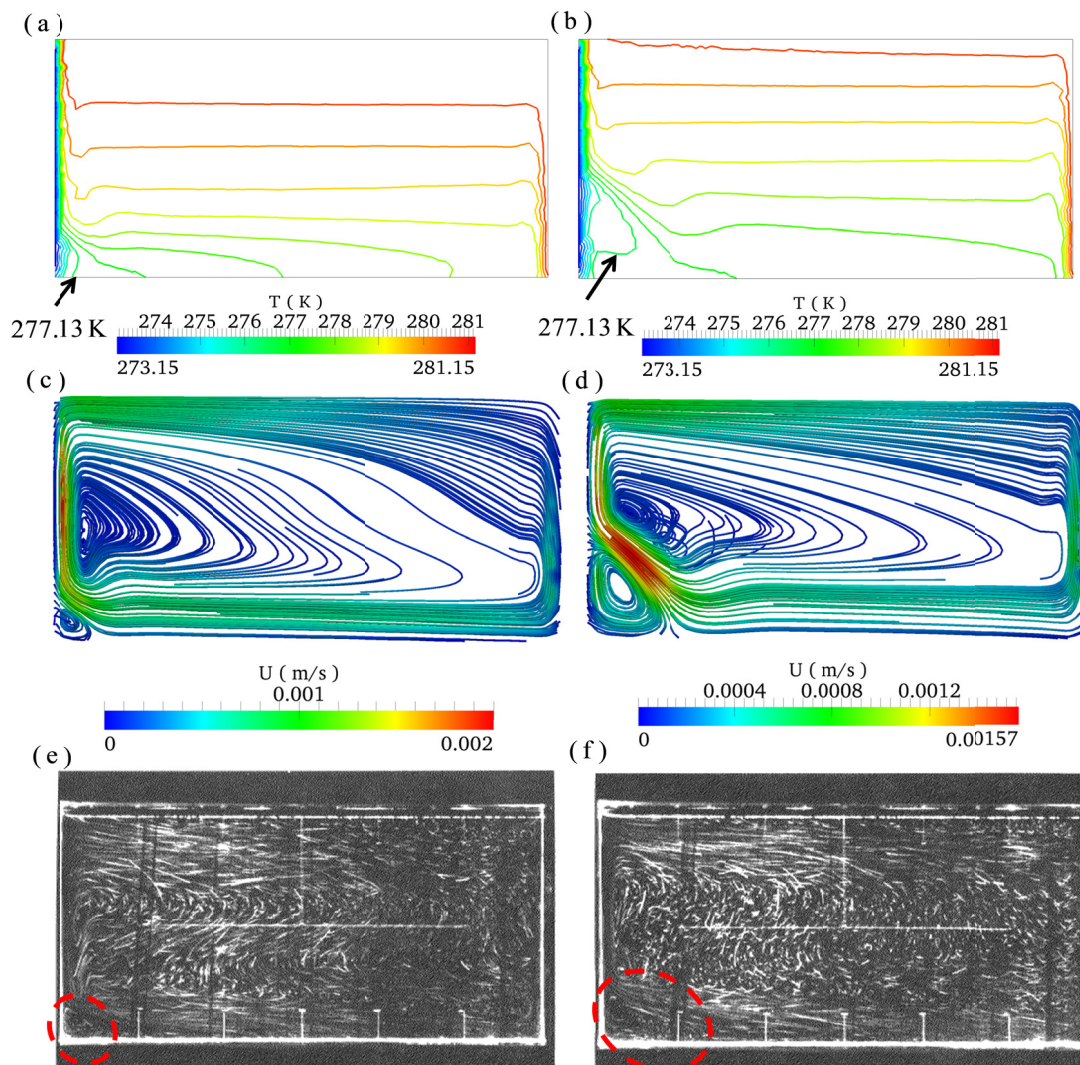


FIG.3. Numerical simulation results on a cross section of height: (a) temperature distributions at $t=15$ min; (b) temperature distributions at $t=30$ min; (c) streamlines at $t=15$ min; (d) streamlines at $t=30$ min; (e) observed streamlines at $t=15$ min; (f) observed streamlines at $t=30$ min (observed photos are copied from Braga and Viskanta (1992)).

Interesting flow patterns caused by natural convection were observed as time elapsed. At $t=15$ min, the fluid that had been cooled to the density inversion (Fig. 3a) exhibited two circulations. One circulation is that the flow along the cold wall at the corner is forced to

move up and then to move down along the 277.13 K isotherm due to buoyancy as shown in Fig. 3c. The other circulation followed a similar flow pattern obtained at $t=5$ min. The flow patterns at $t=15$ min show very good agreement with the observed flow patterns in Fig. 3e. This phenomenon is also confirmed by the results obtained at $t=30$ min in Fig. 3b and Fig. 3d. Due to the heat convection, two separate flow circulations are more obvious. The observed flow patterns in Fig. 3f reaffirm this phenomenon with very a good comparison.

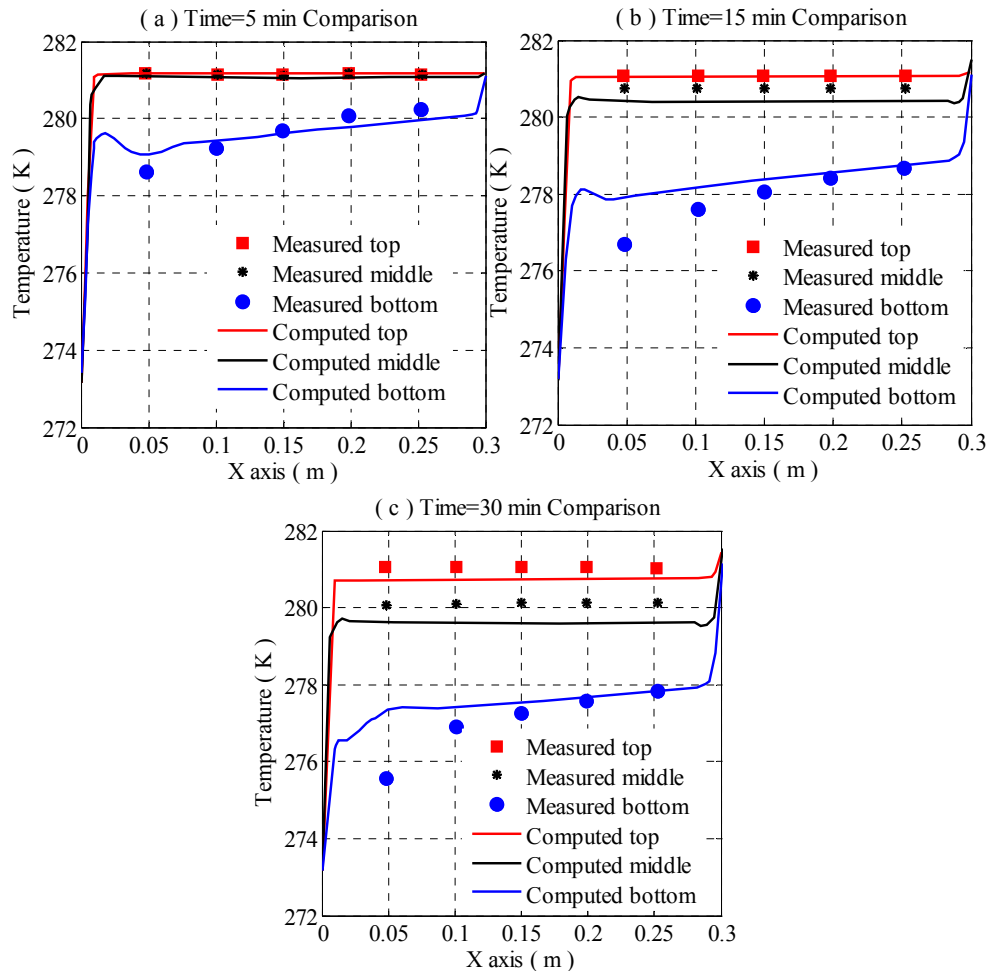


FIG.4. Numerical computed temperatures compared with measured temperatures: (a) $t=5$ min; (b) $t=15$ min; and (c) $t=30$ min (measured data are reproduced from Braga and Viskanta (1992)).

Good comparisons between the computed and measured temperatures further proved the good accuracy of the model. As presented in Fig 4, it can be clearly seen that the distributions of computed temperatures match very well with that of measured temperatures at all different positions for all different times. A slightly difference in the comparison between the computed temperatures and measured temperatures at the bottom was primarily caused by heat conduction along the thermocouple probes (Braga and Viskanta 1992). This heat conduction is particularly significant at locations close to the lower left corner where the density inversion appears. Therefore, the measured temperatures are slightly smaller than the computed values.

SIMULATION OF REPRESENTATIVE CASE

Good comparisons between simulation results and measured data presented in the above section have exhibited the good capacity and accuracy of the proposed 3D FVM model. In this section, a realistic case regarding thermo-hydrodynamic modeling of an inclined and flooded underground mine in the Upper Peninsula (U.P.) in Michigan was investigated to shed light on the understanding of the complicated physical processes in mine water. As reported by Liu et al. (2015), 90% of underground mines were abandoned and flooded with water after closure in the U.P., which results in a huge potential of exploring geothermal energy from those flooded mines to meet the heating demands of the adjacent communities. Therefore, it is of significant meaning and of great interest to study this thermo-hydrodynamic system, with focuses on the transient natural convective motion of water and heat transfer in the system.

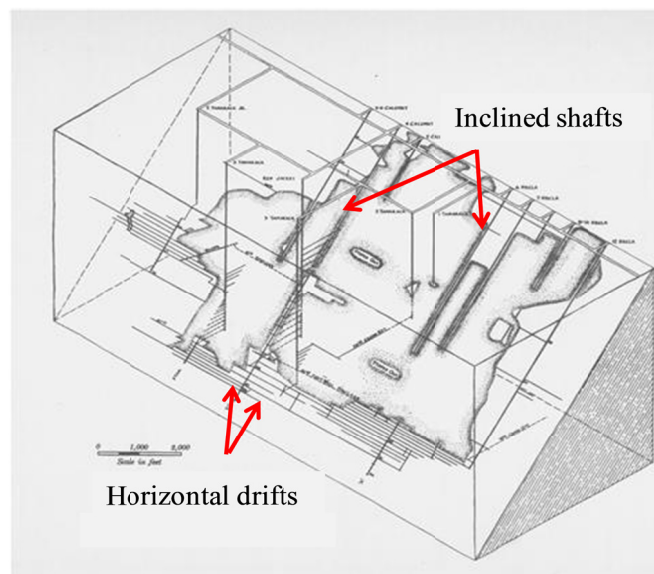


FIG.5. Sketch of a typical underground mine structure (copied from Keweenaw Digital Archives (Book TN443M5V5-002 Figure 1)).

A typical underground mine structure that consists of inclined mine shafts and horizontal drifts connecting those shafts is shown in Fig. 5. For simplicity, an inclined mine shaft was investigated without horizontal drifts as shown in Fig. 6, including information about the computational domain. In order to represent the geothermal gradient in the domain, the temperature was linearly distributed within the water body and surrounding rocks (basalt) from 290 K to 300 K to represent the linear geothermal gradient. The temperature of rocks at the bottom was uniform and fixed to 300 K within the whole domain. In this case, the classical Boussinesq approximation (Eq. 4) can be used due to the absence of density inversion. The interface between different regions was coupled by using “baffles” to simulate heat exchange between two sides of the baffle. Due to a high computing cost in the large-scale simulations, this study presents the results for a process lasting 18 days. The thermal properties of water used in the simulation were chosen at the normal temperature of 299.15 K, and the thermal properties rocks were selected using typical values.

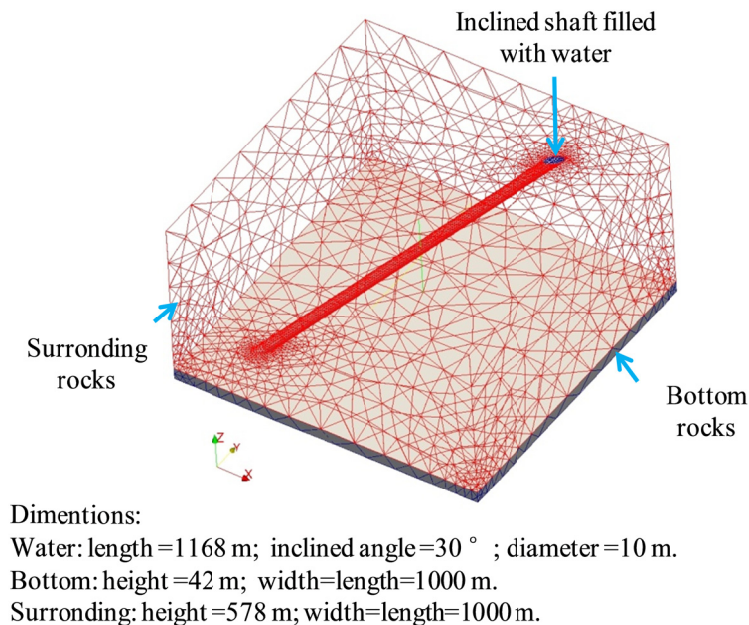


FIG.6. 3D model of the system and its dimensions.

The flow pattern in the center of the water body is depicted in Fig. 7. Due to the density difference caused by the geothermal gradient, the mine water circulates in the shaft, in which the water at the bottom with high temperatures is relatively lighter so that it moves up. Then the water from the bottom is mixed and cooled by the cold water at the top. The cooled water tends to be heavier and therefore moves down and returns to the bottom. This flow phenomenon can be clearly seen in Fig. 7 using flow vectors and streamlines.

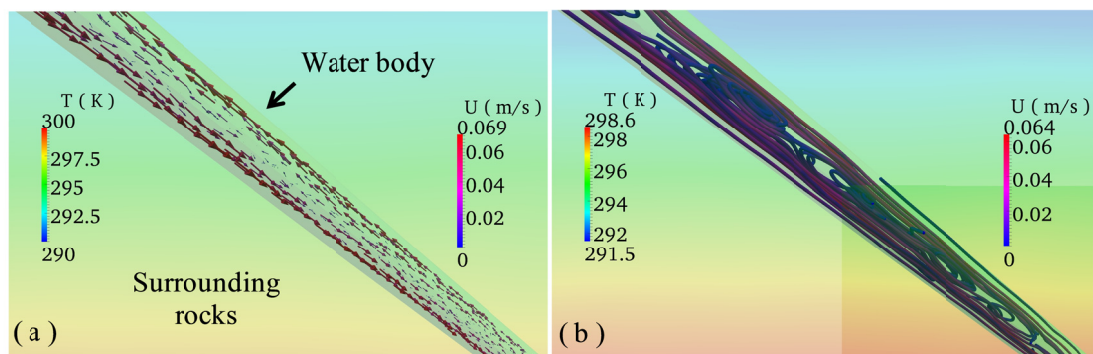


FIG.7. Flow patterns in the center of the water body at $t=1$ day: (a) flow circulation and (b) the corresponding streamlines.

The temperature distribution and its variation along the water body are critical to understanding the thermal energy, which triggers and maintains the buoyancy-driven flow. For this purpose, three representative points, which were captured from the surface, middle and bottom of water body, respectively, were chosen to investigate temperature variations with respect to time. As shown in Fig. 8a, the temperature at the bottom decreases

significantly at the beginning and then tends to be uniform. Opposite results were obtained in which the temperature at the top increases significantly at the beginning and then tends to be uniform. The temperature at the middle almost maintains unchanged. These results provide evidence to explain the simulated flow pattern in Fig. 7. The temperature distribution along the water body in Fig. 8b also elucidates what showed in the flow pattern in Fig. 7. The difference between the temperatures on the top and bottom increases from 10 K to 2 K as time elapses. The temperature of mine water is mixed and tends to be uniform gradually due to the natural convective motion of mine water. This well mixing condition is consistent with most field observations in flooded mines (Wolkersdorfer 2008).

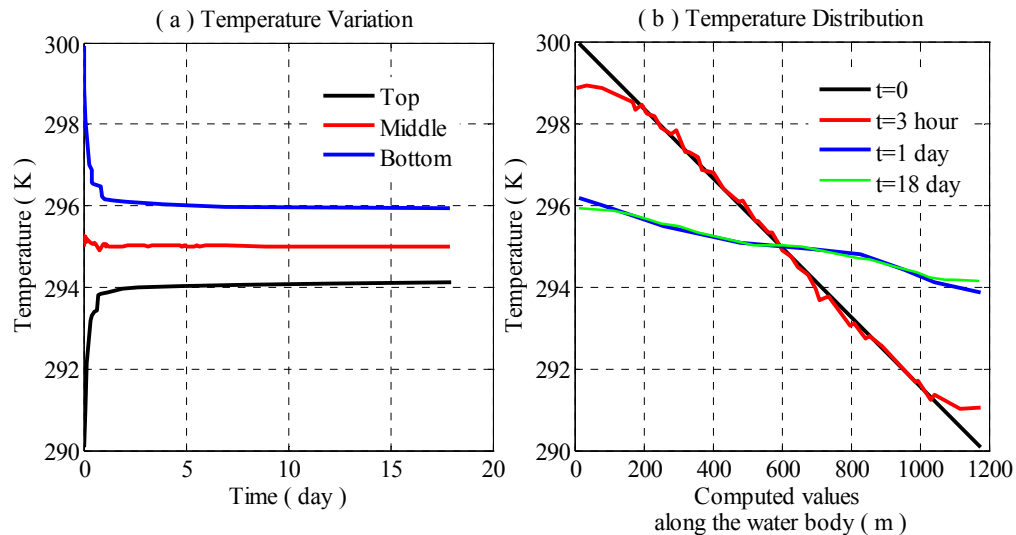


FIG.8. Numerical computed temperatures: (a) temperature variation at different positions, and (b) temperature distribution along the water body.

CONCLUSIONS

A fully coupled 3D thermo-hydrodynamic model was developed using the Boussinesq approximation to numerically solve the coupled multiphysical processes in the mine water-geologic formation system. The fully coupled 3D model was validated against a documented experiment. Good agreement obtained from the comparison revealed a good accuracy of the developed model. Based on that, a realistic case involving thermo-hydrodynamics of an inclined and flooded underground mine in the Upper Peninsula (U.P.) in Michigan was investigated to shed light on the interesting phenomena in mine water induced by natural convective motion of mine water. The simulation results exhibited how the buoyancy-driven flow is triggered and maintained by the temperature difference in mine water. The results in this study are not only significant to understanding the underlying multiphysics mechanisms associated with recovering geothermal energy from mine water, but also practically valuable to further geothermal applications by efficiently exploring geothermal energy from mine water with more complicated underground mine structures.

REFERENCES

- Allen, D., Ghomshei, M., Sadler-Brown, T., Dakin, A., and Holtz, D. (2000). "The current status of geothermal exploration and development in Canada." *Proceedings from World Geothermal Congress*, Japan, 55-58.
- Arias, C. A., Alonso, A. O., and García, R. Á. (2014). "Hydrogeological and Thermal Modelling of an Underground Mining Reservoir." In *Mathematics of Planet Earth*, 419-423. Springer.
- Bazargan, B., Demollin, E., and Van Bergermeer, J.-J. (2008). "Geothermal use of deep flooded mines." *Proc. of the Post Mining Symposium*, Nancy, France, 1-10.
- Bertani, R. (2012). "Geothermal power generation in the world 2005–2010 update report." *Geothermics*, 41: 1-29.
- Braga, S., and Viskanta, R. (1992). "Transient natural convection of water near its density extremum in a rectangular cavity." *International journal of heat and mass transfer*, 35(4): 861-875.
- Ferziger, J. H., and Peric, M. (2012). *Computational methods for fluid dynamics*. Springer Science & Business Media.
- Hall, A., Scott, J. A., and Shang, H. (2011). "Geothermal energy recovery from underground mines." *Renewable and Sustainable Energy Reviews*, 15(2): 916-924.
- Hamm, V., and Sabet, B. B. (2010). "Modelling of fluid flow and heat transfer to assess the geothermal potential of a flooded coal mine in Lorraine, France." *Geothermics*, 39(2): 177-186.
- Hasche-Berger, A. (2013). "Hydrodynamics in a flooded underground limestone mine." *Reliable Mine Water Technology*, IMWA, Golden CO, USA, 1165-1172.
- J. Oliveira, R. I. I., Paulo. (2001). "An improved PISO algorithm for the computation of buoyancy-driven flows." *Numerical Heat Transfer: Part B: Fundamentals*, 40(6): 473-493.
- Jessop, A. (1995). "Geothermal energy from old mines at Springhill, Nova Scotia, Canada." *Proceedings*, 463-468.
- Liu, Z., Meldrum, J., Xue, P., and Green, C. (2015). "Preliminary Studies of the Use of Abandoned Mine Water for Geothermal Applications." *IFCEE 2015*, ASCE, 1678-1690.
- Loredo, J., Ordóñez, A., Jardón, S., and Álvarez, R. (2011). "Mine water as geothermal resource in Asturian coal mining basins (NW Spain)." *Proceedings of 11th International Mine Water Association Congress*, Rude TR, Freund A, Wolkesdorfer C (eds) Mine water: managing the challenges, Aachen, Germany, 177-182.
- Lund, J. W., Freeston, D. H., and Boyd, T. L. (2005). "Direct application of geothermal energy: 2005 worldwide review." *Geothermics*, 34(6): 691-727.
- Malolepszy, Z. (2003). "Low temperature, man-made geothermal reservoirs in abandoned workings of underground mines." *Proceedings of the 28th workshop on geothermal reservoir engineering*, Stanford University, USA, 259-265.

- McDonough, M., and Faghri, A. (1994). "Experimental and numerical analyses of the natural convection of water through its density maximum in a rectangular enclosure." *International journal of heat and mass transfer*, 37(5): 783-801.
- Milora, S. L., and Tester, J. W. (1977). "Geothermal energy as a source of electric power." *Geological Magazine*, 114(5): 1-3.
- Preene, M., and Younger, P. (2014). "Can you take the heat?-Geothermal energy in mining." *Mining Technology*, 123(2): 107-118.
- Ramos, E. P., Breede, K., and Falcone, G. (2015). "Geothermal heat recovery from abandoned mines: a systematic review of projects implemented worldwide and a methodology for screening new projects." *Environmental Earth Sciences*, 73(11): 6783-6795.
- Raymond, J., Therrien, R., and Hassani, F. (2008). "Overview of geothermal energy resources in Québec (Canada) mining environments." *10th International Mine Water Association Congress: mine water and the environment*, Technical University of Ostrava, Ostrava, Czech Republic, 1-12.
- Renz, A., Rühaak, W., Schätzl, P., and Diersch, H.-J. (2009). "Numerical modeling of geothermal use of mine water: challenges and examples." *Mine Water and the Environment*, 28(1): 2-14.
- Rybach, L. (2003). "Geothermal energy: sustainability and the environment." *Geothermics*, 32(4): 463-470.
- Self, S. J., Reddy, B. V., and Rosen, M. A. (2013). "Geothermal heat pump systems: status review and comparison with other heating options." *Applied Energy*, 101: 341-348.
- Streb, C., and Wieber, G. (2011). "Geothermal energy from a flooded mine: a hydraulic model." *Rüde RT, Freund A, Wolkersdorfer Ch (Eds), Mine Water—Managing the Challenges, IMWA*: 189-193.
- Wieber, G., and Pohl, S. (2008). "Mine water: a source of geothermal energy—examples from the Rhenish Massif." *10th International Mine Water Association Congress: Mine Water and the Environment*, Citeseer, Technical University of Ostrava, Ostrava, Czech Republic, 1-4.
- Wolkersdorfer, C. (2008). *Water management at abandoned flooded underground mines: fundamentals, tracer tests, modelling, water treatment*. Springer Science & Business Media.

Thermal Protection Analyses of Underground Steam Pipes

Chanjuan Han¹ and Xiong (Bill) Yu²

¹Graduate Assistant, Dept. of Civil Engineering, Case Western Reserve Univ., Cleveland, OH. E-mail: cxh432@case.edu

²Professor, Dept. of Civil Engineering, Case Western Reserve Univ., Cleveland, OH. E-mail: xyy21@case.edu

Abstract: HDPE pipes are widely used for domestic sewage applications. Accidents have happened in major cities where the leakages of steam pipe caused melting of HDPE pipes adjacent to underground steam pipe. Proper spacing or thermal protection are needed for HDPE pipes located adjacent to the steam pipe, particularly in light of potential leakages. This paper conducts computational simulations to determine the safe distance away from the steam pipe under normal operation conditions and conditions with leakage. From these, design criteria are provided to ensure the safety of HDPE sewage pipe adjacent to steam pipes.

INTRODUCTION

Underground steam pipe is commonly used to provide heating services in cold regions. It operates with high temperature and high pressure steam, which can lead to safety issues. Over 12 incidents of steam pipe explosion have been reported in New York City since 1987 (Belson and DePalma, 2007), due to water pressure hammer, corrosion, or other reasons. Besides catastrophic explosions, leakage of steam pipe has caused various distresses in urban infrastructures, such as melting of adjacent HDPE pipes or pavement. The increasing use of HDPE pipes for domestic sewage applications make it important to design and protection of HDPE pipe installed adjacent to steam pipe.

Studies have been conducted on steam pipe system design (Stevanovic, Studovic et al. 1994, Gandhi, Ganguli et al. 2012), its creep behaviors (Tapsell 1944, Liaw, Saxena et al. 1989, Singh and Singh 1997, Morris, Dear et al. 2006) and life-time analysis (Liaw, Saxena et al. 1989, Jaske 1990, Liaw, Saxena et al. 1993). There are, however, few studies on the influences of steam pipe on its surrounding utility lines, especially when leakage happens. This study intends to provide guidelines on the safety assurance for HDPE pipe adjacent to steam pipe. The temperature field adjacent to steam pipe operating under both normal operation condition and leaky condition are

discussed. This is followed by methods and schema for thermal protection of HDPE pipes. A general design criterion is proposed for practical application.

FINITE ELEMENT MODELING

This study starts with developing theoretical framework to describe the heat exchange between steam pipe and its surroundings soils. The heat transfer process of steam in pipeline for both normal operation condition and leaky operation condition are simulated (FIG. 1). For simplification, 2D numerical model other than 3D model is used. The physics involved in the simulation are described in the following context.

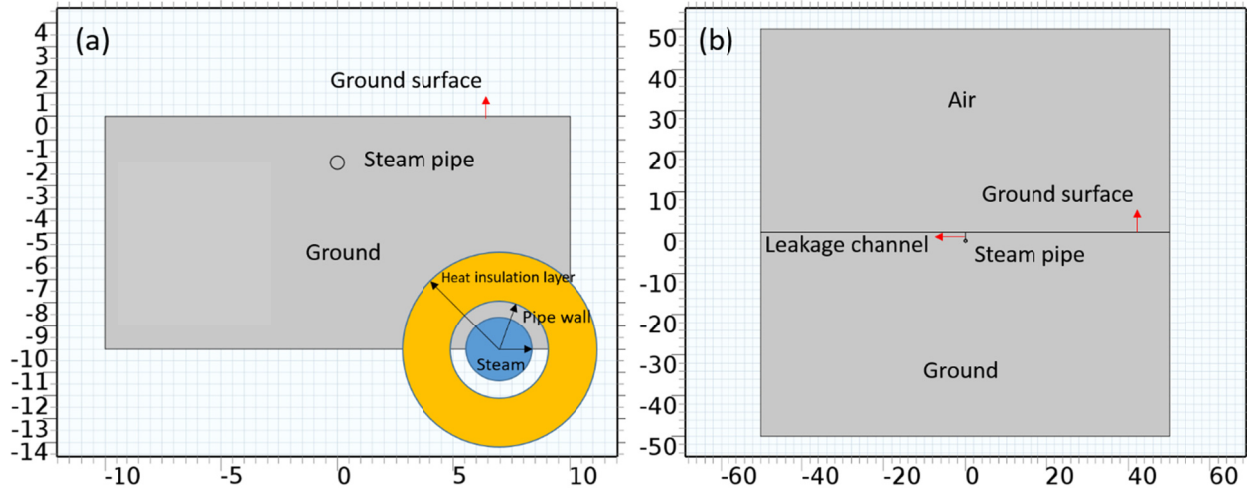


FIG. 1. Configuration of 2D steam pipe under (a) normal condition; (b) leaky condition
Steam pipe operated in normal condition

FIG. 1(a) shows the configuration of 2D steam pipe operating under normal condition. The heat transfer process is driven by the thermal gradient between steam and its surroundings, and only conductive heat transfer is involved in this process. The temperature profile can be acquired by solving equation as follows.

Heat transfer in solid:

$$0 = \nabla \cdot (k \nabla T) \quad (1)$$

where k denotes to the thermal conductivity, and T is the temperature.

Equation (1) is energy conservation equation that neglects the convection in radial direction and energy dissipation along pipeline direction. This is reasonable because the flow velocity in radial direction is generally negligible compared with that along pipeline direction. Besides, considering the steam pipe is usually well insulated in normal operation condition, the corresponding thermal dissipation along pipeline is also negligible. Those simplifications account for the reason why we adopt 2D numerical model instead of 3D model, and they also provide support for that the application of 2D model is both computational accurate and efficiency.

Steam pipe operated in leaky condition

FIG. 1(b) illustrates the configuration of steam pipe operated in leaky condition, in which, non-isothermal fluid flow is taken into account. To avoid the water hammer happening, the steam flowing in the pipeline is normally overheated saturate steam. Once leakage happens, the high temperature and pressure steam will jet to the ambient air resulting in non-isothermal fluid flow, and this process can be mathematically expressed as follows.

Heat transfer in fluid:

$$\rho C_p u \cdot \nabla T = \nabla \cdot (k \nabla T) \quad (2)$$

where ρ is the density. u is the leaky fluid velocity, which can be calculated by solving Equation (5). C_p is the heat capacity. k is the thermal conductivity. T is the temperature.

k - ε turbulent flow:

The Reynold-averaged Navier-Stokes (RANS) equations are applied to simulate the leakage caused turbulent flow, which assumes that the fluid is compressible with the Mach number $Ma < 0.3$. It can be expressed as:

$$\begin{cases} \rho(u \cdot \nabla)u = \nabla \cdot \left[-p + (\mu + \mu^T)(\nabla u + (\nabla u)^T) - \frac{2}{3}(\mu + \mu^T)(\nabla \cdot u)I - \frac{2}{3}\rho k I \right] \\ \nabla \cdot (\rho u) = 0 \end{cases} \quad (5)$$

where ρ represents the fluid density, which is the function of both pressure and temperature. u is the leaky fluid velocity, μ is the dynamic viscosity, and μ^T is the turbulent viscosity that is defined by $\mu^T = \rho C_\mu \frac{k^2}{\varepsilon}$. k stands for the turbulent kinetic energy, which is related with the other variable: turbulent dissipation rate ε . The two dependable variables can be calculated by:

$$\begin{cases} \rho(u \cdot \nabla)k = \nabla \cdot \left[\left(\mu + \frac{\mu^T}{\sigma_k} \right) \nabla k \right] + P_k - \rho \varepsilon \\ \rho(u \cdot \nabla)\varepsilon = \nabla \cdot \left[\left(\mu + \frac{\mu^T}{\sigma_\varepsilon} \right) \nabla \varepsilon \right] + C_{\varepsilon 1} \frac{\varepsilon}{k} P_k - C_{\varepsilon 2} \rho \frac{\varepsilon^2}{k} \end{cases} \quad (6)$$

in which, σ_k , σ_ε , $C_{\varepsilon 1}$ and $C_{\varepsilon 2}$ are model constants with magnitude of 1.0, 1.3, 1.44 and 1.92, respectively (Wilcox 1998). P_k is a production term that can be written as:

$$P_k = \mu^T \left[\nabla u : \left(\nabla u + (\nabla u)^T - \frac{2}{3}(\nabla \cdot u)^2 \right) \right] - \frac{2}{3} \rho k \nabla \cdot u \quad (7)$$

Since the heat convection relies on the leaky flow velocity and the flow properties depend on temperature, the two modules are both flow and temperature coupled to realize non-isothermal fluid flow.

Although 2D numerical model greatly save the computational efforts, the limitation on simulation of steam flow along pipeline direction made it impossible to obtain the leaky velocity automatically. Thus, it is necessary to introduce another independent model that aims to estimate the inlet leaky velocity. The physical description of this model is:

Pipe flow:

$$\begin{cases} 0 = -\nabla p - \frac{1}{2} f_D \frac{\rho}{d_h} |u|u + F \\ \nabla \cdot (A\rho u) = 0 \end{cases} \quad (8)$$

where p is the fluid pressure, f_D is the Darcy friction factor, d_h is the hydraulic pipe diameter, F is the volume force due to fluid density variation, A is the cross section area and u is the fluid velocity.

Accordingly, the leaky velocity can be estimated under appropriate boundary conditions via this 1D Pipe Flow Model (FIG. 2).

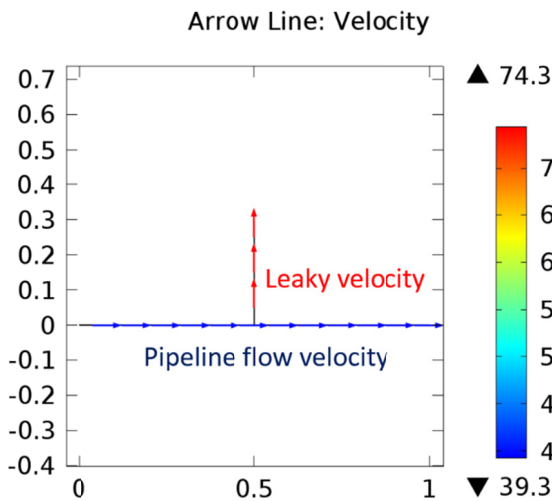


FIG. 2. Calculation of leakage velocity

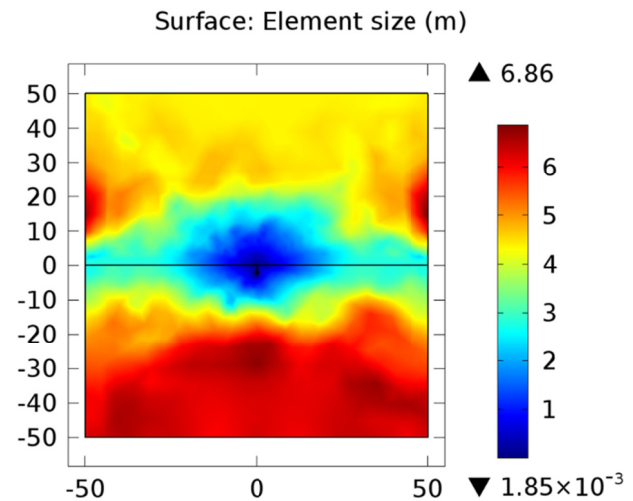


FIG. 3. Mesh element size

Geometry, boundary conditions and mesh schema

As shown in FIG. 1, the computational domain for ground is set to be a rectangular with dimension of 20m width by 10m depth for model in normal operation condition, while the ground domain with dimension of 100m width by 50m depth is applied for model under operation condition with leakage. The steam pipe is stainless steel pipe that covered by insulation layers, which feature high temperature resistant and thermal insulation. Eight types of steam pipes with standard size are selected to analyze the corresponding safety distance. The size and pipe thickness (ASTM A53/A53-12 2012) as well as corresponding required insulation layer thickness (The Engineering ToolBox) are listed in Table 1.

Since the practical temperature of heating steam pipe are usually limited below 230°C (ASHRAE 2008), temperature of 230°C is set as the steam temperature flowing in the pipe. Besides, the temperature of 130 °C is applied as criteria to determine the minimum safety distance (center to center) between steam pipe and HDPE pipe as the melting temperature for HDPE pipe is around 130 °C. The ground temperature is assumed to be constant beyond 10m depth with the magnitude of 13°C, and the temperature linearly decreases to 5°C to ground surface. The ambient air temperature is assumed to be 5°C. The Dirichlet boundary condition is applied on all boundaries of the computational domain. In addition, the numerical model is

meshed with physics-controlled mesh in normal size (FIG. 4), and the material thermal properties are listed in Table 2.

Table 1. Steam pipe size and corresponding insulation thickness

Pipe NO.	Pipe Size (in)	Diameter (in)		Nominal Thickness (in)	Recommended Minimum Thickness of Insulation (in)
		External	Internal		
1	1	1.32	1.05	0.13	2.5
2	2	2.38	2.07	0.15	2.5
3	3	3.5	3.07	0.22	3
4	5	5.56	5.05	0.26	3.5
5	10	10.75	10.02	0.37	3.5
6	16	16	15	0.5	3.5
7	20	20	18.81	0.59	3.5
8	24	24	22.63	0.69	3.5

Table 2. Material thermal properties

Item	Pipe wall	Insulation layer	Ground
Thermal conductivity (W/m/K)	44.5	0.035	2.55

RESULTS AND DISCUSSION

The PDE equations are solved numerically by use of the commercial PDE solver COMSOL[®]. From the results, the temperature profiles are determined. FIG. 4 and FIG. 5 plots the 130°C temperature contour of 8 different types of steam pipes covered with/without insulation layers. Fig 4 shows that application of insulation layer successfully prevented heat from spreading to its adjacent area, as the temperature contour of 130°C always stays within the insulation layer for all these steam pipes. Therefore, there is no safety threat for HDPE pipe installed adjacent to them when the insulation is intact. However, once the insulation layer failed, the 130°C contour expanded significantly (Fig. 5). The required minimum safety distance increases to up to 1m (FIG. 5 pipe (8)). In the practical aspect, the minimum safety distance should be guaranteed to ensure the safety of HDPE pipe. There are, however, space constraints that can make this requirement difficult to meet. In this case, thermal protection is a possible approach to protect HDPE pipe adjacent to steam pipes.

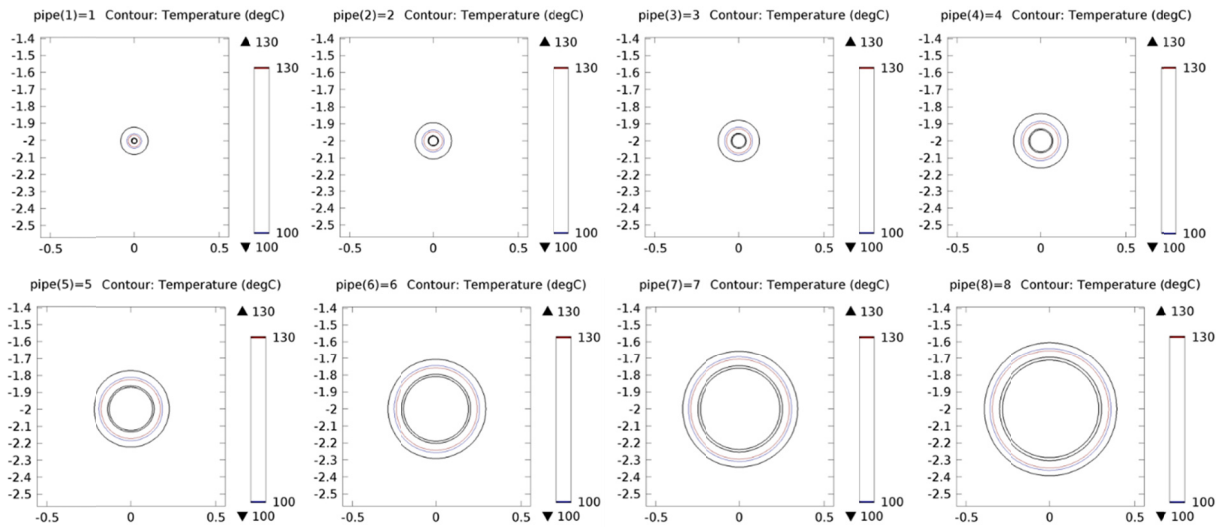


FIG. 4. Contour of 130°C around steam pipe with insulation layer

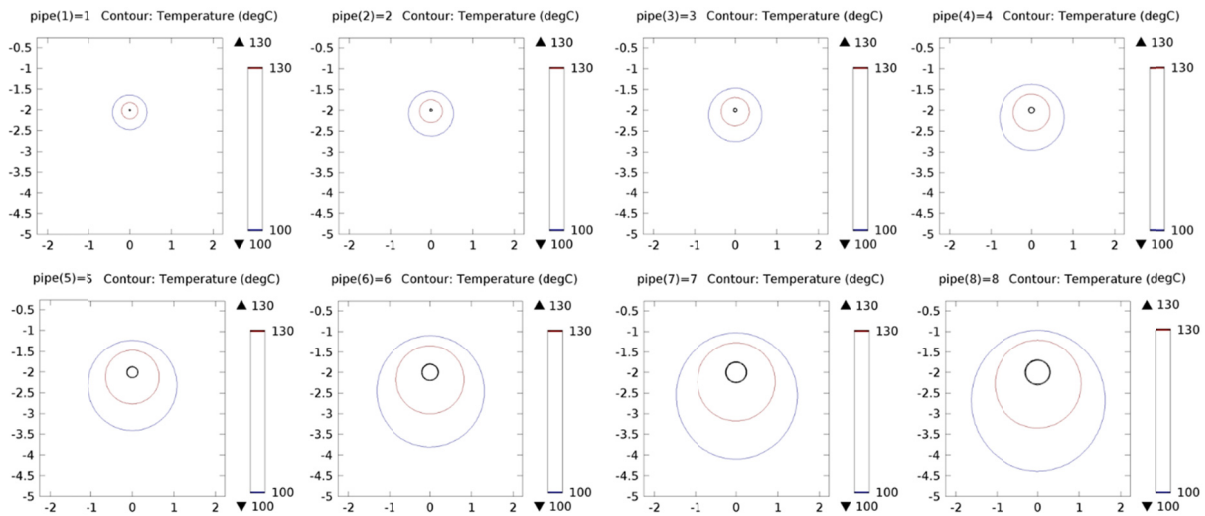


FIG. 5. Contour of 130°C around steam pipe after insulation layer is peeled off

In this paper, a thermal protection channel is defined as a manually excavated channel that is refilled with thermal insulation material. A thermal insulation channel is assumed to be located 0.5m away from the steam pipe center. Sensitivity study is conducted on the thermal conductivity of refilling material in providing thermal shielding (or change the range of 130°C contour). The steam pipe is assumed to have 24 inch diameter as representative of extreme conditions. The results are shown in Fig. 6. The results confirm the fact that lower the thermal conductivity the higher the effectiveness of thermal protection. It demonstrates that the application of thermal protection channel with proper thermal conductivity can effectively decrease the minimum safety distance. However, when the thermal conductivity is larger than 0.5 W/m/K, there is no obvious thermal insulation effect. In addition, the temperature contour of 130 °C features similar shape for thermal conductivity of 0.01 and 0.05 W/m/K. In this case,

the selection of refilling material should primarily consider other factors (i.e., economical efficiency, space limitation, structure requirement, etc.).

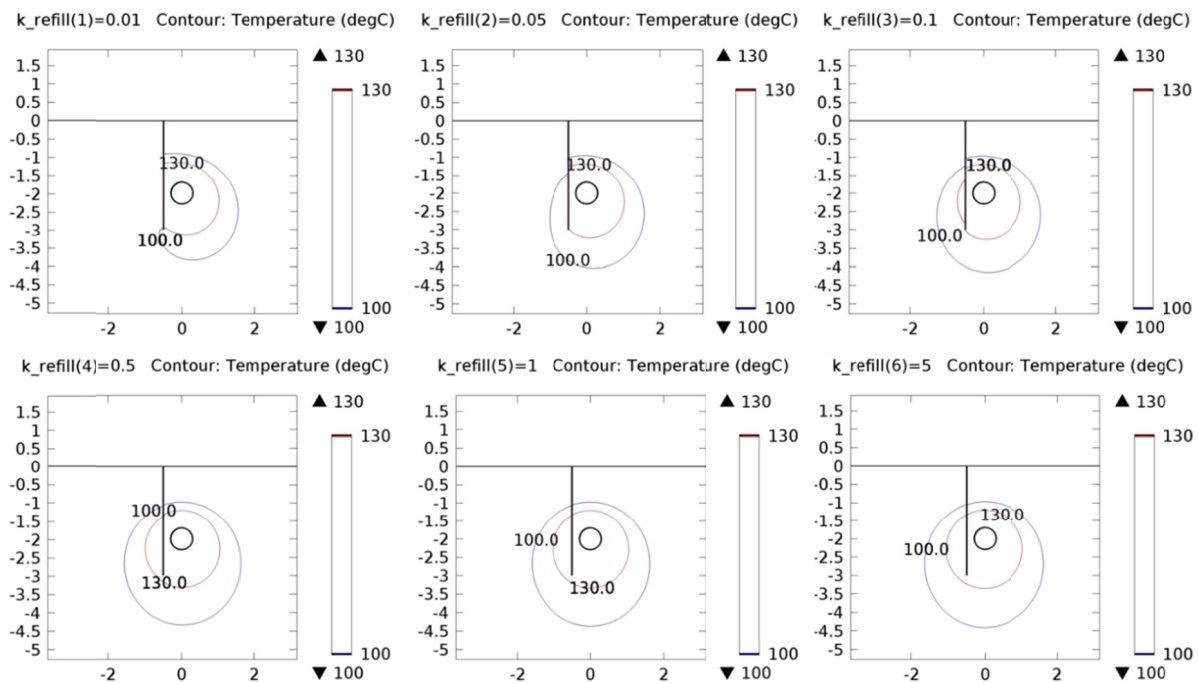


FIG. 6. Sensitivity analysis of effects of thermal conductivity on 130°C contour

In the reality, leaks might happen in the steam pipe leakage than completely peer of insulation layer. To consider this condition, simulations are conducted on the steam pipe with leakage. The leakage channel in the study is assumed to be 5cm in width. The steam pipe is assumed to have diameter of 24 inches. The leakage channel inlet velocity is obtained from Pipe Flow Model with the magnitude of 74.3m/s when the steam flow velocity in the pipe equals to the commonly recommended flow velocity of 40 m/s (The Engineering ToolBox). FIG. 7 illustrates the flow velocity field and temperature field of steam pipe with leakage. The thermal insulation effect of the insulation layer is significantly affected when leakage occurs. This leakage significantly increases the minimum safety distance (from 0 to around 0.9m in lateral direction) (FIG. 8), which is similar with the result when the insulation layer is peeled off (FIG. 5). A sensitivity study is conducted on the thermal conductivity of thermal protection channel when steam pipe has leakage, and the results are presented in FIG. 9. The overall trends are similar to those observed in FIG. 8. FIG. 10 provides more details of temperature distribution after the application of thermal protection channel with thermal conductivity of 0.01 W/m/K. The temperature field distribution is changed significantly by the thermal protection layer. The results show that installation of thermal protection channel is effective to protect possible HDPE thermal melt down due to steam pipe leakage.

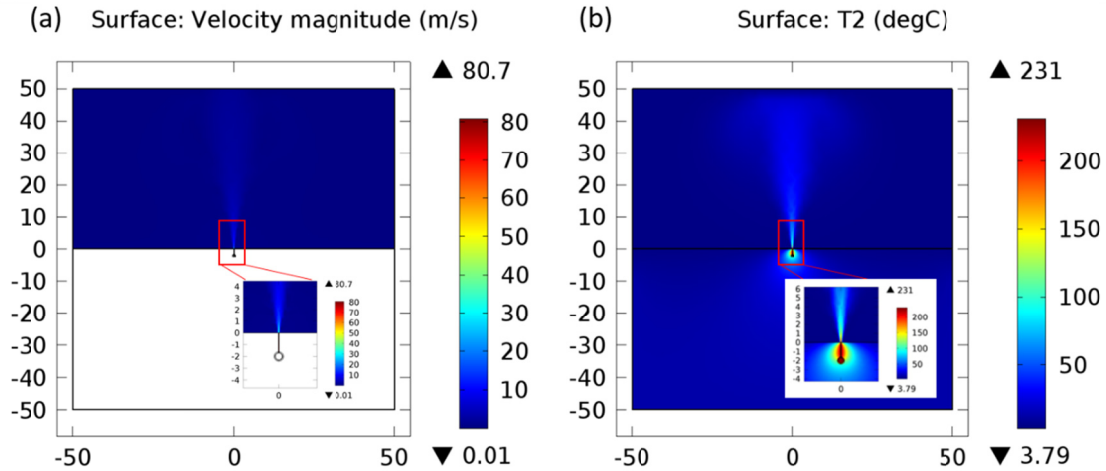


FIG. 7. Simulation results of steam pipe with leakage: (a) Flow velocity field; (2) Temperature field

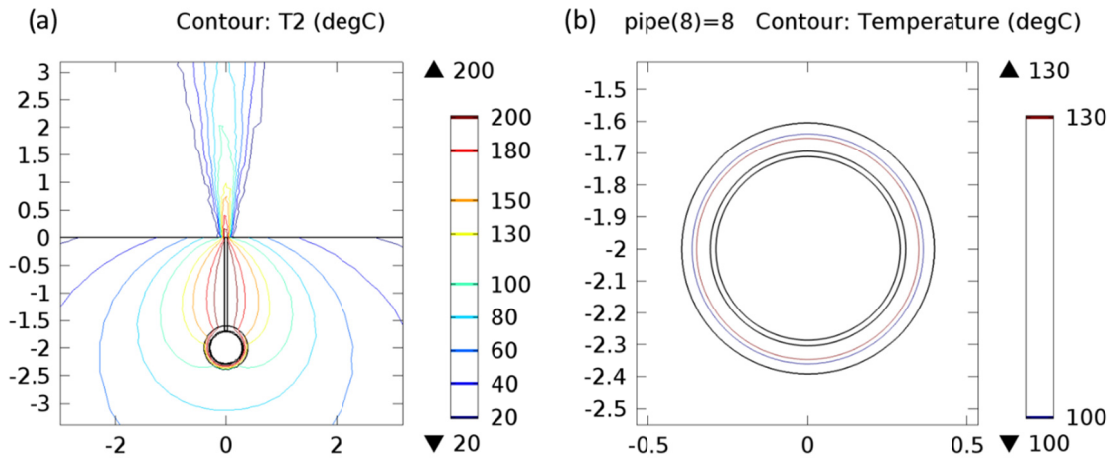


FIG. 8. Temperature distribution of steam pipe in (a) leaky operation condition; (b) normal operation condition

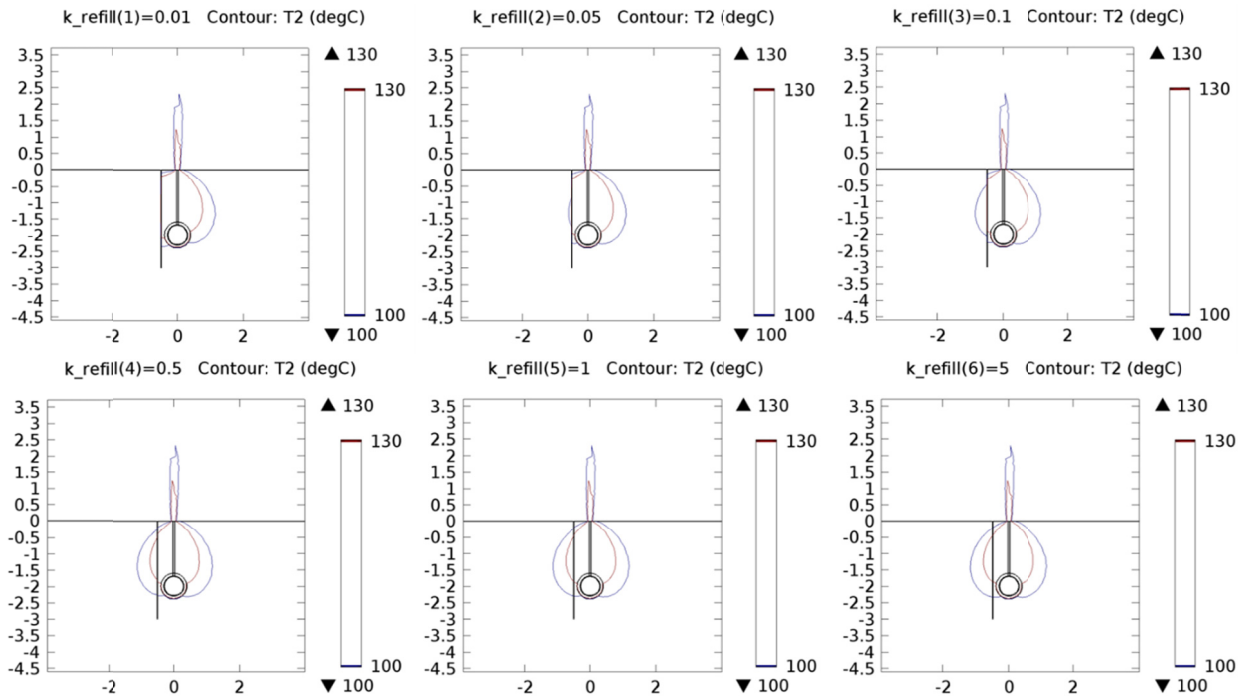


FIG. 9. Sensitivity analysis on the thermal conductivity of thermal protection channel in leaky operation condition
 $k_{refill}(1)=0.01$ Contour: T2 (degC)

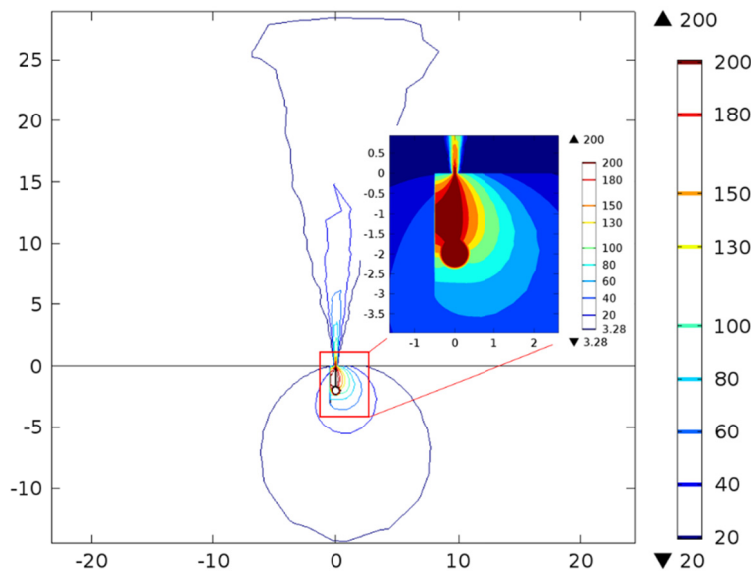


FIG. 10. Temperature distribution of steam pipe in leaky operation condition with thermal protection channel

CONCLUSIONS

This paper simulated the heat transfer process around steam pipe under both normal operation and operation with leakage. To prevent damages to adjacent urban infrastructures due to leakage of hot steam, the required safety distance from steam pipe and design of thermal protection channel are analyzed with the finite element simulations. The results show that maintaining the

minimum safety distance can provide protection to prevent damages of HDPE pipe by leakages of steam pipe. Otherwise, thermal protection channel refilled with proper thermal insulation material can be used, particularly for locations with limited underground space. The thermal properties of refill materials need to be carefully chosen to ensure such thermal protection is effective. Overall, this paper provides insight on the design criteria to ensure the safety of HDPE sewage pipe adjacent to steam pipes.

REFERENCE

- ASHRAE (2008). ASHRAE Handbook: 2008 HVAC Systems and Equipment, American Society of Heating, Refrigerating and Air-Conditioning Engineers, Inc., Atlanta, GA 30329.
- ASTM A53/A53-12 (2012). "Standard Specification for Pipe, Steel, Black and Hot-Dipped, Zinc-Coated, Welded and Seamless." ASTM International, West Conshohocken, PA.
- Belson, K. and A. DePalma (2007). Asbestos and Aging Pipes Remain Buried Hazards. The New York Times. July 19.
- Gandhi, M. S., A. A. Ganguli, J. B. Joshi and P. K. Vijayan (2012). "CFD simulation for steam distribution in header and tube assemblies." *Chemical Engineering Research and Design* 90(4): 487-506.
- Jaske, C. E. (1990). "Life Assessment of Hot Reheat Steam Pipe." *Journal of Pressure Vessel Technology* 112(1): 20-27.
- Liaw, P. K., A. Saxena and J. Perrin (1993). "Life extension technology for steam pipe systems—I. Development of material properties." *Engineering Fracture Mechanics* 45(6): 759-786.
- Liaw, P. K., A. Saxena and J. Schaefer (1989). "Estimating remaining life of elevated-temperature steam pipes—Part I. Materials properties." *Engineering Fracture Mechanics* 32(5): 675-708.
- Liaw, P. K., A. Saxena and J. Schaefer (1989). "Estimating remaining life of elevated-temperature steam pipes—Part II. Fracture mechanics analyses." *Engineering Fracture Mechanics* 32(5): 709-722.
- Morris, A., J. Dear and M. Kourmpetis (2006). "High Temperature Steam Pipelines – Development of the ARCMAC Creep Monitoring System." *Strain* 42(3): 181-185.
- Singh, R. and S. R. Singh (1997). "Remaining creep life study of Cr-Mo-V main steam pipe lines." *International Journal of Pressure Vessels and Piping* 73(1): 89-95.
- Stevanovic, V., M. Studovic and A. Bratic (1994). "Simulation and analysis of a main steam line transient with isolation valves closure and subsequent pipe break." *International Journal of Numerical Methods for Heat & Fluid Flow* 4(5): 387-398.
- Tapsell, H. J. (1944). "Creep Properties of Steels Utilized in High-Pressure and High-Temperature Superheater and Steam Pipe Practice. Part I: Carbon Steels*." *Proceedings of the Institution of Mechanical Engineers* 151(1): 54-62.
- The Engineering ToolBox. "http://www.engineeringtoolbox.com/flow-velocity-steam-pipes-d_386.html."
- The Engineering ToolBox "http://www.engineeringtoolbox.com/pipes-insulation-thickness-d_16.html."
- Wilcox, D. C. (1998). *Turbulence Modeling for CFD*, 2nd ed., DCW Industries.

The Use of Recycled Materials as Thermal Insulation in Underground Construction

James L. Hanson, M.ASCE, Ph.D., P.E.¹; Kevin B. Kopp, S.M.ASCE²; Nazli Yesiller, A.M.ASCE, Ph.D.³; Craig M. Cooledge, S.M.ASCE²; and Emily Klee, S.M.ASCE⁴

¹Professor, Civil and Environmental Engineering Dept., California Polytechnic State Univ., San Luis Obispo, CA 93407.

²Graduate Research Assistant, Civil and Environmental Engineering Dept., California Polytechnic State Univ., San Luis Obispo, CA 93407.

³Director, Global Waste Research Inst., California Polytechnic State Univ., San Luis Obispo, CA 93407.

⁴Undergraduate Student, Environmental Resources Engineering Dept., Humboldt State Univ., Arcata, CA 95521.

Abstract: This investigation was conducted to evaluate the use of recycled materials in underground construction. Facilities constructed underground benefit from stable thermal boundary conditions resulting in reduced heating and cooling requirements. Numerical analysis using 2D finite element method was conducted to investigate a simulated underground facility (i.e., warehouse). The cross-sectional dimensions for the warehouses were 50 m x 10 m. Analyses were conducted for three locations representing cold, temperate, and arid climates. The required heating and cooling energy demands to maintain a target temperature inside the warehouses were determined. Three target temperatures were evaluated: -25°C (cold storage), 10°C (specialized storage), and 20°C (human occupancy). Different insulation materials including waste-derived materials were assessed. Simulations using conventional XPS insulation and no insulation were compared to shredded tires and waste textiles. The heating energy demands were between 0 and 268.0 GJ/year and the cooling energy demands were between 3.1 and 1491.5 GJ/year. The results indicated that the recycled waste materials were effective in providing insulation function. In particular, the textile waste materials matched or exceeded the performance of conventional insulation indicating viability for use as thermal insulation in underground construction applications.

INTRODUCTION

Energy used for heating and cooling constitutes a significant fraction of total energy consumed in various parts of the world. In the U.S., the energy used for heating and cooling exceeds 40% of total energy consumption in commercial applications and is approximately 50% of total energy consumption for residential applications (EIA

2015). Underground space utilization has been demonstrated to be efficient for energy savings for a broad range of building functions and climatic conditions (Carmody and Sterling 1993). Heat transfer analysis is required when subsurface is used as an insulating or dissipating medium for underground utilities (e.g., electrical, water, and liquid natural gas lines), for storage of cold and hot materials (e.g., storage of perishable goods), and for buildings with variable functions (e.g., commercial space, residential space). Conductive heat transfer analysis is often used for investigation of ground temperature variations, as the primary mechanism responsible for heat transfer in soils is conduction (Persaud and Chang 1983, Mitchell 1993).

Effectiveness of underground structures in different climatic regions has been demonstrated in various investigations. As an example, Kuraoka and Hane (1985) documented energy savings for underground food storage in a temperate climate. Van Dronkelaar et al. (2014) presented an extensive parametric evaluation related to thermal energy requirements for underground facilities for six different functions in fifteen distinct climatic regions representative of habitable areas with approximately 90% of the world population.

Use of thermal insulation affects the energy demands for maintaining controlled temperatures. Variations in insulation material thermal conductivity requirements were determined for residential application as a function of depth of placement of the structure for climatic conditions in Korea (Kim and Kim 2004). Use of recycled plastic waste materials derived from municipal solid waste as insulation for basements was investigated (Cherif Megri 2010). Comprehensive analysis of variable waste materials, climatic conditions, and intended use of the underground space had not been conducted in previous studies. This study was conducted to investigate the use of waste- and byproduct-derived insulation materials in underground structures with variable functions located in multiple climatic regions. Numerical analysis was used to evaluate the effectiveness of waste and byproduct insulation materials.

MODEL FORMULATION

Numerical simulations were conducted using a 2D finite element analysis approach (Abaqus CAE version 6.11 software). Quadrilateral elements ranging from approximately 0.1 m x 0.1 m to 1 m x 5 m were used for the analysis. The model consisted of approximately 10,000 elements. The time step was established as 1 day for the simulations. Initially, the entire model for a given site was set to a constant temperature representing the mean annual earth temperature at the site. Next, the model was allowed to run under the influence of variable (i.e., seasonal) ground surface temperature fluctuations over a start-up simulation period of 20 years to reach thermal stasis. Then, the model was run to generate specified target temperatures in the warehouse. A user-defined subroutine was developed to iteratively solve, at each time step, the incremental heat flux required to maintain the constant target temperature and to apply this flux to appropriate nodes along the warehouse boundary. This stage of modeling included a 4-year-simulation period to reach the new thermal stasis for the target constant working warehouse temperature conditions and a follow-up one-year period under quasi steady-state working conditions. Finally, the required heating and cooling demands to maintain the target temperature inside

the selected facility were determined. Heating and cooling requirements were established using heat flux over the entire surface area of the simulated underground facility for the final one-year period. The finite element model was verified using an analytical solution for a fundamental conductive half-space model subjected to periodic temperature variation at the surface (Carslaw and Jaeger 1959).

Geometry

The 2-D simulations were conducted for a warehouse with cross sectional dimensions of 50 m width x 10 m height. When used, insulation materials were configured in a 1 m-thick layer surrounding the exterior surface area of the entire warehouse. The warehouse contained 1 m thick concrete walls, floor, and roof. The top surface of the warehouse roof was situated 2 m below the ground surface. A schematic depiction of the model geometry is provided in Figure 1.

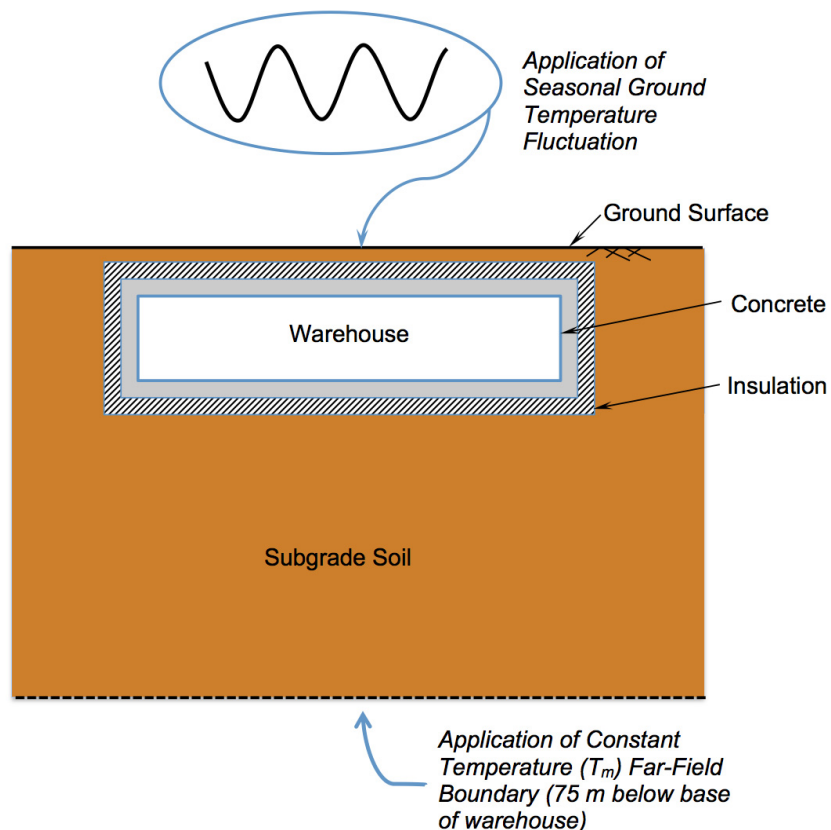


FIG. 1. Schematic of model.

Test Sites

Modeling and analysis were conducted for three locations across the U.S. in different climatic regions (Figure 2). Details of climate classification using the Köppen-Geiger Climate Classification System as presented in Peel et al. (2007) and the relevant climatic statistics are presented in Table 1. The sites were selected to

provide data and analysis for variable climatic conditions. At each site, constant warehouse temperatures of -25°C , 10°C , and 20°C were used representing bulk cold storage, specialty storage applications, and human occupancy conditions, respectively.

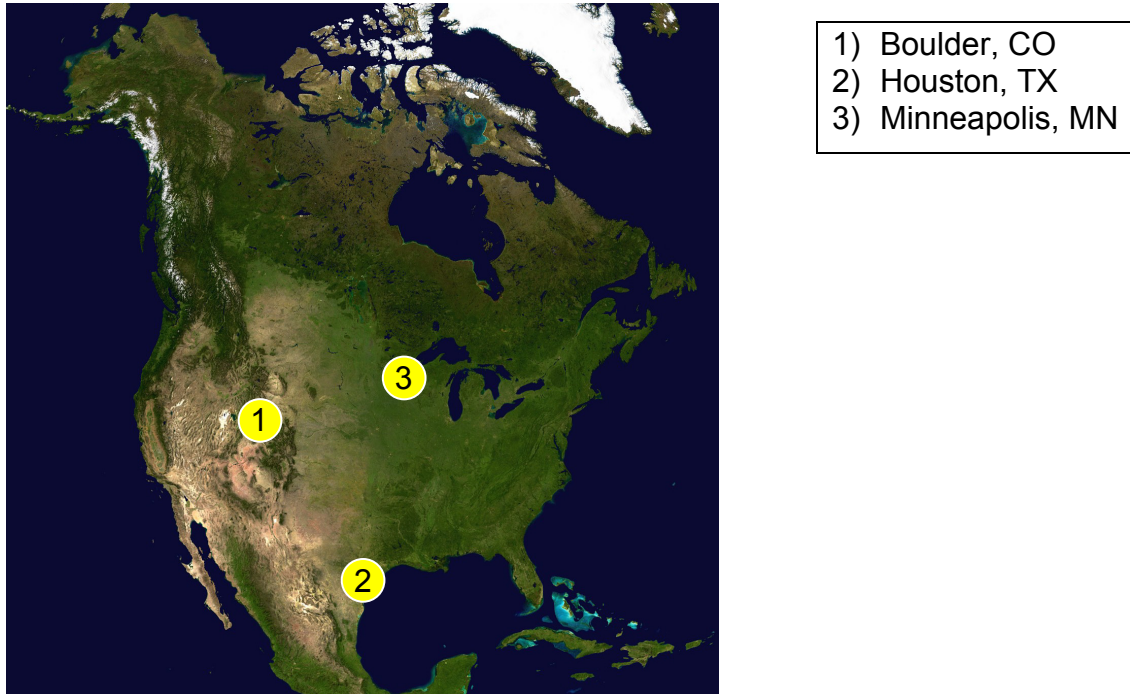


FIG. 2. Locations of model test sites.

Table 1. Climate Data

Parameter	Boulder Colorado	Houston Texas	Minneapolis Minnesota
Climate Zone and Description	Arid, steppe, cold	Temperate, without dry season, hot summer	Cold, dry winter, warm summer
Köppen-Geiger Climate Classification	BSk	Cfa	Dwb
Average daily high temperature ($^{\circ}\text{C}$) ^a	18.7	26.6	13.0
Average daily low temperature ($^{\circ}\text{C}$) ^a	3.4	15.3	3.1
Average daily temperature ($^{\circ}\text{C}$) ^a	11.1	21.0	8.0
Annual normal precipitation (mm) ^a	533	1224	770
Annual normal snowfall (mm) ^a	2264	5	1266
Mean annual earth temperature ($^{\circ}\text{C}$) ^b	11.1	24.4	7.8

^aFrom NCDC (2015)

^bFrom ORNL (1981)

Material Properties and Boundary Conditions

The materials used in the simulations included soil, concrete, internal space of the warehouse, and thermal insulation. A total of four insulation conditions were simulated: no insulation, conventional insulation, shredded waste rubber tires, and waste textiles. The thermal properties of the materials used in the analyses are provided in Table 2.

Table 2. Thermal Properties

Material	Thermal Conductivity (W/mK)	Density (kg/m ³)	Heat Capacity (J/kgK)
Soil	2.0	2000	1300
Concrete	1.70	2500	670
Internal Space ^a	0.093	275	1876
Conventional XPS Thermal Insulation ^b	0.029	48.1	1500
Shredded Tire Insulation ^c	0.24	660	1470
Textile Insulation ^d	0.03	350	1250

^arepresents weighted average for a warehouse

^bOwens Corning (2015)

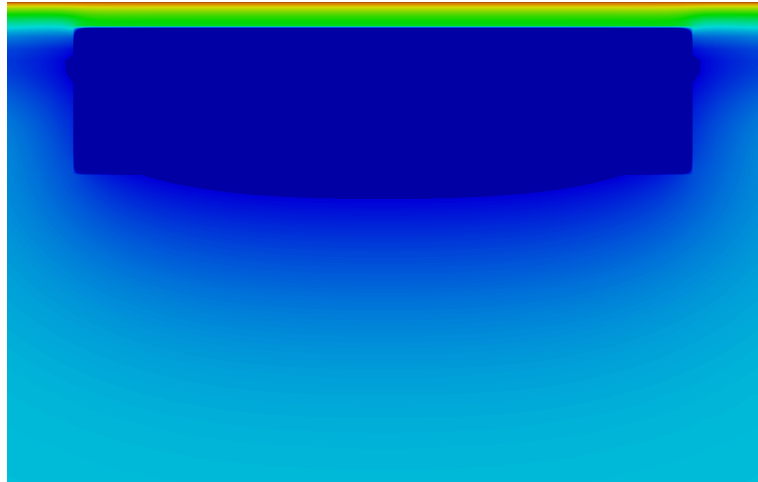
^cHumphrey (1999) and Balunaini et al. (2009)

^dStankovic et al. (2008)

Boundary conditions required in modeling heat transfer associated with the underground storage facility consisted of seasonal ground surface temperature fluctuations and a far field boundary at depth. The seasonal ground surface temperature fluctuations were established using surface n -factors to convert air temperatures to ground temperatures (Andersland and Ladanyi 1994). The freezing and thawing n -factors used were 0.9 and 1.3, respectively. The conventional 30-year definition of n -factors was applied, providing statistically representative conditions for each site. The far field (i.e., bottom) boundary was established at constant mean annual earth temperature for each test site. The far-field boundary condition was applied at a depth that was 75 m below the base of the warehouse. The distance to the far-field boundary was determined by analyzing the temperature response of different model geometries using increasingly greater depths to establish constant temperature.

RESULTS AND DISCUSSION

Example contour plots representing underground temperature distributions for the site located in Boulder are presented in Figure 3. Data are presented for the vicinity of the warehouse (not the entire model configuration) for textile insulation and all three target warehouse temperatures. The graphics represent conditions on July 1 of a given year. The highest influence of the warehouse was observed for the coldest target warehouse temperature conditions. High temperature variations occurred above the warehouse near the ground surface. The presence of the warehouse interrupted the baseline seasonal temperature variations with depth in the subsurface.



a) Warehouse at -25°C



b) Warehouse at 10°C



c) Warehouse at 20°C

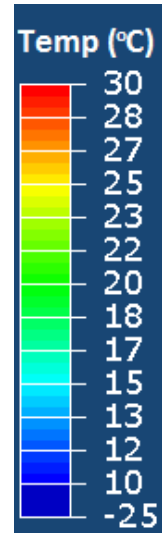


FIG. 3. Model results for Boulder with waste textile insulation.

Thermal gradients (defined as change in temperature per unit length) were largest near the warehouse due to presence of abrupt temperature changes at the facility boundary and to a lesser degree, at the ground surface due to presence of seasonal temperature variations. The magnitudes of thermal gradients were a function of target warehouse temperature, site location and season, as well as type of insulation. Highest thermal gradients were observed when the difference between target warehouse temperature and ambient ground temperatures were greatest. This generally occurred at the top of the warehouse where seasonal ground temperature extremes were present. Maximum thermal gradients were on the order of $32^{\circ}\text{C}/\text{m}$. Presence of the warehouse affected the ambient ground temperature fluctuations for a zone surrounding the warehouse. At distances up to approximately 11 m away from the warehouse (i.e., outside of the insulation/soil interface), the thermal regime approached ambient ground temperature conditions. At depths below approximately 30 m, thermal gradients were negligible.

A summary of the results of the numerical simulations for the three climatic regions, four insulation conditions, and three target warehouse temperatures is provided in Table 3. Data are provided for heating energy demands (heating energy required to reach and remain at target warehouse temperature) and cooling energy demands (cooling energy required to reach and remain at target warehouse temperature) for the different scenarios. Heating and cooling energy demands at a given site were controlled by the target warehouse temperature and the climatic conditions including seasonal ground surface temperature variations, constant earth temperature at depth, and presence of thermal insulation. Thermal energy requirements are reported in GJ/year for a unit length of warehouse into the page (1 m for this case). Heating energy demands were greatest in Minneapolis and lowest in Houston, whereas cooling energy demands were highest in Houston and lowest in Minneapolis. Intermediate energy demands were generally observed for Boulder (Table 3).

Overall, the inclusion of thermal insulation reduced heating and cooling energy demands for all simulations (Table 3). The waste and byproduct-derived insulations were effective in reducing energy demands. Textile insulation was more effective at providing thermal energy savings for all simulations compared to shredded tire insulation. In general, the energy demands were similar for conventional XPS insulation and waste textile insulation. The temperature profiles for the unconventional waste-derived insulation materials approached that for the conventional XPS insulation based on analysis of the numerical simulations of the underground thermal conditions. While the density of the waste textile insulation was higher than that of XPS insulation and the heat capacity of the waste textiles was lower than that of XPS insulation, the thermal conductivity of the two materials were similar. The heat capacities for XPS and shredded tire insulation were similar, whereas both the thermal conductivity and density of the tires were higher than those for XPS insulation. The thermal response simulated herein likely was controlled by the thermal conductivity of the materials with similar results obtained for the materials with similar thermal conductivity values (Table 3).

Table 3. Results of Simulations

Site	Target Temperature (°C)	Heating and [Cooling] Energy Demands (GJ/year)			
		None	XPS	Tires	Textiles
Boulder Colorado	-25	0 [1190.0]	0 [203.0]	0 [767.5]	0 [209.0]
	10	49.5 [184.0]	5.0 [27.8]	26.5 [112.8]	4.2 [27.8]
	20	207.5 [42.0]	32.1 [4.1]	128.3 [22.2]	32.2 [3.3]
Houston Texas	-25	0 [1491.5]	0 [254.3]	0 [961.8]	0 [261.9]
	10	1.4 [438.0]	0 [74.5]	0.2 [281.8]	0 [76.7]
	20	39.7 [174.3]	3.9 [26.8]	21.1 [107.6]	3.2 [26.9]
Minneapolis Minnesota	-25	0 [1129.7]	0 [192.7]	0 [728.6]	0 [198.4]
	10	81.4 [155.4]	8.8 [21.3]	44.3 [91.7]	7.9 [20.8]
	20	268.0 [42.2]	42.2 [3.9]	167.0 [22.0]	42.6 [3.1]

Total annual thermal energy demands (summation of heating and cooling energies) ranged from 28.7 GJ/year (warehouse in Minneapolis, waste textile insulation, maintained at 10°C) to 1491.5 GJ/year (warehouse in Houston, no insulation, maintained at -25°C). The greatest thermal energy demands for warehouses maintained at -25°C, 10°C, and 20°C were 1491.5, 439.4, and 310.2 GJ/year, respectively. These three cases with maximum thermal energy demands were for no insulation scenarios. For comparison, maximum energy requirements for scenarios with insulation were obtained for waste tire insulation and were 961.8, 282.0, 189.0 GJ/year for -25°C, 10°C, and 20°C warehouse temperatures, respectively with lower values for the XPS and textile insulations. Comparisons were made for energy savings between no insulation and insulation conditions. Savings in total annual energy demands ranged from 82 to 87%, 36 to 43%, and 82 to 88% for XPS, waste tire, and waste textile insulations. These comparisons demonstrate that use of insulation directly increases the effectiveness of underground building construction applications. Type of insulation (i.e., thermal properties) significantly affects the extent of energy savings.

CONCLUSIONS

While the use and benefits of insulation in above ground applications is well documented, limited information is available on insulation for underground construction. This investigation was conducted to evaluate the use of waste-derived thermal insulations in underground construction applications. The investigation included three climatic regions representing arid (Boulder, Colorado), temperate (Houston, Texas), and cold (Minneapolis, Minnesota) climates. Four insulation conditions (no insulation, conventional XPS insulation, shredded rubber tires, and

waste textiles) and three target warehouse temperatures (-25°C, 10°C, and 20°C) representing numerous storage and occupancy applications were modeled. Analysis was conducted using 2D finite element modeling. The heating energy demands per unit length for the model warehouse were between 0 and 268.0 GJ/year and the cooling energy demands were between 42.0 and 1491.5 GJ/year for no insulation scenarios, whereas heating energy demands were between 0 and 167.0 GJ/year and the cooling energy demands were between 3.1 and 961.8 GJ/year with the use of insulation materials. Maximum thermal gradients in the immediate vicinity the warehouse were on the order of 32°C/m. Textile insulation was more effective at providing thermal energy savings for all simulations compared to shredded tire insulation. In general, the energy demands were similar for conventional XPS insulation and waste textile insulation with energy savings on the order of 85% compared to no insulation conditions. Use of waste materials and byproducts provides a viable alternative for beneficial reuse of these materials.

ACKNOWLEDGMENTS

This study was partly supported by the Global Waste Research Institute. Mr. Kevin Kopp and Ms. Emily Klee were supported by NSF REU Site Grant No. 1263337.

REFERENCES

- Andersland O. B. and Ladanyi B. (1994). *An Introduction to Frozen Ground Engineering*. Chapman and Hall, New York.
- Balunaini, U., Yoon, S., Prezzi, M., and Salgado, R. (2009). "Tire shred backfill in mechanically stabilized earth wall applications." Final Report, FHWA/IN/JTRP-2857, U.S. Department of Transportation Federal Highway Administration, Washington, D.C.
- Carmody, J. and Sterling, R.L. (1993). *Underground Space Design A Guide to Subsurface Utilization for People in Underground Spaces*, Van Nostrand Reinhold, New York.
- Carlsaw H.S. and Jaeger J.C. (1959). *Conduction of Heat in Solids*, 2nd Ed. Oxford University Press Inc., New York.
- Cherif Megri, A. (2010). "An alternative procedure to recycling plastic waste for basement underground thermal insulation in cold climate buildings." *Journal of Solid Waste Technology and Management*, Vol. 36 (1): 44-53.
- EIA (2015). U.S. Energy Information Administration, Consumption and Efficiency, www.eia.gov/consumption, last accessed 18 May 2015.
- Humphrey, D. (2003). *Civil Engineering Applications Using Tire Derived Aggregate (TDA)*. California Integrated Waste Management Board, Publication #DRRR-2011-038.
- Kim, B.S. and Kim, K. (2004). "Analyses in thermal insulation performance of earth-covered wall for residential underground space by using a numerical simulation program." *Journal of Asian Architecture and Building Engineering*, Vol. 3 (2): 259-266.

- Kuraoka, S. and Hane, T. (1985). "Refrigerated rock cavern for food storage." *Journal, REITO*, Japan Society of Refrigerating and Air Conditioning Engineers, Vol. 60 (687): 95-99.
- Mitchell, J.K. (1993). *Fundamentals of Soil Behavior*, 2nd Ed., Wiley, New York.
- NCDC (2015). National Climatic Data Center "Climate database."
<http://www.ncdc.noaa.gov/>, last accessed 15 August 2015.
- ORNL (1981). *Regional Analysis of Ground and Above-Ground Climate*. Oak Ridge National Laboratory Report No. ORNL/Sub-81/40451/1, U.S. Department of Energy, Office of Buildings Energy R&D.
- Owens Corning (2015). Foamular Extruded Polystyrene (XPS) Product Data Sheet, <http://foamular.com/assets/0/144/172/174/11b5f50a-0f80-4f08-bebe-71f4b6a9fdf7.pdf>
- Peel, M.C., Finlayson, B.L., and McMahon, T.A. (2007). "Updated world map of the Köppen-Geiger Climate Classification." *Hydrology and Earth System Sciences*, Vol. 11: 1633-1644.
- Persaud, N. and Chang, A. C. (1983). "Estimating soil temperature by linear filtering of measured air temperature." *Soil Science Society of America Journal*, Vol. 47, (5): 841-847.
- Stankovic, S. B., Popovic, D. and Poparic, G. B. (2008). "Thermal properties of textile fabrics made of natural and regenerated cellulose fibers." *Polymer Testing* Vol. 27 (2008): 41-48.
- Van Dronkelaar, C., Cóstola D., Mangkuto, R.A., and Hensen, J.L.M. (2014). "Heating and cooling energy demand in underground buildings: Potential for saving in various climates and functions." *Energy and Buildings*, Vol. 71: 129-136.

A Sustainable Perspective for the Long-Term Behavior of Energy Pile Groups

Sherif L. Abdelaziz, A.M.ASCE¹

¹Assistant Professor, Dept. of Civil Engineering, Stony Brook Univ., 116 Heavy Engineering, Stony Brook, NY 11794-2323.

Abstract: This paper discusses the impact of ground-coupled heat pump operation on the performance of energy pile groups. Energy piles are used to support large buildings with groups of energy piles rather than single piles. Furthermore, space-cooling dominates the thermal loads for such buildings corresponding to dominant ground-heating loads. Finite element analysis is used in this paper to investigate the long-term thermal operation of energy pile groups subjected to ground-heating dominant loads considering the thermal operation of the heat pump. While the used thermal loads in this study represents an extreme conditions for ground heat exchange system, the results of this analysis show that the thermal efficiency of energy pile groups subjected to ground dominant loads decays after two years to a significantly reduced capacity. This decay in the performance is attributed to the automatic shut-off of the heat pump. Therefore, different alternatives to ensure that the system operates at its maximum efficiency are considered. The recommended approach is to balance the ground thermal loads applied on energy pile groups. Balanced ground thermal loads cause freezing-heating cycles in soils surrounding energy pile groups for most applications. Further analysis is needed to consider more realistic thermal loads and heat pump operations.

INTRODUCTION

The use of pile foundations as ground-coupled heat exchangers, known as energy piles, is growing worldwide. The use of energy piles for heating and cooling of buildings relies on the fact that the temperature of the ground below the top 5 meters remains relatively constant throughout the year (Kavanaugh and Rafferty, 1997). Thus, utilizing the ground as a heat source when ground is warmer than ambient (i.e., winter) and as a heat sink when the ground is cooler than ambient (i.e., summer) presents a logical technique for heating and cooling of buildings (Brandl, 2006). Ground-coupled systems heat or cool building spaces via a ground-coupled heat pump circulating an exchange fluid in heat-exchange pipes facilitating the exchange of the thermal energy between the building and the ground. Despite the promising utilization of the ground-coupled systems for space heating and cooling, the initial installation costs limit the growth of the technology (Brandl, 1998; Brandl, 2006; Laloui et al., 2006; Olgun et al., 2014; Abdelaziz et al., 2015) especially in the U.S.

market where, until now, building codes do not enforce a mandatory use of sustainable energies in new structures.

In order to reduce the high initial drilling costs, vertical closed-loops may be installed inside deep foundation elements that are structurally needed, known as Energy Piles (Brandl, 1998; Brandl, 2006). Energy piles offer a cost effective way to incorporate the green geothermal heat exchanger in new building constructions. However, enforcing temperature changes in energy piles raises multiple research challenges including (1) the thermo-mechanical response of the pile, and (2) the long-term thermal performance of the energy piles. The former challenges were the focus of numerous research studies that provide an initial understanding of thermal stresses and strains that develop in energy piles throughout their life time (Laloui et al., 2006; Bourne-Webb et al., 2009; McCartney et al., 2010). The latter; i.e., the long-term thermal performance of energy piles, was also presented in multiple research studies which were concerned with the temperature changes in and around the piles given a hypothetical building energy demands (Olgun et al., 2014; Batini et al., 2015). Unfortunately, none of these studies considered the impact of ground-couple heat pump (GCHP) on the approximated long-term thermal performance, which is the focus of this study.

OPERATIONAL BACKGROUND

Structural and Thermal Loads

The economical use of energy piles is for buildings with large structural loads founded on relatively weak soils, which require groups of deep foundation elements for structural safety; therefore, when a building is to incorporate energy piles as the supporting foundation, a group of energy piles is installed rather than a single pile installation. Examples of buildings that are currently supported on energy pile groups include the Dock Midfield at the Zürich Airport in Switzerland (Pahud and Hubbuch, 2007), the rehabilitation center Bad Schallerbach and the Arts Centre in Austria (Brandl, 1998; Brandl, 2006), Keble College at Oxford University (Brandl, 2006), and the Lambeth College in London (Bourne-Webb et al., 2009). In addition to the need for energy pile groups for their structural support, these buildings are characterized by their dominant space-cooling demands, regardless of the geographic locations and ambient weather, due to human activities and/or equipment usages taking place inside the building (Brandl, 2006). Thus, a considerable amount of thermal energy needs to be extracted from the building space and injected into the ground; i.e., dominant ground-heating. Therefore, this paper is focused on understanding the long-term thermal performance of energy pile groups operating under dominant ground-heating loads.

Thermal Operation of Ground Heat Pumps

The long-term thermal performance of energy piles, and any ground heat exchangers, depends on the operation of the ground-coupled heat pump (GCHP), which connects the building's HVAC system to the ground loops. The GCHP

facilitates the heat exchange process between the building and the ground loops through a secondary refrigerant loop inside the GCHP (Siegenthaler, 2010); the refrigerant in the secondary loop evaporates when heated and condenses back to liquid when cooled. Therefore, the internal components of any GCHP include an evaporator and a condenser. These components are very sensitive to the refrigerant temperature being circulated in the secondary loop, which depends on the temperature of the fluid entering the GCHP from the ground; i.e., the return fluid from the ground loops. Therefore, a maximum temperature for the returning fluid from the ground loop is always enforced (Gaspredes et al., 2014). This maximum returning fluid temperature is generally selected as the minimum of (1) the maximum temperature that the GCHP components can handle or (2) the melting temperature of the ground loop material. The melting (rated) temperature for the ground loop is generally less than the maximum temperature for the GCHP components. Therefore, GCHPs are programmed to automatically shut off when the temperature of the returning fluid from the ground loops approaches the melting point for the loop material. The melting temperature for the most commonly used ground loop materials; i.e., high density Polyethylene (HDPE) and Cross-linked Polyethylene (PEX), is about 65 °C; the automatic shut off temperature is generally selected to be about 60 °C considering 5 °C as a safety margin (Gaspredes et al., 2014). The impact of this automatic system shut off on the long-term performance of energy pile groups subjected to dominant ground heating energy wave is investigated in this study using finite element numerical models.

NUMERICAL MODEL

COMSOL Multiphysics finite element package (COMSOL, 2014) is used in this study to investigate the impact of GCHP operation on the performance of energy pile groups subjected to ground-heating dominant loads. This section presents the details of the finite element models used in this study.

Geometry and Material Properties

Since the thermal performance of energy piles is predominant in the radial direction (Lazzari et al., 2010; Abdelaziz et al., 2011; Abdelaziz, 2013; Olgun et al., 2014), two-dimensional horizontal cross-sectional finite element models are used in this study. A 3×3 energy piles group — 600 mm in diameter — embedded in a homogeneous and isotropic loose sandy soil layer is considered. The center-to-center distance between adjacent energy piles equals three times the piles' diameter; i.e., 1.80 m, in accordance to general pile design practices (Federal Highway Administration, 2010). Each of the considered piles is provided with double 34-mm HDPE ground loops at 350 mm away from one another as shown in Figure 1. Table 1 presents the thermal properties for the soil, the piles, ground loops, and the geothermal fluid used in the numerical models. The geothermal fluid is assumed to be circulated at 20 dm³/s in the circulation loops.

Utilizing 2-D finite element models accounts for the heat conduction through the walls of the ground loops, within the pile material, and within the soil. Abdelaziz

(2013) showed that 2-D modeling for energy piles is adequate providing the fact that the ground surface for energy piles is typically insulated as part of good building construction practices. The geothermal fluid is modeled as a solid domain due to the fact that the length of the loops is ignored in the adopted modeling technique. Therefore, the effect of the convection heat between the flowing fluid and the inner surface of the ground loop is not built-in to the adopted modeling approach. The convective heat effects are incorporated into the 2-D model via assigning high thermal conductivity to the fluid domain (1000 W/m·K is used for the models reported herein); meanwhile, the thermal conductivity of the walls of the ground loops is modified to account for the convective heat effects following the technique proposed by Lazzari et al. (2010).

Table 1. Thermal Properties of Various Materials used in the FE Models.

Thermal Property	Soil	Pile	Ground Loop	Fluid
Density (kg/m ³)	2000	2500	960	1000
Thermal Conductivity (W/m·K)	2.00	1.50	0.39	0.594
Specific Heat Capacity (J/kg·K)	1500	1200	2300	4186.9

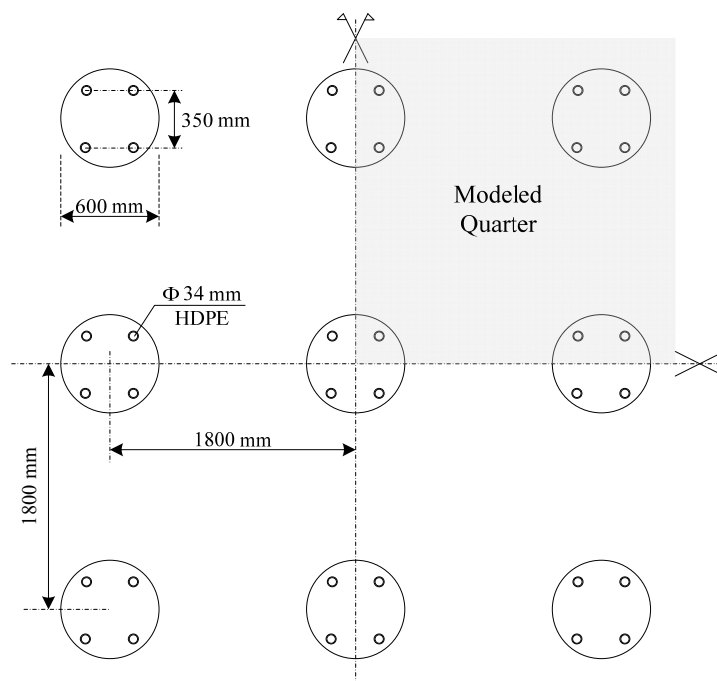


FIG. 1. Considered Energy Pile Group.

Model Extension, and Boundary and Initial Conditions

The selected energy pile group is symmetric in the vertical and horizontal directions, as shown in Figure 1. Due to this symmetry, the models reported in this study considers only one-quarter of the pile group; i.e., the highlight area in Figure 1, by assigning symmetrical boundary conditions at the lower and left boundaries of the modeled quarter.

The extent of the model is selected such that the boundary conditions at the external boundaries; i.e., top and right boundaries of the modeled quarter in Figure 1, do not affect the temperature changes approximated around the pile group. Models with various lateral extents were considered; the external boundaries are altered between constant temperature set to the undisturbed ground temperature and thermal insulation. A 20-m-square soil domain was found sufficient to ensure that the results are independent of the external boundary conditions. In the final models, the external boundaries are thermal insulation.

The initial ground temperature is assumed to be 10 °C representing the undisturbed ground temperature for Chicago, IL. However, this initial ground temperature affects the ground temperature rather than the temperature change (ΔT) during the thermal operation of the system. In other words, ΔT in and around the piles are independent of the initial assigned ground temperature. Therefore, ΔT in and around the piles are used as the basis for assessing the long-term performance of the pile groups.

Applied Thermal Load

As discussed above, energy piles support buildings with space-cooling demands corresponding to ground-heating loads. Therefore, the thermal load applied to the considered group of energy pile is an unbalanced sinusoidal wave representing a dominating ground-heating load. The sinusoidal wave that represents dominating ground heating loads is characterized by (1) longer heating duration compared to the cooling duration, and (2) higher maximum heating amplitude compared to the maximum cooling amplitude. The selected sinusoidal energy wave for the analysis reported in this study is selected according to the equivalent energy wave concept (Abdelaziz et al., 2015) that suggests the durations of the non-dominant and dominant thermal loads to be three and nine months, respectively. Further, the equivalent energy wave concept suggests that the maximum amplitude of the non-dominant thermal load; i.e., the ground-cooling load, to be about one-third of the maximum amplitude of the dominant ground-heating load (Abdelaziz et al., 2015). Therefore, the energy wave applied to each of the considered piles starts with a 3-month cooling period with a maximum cooling amplitude of 20 W/m followed by 9 months heating period with a maximum heating amplitude of 60 W/m. The maximum heating amplitude, i.e. 60 W/m. is selected to be the average ultimate heat exchange capacity between energy piles and surrounding soils (Dupray et al., 2013). The selected energy wave is divided equally between all fluid domains installed inside each of the piles. Further, the energy wave is assumed to remain unaltered over the operational lifetime of the system, assumed 30 years in this study.

Discretization and Time Steps

Triangular finite elements are used to discretize all domains in the considered models; all the elements have quadratic shape function. The size of the elements was decreased incrementally in order to ensure that the results are mesh-independent. The final mesh that is used in the model, which confirm mesh-independent results, is set

with the following characteristics (1) minimum and maximum element size of 0.0025 and 0.75 m respectively, (2) maximum element growth rate of 1.25, and (3) a curvature factor of 0.25. Consequently, the total number of elements is 13,639 divided into 4,403 for the soil domain, 3,238 per a full pile domain, 100 per a full ground loop wall, 144 per each fluid domain.

RESULTS AND DISCUSSIONS

This sections presents the returning fluid temperature from the considered energy pile group and uses this fluid temperature to assess the impact of the ground-coupled heat pump on the long-term thermal operation of the system. Finally, ways to ensure high system efficiency over the expected long-term operation period are discussed.

Returning Fluid Temperature and Operational Time

As discussed earlier, the temperature of the returning fluid from the ground loops to the GCHP affects the thermal operation of the heat pump and, consequently, the thermal operation of the entire system. Figure 2 presents the evolution of the average returning fluid temperature from the considered energy piles, which is shown to increase with time. The annual increase in the temperature of the returning fluid is attributed to the fact that the ground load is heating dominant, which heats up the ground and, therefore, the returning fluid. When the temperature of the returning fluid is less than the maximum temperature of the ambient air; i.e., within segment I in Figure 2, the considered energy pile group operates at its maximum thermal efficiency. As the temperature of the returning fluid exceeds the maximum ambient air temperature in segment II, the thermal efficiency of the considered energy pile group decreases since the ambient air becomes a more efficient medium for cooling the building space. Further increase in the returning fluid temperature above the limiting preset auto turn off temperature; i.e., segment III, shuts down the GCHP and therefore, the system becomes inoperable.

As shown in Figure 2, when the pile spacing (S_{pile}) is three times the pile diameter (D_{pile}), the considered energy pile group operates at its highest thermal efficiency (i.e., segment I) during the ground cooling seasons of the first three years. The system operates at a reduced efficiency during all heating seasons during the first 4 years; while, it becomes inoperable at the peak of the heating season in the fifth year. By the tenth year, the system is inoperable for the entire heating season. In other words, the system is not operating for most of the time given that the applied ground thermal loads are heating dominant. It should be noticed that the current models do not account for the reduced fluid temperature upon GCHP termination; thus, it is expected that energy pile groups will continue to operate but a reduced capacity.

Mitigating Efficiency Losses

Since energy pile groups installed following traditional geotechnical engineering practices become inoperable in few years, as presented in Figure 2, this section presents viable solutions to ensure that the system operates at all times with its

maximum thermal efficiency. Two alternatives are considered (1) widening the pile-to-pile spacing, and (2) balancing the ground thermal loads applied to the group.

Wider Pile Spacing: The typical pile-to-pile spacing in geotechnical/foundation engineering practices — i.e., $S_{pile} = 3 D_{pile}$ — is selected to ensure minimal mechanical/structural interaction between adjacent piles. This spacing may not be sufficient to minimize the thermal interaction between the piles causing an overall increase in the fluid temperature above the desired limits; i.e., maximum ambient air temperature and the auto shut off temperature for GCHP.

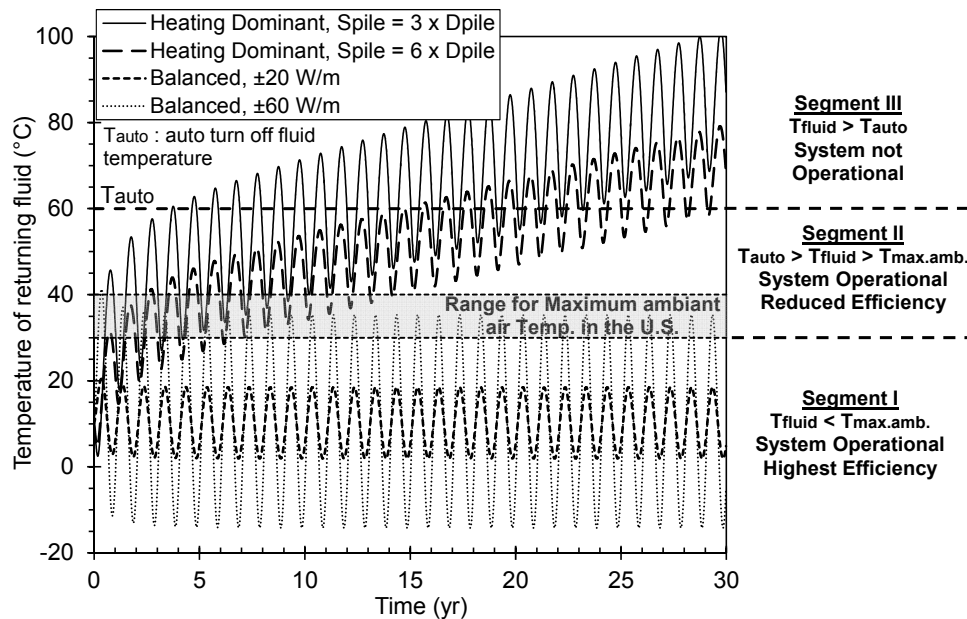


FIG. 2. Returning fluid temperature and effect of GCHP on system operation.

Widening the pile-to-pile spacing can be achieved by increasing the overall pile grade spacing reducing the total number of piles available to support the building structurally. This might not be an economic solution since the capacity of each individual pile would have to be increased via enlarging the pile diameter or length; further, achieving the desired group capacity with the reduced number of piles might be challenging. The other alternative to widen the pile-to-pile spacing is done by selectively switching some of the piles in the original grade into energy piles. In other words, maintaining the original overall pile-grad spacing at three times the pile diameter with the energy piles spacing set as a multiplier of the original overall pile-grad spacing. This alternative will not reduce the total number of piles needed to structurally support the building; however, the total number of energy piles is reduced which might not be sufficient to meet all the required thermal loads for the supported building. Thus, it is the engineer's responsibility to select the approach that meets the structural and thermal needs of the supported building.

In order to study the effect of increasing the spacing between energy piles in this study, the spacing between the considered energy piles is doubled; i.e., pile spacing equal to 6 times the pile's diameter (3.6 m). As shown in Figure 2, doubling the spacing reduced the maximum temperature of the returning fluid. Therefore, the

considered energy pile group will be able to meet all thermal demands of the supported building for about 15 years. Over this period, the system will operate at its highest efficiency only during the first year followed by 14 years operating at a reduced efficiency. Beyond the first 15 years, the system will fail to meet the peak building cooling needs until it becomes completely inoperable after 25 years. Widening the spacing between energy piles even more will increase the system operational period but it will not enhance the efficiency since the temperature of the returning fluid will exceed the maximum ambient air temperature, segment II, as a result of the applied ground heating dominant loads.

Balanced Ground Thermal Loads: The second alternative to ensure that energy pile groups operate at the maximum efficiency over the desired design period is achieved by balancing the applied ground thermal load. Balanced ground thermal loads refers to ground loads with equal heating and cooling episodes (6 months each) with equal heating and cooling maximum amplitudes (Abdelaziz et al., 2015). Two approaches can be followed to balance the applied ground thermal loads. The first is to limit the maximum ground heating load to the maximum ground cooling load which for the considered energy piles group equal 20 W/m; the remaining of the building's cooling load in the summer should be supplemented via external cooling towers. Following this approach, the system is ensured to be operating with the maximum efficiency over the considered 30 years period as shown in Figure 2. However, only a fraction of the maximum heat exchange capacity between energy piles and the surrounding grounds is utilized with additional expense needed for the external cooling towers. Therefore, this approach is not favored.

The other alternative is to utilize the maximum heat exchange capacity of the system in both heating and cooling modes. This can be achieved by using energy pile groups in winter to meet the heating needs of the building in addition to, possibly, providing hot water or other heating demands. In addition to utilizing the maximum heat exchange capacity of the ground, this approach ensures that the system is operating at its maximum efficiency over the considered 30 years operational period as shown in Figure 2. In other words, this approach offers a better use of the available resources and therefore it is recommended over the former approach.

Temperature Changes in and Around Energy Pile Groups

According to the previous discussions, balancing the ground thermal loads applied to energy pile groups is the most efficient approach to ensure a high efficiency for the system over the desired long-term operational duration. As presented in Figure 2, the balanced ground thermal loads cause ± 25 °C fluctuation in the average fluid temperature change. Similar temperature fluctuation occurs in the ground surrounding the pile group. The fluctuation of the ground temperature is of special interest for adequate design of energy pile groups since such fluctuation affects the thermo-mechanical behavior of the piles. As presented in Figure 3, the considered balanced ground thermal loads result cause ± 25 °C fluctuation in the temperature changes in the ground surrounding the pile group.

The approximated temperature change in and around energy piles is independent of the initial ground temperature; rather it depends on the magnitude of the applied thermal loads, the spacing between energy piles, and the thermal properties of the piles and the surrounding ground. Therefore, considering the approximated ± 25 °C ground temperature changes and given that the initial ground temperatures in U.S. are less than 25 °C, energy pile groups are expected to cause cycles of freezing-heating in the ground surrounding energy pile groups in the U.S.

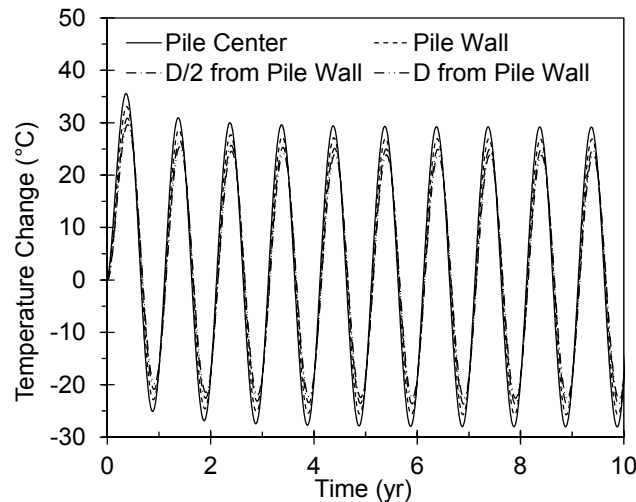


FIG. 3. Effect of balanced ground thermal loads applied to energy pile groups on the temperature change in and around the group.

CONCLUSIONS

Energy piles are most applicable for structures requiring pile foundations. Such structures are characterized with (1) large structural loads, which necessitates the use of groups of piles, and (2) dominant space cooling needs. These dominant space cooling needs are transferred into dominant ground heating loads. Thus, typical energy piles applications include an energy piles group operating under dominant ground thermal heating demands. Operating energy pile groups under dominant thermal heating loads results in a rapid increase in the temperature of the fluid returning from the ground loops to the ground coupled heat pump. Such increase in the returning fluid temperature reduces the thermal efficiency of the system after two to three years from the beginning of system operation. The numerical models showed that, after ten years, the system becomes completely inoperable as the returning fluid temperature exceeds the automatic shut-off temperature preset in the ground coupled heat pump to protect system components. However, the current models do not account for the reduced fluid temperature upon GCHP termination; thus, it is expected that energy pile groups will continue to operate but a reduced capacity. More accurate models are needed to approximate the expected decay in the system's capacity.

Balancing the ground thermal loads applied on energy pile groups was shown to be the most effective approach to ensure that the system operates at its maximum efficiency throughout the desired operational life. The balanced ground thermal

loads, when applied to energy pile groups, are expected to develop freezing-heating cycles in and around the group. Therefore, adequate and economical designs of energy pile groups require characterizing the soil behavior and pile-soil interaction when subjected to freezing-heating thermal cycles.

REFERENCES

- Abdelaziz, S., Olgun, C.G. and Martin, J.R. (2011). "Design and operational considerations of geothermal energy piles." *Geo-Frontiers 2011: Advances in Geotechnical Engineering* (GSP 211), ASCE, Reston/VA: 450-459.
- Abdelaziz, S.L. (2013). "Deep energy foundations: geotechnical challenges and design considerations." *The Charles E. Via Department of Civil and Environmental Engineering, Virginia Polytechnic Institute and State University*. Ph.D. Thesis, pp. 368.
- Abdelaziz, S.L., Olgun, C.G. and Martin, J.R. (2015). "Equivalent energy wave for long-term analysis of ground coupled heat exchangers." *Geothermics*, Vol. 53 (1): 67-84.
- Batini, N., Rotta Loria, A.F., Conti, P., Testi, D., Grassi, W. and Laloui, L. (2015). "Energy and geotechnical behaviour of energy piles for different design solutions." *Applied Thermal Engineering*, Vol. 86 (1): 199-213.
- Bourne-Webb, P.J., Soga, K., Amis, T., Davidson, C., Payne, P. and Amatya, B. (2009). "Energy pile test at Lambeth College, London: geotechnical and thermodynamic aspects of pile response to heat cycles." *Géotechnique*, Vol. 59 (3): 237-248.
- Brandl, H. (1998). "Energy piles for heating and cooling of buildings." *Seventh International Conference and Exhibition on Piling and Deep Foundations*, Westrade Group, Vienna/Austria.
- Brandl, H. (2006). "Energy foundations and other thermo-active ground structures." *Géotechnique*, Vol. 56 (2): 81-122.
- COMSOL (2014). "COMSOL Multiphysics™ Version 4.4: User's Guide and Reference Manual." COMSOL Inc., Burlington, MA.
- Dupray, F., Bachler, M. and Laloui, L. (2013). "Effect of groundwater flow on the THM behavior of an energy pile." *Coupled Phenomena in Environmental Geotechnics*, CRC Press, Boca Raton/FL: 483-489.
- Federal Highway Administration, F. (2010). "Drilled shafts: Construction procedures and LRFD design method" Federal Highway Administration, Reprot No. FHWA NHI-10-016, 970 p.
- Gaspredes, J.L., Masada, G.Y. and Moon, T.J. (2014). "A Simulink®-based building load-ground source heat pump model used to assess short-and long-term heat pump and ground loop performance." *J. Thermal Science & Engineering Applications*, Vol. 6 (2): 021013.
- Kavanaugh, S. and Rafferty, K. (1997). "Ground source heat pumps: Design of geothermal systems for commercial and institutional buildings." *ASHRAE*, Atlanta, Georgia: 175 p.
- Laloui, L., Nuth, M. and Vulliet, L. (2006). "Experimental and numerical investigations of the behaviour of a heat exchanger pile." *International Journal for Numerical and Analytical Methods in Geomechanics*, Vol. 30 (8): 763-781.
- Lazzari, S., Priarone, A. and Zanchini, E. (2010). "Long-term performance of BHE (borehole heat exchanger) fields with negligible groundwater movement." *Energy*, Vol. 35 (12): 4966-4974.
- McCartney, J.S., LaHaise, D., Lahaise, T. and Rosenberg, J. (2010). "Application of geoechange experience to geothermal foundations." *The Art of Foundation Engineering Practice* (GSP 198), ASCE, Reston/VA: 411-422.
- Olgun, C.G., Ozudogru, T.Y., Abdelaziz, S.L. and Senol, A. (2014). "Long-term performance of heat exchanger piles." *Acta Geotechnica*, Vol. 10 (5): 1-17.
- Pahud, D. and Hubbuch, M. (2007). "Measured thermal performances of the energy pile system of the Dock Midfield at Zürich airport." *European Geothermal Congress 2007*, Unterhaching, Germany.
- Siegenthaler, J. (2010). "It all adds up. Tracking energy flows in a ground-source heat pump." *Plumbing and Mechanical*, pp. 22-32.

Fully Instrumented Life-Cycle Analyses for a Residential Geo-Exchange System

Eleanor F. Bloom¹ and James M. Tinjum, Ph.D., P.E., M.ASCE²

¹M.S. Student, Geological Engineering Program, Univ. of Wisconsin-Madison, Madison, WI. E-mail: efbloom@wisc.edu

²Associate Professor, Dept. of Engineering Professional Development, Geological Engineering Program, Univ. of Wisconsin-Madison, Madison, WI. E-mail: jmtinjum@wisc.edu

Abstract: A ground-source heat pump (GSHP) was installed and fully instrumented at an upper Midwest residential site to provide real-time data for a life-cycle assessment (LCA), coefficient of performance (COP) analysis, and life-cycle cost analysis (LCCA). An LCA of modeled GSHP systems at the residence showed that the GSHP emits fewer greenhouse gases than conventional systems (20% reduction). Site-specific measurements include water temperatures, mass flow rates, energy flows, and outdoor temperature. The real-time study of three vertical, closed-loop wells with total length of 700 m revealed an average system COP of 3.2 (i.e. the useful energy from the heat pumps over the electrical consumption of the heat and circulation pumps), reducing the annual equivalent energy consumption by over 23,000 kWh (45% reduction). Most LCCAs of GSHPs use modeled COPs of the heat pumps and do not routinely evaluate the electrical fuel mix or the system's energy balance. This LCCA specifically evaluated the residence's fuel mix and revealed savings of \$37,000 over 30 years. Even with a large initial installation cost, annual utility savings result in an 8-year payback period. This study documents how residential geothermal exchange can efficiently reduce energy consumption and environmental impacts as an economically feasible renewable energy option.

INTRODUCTION

The use of geothermal exchange to heat and cool buildings has become increasingly common because of public concern about rising energy costs and climate change related to greenhouse gas (GHG) emissions. In 2006, the annual energy consumption of the U.S. ground-source heat pump (GSHP) market was estimated to be over 7.5 TWh (Goetzler et al. 2009). For example, since 2001, over 1,900 vertical, closed-loop geothermal systems have been approved in Wisconsin alone (Randell Clark, personal communication, November 13, 2014). While many assume that geothermal exchange is one of the most efficient, sustainable systems for space heating and cooling, studies have found that the cost to operate the GSHP may not outweigh the benefits of the system (Greening and Azapagic 2012, Puttagunta 2010).

In this paper, a life-cycle assessment (LCA) is used to evaluate the long-term environmental impact of a GSHP, while a life-cycle cost analysis (LCCA) is used to

analyze the GSHP's economic feasibility. Most LCAs use modeled systems and coefficients of performance (COPs) from manufacturers to evaluate a GSHP's potential to save energy and therefore GHG emissions (Sauner et al. 2010, Greening and Azpagic 2012). However, studies have found that best-case, manufacturer-recommended COP values are substantially higher than those of actual systems, and the extensive monitoring of GSHP systems provides valuable data that cannot be duplicated through laboratory testing and energy modeling (Puttagunta and Shapiro 2012). A study of residential GSHPs conducted by the Energy Center of Wisconsin collected actual energy use data and calculated COPs of seven residences to understand the emissions and economics of GSHPs in Wisconsin (Hackel 2009). A similar methodology is used to conduct the analyses in this report, except with actual heating and electrical fuel mixes at the residence rather than generalized state-wide data.

This unique case study of an unbalanced, heating-dominated residential geothermal exchange in the upper Midwest uses real, site-specific data as opposed to generic or modeled performance metrics and costs. Instrumentation was installed to analyze the performance of a vertical ground heat exchanger (GHX) configuration with three boreholes of 700-m total loop length at a Midwestern residence. The COP was specifically measured such that the input to the LCA and LCCA represent common operating performance. Actual measurements of all energy flows and costs before and after GSHP installation were used to conduct an in-depth LCCA.

BACKGROUND

Space heating and cooling and water heating accounts for 66% of residential energy use in the U.S. (EIA 2009). Typically, residences are heated by gas or oil furnaces and cooled by air conditioning (AC) units, both of which are predominantly fueled by non-renewable fossil fuels (Greening and Azapagic 2012). The burning of fossil fuels, which account for 77.5% of U.S. energy use (Tans and Keeling 2014), has been directly tied to the exponential increase in atmospheric CO₂ levels since the Industrial Revolution (Etheridge et al. 1996). GSHP systems use the thermal energy stored in the earth to provide an environmentally friendly, low-cost, and sustainable source for heating and cooling. Use of GSHP systems can correspond to a 44% reduction in GHG emissions in comparison to a conventional gas boiler (Jenkins et al. 2009).

Vertical GHXs are low-enthalpy systems used for space heating and cooling (ASHRAE 2011). GSHP systems include ground heat exchangers (GHEs) that have a sealed loop buried in the ground and connected to a heat pump through which carrier fluid is circulated. The carrier fluid is circulated in a closed-loop system to deliver relatively warm (or cool) fluid to heat exchangers to regulate building temperature. GSHP systems rely on relatively constant subsurface temperature to about 50 m deep (Hart and Couvillion 1986) resulting from hemostatic heat flux from above (the sun) and below (radioactive decay within the earth's interior). GSHP systems transfer heat rather than generate heat and can provide an equivalent temperature environment for as little as one quarter of the cost of operating conventional heating, ventilation, and air conditioning (HVAC) (Hackel 2009). Although commercial and residential GSHP installations are expected to grow exponentially (Akella et al. 2009, Lo Russo et al.

2009, Blum et al. 2010), these systems are still not widely used in comparison to conventional HVAC systems because of higher initial cost associated with installation (drilling), borefield space requirements, the limitation in installation and business planning infrastructure, and a lack of reliable system design tools (Hughes 2008).

Life-Cycle Assessment

LCAs provide a scientific approach to the evaluation of long-term environmental performance of GSHPs. Ozdogan-Dolcek (2015) describes the five-stage life cycle of an average GSHP: material production, material transportation, earthwork and construction, use, and disposal. This model was used to conduct a preliminary LCA of the residential site using four theoretical configurations with assumed COP values, including a typical triple-well vertical GHX. The results of the LCA revealed that the vertical GHX reduced GHG emissions by 20%. The reduction is less than indicated in literature primarily because of the assumed COP of 3.5 (Wu et al. 2014, Hackel 2009). Jenkins et al. (2009) uses an idealized case of GSHP operation meeting 100% of peak thermal demand with a COP of 4.4 to predict a 44% reduction in CO₂ emissions.

Two major conclusions from Ozdogan-Dolcek's (2015) study are 1) COP is a significant factor in environmental performance and 2) LCAs depend on the fuel mix of the local electric utility, particularly the percentage of non-fossil fuel burning energy sources. Similarly, an LCA of GSHPs in the UK found that by increasing the COP from 2.8 to 5.0, GHG emissions were reduced by 38% due to a decrease in the amount of electricity used to operate the heat pumps (Greening and Azapagic 2012). Considering the potential influence of COP on environmental impact, a case study of the actual GSHP installation and operation at the Midwestern residence was conducted to further examine the effects of COP.

COP ANALYSIS

Site Description

The project site is located in central Wisconsin. The residence was constructed in the 1930's with additions built in 1980 and 2009 for a total footprint of 325-m². The residential-scale, closed, vertical triple-well, 700-m total length GSHP system began operation on December 15, 2013. Walker (2015) describes the system in detail, and the instrumentation is described by Meyer (2013). The GSHP is used for space heating and cooling, and for heating the domestic hot water (DHW). The site has a colder climate relative to most studied GSHP sites. According to the Wisconsin State Climatology Office (2006), the average annual temperature in central Wisconsin is 6.8 °C. The location averages 4,375 heating and 275 cooling degree days (°C with a temperature base of 18 °C) per year. Over the one-year study, the measured heating and cooling degree days are 4,332 °C and 274 °C, respectively. The average measured annual temperature is 6.9 °C. This indicates that the period of study is representative of average climate conditions at the site.

Prior to the GSHP installation, the residence was heated from a liquefied petroleum (propane) forced-air, 22-kWh-capacity Bryant furnace with propane stored in an outside, bulk storage tank. The house was space cooled by an electrically powered Lennox AC unit. DHW was heated by an A.O. Smith 190-L electric water heater.

The GSHP is comprised of three, vertical GHEs of 700-m total loop length. The GHEs are conventional, closed-loop u-tubes with 6-cm outer diameter high-density polyethylene pipe. A schematic of the GHEs' layout and depths is shown in Fig. 1. The horizontal sections sit in an approximately 2-m-deep trench. Geologically, sandy overburden exists to a depth of 55 m, followed by sandstone to 108 m. Granite begins at 108-m depth, which generally limited significant drilling into this formation.

At the residence, all three GHE loops enter a manifold that allows the system user to specify the flow pathway through the GHEs. The three loops run in parallel flow so as to minimize the pumping power required to reach a specified flow rate (Walker 2015). From the manifold, the water in the GHE loop is piped into a dual-heat pump system connected in series. The water first enters a Water Furnace Envision NSW025 DHW water-to-water (W2W) heat pump, then enters a Water Furnace 7 Series NV036 water-to-air (W2A) heat pump. The water exits the W2A heat pump and is piped back through the manifold out to the field.

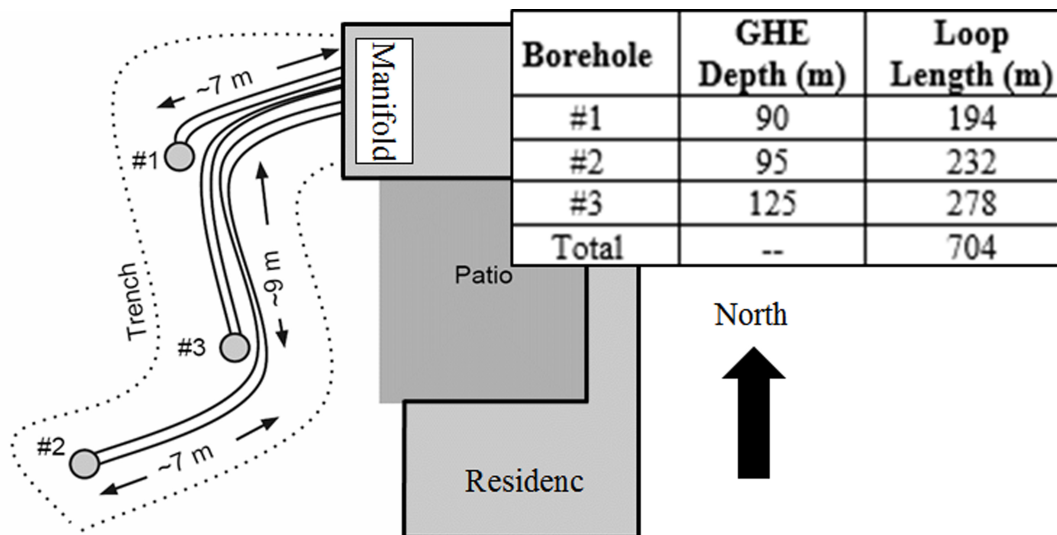


FIG 1. Aerial view of approximate locations of GHE boreholes and horizontal lengths. The GHEs field into the house's (gray) northwest corner.

Heat is extracted from the W2W heat pump to meet the residence's DHW requirements. Additionally, radiant under-floor heating in the household's basement is delivered through a water loop connected to the DWH tank via a plateframe heat exchanger. Heat extracted or rejected by the W2A heat pump meets the residence's space heating and cooling requirements. The W2A heat pump's compressor is also equipped with a desuperheater. The desuperheater uses waste heat from the W2A heat pump to preheat cold well water supplied to the DHW system.

To circulate the water in the GHE system, three circulation pumps are used. A smaller alpha pump circulates water at 19 L/min at all times. The two larger pumps

activate incrementally with increased thermal load on the system. Flow rates are controlled to prevent freezing because the circulation fluid does not contain anti-freeze agents. Additional circulation pumps are required for the DHW, radiant floor heating, plateframe, and desuperheater loops. The energy required to run all of these pumps is measured and the data archived.

Monitoring Equipment and Data Collection

Real-time data is collected and archived such that the COP of the GSHP system is continually calculated. The COP is defined as the useful energy produced by the GSHP divided by the input electrical energy, E . During the cooling season, the useful energy is the heat transferred from the ground, Q (Eq. 1). During the heating season, the useful energy is the heat transferred from the ground plus the input electrical energy, $Q + E$ (Eq. 2). Equation 3 is the calculation for useful energy transferred from the ground, Q .

$$COP_{Cooling} = \frac{Q}{E} \quad (1)$$

$$COP_{Heating} = \frac{Q+E}{E} \quad (2)$$

$$Q = 12mC_p\Delta T \quad (3)$$

where m is the flow rate, C_p is the specific heat of the exchanger fluid, and ΔT is the change in temperature across the system; i.e., across the heat pumps. The constant, 12, is required to calculate consistent units (kW) for the COP.

These equations require measurements of flow rate, temperature, and electrical consumption. Table 1 lists the measurement equipment, and a schematic of the measurement sites is shown in Fig. 2. Flow rate, m , is measured with a flow meter. Temperature measurements are made with four thermistors attached on the outside of metal pipe, in good contact with the pipe surface and insulated. The thermistors measure the W2W and W2A heat pump's entering and leaving water temperatures (EWT_{W2W} , LWT_{W2W} , EWT_{W2A} , and EWT_{W2A} , see Fig. 2).

TABLE 1. Instruments used for COP analysis

Instrument	Model	#	Measurement	Units
Flow meter	Grundfos VFS QT sensors	1	Flow	L min ⁻¹
Thermistor	Campbell Scientific 109 SS	4	Temperature	°C
WattNodes TM	Continental Control Systems LLC WNB-3Y-208-P	12	Electricity	W·h
Datalogger	Campbell Scientific CR10X	1	Voltage response	V

Four WattNodesTM measure the electrical energy supplied to all components of the GSHP system, including the W2W heat pump, W2A heat pump, DHW circulation pump, radiant floor circulation pump, desuperheater circulation pump, plateframe circulation pump, and GHE circulation pump. All measurements are recorded and collected from a datalogger connected to a remote-access computer.

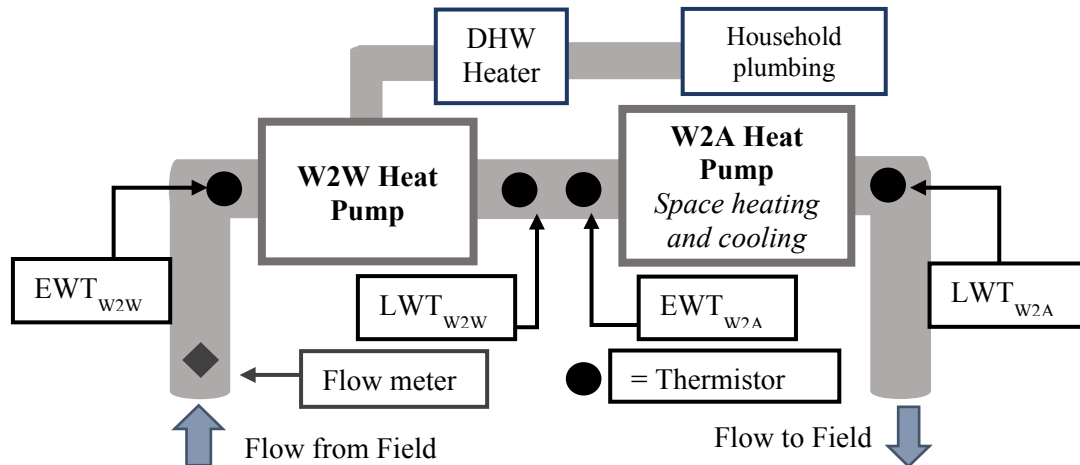


FIG. 2. Schematic of GSHP temperature and flowrate measurement sites relative to heat pumps (not to scale)

Performance Results

The average COP based on typical equipment efficiency data and experimental measurements for a conventional vertical GHX system is 3.5 (Wu et al. 2014, Hackel 2009). However, the COP can be highly situational for a given GSHP system. Based on data collection from the project site, a COP of 3.2 has been recorded to date, reducing the annual energy consumption by 23,000 kWh (45% reduction compared to previous conventional system). There are a number of factors affecting the performance, including the configuration of the heat pumps. Figure 3 shows the average monthly system COP, W2A and W2W COPs, and outdoor temperature. The system COP indicates the total useful energy produced by both heat pumps over all electricity consumed by the system, including heat pump and circulation pump energy. The W2A and W2W COPs indicate the useful energy produced by an individual heat pump over the electricity consumption of that heat pump alone, excluding circulation energy. The lowest COP (2.8) was recorded in March, which is near the end of the heating season and for which the ground has had the most heat extracted. The trend also indicates that the COP of the system increases in warm weather. The series connection of the heat pumps with W2A following W2W is advantageous for space cooling. From the field, the water first reaches the W2W heat pump, which extracts energy for heating the DHW. Therefore, the water is at a lower temperature when it enters the W2A heat pump, establishing a better heat sink for space cooling.

Another factor effecting the performance are the efficiencies of the individual heat pumps. As indicated by Ozdogan-Dolcek's (2015) LCA, the largest electrical energy consumption occurs during GSHP operation, and the majority of the energy is used by the heat pumps. In general, the COP of the system falls somewhere between the higher W2A COP and lower W2W COP (Fig. 3). Considering times when only the W2A heat pump is operating, the average COP of the W2A heat pump is 4.4. Considering times when only the W2W heat pump is operating, the average COP of

the W2W heat pump is 2.3. This indicates that the W2A heat pump performs at a higher efficiency than the W2W heat pump, which can be explained by a few factors. The W2W heat pump has a single-speed compressor that frequently cycles on and off to meet the variable DHW heating demands (Walker 2015). The W2A heat pump has a variable-speed compressor, which more efficiently adapts to variable space heating and cooling demands. Additionally, the W2W heat pump requires more energy to heat the DHW to 48 °C than the W2A requires to maintain an average air temperature of 20 °C.

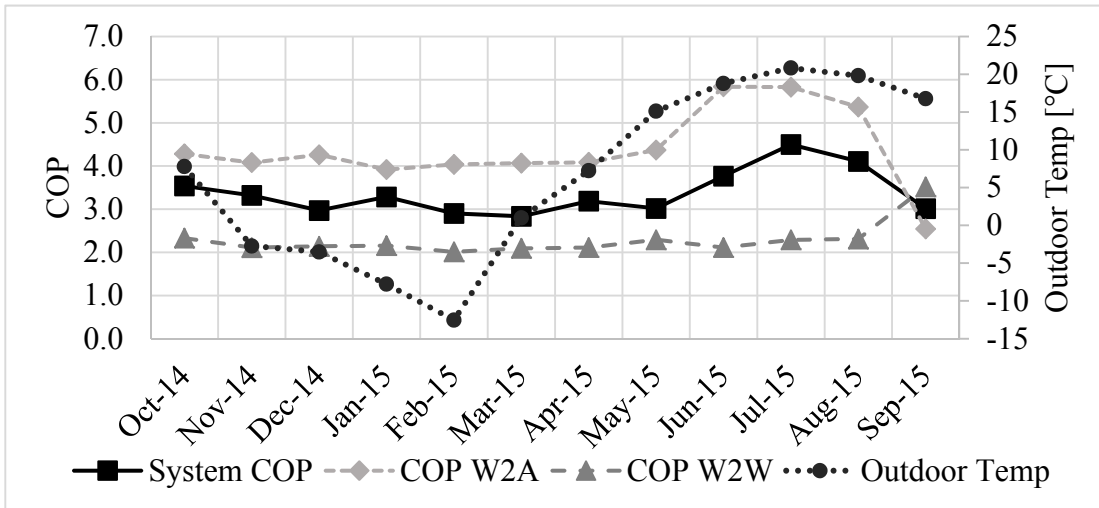


FIG. 3. Average monthly GSHP COPs and outdoor temperature at residence

Fig. 4 further demonstrates the effects of the differing heat pump efficiencies. The dashed line represents the daily system COP from October 3, 2014, to September 30, 2015. The bar graphs represents the energy consumed by all circulation pumps, the W2W heat pump and the W2A heat pump.

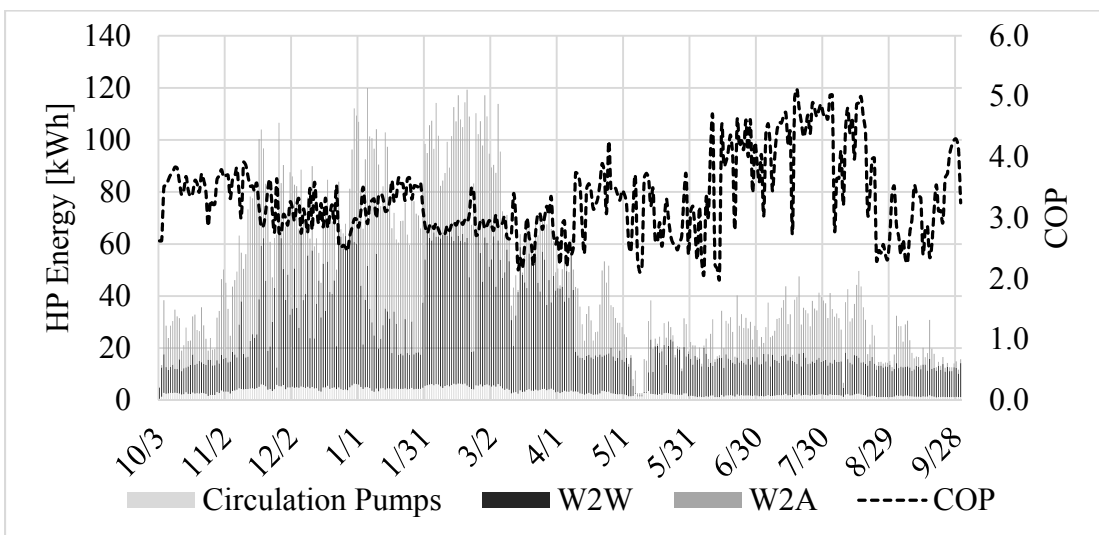


FIG. 4. Daily energy consumption and average system COP of the GSHP system

The circulation pumps require less energy at a more constant amount than the heat pumps. The energy use of the heat pumps varies depending on the household's demands, but the circulation pumps run constantly, whether or not the heat pumps are active. Over the year of study, 94% of the energy used by the GSHP system was consumed by the heat pumps. The COP decreases on days when the W2W heat pump draws a proportionally greater amount of electrical energy than the W2A heat pump. This occurred around late December, when the household had guests for the holidays, which increased use of DHW. On days when there is little W2W energy usage relative to the W2A heat pump, the COP increases. This is evident in mid-January, when the homeowners were on vacation and DHW use was at a minimum while nominal space heating was employed. Regardless, the W2W heat pump's average COP of 2.2 is 100% more efficient than burning fuel oil, which cannot have a COP greater than 1.0.

LIFE-CYCLE COST ANALYSIS

The COP is a required input to conduct the full-life LCCA of the Midwestern residence. LCCAs are useful tools for economic evaluations because they consider both the operating and initial costs (Hakkaki-Fard 2015). The LCCA of this case study compares the costs of the GSHP to the homeowner's previous propane-fueled furnace/AC unit/electric water heater (conventional) HVAC system. A payback analysis and net present value (NPV) calculations were used to determine the system's economic benefits. The expected lifetime of the heat pump equipment, 30 years, was chosen for the length of the LCCA.

Cost Data Collection

The GSHP installation expense in 2013 includes the cost of GHE drilling and piping (\$13,500), heat pump installation and interconnection (\$12,030), and borehole completion (\$2,624) for a total cost of \$28,288. The drilling contractor provided the GHE installation cost, and invoices specified the other costs. At the time of installation, a tax credit was available for 30% of the initial installation cost (\$8,446). Therefore, the total initial cost incorporating the tax credit was \$19,708. The comparable/differential conventional system expense included equipment costs (furnace, AC unit, and water heater). The lifetimes and subsequent replacement of the conventional equipment were also considered. Representative costs and lifetimes of the equipment are as follows:

- 29 kWh, 92% furnace (propane): \$3,000; lifetime of 20 years
- Four-ton AC unit, 13 SEER: \$3,700; lifetime of 20 years
- 190-L electric water heater: \$1,300; lifetime of 12 years

If the conventional system was installed instead of the GSHP, the homeowners would pay \$8,000 for the initial equipment, \$1,300 for a new water heater in years 12 and 24, and \$6,700 for a new furnace and AC unit in year 20.

Utility histories from 2010 to present were available to assist with annual cost calculations. The average yearly electricity and propane consumption prior to installation of the GSHP was compared to the amount of electricity used after the

GSHP became operational (no propane was used after the GSHP became operation). If the system is operating efficiently, the average cooling season electrical usage would decrease due to the use of the GSHP instead of an AC unit. In the heating season, the energy savings associated with not burning propane exceeded the added electricity required to operate the GSHP for heating purposes. For the 30-year analysis, it was assumed that annual energy consumption remained constant, but utility rates increased. The U.S. Energy Information Administration's (EIA) Annual Energy Outlook report (2015) projected propane and electricity prices to increase by 0.5% and 0.6% per year, respectively, at present value from years 2013 to 2040. This led to a 15% increase in annual cost savings from year 1 (\$1,300) to year 30 (\$1,500).

LCCA Results

The results of the simple payback analysis are shown in Fig. 5. The initial deficit between a new GSHP and conventional system was approximately \$11,700 (when considering the available tax incentives). Between years 8 and 9, the payback becomes positive. The jumps in the linear trend indicate years in which the conventional equipment required replacement, further increasing the value of the GSHP system.

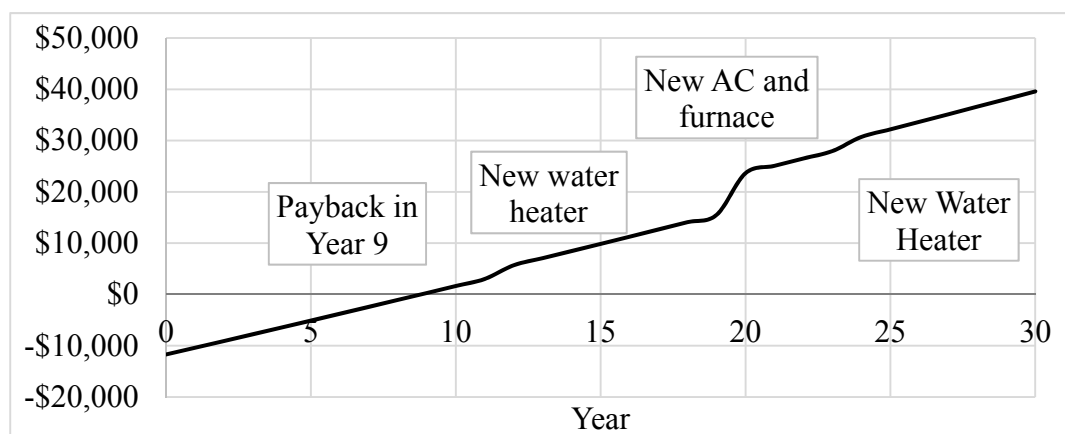


FIG. 5. Simple payback analysis of GSHP

The total NPV of the GSHP, including initial and annual expenses, is \$136,000. Comparatively, the NPV of an equivalent conventional system is \$173,000, indicating savings of \$37,000 in 30 years. Annualized, the homeowners would spend \$4,500 per year for the GSHP, compared to \$5,800 for the conventional system, saving approximately \$1,300 each year. The savings associated with this GSHP are largely attributed to reduced purchases of propane. The GSHP system increased annual electricity consumption by about 3,000 kWh per year. At \$0.13–\$0.15 per kWh, this leads to an increased cost of \$380–\$450 per year. However, the approximate 3,800 L of propane saved by using the GSHP equate to savings ranging from \$1,700 to nearly \$2,000 per year. In general, the GSHP system at the Midwestern residence would cost less over a 30-year period than a comparable conventional system, thus suggesting that significant economic benefits can be recognized by using geothermal exchange.

CONCLUSION

This case study demonstrates the advantages of systematic monitoring and data collection at residential geothermal exchange sites. For a typical residential site in the upper Midwest, a fairly conventional vertical geothermal exchange performed at near-expected efficiencies and at a lower cost relative to conventional HVAC systems. In addition, there are intangible benefits of geothermal exchange that are not evident from data collection or mathematical constructs. Homeowners may be able to heat and cool their homes to more comfortable temperatures with marginal increases to their utility bill. The ground energy utilized for geothermal exchange is free, thus decoupling risks related to long-term fluctuation in energy prices. Quantitative assessments, including life-cycle analyses, are crucial to improving the prediction of performance and promoting the adoption of geothermal exchange.

ACKNOWLEDGMENTS

This material is based upon work supported by the National Science Foundation under Grant Number 1156674, REU Site: Geothermal and Energy Geotechnics, by the University of Wisconsin-Madison Innovation and Economic Development Research Program, and a Seed Grant from the Wisconsin Energy Institute. Any opinions, finding, and conclusions or recommendations expressed in this material are those of the authors and do not necessarily reflect the views of the National Science Foundation, the University of Wisconsin-Madison Graduate School, or the Wisconsin Energy Institute. Special thanks are offered to Rachel Woods-Robinson and Ayse Ozdogan-Dolcek for their corollary efforts in LCA perspectives for this field site.

REFERENCES

- American Society of Heating, Refrigeration and Air-Conditioning Engineers, Inc. (ASHRAE). (2011). "Geothermal Energy." *2011 ASHRAE Handbook – HVAC Applications*, Ch. 34.
- Akell, A., Saini, R., and Sharma, M. (2009). "Social, economic and environmental renewable energy systems." *Renewable Energy*, 34(2), 390–396.
- Blum, P., Campillo, G., Munch, W., and Kobel, T. (2010). "CO₂ savings of GSHP systems-A regional analysis." *Renewable Energy*, 35(1), 112–127.
- Etheridge, D., Steel, L., Langenfelds, R., Francey, R., Barnola, J., and Morgan, V., (1996). "Natural and anthropogenic changes in atmospheric CO₂ over the last 1000 years from air in the Antarctic ice and firn." *Geophysical Research*, 101(D2), 4115–4128.
- Goetzler, W., Zogg, R., Lisle, H., and Burgos, J. (2009). "Ground-source heat pumps: Overview of Market Status, Barriers to Adoption, and Options for Overcoming Barriers." *U.S. Department of Energy*.
- Greening, B. and Azapagic, A. (2012) "Domestic heat pumps: Life cycle environ. impacts and potential implications for the UK." *Energy*, 39(1), 205–217.
- Hackel, S. (2009). "10 Year Update: Emissions and Economic Analysis of Geothermal Heat Pumps in WI." *Energy Center of Wisconsin*, Madison, WI.

- Hakkaki-Fard, A., Eslami-Nejad, P., Aidoun, Z., and Ouzzane, M. (2015). "A techno-economic comparison of a direct expansion ground-source and an air-source heat pump system in Canadian cold climates." *Energy*, 87, 49–59
- Hart, D. and Couvillion, R. (1986). "Earth-Coupled Heat Transfer." *National Water Well Association*, Dublin, OH, 192 pp.
- Hughes, P. (2008). "Geothermal heat pumps: market status, barriers to adoption, and actions to overcome barriers." Oak Ridge National Laboratory: U.S. DOE, 42 pp.
- Jenkins, D., Tucker, R., and Rawling, R. (2009). "Modelling the carbon-saving performance of domestic GSHP." *Energy and Buildings*, 41, 587–595.
- Lo Russo, S., Boffa, C., and Civita, M., (2009). "Low-enthalpy geothermal energy: an opportunity to meet increasing energy needs and reduce CO₂ and atmospheric emissions in Piemonte, Italy." *Geothermics*, 38(2), 254–262.
- Meyer, L. (2013). "Thermophysical properties of wisconsin rocks for application in geothermal energy." M.S. Thesis, Dept. of Geological Engineering, UW-Madison, Madison, WI.
- Ozdogan-Dolcek, A. (2015). "Numerical modeling of heat transport for ground-coupled heat pump (GCHP) systems and associated life cycle assessment." Ph.D. Dissertation, Dept. of Geological Engineering, UW-Madison, Madison, WI.
- Puttagunta, S., Aldrich, R., Owens, D., and Mantha, P. (2010). "Residential ground-source heat pumps: In-field system performance and energy modeling." *GRC Transactions*, 34, 941–948.
- Puttagunta, S. and Shapiro, C. (2012). "An in-depth look at ground source heat pumps and other electric loads in two GreenMax homes." *Energy Efficiency and Renewable Energy*, U.S. Department of Energy, Oak Ridge, TN.
- Saner, D., Juraske, R., Kubert, M., Blum, P., Hellweg, S., and Bayer, P. (2010). "Is it only CO₂ that matters? A life cycle perspective on shallow geothermal systems." *Renewable and Sustainable Energy Reviews*, 14(7), 1798–1813.
- U.S. Energy Information Administration (EIA). (2009). "Residential Consumption Survey (RECS)."
- U.S. Energy Information Administration (EIA). (2015). "Annual Energy Outlook 2015."
- Walker, M. (2015). "Residential and district-scale ground-coupled heat pump performance with fiber optic distributed temperature sensing." M.S. Thesis, Dept. of Geological Engineering, UW-Madison, Madison, WI.
- Wisconsin State Climatology Office. (2006). "Historical Climate Data." *Past Wisconsin Climate*, <<http://www.aos.wisc.edu/~sco/clim-history/division/4705-climo.html>> (August 24, 2015).
- Wu, Y., G. Gan Guo-hui and A. Verhoef. (2010). "Experimental measurement and numerical simulation of horizontal-coupled slinky ground source heat exchangers." *Applied Thermal Engineering*, 30(16), 2574–2583.

Impact of a Thermo-Hydraulic Insulation Layer on the Long-Term Response of Soil-Borehole Thermal Energy Storage Systems

Tugce Baser, M.S., S.M.ASCE¹; John S. McCartney, Ph.D., P.E., M.ASCE²;
Ali Moradi, M.S.³; Kathleen Smits, Ph.D.⁴; and Ning Lu, Ph.D., F.ASCE⁵

¹Graduate Research Assistant, Dept. of Structural Engineering, Univ. of California San Diego, 9500 Gilman Dr. La Jolla, CA 92093-0085. E-mail: tbaser@ucsd.edu

²Associate Professor, Dept. of Structural Engineering, Univ. of California San Diego, 9500 Gilman Dr. La Jolla, CA 92093-0085. E-mail: mccartney@ucsd.edu

³Graduate Research Assistant, Dept. of Civil and Environmental Engineering, Colorado School of Mines, 1500 Illinois St. Golden, CO 80401. E-mail: amoradig@mines.edu

⁴Associate Professor, Dept. of Civil and Environmental Engineering, Colorado School of Mines, 1500 Illinois St. Golden, CO 80401. E-mail: ksmits@mines.edu

⁵Professor, Dept. of Civil and Environmental Engineering, Colorado School of Mines, 1500 Illinois St. Golden, CO 80401. E-mail: ninglu@mines.edu

Abstract: This study focuses on the effect of including a surficial insulation layer above a soil-borehole thermal energy storage (SBTES) system installed in a low plasticity clay deposit in the vadose zone. SBTES systems function by injecting heat collected from solar thermal panels into an array of vertical boreholes containing closed-loop geothermal heat exchangers. The goal of placing an insulation layer on top of the soil layer is to retain as much heat as possible within the borehole array to increase the efficiency by preventing the heat loss from the system to the atmosphere. A two-dimensional (2D), transient finite element model was built in COMSOL to consider the coupled heat transfer and water flow processes in the unsaturated soil layer within the SBTES system. Results indicate that presence of an insulation layer leads to a lower upward heat loss from SBTES system, but it is not significant. The insulation was observed to play a more significant role when coupled heat transfer and water flow was considered than when heat transfer was due to conduction alone.

INTRODUCTION

Soil-Borehole Thermal Energy Storage (SBTES) systems are used to store heat collected from renewable sources so that it can be used later for heating of buildings (Sibbitt et al. 2012; Zhang et al. 2012; McCartney et al. 2013; Başer and McCartney 2015). They function in a similar way to conventional geothermal heat exchange (GHE) systems, where heat is transferred from a source to a sink via circulation of fluid through a series of closed-loop heat exchangers. Because SBTES systems are meant to store heat, the spacing of the heat exchangers in SBTES systems is closer

than that in conventional GHE systems (Başer and McCartney 2015). During operation of SBTES systems use of solar thermal panels as the heat source, the temperature of the ground within the array is expected to increase from its initial temperature (approximately 10-20 °C) to potentially more than 60 °C (Sibbitt et al. 2012; Bjoern 2013), which is much higher than that encountered in GHE systems. McCartney et al. (2013) noted the potential advantages of installing SBTES systems in the vadose zone, where the thermal conductivity of the surrounding soil is relatively low and lateral heat loss will be minimized. The relatively high temperatures associated with SBTES systems may lead to different mechanisms of heat transfer in the vadose zone than those expected under lower temperatures (Lu 2001; Smits et al. 2013). An additional difference between SBTES and GHE systems is that the borehole heat exchanger array in a SBTES system is usually overlain by a hydraulic barrier to retain pore water within the subsurface and a thermal insulation layer to minimize heat losses to the atmosphere. A schematic of a typical SBTES system with the location of the surficial insulation layer and hydraulic barrier is shown in Figure 1. The objective of this paper is to understand the impact of the insulation layer, and whether it has a major effect on the heat storage performance of SBTES systems. To achieve this objective, simulations of coupled heat transfer and water flow in the unsaturated soil within the SBTES system were performed using COMSOL to evaluate the role of the surficial boundary conditions.

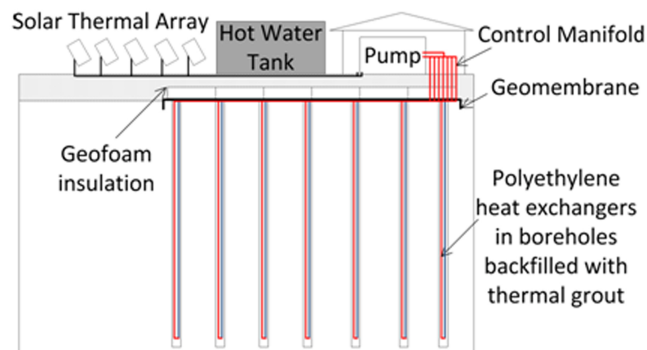


FIG. 1: Schematic of a SBTES system with heat from solar thermal panels

BACKGROUND

While SBTES systems are gaining popularity throughout the world, a better understanding of their thermal performance is required as their thermal storage capacity and heat loss highly depend on the average soil temperature during a heating or cooling period. The capacity of a SBTES system is the quantity of heat that the ground can retain and depends on the thermal properties of the subsurface. Heat loss could occur in all directions (upward, downward and laterally), and is dependent on the spacing of boreholes, number of boreholes, heat injection rate, and heat injection duration, along with the subsurface thermal properties (Chapuis and Bernier 2009; Başer and McCartney 2015). The primary mode of heat loss from an SBTES system is laterally to the surrounding subsurface. The upward and downward heat losses are not as significant because the small area of heated soil around each borehole heat exchanger. Further, the upper surface of an SBTES system is typically insulated with

layers of expanded polystyrene (EPS) even though there has not been thorough evaluation of the role of the insulation. In addition to the insulation, the SBTES system is typically installed beneath the frost depth at a particular location, so the surficial soil layer also provides an insulating effect. Heat loss decreases as the size of the system increases, while it increases with the temperature difference between the storage and ambient ground temperature (Nordell and Hellström 2000).

During operation of a typical SBTES system, heat is injected at a relatively constant rate during the summer months. During this time, the soil within the array increases in temperature. Heat is injected into the central borehole heat exchanger first, then to the surrounding borehole heat exchangers. Although the heat supply in most SBTES systems is from solar thermal panels that only produce heat for a certain period of time during the day, the heat injection rate is stabilized through the use of an intermediary fluid-filled heat storage tank (Sibbitt et al. 2012). The temperature of the soil increases rapidly due to the high thermal gradient, and the rate of increase in temperature decreases as the soil reaches its storage capacity. During the fall, heat may continue to be injected into the array depending on the climate setting, or the heat injection may be stopped at the end of the summer. After heat extraction in the winter, the system may rest after which the cycle begins again. As some heat is typically retained around the perimeter of the SBTES array, the heat extraction efficiency of SBTES systems increases over time (Sibbitt et al. 2012; Zhang et al. 2012; Catolico et al. 2015).

Design parameters of SBTES systems include energy injection and extraction rates, borehole spacing as well as thermal properties of the unsaturated soil. Two commonly used design models available for predicting the heat storage in SBTES arrays for variable injection and extraction rates are the duct storage (DST) model developed by Claesson and Hellström (1981) and Hellström (1989) and the superposition borehole model (SBM) developed by Eskilson (1987). As the borehole array investigated in this study was constructed for research purposes, it was not designed using these models to reach a certain energy storage needed for a building. Claesson and Hellström (1981) also proposed several analytical formulae based on the DST model for selecting the spacing of the boreholes, and found that the optimal spacing between borehole heat exchangers in an SBTES system is 1.5-4.0 m. Başer and McCartney (2015) performed a series of simplified numerical analyses of heat conduction that indicate that soils with lower thermal conductivity have less lateral heat loss, and that arrays with smaller borehole spacing permit more concentrated storage of heat at higher temperatures.

Although there have been several successful SBTES systems in Scandinavia since the late 1970's (Claesson and Hellström 1981), there are two recent examples of successful community-scale SBTES systems. The SBTES system in Braedstrup, Denmark, supplies heat from 18,000 m² of solar thermal panels to an array of 50 boreholes having a depth of 47-50 m and 3 m spacing (Bjoern 2013). This system provides 14000 homes with 20% of their heat. The Drake Landing Solar Community (DLSC) site in Alberta, Canada includes an SBTES system in operation since 2007. This system supplies heat from solar thermal panels to an array of 144 boreholes that are 35 m-deep and equally spaced at 2.25 m within a 35 m-wide grid. The SBTES system at this site has provided more than 90% of the heating requirements to 52

houses (Sibbit et al. 2012). Zhang et al. (2012) performed a numerical simulation of the heat exchange processes at the DLSC site using TOUGH2, and found that the efficiency of heat transfer, defined as the amount of heat extracted divided by the amount of heat injected, is approximately 27%. Although this seems low, the thermal energy injected into the SBTES system is from a renewable source and the heat extracted met the heating needs. The TOUGH2 analysis was further developed by Catolico et al. (2015), who matched simulation results with observed data from the DLSC site and considered conditions leading to a convective cycle in SBTES systems with saturated soils. At both sites, heat is permitted to escape laterally from the SBTES array. The DLSC site also includes a surficial hydraulic barrier to minimize evaporation of water from the soil as the groundwater table is 6 m below the surface.

NUMERICAL MODEL

A transient finite element model developed in COMSOL Version 4.4 was used to predict the temperature distributions and heat flux within the soil inside and around a SBTES array. For simplicity, a 2-dimensional cross-section of an array consisting of three equally-spaced boreholes having a depth of 10 m was used, as shown in Figure 2. The purpose of the simulations is to understand the effect of an insulation layer on heat transfer in unsaturated soil within a SBTES array for the situations that heat transfer occurs due to conduction alone or due to coupled heat transfer and water flow. Although the 2-dimensional analysis, which was performed for speed of simulation of coupled processes, does not represent the 3-dimensional flow processes in SBTES systems, it still permits comparison between simulations to understand the role of different processes on the performance of the SBTES system. When included, the insulation layer above borehole array has a thickness of 0.1 m and a thermal conductivity of 0.2 W/mK. The results of interest are the temperature distributions in the soil and heat loss vertically and laterally from the array.

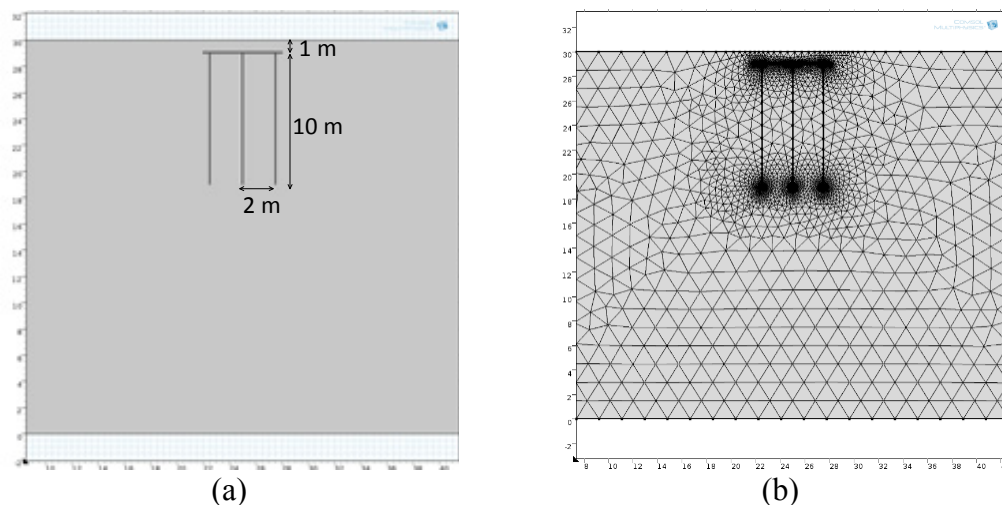


FIG. 2. Details of the model simulated in COMSOL: (a) Geometry; (b) Mesh

First, a simplified model was built assuming that heat transfer is due to conduction alone. The governing equation for conductive heat transfer in soils is:

$$(\rho C_p) \frac{\partial T}{\partial t} - \nabla \cdot (-\lambda \nabla T) = Q \quad (1)$$

where ρ (kg/m³) is the total density of soil, C_p (J/(kgK)) is the specific heat capacity of the soil, T (K) is the absolute temperature, t (s) is time (s), λ (W/(mK)) is the apparent thermal conductivity of soil, and Q (W/m³) is the heat source/sink.

A second model using the same geometry was built to incorporate coupled heat transfer and water flow. When either a partially- or water-saturated soil is subjected to a temperature gradient, convection occurs in the fluid phases due to thermally-induced changes in density of both wetting (water) and not-wetting (gas) fluids. The role of coupled heat transfer and water flow has been considered in several studies (Philip and de Vries 1957; Lu 2001; Smits et al. 2011, Moradi et al. 2015), who found that the convective movement of fluids can play a major role in the total heat transfer in soils. To consider the convective fluid flow, two different equations are defined for flow of the liquid and gas phases. The total gas phase is assumed to be dry air. These two equations are related by capillary pressure to form the following coupled differential equations (Bear 1972; Moradi et al. 2015):

$$n \frac{dS_w}{dP_c} \frac{\partial(\rho_w P_c)}{\partial t} + \nabla \cdot \left(\frac{-\rho_w k_{rw} k_{int}}{\mu_w} (\nabla P_w + \rho_w g) \right) = -Q_m \quad (2)$$

$$n \frac{dS_g}{dP_c} \frac{\partial(\rho_g P_c)}{\partial t} + \nabla \cdot \left(\frac{-\rho_g k_{rg} k_{int}}{\mu_w} (\nabla P_g + \rho_g g) \right) = Q_m \quad (3)$$

where n is the porosity, S_w and S_g (dim.) are the degrees of saturation of water and gas, respectively, μ_w and μ_g (Pa·s) are the dynamic viscosities of water and gas respectively, P_c (kPa) is the capillary pressure, equal to the difference between the pore gas pressure P_g and pore water pressure P_w , k_{int} is the intrinsic permeability of soil (m²), k_{rw} and k_{rg} (dim.) are the relative permeabilities of water and gas, respectively, g is the gravitational acceleration (m²/s), and Q_m (kg/(m³s)) is the mass source per unit volume. Since phase change between liquid water and water vapor was neglected in this study, Q_m was assumed to be zero. By taking averages at the scale of a representative elementary volume, the energy equation can be applied for each phase separately. Assuming local thermal equilibrium, the energy equations for each phase are combined to yield a general form of the heat transfer equation for porous media, as follows:

$$(\rho C_p)^* \frac{dT}{dt} + \nabla \cdot ((\rho_w C_{p,w}) v_w T + (\rho_g C_{p,g}) v_g T) - \nabla \cdot (-\lambda \nabla T) = Q \quad (4)$$

where v_w and v_g are the water and gas velocities (m/s), respectively, ρ_w and ρ_g are the temperature-dependent densities of water and gas, $C_{p,w}$ and $C_{p,g}$ are the water and gas specific heat capacities, and $(\rho C_p)^*$ represents the effective heat capacity of the soil.

The van Genuchten (1980) model is used for the soil water retention curve (SWRC), and the relative permeabilities for water and gas in the unsaturated soil were calculated using the van Genuchten-Mualem model (van Genuchten 1980). The thermal conductivity function (TCF) for unsaturated soil proposed by Lu and Dong (2015) was used, which estimates the apparent thermal conductivity from the degree of saturation and the parameters of the van Genuchten SWRC. The parameters of the different constitutive relationships for the soil and insulation are summarized in

Table 1. The soil properties are representative of a low-plasticity clay, with high air entry suction and low saturated hydraulic conductivity. The nonisothermal properties of water and air were obtained from Moradi et al. (2015). After defining the initial and boundary conditions, equations (2), (3), and (4) were solved simultaneously.

Table 1. Material properties used in the analyses

Layer	Insulation	Low plasticity clay
Thermal conductivity for Conduction-only model, λ (W/mK)	0.03	1.39
Specific heat capacity for saturated conditions, C_p (J/kgK)	900	1000
Total density, ρ (kg/m ³)	1200	1750
van Genuchten parameter, α_{vG} (kPa ⁻¹)	-	0.03
van Genuchten parameter, n_{vG}	-	1.45
Residual volumetric water content, θ_r	-	0.08
Saturated volumetric water content, θ_s	-	0.36
Saturated hydraulic conductivity, k_s (m/s)	-	3.5×10^{-7}

The initial ground temperature was assumed to be uniformly equal to 12 °C. and The water table was assumed to be at a depth of 30 m, and the initial conditions for degree of saturation and matric suction are assumed to be hydrostatic as shown in Figures 3(a) and 3(b). Zero heat flux boundary conditions were applied on the sides of the domain, and the temperature at a depth of 30 m was fixed at 12 °C. The surface temperature was assumed to be a sinusoidal function fitting the ambient air temperature in Golden, CO presented by Başer et al. (2015). Heat flux was applied to the outer borehole boundaries for 90 days. For water transfer, zero mass flux was applied to all boundaries. The soil within the region of the borehole array has an average initial degree of saturation of 0.65. Using the model of Lu and Dong (2015), this corresponds to a soil thermal conductivity of 1.39 W/mK.

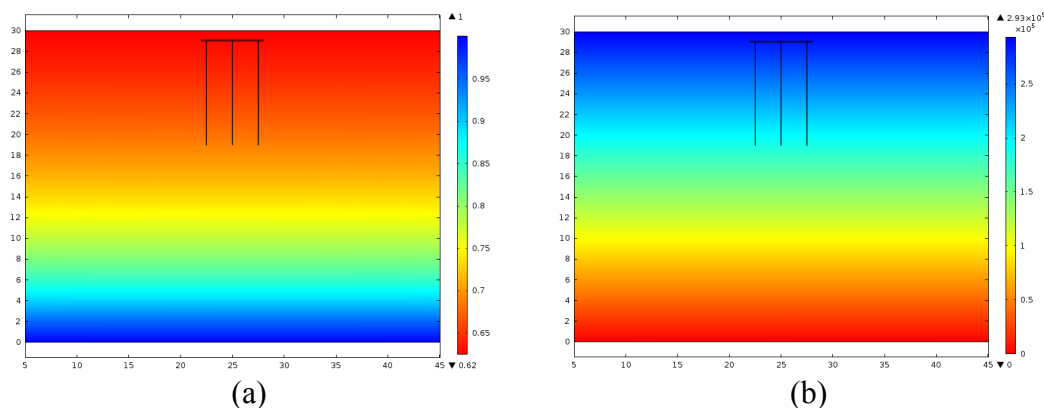


FIG. 3. Initial conditions: (a) Degree of saturation; (b) Matric suction in Pascals

RESULTS

The temperature distributions with radial distance within the soil above the borehole array from the conduction-only analysis are shown in Figure 4 for the time at the end of 90 days of heat injection. Temperature values above the insulation layer is lower than the array without insulation as expected. Also the temperature behavior of the soil is highly dependent on thermal conductivity of insulation material as well as ambient temperature. Although not shown, a lower thermal conductivity for the insulation layer was observed to result in lower increase in temperature in the soil above the borehole array surface.

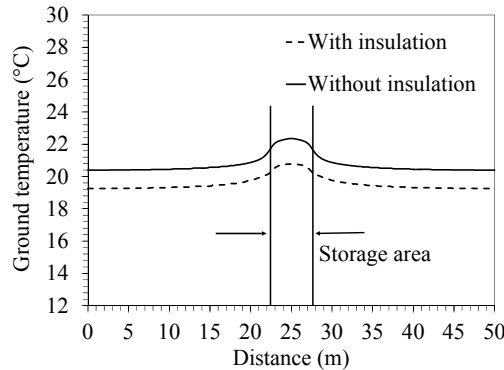


FIG. 4. Temperature distributions within the soil above the borehole array (depth of 0.5 m) for conduction-only heat transfer after 90 days of heat injection

The upward heat loss is shown in Figure 5(a) for the situations with and without insulation. The insulation leads to only a slight decrease in heat loss. Although not shown, the upward heat loss did not change significantly when the thermal conductivity of the insulation layer was changed. To evaluate lateral heat loss from the SBTES array, Başer and McCartney (2015) defined the storage volume of the array as 2 radial spacings from the center. Although this assumption is conservative as the borehole heat exchangers may be able to extract heat from the subsurface outside of the array as well. Using this definition of the array size, the lateral heat losses from the borehole arrays with and without surficial insulation are shown in Figure 5(b). According to energy conservation, when the heat flow is limited at the upper boundary, there should be an increase in lateral heat loss assuming that downward heat loss is negligible.

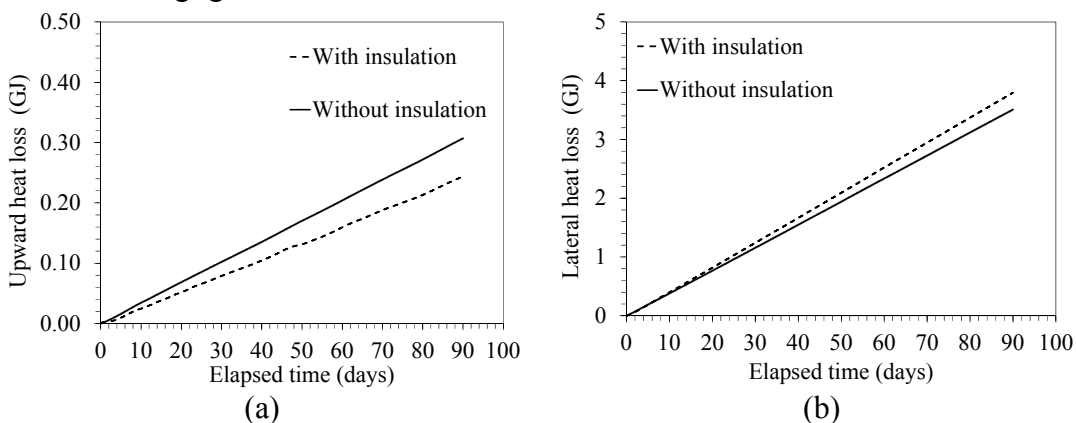


Fig. 5. Conductive heat loss from the borehole array: (a) Upward; (b) Lateral

The second analysis considers coupled heat transfer and water flow in the unsaturated soil layer in and around the SBTES system. In this case, the thermal conductivity was initially similar to that in the conduction analysis due to the relatively uniform initial degree of saturation in the soil. The temperature distribution in the soil above the borehole array is shown in Figure 6. Different from the analysis with conduction alone, the temperature distributions for the situations with and without insulation are similar, possibly due to heat homogenization by convection.

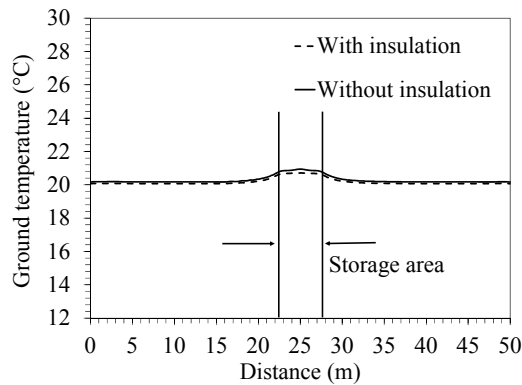


FIG. 6. Temperature distributions in the soil above the borehole array (depth of 0.5 m) for coupled heat transfer and water flow after 90 days of heat injection

The analyses of upward and lateral heat losses considering convection are given in Figures 7(a) and 7(b), respectively. Similar magnitudes of upward heat loss are observed to the simulations with conduction only, although the insulation layer has a greater effect in this case. The lateral heat loss is unaffected by the insulation layer, likely due to the patterns of heat flux created by the convective cell. The magnitude of the lateral heat loss is lower when considering coupled heat transfer and water flow than when considering conduction alone. Although the differences in behavior of the arrays are similar for the two analyses with and without convection, upward heat loss in the coupled case is lower when the insulation layer is present. Although not presented here, the total heat injection after 90 days of heating was 9.8 GJ. The upwards heat loss of 0.31 GJ is only 3% of the total heat injected.

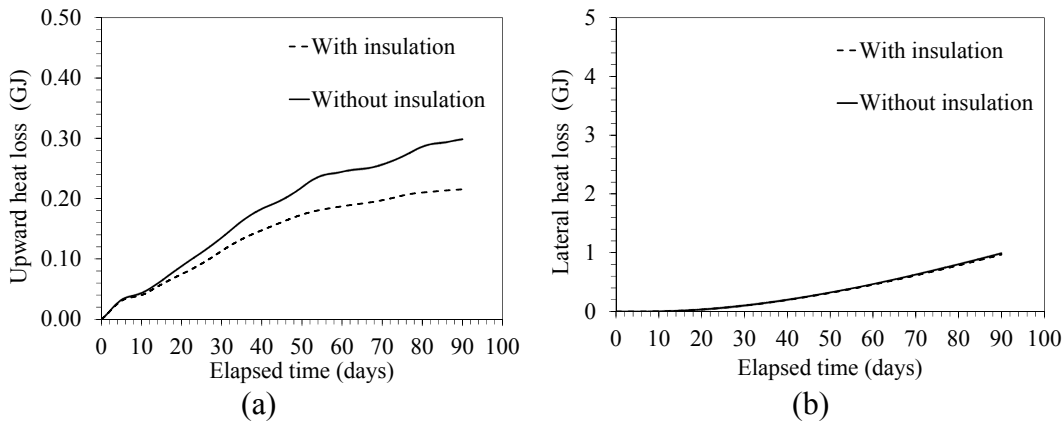


FIG. 7. Heat loss from the array in coupled conditions: (a) Upward; (b) Lateral

The lower lateral heat loss observed in the coupled analysis may be due to the patterns of heat flow within the system. Consideration of convection was found to preserve a greater amount of heat within the array as shown in Figure 8(b). This behavior was also observed by Catolico et al. (2015) in the simulation of the DLSC site using TOUGH2. Lu (2001) and Catolico et al. (2015) observed that the hydraulic conductivity of the soil needs to be sufficiently high for convection to play a major role in heat transfer, or for a convective cycle to start forming.

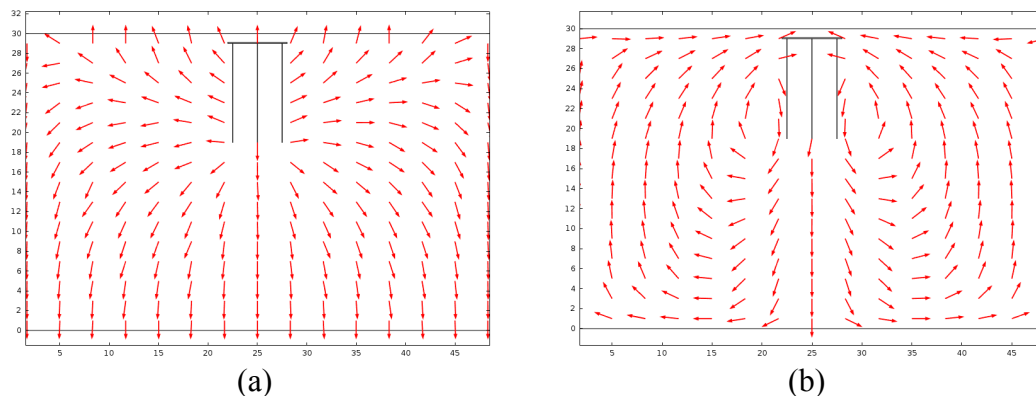


FIG. 8. Heat flux directions: (a) Conduction alone (b) With convection

CONCLUSIONS

This study focused on comparative numerical simulations of the thermal response of soil-borehole thermal energy storage (SBTES) systems with and without a surficial insulation layer. A transient finite element model was built to consider the coupled heat transfer and water flow processes in an unsaturated soil layer in and around the SBTES system. Although the upward heat loss was always found to be reduced by including an insulation layer, this reduction is relatively small due to the small area of heated soil around the borehole heat exchangers. Consideration of coupled heat transfer and water flow in the unsaturated soil caused the insulation to have a slightly greater role in reducing the upward heat loss, potentially due to the formation of a convective cell in the soil. When only conduction is assumed, including an insulation layer causes the lateral heat loss to increase. However, when considering both conduction and convection, the lateral heat loss was lower and the insulation layer did not have a major effect on the lateral heat loss.

ACKNOWLEDGEMENTS

Funding from National Science Foundation (NSF 1230237) is much appreciated. The opinions are those of the authors alone and do not reflect those of the sponsor.

REFERENCES

- Başer, T. and McCartney, J.S. (2015). "Development of a full-scale soil-borehole thermal energy storage system." Proc. Int. Foundations Conference and Equipment Exposition (IFCEE 2015). ASCE. pp. 1608-1617.

- Bear, J. (1972). *Dynamics of Fluids in Porous Media*. Dover, Mineola, N. Y., 764 p.
- Bjoern, H. (2013). "Borehole thermal energy storage in combination with district heating." *European Geothermal Congress 2013*. Pisa. June 3-7. 1-13.
- Catolico, N., Ge, S., and McCartney, J.S. (2016). "Numerical modeling of a soil-borehole thermal energy storage system." *Vadose Zone Hydrology*. 1-17. doi:10.2136/vzj2015.05.0078.
- Chapuis, S. and Bernier, M. (2009). "Seasonal storage of solar energy in borehole heat exchangers." *Proc. of the IBPSA Conf. on Building Sim*. Glasgow. 599-606.
- Claesson, J. and Hellström G. (1981). "Model studies of duct storage systems." *New Energy Conservation Technologies and their Commercialization*. J.P. Millhone and E.H. Willis, Eds. Springer-Verlag, Berlin. 762-778.
- Eskilson, P. (1987). *Thermal Analysis of Heat Extraction Boreholes*. Lund, Sweden: Dept. of Mathematical Physics, University of Lund.
- Hellström, G. (1989). *Duct Ground Heat Storage Model: Manual for Computer Code*. Lund, Sweden: University of Lund.
- Lu, N. (2001). "An analytical assessment on the impact of covers on the onset of air convection in mine wastes." *Int. J. of Num. Anal. Meth. Geomech.* 25, 347-364.
- Lu, N. and Dong, Y. (2015). "A closed form equation for thermal conductivity of unsaturated soils at room temperature." *Journal of Geotechnical and Geoenvironmental Engineering*. 141(6), 04015016.
- McCartney, J.S., Ge, S., Reed, A., Lu, N., and Smits, K. (2013). "Soil-borehole thermal energy storage systems for district heating." *EGC 2013*. Pisa. 1-10.
- Moradi, A., Smits, K., Massey, J., Cihan, A., and McCartney, J.S. (2015). "Impact of coupled heat transfer and water flow on soil borehole thermal energy storage (SBTES) systems: Experimental and modeling investigation." *Geothermics*. 57(September). 56-72.
- Nordell, B. and Hellström, G. (2000). "High temperature solar heated seasonal storage system for low temperature heating of buildings." *Solar Energy*. 69(6), 511-523.
- Philip, J.R., and de Vries, D.A. (1957). "Moisture movement in porous materials under temperature gradients." *Trans. Amer. Geophys. Union* 38:222-232.
- Sibbitt, B., McClenahan, D., Djebbara, R., Thornton, J., Wong, B., Carriere, J., and Kokko, J. (2012). "The performance of a high solar fraction seasonal storage district heating system – Five years of operation." *Energy Procedia*, 30, 856-865.
- Smits, K.M., Sakaki, S.T., Howington, S.E., Peters, J.F., and Illangasekare, T.H. (2013). "Temperature dependence of thermal properties of sands across a wide range of temperatures (30-70 °C)." *Vadose Zone J.*, doi: 10.2136/vzj2012.0033.
- Smits, K.M., Cihan, A., Sakaki, T., and Illangasekare, T.H. (2011). "Evaporation from soils under thermal boundary conditions: Experimental and modeling investigation to compare equilibrium and nonequilibrium-based approaches." *Water Resources Research*, 47, W05540, doi:10.1029/2010WR009533.
- van Genuchten, M.T. (1980). "A closed-form equation for predicting the hydraulic conductivity of unsaturated soils." *Soil Sci. Soc. Am. J.*, 44(5), 892-898.
- Zhang, R., Lu, N., and Wu, Y. (2012). "Efficiency of a community-scale borehole thermal energy storage technique for solar thermal energy." *Proc. GeoCongress 2012*. ASCE. 4386-4395.

Mechanical Behavior of a Pile Used for Small-Scale Compressed Air Energy Storage

Sihyun Kim¹; Seunghye Kim, A.M.ASCE²; Hoyoung Seo, M.ASCE³, and Jongwon Jung⁴

¹Assistant Professor, Bradley Univ., 1501 W Bradley Ave., Peoria, IL 61625-0001.

²Assistant Professor, Western New England Univ., 1215 Wilbraham Rd., Springfield, MA 01119-2684.

³Assistant Professor, Texas Tech Univ., P.O. Box 41023, Lubbock, TX 79409.

⁴Assistant Professor, Louisiana State Univ., 3418 Patrick F. Taylor, Baton Rouge, LA 70803.

Abstract: Intermittent availability of renewable energy sources requires an energy storage system, and small-scale compressed air energy storage (CAES) has been brought up as an attractive option to store excess energy as a pressurized air. Here, we explore the idea of using a close-end steel pile as a vessel to store pressurized air. Small-scale CAES pile is expected to experience unusually a large number of cyclic loading during the operation. This paper frameworks the preliminary results from lab- and field-scale finite element simulations: plane-strain and axisymmetric models are adopted to examine mechanical behavior of a steel pile during a loading-unloading cycle by internal air pressure. Computational models include simple constitutive models of pile, soil, and pile-soil interface. Preliminary results reveal the stability condition of CAES pile as well as deformation pattern.

INTRODUCTION

Active utilization of renewable energy is important to attain the sustainability of energy and environmental systems. Renewable energy sources, such as solar and wind energy, differ from conventional energy sources, such as oil, natural gas, coal, and nuclear, as they heavily depend on the climate conditions for the production. The inevitable intermittency requires a comprehensive renewable energy system to equip with an energy storage option. There are several energy storage options at practice, such as batteries, fuel cells, pumped hydro storage, and compressed air energy storage (CAES) [Aksen *et al.*, 2008; Bullough *et al.*, 2004; Burke, 2008; DTI, 2004; Smith *et al.*, 2008; Succar and Williams, 2008; Van der Linden, 2006].

Among these different technologies, CAES has distinct merits because it can overcome several limitations of other energy storage options. CAES entails storing compressed air in an underground cavity, reservoir, or storage vessel by using excess electricity generated during off-peak hours (day time). The stored air is later released and expanded with heat provided by fossil fuels to drive turbines that generate electricity during peak periods (evening time) [Pasten and Santamarina, 2011]. CAES can be further divided into two categories: (1) large-scale, or (2) small-scale storage, depending on the required storage capacity. Small-scale CAES stores compressed air in flexible bags under water, steel tanks or pipelines above or below ground surface

[Zhang *et al.*, 2012]. Small-scale CAES can be an attractive option for single-standing units because the required volume is small and no specific underground geologic formation is needed.

The required volume V [m^3] of a storage system is a function of the stored energy density e_V [kJ/m^3], either the stored energy E [J] or the delivered power P [W], and the time of supply t [s] as follows [Pasten and Santamarina, 2011]:

$$V = \frac{E}{e_V} = \frac{P \cdot t}{e_V}, \text{ where } e_V = p_{\max} \ln \frac{p_{\max}}{p_{\min}} \quad (1)$$

Let's consider a volume of $V = 2m^3$ and compressed air pressure ranges from $p_{\min} = 0.1MPa$ to $p_{\max} = 8MPa$ (and the estimated energy density is $e_V = 35MJ/m^3$). Assuming a recovery efficiency $\eta = 0.75$, the stored energy can then provide ~ 7 hours of power supply assuming a house power consumption of $2kW$ [Pasten and Santamarina, 2011].

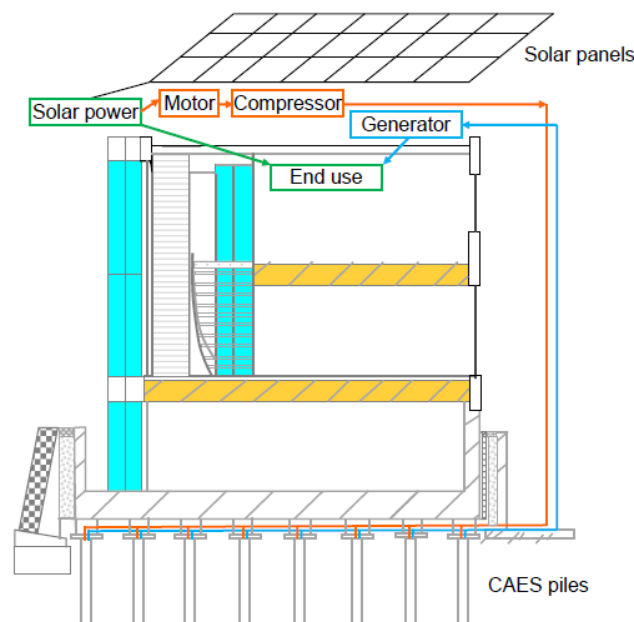


FIG. 1. Schematic illustration of utilizing pile foundations for compressed air energy storage (CAES). Original image is from [Zhang *et al.*, 2012].

Pile foundations of buildings have been studied as “heat exchangers” (so-called “energy-piles”) in the way that fluid circulates in a pile foundation as well as inside building to save energy usage [Hamada *et al.*, 2007; Laloui *et al.*, 2003]. The application ascertains the potential of the building foundation to be part of a comprehensive renewable energy system. Zhang *et al.* [2012] suggested the idea that air is compressed using an excess energy generated from solar panels and then it is stored in a hollow steel pipe pile so that the stored compressed air can be used later (concept is shown in **FIG. 1**). While they showed that additional loading due to the compressed air is not expected to compromise the bearing capacity of a pipe pile, further extensive study is needed to confirm mechanical integrity of the whole system that is subjected to repetitive pressure loadings. Repeated loading is known to cause

progressive shear stress degradation due to gradual densification of soil layer adjacent to structural surface as well as reduction in normal stress [Fakharian and Evgin, 1997; Mortara et al., 2007; Poulos, 1989]. In this study, we attempt to explore in detail the mechanical behavior of a pile when internal pressure is increased and then decreased back to an original value as a result of compressed air energy storage (i.e., one pressure cycle) using numerical simulations. Results in this study will then be used to extend our investigation to the long-term behavior of a CAES pile, such as strain-ratcheting and plastic deformation around a pile.

FINITE ELEMENT MODELS

A commercial finite element software (Abaqus 6.13-2) is utilized to explore the behavior of a CAES pile when the pile is internally pressurized and depressurized during the operation. A close-end pipe pile is selected as an example of the CAES pile. Pressurizing (loading) the pile to p_{\max} is equivalent to storing compressed air during the day time and depressurizing (unloading) back to $p_{\min} = 0.1\text{MPa}$ implies the compressed air is released to generate electricity in the night. Vertical load from superstructure is not considered in this preliminary analysis to focus on the impact of air pressure inside the CAES pile.

Although a large number of loading-unloading cycles should be applied to practically test the stability of CAES pile, as a preliminary study, we simply apply p_{\max} and then decrease to p_{\min} (i.e., one pressure cycle). Maximum air pressure is set as $p_{\max} = 10\text{MPa}$ which is slightly larger than 8MPa in expression (1), so that the analysis here accounts for a bit more conservative condition. We choose a steel pipe pile that has an inner diameter of 0.2m , 0.01m thick, and 20m long. The pile is considered as an elastic material with Young's modulus of 200GPa and Poisson's ratio of 0.3 . Mohr-Coulomb model is chosen for the soil material used in this paper as the simplest plastic model, which has 100MPa of Young's modulus, 0.25 of Poisson's ratio, 1kPa of cohesive strength, and 30° of friction angle. An elastic perfectly-plastic constitutive model is used at the pile-soil interface to examine a slip between the pile and the soil [e.g., Ozudogru et al., 2015]. At the interface, a friction coefficient is assumed to be 0.3 and a threshold elastic strain is 1% . The interface properties used here are generic, thus exact values are to be determined from the laboratory test under cyclic loading condition [e.g., Di Donna and Laloui, 2015; Fakharian and Evgin, 1997; Mortara et al., 2002; Mortara et al., 2010].

PLANE-STRAIN ANALYSIS

Under the inner pressure escalation, a pile expands in both radial and axial directions similar to a pressurized vessel. However, since pile length is typically much greater than its diameter, at least by few orders of magnitude, plane-strain analysis could be a feasible approach to understand the fundamental behavior in the horizontal direction. In this study, using the cavity expansion theory [e.g., Yu, 2000] (FIG. 2a), the deformation of surrounding soil by the pressurized steel pile is tested.

Here, pile has 0.2m of inner diameter and 0.01m of thickness, and soil is considered as Mohr-Coulomb material. Understanding cavity expansion model gives

some insights to the elasto-plastic behavior of soil. For example, the radius of plastic zone in soil, c , is obtained as:

$$c = a \left\{ \frac{(\alpha + 1)[Y + (\alpha - 1)p_{int}]}{2\alpha[Y + (\alpha - 1)p_0]} \right\}^{\frac{\alpha}{\alpha-1}} \quad (2)$$

where $Y = \frac{2C \cos \phi}{1 - \sin \phi}$, $\alpha = \frac{1 + \sin \phi}{1 - \sin \phi}$ [Yu, 2000], C is the cohesive strength, ϕ is the friction angle of soil, and p_0 is the preloaded (initial) pressure inside the pile and the soil mass. Here, p_0 is equal to the minimum air pressure p_{min} inside the CAES pile in our analysis. p_{int} is the actual pressure applied to the surrounding soil, which is not found yet. Numerical computation is used to find the interface stress, p_{int} , as a function of internal air pressure, p , from **FIG. 2b**. Normal stress acting on interface between outer surface of pile and the surrounding soil increases from $p_{int} = p_0$ to $p_{int} = 7.258p_0$ as the internal air pressure increases from $p = p_0$ to $p = 10,000p_0$.

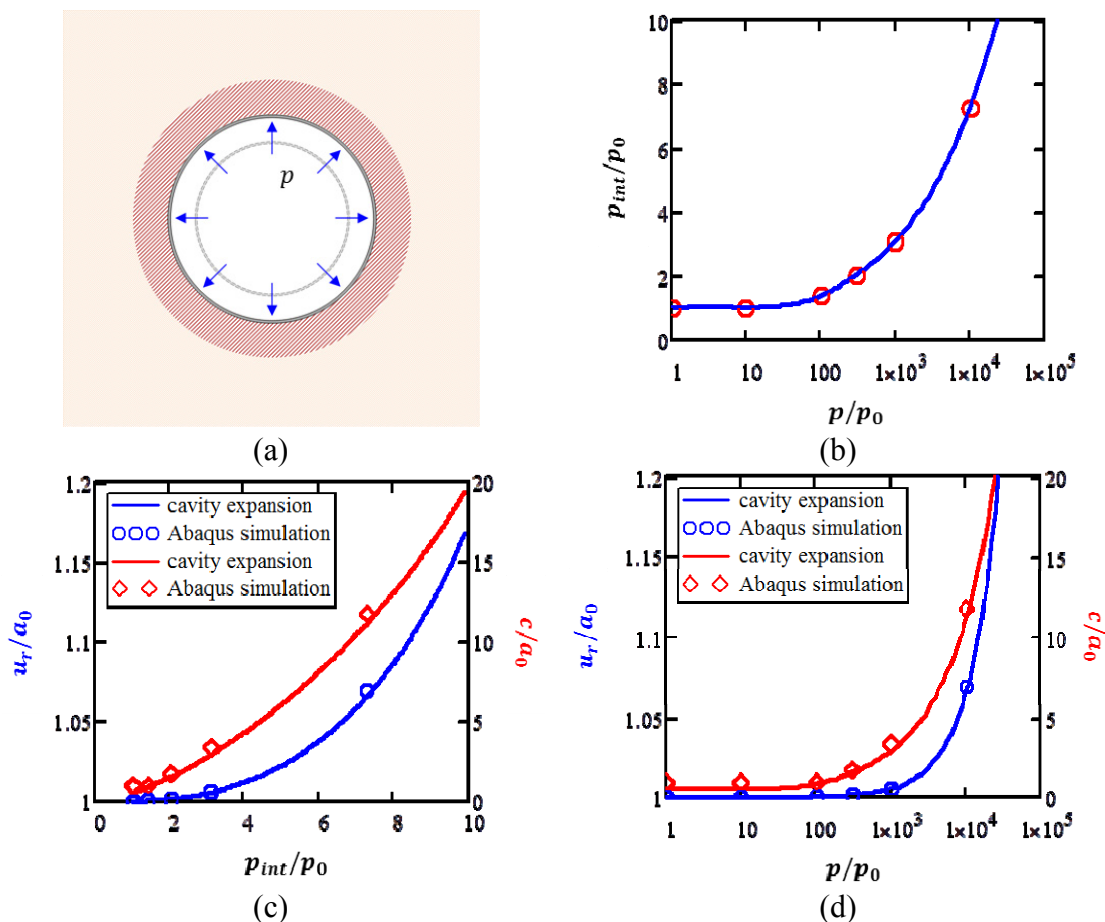


FIG. 2. Cavity expansion analysis. (a) Cross-section of CAES pile with original (dashed lines), deformed (solid) condition, and plastic zone (shaded area), (b) soil-pile interface stress response with air pressure inside CAES pile, (c) radial displacement and plastic zone variation with soil-pile interface stress, and (d) radial displacement and plastic zone variation with air pressure.

Cavity expansion model can analytically expect radial displacement and plastic zone size with the change in interface stress. Then the estimated values are compared with simulation result, which show a good agreement each other (**FIG. 2c**) to assess the radial displacement at the interface, u_r , and the size of plastic zone, c , where a_0 is the initial inner radius of soil (= the outer radius of the pile). In turn, variations of radial displacement and plastic zone size with respect to the applied air pressure p can be calculated as depicted in **FIG. 2d**.

Through the cavity expansion study, we can accurately calculate the magnitude of the applied stress to initiate the plastic zone in the surrounding, which will lead to a permanent deformation after the stress is unloaded. Given soil properties in expression (2), $p_{\text{int}} = 1.5p_0$ of applied stress (interface stress in this case) is expected to cause the plastic strain, and it corresponds to approximately $p = 11\text{MPa}$ of internal air pressure (per **FIG. 2b**). This indicates that CAES pile with the internal pressure less than 11MPa would not generate any irrecoverable strain in the soil outside, but the internal pressure of larger than 11MPa will cause a plastic strain accumulation with the cyclic loading in the soil outside the pile.

Here, 11MPa of internal pressure is larger than the air pressure level currently in use (8MPa). That is, CAES pile does not produce the significant radial deformation, which would not be accompanied by the irreversible strain. Also, please note this result is consistent with the analysis of thermal pile [Knellwolf *et al.*, 2011; Olgun *et al.*, 2014].

AXISYMMETRIC ANALYSIS

Axisymmetric model enables us to assess both radial and vertical displacements of a CAES pile as well as the slip at the pile-soil interface (**FIG. 3a**). We considered a single pile in our analysis for simplicity. The considered pile is close-end, circular in cross section, and vertically preinstalled in the ground. We also choose a same steel pipe pile described earlier that has 0.2m of inner diameter, 0.01m of thickness, and 20m long (inner volume of 0.628m^3). Simulation domain is 50m far from the axis of symmetry and 100m deep from the ground surface which ensures any boundary effect is negligible. The contact between pile and soil is considered as elastic perfectly-plastic [e.g., Ozudogru *et al.*, 2015], which means strength degradation in the interface is not considered. Compressed air pressure $p_{\text{max}} = 10\text{MPa}$ is applied inside the pile, which is expected not to create any plasticity in the surrounding of the pile from the plane-strain study.

When the CAES pile is pressurized with p_{max} , the pile expands not only radially but also stretches vertically. Both radial and vertical displacements of the pile do not change dramatically with depth, but the radial value is much smaller than the vertical displacement by two orders of magnitude (**FIG. 3b**). This result is consistent with the result from the plane-strain study in the aspect that radial deformation does not make a critical contribution to the structure stability, and also validates the necessity of axisymmetric analysis of the CAES pile rather than using the plane-strain model.

We also investigated the case when the CAES pile is depressurized back to the original pressure $p_0 = p_{\text{min}}$ in the axisymmetric analysis. Some residual values of slip (blue lines), shear and normal stresses are observed at the pile-soil interface, especially

within around 2m depth (FIG. 3c). Even though the calculated slip in this simple axisymmetric model seems to be not significant, this irreversible slip can be accumulated during a huge number of working cycles (i.e., 20,000 or more).

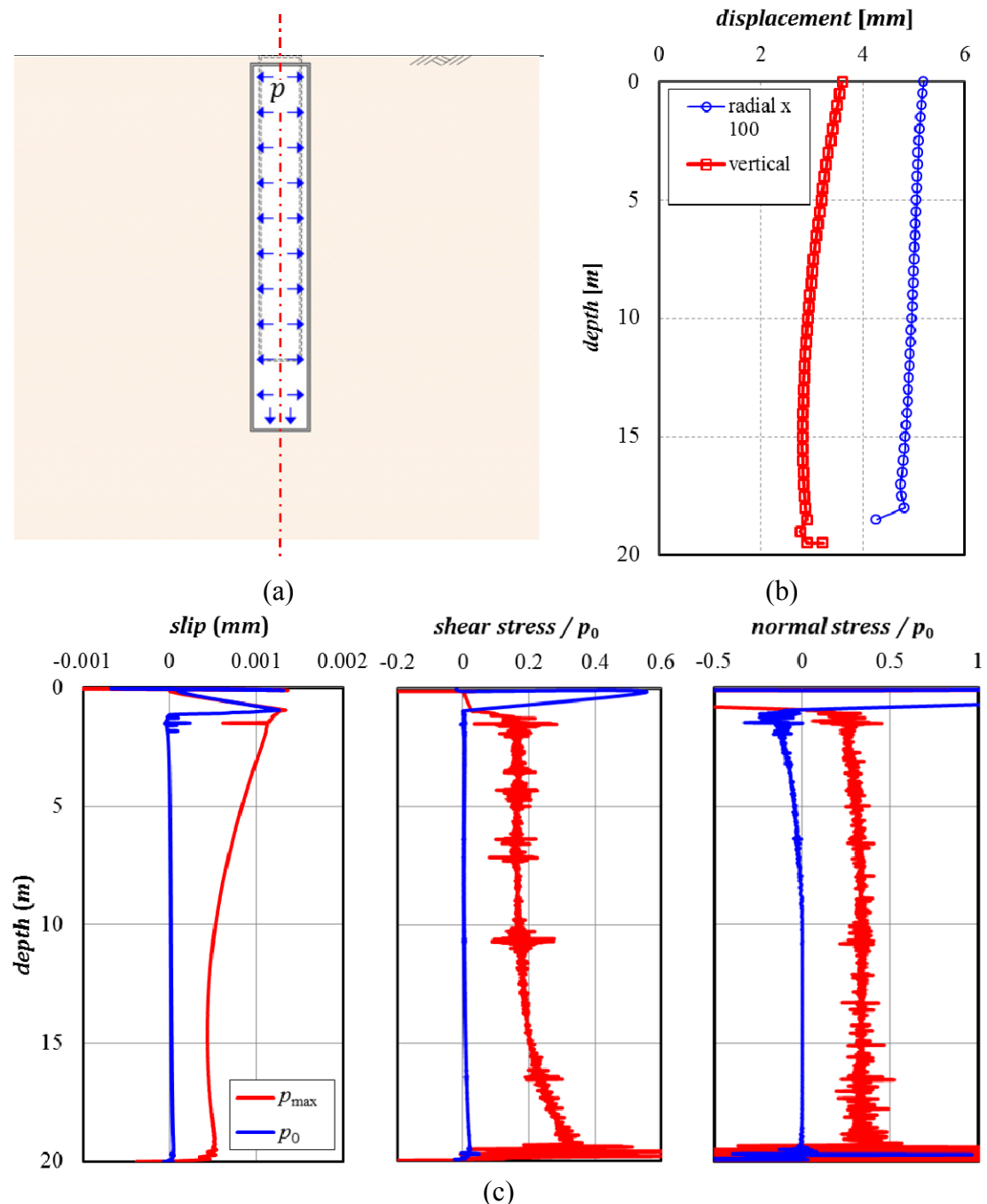


FIG. 3. Axisymmetric analysis of CAES pile. (a) Side view of CAES pile with original (gray, dashed lines), deformed (gray, solid) conditions, and axis of symmetry (red, dashed line) (b) depth profile of radial and vertical displacements at p_{max} , and (c) profile changes in pile-soil interface after pressure drops from p_{max} to p_0 .

As also described in plane-strain analysis, mechanical behavior of the CAES pile has some analogies with a thermo-active pile subjected to heating-cooling cycles. In this regard, it seems logical that similar responses are observed for these two different applications; for example, vertical displacement is much greater than horizontal deformation [Knellwolf *et al.*, 2011; Olgun *et al.*, 2014], and irrecoverable settlement of pile structure is observed after unloading [Laloui *et al.*, 2006; Suryatriyastuti *et al.*, 2014].

CONCLUSIONS

This paper attempts to build a groundwork for the study on mechanical behavior of a CAES pile and presents preliminary results for extending them to the long-term stability of the structure under cyclic loading conditions. Key points from the pilot studies reported here are listed below.

- Results from numerical simulation of the CAES pile in the plane-strain condition and cavity expansion analysis show good agreement.
- Cavity expansion approach and plane-strain simulation suggest the maximum internal pressure that does not generate plastic deformation in the surrounding soil.
- Axisymmetric simulation confirms that horizontal deformation around the CAES pile is much smaller than the vertical deformation.
- Irreversible slip is observed at the pile-soil interface after the CAES pile is depressurized back and can be possibly accumulated with a large number of loading-unloading cycles.
- Fundamental behavior of the CAES pile is similar to that of a thermo-active pile.

REFERENCES

- Axsen, J., A. Burke, and K. S. Kurani (2008), "Batteries for plug-in hybrid electric Vehicles (PHEVs): goals and the state of technology circa 2008" *Rep. UCD-ITS-RR-08-14*, Institute of Transportation Studies, University of California-Davis.
- Bullough, C., C. Gatzen, C. Jakiel, M. Koller, A. Nowi, and S. Zunft (2004), "Advanced adiabatic compressed air energy storage for the integration of wind energy", paper presented at Proceedings of the European Wind Energy Conference, EWEC 2004, London UK, 22-25 November.
- Burke, A. F. (2008), "Materials research for high energy density electrochemical capacitor", paper presented at MRS Proceedings, Cambridge Univ Press.
- Di Donna, A., and L. Laloui (2015), "Response of soil subjected to thermal cyclic loading: Experimental and constitutive study", *Engineering Geology*, 190, 65-76, doi:10.1016/j.enggeo.2015.03.003.
- DTI (2004), "Review of electrical energy storage technologies and systems and of their potential for the UK. Contract number: DG/DTI/00055/00/00" *Rep.*

- Fakharian, K., and E. Evgin (1997), "Cyclic simple-shear behavior of sand-steel interfaces under constant normal stiffness condition", *Journal of Geotechnical and Geoenvironmental Engineering*, 123(12), 1096-1105.
- Hamada, Y., H. Saitoh, M. Nakamura, H. Kubota, and K. Ochifuji (2007), "Field performance of an energy pile system for space heating", *Energy and Buildings*, 39(5), 517-524.
- Knellwolf, C., H. Peron, and L. Laloui (2011), "Geotechnical analysis of heat exchanger piles", *Journal of Geotechnical and Geoenvironmental Engineering*, 137(10), 890-902.
- Laloui, L., M. Moreni, and L. Vulliet (2003), "Behavior of a dual-purpose pile as foundation and heat exchanger", *Canadian Geotechnical Journal*, 40(2), 388-402.
- Laloui, L., M. Nuth, and L. Vulliet (2006), "Experimental and numerical investigations of the behaviour of a heat exchanger pile", *Int. J. Numer. Anal. Meth. Geomech.*, 30, 763-781, doi:10.1002/nag.499.
- Mortara, G., M. Boulon, and V. N. Ghionna (2002), "A 2-D constitutive model for cyclic interface behaviour", *International Journal for Numerical and Analytical Methods in Geomechanics*, 26(11), 1071-1096.
- Mortara, G., D. Ferrara, and G. Fotia (2010), "Simple model for the cyclic behavior of smooth sand-steel interfaces", *Journal of Geotechnical and Geoenvironmental Engineering*, 137(7), 1004-1009, doi:10.1061/ASCEGT.1943-5606.0000315.
- Mortara, G., A. Mangiola, and V. N. Ghionna (2007), "Cyclic shear stress degradation and post-cyclic behaviour from sand-steel interface direct shear tests", *Canadian Geotechnical Journal*, 44(7), 739-752.
- Olgun, C. G., T. Y. Ozudogru, and C. F. Arson (2014), "Thermo-mechanical radial expansion of heat exchanger piles and possible effects on contact pressures at pile-soil interface", *Géotechnique Letters*, 4, 170-178, doi:10.1680/geolett.14.00018.
- Ozudogru, T. Y., C. G. Olgun, and C. F. Arson (2015), "Analysis of friction induced thermo-mechanical stresses on a heat exchanger pile in isothermal soil", *Geotechnical and Geological Engineering* 33, 357-371, doi:10.1007/s10706-014-9821-0.
- Pasten, C., and J. C. Santamarina (2011), "Energy geo-storage—analysis and geomechanical implications", *KSCE Journal of Civil Engineering*, 15(4), 655-667.
- Poulos, H. G. (1989), "Cyclic axial loading analysis of piles in sand", *Journal of Geotechnical Engineering*, 115(6), 836-852.
- Smith, S. C., P. Sen, and B. Kroposki (2008), "Advancement of energy storage devices and applications in electrical power system", paper presented at Power and Energy Society General Meeting—Conversion and Delivery of Electrical Energy in the 21st Century, IEEE.

- Succar, S., and R. H. Williams (2008), "*Compressed air energy storage: theory, resources, and applications for wind power*", Princeton Environmental Institute, Princeton University, Princeton/NJ.
- Suryatriyastuti, M., H. Mroueh, and S. Burlon (2014), "A load transfer approach for studying the cyclic behavior of thermo-active piles", *Computers and Geotechnics*, 55, 378-391.
- Van der Linden, S. (2006), "Bulk energy storage potential in the USA, current developments and future prospects", *Energy*, 31(15), 3446-3457.
- Yu, H.-S. (2000), "*Cavity Expansion Methods in Geomechanics*", 385 pp., Springer Science+Business Media Media, B.Y.
- Zhang, L., S. Ahmari, B. Sternberg, and M. Budhu (2012), "Feasibility study of compressed air energy storage using steel pipe piles", paper presented at GeoCongress 2012.

Settlement Response of a Geothermal Energy Pile Group in Sand

Rajni Saggu¹ and Tanusree Chakraborty²

¹Assistant Professor, Dept. of Civil Engineering, Amity School of Engineering and Technology, Amity Univ. Uttar Pradesh, Sector 125, Noida 201313. E-mail: rsaggu@amity.edu

²Assistant Professor, Dept. of Civil Engineering, Indian Institute of Technology (IIT) Delhi, Hauz Khas, New Delhi 110016. E-mail: tanusree@civil.iitd.ac.in

Abstract: The geothermal piles are used as a group in major construction projects. Geothermal energy piles provide sustainable energy alternative for residential and commercial buildings worldwide. In spite of the growing recognition of the benefits of energy piles, there is still a knowledge gap about the load transfer mechanism of pile groups under thermo-mechanical loading. In the present study, thermo-mechanical response of geothermal energy pile groups in sand has been studied using three dimensional nonlinear finite element analysis procedure. A pile cap is considered on the piles. Stress-strain responses of piles and pile cap are considered linear elastic. The stress-strain response of sand is simulated using a state parameter based constitutive model CASM. The CASM model has been implemented in finite element software Abaqus through user defined material subroutine. The geothermal energy pile group has been analyzed for different combinations of thermal and non-thermal piles in the group in a single layer of Ottawa sand. Analyses have been performed by varying the spacing between the piles. Analysis results have been studied for the displacement at the base of the piles. It is observed from the results the load carried by the thermal piles increases due to heating induced excess load in the pile. For non-thermal piles however, unloading of the pile happens during heating of the thermal piles and base displacement decreases. Heating of thermal piles also causes expansion of these piles in upward direction, thus, the piles pushing the pile cap along with it in the upward direction. Differential settlement at the pile base is observed for the groups containing both thermal and non-thermal piles.

INTRODUCTION

Geothermal energy pile foundations represent an innovative technology for the energy efficient residential and commercial buildings in Europe, the United States, Australia and some countries in Asia (Brandl 2006, McCartney 2011). In order to support the load from the superstructure, piles are often used in group and depending on the heating and cooling requirements of the building, all or only certain number of piles in the group may be used as thermal piles (Koene and Geelen 2000, Salciarini et al. 2013).

The geothermal piles are used as a group in major construction projects. However, very few scientific studies on geothermal pile groups exist in the literature, due to the complexity involved in experimental and numerical investigation of the pile groups. In one study, Sanner et al. (2003) has mentioned that the distance between two energy piles in the group should be at least 4 m. Brettman and Amis (2011) performed thermal conductivity tests of geothermal energy pile groups where piles were placed at 4.5 m center to center. They observed that soil temperature surrounding the pile increases during thermal heating of the pile; however, at the centre between the two piles, soil temperature remains unchanged. Dupray et al. (2014) performed two dimensional thermo-hydro-mechanical finite element analyses of multiple piles in clay. They observed that heating and cooling of all the piles together has a positive impact on the mechanical behaviour of piles in comparison to heating and cooling of isolated piles. They also reported that higher vertical displacement occurs when the piles are under thermal loading. Saggu and Chakraborty (2016) have reported the results of numerical analysis of geothermal energy pile groups and stated that geothermal energy piles exhibit thermally induced axial stress in addition to axial stress due to mechanical loading of these piles. Apart from these studies, three dimensional nonlinear finite element (FE) analysis based predictions for the stresses and displacement of the energy piles in groups under thermo-mechanical loading are rare in the literature.

The present study focuses on the response of geothermal energy pile groups in sand subjected to thermo-mechanical loading, considering different combinations of thermal and non-thermal piles in the group under a single pile cap. Saggu and Chakraborty (2015) have shown that the shaft capacity of the geothermal energy piles does not change significantly as compared to the piles under only mechanical load, whereas, axial stress in the pile and pile base displacement increase with increasing temperature in the pile. Therefore, in the present work, effort has been given in understanding the displacement at the pile base for the geothermal energy pile group as compared to the pile group subjected to only mechanical loading. In order to accomplish the above stated objective, three dimensional (3D) nonlinear finite element (FE) analyses of geothermal energy pile groups, with six piles in the group, have been performed herein using the FE software Abaqus (Abaqus Manual Version 6.11). Analyses have been performed for different combinations of thermal and non-thermal piles in the group and different spacing between the piles. The pile has been assumed to behave linear elastically. The soil behavior has been simulated using a critical state soil mechanics based constitutive model CASM (Yu 1998 and 2006). The constitutive model has been implemented in Abaqus through a user defined material subroutine, e.g. UMAT for defining the mechanical stress-strain behavior of soil and a user defined material subroutine, e.g. UMATHT for defining the thermal soil parameters. The temperature change on pile has been assumed to be uniform over the entire length of the pile (Laloui et al. 2006).

DETAILS OF NUMERICAL ANALYSES

Finite Element Model

The three dimensional finite element analyses reported herein have been performed using the finite element software Abaqus. In these analyses, the pile, pile cap and soil geometries are created as separate parts. Both the pile and the pile cap are considered to be made of concrete with ultimate compressive strength of 45 MPa. The stress-strain response of concrete is considered linear elastic with Young's modulus (E) = 33.7 GPa and Poisson's ratio (ν) = 0.2. Table 1 presents the material properties of Ottawa sand, pile and pile cap.

Table 1. Material Parameters used for Ottawa Sand, Pile and Pile cap

CASM model and thermal parameters for Ottawa sand		
Mechanical Parameters	Value	References
Slope of critical state line in e - $\ln(p')$ space, λ	0.02	Sasitharan et al. (1994), Carraro (2006), Loukidis (2006)
Slope of unloading-reloading line in e - $\ln(p')$ space, κ	0.005	Yu (2006)
Critical state line intercept at 1 kPa pressure, Γ	0.8	Model simulation
Reference state parameter, ξ_R	0.075	Yu (2006)
Model parameter, n	4.5	Model simulation
Slope of critical state line in q - p' space, M_{cc}	1.2	Yu (2006), Loukidis (2006)
Poisson's ratio, ν_s	0.3	Yu (2006)
Shear modulus, G	32.6 MPa	Laloui et al. (2006)
Bulk modulus, K	15 MPa	
Thermal conductivity, k_s	0.274 W/m°C	Tarnawski et al. (2009)
Specific heat, C_s	722 Joule/°C	
Coefficient of thermal expansion, α_s	$10^{-4}/^\circ\text{C}$	
Elastic and thermal parameters for pile and pile cap		
Modulus of elasticity, E	33 GPa	Pile and pile cap material parameters assumed to be same as concrete.
Poisson's ratio, ν	0.2	
Thermal conductivity, k	2.1 W/m°C	
Specific heat, C	800 Joule/°C	
Coefficient of thermal expansion, α	$10^{-5}/^\circ\text{C}$	

Tie constraint has been provided between the pile cap and the piles to tie all vertical and the horizontal degrees of freedom together. The pile is placed in a single layer of Ottawa sand. The Ottawa sand has been modeled with critical state soil mechanics based material constitutive model CASM. Figure 1 shows typical finite element mesh of the piles, pile cap and the surrounding soil. Here each pile is 20 m long with 1 m diameter. The pile cap is 15.5 m long, 12.9 m wide and 1.2 m thick. The vertical far-field soil boundaries have been placed at a distance of 6.5 m and 7.5

m from the side of the pile cap, along the shorter and the longer dimensions of the pile cap, respectively as shown in the Figure 1. The bottom soil boundary is placed at a distance of one pile length from the bottom of the piles. The finite element domain size and element size in the mesh have been determined through boundary and mesh convergence studies. The far-field vertical soil boundaries have been restrained in horizontal directions and the bottom soil boundary has been restrained in both vertical and horizontal directions. Among the thermal boundary conditions, heat flow has been allowed through the far-field sides and the bottom boundaries of the mesh. A constant temperature of 15°C has been assumed at the top soil boundary. Also, the ambient ground temperature is assumed to be 15°C (Laloui et al. 2006).

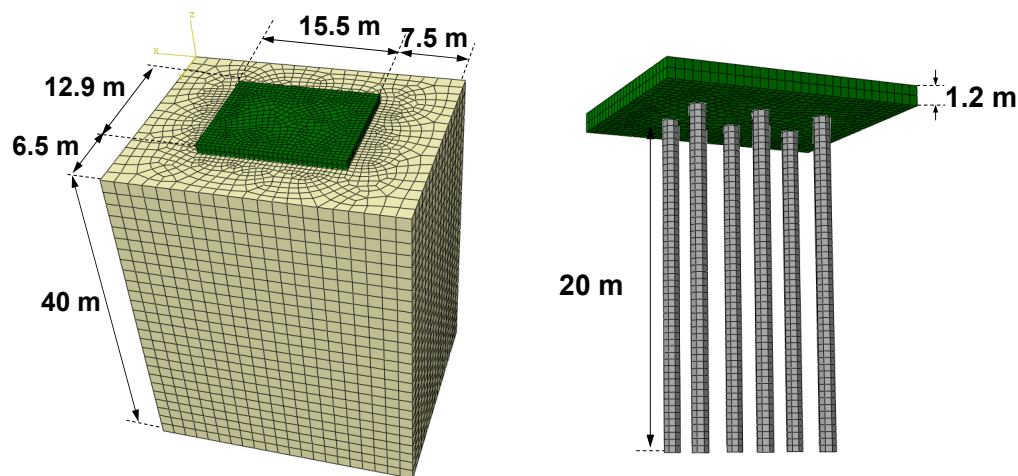


FIG. 1. Finite element mesh for geothermal pile group and pile cap

The analysis domain has been discretized using eight node thermally coupled brick, trilinear displacement and temperature (C3D8T) elements for both pile and soil. The minimum element size in soil domain is 0.5 mm surrounding the pile and the maximum element size is 1.5 mm in the far-field regions. The interfaces between the pile and the soil surfaces have been modeled as frictional contact in the tangential direction with a coefficient of friction $\mu (= \tan\delta)$ between soil and concrete of 0.55. In the normal direction between the pile and soil, hard contact has been considered. Heat conduction between pile and soil has been made possible by defining a thermal conductance at the pile-soil interface same as the soil thermal conductance.

Sand Constitutive Model CASM

The current CASM formulation has seven parameters which can be determined from triaxial test data. In the present study, a FORTRAN code has been written for drained and undrained triaxial compression test simulation for the determination of the CASM model parameters. Herein, the model parameters have been determined for Ottawa sand with minimum void ratio $e_{\min} = 0.48$ and maximum void ratio $e_{\max} = 0.78$ (Murthy et al. 2006). The thermal constitutive model is implemented in Abaqus through user defined material subroutine UMATHT. The thermal response of pile-soil system is considered to follow the energy balance equation given by Green and Naghdi (1992).

Calculation of Settlement for Piles in Group

The settlement of piles when in group is different from the settlement that a single pile would undergo under the same applied load (Salgado 2008). According to Mylonakis and Gazetas (1998) the head displacement w_i of any pile i in the group where total number of piles, $n_p = i \times j$ under the total applied load Q would be a summation of the effects of the loads on adjacent piles considering the soil resistance. The settlement of the pile head is thus given by

$$w_i = \sum_{j=1}^{n_p} \alpha_{ij} \frac{Q}{K_{ij}} \quad (1)$$

where K_{ij} is stiffness of pile j , α_{ij} is the influence factor between piles i and j given by

$$\alpha_{ij} = \Lambda(\lambda L, \Omega) \ln \frac{(r_m / s_{pij})}{(2r_m / B)} \quad (2)$$

where r_m is the “magical” radius (Randolph and Wroth 1978) at which the settlement w of the ground surface becomes zero, s_{pij} is the spacing between the pair of interacting piles considered, e.g. pile i and pile j , B is the diameter of the pile, and $\Lambda(\lambda L, \Omega)$ is the factor containing the pile-reinforcing effect. Graphs for obtaining Λ for different lengths of the piles are given in Salgado (2008). The parameter λ ($= \sqrt{k/E_p A_p}$), k is soil subgrade modulus, E_p is the elastic modulus of the pile and A_p is the cross sectional area of the pile) is the Winkler factor and Ω is the dimensionless pile base stiffness given by

$$\Omega = \frac{4G_b r_s}{(1-\nu) \lambda E_p A_p} \quad (3)$$

where G_b is soil shear modulus at pile base, r_s is radius of pile and ν is Poisson’s ratio of soil at pile base.

In the present study, pile base settlement w_{bi} has been calculated analytically by using equation (4) as given by

$$w_{bi} = \sum_{j=1}^{n_p} \alpha_{ij} \frac{Q_b}{K_b} \quad (4)$$

where Q_b is the load carried by pile base and K_b is the stiffness of soil at the pile base. Herein, Q_b has been obtained from the simulation results and the influence factor α_{ij} has been calculated using equation (2) with $\Lambda(\lambda L, \Omega)$ obtained from the charts provided in Salgado (2008).

VALIDATION OF FINITE ELEMENT MODEL UNDER THERMO-MECHANICAL LOADING

The thermo-mechanical analysis of geothermal energy piles using CASM has been validated by comparing the numerical simulation results with the field pile load test data and the results of numerical simulations performed by Laloui et al. (2006). Laloui et al. (2006) performed thermal pile load tests in Lausanne, Switzerland for a duration of 28 days within which heating period consisted of 12 days followed by 16 days of cooling period. The thermal load was of the order of $\Delta T = 21^\circ\text{C}$. The axial load Q applied at the pile head was 1300 kN. The length and diameter of the pile were 26 m and 1 m, respectively. In the present study, the field pile load test performed by Laloui et al. (2006) has been simulated using the coupled temperature-displacement procedure in Abaqus and the CASM material model. Axisymmetric, thermo-mechanical finite element analysis has been performed. The elastic and thermal material properties for the concrete pile and the soil layers have been taken from Laloui et al. (2006). The soil stress-strain response is simulated using CASM material model. The model parameters were assumed same as that of Ottawa sand. Figure 2 shows the comparison of vertical stress generated in the pile due to thermo-mechanical loading when subjected to an axial load of 1300 kN and $\Delta T = 21^\circ\text{C}$.

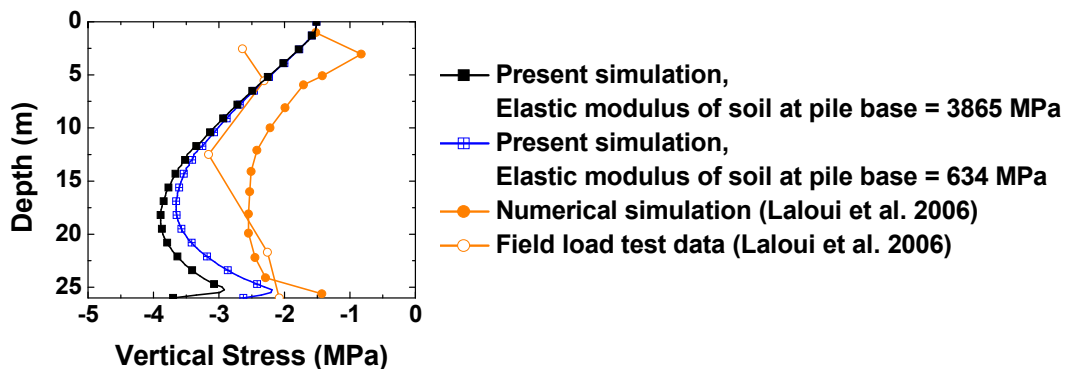


FIG. 2. Comparison of axial stress in pile at the end of heating obtained from simulation with field load test data from Laloui et al. (2006)

The present simulation results compare with the field pile load test data and the numerical simulation results given in the literature with reasonable accuracy. For the upper part of the pile, the axial stress along the pile depth follows the same trend as presented in Laloui et al. (2006). The difference in results may be attributed to the assumption of some parameters.

FINITE ELEMENT SIMULATION OF PILE GROUP

Three dimensional nonlinear finite element analyses of pile groups in Ottawa sand, with six piles in the group, have been carried out under thermo-mechanical loading using Abaqus in two steps- (i) a static step to apply the gravity loading and bring the model in geostatic equilibrium and (ii) a coupled temperature-displacement step to

apply the thermal and mechanical loads. Four sets of analyses have been carried out, e.g. (i) all six piles are geothermal, (ii) only the corner piles are geothermal, (iii) only the middle piles are geothermal and (iv) no piles are geothermal. For all analysis cases, two different pile spacing have been considered, e.g. (i) 4 m centre to centre and (ii) 2.5 m centre to centre. The mechanical axial load is applied on the pile cap instantaneously and maintained constant for the complete analysis run time. The temperature variation in pile, $\Delta T = 21^\circ\text{C}$ (Laloui et al. 2006) with 12 days of heating and 16 days of cooling is applied to the pile. The soil is initially at an ambient temperature of 15°C . The analyses have been performed for sand with relative density $D_R = 50\%$. The soil is modeled as Ottawa sand using CASM constitutive model. The coefficients of lateral earth pressure at rest (K_0) are assumed to be 1 in all analyses. An axial load, Q of 6000 kN is applied on the pile cap. For the pile group analyses, tensile axial stress and upward displacement are considered as positive; depth is considered positive in the downward direction from the ground surface.

ANALYSIS RESULTS AND DISCUSSIONS

Load-Displacement Response at Pile Base

Figures 3(a) through 3(d) show the load-displacement response at pile base at the end of heating of the pile, for one corner pile and one middle pile in all analyses. Here, it may be noted that the non-thermal piles exhibit displacement only under mechanical loading. It is observed from the figures that base displacement of the piles increase under mechanical load irrespective of thermal or non-thermal pile. Upon heating, the base displacement of thermal piles increases due to expansion of the piles in downward direction. The load carried by the thermal piles also increase due to heating induced excess load in the pile. For non-thermal piles however, unloading of the pile happens during heating of the thermal piles and base displacement decreases. It may be noted that the heating of thermal piles also cause expansion of these piles in upward direction, thus, the piles pushing the pile cap along with it in the upward direction. As a result, redistribution of axial load happens on the piles during heating and cooling - the load on non-thermal piles decreases whereas the load on thermal piles increases.

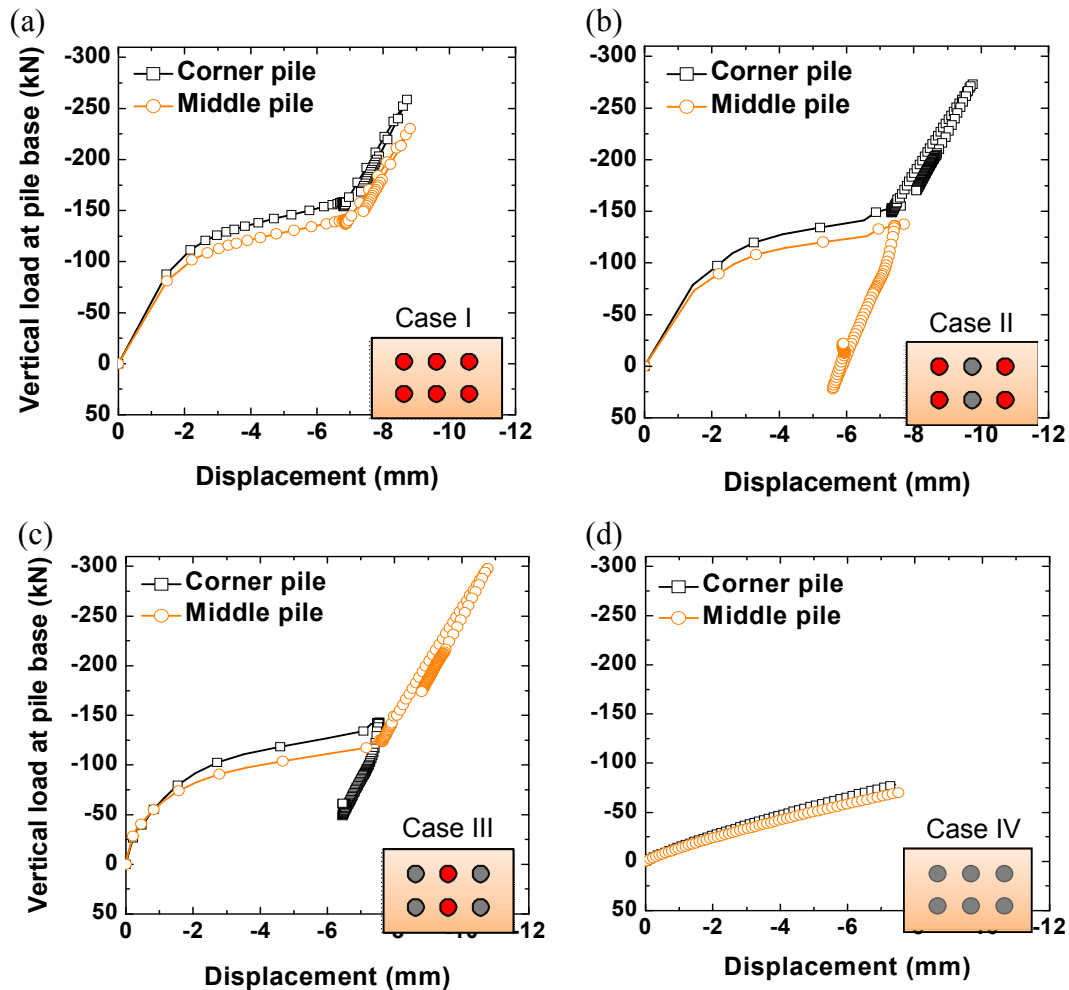
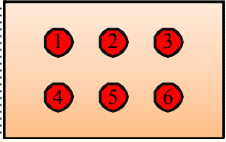
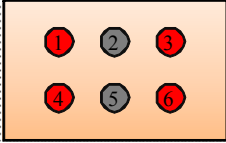
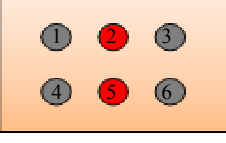
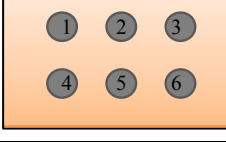


FIG. 3. Load-displacement response at pile base for piles with spacing 4 m center to center

Table 2 summarizes the base displacement of thermal and non-thermal piles for all analyses. The piles under thermal loading exhibit higher base displacement as compared to the non-thermal piles. In Case I, i.e. all piles are thermal and piles are at 4 m center to center spacing, the maximum pile base displacement is 8.81 mm. In the pile group where only mechanical load has been applied (Case IV) and at 4 m center to center spacing, the maximum pile base displacement is observed to be 7.5 mm. However, in Case II, where only corner piles are the thermal piles, maximum base displacement is 9.79 mm for the thermal piles. For non-thermal piles in the same group, the displacement reaches up to 7.72 mm and then decreases to 5.61 mm at the end of heating. In Case III, where only middle piles are thermal piles, the maximum displacement reaches 10.83 mm for the thermal piles. For non-thermal piles in the same group, the displacement reaches up to 7.67 mm and then decreases to 6.51 mm at the end of heating.

Table 2. Vertical Displacement at Pile Base for Different Thermal and Non-thermal Pile Combinations

Thermal Loading Cases	Pile no.	4 m spacing	2.5 m spacing
		Vertical Displacement (mm)	Vertical Displacement (mm)
Case I All piles thermal 	1	8.72	10.08
	2	8.81	10.19
	3	8.70	10.08
	4	8.73	10.08
	5	8.81	10.18
	6	8.70	10.08
Case II Corner piles 	1	9.74	11.02
	2	5.59 (7.71)	7.65 (8.67)
	3	9.77	11.02
	4	9.79	11.02
	5	5.61 (7.72)	7.64 (8.66)
	6	9.79	11.01
Case III Middle piles 	1	6.45 (7.64)	8.10 (8.62)
	2	10.81	11.64
	3	6.51 (7.67)	8.10 (8.62)
	4	6.50 (7.66)	8.09 (8.61)
	5	10.83	11.63
	6	6.45 (7.64)	8.09 (8.61)
Case IV Mechanical piles 	1	7.43	7.86
	2	7.50	7.91
	3	7.43	7.86
	4	7.43	7.87
	5	7.50	7.91
	6	7.43	7.86
Mechanical piles <i>Elastic Analysis and Equation</i>	Simulation Average	2.01	2.30
	Equation (4)	1.85	2.01

For the pile group with 2.5 m center to center pile spacing, higher base displacement is observed as compared to the group with piles at 4 m center to center spacing. Hence, for the design of geothermal energy pile groups, it is not recommended to use thermal and non-thermal piles in the same group. Two different pile groups, one for all thermal piles and the other for all non-thermal piles may be designed under different pile caps with different pile cap thicknesses in order for taking the differential settlement into consideration (Poulos 2001).

In order to compare the displacement of thermal piles with the analytical results, herein, the base displacement of thermal and non-thermal pile groups have been compared with the displacement values predicted by equation (4). For the purpose of

comparison, one set analysis of pile group under only mechanical loading has been carried out considering linear elastic stress-strain response for both soil and pile. Analyses have been performed for both 4 m and 2.5 m pile spacing under 6000 kN axial load on the pile cap. The modulus of elasticity and Poisson's ratio of soil have been considered same as that used in the analysis with CASM. Table 2 presents the pile base displacement results obtained using equation (4) and also through linear elastic finite element analyses. It is observed that for linear elastic analyses, the simulation results compare well with the displacement values calculated using the equation. However, the pile base displacement increases almost four times in elastoplastic analysis with piles subjected to only mechanical loading than that calculated using the equation (4). For thermal piles, a maximum of 47% increase in displacement is observed as compared to the piles under only mechanical load for the group with 2.5 m pile spacing. Thus, for thermal piles, nearly six times higher displacement may be expected as compared the displacement calculated using equation (4). Hence, it is recommended to use at least 4 m spacing between the thermal piles for the cases considered herein.

CONCLUSIONS

Thermo-mechanical response of geothermal energy pile groups with pile cap and different combination of thermal and non-thermal piles placed in a single layer of Ottawa sand has been investigated herein using three dimensional nonlinear finite element analysis procedure. Stress-strain response of piles and pile cap has been considered linear elastic. The stress-strain response of sand has been reproduced using a state parameter based constitutive model CASM. The base displacement of the piles in the group under combined thermo-mechanical loading have been studied for two different pile spacing.

It is concluded from the analysis results that pile base displacement increases under mechanical loading and further increases under thermal heating. However, displacement for non-thermal piles decreases during heating. The base displacement of piles increase by almost four times in elastoplastic analysis than that calculated using the analytical equation. For thermal piles, as much as 47% increase in displacement happens as compared to the piles under only mechanical load for 2.5 m pile spacing. Thus, for thermal piles, nearly six times higher displacement may be expected as compared to the displacement calculated using analytical equation. Hence, it is recommended to use at least 4 m spacing between the thermal piles in field for the cases considered herein.

REFERENCES

- Abaqus/Standard User's Manual, Version 6.11, 2011. Dassault Systèmes Simulia Corporation, Providence, Rhode Island, USA.
- Brandl, H. (2006). "Energy foundations and other thermo-active ground structures." *Géotechnique*, Vol. 56 (2): 81-122.
- Brettmann, T. and Amis, T. (2011). "Thermal conductivity evaluation of a pile group using geothermal energy piles." *Geo-Frontiers*, ASCE 2011: 499-508.
- Carraro, J. A. H. (2006). "Mechanical behavior of silty and clayey sands." *Ph.D. Dissertation*, Purdue University, USA.

- Dupray, F., Laloui, L. and Kazangba, A. (2014). "Numerical analysis of seasonal heat storage in an energy pile foundation." *Computers and Geotechnics*, Vol. 55: 67-77.
- Green, A. E. and Naghdi, P. M. (1992). "On undamped heat waves in an elastic solid." *Journal of Thermal Stresses*, Vol. 15: 253-264.
- Koene, F. and Geelen, C. (2000). "Energy piles as an efficient way to store heat." *CADDET Energy Efficiency*. Special issue on Netherlands 2000.
- Laloui, L., Nuth, M. and Vulliet, L. (2006). "Experimental and numerical investigations of the behavior of a heat exchanger pile." *International Journal for Numerical and Analytical Methods in Geomechanics*, Vol. 30: 763-781.
- Loukidis, D. (2006). "Advanced constitutive modeling of sands and applications to foundation engineering." *Ph.D. Dissertation*, Purdue University, USA.
- McCartney, S. J. (2011). "Engineering performance of energy foundations." *Pan-Am CGS Geotechnical Conference*, Toronto, Canada, October 2-6, 2011.
- Murthy, T. G., Loukidis, D., Carraro, J. A. H., Prezzi, M. and Salgado R. (2006). "Undrained monotonic response of clean and silty sands." *Géotechnique*, Vol. 57(3): 273-288.
- Mylonakis, G. and Gazetas, G. (1998). "Settlement and additional internal forces of grouped piles in layered soil." *Géotechnique*, Vol. 48(1): 55-72.
- Poulos, H. G. (2001). "Piled raft foundations: design and applications." *Géotechnique*, Vol. 51(2): 95-113.
- Randolph, M. F. and Wroth, C. P. (1978). "Analysis of vertical deformation of vertically loaded piles." *Journal of Geotechnical Engineering Division*, ASCE, 1978, Vol. 104(12): 1465-1488.
- Saggu, R. and Chakraborty, T. (2015). "Cyclic thermo-mechanical analysis of energy piles in sand." *Geotechnical and Geological Engineering*, Vol. 33: 321-342.
- Saggu, R. and Chakraborty, T. (2016). "Thermo-mechanical response of geothermal energy pile group in sand." *International Journal of Geomechanics*, doi:10.1061/(ASCE)GM.1943-5622.0000567.
- Salciarini, D., Ronchi, F., Cattoni, E. and Tamagnini, C. (2013). "Some remarks on the thermomechanical effects induced by energy piles operation in a small piled raft." *International Journal of Geomechanics*. doi:10.1061/(ASCE)GM.1943-5622.0000375.
- Salgado R. (2008). "Engineering of foundations." *Mc Graw-Hill*, New York, USA.
- Sanner, B., Mands, E. and Sauer, M. K. (2003). "Larger geothermal heat pump plants in the central region of Germany." *Geothermics*, Vol. 32: 589-602.
- Sasitharan, S., Robertson, P. K., Sego, D. C. and Morgenstern, N. R. (1994). "State-boundary surface for very loose sand and its practical implications." *Canadian Geotechnical Journal*, Vol. 31(3): 321-334.
- Tarnawski, V. R., Momose, T., Leong, W. H., Bovesecchi, G. and Coppa, P. (2009). "Thermal conductivity of standard sands. Part I. Dry state conditions." *International Journal of Thermophysics*, Vol. 30(3): 949-968.
- Yu, H. S. (2006). "Plasticity and Geotechnics." *Springer Publishers*, New York, USA.

Temperature-Induced Alterations of the Shaft and Base Resistances of a Model Geothermal Pile in Dry Sand

Amir Ahmadipur, S.M.ASCE¹; and Prasenjit Basu, A.M.ASCE²

¹Ph.D. Student, The Pennsylvania State Univ., University Park, PA 16802. E-mail: amir@psu.edu

²Assistant Professor, Indian Institute of Technology Bombay, Mumbai 400076, India. E-mail: pbasu@civil.iitb.ac.in

Abstract: Geotechnical performance of geothermal piles can be affected by the heating-cooling cycles that these piles are subjected to during their thermal operations. This paper investigates thermo-mechanical behavior of a model geothermal pile installed in dry sand through a series of instrumented load tests performed under laboratory controlled conditions. One U-shaped polyvinyl chloride (PVC) tube was embedded in the model concrete pile for circulating heat carrier fluid. The pile was instrumented with embedded strain gauges and thermocouples. Mechanical load tests were performed before and after imposing different thermal loadings (heating and cooling) on the pile. Pile shaft and base resistances are calculated using the strain measurements gathered during the pile load tests. Results from these experiments showed increase in both shaft and base resistances with increase in the average pile temperature. A 15% increase in the limit load was observed when the average pile temperature was increased by 31.6°C.

INTRODUCTION

Geothermal piles act as heat exchangers and can be used as an auxiliary mechanism to partially meet heating and cooling energy demand for residential and commercial buildings. Such foundations utilize nearly constant temperature that persists beyond a depth of couple of meters below the ground surface (Bouazza et al. 2011). During summer days, heat extracted from buildings is carried by fluid circulating through one or more closed loops embedded within geothermal piles and part of the extracted heat is eventually rejected to the ground; the reverse is true for winter days when heat is extracted from the ground. An important question to answer in this regard is whether pile temperature change caused by the thermal cycles affect the geotechnical performance of these piles. At present geothermal piles are mostly designed using conventional pile capacity calculation methods along with empirical rules that decide the length of the pile based on energy harvesting demand (Brandl 2006). This is because the potential effects of thermal cycles on geotechnical performance of geothermal piles are not yet fully understood. Full-scale instrumented load tests on geothermal piles revealed the generation of thermally-induced non-uniform thermo-

elastic stresses along the pile length (Laloui et al. 2006; Bourne-Webb et al. 2009; Amatya et al. 2012; McCartney and Murphy 2012; and Sutman et al. 2014). The existence of such additional stresses, magnitude and nature of which would intuitively depend on soil type and pile end conditions, can have non-negligible bearings on load carrying capacity of geothermal piles (Bourne-Webb et al. 2009; Knellwolf et al. 2011).

The effect of temperature change on the capacity of geothermal piles has been investigated by different researchers through analytical and numerical models (Knellwolf et al. 2011; Bourne-Webb et al. 2011; Mimouni and Laloui 2013; Suryatriyastuti et al. 2013; Suryatriyastuti and Mroueh 2014; Olgun et al. 2014; Saggi and Chakraborty 2015) and through physical model and field tests (McCartney and Rosenberg 2011; Wang et al. 2011; Wang et al. 2012; Kramer and Basu 2014; Goode et al. 2014; and Goode and McCartney 2015). McCartney and Rosenberg (2011) performed centrifuge tests on a model geothermal pile embedded in dry silt; about 40% increase in pile shaft resistance was reported as a result of increasing the pile temperature by 41 °C. Based on thermo-mechanical load tests on a model geothermal pile (the model pile was not instrumented with strain gauge) installed in dry Ottawa sand, Kramer and Basu (2014) reported about 5% increase in limit load due to 20 °C increase in the inlet fluid temperature. Goode et al. (2014) performed centrifuge tests on a geothermal pile embedded in dry sand and no change in pile shaft resistance due to increase in pile temperature was recorded. Laboratory experiments on a model steel pile embedded in unsaturated sand showed a 50% decrease in the shaft resistance as a result of increasing the pile temperature by 20 °C (Wang et al. 2011). Wang et al. (2012) conducted similar experiments in dry sand as well as in sand with moisture content of 2% and 4%. No significant change in the shaft resistance was recorded when pile temperature was raised from 20 °C to 60 °C. However, a reduction in the shaft resistance for the same pile temperature change was reported for the tests with higher moisture contents. This paper presents some results from a series of instrumented load tests, under laboratory-controlled conditions, on a model geothermal pile installed in dry sand. The primary objective of the study is to evaluate the effects of pile temperature change in altering shaft and base resistances.

MODEL PILE LOAD TEST SETUP

A large steel tank (1.83 m × 1.83 m × 2.13 m) was used to prepare the test bed of dry F50 Ottawa sand. Some physical, mechanical and thermal properties of the test sand are given in Table 1. In order to avoid the effect of laboratory air temperature fluctuations on the temperature of the soil bed, a layer of hard panel insulation (R Value = 13.1) was placed around the soil tank and a layer of soft rock-wool insulation (R Value = 50) was placed at the soil surface. A concrete pile with the diameter of 10 cm and the length of 1.39 m (of which 1.22 m was embedded in the test bed) was used as the model geothermal pile. The ratio of pile diameter to tank width is 1:18 and that of pile diameter to soil height under the pile base is 1:6. For nondisplacement piles, like the one used in this research, such boundary distances do not affect the mechanical performance of the pile (Kraft 1991; Schnaid and Houlsby 1991; Salgado 2008). One U-shaped polyvinyl (PVC) tube was embedded in the pile to circulate the

heat carrier fluid. The test bed was prepared (at a target relative density $D_R \approx 80\%$) using sand pluviation technique. Figure 1 shows the test setup and sand pluviation device used in this study. Sand pluviation calibrations for different target values of relative density were performed a priori. Such calibration is important in order to ensure uniformity in the test bed and to find required drop height and optimal combinations of sieves for a target value of relative density. The fluid inlet and outlet points of the model pile were connected to a temperature-controlled fluid circulation bath that maintained a constant temperature at the fluid inlet point.

Table 1. Some physical, mechanical and thermal properties of F50 Ottawa sand

Parameter	Value
Shape	Subangular
Mineral composition	> 99% Quartz
Mean Particle Size D_{50} (mm)	0.25
Coefficient of Uniformity, C_u	1.83
Coefficient of Curvature, C_c	0.95
Specific gravity, G_s	2.65
Minimum void ratio, e_{min}	0.48
Maximum void ratio, e_{max}	0.78
Critical state friction angle, ϕ_c	31.8°
Thermal conductivity in dry condition ($W \cdot m^{-1} \cdot K^{-1}$)	0.25



FIG. 1. Test setup and sand pluviation device

In order to quantify stress distribution along the pile and to segregate pile shaft and base resistances, 8 electrical resistance (ER) type strain gauges were embedded inside the pile. T-type thermocouple (hot junction) was placed just beside each strain gauge to measure local temperature. Additionally 16 thermocouples were attached to the pile surface at the same elevations as of the strain gauges. FIG. 2 shows the locations of the strain gauges and thermocouples placed within and on the surface of the pile. Moreover, thermocouples were placed at 98 different locations within the soil bed. Fluid temperature at the inlet and outlet points were measured using two resistance temperature detectors (RTDs) with the accuracy of $\pm 0.1 \times (0.3 + 0.005 |t|)$ °C. The pile head and base displacements were measured using two linear variable displacement transducers (LVDTs). In order to measure the base displacement, a tell-tale sheath assembly was utilized. A load cell was placed at the pile head in order to continuously capture the applied load on the pile during mechanical loading. FIG. 3 shows the load frame, data acquisition system and the instrumented model pile installed in the sand bed.

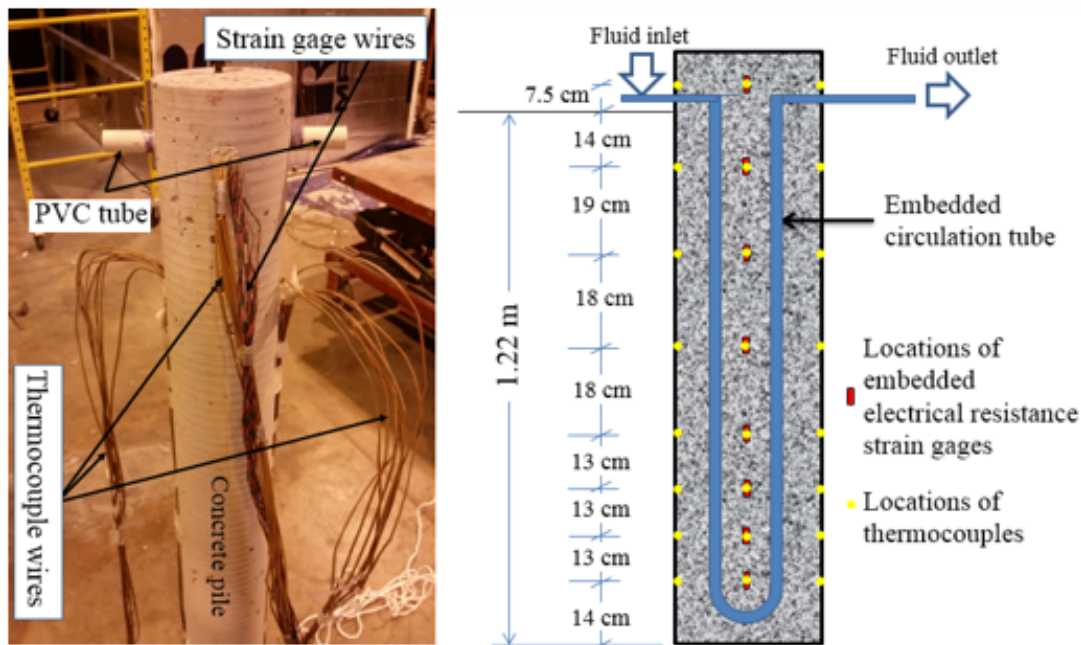


FIG. 2. Model geothermal pile and instrumentation (thermocouples and strain gauges) locations

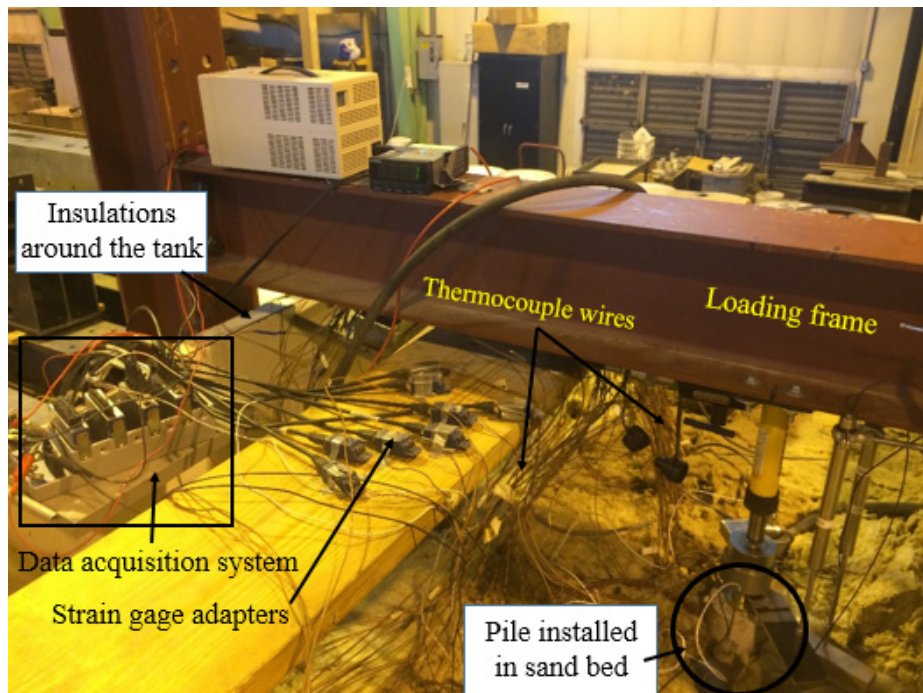


FIG. 3. Instrumented model geothermal pile installed in the sand bed

ER type strain gauges measure strain based on the change in the electrical resistance due to extension or shortening of the gauge length. Change in strain gauge temperature additionally alters the electrical resistance of the gauge material and, therefore, calculated strain includes an error, commonly known as *thermal output*. Thermal output must be compensated in order to get correct strain values in the presence of temperature fluctuations. Considering the difference between the coefficients of thermal expansion of the strain gauge and the substrate materials thermal output can be calculated as (Vishay 2014)

$$\varepsilon_{t/o} = \left[\beta_G + F_G \left(\frac{1 + K_t}{1 + K_t \nu_0} \right) (\alpha_s - \alpha_G) \right] \Delta T / F_G \quad (1)$$

where $\varepsilon_{t/o}$ = the thermal output; β_G = temperature coefficient of resistance of grid conductor which is equal to 0.005 ($^{\circ}\text{C}$) for the strain gauges used in this research; F_G = the gauge factor (= 2.11 for the used strain gauges); K_t = transverse sensitivity of strain gauge; ν_0 = Poisson's ratio of concrete (for the concrete used in this research ν_0 is measured to be equal to 0.12); $(\alpha_s - \alpha_G)$ = difference between coefficients of thermal expansion of concrete and strain gauge (this difference was measured to be equal to 7.3 ($^{\circ}\text{C}$)); and ΔT = temperature change at the strain gauge location. Equation 1 was used to calculate thermal output $\varepsilon_{t/o}$ and the calculated $\varepsilon_{t/o}$ values were subtracted from the strain gauge readings to obtain the corrected strain values.

RESULTS

For each test the initial average pile temperature was set to be approximately equal to 20 °C (this value was confirmed from thermocouple readings). For different tests, fluid temperature at the inlet point was kept constant at 2 °C, 40 °C, 50 °C, and 60 °C (tests TC1, TH1, TH2 and TH3, respectively) during the thermal loading stage. Thermal loading was stopped when the pile and the surrounding soil temperature nearly approached a stable temperature without significant changes (approximately around 4-6 days after the start of the thermal loading). Table 22 shows relevant details for the thermal loading stage for each test. Recorded temperature profiles along the pile length and average pile temperature at different elevations are plotted in Figure 4 for test TH3. As heat is rejected to the soil bed for Test TH3, pile surface temperature measured on the inlet side is always higher than that measured on the outlet side (maximum measured difference is $\approx 2.4^\circ\text{C}$). At depths of 50 cm and 112 cm, recorded pile surface temperature on the outlet side do not meet the theoretical expectations. This discrepancy may have been caused by detachment of thermocouple hot junctions from the pile surface at these two points.

Table 2. Details of different thermal loading tests

Test name	TC1	TH1	TH2	TH3
Fluid temp at inlet (T_{inlet})	2 °C	40 °C	50 °C	60 °C
Initial average pile temperature (T_{p0})	20.4 °C	20.4 °C	21.0 °C	20.1 °C
Initial average ground temperature (T_{g0})	21.1 °C	21.3 °C	20.8 °C	20.6 °C
Average pile temperature at stable condition (T_p)	6.4 °C	35.2 °C	43.3 °C	51.7 °C
Change in average pile temperature ($\Delta T_p = T_p - T_{p0}$)	-14.0 °C	14.8 °C	22.3 °C	31.6 °C

Mechanical pile load tests were performed immediately after the end of the thermal loading stages. Axial load was applied using a hydraulic jack and the load was recorded using the load cell placed at the pile head. During the pile load tests, the load was increased at a rate of 100 N/minute until a limit load (signified by continuing pile head settlement without any increase in axial load) was reached. Some mechanical load tests were repeated (under the same thermal condition) in order to ensure repeatability of test results. The load-displacement curves obtained from mechanical load tests performed immediately after thermal loading tests TC1, TH1, TH2 and TH3 and that performed under initial condition (i.e., prior to application of any thermal loading) are shown in FIG. 5. It is observed that for the cooling test (TC1) the limit load is almost the same as obtained from the mechanical load test performed under initial condition (i.e., at $T_p = T_{p0}$). However, limit load capacity of the model pile increased with increase in average pile temperature T_p . The maximum increase in limit capacity was recorded to be as much as 15% when T_p was raised by 31.6 °C. An increase in the pile head stiffness with increase in pile temperature was also evident.

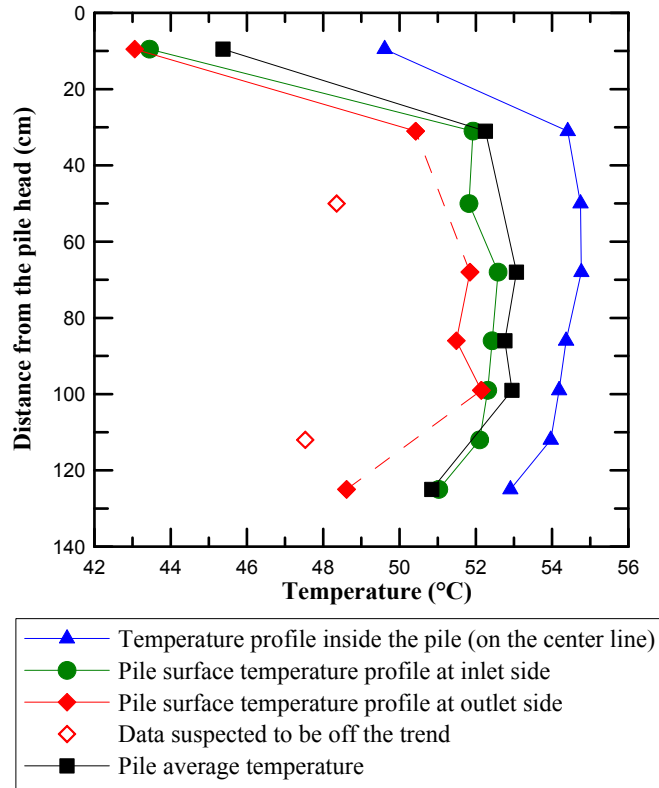


FIG. 4. Temperature profile along the model geothermal pile during Test TH3

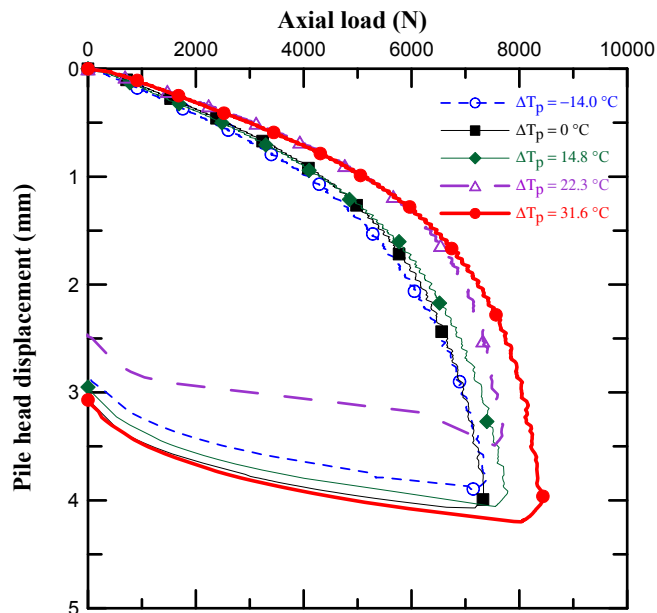


FIG. 5. Pile load-displacement curves obtained from mechanical load tests performed at different values of ΔT_p (i.e., after different thermal loading)

The increase in limit capacity at elevated temperature can be attributed to an increase in the base resistance, in the shaft resistance, or in both. It is thus important to distinguish the effects of temperature change in altering pile shaft and base resistances. Evolutions of shaft and base load (at different values of T_p) with pile head displacements are deduced using the strain gauge data recorded during the mechanical load tests. These evolutions are shown in FIG. 6. Both base and shaft resistances exhibit an increasing trend with increase in T_p . The maximum recorded increase in shaft and base resistances are about 16% and 10%, respectively. Several factors may contribute to such increase in shaft and base resistances. An expansion of the pile may have increased the lateral confinement at the pile-soil interface (Knellwolf et al. 2011; Wang et al. 2013; and Saggi and Chakraborty 2014) and possibly altered the shear stresses along the shaft. Additionally, relative pile-soil movements (in the vertical direction) during thermal loading might have helped mobilization of upward shear stresses along some part of the pile and part of the additional shaft capacity can be attributed to the additional shaft resistance mobilized purely due to thermal loading. Both of these mechanisms would be more prominent under field stress conditions, as previously observed in centrifuge tests reported by McCartney and Rosenberg (2011). Moreover, the additional effective stress generated at the pile base as the base pushes against the soil (just beneath the pile base) at elevated temperature may contribute towards an increase in pile base resistance at elevated temperature.

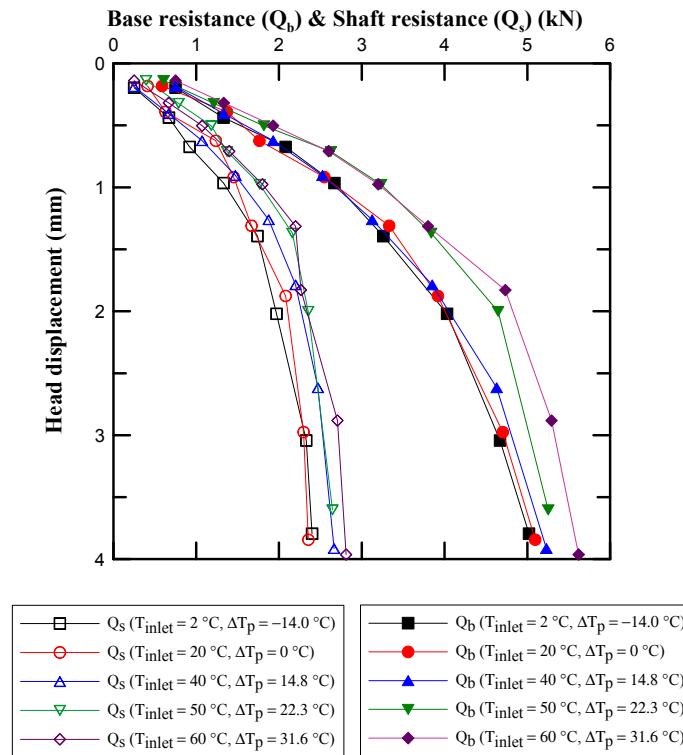


FIG. 6. Shaft and base resistance evolution during mechanical load tests performed at different average pile temperature

CONCLUSIONS

Results from a series of thermo-mechanical load tests on a model geothermal pile revealed that limit load increases with increase in average pile temperature. It was observed that both shaft and base resistances of the model pile increased due to temperature increase. Raising the pile temperature results in an increase in the lateral confinement and mobilization of additional shaft resistance; additional effective stress generated at the pile base at elevated temperature may have contributed towards the increase in base resistance. For a 31.6 °C increase in average pile temperature, the limit load was increased by about 15%. For this test, shaft and base resistance of the pile increased, respectively, around 16% and 10%. Further theoretical studies, aptly supported by field and laboratory test data, are warranted to identify the evolution of pile load transfer mechanism in the presence of thermal cycles.

REFERENCES

- Amatya, B. L. Soga, K. Bourne-Webb, P. J. Amis, T. and Laloui, L. (2012). "Thermo-mechanical behaviour of energy piles." *Géotechnique*, Vol. 62 (6): 503–519.
- Bouazza, A. Singh, R. M. Wang, B. Barry-Macaulay, D. Haberfield, C. Chapman, G. Baycan, S. Carden, Y. (2011). "Harnessing on site renewable energy through pile foundations." *Aust. Geomech*, Vol. 46 (4): 79–90.

- Bourne-Webb, P. J. Amatya, B. Soga, K. Amis, T. Davidson, C. and Payne, P. (2009). "Energy pile test at Lambeth College, London: geotechnical and thermodynamic aspects of pile response to heat cycles." *Géotechnique*, Vol. 59 (3): 237-248.
- Brandl, H. (2006) "Energy foundations and other thermo-active ground structures." *Géotechnique*, Vol. 56 (2): 81-122.
- Goode, J. C. III, Zhang, M. and McCartney, J. S. (2014). "Centrifuge modeling of energy foundations in sand." *Proc. 8th Int. Conf. on Physical Modelling in Geotechnics* (ICPMG 2014), Perth, Australia, CRC Press, Boca Raton, FL, 729–736
- Goode, J. C. McCartney, J. S. (2015). "Centrifuge Modeling of End-Restraint Effects in Energy Foundations." *Journal of Geotechnical and Geoenvironmental Engineering*, Vol. 141 (8): 04015034.
- Knellwolf, C. Peron, H. and Laloui, L. (2011). "Geotechnical analysis of heat exchanger piles." *Journal of Geotechnical and Geoenvironmental Engineering*, Vol. 137 (10): 890-902.
- Kraft, L. (1991), "Performance of axially loaded pipe piles in sand", *Journal of Geotechnical and Geoenvironmental Engineering*, Vol. 117 (2), pp. 272-296.
- Kramer, C. A. and Basu, P. (2014). "Performance of a model geothermal pile in sand." *Proc. 8th Int. Conf. on Physical Modelling in Geotechnics* (ICPMG 2014), Perth, Australia, CRC Press, Boca Raton, FL, 771–777.
- Laloui, L. Nuth, M. and Vulliet, L. (2006). "Experimental and numerical investigations of the behavior of a heat exchanger pile." *International Journal for Numerical and Analytical Methods in Geomechanics*, Vol. 30: 763–781.
- McCartney, J. S. and Murphy, K. D. (2012). "Strain distributions in full scale energy foundations." *DFI Journal*, Vol. 6 (2): 28–36.
- McCartney, J. S. and Rosenberg, J. E. (2011). "Impact of heat exchange on side shear in thermo-active foundations." *ASCE Geo-Frontiers*, 488–498.
- Mimouni, T. Laloui, L. (2013). "Thermo-pile: a numerical tool for the design of energy piles." *Energy Geostructures: Innovations in underground engineering*, Laloui, L. Di Donna, A. (eds), Wiley-ISTE, 265–278.
- Olgun, C. G. Ozudogru, T. and Arson, C. F. (2014). "Thermo-mechanical radial expansion of heat exchanger piles and possible effects on contact pressures at pile-soil interface." *Géotechnique. Letters* Vol. 4: 170–178.
- Salgado, R. (2008). *The Engineering of Foundations*. McGraw-Hill.
- Saggu, R. and Chakraborty, T. 2014. "Thermal analysis of energy piles in sand." *Geomechanics and Geoengineering: An International Journal*, Vol. 10 (1), 10-29. [doi: 10.1080/17486025.2014.923586].
- Saggu, R. and Chakraborty, T. (2015). "Cyclic Thermo-Mechanical Analysis of Energy Piles in Sand." *Geotechnical and Geological Engineering* Vol. 33: 321–342.
- Schnaid, F. and Houlsby, G. T. (1991). "An assessment of chamber size effects in the calibration of in situ tests in sand," *Geotechnique*, Vol. 41 (3): 437–445.
- Suryatriyastuti, M. E. Mroueh, H. and Burlon, S. (2013). "Numerical analysis of the bearing capacity of thermoactive piles under cyclic axial loading." *Chapter 7, Energy geostructures*, L. Laloui and A. DiDonna, eds. Wiley, London.

- Suryatriyastuti, M. E. Mroueh, H. and Burlon, S. (2014). "A load transfer approach for studying the cyclic behavior of thermo-active piles." *Computers and Geotechnics*, Vol. 55: 378–391.
- Sutman, M. Brettmann, T. and Olgun, C. G. (2014). "Thermo-mechanical behavior of energy piles: Full-scale field test verification." *DFI 39th Annual Conf. on Deep Foundations*, DFI, Hawthorne, NJ, 1–11.
- Vishay Precision Group. (2014). "Strain gage thermal output and gage factor variation with temperature." *Technical note TN-504-1. Micro Measurements, Inc.* Wendell, North Carolina.
- Wang, B. Bouazza, A. and Haberfield, C. (2011). "Preliminary observations from laboratory scale model geothermal pile subjected to thermo-mechanical loading." *ASCE Geo-Frontiers*, 430–439.
- Wang, B. Bouazza, A. Barry, D. M. Singh, R. M. Webster, M. Haberfield, C. Chapman, G. and Baycan, S. (2012). "Field and laboratory investigation of a heat exchanger pile." *ASCE Geo-Congress*, 4396–4405.
- Wang, B. Bouazza, A. Singh, R. M. Barry, D. M. Haberfield, C. Chapman, G. and Baycan, S. (2013). Field investigation of geothermal energy pile: Initial observations. *Proceedings of the 18th International Conference on Soil Mechanics and Geotechnical Engineering*, Paris 2013, 3415-3418

The Average Temperature of Energy Piles

Fleur A. Loveridge¹ and William Powrie²

¹Royal Academy of Engineering Research Fellow and Lecturer in Geomechanics, Univ. of Southampton, Southampton SO17 1BJ, U.K.

²Professor of Geotechnical Engineering and Dean of the Faculty of Engineering and the Environment, Univ. of Southampton, Southampton SO17 1BJ, U.K.

Abstract: The geotechnical design of energy piles requires confirmation that the foundations can continue to carry safely the required load from the overlying structure and that no detrimental effects from the additional imposed temperature changes will occur. These additional design checks require assumptions to be made about the temperature changes within the pile. However, there is no universal approach for determining these, and routine application of over-conservative pile temperatures can lead to unrealistically adverse geotechnical design scenarios. This paper considers how the average temperature of a pile can be determined based on the analysis steps already carried out for the thermal design. The aim is to be able use the calculated fluid temperatures, along with readily available pile and ground parameters, to provide better assessments of the actual pile temperature so that the outputs of the geotechnical design can be improved. Two dimensional numerical simulations are used to determine the average pile temperature for different pipe, pile and concrete properties. The results of the simulations are compared with analytical approaches, allowing these to be validated for use on a routine basis. It is shown that the temperature of the center of the pile, which can be determined easily by analytical methods, can be used as a proxy for the average pile temperature.

INTRODUCTION

Energy piles, where foundation piles are equipped with heat transfer pipes to allow them to become part of a shallow ground energy system, are a technology of increasing interest owing to their carbon and energy savings benefits. The geotechnical design of energy piles requires confirmation that the foundations can carry safely the required load from the overlying structure and that no detrimental effects from the additional imposed temperature changes will occur (GSHPA, 2012). These additional design checks may be carried out by adapted load transfer methods, by numerical simulation or by design charts (e.g Knellwolf et al, 2011, McCartney & Rosenberg, 2011, Laloui et al, 2006, Bodas-Freitas et al, 2013). With the exception of full numerical simulation, which is computationally very expensive, most of these approaches require simplifying assumptions to be made about the heat transfer rate or

temperature boundary conditions related to the pile. Load transfer methods tend to assume a homogeneous pile temperature change so it is important to be able to make an appropriate assumption regarding this value, which would be equivalent to the average pile temperature. However, current thermal design methods focus on delivery of the temperature of the heat transfer fluid as it enters and leaves the heat pump. This will always cover a greater range than the pile temperatures. Hence if extreme fluid temperatures are used to define the thermal load cases, an over-conservative design may result. Better means of determining the average temperature of the pile as part of the thermal design process are required.

The aim of this paper is to be able use the calculated fluid temperatures, along with readily available pile and ground parameters, to provide better assessments of the actual pile temperatures so that the outputs of the geotechnical design can be improved. Consequently, this paper considers how the average temperature of a pile can be determined based on the analysis steps already carried out for the thermal design. The average temperature is chosen as the most suitable parameter for use in predictions of expansion and contraction of the pile during heating and cooling. Two dimensional numerical simulations are used to determine the average pile temperature for different combinations of pipe, pile and concrete properties. The results of the simulations are compared with analytical approaches, allowing these to be validated for use on a routine basis.

THERMAL DESIGN

The thermal design of energy piles uses a variety of analytical solutions to calculate the temperatures of the heat transfer fluid entering and leaving the heat pumps (for example Eskilson, 1987, Hellstrom, 1989, Claesson & Hellstrom, 2011). These are typically determined by superposition of the temperature changes in the ground, across the pile concrete and between the fluid and the edge of the heat transfer pipes embedded in the concrete:

$$\Delta T_f = \Delta T_{ground} + \Delta T_{concrete} + \Delta T_{pipe} \quad (1)$$

The ground temperature change is normally calculated using a transient temperature response function (G_g) evaluated at a radial coordinate $r=r_b$, where r_b is the pile radius.

$$\Delta T_{ground} = \frac{q}{2\pi\lambda_g} G_g(t, r) \quad (2)$$

where λ_g is the thermal conductivity of the ground in W/mK, q is the applied thermal power in W/m and t is the elapsed time in seconds.

Traditionally $\Delta T_{concrete}$ and ΔT_{pipe} are calculated using thermal resistances and assuming a thermal steady state (Eq. 3 & 4). However, for large diameter energy piles a transient approach to the temperature change in the pile is preferable (Eq. 5).

$$\Delta T_{concrete} = T_p - T_b = qR_c \quad (3)$$

$$\Delta T_{pipe} = T_f - T_p = qR_p \quad (4)$$

$$\Delta T_{concrete} = T_b - T_p = qR_c G_c(t) \quad (5)$$

where R is a thermal resistance in mK/W and G_c is a transient response function. T_b and T_p are the temperatures at the pile edge and pipe edge respectively (see Figure 1).

In the following sections of the paper the thermal resistance values, which are standard input parameters for the design, will be used to determine an approximation for the average value of the pile temperature based on the fluid temperature which is a routine thermal design output.

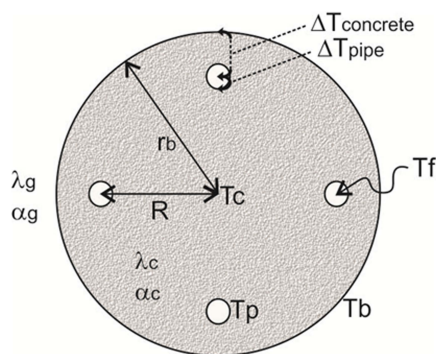


FIG. 1. Typical arrangement of an energy pile showing four pipes.

AVERAGE PILE TEMPERATURE BY ANALYTICAL SOLUTIONS

It is proposed that to determine the thermal design cases for the geotechnical analysis, the extreme fluid temperatures calculated from the thermal design may be used as a starting point for simple calculations to determine the extreme average pile temperatures.

Approach

It is hypothesized that the temperature of the center of the pile could be used as a proxy for the average temperature of the pile. This hypothesis will be tested subsequently by numerical simulation.

Equation 6 gives the change in temperature at the pile center (ΔT_c), after Bozis et al (2011). This assumes that the heat flux to each pipe, q_i , is an equal proportion of the total flux q , such that $q = q_i n_p$, where n_p is the total number of pipes.

$$\Delta T_c = \frac{q}{4\pi\lambda_c} Ei \left(\frac{R^2}{4\alpha_c t} \right) \quad (6)$$

where R is the injection radius, i.e. the distance of the heat transfer pipes from the center of the pile (Figure 1), and the subscript “c” indicates properties of the pile concrete. Ei is the exponential integral. The heating power, q , is variable over the lifetime of a pile, so it is time consuming to calculate the ΔT_c over the full design time sequence. It is instead desirable to determine the value at the extreme conditions only. To investigate how this might be done, the value of the pile center temperature is compared with the temperature values at the pile and pipe edge (T_b and T_p on Figure 1, respectively). For this comparison, the values for the pile edge temperature are determined using a line source approach (Eq. 7). To avoid limiting the time frame for which the results are valid, the full implementation of the exponential integral was used rather than the common log linear simplification.

$$\Delta T_b = \frac{q}{4\pi\lambda_g} Ei \left(\frac{r_b^2}{4\alpha_g t} \right) \quad (7)$$

The results from Eq. 7 were then input into Eq. 3 to determine the pipe temperature, additionally applying values of thermal resistance determined according to the methods of Loveridge & Powrie (2014) or Claesson & Hellstrom (2011). As Eq.6 is based on the thermal properties of the pile and Eq. 7 is based on the thermal properties of the ground, for the two approaches to be directly comparable it must be assumed initially that the pile and the ground have the same properties. The effect of different pile and ground properties will be tested subsequently by numerical analysis.

Results

Figure 2 shows example results of the calculation for the case of a 600 mm diameter pile with two 30 mm diameter pipes installed 75 mm from the pile edge. For ease of interpretation and general applicability of the results the calculations are presented using normalized temperatures and time:

$$\Phi = \frac{2\pi\lambda_g}{q} \Delta T \quad (8)$$

$$FO = \frac{\alpha_g t}{r_b^2} \quad (9)$$

The results assume a constant applied thermal power and so evolve to show a log-linear relationship after a period of time has elapsed. The temperature at the pipe edge starts at a non-zero value which is a reflection of the steady state resistance value used in Eq. 3. Consequently, the values at later times in Figure 2 should be considered when the whole pile is approaching steady conditions. In these circumstances, and for this specific example, the center pile temperature is approximately a quarter of the way between the pile edge temperature and the pipe temperature.

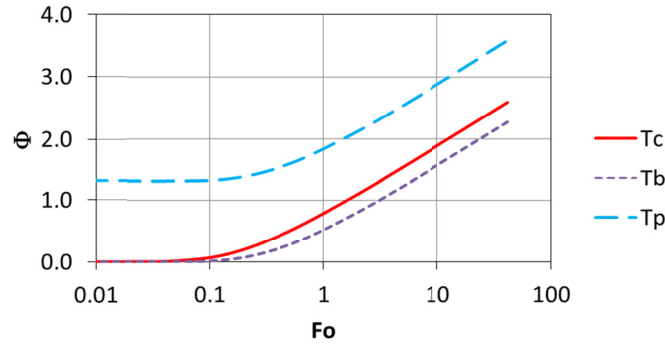


FIG. 2. Example temperature evolution from analytical calculation for 600 mm diameter energy pile with two 30 mm diameter pipes installed at 75 mm offset from the pile edge.

A parametric study was completed to investigate a range of pile sizes and pipe numbers, keeping the pipe size and offset from the pile edge constant (Figure 3) and maintaining evenly spaced pipe arrangements. In all cases the center pile temperature was between that of the pile edge and the pipe edges. In relative terms, the bigger the pile and the fewer the number of pipes, the closer the center pile temperature is to pile edge temperature. This corresponds to the case of the largest pile resistance where there is the biggest temperature difference between the pipe edge and the pile edge.

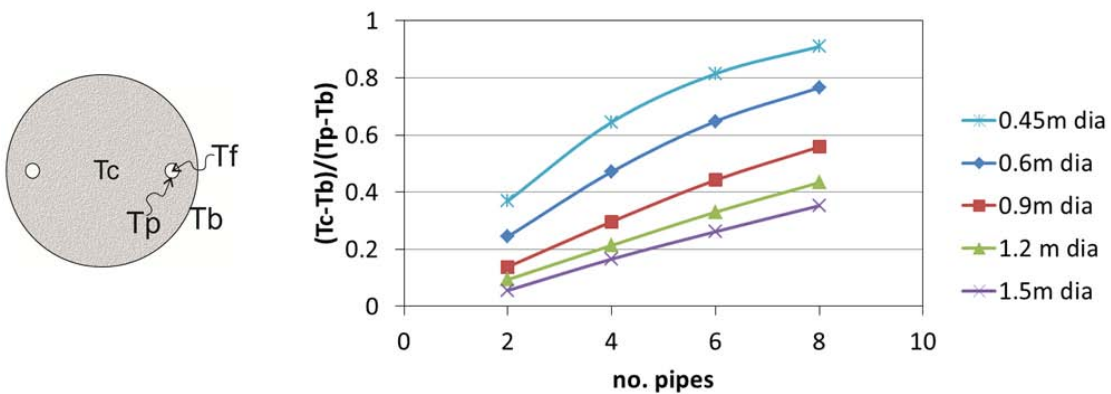


FIG. 3. Relative value of the center pile temperature for different pile sizes and numbers of pipes installed (assuming 30 mm diameter pipes installed at 75 mm offset from the pile edge).

Design Charts

The results of the parametric study are summarized in Figure 3. Such charts could be used to determine the center pile temperature based on the thermal design output, i.e. the fluid temperature. With the extreme fluid temperature values known, Eq. 3 and Eq. 4 can be used to determine T_p and T_b , from which T_c can be estimated from Figure 3. The only other input parameters are the pipe and pile concrete resistances (R_p and R_c), which should already have been estimated (from the geometry and design thermal

properties) as input parameters to the thermal design, or can be determined according to the approaches of Loveridge & Powrie (2014) or Claesson & Hellstrom (2011).

NUMERICAL VALIDATION

The proposed approach set out above relies on a few important assumptions:

1. That the pile center temperature is a good proxy for the average pile temperature.
2. That the ground and pile thermal properties are equal.
3. That the pile is at a thermal steady state.

The first point is expected to be a reasonable assumption and will be tested in this section of the paper. However, it is known that both the relative pile and ground properties and the tendency of large diameter piles to not attain a steady state (especially at peak thermal load) will affect their short term thermal behavior. How this impacts on the average pile temperature is now the subject of investigation.

Model Details

For this initial investigation a two dimensional numerical model was built in COMSOL, as described in Loveridge & Powrie (2014). The model comprised a slice through the pile and surrounding ground. The pipes were not explicitly modelled and the pipe edge temperature and temperatures within the full domain are determined following application of a constant heat flux applied at the position of the pipe outer edge. Boundary conditions within the ground were sufficiently far away so as to not influence the simulation results. The simulation duration was 45 days, since 2D simulations are only appropriate for short time periods.

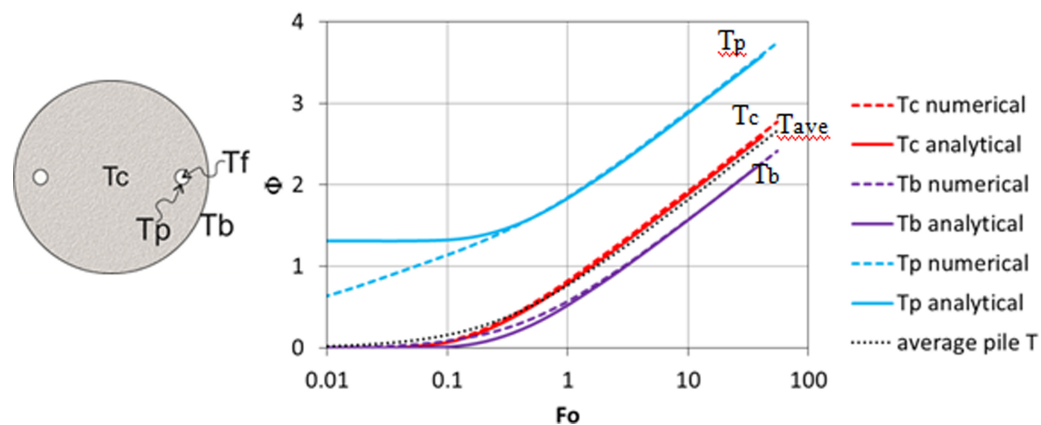


FIG. 4. Temperature evolution from numerical simulation (dashed lines) and analytical calculation (solid lines) for a 600 mm diameter energy pile with two 30 mm diameter pipes installed at 75 mm offset from the pile edge.

Figure 4 shows the model and analytical results for the case of a 600 mm piles with 30 mm pipes installed 75 mm from the pile edge, assuming that the ground and concrete thermal properties are the same. For the numerical model the average temperature at the pipe (T_p) and pile edges (T_b) are used for comparison. The results show good consistency between the two approaches and also that the average temperature of the pile (T_{ave}) is just below the temperature of the pile center (T_c). The difference is approximately 4%. Additionally, as the analysis was carried out for heat injection, and the center pile temperature is higher than the average pile temperature, this result is conservative. This suggests that the pile center temperature could make a good proxy for the average pile temperature.

Impact of Differing Ground and Concrete Properties

The model was then used to investigate the effect of the soil and ground thermal properties for two different pipe arrangements. When the conductivity of the ground becomes less than that of the pile concrete temperature changes are reduced. This means that all the pile edge, pile average and pipe edge temperatures bunch together. Conversely, when the pile concrete is less conductive than the ground, the temperature changes increase and spread out. The effect of these changes on the pile center and average temperature are summarized in Tables 1 and 2.

Table 1. Difference in Relative Value of Pile Center Temperature between Analytical and Numerical Approaches

Pile Arrangement	$(T_c - T_b) / (T_p - T_b)$			
	Analytical $\lambda_c = \lambda_g$	Numerical $\lambda_c = \lambda_g$	Numerical $\lambda_c = 2\lambda_g$	Numerical $2\lambda_c = \lambda_g$
600mm pile, 2 pipes	0.22	0.27	0.27	0.28
600mm pile, 8 pipes	0.77	0.86	0.86	0.86

Table 2. Average Pile Temperature as Percentage of Pile Center Temperature

Pile Arrangement	Analytical $\lambda_c = \lambda_g$	Numerical $\lambda_c = \lambda_g$	Numerical $\lambda_c = 2\lambda_g$	Numerical $2\lambda_c = \lambda_g$
600mm pile, 2 pipes	-	96%	98%	93%
600mm pile, 8 pipes	-	96%	97%	93%

It can be seen that for the numerical analyses, the calculated value of the pile center temperature is always slightly greater than for the analytical approach. However, no significant difference is apparent for the cases with different ground to pile conductivity ratios. In all cases the pile average temperature remained within 7% of the pile center temperature. As the pile center is higher than the average temperature in heat injection, again this indicates the results to be conservative with respect to

geotechnical design. Therefore these initial findings suggest that the analytically determined pile center temperature would be both appropriate and safe if used to determine the thermal design cases for the geotechnical pile analysis.

Impact of Transient Thermal Load

The above analyses all assume that the pile is at a thermal steady state, which may not be the case in reality (Loveridge & Powrie, 2013). To investigate the impact of a time varying thermal load on the average pile temperature, the constant applied heat flux in the COMSOL model was replaced with one that was “on” for 12 hours a day and “off” for 12 hours a day. When the applied heat flux was “on” it was set at twice the value as previously so that the overall average thermal load was the same as in previous simulations.

The results of the transient thermal load simulation are shown in Figure 5. The analysis assumes a 600 mm diameter pile with two 30 mm diameter pipes installed at 75 mm offset from the pile edge with equal ground and concrete thermal properties. At peak loads there is large separation between the pile edge and the pipe temperatures. However, this reduces substantially during the “off” periods when there is no applied thermal load. Steady state conditions do not appear to occur within the pile concrete since $\Delta T_{concrete} = T_p - T_b$ is not constant. Of relevance for this study is the fact that the pile center temperature remains an acceptable proxy for the average pile temperature. However, what needs to be investigated is whether use of the center temperature calculated from steady state resistances will still give a useful indicator of the average pile temperature.

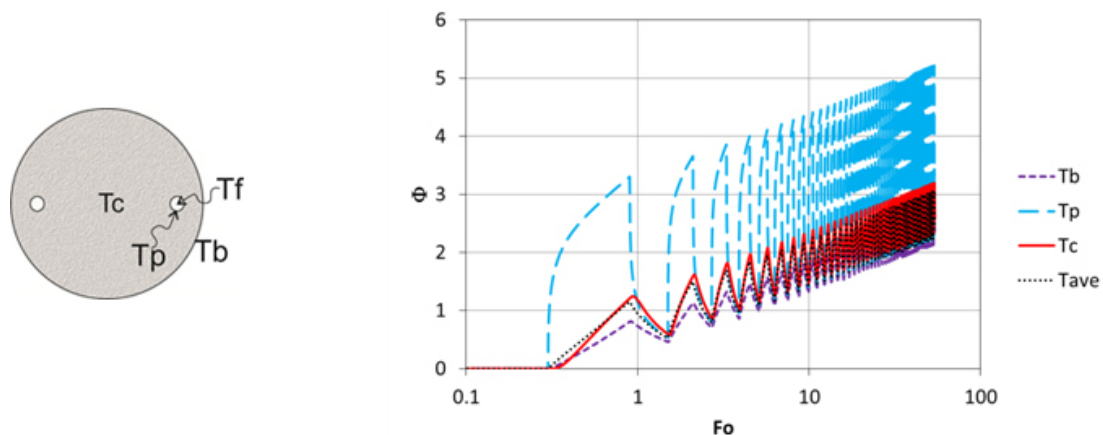


FIG. 5. Temperature evolution during transient thermal load for a 600 mm diameter energy pile with two 30 mm diameter pipes installed at 75 mm offset from the pile edge.

To assess this, the center of pile temperature has been calculated based on the maximum pipe edge temperature from the numerical simulation in Figure 5 and the results compared with the simulated value for the average pile temperature. The steps in the calculation are as follows, with results given in Table 3 below:

1. Read off simulated maximum normalized pipe edge temperature, Φ_{p-max}
2. By application of Eq. 3 and Eq. 8, determine the calculated maximum pile edge temperature $\Phi_{b-max} = \Phi_{p-max} - 2\pi\lambda_g R_c$
3. For the calculated Φ_{b-max} , determine Φ_{c-max} by reading off the design chart in Figure 3.
4. Compare the results with the simulated values of Φ_{c-max} and $\Phi_{ave-max}$.

Table 3. Calculated and Simulated Pile Temperatures under Transient Thermal Load (assuming $q=50$ W/m, $\lambda_g=2$ W/mK, $R_c=0.104$ W/mK)

Normalized Pile Temperatures	Simulated Value (Transient)	Calculated Value (Steady State)
Φ_{p-max}	5.22	
Φ_{b-max}	2.67	3.91
Φ_{c-max}	3.36	4.26
$\Phi_{ave-max}$	3.06	

Table 3 shows how the calculations assuming a steady state resistance overestimate the average temperature of the pile. The calculated normalized pile center temperature is 4.26 and which is approximately 25% more than the simulated pile center temperature and 40% more than the simulated average pile temperature. Nonetheless the calculated values remain both conservative and critically less than the simulated pipe temperature. As such, even in transient conditions, the steady state calculation of the pile center temperature, as a proxy for the average temperature, represents an improvement on simply applying the fluid or pipe edge temperatures as an input for the geotechnical design.

FURTHER WORK

This initial study has focused on numerical simulation of only a small number of pile cases. To increase confidence in the results a greater range of pile geometries need to be assessed such that the design chart presented in Figure 3 can be improved. Additionally, it is clear that the approach can be further developed to better account for transient conditions. This will be especially important for larger diameter energy piles. Validation using 3D simulation that accounts for the non-uniform heat flux distribution between the different pipes would also be beneficial.

CONCLUSIONS

To assess the thermo-mechanical effect of heating and cooling on energy piles it is necessary to make assumptions regarding the temperature changes that will occur within the pile. It is simple to use the extreme values of the fluid temperature for this purpose but the approach is conservative as a temperature gradient exists across the piles and the bounds to the average pile temperature will be reduced compared with the fluid temperature. This paper presents a simple approach to estimate the

temperature at the center of the pile which has been shown to be a good proxy for the average pile temperature. Using the thermal resistances, which are a necessary design input parameter for the thermal design, along with the predicted fluid temperature, which is an output of that process, it is possible to calculate the pile edge and pipe edge temperatures. Using design charts these values can be converted to a value for the center pile temperature. The proposed approach has been tested against numerical simulation and shown to be appropriate for steady conditions. Under transient thermal loads the approach may be conservative for large diameter piles, but less conservative than simply adopting the fluid temperature values instead.

ACKNOWLEDGMENTS

The authors acknowledge funding from the Royal Academy of Engineering under their Research Fellowship scheme.

REFERENCES

- Bodas Freitas T.M., Cruz Silva F. and Bourne-Webb P.J. (2013). The response of energy foundations under thermo-mechanical loading. In *Proceedings 18th Intl. Conf. on Soil Mech. & Geot. Eng., Paris*, Intl. Society for Soil Mechanics & Geotechnical Engineering.
- Bozis D., Papakostas N. and Kyriakis, N. (2011). On the evaluation of design parameters effects on the heat transfer efficiency of energy piles, *Energy and Buildings*, 43, 1020 – 1029.
- Claesson J. and Hellström G. (2011). Multipole method to calculate borehole thermal resistances in a borehole heat exchanger. *HVAC & R Research*, 17(6), 895-911.
- Eskilson P. (1987). *Thermal analysis of heat extraction boreholes*. Doctoral Thesis, Department of Mathematical Physics, University of Lund, Sweden.
- GSHPA (2012). *Thermal pile design installation and materials standards*, Issue 1.0. Ground Source Heat Pump Association, Milton Keynes, UK, p. 85.
- Hellstrom G. (1989). *Duct Ground Heat Storage Model, Manual for Computer Code*. Department of Mathematical Physics, University of Lund, Sweden.
- Knellwolf C., Peron H. and Laloui L. (2011). Geotechnical analysis of heat exchanger piles. *J. Geotechnical & Geoenvironmental Engineering*, 137(10), 890-902.
- Laloui L., Nuth M. and Vulliet L. (2006). Experimental and numerical investigations of the behaviour of a heat exchanger pile. *Intl. J. Num. & Anal. Meth. Geom.*, 30(8), 763-781.
- Loveridge, F. and Powrie, W. (2014). On the thermal resistance of pile heat exchangers, *Geothermics*, 50, 122 – 135.
- Loveridge, F. and Powrie, W. (2013). Performance of Piled Foundations Used as Heat Exchangers, In *Proceedings 18th Intl. Conf. on Soil Mech. & Geot. Eng., Paris*, Intl. Society for Soil Mechanics & Geotechnical Engineering.
- McCartney J.S. and Rosenberg J.E. (2011). Impact of heat exchange on the axial capacity of thermo-active foundations. In *Proceedings Geo-Frontiers: Advances in Geotechnical Engineering*, GSP 211, ASCE, pp. 488-498.

Thermally-Induced Pore Pressure Fluctuations around a Geothermal Pile in Sand

Omid Ghasemi-Fare, A.M.ASCE¹; and Prasenjit Basu, A.M.ASCE²

¹Assistant Professor, Univ. of Louisville, 132 Eastern Pkwy, Louisville, KY 40292. E-mail: omid.ghasemifare@louisville.edu

²Assistant Professor, Indian Institute of Technology Bombay, Mumbai, 400076 India. E-mail: pbasu@civil.iitb.ac.in

Abstract: Heat conduction is commonly considered as the major heat transfer mechanism within the ground surrounding geothermal piles. However, temperature gradient induced by thermal operation of heat exchanger piles alters in situ spatial distribution of pore fluid density. Consequently, buoyant flow can occur, even under hydrostatic condition, in the vicinity of heat exchanger piles installed in saturated soils. Controlled laboratory-scale model tests were performed to investigate thermal operation of a model geothermal pile installed in dry and saturated sand. The test bed was instrumented using several thermocouples and pore water pressure sensors. Comparison of thermal tests under dry and saturated conditions reveals that convective heat transfer plays a definite role in heat exchange through geothermal piles. Results obtained from the model tests also indicated an increase in excess pore pressure within a zone adjacent to the pile during a heating phase (i.e., heat rejection to the ground).

INTRODUCTION

Ground temperature below a certain depth, usually couple of meters depending on the region, remains nearly constant throughout the year. Such thermal potential can be used as an auxiliary heat source (or sink) for residential or commercial buildings. Since the ground temperature is more stable than air temperature, ground source heat pump (GSHP) systems show higher coefficient of performance compared to other conventional systems like air source heat pump (ASHP). Geothermal piles, also known as heat exchanger piles, are widely being used around the world as part of GSHP systems to harvest geothermal energy from the ground. Thermal conductivity of soil surrounding the geothermal piles has a crucial role in determining the nature and amount of heat transfer to and from the ground. Dry soil has a much lower thermal conductivity compared to that of the same soil at saturated condition. The value of thermal conductivity increases with increase in soil water content; for fine-grained soils it usually ranges between 0.3 and 2.1 $\text{Wm}^{-1}\text{K}^{-1}$, respectively, for dry and saturated conditions, and the range is around 0.9–4.2 $\text{Wm}^{-1}\text{K}^{-1}$ for coarse-grained soils (Brandl 2006, Tarnawski et al. 2011).

Temperature in the ground surrounding geothermal piles increases as a result of heat rejection to the ground. This increment alters in situ spatial distribution of pore water density and such temperature-induced changes in pore water density result in pore water

pressure variations (Ghasemi-Fare and Basu 2015). Apart from this, the heat rejected to the media can be absorbed by the moisture present in the soil surrounding geothermal piles and the absorbed heat energy facilitates drying of the surrounding media.

Several published research focused on heat transfer mechanism and efficiency of geothermal piles (Jalaluddin et al. 2011, Ghasemi-Fare and Basu 2013, Kramer et al. 2014, Ozudogru et al. 2014, Li and Lai 2015, Leroy and Bernier 2015, Ghasemi-Fare and Basu 2016, to name a few). Although there are some studies which investigated the natural convection flow (Kaviany 1986, Hossain and Wilson 2002, and Hossain et al. 2013), potential variation of pore water pressure in soil surrounding geothermal piles has not been explored so far. Nevertheless, a few studies explored variations in soil moisture content before and after thermal loading. Low et al. (2013) reported reduction in soil moisture content after thermal loading during laboratory tests to measure soil thermal conductivity using a thermal needle probe. Krishnaiah and Singh (2003, 2004) also reported reduction in normalized water content during thermal loading.

This paper presents some data gathered during instrumented laboratory thermal tests on a model geothermal pile installed in dry and saturated sand. Temperature increments (after four days of heat injection) recorded at same locations for dry and saturated soil are compared. The variations of pore water pressure at different depths and radial distances from the model geothermal pile were also monitored during the test in saturated sand.

EXPERIMENTAL SETUP

A 1.38-m-long concrete pile with a diameter of 0.1 m and embedment depth of 1.22 m was installed in a large soil tank (1.83 m \times 1.83 m \times 2.13 m). One U-shaped PVC circulation tube, with inner and outer diameters equal to 12.4 and 15.8 mm, respectively, was embedded within the model pile. Preliminary heat transfer analysis indicated that thermal tests may be performed at least for 7 and 4 days, respectively, for dry and saturated conditions, before the thermal boundary conditions start to have a bearing on the test results. Sand raining technique was used to fill the tank with a target relative density ($D_R = 70\%$). A constant temperature water bath was used to circulate a laboratory-standard mixture of ethylene glycol and distilled water (1:1 mixture) through the PVC tube. Temperature variations were monitored at 106 different locations within the pile and soil, at pile-soil interface and at the tank boundaries. To monitor the variation of pore water pressure during the thermal loading, 8 vibrating wire (VW) pressure transducers (Geokon model # 4580) were embedded within the soil bed. The VW pressure transducers (ranges within 0.00175 kPa to 14 kPa) were placed at different depths and radial distances to explore the potential of thermally-induced flow vortex formation within a zone surrounding the geothermal pile. Figure 1 shows the schematic view of the model on the vertical plane passing through the PVC tube.

VW pore pressure transducers had to be calibrated before those could be used for monitoring pore water pressure. During the calibration process, all transducers were placed in a water bucket following the calibration specifications supplied by the manufacturer (Figure 2). Pore water pressure readings gathered using all pressure transducers were recorded over a period of one day to check the validity of the calibration procedures. Low volume of water was further added to the calibration water

bucket to check the accuracy of reading variations in all pressure transducers. The pore water pressure variations sensed by all VW piezometers were exactly same as that expected due to the increment in water height.

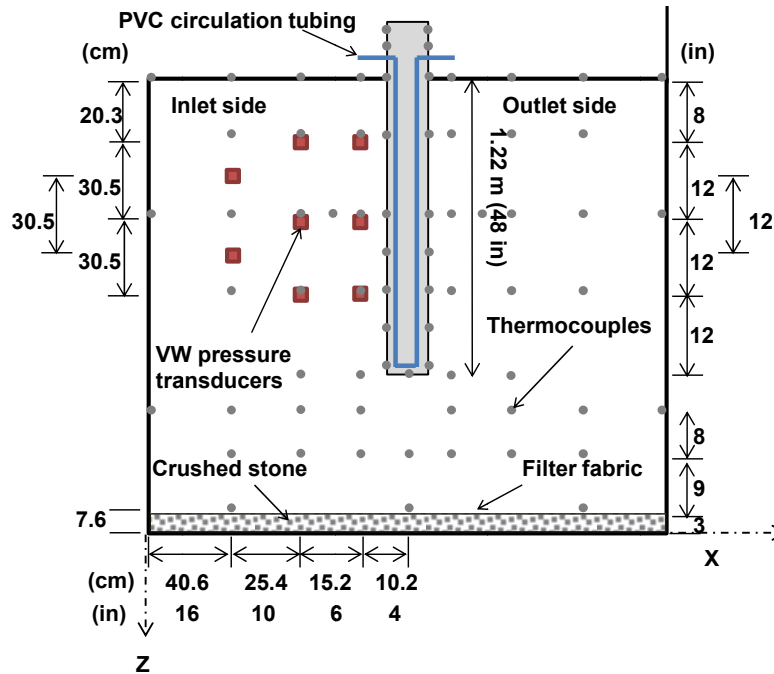


FIG. 1. Schematic view of the test setup and instrumentation details



FIG. 2. Calibration test setup for VW piezometers

The calibrated VW piezometers were embedded at specified locations within the soil bed (Figure 3). Values of test design variables and physical and thermal properties of circulation fluid, concrete, soil and PVC tube are presented in Table 1.

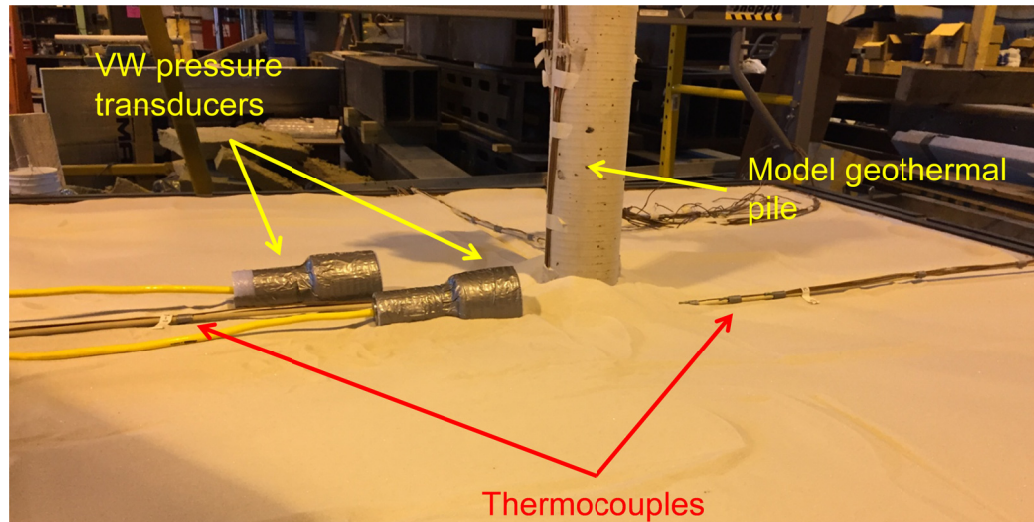


FIG. 3. VW piezometers transducers and thermocouples placed within the testbed

Table 1. Physical and thermal properties for different model components

Fluid circulation velocity	$v = 0.66 \text{ m.s}^{-1}$
Mass density of heat carrier fluid	$\rho_f = 1060 \text{ kg.m}^{-3}$
Length of the model pile	$L = 1.2 \text{ m}$
Radius of the model pile	$r_p = 0.05 \text{ m}$
Inner radius of circulation tube	$r_t = 0.006 \text{ m}$
Specific heat of heat carrier fluid	$C_{pf} = 3455 \text{ J.kg}^{-1}.\text{K}^{-1}$
Thermal conductivity of concrete	$k_c = 1.5 \text{ (W.m}^{-1}.\text{K}^{-1})$
Thermal conductivity of saturated soil	$k_s = 3.2 \text{ (W.m}^{-1}.\text{K}^{-1})$
Thermal conductivity of dry soil	$k_{s,dry} = 0.25 \text{ (W.m}^{-1}.\text{K}^{-1})$
Thermal diffusivity of dry soil	$\alpha_{s,dry} = 1.5 \times 10^{-7} \text{ (m}^2.\text{s}^{-1})$
Thermal diffusivity of concrete	$\alpha_c = 4.8 \times 10^{-6} \text{ (m}^2.\text{s}^{-1})$
Thermal diffusivity of saturated soil	$\alpha_s = 7.6 \times 10^{-6} \text{ (m}^2.\text{s}^{-1})$
Thermal conductivity of PVC tube	$k_t = 0.15 \text{ (W.m}^{-1}.\text{K}^{-1})$
Thermal diffusivity of PVC tube	$\alpha_t = 0.72 \times 10^{-7} \text{ (m}^2.\text{s}^{-1})$
Dynamic viscosity of fluid	$\mu_f = 6.5 \times 10^{-3} \text{ Pa.s}$
Thermal conductivity of fluid	$k_f = 0.41 \text{ W.m}^{-1}.\text{K}^{-1}$

RESULTS

A series of thermal performance tests on model geothermal pile installed in saturated sand were performed in this study. Results obtained from these tests are compared with results of similar tests performed on model pile installed in dry sand (reported by Kramer et al. 2014). Test results reveal that for most part of a heating test (i.e., heat rejection to the ground) soil temperature increments near the geothermal pile installed in saturated sand is as low as 8°C compared to that recorded from a similar test under dry

condition (Figure 4). Following Boussinesq’s theorem (Nield and Bejan 2013) temperature changes in saturated soil would result in spatial variation of fluid mass density. Consequently, following the Brinkman momentum equation, pore fluid flow is expected within the medium surrounding geothermal piles. Comparison of ground temperature increments for dry and saturated sands confirms this notion (See Figure 4). Heat can easily transfer through a saturated medium which has higher thermal conductivity compared to the same medium in dry condition. Based on the heat transfer equation in porous medium (Nield and Bejan 2013), apart from heat conduction through the solid particles, convection through pore fluid flow in saturated medium makes it easier for heat to dissipate away from the heat source (i.e., the geothermal pile for the present case). This results in lower ground temperature in the vicinity of the pile but higher temperature in regions farther from the geothermal pile. To capture thermally induced variations of excess pore water pressure, if any, pore water pressure at 8 different locations were measured during the thermal tests, which comprised of a heating period followed by a relaxation (i.e., cooling back to the room temperature) phase.

A full heat cycle test with a relaxation period was performed to study the excess pore water pressure development in the medium. Hot fluid with inlet point temperature of 60°C was injected for 90 hours (= 3.75 days) and then the water heater was turned off for 50 hours (relaxation phase) to revert back to the initial condition. Temperature was controlled at the fluid inlet point and monitored at both inlet and outlet points and within the soil bed. Figure 5 shows the variation of inlet and outlet fluid temperatures during the thermal (heating) test and relaxation period. Evolution of excess pore water pressure was also monitored and recorded during the entire test.

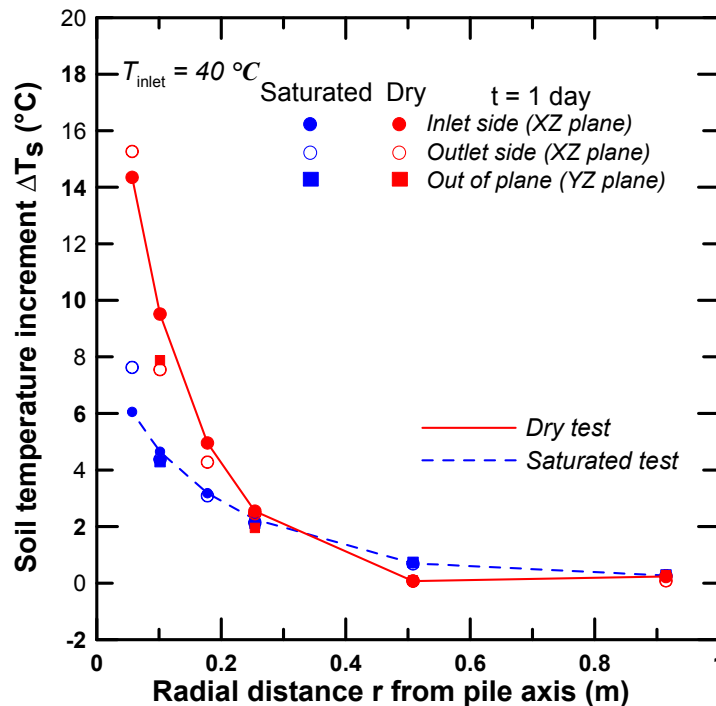


Fig. 4. (a)

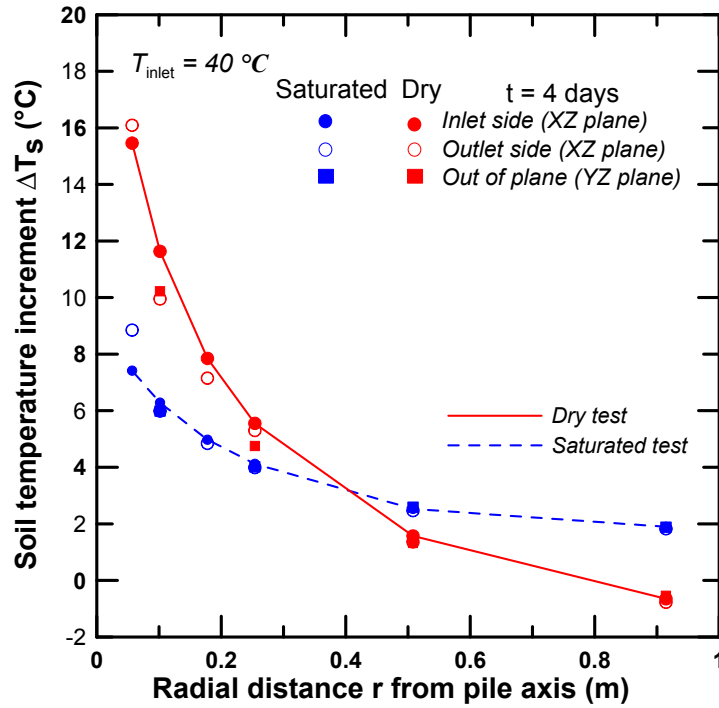


Fig. 4. (b)

FIG. 4. Comparison of soil temperature increments for dry and saturated conditions at different locations (a) $t = 1\text{ days}$ (b) $t = 4\text{ days}$

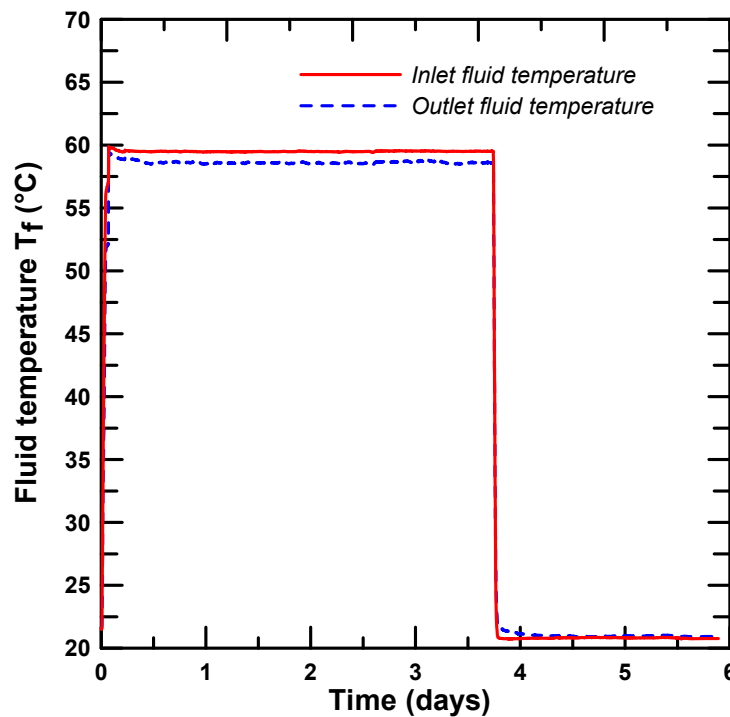


FIG. 5. Evolution of inlet and outlet fluid temperature during the thermal test

Figure 6 shows variations of excess pore water pressure for both heat rejection and relaxation periods with both real and normalized time expressed by Fourier number Fo ($= \alpha_s t / r_t^2$). Results obtained from three different VW pressure transducers at different radial distances and depths are selected to compare the variation of excess pore water pressure at different depths and radial coordinates. As Figure 6 shows, initially pore water pressure increases for the locations close to the pile (radial distance $r = 10.2$ cm). However, generation of excess pore water pressure at a location far from the model pile ($r = 50.2$ cm) starts one day after the start of the thermal test. Comparison of results recorded from the VW transducers shows that the transducer placed near the geothermal pile at higher depth ($r = 10.2$ cm and $z = 81.3$ cm) recorded higher change (increase) in pore water pressure during the heating phase. In contrast, the VW transducer placed near the ground surface (at the same radial distance $r = 10.2$ cm) sensed higher drop in excess pore water pressure during the relaxation phase.

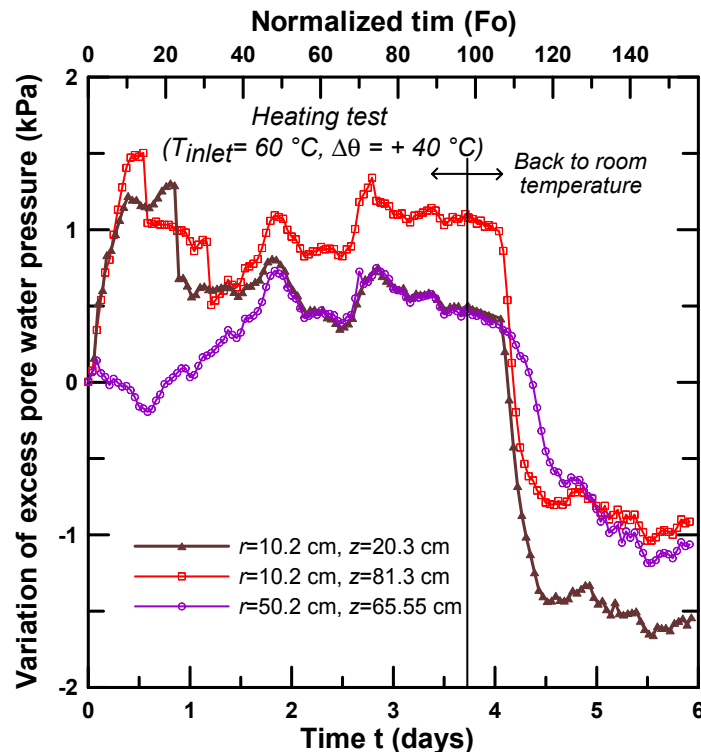


FIG. 6. Variation of excess pore water pressure during the thermal test followed by a relaxation period

Change in excess pore water pressure in the vicinity of the model geothermal pile, as evident in Figure 6, can be attributed to temperature-induced spatial variation of pore fluid density. This figure also demonstrates the reduction in excess pore water pressure soon after starting of the relaxation period. The reason for reduction in excess pore pressure is that heat rejection to the ground reduces soil moisture content within a zone surrounding a geothermal pile. This reduction is higher in the zone (with radius $r \approx 2r_p$) adjacent to the geothermal pile. The rate of excess pore pressure reduction is different at

different radial distances because heat dissipation ΔT_g , is higher in the region close to the pile and thus variation in induced pore pressures will be more drastic in this zone compared to that in the farther zones. Additionally, the drop in excess pore pressure is higher at locations closer to the ground surface (i.e., where water could evaporate easily) compared to that at greater depths. Low et al. (2013) and Loveridge et al. (2014) reported similar reduction in moisture content at the end of thermal conductivity tests using a thermal needle probe. Note that the reduction in pore water pressure might start even during the heating period but the thermally induced excess (positive) pore water pressure prohibits its visibility and we can only observe the reduction in pore pressure during the relaxation period where the temperature gradient and consequently thermally induced excess pore pressure is going to decrease. The negative values of recorded excess pore pressure may be regarded as a direct consequence of drying of a thin soil layer at the top of the soil bed due to thermal loading.

CONCLUSIONS

The role of heat convection through temperature-induced pore fluid flow in pile-soil heat exchange is studied through instrumented thermal tests on model geothermal pile installed in dry and saturated sand. Comparison of temperature recorded in dry and saturated soils confirms that temperature increment is higher at locations close to the pile for dry condition; however, in case of saturated soil, higher temperature increments are recorded at zones farther from the geothermal pile. Heat rejection to the ground results in a positive change in excess pore pressure within a zone surrounding a geothermal pile. The increase in positive pore water pressure is higher for the deeper zone close to the model geothermal pile where the temperature increments are higher. Reduction in excess pore pressure built up during the heating phase is recorded during the relaxation phase.

REFERENCES

- Brandl, H. (2006) "Energy foundations and other thermo-active ground structures." *Géotechnique*, Vol. 56 (2): 81-122.
- Ghasemi-Fare, O. and Basu, P. (2013). "A practical heat transfer model for geothermal piles." *Energy and Buildings*, Vol. 66: 470-479.
- Ghasemi-Fare, O. Basu, P. (2015). "Numerical modeling of temperature-induced moisture migration in soil surrounding geothermal piles", *IFCEE 2015*: pp. 1668-1677. DOI: 10.1061/9780784479087.151
- Ghasemi-Fare, O. Basu, P. (2016). "Predictive assessment of heat exchange performance of geothermal piles", *Renewable Energy*: Vol. 86, 1178-1196. DOI: 10.1016/j.renene.2015.08.078
- Hossain, M. A. and Wilson, M. (2002). "Natural convection flow in a fluid saturated porous medium enclosed by non-isothermal walls with heat generation." *International Journal of Thermal Science*, Vol. 41: 447-454.
- Hossain, A. Saleem, M. Saha, S. C. and Nakayama, A. (2013). "Conduction-radiation effect on natural convection flow in fluid-saturated non-Darcy porous medium enclosed by non-isothermal walls." *Applied Mathematics and Mechanics*, 34(6), 687-702.

- Jalaluddin, E. Miyara, A. Tsubaki, K. Inoue, S. Yoshida, K. (2011). "Experimental study of several types of ground heat exchanger using a steel pile foundation." *Renewable Energy*, Vol. 36: 764–771.
- Kaviany, M. (1986). "Non-Darcian effects on natural convection in porous media confined between horizontal cylinders." *International Journal Heat Mass Transfer*, Vol. 29 (10): 1513-1519.
- Kramer, C. A. Ghasemi-Fare, O. and Basu, P. (2014). "Laboratory thermal performance tests on a model heat exchanger pile in sand." *Journal of Geotechnical and Geological Engineering, Special Issue on Thermo-mechanical Response of Soils, Rocks, and Energy Geostructures*, Vol 33: 253-271.
- Krishnaiah, S. and Singh, D. N. (2003). "A methodology to determine soil moisture movement due to thermal gradients." *Experimental Thermal and Fluid Science*, Vol. 27: 715-721.
- Krishnaiah, S. and Singh, D. N. (2004). "Centrifuge modeling of heat migration in soils." *International Journal of Physical Modeling in Geotechnics*, Vol. 3: 39-47.
- Laloui, L., Nuth, M., and Vulliet, L. (2006). "Experimental and numerical investigations of the behavior of a heat exchanger pile." *International Journal for Numerical and Analytical Methods in Geomechanics*, Vol. 30: 763–781.
- Leroy, A. Bernier, M. (2015). "Development of a novel spiral coil ground heat exchanger model considering axial effects." *Applied Thermal Engineering*, Vol. 84: 409-419.
- Li, M. Lai, A.C.K. (2015). "Review of analytical models for heat transfer by vertical ground heat exchangers (GHEs): A perspective of time and space scales." *Applied Energy*, Vol. 151: 178-191.
- Loveridge, F. Powrie, W. and Nicholson, D. (2014) "Comparison of two different models for pile thermal response test interpretation." *Acta Geotechnica*, Vol. 9: 367-384.
- Low, J. E. Loveridge, F. A. and Powrie, W. (2013). "Measuring soil thermal properties for use in energy foundation design." *18th International Conference for Soil Mechanics and Geotechnical Engineering*, Paris, France, 3375-3378.
- Nield, D. and Bejan, A. (2013). "Convection in porous media". 4th edition, Springer, New York.
- Ozudogru, T.Y. Ghasemi-Fare, O. Olgun, C.G. and Basu, P. (2014). "Numerical modeling of vertical geothermal heat exchangers using Finite Difference and Finite Element Techniques." *Journal of Geotechnical and Geological Engineering, Special Issue on Thermo-mechanical Response of Soils, Rocks, and Energy Geostructures*, Vol. 33: 291-306.
- Tarnawski, V.R. Momose, T. and Leong, W.H. (2011). "Thermal conductivity of standard sands II". Saturated conditions, *International Journal of Thermophysics* Vol. 32: 984-1005.

A New Model Concrete for Reduced-Scale Model Tests of Energy Geo-Structures

Davide Vitali¹; Anthony K. Leung²; Andrew Minto¹; and Jonathan A. Knappett³

¹Ph.D. Student, Univ. of Dundee, Nethergate, Dundee DD1 4HN, U.K.

²Lecturer, Division of Civil Engineering, Univ. of Dundee, Nethergate, Dundee DD1 4HN, U.K. (corresponding author). E-mail: a.leung@dundee.ac.uk

³Reader, Division of Civil Engineering, Univ. of Dundee, Nethergate, Dundee DD1 4HN, U.K.

Abstract: Concrete energy geo-structures such as piles and diaphragm walls exhibit complex thermomechanical behaviour and interaction with the surrounding soil. Small-scale physical model tests including the use of geotechnical centrifuges have been utilised to study such soil-structure interaction. However, existing materials used to model concrete energy geo-structures do not simultaneously scale both the mechanical and thermal properties. This study attempts to develop a new material that could have representative thermal and mechanical behaviour of concrete. The new material is a plaster-based mortar with the addition of fine copper powder. It is revealed that adding copper powder from 0 to 6% (by volume) to the mortar resulted in a 90% increase in thermal conductivity. More importantly, such an addition was not found to cause significant increase or reduction of the mechanical strength, including both the unconfined compressive strength and modulus of rupture. These findings suggest that while the thermal properties of concrete can be properly scaled, the new type of mortar can maintain its ability to also correctly scale the mechanical behaviour of concrete simultaneously. This will allow the study of a range of geotechnical problems, where thermal properties and structural strength are important, such as slope reinforcement using concrete energy piles.

INTRODUCTION

The use of energy geo-structures, which exploit shallow geothermal energy as a heating and cooling source, has been recognised to be a sustainable engineering solution that can reduce carbon emissions from civil infrastructure (Brandl 2006; Lund et al. 2004). Energy piles and diaphragm walls are the two energy geo-structures that have been given close attention due to their cost-effectiveness in reducing building energy requirements (Brandl 2006; Laloui et al. 2006; Adam and Markiewicz 2009). In addition to field testing (Laloui et al. 2006; Bourne-Webb et al. 2009; Murphy and McCartney 2014), the centrifuge modelling technique has been increasingly used to study the thermomechanical behaviour of energy geo-structures and their interaction with the surrounding soil (Ng et al. 2015; Stewart and McCartney 2014). This technique enables small-scale physical models to be tested at the stress levels identical to those experienced by much larger prototypes and under much more tightly controlled test conditions than are possible in field experiments.

In order to carry out a meaningful centrifuge test to study the behaviour of an energy geo-structure, one major challenge is to correctly scale the material properties of the structure. A common model material is aluminium alloy (Ng et al. 2015), as its axial or flexural rigidity can be scaled rather conveniently through the change of second moment

of area of the model pile (e.g., by changing the internal diameter). However, aluminium model piles cannot be used to model the behaviour of energy concrete pile, as the thermal properties between aluminium and concrete are different. The coefficient of thermal expansion of aluminium ($22.2 \times 10^{-6} \text{ m}/(\text{m}\cdot\text{K})$) is two to three times higher than that of concrete ($6 \text{ to } 9 \times 10^{-6} \text{ m}/(\text{m}\cdot\text{K})$). The thermal conductivity of aluminium ($205 \text{ W}/(\text{m}\cdot\text{K})$) is at least 200 times higher than that of concrete (at least $1 \text{ W}/(\text{m}\cdot\text{K})$; GSHP 2012). Another disadvantage of aluminium elements is that stiffness and strength cannot be scaled simultaneously, i.e. if the flexural rigidity is matched through varying the pile cross-section, the moment or shear capacity will not be correct (Knappett et al. 2011). To more correctly model the thermomechanical behaviour of energy concrete geo-structures as well as the soil-structure interaction such as axial and lateral load mobilisation, both the thermal and mechanical properties of a model material needs to be simultaneously scaled.

An alternate approach to model concrete energy piles is the direct use of concrete (Stewart and McCartney 2014). Although the thermal properties of concrete energy piles at prototype might be captured by this approach, the particle-size of coarse aggregates in concretes generally does not scale properly, resulting in an over-strength of the model material. Scaling of the particle size in concrete is extremely important for correctly capturing the failure mechanism and the cracking process of this kind of quasi-brittle and non-linear material, especially when concrete is prone to be subjected to lateral and bending loadings.

Efforts have been made to develop a plaster-based mortar to capture the quasi-brittle nature of concrete (Sabnis and White 1967; Knappett et al. 2011). In particular, Knappett et al. (2011) developed various types of mortar, in which fine silica sand was used to geometrically scale the coarse aggregate found in concrete. Such model concrete is shown to be capable of mimicking the nonlinear quasi-brittle behaviour of concrete and have representative mechanical strengths (i.e., unconfined compressive strength from 26.3 to 81.7 MPa and modulus of rupture from 2.02 to 4.42 MPa). These types of model concrete have been successfully used for modelling various engineering structures such as piles (Al-Defae and Knappett 2014) and bridge piers (Loli et al. 2014). For modelling energy concrete geo-structures, this type of model concrete requires further modification to ensure correct scaling of thermal properties.

This study aims to develop a thermally-enhanced mortar as a new model concrete that attempts to simultaneously scale both the mechanical and thermal properties of concrete at prototype scale. Fine copper powder with a relatively high thermal conductivity is added as a new constituent to a type of mortar, for which the mechanical properties have already been properly scaled by Knappett et al. (2011). Any change in thermal conductivity of the new model concrete due to the addition of different copper powder content was determined. In order to investigate any effects of the addition of copper powder on the mechanical properties of the new model concrete, unconfined compressive strength and modulus of rupture were measured. The test results are interpreted with the aid of some microstructural analyses of the new model concrete by means of scanning electronic microscope (SEM).

MATERIALS AND METHODS

Constituents of the New Model Concrete

The new model concrete developed in this study is a plaster-based mortar, which composes of β -form surgical plaster (manufactured by Saint Gobain), water, silica sand (Congleton HST95) and copper powder (manufactured by Phoenix Scientific Industries). The use of silica sand aims to geometrically scale (approximately) the aggregate used in concrete at prototype scale. Copper powder is a new constituent that attempts to enhance the thermal conductivity of the mortar as it has a high value of $400 \text{ W}/(\text{m}\cdot\text{K})$ as compared to plaster ($0.29 \text{ W}/(\text{m}\cdot\text{K})$; Wakili et al. 2015) and quartz (i.e., the core mineral of the sand; $6.5 \text{ W}/(\text{m}\cdot\text{K})$; Clauser and Huenges 1995). The particle-size distribution of the sand and copper powder were measured by a laser diffraction analyser and they are compared in Figure 1.

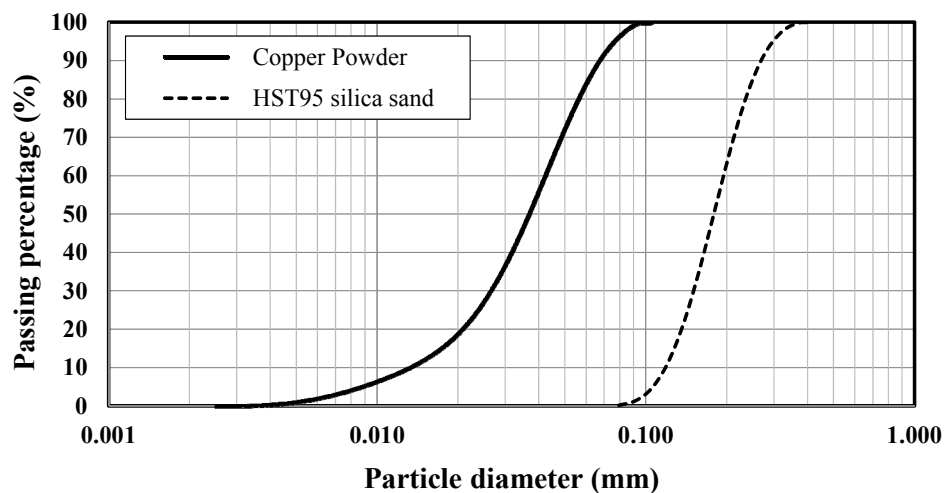


FIG. 1. Particle-size distribution of silica sand and copper powder

The D_{10} (the particle diameter at 10% passing), D_{30} and D_{60} of the sand are 0.12, 0.15 and 0.20 mm, respectively. The coefficients of uniformity and curvature of the sand are 1.7 and 1.0, respectively, and the sand is thus a uniformly-graded sand. The copper powder is finer than the sand, with diameter ranging between 0.002 to 0.1 mm. The powder has D_{10} (0.013 mm), D_{30} (0.026 mm) and D_{60} (0.042 mm) and it is also categorised as a uniform powder.

Sample Preparation

The design mix of the new model concrete is to use a water/plaster (W/P) ratio of 0.9:1 and a sand/plaster (S/P) ratio of 1:1. These ratios have shown to be capable of producing a mortar that can realistically mimic the mechanical properties of concrete in prototype (Knappett et al. 2011). In addition, four different percentages of copper powder by volume (i.e., 0, 1.5%, 3.0% and 6.0% with respect to the volume of sand) were added to the mix. Note that these volumetric percentages were trial values that aim to validate the potential use of copper powder to enhance the thermal conductivity of the

design mortar. The exact range of percentage that can reproduce the thermal conductivity of concrete was not known prior to testing.

According to the designed ratios and percentages selected in this study, each mortar was produced by first mixing all the dry constituents (i.e., sand, plaster and copper powder) for at least three minutes using a whisk and then followed by adding appropriate amount of water for hydration to take place in the plaster. Each mix was then cast in moulds with different dimensions, depending on the type of tests described in the following sections. All samples were air-cured, in a room where the temperature was controlled at 20 – 25 °C, for 28 days before testing.

Thermal Testing

In this study, the thermal conductivity of each mix, λ [W/(m·K)], was measured using a steady-state method based on Fourier's law as expressed below:

$$\lambda = \left(\frac{Q}{A \cdot t} \right) \cdot \frac{1}{\Delta T} \cdot d \quad (1)$$

where Q is the heat rate [W]; d is the thickness of specimen [m]; t is the test duration [s]; ΔT is the temperature difference across the two surfaces of the specimen [°C]; and A is the surface area of the specimen [m²]. The quotient inside the bracket refers to heat flux, q [W/m²]. For a given known geometry of specimen, λ can be obtained by controlling Q and measuring ΔT when a thermal gradient is applied across the specimen.

In order to achieve this testing condition, a hot-box apparatus developed by Jones et al. (2007), as shown in Figure 2, was adopted. The apparatus consists of two units, namely the heating unit and the cooling unit, aiming to create a thermal gradient across a specimen. The heating unit has a feedback system, which includes a 15 W light bulb, a thermal probe and a computer, for applying and controlling a constant temperature of 35 °C. When the temperature in the unit rises beyond 35 °C due to the continuous heat release from the bulb, the thermal probe would transmit a signal to the computer to switch off the bulb. The light bulb would be switched on again when the temperature recorded by the probe drops below 35 °C. In order to prevent direct heating of the sample by radiation, a square wooden baffle was placed between the sample and the bulb. The temperature in the cooling unit was controlled so that the temperature difference between the two units was fixed to be greater than 25 °C during testing, following the suggestions in the standard BS 874-3-1990. Outside the two units, a thermal insulating layer made of expanded polystyrene surrounds the test cell to thermally seal the system.

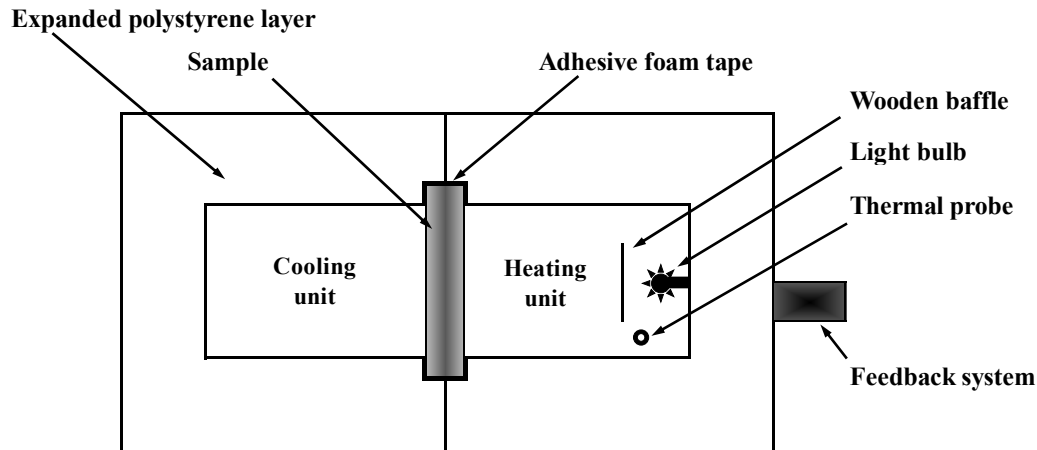


FIG. 2. A schematic diagram showing the plan view of the hot-box apparatus

Slab-shaped mortar specimens with a dimension of 45 x 150 x 150 mm were used for determining λ . Each specimen, after 28 days of curing, was installed in the apparatus and carefully sealed with adhesive foam tape onto the thermal insulating layer, aiming to prevent undesirable heat flow across the two units through gaps.

When a test commenced, the heat flux applied by the light bulb, q , was determined by multiplying the power of the bulb (i.e., 15 W) by the time interval when the bulb is switched on and then dividing this product by the overall test duration (t) as well as the mortar surface area (A). The temperature on each side of each specimen was monitored by five thermocouples to ensure that the specimen has achieved a uniform temperature distribution. When equilibrium is reached (i.e., q reaches an apparent constant value), λ can be determined by Eq. 1. In order to account for any sample variability, three replicates were tested for each percentage of copper powder added (i.e., 12 samples in total).

Mechanical Testing

Two types of tests were conducted to determine the mechanical properties of each mortar mix, namely unconfined compression (UC) tests and four-point bending (FPB) tests. For each UC test, cube-shaped specimens with a length of 100 mm each side were tested. According to the test procedure outlined in the standard BS EN 12390-3:2009, each specimen was compressed vertically by a loading machine at a rate of 7 kN/s until crushing of mortar was achieved. The ultimate strength of each sample (f_c) was then recorded. Three replicates were tested for each percentage of copper powder added (i.e., 12 samples in total).

For each FPB test, beam-shaped specimens with a dimension of 25 x 25 x 250 mm were used to determine the modulus of rupture f_r . It should be noted that f_r is dependent upon specimen dimension (Bažant and Novák 2001). The reason for selecting this dimension in this study is to obtain relevant values of f_r for future centrifuge testing of a model energy pile at 1:20 scale. Figure 3 shows a test setup for a FPB test. Before testing, each specimen was rested on two supports symmetrically separated by 210 mm. Then, the specimen was point-loaded symmetrically at two locations, each of which is 35 mm away from the centreline of the specimen. The test was terminated when an abrupt decrease in the load applied was recorded due to the cracking of mortar. The test

setup and procedures are similar to those described in the standard BS 1881: Part 118:1983. Six repeated FPB tests were conducted for each percentage of copper powder added (i.e., 24 samples in total).

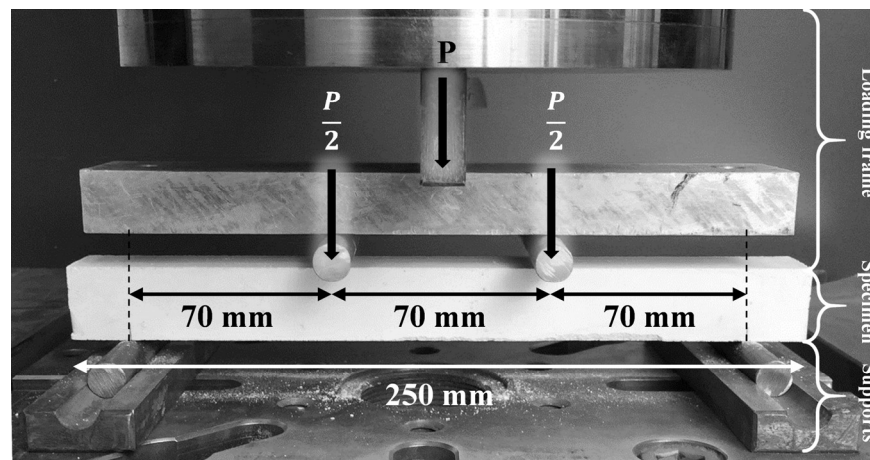


FIG. 3. A picture showing the setup of a typical FPB test

Microstructural Testing

After testing, the microstructure of one of the slab-shaped mortar specimens with 6% copper powder content was imaged by scanning electron microscope (SEM) to study the form of existence and the distribution of each constituent within the matrix. Ten samples were collected at 5 mm depth from the surface of the mortar slab at ten different locations. Each sample was mounted on an aluminium stub using a carbon adhesive stab and epoxy resin. It was then coated with a 30 nm layer of Au/Pd using a Cressington 208HR sputter coater. Each sample was imaged using a microscope (model: JEOL-JSM7400F), with an applied accelerating voltage of 5 kV. Images were taken at magnifications from x25 to x1500.

RESULTS AND DISCUSSION

Microstructure of the New Model Concrete

Figure 4(a) depicts a SEM image showing some grains of silica sand attached in the mortar matrix at a magnification of x55. In general, the sand grains appear to distribute reasonably uniformly within the matrix. The copper particles are too small to be visualised at this magnification level, but they can be identified in a closer view at x500 in Figure 4(b). The fine copper particles exist in spherical shape and they are being entangled by the fibre-like irregular structure of the plaster matrix. Such micro-structure is a key feature of β -form plaster due to the rapid evolution of its pore structure during the hydration phase (Song et al. 2009).

Figure 4(c) shows another view of the mortar matrix at x300. It can be seen that there are noticeable gaps (up to a few microns) at the interface between the plaster and the sand grains, but such gapping is less obvious or negligible at the plaster-copper particle interface. It should be pointed out that no chemical bonding is formed among the plaster, the sand grains and the copper particles after the hydration process. These three constituents are attached together mainly physically through weak inter-particle van der Waal force. The presence of gaps or weak planes at the interface of constituents is the

main reason for the mortar to exhibit and mimic the important quasi-brittle behaviour of concrete.

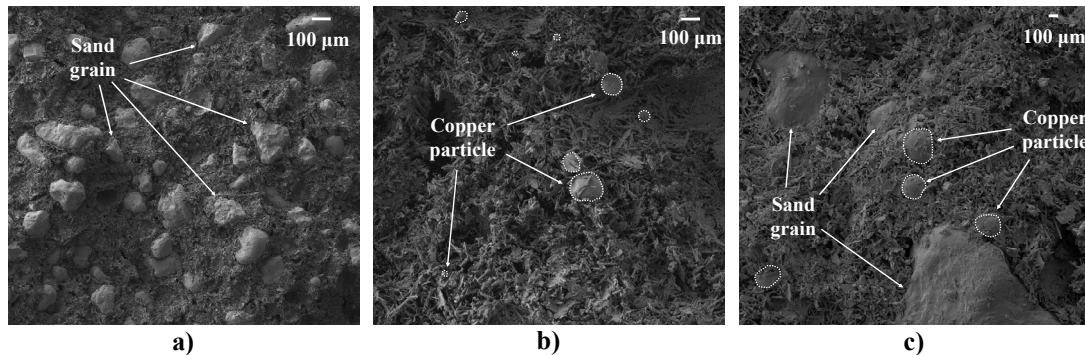


FIG.4. SEM images of a) distribution of sand grains; b) distribution of copper particles; and c) interface of plaster, sand grain and copper particle

Thermal Properties

Figure 5 shows the variation of λ with the percentage of copper powder added to the mortar. All data are expressed in mean values and standard errors obtained from the repeated tests. The mean λ with zero powder content is 0.38 W/(m·K), which is 23.7% higher than of that of gypsum plasterboard (0.29 W/(m·K); Wakili et al. 2015). The reason is that the mortar made in this study was mixed with silica sand, of which the mineral, quartz, has a higher λ than gypsum.

The test results show that there is a substantial increase in λ as the content of copper powder increases. At the highest powder content of 6% considered in this study, the λ rises by 90% and is up to 0.73 W/(m·K). Although the attempt to use copper powder to enhance λ of the mortar is shown to be successful in this study, the magnitude for copper powder of up to 6% is not far from the targeted λ (1 W/(m·K)) of concrete at prototype scale. If the relationship between λ and copper powder content is linear, extrapolation suggests that 10% of copper powder by volume would be adequate to achieve λ of 1 W/(m·K). Further testing of λ of the mortar mixed with a higher copper powder content is currently underway to match the targeted value.

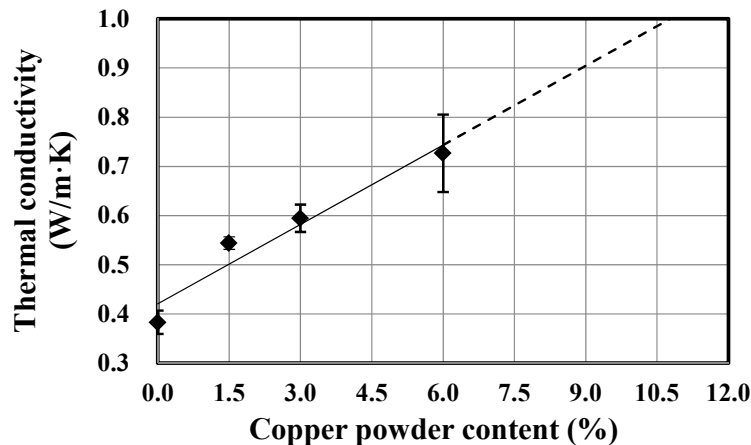


FIG. 5. Effects of the addition of copper powder on the thermal conductivity of the new model concrete

Mechanical Properties

Figures 6(a) and (b) show the effects of the addition of copper powder on the unconfined compressive strength and modulus of rupture, respectively. Similarly, all data are expressed in mean values and standard errors obtained from the repeated tests. Each measured f_c and f_r is normalised with the respective value obtained without adding copper powder (denoted as f_{c0} and f_{r0}).

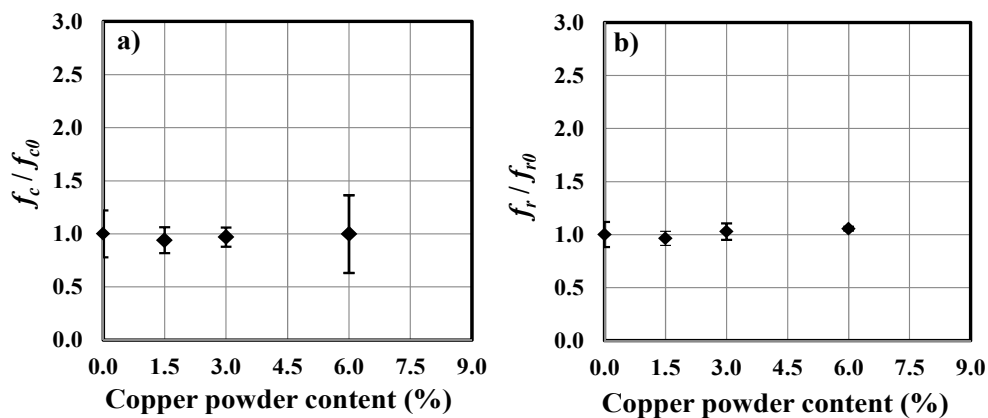


FIG. 6. Effects of copper powder on (a) unconfined compression strength and (b) modulus of rupture of the new model concrete

It can be seen in both figures that the addition of copper powder of up to 6% to the mortar does not result in significant reduction or increase in the mean value of both the unconfined compressive strength and modulus of rupture of the mortar. This observation might be because the fine nature and spherical-shaped copper powder (see SEM image in Figure 4(c)) does not seem to create much appreciable interlocking or weak planes within the plaster matrix to affect the strength of the mortar. The test results of f_c and f_r suggest that the ability of this new model concrete to mimic the mechanical behaviour of concrete is not affected significantly due to the addition of copper powder in the mix.

CONCLUSIONS

This study has developed a new type of model concrete, which has its mechanical and thermal properties more properly scaled for potential use in modelling energy geo-structures such as piles and diaphragm walls in small-scale physical model tests. The new model concrete is a plaster-based mortar, which comprises β -form plaster, water, silica sand (to geometrically scale the aggregates of concrete at prototype scale) and copper powder (to control the thermal conductivity of the mix). The basic mechanical properties, including unconfined compression strength and modulus of rupture, and the thermal conductivity of the new model concrete was determined for different percentages of copper powder by volume (i.e., 0, 1.5, 3 and 6%).

The test results show that adding 6% of copper powder content to the new mix of mortar led to a 90% increase in the thermal conductivity from 0.38 to 0.73 W/(m·K). Such an addition is shown not to cause significant changes in either the unconfined compression strength or the modulus of rupture. The mechanical properties remained almost unaffected because, according to a qualitative assessment of the microstructure of the mortar through SEM, the presence of the spherically-shaped copper powder did not create much appreciable interlocking or weak planes within the matrix. Thus, adding copper powder could enhance the thermal conductivity of the mortar, while maintaining its ability to mimic the mechanical properties of concrete.

A wider testing programme is currently underway to use this new type of mortar to produce small-scale model reinforced concrete energy piles and diaphragm walls for subsequent use in centrifuge testing. Further experiments will be performed to examine the thermomechanical behaviour of these model energy geo-structures and their interaction with the surrounding soil when different temperature fluid is circulated within these geo-structures.

ACKNOWLEDGEMENTS

The authors would like to acknowledge the studentship and the research cost supported by Energy Technology Partnership (ETP), Scottish Road Research Board (SRRB) from Transport Scotland, the EPSRC Doctoral Training Award as well as the Scottish Funding Council (SFC). We would also like to thank Mr. Yiqi Ni for help preparing some mortar specimens for the tests presented in this paper.

BIBLIOGRAPHY

- Adam, D., and Markiewicz, R. (2009). "Energy from earth-coupled structures, foundations, tunnels and sewers." *Géotechnique*, 59(3): 229-236.
- Al-Defae, A. H., and Knappett, J. A. (2014). "Centrifuge modeling of the seismic performance of pile-reinforced slopes." *J. Geotech. Geoenviron. Eng.*, ASCE, 140(6), 04014014.
- Bažant, Z. P., and Novák, D. (2001). "Proposal for standard test of modulus of rupture of concrete with its size dependence." *ACI Mater J.*, 98(1): 79-87.
- Bourne-Webb, P., Amatya, B., Soga, K., Amis, T., Davidson, C., and Payne, P. (2009). "Energy pile test at Lambeth College, London: geotechnical and thermodynamic aspects of pile response to heat cycles." *Géotechnique*, 59(3): 237-248.
- Brandl, H. (2006). "Energy foundations and other thermo-active ground structures." *Géotechnique*, 56(2): 81-122.
- Clauser, C., and Huenges, E. (1995). "Thermal conductivity of rocks and minerals." In *Rock physics & phase relations: A handbook of physical constants*, eds. T. J. Ahrens, American Geophysical Union, Washington, D. C., 105-126.

- GSHP (Ground Source Heat Pump Association). (2012). "Thermal pile design, installation and materials standards." Issue 1.0, Ground Source Heat Pump Association, Milton Keynes, UK.
- Jones, M. R., Zheng, L., McCarthy, A., Dhir, R. K., and Yerramala A. (2007). "Increasing the use of foamed concrete incorporating recycled and secondary aggregates." WRAP Project Report:AGG79-001.
- Knappett, J. A., Reid, C., and O'Reilly, K. (2011). "Small-scale modeling of reinforced concrete structural elements for use in a geotechnical centrifuge." *J. Struct. Eng.*, 137(11): 1263-1271.
- Laloui, L., Nuth, M., and Vulliet, L. (2006). "Experimental and numerical investigations of the behaviour of a heat exchanger pile." *Int. J. Numer. Anal. Methods Geomech.*, 30(8): 763-781.
- Loli, M., Knappett, J. A., Brown, M. J., Anastasopoulos, I., and Gazetas, G. (2014). "Centrifuge modeling of rocking-isolated inelastic RC bridge piers." *Earthquake Eng. Struct. Dyn.*, 43(15): 2341-2359.
- Lund, J., Sanner, B., Rybach, L., Curtis, R., and Hellström, G. (2004). "Geothermal (ground-source) heat pumps—a world overview." *Geo-Heat Centre Quarterly Bulletin*, 25(3): 1-10.
- Murphy, K. D., and McCartney, J. S. (2014). "Seasonal response of energy foundations during building operation." *Geotech. Geol. Eng.*, 33(2): 343-356.
- Ng, C. W., Shi, C., Gunawan, A., Laloui, L., and Liu, H. L. (2015). "Centrifuge modelling of heating effects on energy pile performance in saturated sand." *Canadian Geotechnical J.*, 52 (8): 1-13.
- Sabnis, G. M. And White, R. N. (1967). "A gypsum mortar for small-scale models." *Proc. Am. Concr. Inst.*, 64(11), November: 767-774.
- Song, K. M., Mitchell, J., and Gladden, L. F. (2009). "Observing microstructural evolution during plaster hydration." *Diffusion Fundamentals*, 10: 22.1-22.3.
- Stewart, M. A. and McCartney, J. S. (2014). "Centrifuge modeling of soil-structure interaction in energy foundations." *J. Geotech. Geoenviron. Eng.*, ASCE, 140 (4), 04013044.
- Wakili, K. G., Koebel, M., Glaettli, T., and Hofer, M. (2015). "Thermal conductivity of gypsum boards beyond dehydration temperature." *Fire Mater.*, 39(1): 85-94.

Consideration of the Cyclic Degradation of Cohesive Soils in Pile Foundation Design for Onshore Wind Turbines

Hao Yu, Ph.D., A.M.ASCE¹; Carlos Guzman, P.E., M.ASCE²; and Eric Ntambakwa, P.E., M.ASCE³

¹Civil/Geotechnical Engineer, DNV GL, 1601 Rio Grande St, Suite 400, Austin, TX 78701. E-mail: chris.yu@dnvgl.com

²Civil/Geotechnical Engineer, DNV GL, 1601 Rio Grande St, Suite 400, Austin, TX 78701. E-mail: carlos.guzman@dnvgl.com

³Principal Civil/Geotechnical Engineer, DNV GL, 9665 Chesapeake Dr., Suite 435, San Diego, CA 92123. E-mail: eric.ntambakwa@dnvgl.com

Abstract: An onshore wind turbine foundation is typically designed for an intended life of 20 years, and often considered for an extended lifetime of 25 to 30 years. A wind turbine supported on a pile foundation is subjected to long-term cyclic axial loading and cyclic lateral loading due to dynamic vibrations primarily caused by wind loads and rotation of the blades. The cyclic loading may result in strength and stiffness degradation, accumulation of pile head displacement, significant reduction of pile capacity or even the failure of the wind turbine foundation. The potential for changes in the foundation stiffness could impact the operation frequency and foundation loads over time which could adversely influence wind turbine production and have implications for fatigue and ultimate loads on the foundation system. However, the long-term performance of pile foundations under cyclic loading has not been well incorporated in design standards of onshore wind turbine foundations. In this study, a comprehensive literature review has been performed on mechanisms of cyclic degradation of pile foundations in cohesive soil as well as the potential impact on the long-term performance of wind turbines. Additionally, this paper summarizes existing methods in evaluating cyclic behavior of pile foundations in cohesive soils and provides a framework for analysis of both axial and lateral cyclic degradation of soils supporting pile foundation designs for onshore wind turbines.

Keywords: Onshore, Wind turbine, Pile foundation, Cyclic loading, Degradation, Cohesive soil.

INTRODUCTION

In 2014, a total of 182 terawatt-hours of electricity was produced from wind power and accounted for nearly 5% of all generated electrical energy in the United States.

The growth of onshore wind power remains at a fast and steady pace in the U.S. energy market.

Pile foundations are one of the most favorable foundation types used for support of onshore wind turbines and are typically suitable for use in regions where stratum of adequate capacity is found at much greater depths (Morgan and Ntambakwa 2008). Due to dynamic vibrations caused by continuous wind loads and rotation of blades, pile foundations are often subjected to axial and lateral cyclic loading over the design life. Long-term cyclic loads can lead to cyclic degradation of pile foundation support soils in the form of accumulation of pile head displacement, reduction of foundation stiffness and gradual loss of skin friction or bearing capacity. The degradation of pile bearing capacity and stiffness due to cyclic loading has not typically been directly incorporated into wind turbine pile foundation designs in the earlier standards and codes (Hauschildt et al. 2011). Cyclic behavior of piles is indirectly considered in the design of wind turbine foundations and only general guidelines to account for effects of cyclic loading on soil properties are provided in current codes and guidelines (e.g. DNV/RISØ 2002 and DIN 2010).

The aim of the paper is to discuss the mechanisms of cyclic degradation of cohesive soils supporting pile foundations as well as the potential impact on the long-term performance of onshore wind turbines through a comprehensive literature review of existing design codes, standards and research findings. In addition, this paper summarizes existing methods in evaluating cyclic behavior of pile foundations in cohesive soils and provides a framework for analysis of both axially and laterally cyclic degradation of pile foundation designs for onshore wind turbine.

An important aspect of wind turbine foundation loads which facilitates practical implementation of soil cyclic degradation principles is that design loads are typically developed by turbine manufactures through simulations of the wind regime expected for the design life of 20 years. Project owners are also commonly considering extended life operations to 25 or 30 years which requires that cyclic loading aspects are evaluated for the additional operation. The turbine manufacturer typically provides loads representing normal (average) turbine operating conditions, extreme loading events (e.g. a 1 in 50 year gust) as well as fatigue loading information. The fatigue loading information includes loads (overturning moment, shear and torsion) and the corresponding load cycles for each load or range of loads. The fatigue loading information is useful for evaluating the fatigue life of reinforced concrete and steel and can be utilized to evaluate cyclic degradation effects for the foundation support materials following appropriate frameworks available in the literature. If extended life operation of the turbines is being considered, appropriate cyclic loading data for the additional years should be provided by the turbine manufacturer for use in foundation design validations.

STANDARDS REVIEW

Various codes and standards which provide guidance for considering cyclic degradation effects in designing of pile foundations for onshore wind turbines have been reviewed in this paper. Widely-used standards for offshore wind turbines and other offshore structures (i.e. offshore oil and gas infrastructure) were also reviewed

considering that the existing design codes for onshore wind turbines do not provide direct recommendations to cover the full range of impacts of cyclic loading on the soils supporting the turbine foundations. General recommendations for evaluating pile behavior under cyclic loading conditions are summarized in Table 1.

Table 1. Recommendations for Evaluating Cyclic Pile Behavior in Design Codes

Design Codes	Recommendations
DNV/RISØ Guideline (2002)	<ul style="list-style-type: none"> • Laboratory testing (i.e. cyclic triaxial test and resonant column tests) for assessment of strength and stiffness degradation of turbine foundations under cyclic loading
DNV-OS-J101 (2011) BSH (2007)	<ul style="list-style-type: none"> • Incorporating cyclic effects on shear strength of the soil in the applicable limit state and cyclic effects on soil shear modulus in the serviceability limit state (no detailed methods) • Cyclic pile behavior is more evident in cohesive soils than in medium to coarsely grained cohesionless soils
API-RP-2A-WSD (2000) API-RP-2GEO (2014)	<ul style="list-style-type: none"> • Lab/on-site soil testing and pile load testing in determining the elastic properties of the soil and resistance-displacement relationship along the vertical and horizontal direction of the pile • Framework for evaluation of cyclic response of pile foundations using discrete element or continuum models

Overall, the analyses of cyclic behavior of pile foundation and assessment of cyclic degradation are not directly addressed in current design standards for onshore wind turbine foundation.

EFFECTS OF CYCLIC DEGRADATION ON PILE FOUNDATIONS

Over the past few decades, the mechanisms of cyclic effects on pile foundations in cohesive soils have been well studied. The degradation behavior of cyclically loaded pile foundations can be generally characterized by effects on the bearing capacity (skin friction, end bearing and lateral capacity), stiffness of the pile-soil system and pile head displacement. A number of experimental investigations on cyclic behavior of pile foundation in cohesive soils have been carried out and the results indicate that the extent of cyclic degradation is dependent on the soil type, characteristics of the cyclic load (i.e. amplitude, number of cycles and loading rate) and group effects. Based on a literature review some significant observations are summarized in Table 2.

Table 2. Summary of Research on Cyclic Degradation Effects

Author	Testing Method	Comments
Steenfelt et al. (1981)	Model piles in clay	<ul style="list-style-type: none"> • Decrease in skin friction during cyclic loading with the development of excess pore water pressure in the soil adjacent to the pile foundation
Poulos (1981)	Model piles in remoulded clay	<ul style="list-style-type: none"> • Increasing cyclic displacement resulted in degradation and loss of pile skin friction • Degradation depended on number of cycles but majority of degradation occurred in the first 10-20 cycles
Bea et al. (1980)	Review of lab & field pile load test data	<ul style="list-style-type: none"> • Maximum of 10 to 20% reduction in load capacity under “one-way” cyclic loading and greater than 20% reduction might occur under “two-way” loading • A trend of increasing pile head displacement with number of cycles and level of cyclic loading
Yilmaz et al. (2004)	Cyclic triaxial tests on natural clay soil	<ul style="list-style-type: none"> • Cyclic behavior was dependent on load reversal and level of stress range • Strain accumulation was smaller when the peak cyclic stress below monotonic strength
Tuladhar et al. (2007)	Full-scale model pile in cohesive soil	<ul style="list-style-type: none"> • Maximum lateral capacity under cyclic loading was about 60% of the lateral capacity under static loading
Shahin et al. (2011)	Cyclic triaxial tests on reconstituted soft clay	<ul style="list-style-type: none"> • Confirmed concept of critical stress level below which a state of non-failure stress equilibrium exists • No degradation occurred up to CSR=0.63 • Degradation was dependent on the value of OCR
Garnier (2013)	Cyclic tests on sand and clay samples, static load testing, centrifuge testing	<ul style="list-style-type: none"> • Increasing pile head displacements with applied cycles at service loads • Displacements dependent on severity of applied cyclic loads • Displacements higher than API predicted values above 10 cycles
Jardine (2012)	Literature review	<ul style="list-style-type: none"> • Rate effects impact clays more than sands • Cyclic load thresholds exist below which no degradation occurs • Cyclic failure affected by local shaft capacity

EVALUATION OF CYCLIC DEGRADATION IN COHESIVE SOIL

Axial Cyclic Degradation

In order to evaluate the overall stability under cyclic loading, various simplified analysis methods have been proposed based on results of experimental results by various researchers. The general approach primarily consists of comparing the amplitude of cyclic loading with the static capacity and defining thresholds for cyclic failure (e.g., Jardine, et. al. 2012; Steenfelt et al. 1981). Design charts are typically presented in the form of interaction diagrams relating the average and cyclic load components normalized with the static capacity (Figure 1).

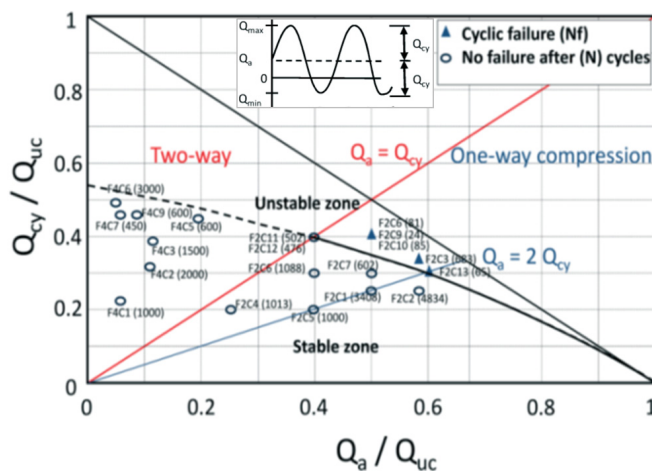


FIG. 1. Cyclic interaction diagram for bored pile in high OCR clay (after Puech, 2013).

(Q_{cy} is cyclic load, Q_a is average load and Q_{uc} is ultimate static capacity)

The interaction diagrams indicate that cyclic degradation would not be anticipated when cyclic loading levels remain below a certain threshold. Puech (2013) found that the threshold was largely dependent on the amplitude of cyclic load Q_{cy} and the average value of the load Q_a and developed a cyclic interaction diagram for screening analysis of pile's potential sensitivity to cyclic loading. The data points below the unstable zone curve indicate no cyclic failure. Cyclic loading of relatively small magnitude was also reported to potentially increase pile capacity by accelerating the ageing process (Jardine 1998) similar to effects previously indicated by others (Bea et al. 1980; Poulos, 1981). A simplified threshold for pile degradation under one-way cyclic loading was defined as the ratio of $(Q_{cy} + Q_a)/Q_{uc}$ of about 0.8 (Jardine et al., 2012). Overall, the reviewed information suggests that the potential for cyclic degradation would be expected to be low if the cyclic load components remain below about 20% of the ultimate static axial pile capacity.

A variety of degradation criteria have also been postulated for skin friction and end bearing. Poulos (1981) presented cyclic degradation criteria in terms of degradation factors D_N defined as the ratio of the property after cyclic loading and the property under static loading. Matlock and Foo (1979) similarly studied cyclic axial behavior

of pile foundation by using a hysteretic and degrading soil model. They developed a relatively simple degradation model which is expressed as:

$$D_N = (1 - \lambda)^N + [1 - (1 - \lambda)^N]D_{\min} \quad (1)$$

Poulos (1988) recommends the following values for degradation parameters λ and D_{\min} :

Table 3. Recommended Values of Degradation Parameters (after Poulos 1988)

Pile Type	Soil Type	λ	D_{\min}
Driven or Jacked Pile	Clay	0.2 – 0.4	0.4 – 0.6
	Silica Sand	0.2 – 0.4	0.5 – 0.7
	Calcareous Sand	0.3 – 0.6	0.2 – 0.6
Drilled Pile	Clay	-	-
	Silica Sand	0.3 – 0.5	0.2 – 0.4
	Calcareous Sand	0.4 – 0.6	0.05 – 0.1

For clay soils, the model indicates maximum degradation of between 40 and 60% although corresponding stress or strain levels which would be expected to impact the level of degradation are not directly incorporated. The degradation level of between 40 and 60% also appears to be within the typical range indicated by various researchers based on conducted literature review.

The reviewed cyclic degradation models for pile foundations are also consistent with the general behavior of soils under cyclic loads discussed in the literature. Idriss et al. (1978) studied cyclic degradation properties of soft clay based on the results of cyclic triaxial tests and proposed a degradation model to describe the relationship between degradation index and number of cycles. The test results indicated that the rate of degradation was essentially controlled by the amplitude of the cyclic axial strain and the degradation factor is expressed as:

$$D_N = N^{-t} \quad (2)$$

Correlations between the degradation parameter (t), cyclic shear strains and plasticity index have been obtained by Tabata and Vucetic (2010) and appropriate values can therefore be selected for specific values of plasticity index and applicable cyclic shear strains for assessment of stiffness degradation. For reference, cyclic shear strains of about 0.1% are typical of wind turbine foundation loading (DNV/RISØ, 2002).

With regard to threshold levels of loading below which degradation would not be expected, Sangrey, et. al. (1969) discussed the concept of Critical Level of Repeated Loading (CLRL). Based on results of cyclic load tests, at levels of loading below the CLRL, cyclic degradation of the soil would not be expected. Strain-based thresholds have also been developed (Vucetic, 1994) which define cyclic shear strain levels

below which soil stiffness degradation would not be expected. Degradation relationships provide a useful tool in evaluating potential cyclic degradation for wind turbine pile foundations relative to the applied cyclic stresses, expected strains and the number of load cycles. Since the resulting levels of degradation may vary depending on the analysis framework or model selected, considering various approaches applicable to the soil type and anticipated loading conditions appears to be a prudent approach. Additional discussion of the unique nature of design loads for utility scale wind turbines, which makes them ideal for applying cyclic degradation principles for foundation designs, is presented later in this paper.

Lateral Cyclic Degradation

Laterally loaded piles are typically analyzed by using the p-y concept which provides a relationship between the mobilized resistance of the surrounding soil and pile deflection. Although several references (DNV/RISØ 2002 and API-RP-2A-WSD 2000) provide guidance for generating p-y curves considered to be representative of cyclic loading the formulations do not reduce the static ultimate lateral resistance p_u by capturing the effects of the cyclic load characteristics and the number of cycles (Garnier, 2013). Therefore, the main objective should be to consider the amplitude of the cyclic loading and the number of cycles applied that will result in soil strength degradation and to determine a degradation coefficient that can be used to calculate the degraded lateral resistance.

Cyclic p-y curves for clay soils provide an envelope to the behavior of a pile under cyclic loading (Figure 2) and can be approximately derived from the static curves by introducing a degradation coefficient r_c which was found to be a function of cyclic load characteristics (Q_{cy} and Q_a), number of cycles, depth below the pile head and the cyclic load to static pile capacity ratio (Khemakhem, 2012).

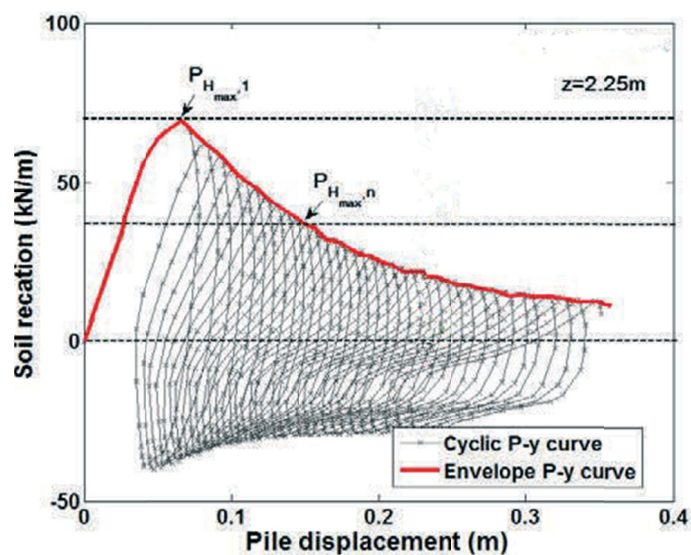


FIG. 2. Example of envelope P-y curve (after Khemakhem 2012).

Garnier (2013) proposed a global analysis based on the results of centrifuge modelling tests in regard to the lateral cyclic response of pile foundations under operational condition where pile loads are less than 1/3 of the ultimate static pile capacity. The global analysis method estimates the evolution of normalized pile head displacement and maximum bending moment under the cyclic loading and is expressed for cohesive soils as follows:

$$\frac{y_N}{y_1} = k \times N^\alpha ; \frac{M_{\max,N}}{M_{\max,1}} = \mu \times N^\beta \quad (3)$$

where y_N and $M_{\max,N}$ are displacement and maximum bending moment at cycle N ; y_1 and $M_{\max,1}$ are displacement and maximum bending moment at cycle 1 (or end of static loading phase); k, α, β, μ are empirical parameters and dependent on the cyclic load level, soil conditions and pile geometry (stiffness).

As discussed for axial loading, it is apparent that under smaller cyclic stresses the soil is not likely fail (for lateral cyclically loaded soils, failure can be defined in terms of accumulated strain) even when subjected to a large number of cycles similar to the CLRL or threshold strain concepts discussed herein. In addition, Lee and Focht (1976) indicate that cyclic deterioration appears to be a strain dependent process by which cyclic strains develop large excess pore pressures that in turn lead to softer and weaker soil and therefore a lower threshold value should be considered for saturated soils.

DISCUSSION

As discussed herein, various researchers have developed models and frameworks for evaluating both axial and lateral behavior of pile foundations under cyclic loading. Cyclic behavior of pile foundations is noted to be a function of various factors including the cyclic load level, number of load cycles, loading rate and direction of loading. “Two-way” cyclic loading tends to cause much more dramatic degradation than “one-way” loading (Poulos, 1983; Seed, 1966). In the design of onshore wind turbine pile foundations, degradation effects are typically indirectly accounted for by limiting two-way cyclic loading in the piles under normal operating conditions. The design approach for axial cyclic loading essentially involves evaluating specific pile configurations and ensuring that all piles only experience compressive forces during normal operation (i.e. no two-way loading in the piles). For lateral loading, the approach essentially consists of developing P-y relationships for static loading conditions and applying factors to account for additional deformations. Although the current typical approaches appear to result in reliable foundation performance, they may also lead to overly conservative designs and translate into increased foundation costs for projects. Optimizing the foundation designs by utilizing the available body of research on cyclic degradation of soils is therefore beneficial and would lead to reduced costs for foundations. On-going studies such as those described by Peuch (2013) are providing encouraging results which appear to represent enhancements to current typical approaches by incorporating cyclic loading characteristics and number of loading cycles in the frameworks.

Although there are a wide range of approaches that can be adopted, frameworks that incorporate appropriate strength and deformation properties of the soil, number of load cycles, representative pile loads and strains due to cyclic loading and cyclic thresholds for loads and strains would be expected to provide reliable results. An example framework based on recommendations by Jardine et al. (2012) is presented in Figure 3 for evaluating potential cyclic effects on wind turbine pile foundations.

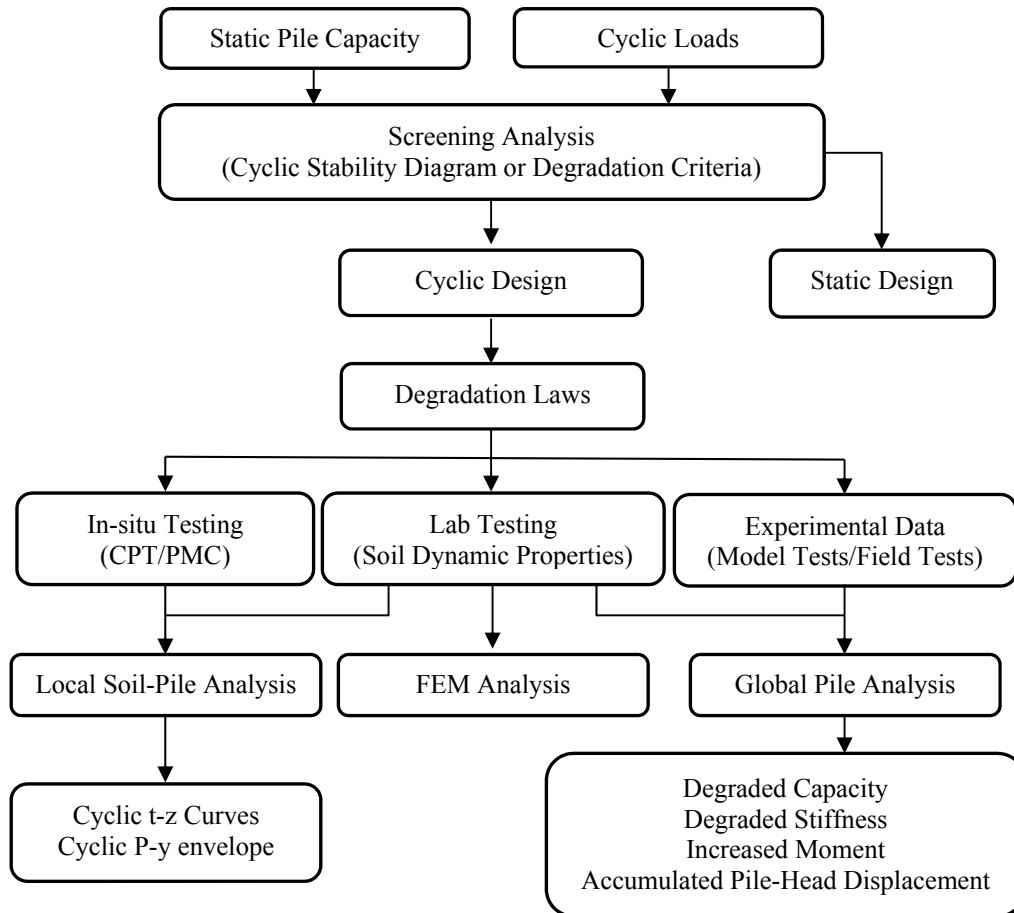


FIG. 3. Example framework for evaluating soil cyclic degradation for wind turbine pile foundations (After Jardine, et. al., 2012).

Overall, the pile foundation design parameters including pile dimensions and embedment depths should be determined by incorporating appropriate safety margins and ideally be based on the results of laboratory cyclic soil testing and full scale axial and lateral pile load testing.

CONCLUSIONS

In this study, a comprehensive review has been performed on available standards and codes for designing of pile foundations for wind turbines. It is noted that the effects of cyclic loading for pile foundation design are not addressed in great detail in

these standards. The mechanisms of cyclic effects on pile foundations in cohesive soils have been summarized in this paper based on a review of research findings reported in the literature.

Current typical practice for design of onshore wind turbine pile foundations indirectly accounts for axial loading degradation effects by limiting two-way cyclic loading in the piles under normal operating conditions. Commonly used standards (e.g. DNV/RISØ 2002 and API-RP-2GEO 2014) provide guidance for generating P-y curves considered to be representative of cyclic loading but do not directly incorporate the effects of the cyclic load characteristics and the number of cycles. The approaches which are currently in use for cyclic loading design for onshore wind turbine pile foundations appear to be reliable but may also lead to overly conservative designs and translate into increased foundation costs for projects in poor soil conditions or as turbines continue to increase in size with increasing design cyclic and extreme loads. Therefore, approaches which consider the amplitude of the cyclic loading and the number of cycles applied as discussed herein provide more reliable results to represent soil strength degradation and cyclic load response and deformations of the piles. Wind turbine pile foundation designs could be further optimized by utilizing the available body of research on cyclic degradation of soils and foundation response to develop more efficient designs and reduce foundation costs.

REFERENCES

- API (2014). "Geotechnical and Foundation Design Considerations." *ANSI/API Recommended practice 2GEO*, Addendum 1, October 2014, American Petroleum Institute.
- API (2000). "Recommended practice for planning, designing and constructing fixed offshore platforms – working stress design." 21st Edn. Washington, DC, American Petroleum Institute; 2000 RP2A-WSD.
- Bea, R.G., Audibert, J.M.E., and Dover, A.R. (1980). "Dynamic response of laterally and axially loaded piles." *Proc. 12th OTC Conf.*, Houston, Paper OTC 3749, 129-139.
- BSH (2007). "Design of offshore wind turbines." *Standard*, Federal Maritime and Hydrographic Agency, Hamburg and Rostock, 20 December 2007.
- DIN 1054: 2010-12 (2010). "Subsoil - Verification of the safety of earthworks and foundations - Supplementary rules to DIN EN 1997-1." *Standard*, December 2010.
- DNV Offshore Standard DNV-OS-J101 (2011). "Design of offshore wind turbine structures." *Standard*, Det Norske Veritas, September 2011.
- DNV/RISØ (2002). "Guidelines for design of wind turbines." Second Edition.
- Garnier, J. (2013). "Advances in lateral cyclic pile design: contribution of the SOLCYP project." *Proc. Of TC 209 Workshop*, 18th ICSMGE, Paris, September 2013.
- Grosch, J.J. and Reese, L.C. (1980). "Field tests of small-scale pile segments in a soft clay deposit under repeated axial loading." *Proc. 12th OTC Conf.*, Houston, Paper OTC 3869, 143-151.

- Hauschidt, M., Kirsch, F., and Richter, T. (2011). "Analysis of axial-cyclic loaded piles from the certifier's view." *Proc. of EWEA Offshore 2011 conference*, Amsterdam.
- Idriss, I.M., Dobry, R. and Singh, R.D. (1978). "Nonlinear behavior of soft clays during cyclic loading." *J. Geotechnical Engineering. Div., ASCE*, Vol.104 (12): 1427-1447.
- Jardine, R.J. (1998). "Interim Report on Cyclic Loading Model and Synthetic Soil Profile for HSE Funded Pile Cyclic Loading Study", Imperial College Consultants (ICON), 1998.
- Jardine, R.J., Puech A. and Andersen, K.H. (2012). "Cyclic Loading of Offshore Piles: Potential Effects and Practical Design." *7th Int. Conf. on Offshore Site Investigations and Geotechnics*, Society for Underwater Technology, 59-100.
- Khemakhem M. (2012). "Experimental study of a bored pile response under monotonic and cyclic lateral loads in clay", *Thèse, Ecole Centrale de Nantes*, 314.
- Lee, K.L. and Focht, J.A. (1976). "Strength of clay subjected to cyclic loading." *Marine Geotechnology*, Vol. 1 (3): 165-185.
- Lombardi D., Bhattacharya, S. and Wood D.M. (2013). "Dynamic soil-structure interaction of monopile supported wind turbines in cohesive soil." *J. Soil Dyn. Earthquake Engrg.*, Vol.49: 165-180.
- Matlock, H. and Foo, S. C. (1979). "Axial analysis of a pile using a hysteretic and degrading soil model." *Proc., Numerical Methods in Offshore Piling*, Institution of Civil Engineers, London, England, 165-185.
- Morgan, K. and Ntambakwa, E. (2008). "Wind turbine foundation behavior and design considerations." *AWEA WINDPOWER Conference*, Houston, 1-14.
- Puech, A. (2013). "Advances in axial cyclic pile design: contribution of the SOLCYP project." *Proc. Of TC 209 Workshop*, 18th ICSMGE, Paris, September 2013.
- Poulos, H.G. (1981). "Some aspects of skin friction of piles in clay under cyclic loading." *Jnl. Geot. Eng.*, Vol. 12 (1): 1-17.
- Poulos, H.G. (1983). "Cyclic axial pile response – alternative analyses." *Spec. Conf. on Geot. Practice in Offshore Eng.*, ASCE, Austin, 403-421.
- Poulos, H.G. (1988). "Cyclic stability diagram for axially loaded piles. " *Jnl Geotechnical and Geoenvironmental Engineering*, Vol.114 (8): 877-895.
- Puech, A. and Jezequel, J.F. (1980). "The effect of long time cyclic loadings on the behavior of a tension pile." *Proc. 12th OTC Conf.*, Houston, Paper OTC 3870, 153-162.
- Steenfelt, J.S., Randolph, M.F. and Worth, C.P. (1981). "Model tests on instrumented piles jacked into clay." *Proc. 10th Int. Conf. S.M. & F.E.*, Stockholm, Vol. 2: 857-864.
- Sangrey, D. A., Henkel, D. J., and Esrig, M. I. (1969). "The effective stress response of a saturated clay soil to repeated loading." *Canadian Geotechnical Journal*, Vol. 6 (3): 241-252.
- Seed, H.B. and Chan, C.K. (1966). "Clay strength under earthquake loading conditions." *J. Soil Mech. and Fnds. Div.*, ASCE, Vol. 92(2): 53-78.
- Shahin, M.A., Loh, R.B.H., and Nikraz, H.R. (2011) "Some Observations on the Behavior of Soft Clay under undrained cyclic loading." *J. GeoEngineering*, Vol. 6 (2): 109-112.

- Tabata, K. and Vucetic, M. (2010). "Threshold Shear Strain for Cyclic Degradation of Three Clays." *Proc. 5th Intl. Conf. on Recent Advances in Geotechnical Earthquake Engineering and Soil Dynamics and Symposium in Honor of Professor I.M. Idriss*, No. 1.15a, San Diego, California.
- Tuladhar, R., Maki, T. and Mutsuyoshi, H. (2008). "Cyclic behavior of laterally loaded concrete piles embedded into cohesive soil." *Earthquake Engng. Struct. Dyn.*, 37: 43–59.
- Vucetic, M. (1994). "Cyclic Threshold Shear Strains in Soils." *J. Geotech. Engrg.*, ASCE Vol. 120 (12): 2208-2228.
- Yilmaz, M.T., Pekcan, O. and Bakir, B.S. (2004) "Undrained cyclic shear and deformation behavior of silt-clay mixtures of Adapazari, Turkey." *Soil Dynamics and Earthquake Engineering*, 24: 497-507.

Deep Foundations under Wind Turbines—A Case Study

Önder Akçakal, M.Sc.¹; Ertun Sözen, B.Sc.²; Turhan Karadayılar, M.Sc.³;
Selim İkiz, M.Sc.⁴; and H. Turan Durgunoğlu, Ph.D., P.E., G.E., F.ASCE⁵

¹Technical Office Manager, ZETAŞ Alemdağ Reşadiye Caddesi 69/A Çekmeköy, Istanbul, Turkey. E-mail: onder.akcakal@zetas.com.tr

²Business Development and Contract Manager, ZETAŞ, Turkey. E-mail: ertun.sozen@zetas.com.tr

³Executive Committee Member, ZETAŞ, Istanbul, Turkey. E-mail: karadayilart@zetas.com.tr

⁴Executive Committee Member, ZETAŞ, Istanbul, Turkey. E-mail: selim.ikiz@zetas.com.tr

⁵Chairman, ZETAŞ, Istanbul, Turkey. E-mail: durgunoglut@zetas.com.tr

Abstract: Wind is an essential way of renewable energy which adopted by many countries as a part of their strategy to reduce dependence on fossil fuels. In the last decades, wind farm investments that consist of a series of wind turbines are widely being constructed in the western part of Turkey. One of them with 15 wind turbines was planned on Söke plain where thick alluvial deposit exists with loose sand and soft clay layers under high water table. Due to the wind forces, high seismicity of the area and unfavorable subsoil conditions bored piling under the foundation was recommended. In the planning stage of the project, 52 numbers of 40 m long bored piles with 800 mm diameter under each turbine were proposed by the super-structural engineer. To provide economy to the project and fulfill the time requirement of the employer 6 numbers of 2,000 mm diameter bored piles were proposed by the contractor company. Soil investigation boreholes were conducted under each turbine and mechanical properties of soil layers were determined precisely based on SPT, CPT, SDMT and UU test results. Bored piles were designed with a depth between 35 and 39 m. Also due to the high seismicity and liquefaction risk 15 m deep soil improvement with jet grouting columns was proposed between the piles. Intense sulfate aggressiveness was pointed within the chemical test results therefore sulfate resistant type cement was used. In addition, reinforcement cage was designed considering crack width criteria and coated with epoxy. Performance of the bored piles was tested with bi-directional static loading test; bearing capacity and settlement of the pile were recorded as accomplishing the project requirements. 2000 mm diameter bored piles with soil improvement alternative provided economy to the project and completed successfully in timely manner.

Keywords: Wind turbines, Deep foundations.

INTRODUCTION

Energy demand of Turkey is increasing in parallel with the development of industry and Ministry of Energy and Natural Sources (2015) announced that

electricity consumption is expected to rise to 357.4 TWh in the year 2020 by an annual average rate of 5.5%. Total electricity output was declared as 239.3 TWh in 2013 and this means that demand will be 50% higher than this capacity in 2020. Therefore, new thermal and hydraulic power plant investments are being constructed by private sector to catch up with the increasing energy demand and to reduce the energy import. There are also some studies on two nuclear power plant projects. Beside these, investors are encouraged for renewable sources, as a part of the strategy to reduce dependence on fossil fuels. Contribution of the renewable sources is only 4% in 2013, where 43.8% contribution comes from natural gas, 24.5% from coal, 24.8% from hydraulic energy and 2% from liquid fuels (MENS, 2015). Portion of the renewable energy is expected to be increased with the new wind, solar and biomass power plant projects in near future.

In Turkey, wind energy was firstly used for electricity generation in 1986 with 55kW nominal energy for general use however; first power plant was constructed in 1998 with a capacity of 1.5 MW (Hepbasli & Ozgener, 2004). Total available potential for wind power is approximately 88,000 MW annually and most attractive locations for wind energy are southeastern part and west coast of Anatolia (Hepbasli & Ozgener, 2004). Today there are 101 wind power plants under operation and cumulative installed capacity for wind power is increased up to 3762 MW in the end of 2014 (TWEA, 2015).

One of the wind power plant investments was planned in Söke Plain, which extends on the fertile alluvial deposits of Greater Menderes River in Aydın province on the west coast of Turkey. Design and construction of deep foundations for the wind turbines of this project are summarized within this study.

PROJECT PROPERTIES

Turbine locations were determined between the farms lay alongside the Söke – Milas state road D525 in Aydın Province. This location is on the northern side of the Söke Plain and the south side of the Dilek Mountain that orients and concentrates the wind flows. As given in the Figure 1, wind speed (50m) of this area is indicated as between 7.0 and 7.5 m/s by MENS (2015).

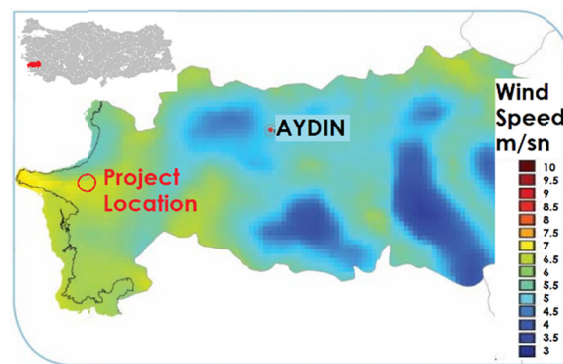


FIG. 1. Wind Speed Distribution Map of the Province, (MENS, 2015)

Construction of fifteen wind turbines was planned with a total 30 MW installed capacity within the project. Turbines were located with an average 400 m distance to each other and connected with a stabilized road for construction and maintenance purpose. Turbines have a hub height of 78 meters and a rotor with three blades. Aerial view of the project and locations of the turbines are given in the Figure 2.

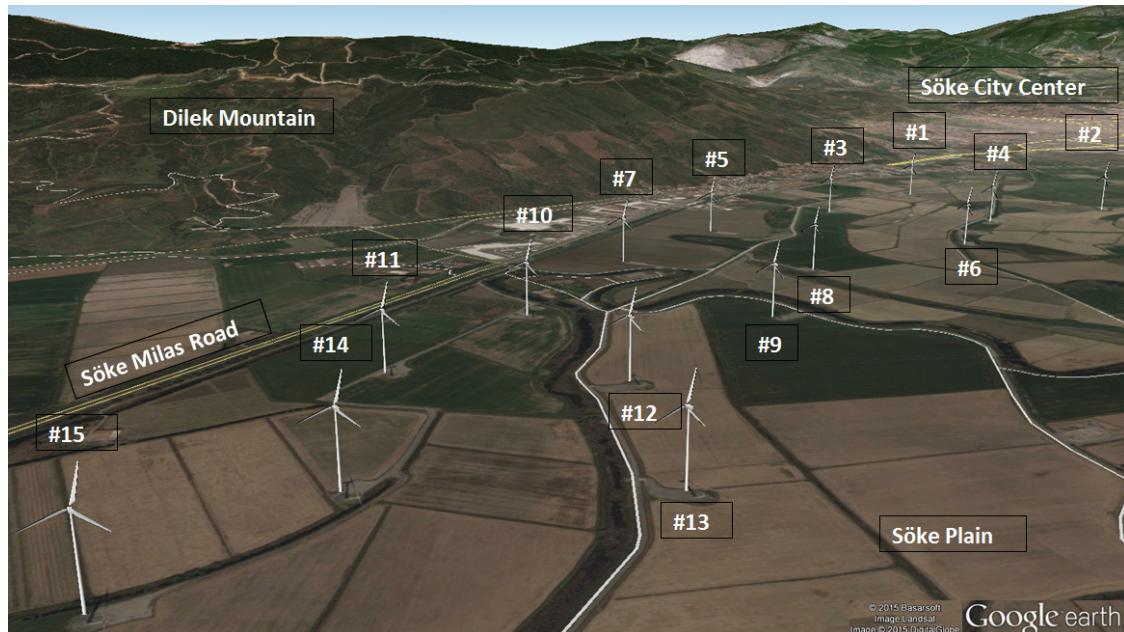


FIG. 2. Aerial view of the project and locations of the turbines (Google Earth, 2015)

SOIL PROFILE

To determine the soil profile 3 boreholes with Standard Penetration Tests (SPT), 28 Cone Penetration Test (CPT) and 5 Marchetti's Dilatometer Test with additional seismic measurement (SDMT) were conducted within the soil investigation studies.

As illustrated in Figure 3 mainly clayey sand and sandy clay layers were encountered. Sand layers were described as loose to dense and contain silt particles with high plasticity. Clay and silt layers were defined as soft to stiff with sand content. Bedrock was not encountered during the soil investigation studies (Ozmen et al., 2010).

Shear parameters are calculated based on conducted SPT, CPT, SDMT and UU tests. Distribution of the shear strength parameters based on the different in-situ and laboratory tests are plotted in the Figure 4.

Soil profiles under the wind turbines are classified in five (5) groups according to the encountered soil types and test results (Table 1). Shear strength parameters are determined based on the in-situ and laboratory test results which summarized all together in the Figure 4. They were separated into groups regarding the Turbine locations.

Soil parameters for each Turbine groups were determined. Although CPT results pointed high friction angles for the top layers, maximum 32° value was selected to be on the safe side.

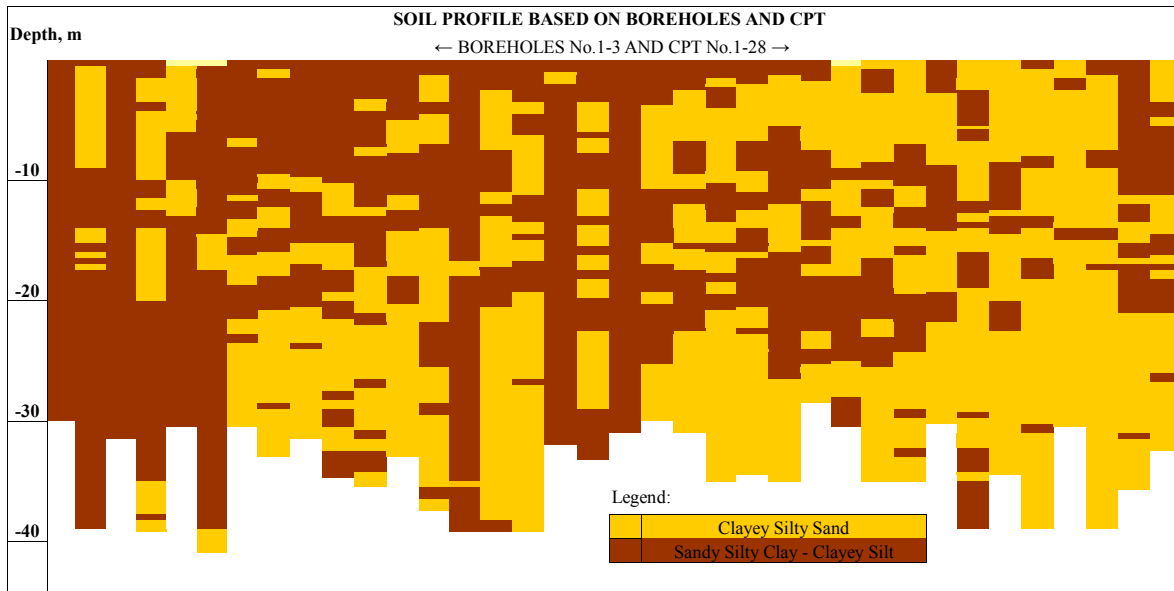


FIG. 3. Soil Profile based on Boreholes and CPT (Ozmen et al., 2010)

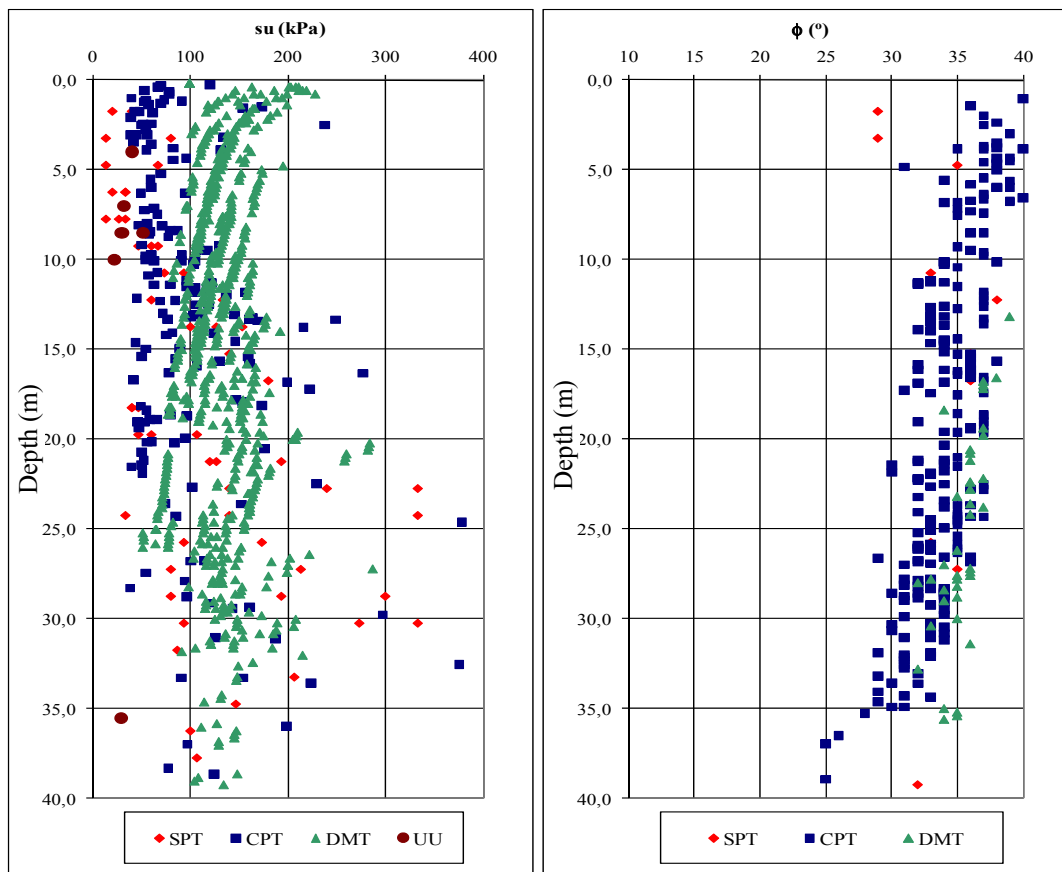


FIG. 4. Distribution of the Shear Strength Parameters Based on the Different In-situ and Laboratory Tests (Ozmen et al., 2010)

Table 1. Soil Profiles under the Wind Turbine Groups

Soil Profile	Soil Profile				
	Turbines; 1-3-4	Turbines; 2-6	Turbines; 5-7-8	Turbines; 9-10-11-15	Turbines; 12-13-14
	Group 1	Group 2	Group 3	Group 4	Group 5
0 m	$\phi=32^\circ$	$su=40 \text{ kPa}$	$\phi=32^\circ$	$su=50 \text{ kPa}$	$su=50 \text{ kPa}$
5 m	$\phi=32^\circ$	$\phi=32^\circ$	$\phi=32^\circ$	$\phi=32^\circ$	$\phi=32^\circ$
10 m	$\phi=32^\circ$	$\phi=32^\circ$	$su=75 \text{ kPa}$	$\phi=32^\circ$	$\phi=32^\circ$
15 m	$su=75 \text{ kPa}$	$su=75 \text{ kPa}$	$su=75 \text{ kPa}$	$su=75 \text{ kPa}$	$su=50 \text{ kPa}$
20 m	$\phi=30^\circ$	$\phi=31^\circ$	$\phi=31^\circ$	$\phi=32^\circ$	$\phi=31^\circ$
25 m	$su=50 \text{ kPa}$	$\phi=31^\circ$	$su=75 \text{ kPa}$	$su=50 \text{ kPa}$	$\phi=31^\circ$
30 m	$su=50 \text{ kPa}$	$\phi=31^\circ$	$\phi=31^\circ$	$\phi=31^\circ$	$\phi=30^\circ$
35 m	$su=50 \text{ kPa}$	$\phi=31^\circ$	$\phi=30^\circ$	$\phi=31^\circ$	$\phi=30^\circ$
40 m	$su=75 \text{ kPa}$	$\phi=31^\circ$	$\phi=30^\circ$	$\phi=31^\circ$	$\phi=30^\circ$
45 m	$su=75 \text{ kPa}$	$\phi=31^\circ$	$\phi=30^\circ$	$\phi=31^\circ$	$\phi=30^\circ$
	Sandy Silty Clay - Clayey Silt			Clayey Silty Sand	

Greater Menderes River is the main stream of the area and there are irrigation and drainage canals used for collecting and distribution of source water inside the plant site. Groundwater level increases to the ground surface level with the seasonal precipitation in the area. Besides, sometimes floods are encountered on the Greater Menderes River and its branches. Groundwater level with respect to the ground level is found to be varying between the depths 0.3-0.5 m (Zemin Etüd, 2010).

TENDER PHASE AND PRELIMINARY DESIGN

An appropriate deep foundation system was needed under the turbines because of the weak subsoil conditions, high ground water table and seismicity of the area. In the tender phase employer requested a preliminary design from the super-structural designer and as illustrated in Figure 5, a deep foundation design was submitted with 52 numbers of 40 m long bored piles with 800 mm diameter under each turbine.

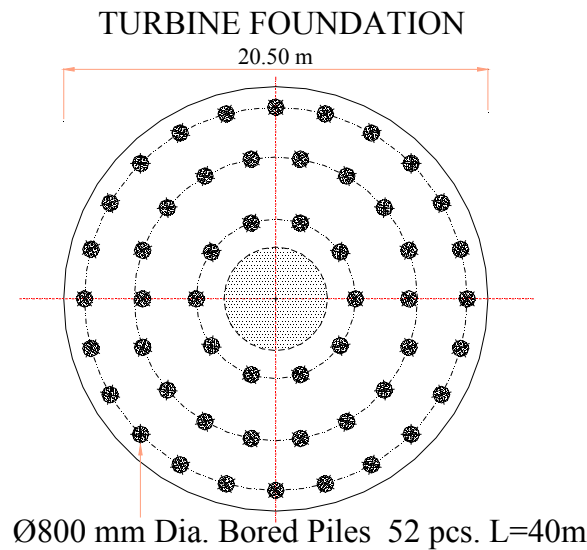


FIG. 5. Preliminary Design Submitted by Employer in the Tender Phase

Preliminary design was prepared after the demobilization of the soil investigation equipment from the site therefore additional studies deeper than 40 m could not be performed. Bored piles were scattered on three numbers of radial axes under the foundation. To cover all of these bored piles, construction of 20.50 m diameter foundation was planned. Thickness of the foundation was given as 180 cm in the drawings.

VALUE ENGINEERING STUDIES

Site was also located in a seismic region and existence of the high groundwater table brings a serious liquefaction risk. The spacing between the bored piles was not close sufficiently in the preliminary design; therefore, liquefaction of the subsoil between the piles was likely to occur during the earthquake. To eliminate the liquefaction risk, jet grouting was planned between the bored piles to improve the shear properties of the soil against earthquake loads. Magnitude of the earthquake and maximum lateral earthquake acceleration were considered as 7.0 (Richter scale) and 0.4g respectively.

Liquefaction risk of the sand layers was determined based on the method offered by Youd and Idriss (2001). Also method offered by Robertson and Fear (1997) was followed for an assessment with CPT data. Safety against liquefaction is determined as a ratio of Cyclic Resistance Ratio (CRR) and Cyclic Stress Ratio (CSR) which can be derived from results of soil investigation studies.

$$FS = \frac{CRR}{CSR_{design}}$$

Shear stresses induced by earthquake concentrate on jet grout columns because of their shear modulus contrast with soil. Therefore, CSR_{design} for the soil between jet grout columns can be calculated with considering a reduction factor (S_G). This reduction factor (S_G) is calculated considering the area replacement ratio (a_r) and shear modulus ratio (G_r) between the jet grout columns and soil.

$$S_G = \frac{1}{G_r} \times \frac{1}{\left[a_r + \frac{1}{G_r} \times (1 - a_r) \right]}$$

$$CSR_{design} = S_G \times CSR$$

Required area replacement ratio is calculated as 8% for the project therefore Ø800 mm diameter jet grout columns were planned with minimum 2.50 m spacing center to center. Length of the jet grout columns was selected 15 m to provide mitigation of liquefiable layers.

Beside the liquefaction phenomena, to provide economy and satisfy the tight construction schedule it is planned to reduce the number of the bored piles with larger diameters. Therefore, six (6) numbers of Ø2000 mm bored piles with depths varying between 35 and 39 m were planned under the turbine foundation. Pile loads were calculated considering the reported forces (Table 2) and bending moments transferred from tower to foundation under both static and seismic conditions.

Table 2. Transferred Loads, Bending Moments and Calculated Bored Pile Loads

	F vertical, kN	M _x , kNm	M _y , kNm	F _{max, pile} Compression, kN	F _{max, pile} Tension, kN
Operational Loading	13275	31232	1545	3814	-
Extreme Wind Condition	13015	58738	177	5181	843
Seismic Condition	13275	56920	1545	5131	706

Applied axial pile load in compression was calculated as 3814 kN under the repetitive static loads and 5181 kN under the seismic or extreme wind load conditions. Maximum tension load was calculated as 843 kN under the seismic or extreme wind load conditions. Due to the strict differential settlement criteria (1mm/m), bearing capacities were calculated considering only skin friction.

Typical layout and section of the proposed deep foundation and soil improvement applications are given in the Figure 6. The diameter and the height of the foundation were calculated as 16 m and 2 m respectively.

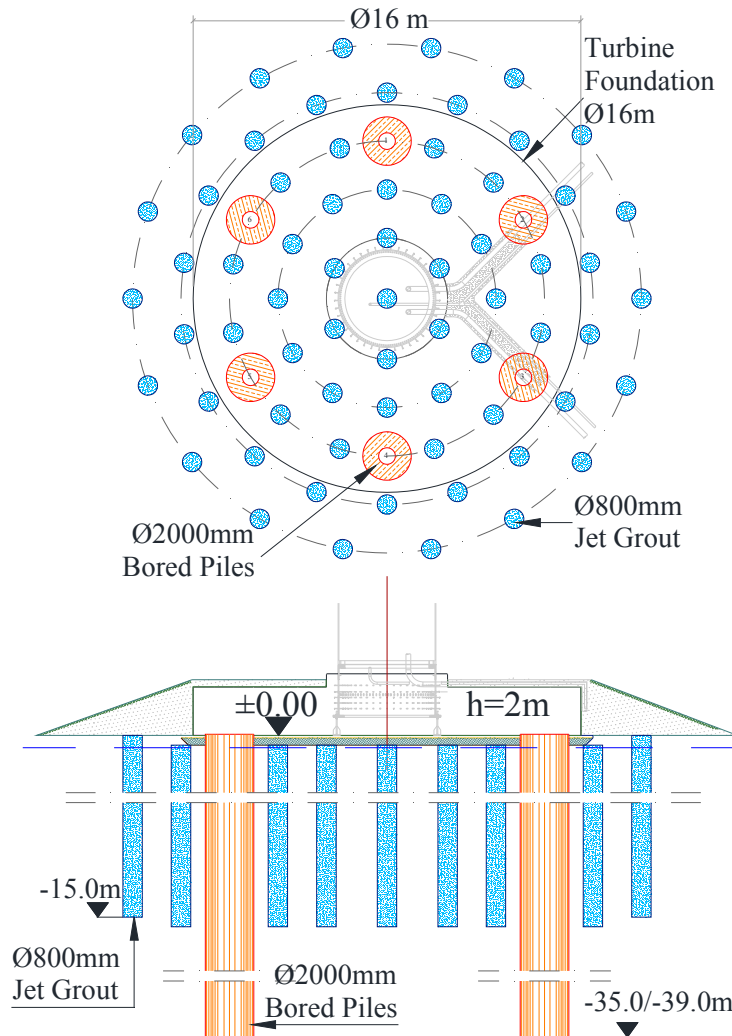


FIG. 6. Proposed Design, Deep Foundation and Soil Improvement Applications

Selected lengths and calculated bearing capacities of the piles for each wind turbine groups are calculated and summarized in the Table 3.

Table 3. Wind Turbine Groups and Calculated Lengths

	Pile Length	Pile Dia.	Pile Number	Allowable Vertical Capacity, kN		Allowable Tension Capacity, kN	
				Static	Dynamic	Static	Dynamic
Group 1 (Turbines; 1,3,4)	39 m	200 cm	6 nos	3880	5960	3570	5530
Group 2 (Turbines; 2,6)	35 m	200 cm	6 nos	3880	5970	3480	5360
Group 3 (Turbines; 5,7,8)	35 m	200 cm	6 nos	3890	5990	3500	5380
Group 4 (Turbines;	35 m	200 cm	6 nos	3860	5940	3470	5340
Group 5 (Turbines; 12,13,14)	37 m	200 cm	6 nos	3840	5910	3500	5390

DESIGN, CONSTRUCTION AND TESTING

Existing farm roads and bridges were found to be insufficient for transportation of the machinery and turbine components. Also due to the weak subsoil properties and high water level working platforms had to be designed and prepared prior to the commencement of the construction works.

Site roads were designed and constructed with 1 m thick compacted (modified proctor 98%) fill. Geotextile was applied under the fill to separate it from the subsoil. Bridges were replaced with precast reinforced concrete panels that supported with jet grout columns under the abutments. For working platform 1 m thick granular material was filled and compacted (modified proctor 98%) with 3 layers of geogrids to improve the bearing capacity of the fill.

Average sulfate content is determined as 2064 mg/L in the soil investigation report therefore sulfate aggressiveness is determined as “intense” based on DIN 4030 for concrete. Concrete cover is determined to be 10 cm and cement type is determined as sulfate resistant which face groundwater for the jet grout columns and of concrete mixes. To limit the crack width of the piles in tension and bending reduced yield strength is considered in calculation of the required longitudinal bar area. Furthermore, to increase the resistance against aggressiveness of the groundwater epoxy coated reinforcement is used for top 12 m of the cage.

Bored piles were constructed with a 260 kNm installed torque capacity piling rig (Fig.7a-b). Except mobilizations between turbine locations, average production rate was recorded as one pile per day. Six numbers of bored piles were constructed in parallel with the soil improvement works in nine days for each turbine (Fig.7c). Bored piles were constructed after the neighboring jet grout columns to prevent any bending or damage during jet grouting.



FIG. 7a, 7b and 7c Construction of the bored piles (left-center) and jet grout columns (right)

Performance of the bored piles was tested with bi-directional static loading test. Hydraulic jacks with 2 x2500 kN capacity were located 19.60 m below the ground surface to equalize the friction of upper and lower parts of the pile. Test pile was loaded up to 7720 kN, which is approximately two times of the working load. Load-displacement and equivalent top load – settlement charts are given in the Figures 8 and 9 respectively. Total top settlement was calculated as 2.7 mm as a result of the test.

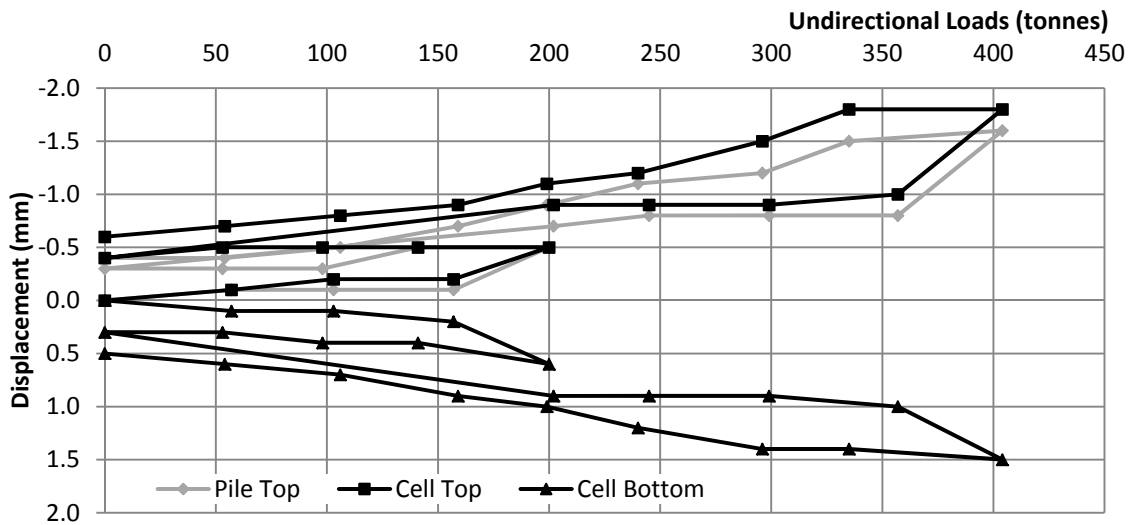


FIG. 8 Bi-directional Static Pile Test, Load - Movement Plot (Cherian et al.)

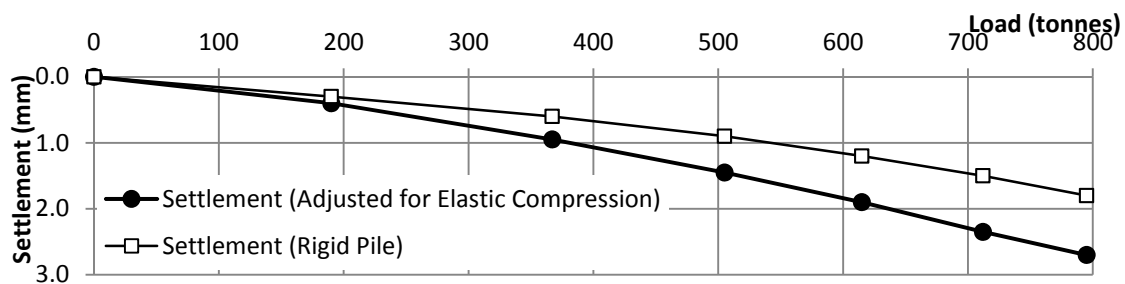


FIG. 9 Equivalent Top Load vs Settlement Chart (Cherian et al.)

Differential settlement was limited with 1mm/m and maximum settlement was calculated as 16 mm for the foundation with 16 m diameter. Test results showed that

project requirements are sufficiently provided. Bearing capacity and settlement of the test pile were reported as accomplishing the project requirements as a result of the test.

CONCLUSION

Foundation system of a wind farm project which was planned to be constructed on weak alluvium deposits of Grater Menderes River was studied and a concept of large diameter piles with soil improvement was proposed to fulfill the difficult project and schedule requirements. 2000 mm diameter bored piles and jet grout columns mitigating the top layers against liquefaction were designed after a comprehensive value engineering study. Six numbers of bored piles were constructed under each turbine with lengths varying between 35 and 39 m regarding the categorized soil profiles. Site roads and working platforms were improved with compacted fill and geogrids prior to the mobilization. Bi-directional static loading test was performed on a test pile and the design was proofed prior to the construction. With the proposed foundation system, approximately 20% economy could be provided to the project and large diameter bored piles with jet grouting could be completed in a successful and timely manner.

REFERENCES

- Hepbasli, A. and Ozgener, O. (2004). "A review on the development of wind energy in Turkey." *Renewable and Sustainable Energy Reviews*, Vol. 8, Pages 257–276.
- Cherian, A. (2010) *Wind Power Plant Project Bi-directional Static Load Test Report*, Dubai, Strain-stall Middle East LLC.
- Deutsches Institut Fur Normung E.V., Assessment of water, soil and gases for their aggressiveness to concrete -Part: Principles and limiting values, 2008, DIN 4030-1
- Google Earth 7.1.5.1557. 2015. Söke Plain 37°41'59.03"N, 27°23'19.95"E, elevation 660m. 3D Buildings data layer. <http://www.google.com/earth/index.html> Viewed 25 August 2015.
- Ozmen, G., Hacialioglu, E. and Uncu, E. (2010). *Wind Power Plant Subsoil and Foundation Investigation Report*, Istanbul, Zemin Etüd ve Tasarım A.Ş.
- Republic of Turkey Ministry of Energy and Natural Sources (MENS) (2015). Retrieved from <http://www.enerji.gov.tr/en-US/Pages/Electricity>
- Robertson, P.K., Fear, C. E. Cyclic Liquefaction and its Evaluation based on SPT and CPT, Proceedings of the NCEER Workshop on Evaluation of Liquefaction Resistance of Soils, Technical report NCEER-97-0022, pp.41-87, 1997
- Turkish Wind Energy Association (TWEA) (2015). Turkish Wind Energy Statistics Report, Retrieved from <http://www.tureb.com.tr/attachments/>
- Turkish Wind Energy Association (TWEA) (2015). Wind Energy Potential Maps, Retrieved from <http://www.eie.gov.tr/YEKrepa/AYDIN-REPA.pdf>
- Youd, T.L. and Idriss, I.M. (2001) "Liquefaction resistance of soils: Sum. Report from the 1996 NCEER and 1998 NCEER/NSF workshops on evaluation of liquefaction resistance of soils", *Journal of Geotechnical and Geoenvironmental Eng.*, Vol. 4, Pages 297-313

Design and Analysis of Foundations for Onshore Tall Wind Turbines

Shweta Shrestha¹ and Nadarajah Ravichandran²

¹Graduate Student, Glenn Dept. of Civil Engineering, Clemson Univ., 123 Lowry Hall, Clemson, SC 29634. E-mail: shwetast@clemson.edu

²Associate Professor, Glenn Dept. of Civil Engineering, Clemson Univ., 202 Lowry Hall, Clemson, SC. E-mail: nravic@clemson.edu

Abstract: Wind turbines play vital role in producing sustainable and clean energy to fulfill the growing need of energy. However, the design of foundation to support wind turbines, especially the taller tower which access steady and higher speed wind is always a challenge due to larger loads exerted at the foundation level. In this paper, the economic advantage of using raft foundation, pile group foundation, and piled-raft foundation is discussed based on the preliminary design results and parametric studies. For the sample design, the axial load, lateral load, and moment at the base of the tower were computed assuming the tower height of 130 m and mean wind speed of 160 mph. The comparison of the volume of material required for each foundation type showed that the piled-raft is the most economical option for the given site and loading conditions. A parametric study conducted by increasing the wind speed, tower height, and pile size resulted in increase in volume of material for the piled-raft. Another study on the effect of number of piles on the settlement revealed that the increase in number of piles while keeping the size and length constant, resulted in significant decrease in settlement up to certain number of piles and thereafter the addition of piles had negligible contribution in reducing the settlement.

INTRODUCTION

Over the past few decades, the generation of electricity from wind turbine has increased rapidly to meet the ever growing demand. Various government and non-government agencies, industries, and researchers around the globe have worked persistently to increase wind energy production. Unlike fossil fuels, it is more environmentally sustainable as the problems of heavy metal emission in air, production of toxic solid waste, and green house emission are not associated with the production of wind energy. It is also found to be a cost effective and reliable source of energy if designed and constructed at suitable sites. Wind turbine use has increased at a rate of more than 25 % a year, but it is still a small fraction of the world's energy demand. The worldwide operating wind power capacity by the end of the year 2014 was 369,597 MW and the percentage growth from the preceding year was 15.99 %

(GWEC, 2015). In the United States, the operating wind power capacity was 66,146 MW by the end of 2014 and the percentage growth from the preceding year was 7.9 % (BP, 2015). Researchers have been working continuously to increase the wind energy production and found that amount of energy available for extraction increases with the third power (cube) of wind speed. Lewin (2010) stated that an increase of turbine elevation from 80 m to 100 m would result in a 4.6% larger wind speed and a 14% increase in power output and an increase from 80 m to 120 m would result in an 8.5% greater wind speed and a 28% increase in power production. Hence, a logical cost-effective solution to increase wind energy production is to build taller wind turbine towers to access higher wind velocities. However, when the tower height increases, the size of the foundation also increases and the design becomes complex. Since a significant percentage of the total cost goes into the construction of foundation, it is necessary to develop cost effective foundations to support tall towers.

In this study, three foundation types (raft, pile group with pile cap, and piled-raft) were investigated to support a sample 130 m tall wind turbine at a potential wind farm site Charleston, SC in this case. Although Charleston lies in seismically active zone, the seismic load has not been presented in this paper. It was found that the piled-raft foundation is the most cost effective solution for the prevailing site conditions and loading. The detail discussion on piled-raft design is presented in the relevant section of this paper. But the pile group and raft foundation are discussed briefly due to page limitation. A parametric study was also performed on piled-raft foundation to evaluate the effect of design parameters on the foundation design and its response.

ASSESSMENT OF DESIGN PARAMETERS FOR A SAMPLE PROBLEM

Design load calculation

The design load consists of dead load and wind load. The dead load was calculated as sum of weight of tower and other components of wind turbine such as nacelle and rotor. The wind turbine tower considered in this study is a hybrid hollow cylindrical tapering tower with lower 93 m made of concrete (base diameter 12.0 m) and upper 37 m made of steel (top diameter 4.0 m). The dead load of tower was calculated using the corresponding unit weights of concrete and steel. The weight of nacelle and rotor was obtained from Malhotra (2011). For simplicity, the dead load is assumed to act at the center without considering the length of nacelle. The final dead weight was calculated to be 51.71 MN. The wind load was calculated considering the wind speed of 160 mph corresponding to Charleston, SC and following the procedure described in ASCE 7-10 (2010). The lateral load and moment acting at the base of the tower were obtained by considering the wind load along the tower height and drag force acting on the nacelle. The total lateral load and the bending moment were calculated to be 3.71 MN and 237.37 MNm, respectively.

Soil properties

The necessary geotechnical parameters of soil required for the design of piled-raft foundation were obtained from the geotechnical report of North Charleston, SC

(WPC, 2010). It is worth noting that geotechnical report was produced for constructing one of the world's largest turbines testing facility in Charleston, SC. The summary of the soil profile and geotechnical parameters are given in Table 1. At this site, the location of ground water table was 1.52 m below the ground surface.

Table 1. Generalized soil properties

La- yer	Soil	Depth (m)	Thick- ness (m)	Unit weight (kN/m ³)	c' (kPa)	φ' (°)	E (kPa)	Poisson 's ratio
1	Medium dense sand	0 - 1.22	1.22	17.28	100	34	6.00 x 10 ⁴	0.49
2	Soft to firm clay	1.22 - 9.15	7.93	16.50	100	0	3.74 x 10 ⁴	0.5
3	Cooper Marl	Below 9.15	21.34	19.64	100	35	3.00 x 10 ⁴	0.5

GEOTECHNICAL DESIGN OF FOUNDATIONS FOR TALL WIND TURBINES

Since foundation failure (bearing capacity or settlement) may result in complete collapse of wind turbine system or will create safety concerns, selection of cost effective foundation type and its design considering site specific data is essential for its safe operation. Various foundation options are available for onshore wind turbine tower such as rafts, piles in group, and hybrid foundations such as piled-raft. The selection of the foundation is not only affected by the loads from above the ground components but also by the soil condition at the site. In this section, three types of foundations are designed and compared for economic advantage.

Raft foundation

The design of raft foundation was performed following the allowable bearing pressure method presented in Coduto (2001) with a target factor of safety of 3. The adequacy of the foundation to carry the given loads was checked for bearing capacity, lateral load, eccentricity due to moment, and settlement. It was found that the settlement criterion controlled the design. The final design resulted in a circular raft with radius of 18 m, thickness of 1 m, and depth of foundation of 1.5 m. The total settlement (δ) was calculated to be 55.13 mm using the Janbu et al. method given in Das (2007). The differential settlement was calculated to be 27.56 mm using the method described in Coduto (2001) considering the generic δ/δ_D ratio of 0.5.

Pile group with pile cap

The driven piles or piles are generally installed in group. When piles are installed in group the complex interaction between piles and the adjacent soil complicates the design because of which the proper design procedure is not yet available in the literature. In this study, the pile group was designed for vertical load capacity, lateral

load capacity, and moment capacity following the simplified design procedure (Rao, 2011; Gudmundsdottir, 1981; Poulos and Davis, 1980). The total vertical design load acting on each pile was calculated as the sum of dead load and vertical load (tension or compression) contribution due to moment using the method proposed by Rao (2011). This was done to incorporate the effect of moment. The resulting load acting on each pile was compared with the ultimate downward or uplift pile capacity to ensure that the vertical design load on each pile is less than pile capacity. The vertical load capacity of the pile group was determined as the lesser of the sum of ultimate pile capacity of individual piles in the group and the ultimate capacity of the block as described in Das (2007) and AASHTO (2012). In order to meet the design requirements in both compression and tension, it was required to increase the length of some of the piles which are located around the circumference (in the direction of moment). The final design resulted in 40 pre-stressed concrete piles of width 0.61 m (24 in.) and length varying from 25 m to 40 m. Out of the 40 piles, 18 piles were arranged at a radius of 5.3 m and the rest were arranged at a radius of 6.7 m.

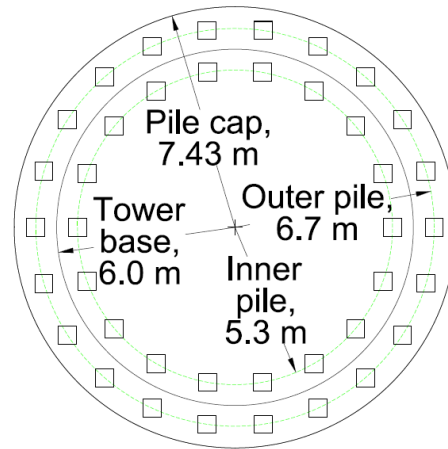


FIG. 1. Plan view of pile group with pile cap

The minimum dimension of the pile cap was determined according to Section 10.7.1.2 of AASHTO (2012), which requires that the top of pile should project at least 0.31 m into the pile cap and distance from the side of any pile to the nearest edge of the pile cap should not be less than 0.22 m. The final design resulted in the pile cap thickness of 1.0 m and radius of 7.43 m. The plan view of the designed pile group foundation with pile cap is shown in Fig. 1.

Piled-raft foundation (Hybrid foundation)

Quantifying the percentage of applied load shared by each foundation element (i.e., raft and piles) is the most challenging task in the design of piled-raft foundation. The combined action of the raft and the piles can increase the bearing capacity, reduce the settlement, and strategic arrangement of the piles can reduce the differential settlement. In spite of the benefits of the piled-raft foundation, reliable design guideline is not yet available, especially for foundation subjected to axial, lateral, and moment loads due to lack of understanding of complex interaction among soil, raft, and piles. The various procedures currently available in the literature can be broadly classified as simplified methods, approximate computer-based methods, and more rigorous computer-based methods.

In this study, a preliminary geotechnical design of the piled-raft foundation was performed following the procedure outlined by Hemsley (2000) in which the

procedure proposed by Poulos and Davis (1980) and Randolph (1994) have been incorporated. The factors considered in the preliminary design are: ultimate vertical, moment and lateral geotechnical capacity, total and differential settlement, rotation of the tower due to wind load, and lateral movement of the foundation. The size of raft and the size and number of piles required to satisfy the design requirements were determined in the preliminary design stage. The capacity of piled-raft foundation was checked for vertical load, lateral load, bending moment, and total and differential settlements. A minimum factor of safety of 2 was considered to be safe for vertical load, lateral load, and bending moment (Hemsley, 2000).

Vertical loading: The vertical capacity of the piled-raft was calculated as the lesser of: **(i)** the sum of ultimate capacities of raft and all the piles and **(ii)** the ultimate capacity of a block containing piles and raft, plus that of the portion of the raft outside the periphery of the pile group. The calculated vertical load capacity of the piled-raft was compared with the vertical design load. Block failure was observed in this case. The final factor of safety for axial load capacity was determined to be 3.55, which meets the design requirement.

Moment loading: The ultimate moment capacity of the piled-raft foundation was estimated as the lesser of: **(i)** the ultimate moment capacity of raft and the individual piles and **(ii)** the ultimate moment capacity of a block containing the piles, raft, and soil. The ultimate moment capacity of the raft, pile group, and block of piled-raft were determined using the method presented in Hemsley (2000). It was observed that the design was controlled by block failure. The final factor of safety for moment capacity was determined to be 1.16. Although the factor of safety appeared to be low, it is considered safe because the factor of safety for lateral capacity (discussed in following section) is in acceptable range.

Lateral loading: The lateral pile capacity of a single pile was determined using the solutions by Broms outlined in Gudmundsdottir (1981). The ultimate lateral load capacity and lateral deflection of single pile were calculated using the horizontal coefficient of subgrade reaction. The lateral load capacity of piled-raft was compared with the design lateral force. The factor of safety for lateral load capacity was found to be 6.14 and lateral deflection of 13.29 mm was observed.

Load – settlement curve: The load-settlement behavior of the piled-raft was estimated by the approach proposed by Poulos (2001) in conjunction with the method of estimating load sharing between the raft and piles presented in Randolph (1994). The load sharing between the raft and the piles can be estimated on the basis of stiffness of the raft, piles and piled-raft. The stiffness of piled-raft, K_{pr} was estimated by Eq. 1 according to Randolph (1994).

$$K_{pr} = X K_p; \quad X = \frac{1 + (1 - 2\alpha_{rp}) K_r / K_p}{1 - \alpha_{rp}^2 (K_r / K_p)} \quad (1)$$

where K_r is the stiffness of raft, K_p is the stiffness of pile group, and α_{rp} is the raft-pile interaction factor. The raft-pile interaction factor was assumed to be 0.8 because as the number of pile in the group increases, the interaction factor increases and tends towards a constant value of 0.8 as reported by Randolph (1994). Among the various methods to estimate the raft stiffness, the method outlined by Randolph (1994) was used. For the estimation of stiffness of the pile, the approach proposed by Poulos (2001) was adopted, where the target stiffness of the piled-raft was first determined by dividing the total axial load by the assumed allowable settlement. Then Eq. 1 was solved for the stiffness of the pile group. The stiffness of piled-raft will remain operative until the pile capacity is fully mobilized at load P_A . The load-settlement relationships established in Eq. 2 were used to obtain the load-settlement (P vs. S) curve for piled-raft foundation.

$$\text{For } P \leq P_A; S = \frac{P}{K_{pr}} \quad \text{For } P > P_A; S = \frac{P_A}{K_{pr}} + \frac{P - P_A}{K_r} \quad (2)$$

The load-settlement curve for the piled-raft is shown in Fig. 2. For the comparison purpose, the load-settlement curves for the raft and the pile group alone calculated in the same way as piled-raft are also presented in the same plot. For load-settlement curve for raft the stiffness of piles was considered to be zero and for pile group, the stiffness of raft was considered to be zero. For the axial load of 51.71 MN, the settlements of the raft and the pile group alone are found to be more than two times higher than the piled-raft. The differential settlement of the piled-raft foundation was determined according to the method developed by Randolph (1994). The differential settlement was calculated to be 10.22 mm and with this settlement, the rotation at the tower top was computed to be 0.078°.

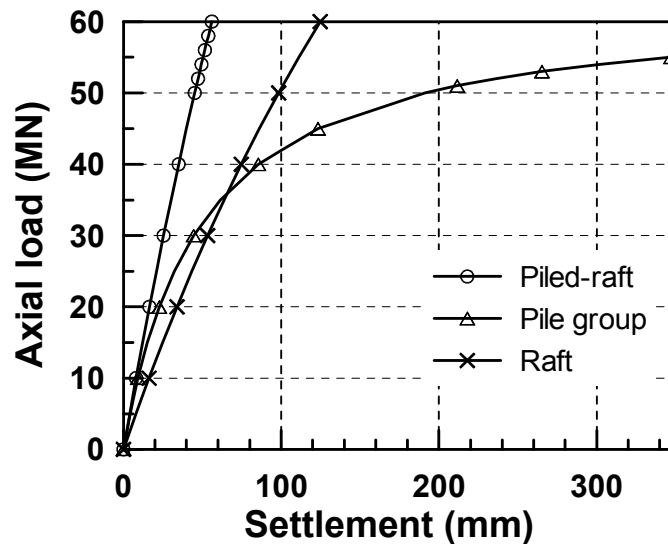


FIG. 2. Calculated load-settlement curve for raft, pile group, and piled-raft

The final design resulted in a raft of radius of 7.5 m, thickness of 1.2 m and 32 prestressed concrete piles of 0.46 m (18 in.) width with 10 m length. The piles were arranged at a center-to-center spacing of at least three pile diameters to avoid group effect. The piles were arranged in two radii: 16 inner piles at 5.3 m radius and 16 outer piles at 6.7 m radius. The piles were arranged at a center-to-center spacing of at least three pile diameters to avoid group effect. The final design is shown in Fig. 3

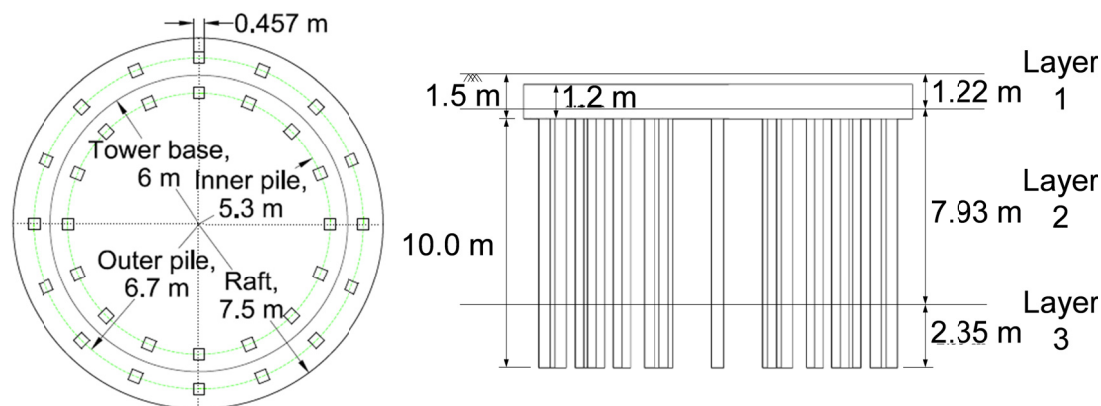


FIG. 3. Plan and side views of the designed piled-raft foundation

COMPARISON OF FOUNDATION

The results of geotechnical design of the three foundation systems are summarized in Table 2. It can be observed that the use of raft and pile group as foundation for tall wind turbine tower will require almost 4 and 2.5 times more volume of material than piled-raft, respectively. Due to the presence of longer and large number of piles, the differential settlement of the pile group is observed to be smaller than that of piled-raft. However, the differential settlement of the piled-raft is also within the acceptable limit, which gives acceptable rotation at the top of the tower and would not cause any problem due to additional moment at the base due to rotation of tower. Hence, it is clear from the investigation of design results that the piled-raft foundation is the most economical choice for the given site conditions based on the volume of foundation material. In addition, the prevailing soil condition i.e. soft to stiff clay favors deep foundation rather than shallow foundation.

Table 2. Comparison of foundations

Foundation	Volume (m ³)	Settlement (mm)	Differential settlement (mm)
Raft	1017.88	55.13	27.56
Pile group	667.68	57.96	6.80
Piled-raft	278.95	46.96	10.22

PARAMETRIC STUDY

A parametric study was performed for the piled-raft foundation to develop relationship between the volume of material required versus input and design parameters such as wind speed, tower height, pile size, and number of piles. It is well known that for parametric study, only one variable should be changed keeping other constant. However, in this study, it was required to change the number and length of pile in order to meet the minimum safety and settlement requirements, otherwise the design would be either overdesigned or under designed. Since more than one variable are changed for parametric study, there should be a common benchmark based on

which the results can be compared. For this purpose, the settlement of the piled-raft for each case of parametric study was maintained in the range of 47 ± 1.6 mm. The volume of material required for each increment of the variable was compared to establish the relationship between the cost and the design parameter since the volume can be directly related to the cost (the construction cost is not considered in this study). The width of the pile was kept constant in the case where the wind speed, tower height, and number of piles were considered as variables while adjusting the number and length of piles to satisfy the design requirements. In the cases where width of the pile was considered as variable, the number of piles was adjusted keeping the length constant to satisfy the minimum design requirements.

The detailed results of parametric study are summarized in Table 3 where n_p , L, s, and vol. represent the number of piles, length of pile, settlement, and volume of material required. An effort was made to bring the settlement of all the foundations in the parametric study in the same range to make the comparison reasonable and meaningful.

Table 3. Results of parametric study for piled-raft

Variables	n_p	L (m)	s (mm)	vol. (m ³)	
Wind speed (mph)	120	32	8	48.01	265.57
	140	28	10	47.33	270.59
	160	32	10	46.96	278.95
	180	28	12	46.85	282.29
	200	28	14	46.05	294.00
Tower height (m)	90	16	8	48.6	238.81
	110	20	10	47.11	253.86
	130	32	10	46.96	278.95
	150	32	12	46.45	292.33
	170	32	14	46.42	305.70
Pile size (m)	0.46	32	10	46.96	278.95
	0.51	28	10	46.88	284.32
	0.61	24	10	46.35	301.24
	0.76	16	10	47.22	304.96
	0.91	12	10	47.59	312.39
Number of piles	24	24	17	46.24	297.34
	28	28	13	46.59	288.15
	32	32	10	46.96	278.95
	36	26	10	46.14	287.31
	40	40	10	45.47	295.67

It can be seen in Table 3 that an increase in wind speed and tower height resulted in an increase in required volume of material. This is because the increase in wind speed and tower height imposes higher design loads demanding bigger foundation. Similarly, the required volume of material increased when the pile size was increased. On the other hand, the required volume of material decreased up to a certain number and then increased when the number of piles was increased. Such plot can be used to avoid the uneconomical use of piles. It is interesting to note that the optimum number of piles from this result is in agreement with the design results.

Since one of the major objectives of adding piles to the raft is to decrease the settlement, the effect of number of piles on settlement was studied. The result is shown in Fig. 4, where the corresponding settlements for different number of piles with same size and length of pile are plotted. Fig. 4 shows that the increase in number of piles while keeping the size and the length constant results in significant decrease in settlement up to certain number of piles (~20) and thereafter the addition of piles has negligible contribution in reducing the settlement. Hence while designing the piled-raft foundation, the number of piles should be decided tactfully to neglect the redundant piles.

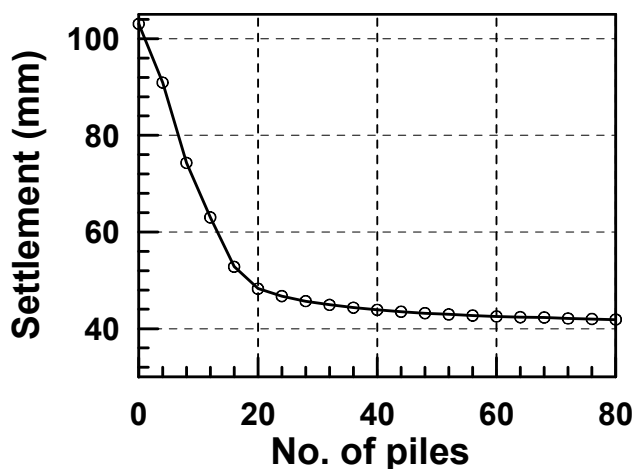


FIG. 4. Effect of number of piles on the settlement of piled-raft foundation

CONCLUSION

Based on the comparison of geotechnical design results of three possible foundation systems, it can be concluded that the piled-raft is the cost effective and stable foundation solution for a tall onshore wind turbine for the site conditions corresponding to Charleston, SC. The parametric study results showed that the increase in wind speed, height of tower, and width of pile resulted in increase in the volume of material required. On the other hand, it is interesting to know that the increase in the number of piles resulted in decrease in volume at first and then increase. While analyzing the settlement of piled-raft, it was observed that the addition of pile contributed significantly in the reduction of the settlement only up to certain number of piles. The results of parametric study can be used as design chart to decide the most economical configuration of the piled-raft foundation. It should be noted that all the results and analysis presented in this study are based on the preliminary design methods and it is recommended to perform more detailed analysis to obtain more accurate results.

It should be noted that the selection of foundation based on design and analysis results is site specific and therefore it may be beneficial to the agencies that construct and manage wind turbines to perform similar analysis and develop recommendations for potential wind farm sites in the USA for quicker construction and operation of turbines.

REFERENCES

- American Association of State Highway and Transportation Officials (AASHTO, 2012). "Design Specifications", Publication code: *LRFDUS-6*, ISBN: 978-56051-523-4.
- American Society of Civil Engineers (ASCE 7-10, 2010). "Minimum Design Loads for Buildings and Other Structures", ISBN 978-0-7844-1085-1.
- BP (2015). "BP Statistical Review of World Energy June 2015." <<http://www.bp.com/statisticalreview>>.
- Coduto, D.P. (2001). "Foundation Design: Principles and Practices, 2nd Edition" *Prentice Hall*, Upper Saddle River, NJ, USA ISBN-0-13-589706-8.
- Das, B.M. (2007). "Principles of Foundation Engineering, 7th Edition" *Cenage Learning*, 200 First Stamford Place, Suite 400, Stamford, CT, USA ISBN-13: 978-0-495-66812-1.
- Gudmundsdottir, B. (1981). "Laterally loaded piles." M.S. thesis, University of Alberta, Edmonton, Alberta, Canada.
- Global Wind Energy Council (GWEC, 2015). "Global Wind Statics, 2014." <<http://www.gwec.net/global-Fig.s/graphs/>>.
- Hemsley, J.A. (2000). "Design applications of raft foundations." *Thomas Telford Ltd.*, Heron Quay, London, ISBN: 0727727656.
- Lewin, T.J. (2010). "An investigation of design alternatives for 328-ft (100-m) tall wind turbine towers." Master's Thesis, Iowa State University.
- Malhotra, S (2011). "Selection, Design and Construction of Offshore Wind Turbine Foundations, Wind Turbines." Dr. Ibrahim Al-Bahadly (Ed.), *InTech*, ISBN: 978-953-307-221-0.
- Poulos, H.G. and Davis, E.H. (1980). "Pile foundation analysis and design." *John Wiley*, New York.
- Poulos, H.G. (2001). "Piled raft foundation: design and applications." *Geotechnique*, Vol. 51 (2): 95-113.
- Randolph, M.F. (1994). "Design methods for pile groups and piled rafts." *State-of-the-Arts Report, 13th International Conference on Soil Mechanics and Foundation Engineering*, New Delhi, India, Vol. 5: 61-82.
- Roa, K.N.S.V. (2011). "Foundation Design: Theory and Practice, 1st edition" *John Wiley and Sons (Asia) Pte Ltd*, 2 Clementi Loop, #02-01, Singapore 129809, ISBN-13: 978-470-82534-1.
- WPC, A Terracon Company (2010). "Geotechnical Engineering Report: Clemson Wind Turbine Testing Facility North Charleston, South Carolina." WPC Project No. EN105060.

Micromechanical Modeling of Proppants for Hydraulic Fracturing

Mehmet. B. Cil¹ and Giuseppe Buscarnera²

¹Postdoctoral Research Fellow, Dept. of Civil and Environmental Engineering, Northwestern Univ., 2145 Sheridan Rd., Tech A236, Evanston, IL 60208-3109.

²Assistant Professor, Dept. of Civil and Environmental Engineering, Northwestern Univ., 2145 Sheridan Rd., Tech A124, Evanston, IL 60208-3109.

Abstract: The durability of hydraulic fracture stimulation is a major requirement for the success of fossil fuel recovery from rock formations with low permeability such as gas-shale. To improve this property, proppants are generally used to hinder the closure of fractures and promote higher fluid conductivity. The efficacy of proppant placement, however, depends among various things also on their mechanical response under high compressive stresses. 3D compression simulations were performed in this study using the distinct element method (DEM) to investigate the interaction between proppants and rock formation, giving emphasis to the role of the crushing resistance of proppant packs. To capture the size-dependence of the particle strength, proppants were modeled by bonded agglomerates with strength assigned randomly via a Weibull statistics. The stress-strain behavior and particle size evolution of specimens characterized by different packings were then studied numerically. The results revealed that packings consisting of multiple layers can sustain higher stresses and producing considerably less fines compared to mono-layer packings subjected to the same extent of fracture closure. Such analyses show that DEM modeling has considerable potential to incorporate the size-dependence of grain fracture processes, i.e. a key element to evaluate alternative types of proppants and select an optimal mixture for site-specific stress conditions.

INTRODUCTION

Hydraulic fracturing is extensively used to increase the permeability of reservoirs in oil/gas recovery, as well as in enhanced geothermal systems. During the last decade, the use of this technology has expanded tremendously, mostly due to the economic relevance of unconventional resources (Economides and Nolte, 2000). Hydraulic fracturing involves the onset, propagation and coalescence of cracks in deep rock formations by injecting pressurized fluids into vertical or horizontal wells (Donaldson, et al., 2014). A common strategy to increase the productivity of the extraction process is to inject granular media together with the fracturing fluid (so-called proppants) with the purpose to pack the stimulated fractures and maintain their opening throughout the process. The performance of granular proppants subjected to

the extreme temperature and pressure conditions typical of rock formations at depth plays a critical role in the resulting productivity and efficiency of the intervention, as indeed the damage of the injected proppant over time (e.g., breakage) may lead to the closure of the opening, as well as to loss of permeability and clogging of narrow fracture zones (Parker, et al., 1999). Design and selection of the optimum type of proppants (e.g., ceramics, natural sands, or resin coated sands) and their properties (e.g., size and shape) for hydro-fracture applications require a thorough understanding of the mechanical response of proppants. Furthermore, it is important to connect single particle characteristics and bulk strength to classify proppants and define solutions to improve their durability (Raysoni, et al., 2013, Zhang and Buscarnera, 2014, Zhang, et al., 2016).

Previous Distinct Element Method (DEM) studies have focused on transport, flowback and compressive response of proppants (Deng, et al., 2014, Tomac and Gutierrez, 2015). The evolution of the microstructure of a pack upon fracture closure (increase in compressive stress) has been shown to be crucial, as it may affect the physical properties that control the success of the stimulation activity. This study presents a multi-scale analysis of the mechanical behavior of proppants under high compressive stresses. The interaction between rock formation and packed layers of proppant was investigated through DEM. Proppants were modeled by crushable agglomerates of bonded spheres (Cil and Alshibli, 2014, Cil and Alshibli, 2015) and their deformation response to increasing values of in situ stress was examined by considering the size-dependent fracture of brittle grains, as well as different fracture apertures. In addition, the evolution of the fines content due to proppant fragmentation has been tracked, with the goal to assess the role of packing conditions on their expected performance.

DEM SIMULATIONS

PFC3D 5.0 (Itasca, 2014) was here employed to perform 3D DEM simulations. First, diametrical compression simulations were conducted on particle agglomerates of different sizes (e.g., 0.5 mm, 1 mm and 2 mm) (Figure 1). The agglomerates were generated by algorithms for bonded particle models (BPM) proposed by Potyondy and Cundall (2004). After completing the agglomerate generation stage, position and size of the spherical sub-particles constituting each agglomerate were saved as a template to be used in subsequent 1D compression simulations. In order to capture the strength variability of individual particles as a function of their size, the normal bond strength of each agglomerate, σ_n , was assigned by using the following equation:

$$\sigma_n = \sigma_0 \left(\frac{d}{d_0} \right)^{-3/w} \ln \left(\frac{1}{P} \right)^{1/w} \quad (1)$$

where σ_0 is the reference tensile strength of an intra-particle bond within a grain of size d_0 , w is the Weibull modulus, P is a uniformly distributed random variable ranging from 0 to 1. At each occurrence of an agglomerate fragmentation event, the bond strength of the remaining fragments was updated according to Equation (1). The

size of each particle was assumed to coincide with the diameter of a sphere with same volume. For this purpose, the overall volume of each agglomerate V_{agg} was calculated as:

$$V_{agg} = \frac{\sum V_{sub-particles}}{n_{int}} \quad (2)$$

where $V_{sub-particles}$ is the volume of the sub-particles in the agglomerate and n_{int} is the internal porosity of the agglomerate (here set equal to 0.36). Diametrical compression simulations revealed that the mean failure stress of an agglomerate is proportional to the average strength of the internal bonds, σ_n . In addition, the simulations pointed out that such approach enables the size dependence of the grain strength to be reproduced successfully during fragmentation. Specifically, the variation of the particle strength for a given reference grain size was captured by assigning randomly the bond strength in accordance with a probability distribution based on Equation (1).

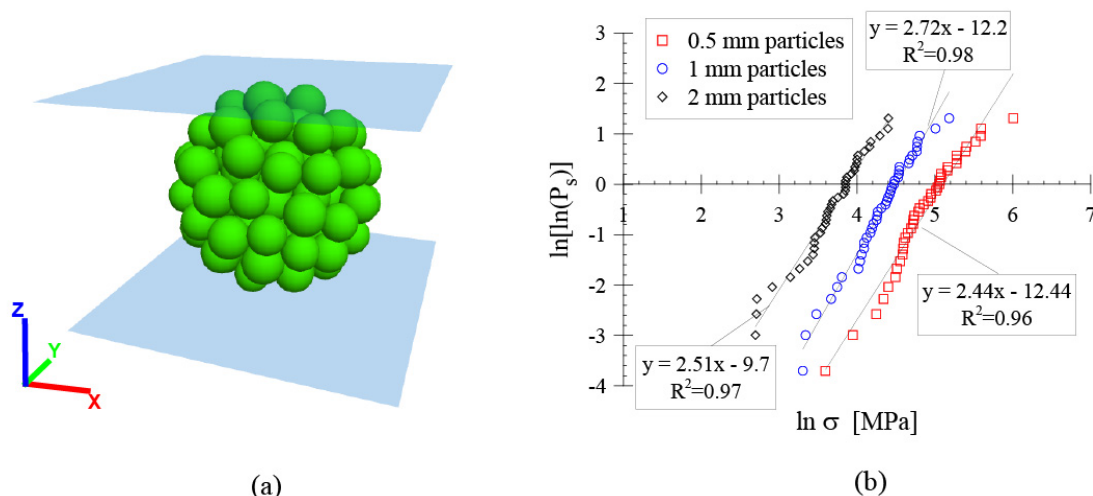


Figure 1. (a) Close up view of an agglomerate before diametrical compression; (b) results of diametrical compression simulations for different particle sizes.

Once the particle strength variability in diametrical compression simulations was captured, 1D compression tests were simulated on agglomerate assemblies. Initially, assemblies consisting of rigid spherical particles were generated in a prismatic container based on a given porosity. Then, several computational timesteps were imposed to eliminate particle overlaps and reach a stable configuration. This task was carried out by allowing particles to rearrange with zero inter-particle friction. Then, each rigid particle was replaced with a crushable agglomerate composed of bonded spherical sub-particles. After the generation of agglomerates, the final contact parameters were assigned and additional computational steps were applied to reach a

stable configuration before loading. 1D compression was implemented by moving the top and bottom axial walls towards the specimen. The progression of bond breakage events and the accumulation of deformations were examined during the compression process. DEM simulations were carried out by using a linear parallel bond model with the method of deformability which relates macroscopic elastic parameters of the specimen such as the Young's modulus to microscopic parameters (see Itasca (2014)). Therefore, the model parameters were determined based on the elastic properties of the selected proppant. Although different proppant types (e.g., sand, resin coated sand and ceramic) are employed in hydraulic fracturing applications, this study focused on the mechanical behavior of sand proppants because of its common usage. A summary of the DEM model parameters is listed in Table 1.

1D COMPRESSION SIMULATION RESULTS

Hereafter, two types of packing (i.e., multi-layer and mono-layer) usually observed in hydraulic fracturing operations were considered to identify the influence of packing conditions on their compression/fracture behavior. The initial packing configuration of each simulation is showed in Figure 2. In multi-layer packings, 5-7 times more layers were present along the vertical direction compared to mono-layer packings. Both simulations extended along the horizontal direction to replicate a small section of a long fracture filled with proppants.

Table 1. Summary of the DEM model parameters

Parameter	Value
<i>General model properties</i>	
Agglomerate size (D_{\min} - D_{\max})	0.8 mm - 1.5 mm
Initial specimen porosity	0.49 (Multi-layer packing) 0.58 (Mono-layer packing)
<i>Linear contact parameters</i>	
Effective stiffness	70 GPa
Stiffness ratio (k_n/k_s)	1.0
Friction coefficient	0.5
<i>Parallel bond parameters</i>	
Installation gap	$D_{\min}/34$
Radius multiplier	1.0
Bond effective stiffness	70 GPa
Bond stiffness ratio	1.0
Cohesion	$\sigma_n * 10$
<i>Weibull function parameters</i>	
Reference particle size (d_0)	2.0 mm
Characteristic bond strength (σ_0)	50 MPa
Weibull modulus w	3.3

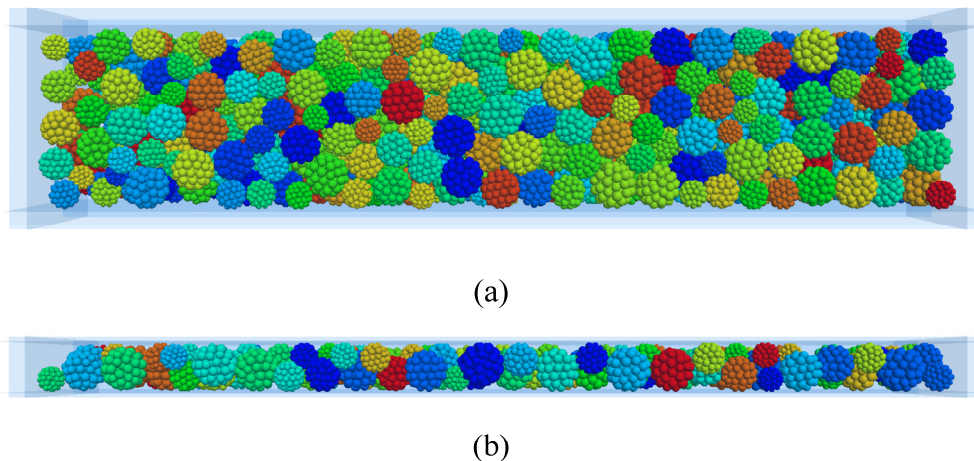


Figure 2. Initial configuration of the (a) multi-layer pack (464 agglomerates) and mono-layer pack (104 agglomerates) bounded by rectangular wall elements.

The deformation response obtained from 1D compression simulations is shown in Figure 3, where the evolution of the axial stress acting on the packing is plotted as a function of axial strains and displacements. Agglomerates in mono-layer packing had limited possibility to rearrange at the beginning of the compression stage, having that breakage events can lead to considerable stress fluctuations. By contrast, in multi-layer packings the stress increased more gradually during the initial stages of loading, until achieving the onset of substantial grain breakage, after which a limited variation in stress upon increasing compressive strains was found and larger stress fluctuations were observed. Also in the latter case, the stress fluctuations can be attributed to the small number of particles in the analyses. It is worth noting that the agglomerates in multi-layer packings were predicted to sustain higher compressive stresses compared to mono-layer packings, thus stressing the role of a range of grain-scale phenomena, as particle rearrangement and force redistribution in the definition of the performance of the different packing configurations.

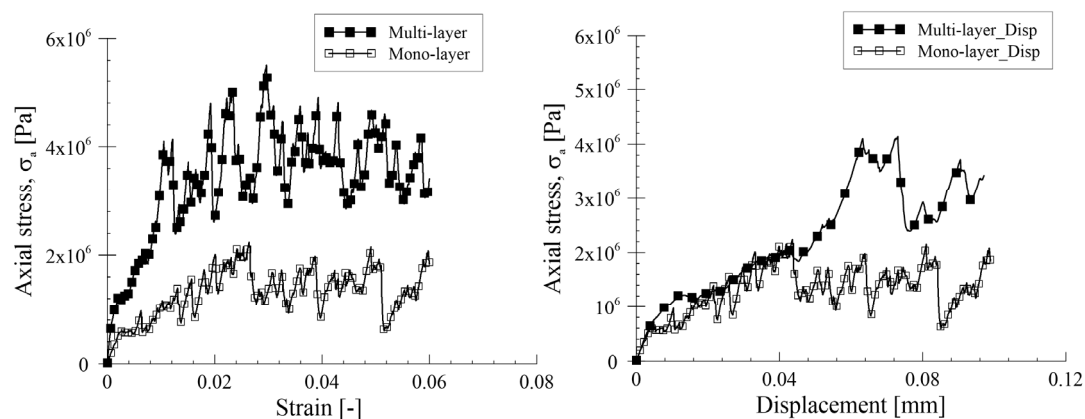


Figure 3. Stress-strain and stress-displacement relationships resulting from 1D compression simulations.

The distribution of produced fragments as a result of agglomerate breakage is showed in Figure 4, which illustrates that breakage events tended to occur randomly throughout the specimen in both simulations. In the mono-layer packing, fragments appear at discrete locations, possibly because of early fractures taking place in particles in contact with the fracture walls, where the largest fraction of axial forces are sustained. By contrast, in the multi-layer packing agglomerate fractures occurred at the interface between specimen and loading walls, as well as within the specimen.

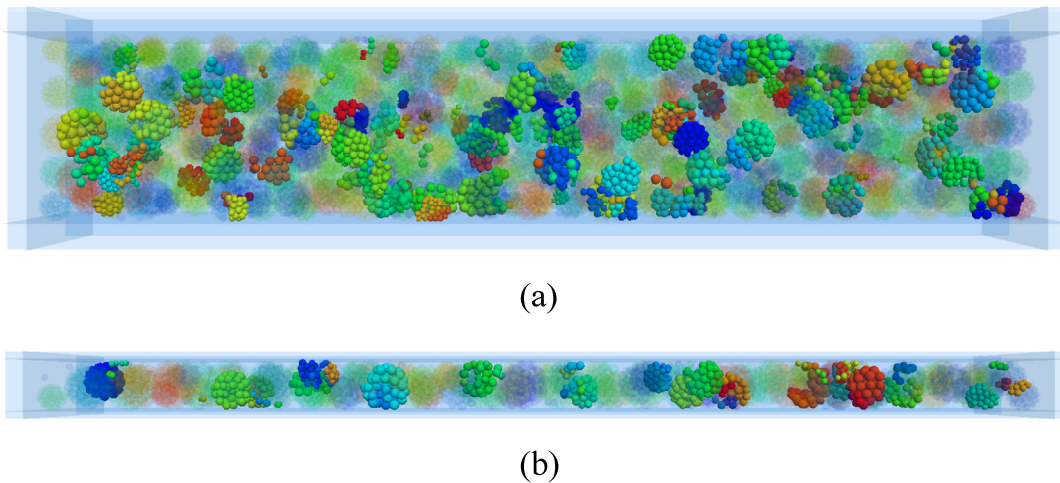


Figure 4. Distribution of fragments generated at the end of the simulated stage of compression in (a) multi-layer and (b) mono-layer packing. Broken agglomerates are highlighted and the rest of the specimen is shown with transparent shading.

Since the goal of proppant placement in hydraulic fracturing is to guarantee high hydraulic conductivity under sustained in situ compressive stresses, it is important to keep track of the fines that may be generated during the fracture closure stage, which may indeed have detrimental consequences for the overall success of the placement intervention. To examine the process of fines generation upon compression-induced crushing with the proposed DEM model, the evolution of the particle size distribution (PSD) has been tracked for the two different packing configurations considered in the previous section. Such analysis are summarized in Figure 5. The results indicate that in both cases the amount of fine particles gradually increased during the compression process. At any given strain level, the fines content resulted to be slightly higher in the multi-layer packing than in the mono-layer packing, which may be a consequence of the higher stresses to which proppant packings were subjected at comparable strain levels. However, if the same property is inspected at fixed stress level (e.g., a constant stress imparted by the surrounding rock formation) as well as for a fixed amount of fracture closure (i.e., by plotting the PSD as a function of the axial displacement), it is possible to notice that the change of the PSD in the case of a multi-layer packing was negligible small compared to that computed for the mono-layer system.

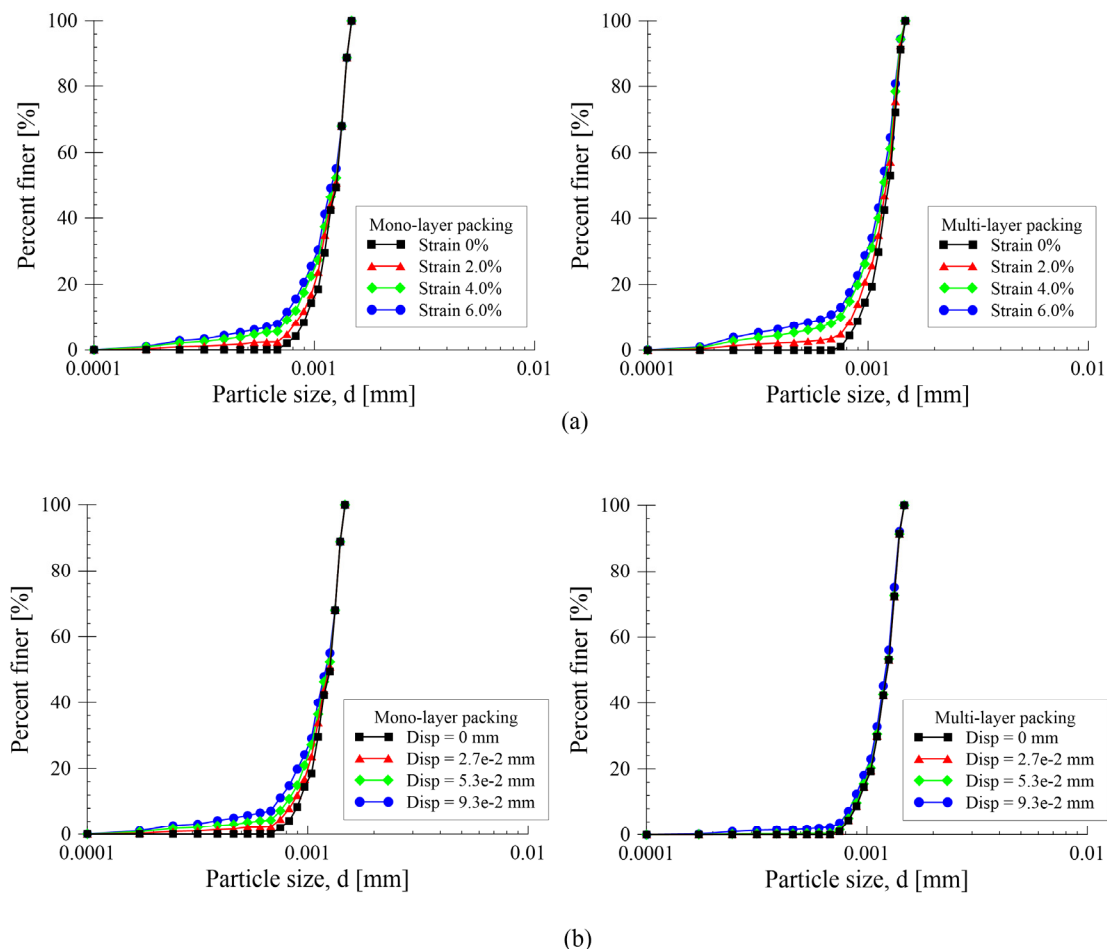


Figure 5. Evolution of the particle size distribution (PSD) at given levels of (a) axial strains and (d) axial displacements (i.e., fixed amount of fracture closure).

CONCLUSIONS

The deformation/crushing characteristics of proppants were investigated using 3D DEM simulations. The bond strength of numerical agglomerates was assigned via a Weibull statistics to capture the size-dependency of the particle strength that is often observed in diametrical compression tests. The stress-strain response and particle size evolution for simulations based on different packing configurations (i.e., multi-layer and mono-layer) have been examined. The results indicate that multi-layer packings may sustain higher compressive stresses compared to mono-layer packings, as well as that they can mitigate the production of fines generated by confined comminution at constant levels of applied stress and/or fracture closure. The simulations also revealed that increasing axial stresses may result in considerable grain breakage and alterations of the PSD of the proppant packing. Such micro-scale analyses provide insight on the evolution of fragmentation in granular media subjected to extreme stress conditions

and have the potential to assist the design/selection of granular proppants to be used for hydraulic fracture interventions under site-specific reservoir conditions.

ACKNOWLEDGMENTS

Financial support of the Petroleum Research Fund of the American Chemical Society through project #55647-ND8 is gratefully acknowledged.

REFERENCES

- Cil, M. B., and Alshibli, K. A. (2014). "3D evolution of sand fracture under 1D compression." *Géotechnique*, 64, 351-364.
- Cil, M. B., and Alshibli, K. A. (2015). "Modeling the influence of particle morphology on the fracture behavior of silica sand using a 3D discrete element method." *Comptes Rendus Mécanique*, 343(2), 133-142.
- Deng, S., Li, H., Ma, G., Huang, H., and Li, X. (2014). "Simulation of shale-proppant interaction in hydraulic fracturing by the discrete element method." *Int J Rock Mech Min*, 70, 219-228.
- Donaldson, E. C., Alam, W., and Begum, N. (2014). *Hydraulic Fracturing Explained: Evaluation, Implementation, and Challenges*, Elsevier.
- Economides, M. J., and Nolte, K. G. (2000). "Reservoir Stimulation." John Wiley & Sons, LTD, New-York.
- Itasca, C. G. I. (2014). *PFC (particle flow code in 2 and 3 dimensions), version 5.0 [User's manual]*. Minneapolis, MN.
- Parker, M., Weaver, J., and Van Batenburg, D. (1999). "Understanding proppant flowback." *Proc., SPE annual technical conference*, 681-693.
- Potyondy, D. O., and Cundall, P. A. (2004). "A bonded-particle model for rock." *Int J Rock Mech Min*, 41(8), 1329-1364.
- Raysoni, N., Pinto, M., and Kothamasu, R. (2013). "Insights into the Relationship between Single Grain and API/ISO Crush Strength when applied to Proppants with or without Diagenesis." American Rock Mechanics Association.
- Tomac, I., and Gutierrez, M. (2015). "Micromechanics of proppant agglomeration during settling in hydraulic fractures." *J Petrol Explor Prod Technol*, 1-18.
- Zhang, Y. D., and Buscarnera, G. (2014). "Grainsize dependence of clastic yielding in unsaturated granular soils." *Granular Matter*, 16(4), 469-483.
- Zhang, Y. D., Buscarnera, G., and Einav, I. (2016). "Grain size dependence of yielding in granular soils interpreted using fracture mechanics, breakage mechanics and Weibull statistics." *Géotechnique*, 66(2), 149-160.

Thermo-Hydro-Chemo-Mechanical Formulation for CH₄-CO₂ Hydrate Conversion Based on Hydrate Formation and Dissociation in Hydrate-Bearing Sediments

Shun Uchida, A.M.ASCE¹; Christian Deusner²; Assaf Klar, M.ASCE³; and Matthias Haeckel⁴

¹Assistant Professor, Dept. of Civil and Environmental Engineering, Rensselaer Polytechnic Institute, Troy, NY 12180. E-mail: uchids@rpi.edu

²Postdoctoral Researcher, GEOMAR Helmholtz Centre for Ocean Research Kiel, Kiel 24148, Germany.

³Associate Professor, Faculty of Civil and Environmental Engineering, Technion – Israel Institute of Technology, Haifa 32000, Israel.

⁴Research Scientist, GEOMAR Helmholtz Centre for Ocean Research Kiel, Kiel 24148, Germany.

Abstract: Gas production from gas hydrate-bearing sediments has been attracting global interests because of its potential to meet growing energy demand. Methane (CH₄) gas can be extracted from CH₄ hydrates by depressurization, thermal stimulation or chemical activation. However, it has never been produced on a commercial scale and the past field trials faced premature termination due to the technical difficulties such as excessive sand flow into the well, a phenomenon known as sand production. One exception is the trial at the Ignik Sikumi, Alaska in 2012, which was conducted by chemical activation followed by depressurization. During the trial, initial sand production ceased after two weeks while CH₄ gas production continued for five weeks. The mitigation of sand production is deemed attributed to mechanical or hydraulic effects through formation of CO₂-rich gas hydrates. This incident has highlighted the favorable effect of CO₂ hydrate formation and needs to incorporate the chemo-processes into existing thermo-hydro-mechanical formulations. This paper presents an analytical formulation to capture the coupled thermo-hydro-chemo-mechanical behavior of gas hydrate-bearing sediments during gas production via CO₂ injection. The key features of the formulation include hydrate formation and dissociation, gas dissolution and multiphase flow for both CH₄ and CO₂, facilitating CH₄-CO₂ hydrate conversion.

BACKGROUND

CH₄ hydrate has been attracting growing international interest because of its potential as an abundant and widespread source of natural gas that could provide nations with long term energy security. Conservative estimates suggest that more than 10 trillion m³ of CH₄ gas resides in oceanic gas hydrate deposits throughout the globe, exceeding the known volume of technically recoverable remaining conventional natural gas (e.g. Burwicz et al., 2011; Milkov, 2004). An economic means of extracting gas from gas hydrate-bearing sediments could therefore meet many decades worth of global energy demand. Three methods have been proposed as being feasible for hydrate dissociation (i.e. phase change of CH₄ from hydrate into gas) at in-situ: [1] depressurization – the use of depressurized wells to reduce the pressure in the soil around the wells; [2] thermal stimulation – the use of thermal injection well to increase the temperature in the surrounding soil; and [3] chemical activation – the use of CO₂ injection to release the CH₄ gas from the hydrate and convert it into more stable CO₂ hydrate.

To date, only a few short-term field trials of gas production from hydrate-bearing sediments have been reported, most notably the trials conducted at the Mallik gas hydrate site, Canada, in 2007 (Dallimore et al., 2008), at the Ignik Sikumi well, Alaska, in 2012 (Schoderbek et al., 2013) and at the Eastern Nankai Trough, Japan in 2013 (Yamamoto, 2014). During these trials, gas extraction via depressurization encountered sand production problems, leading to a premature termination of the trials in 2007 and 2013. In contrast, during the trial in 2012, gas production was operated by depressurization plus chemical activation by CO₂/N₂ injection and it is found that the initially occurred sand production ceased after two weeks while gas production continued for five weeks. Although the mechanism is yet to be fully understood, it is proposed that the stabilization of sand production during the 2012 trial was attributed to CO₂ hydrate formation.

For sustainable gas exploitation from hydrate-bearing sediments in the future, therefore, an implementation of realistic mechanical behavior of hydrate-bearing sediments into thermo-hydro models was and still remains the next logical progression. As of today, a limited number of coupled thermo-hydro-mechanical formulations for behavior of hydrate-bearing sediments are available (e.g. Kim et al., 2011; Kimoto et al., 2010; Klar et al., 2013). However, these formulations only deal with the dissociation process induced by depressurization or thermal stimulation and no analytical work exists to capture the chemical activation induced thermo-hydro mechanical process during hydrate dissociation. This paper presents a first step towards completing an analytical framework to capture the coupled behavior of gas hydrate-bearing sediments during gas production via chemical activation.

MASS BALANCE EQUATIONS INCLUDING METHANE AND CARBON DIOXIDE

Methane exists as CH₄ hydrate, aqueous CH₄ and gaseous CH₄. Likewise, carbon dioxide can exist as CO₂ hydrate, aqueous CO₂, gaseous CO₂ and liquid CO₂. For simplicity, this study assumes that the gaseous phase and liquid phase of CO₂ are indistinguishable. This implies that liquid CO₂ behaves identically to that of gaseous

CO₂. In this study, CH₄ hydrate is denoted as “mh”, aqueous methane as “mw” and gaseous methane as “mg”, CO₂ hydrate as “ch”, aqueous CO₂ as “cw” and gaseous/liquid CO₂ as “cg”.

There are two phenomena changing the phase of methane or carbon dioxide: hydrate formation/dissociation and gas dissolution. Methane (or carbon dioxide) hydrate consists of one molecule of CH₄ (or CO₂) and N_{mh} (or N_{ch}) molecules of pure water. For simplicity, this study assumes that the hydrate forms only from the gaseous phase and thus dissociation releases only gaseous methane (or carbon dioxide). This implies hydrate formation/dissociation does not affect m_{mw} (or m_{cw}) where m is the mass per control volume. On the other hand, gas dissolution increases m_{mw} (or m_{cw}) and decreases m_{mg} (or m_{cg}). Introducing the rate of gas dissolution R_{mw} (or R_{cw}) and that of hydrate formation/dissociation R_{mh} (or R_{ch}), formation positive and dissociation negative, the mass balance equations of pure water, aqueous CH₄ and aqueous CO₂ can be expressed as:

$$dm_{w(pure)} = -\nabla \cdot (\rho_{w(pure)} \mathbf{q}_{w(pure)}) dt - N_{mh} M_{w(pure)} R_{mh} dt - N_{ch} M_{w(pure)} R_{ch} dt \quad (1)$$

$$dm_{mw} = -\nabla \cdot (\rho_{mw} \mathbf{q}_{mw}) dt + m_w R_{mw} dt \quad (2)$$

$$dm_{cw} = -\nabla \cdot (\rho_{cw} \mathbf{q}_{cw}) dt + m_w R_{cw} dt \quad (3)$$

where the subscript $w(pure)$ represents pure water, ρ is the density, \mathbf{q} is the discharge, M is the molecular mass and t is the time. The rate R is approximated by a first-order kinetics and described in the next section. Similarly, the mass balance equations of gaseous CH₄ and CO₂ are:

$$dm_{mg} = -\nabla \cdot (\rho_{mg} \mathbf{q}_{mg}) dt - M_{mg} R_{mh} dt - m_w R_{mw} dt \quad (4)$$

$$dm_{cg} = -\nabla \cdot (\rho_{cg} \mathbf{q}_{cg}) dt - M_{cg} R_{ch} dt - m_w R_{cw} dt \quad (5)$$

The mass balance equations of the two pure hydrates are:

$$dm_{mh} = N_{mh} M_{w(pure)} R_{mh} dt + M_{mg} R_{mh} dt \quad (6)$$

$$dm_{ch} = M_{ch} M_{w(pure)} R_{ch} dt + M_{cg} R_{ch} dt \quad (7)$$

Formation of mixed CH₄-CO₂ hydrates is not explicitly considered in this study.

Both the aqueous CH₄ and CO₂ and gaseous CH₄ and CO₂ are treated as fully miscible, resulting in an aqueous CH₄-CO₂ mixture and a gaseous CH₄-CO₂ mixture. In other words, these mixtures can be represented as a single material:

$$dm_w = dm_{w(pure)} + dm_{mw} + dm_{cw} \quad (8)$$

$$dm_g = dm_{mg} + dm_{cg} \quad (9)$$

where the subscripts w and g represent the aqueous CH₄-CO₂ mixture and the gaseous CH₄-CO₂ mixture, respectively. This study assumes that Darcy's law is valid for the mixtures controlled by the mixture pressure. Since the mixture behaves together, the discharge for each component holds the same quantity as that of the mixture:

$$\mathbf{q}_w = -\frac{\mathbf{K}_h}{\mu_w} k^r (\nabla P_w - \rho_w \mathbf{g}) = \mathbf{q}_{w(pure)} = \mathbf{q}_{mw} = \mathbf{q}_{cw} \quad (10)$$

$$\mathbf{q}_g = -\frac{\mathbf{K}_h}{\mu_g} k^r (\nabla P_g - \rho_g \mathbf{g}) = \mathbf{q}_{mg} = \mathbf{q}_{cg} \quad (11)$$

where μ is the viscosity, k^r is the relative permeability factor, P is the pressure, \mathbf{g} is the gravitation vector and \mathbf{K}_h is the intrinsic permeability tensor of the hydrate-sediments.

The density of each component in the mixture is defined as the mass concentration of its component (i.e. mass of a constituent divided by the volume of the mixture):

$$\rho_w = \rho_{w(pure)} + \rho_{mw} + \rho_{cw} = \frac{1}{nS_w} (m_{w(pure)} + m_{mw} + m_{cw}) \quad (12)$$

$$\rho_g = \rho_{mg} + \rho_{cg} = \frac{1}{nS_g} (m_{mg} + m_{cg}) \quad (13)$$

KINETIC MODELS FOR GAS DISSOLUTION, HYDRATE FORMATION AND HYDRATE DISSOCIATION

Dissolution for gaseous phase substances into their aqueous phase is assumed to be driven by the difference between the maximum mass concentration of the aqueous solute and the current mass concentration of aqueous solute. Thus, the rates of dissolution for CH₄ and CO₂ can be obtained by:

$$R_{mw} = D_{mw} \left\langle c_{mw(max)} - \frac{m_{mw}}{m_w} \right\rangle \quad (14)$$

$$R_{cw} = D_{cw} \left\langle c_{cw(max)} - \frac{m_{cw}}{m_w} \right\rangle \quad (15)$$

where $c_{mw(max)}$ and $c_{cw(max)}$ are the maximum mass concentrations above which no dissolution occurs for gaseous CH₄ and CO₂ respectively, D is the rate of dissolution coefficient (i.e. the phase transition coefficient multiplied by the volumetric specific liquid-gas surface area) and $\langle \cdot \rangle$ is the Macaulay bracket. The above rates are expressed in a control volume.

Formation and dissociation of gas hydrate is assumed to be governed by first-order kinetics, controlled by partial pressures of gaseous CH₄ and CO₂, rather than the total gas pressure. The partial pressure (molar fraction) of each gas is given by:

$$P_{mg} = \frac{m_{mg} / M_{mg}}{m_{mg} / M_{mg} + m_{cg} / M_{cg}} P_g = \frac{m_{mg} M_{cg}}{m_{mg} M_{cg} + m_{cg} M_{mg}} P_g \quad (16)$$

$$P_{cg} = \frac{m_{cg} M_{mg}}{m_{mg} M_{cg} + m_{cg} M_{mg}} P_g \quad (17)$$

Thus, the rate of hydrate formation and dissociation in moles per control volume (formation positive) can be expressed by:

$$R_{mh} = nS_g K_{mh}^f A_{mh}^s \langle P_{mg} - P_{mh}^{eq} \rangle - nS_{mh} K_{mh}^d A_{mh}^s \langle P_{mh}^{eq} - P_{mg} \rangle \quad (18)$$

$$R_{ch} = nS_g K_{ch}^f A_{ch}^s \langle P_{cg} - P_{ch}^{eq} \rangle - nS_{ch} K_{ch}^d A_{ch}^s \langle P_{ch}^{eq} - P_{cg} \rangle \quad (19)$$

where S is the saturation, K^f is the hydrate formation constant, A^s is the hydrate surface area for unit volume of the hydrate, P^{eq} is the phase-equilibrium pressure of hydrate dependent on temperature and K^d is the hydrate dissociation constant.

THERMO-HYDRO-CHEMO-MECHANICAL SOLUTION

The storage terms for aqueous CH₄-CO₂ mixture, gaseous CH₄-CO₂ mixture, CH₄ hydrate and CO₂ hydrate can be expressed as:

$$dP_w = \frac{K_w}{nS_w} \left(\frac{1}{\rho_w} dm_w - ndS_w - S_w d\varepsilon_v + S_w ((1-n)\beta_s + n\beta_w) dT \right) \quad (20)$$

$$dP_g = \frac{K_g}{nS_g} \left(\frac{1}{\rho_g} dm_g - ndS_g - S_g d\varepsilon_v + S_g ((1-n)\beta_s + n\beta_g) dT \right) \quad (21)$$

$$dS_{mh} = \frac{1}{n\rho_{mh}} dm_{mh} - \frac{S_{mh}}{n} d\varepsilon_v + S_{mh} \left(\frac{1-n}{n} \beta_s + \beta_{mh} \right) dT \quad (22)$$

$$dS_{ch} = \frac{1}{n\rho_{ch}} dm_{ch} - \frac{S_{ch}}{n} d\varepsilon_v + S_{ch} \left(\frac{1-n}{n} \beta_s + \beta_{ch} \right) dT \quad (23)$$

where K is the bulk modulus, ε_v is the volumetric strain (compression negative), T is the temperature and β is the thermal expansion coefficient. Substituting the mass changes of the substances (i.e. Eq. (8) & Eqs. (1)-(3) for dm_w , Eq. (9) & Eqs. (4)-(5) for dm_g , Eq. (6) for dm_{mh} and Eq. (7) for dm_{ch}) into the above four storage equations, together with two more differential equations of: [1] capillary pressure relation (i.e.

$dP_g - dP_w = P'_c \frac{dS_w S_g - dS_g S_w}{(S_w + S_g)^2}$); and [2] the pore space condition (i.e. $dS_w + dS_g +$

$dS_{mh} + dS_{ch} = 0$), the six unknowns dP_w , dP_g , dS_w , dS_g , dS_{mh} and dS_{ch} can be solved as simultaneous equations. For example, the solution of aqueous mixture pressure dP_w can be given by:

$$\begin{aligned} dP_w = & -\frac{dt}{nD} \left[\frac{\nabla \cdot (\rho_w \mathbf{q}_w)}{\rho_w} \Gamma + \frac{\nabla \cdot (\rho_g \mathbf{q}_g)}{\rho_g} \right] \\ & - \frac{1}{nD} \frac{S_w \Gamma + S_g}{S_w + S_g} d\varepsilon_v \\ & + \frac{dt}{D} \left[S_w \Gamma - S_w \frac{\rho_w}{\rho_g} \right] R_{mw} \\ & - \frac{dt}{nD} \left[\frac{N_{mh} M_{w(pure)}}{\rho_w} \Gamma + \frac{M_{mg}}{\rho_g} - \frac{M_{mh}}{\rho_{mh}} \frac{S_w \Gamma + S_g}{S_w + S_g} \right] R_{mh} \\ & + \frac{dt}{D} \left[S_w \Gamma - S_w \frac{\rho_w}{\rho_g} \right] R_{cw} \\ & - \frac{dt}{nD} \left[\frac{N_{ch} M_{w(pure)}}{\rho_w} \Gamma + \frac{M_{cg}}{\rho_g} - \frac{M_{ch}}{\rho_{ch}} \frac{S_w \Gamma + S_g}{S_w + S_g} \right] R_{ch} \\ & + \frac{1}{D} \left[S_w \beta_w \Gamma + S_g \beta_g + \left(S_{mh} \beta_{mh} + S_{ch} \beta_{ch} + \frac{1-n}{n} \beta_s \right) \frac{S_w \Gamma + S_g}{S_w + S_g} \right] dT \end{aligned} \quad (24)$$

where $D = \frac{S_w}{K_w} + \frac{S_g}{K_g} - \frac{S_w S_g P'_c}{K_w K_g (S_w + S_g)}$ and $\Gamma = 1 - \frac{S_g P'_c}{K_g (S_w + S_g)}$. As can be seen,

the above equation has seven terms. The first term represents the effect of fluid mixture flow, the second term is the effect of mechanical deformation, the third is the effect of CH₄ gas dissolution, the fourth is the effect of CH₄ hydrate formation/dissociation ($M_{mh} = N_{mh}M_{w(pure)} + M_{mg}$), the fifth is the effect of CO₂ gas dissolution, the sixth is the effect of CO₂ hydrate formation/dissociation ($M_{ch} = N_{ch}M_{w(pure)} + M_{cg}$) and the seventh is the thermal effect, which is given by:

$$\begin{aligned}
 dT = & \frac{dt}{c^{T*}} [-\nabla \cdot (\mathbf{K}^{T*} \nabla T)] \\
 & - \frac{dt}{c^{T*}} [\nabla \cdot (\rho_w c_w^T \mathbf{q}_w T) + \nabla \cdot (\rho_g c_g^T \mathbf{q}_g T)] \\
 & + \frac{dt}{c^{T*}} [\Delta H_{mh} R_{mh}] \\
 & + \frac{dt}{c^{T*}} [\Delta H_{ch} R_{ch}] \\
 & + \frac{1}{c^{T*}} [\boldsymbol{\sigma}' d\boldsymbol{\varepsilon}^p]
 \end{aligned} \tag{25}$$

where \mathbf{K}^{T*} is the volumetric mean of each thermal conductivity tensor, c^{T*} is the volumetric mean of each specific heat, ΔH is the enthalpy of the hydrate, $\boldsymbol{\sigma}'$ is the effective stress vector and $\boldsymbol{\varepsilon}^p$ is the plastic strain vector. This study assumes the effect of gas dissolution on temperature change is negligible. Each term of the right-hand side of Eq. (25) represents heat conduction, heat convection due to the mixture flow, CH₄ hydrate formation/dissociation, CO₂ hydrate formation/dissociation and plastic energy dissipation by mechanical deformation.

A SIMULATION OF CO₂ INJECTION INTO CH₄ HYDRATE-BEARING SEDIMENTS

Klar et al. (2013) developed a coupled thermo-hydro-mechanical simulator for hydrate-bearing sediments during gas production based on explicit time-marching scheme. The equations presented in the previous sections are incorporated and implemented into the simulator. Table 1 summarizes the physical parameters regarding CH₄ and CO₂. The other parameters including the geomechanical properties are presented in Klar et al. (2013).

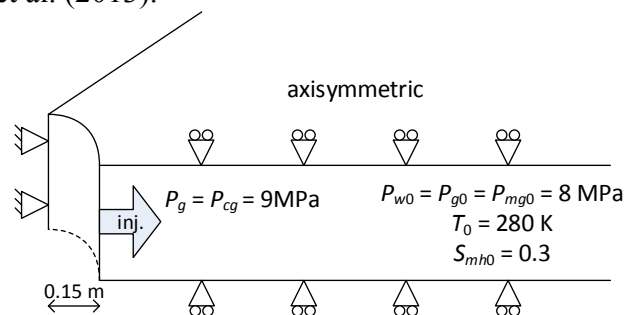


FIG. 1. Considered axisymmetric geometry and boundary conditions.

Fig. 1 shows geometry and boundary conditions considered in this study. The CH₄ hydrate-bearing sediments are assumed to be homogeneous with the initial saturation of $S_{mh0} = 0.3$. The well radius is 0.15 m and the well boundary is fixed in the radial direction. The vertical boundaries are roller, facilitating the radial deformation of the sediments. Gaseous CO₂ is continuously injected from the well at $P_g = P_{cg} = 9$ MPa, thus no water is produced. The initial temperature is set to be $T_0 = 280$ K and the initial water pressure is $P_{w0} = 8$ MPa. Under this condition, both CH₄ and CO₂ hydrates are stable and the phase equilibrium pressures are $P^{eq}_{mh} = 5.7$ MPa and $P^{eq}_{ch} = 3.4$ MPa, respectively. The phase equilibrium pressure is illustrated in Fig. 2. The well is assumed to be insulated. Based on the fact that the sediments bears CH₄ hydrate, the initial partial gas pressures are set to be $P_{mg0} = 8$ MPa and $P_{cg0} = 0$ MPa.

Table 1. Parameters regarding CH₄ and CO₂

Parameters	CH ₄	CO ₂
Aqueous phase		
Density	$\rho_{mw} = m_{mw} / (nS_w)$	$\rho_{cw} = m_{cw} / (nS_w)$
Viscosity	$\mu_{mw} = \mu_{w(pure)}$	$\mu_{cw} = \mu_{w(pure)}$
Specific heat	$c^T_{mw} = c^T_{w(pure)}$	$c^T_{cw} = c^T_{w(pure)}$
Thermal conductivity	$k^T_{mw} = k^T_{w(pure)}$	$k^T_{cw} = k^T_{w(pure)}$
Thermal expansion	$\beta_{mw} = \beta_{w(pure)}$	$\beta_{cw} = \beta_{w(pure)}$
Solubility (g/g)	$c_{mw(max)} = 0.001$	$c_{cw(max)} = 0.07^s$
Gaseous phase		
Density (g/cm ³)	$\rho_{mg} = M_{mg}P_{mg}/(RT)$	$\rho_{cg} = M_{cg}P_{cg}/(RT)$
Viscosity ratio	$\mu_{w(pure)}/\mu_{mg} = 1050 - 3.3T$	$\mu_{w(pure)}/\mu_{cg} = 940 - 3.0T$
Dissolution const. (1/s)	$D_{mw} = 3 \times 10^{-5}$	$D_{cw} = 3 \times 10^{-5}$
Specific heat (J/g/K)	$c^T_{mg} = 1.24 + 0.003T$	$c^T_{cg} = 0.52 + 0.001T$
Therm. cond. (W/m/K)	$k^T_{mg} = 0.034$	$k^T_{cg} = 0.015$
Therm. exp (1/K)	$\beta_{mg} = 1/T$	$\beta_{cg} = 1/T$
Hydrate phase		
Density (g/cm ³)	$\rho_{mh} = 0.90$	$\rho_{ch} = 1.1$
Hydrate number	$N_{mh} = 6$	$N_{ch} = 6$
P^{eq} (kPa) when $T \leq 281.5$	$P^{eq}_{mh} = \exp(39-8520/T)$	$P^{eq}_{ch} = \exp(45-10360/T)$
P^{eq} (kPa) when $T > 281.5$		$P^{eq}_{ch} = \exp(199-53542/T)$
Enthalpy (kJ/mol)	$\Delta H_{mh} = 57-0.02T$	$\Delta H_{ch} = 208-0.53T^-$
Form. const. (mol/m ² /Pa/s)	$K^f_{mh} = 0.60 \times 10^{-11\#}$	$K^f_{ch} = 4.8 \times 10^{-9*}$
Dis. const. (mol/m ² /Pa/s)	$K^d_{mh} = 3.6 \times 10^4 \exp(-9742/T)$	$K^d_{ch} = 1.8 \times 10^8 \exp(-12376/T)^+$
Surface area per vol. (1/m)	$A^s_{mh} = 0.375 \times 10^{-6}$	$A^s_{ch} = A^s_{mh}$
Specific heat (J/g/K)	$c^T_{mh} = 2.01$	$c^T_{ch} = c^T_{mh}$
Therm. cond. (W/m/K)	$k^T_{mh} = 0.62$	$k^T_{ch} = 0.49$
Therm. exp (1/K)	$\beta_{mh} = 4.6 \times 10^{-4}$	$\beta_{ch} = 2.3 \times 10^{-4}$

^s Andersen et al. (1992); ⁻ Anderson (2003); [#] Englezos et al. (1987)

^{*} Clarke and Bishnoi (2005); ⁺ Clarke and Bishnoi (2004)

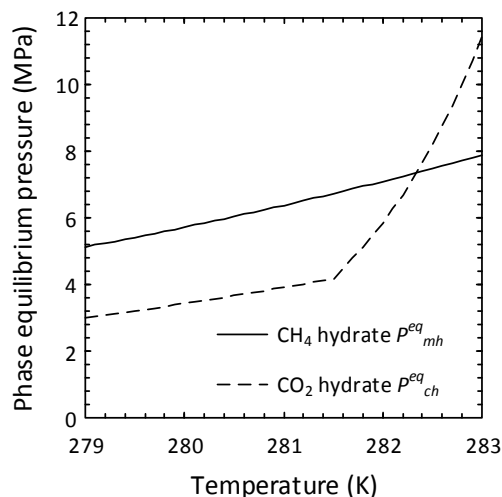


FIG. 2. Phase equilibrium pressures of CH₄ and CO₂ hydrates.

Fig. 3 shows (a) saturation change and (b) pressure change over $t = 10, 20$ and 40 hours. The injected CO₂ gas increases P_{cg} (initially $P_{cg0} = 0$), leading to $P_{cg} > P_{ch}^{eq}$. Consequently, the presence of CO₂ gas is transformed into CO₂ hydrate, raising S_{ch} (black dashed-line). Simultaneously, since chemical reaction is controlled by the partial pressure, the injection of CO₂ gas leads to reduction in P_{mg} (initially $P_{mg0} = 8$ MPa) at given P_g as $P_g = P_{mg} + P_{cg}$. This results in CH₄ hydrate dissociation, reducing S_{mh} (black normal-line) and production of CH₄ gas, increasing P_{mg} (red normal-line in Fig. 3b).

It is interesting to note that, initially, the exothermic nature of CO₂ hydrate formation and endothermic nature of CH₄ hydrate dissociation is in balance. This brings the situation where $P_{ch}^{eq} = P_{cg}$ and $P_{mh}^{eq} = P_{mg}$ (e.g. the location $r = 1.7, 2.6$ and 4.3 m at $t = 10, 20$ and 40 hours, respectively). However, once CH₄ hydrate completely dissociates, the temperature keeps increasing. Consequently, P_{ch}^{eq} reaches 9 MPa, equilibrating with the well pressure, and thus CO₂ hydrate formation ceases at this point. This results in the existence of the sharp fronts of CO₂ hydrate formation and CH₄ hydrate dissociation and these two fronts are very close to each other. In other words, CO₂ hydrate formation could cease in the earlier stage if there was no endothermic effect (i.e. if there was no CH₄ hydrate).

With time, the fronts of CO₂ hydrate formation and CH₄ dissociation propagate further into the sediment. In addition, it becomes more evident that traveled CH₄ gas forms CH₄ hydrate, showing a gradual increase in S_{mh} away from the dissociation front. The produced CH₄ gas travels further into the sediment together with CO₂ gas because of CH₄-CO₂ gas mixture pressure gradient, that is, the value of $P_{mg} + P_{cg}$ is greater than the initial gas pressure of 8 MPa. Until P_{mg} drops to P_{mh}^{eq} (either due to temperature increase or CO₂ gas invasion), formation of CH₄ hydrate continues. The invasion of CO₂ gas is, in effect, prevented by formation of CO₂ hydrate. This implies that the sharp front of CH₄ dissociation is followed by the moderate front of CH₄ hydrate formation. For example, CH₄ formation fronts expand from $r = 2.0$ – 3.3 m at $t = 10$ hours to $r = 5.0$ – 7.5 m at $t = 40$ hours.

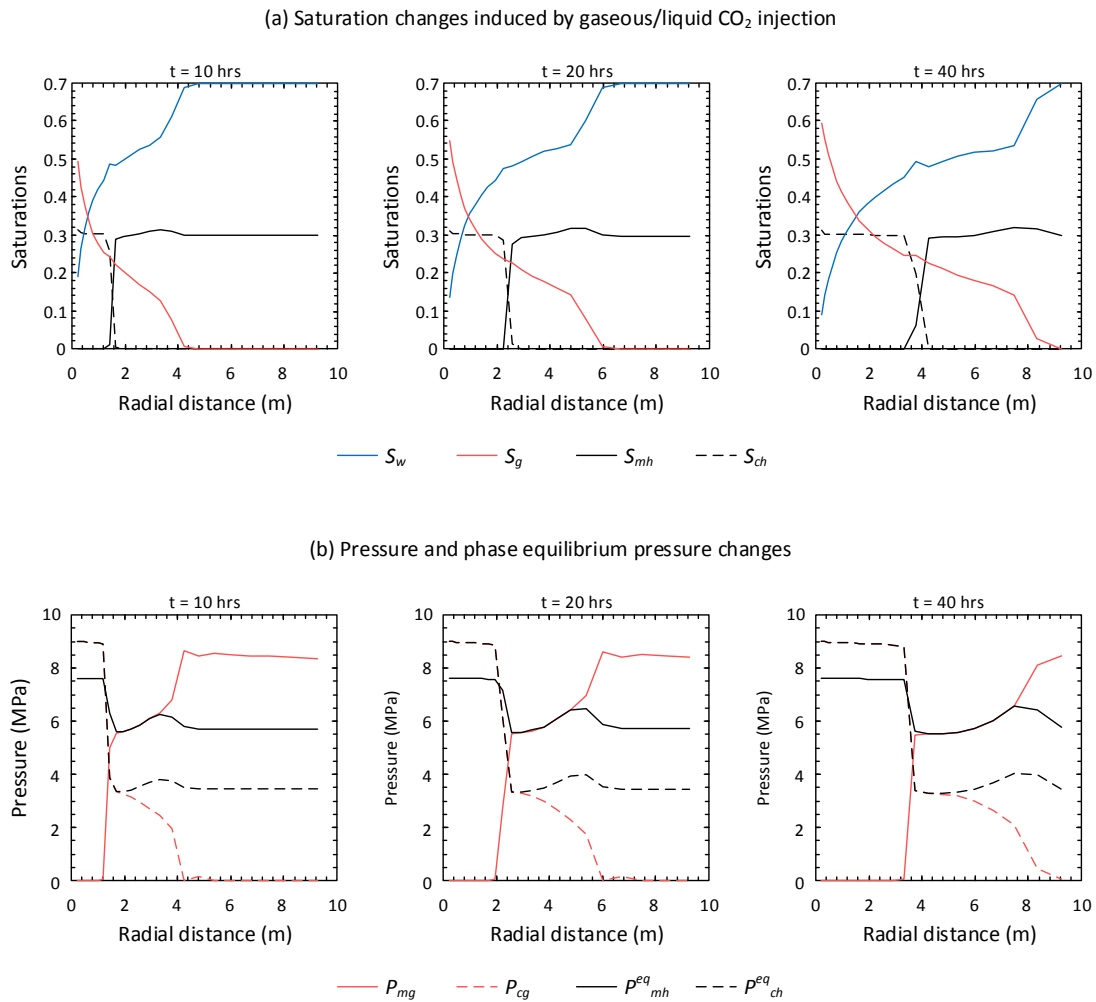


FIG. 3. CO₂ gas injection in hydrate-bearing sediments, leading to (a) saturation change and (b) gas pressure change.

CONCLUSIONS

This paper presented the comprehensive analytical formulation for coupled thermo-hydro-chemo-mechanical behavior of gas hydrate-bearing sediments including the effect of chemical activation. The formulation facilitated the effect of gas dissolution, hydrate formation and hydrate dissociation for both CH₄ and CO₂. As a preliminary study, hydrate conversion (from CH₄ hydrate into CO₂ hydrate) by injection of CO₂ gas into CH₄ hydrate-bearing sediments was simulated. It was found that CO₂ injection resulted in the increase in P_{cg} (thus CO₂ hydrate formation) and also in the decrease in P_{mg} (thus CH₄ hydrate dissociation). The formation of CO₂ hydrate was primarily helped by the endothermic nature of CH₄ hydrate dissociation. Thus, the efficiency of hydrate conversion would likely be controlled by the temperature change.

REFERENCES

- Andersen, G., Probst, A., Murray, L., and Butler, S. (1992). "An accurate PVT model for geothermal fluids as represented by H₂O-CO₂-NaCl mixtures." *The 17th Workshop on Geothermal Reservoir Engineering*, 29-31 January, California, Stanford University, 239–248.
- Anderson, G. K. (2003). "Enthalpy of dissociation and hydration number of carbon dioxide hydrate from the Clapeyron equation." *Journal of Chemical Thermodynamics*, 35(7), 1171–1183.
- Burwicz, E., Rupke, L., and Wallmann, K. (2011). "Estimation of the global amount of submarine gas hydrates formed via microbial methane formation based on numerical reaction-transport modeling and a novel parameterization of Holocene sedimentation." *Geochimica et Cosmochimica Acta* 75, 4562–4576.
- Clarke, M. A., and Bishnoi, P. (2004). "Determination of the intrinsic rate constant and activation energy of CO₂ gas hydrate decomposition using in-situ particle size analysis." *Chemical Engineering Science*, 59(14), 2983–2993.
- Clarke, M. A. and Bishnoi, P. (2005). "Determination of the intrinsic kinetics of CO gas hydrate formation using in situ particle size analysis." *Chemical Engineering Science*, 60(3), 695–709.
- Dallimore, S. R., Wright, J. F., Nixon, F. M., Kurihara, M., Yamamoto, K., Fujii, K., Numasawa, M., Yasuda, M., and Imasato, Y. (2008). "Geologic and porous media factors affecting the 2007 production response characteristics of the JOGMEC/NRCAN/AURORA Mallik Gas Hydrate Production Research well." *6th International Conference on Gas Hydrates*, 06-10 July, Vancouver, Canada.
- Englezos, P., Kalogerakis, N., Dholabhai, P. D. and Bishnoi, P. R. (1987). "Kinetics of Formation of Methane and Ethane Gas Hydrates." *Chemical Engineering Science*, 42(11), 2647–2658.
- Kim, J., Yang, D., Moridis, G. J., and Rutqvist, J. (2011). "Numerical studies on two-way coupled fluid flow and geomechanics in hydrate deposits." *SPE Reservoir Simulation Symposium*, 21-23 February, The Woodlands, USA.
- Kimoto, S., Oka, F., and Fushita, T. (2010). "A chemo-thermo-mechanically coupled analysis of ground deformation induced by gas hydrate dissociation." *International Journal of Mechanical Sciences*, 52(2), 365–376.
- Klar, A., Uchida, S., Soga, K., and Yamamoto, K. (2013). "Explicitly coupled thermal-flow-mechanical formulation for gas hydrate sediments." *SPE Journal*, 18(2), 196–206.
- Milkov, A. V. (2004). "Global estimates of hydrate-bound gas in marine sediments: how much is really out there?." *Earth-Science Review*, 66, 183–197.
- Schoderbek, D., Farrell, H., Hester, K., Howard, J., Raterman, K., Silpngarm, S., Martin, K. L., Smith, B., and Klein, P. (2013). "ConocoPhillips gas hydrate production test." *Final Technical Report*, United States Department of Energy.
- Yamamoto, K., Terao, Y., Fujii, T., Terumichi, I., Seki, M., Matsuzawa, M., and Kanno T. (2014). "Operational overview of the offshore production test of methane hydrates in the Eastern Nankai Trough." *Offshore Technology Conference*, 05-08 May, Houston, USA.

Centrifuge Modeling of Mine Tailings and Waste Rock Co-Disposal, Consolidation, and Dynamic Loading

Nonika Antonaki¹; Tarek Abdoun²; and Inthuorn Sasanakul, A.M.ASCE³

¹Graduate Student, Civil and Environmental Engineering, Rensselaer Polytechnic Institute, Troy, NY 12180. E-mail: antonn@rpi.edu

²Professor, CEE, RPI, Troy, NY 12180.

³Assistant Professor, CEE, Univ. of South Carolina, Columbia, SC 29208.

Abstract: Tailings from a planned copper-gold mining project located at the earthquake-prone Andean region of South America were obtained from the metallurgical pilot plant in order to perform centrifuge tests at the center for earthquake engineering simulation (RPI). Consolidation and shaking table tests were conducted to evaluate the properties and liquefaction potential of mildly sloped consolidated mine tailings. A gentle slope at the surface of a tailings impoundment can significantly add to the stored volume. Due to long consolidation time, large settlement and clear signs of liquefaction after a few cycles of dynamic loading, the need for improvement arose. One of the alternative management methods that can improve physical stability and geochemical properties is co-disposal of mine tailings and waste rock. In this study, co-mixing of the materials at a specified ratio of dry mass (waste rock to tailings) prior to disposal was examined. The behavior was compared to that of tailings with respect to consolidation rate, settlement accumulation, slope stability and response to dynamic loading. In the field, the tailings are thickened and hydraulically deposited into the containment structure in layers. In the centrifuge, tailings were prepared in layers and consolidated, thus allowing instrumentation of each layer before consolidation of the complete impoundment.

INTRODUCTION

Conventional mining activity produces large quantities of both tailings with high water content and dry waste rock. Tailings are commonly discharged as a slurry with slow consolidation properties and low shear strength, often causing failures in tailings impoundments due to physical instability. In contrast, the waste rock is characterized by high shear strength and is commonly disposed of in large dumps. The unsaturated conditions allow weathering of the waste rock, which may cause long-term acid drainage and metal leaching. Blending the two materials could produce self-sealing

deposits with high shear strength, low compressibility and density higher than either material on its own, thereby reducing the total volume and surface area requirements for impoundment design and final reclamation (Bussiere 2007, Wilson et al. 2009).

To date, most experimental research on mine tailings has consisted of small scale laboratory tests, such as simple or direct shear tests, triaxial tests, etc. (Aubertin et al. 1996, Dimitrova et al. 2011, Garga et al. 1984, Hight and Tobin 1980, Hight and Vallee 1980, Proskin et al. 2010, Qiu et al. 2001, Sanin et al. 2012, Wijewickreme et al. 2005, etc). Laboratory investigations have also been conducted on mixtures by a few researchers (Leduc et al. 2003, Wickland et al. 2005, Wickland et al. 2006, Wickland et al. 2010). In Australia, the co-disposal of coarse and fine coal wastes by combined pumping was pioneered in 1990 by Jeebropilly colliery in southeastern Queensland (Morris et al. 1997). Very few attempts of physical modeling tests using a centrifuge have been made with mine tailings (Stone et al., 1994).

In this study, fine-grained tailings from a planned copper-gold mine in an earthquake-prone zone of South America were used in centrifuge tests. The main objectives were to model the deposition of tailings in layers on the centrifuge, examine the consolidation behavior in terms of time, pore pressure dissipation rate and settlement and, finally, to evaluate the liquefaction potential and slope stability under dynamic loading. When the material is able to sustain a sloped surface the stored volume within a specific area can be increased. Subsequently, the same testing scenario was repeated using a mixture at a selected ratio of waste rock to tailings by dry mass for comparison purposes. Geotechnical centrifuge testing can offer several advantages. Consolidation is accelerated and simulating prototype stress conditions in a small scale model is enabled (Taylor 1995). A new technique for monitoring settlement of the layers during consolidation was also developed and has been presented by Antonaki et al. (2014).

TEST DESCRIPTION

A series of tests were carried out at the Center for Earthquake Engineering Simulation at Rensselaer Polytechnic Institute (Troy, NY). The centrifuge is a 150 g-ton machine with a nominal radius of 2.7 m. These tests were conducted at 80g centrifugal acceleration to model a 20 to 25 m high deposit. In an attempt to simulate field conditions the models were constructed in four layers. Drainage was only allowed at the surface to model the in situ conditions.

The tailings were shipped from the site thickened to 59% water content. The material had a specific gravity of 2.73, about 60% passing through the #200 mesh and was classified as low-plastic (CL-ML). For the centrifuge tests, initial water content was re-adjusted to the field pumping water content of 59%. Uniform crushed stone (1/8") was purchased and then sieved using a 0.203" sieve to remove particles larger than 5mm or about 37 cm in prototype scale. Measurements and calculations resulted in 2.3:1 (rock waste to mine tailings by dry mass) as the ratio leading to fine material just filling the voids of the waste rock skeleton at the consolidated state, which is considered to be the optimal scenario when designing a mixture (Wickland et al. 2006). The 2:1 mixture presented herein was selected as a starting point for a parametric study.

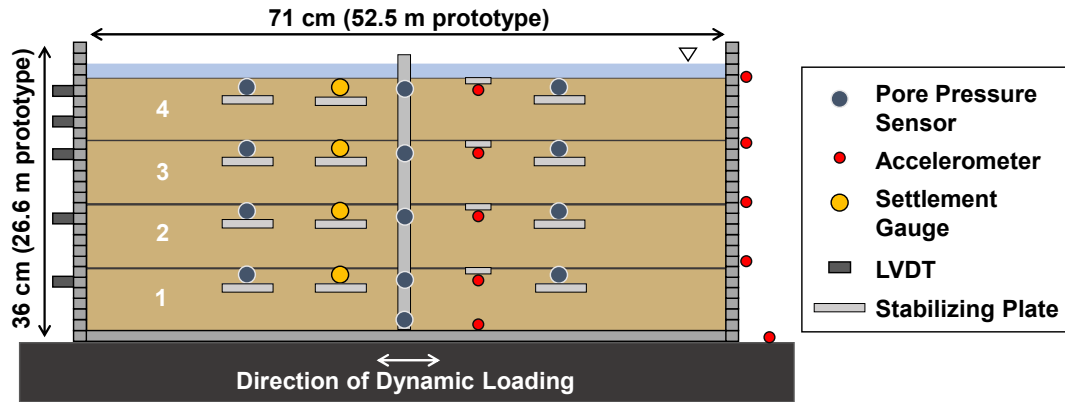


FIG. 1. Test set-up, layer numbering and sensors used.



FIG. 2. (a) Laminar container bolted on shaker attached to the centrifuge basket, (b) Pore pressure sensors taped on ruler attached to the wall of the container and measuring tape used to monitor settlement, (c) Sensor glued on plastic plate floating on surface of mine tailings and (d) same sensor on surface of 2:1 mixture.

The deformable laminar container with internal dimensions of 71 cm x 36 cm x 37 cm that was used is depicted in Figure 1. This type of container consists of stacked thin rectangular “rings” which can slide with respect to each other on bearings, thus allowing the model to deform laterally as opposed to imposing unrealistic fixed boundary conditions during dynamic loading. Removable rigid side walls ensured fixed boundaries during the deposition and consolidation phases of the tests. Figure 2 (a) depicts the container on the centrifuge while its rigid ends are still attached. A membrane fitted to the inside of the container was fabricated to safely contain the material, since the interface between rings cannot prevent seepage of water.

The final instrumentation setup is shown in Figure 1. Settlement gauges, pore pressure sensors, accelerometers and LVDTs were used to obtain data corresponding to each layer. Pore pressures and settlements were monitored to evaluate the consolidation progress with time and depth. The consolidation phase of the tests could conclude once these parameters became close to constant with time, especially relying on pore pressure transducers fixed on the container wall, as depicted in Figure 2 (b). Measuring tape was glued on the fabricated membrane in order to observe settlement throughout the tests (Figure 2(b)). Accelerometers were embedded below the surface of each layer, as well as glued on the rings of the container at the level of each layer surface after consolidation, as estimated from previous tests. LVDTs were used to monitor lateral deformation of the container during dynamic loading. All sensors placed inside the soil model needed to be glued to small plastic or aluminum plates, in order to maintain their position and direction throughout the tests (Figure 2 (c), (d)). Accelerometer cables were additionally wrapped in aluminum foil while the rest of the sensor plates went through vertical strings that prevented lateral movement. During the tests, videos were recorded via centrifuge onboard cameras.

All tests consisted of three phases: brief consolidation of each deposited layer before deposition of the next, consolidation of the complete model and dynamic loading of the sloped model. The first phase was conducted for 30 hours (prototype time) at a lower g-level (20g). This procedure allowed the material to gain enough strength for sensors to be placed at the surface. In addition, the short-term consolidation of tailings as the impoundment is gradually filled was modelled. Consolidation of the impoundment at 80g centrifugal acceleration followed, with duration depending on the material. After consolidation was completed water was drained from the surface of the model and a mild slope ($\approx 4\%$) was formed. Thickened tailings can be deposited to form a gentle beach slope (typically between 2% and 6%). The model was spun back to 80g and a harmonic motion was applied at the base of the model by the shaking table (Figure 3 (a), (b)). The motion consisted of 50 cycles, with linearly increasing amplitude that reached its maximum (approximately 0.10 g) after the first 10 cycles. Figure 3 (c) depicts the container on the shaker after the rigid sides were removed prior to dynamic loading. The LVDT set-up can also be observed in the same figure. Figure 3 (d) exhibits the deformed container at the end of a test. After completion of each test the model was carefully dissected in order to identify the final location of sensors and collect soil samples for water content measurements. Figure 3 (e) and (f) depict accelerometers during dissection after a test with just mine tailings and the 2:1 mixture respectively. The specific sensors successfully maintained their orientation, but that was not the case for all sensors placed in mine tailings. Sensor stability was more easily achieved in mixtures.

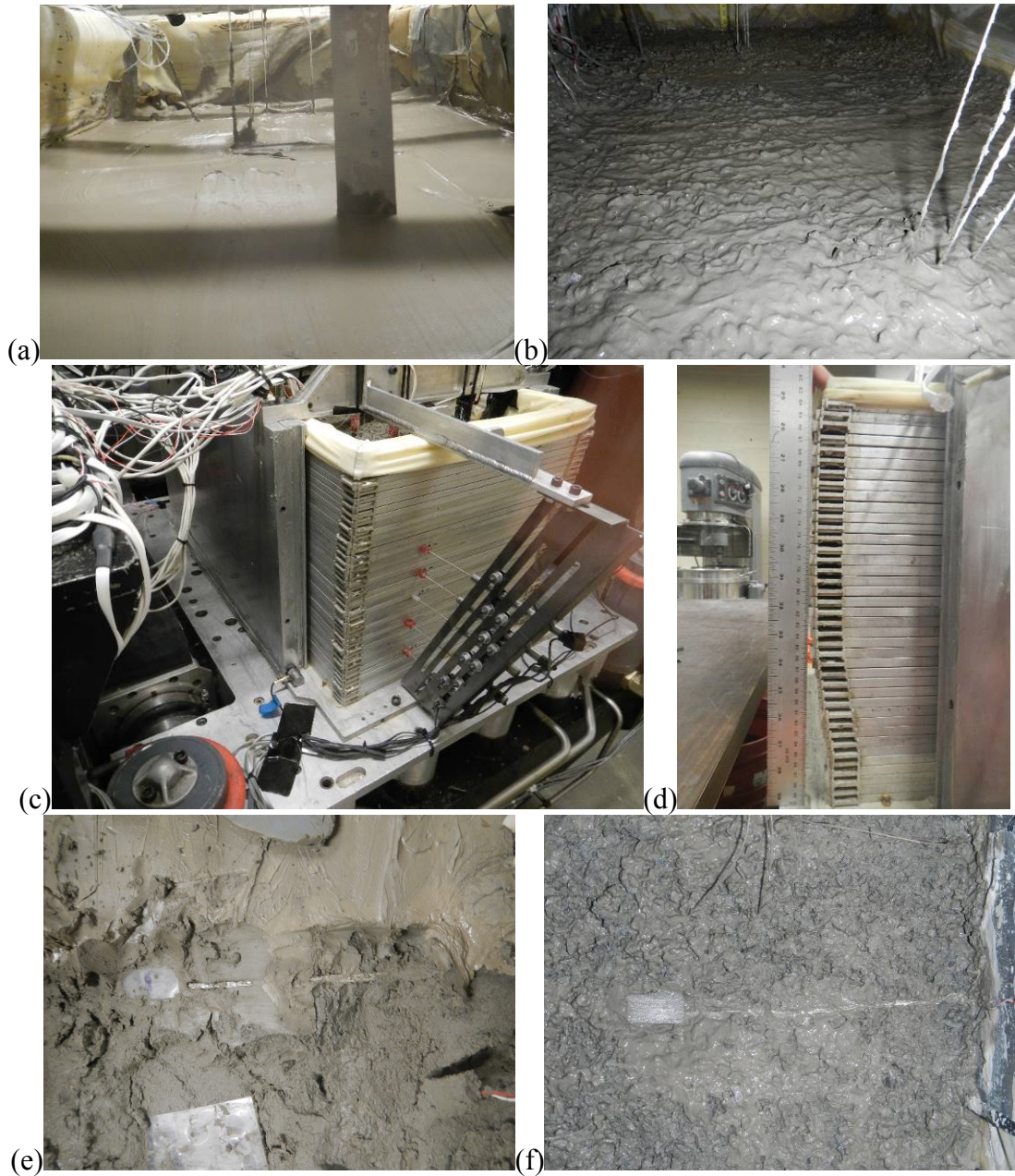


FIG. 3. (a) Laminar container after removal of rigid sides and LVDT set-up on sliding container rings, (b) Example of deformed soil profile after completion of a test, (c) Sloped surface of mine tailings before shaking, (d) Sloped surface of 2:1 mixture before shaking, (e) Accelerometer successfully stabilized in mine tailings until post testing dissection and (f) the same in 2:1 mixture.

TEST RESULTS

Data from a test performed with mine tailings and a test performed with a 2:1 mixture are compared in prototype scale.

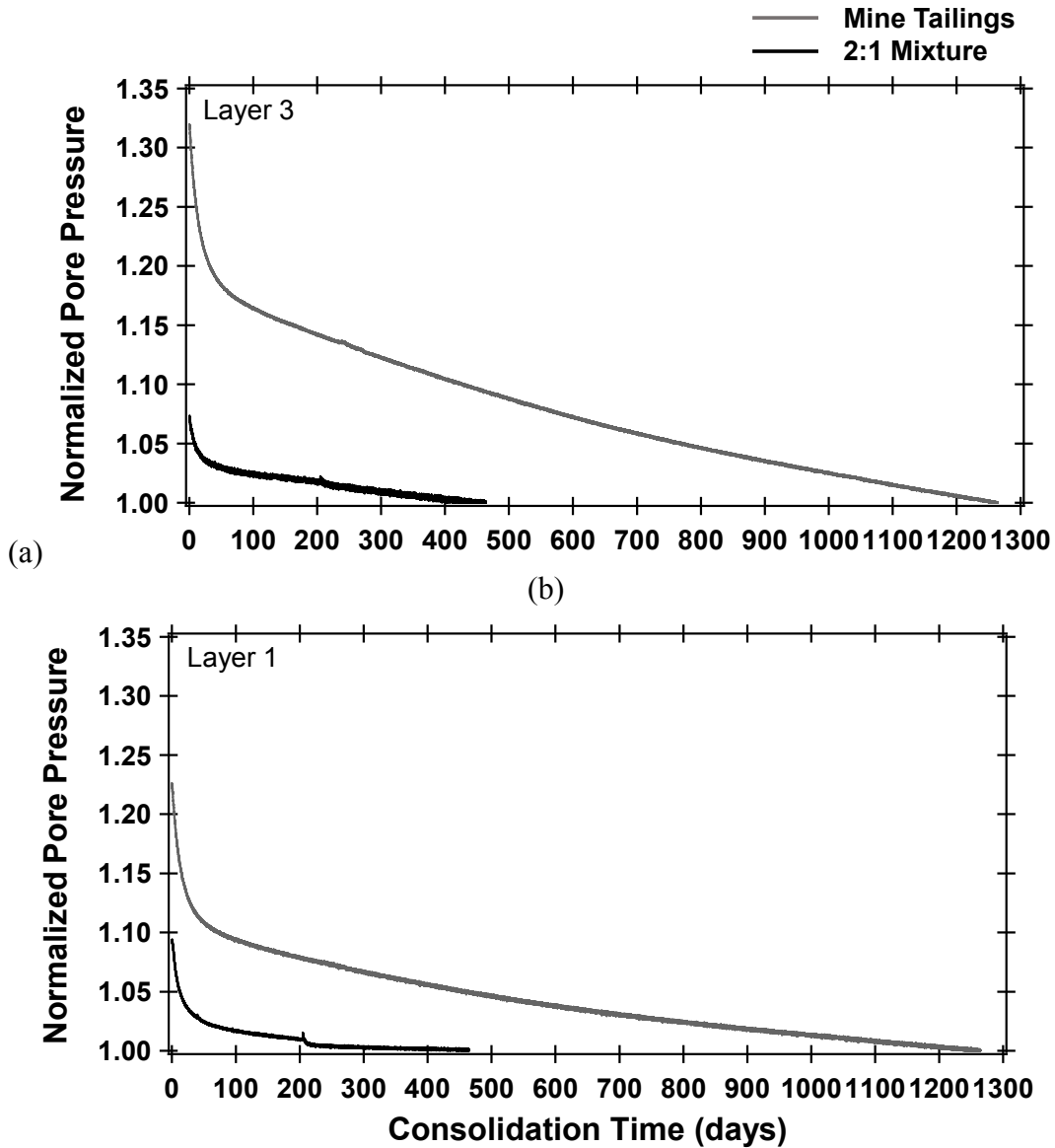


FIG. 4. Pore pressure dissipation (normalized with final value) measured in (a) third layer and (b) first layer during consolidation of mine tailings and 2:1 mixture.

Figure 4 presents pore pressure dissipation as measured by two selected fixed pore pressure sensors (shown in Figure 2 (b)) during consolidation of the deposits at 80g. Excess pore pressure dissipation at similar depths for both materials is plotted in each graph. Every pore pressure curve was normalized with the final value to eliminate the effect of small differences in sensor depth between the two tests (≈ 4 m). The top graph shows pore pressure measured in the third of four layers for both materials (4 – 8 m from the water surface) and the bottom graph shows pore pressure measured in the first or bottom layer (15 – 19 m from the water surface), as numbered in Figure 1.

Curves are qualitatively similar for both tests, consisting of an initial steep part followed by a much flatter part that asymptotically approaches the hydrostatic value. However, mine tailings started with significantly higher build-up and took much longer to consolidate. The mine tailings were left to consolidate for three times the consolidation time of the mixture. In both cases a small part of what appears as pore pressure dissipation was evaporation. As indicated by the final slope of the curves, mine tailings were still slowly consolidating three and a half years after deposition.

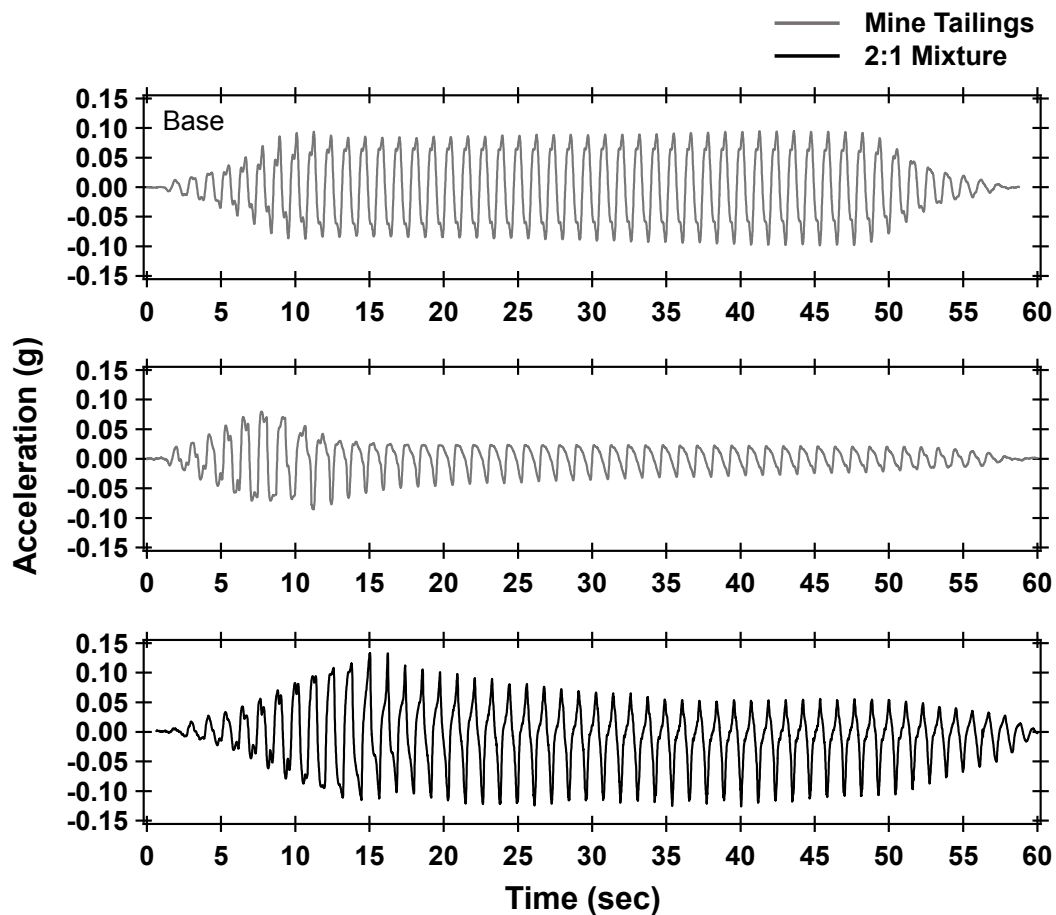


FIG. 5. Acceleration measured during dynamic loading: at base of mine tailings (top graph), at surface of mine tailings (middle graph) and at surface of 2:1 mixture (bottom graph).

For the purpose of dynamic response comparison, Figures 5 and 6 depict selected acceleration and horizontal displacement data from the two tests. The top graph in Figure 5 shows acceleration measured at the base of the container during dynamic loading of mine tailings. The maximum acceleration applied was approximately 0.096 g. The same excitation was applied to the mixture but the amplitude was 0.074 g due to variation of shaker response for different soil models. The middle and the bottom graphs in Figure 5 correspond to acceleration measured right underneath the surface of the tailings and the mixture. In mine tailings, a visible drop in the acceleration data

occurred even before the maximum base acceleration was reached and the acceleration became practically zero (less than 0.05 g) a few cycles later, indicating liquefaction of the slope. In contrast, the mixture surface acceleration kept increasing even after the maximum excitation amplitude was reached. A smaller and asymmetrical decrease was present in the acceleration data and indicated softening but not liquefaction. Accelerations measured at deeper layers are not included herein, but showed that liquefaction did not reach the bottom layer of the mine tailings deposit.

The behavior of the two deposits was similar with respect to lateral displacement of the soil profile. Displacement of the top of the deposits measured by LVDTs was not very large (Figure 6). It appears that the residual displacement of the mixture was slightly higher, but the top LVDT was right at the level of the surface in that test and 1.5 m below the surface in the mine tailings test. The tendency has been for deformation to increase closer to the surface, so the residual displacements at the top can be considered comparable for the two tests. The mine tailings profile deformed in the direction towards the toe of the slope as expected, whereas the mixture profile deformed in the opposite direction. Deformations are small in both cases, so the direction is considered coincidental and not of huge significance.

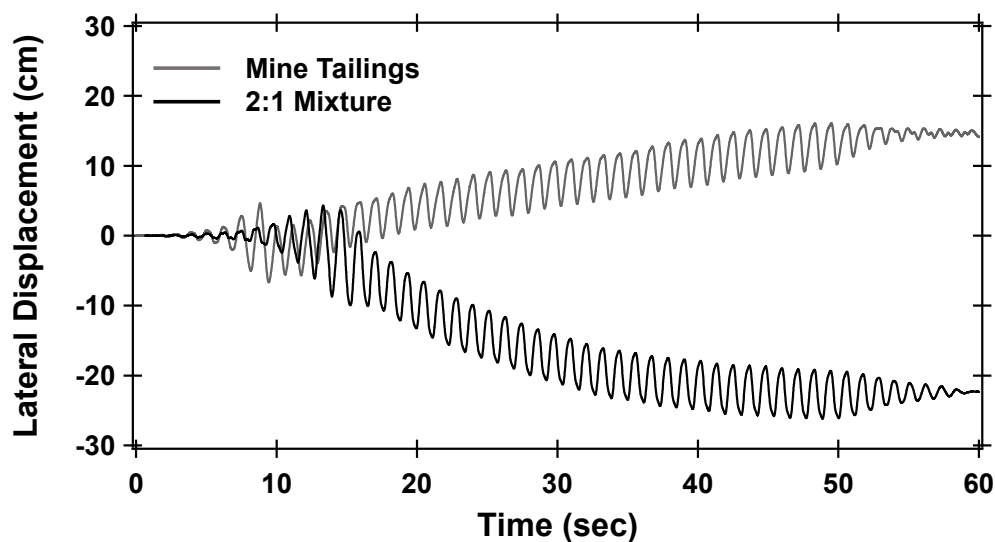


FIG. 6. Horizontal displacement measured at the surface level of mine tailings and 2:1 mixture during dynamic loading.

A summary of observed settlements is included in Table 1 for the two tests presented. Settlement was normalized with height and presented in percent. The last column of the table corresponds to the ratio between the settlements of the tailings (T) and the mixture (M) during each testing phase. The mine tailings settled 1.8 times more during the brief consolidation phase following deposition of each layer and 3.4 times more during consolidation of the entire deposit. Dynamic settlements were similar for the two materials. The negative settlement of the toe of the slope for the mixture indicates that some surficial material moved downslope. In the case of mine tailings the slope started at an inclination of 3.5% and ended up at 2.8% after the

motion was applied, whereas in the case of the mixture the slope started at approximately 4.2% and ended up at 2.8%.

Table 1. Comparison between settlements normalized with model height of mine tailings and 2:1 mixture during each phase of the tests.

Testing Phase	Layer	Settlement/Height (%)		Settlement Ratio (T/M)
		Tailings	2:1 Mixture	
Consolidation at 20g	1	15%	7%	2.2
	2	20%	13%	1.6
	3	22%	13%	1.6
	4	24%	12%	1.9
	Sum	20%	11%	1.8
Consolidation at 80g	All	13%	4%	3.4
Shaking at 80g	Head	4%	3%	1.2
	Toe	2%	-1%	-1.8

CONCLUSIONS

To summarize this study, mine tailings and a mixture of mine tailings and coarse waste rock at 2:1 ratio of waste rock to tailings by dry mass were deposited in layers, consolidated and dynamically loaded on the centrifuge. Co-disposal offered advantages regarding space requirements, consolidation time, compressibility and liquefaction potential. Slope stability was not significantly improved. Based on these results, more tests need to be conducted to examine mixture behavior and further improve the physical stability of the deposit. A centrifuge test with a 3:1 mixture was planned shortly after these conclusions were reached.

ACKNOWLEDGMENTS

The authors appreciate the support of Golder Associates Ltd..

REFERENCES

- Antonaki, N., Sasanakul, I., Abdoun, T., Sanin, M.V., Puebla, H. and Ubilla, J. (2014). "Centrifuge Modeling of Deposition and Consolidation of Fine-grained Mine Tailings." *Proceedings of Geotronics 2014*, Atlanta, Georgia.
- Aubertin, M., Bussiere, B., and Chapuis, R.P. (1996). "Hydraulic Conductivity of Homogenized Tailings from Hard Rock Mines." *Canadian Geotechnical Journal*, Vol. 33: 470-482.
- Bussiere, B. (2007). "Colloquium 2004: Hydrogeotechnical properties of hard rock tailings from metal mines and emerging geoenvironmental disposal approaches." *Canadian Geotechnical Journal*, Vol. 44: 1019-1052.

- Dimitrova, R.S., and Yanful, E.K. (2011). "Undrained Strength of Deposited Mine Tailings Beds: Effect of Water Content, Effective Stress and Time of Consolidation." *Geotechnical and Geological Engineering*, Vol. 29: 935-951.
- Garga, V. and McKay, L.D. (1984). "Cyclic Triaxial Strength of Mine Tailings." *Journal of Geotechnical Engineering*, Vol. 110 (8): 1091-1105.
- Highter, W.H, and Tobin, R.F. (1980). "Flow Slides and the Undrained Brittleness Index of Some Mine Tailings." *Engineering Geology*, Vol. 16: 71-82.
- Highter, W.H, and Vallee, R.P. (1980). "The Liquefaction of Different Mine Tailings under Stress-controlled Loading." *Engineering Geology*, Vol. 16: 147-150.
- Leduc, M., and Smith, M.E. (2003). "Tailings Co -Disposal™ Innovations for Cost Savings and Liability Reduction." *The Latin America Mining Record*, July/Aug. 2003.
- Morris, P.H., and Williams, D.J. (1997). "Co-disposal of washery wastes at Jeebropilly colliery, Queensland, Australia." *Trans. Instn. Min. Metall. (Sect. A: Min. Industry)*, Vol. 106.
- Proskin, S., Segó, D., and Alostaz, M. (2010). "Freeze-thaw and consolidation tests on Suncor mature fine tailings (MFT)." *Cold Regions Science and Technology*, Vol. 63: 110-120.
- Qiu, Y., and Segó, D.C. (2001). "Laboratory properties of mine tailings." *Canadian Geotechnical Journal*, Vol. 38: 183-190.
- Sanin, M.V., Puebla, H., and Eldridge, T. (2012). "Cyclic behavior of thickened tailings." *Proceedings of Tailings and Mine Waste 2012*, Keystone, Colorado.
- Stone, K.J.L., Randolph, M.F., Toh, S., and Sales, A.A. (1994). "Evaluation of Consolidation Behavior of Mine Tailings." *Journal of Geotechnical Engineering*, ASCE, Vol. 120: 473-490.
- Taylor, R.N. (1995). "Geotechnical Centrifuge Technology." 1995 Chapman & Hall.
- Wickland, B.E., and Wilson, G.W. (2005). "Self-weight consolidation of mixtures of mine waste rock and tailings." *Canadian Geotechnical Journal*, Vol. 42: 327-339.
- Wickland, B.E., Wilson, G.W., Wijewickreme, D., and Klein, B. (2006). "Design and evaluation of mixtures of mine waste rock and tailings." *Canadian Geotechnical Journal*, Vol. 43: 928-945.
- Wickland, B.E., Wilson, G.W., and Wijewickreme, D. (2010). "Hydraulic conductivity and consolidation response of mixtures of mine waste rock and tailings." *Canadian Geotechnical Journal*, Vol. 47: 472-485.
- Wijewickreme, D., Sanin, M.V., and Greenaway, G. (2005). "Cyclic Shear Response of Fine-grained Mine Tailings." *Canadian Geotechnical Journal*, Vol. 42: 1408-1421.
- Wilson, G.W., Wickland, B.E., Palkovits, F., and Longo, S. (2009). "The implementation of paste rock systems for preventing acid rock drainage from waste rock and tailings impoundments." *Submitted for oral presentation at the 8th ICARD*, 22-26 June 2009, Skelleftea, Sweden.

Compressibility Behavior of Synthetic Mine Tailings Amended with Fly Ash

Mohammad H. Gorakhki¹ and Christopher A. Bareither²

¹Graduate Research Assistant, Civil and Environmental Engineering, Colorado State Univ., Fort Collins, CO 80523. E-mail: mrhg@colostate.edu

²Assistant Professor, Civil and Environmental Engineering, Colorado State Univ., Fort Collins, CO 80523. E-mail: christopher.bareither@colostate.edu

Abstract: The objective of this study was to evaluate the effects of fly ash amendment on compression behavior of mine tailings. The study included one synthetic mine tailings and two types of fly ash. A synthetic fine-grained mine tailings was created as a combination of silica powder and kaolin clay. The two fly ashes used classified as off-specification, but had sufficient calcium oxide (CaO) content (12 % and 17 %) to promote pozzolanic activity. Tailings-fly ash compression specimens were prepared at solids content of 60 and 70 % (water content = 67 and 43 %, respectively), water-to-fly ash ratios of 2.5 and 5, and were cured for 0.1 d (2 h), 7 d, and 28 d. Bi-linear compression curves on semi-log plots were observed in most of the fly ash amended tailings specimens. The break in slope on the compression curve was identified as the breaking stress, whereupon cementitious bonds are broken and there is a subsequent increase in the magnitude of compression for a given applied vertical stress. In general, higher fly ash content, lower water-to-fly ash ratio, longer curing time, and/or increase in CaO content of fly ash resulted in improved mechanical performance of tailings-fly ash mixtures. Improved mechanical performance coincided with a higher breaking stress, lower compression index, and reduced total settlement.

INTRODUCTION

The Mining, Minerals, and Sustainable Development Project reports that approximately 3500 active tailings management facilities exist worldwide (MMSD 2002). Disposal and management of mine tailings in impoundment facilities can be challenging due to variability in physical and chemical properties of the tailings (Bussi re 2007). Storing mine tailings in impoundments can result in contamination of surface and ground water and soil (Bussi re 2007), and tailings impoundment failures have been observed at a rate 10 times higher than traditional water dams (Davies 2002). The risks associated with tailings storage and long-term management in impoundment facilities highlights the importance of finding alternative methods for mine tailings management.

Incorporating mine tailings in earthwork construction applications can provide an alternative to circumvent disposal and management challenges. However, tailings

typically have high water contents (solids content ranging between 25 and 45 %) that correspond to low shear strength and high compressibility (Bussi re 2007; Gorakhki and Bareither 2015), and tailings strength must be enhanced prior to use in earthwork applications. High water contents of mine tailings reduce the number of particle-to-particle contacts and can result in low effective stress (σ') within tailings deposits. Dewatering approaches have been developed to enhance the mechanical properties of tailings. There are three common types of dewatered tailings: (i) thickened tailings, which increases the solids content (SC) to 50-70 %; (ii) paste tailings, which increases the SC to 70-85 %; and (iii) filtered tailings, which increases the SC above 85 % (Bussi re 2007). Progressive dewatering from thickened to paste to filtered tailings requires additional time, energy, and economic investment at a given mine.

Thickened and paste tailings still contain considerable water in addition to a large portion of fine-grained material, which can prolong consolidation and limit strength gain within reasonable timeframes for construction applications. The addition of a binder (e.g., cement or fly ash) has been shown to enhance the mechanical properties of fine-grained soils (e.g., Horpibulsuk et al. 2005; Kesimal et al. 2005; Benzaazoua et al. 2004, Yilmaz et al. 2010, Yilmaz et al. 2015). Horpibulsuk et al. (2005) investigated the effect of cement addition on compression behavior of soft clay at high water contents ($w = 120, 150, \text{ and } 250 \%$). They reported a threshold in compression behavior of cemented specimens, whereby limited deformation was observed with increasing vertical stress to a certain stress level, and subsequent increases in stress yielded larger deformation. This threshold coincided with breakage of cementitious bonds in the cement-amended clay. Yilmaz et al. (2015) evaluated the efficacy of three different binders (slag; Portland cement; and slag + Portland cement) on reducing the compressibility of mine tailings (SC = 81 %; fine content $\approx 70 \%$). Specimens were cured for 0, 1, 3, and 7 d, and a reduction in the compression index (C_c) was reported with an increase in binder content and/or curing time.

This study included an evaluation of the roles of fly ash content, curing time, solids content, and fly ash type on tailings-binder compression behavior. This study had three objectives: (1) evaluate the effects of fly ash type on compressibility of fine-grained tailings amended with fly ash; (2) evaluate the effect of fly ash content on the compressibility behavior of tailings-fly ash mixtures; and (3) evaluate the effect of curing time on the compressibility behavior of tailings-fly ash mixtures.

METHODS AND MATERIALS

Materials

Hard rock mine tailings typically classify as low plasticity silt (Bussi re 2007). Tailings plasticity and particle-size distribution (PSD) depend on the parent material and ore processing. Compiled PSDs of tailings from different studies are shown in Fig. 1 as average, coarse, and fine. These three PSDs represent the average and upper and lower bounds of tailings particles sizes generated from hard rock mines. The synthetic tailings blend shown in Fig. 1 was created for this study to approximate the fine tailings PSD. The synthetic tailings blend contained 60 % kaolin clay and 40 % silica powder. Kaolin clay primarily contained kaolinite minerals and was obtained

from Thiele Kaolin Company (Georgia, USA). Silica powder primarily contained quartz minerals and was obtained from US Silica (Maryland, USA). Synthetic tailings was used in this project to control tailings composition and limit the number of experimental variables in the testing program.

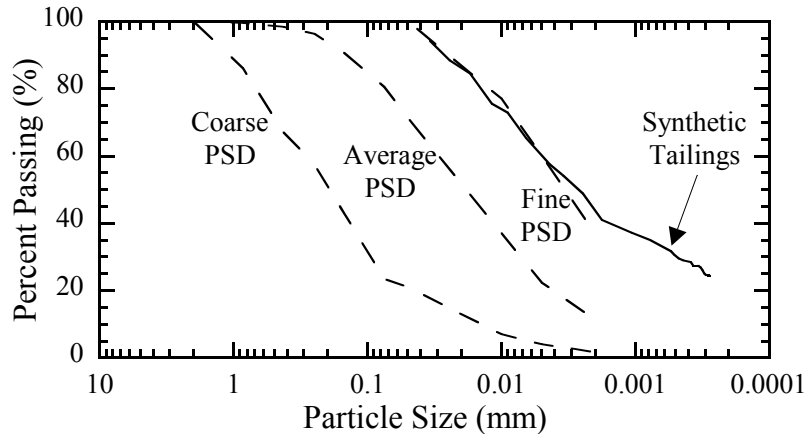


Fig. 1. Range (coarse and fine) and average particle-size distributions (PSDs) for mine tailings compiled from Qiu and Sege (2001), Morris and Williams (2005), Bussi re (2007), Khalili et al. (2010), and Wickland et al. (2010). Synthetic tailings PSD represents the material used in this study.

Two types of fly ash were used in this study. Fly ash A was collected from Stanton Station in Stanton, North Dakota and fly ash B was obtained from Coal Creek Station in Underwood, North Dakota. Chemical composition of fly ash A and B based on X-ray fluorescence (XRF) analysis are in Table 1. Calcium oxide, which is the main constituent responsible for cementitious properties, was 17 % in fly ash A and 12 % in fly ash B. The ternary plot of two types of fly ash is shown in Fig. 2. Fly ash A had a higher $(\text{CaO}+\text{MgO})/\text{SiO}_2$ in comparison with fly ash B, which suggests a higher pozzolanic behavior of fly ash A rather than fly ash B (Tastan et al. 2011). X-ray fluorescence analyses were conducted by Mineralogy Inc. (Oklahoma, USA).

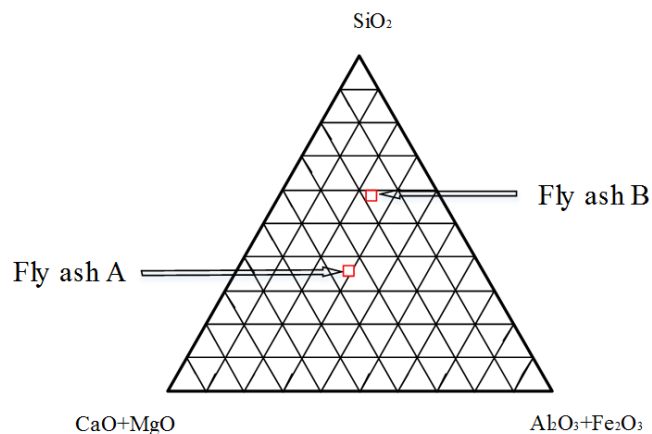


Fig. 2. Ternary plot of fly ash A and fly ash B following Benzaazoua et al. (2002).

Compression Testing

Incremental one-dimensional compression tests were performed in conventional fixed-ring consolidation cells on mixtures of synthetic tailings and fly ash. A summary of all compression tests performed in this study is in Table 2. In all experiments, synthetic tailings were mixed with de-aired water to solids contents of 60 and 70 % ($w = 67\%$ and 43% , respectively) to create a slurry that approximated dewatering levels in thickened tailings ($SC = 60\%$) and paste tailings ($SC = 70\%$). The required quantity of fly ash (A or B) was added to tailings in slurry form to obtain water-to-fly ash ratios of 2.5 and 5, which are common ratios for cemented paste backfills (Kesimal et al. 2005). The tailings-fly ash slurry was then poured into consolidation rings and specimens were leveled to fill the ring. Specimens were sealed in plastic bags and cured for 0.1 d (2 h), 7 d, and 28 d.

Compression tests were performed in one-dimensional (1-D) compression cells, and all specimens were inundated with de-aired water during testing. Incremental vertical loads were applied every 24 h following Method A in ASTM D2435. An example of temporal deformation behavior for specimen B6 is shown in Fig. 3a for an applied vertical effective stress (σ'_v) of 160 kPa. The temporal compression behavior in Fig. 3a is representative of all specimens tested in this study. Primary compression ended after approximately 15-30 min for all specimens. The difference between void ratio at the end of primary compression ($t \approx 15\text{-}30$ min) and void ratio at 24 h was less than 0.002 in specimen B6 and less than 0.006 for all specimens. The continued decrease in void ratio that was attributed to secondary compression between end-of-primary and 24 h was considered negligible such that the void ratio at 24 h was used as end-of-primary in all compression tests.

The relationship between void ratio (e) at 24 h and σ'_v for the fly ash amended specimen A11 is shown in Fig. 3b. A change in slope of the compression curve is apparent and the Casagrande method for determining the pre-consolidation stress (Casagrande 1936) was applied to determine the breaking stress (σ'_B) in fly ash amended specimens. The e - σ'_v relationship in Fig. 3b is typical of fly-ash amended specimens evaluated in this study that exhibited cementitious behavior.

Table 1. Chemical constituents of fly ash A and fly ash B based on X-ray fluorescence.

Element	Fly Ash A (%)	Fly Ash B (%)
SiO ₂	19.76	47.86
CaO	17	12.13
SO ₃	15.76	0.79
Al ₂ O ₃	12.24	13.67
Na ₂ O	11.62	1.87
Fe ₂ O ₃	3.62	5.64
MgO	2.36	2.52
K ₂ O	1.15	2.59
TiO ₂	1.15	0.27
BaO	1.11	0.57

Table 2. Summary of compression tests performed in this study.

Name ^a	SC (%)	FA Type	FA (%)	W/FA	Curing Time (d)	Breaking Stress (kPa)	C _c	e _f	e _i - e _f
N1	60	-	0	-	-	0	0.21	0.27	1.49
N2	70	-	0	-	-	0	0.12	0.36	0.78
A1	60	A	13.3	5	0.1	18	0.19	0.81	0.95
A2	60	A	13.3	5	7	9	0.16	0.83	0.93
A3	60	A	13.3	5	28	55	0.17	1.13	0.63
A4	60	A	26.7	2.5	0.1	25	0.15	0.94	0.82
A5	60	A	26.7	2.5	7	100	0.20	1.09	0.67
A6	60	A	26.7	2.5	28	90	0.22	1.02	0.74
A7	70	A	8.5	5	0.1	15	0.13	0.52	0.61
A8	70	A	8.5	5	7	20	0.10	0.68	0.45
A9	70	A	8.5	5	28	20	0.13	0.51	0.62
A10	70	A	17	2.5	0.1	30	0.14	0.54	0.60
A11	70	A	17	2.5	7	75	0.13	0.71	0.42
A12	70	A	17	2.5	28	75	0.16	0.58	0.55
B1	60	B	13.3	5	0.1	0	0.18	0.50	1.26
B2	60	B	13.3	5	7	0	0.14	0.83	0.93
B3	60	B	13.3	5	28	0	0.14	0.85	0.92
B4	60	B	26.7	2.5	0.1	0	0.13	0.81	0.96
B5	60	B	26.7	2.5	7	0	0.12	0.87	0.89
B6	60	B	26.7	2.5	28	0	0.11	1.00	0.76
B7	70	B	8.5	5	0.1	0	0.11	0.32	0.81
B8	70	B	8.5	5	7	0	0.13	0.20	0.93
B9	70	B	8.5	5	28	21	0.12	0.58	0.56
B10	70	B	17	2.5	0.1	15	0.13	0.51	0.62
B11	70	B	17	2.5	7	18	0.09	0.64	0.50
B12	70	B	17	2.5	28	15	0.14	0.48	0.65

Notes: SC = solids content; FA Type = fly ash type; FA (%) = fly ash content (dried mass); C_c = compression index; e_f = final void ratio at $\sigma \approx 1200$ kPa; e_i = initial void ratio at SC = 60 and 70 %

^a N is representative of specimens with no fly ash amendment, A is representative of specimens amended with fly ash A, and B is representative of specimens amended with fly ash B

RESULTS

Schematics of cemented and non-cemented tailings mixtures are shown in Figs. 4a and 4b. The presence of a binder (e.g., fly ash or cement) in tailings specimens results in the formation of cement bonds between adjacent particles. Effective stress in non-cemented materials is due to self-weight of the soil and any applied load carried through the soil skeleton. However, Horpibulsuk et al. (2005) suggest that σ' in cemented specimens is equal to summation of the effective stress transferred through particle contacts and stress generated due to the cementitious bonds. The summation of these two effective stress components coincides with σ'_B . For $\sigma' < \sigma'_B$, an increase in σ' results in a low magnitude of settlement as loading is resisted by the cementitious bonds (Fig. 4b). In contrast, as σ'_v increases above σ'_B , cementitious bonds are broken, which leads to larger magnitudes of settlement.

Compression curves for specimens N2 and A11 are shown in Fig. 4c. Specimen N2 was non-cemented synthetic tailings, whereas specimen A11 included 17% fly ash A

and was cured for 7 d (Table 2). Compression behavior of N2 is characteristic of a normally consolidated material, which was anticipated as the specimen was remolded from slurry. The addition of fly ash to specimen A11 resulted in reduced compressibility relative to N2 and the development of a bilinear compression curve that includes $\sigma'_B = 75$ kPa. For $\sigma'_v > \sigma'_B$, the C_c of specimen A6 = 0.13, which is remarkably similar to the C_c of 0.12 for specimen N2. The uniqueness of the C_c between specimens N2 and A11 suggests that for $\sigma'_v > \sigma'_B$ compression for both cemented and non-cemented specimens was controlled by the tailings matrix.

Relationships between e and σ'_v of fine synthetic tailings amended with fly ashes A and B are shown in Fig. 5. A summary of the σ'_B , C_c , final void ratio (e_f), and total settlement, defined as a change in void ratio, for all tests is in Table 2. Breaking stress was identified for all fly ash amended specimens that exhibited a bilinear compression curve. The C_c was determined for the linear portion of all compression curves, which coincided with $\sigma'_v > \sigma'_B$ for fly ash amended specimens. In general, total compression of fly ash amended specimens was less than specimens without fly ash for a given σ'_v .

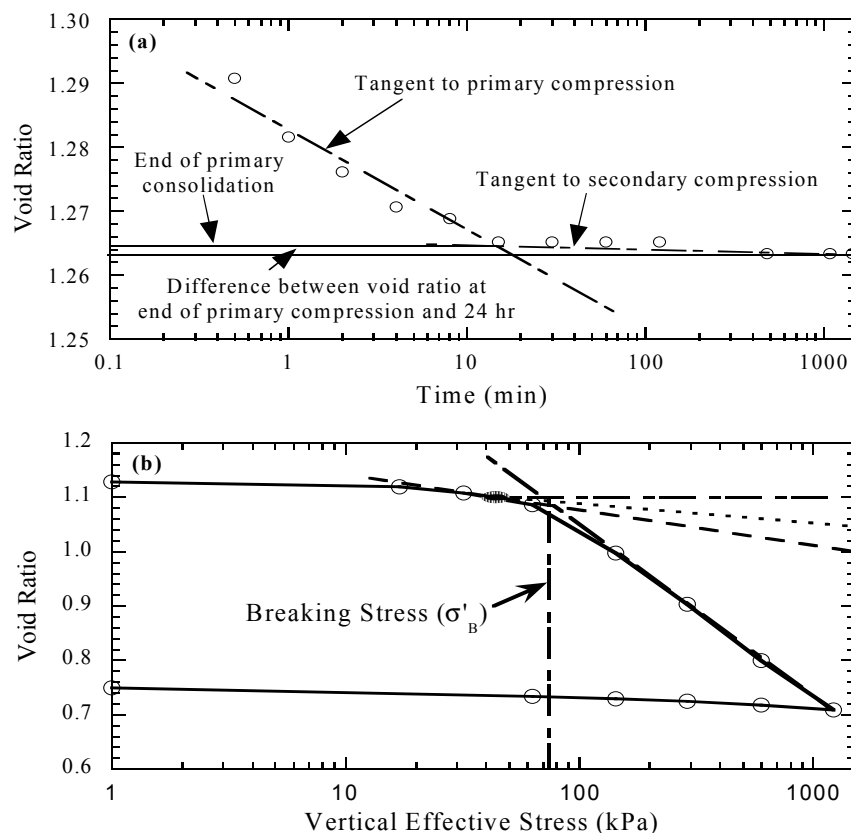


Fig. 3. (a) Temporal relationship of void ratio for specimen B6 (SC = 60 %, fly ash B, fly ash content = 26.7 %, and curing time = 28 d) under an applied load of 160 kPa, and (b) identification of the breaking stress for fly ash amended specimen A11 (SC = 70 %, fly ash A, fly ash content = 17 %, and curing time = 7d) based on the Casagrande method for pre-consolidation stress.

Compression behavior of specimens amended with fly ash A exhibited higher and more defined σ'_B , but comparable total settlement relative to specimens amended with fly ash B (Fig. 5 and Table 2). This contrast in compression behavior was attributed to the higher CaO content in fly ash A. A higher CaO content results in an increase in cementation in tailings-fly ash mixtures. Specimens prepared with fly ash B and synthetic tailings at 60 % solids content did not exhibit a σ'_B ; however, some cementation of fly ash B was observed for specimens prepared at SC = 70 %. The initial void ratios of specimens prepared at SC = 60 % were higher compared to specimens prepared at SC = 70 % (Fig. 5). These higher initial void ratios coupled with the lower CaO content of fly ash B may have prevented cementitious bonds from effectively bridging the void spaces between adjacent particles.

Effect of Fly Ash Content

The effect of fly ash content on σ'_B of tailings-fly ash mixtures for different solids content, curing times, and water-to-fly ash ratios for fly ash A is shown in Fig. 6. In general, σ'_B increased with an increase in fly ash content for a given SC and curing time. The additional fly ash generated a larger number of cementitious products that increased stiffness and yielded a higher σ'_B .

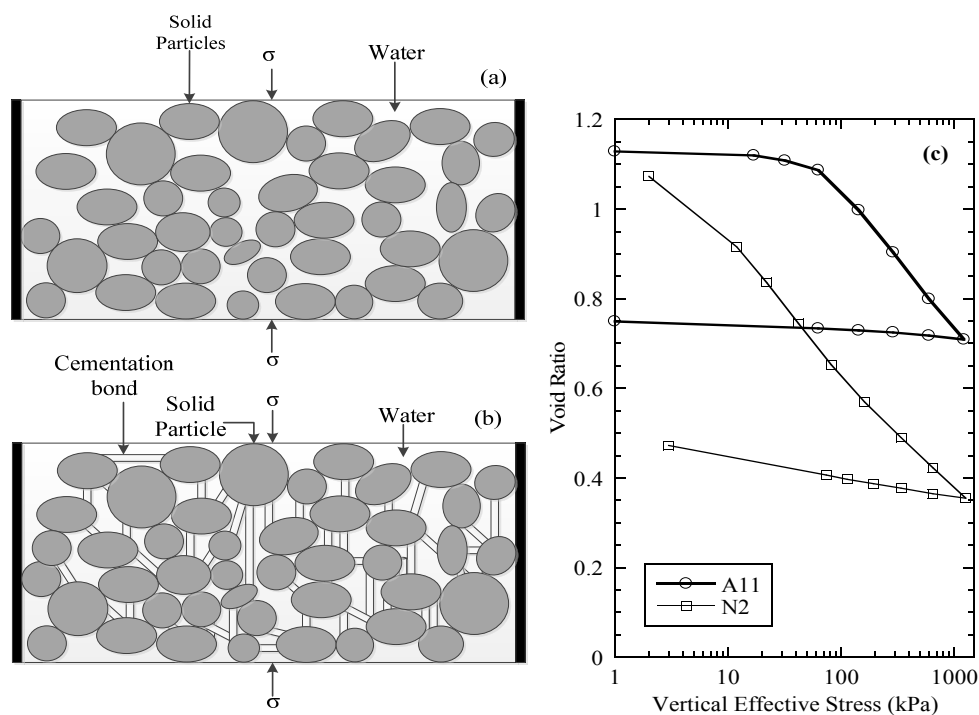


Fig. 4. Schematic and example of compression behavior of non-cemented and cemented soils: (a) non-cemented soil, and (b) cemented soil, and (c) relationship between void ratio and vertical effective stress for non-fly ash amended (N2) and fly ash amended (A11) synthetic tailings.

The difference in initial and final void ratio ($e_i - e_f$) and C_c for all specimens are in Table 2. Total settlement (i.e., $e_i - e_f$) decreased with an increase in fly ash content,

which was attributed to the increase in specimen stiffness. Compression indices were comparable between non-fly ash amended and fly ash amended specimens for $\sigma' > \sigma'_B$, and no discernable trend was identified. The C_c fall within a close range of $0.11 < C_c < 0.22$ for solids content = 60 %, and $0.09 < C_c < 0.16$ for solids content = 70 %. This behavior suggests that for the synthetic tailings and fly ash mixtures evaluated in this study, C_c determined for $\sigma' > \sigma'_B$ was independent of fly ash content. The range of C_c for tailings and fly ash amended tailings was comparable to C_c reported in literature (Pierce 1997; le Roux 2004; Yilmaz 2010).

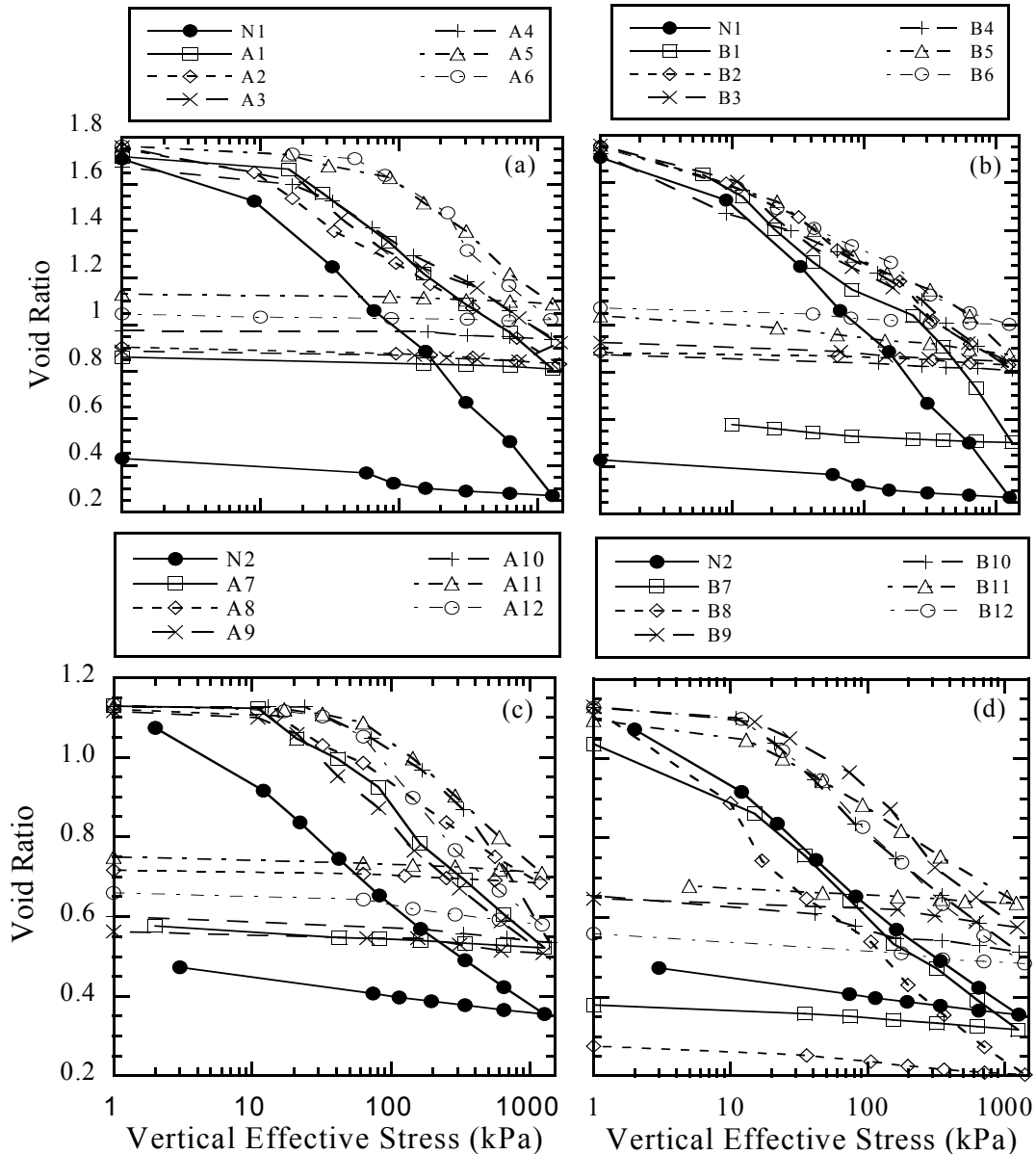


Fig. 5. Compression behavior of tailings-amended with fly ash for curing times = 0.1 d, 7 d, and 28 d: (a) SC = 60 % and fly ash A, (b) SC = 60 % and fly ash B, (c) SC = 70 % and fly ash A, and (d) SC = 70 % and fly ash B.

Compression behavior of fly ash amended specimens is influenced by two contrasting mechanisms: (i) formation of cementitious bonds from reactions between fly ash and water and (ii) breakage of cementitious bonds following an increase in applied stress. Incremental loads were applied every 24 h in all compression experiments. For specimens cured under short-duration curing times (i.e., 0.1 d and 7 d), cementitious bonds were continually forming during incremental loading. As water is expelled from the soil during compression, the water-to-fly ash ratio decreases, which can lead to an increase in cementitious bonding. However, an increase in σ' of a fly ash amended specimen prior to full formation of cementitious bonds can damage the bonds, reduce or nullify the σ'_B , and lead to larger than anticipated settlement. These competing mechanisms of formation and breakage of cementitious bonds during loading results in a confounded relationship between C_c and fly ash content. Yilmaz et al. (2010) considered this competing behavior between damage to particles and formation of more bonds with a relationship between unconfined compressive strength (UCS) of cemented paste backfill (CPB) cured under pressure and UCS of CPB cured in molds.

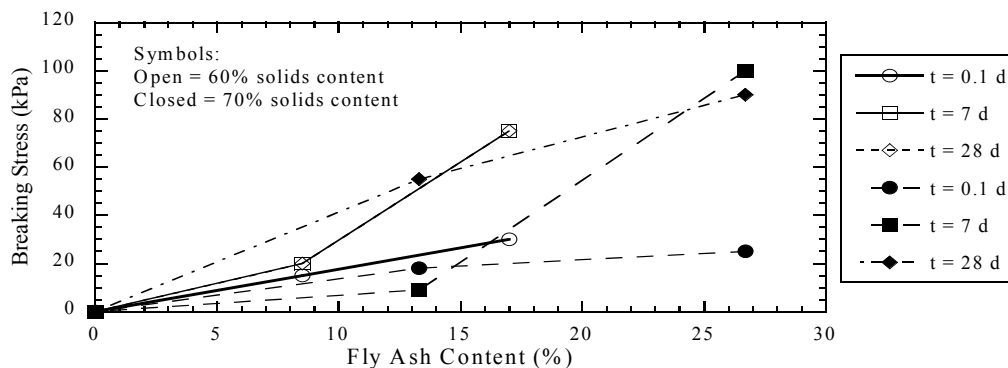


Fig. 6. Relationship between breaking stress and fly ash content for tailings-fly ash mixtures prepared with fly ash A.

Effect of Curing Time

The relationship between breaking stress and curing time of synthetic tailings amended with fly ash A at different fly ash contents for 60 % and 70 % solids content is shown in Fig. 7. In general, σ'_B increased with an increase in curing time from immediate curing (0.1 d) to short duration curing (7 d). However, σ'_B did not change considerably when curing time was increased to 28 d. This is because most of cementitious products are generated within the first few days following amendment with fly ash for non-sulfidic tailings (Yilmaz et al. 2014).

Total settlement and C_c of tailings amended with fly ash A are in Table 2. Settlement was lowest in specimens cured for 7 d and no identifiable trend was observed between C_c and curing time. This was attributed to contrasting mechanisms of cementitious bond formation and breakage that occurs during compression of specimens for $\sigma' > \sigma'_B$. These competing mechanisms during loading resulted in confounded relationship between C_c and curing time.

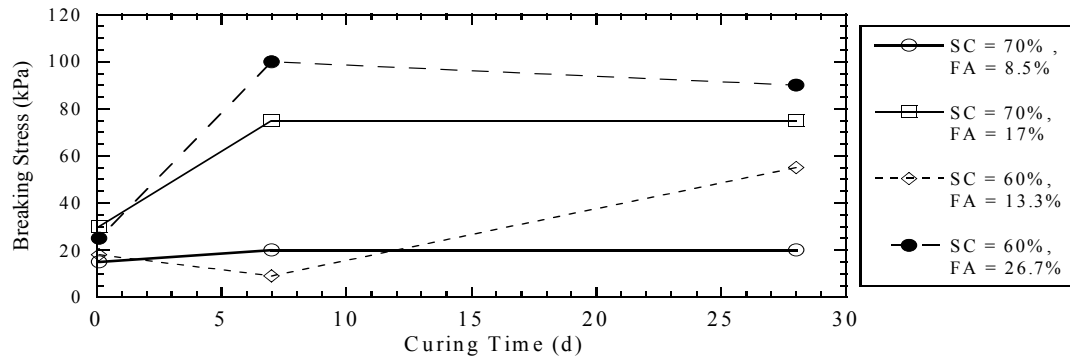


Fig. 7. Relationship between breaking stress and curing time for tailings-fly ash mixtures prepared with fly ash A.

CONCLUSIONS

One-dimensional compression tests were conducted to assess the effect of fly ash amendment on compressibility of tailings-fly ash mixtures. Total settlement, breaking stress, and compression index were determined for synthetic fine-grained mine tailings mixed with two different off-specification fly ashes. The following conclusions were drawn from this study.

- Specimens amended with fly ash A that contained 17 % CaO had lower settlement and higher breaking stress in comparison with specimens amended with fly ash B that contained 12 % of CaO. Higher CaO in fly ash generates more cementitious products that can reduce total settlement and increase the breaking stress of the amended specimen.
- Settlement decreased and breaking stress increased with an increase in fly ash content. This behavior was more pronounced in specimens amended with fly ash A due to the enhanced cementitious potential with a higher CaO content.
- Breaking stress increased with an increase in curing time from 0.1 d to 7 d due to an increase in the cementitious bonds. However, the breaking stress was comparable for specimens cured for 7 d and 28 d. This effect of curing time on breaking stress was attributed to the majority of cementitious bonds forming during the first few days of curing.

ACKNOWLEDGMENTS

Financial support for this study was provided in part by the Mountain Plains Consortium awarded to North Dakota State University. Support also was provided by the Colorado State University. The opinions, findings, and conclusions expressed herein are those of the authors and do not represent the views of the Mountain Plains Consortium, North Dakota State University, or Colorado State University.

REFERENCES

- Benzaazoua, M., Belem, T., and Bussi re, B. (2002). Chemical factors that influence the performance of mine sulphidic paste backfill. *Cement Concrete Res.* 32(7), 1133-1144.
- Benzaazoua, M., Fall, M., and Belem, T., (2004). A contribution to understanding the hardening process of cemented pastefill. *Minerals Engineering.* 17(2), 141-152.
- Bussi re, B. (2007). Colloquium 2004: Hydrogeotechnical properties of hard rock tailings from metal mines and emerging geoenvironmental disposal approaches, *Can Geotech J*, 44(9), 1019-1052.
- Casagrande, A. (1936). The determination of the pre-consolidation load and its practical significance. In *Proceedings of the international conference on soil mechanics and foundation engineering*, 3, 60-64.
- Davies, M. P. (2002). Tailings impoundment failures: are geotechnical engineers listening? *Geotechnical News*, 31-36.
- Gorakhki, M. H., and Bareither, C., A. (2015). Salinity effects on sedimentation behavior of kaolin, bentonite, and soda ash mine tailings. *Appl Clay Sci*, 114, 593-602.
- Horpibulsuk, S., Norihiko, M., and Nagaraj, T.S., (2005). Clay-water/cement ratio identity for cement admixed soft clays. *J. Geotechnical & Geoenv. Engrg*, 131(2), 187-192.
- Kesimal, A., Yilmaz, E., Ercikdi, B., Alp, I., and Deveci, H. (2005). Effect of properties of tailings and binder on the short-and long-term strength and stability of cemented paste backfill. *Materials Letters*, 59(28), 3703-3709.
- Khalili, A., Wijewickreme, D., and Wilson, W. (2010). Mechanical response of highly gap-graded mixtures of waste rock and tailings. Part I: Monotonic shear response, *Can Geotech J*, 47(5), 552-565.
- le Roux, K. A., (2004). Properties and liquefaction analysis of cemented paste backfill, Ph.D dissertation, University of Toronto, Ontario, Canada. Mining, Minerals, and Sustainable Development Project. (2002). *International Institute for Sustainable Development*
- Morris, P.H. and Williams, D.J. (1997). Results of field trials of co-disposal of coarse and fine coal waste, *Transactions of the Institution of Mining and Metallurgy*, 106, A38-A41.
- Pierce, M. E., (1997) Laboratory and numerical analysis of strength and deformation behavior of paste backfill. M.Sc. thesis, Queen's University, Kingston, Ontario, Canada.
- Qiu, Y. and Sego, D.C. (2001). Lab properties of mine tailings, *Can Geotech J*, 38(1), 183-190.
- Tastan, E., Edil, T., Benson, C., and Aydilek, A (2011). Stabilization of organic soils with fly ash. *J. Geotech Geoenviron Eng.* 137(9), 819-833.
- Wickland, B.E., Wilson, G.W. and Wijewickreme, D. (2010). Hydraulic conductivity and consolidation response of mixtures of mine waste rock and tailings, *Can Geotech J*, 47(4), 472-485.
- Yilmaz, E., Belem, T., Benzaazoua, M., and Bussi re, B. (2010). Assessment of the modified CUAPS apparatus to estimate in situ properties of cemented paste backfill. *Geotech Test J.* 33(5). 1.

- Yilmaz, E., Benzaazoua, M., Belem, T., and Bussi re, B. (2009). Effect of curing under pressure on compressive strength development of cemented paste backfill. *Miner Eng*, 22(9), 772-785.
- Yilmaz, E., Belem, T., and Benzaazoua, M. (2014). Effects of curing and stress conditions on hydromechanical, geotechnical and geochemical properties of cemented paste backfill. *Eng Geol*, 168, 23-37.
- Yilmaz, E., Belem, T., Bussi re, B., Mbonimpa, M., and Benzaazoua, M. (2015). Curing time effect on consolidation behavior of cemented paste backfill containing different cement types and contents. *Construction and Building Materials*. 75, 99-111.

Design, Construction, and Preliminary Results of Two Insulation Covers at the Meadowbank Mine

Sylvette A. Awoh, R.O. RIME¹; Bruno Bussière, P.RIME²; Charles Batzenschlager, S.RIME³; Vincent Boulanger-Martel, S.RIME⁴; Thomas Lepine, G.C AEM⁵; and Erika Voyer, E.C. AEM⁶

¹Research Officer, Research Institute of Mine and Environment, Univ. du Québec en Abitibi-Témiscamingue, 445 Blvd. de l'Université, Rouyn-Noranda, QC, Canada J9X 5E4. E-mail: akue-sylvette.awoh@uqat.ca

²Professor, Research Institute of Mine and Environment, Holder of the industrial CRNSG-UQAT chair, Univ. du Québec en Abitibi-Témiscamingue, 445 Blvd. de l'Université, Rouyn-Noranda, QC, Canada J9X 5E4. E-mail: Bruno.Bussière@uqat.ca

³Student, Research Institute of Mine and Environment, Univ. du Québec en Abitibi-Témiscamingue, 445 Blvd. de l'Université, Rouyn-Noranda, QC, Canada J9X 5E4. E-mail: Charles.Batzenschlager@uqat.ca

⁴Student, Research Institute of Mine and Environment, Univ. du Québec en Abitibi-Témiscamingue, 445 Blvd. de l'Université, Rouyn-Noranda, QC, Canada J9X 5E4. E-mail: Vincent.Boulanger-Martel@uqat.ca

⁵Geotechnical Coordinator, Agnico Eagle Mines Limited –Meadowbank Division Baker Lake, Nunavut, CA X0C 0A0. E-mail: thomas.lepine@agnicoeagle.com

⁶Environmental Coordinator, Agnico Eagle Mines Limited –Meadowbank Division Baker Lake, Nunavut, CA X0C 0A0. E-mail: erika.voyer@agnicoeagle.com

Abstract: Two experimental insulation covers made of inert waste rocks and were of 2 and 4 m-thick respectively were tested at the Meadowbank mine site to assess the performance of insulation covers tailings storage facility. On each experimental cell, volumetric water content, matric suction and temperature sensors were installed at three stations and at various depths. Oxygen consumption tests were also performed below the cover and in the tailing pond to estimate the reactivity of the covered and uncovered Meadowbank tailings. This paper focuses on the design, the construction and the instrumentation of the tested insulation covers. Preliminary results of the monitored temperatures at the central station and of the OC tests are presented for each cell. For both tested covers, results indicate good thermal insulation performances since the covered mine tailings remain below the freezing point during the warmest period of the year. The reactivity of the tailings under the two tested covers is below the detection limit (10 moles of O₂/m²/year) of the OC method while the reactivity of uncovered tailings during Summer is between 20-85 moles of O₂/m²/year.

INTRODUCTION

In Canada, many mine sites are located in Nordic environment where permafrost can be found almost everywhere. Permafrost is defined as a soil with a temperature at or below 0 °C for at least two consecutive years (Andersland and Ladanyi 2004). This definition does not take into account any phenomenon that could affect the physical and chemical characteristics of permafrost (Coulombe et al. 2012).

Reclamation of mine tailings impoundment is a significant environmental challenge for mining companies, especially when tailings can generate acid mine drainage (AMD). The reclamation of Nordic mine sites is even more complex because it is affected by many additional factors. The presence of permafrost, the limited availability of cover materials close to the construction site, the possible effect of freeze-thaw cycles on the properties of cover materials and the effects of climate change on cover performance are important parameters to consider when designing the reclamation strategy (i.e. Bussière and Hayley 2010). Other constraints such as the shortness of Nordic summers, difficult climatic conditions and remoteness may also have a significant impact during the construction

Few methods have been used over the years to control AMD in Nordic environment: water covers, covers made of low saturated hydraulic conductivity materials (natural or synthetic materials), multi-layer covers, elevated water table covers, and insulation covers). Among those methods, the insulation cover is the main reclamation strategy proposed for tailings storage facilities located in continuous permafrost regions (MEND 2004a).

Insulation covers aims at integrating mine tailings into permafrost in a permanently frozen state. To prevent seasonal thawing of tailings, a layer of non-reactive material is placed over the tailings, allowing their thermal insulation during the warm seasons. Hence, the active layer (the portion of the soil above permafrost that thaws and freezes seasonally) is contained within the cover (Andersland and Ladanyi 2004). Generally, the low temperatures will slow down significantly both chemical and biological oxidation reactions (Elberling et al. 2000) while permafrost will limit water seepage and thus contaminant transport. Depending on the tailings properties (i.e. reactivity, unfrozen water content), a target maximum tailings temperature (usually between -2°C and -6°C) at which sulfide oxidation and contaminant migration is significantly reduced should be determined for cover design.

Freezing of tailings as a control strategy for limiting AMD has already been used at several mine sites in Northern Canada for the reclamation of tailings impoundment. One can mention the Rankin inlet mine, Nunavut, Canada (Meldrum et al. 2001) and the Nanisivik mine, Nunavut, Canada (Kyhn and Elberling 2001; Elberling 2005). This method has been proposed as a reclamation option at other Canadian mine sites where various granular soils (gravel and sand) are proposed as insulation cover material, the Raglan mine, Quebec (Coulombe et al. 2012), Diavik mine, North-West Territories and Ekati mine, North-West Territories (MEND 2009).

This study focusses on potential reclamation scenarios for the Meadowbank mine (Nunavut, Canada) tailings storage facility (TSF), where two insulation covers made of non-reactive waste rocks are presently tested. More specifically, this article presents the methodology that was followed to evaluate the *in situ* performance of

two insulation cover experimental cells (2 and 4 m thick covers) built on Meadowbank's TSF. The main physical, chemical, mineralogical and geotechnical properties of the tailings and waste rock cover materials are first presented. Then, the experimental cells built to assess the insulation performances of the tested covers are described. Finally, preliminary results of the cover's thermal regime and of the reactivity of the covered and uncovered tailings measured during the first year of monitoring are provided.

MATERIAL AND METHOD

Site description

The Meadowbank gold mine (65° N) operated by Agnico Eagle is located in the Kivalliq Region, Nunavut (a low Arctic ecoclimate described as one of the coldest and driest region of Canada), approximately 100 km north of Baker Lake (Agnico Eagle Mine AEM, unpublished report 2009). Historical meteorological data indicate that, at the mine site, the mean annual air temperature is approximately -11°C and that the average annual rainfall is approximately 280 mm for snow and rain combined (AEM, unpublished report 2009). Based on previous thermal studies, and on measurements of ground temperatures, the depth of permafrost at the site is estimated between 450 and 550 m, depending on the proximity to lakes (AEM, unpublished report 2009). The depth of the active layer in the surrounding natural ground ranges from 1.3 m in areas with shallow overburden, to about 4 m in areas close to lakes (AEM, unpublished report 2009).

Materials properties

The two insulation covers were built over mine tailings stored in the TSF with non-reactive waste rock. The TSF is located in a topographic depression. The material's grain size distributions were obtained using a Malvern Mastersizer laser particle size analyzer for fine particles (<1 mm) and by mechanical sieving for coarser particles (ASTM standard D422) The D_{10} , D_{30} , and D_{60} , corresponding to 10, 30 and 60 % of particles passing on the cumulative curves, are respectively 3.9 μm , 12.0 μm , 33.6 μm for the tailings and 41.4 μm , 2400 μm and 13000 μm for the waste rock. The coefficient of uniformity ($C_u=D_{60}/D_{10}$) and the coefficient of curvature ($C_c=(D_{30})^2/(D_{10}\times D_{60})$) are 8.6 and 1.1 for the tailings and 314 and 10.7 for the waste rock respectively. Based on Unified Soil Classification System classification, the Meadowbank tailings are classified as non-plastic silt (ML) and the waste rock as well-graded gravel with silt (GW-GM).

The specific gravity (G_s) of materials was determined using a Micromeritics Accupyc 1330 helium pycnometer following ASTM-D5550 standard (accuracy within 0.03 % of reading, plus 0.03 % of nominal full-scale sample chamber volume). The obtained values are similar with values of 3.03 for the tailings and 2.90 for the waste rock.

The mineralogical composition of the two materials was determined using X-ray diffraction (XRD) data and, the quantitative Rietveld method (relative precision of \pm

0.5 %) with the TOPAS software. The main minerals of the waste rock are chlorite (30%), talc (22%), tremolite (15 %) and biotite (8%). The mineralogical composition of the tailings is mainly quartz (59%), chlorite (14%), and pyrite (2%).

Sulfur and carbon analysis were also conducted on the two materials using an induction furnace. The obtained results show that the tailings contain 2.3 % sulfur (as pyrite, Fe_2S) and less than 0.4 % carbon while the waste rock contains 0.1 % sulfur and 2.0 % carbon.

The acid generation potential was determined using a static test (Acid Base Accounting). The net neutralizing potential (NNP) of tailings is negative, with values ranging between -11 and -26 kg CaCO_3/t . These values are less than the minimal criterion of 20 kg CaCO_3/t (Miller et al. 1999) and suggest that the tailings are potentially acid generating (PAG). On the other hand, the NNP of the waste rock is positive with a value of 119 kg CaCO_3/t . This value is greater than the 20 kg CaCO_3/t criterion and suggests that the waste rocks are non-potentially acid generating (NPAG).

The saturated hydraulic conductivity (k_{sat}) tests were performed to characterize the hydrogeological properties of the two materials. The k_{sat} of the waste rock was determined in large scale columns of 30 cm in diameter and 150 cm in height following the method described in Peregoedova (2012). For the tailings, the k_{sat} was obtained through permeability testing following ASTM standard D5856. At the loose state (porosity around 0.4), an average saturated hydraulic conductivity of 1.5×10^{-1} cm/s was measured for waste rock samples having particle diameter smaller than 50 mm. The average saturated hydraulic conductivity of the tailings is 1.3×10^{-5} cm/s, which corresponds to values found in the literature for hard rock mine tailings (Bussiere 2007). Other characterization work such as the determination of the thermal conductivities and water retention curves of those materials are presently underway.

Field experimental cells description

Design and construction

Two experimental cells were built in the northern part of Meadowbank TSF (Figure 1 - not to scale) in June 2014 in order to study the performance of two reclamation scenarios: a 2 m insulation cover made of non-acid generating (NPAG) waste rock (cell 2 m), and a 4 m (cell 4 m) insulation cover with the same material. These two insulation covers represent two potential scenarios investigated by the mine as their final reclamation plan. Each experimental cell has a flat top surface of approximately 100 m² (10 x 10 m). There is about a 1.0 m thick layer of deposited tailings in the area where the experimental cells were constructed. Figure 2 shows a schematic representation of the experimental cells and the instrumentation locations.

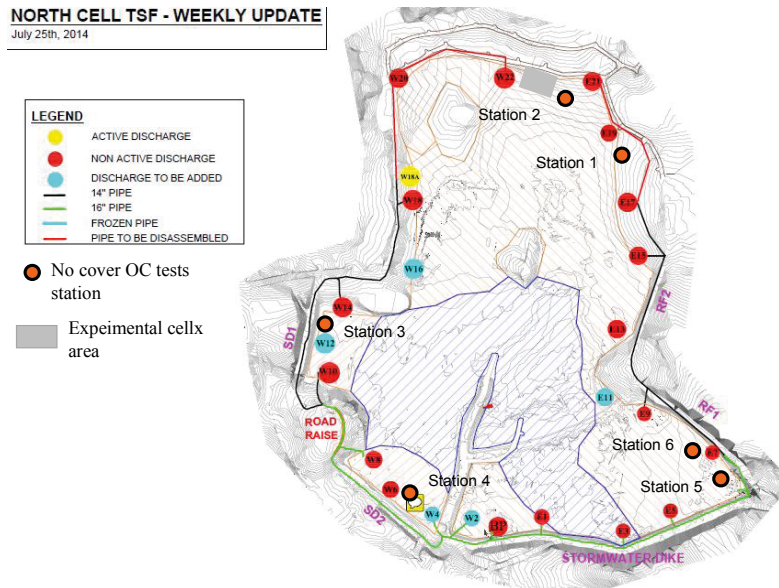


FIG. 1. Experimental cells area and no cover OC tests (NC-OC) station

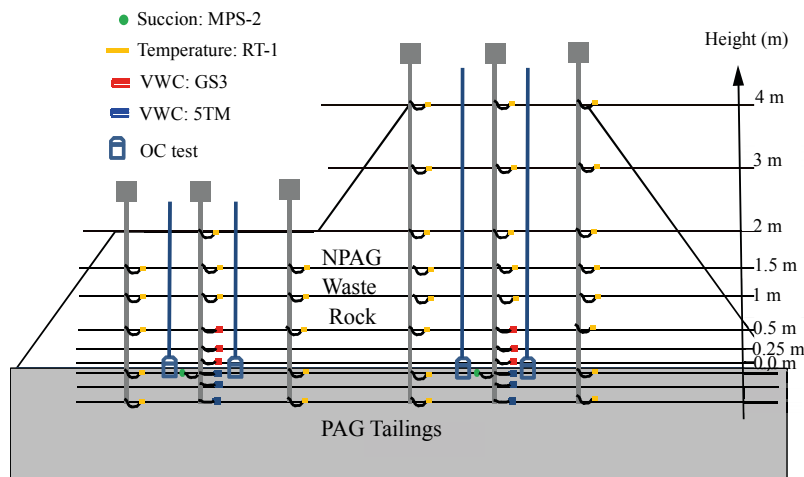


FIG. 2. Schematic representation of the experimental cells and their instrumentation. VWC (volumetric water content)

Before the experimental cells were constructed, a first 2 m of NPAG waste rock was deposited (in early spring 2014) on top of the tailings as a temporary insulation cover to maintain the tailings frozen until the beginning of construction in June 2014 (Figure 3A). Then, in order to allow instrumentation set-up, a trench was excavated with an excavator in the center of both cells until the tailings were reached (Figure 3B). At that point, the tailings were still frozen and the use of a jackhammer was necessary to excavate holes of about 1-2 m wide by 50 cm deep used to install the instrumentation (Figure 3C). Since the tailings were deposited during winter, there was an alternation of layers of tailings and ice lenses which had a thickness ranging from a few centimetres up to 10 cm. With the thawing of the ice lenses (during

construction), a thaw settlement was observed close to the holes. Water progressively filled the hole and had to be pumped regularly.

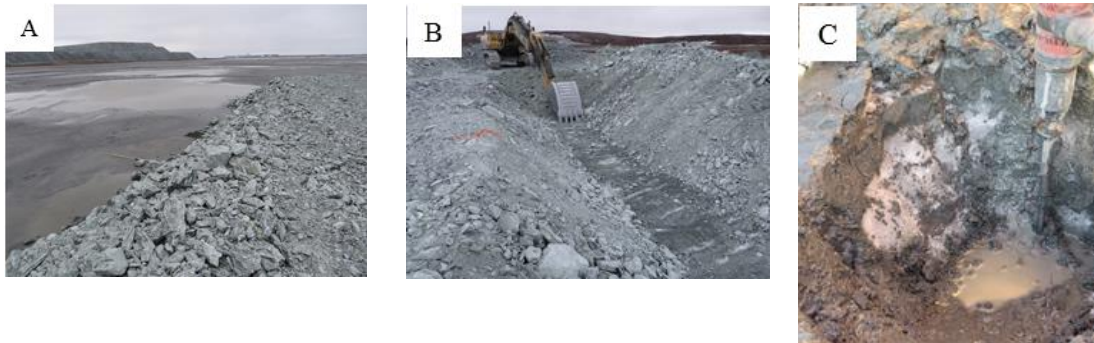


FIG. 3. Photos illustrating the field insulation cover construction steps

Field cells instrumentation and monitoring

In this study, three main parameters are monitored to assess the performance of the tested insulation covers: volumetric water content (VWC), temperature profiles, and oxygen consumption of covered and uncovered mine tailings; suction was also measured but will not be discussed further in this article. The volumetric water contents and temperatures are continuously monitored, whereas oxygen consumption tests are conducted a few times per year.

Temperature, VWC probes set up

Six (6) 50 cm-deep holes were excavated using the jackhammer to install probes in the tailings. The probes were previously assembled on a vertical support (called probe tree) before being installed in the tailings (Figure 4A). One probe tree equipped with VWC probes (5TM for tailings and GS3 for waste rock, Decagon) and temperature (RT-1, Decagon), was installed in the center of each cell. Also, two probe trees, only equipped with temperature probes (RT-1, Decagon) were installed on both sides of each cell to see the boundaries influence. Temperature sensors were attached to the probe trees (Figure 4B) while the VWC and matric suction probes were directly inserted into the tailings and the waste rock (Figure 4C).

The probes were connected to dataloggers through ABS tubes to monitor continuously temperature, VWC in the insulation cover and in the tailings. Data are collected and compiled every month.

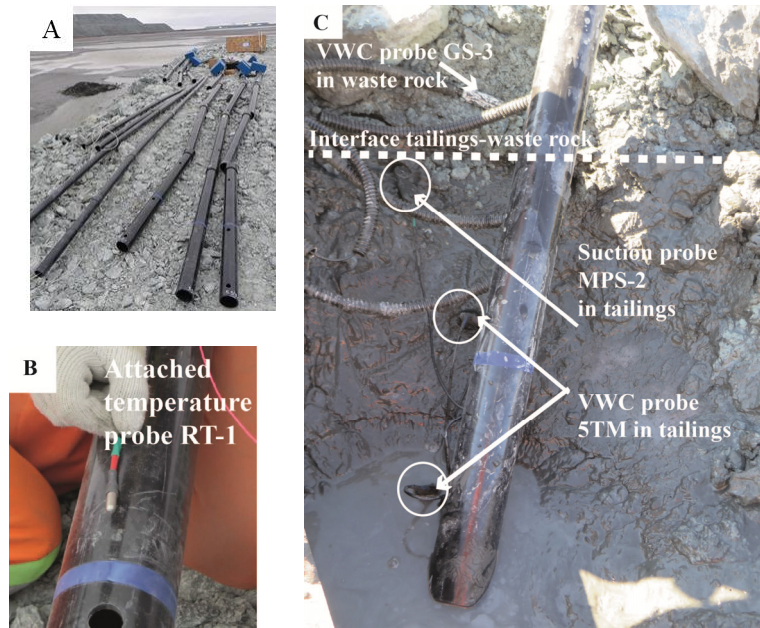


FIG. 4. Photos illustrating the field cells instrumentation

Oxygen consumption test set up

Oxygen consumption (OC) tests are performed on covered and uncovered tailings to compare the tailing's reactivity in both conditions.

In the tailings pond (uncovered) the common OC test described by Elberling et al. 1994) was used to measure oxidation rates in sulphide tailings (Elberling 2001; Coulombe et al. 2012). The OC test consists of measuring the decrease in oxygen concentration with an oxygen sensor (starting at 20.9 %; the standard oxygen concentration in the atmosphere) in a sealed chamber over the tailings for a period of 3 to 5 hours. The oxygen decrease over time is caused by oxygen diffusion through the tailings and by oxygen consumption resulting from the oxidation of sulphide minerals. The higher the oxygen decrease, the more reactive the tailings are. Tests were performed in 30 cm stainless steel cylinders, having a 15 cm diameter. The cylinders were inserted in the tailings leaving an empty space "h" at the top of the cylinder. An aluminium cap equipped with two valves and an oxygen sensor is placed on top of each cylinder to create a sealed chamber during the test. The sensor used in this study is the SO-110 galvanic type cell sensor manufactured by Apogee Instruments, with an accuracy of $\pm 0.02\%$ O₂. The OC tests were performed at 6 stations of uncovered tailings. Those tests are referred as no cover OC test (NC-OC) on Figure 1. The NC-OC tests were performed during the summer period when the tailings were in the appropriate hydrogeological conditions for their oxidation (i.e. with a degree of saturation (S_r) between 48 and 62%). Mine tailings are more reactive when the S_r is between 40 and 60% (Bouzahzah et al. 2015).

The common OC test setup (Elberling et al. 1994) was modified for the tests performed below the insulation covers. In these conditions, cylinders of 40 cm high

and 14 cm wide were placed in the tailings through the excavated holes (Figure 5A). The cylinders were then filled with tailings collected in the tailings pond and were left at rest allowing them to settle. After settlement, a headspace between 5 and 10 cm was created above the tailings and the voids around the cylinders were backfilled with tailings from the excavations. Bentonite seals were also placed around the cylinders to limit oxygen ingress along the cylinder's wall (Figure 5B). Sealed caps and protection systems were then placed over the cylinders (see Figure 5B).

For a given OC test set up, an oxygen probe and flexible pipes (1/4") were connected to the aluminum lid which was then installed on the aluminium cylinder (Figure 6B). At each station, the probes and the flexible pipes were connected to the surface of the cover through an ABS protective tube (Figure 6B). The flexible pipes (1/4") are used to push fresh air in the reservoir above the tailings from the surface. The objective is to start the OC test with an initial concentration of oxygen close to 20.9% O₂. For each cell, one of the cylinders has a control sensor located outside the cylinder, under the protective shell, to correct sensor readings for temperature effects. The interested reader can find more information on OC tests performed on similar *in situ* conditions in Coulombe et al. (2012).

Trenches and holes filling

All the sensors located in the tailings were installed and connected to the ABS tube (connection to surface) and the holes in the tailings and the trenches in the waste rock were backfilled (Figure 6A, B, and C). During backfilling, the probes stations were held vertically with all the necessary precautions to put in place and protect the sensors. When the experimental cell's instrumentation setup was completed (after compaction and securing of slopes), dataloggers were installed at the surface and connected to the sensors. Dataloggers are protected with waterproof cases and wooden boxes attached to the ABS tubes (see Figure 6D).

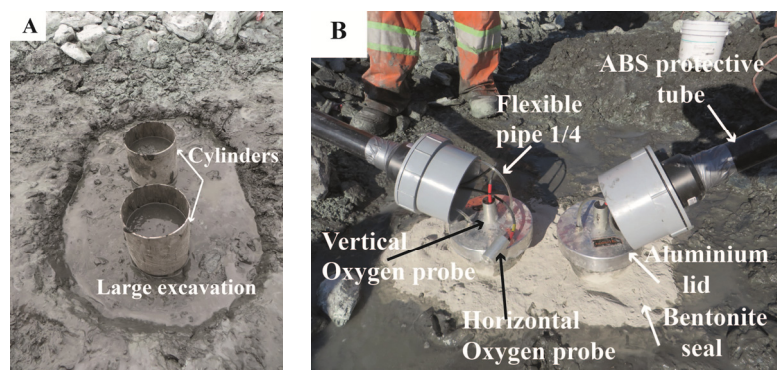


FIG. 5. Photos illustrating oxygen consumption test set up below the insulation cover

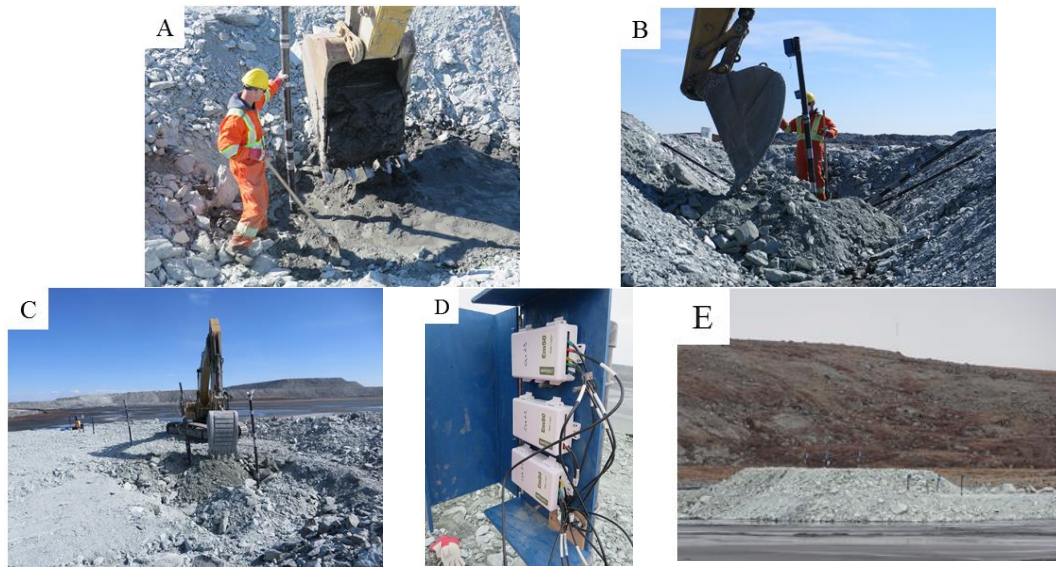


FIG. 6. Photos illustrating holes and trenches backfilling (A, B and C), the installed dataloggers (D) and the completed cells (E)

PRELIMINARY RESULTS

Temperature results collected during the first monitoring months are presented for each station and each cell. In this article, the emphasis is on results obtained for the central station (station 1) in the two (2 and 4 m) experimental cells. The thermal behaviors of the tailings and the insulation covers are analyzed from June 2014 to April 2015. The *in situ* temperature profiles are presented as the average monthly data.

Temperature profiles

The temperature profiles measured in the center (station 1) of the 2 m and the 4 m cells are shown in Figure 7A, B. The curves that were obtained indicate that the insulation properties of the tested covers allow controlling the tailings' temperature. As expected, in both cases, the monitored temperatures within the cover are at the highest in summer and at the lowest in winter. The hottest month recorded being July (temperatures at the cover/tailings interface varied between -0.2°C and 0.9°C for the 2m cover and between -0.5°C to -1.2°C for the 4m cover) and February (temperatures at the cover/tailings interface varied between -21°C and -18°C for the 2m cover and between -7°C and -10°C for the 4m cover) the coldest. In the performance evaluation of insulation covers, the main point of interest is the temperature at the cover/tailings interface. In the case of the 2 m cell, the measured temperatures varied between -21 and 0.5°C and between -12.3°C and -0.1°C for the 4 m cell. Therefore, the overall temperature variations of the tailings' sub-surface are greater in the 2 m cell than the 4 m cell with colder and hotter temperatures measured in the 2 m cell. This phenomenon was expected since a thicker cover should provide more insulation capability than a thinner cover made of the same material. More specifically, it is

observed that the maximal temperature shifts permanently below 0°C roughly at a depth of 0.0 to 0.5 m within the tailings for the 2 m cell while this shift is observed between 0.5 to 0.7 m above the tailings for the 4 m cell. Also, the temperature drop below the freezing point appears faster in the 4 m cell than in the 2 m cell. However, it is important to consider that the two profiles obtained represent only a part of the first year of monitoring and that the thermal regime might not be at equilibrium. Therefore, the temperatures monitored in the first months of the survey might be warmer than it will appear in the subsequent years of survey where a stable thermal regime will be reached.

Nevertheless, these results suggest that in the 4 m cell, the tailings remain below the freezing point all year long while in the 2 m cell, the temperature at the tailings-waste rock interface is very close to the freezing point (0 to 0.5 °C).

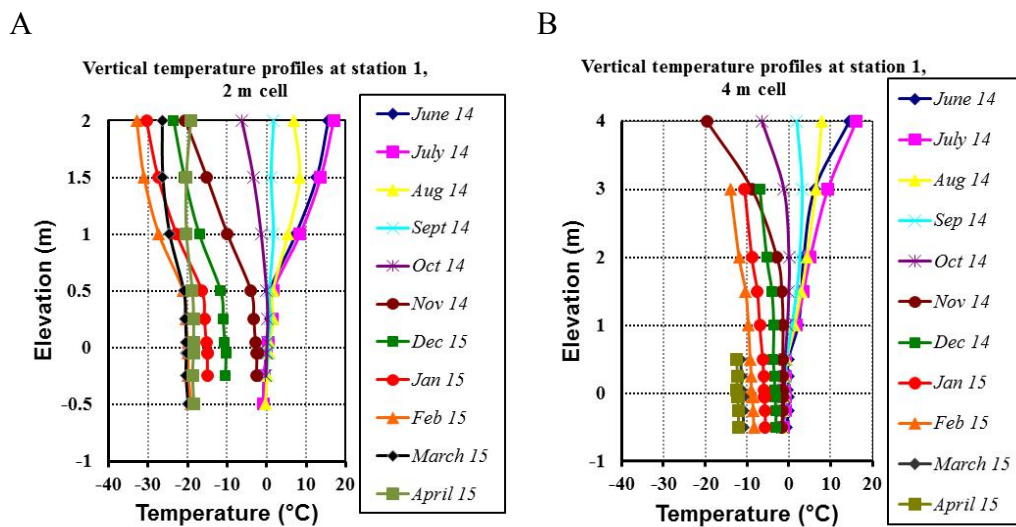


FIG. 7. Temperature profiles measured at station 1 in (A) 2 m and (B) 4 m experimental cell

Oxygen consumption tests

The OC tests were interpreted with the analytical method described by Elberling et al. (1994) in order to evaluate the steady-state O_2 fluxes at the surface of covered and uncovered tailings. The OC tests were performed at 6 stations on the TSF (uncovered tailings) in July and August 2014 at temperatures between 19 and 22°C and with S_r between 48 and 60%. The calculated values of oxygen fluxes are between 20 and 85 moles.m⁻².year⁻¹ at the surface of uncovered tailings. These flux values are relatively low compared to the results of other studies in Nordic environment. Values of oxygen fluxes between 44 and 183 moles.m⁻².year⁻¹ and between <25 and 544 moles.m⁻².year⁻¹ were measured at the Nanisivik mine (Elberling, 2001) and the Raglan mine respectively.

Below insulation covers, OC tests were conducted at temperatures between -1.2 and 0.5°C and with S_r between 80 and 100%. The obtained oxygen fluxes were below 10 moles.m⁻².year⁻¹ at the surface of the covered tailings. Two main factors can explain

the low reactivity of the covered tailings.. First, the measured temperatures were generally low under the insulation cover. Under these thermal conditions, both chemical and biological oxidation reactions may be slowed down. Secondly, the tailing's S_r were high (80-100%). Oxygen flux can be reduced by maintaining a high S_r in the tailings prone to generate AMD. O_2 fluxes measured below the insulation cover are much lower than those measured in the uncovered tailings. These results suggest that the insulation covers contribute to limit O_2 consumption/diffusion by the reactive tailings.

LAST REMARKS

The objective of this study is to evaluate the insulation cover reclamation option at Meadowbank mine (Nunavut, Canada) TSF. Two cover scenarios (2 and 4 m insulation covers) are currently tested to validate this reclamation technique. VWC, temperatures and oxygen consumption of covered and uncovered tailings are measured to assess the thermo-hydraulic performance of the tested covers.

The thermal profiles obtained during the first year for the two central stations showed a fairly good efficiency of the insulation covers to control tailings' temperature. Based on the temperature profiles, the 4 m cover indicated better insulation properties than the 2 m cover. For the 4 m cover, the temperatures measured at the tailings-cover interface were constantly below the freezing point, despite the warm surface temperatures measured at the site during summer (which reached up to 20 -30 °C). The 2 m cover maintained, for most of the time, a tailings temperature below the freezing point. The OC tests conducted on covered and uncovered mine tailings showed that covered tailings have lower oxygen consumption rates and thus the tested covers help limit sulphide oxidation. This paper focused on the design, the construction and the instrumentation of the tested insulation covers. The covers' hydrogeological behavior is still under monitoring. Results as of April 2015 showed that, for both covers, the unfrozen VWC values stabilized between 0.02 and 0.06 (close to the residual water content) in cover materials. For the tailings, unfrozen VWC values close to saturation are observed when the tailings are completely thawed.

The monitoring of the two experimental cells will be continued for a total period of 3 years. Also, a new experimental cell was constructed in summer 2015 to test the possible suitability of an insulating cover with capillary barrier effects as a reclamation scenario for Meadowbank's TSF. This cover was built and instrumented similarly to the herein insulation covers and aims at controlling both the availability of oxygen to the reactive tailings and tailings' temperature. The following testing steps will include a detailed laboratory characterization of the thermal, hydrogeological and geotechnical properties of cover materials. Further, the VWC and the temperature monitoring data will be used to develop a numerical model to predict the long term performance of the tested covers.

ACKNOWLEDGEMENTS

The authors would like to acknowledge the financial support of the NSERC-UQAT Industrial Chair on Mine sites reclamation and the RIME UQAT-Polytechnique industrial partners (www.rime-irme.ca).

REFERENCES

- Andersland, O. and Ladanyi, B. (2004). *Frozen Ground Engineering*. John Wiley & Sons Inc., Hoboken, New Jersey.
- Bouzaah, H., Benzaazoua, M., Bussière, B., and Plante, B. (2015). "ASTM normalized humidity cell kinetic test: protocol improvements for optimal sulfide tailings reactivity." *Mine Water Environ.* 34: 242-257.
- Bussière, B., and Hayley, D. W. (2010). "Effects of Climate Change on Mine Waste Disposal in the Arctic." *Geo-Strata* 14 (5): 44-46
- Bussière, B. (2007). "Hydrogeotechnical properties of hard rock tailings from metal mines and emerging geoenvironmental disposal approaches." *Can. Geotech. J.* 44 (9): 1019-1052.
- Coulombe, V., Bussière, B., Côté, J. and Garneau, P. (2012). "Performance of insulation covers to control acid mine drainage in cold environment." *Proc. 15th International Conference on Cold Regions Engineering*, Qc, Ca, 789-799.
- Elberling, B., Nicholson, R.V., Reardon, E.J. and Tibble, P. (1994). "Evaluation of sulphide oxidation rates: a laboratory study comparing oxygen fluxes and rates of oxidation product release." *Can. Geotech. J.* 13: 375-383.
- Elberling, B., Schippers, A., and Sand, W. (2000) "Bacterial and chemical oxidation of pyritic mine tailings at low temperatures." *J. Contam. Hydrol.* 41: 225-238.
- Elberling, B. (2005). "Temperature and oxygen control on pyrite oxidation in frozen mine tailings." *Cold Reg. Sci. Technol.* 41(2): 121-133.
- Kyhn, C. and Elberling, B. (2001). "Frozen cover actions limiting AMD from mine waste deposited on land in Arctic Canada." *Cold Reg. Sci. Technol.* 32(2-3): 133-142.
- Meldrum, J.L., Jamieson, H.E. and Dyke, L. D. (2001). "Oxidation of mine tailings from Rankin Inlet, Nunavut, at subzero temperatures." *Can. Geotech. J.* 38 (5): 957-966.
- MEND. (2004a). *Covers for reactive tailings located in permafrost regions review*. Report 1.61.4. Mine Environment Neutral Drainage (MEND) Canada Center for Mineral and Energy Technology (CANMET), Ottawa, Ont.
- MEND. (2009). *Mine waste covers in cold regions*. Report 1.61.5a. Mine Environment Neutral Drainage (MEND) Canada Center for Mineral and Energy Technology (CANMET), Ottawa, Ont.
- Miller, S.D., Jeffrey, J.J. and Wong, J.W.C. (1991). "Use and misuse of the acid-bas accounting for AMD prediction". *Proc. 2nd ICARD*, Montréal, Ca, 3: 489-506.
- Peregoedova, A. (2012). "Étude expérimentale des propriétés hydrogéologiques des roches stériles à une échelle intermédiaire de laboratoire". M.S. thesis, École Polytechnique Montréal, Qc, Ca.

Estimating the Cyclic and Post-Earthquake Behavior of Coal Mine Tailings at a Site in Eastern Kentucky

M. E. Kalinski, Ph.D., P.E.¹; and A. Salehian, Ph.D.

¹Associate Professor, Univ. of Kentucky, 161 Raymond Bldg., Lexington, Kentucky 40506-0281.

²Project Engineer, Engeo Incorporated, 2010 Crow Canyon Pl., Ste. 250, San Ramon, CA 94583.

Abstract: Tailings impoundments are constructed to contain tailings produced from mining activities. Methods to analyze liquefaction resistance and post-earthquake behavior exist for soil, but less information is available for mine tailings. This study was undertaken to contribute to the understanding of the cyclic and post-earthquake behavior of coal mine tailings for an impoundment in eastern Kentucky. Cyclic triaxial testing was used to determine liquefaction resistance. Special measures were taken to recover specimens for laboratory testing, including fixed piston sampling and construction of work pads. Field vane shear testing was also performed and relationships between strength and field geotechnical measurements were developed. The three main conclusions of this study are: (1) cone penetrometer testing (CPT) is recommended over standard penetration testing and shear wave velocity testing to estimate shear strength of fine coal tailings; (2) a relationship was derived which may be useful to estimate the cyclic resistance of fine coal tailings based on CPT tip resistance; and (3) correlations between CPT tip resistance and strength were developed which may be useful to estimate the post-earthquake strength of fine coal tailings.

INTRODUCTION

Tailings impoundments are constructed to contain waste materials produced as a result of mining activities associated with coal and metals. Tailings impoundments consist of a dike of coarse-grained refuse with fine-grained tailings hydraulically placed behind the dike from a discharge point near the embankment crest. The three basic construction methods include upstream, centerline, and downstream construction, although impoundments constructed using the upstream method tend to be the least stable (Fig. 1). As the pool of fine refuse fills behind the dike, the dike is expanded upward and tailings impoundments can reach hundreds of feet in depth. Of the three construction types, the upstream construction method is most critical with respect to slope stability because most of the critical failure surface passes through the weaker fine refuse. However, the upstream method is popular because it requires

the least amount of effort and materials to construct the dike and does not progressively move downstream to crowd existing structures and appurtenances.

There are around 1,600 tailings impoundments in the United States, with coal tailings impoundments concentrated in Appalachia and metal tailings impoundments concentrated in the west (NSF, 2003). According to the National Inventory of Dams, approximately one-third of these structures are determined to be high-hazard potential, where failure would result in loss of human life. Tailings impoundments are also common throughout the world. Over the past 60 years, approximately 80 tailings impoundments have failed worldwide with a resulting uncontrolled release. Fifteen of these failures were the result of liquefaction due to earthquake shaking. A noteworthy example is the March 28, 1965 El Cobre Dam system failure in Chile, where over 200 people were killed with an associated release of roughly 2 million tons of material (Dobry and Alvarez, 1967). Another example is the January 15, 1978 Mochikoshi tailings impoundment failures in Japan, where one dam failed during the earthquake, while another failed 24 hours later due to the gradual increase in pore pressures from liquefaction of material behind the dike (Ishihara, 1993). These failures had associated with them liquefaction of fine-grained materials that are often considered to be liquefaction resistant.

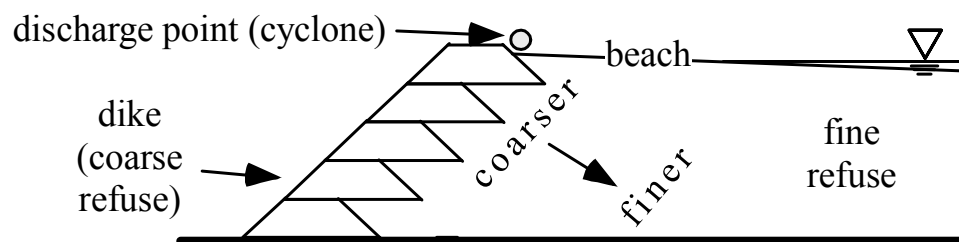


FIG. 1. Upstream construction method for mine tailings impoundments.

Methods to analyze liquefaction resistance in soil deposits, such as the National Center for Earthquake Engineering Research (NCEER) approach summarized by Youd et al. (2001), may be useful to delineate liquefied zones within tailings dams if appropriate modifications are made. This approach consists of estimating the cyclic resistance ratio (CRR) based on laboratory methods (cyclic triaxial or cyclic simple shear) or in situ methods (standard penetration test (SPT), cone penetration test (CPT), or shear wave velocity (v_s) measurement). The factor of safety against liquefaction for horizontally layered sites is calculated by dividing the CRR by the cyclic stress ratio (CSR), which is a function of anticipated peak ground surface acceleration, a_{max} , due to earthquake loading.

However, mine tailings are inherently different than soil. Fine refuse is silty and normally consolidated with a high water content and is more akin to rock flour than naturally occurring soil. The particle shape, angularity, specific gravity of soil solids (G_s), and mineralogical composition of fine refuse is different than fine-grained soil, which is often considered to be liquefaction-resistant. As a result, fine refuse is not necessarily resistant to liquefaction just because it is fine-grained.

Some previous research has been conducted on understanding the dynamic behavior of tailings during strong ground motion loading (Thacker et al., 1988; Zeng

et al., 1998; Zeng et al., 2008), but less data exist for tailings materials because of the difficulties involved with obtaining samples. Fine refuse is soft and should be sampled using specialized methods such as fixed piston sampling or freezing (Poulos et al., 1985), but access to the refuse may be impeded by the fact that large equipment cannot be operated directly on the soft “beach” portion of an impoundment structure. Thus, it would be advantageous to develop in situ methods as an alternative to laboratory-based methods to minimize the need for recovery of specimens.

The National Science Foundation (NSF) funded a research study from 2005-2010 to address these concerns. The scope of the study included piston sampling of fine coal tailings at a representative impoundment in Appalachia, performing various field geotechnical measurements, performing laboratory cyclic testing of undisturbed specimens, and developing correlations between the field measurements and cyclic behavior. The recovery and testing of undisturbed specimens of mine tailings is beyond the capabilities of most practitioners, so the objective of this research was to develop useful correlations between common geotechnical field parameters and cyclic behavior in fine tailings. Herein, the study is discussed.

DESCRIPTION OF TEST LOCATION

An impoundment containing relatively soft tailings was selected to represent the most critical and common case of upstream construction. The Big Branch impoundment was selected as described in Fig. 2. The Big Branch Impoundment is located in Knott County, Kentucky. This impoundment was originally constructed in the early 1980’s and sat dormant for nearly two decades as coal mining operations supporting the preparation plant were suspended. Mining operations on the property resumed in late 2006. The Big Branch Impoundment is an upstream, cross-valley dike system. The maximum permitted pool elevation is 1,298 ft (395.6 m), while the toe of the dam is at 940 ft (286 m).

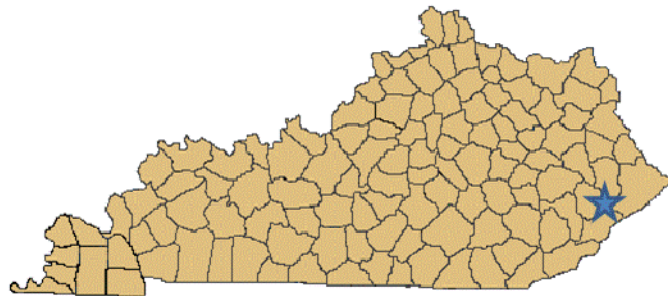


FIG. 2. Approximate location of the Big Branch impoundment in Kentucky.

Detailed records describing tailings placement history and methods at Big Branch were not available, but it was expected that the material encountered beneath the dike would be a combination of mixed refuse underlain by fine refuse. Fine refuse was expected to consist of fine-grained low plasticity silts. Based on previous sampling experience by others, the fine tailings were expected to be relatively soft.

DESCRIPTION OF FIELD AND LABORATORY TESTING METHODS

Field Testing Program. In situ sampling and testing at the Big Branch was performed at two locations at the crest and upstream toe as depicted in Fig. 3. Testing at the crest of the dike was performed because the ground at the crest of the structures was expected to be relatively stable. However, the material encountered below the sampling point at the crest was expected to contain mostly coarse refuse with relatively little fine refuse. Therefore, testing was also performed at a point on the upstream toe of the dike in an effort to sample and recover a larger amount of fine tailings. Testing at these locations was performed by pushing a pad of coarse refuse out into the impoundment, which served to distribute surface pressures and allow equipment to be operated on a peninsula that extended out into the beach area. This approach has been used for other tailings impoundment investigations (Vidich et al., 1998) and proved to be a successful method in this study.

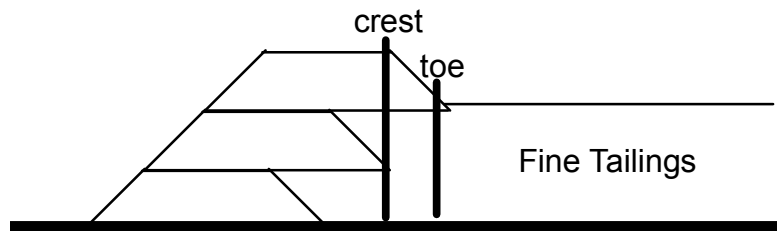


FIG. 3. Schematic illustration of in situ testing and sampling locations at each impoundment.

Field testing and sampling included seismic cone penetrometer testing with pore pressure (u) measurements (sCPTu), standard penetration testing (SPT), in situ vane shear testing, piston sampling, and downhole seismic testing. Cone penetrometer testing was performed by installing a cased pilot hole in the coarse refuse approximately 6 m (20 ft) from the borehole where the other testing was performed. Cone penetrometer testing was not performed in coarse or mixed refuse to avoid damaging the cone and a cone with an area of $(2.33 \text{ in}^2) 15.0 \text{ cm}^2$ was used. Soil sampling and testing in the SPT borehole was facilitated by using hollow stem auger drilling.

Laboratory Testing Program. The objective of this study was to develop methods to assess liquefaction potential and predict post-liquefaction strength based on in situ testing techniques commonly used in geotechnical engineering practice (either SPT, sCPTu, or shear wave velocity). Therefore, it was necessary to recover undisturbed piston samples of fine tailings which could be used for laboratory cyclic triaxial testing per the ASTM D5311 standard. All the triaxial tests in this study were performed using a GCTS cyclic triaxial system at the University of Kentucky.

Cyclic triaxial testing was performed at a loading frequency of 1.0 Hz and pore pressure was measured using a pore pressure transducer. Since most of the specimens were low-plasticity silts, this loading rate was considered slow enough to allow for pore pressure equilibration in the specimen during the test. Specimens were

backpressure saturated prior to testing to obtain a degree of saturation of 100% and tested at an effective stress that was approximately equal to the in situ effective stress of the specimen.

RESULT FROM FIELD TESTING

Field testing was performed at the Big Branch impoundment during the Summer of 2007. Testing was performed at the crest and on a pushout near the upstream toe (Figs. 4 and 5). In general, the fine tailings encountered at Big Branch were relatively soft. Specific gravity testing of representative samples of tailings indicated a specific gravity of soil solids of around 1.8-2.2, which is typical for organic-rich rock that accompanies coal deposits. Plasticity indices were found to be around 5-14% with a USCS classification of mostly ML with some lean clay (CL). In situ moisture content of the tailings varied from 35-40%.

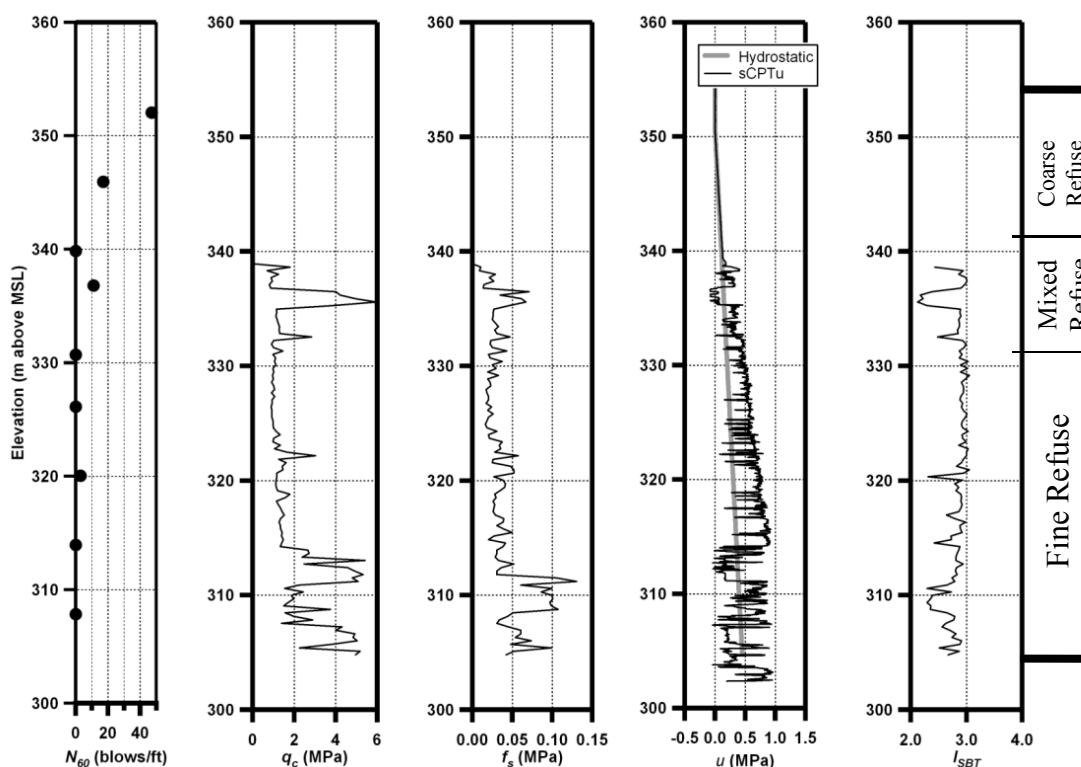


FIG. 4. Field data from the crest location (ground surface elevation = 355 m).

A full suite of sCPTu tests was performed at the Big Branch site, including tip resistance (q_c) and side friction (f_s). Tip resistance and side friction were used to calculate Soil Behavior Type Index (I_{SBT}) according to the updated recommendation provided by Robertson (2010). As indicated in this figure, the borings encountered coarse tailings overlain by fine tailings with an interval of mixed tailings in between. The fine tailings were observed to be a mixture of clayey and silty materials based on visual inspection and soil classification. The I_{SBT} values for the Big Branch

impoundment derived from sCPTu testing indicated that some of the fine tailings were in the silt-sand mixture range (i.e. I_{SBT} between 2.05 and 2.60), with most intervals being in the silty range (i.e. I_{SBT} between 2.60 and 2.95) and some intervals crossing into the clayey range (i.e. I_{SBT} between 2.95 and 3.60). Reliable shear wave velocity data could not be acquired at Big Branch using sCPTu downhole seismic, or SASW due to high amounts of wave attenuation in the soft material. Pore pressure dissipation tests indicated that the long-term pore pressure after dissipation was approximately equal to the predicted hydrostatic pore pressure, so the tailings were assumed to be normally consolidated rather than underconsolidated.

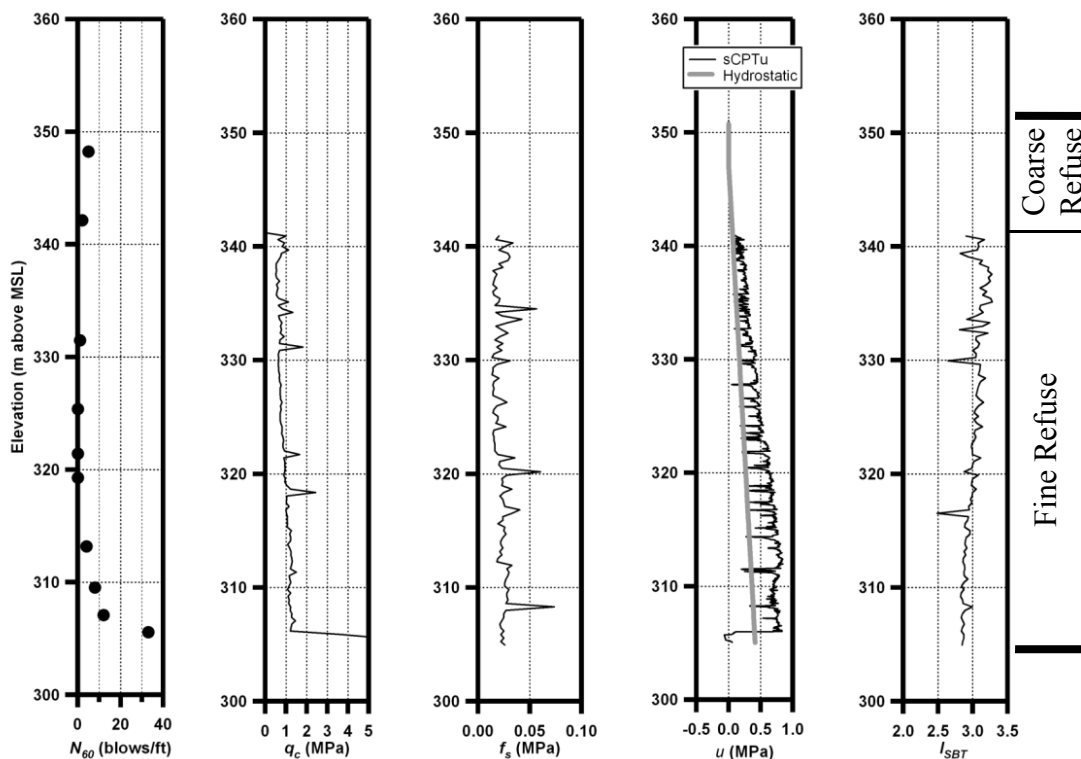


FIG. 5. Field data from the upstream toe location (ground surface elevation = 351 m).

In situ vane shear testing was performed at the Big Branch site following the ASTM D2573 standard. Testing was performed at an interval of around 3 m (10 ft). Forces were measured using a torque wrench and both peak and residual forces were recorded to calculate peak and residual strength. Calculated values for peak shear strength S_p and residual shear strength S_r are included in Table 1 in along with depth, elevation, σ_v , and q_c for the corresponding depth. Peak strength was typically around two to three times higher than residual strength, which is typical for fine tailings (e.g. Poulos et al., 1985). Relationships between strength and CPT tip resistance were expressed using the form:

$$S = \frac{q_c - \sigma_{v0}}{N_k}, \quad (1)$$

where N_k is an empirical cone factor. Values for the cone factor for peak and residual strength (N_{k-Sp} and N_{k-Sr} , respectively) are listed in Table 1.

Table 1. Values for vane shear strength and CPT tip resistance in fine tailings for the Big Branch impoundment

Depth (m)	Elevation (m)	σ_v (kPa)	q_c (kPa)	S_p (kPa)	S_r (kPa)	N_{k-Sp}	N_{k-Sr}
Crest							
26.8	327.9	412	1051	20.8	10.4	30.8	61.5
30.5	324.3	468	1122	26.0	5.2	25.2	125.9
32.9	321.8	505	1253	26.0	10.4	28.7	71.9
36.6	318.2	561	1143	31.2	15.6	18.7	37.3
39.0	315.8	599	1345	26.0	10.4	28.7	71.8
42.7	312.1	655	4906	36.4	15.6	116.8	272.5
45.1	309.7	692	1977	31.2	15.6	41.2	82.3
Upstream Toe							
11.6	339.5	173	784	31.2	15.6	19.6	39.2
15.5	335.5	232	653	15.6	5.2	27.0	81.1
17.7	333.4	263	800	31.2	10.4	17.2	51.6
21.6	329.4	322	641	10.4	5.2	30.6	61.2
23.8	327.3	354	720	10.4	5.2	35.2	70.4
27.7	323.3	413	846	20.8	10.4	20.8	41.6
29.9	321.2	445	938	31.2	10.4	15.8	47.4
33.8	317.2	504	1143	20.8	10.4	30.7	61.5
36.0	315.1	536	1262	31.2	10.4	23.3	69.9
39.9	311.1	595	1155	20.8	10.4	26.9	53.9
42.1	309.0	627	1152	41.6	26.0	12.6	20.2

RESULTS FROM LABORATORY TESTING

Fixed piston sampling was performed at the Big Branch site to minimize sample disturbance. Table 2 presents a summary of the fixed piston samples used for laboratory cyclic testing. Cyclic triaxial testing was performed on these specimens following the ASTM D5311 standard. Typical results from a representative cyclic triaxial test indicate that mine tailings, like many fine-grained silty materials, exhibit strain hardening and cyclic mobility with limited strain as the pore pressure ratio approaches unity.

Measured values of CRR are plotted as a function of number of cycles to liquefaction in Fig. 6. Despite variations in void ratio among the different specimens, there was not a distinct trend in the CRR data to demonstrate the type of relationship between void ratio and cyclic behavior that is typically observed in soil, nor could a relationship between CRR and q_c be established. Nevertheless, a relationship between CRR and N_L was developed which may be useful for estimating cyclic behavior of soft coal tailings similar to those found at the Big Branch site:

$$CRR = 0.435 - 0.131[\log(N_L)]. \quad (2)$$

CORRELATION OF FIELD AND LABORATORY DATA

Shear wave velocity data were not considered as a reliable parameter for correlation due to the lack of data (shear wave velocities could not be reliably measured in the soft Big Branch tailings using sCPTu, SASW, or borehole seismic methods), and SPT blow counts were not considered as a reliable parameter for correlation because blow counts of zero (i.e. “weight-of-tool”) are of little practical use. Therefore, CPT was considered to be the most reliable method for correlation and the remainder of this discussion is dedicated to developing CPT-based methods for estimating shear strength in tailings.

Table 2. Summary of piston specimens used for cyclic triaxial testing (ASTM D5311).

Sample ID	Recovery Depth (m)	Elevation (m)	σ_v (kPa)	USCS Class.	e_o	q_c (kPa)	CRR	N_L
D1S3	26.1	328.7	400	ML	0.58	873	0.32	6
D2S2	32.2	322.6	494	ML	0.97	1073	0.36	4
D2S3	32.3	322.4	496	ML	0.97	1162	0.27	20
D4S1	44.2	310.6	678	ML	0.72	1652	0.29	12
A13S4	23.5	327.7	348	CL	0.62	754	0.28	11
A14S3	29.4	321.6	438	CL	0.97	854	0.29	11
A14S4	29.6	321.5	440	CL	1.07	901	0.26	20
A15S2	35.3	315.8	526	ML	0.62	1053	0.34	6
A15S3	35.5	315.6	528	ML	0.62	1070	0.28	24
A16S1	41.1	309.8	614	ML	0.96	1140	0.43	2
A16S2	41.5	309.6	617	ML	1.23	1222	0.34	3

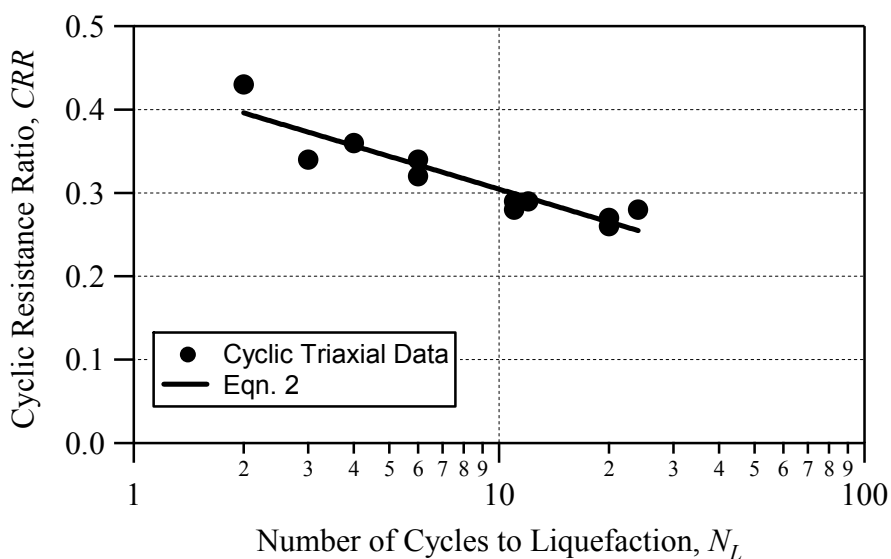


FIG. 6. Cyclic Resistance Ratio versus Number of Cycles to Liquefaction derived from Cyclic Triaxial Testing of Mine Tailings Specimens.

Values for N_k were calculated for peak and residual in situ vane strength and are listed in Table 1. There was a large amount of variability in these calculated values. This large amount of variability is typical in soils where a wide range in N_k can exist due to naturally occurring heterogeneity. Attempts were made to correlate the values of N_k to various parameters, including σ_v , q_c , f_s , R_f , and I_{SBT} , in an effort to develop a CPT-based method to predict strength, but no usable correlations were observed.

An approach of plotting shear strength versus CPT tip resistance ($q_c - \sigma_v$) was also employed and results of this correlation are shown in Fig. 7. Linear regression analyses reveal best-fit curves in the form of:

$$S_p = 5.32 + 0.0355(q_c - \sigma_v) \quad (3)$$

and

$$S_r = 4.42 + 0.0119(q_c - \sigma_v) \quad (4)$$

for peak and residual strength, respectively, where the stress and strength are in units of kPa.

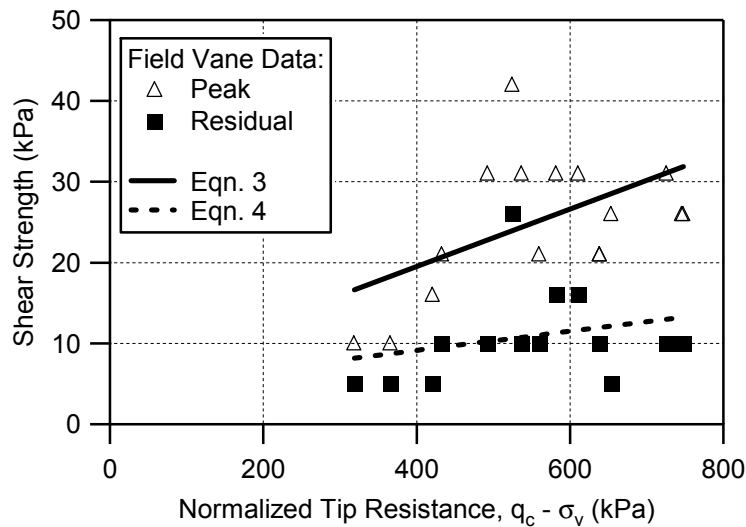


FIG. 7. Shear strength versus CPT tip resistance from in situ vane shear testing.

CONCLUSIONS

The objective of this study was to contribute to the understanding of the cyclic and post-earthquake behavior of coal tailings materials using field and laboratory data acquired at a tailings impoundment in eastern Kentucky. As a result of this study, the following general conclusions can be drawn, which may be applied to other similar coal tailings impoundments:

- Cone penetrometer testing is recommended over SPT and shear wave velocity testing as a means to ascertain the shear strength of fine tailings. Blow counts from SPT testing may be of limited use in softer materials where a blow count of zero (“weight of tool”) is encountered, and in situ shear wave velocity data may not be obtainable due to high attenuation rates in soft tailings.
- A cyclic resistance relationship was derived for soft coal tailings which may be useful to estimate the cyclic behavior of other similar materials.
- Results from in situ vane testing were used to develop correlations between CPT tip resistance and strength (Figs. 6 and 7). The strengths derived from this correlation may be useful to estimate the post-earthquake the post-earthquake strength of other similar materials.

REFERENCES

- Dobry, R. and Alavarez, L. (1967). “Seismic Failures of Chilean Tailings Dams,” *J. Soil Mech. Found. Div., Proc. of the ASCE*. 93: 237-260.
- Ishihara, K. (1993). “Post-Earthquake Failure of a Tailings Dam Due to Liquefaction of the Pond Deposit,” *Proceedings of the Third International Conference on Case Histories in Geotechnical Engineering*, July 1-4, 1993, Saint Louis, Missouri, pp. 1129-1143.
- NSF (2003). “Proceedings of the International Workshop on Seismic Stability of Tailings Dams,” Case Western Reserve University, November 10-11, 2003, National Science Foundation.
- Poulos, S., Castro, G., and France, J. (1985). “Liquefaction Evaluation Procedure,” *J. Geotech. Eng.* 111: 772–792.
- Robertson, P. K. (2010). “Soil Behaviour Type from the CPT: an Update,” *Proceedings of the Second International Symposium on Cone Penetration Testing*, May 9-11, 2010, Huntington Beach, California.
- Thacker, B. K., Ullrich, C. R., Athanasakes, J. G. and Smith, G. (1988). “Evaluation of a Coal Refuse Impoundment Built by the Upstream Method,” *ASCE Geotechnical Special Publication No. 21*, pp. 730-749.
- Vidich, D., Beckwith, G. H. and J. R. Keaton. (1998). “Liquefaction Assessment of Mine Tailings Dams,” *Geotechnical Site Characterization*, P. Robertson and P. Mayne, Eds., Balkema, pp. 543-548.
- Youd, T. L., Idriss, I. M. Andrus, R. D., Arango, I., Castro, G., Christian, J. T., Dobry, R., Finn, W. D. L., Harder Jr., L. F., Hynes, M. E., Ishihara, K., Koester, J. P., Liao, S. S. C., Marcuson III, W. F., Martin, G. R., Mitchell, J. K., Moriwaki, Y., Power, M. S., Robertson, P. K., Seed, R. B. and Stokoe II, K. H. (2001). *Liquefaction Resistance of Soils: Summary Report from the 1996 NCEER and 1998 NCEER/NSF Workshops on Evaluation of Liquefaction Resistance of Soils*, *J. Geotech. Geoenviron. Eng.* 127: 817–833.
- Zeng, X., Wu, J. and Rohlfs, R. A. (1998). “Seismic Stability of Coal-Waste Tailings Dams,” *ASCE Geotechnical Special Publication No. 7. 2*: 950-961.

Field Experiments to Test the Elevated Water Table Concept Combined with a Desulfurized Tailings Cover Layer

Nicolas J. Rey, S.RIME¹; Isabelle Demers, P.RIME²; Bruno Bussière, P.RIME³; Mamert Mbonimpa, P. RIME⁴; and Sylvain Lortie, SupI. Iamgold⁵

¹Student, Research Institute of Mine and Environment, Univ. du Québec en Abitibi-Témiscamingue, 445 Blvd. de l'Université, Rouyn-Noranda PQ, Canada J9X 5E4.

²Professor, Research Institute of Mine and Environment, Univ. du Québec en Abitibi-Témiscamingue, 445 Blvd. de l'Université, Rouyn-Noranda PQ, Canada J9X 5E4.

³Professor, Research Institute of Mine and Environment, Holder of the industrial CRNSG-UQAT Chair, Univ. du Québec en Abitibi-Témiscamingue, 445 Blvd. de l'Université, Rouyn-Noranda PQ, Canada J9X 5E4.

⁴Professor, Research Institute of Mine and Environment, Univ. du Québec en Abitibi-Témiscamingue, 445 Blvd. de l'Université, Rouyn-Noranda PQ, Canada J9X 5E4.

⁵Superintendent, Westwood Environment Dept., Iamgold, CP 970, Rouyn-Noranda, QC, J9X 5C8.

Abstract: The monolayer cover combined with an elevated water table (EWT) concept is an emerging method that appears to be particularly promising in the field of reclamation of sulfidic tailings ponds which may generate acid mine drainage (AMD). The principle of this technical approach relies on the fairly high matric potential of tailings. By controlling the level of the water table inside the pond, one can maintain the degree of saturation of the reactive material sufficiently high to prevent oxygen migration, and therefore limit sulfide minerals oxidation and AMD generation. Desulfurized tailings produced directly at the treatment plant can be used instead of natural material to constitute a cover able to maintain the sulfidic tailings close to saturation, thus reducing the environmental footprint. Previous studies confirmed the performance of the EWT through laboratory experiments and suggested that water table position and cover thickness are important parameters. To further test the concept in real climatic conditions, experimental cells were installed on Doyon-Westwood mine site, in Rouyn-Noranda, Quebec, in summer 2015. This paper presents the design, construction, and instrumentation of three in-situ experimental cells. They are instrumented to enable the evaluation of the hydrogeological behavior of the setting in relation with climatic conditions and the oxygen migration through the cover. Water samples are analyzed to assess sulfide mineral oxidation.

INTRODUCTION

Acid mine drainage (AMD) is the consequence of sulfidic minerals oxidation that were exposed to atmospheric conditions by mining operations. The oxidation reaction results in sulfate liberation and acid generation, which may trigger dissolution of metal contaminants normally stable at neutral pH (Blowes et al. 1990). Engineered covers are often considered as a reclamation option for sulfidic tailing ponds in order to control and/or prevent AMD. Under humid climatic conditions such as in Abitibi, Quebec, the use of the low gas diffusivity property of water is a commonly adopted strategy to limit oxygen migration and to control the oxidation of sulfidic minerals (Bussière 2007). Water covers and covers with capillary barrier effects (CCBE) are designed based on this low gas diffusion property of water and saturated soils. Water covers used to be a prevalent approach during the previous decades, but suffered recent growing concerns about the long term stability and maintenance costs of the dams supposed to maintain the water level. CCBE proved to be a reliable reclamation method when correctly set up (Aubertin et al. 1995; Bussière et al. 2006). However, it requires significant volumes of borrowed material that may be costly to transport if not available in proximity of the site. For sites where the water table is near the surface or can be controlled, a monolayer cover is an economic and effective solution (Demers 2008; MEND 1996; Ouangrawa 2007).

The material used as retention layer in a CCBE or monolayer cover has to be sufficiently fine-grained to remain close to saturation ($S_r \geq 85\%$) in field conditions to correctly limit oxygen migration. Nevertheless, as the grain-size becomes finer, the material becomes more plastic and its hydrogeological properties may become altered by freeze-thaw and/or dry-wet cycles (Dagenais 2005; Kim and Daniel 1992). Therefore, in regions affected by those phenomena the recommended compromise is the use of silty materials which can meet water retention requirement while having a self-healing potential allowing regeneration after each cycle (Aubertin et al. 1995; Bussière 2007).

Engineered covers require significant amounts of materials. Large surface areas may be disturbed to obtain enough natural cover material. In remote regions such as the north of Quebec, silty materials are scarce or not present in sufficient amounts. Alternative solutions are developed to reduce the use of natural materials in cover construction. Researchers have studied the possibility of using low sulfide tailings (Aubertin 1999; Aubertin and Chapuis 1991) or desulfurized tailings (Bussière et al. 2004; Bussière et al. 1995; Demers 2008; Demers et al. 2009a; Demers et al. 2008; Demers et al. 2009b; Dobchuk et al. 2013) to constitute a reclamation cover. Despite the fact that those materials must be characterized in order to anticipate any risks of contaminated and acid mine drainage generation, their use present several advantages: (i) the cover material is produced on site, so transportation costs are reduced; (ii) residual sulfides present in the cover material can temporarily consume a portion of oxygen going through the cover, and thus limit its flux; (iii) using recycled mine materials instead of natural ones reduces the environmental footprint of the project (Demers et al. 2009b; Mbonimpa et al. 2003; Mbonimpa et al. 2011).

Most published experimental studies about monolayer covers with elevated water table (EWT) consisted of laboratory column tests. This project proposes to evaluate

the behavior of such a cover at an intermediate field scale in real field conditions. The experimental site is the Doyon/Westwood mine, located near Rouyn-Noranda, Quebec. Laboratory column tests and numerical modeling are also used to validate field results; however they are not discussed in this paper.

In a first section, the monolayer cover combined with the EWT as tailings impoundment reclamation scenario will be explained. In a second section, the historical context of the Doyon/Westwood mine will be broadly overviewed as well as the motivations that led its current operator, IAMGOLD, to explore the feasibility of this reclamation approach. Then, the experimental design, construction sequence and the properties of the different materials will be described. Finally, the upcoming work will be presented briefly along with some conclusions of this preliminary work.

MONOLAYER COVERS COMBINED WITH EWT

The monolayer cover combined with EWT approach is based on the control of oxygen flux to prevent the formation of AMD. The water level is maintained sufficiently high for tailings to remain close to full saturation. Indeed, the oxygen diffusion coefficient of water is approximately 10^4 times lower than that of air (Aachib et al. 2004; Mbonimpa et al. 2003) therefore saturated soil or tailings can act as an oxygen barrier. The role of the cover is to prevent desaturation by evaporation during the dry periods and erosion during floods. It can also allow the maintenance of a certain height of saturated soil above the sulfidic tailings by capillary rise, which may prevent oxidation of its most superficial horizons. According to previous studies, cover thickness has a small but visible impact on the oxygen flux (Demers 2008; Ouangrawa 2007).

The water table level required to control oxidation depends on the water retention curve (WRC) of the tailings, and more specifically on the air entry value (AEV). This value corresponds to the pressure at which a material begins to drain. It is also equivalent to the vertical distance above the water table along which the material may remain fully saturated due to capillarity. Theoretically, a distance of one AEV between the reactive tailings surface and the water table should suffice to maintain saturation in the tailings. However, previous studies have shown that a distance of $\frac{1}{2}$ AEV is more appropriate (Ouangrawa 2007). Indeed, a safety margin is preferable to compensate for heterogeneity that might affect the hydrogeological properties of the material, and variable climatic conditions.

EXPERIMENTAL SITE: DOYON/WESTWOOD MINE

The Doyon gold deposit was exploited from 1978 to 2010. 110 ha of sulfidic tailings have been generated and stored in three different ponds (see FIG. 1). Recently, IAMGOLD, who operated the Doyon mine, began operation of the underground Westwood deposit located two kilometers away from the Doyon mine. This new project brought up the opportunity to use tailings desulfurized in the mineral processing circuit to constitute a cover for the Doyon ponds #2 and #3. Westwood tailings (stream that is not desulfurized) and the concentrate from the desulfurization process will be deposited in Doyon open pits and/or used as backfill for Westwood underground stopes.

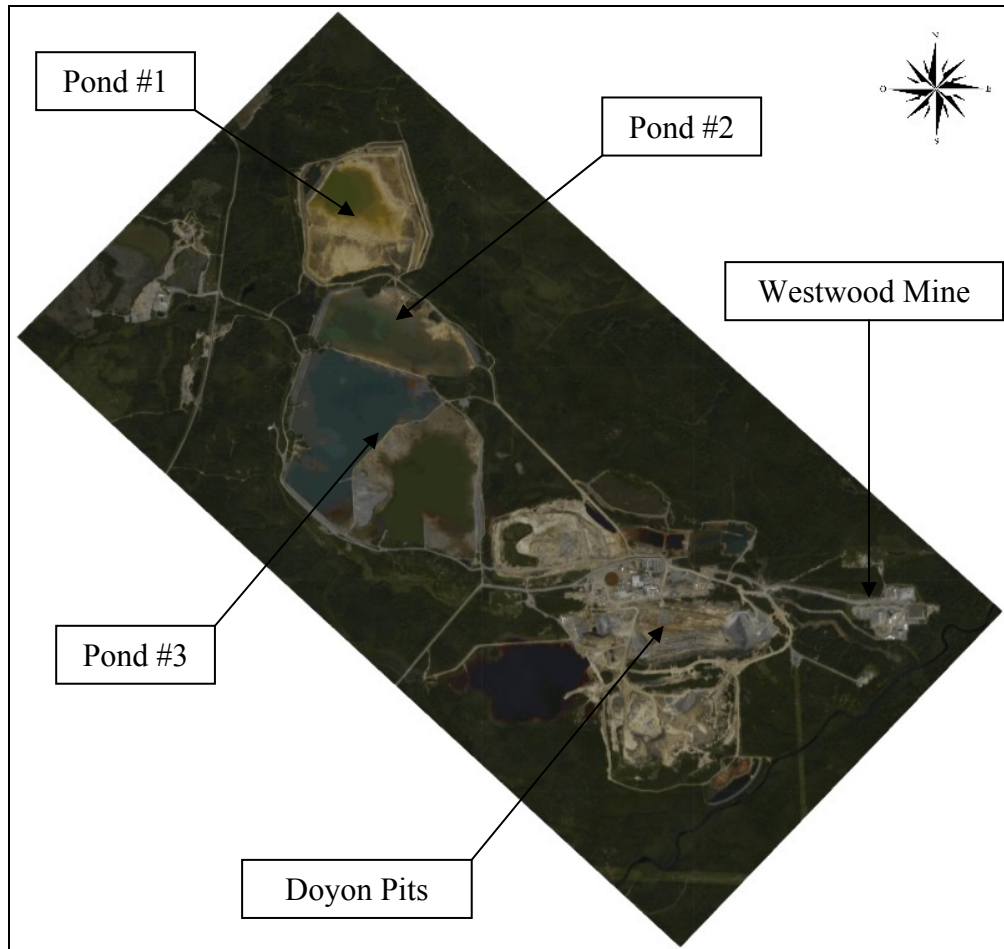


FIG. 1. Aerial photography and display of main installations of the Doyon-Westwood mine site

CONSTRUCTION AND MONITORING OF THE EXPERIMENTAL CELLS

IAMGOLD considered a monolayer cover combined with EWT for the reclamation of ponds #2 and #3 because (i) the water table lays naturally close from the surface of the tailings and can be controlled; and (ii) desulfurized tailings will be produced on site. Three experimental cells were constructed and instrumented in July 2015 in order to evaluate the performance of this scenario at an intermediate scale under in-situ natural climatic conditions. The general design of the cells was based on the set up used in previous studies by RIME researchers such as in Bussi re et al. (2007) whereas the cover thicknesses and AEV position ranges were inspired from Ouangrawa (2007) and Demers (2008). Through this experiment, three main parameters are tested: (i) the thickness of the cover, (ii) the level of the water table, and (iii) the presence of an evaporation barrier. The cells (see FIG. 2A and FIG. 3) are shaped as an inversed pyramid with a square truncated apex of 1 m². The upward square basis surface depends on the thickness of the cover. Cells #1 and #2 are 9 by 9 m large and Cell #3 is 7.6 by 7.6 m large. A constant pyramid slope of 2L:1V was chosen for geotechnical stability during construction.

The cells were constructed on a waste rock pile at Doyon site. The broad form of the cells was first excavated into the waste rocks, and 30 cm of fine sand was then deposited at the bottom to shape the cells more precisely and to protect the geomembrane from the sharp angles of the rocks. A geomembrane was used for impermeability (to separate the rock pile from the inside of the cells). A drain was also installed at the bottom of the cells through the membrane to adjust the water table level and allow the collection of effluent water samples. Its outer end is bent so the pipe remains full of water thus preventing air inflow to the cell that would trigger oxidation of the tailings from the bottom of the cell (see FIG. 3). For cells #1 and #3 the drain is set horizontally, so the outlet of the pipe is 1 m underneath the tailings/cover interface and cells #2 drain is set up with a gentle slope so its outlet is 2 m underneath the tailings/cover interface. Those elevations of 1 and 2 m are respectively equivalent to $\frac{1}{2}$ AEV and 1 AEV of the sulfidic tailings (which is approximately 200 cm (from modified Kovacs (Aubertin et al.2003))). Also, flowmeters are installed at the exit of the drains.

The three cells are filled with one meter of sulfidic tailings ($V1 = 10.34 \text{ m}^3$) collected from Doyon pond #3. In cells #1 and #2 the Doyon tailings are covered with a one meter thick desulfurized tailings ($V2 = 50.35 \text{ m}^3$), whereas cell #3 is covered by a 50 cm layer of desulfurized tailings ($V2' = 18.17 \text{ m}^3$) and a 15 cm layer of inert sand and gravel ($V3 = 8.00 \text{ m}^3$) as evaporation protection layer. This last material was imported from a nearby alluvial deposit. Concerning the desulfurized tailings, since the Westwood treatment plant was not yet operational to produce such volume (about 120 m^3) a similar desulfurized material was transported from the Goldex mine in collaboration with its operator Agnico Eagle.

Sensors are set up at different levels from either side of a pipe installed vertically at the center of the cell. The lower tip of the pipe rests at the bottom of the cells and the sensor cables are attached to it so they can't be towed nor damaged during the construction (see FIG. 2C and FIG. 3). In all three cells, volumetric water content and temperature sensors (Decagon 5TM) were placed 10 cm below the desulfurized tailings surface and 10 cm below and above the sulfidic tailings surface. Also, another sensor was placed in the middle of the 15 cm thick sand and gravel cover in cell #3. Suction sensors (Watermark) were installed at the exact same levels, except for the bottom ones inside the sulfidic tailings, where punctual measurement will be taken regularly with a tensiometer (Jetfill). Volumetric water content and suction sensors are connected to adapted dataloggers (respectively Em50 and Watermark).

Two flexible tubes are also installed inside each of the desulfurized covers to collect air samples for oxygen analysis. The lower end of each tube is pierced and wrapped into geotextile to allow air circulation without clogging. The upper ends of the tubes remain at the surface of the cell and are plugged when not in use so air circulation is prevented. The lower ends of the tubes are placed 10 cm below the top and above the bottom of the layer. Small amounts of air (with negligible impact on whole system) can be suctioned with a peristaltic pump and analyzed by an oxygen sensor (Optopod PSt3) and its acquisition system (OXY-10). Those measurements realized once every month allow the assessment of the oxygen concentration gradient in interstitial air at those specific levels of the cover.

Major climatic parameters will also be assessed. A pluviometer is installed near the cells, and the temperature sensor (5TM) placed just below the surface (7.5 cm deep) in the sand and gravel layer of Cell #3 will give a fair indication of the temperature. Climatic data from the Rouyn-Noranda airport meteorological station (approximately 20 km away from the installation) will also be used.

Water samples are collected regularly at the drain outlets and analyzed at the URSTM-UQAT laboratory to evaluate sulfate and metal concentrations, acidity and alkalinity, while pH, Eh and conductivity measurement will be performed on site with electrodes. The monitoring of the cells started in July 2015 and is expected to be pursued at least until the end of 2017, for a minimum duration of two years. The acquired data will be compared to a consistent database collected from a control cell made of similar sulfidic tailings which were exposed without any protection. This control cell was set up in 2012 as part of an anterior project on reclamation scenarios for the Doyon-Westwood mine site and is still monitored (Demers et al. 2015).

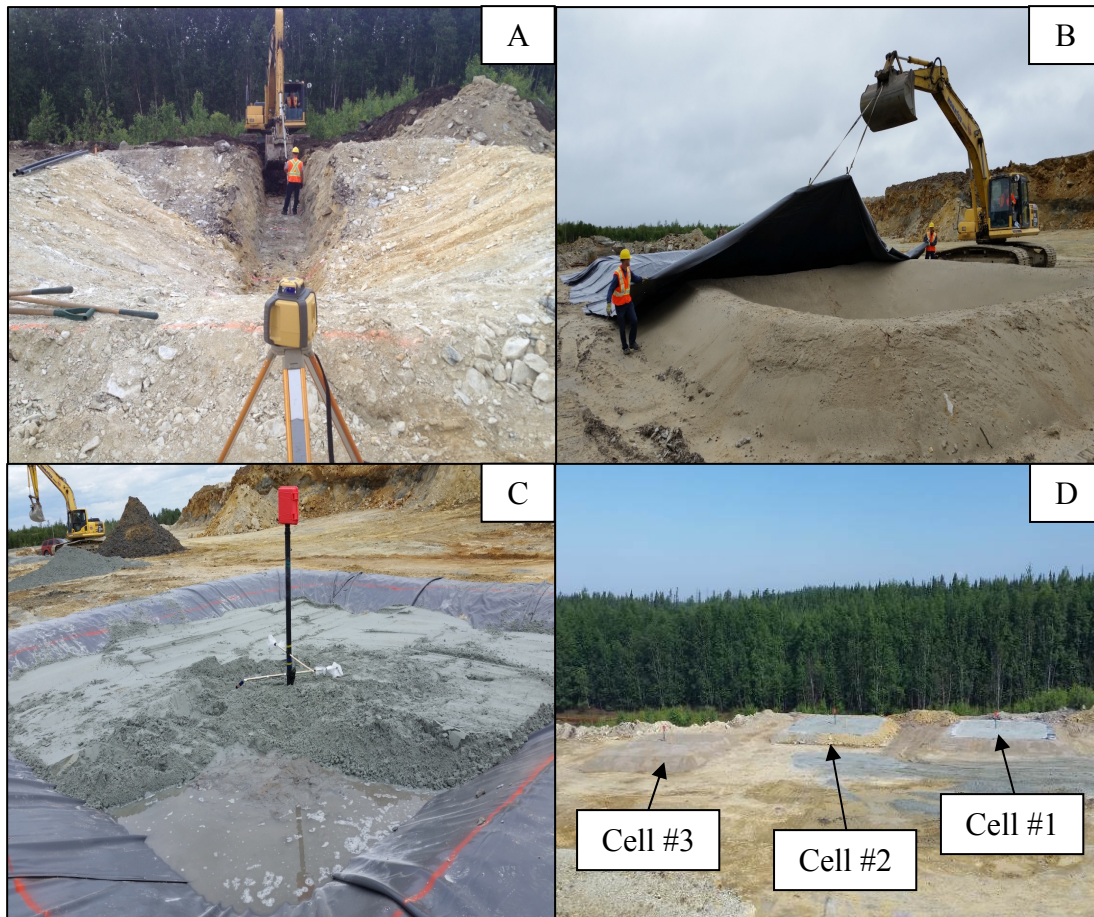


FIG. 2. Photos of key steps of cells construction (A: excavation of the shape of the cell; B: setting of the geomembrane; C: filling of the cell and installation of the monitoring system; D: end of the construction)

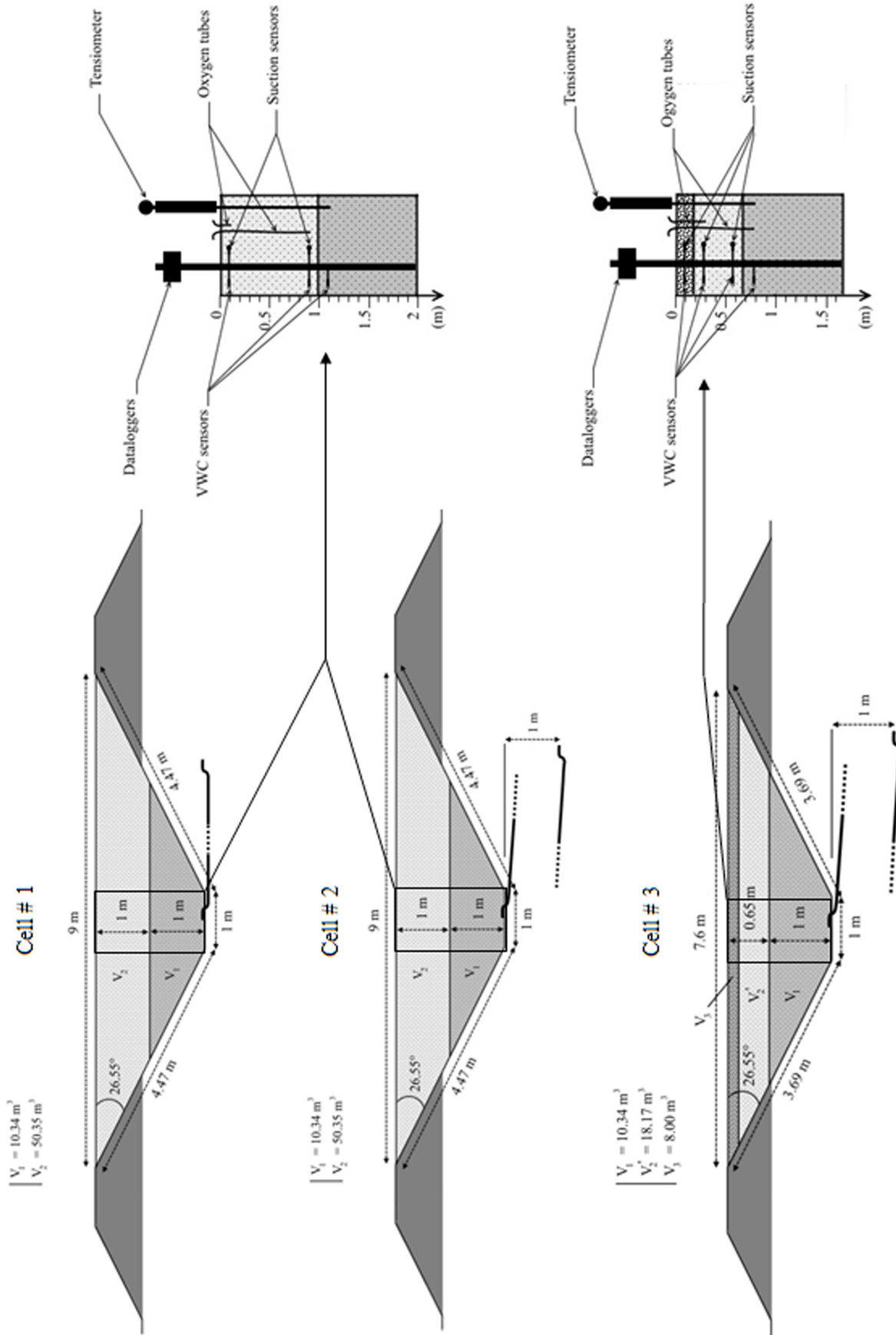


FIG. 3. Lateral illustration of the geometry of the experimental cells and their instrumentation

PRELIMINARY MATERIAL CHARACTERIZATION

Samples of both sulfidic and desulfurized tailings were subjected to characterization of grain size (laser diffraction analysis), specific gravity (G_s) (helium pycnometer), and void ratio (weighing, drying protocol). The grain size of the sand and gravel of the anti-evaporation layer was obtained with standard sieving procedure. The sulfide contents (essentially pyrite) are 3.58% for the Doyon tailings, and 0.10% for the desulfurized cover material, which is considered non-PGA. A complete chemical and mineralogical was not considered relevant for the topic of this paper and will therefore be presented in further publications.

Four samples of sulfidic tailings and two of desulfurized tailings were collected per cell at the moment of their placement. The G_s measured was 2.81 and 2.72 respectively. The void ratios (e) were estimated at 0.48 and 0.45 with a calculated variance of $6 \cdot 10^{-3}$ and 10^{-3} respectively. The grain size properties characterized are displayed below (see Table 1).

Table 1: Results of the grain size characterization of tailings

Tailings	D ₁₀ (μm)	D ₃₀ (μm)	D ₅₀ (μm)	D ₆₀ (μm)	D ₉₀ (μm)	C _u (-)
Sulfidic	6.18	16.71	34.89	49.61	172.28	8.02
Desulfurized	25.22	109.12	173.83	206.32	350.15	8.18
Sable	112.04	336.12	560.2	672.24	1008.36	6.00

From these physical properties, an estimation of the WRC of the sulfidic tailings was calculated with the Modified Kovacs (MK) model (Aubertin et al. 2003). The void ratio, D_{10} , and C_u input values are the ones above ($e = 0.48$, $D_{10} = 6.18$, $C_u = 8.02$). An estimated AEV of 200 cm was determined graphically. The WRC will be measured experimentally in the laboratory using a Tempe pressure cell.

CONCLUSION AND UPCOMING WORK

The monitoring of the experimental cells will provide new insight concerning the performance of desulfurized tailings as a material to control the production of AMD in natural climatic conditions. As part of the present project, laboratory column tests will also be conducted to compare the behavior of Westwood desulfurized tailings to the ones used as in the construction of the described cells (Goldex tailings). The column experiments will also allow the testing of more diverse combination of the aforesaid parameters (water table level, cover thickness, and evaporation protection) as well as other parameters (particle size of desulfurized tailings). Finally, the database collected will be used to conduct a numerical modelling study using VADOSE/W (GEO-SLOPE) and MIN3P (Mayer et al. 2002) software. The numerical model will simulate the system on a long term scale (a hundred years), as well as the impact of climate change on the efficiency of such cover systems. The knowledge acquired from the study will provide insights on the installation, monitoring and optimization of monolayer covers made of desulfurized tailings combined with an

elevated water table, which can most certainly be incorporated into a mine waste integrated management plan.

ACKNOWLEDGMENTS

The authors appreciate the help of the Westwood – IAMGOLD partners, as well as the URSTM technicians, the RIME UQAT-Polytechnique partnership, the trainee student Claudia Grondin, and the Goldex - AGNICO EAGLE team for their collaboration to this project. The authors also acknowledge the financial support of the NSERC-UQAT Industrial Chair partners, and of the CRSNGNSERC-FRQNT through the BMP scholarship.

REFERENCES

- Aachib, M., Mbonimpa, M., and Aubertin, M. (2004). "Measurement and prediction of the oxygen diffusion coefficient in unsaturated media, with applications to soil covers." *Water Air Soil Pollut.* 156(1-4): 163-193.
- Aubertin, M. (1999). "Etudes de laboratoire sur l'efficacité de recouvrements construits à partir de résidus miniers." *MEND report 2.22.2B*, Ottawa, ON, Canada.
- Aubertin, M., and Chapuis, R.P. (1991). "Considération hydrogéotechniques pour l'entreposage des résidus miniers dans le nord-ouest du Québec." *2nd Int. Conf. on the Abatement of Acidic Drainage*, Montréal, QC, Canada. pp. 1-22.
- Aubertin, M., Chapuis, R.P., Bussière, B., Ricard, J.-F., and Tremblay, L. (1995). "Evaluation en laboratoire de barrières sèches construites à partir de résidus miniers." *MEND Report 2.22.2a*.
- Aubertin, M., Mbonimpa, M., Bussière, B., and Chapuis, R.P. (2003). "A physically-based model to predict the water retention curve from basic geotechnical properties." *Can. Geotech. J.* 40(6): 1104-1125.
- Blowes, D.W., Reardon, E.J., Jambor, J.L., and Cherry, J.A. (1990). "The formation and potential importance of cemented layers in inactive sulfide mine tailings." *Geochim. Cosmochim. Acta* 55(4): 965-978.
- Bussière, B. (2007). Colloquium 2004: "Hydrogeotechnical properties of hard rock tailings from metal mines and emerging geoenvironmental disposal approaches." *Can. Geotech. J.* 44(9): 1019-1052.
- Bussière, B., M. Aubertin, M. Mbonimpa, J.W. Molson et R.P. Chapuis. (2007). "Field experimental cells to evaluate the hydrogeological behaviour of oxygen barriers made of silty materials." *Can. Geotech. J.* 44(3): 245-265.
- Bussière, B., Benzaazoua, M., Aubertin, M., and Mbonimpa, M. (2004). "A laboratory study of covers made of low-sulphide tailings to prevent acid mine drainage." *Environ. Geol.* 45(5): 609-622.
- Bussière, B., Lelievre, J., Ouellet, J., and Bois, D. (1995). "On the use of low sulphur tailings as cover to prevent AMD: Technico-economical analysis of two cases study." *Sudbury '95 - Mining and the Environment, Conference Proceedings.* 1(3): 59-68.
- Bussière, B., Maqsoud, A., Aubertin, M., Martschuk, J., and McMullen, J. (2006). "Performance of the oxygen limiting cover at the LTA site, Malartic, Quebec." *CIM Bulletin* 99(1096): 1-11.

- Dagenais, A.M. (2005). "Technique de contrôle du drainage minier acide basées sur les effet de barrière capillaire." *Département des génies civils, géologiques et des mines. École polytechnique de Montréal.* p. 401.
- Demers, I. (2008). "Performance d'une barrière à l'oxygène constituée de rejets miniers faiblement sulfureux pour contrôle la production de drainage minier acide." *Institut de Recherche en Mines et en Environnement. UQAT.* p. 283.
- Demers, I., Benzaazoua, M., Mbonimpa, M., Bouda, M., Bois, D., and Gagnon, M. (2014). "Valorisation of acid mine drainage treatment sludge as remediation component to control acid generation from mine wastes, part 1: Material characterization and laboratory kinetic testing." *Miner. Eng.* 76(2015): 109-116.
- Demers, I., Bussiere, B., Benzaazoua, M., Mbonimpa, M., and Blier, A. (2009a). "Preliminary optimization of a single-layer cover made of desulphurized tailings: application to the Doyon Mine tailings impoundment." *Society for mining, metallurgy, and exploration inc.* 326: 21-33.
- Demers, I., Bussière, B., Benzaazoua, M., Mbonimpa, M., and Blier, A. (2008). "Column test investigation on the performance of monolayer covers made of desulphurized tailings to prevent acid mine drainage." *Miner. Eng.* 21(4): 317-329.
- Demers, I., Bussiere, B., Mbonimpa, M., and Benzaazoua, M. (2009b). "Oxygen diffusion and consumption in low-sulphide tailings covers." *Canadian Geotechnical Journal* 46(4): 438-453.
- Dobchuk, B., Nichol, C., Wilson, G.W., and Aubertin, M. 2013. "Evaluation of single-layer desulphurized tailings cover." *Can. Geotech. J.* 50: 16.
- Kim, W., and Daniel, D.E. (1992). "Effects of Freezing on Hydraulic Conductivity of Compacted Clay." *Journal of Geotechnical Engineering* 118(7): 1083-1097.
- Mayer, K.U., Frind, E.O., and Blowes, D.W. (2002). "Multicomponent reactive transport modeling in variably saturated porous media using a generalized formulation for kinetically controlled reactions." *Water resources research* 38(9, 1174): 21.
- Mbonimpa, M., Aubertin, M., Aachib, M., and Bussiere, B. (2003). "Diffusion and consumption of oxygen in unsaturated cover materials." *Can. Geotech. J.* 40(5): 916-932.
- Mbonimpa, M., Aubertin, M., and Bussière, B. (2011). "Oxygen consumption test to evaluate the diffusive flux into reactive tailings: interpretation and numerical assessment." *Can. Geotech. J.* 48(6): 878-890.
- MEND. (1996). "Review of use of an elevated water table as a method to control and reduce acidic drainage from tailings." *MEND report 1.17.1*, Ottawa, ON, Canada.
- Ouangrawa, M. (2007). "Étude expérimentale et analyse numérique des facteurs qui influencent le comportement hydro-géochimique de résidus miniers sulfureux partiellement saturés." *Département des génies civil, géologique et des mines. Ecole Polytechnique de Montréal.* p. 418.

Geotechnical Characterization of Compacted Bauxite Residue for Use in Levees

Matthew S. Gore, Ph.D., E.I.T., M.ASCE¹; Robert B. Gilbert, Ph.D., P.E., D.GE, M.ASCE²;
Ian McMillan³; and Shannon L. Isovitsch Parks, Ph.D., P.E.⁴

¹Staff Engineer, Golder Associates, 820 S. Main St. #100, Saint Charles, MO 63301.
E-mail: matthew.s.gore@gmail.com

²Brunswick-Abernathy Professor in Civil, Architectural and Environmental,
Engineering, Dept. of Civil Engineering, Univ. of Texas at Austin, Austin, TX 78704.
E-mail: bob_gilbert@mail.utexas.edu

³Graduate Research Assistant, Dept. of Civil Engineering, Univ. of Texas at Austin,
Austin, TX 78704. E-mail: mcmillanfifth@gmail.com

⁴Senior Project Leader, Alcoa Technical Center, 100 Technical Dr., Alcoa Center, PA
15069. E-mail: Shannon.Parks@alcoa.com

Abstract: This paper describes the results from a laboratory test program developed to characterize and evaluate the geotechnical properties of compacted bauxite residue, a byproduct from the production of alumina. Demand for suitable fill materials to construct flood-protection levees, particularly along the U.S. Gulf Coast, prompted this study to determine if bauxite residue could be a feasible solution. The laboratory test program consisted of characterization tests and performance tests including shear strength, hydraulic conductivity, erosion resistance and compressibility. Samples of both untreated bauxite residue and alkalinity-adjusted bauxite residue were tested. The results provide several conclusions. The characterization tests show that bauxite residue behaves like a fine-grained, plastic soil. Oven-drying the material before testing affects its geotechnical behavior and provides impractical results. In a compacted state, bauxite residue has a low hydraulic conductivity that is resistant to internal erosion and suitable for the core of a flood-protection levee. Compacted bauxite residue has a shear strength that is greater than fine-grained soils typically used in levees, potentially reducing the necessary footprint and volume required for a levee constructed with this material. The high alkalinity of untreated bauxite residue makes it necessary for neutralization or encapsulation to minimize its impact on the environment.

INTRODUCTION

Bauxite residue (also called "red mud", "red clay", "alkaline clay", or "cajunite") is a fine-grained reddish-brown waste byproduct from the refining of bauxite ore through the Bayer process, to alumina, a precursor to aluminum. It is composed mostly of iron (20-45%), aluminum (10-22%), and silica (5-30%) content. The refining process includes grinding, digestion, liquor clarification, precipitation of alumina hydrate, and calcination of the ore to alumina (Jones et al. 2011). Bauxite residue is produced when the ground ore is mixed with caustic soda (sodium hydroxide, NaOH), heated and put under pressure, and transformed into sodium aluminate and insoluble solids (bauxite residue). Filtering and washing of the resulting mixture separates the alumina and bauxite residue (a high pH, caustic slurry waste). The EPA classifies the waste, under RCRA Subtitle D and in accordance with the Bevill Exemption, as a solid waste with a high pH; as high as 13 (USEPA 1990). For reference, bauxite, the aluminum ore, is a laterite mined primarily in the tropics 30° North and 30° South of the equator.

Despite advances in refinery processing, demand and production of aluminum continues to create increasing levels of bauxite residue, with approximately 2 billion tons produced worldwide in the last decade (IAI 2013). Refineries typically store the waste in containment ponds or dry stacking facilities located on site. As available storage of current containment facilities decreases and cost of expansion increases, the aluminum industry is in search of a solution to the growing challenge of storage. One possibility is to reuse bauxite residue as a compacted fill for embankments or levees.

The goal of this paper is to present the results from a laboratory testing program studying compacted bauxite residue as a possible fill material from a geotechnical perspective.

LITERATURE REVIEW

The study of bauxite residue as a reuse product has been an ongoing topic for at least 30 years, with studies looking at both the physical and chemical properties of the material. In terms of geotechnical properties of bauxite residue, publically available data show significant scatter, making it difficult to classify using traditional means. Much of the reviewed research classifies bauxite residue as a clayey silt, with a few papers classifying the material as sand. For plasticity, data includes liquid limit (LL), plasticity limit (PL), and plasticity index (PI) ranges were 25 to 66, 17.5 to 40, and 4 to 32, respectively (Somogyi 1976; Jenny 1974; Vick 1981; Cooling 1985; Kirkpatrick 1996; Consoli 1997; Newson 2006; Kehagia 2008; Bodley et al. 2011; Ito 2013; Kola & Das 2013; Deelwal et al. 2014). The reviewed research also shows drained friction angles range from 27° to 46° (Jenny 1974; Somogyi 1976; Li 1998; Newson 2006; Vick 1981; Bodley et al. 2011; Shahin et al. 2011; Nikraz et al. 2007; Kola & Das 2013; Deelwal et al. 2014). Nikraz et al. (2007) provides further details on strength by stating drained friction angle ranges for untreated residue (38° - 46°), carbonated treated residue (37° - 45°), and bittens/carbonated treated residue (41° - 42°).

MATERIALS

Two different refineries in the U.S provided samples for this bauxite residue research. The first refinery (designated Residue 1 or R1) disposed of residue as slurry with water contents exceeding 120 percent. The samples for Residue 1 came from one location approximately half way along the depositional path. The second refinery (designated Residue 2 or R2) disposed of residue in a “dry-stacking” slurry operation, with water contents on the order of 60 to 70 percent. The samples for Residue 2 came from multiple locations along the depositional path.

One concern with tropical/residual soils or rocks is the possibility of extracting water from the minerals themselves during oven drying at 110° C (Blight & Leong 2012). In order to explore this effect with bauxite residue, specimens were dried both in ovens at 110° C and 50° C. The results show that the effect of using a lower drying temperature only change the weight of solids by at most 1 or 2 percent (Gore 2015).

With the initial results on varying the oven drying temperature, the laboratory testing program utilized three different methods of preparing specimens: (1) oven-drying (110°C) and then re-wetting with tap water to the desired water content; (2) air-drying (approx. 23°C) and then re-wetting with tap water to the desired water content; and (3) pressing/squeezing the material to the desired water content with no rewetting.

GRAIN SIZE

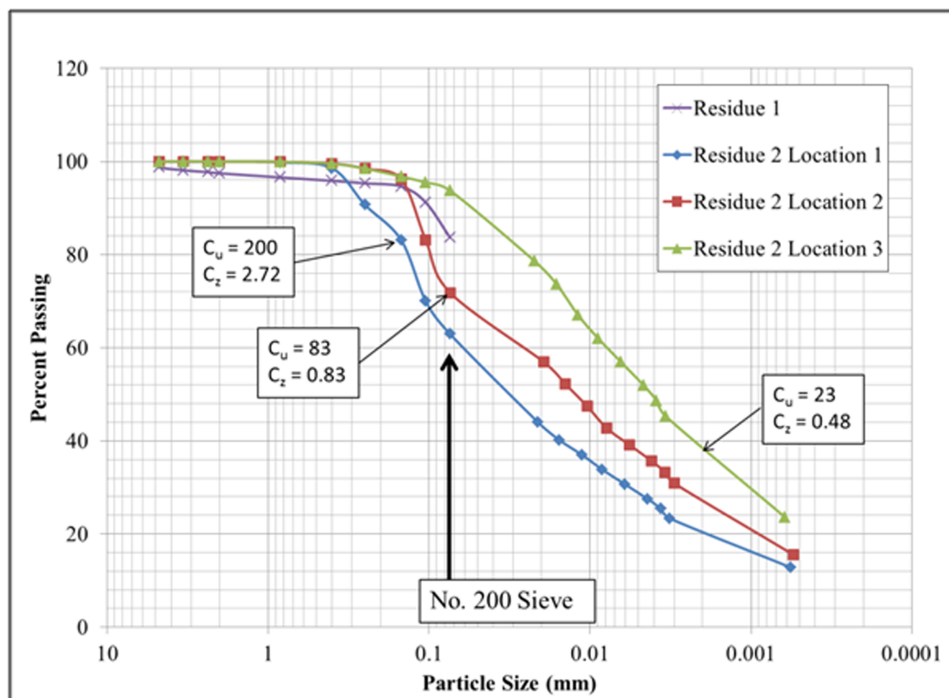


FIG. 1. Grain Size Distribution Results based on Wet Sieving

Wet sieve analysis of bauxite residue (Figure 1) shows 65 to 95 percent passing the U.S. Standard Sieve No. 200 (0.074 mm particle diameter) and a coefficient of

uniformity exceeding 20. However, dry sieving results in substantially fewer particles passing the No. 200 Sieve (Gore, 2015), indicating effects of drying and cementation that would not be representative for practical applications unless the bauxite residue were to be completely de-watered before use in a compacted fill.

Specific gravities range from 3.2 to 3.7. The specific gravities compare well between the two different residues. Also, the specific gravities tend to decrease with distance away from the discharge point in the storage area (Gore, 2015). The high specific gravity for bauxite residue reflects the minerals that constitute it: iron oxide with a specific gravity of 4.8 to 5.3, aluminum oxide with a specific gravity of 3.4 to 4, and titanium oxide with a specific gravity of 3.9 to 4.2.

PLASTICITY

Plasticity of bauxite residue varies significantly depending on how the material is processed prior to testing as described in the MATERIALS section. Oven-dried residue rewetted with tap water exhibits essentially no plasticity. Air-dried residue rewetted with tap water behaves as a silt with moderate plasticity, classifying as an ML material in the Unified Soil Classification System (Figure 2). This second method of preparation is intended to best represent the material preparation in the field for a compacted fill. Press/Squeeze-dried residue (i.e. - residue with caustic liquid as pore fluid) shows the highest level of plasticity. Therefore, care is required in determining how the material was prepared for testing both in future research and in using plasticity data reported in the research literature on bauxite residue. The results may also show that the pore fluid alkalinity may affect plasticity of the material as well.

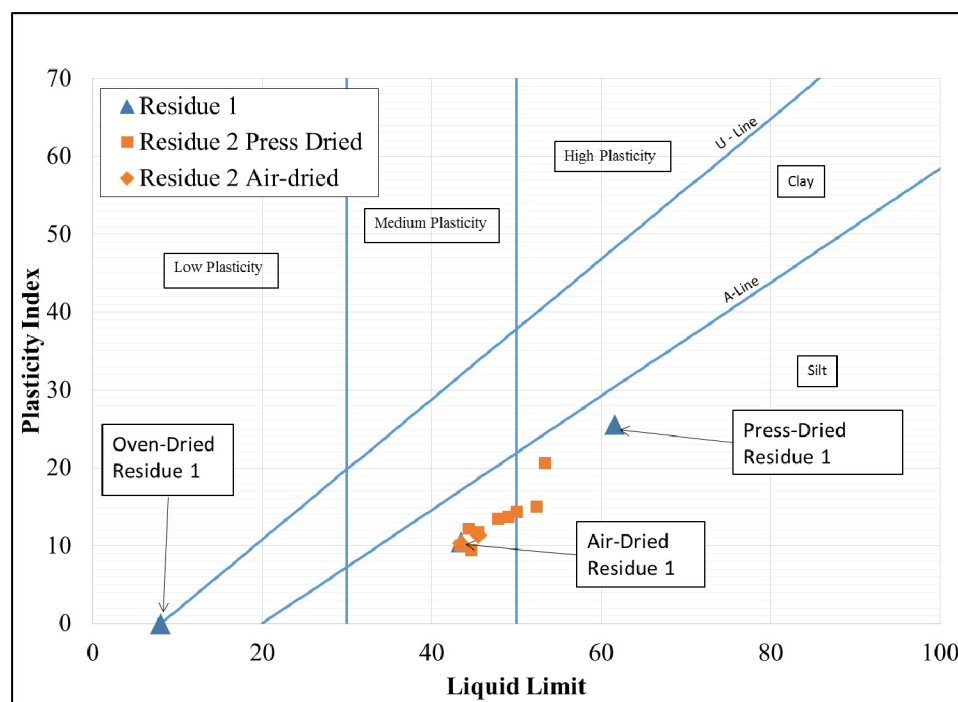


FIG. 2. Plasticity Results

pH

The pH of the pore fluid in the as-disposed bauxite residue is quite high due to the introduction of high concentrations of caustic soda during the Bayer process. Measured values of pH for untreated, unprocessed bauxite residue range from 13.1 to 13.5. When the bauxite residue is air dried, the alkalinity lowers by about two orders of magnitude, likely through carbonation (Cooling et al., 2002) to a pH of about 11 (Gore, 2015).

COMPACTION

Compaction data for Residues 1 and 2 indicate that the material compacts in a relatively narrow range for maximum dry densities and optimum moisture contents, despite the residues produced from ores mined on two different continents (Figures 3 and 4). Press-dried residue shows the highest maximum dry density at approximately 15.5 kN/m³ for standard effort with an optimum moisture content (OMC) of 30% and 17.4 kN/m³ for modified effort with an OMC of 24%. Air-dried specimens show a maximum dry density range from 14.2 to 14.8 kN/m³ with OMC ranging from 30-34%. The relatively flat nature of the curves is indicative of silt soil behavior (ML USCS classification). However, in comparing bauxite residue maximum dry density and OMC points of bauxite residue to typical values of other fine-grained soils, the material compacts most similarly to a high plasticity clay (CH), with higher OMC and lower maximum dry density compared to a typical ML soil (see Figure 5).

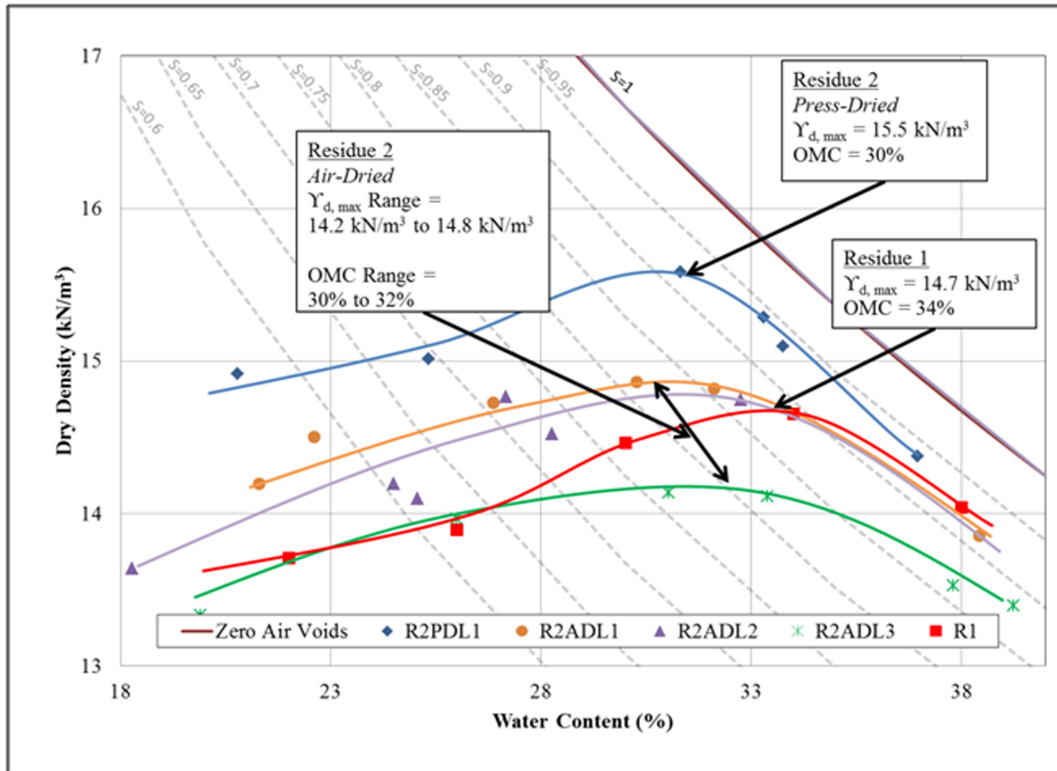


FIG. 3. Standard Proctor Curves (PD=press-dried; AD=air-dried)

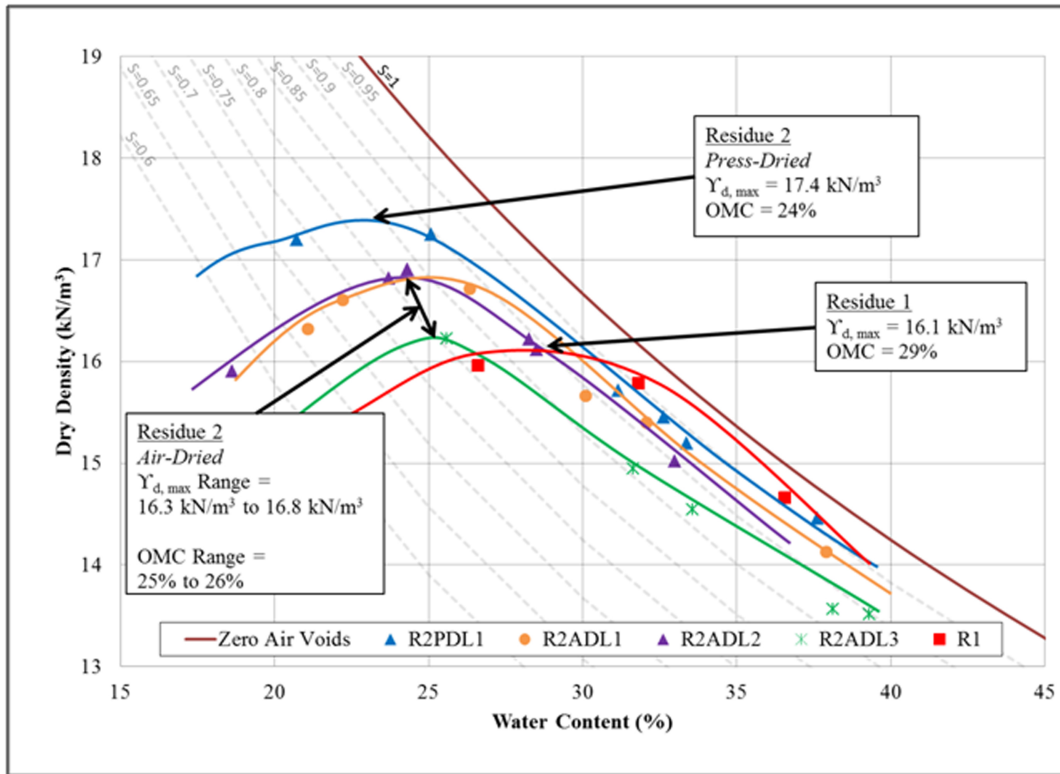


FIG. 4. Modified Proctor Curves (PD = press-dried; AD = air-dried)

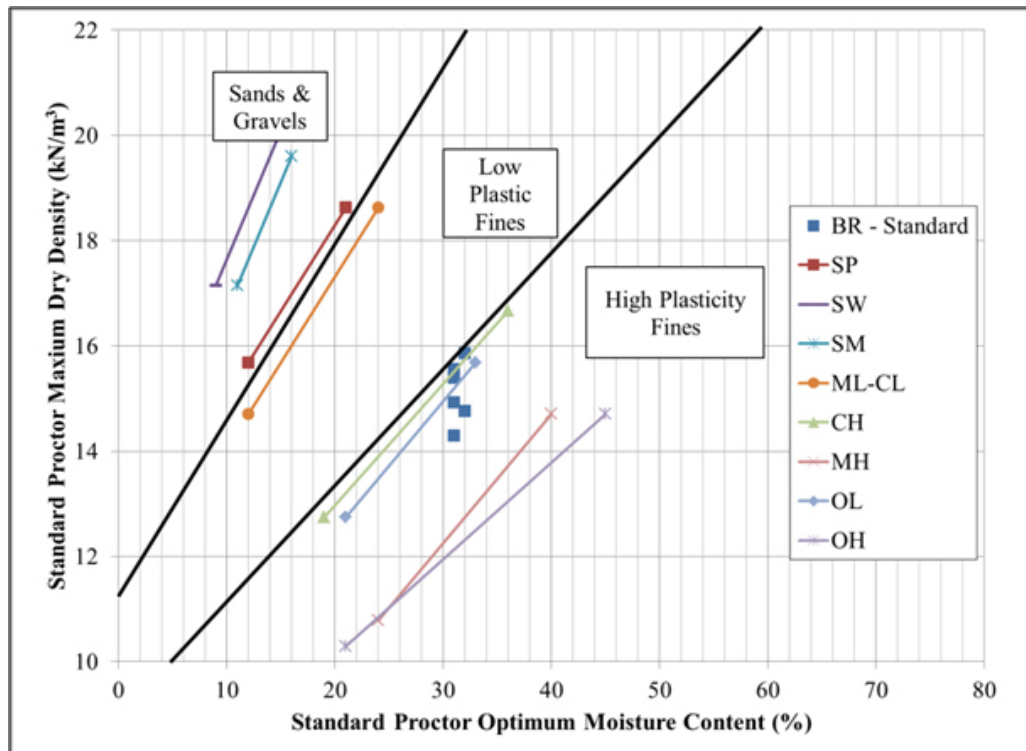


FIG. 5. OMC and Maximum Dry Density Point Comparison (BR= bauxite residue)(typical soil data adapted from Carter & Bentley 1991)

COMPRESSIBILITY

The research studied compressibility behavior using residue prepared by compacting the material at an approximate optimum moisture content of 32% using standard effort. Residue 1 shows a preconsolidation pressure of 230 kPa with C_c of 0.56 and C_r of 0.03. Residue 2 preconsolidation pressures ranges from 150 to 190 kPa with C_c ranging from 0.28 to 0.38 and C_r ranging from 0.025 to 0.03. The results, based on the C_c ranges, indicate that bauxite residue compresses similar to a clay (CH), not a silt (ML). The compressibility and compaction data are important in showing that bauxite residue, despite classification by USCS as a ML soil, behaves more similarly like a CH soil in these two performance tests. Also, the findings from free swell tests performed on Residue 1 indicate no swell potential.

HYDRAULIC CONDUCTIVITY

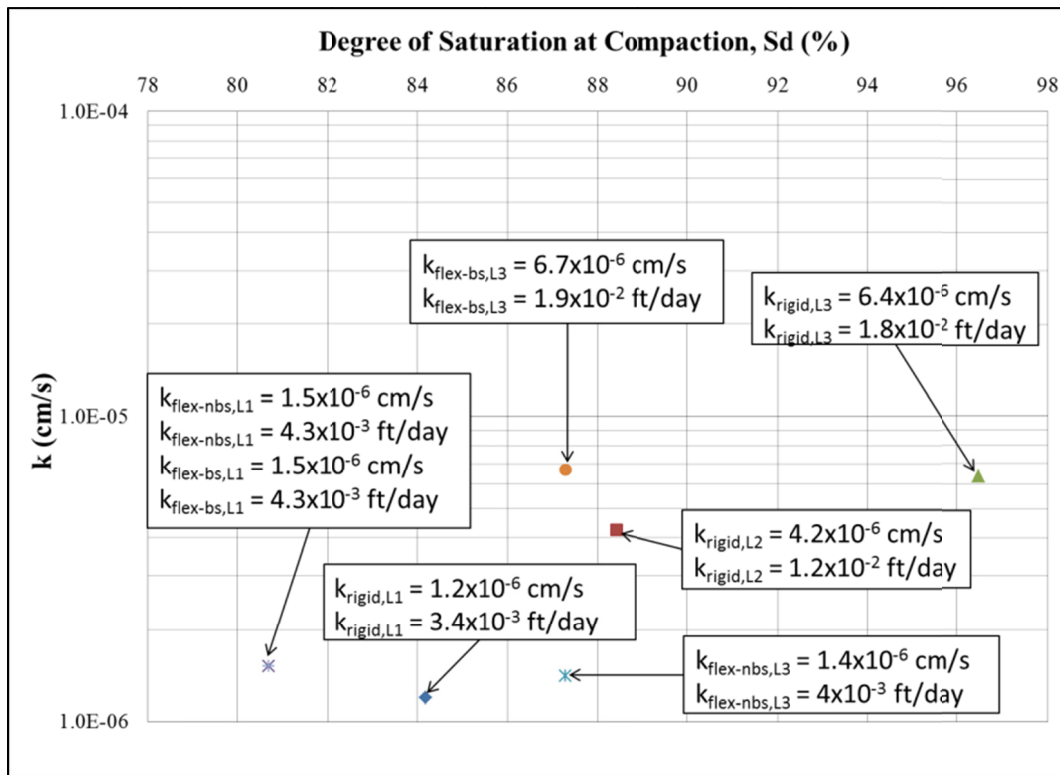


Fig. 6. Hydraulic Conductivity versus Degree of Saturation at Compaction (bs=back-pressure saturated; nbs=no back-pressure saturation; L# = Location #)

Three different hydraulic conductivity testing procedures were used to analyze the material: (1) rigid wall permeameter using the falling head test, (2) flexible wall permeameter with no back pressure using the falling head test, and (3) flexible wall permeameter with back pressure using the falling head/rising tailwater test. As with the compressibility testing, hydraulic conductivity tests used specimens that were compacted at an optimum moisture content of approximately 32% using standard

compaction effort. For the rigid wall tests, the compacted specimens were simply prepared in the mold and then connected to a pressure panel to run the falling head test. For the flexible wall tests, specimens were compacted in a mold as described previously, extracted out of the mold, and then carefully trimmed to an approximate height to diameter ratio of 2.6 for use in a triaxial cell flexible wall permeameter. The results (provided in Figure 6) indicate that bauxite residue has an approximate hydraulic conductivity of 10^{-6} cm/s (10^{-3} ft/day) and that all three testing procedures show similar values. This second conclusion leads to the thought that it may not be necessary to perform more expensive and time consuming flexible wall permeameter tests to obtain the hydraulic conductivity results.

SHEAR STRENGTH

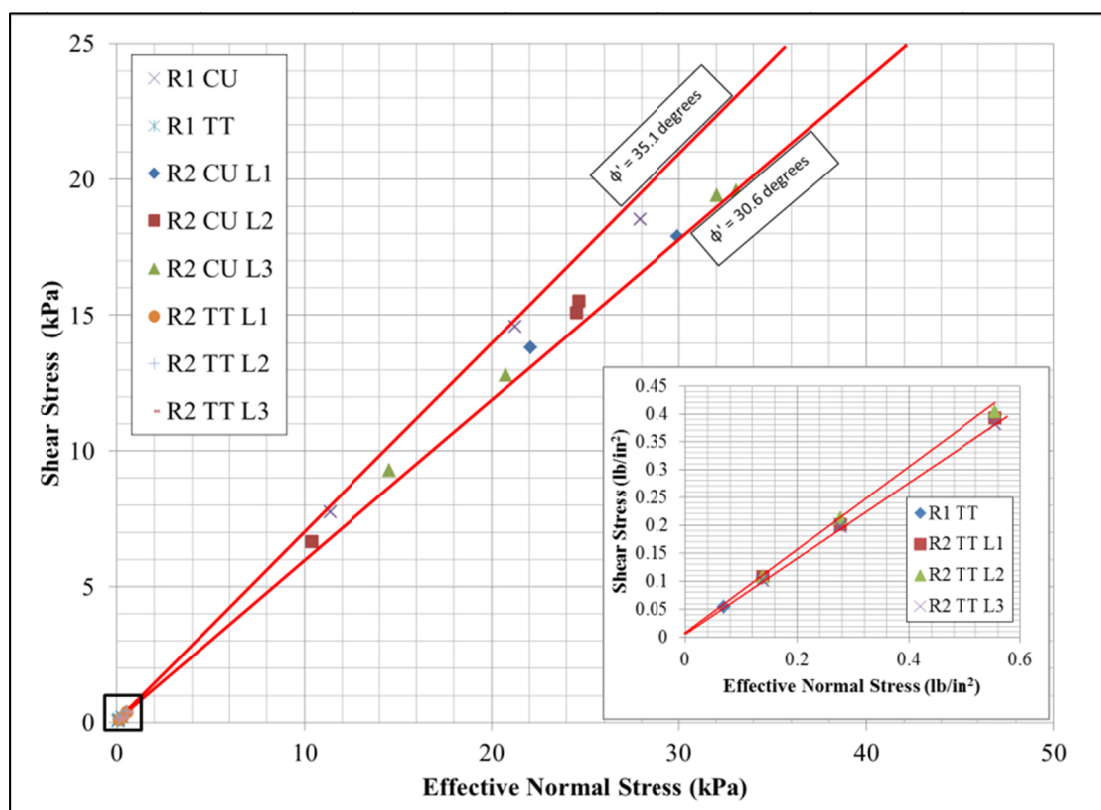


FIG. 7. Effective Shear Strength Results (R# = Residue #; CU=Consolidated Undrained; TT = Tilt Table; L# = Location #)

The combined results of the consolidated-undrained (CU) triaxial tests and tilt table tests indicate that compacted bauxite residue has a high effective shear strength, with a range of friction angles from 30 to 35 degrees (shown in Figure 7). Cohesion values were relatively low and the tilt table data indicated a relatively linear behavior at low confining stresses. In terms of comparison, Residues 1 and 2 show similar behavior indicated by the relatively narrow range of data points. In terms of undrained shear strength, compacted residue also shows dilative behavior, indicative of being on the "good" or left side of the critical state line. This behavior is observed up to a

confining stress of at least 345 kPa (the maximum stress tested and the assumed typical value experienced in a levee).

EROSION RESISTANCE

Two forms of testing for erosion resistance were performed on bauxite residue: crumb test and pinhole dispersion results. The crumb tests show non-dispersive behavior for all tests and pinhole dispersion results indicate non-dispersive to slightly dispersive behavior. The Sherard grain size distribution characterization for fill materials also provide positive results with bauxite residue falling outside the dispersive zones.

CONCLUSIONS

General Conclusions

Bauxite residue is a fine-grained, low plasticity material with a comparatively high specific gravity and a high pH. Under the USCS classification system, bauxite residue typically classifies as a ML soil (inorganic silt). Despite this classification, bauxite residue behaves like a plastic, fine-grained material (CH/CL) when compacted under either standard or modified proctor effort. The optimum moisture contents tests are relatively high and the maximum dry density values are low compared to similar fine-grained soils. Gravimetric water contents targeted for use in a levee are 32% to 36%, compared to the stored gravimetric water contents for dry stacking of 60% to 70% and over 100% for slurry disposal. The hydraulic conductivity of bauxite residue is in the order of 10^{-6} cm/s (10^{-3} ft/day). This magnitude provides reasonably low flow rates for a levee application. Bauxite residue also indicates behavior and total unit weight concerning the applied pressure to the subgrade comparable to a CH/CL material. The drained strength of bauxite residue is relatively high compared to similar fine-grained soils (ML/CH soil). Undrained strength of compacted residue indicates dilative behavior for all confining stresses tested (up to 345 kPa). Compacted residue also demonstrates high erosion resistance in terms of the crumb and pinhole dispersion testing criteria, as well as the empirical Sherard grain size distribution characterization for fill materials. Much of the variability in properties published in the literature can be attributed to differences in the techniques used to process the material before testing.

Suitability for a Levee

General Army Corps of Engineers post-Katrina guideline criteria for levee fill material require a plasticity index greater than 10, a USCS soil classification of CH/CL (fat or lean clay), less than 9% organic matter, less than 35% sand content, and shear strength to facilitate the construction of a levee at a 2H:1V maximum slope. Based on the results found in this research, it was found that compacted bauxite residue meets the guideline for the PI greater than 10, but does not meet the USCS classification of a CH material. Due to the nature of bauxite residue, there is very

little organic material and the material is considered 75% or greater silt, meaning that there is less than 35% sands. In terms of compaction and consolidation, the low swell potential and general behavior similar to a clay indicate that bauxite residue would behave similar to the desired CH/CL material requested in the guidelines. The hydraulic conductivity of 10^{-6} cm/s would be considered good for levee fill. The effective friction angles of greater than 30 degrees would support the construction of 2V:1H or 3V:1H slopes specified in the table for typical levee construction. Finally, the high erosion resistance would be conducive to the use of residue as a levee fill. Overall, compacted bauxite residue shows high strength, low permeability, acceptable compaction/consolidation behavior, no swell potential, and high erosion resistance. The exceptions would be that the material is a ML and not a CH/CL soil and the pH would be considered high. Compacted bauxite residue appears to be a viable option, in terms of geotechnical engineering, as a fill material in a levee or embankment. The classification issue could be addressed by mixing bauxite residue with other materials to create an acceptable CH/CL material. The pH issue could be addressed either through neutralization (lowering of the pH through a chemical process) or encapsulating the material to avoid possible high pH leaching from the bauxite residue into the environment.

ACKNOWLEDGMENTS

The authors would like to thank Alcoa, Remedial Construction Services, and Noranda Alumina for their support in this research.

REFERENCES

- Blight, G.E.; Leong, E.C. (2012); *Mechanics of Residual Soils, 2nd Edition*; CRC Press; Taylor and Francis Group; London, U.K.; 354 pgs.
- Bodley, A.; Chen, S.; Ferrier, M.; Cooling, D. (2011); "Reclamation of a Conventional Tailings Facility for Long Term Dry Stacking Operations in Western Australia"; *Proceedings of Tailings and Mine Waste 2011*; Vancouver, British Columbia, Canada; November 6-9.
- Carter, M.; Bentley, S.P. (1991); *Correlations of Soil Properties*; Pentech Press Ltd.; London, U.K. 130 pgs.
- Cooling, D.J.; Hay, P.S.; Guilfoyle, L. (2002); "Carbonation of Bauxite Residue"; In *Proceedings of the 6th International Alumina Quality Workshop*; Chandrashekar, S., Ed.; AQW Inc.; Brisbane, Australia; 185-190.
- Deelwal, K.; Dharavath, K.; Kulshreshtha, M.; (2014); "Evaluation of Characteristic Properties of Red Mud for Possible Use as a Geotechnical Material in Civil Construction"; *International Journal of Advances in Engineering and Technology*; Vol. 7; Issue 3; 1053-1059.

Deelwal, K.; Dharavath, K.; Kulshreshtha, M.; (2014); "Stabilization of Red Mud by Lime, Gypsum, and Investigating its Possible Use as a Geotechnical Material in the Civil Construction"; *International Journal of Advances in Engineering and Technology*; Vol.7; Issue 4; 1238-1244.

Gore, M.S. (2015), *Geotechnical Characterization of Bauxite Residue (Red Mud)*, Doctoral Dissertation, The University Texas at Austin, 307 pgs.

IAI (2013); "Bauxite Residue Management: Best Practice"; European Aluminum Association. 32 pgs.

Jenny, F.C. (1974); "Ferrosilt (Red Mud): Geotechnical Properties and Soil Mechanical Considerations"; *Light Metals*; 909-914. Republished in *Essential Readings in Light Metals: Alumina and Bauxite*; Edited by Don Donaldson and Benny E. Raahauge (2013); The Minerals, Metals, & Materials Society; John Wiley & Sons, Inc.

Jones, B.E.H.; Haynes, R.J.(2011); "Bauxite Processing Residue: A Critical Review of Its Formation, Properties, Storage, and Revegetation"; *Critical Reviews in Environmental Science and Technology*; Vol. 41, No. 3; 271-315.

Kehagia, F. (2008); "An Innovative Geotechnical Application of Bauxite Residue"; *Electronic Journal of Geotechnical Engineering*; Vol.13; Bundle G; 2008; 1-10.

Kehagia, F. (2010); "A Successful Pilot Project Demonstrating the Re-use Potential of bauxite Residue in Embankment Construction"; *Resources, Conservation and Recycling*; Vol. 54 (2010); 417-421.

Kehagia, F. (2014); "Construction of an Unpaved Road using Industrial By-Products (Bauxite Residue)"; *WSEAS Transactions on Environment and Development*; Vol. 10; 160-168.

Kirkpatrick, D.B. (1996); "Red Mud Product Development"; *Light Metals 1996; Proceedings of the Technical Sessions at the 125th TMS Annual Meeting*; TMS Light Metals Committee; February, 1996; 75-80.

Kola, N.; Das, S.K. (2013); "Lateral Earth Pressure Due to Red Mud Using Numerical Analysis"; *Proceedings of Indian Geotechnical Conference*; Roorkee, Haridwar, India; December 22-24, 2013; 1-6.

Li, L.Y.; Rutherford, G.K. (1996); "Effect of Bauxite Properties on the Settling of Red Mud"; *International Journal of Mineral Processing*; Vol. 48 (1996); 169-182.

Li, L.Y. (1998); "Properties of Red Mud Tailings Produced Under Varying Process Conditions"; *Journal of Environmental Engineering*; ASCE; Vol. 124, No. 3 March (1998); 254-264.

Newson, T.; Dyer, T.; Adam, C.; Sharp, S.(2006); “Effect of Structure on the Geotechnical Properties of Bauxite Residue”; *Journal of Geotechnical and Geoenvironmental Engineering*; ASCE; Vol. 132, No. 2 February (2006); 143-151.

Nikraz, H.R.; Bodley, A.J.; Cooling, D.J.; Kong, P.Y.L.; Soomro, M. (2007);”Comparison of Physical Properties between Treated and Untreated Bauxite Residue Mud”; *Journal of Materials in Civil Engineering*; Vol. 19; Issue 1; January 1, 2007; 2-9.

Shahin, M.A.; Mardesic, T.; Nikraz, H.R. (2011); “Geotechnical Characteristics of Bauxite Residue Sand Mixed with Crumbed Rubber from Recycled Car Tires”; *Journal of GeoEngineering*; Vol. 6; No. 1; April 2011; 63-72.

Somogyi, F. (1976); *Dewatering and Drainage of Red Mud Tailings*; PhD Dissertation; Department of Civil Engineering; University of Michigan; Ann Arbor, MI; 291pgs.

USEPA (1990); *Report to Congress on Special Wastes from Mineral Processing*; EPA530-SW-90-070C; Office of Solid Waste; United States Environmental Protection Agency; July; Volumes 1 and 2.

Vick, S. (1983); *Planning, Design, and Analysis of Tailings Dams*; Wiley Interscience Publication; John Wiley & Sons Inc.; New York, NY; 369 pgs.

Heat Extraction from Mining Waste Piles

Nazli Yeşiller, Ph.D., A.M.ASCE¹; James L. Hanson, Ph.D., P.E., M.ASCE²; Emma H. Yee³; and Kevin B. Kopp⁴

¹Director, Global Waste Research Institute, California Polytechnic State Univ., San Luis Obispo, CA 93407. E-mail: nyesiller@gmail.com

²Professor, Dept. of Civil and Environmental Engineering, California Polytechnic State Univ., San Luis Obispo, CA 93407. E-mail: jahanson@calpoly.edu

³Graduate Student, Dept. of Chemical Engineering, Massachusetts Institute of Technology, Cambridge, MA 02139. E-mail: ehyee@mit.edu

⁴Graduate Student, Dept. of Civil and Environmental Engineering, California Polytechnic State Univ., San Luis Obispo, CA 93407. E-mail: kevinbkopp@gmail.com

Abstract: Significant heat generation occurs in mining waste piles due to the bacterially mediated, highly exothermic oxidation reactions of pyrite minerals commonly present in waste rocks. An opportunity exists to extract the heat from mining waste piles for beneficial use as an alternative energy source while limiting acid producing reactions within a waste pile. Two approaches are outlined to establish available thermal energy: extracting the excess heat above baseline (i.e., ambient) thermal equilibrium conditions and extracting the excess heat above 0°C (i.e., temperature threshold where microbial populations become relatively inactive). The differences between the waste temperatures and the target temperatures were quantified and then multiplied with the heat capacity of the wastes to determine extractable heat energy. Example analyses using data from four sites in different climatic regions indicated that up to 76.0 and 90.3 MJ/m³ of heat energy were available above baseline equilibrium and 0°C target temperature conditions, respectively.

INTRODUCTION

Waste rocks and tailings are generated during extraction and treatment of various types of ores from underground mines as well as from open pit operations. The waste rocks typically are stored in above ground piles exposed to atmospheric conditions. Coupled biogeochemical processes that occur within the waste rocks result in significant heat generation in mining waste piles. In particular, sulfides present in the waste rocks are oxidized in bacterially mediated, highly exothermic reactions leading to heat generation. The oxidation reactions produce acidic conditions and acid mine drainage (AMD), which poses significant threats to the environment.

The most common sulfide mineral present in waste rocks, pyrite, oxidizes naturally when exposed to air and water (Lefebvre et al. 2001). Pyrite is oxidized by direct reaction with oxygen and water, or is oxidized by ferric iron. The oxidation process produces approximately 1400 to 1600 kJ of heat energy for every mole of pyrite oxidized (Lowson 1982, Rohwerder et al. 1998, Rimstidt and Vaughan 2003, Silberberg 2009, Schippers et al. 2010). The calculated heat energy varies as a function of the standard enthalpies of formation ($\Delta_f H^0$) used in the analysis for the specific oxidation pathway and environmental conditions, such as temperature and microbial population characteristics. The direct reaction of pyrite with oxygen and water can be represented as (Lefebvre et al. 2001):



The biochemical pyrite oxidation reaction is influenced by availability of oxygen and water, and the rate of oxidation is controlled by temperature, pH, bacterial populations, and surface area of minerals, as well as the crystalline structure of the sulfides. Optimum temperature ranges for iron-oxidizing bacteria were indicated to be between 25 and 45°C and for thermophilic species between 60 and 80°C (Lefebvre et al. 2001). Increasing temperatures enhance the oxidation reactions, leading to increased potential for acid mine drainage and contaminant migration and pollution at elevated temperatures (e.g., Hollesen et al. 2009). Preventive measures including water and/or oxygen barriers have been developed for limiting the extent of reactions within the piles, which range from low permeability cover systems, to layered construction with benches, to inundation of the piles with water (e.g., Aubertin et al. 2009, Hollesen et al. 2009, Aubertin 2013). An alternative approach is presented herein to control AMD by reducing waste pile temperatures. An opportunity exists to extract heat from mining waste piles for beneficial use as an alternative energy source while limiting acid producing reactions within a waste pile. Heat extraction from mining waste piles had not previously been investigated. Only a numerical study was reported for a gold mine site that simulated operation of a ground source heat pump in the subgrade underneath the mine waste pile and that demonstrated enhanced extraction conditions beneath the heated pile compared to baseline subgrade with no overlying waste mass (Raymond et al. 2011). To evaluate feasibility and potential for extracting heat from waste piles, thermal energy available for extraction was determined in this study. In particular, estimates for heat energy are provided for two distinct heat extraction approaches.

HEAT EXTRACTION SCHEMES

Available thermal energy for extraction of heat from mining waste piles was estimated using two distinct approaches:

- Extracting the excess heat above baseline (i.e., ambient) thermal equilibrium conditions (controlled by the specific waste properties and the climatic region) to beneficially use the heat generated in a waste pile. In this approach, heat extraction results in seasonally variable waste temperatures consistent with unheated baseline waste temperature, $T_{(x,t)}$. The $T_{(x,t)}$ represents mine waste

temperatures at a given depth (x) and time (t) under conditions of no heat generation.

- Extracting the excess heat above a constant target temperature threshold to minimize biochemical activity in the waste pile, which has been reported to range from approximately -5 to 0°C , where microbial populations are relatively inactive. In this approach, the heat extraction results in a constant temperature, T_{cons} at all depths.

The available excess heat energy and the amount of energy that can be extracted from a waste pile are quantified using a series of interrelated parameters. Schematic representations of the two methodologies described above are provided in Figure 1. For the first approach, the target temperature is represented by the baseline unheated temperature, $T_{(x,t)}$. This is the temperature of the mining waste under the influence of only seasonal subsurface temperature fluctuations (and not including any heat generation within the waste pile). The baseline waste temperature can be calculated using conventional near-surface earth temperature theory (ORNL 1981) by adopting physical and thermal properties appropriate for mining waste using Equation 2.

$$T_{(x,t)} = T_m - A_s e^{-x\sqrt{\frac{\pi}{365s\alpha}}} \cos\left[\frac{2\pi}{365s}\left(t - t_o - \frac{x}{2}\sqrt{\frac{365s}{\pi\alpha}}\right)\right] \quad (2)$$

where, $T_{(x,t)}$ is baseline unheated waste temperature ($^{\circ}\text{C}$) at depth x and time t , T_m is mean annual earth temperature ($^{\circ}\text{C}$), A_s is amplitude of the annual surface temperature wave ($^{\circ}\text{C}$), x is the depth below the surface (m), $s = 86,400$ (seconds in a day), α is thermal diffusivity (m^2/s), t is time of year (s, where zero = midnight December 31), and t_o is a phase constant (s, equivalent to 34.6 days). Site-specific thermal diffusivity values (α) for mining wastes are used in calculation of baseline unheated waste temperatures. The thermal diffusivity is calculated as the quotient of thermal conductivity and volumetric heat capacity. For the second approach, the target temperature is T_{cons} , a constant temperature that does not change with depth or time.

Initially, the difference between the elevated temperatures of the mining waste pile and the target temperature levels, either $T_{(x,t)}$ or T_{cons} , is quantified as cumulative temperature differential, ΔT . The ΔT represents the temperature change that a unit volume of the mining waste would undergo due to heat extraction. The ΔT is determined using three steps: temperature versus time data are plotted; the target temperature (either $T_{(x,t)}$ or T_{cons}) is superimposed on the plot; and the area between the two temperature histories is calculated as presented in Figure 1. Then, a time-averaged temperature differential, ΔT_{avg} , is determined to normalize the cumulative temperature differential, ΔT , for temporal fluctuations of temperatures (mining and/or target temperatures). The ΔT_{avg} is determined by dividing the calculated area (Figure 1) by the total period of observation (Hanson et al. 2010, Yeşiller et al. 2015). To avoid seasonal bias, time periods representing full annual cycle(s) are used. The average temperature differential (units of $^{\circ}\text{C}\text{-day/day}$) is designated as $\Delta T_{avg-(x,t)}$ when the target temperature in the heat extraction application is $T_{(x,t)}$ and as $\Delta T_{avg-cons}$ when T_{cons} is used as the target temperature for heat extraction. The ΔT_{avg} calculations are

repeated along the depth of a waste pile using available measured waste temperatures. The ΔT_{avg} calculated at the depth with the maximum mining waste temperatures is termed the peak average temperature differential and designated as $\Delta T_{avg,p-(x,t)}$ or as $\Delta T_{avg,p-cons}$ depending on the extraction approach. In addition, a one-year peak average temperature differential ($\Delta T_{avg,po-(x,t)}$ or $\Delta T_{avg,po-cons}$) is provided for the specific full one-year duration within the temperature measurement period with the highest measured mining waste temperatures.

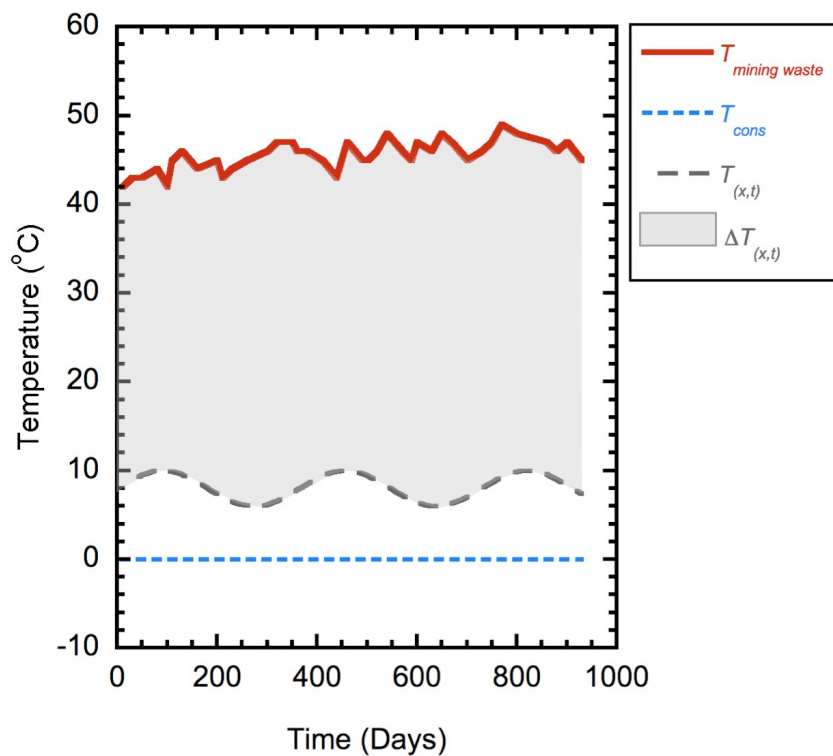


FIG. 1. Heat extraction approaches.

Subsequent to determination of ΔT_{avg} , the thermal energy available associated with the unit volume of waste located at the depth of interest is determined by multiplying the ΔT_{avg} value by the volumetric heat capacity (C) of the mining wastes. The resulting heat energy, designated E_h , describes a one-time heat gain and is reported in units of MJ/m^3 that accounts for accumulation of heat. The heat capacity is a measure of the energy required to increase the temperature of a unit volume of a specific material by 1°C and varies as a function of density and moisture content (e.g., Hanson et al. 2013) as well as mineralogical composition (CRC 2012). Volumetric heat capacity ($\text{MJ}/\text{m}^3\text{K}$) for waste can be calculated by summing heat capacity of individual constituent components of the waste on a volumetric basis. Additional details regarding calculation of C are provided in Hanson et al. (2008, 2013). This energy calculation methodology can be extended to the entire mining waste pile when extensive mine waste pile temperature data are available, wherein the unit volume of heat energy values determined incrementally with depth are summed over the entire

depth and lateral extent of a waste pile to establish total extractable heat energy potential.

HEAT EXTRACTION IN VARIABLE CLIMATIC REGIONS

Data and heat extraction analysis are provided for four mining waste piles located in different climatic regions. Details regarding geographic, physical, and climatic conditions at the sites are summarized in Table 1. Climate classifications were based on Koppen-Geiger Climate Classification System as presented in Peel et al. (2007). The mining wastes disposed at these selected sites were generated from extraction of different types of ores. The pyrite content of the waste rock in the piles varied between less than 1% and 7% by mass (Table 1).

Table 1. Mining Waste Sites

Site Information	Rum Jungle	Doyon Mine	Svalbard	Diavik Mine
Location	Batchelor, Northern Territory, Australia	Rouyn-Noranda, Quebec, Canada	Svalbard, Norway	Yellowknife, Northwest Territories, Canada
Type of Waste	Uranium mining waste	Gold mining waste	Coal mining waste	Diamond mining waste
Type of Waste Rock	Carbonaceous slates, graphitic schists	Sericite schists, dioritic rocks	Sandstone, siltstone, conglomerate, schist	Granite with small amounts of sulfide-bearing biotite schist
Pyrite Mass Fraction (%)	3	1.5 to 7	<1	> 0.08
Climatic Region	Tropical savannah (Aw)	Cold, no dry season, warm summer (Dfb)	Polar tundra (ET)	Cold, no dry season, cold summer (Dfc)
Average Annual Air Temperature (°C)	27.4	2.0	-5.8	-8.9
Average Annual Precipitation (mm)	1500	864	187	280
Pile Dimensions	13 to 18 m high	500 x 900 m, 30 to 35 m high	22 m high	50 x 60 m, 15 m high
Waste Age (years)	20	9 to 14	20-22	0 to 2.5
Reference	Harries and Ritchie (1981)	Lefebvre et al. (1997), Lefebvre et al. (2001)	Hollesen et al. (2009)	Pham et al. (2013)

Temperature data were available with depth for the waste piles at all of the selected sites, whereas variations of the waste pile temperatures with time were available at three sites with the exception of the Rum Jungle waste pile. The temperature profile with depth for this site was assumed to be constant for a duration of one year. This assumption allowed for determination of one-year peak average temperature differential and this value also was used as the peak average temperature differential at the Rum Jungle site. For all four sites, the heat generation parameters determined included two sets of values representing calculations made with baseline unheated waste pile temperatures at a given depth, $T_{(x,t)}$, and calculations with target T_{cons} of 0°C. The results of the analysis for heat extraction for the two schemes described in the previous section are summarized in Table 2. The thermal parameters used in the analysis also are presented in Table 2. Variation of average temperature differential with depth is provided for the four sites in Figure 2.

Table 2. Heat Generation Data

Thermal and Heat Generation Parameters	Rum Jungle	Doyon Mine	Svalbard	Diavik Mine
Mean Annual Earth Temp. (°C)	27.8	7.3	-1.9	-6.5
Thermal Diffusivity (m ² /s)	5.9x10 ⁻⁷	1.2x10 ⁻⁷	3.5x10 ⁻⁷	7.7x10 ⁻⁷
Heat Capacity (MJ/m ³ K)	1.4	2.0	2.0	2.1
Peak Avg. Temp. Diff. (°C-day/day)	25.8 ($\Delta T_{avg,p-(x,t)}$)	38.4 ($\Delta T_{avg,p-(x,t)}$)	6.1 ($\Delta T_{avg,p-(x,t)}$)	2.3 ($\Delta T_{avg,p-(x,t)}$)
	51.3 ($\Delta T_{avg,p-cons}$)	45.6 ($\Delta T_{avg,p-cons}$)	4.2 ($\Delta T_{avg,p-cons}$)	-4.3 ($\Delta T_{avg,p-cons}$)
One-Year Peak Avg. Temp. Diff. (°C-day/day)	25.8 ($\Delta T_{avg,po-(x,t)}$)	39.0 ($\Delta T_{avg,po-(x,t)}$)	7.9 ($\Delta T_{avg,po-(x,t)}$)	3.4 ($\Delta T_{avg,po-(x,t)}$)
	51.3 ($\Delta T_{avg,po-cons}$)	50.2 ($\Delta T_{avg,po-cons}$)	5.6 ($\Delta T_{avg,po-cons}$)	-4.2 ($\Delta T_{avg,po-cons}$)
Peak Average Heat Generation (MJ/m ³)	37.4 ($E_{h-(x,t)}$)	76.0 ($E_{h-(x,t)}$)	12.1 ($E_{h-(x,t)}$)	4.7 ($E_{h-(x,t)}$)
	74.2 (E_{h-cons})	90.3 (E_{h-cons})	8.4 (E_{h-cons})	-9.0 (E_{h-cons})
Waste Age (years)	20	10 to 12	20 to 22	1 to 2
Reference	Harries and Ritchie (1981)	Lefebvre et al. (1997)	Hollesen et al. (2009)	Pham et al. (2013)

Based on the analysis presented in Table 2, for unheated baseline conditions, the peak average temperature differential varied between 2.3 and 38.4°C-day/day and the peak average heat generation varied between 4.7 and 76.0 MJ/m³. For the 0°C constant target threshold temperature, the peak average temperature differential varied

between -4.3 and $51.3^{\circ}\text{C}\cdot\text{day}/\text{day}$ and the peak average heat generation between -9.0 and $90.3 \text{ MJ}/\text{m}^3$. The maximum heat generation was observed at the site with the cold, no dry season, warm summer climate description and annual precipitation of 864 mm . The heat generation rates were low at the sites with cold and dry climates as well as at the site with high precipitation. Heat generation was more directly related to precipitation than air temperatures. Maximum heat generation occurred at a moisture content associated with the site in Quebec, Canada. Both lower and higher precipitation levels resulted in lower heat generation. Heat generation was low at lower moisture contents due to lack of sufficient moisture to support biochemical activity and also low at higher moisture contents due to the high heat capacity of wet wastes that prevented temperature rise and heat gain. Similar precipitation-dependent trends also were observed for additional mine waste sites and for municipal solid wastes. Details related to the climatic effects on waste heat generation are provided in Yeşiller et al. (2015).

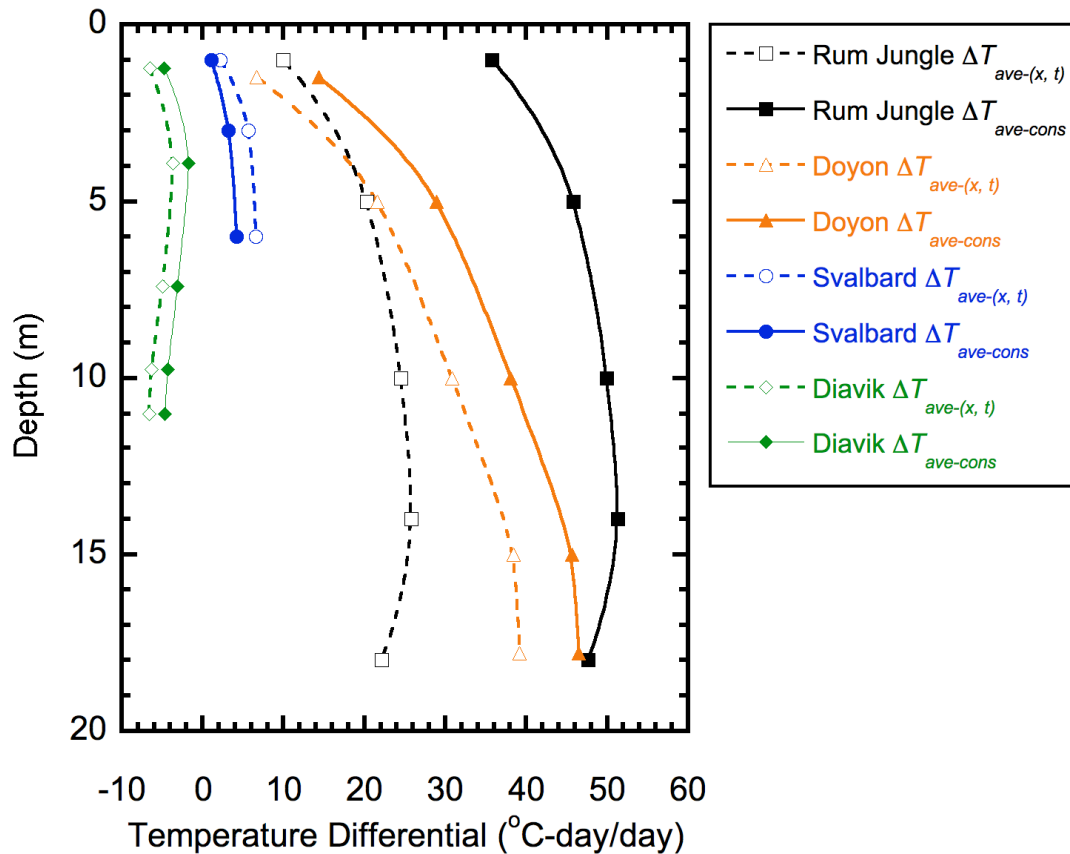


FIG. 2. Variation of temperature differential with depth.

The highest temperatures, average temperature differential, and heat energy in the waste piles typically were obtained at locations away from the top surface and base of the pile. Seasonal temperature variations affected temperatures and heat gain near the top surface. Subgrade temperatures influenced waste temperatures near the base of the pile. In general, the average temperature differential was higher for the constant 0°C

threshold than the baseline unheated mining waste temperature threshold (Figure 2). This trend was reversed at the site in Svalbard, Norway. The unheated baseline waste temperatures were lower than 0°C, which resulted in the lower average temperature differential for the 0°C threshold. Heat generation and unheated baseline waste temperatures also were low at the Northwest Territories, Canada site. However, for this case, the relative variation between the two heat extraction scenarios followed the same trend as the sites with high heat generation due to the relative magnitude of the 0°C threshold in comparison to unheated baseline waste temperatures. Negative average temperature differential values were observed when the waste temperatures were lower than the target values. For these cases, from a practical perspective to limit microbial activity, allowing temperatures to approach ambient conditions would be sufficient and result in more heat drawn off than trying to reach the target threshold.

The heat generated in a waste pile can be extracted to reduce overall waste temperatures to limit conditions that promote acid mine drainage. An extraction system can reduce the environmental risks of a mining waste pile, while at the same time providing an alternative energy source. Use of a passive system for heat extraction (i.e., reducing the temperature of the waste piles to prevent acid mine drainage) that takes advantage of cool surrounding soil and air is envisioned for cold climates whereas active cooling is envisioned for warm climates. The heat extraction process may impact future heat generation potential of the wastes. Modeling and pilot scale studies need to be conducted to verify the effectiveness and feasibility of the use of heat extraction systems in mining waste piles.

CONCLUSIONS

Significant heat generation occurs in mining waste piles due to the bacterially mediated, highly exothermic oxidation reactions of sulfide minerals, in particular pyrite, commonly present in waste rocks. An opportunity exists to extract the heat from mining waste piles for beneficial use as an alternative energy source while limiting acid producing reactions within a waste pile. To evaluate feasibility and potential for extracting heat from waste piles, thermal energy available for extraction was determined using two heat extraction approaches:

- Extracting the excess heat above baseline thermal equilibrium temperatures (controlled by the specific waste properties and the climatic region, and variable with depth and time), $T_{(x,t)}$.
- Extracting the excess heat above a constant target temperature threshold, $T_{cons} = 0^{\circ}\text{C}$, at all depths to limit activity of microbial populations.

The difference between measured waste temperatures and target temperatures (either $T_{(x,t)}$ or T_{cons}) was quantified over time as cumulative temperature differential, ΔT . This ΔT is normalized by the period of analysis to obtain an average value, ΔT_{avg} and multiplied by the volumetric heat capacity (C) of the waste to obtain unit volume of heat energy (termed heat generation). Example analyses were provided for four mining waste sites located in different climatic regions around the world (tropical, cold with warm summer, polar tundra, and cold with cold summer) for which temperature data were available. The results of the analyses indicated that for

unheated baseline conditions, the peak average temperature differential varied between 2.3 and 38.4°C-day/day and the peak average heat generation between 4.7 and 76.0 MJ/m³. For the 0°C constant target threshold temperature, the peak average temperature differential varied between -4.3 and 51.3°C-day/day and the peak average heat generation between -9.0 and 90.3 MJ/m³. The maximum heat generation was observed at the site with the cold, no dry season, warm summer climate description and annual precipitation of 864 mm. The heat generation at the warmer and colder sites was less than the heat generation at this site. The heat generation rates were low at the sites with cold and dry climates as well as at the site with high precipitation. For the site with the cold summer climate classification, the waste pile temperatures were less than the target temperatures for extended periods of time resulting in negative temperature differential and therefore, negative heat generation for the 0°C target threshold. For both heat extraction approaches, the empirically based heat energy that was determined to be available for extraction represents a novel opportunity for providing a new source of alternative energy while at the same time reducing the environmental risks of acid mine drainage.

ACKNOWLEDGMENTS

This investigation was partially supported by the Global Waste Research Institute. Ms. Yee and Mr. Kopp were supported by funds provided by a National Science Foundation REU Site Grant: EEC-1263337.

REFERENCES

- Aubertin, M., Cifuentes, E., Apithy, S.A., Bussiere, B., Molson, J., and Chapuis, R.P. (2009). "Analyses of water diversion along inclined covers with capillary barrier effects." *Canadian Geotechnical Journal*, NRC Research Press, Vol. 46: 1146-1164.
- Aubertin, M. and Bussiere, B. (2013). "Mine wastes management @RIME." *Proceedings Tailings and Mine Waste 2013*, Banff, University of Alberta: 1-10. CRC (2012). *Handbook of Chemistry and Physics*, 93rd Edition, Haynes, W.M., Editor-in-Chief, CRC Press.
- Hanson J.L., Liu W.-L., and Yeşiller N. (2008). "Analytical and numerical methodology for modeling temperatures in landfills." *Geotechnics of Waste Management and Remediation, GSP 177*, Khire et al. (Eds), ASCE: 24–31.
- Hanson J.L., Yeşiller N., and Oettle N.K. (2010). "Spatial and temporal temperature distributions in municipal solid waste landfills." *Journal of Environmental Engineering*, ASCE, Vol. 136 (8): 804–814.
- Hanson J.L., Yeşiller N., Onnen M.T., Liu W.-L., Oettle N.K., and Marinos J.A. (2013). "Development of numerical model for predicting heat generation and temperatures in MSW landfills." *Waste Management*, Elsevier, Vol. 33: 1993-2000.
- Harries, J.R. and Ritchie, A.I.M. (1981). "The use of temperature profiles to estimate the pyritic oxidation rate in a waste rock dump from an opencut mine." *Water, Air, and Soil Pollution*, Springer, Vol. 15: 405–423.

- Hollesen, J., Elberling, B., and Hansen, B.U. (2009). "Modelling subsurface temperatures in a heat producing coal waste rock pile, Svalbard (78°N)." *Cold Regions Science and Technology*, Elsevier, Vol. 58: 68-76.
- Lefebvre, R., Gelinas, P., and Isabel, D. (1997). *Heat Transfer during Acid Mine Drainage Production in a Waste Rock Dump, La Mine Doyon (Quebec)*, MEND Research Program Report 1.14.2c, CANMET, Ottawa, Canada, March 1994, Revised August 1997.
- Lefebvre, R., Hockley, D., Smolensky, J., and Gelinas, P. (2001). "Multiphase transfer processes in waste rock piles producing acid mine drainage 1: Conceptual model and system characterization." *Journal of Contaminant Hydrology*, Elsevier, Vol. 52: 137-164.
- Lowson, R.T. (1982). "Aqueous oxidation of pyrite by molecular oxygen." *Chemical Reviews*, Vol. 82 (5): 461-497.
- ORNL (1981). *Regional Analysis of Ground and Above-Ground Climate*. Oak Ridge National Laboratory Report No. ORNL/Sub-81/40451/1, U.S. Department of Energy, Office of Buildings Energy R&D.
- Peel, M.C., Finlayson, B.L., and McMahon, T.A. (2007). "Updated world map of the Koppen-Geiger Climate Classification," *Hydrology and Earth System Sciences*, EGU, Vol. 11: 1633-1644.
- Pham, N.H., Segó, D.C., Arenson, L.U., Blowes, D.W., Amos, R.T., and Smith, L. (2013). "The Diavik waste rock project: Measurement of the thermal regime of a waste-rock test pile in a permafrost environment." *Applied Geochemistry*, Elsevier, Vol. 36: 234-245.
- Raymond, J., Therrien, R., Gosselin, L., and Lefebvre, R. (2011). "Numerical simulation of geothermal energy transfer beneath exothermic waste rock piles." *HVAC&R Research*, Taylor & Francis, Vol. 17 (6): 1115-1128.
- Rimstidt, D.J. and Vaughn, D.J. (2003). "Pyrite oxidation: A state-of-the-art assessment of the reaction mechanism." *Geochimica et Cosmochimica Acta*, Pergamon, Vol. 67 (5): 873-880.
- Schippers, A., Breuker, A., Blazejak, A., Bosecker, K., Kock, D., and Wright, T.L. (2010). "The biogeochemistry and microbiology of sulfidic mine waste and bioleaching dumps and heaps, and novel Fe(II)-oxidizing bacteria." *Hydrometallurgy*, Elsevier, Vol. 104: 342-350.
- Silberberg, M. (2009). *Principles of General Chemistry*, 2nd Edition, McGraw-Hill.
- Yeşiller, N., Hanson, J.L., and Yee, E.H. (2015). "Waste heat generation: A comprehensive review." *Waste Management*, Elsevier, Vol. 42: 166-179.

Modeling the Effect of Flocculation and Desiccation on Oil Sands Tailings

Nicholas A. Beier, Ph.D., P.Eng.¹; Louis K. Kabwe, Ph.D.¹; J. Don Scott, Ph.D., FEIC P.Eng.¹; Nam H. Pham, Ph.D.¹; and G. W. Wilson, Ph.D., FCAE, FEIC, P.Eng.¹

¹Dept. of Civil and Environmental Engineering, Univ. of Alberta, Edmonton, AB, Canada.

Abstract: Considerable research has been performed by oil sands mining companies to dewater and manage their fluid fine tailings (FFT) in an effort to meet regulatory and closure requirements. One potential dewatering process includes the addition of flocculants to the FFT and using thickeners to increase the solids content. Additional promising technologies are to surcharge the deposited thickened tailings (TT) or to further thicken the tailings by atmospheric drying. It was found that flocculating and thickening treatments increased the hydraulic conductivity of the fine tailings to some degree, but had no effect on the compressibility and shear strength. Atmospheric drying could enhance the shear strength, but the tailings had to be dried to an unsaturated state, which could be difficult to achieve in the field considering the climate in northern Alberta. Using the geotechnical properties of thickened and desiccated tailings, deposition scenarios for the management of the tailings were modeled. The influence of flocculation and thickening with or without atmospheric drying on a tailings deposit is discussed.

INTRODUCTION

The oil sands deposits in northern Alberta, Canada, contain an estimated 2.5 trillion barrels of bitumen. About 20% of the bitumen can be produced through surface mining. The bitumen is extracted from the mined oil sands ore through a hot water extraction process by the addition of steam, hot water and process aides (sodium hydroxide). On average, for every barrel of bitumen produced about 1 m³ of sand and 0.25 m³ of FFT are created. The fluid fine tailings (FFT) are highly dispersed and consolidate extremely slowly (Suthaker and Scott 1994). To date, there are nearly 1 billion m³ of FFT (30-35% solids by mass) currently stored among the oil sands mine sites which require full containment in tailings ponds (AESRD 2014). In order to meet regulatory and closure requirements, the FFT deposits must be dewatered.

These FFT deposits may be dewatered and managed through various chemical, mechanical and environmental processes as outlined by Sobkowicz and Morgenstern (2009). In fact, there were over 550 tailings technologies identified in the Oil Sands Tailings Technology Development Roadmap project that could have potential use for managing tailings in the oil sands industry (Sobkowicz 2012). Several of these

technologies are utilized commercially, and many others are in an advanced development stage. A promising technology is to add flocculants to the FFT and to use thickeners to increase the solids content. Upon deposition of the tailings, atmospheric drying may also be used to further thicken the tailings.

The objective of the research reported in this paper was to investigate the effects of flocculating, thickening and atmospheric drying treatments by modeling deposition scenarios for the management of the tailings. The influence of flocculation and thickening with or without atmospheric drying on a commercial tailings operation will be compared to those of untreated FFT to assess the effects of the treatments.

TAILINGS CHARACTERIZATION

Three FFT samples were utilized in this research: an untreated tailings sample (FFT) and two flocculated and thickened tailings samples (Treat 1 and Treat 2). Samples Treat 1 and Treat 2 were subsequently dried (Dry 1 and Dry 2) to evaluate the influence of atmospheric drying. The FFT samples were received in 25-L plastic pails from the Saskatchewan Research Council in Saskatoon, Saskatchewan, Canada. The FFT samples used in this research were treated with a flocculant dosage of 150 g/t; however, the method of production of the thickener under-flow is beyond the scope of this paper and is not discussed. The material and geotechnical properties of the three samples were determined upon delivery to the University of Alberta Geotechnical Center (Table 1).

Table 1. Initial Tailings Material Properties

Sample	C_w >45 μ (%)	C_{fines} (%)	e	e_{fines}	Clay Size ^a (%)	Clay Size ^b (%)	$C_{\text{But.}}$ (%)	W_L (%)	IP (%)	G_s
FFT	46.1	96	2.85	2.85	15	ND	2.6	50	29	2.44
Treat 1	49	54	2.73	5.06	18	38	1.5	28	10	2.63
Treat 2	49	55	2.71	4.93	8	40	1.5	36	19	2.61

Treat 1 = FF + TH, Treat 2 = FF + TH + 3% flyash.

Notes: FF = flocculated, TH = thickened, C_w = solids content, C_{fines} = fines content, e = void ratio, e_{fines} = fines void ratio, a = by non-dispersed hydrometer test, b = by Methylene Blue Index, $C_{\text{But.}}$ = bitumen content, W_L = liquid limit, IP = plasticity, G_s = specific gravity, ND = not determined

The properties reported for Treat 1 and Treat 2 are after flocculating and thickening and the addition of flyash (Treat 2 only). The type and properties of the flyash used are cited in Sun et al. (2014). The initial gravimetric solids content, C_w (mass of solids over mass of slurry), of the three samples were somewhat similar with FFT at 46% while the C_w of the Treat 1 and Treat 2 samples were 49%. The main difference between the FFT sample and the treated samples was in their fines (or sand-sized) content. In the oil sands industry, fines are defined by the material passing the 45 μ m sieve, and fines solid content is defined by the mass of fines and bitumen/total mass. The FFT sample consists predominantly of fine material with only 4% of it sand-sized, while Treat 1 and Treat 2 contained much less fines with about 45% of it sand-sized. Treat 1 and Treat 2 had similar clay contents as determined by the Methylene

Blue Index test. The large difference between the clay size obtained by the Methylene Blue Index and the non-dispersed hydrometer test is because the Methylene Blue Index test disperses much of the coarse silt-size clay peds and booklets into clay flakes finer than 2 μm . The non-dispersed test does not disperse the clay lumps and peds. The fines void ratio (e_{fines}), defined as the volume of voids/volume of fines, will be used later to evaluate the effect of the treatment method on consolidation and shear strength properties.

The geotechnical properties of the samples are provided in Table 1. Samples for Treat 1 and Treat 2 had lower liquid limits, W_L , (28% and 36%, respectively) than the FFT (50%). For oil sands tailings, the addition of a flocculant would typically raise the W_L ; however, due to the presence of sand in the flocculated samples, the W_L is actually reduced. Due to the lower fines content in the Treat 1 and Treat 2 samples, the bitumen content is slightly lower (mass of bitumen divided by the mass of fines and bitumen). Since the bitumen is generally intermixed with the fines, bitumen is considered as part of the fines for all measurements and calculations.

For numerical modeling of oil sands fine tailings, finite strain consolidation theory is generally accepted (Jeeravipoolvarn et al. 2008; Suthaker and Scott 1994). This theory requires compressibility (void ratio-effective stress relationship) and saturated hydraulic conductivity (K_{sat} -void ratio relationship) to be obtained from a large strain consolidation test. Using the large strain consolidation testing apparatus and method outlined in Scott et al. (2008), the consolidation characteristics of all the tailings samples were determined. A second large strain consolidation test was performed in combination with vane shear measurements to provide undrained shear strength (S_U) relationships (void ratio- S_U). Unsaturated volume change behavior including the water retention curve (or soil water characteristic curve SWCC) and shrinkage curve were determined using the apparatus and methods outlined in Fredlund and Rahardjo (1993) and Kabwe et al. (2013). The SWCC is the relationship between the amount of water in a specimen and various applied soil suctions. The total mass of a specimen is continually monitored during drainage phase of each pressure increment until equilibrium is achieved (i.e. when zero discharge is observed). The water content corresponding to the highest matric suction with the previous changes in weight is used to back calculate the water contents corresponding to the other suction values. The matric suctions are then plotted against their corresponding water contents to yield the SWCC. The consolidation, unsaturated volume change and strength gain behavior and relationships for the tailings samples are reported in Wilson et al. (2014).

MODELING TAILINGS DEPOSITION

A one-dimensional, large strain consolidation computer program developed by the University of Alberta (Pham and Seg0 2014a, b) called FTCD (Freeze-Thaw-Consolidation-Desiccation) was used to simulate the post-depositional behavior of the three tailings samples under natural dewatering processes including consolidation and desiccation. The modeling exercises were conducted to assess the tailings treatments and to optimize the filling of dedicated disposal areas (DDAs).

The FTCD model incorporates the large strain consolidation theory from Gibson et al. (1967) and is coupled with the desiccation model developed by Qui and Segoo (2006). In addition, FTCD can model freeze-thaw dewatering and heat transfer; however, these features were not utilized for the current simulations.

The model parameters for large strain consolidation (compressibility, hydraulic conductivity and shear strength) and drying employed are presented in Figures 1 to 3 (Wilson et al. 2014). The shear strength is plotted as a function of fines void ratio in Figure 2 (D) to explore the effect of sand content on the void ratio-shear strength relationship. With this plot, the effect of the sand is removed and the FFT has the same shear strength as Treat 1.

Five separate depositional scenarios were modeled using the FTCD program incorporating the material properties and volume change relationships reported above: FFT with no treatment, Treat 1 with and without desiccation (Dry 1) and Treat 2 with and without desiccation (Dry 2). In each case, the DDA was filled in 0.15 m lifts every 5 days (one day for filling) for 50 days based on a proposed depositional scheme for one of the oil sands mine sites. The final thickness of this filling scenario is 1.5 m. For the cases in which desiccation was considered, Dry 1 and Dry 2, a potential evaporative flux boundary of 2.6 mm/day, typical of the conditions near the oil sands mine sites, was then applied to the surface of the tailings to represent atmospheric drying. This potential evaporation was applied to tailings surface for 80 days.

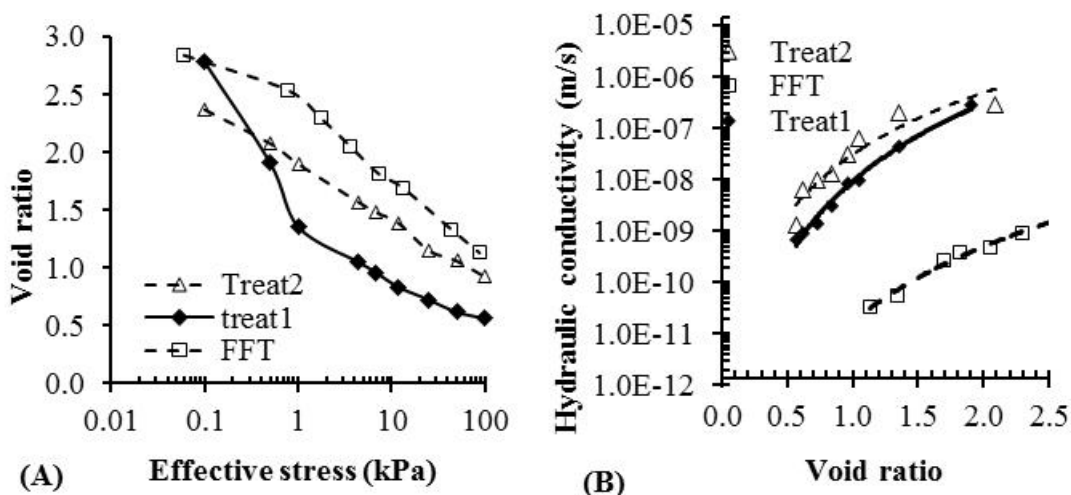


Figure 1. (A) Compressibility and (B) Hydraulic conductivity of FFT, Treat 1 and Treat 2.

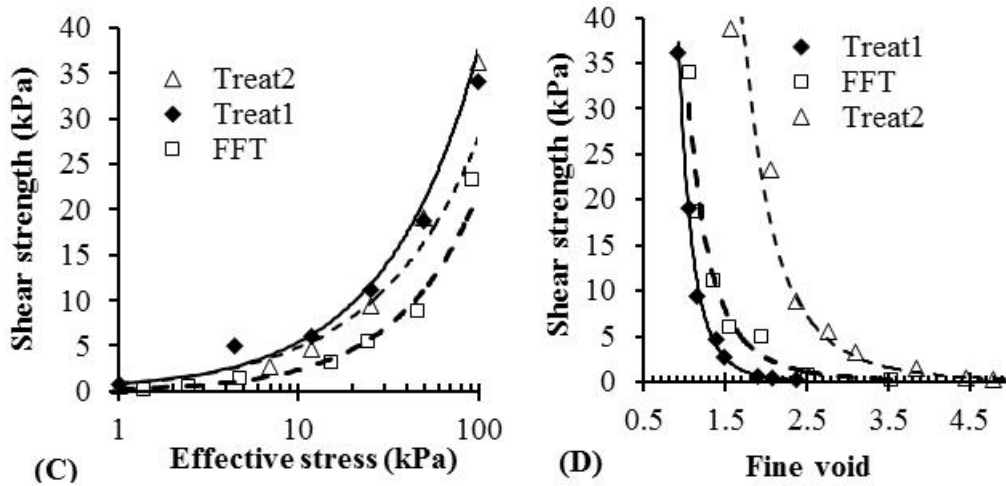


Figure 2. Undrained shear strength: (C) as function of effective stress and (D) fines void ratio for large strain consolidation of FFT, Treat 1, and Treat 2

Model Results

The surface elevations of the tailings deposit after 80 days, including the filling stage for the different scenarios, are shown in Figure 3. After 1 year, the FFT sample has only settled a few centimeters to 1.47 m. Both Treat 1 and Treat 2 dewatered considerably upon deposition with final surface elevations of 0.87 m and 1.06 m, respectively, after 1 year. Evaporation of the tailings reduced the surface elevation in Treat 1 and Treat 2 (represented as Dry 1 and Dry 2, respectively) by nearly 45% to 50% after only 80 days following the start of the filling cycle. After 80 days, no further settlement occurred in the Treat 1 and Treat 2 samples.

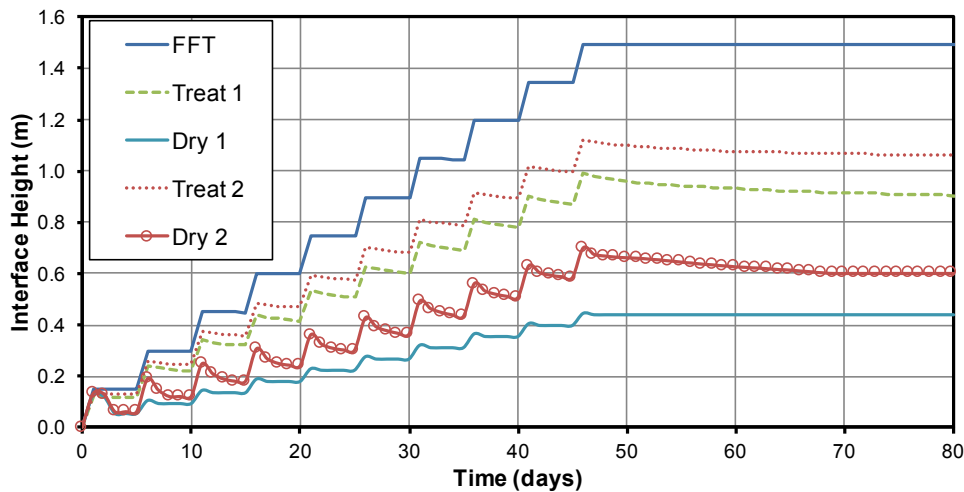


Figure 3. Tailings surface elevation after 80 days.

Fines void ratio profiles at elapsed times of 60, 120, 240, 360, 540 and 720 days are provided for the FFT, Treat 1 and Treat 2 samples and for 80 days only for the Dry 1 and Dry 2 samples (Figure 4).

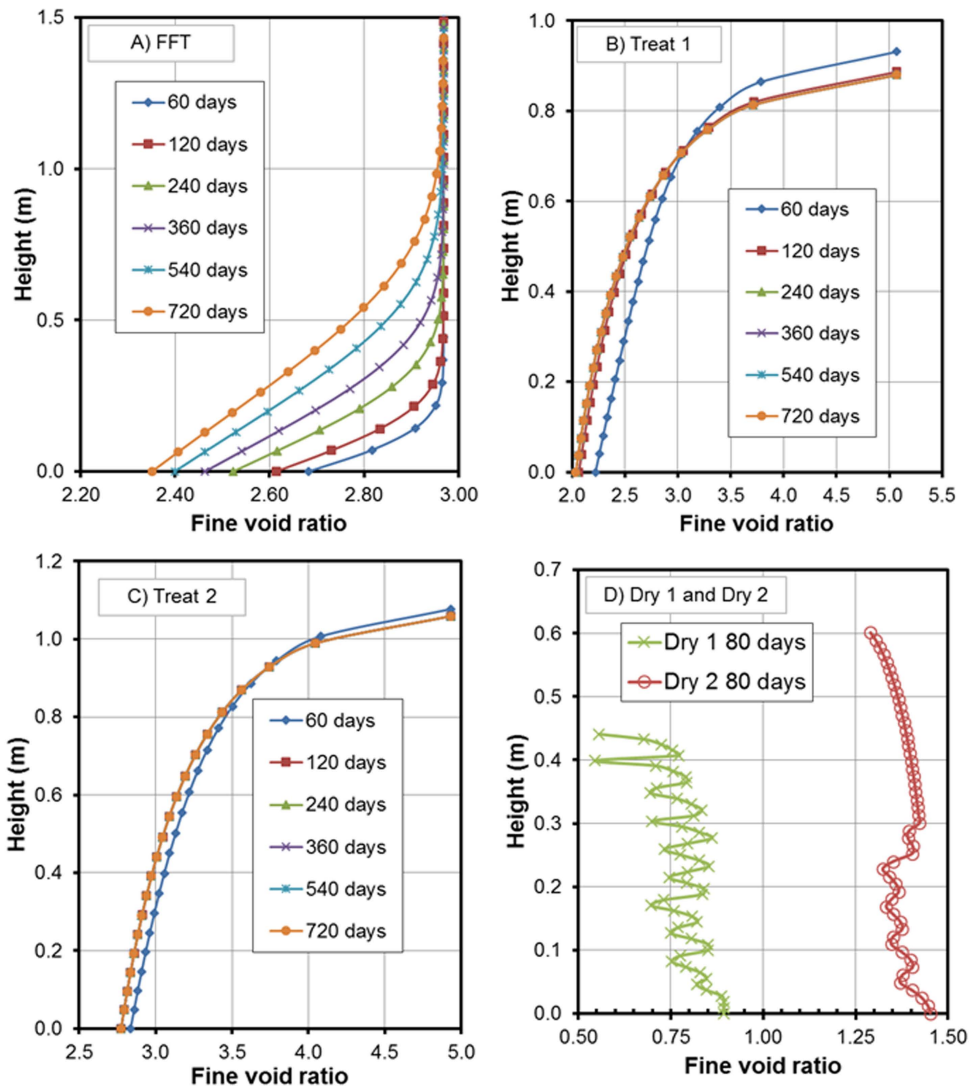


Figure 4. Fines void ratio profiles with height. A) FFT, B) Treat 1, C) Treat 2, D) Dry 1 and Dry 2.

Since no further dewatering occurred after 80 days of drying, the 80-day profiles of the Dry 1 and Dry 2 samples will only be reported on hereafter. Consolidation of the FFT sample starts from the bottom up and at the end of two years, only the bottom 1 m shows a decrease in void ratio. The upper 0.5 m shows no change in void ratio. In the treated samples, Treat 1 and Treat 2, very little dewatering occurs following deposition with no change in void ratios after 120 days. Little dewatering occurred in the final lift after 2 years. Due to the atmospheric drying conditions, significantly lower e_{fines} were calculated for Dry 1 (average of 0.78) and Dry 2 (average of 1.38) samples. The oscillation in the fines void ratio profiles in Figure 2D indicates the

combined effects of consolidation and desiccation. For each lift, the tailings are first consolidated until the upward water flux due to consolidation is less than the applied evaporation at the surface. At this point, the desiccation process will start. These two processes act on tailings consecutively during deposition, which contributes to the oscillations in the fines void ratio results in Dry 1 and Dry 2.

Figure 5 shows the shear strength profiles for the five model scenarios. Very little strength developed in the FFT sample with only a slight increase at depth (up to 0.75 kPa). For the Treat 1 and Treat 2 samples, the strength increased nearly linearly from the surface (0 kPa) to the bottom of the deposit (~2.5 kPa). No relationships were available for calculating the shear stress of the desiccated samples (Dry 1 and Dry 2).

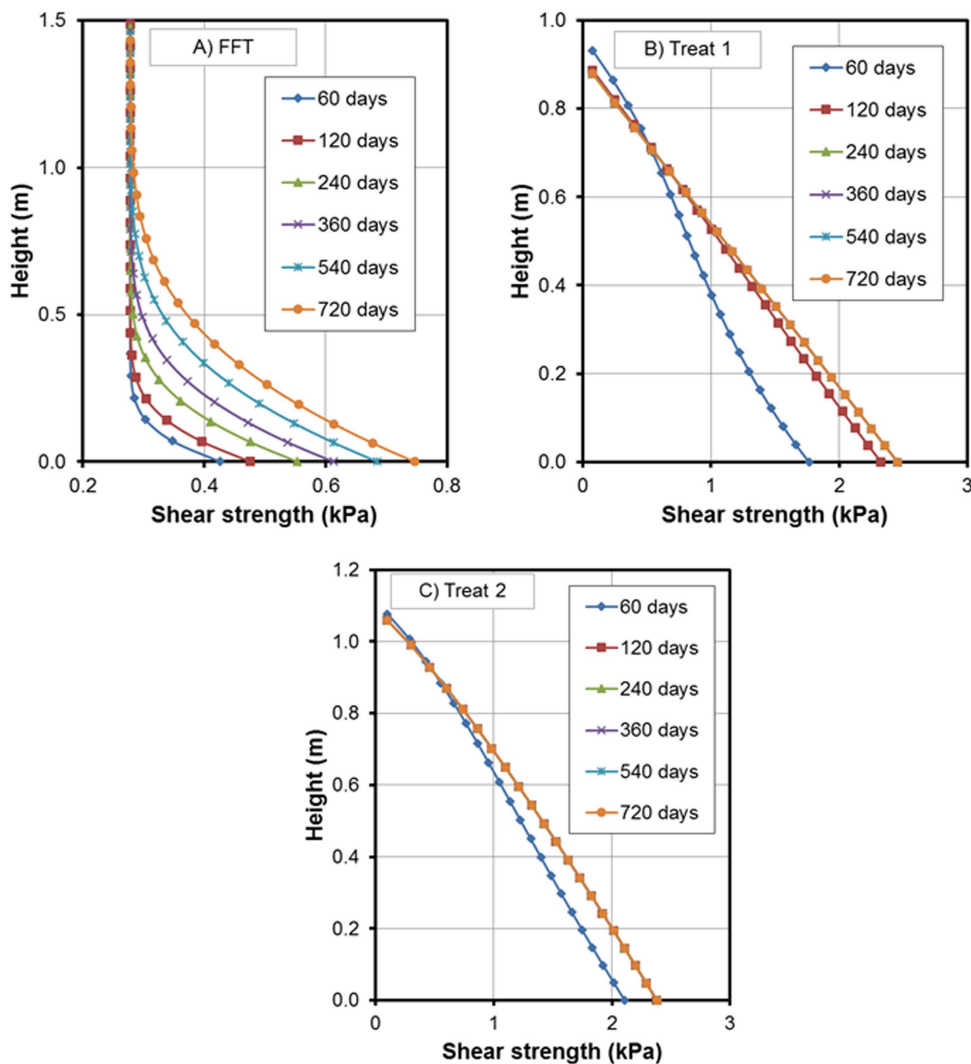


Figure 5. Shear strength profiles with height. A) FFT, B) Treat 1, C) Treat 2.

DISCUSSION

The flocculation, thickening and flyash addition (Treat 1 and Treat 2) resulted in improved settlement behavior compared to the untreated FFT samples. Under the same deposition conditions, the Treat 1 and Treat 2 tailings will settle up to 40% more than FFT (Figure 3). The addition of flyash to a flocculated and thickened tailings (Treat 2) hindered the settlement of the deposit compared to Treat 1 without flyash. Wilson et al. (2014) found that the flyash-amended tailings may actually be slightly resistant to compression due to a cementing of the fines. Atmospheric drying further improved the settlement of the flocculated tailings by another 50% (Dry 1 and Dry 2; Figure 3).

As can be seen in Figure 4, the flocculation and thickening process speed up the consolidation time; however, it did not significantly affect the final e_{fines} in the tailings deposits. It only took the Treat 1 deposit 120 days to reach an average e_{fines} of 2.61, after which further decreases in void ratio did not occur. Compared with the FFT sample, the e_{fines} deposit continued to dewater slowly with an average of only 2.78 after 2 years of settling. The addition of flyash appears to have prevented significant changes in the e_{fines} in Treat 2. Again, this is likely due to the cementation of the fines within the sample (Wilson et al. 2014). In order to reduce the e_{fines} appreciably, atmospheric drying was required. After 80 days, Dry 1 and Dry 2 deposits achieved an average e_{fines} of 0.78 and 1.38, respectively. This demonstrates that the volume change observed in the tailings deposit interface (Figure 3) was due to total void ratio changes and not to changes in the fines void ratio. To affect a significant volume change in the samples, a surface evaporation flux was required.

Previous research (Jeeravipoolvarn 2010) has indicated that flocculation increases the shear strength of oil sands fine tailings. Figure 5 demonstrates that flocculating, thickening and flyash addition has a major effect on increasing the shear strength. The treated samples (Treat 1 and Treat 2) show an improvement in shear strength development over the FFT sample (up to 3 times greater). Treat 2 developed shear strengths faster than the Treat 1 sample. Since the Treat 2 sample had higher e_{fines} within the deposit, it demonstrates that the flyash addition may allow tailings to achieve shear strengths with less compression (Wilson et al. 2014). However, the shear strength profiles developed in the Treat 1 and Treat 2 scenarios would not be sufficient to support soft capping activities, according to (COSIA 2012). Fines-dominated tailings deposits like Treat 1 and Treat 2 require strengths of at least 1 kPa to 2 kPa throughout the deposit profile in order to deploy soft deposit capping activities. Therefore, mechanical enhancements and environmental effects (such as freeze-thaw and desiccation) would be required to assist with surficial strength development for Treat 1 and Treat 2 samples.

Unfortunately, the shear strength – void ratio relationship was not sufficient to calculate shear strength profiles for the Dry 1 and Dry 2 samples due to the very low e_{fines} . However, from previous laboratory and field experience, for thickened tailings dried to a C_w of at least 65%, the shear strength will exceed 10 kPa to 15 kPa.

CONCLUSIONS

The geotechnical properties of thickened and desiccated tailings were used to model deposition scenarios for management of oil sands fine tailings. The influence of flocculation and thickening with or without flyash addition or atmospheric drying was demonstrated through the presentation and discussion of the model results. The modeling exercise demonstrated:

1. The flocculation, thickening and flyash addition (Treat 1 and Treat 2) resulted in improved settlement behavior compared to the untreated FFT samples.
2. Although the flocculation and thickening process accelerated the consolidation time, they did not significantly reduce the final e_{fines} profile in the tailings deposits when compared to FFT.
3. Flocculating, thickening and flyash addition has a major effect on increasing the shear strength; however, these treatments were not sufficient to generate strengths needed for soft capping and reclamation activities.
4. Enhancement by atmospheric drying was shown to significantly improve the post-depositional behavior. Desiccated tailings deposits had greater settlement, lower e_{fines} profiles and greater shear strengths.

ACKNOWLEDGMENTS

The authors would like to thank Total E&P for funding this research project and the Saskatchewan Research Council for providing the flocculated and thickened samples.

REFERENCES

- Alberta Environment and Sustainable Resource Development (AESRD). (2014). "Reclamation Information System, 2013". *Annual Conservation and Reclamation Report Submissions*.
- COSIA, (2012). Technical Guide for Fluid Fine Tailings Management. http://www.cosia.ca/uploads/documents/id7/TechGuideFluidTailingsMgmt_Aug2012.pdf Accessed August 19, 2015.
- Fredlund, D.G., and Rahardjo, H. (1993). Soil mechanics for unsaturated soils. John Wiley & Sons, Inc., New York.
- Gibson, R., England, G., & Hussey, M. (1967). "The theory of one-dimensional consolidation of saturated clays." *Geotechnique* 17(3): 261-273.
- Jeeravipoolvarn, S., Scott, J.D. and Chalaturnyk, R.J. (2008). "Multi-dimensional finite strain consolidation theory: Modeling study." *61st Canadian Geotechnical Conference*, Edmonton, AB, 22-24 September 2008.
- Jeeravipoolvarn, S. (2010) Geotechnical behavior of in-line thickened oil sands tailings. PhD Thesis, Department of Civil and Environmental Engineering, University of Alberta, Edmonton, Alberta, Canada, 431p.
- Kabwe, L.K., Kone, M., Sorta, A., Wilson, G.W., Scott, J.D. and Ulrich, A.C. (2013). "Measurements of unsaturated soil properties of old and new mature fine tailings," *Proceedings of the 8th International Conference on Mine Closure 2013*, Cornwall, UK.

- Qiu, Y. and Sego, D. (2006). "Optimum deposition for sub-aerial tailings disposal: concepts and theories." *International Journal of Mining, Reclamation and Environment* 20(4): 272-285.
- Pham, N.H. and Sego, D. (2014a). "Modeling dewatering of oil sands mature fine tailings using freeze thaw." 4th *International Oil Sands Tailings Conference*, Lake Louise, AB, 7-10 December 2014. 123-130.
- Pham, N.H. and Sego, D. (2014b). "Numerical simulations of freeze-thaw, large strain consolidation and desiccation of thickened tailings." *Report to Total E&P Canada Ltd.* 90 pgs.
- Scott, J.D., Jeeravipoolvarn, S. and Chalaturnyk, R.J. (2008). "Tests for wide range of compressibility and hydraulic conductivity of flocculated tailings". 61st *Canadian Geotechnical Conference*, Edmonton, AB, 22-24 September 2008.
- Sobkowicz, J. (2012). "The oil sands tailings technology roadmap and action plan: Introduction and key recommendations." 3rd *International Oil Sands Tailings Conference*, Edmonton, AB, 2-5 December 2012. 13-22.
- Sobkowicz, J.C. and Morgenstern, N.R. (2009). "A geotechnical perspective on oil sands tailings." 13th *International Conference on Tailings and Mine Waste*, November 1 -4, 2009, Banff, Alberta, 26 pp.
- Sun, R., Spelay, R., Kan, J., Goldszal, A. (2014). "Column consolidation testing of oil sands tailings". 4th *International Conference on Oil Sands Tailings Conference*, Lake Louise, AB, 7-10 December 2014. 163-171.
- Suthaker, N.N. and Scott, J.D. (1994). "Large scale consolidation testing of oil sand fine tails". 1st *International Congress on Environmental Geotechnics*, Edmonton, AB, 10-15 July 1994.
- Wilson, G.W., Kabwe, L.K., Scott, J.D. (2014). "Closure option for oil sands fluid fine tailings ponds." 9th *International Conference on Mine Closure*, Johannesburg, South Africa, 1-3 October 2014.

Pore Water Pressure Variations in Cemented Paste Backfilled Stopes

Mohammad Shahsavari, S.M.ACSE¹; and Murray Grabinsky, P.Eng.¹

¹Dept. of Civil Engineering, Univ. of Toronto, 35 St. George St., Toronto, ON, Canada M5S 1A4.

Abstract: Cemented paste backfill (CPB) has gained popularity over the past decade over other mine waste management techniques due to its high delivery rate and tight characteristics. CPB is a mixture of mine tailings, water and binder (cement). CPB has both environmental and operational benefits to a mine. Fresh CPB is being held in the stope by means of a barricade until it is cured and is self-supportive while mining operations such as blasting are going on. Barricade safety is crucial as the barricade failure would cause injuries and casualties to mining personnel as well as adding additional costs. The pressure acting on the barricade is dependent on the pore pressure that is developed and dissipated in and from CPB. The problem of self-weight consolidation of an accreting material was first studied by Gibson (1958). Shahsavari and Grabinsky (2015) modified the Gibson solution based on a new boundary condition that was inferred from in-situ measurements. However, Shahsavari and Grabinsky (2015) ignored the effect of hydration on pore pressure variations. In this study, a 1D analysis using FLAC3D is performed where the effect of hydration on pore pressure is considered through the change in material properties with time. The time dependent coefficient of permeability and shear modulus are then used to predict the pore pressure variations with time.

INTRODUCTION

Extraction of an orebody creates large underground voids called stopes. These stopes need to be backfilled to provide ground support for further excavation in addition to the reduction of surface disposal of mine waste. The three primary types of mine backfill are hydraulic fill, rock fill, and paste fill. When mixed with binder, the paste fill is called Cemented Paste Backfill (CPB). CPB is a mixture of mine tailing, binder (usually cement), and water. CPB has gained popularity over hydraulic and rock fills due to its relatively high delivery rate, homogenous as-placed properties, and tight-filling characteristics. During and after backfilling, fresh CPB is being held in the stope by using a barricade that is located in the undercut (i.e. the stope's "access tunnel"). Barricade failure would put the mining personnel at great risk and can impose high additional costs to the mining operation (e.g. Sivakugan 2008; Revel and Sainsbury 2007).

The barricade is subjected to horizontal stresses due to the development of effective stresses within CPB in addition to pore water pressure. Initially, the fresh CPB is like a dense fluid. Hence, hydrostatic pressures equal to the unit weight of the CPB times its height are applied to the barricade. With pore pressure dissipation with time, effective stresses develop within CPB. As the effective vertical stresses develop, the effective lateral pressures also increase. The net outcome of the pore pressure dissipation and effective stresses increase is a reduction in the barricade stresses due to arching (Mitchell 1992). Two main mechanisms are responsible for pore pressure reduction in CPB: 1. pore water drainage and hence consolidation and 2. self-desiccation through cement hydration. In the current study, the effect of self-desiccation on pore pressure variation is ignored for the sake of simplification.

CPB is being deposited in the slope in layers. Therefore, the problem of consolidation of CPB can be treated as the consolidation of an accreting soil. Gibson (1958) developed the governing partial differential equation (PDE) for the problem of consolidation of a clay soil that its thickness was increasing with time and proposed the analytical solution to the PDE. The details of the PDE and the solution will be explained in the upcoming sections. Fahey et al. (2010) applied the Gibson's (1958) solution to the consolidation of CPB. Unlike Gibson (1958), Fahey et al. (2010) used strain dependent constrained modulus and hydraulic permeability coefficients in their analysis. The non-linear void ratio-effective stress and void ratio-permeability coefficient relations were incorporated in the analysis which would lead to a variable coefficient of consolidation (Fahey et al. 2010). It was shown that the consideration of a variable coefficient of consolidation (c_v) would impact the pore pressure isochrones that was developed by Gibson (1958) that used constant c_v . However, field measurements show very small deformations (Grabinsky et al. 2014 and 2013) and it seems the consideration of a non-linear void ratio-effective stress relationship would be unnecessary.

On the other hand, Fahey et al. (2010) ignored the effect of binder hydration on both the constrained modulus and hydraulic permeability coefficient. The effect of hydration on CPB consolidation and pore pressure variations with time and depth is studied through using time dependent material properties.

In the previous studies on the numerical simulation of the process of consolidation of CPB, it has always been assumed that the pore pressure remains zero on top of each layer before the next layer is being added (Doherty 2015; El Mkdami et al. 2014; Fahey et al. 2010; Li and Aubertin 2009; Helinski 2008). However, the in-situ measurements (e.g. Grabinsky et al. 2014 and 2013; Thompson et al. 2012) indicate that there is a specific height of CPB that does not show any signs of consolidation and remains slurry for a while (Shahsavari and Grabinsky 2014). Shahsavari and Grabinsky (2015) studied the effect of the presence of this non-consolidating slurry layer on the pore pressure variations with time and depth in a continuous fill using FLAC3D. It was shown that a non-zero hydraulic and mechanical boundary conditions on top of the consolidating CPB would greatly impact the both the magnitude and the location of the maximum pore water pressure (Shahsavari and Grabinsky 2015). Shahsavari and Grabinsky (2015) also showed that for a specific case their numerical simulation was capable of predicting the maximum in-situ pore pressure that was applied to the barricade.

The same modeling approach as Shahsavari and Grabinsky (2015) is followed in the current analysis, but with variable material properties. In the following sections, first, the Gibson (1958) analytical solution is described, then the numerical simulation procedure and material properties are shown. These sections are followed by analyzing the in-situ measurements and the presence of the slurry layer. Then, the effect of hydration on material properties and pore pressure variations is shown.

ANALYTICAL SOLUTION

Gibson (1958) developed the partial differential equation (PDE) governing the pore pressure variations with time and location within a clayey soil that its thickness was increasing with time. Gibson (1958) assumed that the material properties including the coefficient of permeability and constrained modulus were constant. The developed PDE also assumed one-dimensional deformations and water flow. The PDE is shown in Eq.1.

$$c_v \frac{\partial^2 u}{\partial z^2} = \frac{\partial u}{\partial t} - \gamma \frac{dh}{dt} \quad (1)$$

where u is the total pore pressure, γ is the material unit weight, h is the current height of the layer and a function of time (i.e. $h = h(t)$), and z is the vertical distance from the bottom of the soil. c_v is the coefficient of consolidation and is defined as Eq. 2.

$$c_v = \frac{k \cdot M}{\gamma_w} \quad (2)$$

where k and M are hydraulic permeability coefficient and constrained modulus, while γ_w is the water unit weight.

Gibson (1958) solved Eq.1 assuming that pore pressure is zero both at top of the layer and at $z = 0$. In the problem of sedimentation or backfilling the height varies as linear function of time. The solution to Eq.1 considering $h = h(t) = m \cdot t$ is shown in Eq. 3.

$$u = -\gamma z \left(1 + \frac{mz}{2c_v} \right) + \frac{\gamma m}{2c_v} (\pi c_v t)^{-\frac{1}{2}} \cdot \exp\left(-\frac{z^2}{4c_v t}\right) \cdot \int_0^\infty \xi^2 \coth\left(\frac{m\xi}{2c_v}\right) \sinh\left(\frac{z\xi}{2c_v t}\right) \exp\left(-\frac{\xi^2}{4c_v t}\right) \cdot d\xi \quad (3)$$

where z is the vertical distance measured from the bottom of the consolidating soil. Gibson (1958) evaluated the integral in Eq.3 numerically and introduced a set of isochrones using a dimensionless time factor as $T = mt^2/c_v$. The isochrones are shown in Figure 1.

As much as the analytical solution is valuable in early estimation of pore pressure and barricade loads, it does not consider the different interactions and couplings that take place within a consolidating soil. These interactions in a one-dimensional

problem include, the soil-water coupling and chemical interactions in case of cemented soils such as CPB. Therefore, numerical simulations are needed to be able to have a more precise prediction of pore water pressure within depositing CPB.

NUMERICAL SIMULATION

FLAC3D is used to simulate the problem of consolidation of cemented paste backfill. Shahsavari and Grabinsky (2014) showed that FLAC3D is capable of producing the same isochrones as the analytical solution considering the same assumptions as Gibson (1958). Shahsavari and Grabinsky (2014) assumed that the material is linear elastic with constant properties. The comparison of the numerical and analytical solution is shown in Figure 1.

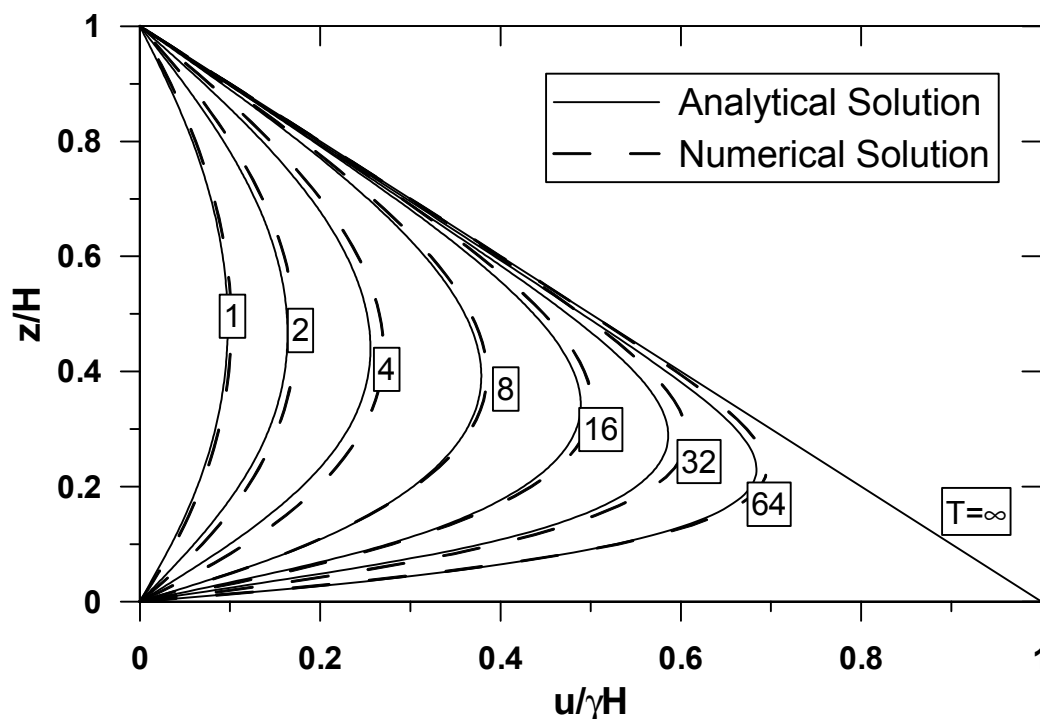


FIG.1 Comparison of the FLAC3D numerical simulation and analytical solution to the consolidation governing PDE (after Shahsavari and Grabinsky 2014)

FLAC3D consolidation formulation is based on Biot's (1941) theory of consolidation. However, if the material is fully saturated and the grains are considered incompressible then the Biot's coupled consolidation PDEs would reduce to the one uncoupled PDE introduced by Terzaghi (1943). In this context, coupled analysis refers to the mechanical and hydraulic coupling. These assumptions were applied to the FLAC3D model in order to be able to make the comparison with the analytical solution (Shahsavari and Grabinsky 2014). The same numerical modeling approach as Shahsavari and Grabinsky (2015) is going to be followed in the current analysis with the addition of the effect of hydration on pore pressure variations with time and space by using time dependent material properties.

Shahsavari and Grabinsky (2015 and 2014) inferred from the in-situ measurements of pore pressure and total stresses (Grabinsky et al. 2013; Thompson et al. 2012) that the pore pressure is not zero on top of the consolidating material. This layer was called the slurry layer due to its nature (Shahsavari and Grabinsky, 2014). The presence of the slurry layer applied non-zero mechanical and hydraulic boundary conditions on top of the consolidating material. The mechanical boundary condition was due to the slurry layer weight. The non-zero hydraulic boundary condition was not considered in other numerical analysis of the problem of CPB consolidation (e.g. Doherty 2015; El Mkdami et al. 2014; Veenstra, 2013; Fahey et al., 2010). Shahsavari and Grabinsky (2015) showed that the presence of such non-consolidating layer would increase the maximum pore pressure. Shahsavari and Grabinsky (2015) predicted the maximum in-situ pore pressure behind the barricade with their numerical approach. In the current study the non-zero pore pressure and the weight of the slurry layer are incorporated into the analysis. CPB is placed in layers of 25 cm high and each layer is divided into 4 zones. Then the appropriate non-zero hydraulic and mechanical boundary conditions are applied on top of the layer. Each layer is then consolidated for an hour before the placement of the new layer. The details of the numerical model can be found at Shahsavari and Grabinsky (2014 and 2015). In the following sections, first the time dependent material properties and their implementation in the FLAC3D code is described. Then the effect of hydration on pore pressure variations considering those time dependent material properties is shown. It must be noted that to be consistent with both the previous analysis and the analytical solution it is assumed that the stress-strain response is elastic and small strain condition prevails.

Effect of Cement Hydration on CPB Properties

As cement reacts with water the calcium silicate hydrate (C-S-H) bonds are formed within the pore space and around the tailings grains. The formation of C-S-H bonds alter the material properties and response. Since the cement hydration is time dependent phenomena, the material properties will in turn be functions of time. The time can be either measured from the initiation of the acceleration phase of hydration initiation or from the time the mixture is ready. In this analysis, time is referenced with the initial mixing time.

The material properties that involve in the current analysis are the shear modulus, coefficient of permeability, and Poisson's ratio. It is assumed that the material is saturated and occluded air bubbles does not exist. Therefore, the Biot's number can be considered to be constant and equal to one. The variation of Poisson's ratio with time are minimal (Abdelaal 2011; Veenstra 2013) and hence a constant value of 0.35 is considered for the Poisson's ratio during the whole analysis. The coefficient of permeability and shear modulus are measured experimentally. The results of these experiments are shown in the following subsections.

Material Tested

The CPB used in this analysis is consists of silica tailings, glacial sand, and binder. All these components were supplied by Xstrata from Kidd mine in sealed pails.

Figure 2 shows the grain size distribution of the mine tailings, sand, and the mixture of 45% solid weight sand and 55% mine tailings. The details of the sieve analysis and hydrometer tests is described by Abdelaal (2011). The specific gravity of the tailings was determined to be 2.79 in accordance to ASTM D854-06 (Abdellaal 2011). CPB samples were obtained by mixing 45% of the solid weight sand with 55% of the solid weight mine tailings and then add 4.5% of the total solid weight binder to the solid mixture. Water then was added to reach a water content of 28% to generate a paste with a slump between 140 mm and 190 mm (Abdelaal 2011). The CPB samples were then used to measure the coefficient of permeability and shear modulus variations with time.

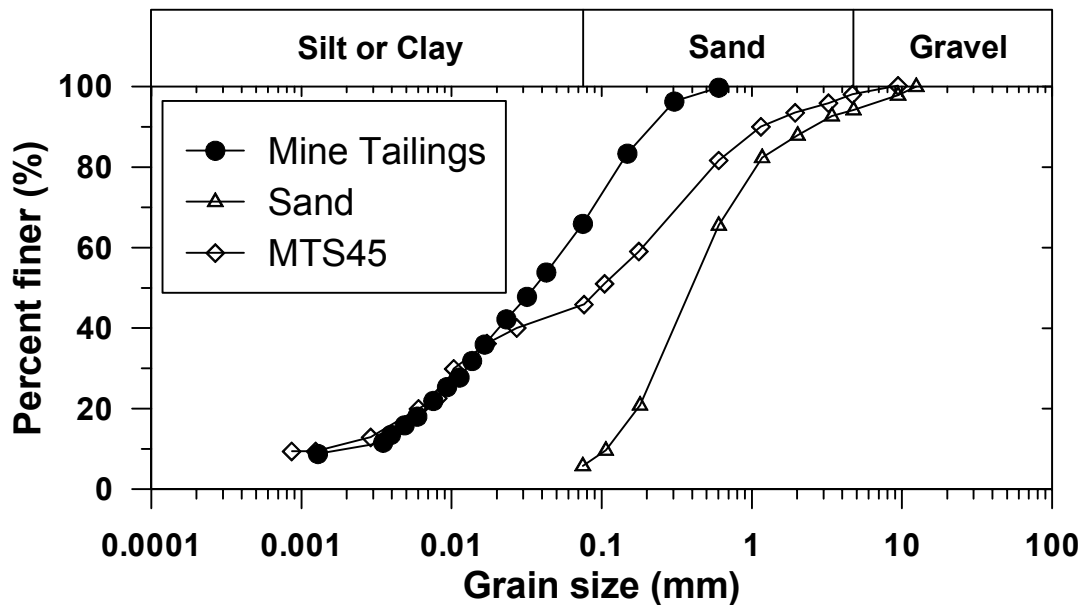


FIG2. Grain size distribution of mine tailings (MT), sand, and mixture of 55% mine tailings and 45% sand (MTS45) (after Abdelaal, 2011)

Coefficient of Hydraulic Permeability

Coefficient of permeability is used in the solution of the diffusion PDE that is coupled with the mechanical deformation PDEs. Coefficient of permeability is a function of the viscosity of the saturating liquid, degree of saturation and a factor that is called the intrinsic permeability. The effect of the variation of water viscosity with temperature is ignored in this analysis for the sake of simplicity. On the other hand, due to the high water content of CPB, the effect of degree of saturation is ignored and the material is assumed to be fully saturated during the whole analysis. The intrinsic permeability is a function of the tortuosity of the pores. Due to the presence of binder, the tortuosity of CPB changes with time and hence the coefficient of permeability changes.

It is easier to measure the coefficient of permeability rather than measuring the intrinsic permeability. UMS KSAT device was used to measure the coefficient of

permeability. The KSAT device is capable of measuring the coefficient of permeability through both constant head and falling head tests. Due to the low permeability of CPB, falling head method was followed. A cylindrical sample with the cross section area of 50 cm² and height of 5 cm was used. Water was forced through the bottom of the sample with an initial gradient of about 1. The gradient was then increased with time as CPB was cured, in order to allow water flow through the sample. Figure 3 shows the variation of coefficient of permeability with time.

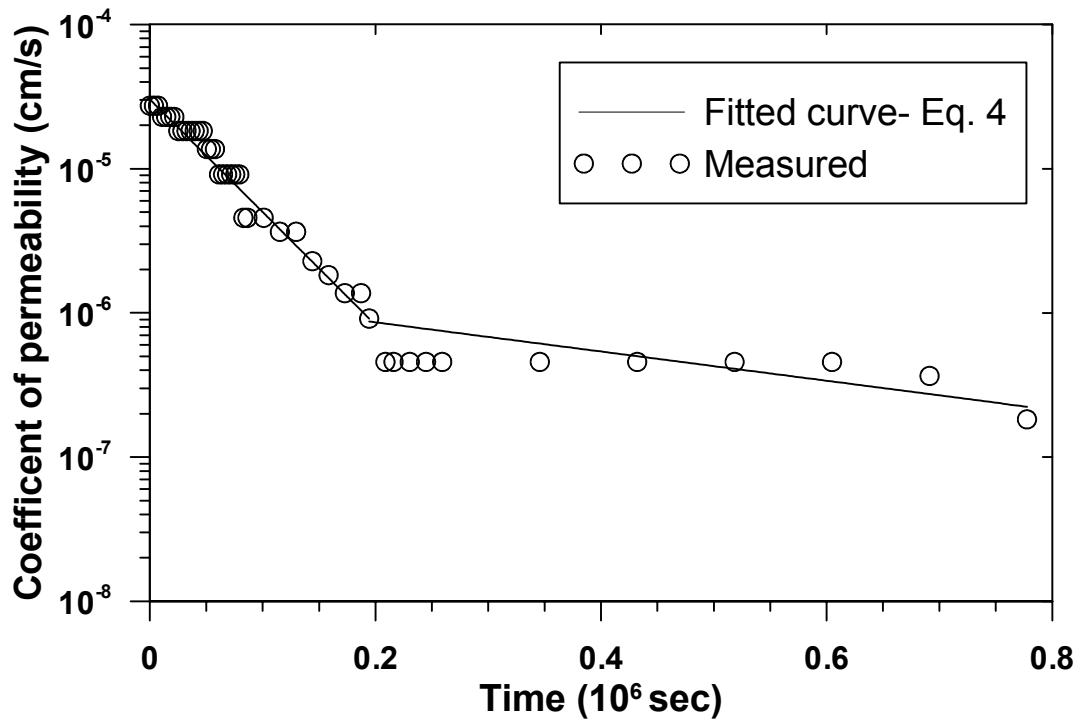


FIG 3. Variation of coefficient of permeability with time

In order to be able to implement the variable coefficient of permeability into the FLAC3D analysis, two curves were fitted to the measured points. The two curves are separated at the 2e5 seconds after the sample was casted. The fitted curves are shown in Eq. 4 where $k = k(t)$ is the coefficient of permeability. It must be noted, since the hydration does not begin before the 3rd hour, the constant value of 2.5e – 5 cm/s is used for $t \leq 3$ hrs.

$$k(t) = \begin{cases} 3.0e - 5 * \exp(-1.8e - 5.t) & 1e4 \text{ sec} < t \leq 2e5 \text{ sec} \\ 1.3e - 6 * \exp(-2.3e - 6.t) & t \geq 2e5 \text{ sec} \end{cases} \quad (4)$$

Shear Modulus

The presence of cement changes the CPB stiffness with time due to the formation of C-S-H bonds and also self-desiccation. For the one dimensional analysis, the constrained modulus (M) is needed. The constrained modulus is a function of shear

(G) and bulk modulus (K). On the other hand, the shear and bulk modulus are related through the Poisson's ratio. Considering a constant Poisson's ratio, only the effect of hydration on the small strain shear modulus is shown and used in the analysis. The constrained modulus is then derived as $M = K + \frac{4}{3}G$. Abdelaal (2011) used triaxial device and bender element tests to measure the development of low strain stiffness of CPB. The details of the tests are beyond the scope of this paper and can be found at Abdelaal (2011). Figure 4 shows the variation of small strain shear modulus with the hydration time.

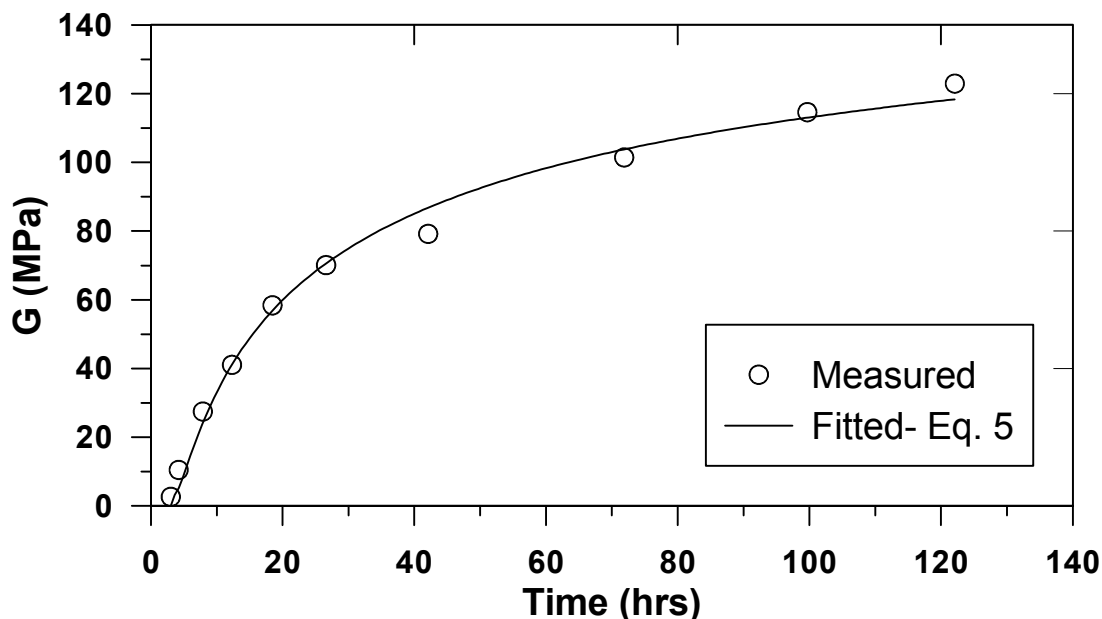


FIG 4. Variation of shear modulus with time (after Abdelaal, 2011)

Illston et al. (1979) introduced an exponential “maturity function” for cemented materials. The maturity function for the CPB used in this study takes the form of Eq. 5.

$$G = G_i + a * \exp\left(-\frac{d}{\sqrt{t - t_i}}\right) \quad (5)$$

where G_i and t_i are the initial shear modulus and time prior to the acceleration phase, respectively. For the CPB used in this analysis, G_i and t_i are 2.7 MPa and 3 hours, respectively. a and d are fitting parameters and have values of 177.31 MPa and 4.67 hour^{1/2}, respectively.

FLAC3D Analysis

The variation of pore water pressure with depth at the end of filling for an 8m high plug layer in a slope is shown in Figure 5. Four different cases are compared; when a 3m high slurry layer is present on top of the consolidating layer and when the top pore

pressure is zero. The effect of hydration on pore pressure variations in both cases is also shown. As shown in Figure 5, as cement hydrates and stiffness increases while the coefficient of permeability is decreased, the maximum pore pressure decreases. Gibson's (1958) solution with zero pore pressure on top, would lead to an over estimation of loads that are applied to the barricade. On the other hand, if Gibson's solution is followed and the effect of hydration is considered but the top boundary condition is not chosen properly, then very low pore pressures are predicted which would lead to an unsafe design of the barricade. The importance of the proper boundary condition selection is shown by Shahsavari and Grabinsky (2015) as they were able to predict the maximum in-situ pressure that was applied to a barricade with a high precision. In addition, the effect of non-zero mechanical and hydraulic boundary conditions become more prominent when variable material properties are used in the analysis.

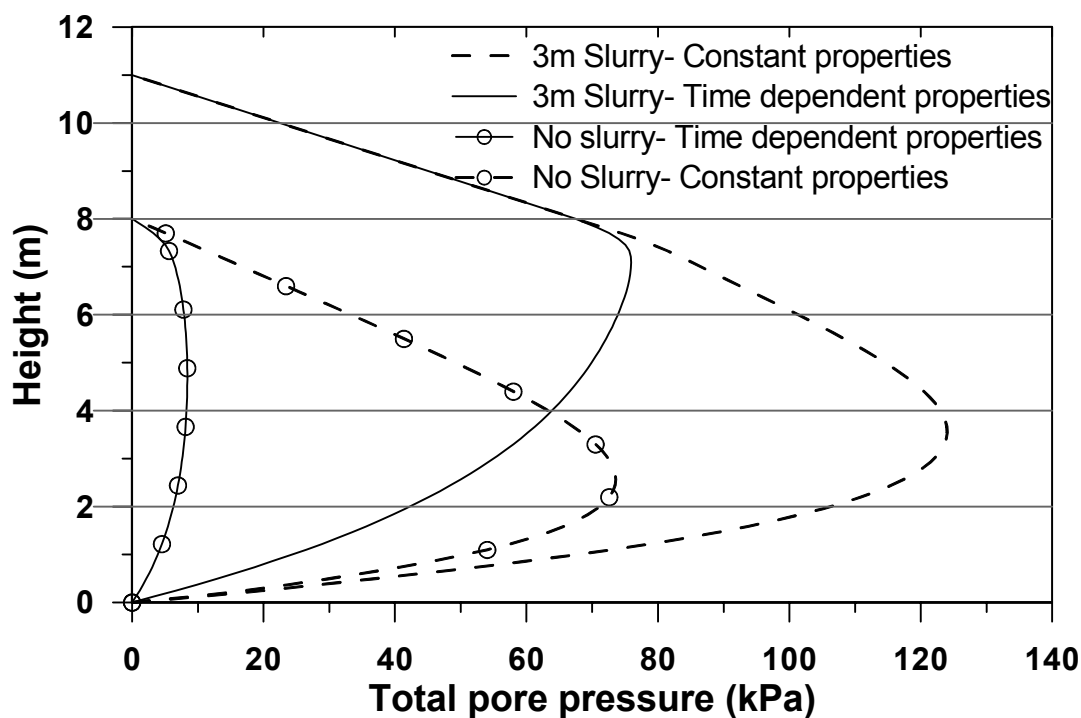


Fig 5. Effect of both the slurry layer presence and hydration on pore pressure variations at the end of backfilling

Another factor that would cause a change in the maximum pore pressure is the height of the slurry layer on top of the consolidating layers. Figure 6 shows the pore pressure variations with depth for two different plug heights and two different slurry layer heights of 1.5m and 3m. As the slurry layer height increases, the maximum pore pressure also increases. However, the magnitude of the maximum pore pressure does not change with the plug height. This almost constant maximum pore pressure can be attributed to the increase in the material stiffness and lower permeability at lower layers. The effect of non-zero boundary conditions does not eliminate even when the material properties are changing.

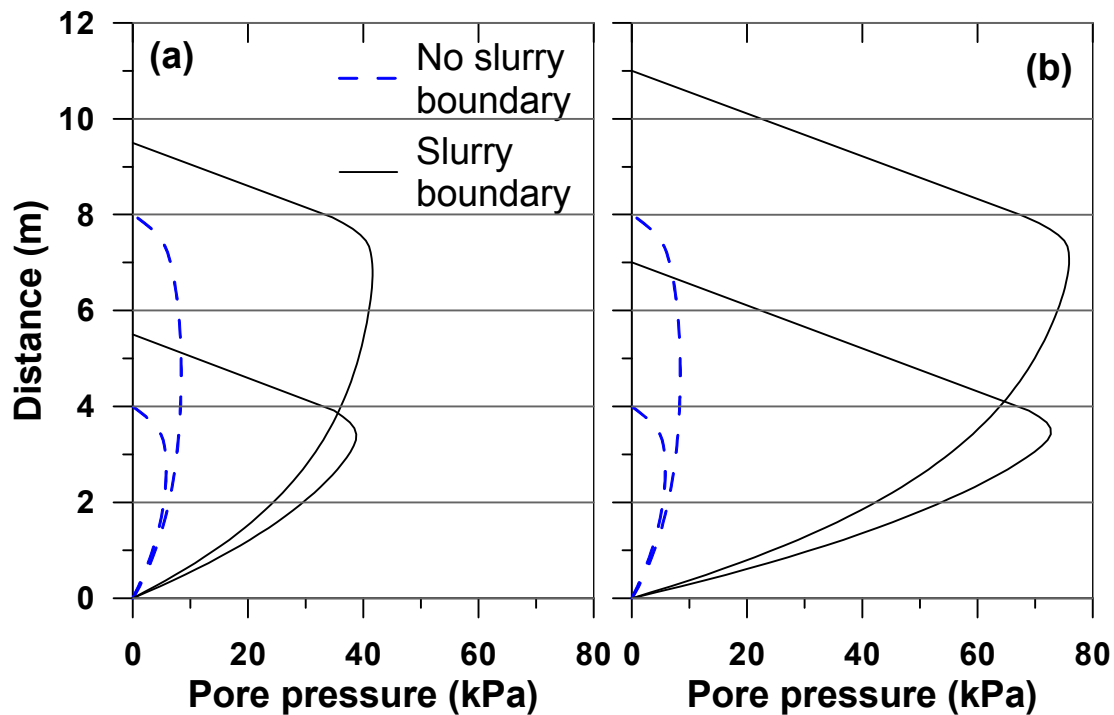


FIG 6. Effect of both hydration and slurry layer height on pore pressure: (a) 1.5m and (b) 3m high slurry layers

CONCLUDING REMARKS

As cement hydrates in CPB, the coefficient of permeability decreases while the material stiffness increases. These are the two key material parameters in the analysis of the consolidation of CPB. These variable material properties are not considered in the analytical solution. It was shown that the consideration of time-dependent material properties would lead to a decrease in the maximum pore pressure within the backfilled CPB.

On the other hand, combined effect of the presence of a slurry layer on top of the consolidating layer and hydration was also studied. It was shown that, it is even more crucial to consider the right boundary conditions when the effect of hydration is also taken into account. When constant material properties are used in the analysis (e.g. Shahsavari and Grabinsky 2015) the ratio of the slurry layer height to the consolidating material height had an effect on the maximum pore pressure, however, when hydration is taken into the account that effect of height ratio is seemed to become less important.

The analysis in this paper was performed assuming an elastic material and one dimensional deformations. The effect of the surrounding rock on CPB consolidation and the interaction with CPB needs to be studied using a 3D analysis. On the other hand, the effect of self-desiccation as described by (Helinski et al. 2007) must also be incorporated in the analysis.

ACKNOWLEDGMENTS

The first author is a recipient of an Itasca Education Partnership which provides training for, and use of Itasca codes including FLAC3D. The support of Jim Hazzard in Itasca's Toronto Office is gratefully acknowledged. Funding for this work has been provided by Barrick Gold Corporation as part of a larger investigation into the behavior of high performance paste backfill.

REFERENCES

- Abdelaal, A., (2011). Early Age Mechanical Behavior and Stiffness Development of Cemented Paste Backfill with Sand. *Ph.D. Thesis*, Dept. of Civil Engineering, University of Toronto, Toronto, Canada.
- ASTM D854-06e1. (2006). "Standard Test Methods for Specific Gravity of Soil Solids by Water Pycnometer." *ASTM International*, West Conshohocken, PA.
- Biot, M.A. (1941). "General Theory of Three-Dimensional Consolidation." *Journal of Applied Physics*. 12(2): 155-16.4.
- Doherty, J.P. (2015). "A numerical study into factors affecting stress and pore pressure in free drainage mine stopes." *Computer and Geotechnics*. 63: 331-341.
- El Mkadmi, N., Aubertin, M., and Li, L. (2014). "Effect of drainage and sequential filling on the behavior of backfill in mine stope." *Canadian Geotechnical J.* 51(1):1-15.
- Fahey, M., Helinski, M. and Fourie, A. (2010). "Consolidation in accreting sediments: Gibson's solution applied to backfilling of mine stopes." *Géotechnique*. 60(11): 877-882.
- Gibson, R.E. (1958). "The progress of consolidation in a clay layer increasing in thickness with time". *Géotechnique*. 8(4): 171-183.
- Grabinsky, M.W., Bawden, W.F., Simon, D., Thompson, B.D. and Veenstra, R.L. (2013). "In situ Properties of Cemented Paste Backfill from Three Mines." *Proc. 66th Canadian Geotechnical Conference*, Montreal, Quebec, Canada.
- Grabinsky, M.W., Simon, D., Thompson B.D., Bawden, W.F. and Veenstra, R.L. (2014). "Interpretation of as-placed cemented paste backfill properties from three mines." *Proc. 11th International Symposium on Mining with Backfill*, Australian Centre for Geomechanics, Perth, Australia.
- Helinski, M. (2008). The Mechanics of Mine Backfill. *Ph.D. Thesis*, University of Western Australia.
- Helinski, M., A.B. Fourie, M. Fahey, and M. Ismail. (2007). "Assessment of the self-desiccation process in cemented mine backfills." *Canadian Geotechnical J.* 44(10):1148-1156.
- Illston, J.m., Dinwoodie, J.M., and Smith, A.A. (1979). "Concrete, timber and metals: the nature and behavior of structural materials." *Van Nostrand Reinhold Company*, NewYork. ISBN 0419154701. 663p.
- Li, L. and Aubertin, M. (2009). "The Influence of Water Pressure on the Stress State in Stopes with Cohesionless Backfill." *Geotechnical and Geological Engineering*. 27(1): 1-11.

- Mitchell, R.J. (1992). "Centrifuge model studies of fill pressures on temporary bulkheads." *Canadian Institute of Mining Bulletin*. 85 (960): 48–54.
- Revell, M.B and D.P. Sainsbury. (2007). "Paste Bulkhead Failures." *Proc.9th International Symposium on Mining with Backfill*, Montreal, Quebec, Canada.
- Shahsavari, M. and Grabinsky, M.W. (2014). Cemented paste backfill consolidation with deposition-dependent boundary conditions, *Proc. 67th Canadian Geotechnical Conference*, Regina, Saskatchewan, Canada.
- Shahsavari, M. and Grabinsky, M.W. (2015). "Mine backfill porewater pressure dissipation: numerical predictions and field measurements." *Proc. 68th Canadian Geotechnical Conference*, Quebec City, Quebec, Canada.
- Sivakugan, N. (2008). "Drainage issues and stress developments within hydraulic fill mine stopes." *Australian J. of Civil Eng.* 5(1): 61-70.
- Terzaghi, K. (1943). "*Theoretical Soil Mechanics*." John Wiley and Sons, New York, NY, USA.
- Thompson, B.D., Bawden, W.F. and Grabinsky, M.W. (2012). "In-situ Measurements of Cemented Paste Backfill at the Cayeli Mine." *Canadian Geotechnical Journal*, 49(7):755-772 (available for free download at www.nrcresearchpress.com/doi/abs/10.1139/t2012-040)
- Veenstra, R. L. (2013). A design procedure for determining the in situ stresses of early age cemented paste backfill. *PhD thesis*, Dept. of Civil Engineering, University of Toronto, Canada.

Review of the Reclamation Techniques for Acid-Generating Mine Wastes upon Closure of Disposal Sites

Michel Aubertin, M.ASCE^{1,4}; Bruno Bussière^{2,4}; Thomas Pabst³;
Michael James^{1,4}; and Mamert Mbonimpa^{2,4}

¹École Polytechnique de Montréal, QC, Canada H3C 3A5.

²Université du Québec en Abitibi-Témiscamingue, QC, Canada J9X 5E4.

³Norwegian Geotechnical Institute, Oslo, Norway 0806.

⁴Research Institute on Mines and Environment (RIME UQAT-Polytechnique).

Abstract: Acid mine drainage (AMD) remains a major environmental challenge for the mining industry. The preferred options for effectively limiting the environmental impact of AMD consist in controlling the reactions through the use of preventative techniques. Their principal objective is to exclude at least one of the constitutive elements of the chemical reactions, i.e. water, oxygen, or sulfidic minerals. The article recalls the basic principles and reviews different approaches for the prevention and control of AMD upon mine closure. The main methods include multi-layer covers, water covers, and an elevated water table (with a mono-layer cover). Their main advantages, limitations and uncertainties are addressed. Alternative approaches, such as environmental desulphurization and co-disposal of waste rock and tailings, are also discussed.

INTRODUCTION

The mining industry contributes significantly to the economy of many regions around the globe. However, there are also some drawbacks associated with mining operations. One of these is the challenge associated with the large amount of wastes produced which need to be managed safely and economically.

As ore reserves are depleted, all mines will reach the closure stage beyond which the site must be reclaimed. The general goal is then to return the mine site to a satisfactory state by eliminating the risks to health and safety, controlling contaminant production and migration, and establishing conditions that require a minimum of monitoring and maintenance in the long term (Aubertin et al. 2002).

Although apparently straightforward, effective closure measures are not easily applied to disposal sites where the mine wastes (tailings and waste rock) contain reactive minerals that can produce acid mine drainage (AMD). The generation of acidic effluents is a well-known phenomenon that has been studied for decades (e.g.

Singer and Stumm 1970; SRK 1989). AMD is typically produced when sulfidic minerals (such as pyrite and pyrrhotite) are exposed to atmospheric conditions. The reactions between the iron sulfides, oxygen and water then reduce the leachate pH (often to around 2), favoring the solubilisation of various elements (including metals) present in the rock. As acid mine (or rock) drainage can be a major threat to local ecosystems, the effluent must be treated before discharge. However, active chemical treatment, often employed during mining operations, is not a viable (nor acceptable) option upon closure due to the long term costs involved, infrastructure requirements and maintenance, and the large amount of sludge produced (Aubertin et al. 2002; Robertson 2011). The primary goal of mine site reclamation should be to prevent the production of AMD.

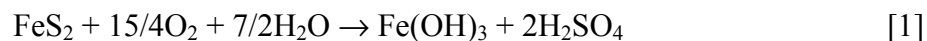
The vast amount of work performed and the experience gained over the last two to three decades clearly indicate that the reclamation of reactive wastes disposal sites is best achieved when it is planned in advance and integrated into the mining production cycle. This guiding principle of “Designing for Closure” has in fact been considered for many years (SRK 1989; Aubertin et al. 2002), but it must be admitted that it is seldom being applied diligently by the industry (Aubertin et al. 2015); this aspect will be addressed further below.

One of the major challenges regarding closure and reclamation of sites producing AMD is the required life time of the engineering works that must be constructed and maintained. This duration can be very long, and it is sometimes considered indefinite (Vick 2001). This has a major impact on the geotechnical (physical) and geo-environmental (chemical) design criteria for various works such as the dikes surrounding tailings impoundments and the external slopes of the waste rock piles (Aubertin et al. 1997, 2002, 2011).

This article summarizes the main techniques available for the reclamation of AMD generating sites, with an emphasis on those that are more commonly applied under relatively wet (and cold) climatic conditions (such as those in the eastern provinces of Canada). The presentation is largely based on previous work conducted by the authors and their industrial and academic collaborators on tailings sites, with some additional information on waste rock.

GLOBAL REACTION AND MAIN PREVENTION METHODS

Pyrite (FeS_2) is usually the most abundant iron sulfide mineral in mine wastes so it is often used to express the reactions leading to the production of sulfuric acid. These reactions can be simplified into a single global expression:



This equation confirms that sulfidic minerals, water and oxygen are required to produce AMD. The detailed reactions include various steps that may also involve contributions from other oxidizing agents (e.g. ferric iron) and bacteria (Kleinman et al. 1981; SRK 1989; Aubertin et al. 2002; INAP 2012; Anawar 2015).

Prevention and control methods target the three components on the left hand site of Eq. 1. In the case of tailings, the sulfidic minerals can be separated (and managed

separately) by using desulfurization techniques (Benzaazoua et al. 2008); this approach can be very advantageous, as will be discussed further below. The availability of water and oxygen can be controlled using different types of barriers placed on top and around the reactive wastes, as will be described in the following. It is also possible to use complementary mitigation methods to reduce the reaction rate, such as temperature control (in cold climate), surface passivation and anti-bacterial agents, but most of these techniques suffer from a number of disadvantages and they are usually considered less reliable; they will not be discussed here.

MULTILAYERED COVERS

Covers made of a few layers of different materials, each playing a distinct role, are commonly used to control water infiltration and/or oxygen ingress at disposal sites (Aubertin et al. 1995, 2002; MEND 2004); they also play various other roles with respect to surface stability and future use (and esthetic) of the sites.

This type of cover is now commonly applied on the nearly horizontal surfaces of tailings impoundments, but they can also be used, with some adjustments, for inclined areas such as the external face of dikes and the slope of waste rock piles (Bussi re et al. 2003; Aubertin et al. 2009). In all cases, the characteristics of the cover must be adapted to the local conditions in terms of climate, hydro(geo)logical site characteristics, available materials, and reactive wastes properties.

As stated above, covers must be able to perform adequately for a very long time. This creates many challenges for their design, construction, and maintenance.

Fig. 1 illustrates a typical multi-layered cover system that contains five layers; the actual number of layers (from two to more than five) depends on a number of factors related to site specific conditions and design criteria. In Fig. 1, the superficial Layer A serves to integrate the surface of the site to the local environment. It is usually made of organic soils that facilitates the controlled establishment of vegetation; care must be taken (with some maintenance) to avoid the potentially negative effects of roots on the cover performance. Layer B is a protection layer that helps stabilize the site and prevents bio-intrusions; it is made of coarse grained materials with a high content of cobbles. Layer C is a drainage layer of granular (sand and/or gravel) material that controls water inflow laterally and vertically. In many cases, layers B and C can be combined into a single one. This coarse-grained layer may also play the role of a capillary break, to prevent moisture loss by evaporation. Layer D is the actual hydrogeological barrier in the cover. It is made of a relatively impervious material such as a fine grained soil, a geomembrane (GM), a geosynthetic clay liner (GCL) or a combination of these; considering its key role, characteristics of layer D will be discussed more extensively below. Layer E is the support layer placed on the reactive waste; the granular material used here may also act as a capillary break that prevents upward or downward moisture movement.

The thickness of the different layers may vary, from a few mm (in the case of a GM) to more than one meter (Aubertin et al. 2002, 2015). The different layers thicknesses must be optimized as these significantly affect the efficiency and cost of the cover.

Infiltration barrier

As stated above, a multilayered cover can be designed to prevent water inflow. In this case, Layer D would typically be made of a fine grained soil (such as a compacted clay layer, CCL), a geomembrane (GM), a geosynthetic clay liner (GCL), or a combination of two of these.

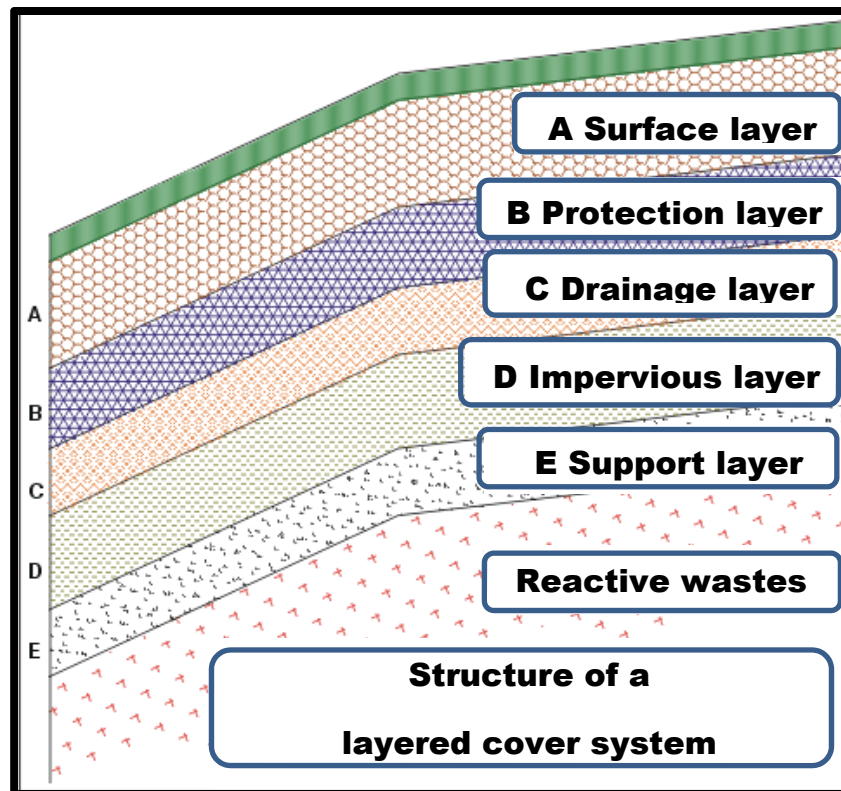


FIG. 1. Configuration of a cover with five layers made of different materials (adapted from Aubertin et al. 1995, 2002)

In the case of soils, care must be taken to select one that is not prone to permanent cracking when exposed to wetting-drying or freezing-thawing cycles. Many plastic clays are susceptible to these problems, so they should be avoided as much as possible when the climatic conditions are critical (Aubertin and Chapuis 1991; Aubertin et al. 1995, 2002). Low plasticity silts may be preferable in many cases (even if they are often somewhat more pervious) because cracks induced in these materials tend to heal upon rewetting. Along the same line, non-acid generating tailings can constitute a good alternative as they often have the required properties to perform well (Aubertin et al. 1995; Bussi re 2007); they may also be cheaper and easier to put in place than clays.

Geomembranes are sometimes used as an impervious layer, but many concerns have been raised regarding their use in covers, particularly regarding the presence of defects and wrinkles which may significantly diminish their efficiency (Rowe et al. 2012; Aubertin et al. 2015). The effect of settlements and risk of sliding along the

slopes are other major concerns (Aubertin et al. 1995, 2002). These issues and others have influenced regulators who now often require double-layer protection with a GM.

But the main objection regarding the use of a geomembrane in covers for acid generating mine sites is their limited lifetimes, which is usually expressed in decades (Koerner et al. 2011; Rowe et al. 2014; Rowe and Ewais 2015). Such fairly short lifetimes are not compatible with the very long term requirements for such cover.

Geocomposite clay liners (GCL), made with bentonite and geotextiles, constitute another alternative for the impervious layer. In this case, attention must be paid to potential problems with the GCL uniformity and integrity, low friction angle, limited efficiency against oxygen diffusion, and the risk of in-situ alteration of their physicochemical properties (Aubertin et al. 2000, 2015; Benson and Scaliar 2008; Liu et al. 2013).

In addition to non-acid-generating tailings, other alternative materials have also been considered (and used) in covers, including pulp and paper or deinking residues, and other types of industrial waste. Documented cases are however relatively scarce and many of these raise serious questions. Each material must thus be assessed in details to meet robust design criteria.

Water retention covers

Under relatively dry climatic conditions, it is possible to design the cover so infiltration water would be stored in the layer close to the surface, and then released during dry spells by evaporation. Such so-called store-and-release (SR, or alternate) covers have been shown to be quite efficient at reducing the quantity of water reaching the underlying waste, provided that the right materials are used to create the required capillary barrier effect (described below) and storage capacity. This type of cover has been constructed at the Barrick Goldstrike operation in Nevada, USA (Zhan et al. 2000), and also applied within experimental cells at the Kettara mine, Morocco (Bossé et al. 2015).

The amount of precipitation (recharge) that can be handled by this type of cover is however limited, so it is usually not appropriate for horizontal covers under humid climates.

For inclined surfaces, moisture retaining covers can be designed to divert part of the infiltrating water toward the side and base of the slope. Such Store-Divert-Release (SDR) covers also take advantage of the unsaturated materials properties to accumulate water in a retention layer, and then force it to flow along the slope until discharge and evaporation reduces the water content. A SDR cover has been constructed on the slope of a heap leach pad at the Barrick Goldstrike operation (Zhan et al. 2001, 2014). The main design criterion in this case is the diversion length (LD), which is illustrated on Fig. 2. This length is associated with the down dip limit (DDL; Ross 1990; Stormont 1996; Zhan et al. 2001; Aubertin et al. 2009). It depends on the different materials hydrogeological properties (i.e. water retention curves and hydraulic functions; see Fig. 3 discussed below), the amount of water (precipitation) to be handled, the thickness (and available porosity) of the layers, and the inclination angle of the surface (Aubertin et al. 2009). The cover design must be adapted to the local conditions, which may require some innovative configuration. It may not be an appropriate solution for all situations; again, specific analyses must be

conducted to ensure the satisfactory cover performance to control the production of AMD.

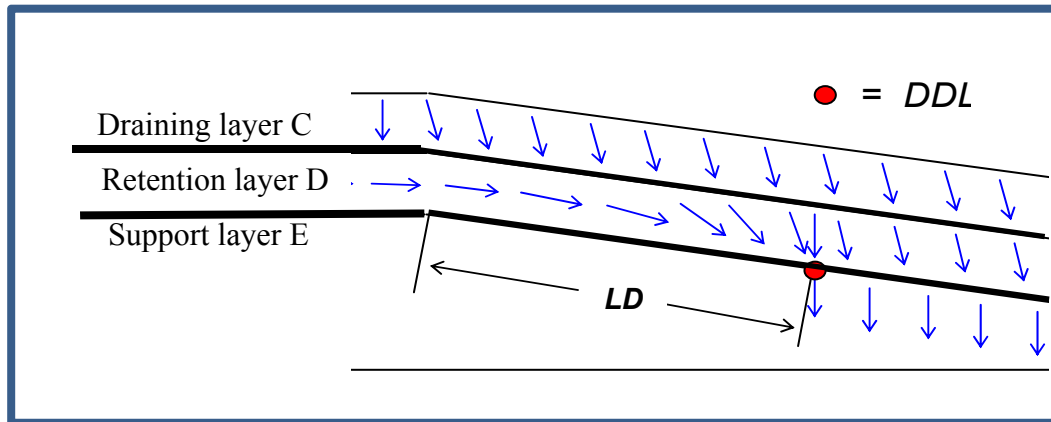


FIG. 2. Schematic representation of the water flow along an inclined SDR cover made of a coarse draining layer (C) placed on a moisture retention layer (D) and a coarser material layer (E) (adapted from Bussi re 1999 and Aubertin et al. 2009).

Oxygen barrier

For regions having a relatively humid climate (with a highly positive annual water budget), it is often more efficient and economical to design the layered cover system to create a barrier against oxygen ingress (Aubertin et al. 2002, 2006).

GM and GCL can, in principle, prevent oxygen migration, but the limitations mentioned above makes these materials less attractive than other alternatives. In practice it is usually preferable to use thick layers made of more durable geomaterials to create an oxygen barrier. The most efficient and practical means is to use a water retention layer that maintains a high degree of saturation at all time, so it can efficiently limit the oxygen flux (by advection and diffusion). To do so, it is usually required to select a material that will be able to create a capillary barrier in the cover above the water table (under unsaturated conditions).

A cover with capillary barrier effects (CCBE) is typically made of layers of materials with distinct hydrogeological properties (Aubertin et al. 1995, 2002, 2006; Bussi re et al. 2003). Water retention in a CCBE is mainly associated with capillary and adhesion forces which are typically more pronounced in unsaturated soils with a finer pore structure.

This is illustrated with the schematic representation of the water retention curves and hydraulic functions shown in Fig. 3 for a coarse grained soil (sand) and a finer grained soil (silt). Fig. 3a shows that the silt has a greater volumetric water content θ (and thus a larger water retention capacity) compared with the sand, at a given suction; this translates into a larger air entry value (AEV or ψ_a) and water entry value (WEV or ψ_r) for the silt. The higher moisture content, at a given suction, means that the unsaturated hydraulic conductivity of the silt is also larger (Fig. 3b).

In a CCBE, the upper fine-grained soil (i.e. layer D in Fig. 1 and 2), located above a coarser material (layer E) that easily desaturates, tends to store moisture

coming from the surface as water does not easily move downward into the underlying material due to its low hydraulic conductivity at the reduced volumetric water content (or degree of saturation). Water then tends to accumulate in the moisture retaining layer (MRL) until the negative pressure (suction) at the interface approaches the water entry value WEV (or ψ_r) of the coarse-grained material. The WEV corresponds, on the water retention curve (WRC), to the suction ψ at which water starts to penetrate significantly into the material on a wetting path; this suction is reached at the residual water content θ_r of the coarse grained material (Fig. 3a). Once water moves across the interface, it progressively increases the degree of saturation and hydraulic conductivity of the coarser material (Fig. 3b), hence dissipating the capillary barrier effect.

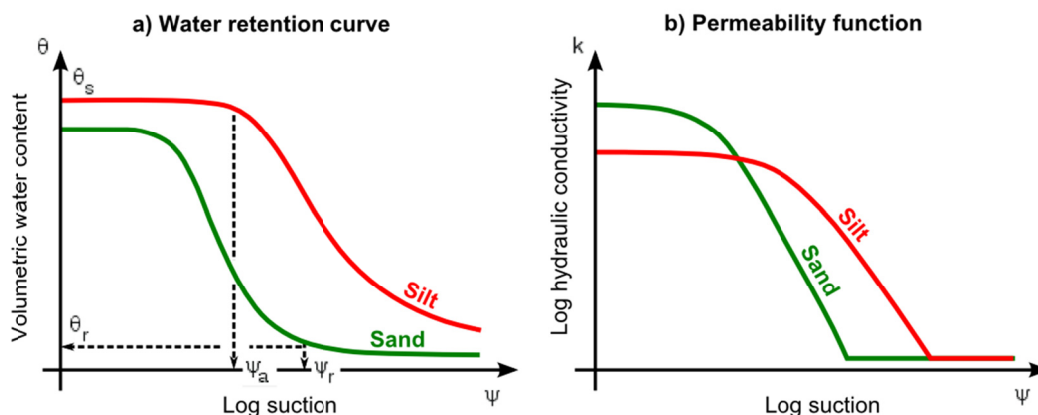


FIG. 3. Schematic hydraulic functions for a fine grained soil (silt) and a granular soil (sand).

An efficient CCBE constructed on a relatively flat surface will be able to maintain a high degree of saturation (> 85 to 90%) over time in the fine-grained, water retention layer (D). This greatly reduces the air permeability in this material (to almost zero) and it significantly diminishes the oxygen diffusion flux F_{O_2} across the moisture retaining layer. Oxygen diffusion can be expressed using the first Fick's law (e.g. Mbonimpa et al. 2003):

$$F_{O_2} = - D_e (\partial C_{O_2} / \partial Z) \quad [2]$$

where the term in parentheses represents the oxygen concentration (C_{O_2}) gradient, over vertical distance (Z -axis), from the surface to below the cover. This diffusive flux depends directly on the value of the effective diffusion coefficient D_e , which in turn varies with the degree of saturation S_r , as illustrated in Fig. 4. The value of D_e is reduced by orders of magnitude when the material goes from a low to a high degree of saturation (Aubertin et al. 1995, 2000, 2006; Aachib et al. 2004). An oxygen barrier is effective when the moisture retaining layer is highly saturated. When the CCBE is well designed and constructed, it can reduce the oxygen flux by more than 99% (compared with exposed tailings), to values below 1 mole $O_2/m^2/year$

(Mbonimpa et al. 2003; Bussière et al. 2003, 2006). This is usually sufficient to effectively control the production of AMD.

Maintaining a high degree of saturation on the relatively flat (almost horizontal) surface of a tailings impoundment is fairly straightforward, but the situation can be quite different along sloping areas such as on tailings dikes and waste rock piles. In this case, care must be taken to assess the possible desaturation of the moisture retaining layer uphill, due to the movement of water induced by the downhill hydraulic gradient (Aubertin et al. 1999; Bussière et al. 2003).

Figure 5 shows a picture of the LTA site located in Abitibi, Québec, Canada, during cover construction. This CCBE was constructed about 20 years ago and it has been monitored, demonstrating that such a cover can be efficient as an oxygen barrier (Bussière et al. 2006). Another somewhat similar layered cover has been successfully applied at the Lorraine mine site, near Latulippe, Québec, Canada (Aubertin et al. 2006).

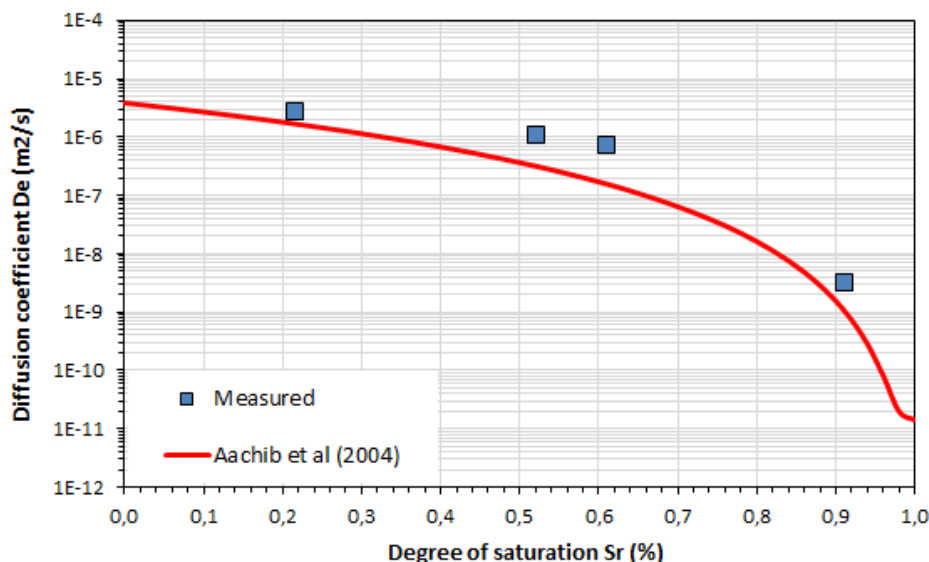


FIG. 4. Value of the effective diffusion coefficient of oxygen D_e based on diffusion tests on silty tailings and on the predictive model of Aachib et al. (2004) (adapted from Pabst 2011).

In addition to the various types of materials and cover configurations mentioned above, it is also possible to use oxygen consuming materials (such as wood chips or low sulfide tailings) to build (part of) a cover. Although these can perform well in the short term, the efficiency of such type of cover tends to diminish over time with the depletion of the oxygen consumption potential.

WATER COVERS AND ELEVATED WATER TABLE

Covering reactive mine wastes with water has long been used to control the production of AMD. The low solubility of oxygen combined with its low diffusion coefficient in water make this a potentially very efficient technique. In practice, this technique has mainly been applied to tailings, such as at the Louvicourt and Solbec-

Cupra mine sites in Québec, Canada (Aubertin et al. 2002). It may require the addition of impervious material along the base (liner) and sides (dikes) of the impoundment. It can also be applied to waste rock under specific circumstances.

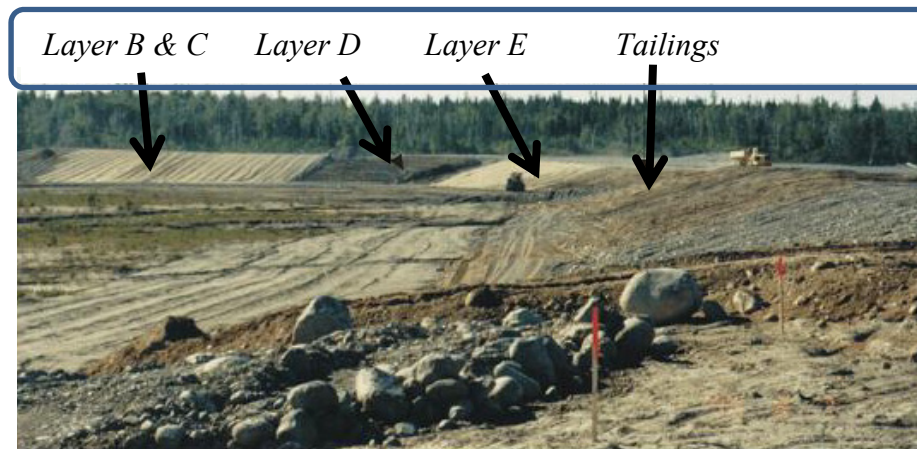


FIG. 5. The LTA tailings disposal site during the construction of a CCBE made of three layers (adapted from Aubertin et al., 2002)

Reactive mine wastes can be deposited immediately under water, thus preventing oxidation from the start, or they can be flooded at a later time during the mine life. Using existing lakes and rivers is tempting, but this practice is often regulated (prevented) by governmental agencies. Hence, engineered structures must usually be constructed to retain the aqueous cover, which must be thick enough to prevent resuspension of the fine grained particles (Li et al. 1997; Yanful and Catalan 2002). The main challenge in this case is to ensure the long term physical (geotechnical) stability of the retaining structures, over an indefinite lifespan (Aubertin et al. 1997, 2002, 2011). As such long term conditions may induce unavoidably high risks for (catastrophic) failure, due to the increasing probability of exceeding the system capacity over time, regulators are now often reluctant to allow the application of this technique if it involves the construction and maintenance of man-made structures.

An alternative is to dispose of the reactive wastes in open pits with stable slopes. This technique has been applied with success at the Don Rouyn site in Abitibi (QC, Canada). In this case, the analysis and design must take into account contaminants migration in the fractured rock mass surrounding the wastes (Aubertin et al. 2015).

Like for all the other types of covers, water (aqueous) covers require extensive monitoring and site surveillance.

A somewhat similar but often more advantageous alternative to water covers is to use an elevated water table (EWT) to prevent tailings oxidation. This technique consists of raising the phreatic surface to a depth less than the height of the saturated capillary fringe in the tailings, i.e. $h < AEV$, as illustrated in Fig. 6 (Aubertin et al. 1999; Ouangrawa et al. 2010; Pabst 2011). Raising the water table is easier when the impoundment was designed to prevent exfiltration. For other cases, it can be done by modifying the water balance of the site, by increasing the water retention capacity of the tailings, or by decreasing the lateral flow of groundwater (Orava et al. 1997).

A monolayer cover made of coarse-grained material is placed above the tailings to increase water infiltration, reduce run-off, and limit water loss by evaporation; such is the case at the Aldermac mine site, Québec, Canada. For sufficiently humid conditions, a fine-grained material (such as tailings that don't produce AMD) can alternatively be used to form the cover, as shown at the Manitou-Goldex mine site, Québec, Canada (Ethier et al. 2013).

A well designed EWT with a monolayer cover has many advantages over a full water cover, including lower pore water pressures in the dikes and foundations, reduced downward and lateral seepage flow, absence of water movement due to the wind (which tends to increase oxygen availability in a water cover), and the strength gain of tailings submitted to suction (negative pore water pressure) in the vadose zone. The free board is also increased (by up to a few meters) by avoiding free water on the surface. Maintenance of the site can also be simpler and less costly than for other types of covers.

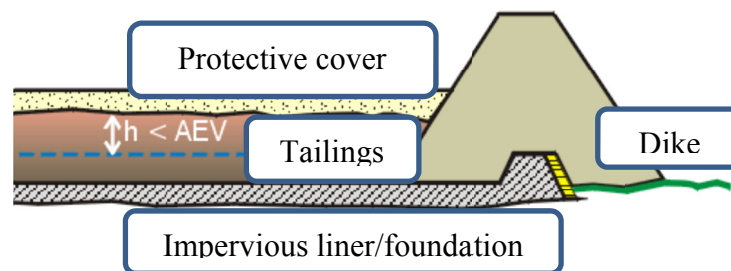


FIG. 6. Schematic view of an elevated water table in a tailings impoundment, with a protection layer made of coarse grained material (adapted from Aubertin et al. 1999).

OTHER COMPONENTS OF THE RECLAMATION PROGRAM

Closure and reclamation of AMD generating sites requires careful planning, rigorous design, and good construction methods. The program also involves many other aspects to complement the main elements of the reclamation works described above. For instance, the establishment of vegetation on the surface of the disposal site is often needed to control erosion, and it is sometimes a requirement included in the regulations. In this case, the effect of the vegetation on the engineered works must be carefully assessed. For example, deep rooting systems may be detrimental for the efficiency of a CCBE acting as an oxygen or water infiltration barrier. Interaction between deep roots and underground water with the EWT must also be considered. A positive contribution of the vegetation to evapotranspiration may be beneficial for store-and-release covers, and also for improving slope stability, but these need to be assessed on a case by case basis (e.g. Cooke and Johnson 2002). Again, this is easier to do when planned in advance.

During the operation and upon closure of mine wastes disposal sites, engineered works and their surroundings must be instrumented and monitored closely. In the case of AMD generating wastes, monitoring must last for a very long time. The

efficiency of the various techniques described above usually requires that specific characteristics be measured on the site, including the depth of the water table (or the pore water pressures near the base of the site), the quality of the surface and underground water, and the settlements and displacements of the various components. The efficiency of the reclamation works also requires specific measurements that should involve the volumetric water content and (negative) pore water pressures near the surface; oxygen concentrations and fluxes also need to be assessed to evaluate the cover efficiency (Aubertin et al. 1999; 2002, 2015; Bussière et al. 2006; Dagenais et al. 2012). The various instruments developed for these types of measurements must be properly installed and maintained so that they can provide reliable information.

Monitoring goes hand in hand with a regular inspection program. All the main components must be targeted during visits from the (independent) specialists involved in evaluating the site conditions and the performance of the reclamation (and related) works. The information gathered from field observations and instrumentation, and comparisons with initial design considerations (assumptions), must be well documented and permanently filed in several places. Corrective measures, when needed, must be applied swiftly, and rigorously.

An emergency plan is also required during the mine operation and upon closure. It must identify all the possible (potential) problems (even the least likely) and the actions to be taken; these must be planned and prepared in advance, by identifying the responsibilities and the resources required (Aubertin et al. 2002, 2011, 2015).

INTERGRATED MINE WASTES MANAGEMENT AND RECLAMATION

Mining is a rapidly evolving industry, and mine waste management practices are expected to progress at the same pace as other technological components. Although much work has been conducted in recent years, some components still lag behind. This is particularly the case with applications of the general principle of “Designing for closure”. As discussed in more details elsewhere (Aubertin et al. 2015), there is often a large gap between the overall objectives of mining companies and the actual measures taken to improve mine wastes management. This is particularly the case when it comes to taking preventive measures to control AMD from the initial stages of the operation.

Many tools and techniques now exist to help with the management of such reactive wastes. Some take advantage of recent developments that favor the integration with other components of the mining operation (Bussière 2007; Benzaazoua et al. 2008). In this regard, environmental desulfurization of the tailings at the mill is a very promising avenue that allows the separation of the reactive fraction, which can then be managed separately from the (often larger) non-acid generating fraction. The former can for example be returned in underground stopes as cemented paste backfill, while the latter can be used to construct single or multi-layer covers (Benzaazoua et al. 2008).

Backfilling with tailings (as hydraulic or paste fill) or waste rock (as rock fill or to construct barricades) is another option that reduces the amount of waste on the surface, while improving ground stability and ore dilution in underground operations (Aubertin et al. 2002, 2011; Benzaazoua et al. 2008). Placing the reactive wastes in

open pits is another option, but care must then be taken to prevent contaminants migration in the surrounding fractured rock mass and groundwater.

Non-reactive waste rock can also be used to construct one (or more) layer(s) in the cover system (i.e. infiltration layer with the EWT or capillary break layer(s) in a CCBE), in addition to their regular use to construct dikes around tailings impoundments.

Another promising avenue involves the construction of waste rock inclusions (WRI) in tailings impoundments to increase the rate of drainage and dissipation of excess pore water pressures and to improve the geotechnical stability of the dikes under static or dynamic (earthquake) loadings (James et al. 2013); this technique is illustrated in Fig. 7. When the waste rocks are reactive, it is also possible to prevent contact with atmospheric oxygen by maintaining an elevated water level in the tailings. A cover can be added on the surface at the end of operations.

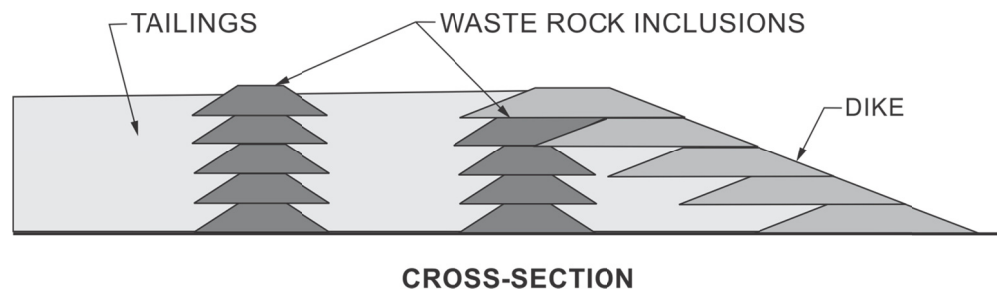


FIG. 7. Schematic illustration of waste rock inclusions in tailings (WRI); a cover can be added on top to control AMD (adapted from James et al. 2013)

When only a part of the waste rock can be placed as WRI in the impoundment (or returned underground as backfill), the remaining waste rock usually has to be placed in piles. In such cases, the waste rock pile should be designed and constructed to ensure the geotechnical and geochemical stability (Aubertin 2013). The construction of reactive waste rock piles must be well documented and monitored.

CONCLUDING REMARKS

Acid generating mine wastes raise many technical, operational and financial challenges for the industry. The costs and efficiency of the reclamation program can be optimized through early and careful planning, and by integrating into operations measures that will facilitate closure and maintenance of the site in the long term. Too often however, the reclamation program is initially limited to conceptual views, proposed in the early stages of the mine, but which are rarely updated sufficiently to establish a detailed reclamation program. This lack of detailed planning can have major economic and environmental consequences upon mine closure. There is also a tendency of idealizing (simplifying) the work to be done and to minimize the challenges and difficulties that will be encountered upon closure. Accounting practices, often based on a Net Present Value analysis (or a variant of it), may also create additional challenges as these often consider postponing investments (seen as

“expenses”) as a way to increase the short term profits of the operation, while underestimating the negative effect that this may have in the long term.

The exceptionally long duration of the works that need to be constructed and maintained is a real challenge when the tailings or waste rocks are prone to produce AMD. Such works need to be designed to resist long term conditions that may affect the material strength and the loading conditions, and hence their factor (and margin) of safety (Aubertin et al. 2011). It can then be asked how will these disposal sites be maintained in the long term, and by whom? Like all corporations, mining companies have a limited operating life (of a few decades in most cases), while governmental agencies may not have the resources to take care of these sites (even when some funding is put aside for this purpose). This is an important issue that may greatly affect the social acceptability of future mining operations. A review of current practices seems to be required in this regard; the authors and their collaborators are directly involved in this process.

ACKNOWLEDGEMENTS

This work is supported by RIME (www.rime-irme.ca/en/)

REFERENCES

- Aachib, M., Mbonimpa, M. and Aubertin, M. (2004). “Measurement and prediction of the oxygen diffusion coefficient in unsaturated media, with applications to silt covers”. *Water, Air and Soil Pollution.*, 156 : 163-193.
- Anawar, H. Md. (2015). “Sustainable rehabilitation of mining waste and acid mine drainage using geochemistry, mine type, mineralogy, texture, ore extraction and climate knowledge.” *J. Environmental Management*, 158:111-121.
- Aubertin, M., and Chapuis, R.P. (1991). "Considérations hydro-géotechniques pour l'entreposage des résidus miniers dans le nord-ouest du Québec". *Proc. 2nd Int. Conf. On Reduction of Acid Rock Drainage*, Montreal, Canada, Vol. III, 1-22.
- Aubertin, M., Chapuis, R.P., Aachib, M., Bussière, B., Ricard, J.F., and Tremblay, L. (1995). *Évaluation en laboratoire de barrières sèches construites à partir de résidus miniers*. École Polytechnique de Montréal, MEND Report 2.22.2a.
- Aubertin, M., Dionne, J., and Marcoux, L. (1997). “Design guidelines and stability criteria of engineering works for water covers.” *Proc 4th Int. Conf. on Acid Rock Drainage*, Vancouver, BC, Canada, Vol. 4, 1851-1866.
- Aubertin, M., Bussière, B., Monzon, M.,..., Chapuis, R.P., and Bernier, L. (1999). *Étude sur les barrières sèches construites à partir des résidus miniers. Phase II-Essais en place*. École Polytechnique de Montréal, MEND Report 2.22.2c.
- Aubertin, M., Aachib, M., and Authier, K. (2000). “Evaluation of diffusive gas through covers with a GCL”. *Geotextiles and Geomembranes*, Vol. 18 : 1-19.
- Aubertin, M., Bussiere, B., and Bernier, L. (2002). *Environnement et gestion des rejets miniers*. Manual on CD-Rom, Presses Int. Polytechnique. Montreal., QC, Canada.
- Aubertin, M., Molson, J., Bussière, B., and Dagenais, A.M. (2006). “Investigations of layered cover systems acting as oxygen barriers to limit acid mine drainage”. *Proc. 5th Int. Conf. Environmental Geotechnics*, Cardiff , UK., Vol. 2, 827-835.

- Aubertin, M., Cifuentes, E., Apithy, S., Bussière, B., Molson, J. and Chapuis, R.P. (2009). "Analyses of water diversion along inclined covers with capillary barrier effects". *Canadian Geotechnical J.*, 46: 1146-1164.
- Aubertin, M., Bussière, B., James, M.,...Mbonimpa, M., and Chapuis, R.P. (2011). "Vers une mise à jour des critères de stabilité géotechnique pour la conception des ouvrages de retenue de résidus miniers" *Proc. Symp. Mines and Environnement*, Rouyn-Noranda, QC, CIM (CD Rom), 38 p.
- Aubertin, M., Pabst, T., Bussière, B. James, M. Mbonimpa, M., Benzaazoua, M., and Maqsoud, A. (2015). "Revue des meilleures pratiques de restauration des sites d'entreposage de rejets miniers générateurs de DMA". *Proc. Symp. Mines and Environnement*, Rouyn-Noranda, QC, CIM (CD Rom), 67 p.
- Aubertin, M. (2013). "Waste rock disposal to improve the geotechnical and geochemical stability of piles". *Proc. 23rd World Mining Congress*, Montreal, 8 p.
- Benson, C.H., and Scaliar, J. (2008). "Field performance of GCLs used as hydraulic barriers in caps" *Proc. Symp. Mines and Environnement*, Rouyn-Noranda, QC, CIM (CD Rom), 12 p.
- Benzaazoua, M., Bussière, B., Demers, I., Aubertin, M., Fried, E., and Blier, A. (2008). "Integrated mine tailings management by combining environmental desulphurization and cemented paste backfill: Application to mine Doyon, Quebec, Canada." *Minerals Engineering*, 21 : 330-340.
- Bossé, B., Bussière, B., Hakkou, R., Maqsoud, A., and Benzaazoua, M. (2015). "Field experimental cells to assess the hydrogeological behaviour of store-and-release covers made with phosphate mine waste". *Canadian Geotechnical J.*, 52 : 1-15.
- Bussière, B (1999). "Étude du comportement hydrique de couvertures avec effets de barrière capillaire inclinées à l'aide de modélisations physiques et numériques." Ph.D. Thesis, École Polytechnique de Montréal, 354 p.
- Bussière, B., Aubertin, M. and Chapuis, R.P. (2003). "The behavior of inclined covers used as oxygen barriers." *Canadian Geotechnical J.*, 40: 512-535.
- Bussière, B., Maqsoud, A., Aubertin, M., Martschuk, J., McMullen, J., and Julien, M. (2006). "Performance of the oxygen limiting cover at the LTA site, Malartic, Quebec". *CIM Bulletin*, 99(1096) : 1-11.
- Bussière, B. (2007). "Colloquium 2004: Hydro-geotechnical properties of hard rock tailings from metal mines and emerging geo-environmental disposal approaches." *Canadian Geotechnical J.* 44(9): 1019-1052.
- Cooke J.A., Johnson, M.S. (2002). Ecological restoration of land with particular reference to the mining of metals and industrial minerals: A review of theory and practice. *Environ. Rev.* 10: 41-71.
- Dagenais, A.M., Mbonimpa, M., Bussière, B. and Aubertin, M. (2012). "The modified oxygen consumption test to evaluate gas flux through oxygen barrier covers." *Geotechnical Testing J.* ASTM, 35(1) : 150-158.
- Ethier, M.P., Bussière, B., Aubertin, M., Maqsoud, A., Demers, I., and Lacroix, R. (2013). "In situ evaluation of the elevated water table technique combined with a monolayer cover on reactive tailings: monitoring strategy and preliminary results." *GeoMontreal 2013: Proc. 66th CGS Conference*, Montreal, Canada, 9 p.
- INAP (International Network for Acid Prevention).(2012). "Global Acid Rock Drainage (GARD) Guide". <<http://www.gardguide.com>>.

- James, M., Aubertin, M., and Bussière, B. (2013). "On the use of waste rock inclusions to improve the performance of tailings impoundments". *Proc. 18th Int. Conf. on Soil Mechanics and Geotechnical Engineering*, Paris, France, 735-738.
- Kleinmann, R.L.P., Crerar, D.A., and Pacelli, R.R. (1981). "Biogeochemistry of acid mine drainage and a method to control acid formation". *Mining Engineering*, March 81:300-304.
- Koerner, R.M., Hsuan, Y.G., and Koerner, G.R. (2011). "Geomembrane lifetime prediction: Unexposed and exposed conditions". *GRI White Paper #6, Geosynthetic Institute*, Updated, February 2011, 27 p.
- Li, M., Aubé, B., St-Arnaud L. (1997). "Considerations in the use of shallow water covers for decommissioning reactive tailings." *Proc. 4th Int. Conf. on Acid Rock Drainage*, Vancouver, Canada, Vol I: 117-130.
- Liu, Y., Gates, W.P. and Bouazza, A. (2013). "Acid induced degradation of the bentonite component used in geosynthetic clay liners." *Geotextiles and Geomembranes*, 36:71-80.
- Mbonimpa, M., Aubertin, M., Aachib, M., and Bussière, B. (2003). "Diffusion and consumption of oxygen in unsaturated cover materials". *Can. Geot. J.* 40: 916-932.
- MEND (2004). *Design, construction and performance monitoring of cover system for waste rock and tailings*. Report 2.21.4. Ottawa, Canada.
- Orava, A.D., Tremblay, G.A., Tibble, A., and Nicholson, R. (1997). "Prevention of acid rock drainage through application in-pit disposal and elevated water table concepts." *Proc. 4th Int. Conf. on Acid Rock Drainage*, Vancouver, Vol. 3, 973-983.
- Ouangrawa, M., Aubertin, M., Molson, J., Bussière, B., and Zagury, G.J. (2010). "Preventing acid mine drainage with an elevated water table: Long-term column experiments and parameter analysis". *Water, Air and Soil Pollution*, 213 : 437-458.
- Pabst, T. (2011). "Étude expérimentale et numérique du comportement hydro-géochimique de recouvrements placés sur des résidus sulfureux partiellement oxydés." PhD Thesis, Ecole Polytechnique de Montréal, Canada, 582p.
- Robertson, A. A. (2011). "Top 10 things that can go wrong with plans for mine closure." *Proc. Int. Conf. on Mine Closure*, Lake Louise.
- Ross, B. (1990). "The diversion capacity of capillary barriers". *Water Resources Research*, 26: 2625-2629.
- Rowe, R.K., Yang, P., Chappel, M.J., Brachman, R.W.I, and Take, W.A. (2012). "Wrinkling of a geomembrane on a compacted clay liner on a slope." *Geotechnical Engineering Journal*, SEAGS & AGSSEA, 43(3): 11-18.
- Rowe, R.K. Abdelaal, F.B., Islam, Z. (2014). "Ageing of high-density polyethylene geomembranes of three different thicknesses." *J. Geotechnical and Geoenvironmental Engng*, 11 p.
- Rowe, R.K., and Ewais, A.M.R. (2015). "Ageing of exposed geomembranes at locations with different climatological conditions". *Canadian Geotechnical J.*, 52: 326-343.
- Singer, P.C., and Stumm, W. (1970). "Acid mine drainage: The rate determining step." *Science*, 167:1121-1123.
- SRK (1989) *Draft Acid Rock Drainage Technical Guide*. BCAMD Task Force.
- Stormont, J.C. (1996). "The effectiveness of two capillary barrier on a 10% slope". *Geotechnical and Geological Engineering*, 14:243-267.
- Vick, S.G. (2001). "Stability aspects of long-term closure for sulphide tailings". *Proc. Safe Tailings Dams Constructions*, Gaellivare, Sweden, 12 p.

- Yanful, E.K., and Catalan, L.J.J. (2002). "Predicted and field measured resuspension of flooded mine tailings". *J. Environmental Engineering*, 128 : 341-351.
- Zhan, G.S., Mayer, A., McMullen, J., and Aubertin, M. (2000). "Capillary cover design for a spent leach pad". *Proc.Int. Symp. Hydrogeology and the Environment*, Wuhan, China Environmental Science Press, Beijing, 144-150.
- Zhan, G., Aubertin, M., Mayer, A., Burke, K., McMullen, J. (2001). "Capillary cover design for leach pad closure". *Transaction SME*, 310:104-111.
- Zhan, G., Keller, J., Milczarek, M., Giraudo, J. (2014). 11 Years of evapotranspiration cover performance at the AA leach pad at Barrick Goldstrike Mines. *Mine Water and the Environment*. DOI 10.1007/s10230-014-0268-6.

Tailings Disposal Challenges and Prospects for Oil Sands Mining Operations

Michel Aubertin, M.ASCE¹; and Gord McKenna²

¹Scientific Director, Research Institute on Mines and Environment; Professor, École Polytechnique, Montréal, QC, Canada H3C 3A7.

²Principal, Geotechnical Engineer, BGC Engineering Inc., Vancouver, BC, Canada V6Z 0C8.

Abstract: The tailings produced from using water to extract the bitumen from oil sands operations in Alberta, Canada, are deposited in ponds behind dykes. Several types of tailings accumulate in large ponds, including coarse tailings and fluid fine tailings generated from the main extraction processes, and froth treatment tailings generated when bitumen is cleaned. These ponds pose significant geotechnical and geo-environmental challenges during tailings disposal and for site reclamation. The main concerns are related to the slow consolidation and slow strength gain of tailings, the quantity, quality and fate of process-affected water, and the long term safety of dykes. This article recalls and discusses some of the key challenges related to tailings management technologies and identifies some prospects for the future, based on the main observations from a report recently produced by an expert panel for the council of Canadian academies.

INTRODUCTION

Surface mining is applied in the North Athabasca region of the oil sands, Alberta, Canada, where the bitumen ore lies within about 75 metres of the surface. This ore zone covers an area of some 4,800 km² (Fig. 1), of which 715 km² has thus far been disturbed. Surface mines currently account for half of bitumen production in this region. These operations use shovels and trucks, and also include bitumen processing facilities and tailings ponds, as illustrated schematically in Fig. 2. Outside the minable areas, in situ methods are used to access bitumen reservoirs, with the aid of steam, at depths below 200 metres. Upgrading facilities are used to partially refine bitumen that can be transported by pipelines. Each of these three processes has a distinct environmental footprint (CCA 2015); this article will concentrate on issues related to tailings produced by surface mines.

The bitumen ore (typically 10% bitumen by weight) involve extraction operations that use shovel excavators and haul trucks that are similar to other types of large-

scale open pit mines (e.g., coal, copper, iron). Most oil sands mines are typically much bigger, five to ten times the size of most large open pit mining operations.

The ore is crushed and transported by conveyor to a slurry preparation plant, where warm water and chemical aids (e.g., sodium hydroxide) are added to make a slurry that is then transported by pipeline. This process starts to liberate bitumen from the solid grains, breaking it into small droplets. The conditioned slurry is then discharged to large stationary primary separation cells where the bitumen floats to the top and is collected as bitumen froth, while the solids and process-affected water are discharged as tailings. Additional tailings result from the final froth treatment stage, which uses solvents to reduce bitumen viscosity and density and help remove the remaining solids and water. About 90% of the bitumen in the mined ore is recovered (CCA 2015).



FIG. 1. Oil sands deposit areas (orange) in Alberta, Canada (adapted from CCA, 2015).

The tailings are deposited behind dykes in tailings ponds (also called impoundments). The tailings slurry is comprised mainly of quartz sand with fine (silt and clay) particles, residual bitumen, connate water, and the water used for hydrotransport and extraction. Several types of tailings accumulate in tailings ponds including coarse tailings and fluid fine tailings generated from the main extraction processes, and the froth treatment tailings (CTMC 2012). Coarse-grained tailings (mostly sand) are used for dyke building or form the tailings beach. The fluid fine tailings segregated slurry of water with silt and clay particles) with some residual bitumen largely remain in suspension in the ponds and accumulate over the mine life. As a result, large tailings ponds are required for storage of fluid fine tailings, posing a significant challenge for reclamation. In 2011, the Government of Alberta estimated that the total surface covered by tailings ponds was 182 km² (including dykes and other structures but excluding reclaimed coarse or fine tailings). Of this area, 830 million cubic metres of fluid tailings cover approximately 77 km² (CAPP 2014).

All disturbed land is to be reclaimed progressively and returned to equivalent land capability that existed prior to development. Such regulation however raises a number of significant geo-environmental challenges. Specific concerns over tailings disposal sites are related to the large areas of land disturbance, the tailings characteristics, and the quantity, quality, and fate of process-affected water (in the tailings pores and as free water on the ponds). Additional hazards include dusting from tailings sand beaches and the risk of catastrophic dam breaches (CCA 2015).

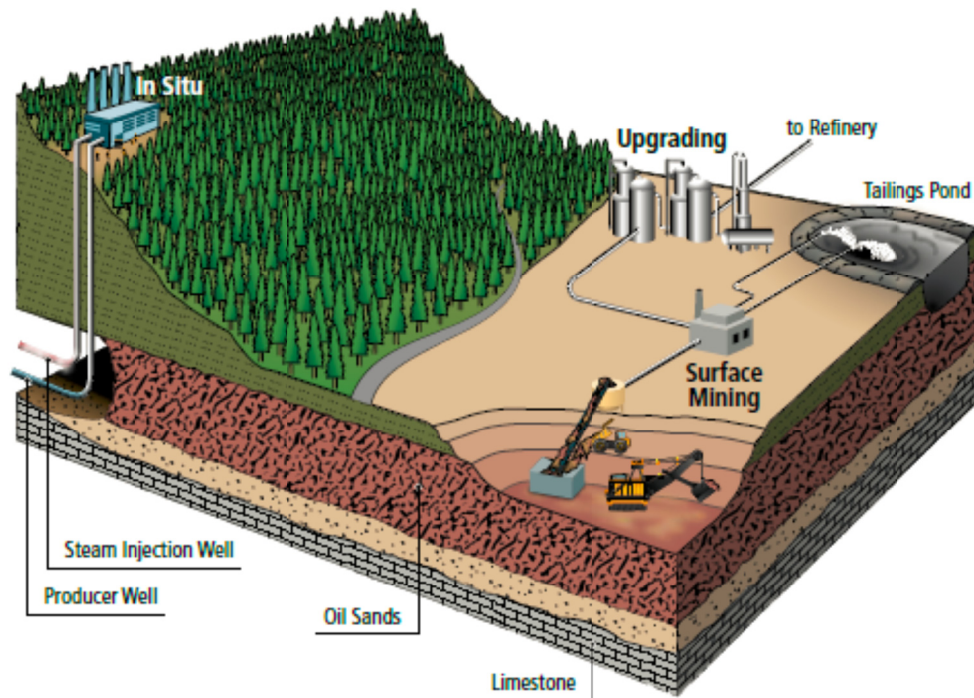


FIG. 2. Simplified illustration of bitumen extraction and processing (CCA 2015).

This article summarizes sections from a report on the environmental footprint of Canadian oil sands that focus on surface mining and tailings production; this report (available online) was produced by an Expert Panel assembled by the Council of Canadian Academies, and it describes the main challenges and some solutions to address problematic issues (CCA 2015). The authors were members of this Panel. The article reflects the authors' views on some of the key issues, including the need to better integrate tailings disposal and site reclamation with other components of oil sands mining operations, following an approach known in the industry as "Designing for Closure" (e.g. SRK 1989; Aubertin et al. 2002). The analysis of the situation indicates that there are major challenges and that there is no readily available solution to address some of the key problems. Promising work is underway to develop improved technologies that will help in the coming years, but the pace of technological development needs to be further increased to match and surpass the pace of oil sands development to provide timely solutions.

OVERVIEW OF THE MAIN CONCERNS

In addition to the solid grains and water, oil sands tailings contain a number of organic and inorganic compounds resulting from the extraction process, including naphthenic acids, phthalates, asphaltenes, benzene, phenols, cresols, humic and fulvic acids, and toluene. They also contain petrogenic PAHs, dissolved solids (sodium, chloride, sulphate, and bicarbonate), and metals (lead, mercury, arsenic, nickel, vanadium, chromium, and selenium). The concentration of these contaminants depends on the composition of the oil sands ore, the degree of water recycling, and the type of bitumen cleaning process used (either paraffinic or naphtha based). Among these, the most significant constituents of concern are the naphthenic acids and the salinity (CEMA 2014).

The froth treatment tailings are a small component of the tailings produced (2 to 4%), but raise specific concerns as they contain significant residues of the solvents (3 to 4 volumes per 1,000 volumes of bitumen produced) used to extract the bitumen. Froth tailings also have elevated concentrations of pyrite, naturally occurring radioactive materials, and some metals (CTMC 2012).

Some of these contaminants seep from tailings ponds because most tailings dykes are constructed from relatively pervious compacted tailings, while some ponds and dykes are constructed over sandy aquifers. In recent years, the groundwater issue has become more widely recognized (e.g. Morgenstern 2012; Kupper et al. 2013; Frank et al. 2014).

Another concern is the safety of the retaining structures. Around the world, tailings dam (dyke) failures occur at a rate of about 20 per decade (which is much higher than for other types of dams), often with tragic results for humans and the environment (Azam and Li 2010; Aubertin et al. 2011; Newland Bowker and Chambers 2015). The oil sands operations currently have dozens of large dykes, and their number should continue to grow. Even if their geotechnical performance has been good, there is nonetheless the need to actively manage the cumulative risk in the long term. One way to do so is to reduce their size, and hence the volume of tailings produced by oil sands mining operations.

These key issues, and a few others, are described in more details in the following sections; some solutions are also presented and discussed.

REDUCING TAILINGS VOLUME

Extensive work has been conducted on tailings properties since the 1960s (e.g. CTMC 2012; McKenna et al. 2013; Read 2014). Tailings ponds nonetheless remain an outstanding environmental and financial liability. The concerns are in part related to the accumulation of large amounts of fluid fine tailings, seepage of process-affected water from tailings ponds and the surrounding dykes, and the risk of a dyke breach (Morgenstern 2010, 2012; Kupper et al. 2013). Somewhat similar concerns also exist for other types of mining wastes (Vick 1990; Aubertin et al. 2002, 2011; CDA 2014). For oil sands, much of the efforts have been devoted to reducing the amount of tailings from the operations.

A range of tailings technologies have been implemented or are being tested to reduce the volume of tailings ponds by increasing the density (degree of

consolidation) of mature fine tailings. Each of these technologies is best tailored to particular geological and geotechnical conditions and tailings streams (CTMC 2012). Various classes of technologies have been identified (OSTC & COSIA 2012; CCA 2015), including the three main ones described here.

Thin-Layered Fines-Dominated Deposits are constructed with fine tailings streams that have sand-to-fines ratios of less than 1 and that are discharged subaerially into a disposal site in thin lifts, typically 100 to 500 mm thick. This technology involves initial tailings dewatering through chemical and mechanical treatment, followed by atmospheric evaporation and/or freeze-thaw effects. These dewatered tailings can either be moved to a permanent disposal site or left in place as part of a multi-layer deposit. In some cases, the soft material can be placed in polders designed into overburden disposal structures. In other cases, they may be capped with tailings sand or petroleum coke (another byproduct from bitumen upgrading). These thin-layered deposits are based on three specific technologies known as: i) Thin-Lift Dewatering of In-Line Flocculated Mature Fine Tailings, which involves pumping or dredging out mature fine tailings from a tailings pond and injecting flocculants into the tailings; ii) Centrifugation of Flocculated Mature Fine Tailings that involves pumping or dredging out mature fine tailings from a tailings pond, treating the fine tailings with flocculants and using a decanter centrifuge to separate the solids and water; iii) Thin-Lift Freeze-Thaw that consists of depositing mature fine tailings in thin layers submitted to natural freezing and thawing cycles. There are numerous operational challenges and expenses related to placement and drying of thin lifts, and subsequent capping.

Deep Fines-Dominated Deposits consist of a fluid fine tailings stream discharged on a continuous basis into a deep disposal site, which accumulates a significant thickness over time. Initial water release is accomplished with flocculants. The balance of water release and volume reduction occurs through self-weight consolidation, which is a very slow process. This densification allows modest strength gains with time. The surface will be capped, typically with sand, to provide a trafficable layer and add weight to improve consolidation of the upper part of the deposit. These fines-dominated deposits are generally favoured where in-pit area and volume are available. Thinner, out-of-pit deposits in a suitable containment structure may be necessary for new mine start-ups. However, the consolidation rates for thick deposits are slow, bearing capacities are extremely low, and post-reclamation settlements may be high. Specific tailings technologies considered for such deep deposits include: i) Thickened Tailings where the sand fraction is removed with hydrocyclones and the finer fraction is fed into thickeners with flocculants; ii) Accelerated (or rim ditch) Dewatering that involves a deep polymer treated fine-rich tailings deposit with a perimeter ditch that is slowly deepened over time to enhance drainage and densification, and fine tailings pumped and treated with a polymer to produce in-line thickened tailings deposited into an engineered cell; iii) Filtered Tailings applied to the whole (unaltered/coarse) tailings stream under a vacuum, using horizontally or vertically stacked plate, drums, or horizontal belts (or other techniques); iv) Centrifuged Tailings where the fine tailings streams are processed with scroll centrifuges to rapidly create a higher density centrifuge cake product.

Fines-Enriched Sands involve co-disposal of a coarse sand stream and a fines stream usually treated with coagulants or flocculants (Pollock et al 2000). When the fines are derived from mature fine tailings, the process is referred to as composite tailings or consolidated tailings. When the fines are derived from a thickener underflow, it is referred to as non-segregated tailings. These tailings form a deposit that has higher hydraulic conductivity and lower compressibility compared with fines dominated materials. The tailings consolidate over several years or decades to form sand-dominated deposits with fines in the pore spaces. Deposits are capped hydraulically with tailings sand soon after deposition, but remain potentially mobile (liquefiable) in the long term. Specific technologies considered for fines-enriched sands are : i) Composite Tailings which consists of mixing coarse and fine tailings streams, with a coagulant, to produce a non-segregating, semi-solid deposit that can be capped for reclamation; ii) Spiked Tailings that are fairly similar to composite tailings but involve adding a fines stream to a whole tailings stream without coagulant; iii) Enhanced Beach Capture aimed at increasing (50 to 75%) the amount of fines captured in the tailings sand beaches and dykes. Commercial implementation of these technologies has been difficult and results have been mixed.

These technologies help increase the density of the tailings in-situ, but they have not met the goals set by the regulations. Directive 074, issued by the Alberta government (AER 2009), committed operators to achieve a fines capture of 50% (in addition to that captured in hydraulically placed dykes and beaches) in dedicated disposal areas where they have to form trafficable deposits. This would have required dewatering tailings to approximately 70 to 80% solids content, which is greater than what has been achieved with the available technologies (OSTC & COSIA 2012; McKenna et al. 2013; Read 2014). Operators were unable to comply with the initial timeframe, and there is currently no single breakthrough (or “silver bullet”) technology that can significantly reduce the volume and improve the consolidation of fluid fine tailings (CCA 2015). A suite of technologies — if used together and tailored for particular geological and geotechnical conditions and tailings streams — may however improve tailings management and could provide a path to acceptable and timely reclamation (Read 2014; CCA 2015).

In March 2015, the Alberta government suspended Directive 074 and released a new framework entitled *Tailings Management Framework for the Mineable Athabasca Oil Sands* (Alberta Government, 2015). This new framework includes two important departures from Directive 074: recognition of the potential need to consider the regulated release of process-affected water to the environment, and requirements for a reduction of legacy tailings volume. These are discussed below.

WATER STORAGE AND SEEPAGE

Approximately 80 to 85% of water used on mine sites is recycled. There are however limits to recycling process-affected water as repeated extraction cycles contribute to a decline in water quality, which disrupts the extraction process by way of scaling, fouling, increased corrosivity, and chemical interference.

Large quantities of process-affected water are also stored in tailings ponds and will need to be dealt with at the time of mine closure, or perhaps before. The major challenges to reducing water impacts and the volume and composition of tailings

include the recovery rate of bitumen (currently around 90%). But as the quality of ore deposits declines, recovery rates are likely to diminish, which implies a larger amount of fine clays in tailings streams and a significantly greater loss of bitumen to tailings.

The regulations for oil sands operation require that all process-affected water must be contained on site (zero discharge) including rainwater run-off, seepage water, and water produced from interceptor wells used to minimize off-site seepage of process affected water. Despite the many precautions taken, it is now recognized that some process-affected water from fine- and coarse-grained tailings may seep through dykes, abutments, and foundations (Morgenstern 2012; Kupper et al. 2013; Frank et al. 2014; CCA 2015). The process-affected water seeping from tailings ponds and dykes can produce environmental impacts on soils, vegetation, wetlands, and streams; it also has the potential to affect the use of groundwater by others.

Tailings seepage from post-closure landscapes can also become an important long term issue, particularly when large amounts of water are retained in the deposition areas (e.g. Aubertin et al. 2002, 2011).

There are options for avoidance, source control, groundwater remediation, and groundwater flow system reconstruction (CCA 2015). Some of these options are based on well-known (proven) technologies, while others are still at the conceptual stage. Some of the greatest improvements for new operations would come from selecting and applying appropriate extraction and tailings disposal technologies and improving the quality of the process water during operation. Most options require a more robust design-for-closure practice for all aspects of tailings management. Closer collaboration of mine operators with the geotechnical, groundwater, and ecological risk assessment communities is needed to improve the state of practice for design, operation, and closure of these facilities.

Also, the need for discharge of suitably treated process-affected water, as is done in just about all other industries, is becoming increasingly apparent. In the absence of discharge standards, process-affected water will continue to accumulate on site, contributing to sprawl, tailings and water containment costs, increasing the risk of a tailings dam breach, and delaying reclamation. Treatment and discharge standards are ultimately required to improve tailings management and reduce the volume of tailings ponds (CCA 2015).

RISK OF A DAM BREACH

The risk of failure of large tailings dams (dykes) in the oil sands constitutes an element of the environmental footprint. Consequently, additional steps to reduce the risk (probability or consequences) would help reduce this footprint (CCA 2015).

In terms of dam safety and design, the track record of the oil sands industry has been good over the last 50 years. The operations have generally applied the best technologies and practices, and follow stringent safety guidelines (e.g. CDA 2014) for design, construction, monitoring, and maintenance (Eshraghian and Becker 2016).

There are nonetheless several areas of concern regarding the stability of oil sands tailings impoundments (Morgenstern 2010; Kupper et al. 2013). These include the complex geotechnical behaviour of tailings, particularly regarding volumetric

straining and pore water pressure, undrained shear strength and risk of (static) liquefaction (McKenna 1998) . There is also a concern about performance under extreme events, with low probability and significant consequences, like large earthquakes and precipitation events, which increase the risk of a dyke breach (Eshraghian and Becker 2016). Tailings ponds are vulnerable to various hazards including extreme weather and seismic events, and the risk evolves over time following an increasing cumulative probability (Vick 1990; Aubertin et al. 1997, 2002, 2011). On an annual basis, the highest risk for dam failure exists during construction and operation, but on an absolute (cumulative) basis, the risk of a breach can become much higher after closure due to the long time period of exposure when dams remain in the reclaimed landscape,. Evolution of the retaining structures (which naturally tend to degrade over time) can also increase the likelihood of a breach over a long time period.

Efforts to reduce the risks have been ongoing for decades, but these are challenged by the increasing number and size of operational tailings dykes, the decommissioning and de-licensing of these dams at closure (Oil Sands Tailings Dam Committee 2014), and the large volumes of water, fluid fine tailings, and other potentially mobile tailings stored behind dykes. The slow rates of consolidation and dewatering of fine tailings is a major obstacle because it means that their strength remains extremely low for a very long time, making them untrafficable for reclamation equipment while it increases their mobility in the event of a breach. Alternative technologies, complementary to those described above, could be used to improve the situation. For instance, inclusions made of coarse-grained materials to construct impoundments with different cells, accelerate drainage, add reinforcement, and help with progressive reclamation is being actively investigated in other types of mining operations (Aubertin et al. 2011; James et al. 2013); somewhat similar approaches may be applicable to tailings ponds from the oil sands operations.

Solvent-based extraction technologies constitute another promising avenue to reduce water use and the production of fluid fine tailings. But these are still in an early stage of development, with little to no information available on performance in large-scale operations, costs, environmental impacts from solvent release; new techniques to remove the residual solvents would also be required to advance this type of technology (CCA 2015).

A reduction of the absolute risk in the oil sands industry may also require more fundamental changes in tailings management. There is a need to improve design-for-closure practices for dykes and impoundments, minimize the number of dykes and other facilities requiring long-term maintenance, and plan for long-term maintenance of various elements of the closure landscapes (Morgenstern 2010, 2012; CCA 2015). Good closure planning is essential to creating tailings deposits that do not require containment dykes and to design dykes and tailings ponds that are easier to decommission and de-license and remain low risk at every stage of construction, operation, and closure.

END-PIT LAKES

End-pit lakes are artificial lakes that are created from mined-out pits after they have been partially backfilled with combinations of overburden, lean oil sands, and

coarse tailings. The remaining void is then converted into an end-pit lake by filling it with fluid tailings (in the case of about half of the proposed oil sands end pit lakes) capped with a thickness of 5 to 50 m of water (CEMA 2012). Once acceptable surface water quality is attained, outflow from surrounding terrain is established to emulate a natural lake system (OSTC & COSIA 2012).

End-pit lakes are expected to provide a natural source of bioremediation, whereby microorganisms break down naphthenic acids (CTMC 2012). The lakes are also predicted to act as bioreactors for process-affected water that seeps from the dykes over time so that the water is diluted and, with a long enough residence time, bioremediated to the extent that it can be released to the environment (CEMA 2012). Some view these lakes as adding a positive environmental footprint to the region, providing new land uses and allowing bioremediation of process-affected waters, potentially avoiding the need for long-term active water treatment. Others view end pit lakes, particularly those with fluid tailings, as having a strong negative environmental footprint (CEMA 2012).

Although industry is planning for and piloting end-pit lakes, this technology has yet to be proven and their use is experimental. A significant concern regarding end-pit lakes revolves around uncertainty in future ecological performance, specifically the quality of in-lake and discharge water (CEMA 2012). There are also risks associated with seepage and geotechnical concerns due to the long-term probability of failure associated with retaining a water cover in perpetuity (e.g., Aubertin et al. 1997, 2011). Long-term containment (geological and otherwise) for end-pit lakes, where large volumes of water and fluid tailings will be permanently stored, requires an even higher level of design safety and care.

In addition, while regulators call for walk-away solutions, the long-term risks posed by tailings and water are likely to require perpetual care and maintenance for some parts of these sites (Morgenstern 2012).

Because of these considerations (and others), stakeholders acceptance of end-pit lakes is not assured. The lack of water discharge criteria and the lack of dialogue on the potential for long term care and maintenance also stifle debate on alternatives or enhancements to end-pit lake technology.

OTHER ENVIRONMENTAL ISSUES AND PROSPECTS

Most oil sands operators currently deliver coarse and fluid fine tailings (from primary and secondary extraction) and froth treatment tailings (from the froth cleaning step) into the same tailings ponds. As previously mentioned, froth treatment tailings are a relatively small stream (only 2 to 4% of the total volume of tailings produced) but have some challenging properties because they contain residual solvents used to clean the bitumen. These hydrocarbons can migrate to the water table and are volatilized by microbial activity. These tailings also have elevated levels of sulphide minerals, which can result in acidic runoff/seepage if the tailings are allowed to oxidize, and also contain low levels of naturally occurring radioactive minerals (CTMC 2012). Some froth tailings segregate upon deposition to form very weak deposits that are untrafficable and prone to large post-reclamation settlement. This disposal method makes stabilization and reclamation of these areas of the tailings ponds much more challenging.

Removal of the residual solvent in froth tailings streams, together with discharging these streams into dedicated engineered containment cells, is a better strategy (CCA 2015). Operators must then keep the froth treatment tailings stream separate and treat it for return to the mine or to recover bitumen and metals. Separating the more toxic froth treatment tailings from the other more voluminous tailings streams and effectively treating this stream for return to the mine or to recover bitumen and metals would address two important tailings problems. It would reduce the potential impacts of solvents on groundwater, soils, and surface water over and around these deposits and reduce fugitive emissions resulting from decomposing solvent that remains in froth tailings after treatment.

FINAL REMARKS

Tailings are the sources of the most significant environmental impacts of surface mining. There is no single breakthrough technology that could be adopted over the next 15 years or less to significantly address these impacts (CCA 2015). Nonetheless, a combination of technologies, new and old — if used together and tailored for particular geological and geotechnical conditions and tailings streams — may constitute a “silver suite” of tailings management solutions that could provide the path to reduced sprawl, reduced risk, and more expedient reclamation.

A number of resource input, business, and regulatory factors may however impede the development and adoption of new technology. From a corporation’s perspective, investing in environmental technology is often perceived as a cost only, with limited benefit to the firm, which is predominantly accountable to its shareholders. Market forces alone often provide insufficient incentives, leading to firms underinvesting in environmental technologies relative to what is optimal from a societal perspective (CCA 2015).

The long technology adoption lead times (typically about 15 years), which are not unusual in resource industries, raise a particular problem because investments with long payback periods may not attract investors. Most firms use stringent investment criterion, going beyond a standard net present value, but their valuation typically implies that a present dollar is worth more than a future dollar (i.e., time value of money). In the context of oil sands, it follows that operators have an incentive to delay investment in tailings management and site reclamation since this investment yields no revenue and is relatively more costly in the present (CCA 2015). These types of valuation don’t adequately capture the cost of environmental liabilities or of the potential erosion of stakeholder and regulator confidence in a firm or the industry (Devenny 2010).

These factors tend to limit industry’s ability to respond to the central environmental challenge. They create a wedge between the potential of a technology and its actual impact on reducing the absolute environmental footprint. Under the current regulatory framework, firms may be reluctant to pay the premium to reduce the environmental footprint in the present when they can delay this expense into the future. This delayed investment increases the magnitude of the environmental footprint, which will have to be addressed later when revenues may be declining (or even non-existent). Indeed, when operators exit the industry, the public could be left

bearing costs of future cleanup. The level of financial assurance for reclamation, which now stands around \$1 billion, is a fraction of what is required (CCA 2015).

Alongside technology investments, operators can adopt complementary management practices to help speed up reclamation. An early win would be the full integration of mine operation, tailings disposal, reclamation, and closure planning to develop and use a single, dynamic mining plan for each organization that fully embraces the design-for-closure approach. This could reduce mine sprawl and lead to less expensive and more robust closure scenarios. More aggressive and progressive reclamation, whereby tailings areas are reclaimed more rapidly would reduce the area under active operation. Another early win would be closing tailings ponds as they reach full capacity rather than keeping them open in case of future need for addition of small tailings volumes. There is also an opportunity for greater collaboration between operators in mine waste management and reclamation, including sharing of tailings disposal areas, fluid fine tailings feedstocks, reclamation stockpiles, and more seamless designs across lease boundaries.

The government can help support a “design-for-closure” approach to oil sands mining sites. This can include incentives that drive the further development of technology and management solutions to discharge water, consolidate tailings, transform tailings pond into non-retaining structures, and earmark funds for future cleanup and reclamation. Water treatment guidelines and discharge standards that define permissible levels of various contaminants could also greatly help with the development of tailings technologies; having these standards in place would expand the range of tailings management options available to operators (CCA 2015). There is also an opportunity for governments and academia to work more closely with oil sands operators to improve the rate of tailings technology development, following research investments models that have been successful in oil sands development.

ACKNOWLEDGEMENTS

The authors thank the Council of Canadian Academies (particularly Tijs Creutzberg) for the permission to use part of its 2015 Expert Panel Report to prepare this article. The first author also acknowledges the support from the Research Institute on Mines and Environment (RIME UQAT-Polytechnique; www.rime-irme.ca/en/).

REFERENCES

- Alberta Government (2015). *Lower Athabasca Region: Tailings Management Framework for the Mineable Athabasca Oil Sands*. Edmonton, AB.
- AER (Alberta Energy Regulator). (2009). *Directive 074: Tailings Performance Criteria and Requirements for Oil Sands Mining Schemes*. Edmonton, AB.
- Aubertin, M., Dionne, J., and Marcoux, L. (1997). “Design Guidelines and Stability Criteria of Engineering Works for Water Covers.” *Proc. Proc. 4th International Conference on Acid Rock Drainage*, Vancouver, BC, Vol. 4 , 1851-1866.
- Aubertin, M., Bussière, B., and Bernier, L. (2002). *Environnement et Gestion des Rejets Miniers*, Manual on CD-ROM, Presses Internationales Polytechnique. Montreal, QC.

- Aubertin, M., Bussière, B., James, M.,...Mbonimpa, M., and Chapuis, R.P. (2011). "Vers une mise à jour des critères de stabilité géotechnique pour la conception des ouvrages de retenue de résidus miniers" *Proc. Symp. Mines and Environnement*, Rouyn-Noranda, QC, CIM (CD Rom), 38 p.
- Azam, S. and Li, Q. (2010). "Talings dam failures : A review of the last one hundred years." *Geotechnical News*. BiTech, 28 (4): 50-54.
- CAPP (Canadian Association of Petroleum Producers). (2014). *The Facts On Oil Sands*. Calgary, AB.
- CCA (Council of Canadian Academies) (2015). *Technological Prospects for Reducing the Environmental Footprint of Canadian Oil Sands*. The Expert Panel on the Potential for New and Emerging Technologies to Reduce the Environmental Impacts of Oil Sands Development. Ottawa, ON.
- CDA (Canadian Dam Association). (2014). *Application of Dam Safety Guidelines to Mining Dams*. Toronto, ON.
- CEMA (Cumulative Environmental Management Association) (2012). *End Pit Lake Guidance Document*. Fort McMurray, AB.
- CEMA (Cumulative Environmental Management Association). (2014). *Guidelines on Reclaimed Oil Sands Leases*. Fort McMurray, AB.
- CTMC (Consortium of Oil Sands Tailings Management Consultants) (2012). *Oil Sands Tailings Technology Deployment Roadmaps*. Vol. 1, 2. Edmonton, AB.
- Deveny D. W. (2010). *A Screening Study of Oil Sand Tailings Technologies and Practices*. Alberta Energy Research Institute, Edmonton, AB.
- Eshraghian, A., and Becker, D.E. (2016). "Application of CDA Dam Safety Guidelines to the Geotechnical Design of Oil Sands Tailings Dams in Northern Alberta." *Canadian Dam Association Bulletin*. 27(1): 26-41.
- Frank, R., Roy, J., Bickerton, G., Rowland, S., ... and Hewitt, M. (2014). "Profiling oil sands mixtures from industrial developments and natural groundwaters for source identification." *Environmental Science & Technology*, 48: 2660-2670.
- James, M., Aubertin, M., and Bussière, B. (2013). « On the use of waste rock inclusions to improve the performance of tailings impoundments." *Proc. 18th Int. Conference on Soil Mechanics and Geotechnical Engineering*, Paris, France.
- Kupper, A. et al. (2013). "Delicensing Oil Sands Tailings Dams – When is a dam no longer a dam?" *Proc. Tailings and Mine Waste Conference*, Banff, AB.
- McKenna, G. (1998). "Celebrating 25 Years." *Syncrude's Geotechnical Review Board*. Geotechnical News, BiTech Publ., Vancouver, 16:34-41.
- McKenna, G., Dawson, R., Hyndman, P., LeSueur, P., & Sobkowicz, J. (2013). "The oil sands tailings technology roadmap and action plan: Oil sands tailings state of practice overview." *Proc. Third International Oil Sands Tailings Conference*, Lake Louise, AB.
- Morgenstern, N. R. (2010). "Improving the Safety of Mine Waste Impoundments." *Proc. 14th International Conference on Tailings and Mine Waste*, Vail, CO.
- Morgenstern, N. R. (2012). "Oil Sands Mine Closure - The End Game: An Update." *Proc. Third Int. Oil Sands Tailings Conference*, Edmonton, AB. 23-34.
- Newland Bowker, L. and Chambers D.M. (2015). *The Risk, Public Liability & Economics of Tailings Storage Facility Failures*. Earthworks Action, Report from Bowker Associates Science & Research In The Public Interest (Maine) and Center For Science In Public Participation(Montana). 56 p.

- Oil Sands Tailings Dam Committee (2014). *De-licensing of oil sands tailings dams. Technical guidance document*. March 2014. Oil Sands Research and Information Network (OSRIN). University of Alberta, Edmonton. 46p.
- OSTC & COSIA (Oil Sands Tailings Consortium & Canada's Oil Sands Innovation Alliance) (2012). *Technical Guide for Fluid Fine Tailings Management*, Calgary, AB.
- Pollock, G.W., McRoberts, E.C., Livingstone, G., McKenna, G.T., Matthews, J.G., Nelson, J.D. (2000). "Consolidation behaviour and modelling of oil sands composite tailings in the Syncrude CT Prototype". *Int. Conf. Tailings and Mine Waste*. Fort Collins, CO. 121-130.
- Read, P. (2014). "Broad Suite of Practice and Technology Key to Success in Tailings Management." *Proc. Fourth International Oil Sands Tailings Conference*, Lake Louise, AB.
- SRK (1989). *Draft Acid Rock Drainage Technical Guide*, BCAMD Task Force.
- Vick, S.G. (1990). *Planning, Design, and Analysis of Tailings Dam*. BiTech Publ., Vancouver, BC.

Vulnerability Assessment of Underground Mine Stopes Filled with Granular Backfills

P. Rajeev¹ and N. Sivakugan²

¹Dept. of Civil and Construction Engineering, Swinburne Univ. of Technology, VIC 3122, Australia. E-mail: prajeev@swin.edu.au

²College of Science, Technology and Engineering, James Cook Univ., Townsville, QLD 4811, Australia. E-mail: siva.sivakugan@jcu.edu.au

Abstract: Satisfactory performance of mine barricade is important in order to avoid any unexpected risk due to barricade failures. The barricades are subjected to various levels of stresses and strains with time as a result of the deposition of the backfill material. Further, the strength of the barricade material degrades over time. The design of barricades relies on simplified analytical methods to determine the barricade capacity and load acting on it. Marston's theory and its modifications are being used to determine the average vertical stress variation with depth within the stope. Then, the load on the barricade is determined on the basis of the vertical stress at the barricade level and setback distance of the barricade. Several models were proposed to determine the load on the barricade, which show significant variation in the prediction. In the past, several failures were recorded in the mine stopes due to inadequate understanding on the loading on the barricade. Therefore, understanding the effect of variation in barricade material strength and load is necessary. In this paper, an attempt is made to quantify the effect of uncertainty in material strength, earth pressure prediction, barricade geometric properties on the safety of the barricade. The probability of failure and reliability index are computed, and then a capacity reduction factor of barricade strength is proposed to increase the reliability index to the acceptable level. The result shows that the variability in the brick strength has a significant effect (i.e., more than 70%) on the safety of the barricade in comparison to other source of uncertainty. The difference in estimated capacity reduction factor for various earth pressures prediction models is not large (~ 0.1). Therefore, a single factor can be used in the design practice to account the total variability.

INTRODUCTION

The failure of barricades in underground mining operations is not acceptable due to high consequences associated with these failures. However, a larger number of barricade failures were recorded in the past, for example, 11 barricade failures were recorded at Mount Isa Mines in both hydraulic and cemented hydraulic fills between 1980 and 1997 in Australia (Kuganathan, 2001); and a failure at the Normandy Bronzewing Mine in Western Australia resulted in a triple fatality, and two failures were reported later that same year as a result of hydraulic fill containment at the Osborne Mine in Queensland (Grice, 2001).

The barricades are constructed with various materials such permeable bricks and concrete and different method of construction such as sprayed shotcrete/ fibrecrete, sprayed aquacrete and hybrid mullock pile and shotcrete (e.g., Berndt et al. 2007, and Revell and Sainsbury 2007). Figure 1 shows the permeable brick and concrete barricades.

Barricade failures happen in early filling due to poor drainage, sudden increase of pore pressure from adjacent blasts, reduction of backfill shear strength and liquefaction, and also piping in stope. This piping, where an erosion channel is formed near the barricade inside the fill, grows up to the fill surface imposing extra load on barricade due to the formed water column (Sivakugan, 2008; Bloss and Chen, 1998). Especially in brick barricades the failure occurs mainly due to incomplete comprehension of (i) the barricade material properties, (ii) the strength

achieved through design and construction and (iii) the operational stresses of the barricade (Berndt et al. 2007). For example, the strength of the brick depends on the condition of the brick (i.e., wet or dry) and varies significantly within the same condition.

The design of barricades relies on simplified analytical methods to determine the barricade capacity and load. Marston's theory and its modifications are being used to determine the average vertical stress variation with depth within stope. Then, the load on the barricade is determined on the basis of the vertical stress at the barricade level and setback distance of the barricade. Several models were proposed to determine the load on the barricade and they show significant variations in prediction.



FIG. 1. Examples of barricade: (a) permeable brick barricade in place (adopted from Berndt et al. 2007) and (b) typical sprayed shotcrete/fibrecrete paste barricade (adopted from Revell and Sainsbury, 2007)

Therefore, understanding the effect of variation in barricade material strength and load on safety is necessary. In this paper, an attempt is made to quantify the effect of uncertainty in material strength, earth pressure prediction, barricade geometric properties on the safety of the barricade. The probability of failure and reliability index are computed, and then a capacity reduction factor of barricade strength is proposed to increase the reliability index to the acceptable level.

STRESS PREDICTION MODELS FOR BARRICADES

Several analytical stress prediction models for barricades were developed in the past and were reported in literature (e.g., Kuganathan, 2002 and Li and Aubertin, 2009). The models are based on continuum approach to calculate the vertical stress in the stope by modifying the Marston's equation as given in Eq. (1) for a three dimensional square or circular stopes.

$$\sigma_v = \frac{\gamma D}{4K \tan \delta} \left[1 - \exp\left(-4K \tan \delta \frac{z}{D}\right) \right] + q \exp\left(-4K \tan \delta \frac{z}{D}\right) \quad (1)$$

where σ_v is the vertical stress at the base of the stope entrance; γ is unit weight of the fill; K is the lateral earth pressure coefficient; z is the height from top; D is the width or diameter of the stope; q is uniformly distributed surcharge applied at the top; and δ is the wall friction angle.

Then the horizontal stress onto the barricade can be calculated using equation below proposed by Li and Aubertin (2009).

$$\sigma_h = \left[\frac{h}{H_d} \sigma_{hTO} + \left(1 - \frac{h}{H_d} \right) \sigma_{hBO} \right] \exp \left[-l \frac{2 \tan \delta}{K_{dt}} \left(\frac{1}{H_d} + \frac{K_{dt}}{W_d} \right) \right] \quad (2)$$

where σ_h is the horizontal stress at the barricade; h is the elevation of a calculation point in the drift; σ_{hBO} & σ_{hTO} are the horizontal stress at the base and top of the stope entrance, respectively; H_d is the total height of the drive; K_{dl} is the earth pressure coefficient in longitudinal direction within the drive; K_{dt} is the earth pressure coefficient in transverse direction within the drive; W_d is the width of the drive; and l is the setback distance.

Later, Kuganathan (2002) proposed a simplified equation to calculate the stress on barricade as given below.

$$\sigma_h = \sigma_o \exp \left[-\frac{PK_o \tan \phi}{A} l \right] \quad (3)$$

where σ_o is the horizontal stress at the stope entrance; P is the perimeter of the drive; and A is the cross-sectional area of the barricade.

The laboratory experimental study reported in Widinghe et al. (2014) shows that the prediction of horizontal stress at the barricade using both Eqs. (2) and (3) is not always reliable. However, the accuracy of Eqs. (2) and (3) depends on the accuracy of Eq. (1). The Eqs. (2) and (3) significantly under predict the horizontal stress at the barricade for larger q 's with shorter setback distances while over predicting for larger q 's with larger setback distances. Depending on the predictive equation used in the design stage determine the sizing and detailing and the level of safety of the barricade. Therefore the performance reliability of the barricade has to be assessed to understand the effect of earth pressure model variability in the safety of the barricade.

DESIGN METHODS FOR BARRICADE

Several analytical methods were developed over the years to estimate the capacity (i.e., strength) of the barricade with varying levels of accuracy and complexity (Revell and Sainsbury, 2007). The method is mainly based on the assumed possible failure mechanism (i.e., flexural failure mode) for barricade rather than the actual failure as shown in Figure 2. The analytical model was proposed considering the flexural failure mode (Figure 2.a) without considering the possible punching shear failure (Figure 2.b)

The American Concrete Institute (ACI) reinforced concrete building design code is commonly used to design and detail the barricade. Djahanguiri and Abel (1997) analysed the barricade as a two-dimensional simply supported beam to determine the maximum allowable load and they used the ACI code to design the steel reinforcement. However, the simply supported beam analysis of the three-dimensional and partially clamped barricade generally yields an overly conservative design.

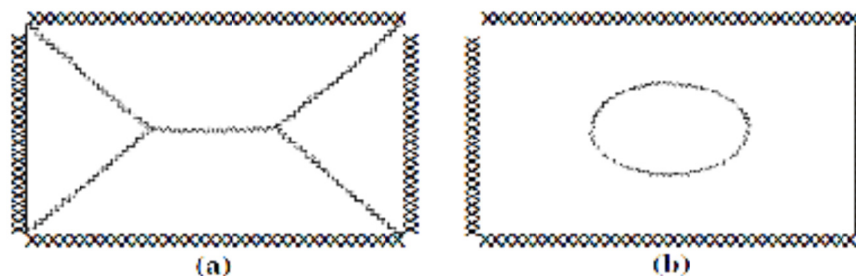


FIG. 2. Mechanisms for barricade failure (a) Theoretical (Duffield et al. 2003), (b) Observed (Kuganathan 2001a, b).

The yield line theory developed to estimate the ultimate load in reinforced concrete slab is also used to design mine barricades. The yield line theory assumes the failure occurs in flexural model and the slab has sufficient shear resistance to prevent the shear failure. However, it has been observed that the yield line method does not accurately determine the failure load of reinforced concrete slabs under all loading and support conditions (e.g., Powell, 1956; Niblock, 1986; Wood, 1961). Specially, the method is unable to account the membrane (arching) forces mobilized at the slab edges in its standard form (Revell and Sainsbury, 2007). Further, the method cannot be used to analyse the masonry wall.

Beer (1986) proposed a yield line based solution to analyse the masonry barricade wall by using the equations to calculate the ultimate load in simply supported slab as given below.

$$m_p = \sigma_c \frac{t^2}{8} \quad (4)$$

$$w_p = \frac{24m_p}{b^2} \quad (5)$$

where w_p is the ultimate uniformly distributed pressure; m_p is the ultimate moment capacity per unit length; b is the length or width of the barricade; t is the thickness of the barricade; and σ_c is the unconfined compressive strength of the mortar.

In Australia, the solution proposed in Beer (1986) is commonly used to design masonry barricades, although there is no theoretical basis to apply the yield line theory to unreinforced masonry wall (e.g., Hendry, 1981; Martini, 1997; and Sinha, 1978) due to the orthotropic nature of masonry structures.

Revell and Sainsbury (2007) carried out numerical analysis to study the ultimate failure load in concrete barricade with varying geometry (i.e., square and horseshoe and both flat and curved) and interface friction between the rock face and barricade with strain-softening material model. The results show that the simply supported square barricade provides perfect correlation with the yield line solution of concrete slab as given in Eq. (6), however, the fully fixed and shear interface barricades provide better correction with modified Beer (1986) solution, where the basic solution is multiply by factor of 1.72. Therefore, the design based on Beer (1986) solution already has a built-in factor of safety of 1.72 before applying additional partial safety factors for loadings and capacities.

$$w_p = \frac{6\sigma_t \cdot t^2}{b^2} \quad (6)$$

where σ_t is the tensile strength of concrete, which can be calculated using the compressive strength of the concrete, given in Thomas et al. (2001) as $\sigma_t = 0.3\sigma_c^{0.67}$.

UNCERTAINTY IN BARRICADE CAPACITY

Even a well-designed barricade may fail due unexpected change in loading condition (i.e., variation in uniformly distributed load applied at the top), prediction of pressure at the barricade (i.e., model uncertainty), variability in material properties of the barricade and backfill parameters and the variation in geometry of the drive. For example, the uniaxial compressive strength (UCS) of barricade bricks may vary from 5 to 26 MPa, although the manufacturer should guarantee a minimum uniaxial compressive strength of 10 MPa (Duffield et al., 2003 and Kuganathan, 2001). Further, a series of uniaxial compressive strength tests undertaken in Berndt

et al. (2007) on a large sample of brick cores have demonstrated that the strength of the brick drops in the order of approximately 25% when it is in saturated stage, as it would occur in the mines (See Figure 3). The load bearing capacity of the barricade reduces significantly from the design strength when the material strength is below the characteristic design value; consequently, failure occurs due to inadequate strength.

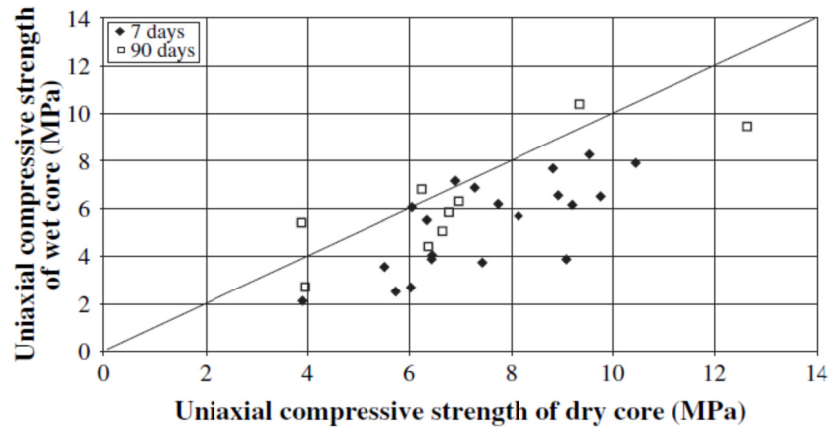


FIG. 3. Uniaxial compressive strength of dry and wet brick (adopted from Berndt et al., 2006)

CASE STUDY

In this paper, the variability in the barricade material and geometry and the earth pressure model on the performance of the barricade is studied. The slope of 250 m depth and 15 m width, with the drive size of 4 m X 4 m is considered in this study. Table 1 provides properties of fill material and brick considered in the design of barricade.

Table 1. Design parameter

Parameter	Unit	Value
Dry density	kg/m ³	2175
Peak friction angle (ϕ)	deg	39
Interface friction (δ)	deg	23
Compressive strength of the brick	MPa	10
Setback distance (l)	m	4

The design of the barricade is carried out using the horizontal earth pressure derived from Eq. (2) where the K_{at} and K_{dt} are taken as 2 and 0.37 (i.e., at-rest pressure coefficient) respectively. The horizontal stress at the base and top of the slope entrance was estimated from the using the vertical stresses computed from Eq. (1) at that location and multiply by K_{dt} . The width of the slope (W_d) is assumed to be 15 m. The lateral earth pressure at the middle of the barricade is

estimated to be 0.12 MPa. The barricade wall thickness of 0.45 m will provide the failure pressure of 0.38 MPa according to Beer (1986) and give a factor of safety slightly greater than 3.0 (i.e., $0.38/0.12 = 3.17$). Therefore, the barricade is in safe state and expected to performance satisfactorily in its lifetime.

The important point to note in the current engineering design practice is that design process does not take into account the variability in the capacity and demand. The design based on the single value (i.e., mostly the mean) of demand and capacity results unsatisfactory performance especially the variability in the material is significantly high such as brick. Therefore, it is important to know the effect of material and loading uncertainty in the safety of the barricade. In this study, an attempt is made to understand the effect of variability in the brick material, loading, and geometry of the barricade in the safety of the barricade. The simulation based reliability analysis for the barricade is performed. The uncertain parameters are sampled from predefined probabilistic distribution for each variable using Latin-Hypercube sampling technique. The statistical properties of the uncertain variables are given in Table 2. The lateral earth pressure on the barricade is calculated using the models proposed by Li and Aubertin (2009) and Kuganathan (2002) in order to understand the model uncertainty. The variability in fill material properties are not considered in this study. Further, the performance of the barricade is checked against the flexural failure mode only and the punching shear failure is not considered.

Table 2. Statistical properties of the uncertain variables

Parameter	Distribution	Mean	CoV (%)	Source
Compressive strength of the brick (MPa)	Log-normal	6.57	34.25	Berndt et al. (2007)
Width and length of the barricade (m)	Uniform	[3.5, 4.5]	-	Rajeev (2008)
Thickness of the barricade (m)	Uniform	[0.4,0.5]	-	Rajeev (2008)
Setback distance (m)	Normal	4.0	10.00	Rajeev (2008)
Earth pressure prediction	-	-	-	Model (1): Li and Aubertin (2009) Model (2): Kuganathan (2002)

RESULTS AND DISCUSSION

The performance of the barricade is assessed using 10,000 samples of uncertain variables drawn from assigned distribution. The factor of safety was computed for each simulation. Figure

4 shows the sampled compressive strength of brick and setback distance. As stated above, the lateral earth pressure is estimated using both Li and Aubertin (2009) and Kuganathan (2002) models and then the Factor of Safety (FoS) for all 10000 simulations. Figure 5 shows the cumulative probability density function for the computed FoS. The probability of unsatisfactory performance (i.e., $FoS < 1$) is 0.045 and 0.169, respectively for Li and Aubertin and Kuganathan. Further, the probability of unsatisfactory performance is nearly 4 times higher for Kuganathan than the Li and Aubertin. The probability of having factor of safety less than 3.0 (i.e., design FoS) is 0.854 and 0.935, respectively for Li and Aubertin and Kuganathan.

On the basis of the computed probability of unsatisfactory performance, the corresponding reliability index can be calculated as follows:

$$p_f = P(FoS < 1) \tag{7}$$

$$\beta = -\Phi^{-1}(p_f) \tag{8}$$

where p_f is the probability of having $FoS < 1.0$, β is the reliability index, and Φ is the standard normal distribution function.

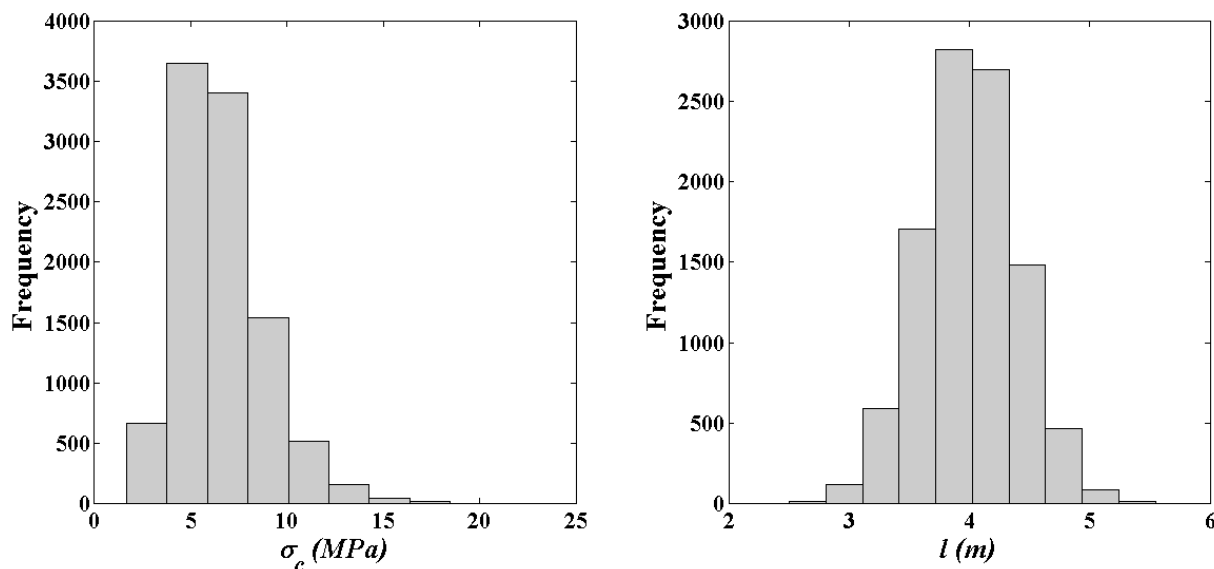


FIG. 4. Sampled compressive strength of brick and setback

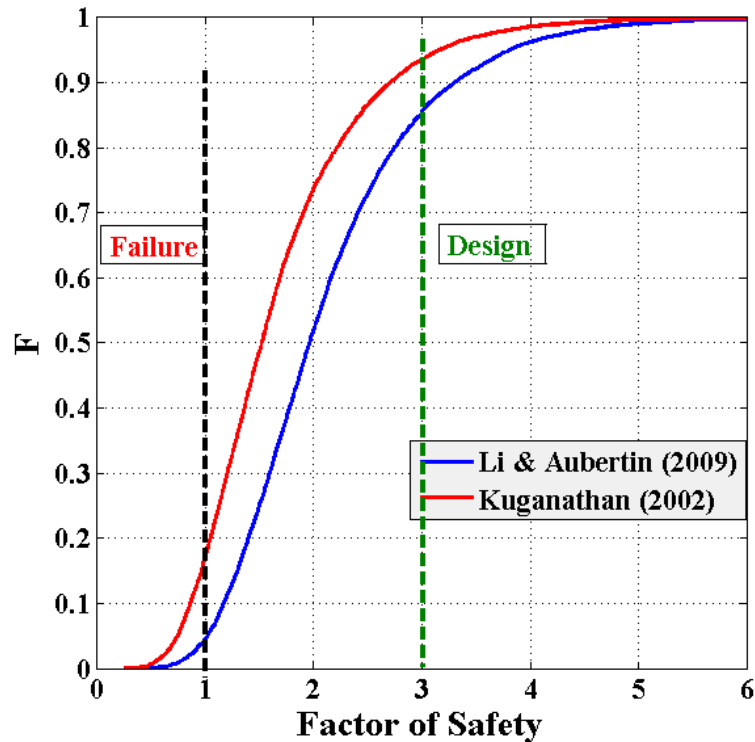


FIG. 5. Empirical cumulative probability density function for computed factor of safety

The estimated reliability index is 1.70 and 0.96 for Li and Aubertin and Kuganathan models, respectively. The reliability index values are very low compared to the values used in the standards which are generally above 3.5 for critical elements. In order to achieve the reliability index close to 3.5 the probability of unsatisfactory performance should be reduced to 0.0002.

Further, parameter sensitivity analysis was carried out to understand the contribution of each uncertain parameter on the factor of safety estimation. The results are shown in Figure 6. The compressive strength of the brick (σ_c) has the highest contribution on the estimation of factor of safety for both Li and Aubertin and Kuganathan models (i.e., 70% to 80%). The width (t) and length (H_d) show nearly 40% to 50% contribution on the factor of safety. The effect of setback distance (l) shows 20% contribution on the factor of safety for Kuganathan's model while less than 10% contribution for the Li and Aubertin's model.

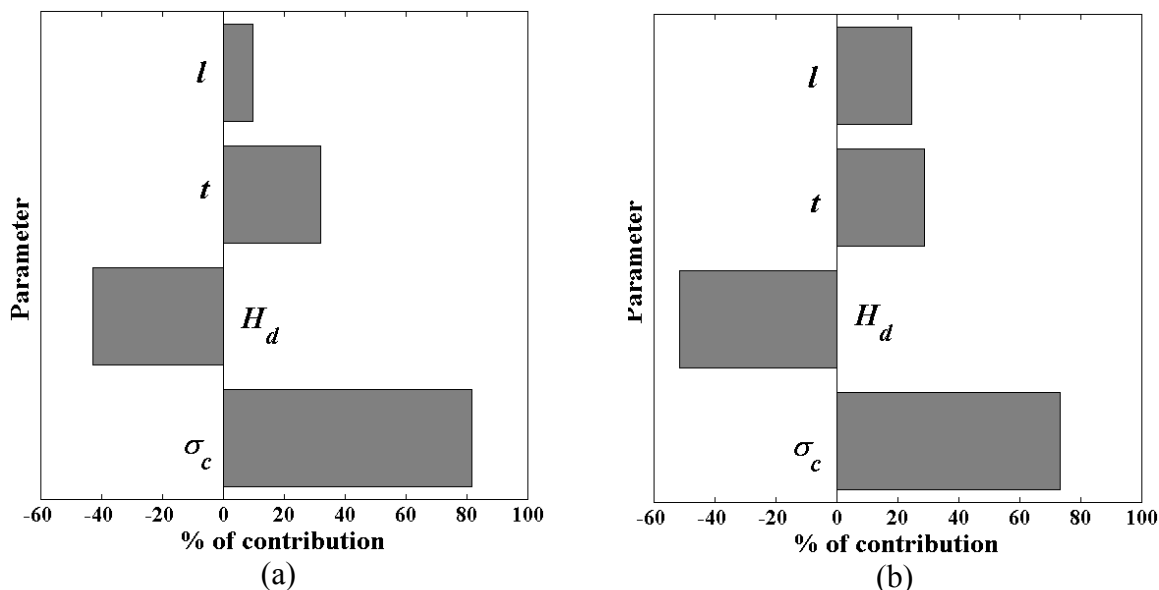


FIG. 6. Parameter sensitivity on factor of safety: (a) Li and Aubertin and (b) Kuganathan

In order to improve the safety of the barricade the variability in compressive strength of brick needs to be quantified accurately. This may require large number of brick specimens to be tested in different conditions (i.e., wet and dry) and is not possible in practice. Alternately, the estimated structural capacity of the barricade using the characteristic strength of the brick can be reduced by using a factor call “capacity reduction factor (ϕ)” to account the larger variability in material strength as explained in Franchin et al. (2010). The ϕ factor helps to achieve the required level of safety. Thus, the probability of unsatisfactory performance can be reduced by applying an appropriate capacity reduction factor, ϕ , for Eq. (4) as below:

$$w_p = \phi \frac{24m_p}{b^2} \quad (9)$$

The capacity reduction factor will shift the cumulative probability density function of FoS (shown in Figure 3) in such a way that the probability of having FoS less than 1 is close to 0.0002. For this particular example, the capacity reduction factor (ϕ) is in the range of 0.3 to 0.4 for both earth pressure prediction models. The difference in the capacity factor for both models is not significant; this implies the effect of variation in earth pressure prediction models is not significant in comparison to the variability in material strength. Therefore, it is possible to use a single value, which take cares the variability in the strength of the brick, to reduce the structural capacity of the barricade.

CONCLUSIONS

In this paper, the effects of variability in barricade material, geometry and loading are studied. Based on results, it is shown that the safety of the barricade is significantly affected by the variability in all above parameters. The reliability index computed for the example barricade shows very low values compared to the values suggested in the standards. In order to achieve the target reliability index, a capacity reduction factor is proposed. However, the proposed capacity reduction factor needs further studies considering different barricade loading conditions, failure mechanism, and geometry etc.

REFERENCES

- Beer, G. (1986). "Design of brick bulkheads: Numerical Modelling." CSIRO Division of Geomechanics, Long Pocket Laboratories, Project Report 1.
- Berndt, C. C., Rankine, K. J. and Sivakugan, N. (2007). "Materials properties of barricade bricks for mining applications." *Geotech Geol Eng*, Vol. 25:449-471.
- Bloss, M. & Chen, J. (1998). Drainage research at Mt Isa Mines Limited 1992-1997", *Proceedings of the Sixth international Symposium in mining with backfill*, Brisbane, Australia, 111-116.
- Duffield, W.A., Gad, E. and Bamford. W. (2003). "Investigation into the structural behavior of mine brick barricades." *Australasian Institute of Mining and Metallurgy 2* (March/April):45-50.
- Djahanguiri, F. and Abel, J. F. (1997). "Design and construction of a bulkhead for a simulated underground leaching stope." *Mining Engineering*. January.
- Franchin, P., Pinto, P. E. and Rajeev, P. (2010). "Confidence Factor?" *Journal of Earthquake Engineering*, Vol. 14(7): 989-1007.
- Grice, T. (2001). "Recent mine developments in Australia." *In: Proceedings of the 7th international symposium on mining with backfill (MINEFILL)*, 351-358.
- Hendry, A. W. (1981). *Structural Brickwork*. New York: John Wiley and Sons.
- Kuganathan, K. (2001). "Mine backfilling, backfill drainage and bulkhead construction - a safety first approach." *Australia's mining monthly February*, 58-64.
- Kuganathan, K. (2002). "A method to design efficient mine backfill drainage systems to improve safety and stability of backfill bulkheads and fills." *Proceedings of the 8th AusIMM Underground Operators' Conference "growing our underground operations"*, Australasian Institute of Mining and Metallurgy, Carlton, 181-189.
- Li, L. and Aubertin, M. (2009). "Horizontal pressure on barricades for backfilled stopes. Part I: Fully drained conditions." *Canadian Geotechnical Journal*, vol. 46 (1) : 37-46.
- Martini, K. (1997). "Finite element studies of out-of-plane failure of unreinforced masonry." *Proceedings of the International Conference on Computing in Civil and Building Engineering*, Korea.
- Niblock, R. A. (1986). "Compressive membrane action and the ultimate capacity of uniformly loaded reinforced concrete slabs, Ph.D. Thesis, The Queen's University of Belfast, UK.
- Powell, D. S. (1956). *Ultimate strength of concrete panels subjected to uniformly distributed loads*, Ph.D. Thesis, Cambridge University, UK.
- Rajeev, P. (2008). *Role of confidence factor in seismic assessment of existing buildings*. Ph.D Thesis, University of Pavia, Italy.
- Revell, M. B. and Sainsbury, D. P. (2007). "Advancing Paste Fill Bulkhead Design Using Numerical Modeling." *MINEFILL2007*.
- Sinha, B. P. (1978). "A simplified ultimate load analysis of laterally loaded model orthotropic brickwork panels of low tensile strength." *Journal of Structural Engineering*, Vol.56 (4): 81-84.
- Sivakugan N. (2008). Drainage issues and stress developments within hydraulic fill mine stopes. *Australian Journal of Civil Engineering*, Vol 5, No 1.
- Wood, R. H. (1961). "Plastic and elastic design of slabs and plates." London: Thames and Hudson.

A Novel Mixed-in-Place Pile System for Offshore Platforms

Giovanni Spagnoli¹; Paul Scheller²; and Paul Doherty³

¹Product Manager, Dept. of Maritime Technologies, BAUER Maschinen GmbH, Schrobenhausen, Germany. E-mail: giovanni.spagnoli@bauer.de

²Director, BAUER Renewables Ltd., Bishops Stortford, U.K. E-mail: paul.scheller@bauer.de

³Managing Director, GDG Geosolutions, Dublin, Ireland, (formerly at School of Civil, Structural and Environmental Engineering, Univ. College Dublin), E-mail: pdohererty@gdgeo.com

Abstract: A novel mixed-in-place pile (MIDOS) has been developed by BAUER for supporting piled offshore platforms. The mechanical technology and in situ pile performance were successfully demonstrated during an in situ test in silica sand, where the tension capacity reached 9MN. This paper investigates the axial bearing capacity on one MIDOS test pile in a silica deposit where a dynamic test has been conducted using the “high-strain” testing method. The interpretation of the results was performed by means of the CAPWAP signal matching method. The static bearing capacity mobilized by the dynamic pressure of the load test reached 15.4MN (12.7MN skin friction and 2.7MN end bearing capacity). Analysis of the loads achieved in the dynamic test suggests that the MIDOS pile performs similarly to conventional bored piles in silica deposits with a D_r of about 80%. The research scope was subsequently extended to include laboratory studies in calcareous deposits. These investigations have shown that the MIDOS pile is a feasible foundation alternative for carbonate sand deposits where extreme compression at high confining stresses results in very low values of skin friction for driven piles. Laboratory tests on the steel-carbonate grout interface show a characteristic slip-stick response, which is thought to be related to the potential energy required to overcome interface locking followed by a relative short movement along a low resistance plane before reaching a similar interlocking resistance.

INTRODUCTION

The majority of offshore platforms constructed over the past five decades have used jacket constructions, where piles have been inserted through the steel substructure by driving through the jacket legs or into an external sleeve connection. These foundation elements may be either vertical or battered, with a range of 1:8 – 1:20 (Poulos 1988). Over the past 60 years, water depths have increased from 6m to 412m. The most common foundation solutions are open ended steel tubular piles driven into the seabed to a prescribed penetration using hydraulic impact hammers. This installation

technique is relatively quick, highly efficient and the small number of marine operations reduces the risk profile of driven piles compared to their alternatives. However, in certain ground conditions, driven piles are not a suitable foundation option, as the high energy imparted to the soil during installation result in excessive friction fatigue and low pile capacities (i.e. poor geotechnical performance). In calcareous sand, the impact energy from the piling hammer causes particle breakage which leads to high levels of contraction and very low pile shaft capacities. The traditional alternative to driven piles is to employ a drilled-and-grouted pile system (D&G), however this technique is time consuming and expensive. The MIDOS (Mixed Drilled Offshore Steel) pile is a novel pile that utilizes mixed-in-place (MIP) technology as an alternative to D&G piles. The MIDOS system minimizes the number of offshore operations, is significantly quicker than D&G piles and is therefore more cost effective. One of the key environmental advantages relative to driven piles is the reduced noise levels during installation. A field trial with static load testing was undertaken to demonstrate the efficiency of this system in a silica sand deposit containing silt and clay layers (see Igoe et al. 2014; Spagnoli et al. 2014). The following paper describes further in situ tests using dynamic load testing techniques in silica deposits. In addition, a subsequent series of laboratory tests on calcareous deposits are described, as the MIDOS pile seems particularly well suited for these kinds of deposits.

THE MIDOS PILE

The MIDOS drilling tool includes an excavation chamber with a diameter larger than the casing diameter, which is mounted at the toe of the casing (Fig. 1). The finished pile consists of a structural steel pile imbedded in a soil-cement-mixture created by using a low pressure grout combined with the in situ soils. The MIDOS pile installation involves advancing the drill bit ahead of the steel casing, facilitating the inward flow of soil into a mixing chamber located behind the rotary head. Paddles within the mixing chamber are used to generate a homogeneous soil-cement-mix. As the drill bit advances, the soil-cement-grout forms an outer annulus around the casing and also fills the internal space within the steel pile. Additional details about the MIDOS technology are available in Igoe et al. (2014), Spagnoli et al. (2014), Spagnoli et al. (2015a; 2015b) and Doherty et al. (2015a; 2015b). The steel pile extends above mudline allowing the jacket legs to be connected to the pile using a conventional jacket sleeve arrangement. One or two rotary drives are clamped inside of the top section of the casing. A mixing tool is positioned at the bottom end of a vertical drive shaft and rotated by the top rotary drive. Specially designed cement slurry exits the mixing tool, so that the loosened soil is immediately mixed with this slurry to a soil-cement-mixture. The soil is mixed in the excavation chamber while simultaneously the casing penetrates into the soil. During the installation of the pile, the soil-grout mixture flows through the openings placed in the casing and passes throughout the annulus created by the difference in diameters between the excavation chamber and the steel pile. When reaching the final depth, the rotary drives with the shaft and the mixing and drilling tools are extracted, while the casing and the starter piece remain in place.

The MIDOS system has several advantages over standard drilled and grouted piles, such as the simultaneous installation of casing during drilling, which eliminates the

need for pre-driven steel casing in weak soils, and the soil-grout mixing system designed to ensure adequate grouting around the pile shaft. Furthermore, as the installation process does not involve any soil excavation or unloading (e.g. due to extracting casing), relaxation of the surrounding soil does not occur, which ensures that the controlling radial stresses are maintained at a constant value. Reverse circulation (RC) top drilling units need more operations such as pipe addition, whereas the MIDOS pile does not.

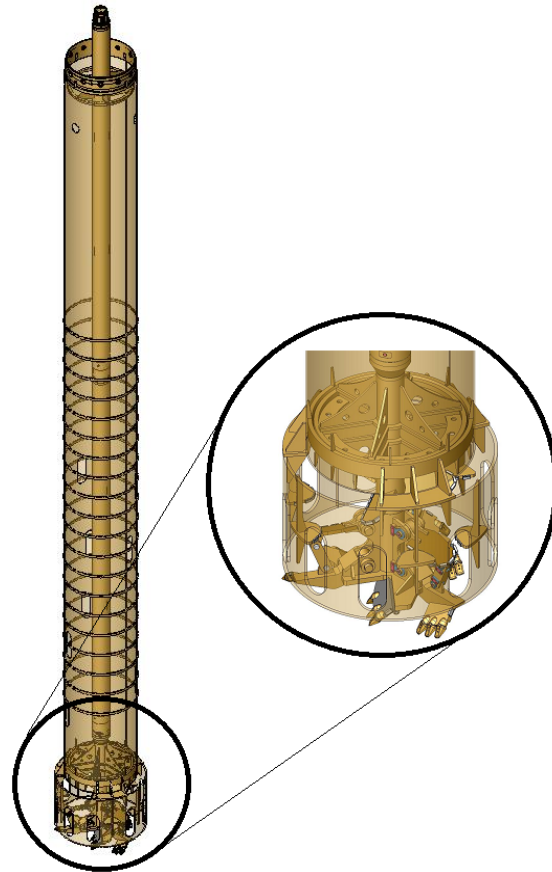


FIG. 1. Sketch of the MIDOS pile with the enlargement of the drilling tool.

DYNAMIC TESTS IN SILICA SANDS

A field trial of the MIDOS pile system was completed using a modified drill rig Bauer BG 42 commonly used for creating standard bored piles, as shown in Fig. 2. The field trial was carried out to verify the suitability of the installation procedure and load carrying performance of the novel technology. The field tests involved the installation and load testing of a large scale test pile, 1.9m external diameter of the mixed-in-place (1.5m diameter of the steel pipe), and penetrating about 18m into a silica sand deposit (with a D_r value of about 80%) near Schrobenhausen (Bavaria, Germany). The installation records show similar drilling rates to onshore bored piles and indicate no conceptual challenges with the proposed installation methodology. Design calculations for traditional D&G piles, were used to estimate the pile capacity and were compared to the measured results. The pile demonstrated an ultimate tension

capacity of more than 9MN, which Igoe et al. (2014) showed to be in good agreement with the expected shaft friction. The unconfined compressive strength of the grout was measured after 28 days as 5MPa.



FIG. 2. The MIDOS pile during the in situ tests in South Germany (left) and the mixing chamber after the installation (right).

Static load tests are in most circumstances prohibitively expensive for use offshore and as a result alternative means of measuring the axial bearing capacity of offshore piles is required. As a result, dynamic tests are often used in combination with various interpretation techniques such as signal matching analysis. In this research programme, a dynamic test using the “high-strain” method was undertaken on an onshore MIDOS test pile and was subsequently evaluated by means of the CAPWAP signal matching process. CAPWAP is an iterative curve-fitting technique where the pile response determined in a wave equation model is matched to the measured response of the actual pile for a discrete hammer blow. The pile model consists of a series of continuous segments and the total resistance of the embedded portion of the pile is represented by a series of springs (static resistance) and dashpots (dynamic resistance). Static resistance is formulated from an idealized elasto-plastic soil model, where the quake parameter defines the displacement at which the soil changes from elastic to plastic behavior. The dynamic resistance is formulated using a viscous damping model that is a function of a damping parameter and the velocity (Goble and Rausche 1979). GSP mbH Mannheim performed this test (GSP, unpublished internal report, September 2014). During the load test, strain and acceleration were recorded to determine the stress on the pile and the induced energy. Through the implementation of one dimensional wave theory, the bearing capacity of the pile was determined separately for skin friction and for end bearing. While the primary motivation for the load test was to measure the pile performance, a secondary objective was to determine whether similar results could be achieved through measurements made on a pile follower rather than by transducers directly mounted on the pile head. Since offshore it is a significant effort to mount a transducer on the pile head by divers, it was deemed

important to determine whether transducers mounted on a retrievable follower gave similar results. The follower was made of the same material of the pile and was mounted through a gravity connection. The follower had the same diameter of the pile (i.e. 1500mm and length of 5m) and for centering and stabilizing it, a tube was welded to the follower and inserted into the pile head, so that no welding connection between pile and follower were needed. In this way compressive forces could be transmitted from follower to the pile. For the tests the pile was prepared such that the pile head was protruding 75cm over the ground level. For the application of the test load, Bauer constructed special test load equipment to guide a 25 ton drop mass which has been installed on top of the follower (Fig. 3). The follower had to fulfill the role of a cap outfitted with strain and acceleration transducers. With the performance of the dynamic load test on this onshore test pile and the simultaneous outfitting of the pile (referred to as the standard sensor system) and the follower it was expected to demonstrate whether the exclusive outfitting of the follower would provide reliable results when applied on offshore tests. The follower was fitted at the same axis as for the pile with 2 electrical resistance strain gauges and 2 accelerometers. The range of the strain transducer was $3,000 \mu\epsilon$, whereas for the accelerometer the range was 5,000g. Two sets of sensors were mounted on the follower, as shown in Figure 3, allowing the measurements from waterproof sensors and standard sensors to be compared.

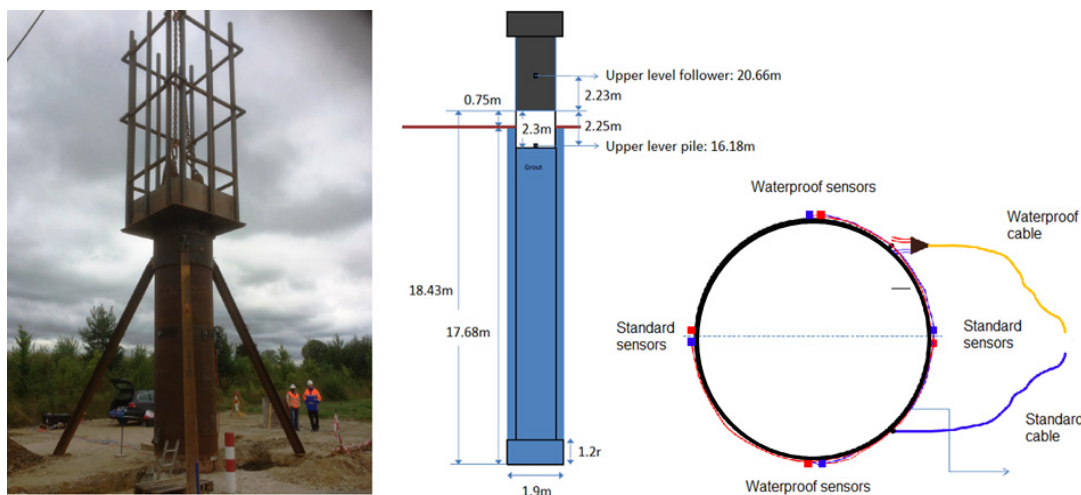
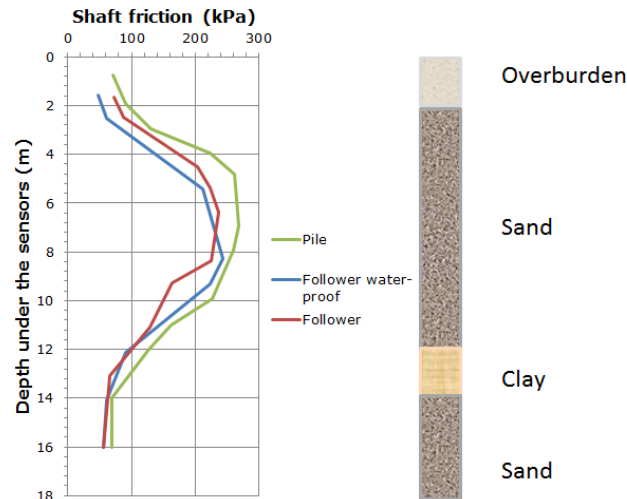


FIG. 3. Special load equipment installed on top of the pile as follower (left); schematic diagram of essential measurements (middle); transducers fitted to follower-view from top (right).

The CAPWAP analysis resulted in compression capacities in the order of 15.3 to 15.4 MN, with approximately 80% of the capacity mobilized along the pile shaft. The results in table 1 as well as the Figure 4 also reveal that similar dynamic capacity measurements can be recorded on the follower and directly on the pile shaft. This is an interesting conclusion as it suggests that in principal it is possible to obtain similar results in dynamic tests offshore without the need to mount the gauges directly on the pile head.

Table 1. Activated Bearing Capacities for the 11th Test

	Static bearing capacity kN	Skin Friction kN	End bearing kN
Pile	15,431	12,458	2,973
Follower (water-proof)	15,371	12,698	2,673
Follower (standard)	15,335	12,917	2,418

**FIG. 4. Distribution of skin friction over the embedded length and soil profile.**

GEOTECHNICAL TESTS IN CARBONATE SANDS

Several geotechnical tests and finite element analysis have been performed in the past on two carbonate sands from Ireland, namely the Dog's Bay (DB) and the Ballyconneely (BC) sands (see Spagnoli et al. 2015a; 2015b; Doherty et al. 2015a; 2015b). The DB sand is a skeletal "foramol" carbonate sand which was also extensively investigated in the past because of its mechanical behaviour similar to the problematic Australian Rankin Field sand deposit (Golightly 1988; Kwag et al. 1999). By contrast, the BC sand is a whitish orange dense rounded uncemented calcitic carbonate algal sand, previously studied by Golightly (1988) and Jian et al. (1991), was chosen because of its chlorozoan grain type, which is normally only found in tropical locations (Golightly 1988) and offers a strong contrast to the DB sand.

The suite of characterization tests (direct shear tests, triaxial tests, SEM and XRD analysis, compression and tension grout tests) undertaken on the calcareous sand samples from the West of Ireland clearly showed potential for particle damage during loading and compression during shearing (see Doherty et al. 2015a). In particular, shearing under high stresses in triaxial conditions was seen to cause a high degree of particle crushing and a migration of sand particles into the "fine" range. Fig. 5 compares the results of carbonate sands tested by Nauroy and Le Tirant (1981) with the DB and the BC carbonate sands. The figure shows that as the confining pressure increases, the peak friction angle decreases. Doherty et al. (2015a) demonstrated that grouted carbonate soils have the same properties of grouted silica soils. This was

deemed particularly important because the MIDOS system has already been shown to be an effective pile installation technique in silica deposits, with the load carrying capacity shown to be in-line with predicted values for conventional D&G piles. The testing regime focused on both the potential geotechnical and structural failure modes. Testing at the geotechnical interface (soil-soil; grout-steel; grout-soil) focused on the comparison between direct shear behaviors of calcareous and silica deposits, when sheared against soil-soil, soil-grout and soil-steel interfaces. Water-cement ratio of 0.4 was chosen with cement-sand ratios of 15%-25% and 35% to simulate different mixing velocities. All of the results showed a similar shearing behavior, with relatively constant volume and peak friction angles observed on both the silica and calcareous sands. The constant volume friction angles decreased with normal stress and approached a constant value of 30° - 33° at high normal stresses for the calcareous sand when tested against the soil-soil and soil-grout interface (Fig. 6). Comparison of the calcareous interface friction angles for the soil-soil, soil-steel and soil-grout tests were nearly identical, suggesting that δ_{cv} for the soil-steel and soil-grout is directly comparable to the ϕ_{cv} for the soil-soil failure. This suggests that the friction angle controlling the failure mechanism at the pile-soil interface of the MIDOS pile will be comparable to the soil friction angle and no reduction is needed to account for the interface properties. Besides, the calcareous sand typically displayed maximum friction angles (soil-soil) that were higher than the comparative tests on the silica sand samples, indicating that the MIDOS pile is able to generate the same friction as in calcareous deposits.

As the MIDOS pile is installed while keeping the in situ horizontal stresses at an approximately constant value, there should be no radial compression of the sand and the overall pile shaft shear stress should be governed by the in situ K_0 conditions and the friction angles measured in this study. This suggests that in terms of the geotechnical resistance the MIDOS pile is likely to work as well in calcareous deposits. In addition to testing the shearing properties of the sand material and the sand material interfacing with steel and grout, a number of tests were undertaken to explore the shearing behavior of the steel grout interface, representative of the casing to MIP bond in the MIDOS system. The configuration proposed was similar to the one used in direct shear test for soil materials specified in ASTM D3080-11. The specimen was formed for a grout block (for the tests 35% c-s ratio was used) with a steel plate embedded in it. To assure the plate remains horizontal and in the same plane as the fracture is produced by the shearing device, a U-shape in the plate was proposed. In addition, this shape assured that one side of the plate is fixed in the grout and the sliding is produced only in one plane. Thus, this test method consisted of placing the bi-phase specimen in the direct shear device, applying a predetermined normal stress, unlocking the frames that held the test specimen, and displacing one frame horizontally with respect to the other at a constant rate of shearing deformation and measuring the shearing force and horizontal displacements as the specimen is sheared. At least three test for each kind of mixture and age were performed, each one with different vertical load. The surface roughness of both materials was measured in the lab using a Keyence VH-Z20UR microscope and imagery software calibrated to an overlapping grid of 3x3mm. The results are as illustrated in Fig. 7. The average roughness, R_a , for

the steel plate is well captured by the Ra value between 0.39 and 0.45, whereas rougher values were obtained for the concrete grout material.

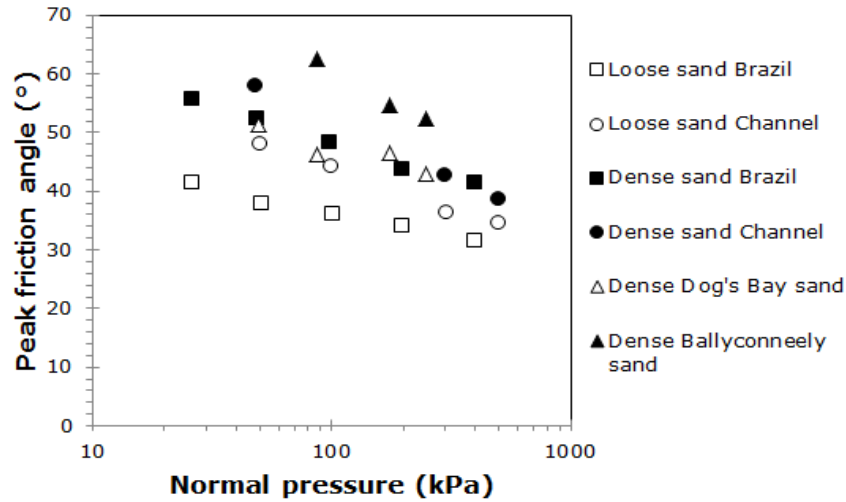


FIG. 5. Comparison of peak friction angles of the ARGEMA results (Nauroy and Le Tirant 1981) with the carbonate sands tested for the R&D program.

The shear results for the grout-steel behavior gave dramatically different results to the previously observed response for the soil-interface testing. A characteristic slip-stick response is observed as shown in Figure 8, which is thought to be related to the potential energy required to overcome interface locking followed by a relative short movement along a low resistance plane before reaching a similar interlocking resistance. It is anticipated that this behavior is a function of the relative roughness of the two materials; however this is outside the scope of this investigation and warrants further study in the future. From Fig. 8 it is possible to see that a slight concrete contraction is observed.

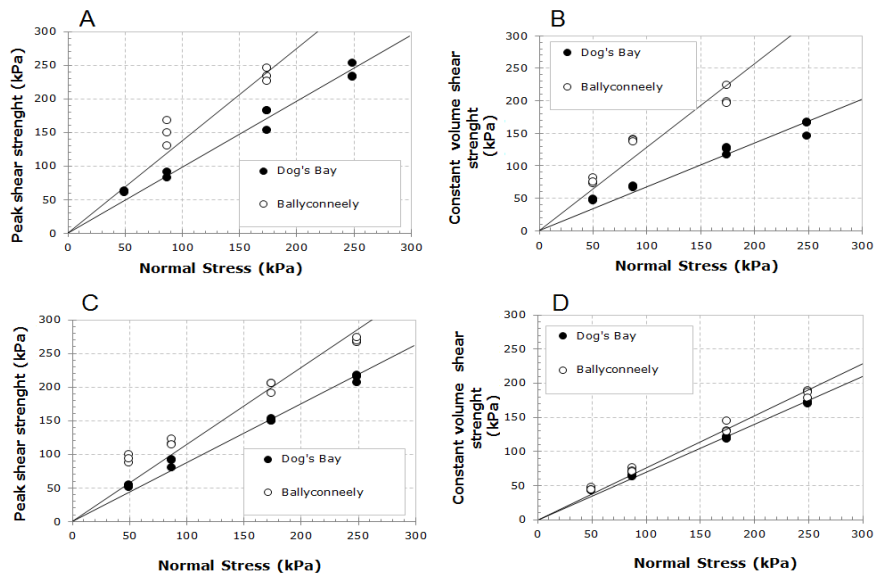


FIG. 6. Comparison of direct shear tests for DB and BC for soil-soil (A-B) and soil-grout (CD) interfaces.

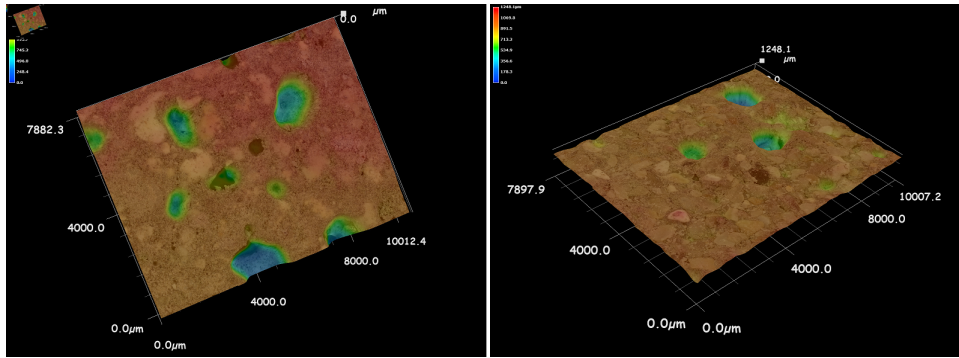


FIG. 7. Measurement of concrete roughness for the BC (left) and DB sands (right) for c-s ratios of 35%.

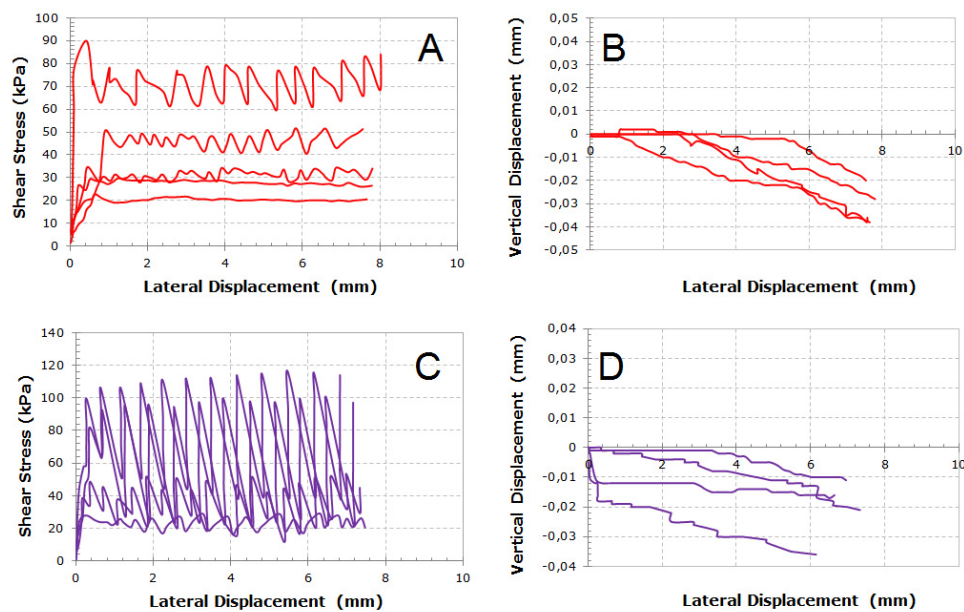


FIG. 8. Shear testing of grout against steel for 50, 87, 175 and 250kPa for the DB (A-B) and BC (C-D) sand.

CONCLUSIONS

Onshore static tension in situ tests for the MIDOS pile showed an uplift capacity of 9MN (indicating an ultimate unit skin friction capacity of 75kPa). The dynamic tests gave values of 12.7MN skin friction and 2.7MN bearing capacity in compression, giving unit skin friction and unit bearing capacities in compression of 120 and 950kPa respectively. As the installation process does not involve any soil excavation or unloading, relaxation of the surrounding soil does not occur, which ensures that the controlling radial stresses are maintained at a constant value. This seems particularly important for carbonate sands, which crush under the impact of driven piles. A series of geotechnical and grout tests have been performed on carbonate sands from Ireland. The results suggest that in terms of the geotechnical resistance the MIDOS pile is

likely to demonstrate similar behavior in calcareous deposits and silica sands. Due to its high bearing capacity and its fast installation time the MIDOS pile is a very economic foundation method for offshore platforms in calcareous sands.

ACKNOWLEDGMENTS

The authors wish to thank the companies BAUER Maschinen GmbH and BAUER Renewables Ltd. for the permission granted to publish these results and to GSP mbH Mannheim for performing the dynamic tests.

REFERENCES

- Doherty, P., Spagnoli, G. and Doherty, M. (2015a). "Laboratory investigations to assess the feasibility of employing a novel mixed-in-place offshore pile in calcareous deposits." *Ships Offshore Struct.*, <http://dx.doi.org/10.1080/17445302.2015.1056579>.
- Doherty, P., Spagnoli, G. and Bellato, D. (2015b). "Mixed-in-place response of two carbonate sands." *P.I.Civil Eng. Geotech.*, doi: [10.1680/jgeen.15.00058](https://doi.org/10.1680/jgeen.15.00058).
- Goble, G.G. and Rausche F. (1979). "Pile drivability predictions by CAPWAP." *Proc., Conf. on Numer. Methods in Offshore Piling*, ICE, London, UK, 29-36.
- Golightly, C.R. (1988) "Engineering properties of carbonate sands." Ph.D. thesis, University of Bradford, U.K.
- Igoe, D., Spagnoli, G., Doherty, P. and Weixler, L. (2014). "Design of a novel drilled-and-grouted pile in sand for offshore oil&gas structures." *Mar. Struct.*, Vol. 39: 39-49, <http://dx.doi.org/10.1016/j.marstruc.2014.06.001>.
- Jian D., Zhu L and Wu X (1991) "The dynamic properties of carbonate sands from seabed." *Proc., 2nd Int. Conf. Recent Advances Geotechnical Earthquake Engineering*. St. Louis, MO, 65-68.
- Kwag, J.M., Ochiai, H, and Yasufuku, N, (1999) *Yielding stress characteristics of carbonate sand in relation to individual particle fragmentation strength*, Engineering for Calcareous Sediments, Al-Shafei, B. ed, Balkema, Rotterdam, Netherlands, 79-86.
- Nauroy, J.F. and Le Tirant, P. (1983). "Comportement des sédiments carbonatés." *Proc., Conf. 10th ICSMFE*, Stockholm, Sweden, 265-268.
- Poulos, H.G. (1988). *Marine Geotechnics*. Unwin Hyman. London, UK.
- Spagnoli, G., Doherty, P., Bellato, D. and Weixler, L. (2014). "Latest technological developments in offshore deep mixing for piled oil and gas platforms." *Proc., 33rd Int. Conf. on Ocean, Offshore and Arctic Engineering (OMAE 2014)*, ASME, New York, NY, doi:[10.1115/OMAE2014-23045](https://doi.org/10.1115/OMAE2014-23045).
- Spagnoli, G., Doherty, P., Wu, D. and Doherty, M. (2015a). "Some mineralogical and geotechnical properties of carbonate and silica sand in relation to a novel offshore mixed-in-place pile." *Proc., Offshore Mediterranean Conf.*, OMC, Ravenna, Italy, OMC-2015-222.

Spagnoli, G.; Doherty, P., Murphy, G. and Attari, A. (2015b). "Estimation of the compression and tension loads for a novel mixed-in-place offshore pile for oil and gas platforms in silica and calcareous sands." *J. Pet. Sci. Eng.*, Vol. 136, 1-11, <http://dx.doi.org/10.1016/j.petrol.2015.10.032>.

Design Charts for Laterally-Loaded Rigid Monopiles in Multilayered Elastic Soil

Bipin K. Gupta¹ and Dipanjan Basu, C.Eng., M.ASCE²

¹Graduate Student, Dept. of Civil and Environmental Engineering, Univ. of Waterloo, 200 University Ave. W, Waterloo, ON, Canada N2L 3G1. E-mail: bkgupta@uwaterloo.ca

²Associate Professor, Dept. of Civil and Environmental Engineering, Univ. of Waterloo, 200 University Ave. W, Waterloo, ON, Canada N2L 3G1. E-mail: dipanjan.basu@uwaterloo.ca

Abstract: A new continuum-based analysis is developed for laterally loaded rigid monopiles and poles. The principle of virtual work is used to obtain the equilibrium equations for the pile and soil displacements. The governing differential equations are solved analytically and numerically to obtain pile head displacement and rotation. Normalized pile head displacement and rotation are plotted as functions of pile slenderness ratio for a variety of soil profiles. These plots can be used in analysis and design of monopiles, poles, and stubby piles like large diameter drilled shafts to quickly estimate the pile head response when the applied load, soil layering and elastic constants, and pile geometry are known.

INTRODUCTION

The slenderness ratio of monopiles supporting offshore wind turbines and the relative stiffness of the monopile-soil systems are such that the monopiles undergo rigid body rotation and translation when subjected to lateral forces and moments (LeBlanc et al. 2010, Klinkvort et al. 2012). Stubby piles and drilled piers carrying lateral loads from structures like transmission lines, power stations, and bridges also often undergo rigid body motion (Laman et al. 1999). There are several methods available for analysis and design of laterally loaded piles, such as (1) the ultimate capacity approach (Brinch Hansen 1961, Broms 1964a, b, Petrasovits and Award, 1972, Prasad and Chari, 1999, Zhang et al, 2005), (2) the subgrade modulus approach (e.g., the p - y method) (Matlock 1970, Reese et al. 1974, Murchison and O'Neil 1984), and (3) the continuum approach (Poulos 1971, Randolph 1981, Sun 1994, Zhang 2000, Gupta and Basu 2016). For flexible laterally loaded piles, the p - y method is widely used and the maximum tolerable pile head displacement is often set as the design criterion. Existing methods of analysis of rigid piles are rather limited (Davidson 1982, Carter and Kulhawy 1992, Varun et al. 2009, Higgins et al. 2013). The p - y method has been used for analysis of rigid piles, but the existing p - y method (API 2000) is strictly not applicable to rigid piles.

In this study, a continuum-based analysis is performed to study the response of laterally-loaded rigid monopiles in multilayered, elastic soil. In the analysis, rational soil and pile displacement fields ensuring continuity of displacements between pile and soil and between soil layers are assumed and the interaction between the pile and surrounding soil is taken into account by considering appropriate external and internal forces acting on the pile and soil. The principle of virtual work is applied on the pile-soil system to obtain the governing differential equations of pile and soil displacements, which are solved analytically and numerically following an iterative algorithm. Normalized pile head displacement and rotation are obtained for homogeneous, two-layer, and linearly varying soil profiles and presented in the form of charts, which can be used in design by appropriate selection of soil elastic constants such as the secant modulus.

ANALYSIS

Fig.1 shows a laterally loaded rigid monopile embedded in an elastic soil deposit consisting of n layers. Each layer i is characterized by Lamé's constants λ_{si} and G_{si} and has a thickness $H_i - H_{i-1}$ ($H_0 = 0$). The goal of the analysis is to obtain pile head displacement and rotation caused by the action of F_a and/or M_a . No slippage or separation between the pile and the surrounding soil or between the soil layers is assumed. Fig. 2 shows the appropriate external and internal forces acting on the pile and soil.

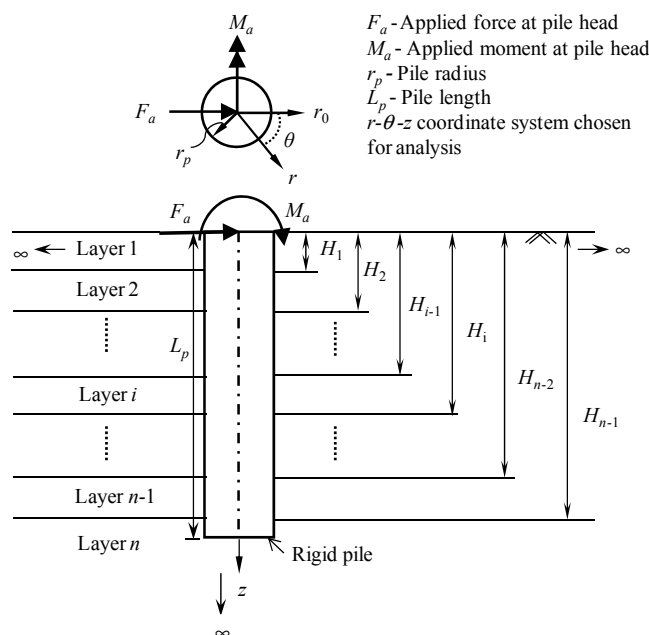


FIG. 1. Laterally loaded rigid pile in multilayered soil.

The pile is assumed to be infinitely rigid because of which it is reasonable to assume a linear pile displacement profile given by (Gupta and Basu 2015)

$$w(z) = w_h - \sin(\Theta_h)z \approx w_h - \Theta_h z \tag{1}$$

where $w(z)$ is the pile displacement at any depth z , and w_h and Θ_h are the pile head displacement and rotation, respectively.

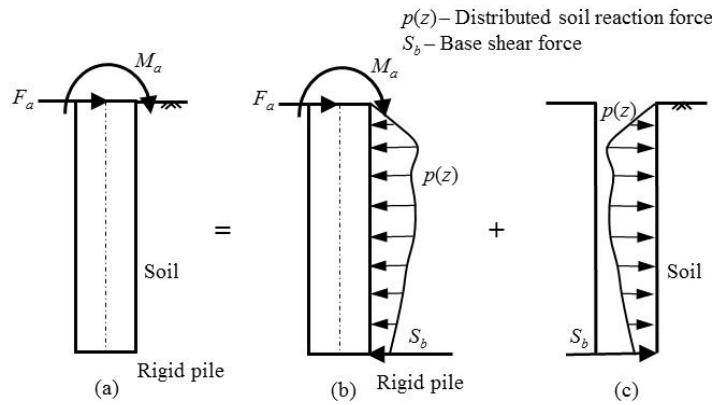


FIG. 2. (a) Pile-soil system with the applied external forces (b) force diagram of the pile (c) force diagram of the soil.

Applying the principle of virtual work $\delta W_E = \delta W_I$, (δ is the variational operator and W_E and W_I are the external and internal virtual work, respectively) to the pile (Fig. 2(b)), and using Eq. (1), the following equilibrium equations are obtained:

$$F_a = \int_0^{L_p} p(z) dz + S_b \tag{2}$$

$$M_a = - \left[\int_0^{L_p} p(z) z dz + S_b L_p \right] \tag{3}$$

For soil, the displacements in the horizontal direction are assumed as

$$u_r = w(z) \phi_r(r) \cos\theta \tag{4}$$

$$u_\theta = -w(z) \phi_\theta(r) \sin\theta \tag{5}$$

where $\phi_r(r)$ and $\phi_\theta(r)$ are dimensionless displacement functions. It is assumed that $\phi_r(r) = 1$ and $\phi_\theta(r) = 1$ at the pile-soil interface, which ensures no gap between the pile and soil, and $\phi_r(r) = 0$ and $\phi_\theta(r) = 0$ at infinite radial distance from the pile, which ensures that displacements in soil because of pile displacement decrease with increase in radial distance from the pile and become zero at large distances. The vertical soil displacement u_z is neglected.

Applying the principle of virtual work to the soil mass (Fig. 2(c)), the following equation is obtained:

$$\int_0^{L_p} p(z) \delta w dz + S_b \delta w_b - \int_0^{\infty} \int_0^{2\pi} \int_{r_p}^{\infty} \sigma_{lm} \delta \varepsilon_{lm} r dr d\theta dz - \int_{L_p}^{\infty} \int_0^{2\pi} \int_{r_p}^{\infty} \sigma_{lm} \delta \varepsilon_{lm} r dr d\theta dz = 0 \quad (6)$$

where σ_{lm} and ε_{lm} are soil stress and strain tensors, respectively, and summation is implied by the repetition of the indices l and m .

Substituting Eqs. (4) and (5) in Eq. (6), and expressing the soil strains in terms of the displacement functions $w(z)$, $\phi_r(r)$ and $\phi_\theta(r)$, an equation of the following form is obtained:

$$\left[A(w) \delta w + B(w) \delta \left(\frac{dw}{dz} \right) \right] + \left[C(\phi_r) \delta \phi_r \right] + \left[D(\phi_\theta) \delta \phi_\theta \right] = 0 \quad (7)$$

Setting the variations δw and $\delta(dw/dz)$ in Eq. (7) equal to the zero for the soil layer below the pile base ($L_p < z < \infty$), denoted by $n+1$, and within each layer $H_{i-1} < z < H_i$, the following differential equations are obtained:

$$-2t_{n+1} \frac{d^2 w_{n+1}}{dz^2} + k_n w_{n+1} = 0 \quad (8)$$

$$-2t_i \frac{d^2 w_i}{dz^2} + k_i w_i - p_i(z) = 0 \quad (9)$$

where the soil parameters k_i and t_i are given by

$$k_i = \pi \left[(\lambda_{si} + 2G_{si}) \int_{r_p}^{\infty} r \left(\frac{d\phi_r}{dr} \right)^2 dr + G_{si} \int_{r_p}^{\infty} r \left(\frac{d\phi_\theta}{dr} \right)^2 dr + 2\lambda_{si} \int_{r_p}^{\infty} (\phi_r - \phi_\theta) \frac{d\phi_r}{dr} dr \right. \\ \left. + 2G_{si} \int_{r_p}^{\infty} (\phi_r - \phi_\theta) \frac{d\phi_\theta}{dr} dr + (\lambda_{si} + 3G_{si}) \int_{r_p}^{\infty} \frac{1}{r} (\phi_r - \phi_\theta)^2 dr \right] \quad (10)$$

$$t_i = \begin{cases} \frac{\pi}{2} G_{si} \left[\int_{r_p}^{\infty} (\phi_r^2 + \phi_\theta^2) r dr \right]; & i = 1, 2, \dots, n \\ \frac{\pi}{2} G_{sn} \left[\int_{r_p}^{\infty} (\phi_r^2 + \phi_\theta^2) r dr + r_p^2 \right]; & i = n+1 \end{cases} \quad (11)$$

The parameter k represents the compressive resistance of soil (it is analogous to the Winkler spring constant) and the parameter t represents the shear force acting between the adjacent soil “springs”.

The displacement in the soil must vanish at infinite vertical distance down from the pile base. Using this condition, the displacement w for $z > L_p$ is obtained by solving Eq. (8) as:

$$w_{n+1} = w_n \Big|_{z=L_p} e^{-\sqrt{\frac{k_n}{2t_{n+1}}}(z-L_p)} \quad (12)$$

Equation (12) is used to obtain the shear force at the pile base S_b :

$$S_b = -2t_n \Theta_h + \sqrt{2k_n \zeta t_n} w_b \quad (13)$$

where $\zeta = t_{n+1}/t_n$, and w_b is the pile displacement at $z = L_p$.

Substituting Eq. (1) in Eq. (9) gives the distributed soil reaction force p :

$$p_i = k_i w_i \quad (14)$$

Substituting Eqs. (13) and (14) into Eqs. (2) and (3) gives the equations relating pile head displacement and rotation to the applied force and moment:

$$F_a = \int_0^{L_p} k_i (w_h - \Theta_h z) dz - 2t_n \Theta_h + \sqrt{2k_n \zeta t_n} (w_h - \Theta_h L_p) \quad (15)$$

$$M_a = - \int_0^{L_p} k_i (w_h - \Theta_h z) dz - \left\{ -2t_n \Theta_h + \sqrt{2k_n \zeta t_n} (w_h - \Theta_h L_p) \right\} L_p \quad (16)$$

Setting the variations $\delta\phi_r$ and $\delta\phi_\theta$ in Eq. (7) are equal to zero within the interval $r_p < r < \infty$ along with the boundary conditions $\phi_r = 1$ at $r = r_p$ and $\phi_r = 0$ at $r = \infty$, the following differential equations of ϕ_r and ϕ_θ are obtained:

$$\frac{d^2\phi_r}{dr^2} + \frac{1}{r} \frac{d\phi_r}{dr} - \left[\left(\frac{\gamma_1}{r} \right)^2 + \left(\frac{\gamma_2}{r_p} \right)^2 \right] \phi_r = \frac{\gamma_3^2}{r} \frac{d\phi_\theta}{dr} - \left(\frac{\gamma_1}{r} \right)^2 \phi_\theta \quad (17)$$

$$\frac{d^2\phi_\theta}{dr^2} + \frac{1}{r} \frac{d\phi_\theta}{dr} - \left[\left(\frac{\gamma_4}{r} \right)^2 + \left(\frac{\gamma_5}{r_p} \right)^2 \right] \phi_\theta = - \frac{\gamma_6^2}{r} \frac{d\phi_r}{dr} - \left(\frac{\gamma_4}{r} \right)^2 \phi_r \quad (18)$$

where $\gamma_1, \gamma_2, \gamma_3, \gamma_4, \gamma_5$ and γ_6 are dimensional constants given by

$$\gamma_1 = \frac{\sqrt{\sum_{i=1}^n (\lambda_{si} + 3G_{si}) \int_{H_{i-1}}^{H_i} (w_h - \Theta_h z)^2 dz + (\lambda_{sn} + 3G_{sn})(w_h - \Theta_h L_p)^2 \sqrt{\frac{\zeta t_n}{2k_n}}}}{\sqrt{\sum_{i=1}^n (\lambda_{si} + 2G_{si}) \int_{H_{i-1}}^{H_i} (w_h - \Theta_h z)^2 dz + (\lambda_{sn} + 2G_{sn})(w_h - \Theta_h L_p)^2 \sqrt{\frac{\zeta t_n}{2k_n}}}} \quad (19)$$

$$\gamma_2 = r_p \frac{\sqrt{\sum_{i=1}^n G_{si} \int_{H_{i-1}}^{H_i} \Theta_h^2 dz + G_{sn} (w_h - \Theta_h L_p)^2 \sqrt{\frac{k_n}{8\zeta t_n}}}}{\sqrt{\sum_{i=1}^n (\lambda_{si} + 2G_{si}) \int_{H_{i-1}}^{H_i} (w_h - \Theta_h z)^2 dz + (\lambda_{sn} + 2G_{sn})(w_h - \Theta_h L_p)^2 \sqrt{\frac{\zeta t_n}{2k_n}}}} \quad (20)$$

$$\gamma_3 = \frac{\sqrt{\sum_{i=1}^n (\lambda_{si} + G_{si}) \int_{H_{i-1}}^{H_i} (w_h - \Theta_h z)^2 dz + (\lambda_{sn} + G_{sn})(w_h - \Theta_h L_p)^2 \sqrt{\frac{\zeta t_n}{2k_n}}}}{\sqrt{\sum_{i=1}^n (\lambda_{si} + 2G_{si}) \int_{H_{i-1}}^{H_i} (w_h - \Theta_h z)^2 dz + (\lambda_{sn} + 2G_{sn})(w_h - \Theta_h L_p)^2 \sqrt{\frac{\zeta t_n}{2k_n}}}} \quad (21)$$

$$\gamma_4 = \frac{\sqrt{\sum_{i=1}^n (\lambda_{si} + 3G_{si}) \int_{H_{i-1}}^{H_i} (w_h - \Theta_h z)^2 dz + (\lambda_{sn} + 3G_{sn})(w_h - \Theta_h L_p)^2 \sqrt{\frac{\zeta t_n}{2k_n}}}}{\sqrt{\sum_{i=1}^n G_{si} \int_{H_{i-1}}^{H_i} (w_h - \Theta_h z)^2 dz + G_{sn} (w_h - \Theta_h L_p)^2 \sqrt{\frac{\zeta t_n}{2k_n}}}} \quad (22)$$

$$\gamma_5 = r_p \frac{\sqrt{\sum_{i=1}^n G_{si} \int_{H_{i-1}}^{H_i} \Theta_h^2 dz + G_{sn} (w_h - \Theta_h L_p)^2 \sqrt{\frac{k_n}{8\zeta t_n}}}}{\sqrt{\sum_{i=1}^n G_{si} \int_{H_{i-1}}^{H_i} (w_h - \Theta_h z)^2 dz + G_{sn} (w_h - \Theta_h L_p)^2 \sqrt{\frac{\zeta t_n}{2k_n}}}} \quad (23)$$

$$\gamma_6 = \frac{\sqrt{\sum_{i=1}^n (\lambda_{si} + G_{si}) \int_{H_{i-1}}^{H_i} (w_h - \Theta_h z)^2 dz + (\lambda_{sn} + G_{sn})(w_h - \Theta_h L_p)^2 \sqrt{\frac{\zeta t_n}{2k_n}}}}{\sqrt{\sum_{i=1}^n G_{si} \int_{H_{i-1}}^{H_i} (w_h - \Theta_h z)^2 dz + G_{sn} (w_h - \Theta_h L_p)^2 \sqrt{\frac{\zeta t_n}{2k_n}}}} \quad (24)$$

Soil Poisson’s ratio ν_s has minimal effect on the lateral pile response and its effect can be taken into account by using an equivalent shear modulus G_s^* given by (Randolph 1981)

$$G_s^* = G_s(1 + 0.75\nu_s) \quad (25)$$

For soil profiles in which the soil shear modulus G_s increases linearly with depth, the rate of change of soil shear modulus with depth dG_s/dz is similarly modified as

$$m^* = (dG_s / dz)(1 + 0.75\nu_s) \quad (26)$$

In addition to the modification of the soil shear modulus described in Eqs. (25)-(26), the Lamé's constant λ_{si} for each layer is set equal to zero to remove the artificial stiffness in the system that arises because of the assumption of the soil displacement field based on Eqs. (4) and (5).

An iterative algorithm is used to obtain w_h and Θ_h . First, initial guesses on γ - γ_6 are made, and for these assumed values, ϕ_r and ϕ_θ are determined by numerically solving Eqs. (17)-(18) simultaneously. Using the calculated values of ϕ_r and ϕ_θ , k_i and t_i are determined from Eqs. (10)-(11), which are then used to calculate w_h and Θ_h using Eqs. (15)-(16). From the calculated values of pile head displacement and rotation, γ - γ_6 are obtained from Eqs. (19)-(24) and compared with the assumed initial values. If the differences in γ - γ_6 are more than a tolerable limit, the same set of calculation is repeated with the newly calculated values of γ - γ_6 as the new initial guesses. Iterations on γ - γ_6 are continued until the values of γ - γ_6 between successive iterations are less than 0.001. After the convergence of γ - γ_6 is ensured, w_h and Θ_h are recorded as the final values of the pile head displacement and rotation.

APPLICABILITY OF THE PRESENT ANALYSIS AND CHOICE OF SOIL MODULUS

Whether a laterally loaded pile behave as a flexible or a rigid element depends on its slenderness ratio L_p/r_p and on the relative stiffness E_p/G_s^* of the pile and soil (E_p is the Young's modulus of the pile). For piles embedded in homogeneous soils, if E_p/G_s^* exceeds a threshold value $(E_p/G_s^*)_{RT}$ given by

$$\left(\frac{E_p}{G_s^*}\right)_{RT} = 44 \left(\frac{L_p}{r_p}\right)^{3.23} \quad (27)$$

then these piles behave as rigid elements (Higgins et al. 2013). For piles embedded in soil profiles in which the soil shear modulus increases linearly with depth from zero at the ground surface, the boundary between flexible and rigid behavior can be demarcated by (Higgins et al. 2013)

$$\left(\frac{E_p}{m^* r_p}\right)_{RT} = 119 \left(\frac{L_p}{r_p}\right)^{3.45} \quad (28)$$

If, for a pile, $E_p/(m^* r_p)$ exceeds $(E_p/(m^* r_p))_{RT}$, then it behaves as a rigid element.

It is evident from Eqs. (10)-(11), Eqs. (25)-(26), and Eqs. (27)-(28) that appropriate values of soil elastic constants (e.g., secant modulus) have to be chosen in order to reliably predict real field pile response. Recommendations on the choice of soil elastic constants are given in Bowles (1996) and Budhu (2011), which are summarized in Table 1.

Table 1: Typical values of Shear Modulus (G_s) and Poisson's ratio (ν_s) for different types of soil

<i>Soil type</i>	<i>Description</i>	G_s (MPa)	ν_s
Clay	Soft	0.5-5	0.35-0.4
	Medium	5-15	0.3-0.35
	Stiff	15-40	0.2-0.3
Sand	Loose	5-10	0.15-0.25
	Medium	10-15	0.25-0.3
	Dense	15-35	0.25-0.35
Silt	-	0.8-8	0.3-0.35

RIGID PILE RESPONSE IN HOMOGENEOUS, TWO-LAYER, AND LINEARLY VARYING SOILS

Pile responses obtained from the present analysis are compared with those of equivalent three-dimensional (3D) finite element (FE) analysis using ABAQUS 6.10 (2010). In ABAQUS, the pile and soil are modeled as a single cylindrical part (domain) with appropriate partitioning to represent the circular hollow monopile and soil separately. Appropriate boundary conditions (with zero horizontal displacements on the outer vertical boundary and zero horizontal and vertical displacements in the bottom horizontal boundary) and mesh size (based on a convergence check) using C3D8R elements are used in the model. A concentrated force and moment are applied to a reference point at the centroid of the pile head to which all the nodes of the rigid pile are connected using a rigid body constraint (this ensured that the entire pile behaves as a rigid body).

In the FE analysis, piles with the same geometries (lengths and diameters) as those of the rigid piles were reanalyzed after removing the rigid body constraint. These "flexible" piles were analyzed to identify the difference in the response that occurs if the rigid body constraints are not imposed in the FE analysis. For the analysis of the flexible piles, the same approach as that of the rigid pile was followed except that only the nodes on the top surface of the pile (i.e., the pile head) were connected to the reference point using the rigid body constraint (this allowed the pile to deform as a flexible element). The pile properties used for the flexible pile analysis are $E_p = 210$ GPa, $\nu_p = 0.3$ (ν_p is the Poisson's ratio of pile), and $t_p = \{6.35 + (2 \times r_p)/100\}$ mm (API 2000) (t_p is the pile wall thickness). It was found that the pile responses obtained from the present analysis matched well with those from 3D FE analysis for both rigid and flexible piles. After the accuracy of the present analysis was verified with FE analysis, parametric studies were performed.

Figs. 3(a)-(b) show the normalized pile head displacement $w_h G_s^* r_p / F_a$ and $w_h G_s^* r_p^2 / M_a$ and normalized pile head rotation $\Theta_h G_s^* r_p^2 / F_a$ and $\Theta_h G_s^* r_p^3 / M_a$, caused by applied force and moment, respectively, as functions of the pile slenderness ratio L_p / r_p for piles embedded in homogenous soil. In these figures, results obtained from the 3D FE analysis are also plotted. The match between the results of the present analysis and 3D FE analysis are quite well. The plots for flexible piles obtained from the 3D FE analysis show that, even if the piles are allowed to behave flexibly in the FE analysis, the head displacements obtained are quite close to those of rigid piles.

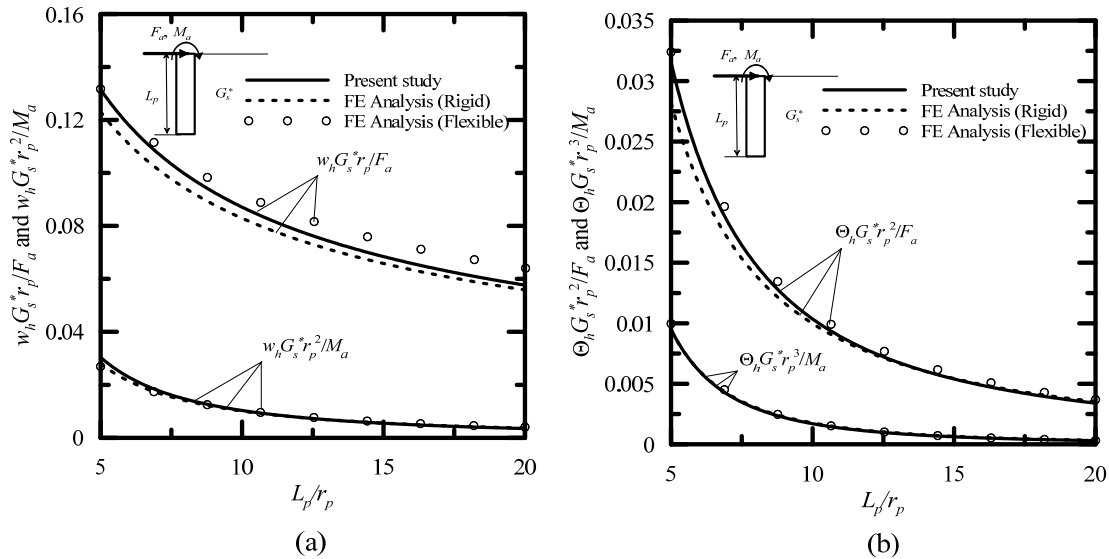


FIG. 3. (a) Normalized pile head displacement and (b) normalized pile head rotation in homogeneous soil profiles.

Figs. 4(a)-(d) show the normalized pile head displacement and rotation caused by applied force and moment in two-layer soil profiles for three cases of G_{s2}^* / G_{s1}^* . The normalization is performed with respect to the modified shear modulus G_{s1}^* of the top layer. Plots are generated for different thickness H_1 of the top layer.

Figs. 5(a)-(d) show the normalized head displacement $w_h m^* r_p^2 / F_a$ and $w_h m^* r_p^3 / M_a$ and rotation $\Theta_h m^* r_p^3 / F_a$ and $\Theta_h m^* r_p^4 / M_a$ caused respectively by applied force and moment as functions of pile slenderness ratio in soil profiles where the equivalent shear modulus G_s^* increases linearly with depth from G_{s0}^* at the ground surface. The plots are obtained for different values of $G_{s0}^* / (m^* L_p)$.

Sometimes, soil profiles have the top layer with spatially constant modulus followed by linearly increasing modulus in the second layer. Normalized pile responses are obtained for such soil profiles for the case with $H_1 / L_p = 0.1$ (Figs. 6(a)-(d)).

NUMERICAL EXAMPLE

A numerical example is provided to illustrate the use of Figs. 3-6. A circular monopile with $L_p = 25$ m, $r_p = 4$ m, $E_p = 210$ GPa, and $\nu_p = 0.3$ is considered embedded in a homogeneous loose sandy soil with Young's modulus $E_s = 20$ MPa

and $\nu_s = 0.2$. The pile is subjected to a force $F_a = 3$ MN and a moment $M_a = 35$ MN at the head. The modified shear modulus G_s^* for the loose sandy soil is calculated as $G_s^* = [E_s / \{2(1 + \nu_s)\}] (1 + 0.75 \nu_s) = [20 / \{2 \times (1 + 0.2)\}] \times (1 + 0.75 \times 0.2) = 9.6$ MPa. For the pile to behave rigid it should satisfy Eq. (27). It was found that, for this pile, $E_p / G_s^* = 21875$ and $44(L_p / r_p)^{3.23} = 16374$, which implies that $E_p / G_s^* > (E_p / G_s^*)_{RT}$. Thus, the pile behaves as a rigid element.

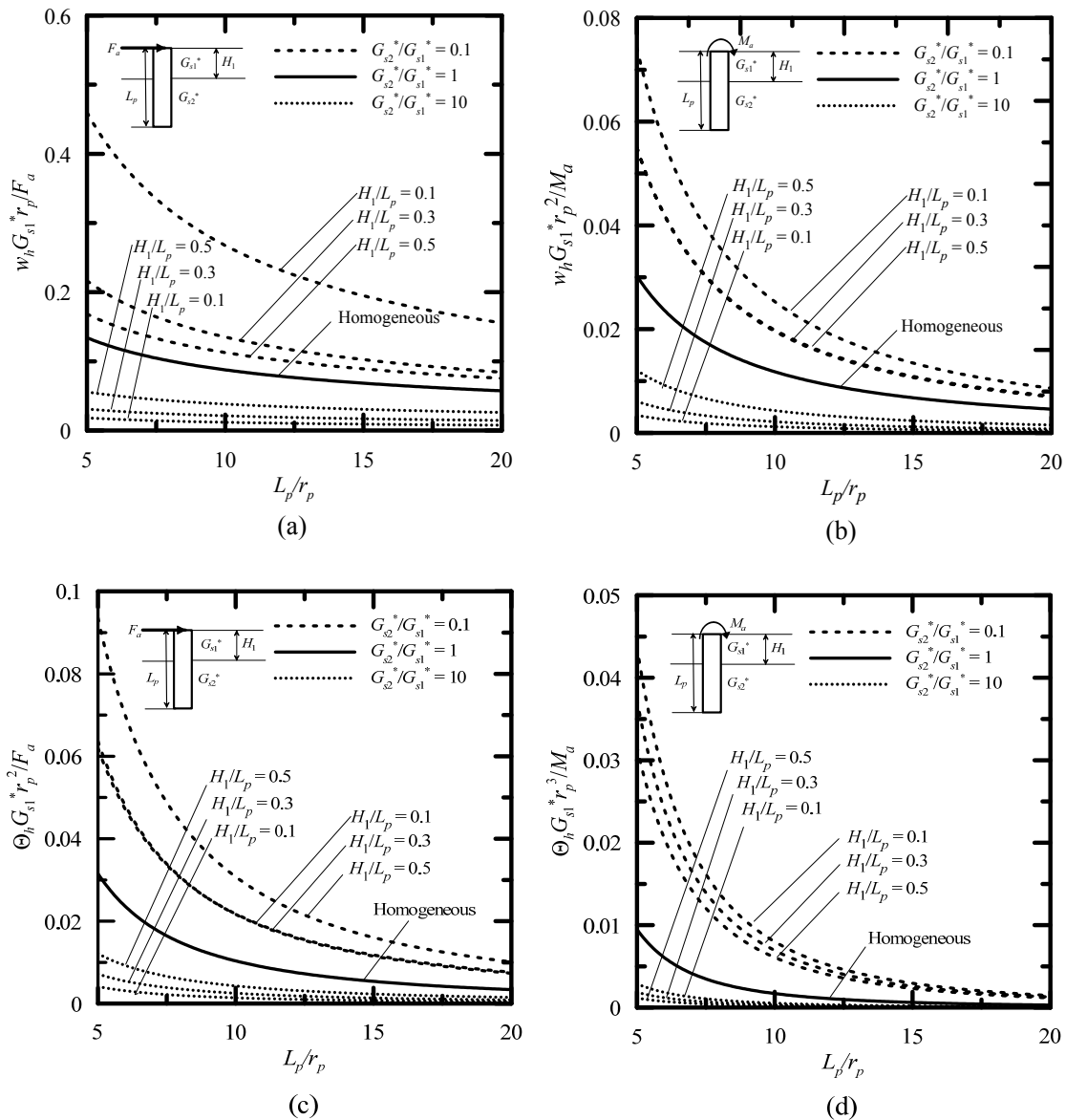


FIG. 4. (a) Normalized pile head displacement due to applied force, (b) normalized pile head displacement due to applied moment, (c) normalized pile head rotation due to applied force, and (d) normalized pile head rotation due to applied moment in two layer soil profiles.

The pile head displacement w_h and rotation Θ_h are determined from Figs. 3(a)-(b). For the pile slenderness ratio $L_p/r_p = 25/4 = 6.25$, the normalized head displacements and rotations $w_h G_s^* r_p / F_a$, $w_h G_s^* r_p^2 / M_a$, $\Theta_h G_s^* r_p^2 / F_a$ and $\Theta_h G_s^* r_p^3 / M_a$ obtained from Figs. 3(a)-(b) are 0.1, 0.017, 0.015, and 0.0026, respectively. Thus, the head displacement is given by $w_h = [(0.1 F_a) / (G_s^* r_p) + (0.017 M_a) / (G_s^* r_p^2)] = [(0.1 \times 3) / (9.6 \times 4) + (0.017 \times 35) / (9.6 \times 4^2)] = 0.012$ m and the rotation is given by $\Theta_h = [(0.015 F_a) / (G_s^* r_p^2) + (0.0026 M_a) / (G_s^* r_p^3)] = [(0.015 \times 3) / (9.6 \times 4^2) + (0.0026 \times 35) / (9.6 \times 4^3)] = 4.41 \times 10^{-4}$ rad.

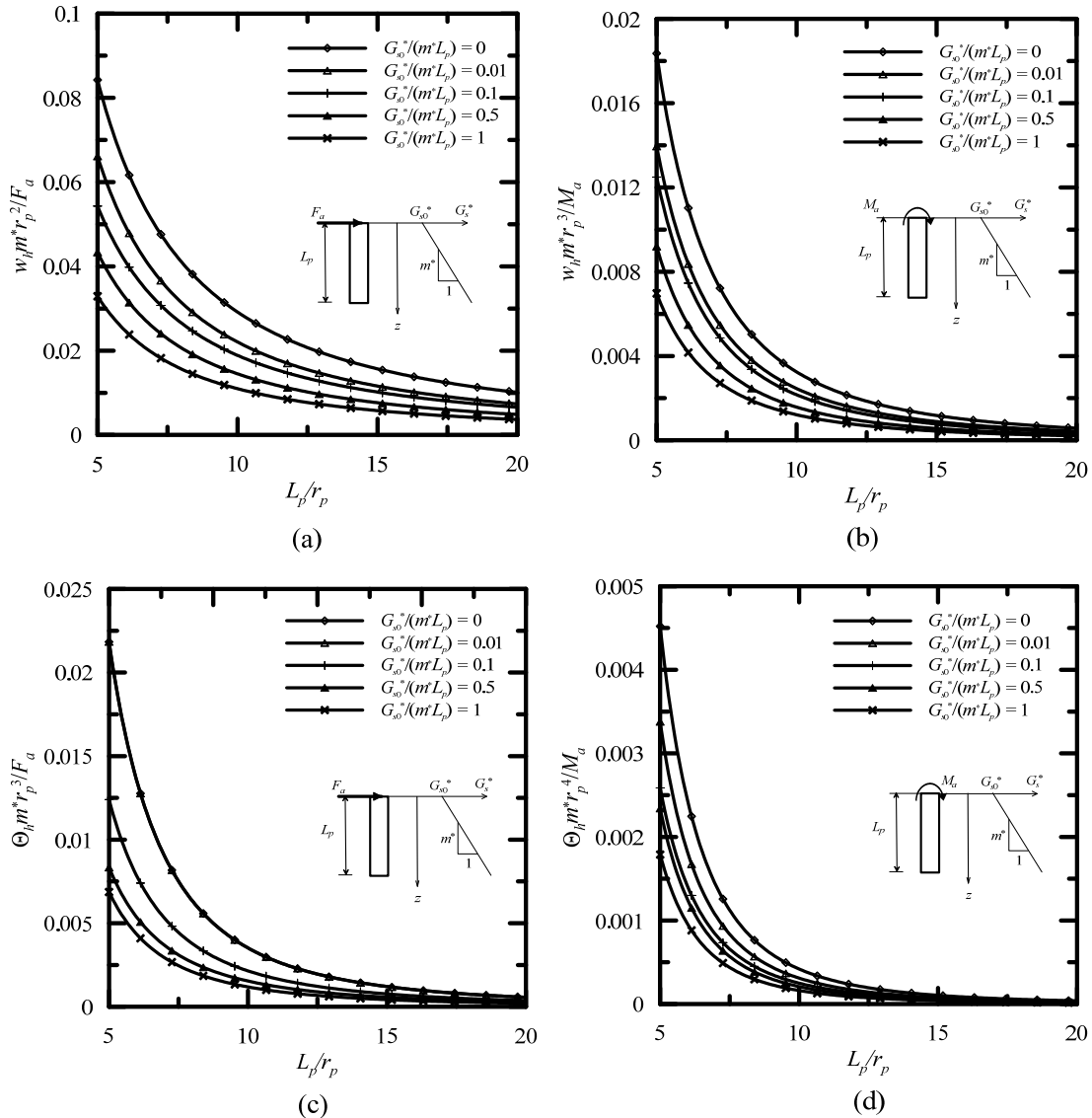


FIG. 5. (a) Normalized pile head displacement due to applied force, (b) normalized pile head displacement due to applied moment, (c) normalized pile head rotation due to applied force, and (d) normalized pile head rotation due to applied moment in linearly varying soil profiles.

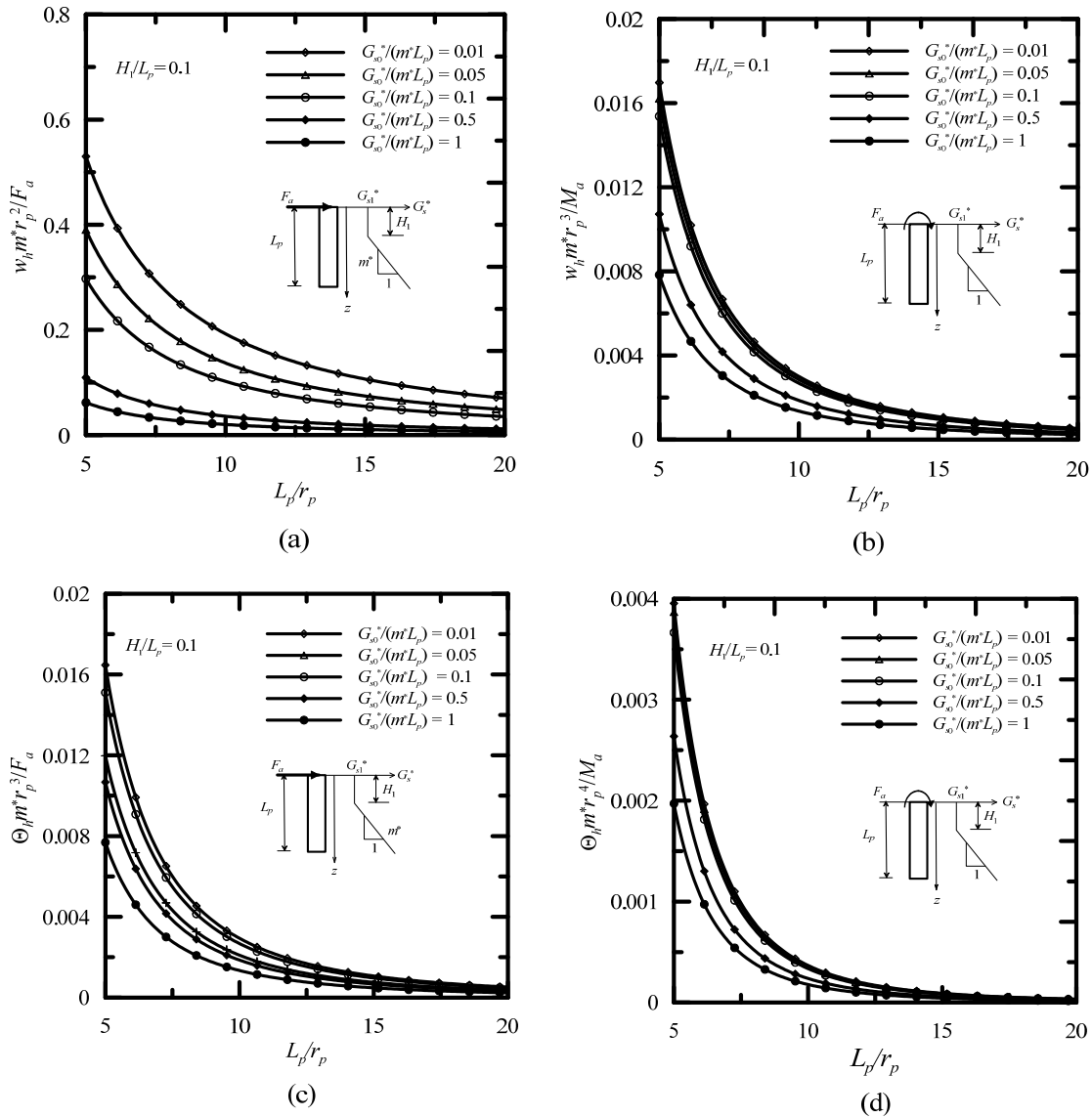


FIG. 6. (a) Normalized pile head displacement due to applied force, (b) normalized pile head displacement due to applied moment, (c) normalized pile head rotation due to applied force, and (d) normalized pile head rotation due to applied moment for soil profiles with constant modulus in the top layer and linearly varying modulus in the second layer.

CONCLUSIONS

A new continuum-based method of analysis for laterally loaded rigid circular monopiles and poles in multilayered elastic soil is presented. The differential equations for the pile and soil displacements are obtained using the principle of virtual work. The equations are solved using an iterative algorithm to obtain the pile head displacement and rotation.

Dimensionless head displacement and rotation caused by the applied horizontal force and moment at the pile head are calculated using the analysis and plotted as functions of pile slenderness ratio for different soil profiles. These design charts can be used to quickly estimate the rigid pile head displacement and rotation, which can be checked against the serviceability limit states of maximum allowable head displacement and rotation.

The inputs required for performing the analysis and for using the design charts are the soil elastic constants and layering, the pile geometry, and the magnitudes of the applied force and moment. These design charts can give accurate predictions of pile head displacement and rotation if the soil elastic constants are reliably determined. A numerical example that illustrates the use of the design charts is provided.

REFERENCES

- ABAQUS 6.10 (2010). Dassault Systemes Simulia Corp, Providence.
- API (2000). "Recommended practice for planning, designing and constructing fixed offshore platforms—working stress design RP 2A-WSD." 21st edn. American Petroleum Institute, Washington.
- Bowles J.E. (1996). "Foundation analysis and design-5th Edition." The McGraw-Hill Companies, Inc.
- Brinch-Hansen, J. (1961). "The ultimate resistance of rigid piles against transversal forces." *Bulletin Rep. No. 12*, Danish Geotechnical Institute, Copenhagen, Denmark, 5–9.
- Broms, B.B. (1964a). "Lateral resistance of piles in cohesionless soils." *J. Soil Mech. and Found. Div.*, 90(3), 123–159.
- Broms, B.B. (1964b). "Lateral resistance of piles in cohesive soils." *J. Soil Mech. and Found. Div.*, 90(2), 27–63.
- Budhu, M. (2011). "Soil Mechanics and foundations-3rd edition." John Wiley & Sons, Inc.
- Carter, J.P., and Kulhawy, F.H. (1992). "Analysis of laterally loaded shafts in rocks." *J. Geotech. Eng.*, 118(6), 839–855.
- Davidson, H.L. (1982). "Laterally loaded drilled pier research, Vol 1: Design methodology, Vol. 2: Research documentation." Final Report by GAI Consultants Inc., to Electric Power Research Institute (EPRI).
- Gupta, B.K., Basu D., (2015). "Analysis of offshore wind turbine rigid monopile foundation." 15th PanAmerican conference on soil mechanics and geotechnical engineering-From fundamentals to application in geotechnics, Buenos Aires, 822-829.
- Gupta, B.K., Basu D., (2016). "Analysis of laterally loaded rigid monopiles and poles in multilayered linearly varying soil." *Computers and Geotechnics*, 72:114–125.
- Matlock H (1970). "Correlations for design of laterally loaded piles in soft clay." In: Proceedings of 2nd annual offshore technology conference, Houston, Texas, 1:577–94.
- Murchison, J.M., O'Neill, M.W. (1984). "Evaluation of p-y relationships in cohesionless soils." In: Analysis and design of pile foundations: proceedings of a symposium sponsored by the asce geotechnical engineering division and a session sponsored by the ASCE technical council on codes and standards in conjunction with the ASCE national convention, San Francisco, California; 174–91.

- Higgins, W., Vasquez, C., Basu, D., and Griffiths, D.V. (2013). "Elastic solutions of laterally loaded piles." *J. Geotech. Geoenviron. Eng.*, 139(7), 1096-1103.
- Klinkvort RT, Springman SM, Hededal O (2012). Scaling issues in centrifuge modelling of monopiles. *International Journal of Physical modelling in Geotechnics*, 13(2):38-49.
- Laman, M., King, G.J.W. and Dickin, E.A. (1999). "Three-dimensional finite element studies of the moment-carrying capacity of short pier foundations in cohesionless soil. *Computers and Geotechnics*, 25, 141-155.
- LeBlanc C, Houlsby GT, Byrne BW (2010). Response of stiff piles in sand to long-term cyclic lateral loading. *Geotechnique*, 60(2):79-90.
- Petravovits, G., and Award, A. (1972). "Ultimate lateral resistance of a rigid pile in cohesionless soil." *Proc., 5th European Conf. on SMFE 3*, The Spanish Society for Soil Mechanics and Foundation, 407-412.
- Poulos, H.G. (1971). "Behavior of laterally loaded piles: I. Single piles." *Journal of Soil Mechanics and Foundations Division ASCE*; 97:711-731.
- Prasad, Y.V.S.N., and Chari, T.R. 1999. "Lateral capacity of model rigid piles in cohesionless soils." *Soils Found.* , 39(2):21-29.
- Randolph, M.F. (1981). "The response of flexible piles to lateral loading." *Geotechnique*; 31(2):247-259.
- Reese L.C., Cox W.R., Koop F.R. (1974). "Analysis of laterally loaded piles in sand." *Proceedings of the offshore technology conference*, Paper No. 2080, Houston, 473-483.
- Sun, K. (1994). "Laterally loaded piles in elastic media." *J. Geotech. Geoenviron. Eng. ASCE*; 120(8):1324-1344.
- Varun D., Assimaki, G., Gazetas, G. (2009). "A simplified model for lateral response of large diameter caisson—Linear elastic formulation." *Soil Dynamics and Earthquake Engineering* 29 (2009) 268-291.
- Zhang, L., Ernst, H., Einstein, H.H. (2000). "A non-linear analysis of laterally loaded rock-socketed shafts." *J. Geotech. Geoenviron. Eng. ASCE*; 126(11):955-968.
- Zhang, L., Silva, R., and Grismala, R. 2005. "Ultimate lateral resistance to piles in cohesionless soils." *J. Geotech. Geoenviron. Eng. ASCE*, 131(1),78-83.

Effect of Climate Change on the Reliability of Offshore Wind Turbine Foundations

Sumanta Haldar¹ and Dipanjan Basu, C.Eng., M.ASCE²

¹Associate Professor, Dept. of Civil Engineering, School of Infrastructure, Indian Institute of Technology Bhubaneswar, Bhubaneswar 751013, India. E-mail: sumanta@iitbbs.ac.in

²Associate Professor, Dept. of Civil and Environmental Engineering, Univ. of Waterloo, 200 University Ave. W, Waterloo, ON N2L 3G1, Canada, E-mail: dipanjan.basu@uwaterloo.ca

Abstract: The reliability of monopile supported offshore wind turbine (OWT) is assessed considering the uncertainties in aerodynamic and hydrodynamic loads and spatial variability of soil. Traditional designs assume that applied loads are constant during the design period of OWTs. However, fluctuations in climatic conditions alter the future wind and wave loads because of which time-dependent reliability assessment of OWTs is performed in this study. Statistical downscaling method using the general circulation model corresponding to the A2 emission scenario is used to predict the future wind and wave responses. The impact of climate change on the probability of failure for the serviceability limit state of maximum allowable mudline rotation is studied. The uncertainties in soil properties, and wind and wave loads are incorporated in the analysis. The reliability of an OWT structure founded in sand is investigated for the period 2015-2050. The OWT system is modeled using a beam supported laterally by a nonlinear Winkler foundation characterized by the American Petroleum Institute recommended cyclic p - y curve for sand. This study shows that the reliability of OWT is changed significantly because of the effects of climate change.

INTRODUCTION

Design of monopile supported offshore wind turbines (OWTs) is primarily driven by the safety and serviceability criteria used in the design of the monopiles (Li *et al.* 2011). The cost of foundations of OWTs is about 30-40% of the total cost because of which developing a rational and robust foundation design strategy for OWTs is necessary (Bhattacharya and Adhikari 2011). In conventional design, it is assumed that the applied loads are constant during the design period of OWTs. However, recent studies show that the future wind speed may vary by 10-74% because of changes in the climatic conditions in various offshore locations across the world (Chan 2011, Deepthi and Deo 2010). Fluctuations in wind speed and wave height because of climate change affect the monopile performance, which may adversely impact the safety, serviceability, and functionality of OWTs. Holland *et al.* (2011) reported that a 10% increase in wave height because of climate change can increase the cost of coastal and offshore structures

significantly. At the same time, the change in wind speed and wave height may cause reduction in wind energy production in the future (Mori *et al.* 2013).

Accounting for the uncertainties associated with the prediction of future wind speed, wave height, and applied loads can substantially change the monopile design outcome (Khan *et al.* 2006). The design becomes more challenging when the inherent heterogeneity and random spatial variability of soil properties (Griffiths and Fenton 2001) in the seabed is considered. In order to obtain a robust design, a probability-based analysis approach is necessary for OWT structures, with the wind and wave loads and the soil properties treated as random variables.

Studies on impact of climate change on OWTs have mostly focused on wind energy production in which the future wind speed and wave height were examined for different green-house gas emission scenarios (Pryor *et al.* 2005). The probabilistic aspects of design of OWT structures have been studied in the past by incorporating the spatial variability of soil properties and uncertainty of applied loads (Carswell *et al.* 2015, Sørensen and Toft 2010). However, in all these studies, the uncertainties in the prediction of wind speed and wave height caused by climate change and in the estimation of soil properties have not been considered together for reliability analysis of monopiles.

In this study, a time-dependent reliability assessment of a 5 MW OWT is performed considering the temporal variations of wind speed, wave height, and wave period. These temporal variations are assumed to be caused by climate change. The wind speed, wave height and wave period data are collected from the observatory at the west coast of India for the period 1998-2001. Realizations of future wind speed, wave height and wave period are predicted using the statistical downscaling model (Wilby *et al.* 2002) for a 50-year time period (2001-2050) using the General Circulation Model (GCM) predictor variables. The high-resolution wind and wave data, obtained from the National Centre for Environmental Prediction (NCEP), are used to calibrate the downscaling model. A monopile supported OWT founded in sand is idealized as an Euler-Bernoulli beam subjected to horizontal loads from wind and waves, and the widely used American Petroleum Institute (API 2011) based cyclic p - y model is used to calculate the lateral resistance of soil surrounding the monopile. The friction angle and unit weight of soil are modeled as one-dimensional non-Gaussian homogeneous random field to capture the spatial variability of soil. Using Monte Carlo simulations, the time-dependent probability of failure of the OWT, based on the serviceability limit state of maximum allowable mudline rotation, is investigated for future climate scenarios.

PREDICTION OF FUTURE WIND AND WAVE CLIMATE

An offshore location with latitude 15.39°N and longitude 73.76°E is selected at a distance of approximately 28 km off the west coast of India. The water depth at this location is assumed to be 20 m. Future wind speed and wave height and period are generally derived using the GCM data, which incorporates the future climate change scenarios. The spatial resolution of GCM data is low because of which the data requires

processing for application to a specific region – this processing is termed downscaling of data (Deepthi and Deo 2010). Future wind speed, and wave height and period are generated for this location considering GCM predictors using an open source program *Statistical Downscaling Model (SDSM)* (Wilby *et al.* 2002). The stochastic weather generator and transfer function method are adopted for downscaling. The weather generator is a statistical approach that replicates the statistical parameters (e.g., mean and variance) from the observed data to generate a similar time series of any length using calibrated regression model. The transfer function method establishes an empirical relationship between local-scale predictands (i.e., wind speed, wave height, and wave period) and regional-scale predictors (e.g., temperature, specific humidity, etc.) using regression analysis. The *SDSM* model has three steps. The first step involves model calibration to develop the transfer function, which needs station data and reliable high resolution predictor variables. The daily maximum wind speed, and wave height and period corresponding to the maximum wind speed are obtained from the buoy deployed by the Indian National Center for Ocean Information Services (INCOIS) (www.incois.gov.in/portal/index.jsp) for the period 1998-2001. The high resolution NCEP predictor data and the station data are used to develop the transfer function. The second step involves validation of the regression equation with respect to station data and downscaled data derived using NCEP data for the period of 1998-2001. The third step involves generation of ensemble of synthetic, daily weather time series using GCM predictors and the regression model for the future period of 2001-2050.

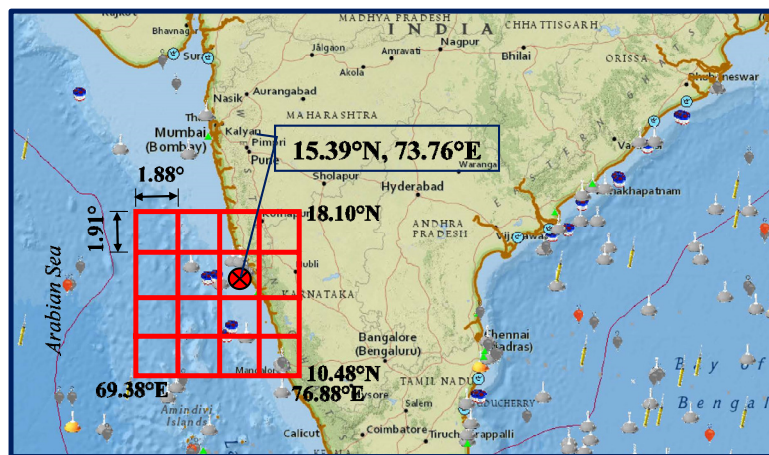


FIG. 1. Selected location at the Indian coastline and NCEP grid superposed on the selected location (www.incois.gov.in/portal/index.jsp).

In this study, five predictor variables, namely zonal wind speed, meridional wind speed, air temperature at 2 m (near surface), specific humidity at 2 m, and sea level pressure are used for the period 1998-2001. The predictor variables are downloaded for an area corresponding to a 5×5 grid of equal interval around the selected location,

spanning over 10.476°-18.091°N and 69.375°-76.875°E, to obtain a more realistic estimate of the neighboring climate (Figure 1). The data sets of five predictor variables are also downloaded for the 25 grid points from the third-generation Canadian coupled GCM for A2 emission scenario for the period 2001-2050. It is important to note that A2 scenario is the worst case scenario which projects about 3.6°C temperature rise by 2100 (Deepthi and Deo 2010). The resolution of NCEP and GCM data are different; hence, re-gridding of GCM data is done using linear interpolation to match with NCEP resolution. After re-gridding, GCM predictor variables for the selected location are estimated from the 25 grid points using a weighted average method. Bias correction for all the predictor variables are done by subtracting the mean from the original data and dividing the difference by the standard deviation for a predefined baseline period. A baseline period of 1998-2014 for NCEP and 2001-2014 for GCM predictor are selected. The durations are considered adequate for establishing a reliable climatology (Wilby *et al.* 2002).

Table 1. Performance of the statistical downscaling model.

Parameters	Correlation coefficient	Mean absolute error
Wind speed (m/sec)	0.6	1.7
Wave height (m)	0.87	0.24
Wave period (sec)	0.82	0.47

The bias corrected data sets are used to develop future climate scenarios using the statistical downscaling technique. The correlation coefficient and mean absolute error of wind speed, wave height and wave period between the observed and predicted data are reported in Table 1. A correlation coefficient of 0.6 can be regarded as reasonably good for the simulation of natural phenomena (Kulkarni *et al.* 2014). Hence, the model is used in the subsequent forecasting of wind speed, wave height, and wave period. An additional check on the performance of the downscaled model is done by comparing the statistics of the predicted daily wind speed based on the GCM model with actual buoy data from INCOIS for the period 2002-2006. The mean and standard deviation of wind speed are 4 m/s and 2.34 m/s for GCM predicted data, respectively, and the corresponding values from observed data are 5.9 m/s and 2.6 m/s. This additional validation lends credence to the use of the GCM model in reproducing the present day climate in terms of wind speed. Realizations of the daily wind speed, and wave height and period are forecasted for the period of 2001-2050. Figure 2 shows 1000 realizations of the annual maximum wind speed and its mean considering the future climatic conditions.

WIND AND WAVE LOADS ON OWT

Wind load acting on the tower can be categorized into load acting on the turbine blades and load acting on the turbine tower. The lateral load F_b acting at hub height due to wind thrust on the turbine blades is given by (Jara 2006)

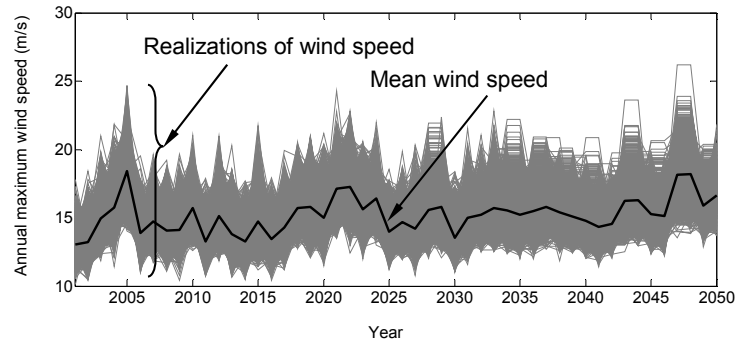


FIG. 2. 1000 realizations of forecasted annual maximum wind speed considering future climate, and mean wind speed.

$$F_b = 0.5 \rho_a \pi R_T^2 V^2 C_T(\lambda_s) \sin(2\pi f_r t) \tag{1}$$

where V = hub height wind speed in m/s, R_T = rotor radius in m, ρ_a = air density = 1.23 kg/m³ at 15°C and 1 atm, f_r = rotor frequency, t = dynamic time, and $C_T(\lambda_s)$ = thrust coefficient which is a function of the tip speed ratio λ_s ($= V_r R_T / V$ in which V_r is the rotor speed in rad/s). The lateral wind load acting on the turbine tower can be estimated based on wind load profile as (DNV-RP-C205 2010)

$$F_{tower}(z) = 0.61 V^2(z) C_h C_s D \tag{2}$$

where $F_{tower}(z)$ = wind load profile in N/m acting along the tower height, $V(z)$ = wind speed profile in m/s; C_h = height coefficient (varies from 1 to 1.58 for a height ranging over 0-100 m), C_s = shape coefficient (= 0.5), and D = tower diameter. The wind speed profile along the tower height is given by (DNV-RP-C205 2010)

$$V(z) = U_{10} \frac{\ln(z/z_0)}{\ln(10/z_0)} \tag{3}$$

where z = tower height in m from the mean sea level (MSL), z_0 = terrain roughness parameter = 0.0001 m in the open sea without waves, and U_{10} = 10-minute average wind speed at 10 m height from the MSL.

The load on the tower, obstructed because of blade rotation (3P loading), is estimated by integrating Equation (2) up to the blade length and applied as lateral point load (F_{1tower}) at the center of gravity with a frequency of $3f_r$. The Load on the tower uncovered by the blade is applied as static equivalent point lateral load (F_{2tower}) at the center of gravity.

The wave force (F_{wave}) on the OWT is estimated using Morison’s equation (DNV-OS-J101 2010)

$$F_{wave}(t) = F_M + F_D = C_M \rho \pi D^2 / 4 \int_{-d_w}^{\eta(t)} \ddot{u}(t) dz_1 + C_D \rho D / 2 \int_{-d_w}^{\eta(t)} \dot{u}(t) |\dot{u}(t)| dz_1 \tag{4}$$

where F_M = inertia force and F_D = drag force, z_1 is the depth below the MSL, C_D = drag coefficient, C_M = mass coefficient, ρ = mass density of the sea water (1030 kg/m^3), D = diameter of the tower and monopile in m, \dot{u} = wave induced velocity of water, \ddot{u} = wave induced acceleration of water, and $\eta(t) = 0.5h_w \cos(\omega_w t)$ in which h_w is the wave height in m and ω_w is the wave frequency in rad/s. The equations of \dot{u} and \ddot{u} are given by (DNV-OS-J101 2010)

$$\dot{u} = \frac{h_w \pi}{T_w} \frac{\cosh\{k(z_1 + d_w)\}}{\sinh(kd_w)} \cos(\omega_w t) \quad (5)$$

$$\ddot{u} = \frac{2h_w \pi^2}{T_w^2} \frac{\cosh\{k(z_1 + d_w)\}}{\sinh(kd_w)} \sin(\omega_w t) \quad (6)$$

where, k is the wave number in m^{-1} , λ is the wave length in m, d_w is the water depth in m, T_w is the wave period in sec.

The annual maximum wind speed is extracted from the forecasted daily wind speed data for the year 2015-2050. This wind speed is assumed to be 10 min average wind speed at 10 m high (U_{10}) and the wind speed profile along the tower is derived using Equation (3). The wind load at the hub height (F_b) is estimated from Equation (1) using the wind speed at hub height calculated using Equation (3). Loads on tower (F_{1tower} and F_{2tower}) are estimated by integrating Equation (2) over the tower height. The wave load is estimated from Equations (4)-(6) using the annual wave height and period corresponding to maximum annual wind speed data. Loads are also estimated for the present-day climate condition based on the annual maximum wind speed and the corresponding wave height and period for the period of 1998-2001 using NCEP predictors.

NUMERICAL ANALYSIS

The response of the OWT is estimated using finite element analysis performed in OpenSees (2007) software. The monopile and tower are modeled as a uniform Euler-Bernoulli beam of flexural rigidity $E_p I_p$ supported laterally by a nonlinear Winkler foundation characterized by the API (2011) recommended cyclic p - y curve for sand. The tower and monopile is discretized into beam elements. The rotor nacelle assembly (RNA) is combined into a single mass M_{RNA} placed at the top of the tower with the second mass moment inertia J_{RNA} .

The properties of a 3 bladed 5 MW OWT are adopted from the National Renewable Energy Laboratory (NREL 2004). The numerical analysis is carried out using rotor diameter = 126 m, hub height from MSL = 80 m, $M_{RNA} = 300$ ton, $J_{RNA} = 4 \times 10^7 \text{ kg-m}^2$, density of steel for tower and monopile = 7850 kg/m^3 , Young's modulus of steel = $2.1 \times 10^{11} \text{ N/m}^2$, diameter of monopile and tower = 6.5 m, thickness of monopile and

tower = 65 m, and embedded length of monopile = 55 m. The rotor frequency (1P) lies in the range of 0.12-0.2 Hz, and the corresponding 3P frequency lies in the range of 0.36-0.6 Hz. The OWT is designed such that the fundamental frequency of the system would lie in the interval between the highest 1P and lowest 3P frequencies (i.e., soft-stiff approach), which is the usual choice for OWT. The wind loading frequency at hub height is applied as 0.2 Hz, which is the highest 1P frequency of the reference OWT.

UNCERTAINTY IN SOIL PROPERTIES

The inherent variability of soil properties, represented by the mean, coefficient of variation (COV), and correlation distance, affects the OWT response. In this study, the friction angle ϕ' is assumed to be bounded by medium to dense sand with a range of 30°-40° and the COV $_{\phi'}$ is assumed to be 5% (Lacasse and Nadim 1996). A bounded distribution, which resembles beta distribution, is assumed for ϕ' (Fenton and Griffiths 2003):

$$\phi'(\tilde{z}) = \phi'_{\min} + 0.5(\phi'_{\max} - \phi'_{\min}) \left[1 + \tanh\left(\frac{sG_{\phi'}(\tilde{z})}{2\pi}\right) \right] \quad (7)$$

where ϕ'_{\min} and ϕ'_{\max} are the minimum and maximum friction angles, respectively, s is a scale factor, \tilde{z} is the spatial position below the mudline at which ϕ' is required, and $G_{\phi'}(\tilde{z})$ is a zero mean-unit variance Gaussian random field. Realizations of $G_{\phi'}(\tilde{z})$ is generated by the *Cholesky decomposition* technique using an exponential isotropic correlation function given by:

$$\rho_{\phi'}(\tau) = \exp(-2|\tau|/\Theta_{\phi'}) \quad (8)$$

where τ is the distance between any two points in the field and $\Theta_{\phi'}$ is the spatial correlation distance. Based on the reported values (Phoon and Kulhawy 1999), $\Theta_{\phi'} = 2$ m is assumed in this study. The value of s is assumed to be 5. According to Lacasse and Nadim (1996), the submerged unit weight of soil γ' follows a normal distribution with COV = 0-10%. In this study, γ' is assumed to be normally distributed with COV $_{\gamma'} = 5\%$. The mean value of γ' is assumed to be 8.2 kN/m³.

TIME DEPENDENT RELIABILITY ANALYSIS

According to DNV-OS-J101 (2010), the serviceability limit for monopile head rotation is 0.5° at the mudline. During the design life of an OWT structure, the limit state function for serviceability limit state (SLS) can be defined as (Carswell *et al.* 2015):

$$g(t) = 0.5^\circ - |\theta_{\text{mudline}}(t)| \quad (9)$$

where $g(t)$ is the safety margin with respect to time t and $\theta_{mudline}(t)$ is the rotation of monopile at mudline in degree. $\theta_{mudline}(t)$ depends on future loading, and soil and monopile properties. Failure occurs when $g(t) \leq 0$ so that the instantaneous failure probability $p_f(t)$ can be defined as:

$$p_f(t) = P(0.5^\circ \leq |\theta_{mudline}(t)|) \quad (10)$$

The instantaneous failure probability can be integrated over the interval $[0, t]$ in order to evaluate the failure probability over that interval. The time dependent failure probability of OWT for its design life T can be divided into finite number of time segments (e.g., month, year, etc.):

$$p_f(T) = 1 - \prod_{i=1}^N (1 - p_i); \quad N = 1, 2, \dots, 50 \quad (11)$$

where p_i is the probability of failure for the i^{th} time step and N is the number of time segments. In this study, p_i is estimated annually using Equation (10) considering the annual maximum $\theta_{mudline}$ value for a 50 year time period (2001-2050) incorporating climate change. The value of p_i is also estimated based on the present climate condition in which the maximum $\theta_{mudline}$ value is estimated within the period of 1998-2001 based on loads estimated from NCEP predictors. In this analysis, 1000 Monte Carlo simulations were performed because the fluctuations in the mean and standard deviation of OWT response fall within a tolerable range. Each realization produced a different $\theta_{mudline}$ values. Hence, the statistics were obtained by ensemble averaging. A first order second moment reliability method (FOSM) was used to estimate the annual probability of failure for the serviceability criterion.

RESULTS

The effect of climate change on the mean maximum rotation of monopile at the mudline ($\bar{\theta}_{mudline}$) is investigated. The values of $\bar{\theta}_{mudline}$ is observed to be 0.23° and 0.38° for the cases without and with climate change effect, respectively. This means $\bar{\theta}_{mudline}$ is increased by about 62% when climate change effects are considered. This increase occurs because wind load and wave load increases substantially when climate change effects are considered.

The variability of $\theta_{mudline}$ is also examined in terms of its coefficient of variation $COV_{\theta_{mudline}}$. It is observed that $COV_{\theta_{mudline}}$ increases marginally when climate change is considered. For example, $COV_{\theta_{mudline}} = 11\%$ and 12% for the cases with and without the effects of climate change, respectively. Realizations of $\theta_{mudline}$ for future periods are obtained from the Monte Carlo simulations and the cumulative density is estimated. It is found using the chi-square goodness of fit tests that there is a good agreement between the estimated data and assumed log-normal distributions (Figures 3(a)-(b)).

Time dependent reliability analysis is performed for OWT based on the failure probability model for the serviceability limit described by Equation (11). The time dependent probability of failure is estimated without and with climate change effects, and the results are presented in Figure 4 for different design life of OWT. Considering climate change, the estimated time dependent failure probability at different reference time (T) is found to be more than that of the case when climate change effect is not accounted for in the analysis.

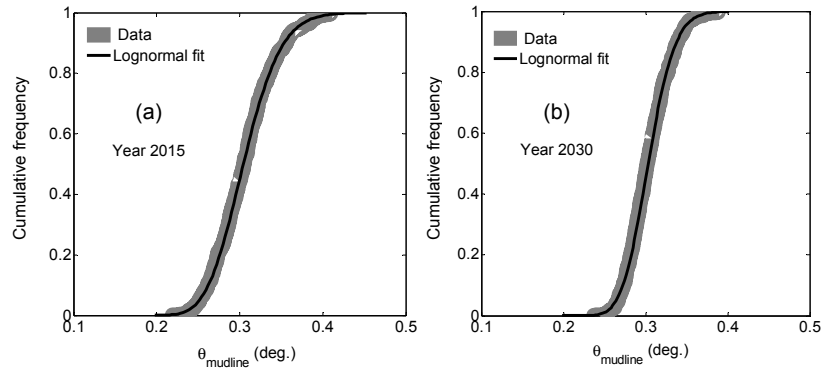


FIG. 3. Cumulative frequency from maximum $\theta_{mudline}$ considering future climate and fitted log-normal distribution for (a) year 2015 and (b) year 2030.

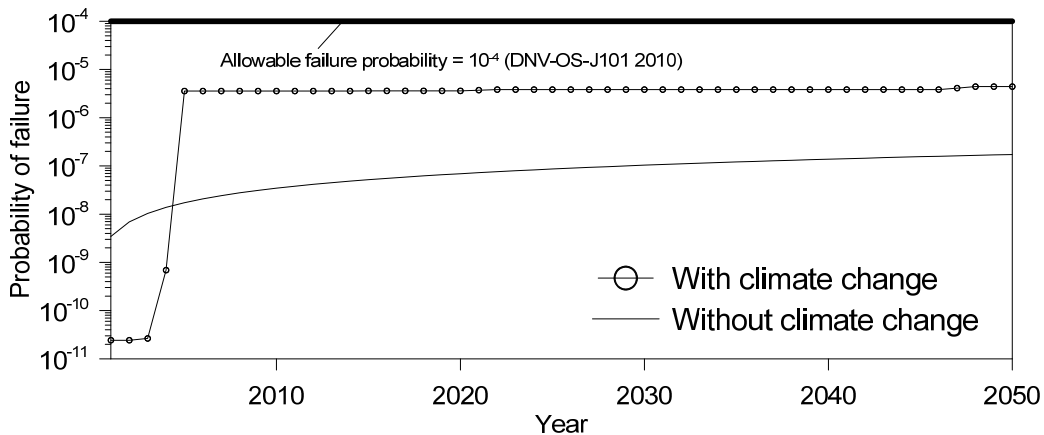


FIG. 4. Probability of failure for present and future climate conditions for different design life of OWT.

CONCLUSIONS

The impact of climate change on time dependent reliability of a 5 MW OWT installed at the west coast of India is assessed. The realizations of future wind speed, wave height and wave period are generated for a period of 2001-2050 considering GCM predictors and A2 scenario, using the Statistical Downscaling Model. Spatial variability of soil is also incorporated in this study. The probability of exceeding the serviceability limit state

criterion of tolerable tilt of OWT is estimated using the First Order Second Moment reliability method. A time-dependent failure probability for the serviceability criterion of OWT is presented. The downscaling model is found to perform reasonably well in forecasting the wind speed, wave height, and wave period using the GCM. The lognormal probability distribution is found to be in good agreement with the estimated maximum mudline rotation of the monopile. The mean value of the maximum rotation at mudline increases significantly when the effect of future climate change is considered. The coefficient of variation of maximum mudline rotation changes marginally because of climate change effects. The rate of increase in failure probability based on the serviceability limit state criterion is substantially higher than that of the case without climate change.

REFERENCES

- API. American Petroleum Institute. (2011). *"Petroleum and natural gas industries-specific requirements for offshore structures. Part 4 – geotechnical and foundation design considerations."*
- Bhattacharya, S., and Adhikari, S. (2011). "Experimental validation of soil-structure interaction of offshore wind turbines." *Soil Dynamics and Earthquake Engineering*, 31: 805-816.
- Carswell, W., Arwade, S. R., DeGroot, D. J., and Lackner, M. A. (2015). "Soil-structure reliability of offshore wind turbine monopile foundations." *Wind Energy*, 18 (3): 483 – 498.
- Chan, B. (2011). "Climate change and wind speeds." *The Structural Engineer*, 89 (10): 12-13.
- Deepthi, R., and Deo, M. C. (2010). "Effect of climate change on design wind at the Indian offshore locations." *Ocean Engineering*, 37: 1061-1069.
- DNV-OS-J101. (2010). *"Design of offshore wind turbine structures."* DET NORSKE VERITAS.
- DNV-RP-C205. (2010). *"Environmental conditions and environmental loads."* DET NORSKE VERITAS.
- Fenton, G. A., and Griffiths, D. V. (2003). "Bearing capacity prediction of spatially random $c-\phi$ soils." *Canadian Geotechnical Journal*, 40: 54 – 65.
- Griffiths, D.V., and Fenton, G.A. (2001). "Bearing capacity of spatially random soil: the undrained clay Prandtl problem revisited." *Geotechnique*, 51(4): 351-359.
- Holland, G. J., Done, J., and Hurrell, J., Webster, P., Bruyere, C., and Suzuki-Parker, A. (2011). "Effect of climate variability and change in hurricane activity in the North Atlantic." *Draft final report on project*, 07121-1801.
- Jara, F. A. V. (2006). *"Model testing of foundations for offshore wind turbines."* Ph.D. thesis, University of Oxford.
- Khan, M. J., Coulibaly, P., and Dibike, Y. (2006). "Uncertainty analysis of statistical downscaling methods." *Journal of Hydrology*, 319: 357 – 382.

- Lacasse, S., and Nadim, F. (1996). "Uncertainties in characterising soil properties." *Proceedings of Uncertainty in Geological Environment*, 96: 49-73.
- Li, M., Zhang, H., and Guan, H. (2011). "Study of offshore monopile behavior due to ocean waves." *Ocean Engineering*, 38: 1946-1956.
- Mori, N., Shimura, T., Nakajo, S., Tsujio, D., Yasuda, T., Mase, H., and Suh, K. D. "Projection of future wave climate change and application to coastal structure design." *Proceedings of Breakwater Conference*, Edinburgh, 9p, 2013.
- NREL (2004). "National Renewable Energy Laboratory." Washington.
- OpenSees (2007). "Open System for Earthquake Engineering Simulation." <http://opensees.berkeley.edu>.
- Phoon, K.-K., and Kulhawy, F. H. (1999) "Evaluation of geotechnical property variability." *Canadian Geotechnical Journal*, 36: 625-639.
- Pryor, S. C., Barthelmie, R. J., and Kjellstrom, E. (2005). "Potential climate change impact on wind energy resources in northern Europe: analyses using a regional climate model." *Climate Dynamics*, 25: 815-835.
- Sørensen, J. D., and Toft, H. S. (2010). "Probabilistic design of wind turbines." *Energies*, 3: 241-257.
- Wilby, R. L., Dawson, C. W., and Barrow, E. M. (2002). "SDSM – a decision support tool for the assessment of regional climate change impacts." *Environmental modelling & Software*, 17: 147-159.

Evaluating the $p - y$ Curve Method of Analysis for Large-Diameter Monopiles Using Centrifuge Modelling

Mr. Steven M. Bayton¹ and Dr. Jonathan A. Black²

¹Ph.D. Researcher, Dept. of Civil and Structural Engineering, Univ. of Sheffield, U.K.

²Senior Lecturer, Dept. of Civil and Structural Engineering, Univ. of Sheffield, U.K.

Abstract: Centrifuge model tests were performed to evaluate the structural response of offshore wind turbine monopile foundations in sand subjected to lateral loading. Model monopile foundation tests were performed at 100 gravities (100g) of a prototype pile 5 m in diameter (D). Three embedment depths (L) of 20 m, 30 m and 40 m ($L/D = 4, 6$ and 8) were evaluated under an increasing monotonic lateral load. Evolution of pile head deflection, lateral force and consequential pile bending moments were monitored. Comparison of the observed and predicted deflected shape and pile bending moments indicates that the design codes $p - y$ methods of analysis (API, 2011; DNV, 2014) may underestimate the two parameters by up to 30 percent. Additionally, upon unloading, the monopile experiences a degree of 'locked-in' moment, which suggests an increase in horizontal restraint due to sand particle restructuring in the principle axis of bending during the initial load application.

INTRODUCTION

In order to become a sustainable, energy-independent society, there is a requirement for a strategic departure from traditional fossil fuel energy sources towards zero carbon electricity generation. The offshore wind energy sector presents a major opportunity to realize this. In the United Kingdom alone, offshore wind has the potential to meet the country's demands three times over (Oswald *et al.*, 2008). That being said, the industry is not expanding as rapidly as required owing to multiple factors, none more so than the high initial capital investment. Improvement of foundation efficiency, through increased knowledge and experience, is one solution which would lead to an increase in the economic feasibility of future projects.

Owing to its simple and robust design, its suitability to mass-production and track record over the past decade, the monopile is likely to remain the leading foundation of choice for designers and contractors alike for water depths of proposed sites in the near future. This paper presents results from a suite of monotonic lateral loading tests performed in the University of Sheffield's 4m diameter 50g-tonne geotechnical beam

centrifuge located in the Centre for Energy and Infrastructure Ground Research to evaluate the current $p - y$ design method applied for monopile design in sand.

P - Y CURVE METHOD OF ANALYSIS

The foundations for an offshore wind turbine have to be able to withstand the most severe of weather conditions presented by the harsh marine environments. The oil and gas industry has vast experience in managing these conditions; however, there are significant differences between the problems faced in this sector and those encountered in the design of wind turbine foundations. Most notably is the relatively large design lateral loads, F_h , applied to the wind turbine structure at great eccentricity, e , in comparison to the small vertical loads from its self-weight, resulting in large overturning moments experienced at the seabed. Figure 1(a) illustrates the applied loading condition that the offshore wind turbine foundation is subjected to.

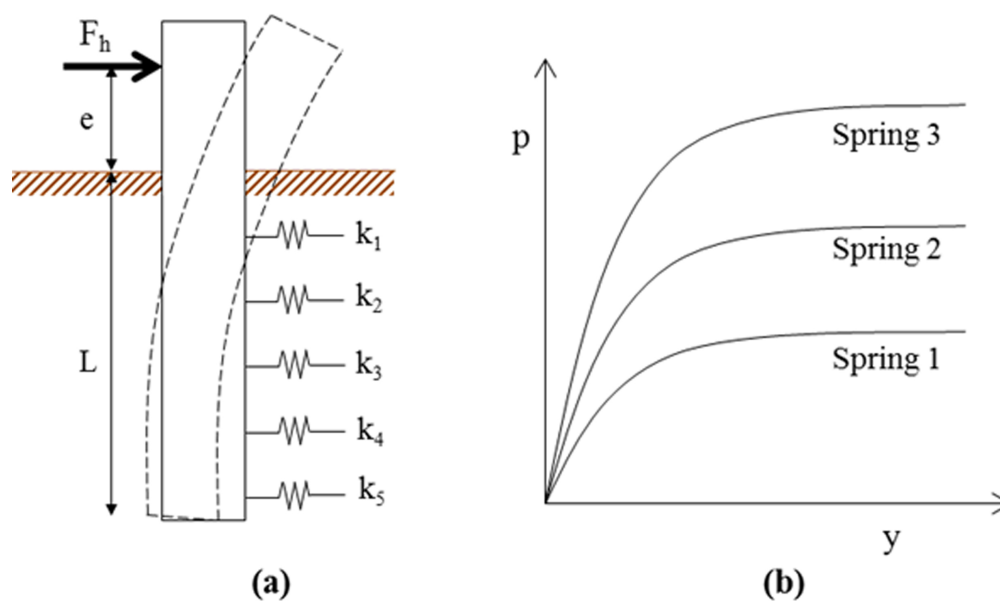


FIG. 1. (a) Schematic Illustration of Applied Loads on an Offshore Wind Turbine; (b) Non-Linear $p - y$ Curve Spring Foundation

Methods of analysis to predict the behavior of piles in sand subjected to these large overturning moments are numerous. Of these, the most widely accepted by designers today is a form of the subgrade reaction theory approximation (Hetenyi, 1946), commonly known as the $p - y$ curve method of analysis. This method combines original theories of the Winkler spring model (Winkler, 1867) with nonlinear soil properties and forms the backbone of the current API (2011) and DNV (2014) design codes. These codes are proven in industry to produce reliable predictions for deflection, and resulting moments, of laterally loaded piles deployed throughout the oil and gas industry. The fundamental Euler-Bernoulli equation to describe pile deflected shape is as follows:

$$EI \frac{d^4 y}{dz^4} + Q_a \frac{d^2 y}{dz^2} - p(y) = 0 \quad (\text{Eq. 1})$$

where EI is the bending stiffness of the pile, y the horizontal deflection, z the depth below the seabed, Q_a the applied axial load and $p(y)$ the soil resistance as a function of the horizontal deflection as defined by the $p - y$ curves in sand (Fig. 1(b)).

However, uncertainties are raised when translating this method to the design of large-diameter wind turbine monopiles. Firstly, the fundamental design curves, on which the $p - y$ method is formed, are based on empirically derived adjustment factors which are calibrated using data obtained from piles of up to just 1.2 meters in diameter (O'Neill and Murchison, 1984). Modern day monopiles already reach over 5 meters in diameter, presenting significant questions over the method's empirical validity upon extrapolation.

One major concern for the method's translation to large-diameter monopiles is the variation of the mechanism of failure as a result of the increased global monopile stiffness. Traditional offshore piles for the oil and gas industry are typically classified as flexible, with high slenderness ratios (high L/D ratio), and failure is generally defined by the realization of bending resistance of the pile, with relatively low yielding of the surrounding soil. Conversely, monopiles for offshore wind turbines, can be considered as more rigid in nature owing to their low L/D ratio and experience both bending and rotational failure mechanisms. This variation in potential mode of failure is largely governed by criteria such as the pile bending stiffness, embedment length and soil properties which present significant complications to design. Several studies, both numerical and experimental (Achmus *et al.*, 2009; Hamre *et al.*, 2011; Haiderali and Madabhushi, 2013) have been performed to investigate the behavior of this rigid mechanism of failure, though few studies evaluate the transition from slender to rigid and the effect this has on the failure mechanism and soil-pile interaction behavior.

It is therefore necessary to assess the current design codes for accurate application to rigid, large-diameter monopiles. In this respect, this paper reports on a series of centrifuge experimental monopile foundation tests in sand to evaluate the effect of pile rigidity for verification of the $p - y$ design method.

CENTRIFUGE EXPERIMENTAL METHOD

Centrifuge modelling techniques have been widely applied to a number of offshore geotechnical engineering problems to provide validation of design methods, verification of numerical predictions and information for geotechnical design (Murff, 1996; Gaudin *et al.*, 2011). Centrifuge modelling presents several advantages over traditional 1g physical model tests, namely the recreation of prototype soil stresses within the sample.

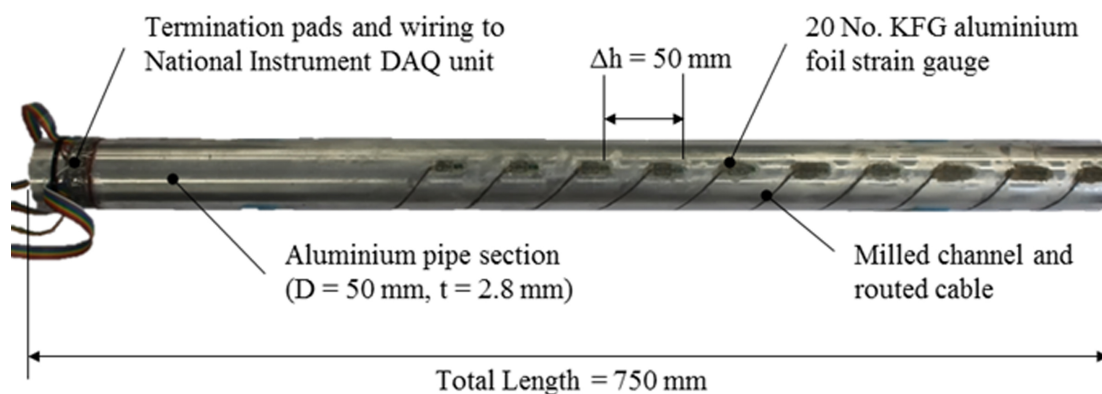
Using The University of Sheffield's 4m diameter 50g-tonne geotechnical beam centrifuge a series of centrifuge model tests, at a centrifugal acceleration of 100g, were conducted to evaluate the structural response of monopile foundations embedded at various depths subjected to lateral monotonic load. Table 1 provides details on the centrifuge.

Table 1. University of Sheffield 50g-tonne Centrifuge Specification

Description	Specification
Platform radius	2.0 m
Payload size	W = 0.8 m (circumferential) L = 0.8 m (vertical in flight) H = 0.9 m (radial in flight)
Maximum acceleration	100g at 500 kg payload or 150g at 330 kg payload

A fine grained sand commercially known as HST95 sand ($d_{50} = 0.2$ mm) was pluviated into the centrifuge strong box in twenty separate layers through a coarse mesh from a drop height of 400 mm to give a loose sample with a relative density (R_d) of 34 %. A high level of repeatability of this value of R_d was achieved ($\sigma = 0.8$ %). Shear box tests revealed the angle of shear resistance at $R_d = 34$ % to be 32° . The cylindrical strong box had an internal diameter and height of both 500 mm, and provided a rigid boundary condition.

An aluminum pipe section with outer diameter 50 mm and wall thickness 2.8 mm was used throughout the test procedure to replicate a 5 meter outer diameter pile. The wall thickness of the model pile (2.8 mm) was selected to reproduce the flexural stiffness (EI) of a typical steel monopile at prototype scale. Ten pairs of strain gauges (KFG type with gauge length 3 mm) in half bridge configuration were positioned on the pile extremity along its embedded length at 50 mm intervals. Bending moment calibration of the strain gauges was performed on each 90 degree orientation as well as in compression. The proportion of out-of-plane bending was recorded to be a maximum of just 8 % of the respective in-plane bending. Application of a compressive stress did not provide any significant excitation of the strain gauges and thus no adjustment to the bending measurements was required to account for this. Milled channels enabled routing of all wiring away from the strain gauges towards the top of the pile. Epoxy was positioned around these channels to protect the wiring. Protruding epoxy was then made flush with the curvature of the pile using fine sandpaper to preserve its original cylindrical profile. Figure 2 presents the arrangement of the model pile.

**FIG. 2. Model Pile Arrangement**

The pile section was driven into position at 1g with the aid of an alignment frame that mounted on the top of the centrifuge strong box to ensure vertical installation was achieved. Three embedment lengths were selected, defined by the length to diameter ratio, L/D , equating to 4, 6 and 8, replicating 20, 30 and 40 meter prototype embedment lengths respectively. Table 2 defines the pile configuration used throughout the experimental program.

Table 2. Pile Configuration – Model and Prototype Scale

Description	Model Dimension	Prototype Dimension
Diameter (D)	50 mm	5.0 m
Thickness (t)	2.8 mm	84 mm (steel equivalent)
Material	Aluminum	Steel
Young's Modulus (E)	69 GPa	205 GPa
Flexural Stiffness (EI)	$8.01 \times 10^3 \text{ Nm}^2$	$8.01 \times 10^{11} \text{ Nm}^2$
Embedment length (L)	200 mm ($L/D = 4$)	20.0 m
	300 mm ($L/D = 6$)	30.0 m
	400 mm ($L/D = 8$)	40.0 m
Maximum Applied Load (F_h)	875 N ($L/D = 4$)	8.75 MN
	1375 N ($L/D = 6$)	13.75 MN
	1525 N ($L/D = 8$)	15.25 MN

A bespoke loading frame was assembled from extruded aluminum sections to ensure that the lateral load was applied at the highest possible location in relation to the dimension constraints of the centrifuge payload. This allowed for the ratio of applied lateral load to overturning moment at the seabed to be as close to prototype as possible, best replicating *in situ* loading conditions. The load application was achieved by the use of an 80 mm diameter dual acting pneumatic cylinder actuator, with a maximum load capacity of 5.0 kN [50 MN at 100g] at 10 Bar air pressure supply. A load cell calibrated over the range of 2.5 kN was attached to the end of the actuator piston that interfaced to the pile via a 'C' shape coupler mating with its curvature. Two linear variable differential transformers were attached to the frame to give values of horizontal displacement. These readings, alongside the bending moment readings from the strain gauges, were necessary to process the deflected shape. Two GoPro™ cameras were mounted to record image data and video to remotely view the test during flight. Figure 3 presents the experimental setup.

Load was applied in approximately 100 N [0.1 MN] increments at an extremity of 300 mm [30 m] from the seabed, relating to z/D equal to 6, until ultimate limit state conditions were reached. This was defined by either the realization of the bending resistance of the pile ($M_{rd,p} = 650 \text{ MNm}$ at steel prototype condition, equivalent to 650 Nm at model scale, marked as the dashed line on Fig. 5), or upon reaching yielding of the soil, defined as excessive plastic deformation. The resulting bending moments experienced within the pile were recorded using the strain gauge measurements.

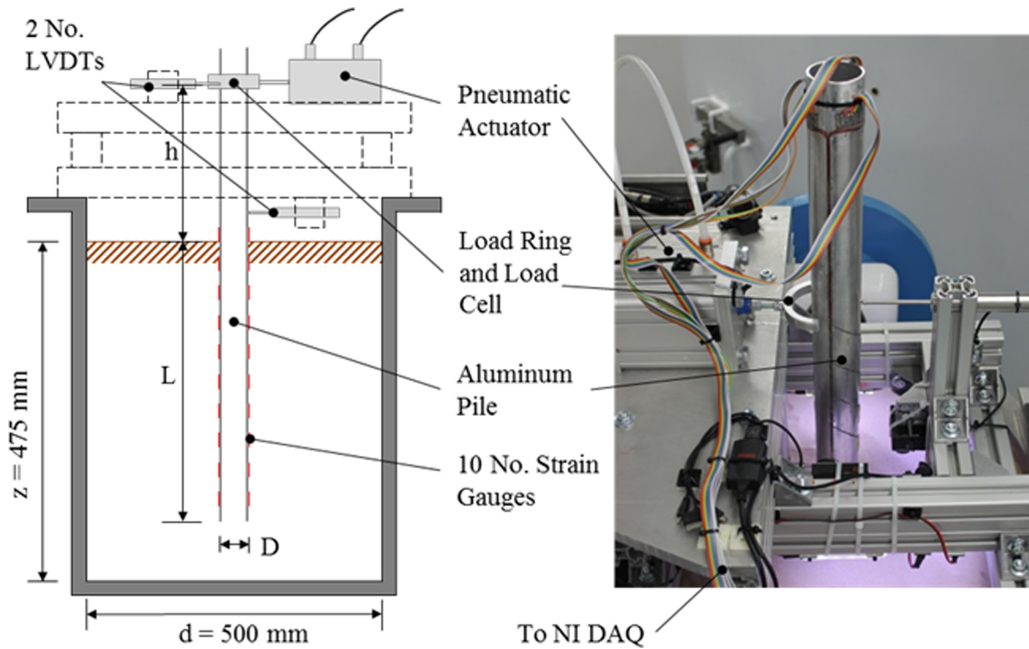


FIG. 3. Centrifuge Lateral Loading Frame Experimental Setup

RESULTS

The lateral load, F_h , displacement, y , relationships observed for each of the three centrifuge tests are plotted using prototype units in Figure 4. The lateral displacement measurement presented is referenced at the same horizontal line of action as the actuator and is normalized by the diameter of the pile (D).

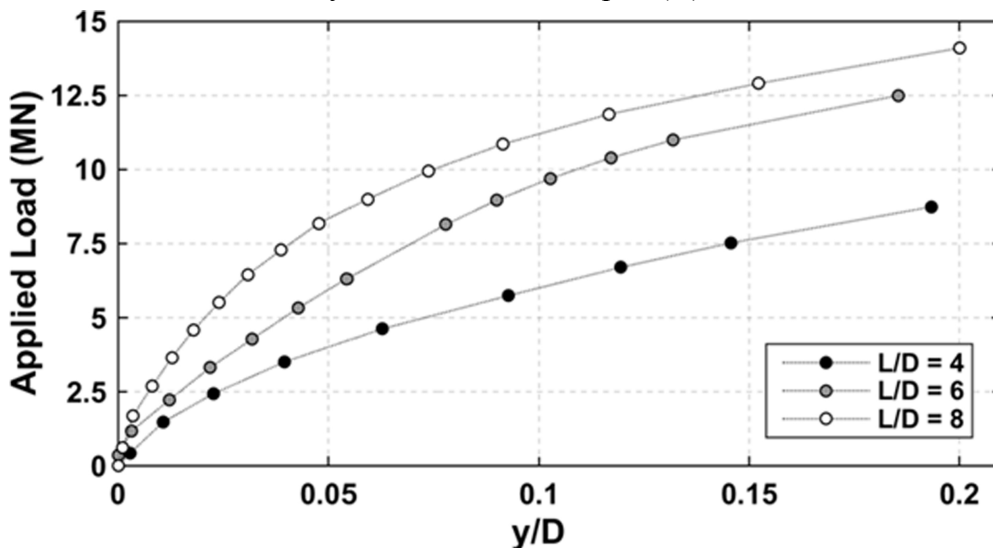


FIG. 4. Lateral Load – Displacement Response Observed

From the above figure, it can be seen that for the pile with the lowest L/D ratio, the deflection experienced is of significantly greater magnitude for the same applied load than for a deeply embedded more flexible pile. The monopiles with greater L/D ratios appear to follow a closer relationship to one another, with the $L/D = 8$ experiencing

only slightly less deflection for the same load than for $L/D = 6$. This may suggest that an optimum embedment length is being approached, whereby any further embedment would produce the same load displacement relationship since the failure mechanism would purely be by excessive bending about this fixed depth.

Observation of the stiffness response of the soil-pile interaction shows that the monopile with greatest L/D ratio produces the stiffest initial response. This would support the hypothesis that the failure mechanism here is by excessive bending, whereas for rigid piles it is by excessive plastic deformation of the surrounding soil. This is due to the much greater stiffness modulus of steel in comparison to sand. It should be noted that original design codes do not take into account this rotational failure mechanism and consequently it is important that further evaluation of this mechanism is made.

In addition to the pile deflection, the bending moment experienced can be evaluated using the measurements from the strain gauges on the pile extremity. Figure 5 presents the evolution of moment with applied load for each of the three L/D ratios. Note zero on the vertical z/D axis corresponds to the sea bed surface.

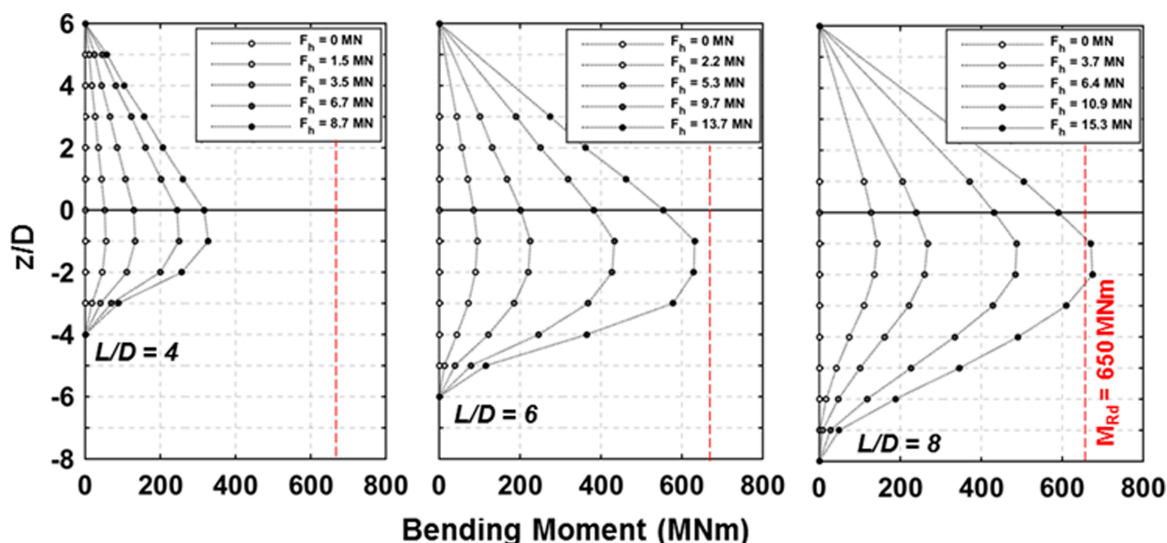


FIG. 5. Evolution of Bending Moment with Successive Applied Load

The first observation to be made is that the general shape of the bending moment diagrams for each of the different L/D ratios is consistent, suggesting that the overall behavior of the soil-pile interaction is similar for each scenario. Also, the piles do not experience a point of inflexion as would be expected for very slender piles. What is clear is the magnitude of maximum bending moment reduces as the L/D ratio reduces, despite experiencing a comparable magnitude of displacement at the location of the applied load. This supports the belief that more rigid piles do not fail by excessive bending since the pile bending resistance is not close to being mobilized.

After the application of load, the piles were unloaded incrementally to evaluate the residual soil-structure interaction state. The bending moment diagrams of the three scenarios are observed in Figure 6 for the successive removal of the applied load. It is evident that in each pile the bending moment did not return to zero and a residual ‘locked-in’ bending moment is observed as the load is reduced.

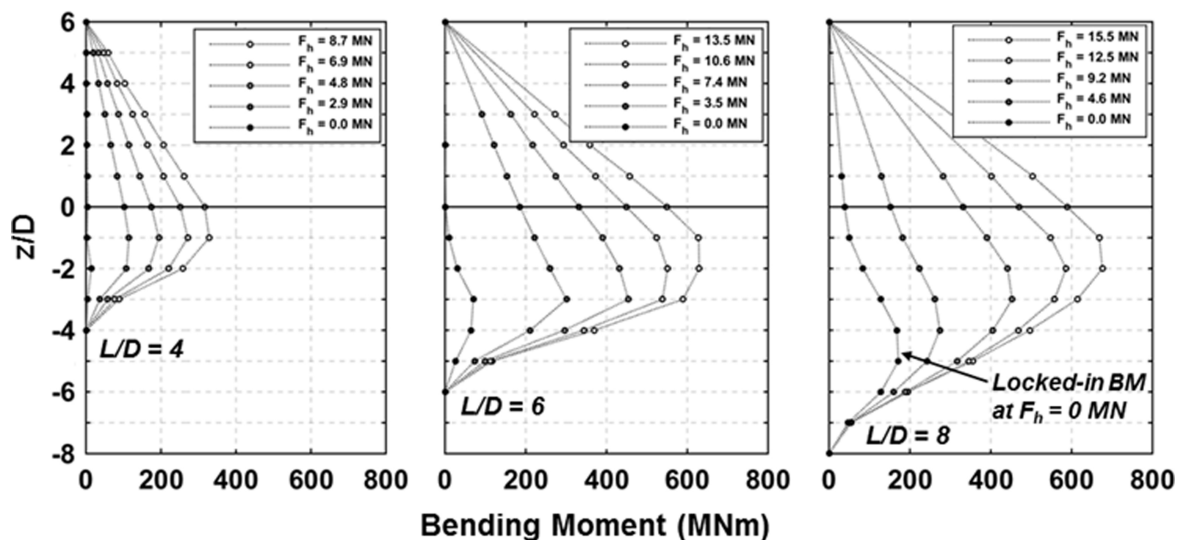


FIG. 6. Regression of Bending Moment with Successive Load Removal

The phenomenon is much more prominent for the monopile with a greater L/D ratio with the proportions of 'locked-in' moment for the L/D ratios of 8, 6 and 4 being 30, 15 and 5 % of the original maximum bending moment generated respectively. An explanation for this observation may be due to changes in soil stiffness that occur upon activation of the monopile as load is applied and then removed. Mobilization of the pile generates passive and active stress states in the soil along the principle axis of bending. The reduction in lateral stress behind the translating pile allows the redistribution and flow of sand which prevents gapping. As observed in Figure 5, pile bending is more prevalent in deeper embedded piles as they flex, as opposed to simple rigid body translation of shallow installed piles; thus the elastic recovery potential of longer piles is considerably greater. As the pile is unloaded it is prevented from returning to its original position by the inflow particles which results in a locked-in internal bending moment within the pile owing to the new soil-structure interaction regime established.

For the monopile with L/D equal to 4, almost all the initial bending moment dissipates on the removal of the applied load as the pile failure mechanism was by rigid body rotation, owing to the shallow embedment depth, and not pile flexure. There is, however, no strong indication from current observations to provide conclusive evidence that this is the case and additional testing is necessary to verify this hypothesis.

Upon spindown of the centrifuge, when the elevated stress field in the soil reduces, the 'locked-in' moments dissipated, confirming that this was indeed a form of increased horizontal stress within the soil restraining the monopile on unload.

NUMERICAL ANALYSIS USING P – Y METHOD OF ANALYSIS

With the aid of MATLABTM programming software, the non-linear, fourth order differential equation, as defined by current design codes of practice to describe pile behavior subjected to lateral load (see Eq. 1), was evaluated for the pile configurations as performed in the centrifuge experimental study.

Firstly, when the monopile predicted and observed deflected shapes are compared (Fig. 7), it can be clearly seen that despite following a very similar general form in terms of rotation, bending and toe-kick, the design method (DNV, 2014) underestimates the deflection for each of the L/D ratios tested by up to 30 per cent. This echoes observations made in finite element modelling studies performed by Achmus *et al.* (2011) and Sørensen *et al.* (2010).

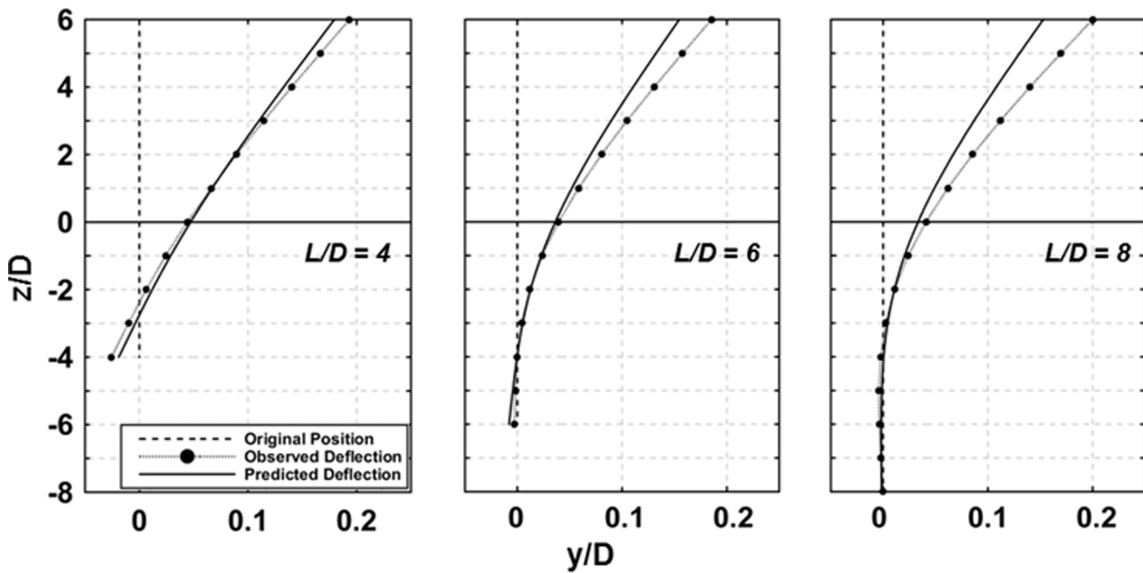


FIG. 7. Comparison of Observed and Predicted Ultimate Deflected Shape ($L/D = 4, 6, 8$)

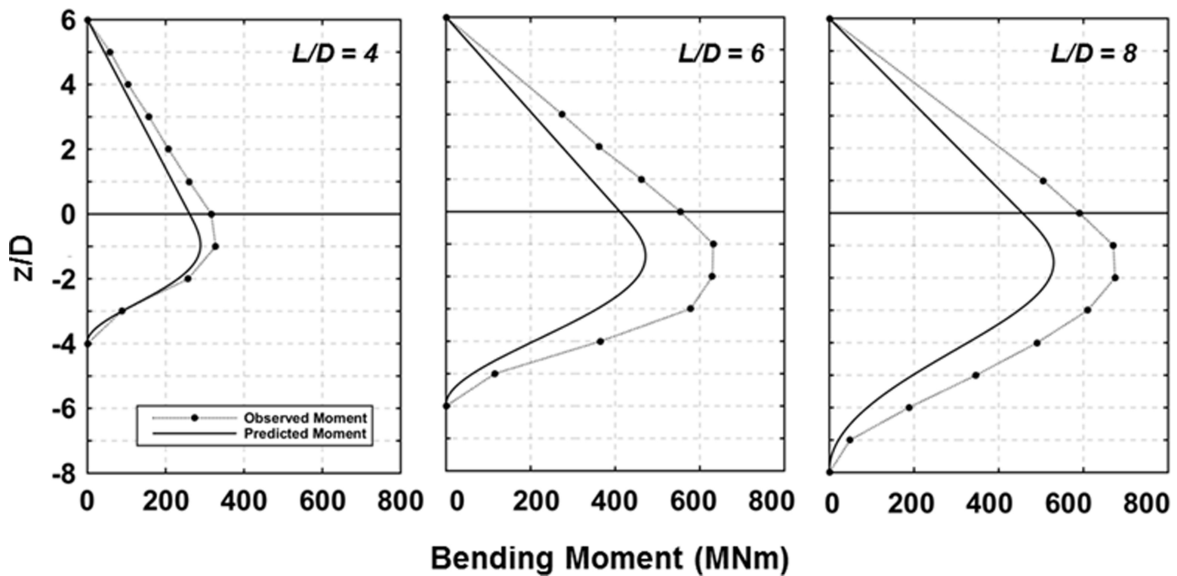


FIG. 8. Comparison of Observed and Predicted Ultimate Bending Moment ($L/D = 4, 6, 8$)

Comparison of bending moment diagrams leads to similar conclusions. The design code provides good accuracy in predicting the general form of the bending moment developed throughout the monopile (Fig. 8) with the location of the maximum moment accurately described. However, the magnitude of maximum moment is underestimated in each test which diverges with increasing L/D ratio. This would be as expected, after evaluation of the deflected shape revealed a prediction lower than observed, given that deflected shape and bending moments are concomitant.

Underestimation of deformation and bending moments by the $p - y$ method may be attributed to the high levels of empiricism within the code not allowing for accurate extrapolation to monopiles with such large diameters or global stiffnesses. Based on this current set of experimental results, it would be inappropriate to assume that the current $p - y$ design methods provide reasonable predictions for large-diameter monopile foundations.

CONCLUSION

A series of centrifuge modelling experiments has been carried out evaluating the behavior of wind turbine monopile foundations subjected to incremental lateral loads in sand. Results indicate the differences in failure mechanisms from flexible ($L/D = 8$) to rigid ($L/D = 4$) piles whereby the former appear to fail by excessive bending, and the latter by plastic deformation of the surrounding soil.

Upon unload of the ultimate lateral load, the monopiles experienced a degree of 'locked-in' moment. This was more pronounced for the most flexible monopile ($L/D = 8$) whereby 30 per cent of the maximum moment is retained. Rigid piles ($L/D = 4$) do not appear to experience this phenomenon to the same extent.

Comparison of observed deflected shapes and those predicted by the $p - y$ method of analysis show a clear underestimation of the design code pile deflection as well as the consequential flexural bending moments generated. A reason for this is likely due to the empirical nature of the $p - y$ curve formulation, having been calibrated with data from piles of up to just 1.2 meters in diameter, which does not allow for accurate extrapolation to monopiles with large diameters.

A method of determining the physical behavior of the soil beneath the surface would provide greater insight into the soil-pile interaction for the transition from a flexible failure mechanism to rigid.

ACKNOWLEDGEMENTS

Funding support provided by the Engineering Physical Sciences Research Council (EPSRC) to establish the 4m diameter beam centrifuge and Centre for Energy and Infrastructure Ground Research at the University of Sheffield is gratefully acknowledged. Continued technical support by Neil Baker and Alan Ainsworth, Thomas Broadbent and Son Ltd. is also appreciated. The lead author is supported via an EPSRC Doctoral Training Grant.

This work is indebted to the invaluable expertise of the Department of Civil & Structural Engineering technical staff, Dr Craig Cox, Alex Cargill, Paul Blackburn and Dave Callaghan for in-house fabrication of the pile and loading systems.

REFERENCES

- Achmus, M., Albiker, J, Peralta, P. and tom Worden, F. (2011). "Scale Effects in the Design of Large Diameter Monopiles". *Scientific Proceedings of the European Wind Energy Association*, 14-17 March 2011, Brussels
- Achmus, M., Kuo, Y.S. and Abdel-Rahmen, K. (2009). "Behaviour of monopile foundations under cyclic lateral load". *Computers and Geotechnics*, Vol. 36, pp. 725-735
- American Petroleum Institute (API) (2011). *RP 2A-WSD Recommended Practice for Planning, Designing and Constructing Fixed Offshore Platforms – Working Stress Design, 21st Edition*. Washington, USA
- Det Norske Veritas AS (DNV) (2014). *DNV-OS-J101 Design of Offshore Wind Turbine Structures*
- Gaudin, C., Clukey, E.C., Garnier, J. and Phillips, R. (2011). "New Frontiers for Centrifuge Modelling in Offshore Geotechnics". *Frontiers in Offshore Geotechnics II*, London
- Haiderali, A.E. and Madabhushi, G.S.P. (2013). "Evaluation of the $p - y$ Method in the Design of Monopiles for Offshore Wind Turbines". In: *Proceedings from the Offshore Technology Conference*, Texas, USA, 6-9 May, pp. 1824-1844
- Hamre, L., Feizi Khankandi, S., Strom, P.J. and Athanasiu, C. (2011). "Lateral Behaviour of Large Diameter Monopiles at Sheringham Shoal Wind Farm". *Frontiers in Offshore Geotechnics II*. Gourvenec & White, London
- Hetenyi, M. (1946). *Beams on Elastic Foundation: Theory with Applications in the Fields of Civil and Mechanical Engineering*. University of Michigan Press, USA
- Murff, J.D. (1996). "The Geotechnical Centrifuge in Offshore Engineering". *Offshore Technology Conference*, OTC 8265
- O'Neill, M.W. and Murchison, J.M. (1984). "Evaluation of p - y Relationships in Cohesionless Soils". In: *Analysis and Design of Pile Foundations. Proceedings of a Symposium in Conjunction with the ASCE National Convention*, pp. 174-191
- Oswald, J., Raine, M. and Ashraf-Ball, H., 2008. *Will British Weather Provide Reliable Electricity? Energy Policy*, Vol. 36, pp. 3212-3225
- Sorensen, S.P., Ibsen, L.B. and Augustesen, A.H. (2010). "Effects of Diameter on Initial Stiffness of $p - y$ Curves for Large-Diameter Piles in Sand". *Numerical Methods in Geotechnical Engineering, Proceedings of the 7th European Conference*, Trondheim, Norway, 2-4 June 2010
- Winkler, E. (1867). *Die Lehre son der Elastizität und Festigkeit*. Prague, pp. 182.

In Situ Geotechnical Early Site Assessment of a Proposed Wave Energy Converter Site in Yakutat, Alaska, Using a Portable Free-Fall Penetrometer

Ali Albatal, S.M.ASCE; and Nina Stark, Ph.D., M.ASCE

Dept. of Civil and Environmental Engineering, Virginia Tech, 200 Patton Hall,
Blacksburg, VA 24061. E-mail: ali2@vt.edu; ninas@vt.edu

Abstract: Wave energy converters (WECs) are promising techniques with regard to the production of sustainable energy. However, the geotechnical and sedimentological site assessment, and the resulting foundation or anchoring design, can still represent a major challenge due to the energetic environmental conditions in the targeted areas. Most recently, portable free-fall penetrometers were suggested for the early site assessment of WEC projects as an innovative cost-effective method to investigate the uppermost layers of the seabed with regard to sediment strength and possible sediment transport processes. In this study, early site assessment was conducted at a proposed WEC site near Cannon Beach, Yakutat, Alaska, using the free fall penetrometer *BlueDrop*. 151 deployments were performed in water depths of 3-40 m during three survey days in May and July, 2014. The results suggested an average quasi-static bearing capacities of 125 ± 18 kPa (normalized for a constant penetration velocity of 2 cm/s) at the uppermost seafloor surface, generally increasing with distance to the shore and water depth. A loose top layer of reworked sediments of up to 4 cm in thickness was detected, indicating moderate sediment remobilization processes. Lower strength and abundance of loose sediment top layers were particularly observed at water depths less than about 15 m.

INTRODUCTION

Ocean energy is one of the most promising sources for the harvesting of renewable energy. The world's oceans offer a large amount of energy in the form of waves, tides, currents and heat (Ghosh and Prelas 2011). This energy potentially covers more than the world's need of power, and the interest of using it is continuously increasing (Pelc and Fujita 2002). Oceans around the world produce up to 10 TW of wave energy (Muetze and Vining 2006). Depending on the wave height, one wave can transmit more than 50 kW per meter length of the wave front (Muetze and Vining 2006; Cornett 2009; Letcher 2014). Considering this amount of energy, researchers and developers are racing to produce the most efficient and reliable designs of wave energy converters (WECs). Alaska is well-known for energetic wave conditions. With a wave power density of about 1,570 TWh/yr, Alaska's continental shelf contains about 60% of the U.S. wave power density (EPRI 2011). Motivated by this potential and the region's demand for an alternative energy source to fossil fuels, Alaska

became a target area for the harvesting of wave energy in the U.S. In this framework, Yakutat, Alaska, was identified as an area of interest (EPRI 2009).

In order to secure an efficient wave energy production, it is essential to choose an appropriate location to deploy the WECs. The potential energy production, the environmental impact, and particularly for bottom-mounted WECs, the seabed stability and sediments dynamics should be considered to determine the appropriate deployment location (Falnes and Løvseth 1991; Cornett 2009; Stark et al. 2014). An energetic environment can jeopardize the stability of the foundation, the mooring and the cable systems, increasing the need for a detailed site assessment (Muetze and Vining 2006). However, the seabed investigation can represent a major challenge at sites characterized by strong hydrodynamics, with regard to the field activities as well as to the associated costs (Letcher 2014; Stark et al. 2014). In addition to the cost of equipment, labor, and the data processing and interpretation, an equipped vessel for the purpose of offshore site investigation can cost up to \$500,000 per day even if only shallow water depths are targeted (Randolph et al. 2005). Thus, budget restrictions, particularly at early stages of such projects, can prohibit the site assessment of the seabed with conventional strategies. This can lead to delays, or even cancellations of projects.

Free fall penetrometers (FFP) have been suggested as an economic and rapid method to investigate the seabed's uppermost sediment layers (Colp et al. 1975; Dayal 1980; Stoll and Akal 1999; Stark and Kopf 2011). The basic idea is to estimate the soil bearing resistance (or even shear strength) by measuring the deceleration of a soil impacting and penetrating probe based on semi-empirical equations and for different penetration depths reached (Dayal 1980; Aubeny and Shi 2006; Stark et al. 2012a).

This article is focusing on the in-situ geotechnical characterization of the seabed surface and the sediment dynamics in the vicinity of a proposed deployment location of a bottom mounted WEC near Cannon Beach in Yakutat, Alaska. The portable FFP *BlueDrop* was suggested for the preliminary site characterization of the uppermost seabed layers at the targeted location and the surrounding area (Stark et al. 2014). During two surveys in May and July 2014, a characterization of sediment type, evaluation of surficial seabed strength and mapping of areas of potential sediment remobilization was conducted. Sediment dynamics were the focus of the investigation, as they may affect scour processes as well as the functionality of the proposed bottom-mounted device. The study also served as a demonstration of how portable free-fall penetrometers can be applied in the framework of early site assessment of WECs, and contributed to a larger geotechnical characterization of the geologically complicated area (Stark et al. 2014).

REGIONAL CONTEXT

Yakutat is enclosed by glaciers and mountains, and is disconnected from a wider electric grid. It is located at the entrance of Yakutat Bay in the Gulf of Alaska, about 360 km northwest of Juneau (Fig. 1). A WEC near Cannon Beach was suggested to reduce the dependency on diesel as a source of energy. The new developments of bottom mounted WECs is particularly encouraging for sites such as Yakutat which

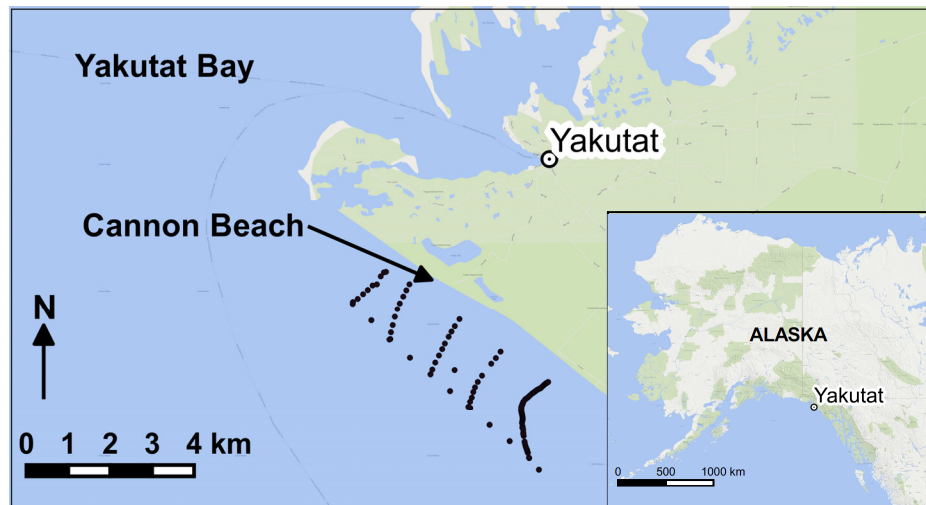


FIG. 1. Location of Cannon Beach in Yakutat, AK. Yakutat City coordinates are 59.5469° N, 139.7272° W. The black dots represent the penetrometer deployments locations.

feature challenges for surface-piercing devices such as the abundance of driftwood and possibly ice.

The average measured significant wave height was about 2-2.5 m with an average dominant wave period of about 9.9 s in 2008, producing an average power density of about 22 kW/m at a water depth of 13 m (EPRI 2009; NDBC 2015).

Ruby (1977) studied the variation of the sediment particle size along the beach face between Yakutat Bay and Dry Bay which is 80 km southeast Cannon Beach (Fig. 1). The sediments at Cannon Beach were identified as fine quartz sand and rock fragments with a mean particle size ranging from 0.2-0.3 mm, and were classified as poorly graded fine sand according to the Unified Soil Classification System (USCS) (ASTM D2487). The finer fractions were found at the upper beach face, while coarser particles were mostly abundant in the lower intertidal zone (Ruby 1977). However, a full description of the regional sediment processes is still lacking (EPRI 2009; Stark et al. 2014).

METHOD

The portable free-fall penetrometer *BlueDrop* (Fig. 2) can be deployed in water depths of up to 200 m (Stark et al. 2014). The device has an approximately streamlined shape, and has a mass of 7.71 kg. The total length of the device is 63.1 cm (Fig. 2). The main body and tail are made of aluminum while the tip is made of steel. The body contains batteries, a pressure transducer behind the tip (i.e. u_2 location) which measures up to about 2 MPa with an accuracy of $\pm 4.67 \times 10^{-4}$ kPa, five vertical microelectromechanical systems (MEMS) accelerometers recording at 2 kHz, with capacities ranging from ± 1.7 -250 g (with g being the gravitational acceleration) and two 3-dimensional MEMS accelerometers with capacities up to ± 55 g. The device records continuously during free fall through the water column and during the soil penetration. The impact and penetration velocity and penetration depth was

derived from the first and second integration of the deceleration-time profile, respectively, during impact and penetration into the soil (Dayal and Allen 1973, Stoll and Akal 1999; Stark and Wever 2009). The sediment resistance force was calculated using Newton's second law, and an equivalent of quasi-static bearing capacity q_{sbc} (normalized for a constant penetration velocity of 2 cm/s) was estimated, based the approach described by Stark et al. (2012a) and the strain rate correction suggested by Dayal and Allen (1973). The water depth was estimated using the measured hydrostatic pressure at impact, because available bathymetric maps are of coarser resolution than the deployment grid.

The FFP *BlueDrop* was deployed 151 times in a water depth ranging from 3-40 m during three survey days in May and July 2014. The deployment locations covered generously the proposed WEC deployment area to enable an assessment of the general geotechnical and morphological characteristics. They included five transects approximately perpendicular to the shore and a shore parallel transect (Fig. 1). In addition to the penetrometer surveys, sediment grab sampling was attempted using a small, hand-deployed Van-Veen grab sampler. Unfortunately, the recovered volumes of sediment were insufficient for further analysis. Three representative samples were retrieved at Cannon Beach during low tide using a shovel. However, the here presented study was focused on the *BlueDrop* deployments.

RESULTS

The water depth based on the *BlueDrop* results ranged between 2.9-39.5 m, being in accord with expected water depths and the available soundings of a single beam echo sounder (Fig. 3). The resulting bathymetric contour map indicated shore parallel shoals crossing transects 2 and 3, possibly representing submerged sand bars (Fig. 3).

The measured maximum decelerations ranged between 20-72 $g \pm 1.56 \times 10^{-5} g$ with an average of about 46 g . The resulting maximum q_{sbc} reached in the penetrated sediment depths (being ≤ 11 cm) 40-215 ± 5 -32 kPa with an average of about 125 ± 18 kPa. Deployment duplicates at approximately the same location showed a good agreement (Fig. 4). The lowest values of the q_{sbc} (< 50 kPa) were observed at a distance of about 600-800 m from the shoreline while the highest values of the q_{sbc} (> 200 kPa) were observed at distances of about 1.2 and 2.1-2.2 km from the shoreline, respectively. Generally, a trend of increasing q_{sbc} with increasing water depth and distance to the shoreline was observed, particularly up to a distance of 2000 m from the shoreline (Fig. 5).

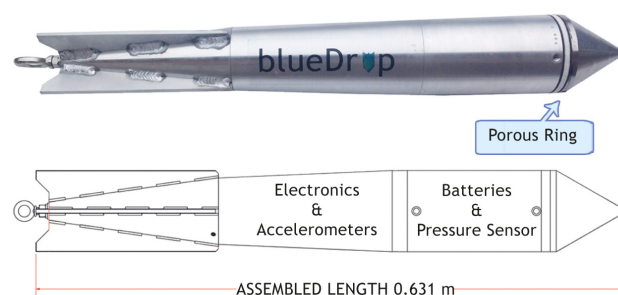


FIG. 2. The FFP *BlueDrop* (modified from www.bluecdesigns.com).

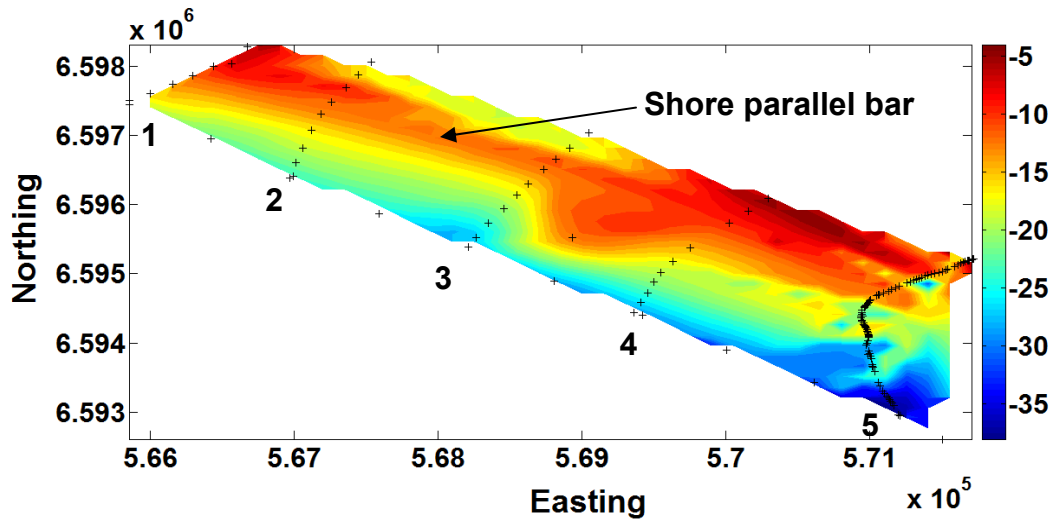


FIG. 3. The bathymetry of the survey area based on the *BlueDrop* deployments (crosses). The numbers 1 through 5 indicate the transect numbers. The arrow indicates a possibly shore parallel bar between transects 2 and 3.

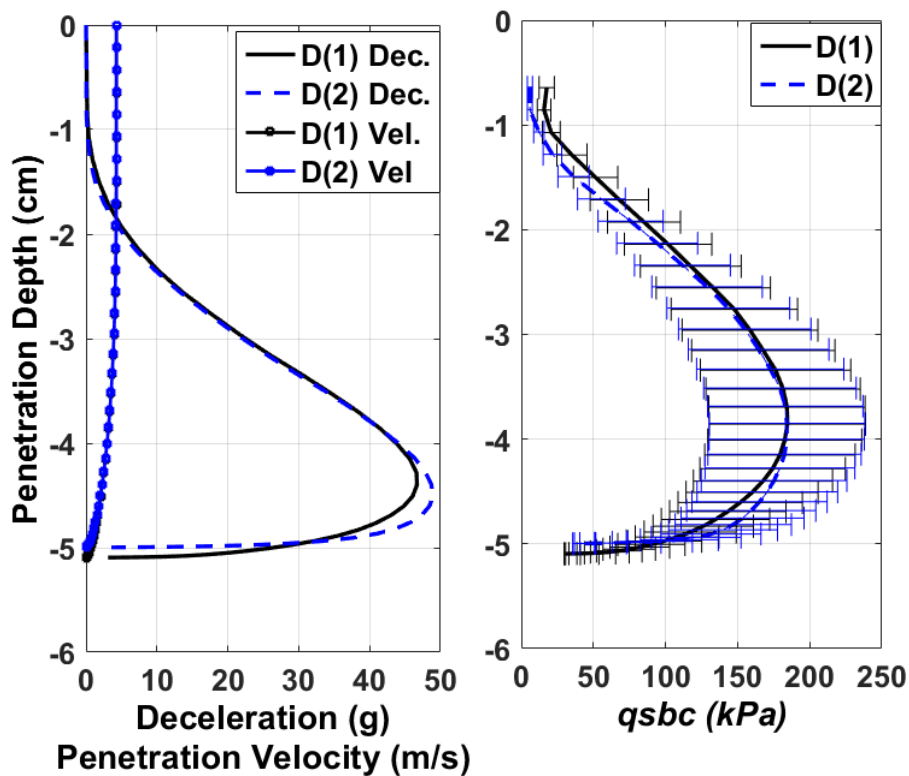


FIG. 4. The deceleration-depth and penetration velocity-depth (left), and q_{sbc} -depth (right) profiles for two deployments (D1-black lines; D2-blue lines) at approximately the same location. The error bars represent the uncertainty ranges resulting from the strain rate factor of 1-1.5. The q_{sbc} values at a sediment depth of < 0.6 cm were impacted by deviations following the calculation approach and were neglected here.

The impact velocity varied between 2.8-5.4 m/s with an average impact velocity of 4.4 m/s. The penetration depth reached between 4-11 cm with an average value of ~6 cm. A trend of decreasing penetration depth with increasing distance from the shore, and water depth, was observed. This trend seemed to be more pronounced at water depths less than about 15 m.

A loose sediment top layer opposing a low resistance against the penetrometer was identified in 99% of the deployments (see Fig. 4 upper 1 cm), representing a thin layer of likely mobile sediments. The maximum thickness of this layer was 4 cm, and was detected at the location of the shore parallel bar, indicating ongoing sediment remobilization processes here. As shown in Fig. 6, which shows the variation of the loose sediment top layer thickness along transect 5, the thickness of this layer decreases with distance from the shore.

DISCUSSION

The presented study aimed at a cost-effective geotechnical early-site investigation of seabed characteristics and sediment dynamics at a location of a proposed bottom mounted WEC, in order to contribute to the choice of the most suitable WEC deployment area. Using the portable FFP *BlueDrop* allowed an economical and rapid characterization of the seabed surface. Deployment duplicates at approximately the same locations showed a high consistency (Fig. 4). The results indicated the abundance of a thin and loose sediment top layer likely associated to wave-driven

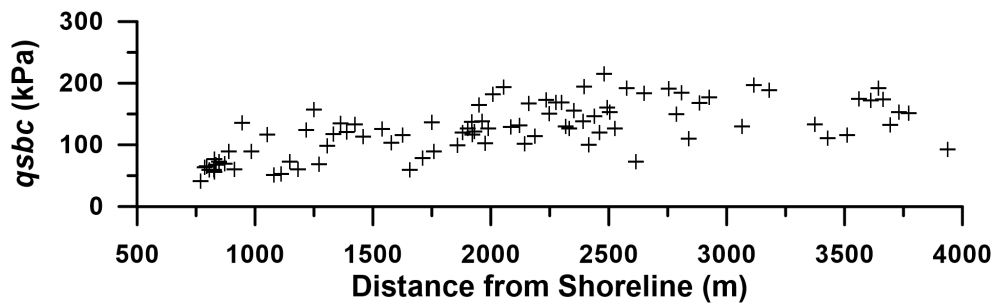


FIG. 5. Estimated q_{sbc} with the distance from shoreline for transect 5. The figure shows an increase of q_{sbc} with the increase of the distance from the shoreline to a distance of about 2000 m from the shoreline.

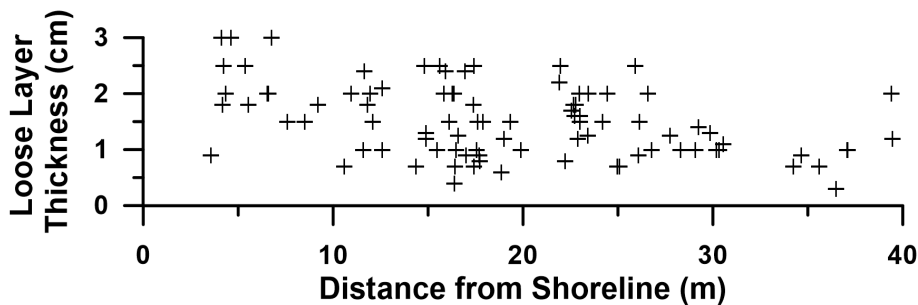


FIG. 6. The loose sediment top layer thickness along transect 5 showing the decrease of its thickness with the increase of the distance from the shoreline.

sediment remobilization processes (Stark and Kopf 2011). This layer reached a thickness of 4 cm at the shore parallel bar, suggesting ongoing morphodynamics. The layer became less significant with further distance from the shore and larger water depth as expected from sediment remobilization due to wave action (Nichols 2009).

The resistance of the soil against impact and penetration of an object depends on the penetrometer geometry, the impact velocity and the soil properties (Mulukutla et al. 2011, Stark et al. 2012b). Although the small penetration depth is a disadvantage when using the FFPs in sandy seabeds, it was possible to derive a first estimate for the soil bearing capacity and the sediment stiffness at the uppermost layers of the seabed surface (Stark et al 2012a). 92% of the impact velocity values ranged between 3.5 - 5.4 m/s. This would allow to classify the soil based on the penetration depth (on average 6 cm) and maximum deceleration (on average 46 g), confirming a consistently sandy seabed in the tested area based on approaches presented by Stoll and Akal (1999); Mulukutla et al. (2011); Stark and Kopf (2011). However, the measured variations in deceleration values indicated a variability in the density of the sandy soils from loose to dense sands (Akal and Stoll 1995). The decrease of the penetration depth with the increase of the water depth was affected by the decrease of the impact velocity due to the increase of the rope drag force, and by the decrease of the loose mobile layer thickness (Stark et al. 2014).

The estimated $qsbc$ suggested an increasing density with distance from the shore until reaching 2000 m and with water depth of up to 15 m (Fig. 5). This may be related to the decreasing impact of waves on the seabed with the increase in the water depth. With less wave-related sediment remobilization, the particles have a larger chance to settle and form denser layers (Stark and Kopf 2011).

Uncertainties in $qsbc$ followed the calculation procedure, and specifically the estimate of the strain rate factor (Stark et al 2012a; Steiner et al. 2014). However, the observed scattering of the $qsbc$ values exceeded the uncertainty due to the strain rate factor range. A reason for that can be changes of the seabed slope and small-scale morphological features. Compared to the horizontal surface, a sloped surface causes a reduction in the bearing capacity (Castelli and Motta 2010). The distance between the deployments is too large to detect small seabed bedforms, but it can be expected to find wave-induced ripples in the shallow areas and even in the deeper parts of the tested area where the ripples may have formed during large storm events in the past (Quick 1982; Mogridge et al. 1994). Such small seabed formations may have caused a variation in the seabed slope and strength at the impact location (Stark et al. 2012b). This would have led to variation in the values of the $qsbc$ even for the same soil characteristics. In addition to the sloped surface, these formations are usually associated with a sediment-sorting pattern of changes in sediment particle sizes between the ripples' crests and the troughs (Foti and Blondeaux 1995; Balasubramanian et al. 2008). This can cause a change in the $qsbc$ results due to the change in the sediment characteristics (Mulukutla et al. 2011, Stark et al. 2012b). However, the effect of the sorting might be small due to the small range of the particle sizes. An evidence for that is the good agreement between most of the duplicated deployments (Fig. 4). Other reasons that may explain the observed deviations are longshore variations in hydrodynamics (e.g. occasional development of rip currents) and their impact on seabed mobilization, or the abundance of localized

gravel at some locations due to the availability of rock fragments in the seabed as described by Ruby (1977).

The results showed high bearing capacity values for the seabed surface in comparison to Stark et al. (2012a), for example, who tested quartz sands in the same size range in the North Sea. This was an encouraging finding for the possibility of deploying a WEC in this area. Although only the uppermost seafloor layers were tested, the estimated values may serve as an indication for deeper sediment depths. However, this is based on the assumption that the uppermost tens of meters of the seabed are composed of the same material. This can be investigated using technologies such as chirp sonar (LeBlanc et al. 1991). The results of this survey can help in choosing priority locations, which would then be subject to a detailed site investigation, including more comprehensive field tests such as, e.g., cone penetrometer testing (CPT), vane shear tests, and/or acquisition of soil samples and cores (Stark et al. 2014).

Scour around the foundation and high amounts of suspended sediments may represent concerns in this case. Finding a shore parallel bar was an important evidence for sediment dynamics in the area, particularly at shallower water depths. However, the current results are not sufficient to get a full picture of the sediment remobilization processes and more investigations are required to assess possible risks associated to scour, as well as larger sediment relocation mechanisms. This is because (i) the bar was only identified crossing only two transects, raising a question about the stability of this bar and if there is a continuous formation and migration of bars in the region. (ii) The contour map included a significant amount of interpolation due to the limited number of transects. A hydrographic survey using e.g. a multi beam echo sounder would give significantly more detail about the local morphology. (iii) The results of the deployments represented a snapshot in time while continuous monitoring or periodic surveying is required to get a full picture of the sediments dynamics (Stark and Kopf 2011). It should also be mentioned that both surveys were conducted during calm to moderate wave conditions. Cannon Beach is classified as an erosional beach, and the sediment remobilization is expected to increase significantly under storm conditions (Ruby 1977; Nichols 2009).

CONCLUSIONS

The impact of the wave action on the proposed WEC area near Cannon Beach was evident. The change of the seabed's geotechnical characteristics with the change of the water depth was likely related to wave action. Deeper water depths were associated with (i) a decrease in the penetration depth, (ii) an increase in the $qsbc$, and (iii) a decrease in the loose mobile layer thickness. Nevertheless, significant scattering was also obvious in the $qsbc$ versus water depth record. Different explanations such as small-scale morphological features, changes in seabed slope, longshore differences in hydrodynamics, or local abundance of gravel must be considered.

The results of the *BlueDrop* deployments showed that the seabed surface in the proposed WEC location is characterized by high bearing capacities, being encouraging to move on to the detailed site characterization. Another survey was conducted in August 2015 focusing on the collection of sediment samples to verify

the promising results via laboratory tests. The noticeable indications for ongoing sediment transport processes emphasized the need to investigate the risk of scour and impacts through large amounts of suspended sediments.

ACKNOWLEDGMENTS

This study was funded by the Institute for Critical Technology and Applied Science at Virginia Tech. The authors thank Brandon Quinn for his assistance during the field investigation. The authors also appreciate the support by Resolute Marine Energy Ltd, and Chris Zobel (Pamplin School of Business, Virginia Tech). On-site support through the City and Borough of Yakutat, and specifically, Rhonda Coston and Bill Lucy is highly appreciated. The authors also acknowledge technical support through Steven Smyth and the BlueCDesigns Ltd team.

REFERENCES

- Aubeny, C.P. and Shi, H. (2006). "Interpretation of impact penetration measurements in soft clays." *J. Geotechnical and Geoenv. Eng.*, 132(6), 770-777.
- Akal, T. and Stoll, R. D. (1995). "An expendable penetrometer for rapid assessment of seafloor parameters." *Proc. MTS/IEEE OCEANS'95. Challenges of Our Changing Global Env. Conference*, 3, 1822-1826.
- Balasubramanian, S., Voropayev, S.I., and Fernando, H.J.S. (2008). "Grain sorting and decay of sand ripples under oscillatory flow and turbulence." *J. of Turbulence*, 9(17), 1-19.
- Castelli, F., and Motta, E. (2010). "Bearing capacity of strip footings near slopes." *Geotechnical and Geological Eng.*, 28(2), 187-198.
- Colp, J.L., Caudle, W.N., and Schuster, C.L. (1975). "Penetrometer system for measuring in situ properties of marine sediment." *Proc. IEEE Ocean 75 Conference*, San Diego, CA, 405-411.
- Cornett, A.M. (2009). "A global wave energy resource assessment." *Sea Technology*, 50(4), 59-64.
- Dayal, U., and Allen, J.H. (1973). "Instrumented impact cone penetrometer." *Canadian Geotechnical J.*, 10(3), 397-409.
- Dayal, U. (1980). "Free fall penetrometer: a performance evaluation." *Applied Ocean Research*, 2(1), 39-43.
- EPRI (Electric Power Research Institute) (2009). *Yakutat conceptual design, performance, cost and economic wave power feasibility study*. Tech. Report No. EPRI-WP-006-Alaska
- EPRI (Electric Power Research Institute) (2011). *Mapping and assessment of the US ocean wave energy resource*. Tech. Report No. 1024637. Palo Alto, CA.
- Falnes, J., and Løvseth J. (1991). "Ocean wave energy." *Energy Policy*, 19(8), 768-775.
- Foti, E., and Blondeaux, P. (1995). "Sea ripple formation: the heterogeneous sediment case." *Coastal Eng.*, 25(3), 237-253.
- Ghosh, T.K., and Prelas M.A. (2011). *Energy Resources and Systems: Volume 2: Renewable Resources*. Springer, New York, NY.

- LeBlanc L.R., Mayer, L., Rufino, M., Schock, S.G., and King, J. "Marine sediment classification using the chirp sonar." *J. Acoustical Soc. of America*, 91(1), 107-115.
- Letcher, T.M. (2014). *Future Energy: Improved, Sustainable and Clean Options for Our Planet*. Second Edition, Elsevier, Boston, MA.
- Mogridge, G.R., Davies, M.H., and Willis, D.H. (1994). "Geometry prediction for wave-generated bedforms." *J. Coastal Eng.*, 22(3), 255-286.
- Muetze, A. and Vining, J. (2006). "Ocean wave energy conversion-a survey." *Proc., Industry Applications Conference, 2006. Conference Record of the 2006 IEEE 41st IAS Annual Meeting*. 3, 1410-1417.
- Mulukutla, G.K., Huff, L.C., Melton, J.S., Baldwin, K.C., and Mayer, L.A. (2011). "Sediment identification using free fall penetrometer acceleration-time histories." *Marine Geophysical Research*, 32(3), 397-411.
- NDBC (National Data Buoy Center) (2015). "Station 46083-historical data." <http://www.ndbc.noaa.gov/station_page.php?station=46083> (June 22, 2015).
- Nichols, G. (2009). *Sedimentology and Stratigraphy*. John Wiley & Sons, West Sussex, UK.
- Pelc, R. and Fujita, R.M. (2002). "Renewable energy from the ocean." *Marine Policy* 26(6), 471-479.
- Quick, M.C. (1982). "Wave-induced sand ripples." *Canadian J. of Civil Eng.* 9(2), 285-295.
- Randolph, M., Cassidy, M., Gourvenec, S. and Erbrich, C. (2005). "Challenges of offshore geotechnical engineering." *Proc., Int. Conference on Soil Mech. and Geotechnical Eng.*, ISSMGE, Osaka, Japan, 16(1), 1-123.
- Ruby, C.H. (1977). *Coastal morphology, sedimentation and oil spill vulnerability, northern Gulf of Alaska*. Tech. Report No. 15-CRD, University of South Carolina.
- Stark, N., and Wever, T.F. (2009). "Unraveling subtle details of expendable bottom penetrometer (XBP) deceleration profiles." *Geo-Marine Letters*, 29(1), 39-45.
- Stark, N. and Kopf, A. (2011). "Detection and quantification of sediment remobilization processes using a dynamic penetrometer." *Proc. IEEE/MTS Oceans 2011 Conference*, Waikoloa, HI.
- Stark, N., Wilkens, R., Ernstsen, V.B., Lambers-Huesmann, M., Stegmann, S., and Kopf, A. (2012a). "Geotechnical properties of sandy seafloors and the consequences for dynamic penetrometer interpretations: quartz sand versus carbonate sand." *J. Geotechnical and Geological Eng.*, 30(1), 1-14.
- Stark, N., Coco, G., Bryan, K.R., and Kopf, A. (2012b). "In-situ geotechnical characterization of mixed-grain-size bedforms using a dynamic penetrometer." *J. Sedimentary Research*, 82(7), 540-544.
- Stark, N. Hay, A.E. and Trowse, G. (2014). "Cost-effective geotechnical and sedimentological early site assessment for ocean renewable energies." *Proc. IEEE/MTS Oceans 2014 Conference*, St. John's, NL.
- Steiner, A., Kopf, A. J., L'Heureux, J. S., Kreiter, S., Stegmann, S., Hafliadason, H., and Moerz, T. (2014). "In situ dynamic piezocone penetrometer tests in natural clayey soils—a reappraisal of strain-rate corrections." *Canadian Geotechnical J.*, 51(3), 272-288.
- Stoll, R.D., and Akal, T. (1999). "XBP-tool for rapid assessment of seabed sediment properties." *Sea Technology*, 40 (2), 47-51.

Installation Torque Measurements of Helical Piles in Dry Sand for Offshore Foundation Systems

Giovanni Spagnoli¹; Soroosh Jalilvand²; and Kenneth Gavin³

¹Product Manager, Dept. of Maritime Technologies, BAUER Maschinen GmbH, Schrobenhausen, Germany. E-mail: giovanni.spagnoli@bauer.de

²Ph.D. Student, School of Civil, Structural and Environmental Engineering, Univ. College Dublin. E-mail: soroosh.jalilvand@ucdconnect.ie

³Professor of Subsurface Engineering, Delft Univ. of Technology, Delft, Netherlands (former Senior Lecturer, School of Civil, Structural and Environmental Engineering, Univ. College Dublin). E-mail: k.gavin@tudelft.nl

Abstract: Helical piles are commonly used onshore as foundation elements for several structures such as bridges, building and towers. The following research considers the use of helical piles as a novel foundation system for the offshore piled facilities. For the design of offshore structures (e.g. renewable energy or oil & gas platforms), the tension on a footing becomes the critical design condition. Among the advantages of helical piles, the high tension bearing capacity is one of the important ones. To investigate the optimum helix-to shaft ratio, the Blessington sand from Ireland has been used for these laboratory tests. CPT tests were performed to determine the consistency of the density for each filling of the sand box. The results suggest that the optimum pile design has a helix-to-shaft diameter (defined as wing ratio) between 1.5 and 2.0.

INTRODUCTION

For the installation of marine structures the piles are normally driven either as an end-on operation with the piling equipment mounted on girders cantilevering from the completed pile bents, or as an operation from a floating or jack-up barge (Tomlinson and Woodward 2008). Offshore foundations are usually subject to significant compressive and tensile axial loads. Besides, conventional offshore monopiles for renewable energy will have to increase significantly in dimensions, due to increase in water depths, to carry such loading which may result in them becoming too expensive to fabricate and impractical to transport and deploy. Alternatives include the use of jacket structures or hybrid structures with smaller deep foundations (Al-Baghdadi et al. 2015). For oil&gas offshore facilities, current deep-water developments offshore Brazil are centered on three basins: the Santos, the Campos, and the Espírito Santo, where water depths of 2,000m are not uncommon (e.g. the Azulão field in the Santos basin with 2,223m water depth). Normally, for such deep-water structures

suction piles are the predominant mooring and foundation system used for oil & gas development projects, with diameter larger than 5m and length of 20-30m (Gerwick 2007).

This manuscript presents some laboratory data about a novel foundation system. Helical piles are already a commonly used tool for onshore structures such as transmission towers or anchors for pipelines. They have also a long history of use for offshore vessels and structures, with specific application in the energy sector primarily relating to anchoring pipelines to the seafloor. There exists a potential niche application to foundations for offshore renewable energy structures in that relatively high anchoring capacity can be achieved with anchors installed using relatively small vessels (Newgard et al. 2015). Helical piles are steel foundations that are rotated into the ground to support structures. They can be an interesting novel foundation method for the offshore industry (e.g. Spagnoli 2013; Byrne and Houlsby 2015; Spagnoli et al. 2015; Spagnoli and Gavin 2015). In fact, they do not cause any noise and vibration into the ground, which is advantageous for environmental reasons. For offshore applications, marine life is relatively unaffected by the installation of screw piles. They do not produce any waste soil during their installation, a large bearing capacity is generated by the consolidation effect of the soil as the pile is screw-driven into the ground and the base enlarging effect of the wing as the wing rotated into the ground. A large pulling capacity is maintained as the passive soil resistance, which acts on the wing part as propulsive force as the pile penetrates into the ground, and it is turned into pulling resistance. The helical piles are very earthquake resistant and since they do not need concrete or lime, they do not need to wait for curing (Nippon Steel 2013). Thanks to their large bearing capacity, piles of a smaller diameter or fewer piles can be used, thus reducing the size of the footing itself. Another major advantage of helical piles is that they are easy to remove once they have reached their service life. Because of their high vertical bearing and large pulling resistance capacity, helical piles might also be an interesting solution for floating structures for deep-water oil and gas projects.

The installation of helical piles is fairly straightforward; however, as with any process, there are a number of parameters that must be taken into account. Helical piles can have various types of geometries and the choice of design for a given screw pile depends on its application. The geometry of a screw pile design is important for many reasons. The shape of the pile can have influencing factors during installation, affect loading capacities and can influence the cost of manufacturing and the torque needed for installing it. This paper presents data obtained from eighteen model screw pile installation and pull-out load tests. Three model screw piles with varying wing ratio geometries were installed in a test bed of loose sand in a laboratory setting. The results are compared with laboratory tests performed in the same sand by Spagnoli et al. (2015) in order to determine the effect of the wing ratio on the required installation torque and on the pull-out capacity of the helical piles. Cone Penetration Tests (CPT) were also conducted for each test bed to ensure a consistent density of the sand throughout the testing. The results of this investigation may improve the efficiency of the screw pile design for the use in offshore structures.

LABORATORY TESTS SET UP

Blessington sand was chosen to create the test bed as it has been used previously to complete a series of research projects similar to this experimental investigation (Spagnoli et al. 2015). According to Doherty et al. (2012) the Blessington sand is also suitable for this experimental investigation as, it is a consistent nature of sand deposit and has similar strength and stiffness properties of the sand to those encountered in offshore seabed deposits in the North Sea.



FIG. 1. Sand box lined with skip bag.

The sand was prepared the same way for each experiment to ensure continuity throughout. A 900mm^3 steel formwork was filled with 750mm^3 of Blessington sand to create the test bed to be used throughout the testing. The sand was refilled after each test to ensure all the properties of the sand, most importantly the density of the sand, remained constant for each test. The refilling of the sand for each test eliminated any compaction or disturbance of the soil from the previous set of testing. For ease of filling the sand into the 900mm^3 box, it was lined with a 900mm^3 skip bag as seen in Fig. 1. To ensure the sand was filled in the same manner each time a sieve was placed on top of the 900mm^3 box. As a full-scale offshore site would consist of a dense sand, to simulate this in a laboratory scaled down version of testing, the Blessington sand needed to be kept of a loose density (ranging between 35-50%). This is consistent with that mentioned by Kelly et al. (2006) who state that keeping the laboratory tests at a lower relative density than that of the field test will account for the reduction of friction angle with stress levels.

The model screw piles used in this experimental investigation were taken from a previous research described by Spagnoli et al. (2015). The pile design needed to be a good representation of a full scale screw pile and therefore the geometry chosen for the screw pile was that of a circular section with a single helix at the base. Three screw piles of varying helix diameter were needed for this investigation. The pile

shaft diameter was kept constant and the helix diameters varied from a ratio of 1.5, 2.0 and 2.5 times the diameter of the shaft. This geometry was chosen as Spagnoli et al. (2015) showed that piles with a helix-to-shaft ratio of 1.2 required larger installation torques and proved to have poor uplift capacities, in comparison to the piles of a wing ratio of 1.5 and 2.0. Piles with a wing ratio of 2.5 had noticeably improved resistance to vertical loads but were difficult to install, thus requiring greater torques and proving difficult to keep vertical during installation, but were used as a control in the experiment for the 1.5 and 2.0 pile geometries. The pile shaft diameter was chosen to be 60.3mm as it is of close proximity to the standard section sizes of circular hollow section to one tenth of full scale screw piles; an example can be seen in Fig. 2.

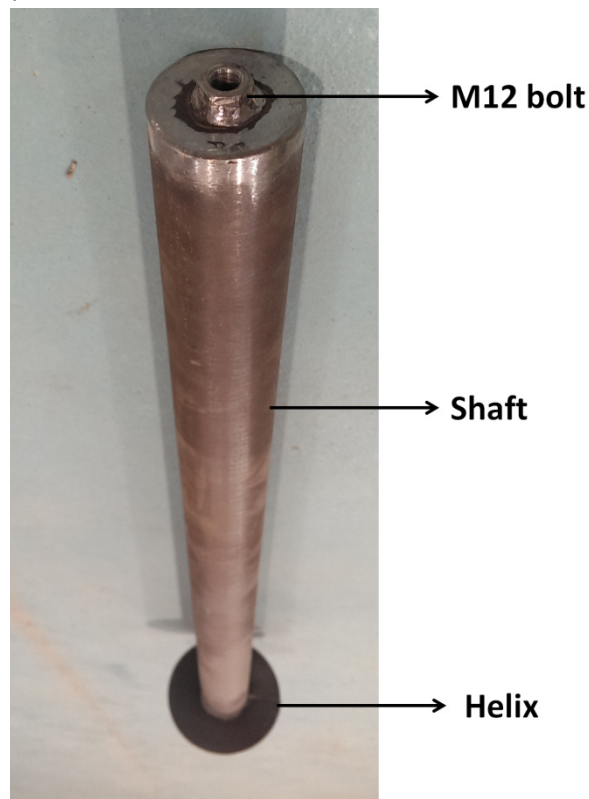


FIG. 2. Model helical pile used for the experiments.

A timber clamp guide was fabricated to ensure an accurate verticality of the model screw piles during installation. The screw piles were then inserted through the 70mm diameter steel pipe fixed on the timber guide. As a result, the verticality of piles was assured while they were screwed into place during the installation phase of the test. A custom drill bit was created, to be attached to the M12 nut on the top of the model screw pile, to allow for the torque from the drill to be applied to the pile in order for the pile to be screwed into place. The drill bit was made by welding a 19mm socket to a regular drill bit.

The pull-out tests were completed by employing a 10 tonne laboratory crane depicted in Fig. 3. To this end, a plastic plate was screwed to the top of the pile at one end and was hooked to the crane at the other end. A load cell was placed in between the plate and the crane to measure the pull-out loads. A drawwire was used to measure the displacement of the pile.

A plank of wood was placed across the top of the sand box and the drawwire was clamped onto the plank of wood using G-clamps and the hook of the drawwire was attached to the underside of the plastic plate. The crane was engaged at a constant rate of 15.5mm/s until the pile was fully extracted from the test bed. The displacement and load were logged during this process and the data was later used to determine the uplift capacity of each geometry of the model screw piles. Each installation and uplift test was repeated six times.

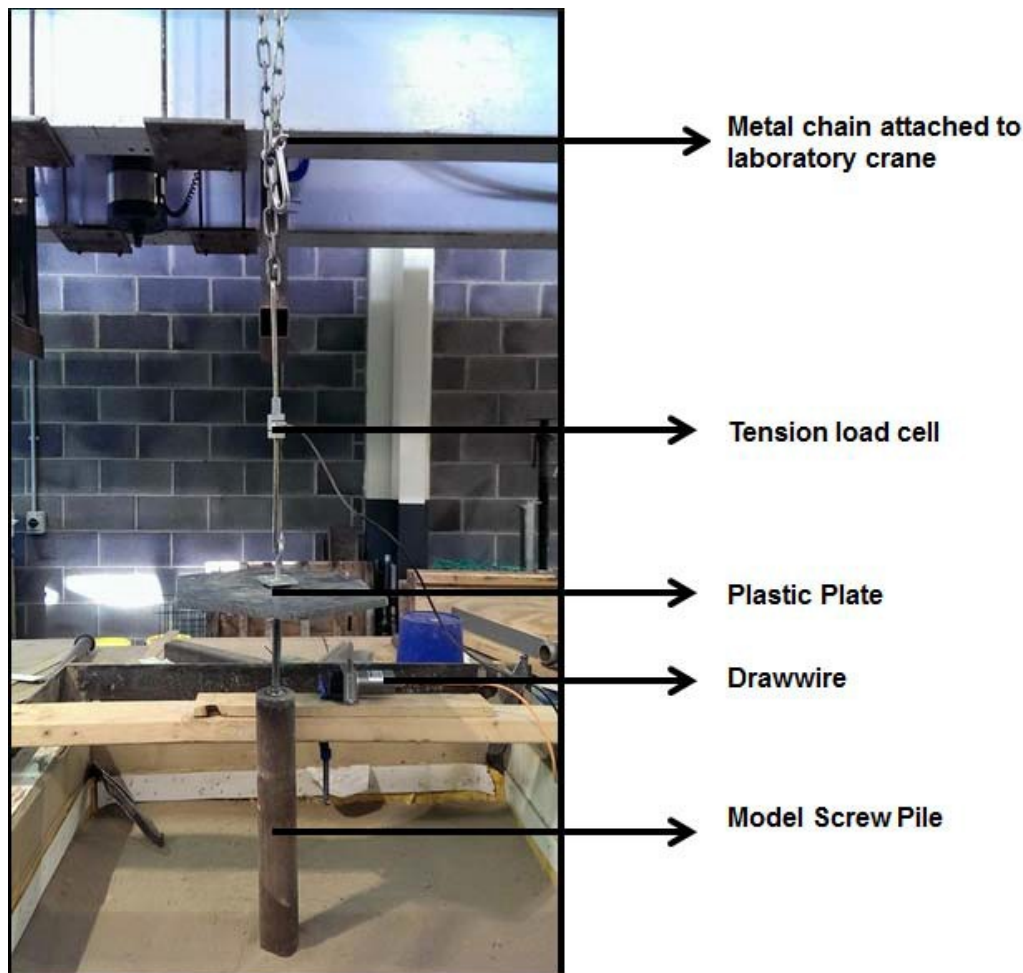


FIG. 3. Pull-out test equipment.

Having a consistent density of each test bed was of great importance in this research project, therefore a cone penetration test (CPT) was completed for each filling of the sand box. The test was not a traditional CPT as the only soil property of interest in this experimental investigation was the cone resistance q_c . The equipment used to measure the cone resistance is composed of a piece of 670mm long close-ended pipe fitted with a pressure sensor on the bottom. The pipe is 35mm in diameter. Fig. 4 shows the CPT sensor. In order to drive the pressure sensor to the desired embedment depth, a loading rig that was used in an earlier study to extract the screw piles (Spagnoli et al. 2015) was adapted to apply downward forces. In the previous setup, the lever arm of the loading rig rested on top of a car jack and was forced in the

upward direction to apply a pullout force on the screw pile. In the new setup, however, the loading rig required to provide a force in the downward direction to derive the CPT tool into the test bed. This was achieved by using a carabiner to make a connection between the top of the car jack and the underside of the lever arm of the rig. The drawwire was used again in this procedure; it was screwed into place on the base of the loading rig. The CPT sensor was placed into the guide and the lever arm gradually drove the sensor to the desired embedment depth by slowly lowering the car jack, at an installation rate of 4mm/s. Extensions for the sensor were attached at two intervals in order for the sensor to be driven to the embedment depth of 650mm. The extensions, as seen in Fig. 4B were fabricated in the UCD laboratory. This procedure was constant for each test and performed after the tests for not disturbing the soil bed.

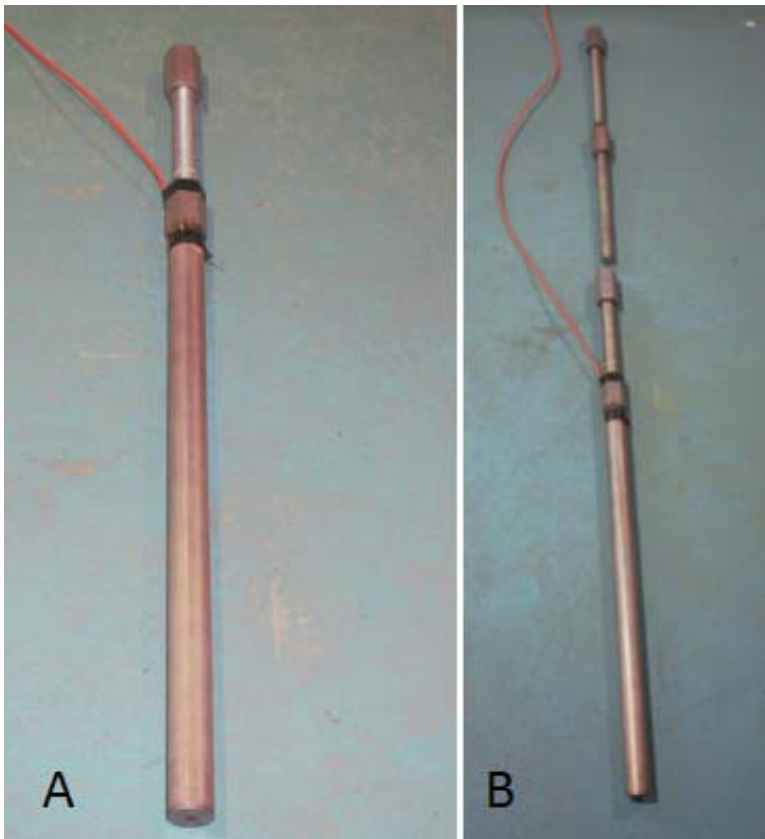


FIG. 4. The CPT sensor (A) with the additional extensions needed to drive the sensor to the appropriate embedment depth (B).

TORQUE AND PULL-OUT TEST RESULTS

The average of each pile geometry was found from all six series of tests and plotted as illustrated in Fig. 5A. From this diagram it is clear to see that with an increase in the wing ratio there is a corresponding increase in the uplift capacity of the screw pile. The average maximum uplift capacity for the wing ratio of 1.5 is 678.8N; this uplift capacity increases to 927.4N for the wing ratio of 2.0. The average maximum uplift capacity increases further to 1131.667N for the wing ratio of 2.5. To investigate this relationship further, the maximum pull-out loads achieved by the model screw piles in testing were plotted against the wing ratios.

As can be seen in Fig. 5B there is a linearly increasing relationship between the two. This was reassured further by completing a linear regression analysis on the data. The R^2 value was found to be 0.9967, indicating a strong linear relationship between the explanatory and dependent variables. In the case of this investigation it means that once the wing ratio increases there is a proportional increase in the pull-out load achieved by the screw pile. This finding may be used in future to predict the maximum pull-out load that may be achieved by a larger wing ratio.

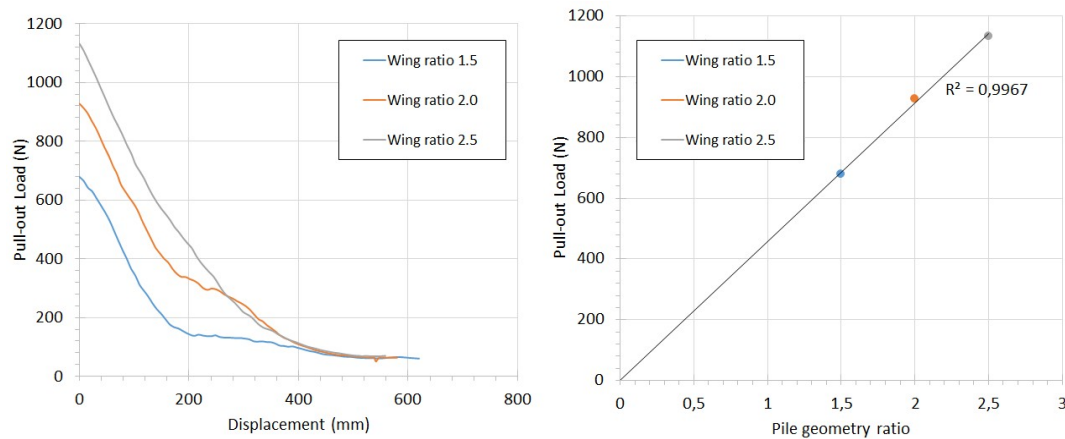


FIG. 5. Average pull-out load results (left); relationship between the helix-to-shaft ratio and the pull-out capacity of the helical piles (right).

The results for all six series of tests were then compared to a previous similar investigation completed by Spagnoli et al. (2015) to determine the reliability of the results overall. The maximum pull-out load test results are clearly illustrated in Table 1 for a comparison in results to be made. Studying the tables below it is found that there is a significant consistency with the maximum pull-out loads achieved by the screw piles of pile geometry 2.5, with average pull-out values of 1131.6N and 1099.69N for the investigations shown in this paper and by Spagnoli et al. (2015), respectively. This is a difference in results of 75.2N or a discrepancy between the results of 7%. Comparisons were also made between the pull-out results obtained by the pile geometry 2.0 for both test series. A difference of 87.53N was calculated between the averages of both periods of testing; in percentage this is a variance of 10.4%. The pile geometry 1.5 was the pile that had the largest discrepancy between the results obtained by each period of testing. The average of the 1.5 wing ratio for this study is recorded at 678.7N, and an average of 818.06N is recorded for Spagnoli et al. (2015). This is a variance in results of 139.36N, or 20%. This is a substantial variance compared to the difference in results seen for the pile geometries of 2.0 and 2.5. The maximum average installation torques measured for the pile geometries 1.5, 2.0 and 2.5 were 15.9 Nm, 14 Nm, and 22.4Nm, correspondingly. The maximum average of all 6 series of installation torque results were then taken and plotted against each other as seen in Fig. 6 to determine a relationship between the wing ratio and the maximum installation torque achieved. As can be seen in the graph below a linearly constant relationship is not present between the wing ratio and the installation torque. This finding indicates that when the wing ratio increased there was not a corresponding increase in installation torque. The results however confirm the previous finding of Spagnoli et al. (2015), who stated that the optimum pile geometry ranges between 1.5 and 2.

Table 1. Comparison of the Maximum Pull-Out tests of this Research with the Results of Spagnoli et al. (2015)

Series no.	Pile geometry 1.5	Pile geometry 2.0	Pile geometry 2.5
1 (this research)	732.8N	951N	1254N
2 (this research)	736.8N	1042N	1097N
3 (this research)	763.3N	932N	1208N
4 (this research)	586.2N	912N	919N
5 (this research)	713.4N	762.4N	1197N
6 (this research)	540.7N	972N	1115N
Average	678.7N	927.4N	1131.6N
1 (Spagnoli et al. 2015)	774N	846 N	1072 N
2 (Spagnoli et al. 2015)	807.99N	801.87N	1085.94N
3 (Spagnoli et al. 2015)	872.21N	n.a.	967.79N
4 (Spagnoli et al. 2015)	n.a.	871.75N	1099.69N
Average	818.06N	839.87N	1056.35N

CPT TESTS

Cone penetration tests were performed in order to determine the consistency of the results obtained from this investigation by measuring the end resistance of the cone, q_c . This parameter was measured to determine the consistency of the density for each filling of the sand box. Fig. 7A shows results from CPT tests performed in the four corners as well as the middle point of a typical sand box prior to pile testing. The results demonstrate the consistency of sand density across a typical test bed. The consistency of the test bed density as a result of successive refills is depicted in Fig 7B, where the average CPT results for each pile geometry are shown. The average maximum q_c values are 302.5kPa for the pile geometry 1.5, 304.6kPa for the pile geometry 2.0 and 302.5kPa for the pile geometry 2.0. This is a clear indication that there is a strong consistency in the density of the sand of each sand box prepared and therefore the density of the sand has little impact on the regularity of the results obtained from the installation and pull- out tests.

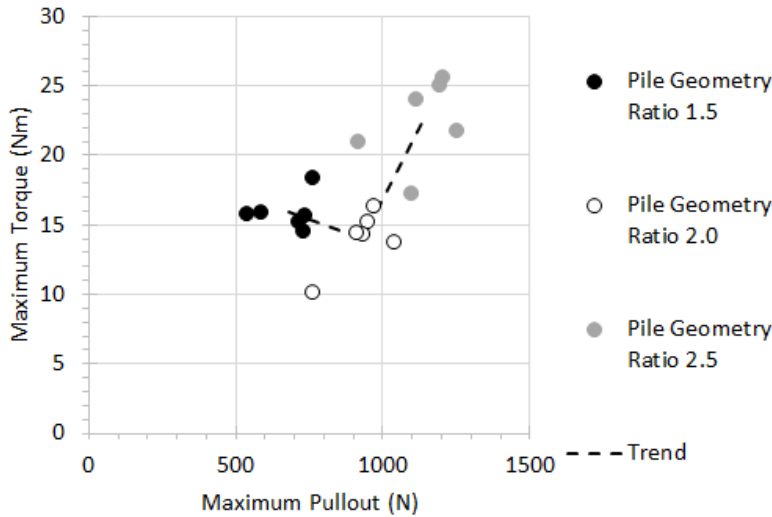


FIG. 6. Relationship between the wing ratio and maximum required installation torque. The trend represents the mean values of both torque and pullout.

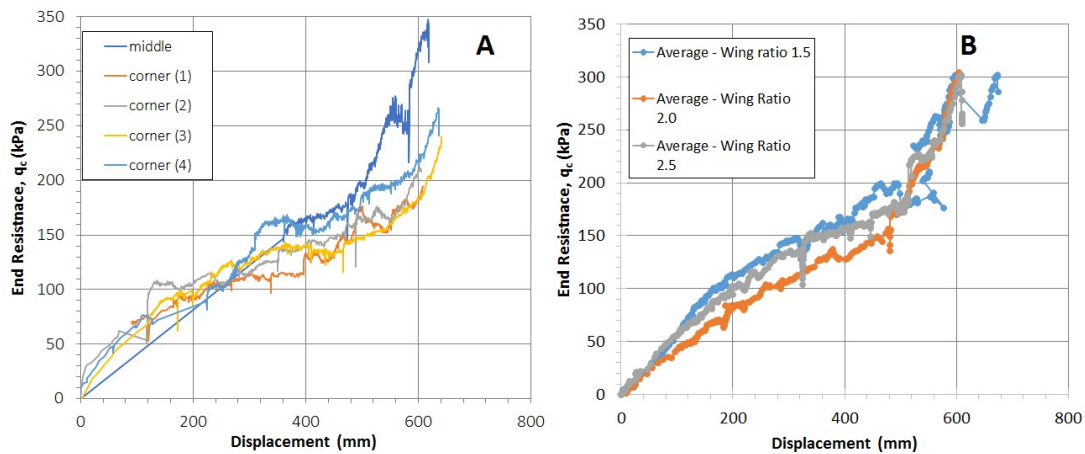


FIG. 7. Spatial distribution of typical CPT data in the test bed (A) and average CPT data for each wing ratio (B).

CONCLUSIONS

A series of experiments were designed based upon similar investigations found in the literature review, and from a previous investigation completed by Spagnoli et al. (2015) upon which this investigation was based. A total of eighteen 1g tests were completed using three varying sized model screw piles. The sizes of these screw piles varied with respect to helix-to-shaft diameter ratios of 1.5, 2.0 and 2.5. As expected, the screw pile with the largest wing ratio showed the highest uplift capacities out of all three sizes. The deviation between the capacities achieved by all three sizes varied linearly, with the smallest pile size reaching a capacity of 679N and the largest 1131N. This concluded that the greater the size of the screw pile the greater the capacity that will be achieved. However it was found that the larger helical piles took

greater installation torques to install the piles to the correct embedment depth, indicating that the larger helical screw pile sizes are not the most efficient design, and should only be used in a practical sense when uplift capacity is of great importance in the design.

ACKNOWLEDGMENT

The authors wish to thank BAUER Maschinen GmbH for the permission granted to publish the results and Kate O'Grady for her work performed during her Master Thesis.

REFERENCES

- Al-Baghdadi, T.A., Brown, M.J., Knappett, J.A. and Ishikura, R. (2015). "Modelling of laterally loaded screw piles with large helical plates in sand." Chapter 56 in *Frontiers in Offshore Geotechnics III*, Vaughan Meyer, editor. CRC Press, Boca Raton, FL, 503-508, [10.1201/b18442-62](https://doi.org/10.1201/b18442-62).
- Byrne, B.W. and Houlsby, G.T. (2015). "Helical piles: an innovative foundation design option for offshore wind turbines." *Phil. Trans. Roy. Soc. A.*, Vol. 373 (2035), [10.1098/rsta.2014.0080](https://doi.org/10.1098/rsta.2014.0080).
- Doherty, P., Kirwan, L., Gavin, K., Igoe, D., Tyrrell, S., Ward, D. and O'Kelly, B. (2012). "Soil properties at the UCD geotechnical research site at Blessington." *Proc., Bridge and Concrete Research in Ireland Conference (BCRI 2012)*, 485.
- Gerwick, B.C. (2007). *Construction of Marine and Offshore Structures*. CRC Press, Boca Raton, FL.
- Kelly, R.B., Houlsby, G.T. and Byrne, B.W. (2006). "A comparison of field and laboratory tests of caisson foundations in sand and clay." *Géotechnique*, Vol. 56(9): 617–626, [10.1680/geot.2006.56.9.617](https://doi.org/10.1680/geot.2006.56.9.617).
- Newgard, J.T., Schneider, J.A. and Thompson, D.J. (2015). "Cyclic response of shallow helical anchors in a medium dense sand." Chapter 122 in *Frontiers in Offshore Geotechnics III*, Vaughan Meyer, editor. CRC Press, Boca Raton, FL, 913-918, [10.1201/b18442-131](https://doi.org/10.1201/b18442-131).
- Nippon Steel (2013). "ECO Pile." <http://www.nsec-steelstructures.jp/data/ns_ecopile/> (August 16, 2015).
- Spagnoli, G. (2013). "Some considerations regarding the use of helical piles as foundation for offshore structures." *Soil Mech. Found. Eng.*, Vol. 50 (3): 102–110, [10.1007/s11204-013-9219-7](https://doi.org/10.1007/s11204-013-9219-7).
- Spagnoli, G., Gavin, K., Brangan, C. and Bauer, S. (2015). "In situ and laboratory tests in dense sand investigating the helix-to-shaft ratio of helical piles as a novel offshore foundation system." Chapter 79 in *Frontiers in Offshore Geotechnics III*, Vaughan Meyer, editor. CRC Press, Boca Raton, FL, 643-648, [10.1201/b18442-85](https://doi.org/10.1201/b18442-85).
- Spagnoli, G. and Gavin K. (2015). "Helical piles as a novel foundation system for offshore piled facilities." *Proc., Abu Dhabi International Petroleum Exhibition and Conference (ADIPEC)*, Abu Dhabi, SPE-177604-MS, <http://dx.doi.org/10.2118/177604-MS>.
- Tomlinson, M. J. and Woodward, J. (2008). *Pile Design and Construction Practice*. Taylor & Francis, Oxford, UK.

Lateral Performance of Helical Piles as Foundations for Offshore Wind Farms

Sherif A. Y. Akl¹; Omar M. Elhami²; and Mustafa A. Abu-keifa³

¹Assistant Professor, SMFRL, Cairo Univ., Giza, Egypt 12613.

²Geotechnical Engineer, Dar Al Handasah, Giza, Egypt 12577.

³Professor, SMFRL, Cairo Univ., Giza, Egypt 12613.

Abstract: Helical piles can be the high capacity foundation needed to meet the growing demand for wind energy production. Predrilling alleviates the need for large torque to install high capacity helical piles, but affect its lateral performance. The paper describes 3D numerical analyses of field pile lateral load tests that have been used to study the effect of predrilling on the lateral resistance of helical piles. The field tests compare between the lateral performances of predrilled helical piles and that of typically installed ones. The paper also compares between predictions of the lateral performance of helical piles using p-y analysis (Lpile Plus 5.0) and the finite element method (FEM, PLAXIS 3D). The study investigates how each analysis captures the effect of predrilling on the lateral capacity. The FEM predictions showed better agreement with measured behavior in field tests for both predrilled and typical cases. The 3D model considers a remolded zone around the pile with reduced stiffness and shear parameters to capture the effect of installation. The analysis showed that similar results are achieved by adjusting the strength reduction factor of the interface element.

INTRODUCTION

To meet the growing demand for clean and renewable energy, the development of wind farms is on the rise. The European Wind Energy Association plans to increase energy production from wind to 40 GW in 2020 and further to 150 GW in 2030 (Rock and Parsons, 2010). Wind farms in 2020 are expected to provide 75 GW of the world's total energy production; with the US and China being major contributors in this field (Spagnoli, 2013). Most offshore wind farms are at an average distance of 29 km from shorelines, and in an average water depth of 22 m to keep costs of energy production economically feasible. The most common type of foundation for offshore wind turbines is the monopile with diameters ranging from 4 to 6 m (Dean, 2009). Typical vertical loads on the monopiles range from 6 to 12 MN for turbines producing 3.5 to 5 MW, respectively. Considerable lateral loads act upon this foundation from wind (1~2 MN) and waves (3 MN).

However, intended growth plans for wind energy production need heavier turbines further from shores, and at water depths up to 65 m and even 100 m. This expansion

requires foundations that carry heavier axial loads and resist larger lateral loads. Some of the existing offshore wind farms use tripods or jacket foundations to carry heavier turbines in deeper waters. On the other hand, several researchers (e.g., Spagnoli (2013); and Byrne and Houlsby (2015)) recommend the use of Helical or Screw Piles. Helical piles are easy to construct and have high load carrying capacity and uplift resistance (Basu and Prezzi, 2009). The construction of wind farms with helical piles will have to use underwater machines with hydraulic torque heads. The installation torque is analytically related to its axial load capacity (Ghaly and Hanna, 1997) and uplift resistance (Hoyt and Clemence, 1989).

To increase the load carrying capacity, helical piles require helices of larger diameters. The required installation torque increases significantly with the increase of helix diameter and helix to pile diameter ratio (Spagnoli, 2013). Underwater machinery able to produce such high torque values may not be available; and one way to offset the torque requirements is to predrill an open hole before the actual pile installation. The installation of helical piles in the ground creates helical paths and remolds the soil around it. Typically, the loss of strength due to remodeling is compensated by soil displacement around the shaft. This compensation mechanism does not occur effectively if the hole of the pile location is predrilled. Sakr (2010) performed several field tests on helical piles in cohesive and cohesionless soils using predrilling as well as typical installation. The measured behavior shows that the lateral capacity of helical piles is vulnerable to predrilling. Sakr (2010) also used p-y analysis to investigate how the reduction in lateral capacity due to predrilling can be estimated. This paper presents numerical analysis of lateral load field tests on helical piles using the FE commercial program Plaxis 3D. The analysis shows a realistic depiction of predrilling effects and suggests a reliable method to estimate the lateral capacity.

FIELD TESTS

Sakr (2010) performed several field tests on helical piles in 4 sites located at about 70 km north of Fort McKay, in northern Alberta, Canada. This paper focuses on two of these field tests in cohesionless soils to determine the pile capacity for resisting lateral loads. The tests are performed on helical piles with double helices made of Grade 3 (ASTM classification) steel with a yield strength of 310 MPa. The pile installation equipment comprised of a drive unit mounted on a tracked excavator that provided the torque for rotation of the screw pile into the ground to a maximum value of 339 KN.m. The test is performed using a 200 ton hydraulic jack applying a horizontal load on the pile head that protrudes 20 cm from ground surface. The lateral displacements are measured using 2 Linear Displacement Transducers (LDTs) with 0.01 mm accuracy and a 150 mm travel range, as well as a dial gauge with 0.025 subdivisions and a 50 mm travel range.

Figure 1 shows the soil condition and helical pile description in Field Test 1 where predrilling was used to decrease the torque necessary for installation. Standard Penetration Test (SPT) blow counts varied between 23 to 37 blows per 300 mm of penetration until a depth of 10 m indicating a fine grained sand to silty sand layer,

which is well graded and dense to very dense. Ground water level is at 5.4 m below the existing ground surface. Predrilling to a depth of 5.5 m leads to torque values at the end of installation of 338.3 KN.m with a total embedment depth of 6.5 m.

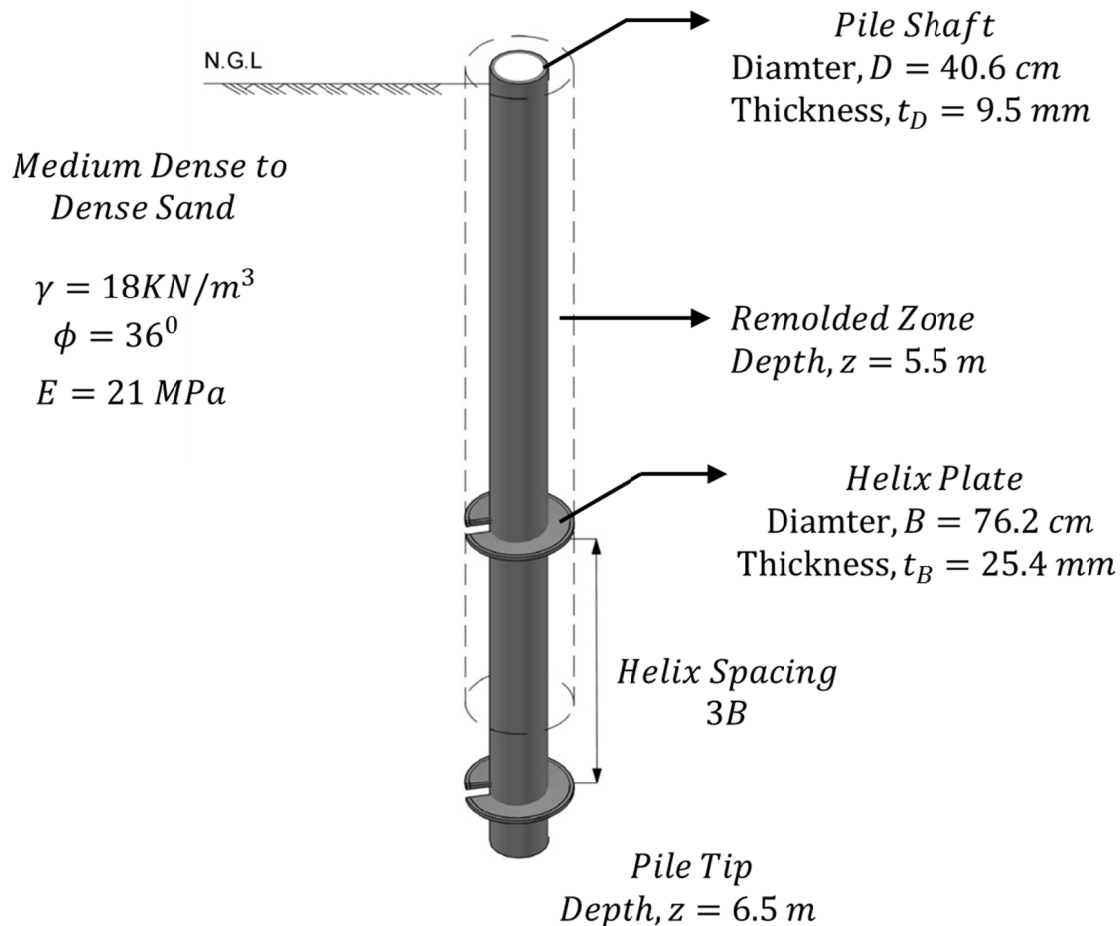


FIG. 1. A schematic diagram showing the helical pile and soil conditions in Field Test 1 (after Sakr, 2010).

Figure 2 shows the soil conditions and pile description of Field Test 2. The soil comprises of a succession of cohesionless soil layers similar to that in Field Test 1, including sandy silt, glacial till and dense to very dense sand. However, there is some cementation in the glacial till layer. No predrilling is used to install the pile and the ground water level is at a depth of about 7.1 m below the existing ground surface. The measured torque at end of installation for helical pile is about 306 KN.m and the corresponding embedment depth is 5.3 m.

Sakr (2010) simulated the pile lateral load test using the p-y analysis program, Lpile Plus 5.0 (Reese et al., 2000). Nonlinear p-y analyses predict the relationship between dimensionless measures of load and deflection. Figure 3 shows the Lpile predictions compared to results from the field tests. Lpile overestimated the lateral resistance of the pile in Field Test 1 and underestimated that in Field Test 2. Sakr (2010) argues

that soil conditions in both field tests are similar and the lower lateral capacity found in Field Test 1 is due to predrilling. Sakr (2010) repeated the simulation of Field Test 1 using y multipliers to take the effect of predrilling into consideration. The p or y multipliers are typically used to account for pile shadowing phenomenon occurring in the performance of pile groups (Clarke and Duncan, 2001). In closely packed pile groups, piles transfer their loads to the same zone, which increases the lateral deflection of the pile. The simulation using a y multiplier equal to 2.5 predicted a behavior very similar to the one observed in Field Test 1. However, this value of the y multiplier is not a true material property and is not linked to the remolding process around the helical pile. Also, the value 2.5 may be less than the true value, because the L_{pile} predictions underestimated the behavior measured in Field Test 2 where no predrilling was used.

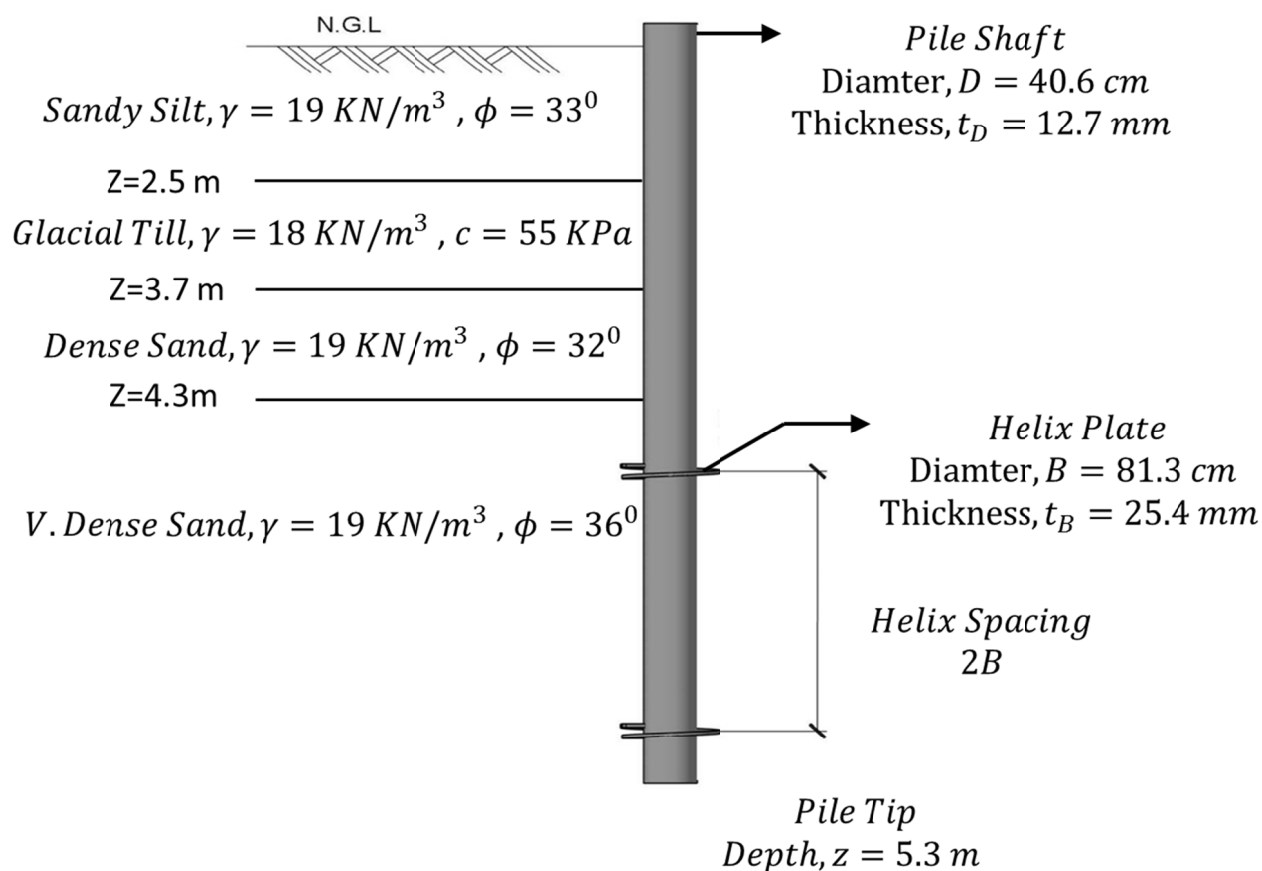


FIG. 2. A schematic diagram showing the helical pile and soil conditions in Field Test 2 (after Sakr, 2010).

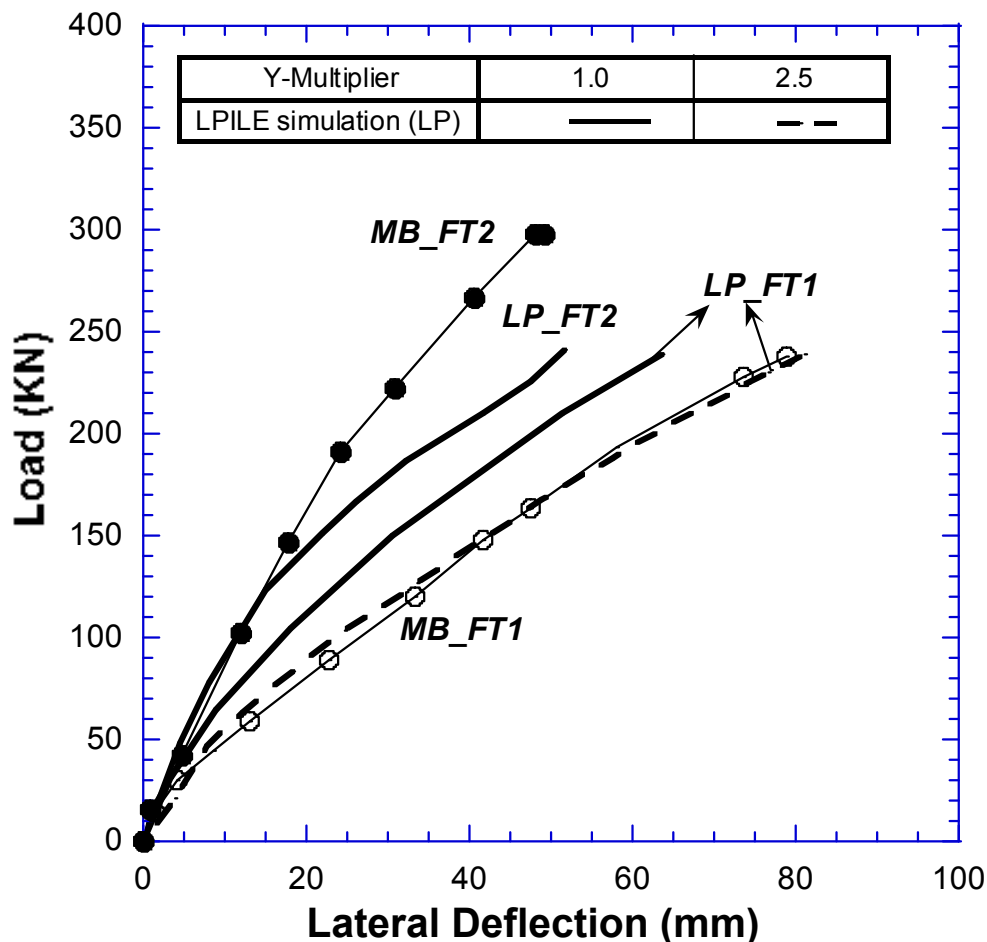


FIG. 3. Comparison between Lpile Plus 5.0 (LP) predictions and measured behavior (MB) in pile lateral load field tests (FT), after Sakr (2010).

FINITE ELEMENT MODEL

The field tests from Sakr (2010) are represented in the FE commercial software PLAXIS 3D (Brinkgreve et al., 2012) by 3D tetrahedron elements with 10 nodes each. The soil continuum extends 20 m in both directions around the pile and is 40 m deep to minimize boundary effects on the pile response. Figure 4b shows the mesh used in the analysis and the variation in element size distribution around the pile. There are few soil properties recorded in Sakr (2010) so that only the elastic-perfectly plastic model is assumed to be suitable for predicting the soil behavior. The Mohr-Coulomb soil model with a tension cut-off describes this behavior in the analyses.

The model represents the hollow shaft of the helical pile, shown in figure 4a, with 6-noded shell elements. A significantly more rigid horizontal plate is added to the top of the pile head. This plate transmits the horizontal force incrementally and equally everywhere in the pile cross-section, and prevents transversal deformations. Helices are represented by circular plates of shell elements and then fixed to the body of the pile shaft. The pile-soil interaction is represented by interface elements consisting of six pairs of nodes, compatible with the 6-noded triangular side of the soil element and the shell element. The aim of these interface nodes is to allow slippage between the soil and pile and the opening of a gap behind the pile when lateral deflection occurs.

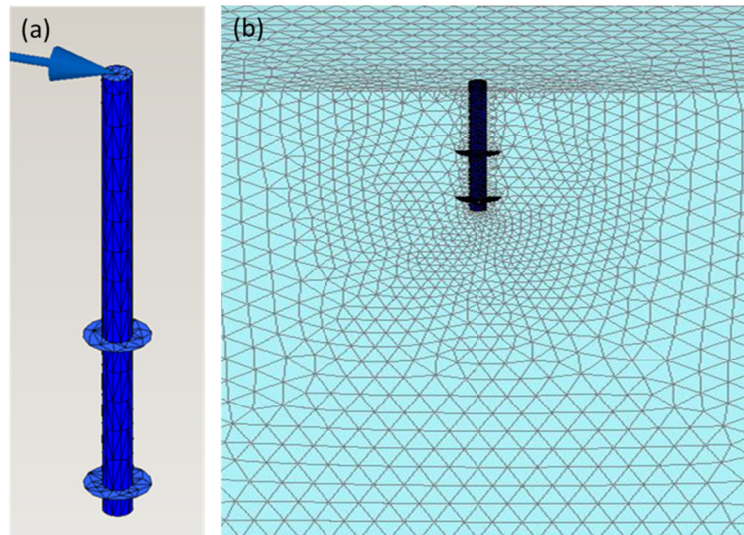


FIG. 4. The 3D finite element mesh representing the helical pile (shell elements in 4a) and the soil (tetrahedron elements in 4b).

For the simulation of Field Test 1, the model assumes that predrilling creates a zone around the pile shaft where soil is remolded as shown in Figure 1. This zone radially extends from the pile shaft to the extent of the helical plate (The volume where the helix plate creates helical paths as the pile is installed). The strength in this zone is close to the residual strength of the soil. Predrilling decreases or eliminates soil lateral displacement with pile installation and hence the strength of this zone remains lower than its original value.

Figure 5 shows the non-linear relationship between the applied increments of lateral loads and the pile head deflection. Similar to figure 3, figure 5 compares the FE model predictions to the behavior measured in Field Tests 1 and 2. When no predrilling is used in pile installation (Field Test 2), the FE predictions match the measured behavior better than that of the p-y analysis. This can be attributed to the fact that the soil is represented as a continuum in the FE model not as a set of isolated non-linear springs as in the Lpile program. The helical plate increases the lateral capacity measured in Field Tests 1 and 2 and FE model captures this increase while the Lpile simulation does not. On the other hand, previous literature recorded that Lpile sometimes underestimates the lateral capacity of piles and overestimates lateral deformations (e.g. Pando et al., 2006; and Choi et al., 2013).

Both Lpile and the FE model overestimated the lateral resistance of the pile in Field Test 1. However, when another simulation includes the disturbed zone around the pile shaft with reduced strength, the predicted response agrees well with that measured in the field. The advantage of the FE program is that the reduction can be related to the actual mechanism of remolding. In this analysis, the remolded strength is assumed to be around 60% of the original strength. This is considered on the high end of strength decrease due to remolding (Mulilis et al., 1977). It is worth noting that there are no element tests carried out on the remolded soil from Field Test (1) in Sakr (2010). This value of reduction percent can be affected by the accuracy of the numerical procedures. The value of the friction angle is reduced from 36° to 20° . In addition, the stiffness in the remolded region is reduced to 25% of its value ($E = 5.25$ KPa).

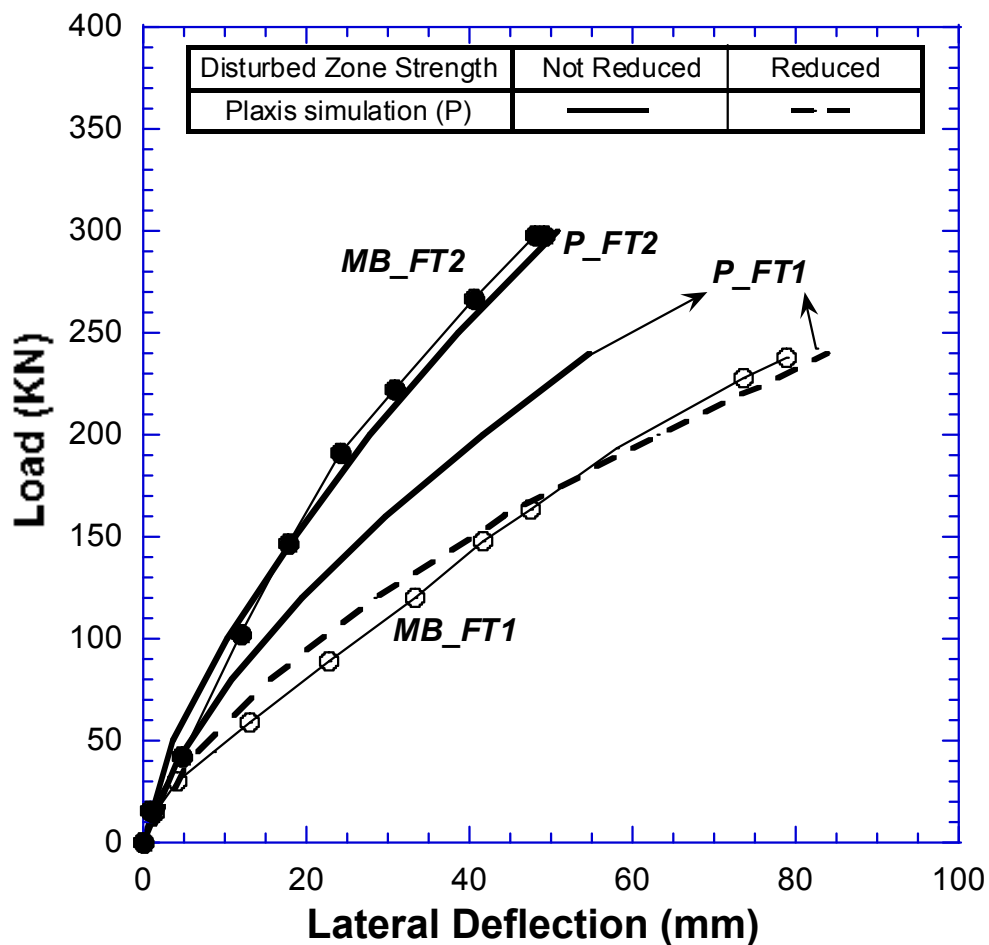


FIG. 5. Comparison between Plaxis predictions (P) and measured behavior (MB) in Field Tests (FT) 1 and 2 from Sakr (2010).

Interface Element Properties

The creation of a small zone around the helical piles to account for installation induced disturbance (remolding) may not be practical when a large number of piles is considered. Typically, in the FEM soil-structure interaction is regulated by the properties of the interface elements. Wehnert and Vermeer (2004) showed how the interface affects the results of a pile load test simulation. In Plaxis 3D, the strength reduction factor, R controls the effect of the interface on the analyses. This study calculates the value of R based on the value of the reduced shear strength (friction angle) chosen for the analysis as shown in Eq (1). The stiffness of the soil adjacent to the pile is calculated from the value of R as shown in Eq (2).

$$R = \frac{\tan(\phi_{\text{red}})}{\tan(\phi)} \quad (1)$$

$$E_{\text{reduced}} = R^2 * E \quad (2)$$

Figure 6 shows the lateral response of the helical pile model corresponding to Field Test 1 using different values of R . The figure shows that the lateral capacity decreases and the lateral deflection increases with the decrease in R as demonstrated in existing literature. The figure also shows the variation in the percentage reduction of friction angle with the variation in R . For $R=0.5$, the model predicts a lateral response very similar to that observed in Field Test 1 and to that predicted by the model, including a remolded zone around the pile. This value corresponds to the reduced friction angle ($\phi_{\text{red}} = 20^\circ$) used in the simulation of the remolded zone.

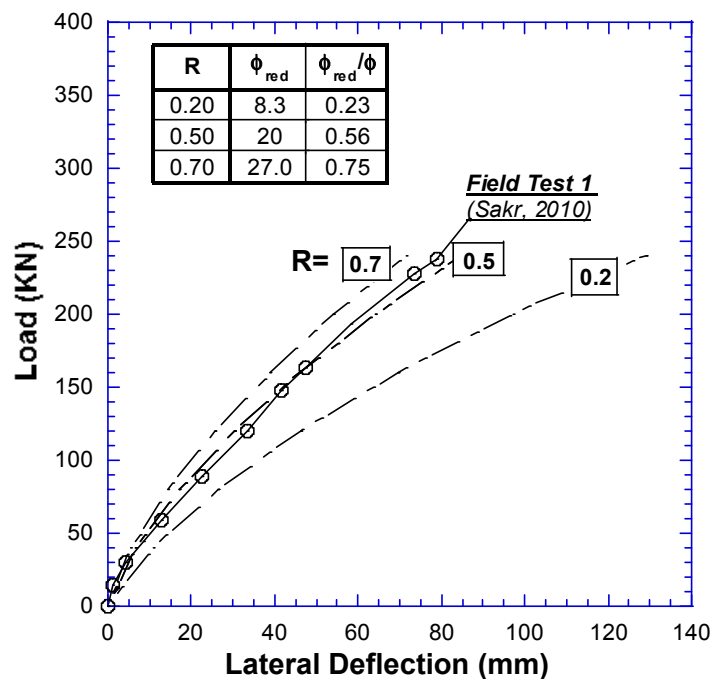


FIG. 6. Effect of Interface Element on helical pile lateral response.

CONCLUSIONS

This research employed numerical analysis to assess the effect of the predrilling needed to install high axial capacity helical piles on the lateral load capacity of such piles. This paper uses published results of two field tests (Sakr, 2010) to validate the predictions of the FE model performed using Plaxis 3D. There is a better agreement between Field Test 2 measurements (no predrilling) and the FE predictions than with Lpile predictions using p-y analysis. The discretized representation of the soil in Lpile overlooks the effect of helical plate on lateral response and underestimates the piles lateral capacity.

Predrilling eliminates the soil displacement occurring with pile installation and hence, the remolding of the soil with the passage of the helix plate is not compensated. The FE model captures the effect of predrilling on the pile lateral response by using the remolded strength and stiffness of the soil around the pile. On the other hand, the Lpile model uses a γ multiplier (originally used for shadowing effect in pile groups) to increase the lateral deflection of the pile.

The simulation of a remolded zone around the pile can be replaced by choosing an appropriate value for the strength reduction factor, R with regards to the properties of the interface elements. Predictions using the value of R that corresponds to the remolded strength of the soil around the pile (0.5) agrees well with those using a remolded zone and with the measurements from the field test.

ACKNOWLEDGMENTS

The authors appreciate the support of Dar Al Handasah and especially Dr. Sherif W. Agaiby for his encouragement.

REFERENCES

- Basu, P. and Prezzi, M. (2009). "Design and applications of drilled displacement (screw) piles." *FHWA/IN/JTRP-2009/2*, Federal Highway Administration, Washington, DC.
- Brinkgreve, R. B. J., Engin, E., and Swolfs, W. M. (2012). "Plaxis 3D 2012 Manual." Plaxis bv, the Netherlands.
- Byrne, B. W., and Houlsby, G. T. (2015). "Helical piles: an innovative foundation design option for offshore wind turbines." *Philosophical Transactions of the Royal Society of London, A: Mathematical, Physical and Engineering Sciences*, 373(2035), 20140081.
- Choi, H. Y., Lee, S. R., Park, H. I., & Kim, D. H. (2012). "Evaluation of lateral load capacity of bored piles in weathered granite soil." *J. Geotechnical & Geoenviron. Engrg.*, 139(9), 1477-1489.
- Clarke, J. A., & Duncan, J. M. (2001). "Revision of the CLM Spreadsheet for Lateral Load Analyses of Deep Foundations." Report of a Study Performed by the Virginia Tech Center for Geotechnical Practice and Research, 22.

- Dean, E. T. (2009). **Offshore geotechnical engineering**. Thomas Telford.
- Hoyt, R. M., and Clemence, S. P. (1989). "Uplift capacity of helical anchors in soil." In *Proceedings of the 12th International Conference on Soil Mechanics and Foundation Engineering*, Rio de Janeiro, Brazil (Vol. 2, pp. 1019-1022).
- Mulilis, J. P., Arulanandan, K., Mitchell, J. K., Chan, C. K., & Seed, H. B. (1977). "Effects of sample preparation on sand liquefaction." *Journal of the Geotechnical Engineering Division*, 103(2), 91-108.
- Pando, M. A., Ealy, C. E., Filz, G. M., Lesko, J. J., and Hoppe, E. J. (2006). "A Laboratory and Field Study of Composite Piles for Bridge Substructures." *FHWA-HRT-04-043*, Federal Highway Administration, Washington, DC.
- Reese, L. C., Wang, S. T., Isenhower, W. M., & Arrellaga, J. A. (2000). "Computer program Lpile plus version 5.0 technical manual". Ensoft, Inc., Austin, Texas.
- Rock, M. and Parsons, L. (2010). "Offshore Wind Energy." Fact Sheet, Environmental and Energy Study Institute, Washington, DC.
- Sakr, M. (2010). "Lateral Resistance of High Capacity Helical Piles – Case Study." 63rd Canadian geotechnical and 6th Canadian Permafrost Conference, Calgary, Alberta, September 12 – 16, 2010, pp. 402 -412.
- Spagnoli, G. (2013). "Some considerations regarding the use of helical piles as foundation for offshore structures." *Soil Mechanics and Foundation Engineering*, 50(3), 102-110.
- Wehnert, M., & Vermeer, P. A. (2004). "Numerical analyses of load tests on bored piles." *Numerical methods in geomechanics—NUMOG IX*, 505-511.

Preliminary Development of a New Concept to Improve the Sustainability of Offshore Foundations

Hande Gerkus, S.M.ASCE¹; Joseph R. Giampa, S.M.ASCE²; Asitha I. Senanayake, S.M.ASCE¹, Ying Lai, S.M.ASCE¹; Yunhan Huang, S.M.ASCE¹; Jose Eugenio Iturriaga Flores¹; Nikolaus B. Breithaupt²; Sven Sivarajah²; Aaron S. Bradshaw, P.E., M.ASCE³; and Robert B. Gilbert, P.E., D.GE, M.ASCE⁴

¹Graduate Research Assistant, Civil Architectural and Environmental Engineering, Univ. of Texas at Austin, 301 E. Dean Keeton St. Stop C1700, Austin, TX 78712.

²Graduate Research Assistant, Civil and Environmental Engineering, Univ. of Rhode Island, 203 Bliss Hall 1 Lippitt Rd., Kingston, RI 02881.

³Assistant Professor, Civil and Environmental Engineering, Univ. of Rhode Island, 203 Bliss Hall 1 Lippitt Rd., Kingston, RI-02881.

⁴Professor, Civil Architectural and Environmental Engineering, Univ. of Texas at Austin, 301 E. Dean Keeton St. Stop C1700, Austin, TX 78712.

Abstract: A foundation concept that uses natural forces to install and mobilize the capacity of the foundation is described. Preliminary research and development on an implementation of this concept using a wing-shaped anchor for floating offshore wind turbines has included conducting model tests in clays and sands in the laboratory and developing simplified predictive models. This work indicates that the concept may be feasible, with the ability to embed the anchor several anchor widths during gravity free-fall and several more anchor widths during loading in service. Also, plasticity-based predictive models are able to capture its behavior during model tests.

INTRODUCTION

This paper describes the preliminary development of a new concept to provide a more sustainable foundation for offshore wind turbines. The future for offshore wind is in deep water (Figure 1) where the wind resources are plentiful, the size of the turbines can be maximized, and the facilities can be located reasonably close to major urban areas without being visible from the shore. The challenge in deep water is the effort and cost required to construct facilities.

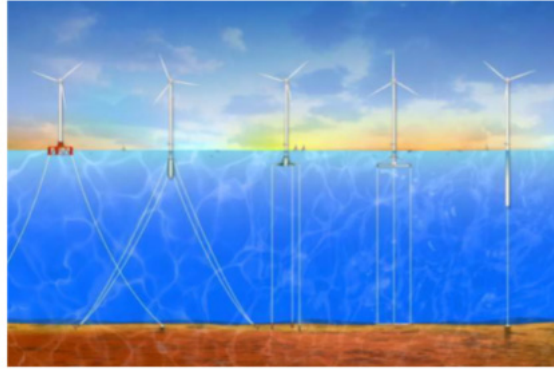


Figure 1. Example Floating Offshore Wind Turbines (NREL 2010)

Conventional offshore foundations, such as driven steel pipe piles, are not efficient and not very sustainable. Also the noise caused by pile driving can be harmful to marine mammals. Long offshore piles typically generate most of their axial capacity in side shear, which is less effective than bearing at utilizing the shear strength of the soil and is susceptible to degradation from installation and cyclic loading. Furthermore, installation of a pile by driving requires a significant amount of work since its axial capacity must be exceeded in order to advance the pile to the target depth. In a sense, this work is wasted because it is extremely unlikely that the full capacity of the foundation will ever actually be needed during service. Lastly, it is virtually impossible to retrieve and re-use a driven pile.

The premise for a foundation concept to improve sustainability is the following:

1. Use natural forces, including gravity and environmental loading, to install and mobilize the capacity of the foundation.
2. Achieve the ultimate holding capacity with the foundation bearing rather than shearing on the soil to utilize the strength of the soil.
3. Utilize multi-directional loading during installation and retrieval so that the foundation is shearing rather than bearing on the soil to minimize the resistance from the soil.

A possible implementation of this concept is a wing-shaped plate anchor (Figure 2). It is embedded using gravity from free-fall through the water column and penetration into the sea floor under self-weight. This penetration method avoids the harming pile driving vibrations on marine mammals. As the tension in the line that attaches the vessel to the anchor increases, the anchor pitches and then begins diving. With increasing environmental loads due to winds, waves and currents, the anchor dives and pitches until the available holding capacity in bearing is maximized over the full bearing surface. The anchor can then be retrieved by pulling on the anchor line in the opposite direction, causing the anchor to slice back up through the soil.

The ability to pursue this novel foundation concept, and to move toward more sustainable foundations, requires a fundamental understanding of soil-structure interaction that considers the orders-of-magnitude range of shear rates during free-fall penetration, line pre-tensioning and environmental loading and the complete six-degree-of-freedom interactions between the wing, the line and the soil under large deformations as the anchor “flies” through the soil. Preliminary research and development work in pursuit of this concept is described here.

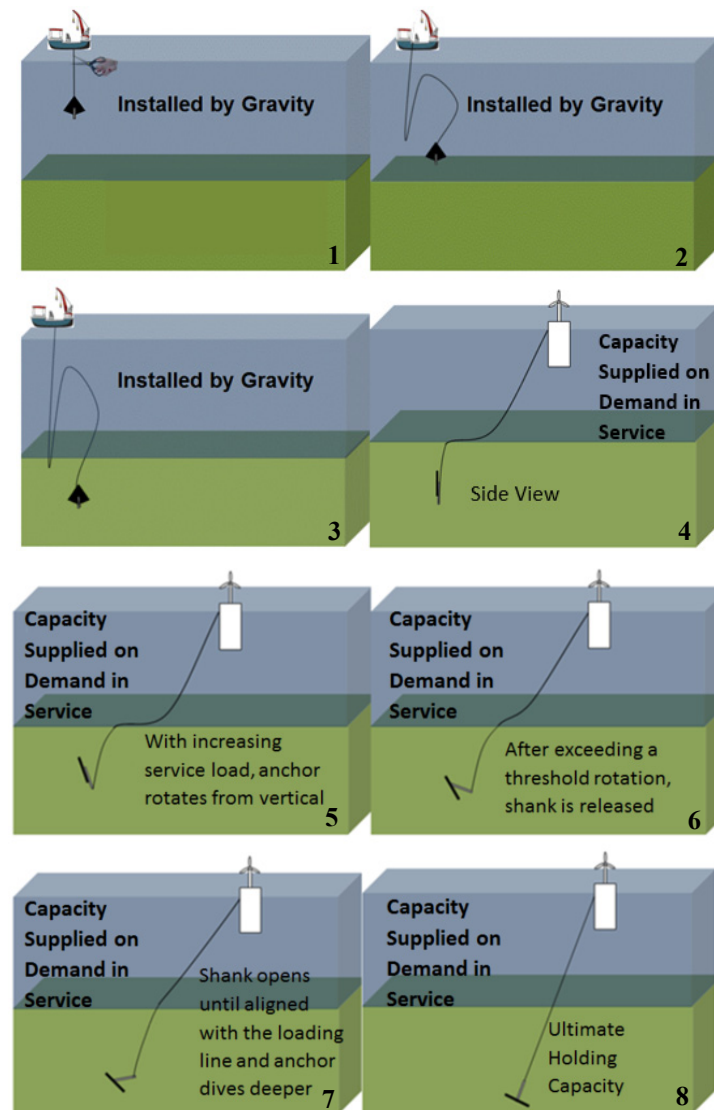


Figure 2. Schematic Illustration of Installation and Service for Flying Wing Anchor (Patent Pending)

RESISTANCE TO PURE BEARING, SHEAR AND ROTATION

The first step to understanding, predicting, and controlling the behavior of the proposed anchor is to establish its resistance to pure bearing, shear, and rotation (Figure 3 and Figure 4). For convenience of comparison, these resistances are expressed as normalized bearing factors (Table 1), where the resistance is non-dimensionally related to the strength of the soil (i.e., the undisturbed undrained shear strength for clay and the vertical effective stress for sand) and the geometry of the anchor (i.e., the bearing area of the fluke).

Model tests have been conducted in test beds of soil to measure these pure bearing capacity factors. Model single-wing shaped anchors (Figure 3) were built with an

equivalent fluke width (B) of about 100 mm and a fluke thickness of about B/10. The anchors were tested in test beds of kaolinite, marine clay, and sand. Additionally, a double-wing shaped model anchor (Figure 4) with a width of 90 mm and a fluke thickness of B/30 was tested in marine clay. The kaolinite has a liquid limit of about 56%, while the marine clay has a liquid limit of about 105%. The undrained shear strength (s_u) of the soil was measured using an in situ t-bar test (El-Sherbiny 2005; Aubeny C. , et al., 2011). Tests in clay were conducted immediately after remolding the test bed (i.e., sensitivity equal to one) and after waiting several days to weeks (i.e., sensitivity greater than one). The anchors were loaded under a relatively quick rate such that undrained conditions applied; the same rate of penetration was used for the t-bar test. The sand test beds were prepared using a beach sand with a mean particle size of 0.3 mm, a minimum void ratio of 0.44 and a maximum void ratio of 0.84. The sand was placed through pluviation to a relative density of about 20% (Bradshaw et al. 2015).

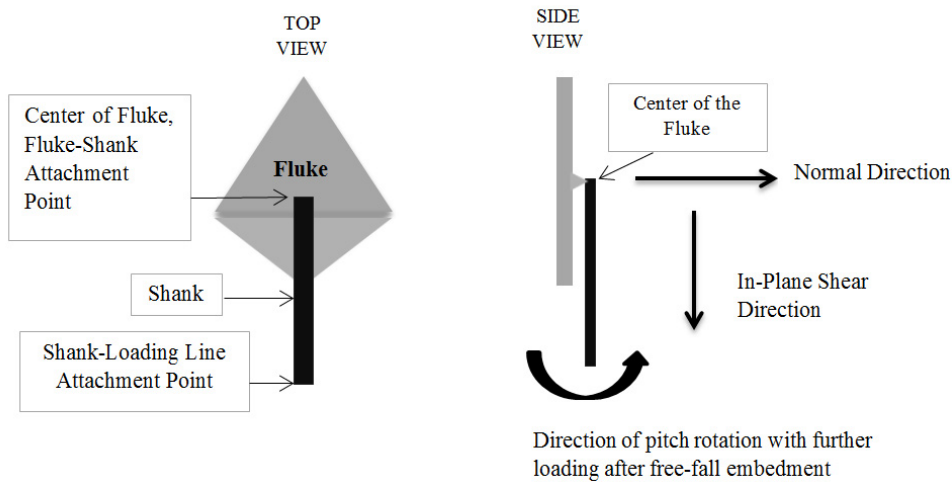


Figure 3. Schematic of Single Wing-Shaped Anchor

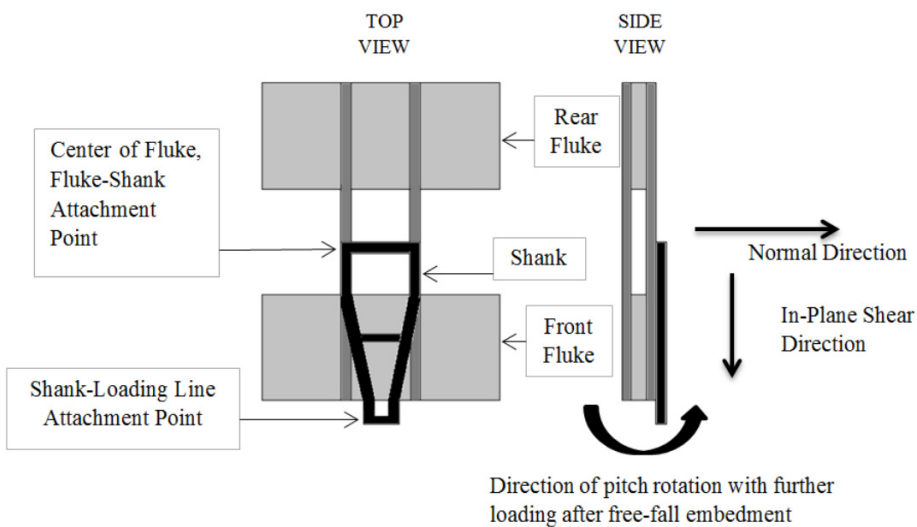


Figure 4. Schematic of Double Wing-Shaped Anchor

Table 1. Non-dimensional Bearing Capacity Factor Equations

Normal Loading and In-Plane Shear Loading in Clay	Pitch Loading in Clay	Normal Loading and In-Plane Shear Loading in Sand	Pitch Loading in Sand
$N_c = \frac{F}{s_u \cdot A_{fluke}}$	$N_c = \frac{M_{max}}{s_u \cdot A_{fluke} \cdot B}$	$N_\gamma = \frac{F}{\gamma' \cdot A_{fluke} \cdot H}$	$N_\gamma = \frac{M_{max}}{\gamma' \cdot A_{fluke} \cdot H \cdot B}$
F: Net anchor resistance		H: Depth of embedment to center of fluke	
M_{max} : Maximum moment		s_u : Undrained shear strength	
B: Equivalent fluke width = $(A_{fluke})^{1/2}$		γ' : Submerged unit weight of sand	

Similar pure bearing capacity factors are measured in both the kaolinite and marine clay (Figure 5). The measured average bearing capacity factor of about 13 for the single wing-shaped anchor and 13.6 for the double-wing shaped anchor for normal loading (Figure 5a) compares well with theoretical values calculated from the finite element method for symmetrical, thin plates (e.g., Martin and Randolph 2001). Also, the measured pure bearing capacity factors for pitch loading (Figure 5b) are similar to that calculated from an upper-bound plasticity solution for symmetrical thin plates of 1.9 (e.g., Aubeny and Chi 2010). The pure bearing capacity factors in shear are about 1/3 of the normal loading bearing capacity factors (Figure 5c). The measured pure bearing capacity factors for shear loading are comparable to those predicted using a simplified plasticity model of summing of the resistances contributed by each surface of the anchor, $N_{c, shear} = 2(1/S_t) + 2 \times 7.5 \times (t/B)$ where S_t is the sensitivity of the clay (i.e., the side shear is assumed to mobilize the remolded undrained shear strength) and t/B is the ratio of the fluke thickness to the fluke width. Unlike the pure bearing capacity factors in normal and pitch loading, the measured and calculated bearing capacity factors in shear loading decrease as the sensitivity of the clay increases.

For pure shear loading in sand with the anchor translating horizontally, a flow-around type of failure mechanism develops and the resistance is essentially proportional to the effective vertical stress (Figure 6). A simplistic comparison with the same anchor under shear in a normally consolidated clay can be obtained by relating the undrained shear strength to the vertical effective stress, s_u/σ_v' : $N_{\gamma, shear} = N_{c, shear} \times (\sigma_v'/s_u)$. Therefore, the horizontal shear resistance in sand, $N_{\gamma, shear}$ of about 5, is smaller than the undrained shear resistance in a normally consolidated clay, $N_{\gamma, shear}$ of about 16 assuming $s_u/\sigma_v' = 1/4$. For pure normal loading the failure mechanism is more complicated and depends on the depth to the surface as well as the direction of loading (e.g., Bradshaw et al. 2015). For vertical uplift of a horizontally-oriented anchor, the non-dimensional bearing capacity factor increases approximately proportionally to the embedment depth (Figure 6); therefore, the uplift resistance is increasing in proportion to the square of the embedment depth.

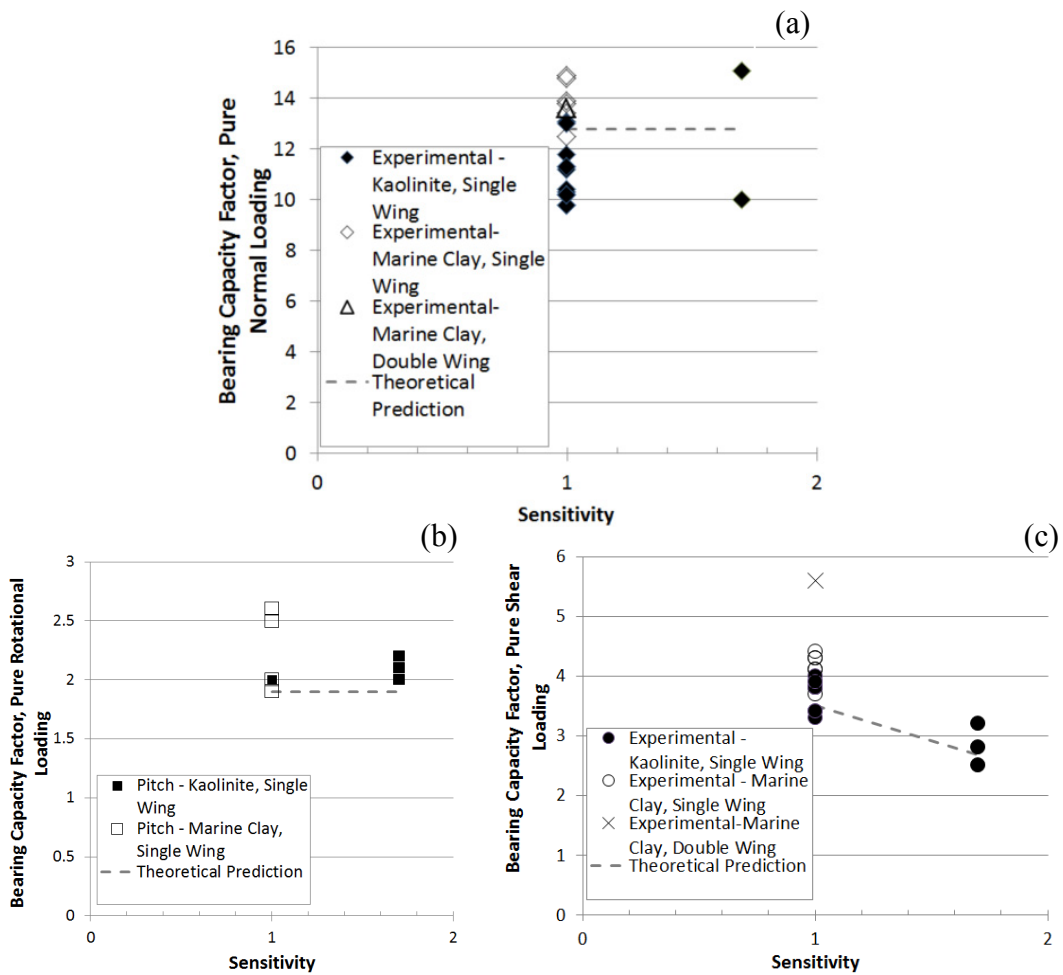


Figure 5. Non-dimensional Bearing Capacity Factors for Normal (a), In-Plane Shear (b) and Pure Rotational (c) Loading in Clay

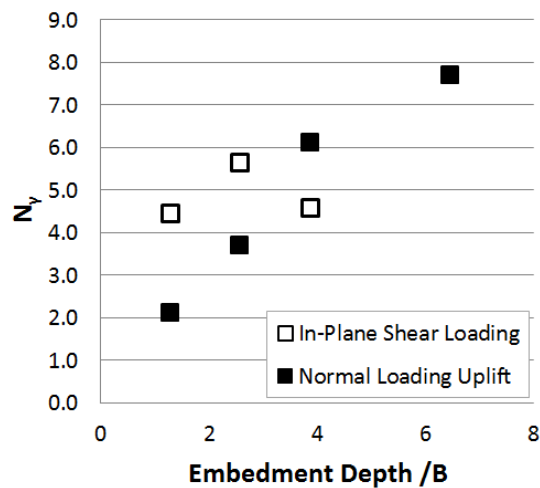


Figure 6. Non-dimensional Bearing Capacity Factors for Normal and In-Plane Shear Loading of Horizontally-Oriented Anchor in Sand

FREE-FALL PENETRATION

Installation for the proposed anchor starts by releasing it in water for free-fall and near vertical penetration under self-weight. The deeper the penetration under free-fall, the greater the ultimate holding capacity will be because the undrained shear strength for a clay tends to increase with depth and the effective stress for a sand increases with depth. Free-fall penetration tests were conducted in test beds of clay using the single wing-shaped and the double-wing shaped scaled anchor models; and using the single wing-shaped scaled anchor model in sand. Scaled anchor models were built of steel with weights of: 0.59 kg for the single wing-shaped anchor tested in clay, 0.67 kg and 1.04 kg for the single wing-shaped anchors tested in sand, and 0.44 kg for the double-wing shaped anchor tested in clay. The impact velocity was varied by varying the drop height. The clay test beds were constituted of marine clay with an undrained shear strength that was nearly constant with depth; in situ undrained shear tests were conducted at different rates to estimate rate effects. A dry sand was tested with a relative density of about 26%, and a saturated sand was tested with a relative density of about 36%.

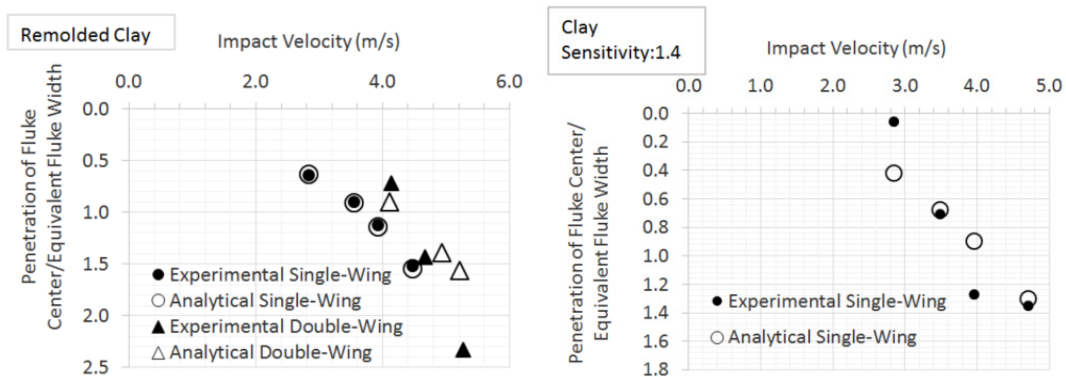


Figure 7. Free-fall Penetration Results in Clay

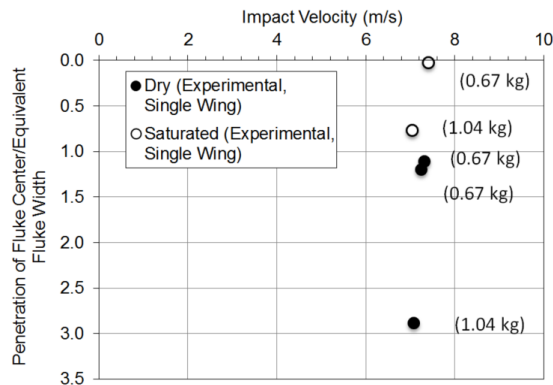


Figure 8. Free-Fall Test Results in Sand

The depth of penetration increases both as the impact velocity increases (Figure 7) and the weight of the anchor increases (Figure 8). In these tests, maximum penetration depths of two to three fluke widths were obtained. However, it is not possible to scale the results from model tests directly to the field because the impact velocities in the field (40 to 50 m/s) will be greater than can be achieved with free-fall in the laboratory (less than 5 m/s) and because the ratio of the weight (proportional to the cube of the anchor width, B^3) and area that resists shear during penetration (proportional to the square of the anchor width, B^2) is about 50 times greater in the field compared to the small-scale laboratory models. Therefore, penetration depths in the field could be significantly larger than those achieved in the laboratory.

In order to scale the laboratory test results, a predictive model is needed to relate the penetration to the properties of the anchor and the soil. A simplified, analytical model developed by True (1976) for the vertical penetration of projectiles into the ocean floor has been successfully adapted to predict the penetration of torpedo piles for offshore foundations (e.g., Richardson 2008). Predictions based on this model for the laboratory tests in clay match reasonably well with the measurements, particularly for the remolded clay (Figure 7). Predicting and interpreting the test results in sand is more complicated and in development to properly account for strain rate and dilation effects (Breithaupt 2015).

DRAG EMBEDMENT

After the free-fall penetration, the anchor dives and embeds deeper as the environmental loads acting on the anchor increase. With increasing load, the anchor starts rotating while the shank is held in the closed position. When a threshold pitch angle is exceeded, the fluke-shank transient attachment mechanism releases the shank to open and the fluke-shank angle increases until the shank is aligned with the loading line. Further increase in the load causes anchor to embed deeper and pitch until the ultimate loading capacity is mobilized.

A simplified analytical model based on plasticity theory has been developed to predict anchor trajectory during drag embedment after free-fall (Huang, 2015). Anchor line geometry and resistance in soil is modeled after Aubeny and Chi (2014), which is an extension of the model presented by Neubecker and Randolph (1995).

The bearing and shear forces acting on the anchor are calculated by the mechanical model proposed by Neubecker and Randolph (1996). The anchor dive initiation after free-fall starts by pitching of the fluke when the applied moment exceeds the anchor's moment capacity while the shank is attached to the fluke on both sides (fluke-shank angle is zero). It is assumed that the mechanism connecting the fluke and shank is located at the center of the fluke, so there is no moment applied on the fluke once the shank is free to move. A plasticity-based solution (e.g., Aubeny and Chi 2014) is used to model the interaction between the anchor and clay during drag (Figure 9). The dive trajectory is calculated in consecutive steps: anchor pitching with the shank attached to the fluke, the shank starting to open up when a threshold angle between the line and the fluke is exceeded, anchor diving and pitching with further drag embedment until the shank and loading line are approximately normal to the fluke to mobilize the ultimate holding capacity.

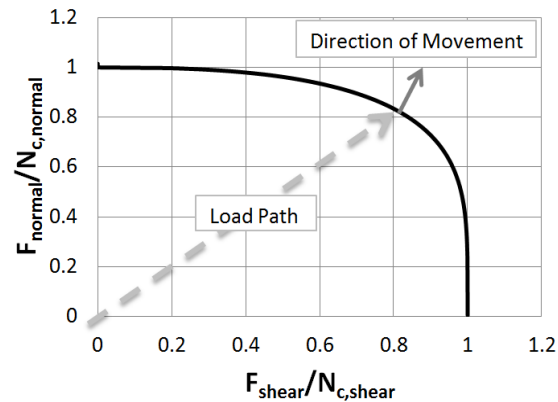


Figure 9. Yield Interaction Surface for Shear and Normal Loading on Anchor

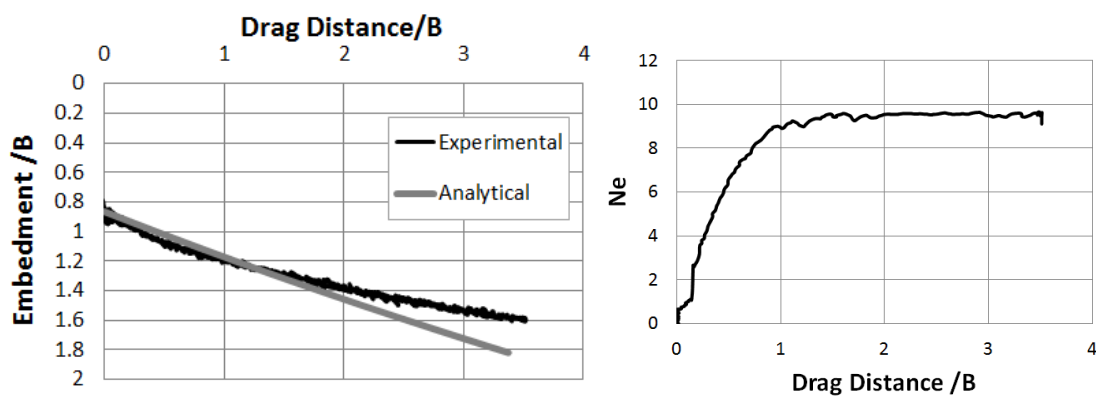


Figure 10. Drag Embedment Test Result for Trajectory and Load

Preliminary anchor drag embedment tests were performed to check the trajectory prediction of the simplified analytical model. Tests were performed in remolded marine clay with constant undrained shear strength by using the double-wing shaped anchor model with a fluke area of 77 cm^2 . Drag embedment tests were performed by initially placing the anchor model at the pitch angle of 50 degrees from the horizontal with the loading line attached at the pad-eye at an angle of 10 degrees from the horizontal. The shank was free to rotate and the anchor center was at $0.8B$ below the mudline.

The anchor was dragged $3.5B$ and embedded approximately $0.8B$ (Figure 10). The line load on the anchor is normalized by the area of the fluke and the undrained shear strength of the soil at the depth of the fluke using an equivalent or mobilized bearing capacity factor, N_e . This mobilized bearing capacity factor increases to a near constant value of about 9.4 (Figure 10). This mobilized bearing capacity factor is in between that for pure shear, about 5.6, and pure bearing, about 13.6 (Figure 5) reflecting the interaction between these components of load during dive. The analytical predictive model produces results comparable to the measurements (Figure 10).

CONCLUSIONS

This paper describes the preliminary development of a new concept to provide a more sustainable foundation for offshore wind turbines. The concept is to use natural forces, including gravity and environmental loading, to install and mobilize the capacity of the foundation and to achieve the ultimate holding capacity with the foundation bearing rather than shearing on the soil to best utilize the strength of the soil. Research and development is in progress to implement this concept with a wing-shaped anchor, both installed into the soil by free-fall penetration and pulled deeper into the soil to develop its holding capacity by loading in service.

The following conclusions are drawn based on the development work thus far:

- The resistance to movement under pure shear loading is about 1/3 that for pure normal loading under undrained shearing conditions in clay.
- The resistance to movement under pure shear and normal loading in sand depends on the direction of movement relative to the ground surface and the depth of embedment. The resistance to horizontal translation under pure shear loading decreases relative to that for pure normal loading under vertical uplift as the depth of embedment increases.
- Depths of penetration under free-fall embedment of at least two to three widths of the anchor are possible. The depth of penetration increases as the impact velocity increases and as the volume relative to the surface area of the anchor increases. For anchors in clay, a simplified predictive model of penetration depth compares reasonably well with model test results.
- The anchor dives as it is loaded in service; the rate of embedment versus horizontal translation is related to the interaction between the yield capacity under pure shear and normal loading. For anchors in clay, a simplified predictive model compares reasonably well with model test results.

This particular anchor concept could be used for a variety of offshore applications, including floating bridges and oil and gas production facilities. More fundamentally, the principle of a foundation that yields plastically as it provides resistance to loading in service, therefore “installing” itself, could potentially be applied to conventional onshore structures, even with small tolerable deformations and distortions, if the structural system is designed to complement the foundation system by distributing load as elements in the foundation yield.

ACKNOWLEDGMENTS

The material is based upon work supported by the National Science Foundation under Grant No. 1301211. The authors also appreciate the valuable contribution of collaborators Kenneth Gavin, Paul Doherty, Soroosh Jalilvand (University College Dublin) and Vinayagamoothy Sivakumar (Queen’s University Belfast).

REFERENCES

- Aubeny, C. P., & Chi, C. (2010). Mechanics of Drag Embedment Anchors in a Soft Seabed. *Journal of Geotechnical and Geoenvironmental Engineering*, Vol. 136 (1): 57-68.
- Aubeny, C., & Chi, C.-M. (2014). Analytical Model for Vertically Loaded Anchor Performance. *Journal of Geotechnical and Geoenvironmental Engineering*, Vol. 140 (1): 14-24.
- Aubeny, C., Gilbert, R., Randall, R., Zimmerman, E., Katelyn, M., Chen, C.-H., et al. (2010). *The Performance of Drag Embedment Anchors*. Contract Number M09PC00028, MMS Project Number 645, OTRC Project 32558-A6960, Minerals Management Service.
- Bradshaw, A. S., Giampa, J., Dietrich, F., Gilbert, R. B., & Gerkus, H. (2015). Pullout Capacity of Plate Anchors in Sand for Floating Offshore Wind Turbines. *Proceedings of the 3rd International Symposium on Frontiers in Offshore Geotechnics* (pp. 833-838). Oslo, Norway: NGI.
- Breithaupt, N. B. (2015). Dynamic Penetration of a Flying Wing Anchor in Sand in Relation to Floating Offshore Wind Turbines. *M.S. Thesis*. University of Rhode Island.
- El-Sherbiny, R. (2005). Performance of Suction Caisson Anchors in Normally Consolidated Clay. *Ph.D. Dissertation*. The University of Texas at Austin.
- Huang, Y. (2015). Designing a Laboratory Model Test Program for Developing a New Offshore Anchor. *Master's Thesis*. The University of Texas at Austin.
- Martin, C. M., & Randolph, M. F. (2001). Applications of the lower and upper bound theorems of plasticity to collapse of circular foundations. *Proc., 10th Int. Conf., Vol 2* (pp. 1417-1428). Tucson, AZ: International Association of Computer Methods and Advances in Geomechanics.
- NREL (2010). *Large-Scale Offshore Wind Power in the United States*. Authored by Musial, W. and Ram, B. for the National Renewable Energy Laboratory, Department of Energy.
- Neubecker, S. R., & Randolph, M. F. (1995). Performance of Embedded Anchor Chains and Consequences for Anchor Design. *Offshore Technology Conference*, (pp. 191-200). Houston, TX.
- Neubecker, S. R., & Randolph, M. F. (1996). The performance of drag anchor and chain system in cohesive soil. *Marine Georesources & Geotechnology*, Vol. 14 (2): 77-96.
- Richardson, M. D. (2008). Dynamically Installed Anchors for Floating Offshore Structures. *Ph.D. Thesis*. Crawley, Australia: The University of Western Australia.
- True, D. G. (1976). Undrained Vertical Penetration Into Ocean Bottom Soils. *Ph.D. Thesis*. University of California, Berkeley, California.

Rotational Behavior of Squat Monopiles in Soft Clay from Centrifuge Experiments

Ryan D. Beemer, S.M.ASCE¹; Madhuri Murali, S.M.ASCE²; Dr. Giovanna Biscontin, M.ASCE³; and Dr. Charles Aubeny, M.ASCE, P.E.⁴

¹Laureate Research Associate, Centre for Offshore Foundation Systems, Univ. of Western Australia, Perth, Australia. E-mail: ryan.beemer@uwa.edu.au

²Geotechnical Engineer, Terracon Consultants, Inc., 11555 Clay Rd., Suite 100, Houston, TX 77043. E-mail: maddy.murali@terracon.com

³Lecturer, Dept. of Engineering, Cambridge Univ., Trumpington St., Cambridge CB2 1PZ. E-mail: gb479@eng.cam.ac.uk

⁴Professor, Zachry Dept. of Civil Engineering, Texas A&M Univ., 3136 TAMU, College Station, TX 77843. E-mail: caubeny@civil.tamu.edu

Abstract: This paper presents initial results from geotechnical centrifuge experiments on squat gravity caissons/monopiles under cyclic rotational loading in soft clay under undrained conditions. These experiments were conducted in the 150g-ton centrifuge at Rensselaer Polytechnic Institute. In total three monopiles with length to diameter aspect ratios of two were tested. Though this aspect ratio is a bit atypical it could be a reasonable option for offshore renewable hydrokinetic systems or a component in tripod or tetrapod wind tower foundation systems. Results are focused on behavior arising from an unrestricted vertical coordinate, allowing self-weight to contribute to combined loading, and the effect of load eccentricity and depth of rotation on rotational resistance.

INTRODUCTION

As the world seeks to develop more diverse and renewable sources of energy geotechnical engineers find themselves pushing the bounds of how to define types of gravity foundations. The variety of caisson type foundations has resulted in a fluidity between shallow foundations and open ended flexible piles, resulting in transitional foundations such as skirted foundations, monopiles, buckets, and caissons. In this paper monopile refers to the entire assembly while caisson refers to the foundation.

Given the dynamic nature of the offshore environment an important design aspect of these transitional foundations will be their behavior under cyclic lateral loading. Traditionally, cyclic lateral capacity of piles can be determined with cyclic p-y curves (Matlock 1970). However; this work was developed for long flexible piles, length to diameter aspect ratios above 10 (Poulos and Davis 1991; Randolph 1981). Additionally, a mean stress method (Andersen 1988) can be used to determine cyclic

capacity, given the appropriate failure mechanism and laboratory data. In recent years there has been more development in this area. Cyclic translational loading of monopiles, in soft clay, with length to diameter aspect ratio of five was investigated by Zhang et al. (2011). These centrifuge experiments were conducted under two-way displacement controlled loading and were restricted in the vertical coordinate. The behavior of monopiles, in clay, with aspect ratios of approximately 5.2 under combined lateral-moment loading has been investigated by Lau (2015). These centrifuge experiments were conducted under both one-way and two-way cyclic force controlled loading.

This paper presents the initial results from centrifuge experiments of monopiles in, soft clay, with aspect ratio of two under combined lateral-moment loading with a constant gravity load from self-weight. Rotational loading was one-way, cyclic, displacement controlled. Model geometry was used to vary load eccentricity between 1.10 and 3.05 diameters. These results should be used to fill the gap in the behavior of transitional caisson type gravity foundations and could be useful for the design of tripod or multi-legged renewable energy structures.

EXPERIMENTAL SETUP

Facilities

This centrifuge experiment was conducted in the 150 g-ton at the Center for Earthquake Engineering Simulations at Rensselaer Polytechnic Institute (RPI) (Elgamal, et al. 1991). All load application and in-flight soil strength testing was conducted with the RPI 4 Degree of Freedom Robot (Ubilla, et al. 2006). Use of the robot limited nominal centrifuge acceleration to 70 g. A custom cup adaptor, was fabricated for the RPI robot from a 3D printed steel-bronze alloy. It allowed multiple monopiles to be loaded sequentially in-flight without spinning down the centrifuge.

Soil Test Bed

The test bed was constructed in the RPI Large Rigid Box. The multi-phase construction involved placement of kaolinite clay (BASF ASP 600) at a water content of approximately 80% using RPI's large standing mixer, partial consolidation on the centrifuge at 100g to an average water content of approximately 62.5%, and finally excavation of 4.5 cm of clay in order to reduce the over-consolidation effects on the surface soils. Partial consolidation of a doubly drained soil results in a non-uniform profile with the surface and bottom being more consolidated than the center. By removing soil from the surface a profile roughly approximating normal consolidation can be created. Teflon sheets along the sides of the box allowed even settlement of the model. The final model had dimensions of 88 cm by 39 cm with a depth of 20 cm in flight at 74 g and 23 cm at 1 g, assuming 3 cm of recompression.

Soil undrained shear strength was measured through T-bar testing, water content correlations developed by Tessari (2012), and SHANSEP analysis as presented in Murali (2015). T-bar tests were conducted adjacent to each monopile before and after each test allowing for measurements in time and space. Measured strength was fairly

consistent apart from the post experiment water content correlations under predicting strength at shallow depths and the first T-bar test. It is believed that the water content correlations do not properly take into account the soil's stress history and it is likely the soil consolidated slightly between T-Bar 1 and the first cyclic test. Prototype time, $1/N^2$ for diffusion (Garnier et al. 2007), between the first T-bar test and the first monopile test was approximately 160 days at 74 g.

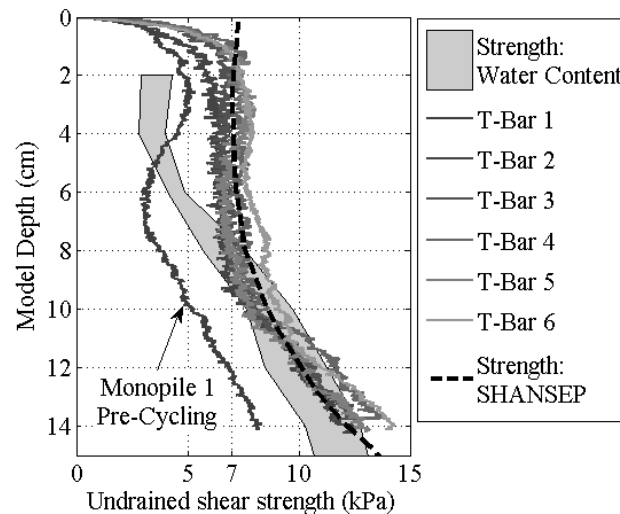


FIG. 1. Shear strength profile of experiment (model scale)

Monopile Models

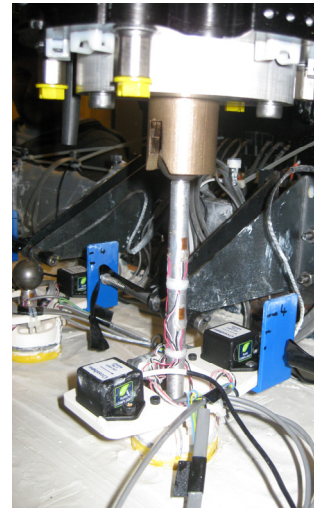
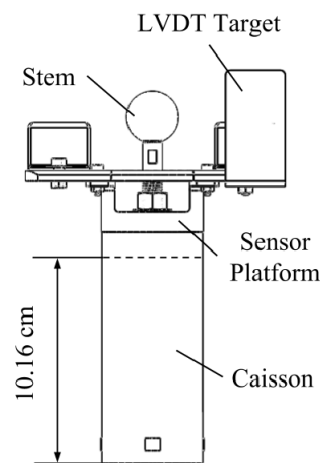
Monopiles consisted of an aluminum caisson, an aluminum or steel stem, and an ABS plastic sensors platform. The caissons were created by turning down an aluminum pipe to an outside diameter of 4.96 cm and welding on a 1.27 cm cap. This resulted in an effective installation length of 10.16 cm. Further details are provided in Table 1 and Figure 2a, including prototype dimensions, given centrifuge gravity of 74 g.

The stems were secured through a thread hole in the cap with a nut and nylon washers. The stems were constructed from 9.52 mm (3/8 in) diameter steel or aluminum rod and were capped with 2.54 cm (1 in) diameter ball, Figure 2a. Load was transferred to the stem through the ball and cup connection. The cup on the RPI robot allowed it to couple with the stem ball in flight and apply rotational loading, Figure 2b. Additionally, this connection was incapable of transferring vertical load. Stem lengths were varied between piles in order to change load eccentricity, taken as distance between the center of ball and the pile cap, Table 2. One to two levels of three strain gages were evenly spaced around the stem circumference to measure applied moment and horizontal force.

Strain gage wiring was secured by wrapping thread around the wires at the base of the stem and the caisson cap, similar to how an eyelet is attached to a fishing rod. The parts were then coated in rubber in order to secure and protect the strain gages and wiring. This was a successful means of securing the gages with only Monopile 3 exhibiting gage loss at high g.

Table 1. Caisson Properties

Property	Model	Prototype
Outside Diameter	4.96 cm	3.47 m
Effective Length	10.16 cm	7.52 m
Total Length	11.43 cm	8.46 m
Shell Thickness	0.61 mm	45.14 cm
Vent Diameter	6.35 mm	47.00 cm
Young's Modulus	69.00 GPa	69.00 GPa

**FIG. 2a. Monopile sketch (not to scale) FIG. 2b. Example monopile loading**

The sensors platform was printed in multiple parts from ABS plastic on a 3D printer and fastened together with screws. The platform provided mounting space for two MEMS accelerometers and a target for the LVDT transducer, Figure 2a-b. The MEMS accelerometers had a ± 10 g range (MEMSIC n.d.) and allowed for measurements of monopile rotation relative to centrifuge gravity.

Model Layout

The model presented below is the same as Experiment Two in Grajales et al. (2015). This paper addresses cyclic behavior of monopiles while Grajales et al. (2015) presented post-cyclic capacity.

After excavation of the soil bed the monopiles were installed by hand in 1 g. Three monopiles were installed on the center line of the box 18.5 cm on center with a foam template, Figure 3. The monopiles were installed until the plug was filled, a depth of 10.16 cm (assuming no plug heave). The vent was then plugged with a cork. LVDT transducers were mounted to the Large Rigid Box to measure pile translation. The LVDT sensors did not work well and are not presented. Displacement data instead comes from the theoretical motion of robot bounded by the MEMS accelerometer data (Beemer 2016). Pore pressure sensors were embedded in the soil during the bed

construction. The sensors were installed at monopile mid-depth, approximately 5 cm, and 3.81 cm away in the +X direction from the monopile. A mudmat 3D printed in ABS plastic was installed at the far end of the box. It carried a 100g MEMS accelerometer (Silicone Design Inc. 2013) at the height of the sensors platform on the monopiles. This was used to increase the accuracy of orientation measurements from the MEMS accelerometers on the monopiles (Beemer et al. 2015).

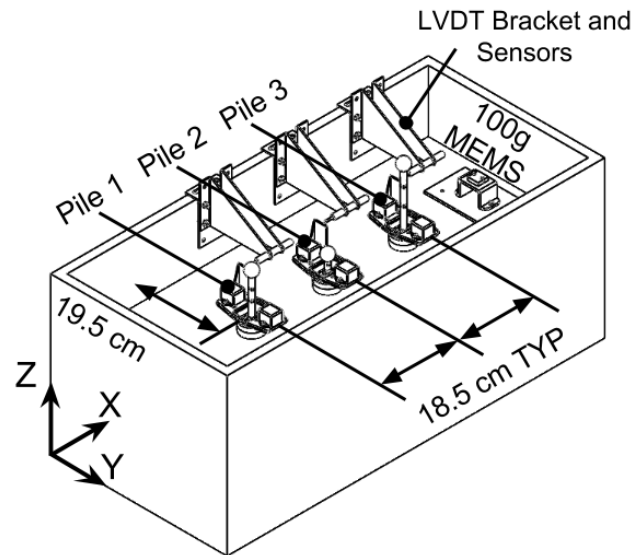


FIG. 3. Sketch of experimental layout

Finally, the model was center on the centrifuge basket such that the three monopiles and mudmat were aligned in the plane of Earth's gravity and centrifugal acceleration and the X-Z plane (Figure 3) was parallel to it.

TEST METHODOLOGY

The nominal centrifuge gravity for the experiment was 70 g; however, gravity at the caisson mid-depth was computed to be 74 g from the 100 g MEMS accelerometer. This acceleration has been used for all prototype scaling. In this experiment displacement magnitude and eccentricity were varied across the three monopiles. Additionally, each pile had a different vertical load due to self-weight from the caisson cap, stem, and sensor platform, Table 2. Monopile vertical capacity was estimated as 225 Newtons. Approximately 60%-78% of vertical capacity was engaged. Each foundation was loaded under three sets of 50 cycle one-way displacement controlled loading. A complete testing matrix for the cyclic loading portion of the experiment is provided in Table 2.

To ensure a constant strain rate over the duration of the one-way motion the maximum horizontal velocity could only be 2 mm/s. This is because the RPI 4 DOF robot's maximum acceleration is 50 mm/s². This combination of acceleration velocity ensured that at least 95% of each motion was at a constant strain rate and the caisson's behavior was undrained. The normalized velocity, $V = vd/c_v$, eccentricity

was of 625; well above the minimum for undrained conditions of 30 (DeJong et al., 2012). Displacement magnitudes in Table 2 are at eccentricity, they were selected to bound working and failure limit states at the soil surface.

Table 2. Experiment Cyclic Loading Matrix

Monopile (#)	Load Eccentricity (\emptyset)	Model Vertical Load (N)	Test (#)	Displacement Magnitude (% \emptyset)	One-Way Load Direction $\pm(X,Y,Z)$	Cycles (#)
1	2.27	175.0	1	2.5	+X	50
			2	5.0	+X	50
			3	10	+X	50
2	1.10	135.0	1	2.5	+X	50
			2	5.0	+X	50
			3	10	+X	50
3	3.05	150.0	1	2.5	+X	50
			2	5.0	+X	50
			3	10	+X	50

where: \emptyset = caisson diameter, 4.96 cm

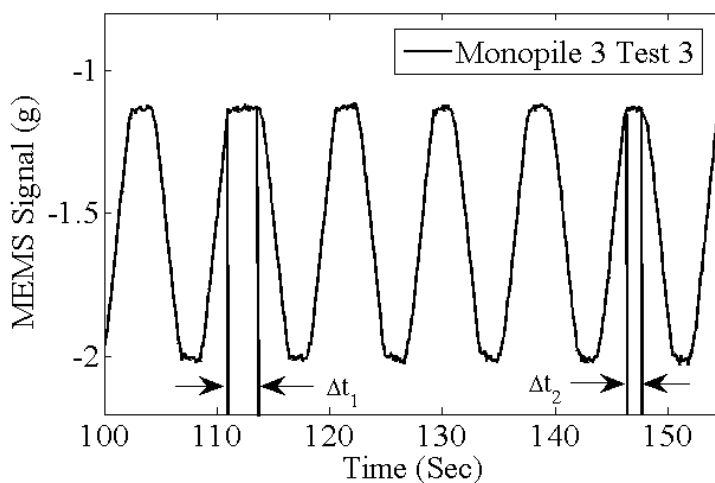


FIG. 4. Example of variation in robot motion due to anti-collision algorithm

Also of note, is that prior to making any motion the RPI 4 DOF Robot runs an anti-collision algorithm. The computation time to complete these calculations varied significantly as seen in MEMS accelerometer signal in Figure 4, $\Delta t_1 > \Delta t_2$. Thus the load frequency and period were not constant. Target load periods (calculated from robot acceleration, velocity, and displacement magnitude) and applied load periods (total cycling time divided by number of cycles) have been provided in Table 3. On average the pauses by the robot added 3.70 seconds to the load period, at model scale. The only foreseeable impact this would have on results is if setup occurred during the

pauses. The average pause time at prototype scale was 2.8 hours. This should not have been enough time for any significant setup to occur.

As discussed in the **Results** section significant settlement of the monopiles occurred during cycling. There was concern that if too much settlement occurred the stem and robot would decouple. To prevent this a small vertical motion of 1.5% of diameter (0.75 mm) was added to the robot cyclic program after 25 cycles.

Table 3. Target vs applied load period

Monopile (#)	Test (#)	Displacement Magnitude (% Ø)	Target Load Period (s)	Applied Load Period (s)	Prototype Applied Period (min)
1	1	2.5	1.64	5.48	6.76
	2	5.0	2.88	6.56	8.09
	3	10	5.38	8.81	10.87
2	1	2.5	1.64	5.65	6.97
	2	5.0	2.88	6.54	8.07
	3	10	5.38	9.02	11.12
3	1	2.5	1.64	5.52	6.81
	2	5.0	2.88	6.53	8.05
	3	10	5.38	8.85	10.92

RESULTS

Initial Orientation of Piles

During centrifuge spin up all three monopiles tilted slightly in the $-X$ direction. There was concern that these initial movements of the monopiles would result in the LVDT sensors going out of range during testing; so, Monopiles 1 and 3 were straightened to ensure this would not occur. Both piles were allowed to sit for 5 minutes, 19 days in prototype time at 74 g, to allow any generated excess pore pressures to dissipate. Adjusted locations and initial monopile tilts from MEMS accelerometers, after adjustment, are provided in Table 4. It should be noted initial tilt of the pile is difficult to ascertain because the basket orientation relative to centrifuge gravity was not measured during the experiment. The largest sources of uncertainty in orientation of the basket comes from the robot changing the model's center of gravity and applied moment about the basket hinge, see Beemer et al. (2016). However, given that the model was centered in the basket and the RPI robot was center when over Monopile 2 it is likely error in initial tilt is on the order of $\pm 1^\circ$ - 3° .

Pile Settlement

As noted previously significant settlement occurred during cycling. The RPI robot was used to measure settlement. After each test the robot was stepped in 0.1 mm increments until it fully connected with the stem. The measurement was taken as change in robot vertical coordinate. Settlement appears to be dependent on load

eccentricity, Table 5, and is not due to consolidation. As seen in Table 2 Monopile 1 had the largest gravity load, but it settled less than Monopile 3 which had a much lighter load. Additionally, the model sat for 7 months of prototype time at 74 g (excluding centrifuge spin up); enough time for the majority primary consolidation to be completed, before testing. It is possible that the combined lateral-vertical load results in plastic failure; given the high ratio of vertical to horizontal load any plastic deformation would include a significant vertical movement.

Table 4. Initial Pile Orientation

Monopile (#)	Pre-Spin Up Robot X-Location (mm)	Post-Spin Up Robot X-Location (mm)	Adjusted Robot X-Location (mm)	Adjusted Tilt MEMS (°)
1	227	213.0	227	4.63
2	417	412.0	413	1.20
3	598	579.5	585	2.15

Table 5. Monopile Settlement

Test (#)	Monopile 1	Monopile 2	Monopile 3
	Eccentricity = 2.25 \emptyset	Eccentricity = 1.10 \emptyset	Eccentricity = 3.05 \emptyset
Prototype Settlement (cm)			
1	29.6	22.20	37.0
2	22.2	14.80	22.2
3	22.2	22.20	22.2
Total:	74.0	59.20	81.4
Total (d/L):	9.80 %	7.90 %	10.80 %

Effects of Load Eccentricity and Depth of Rotation

The following section discusses the impact of varying load eccentricity on monopile cyclic behavior. A sketch of monopile reaction has been provided in Figure 5 for reference. Monopile 1 with an eccentricity of 2.25 had the largest resistance to rotation across all displacement magnitudes at eccentricity, example in Figure 6. This is in spite of the fact that Monopile 2 rotated and displaced more than Monopile 1, Figure 7a-b. Reactive moment appears to be dependent on depth of rotation and not load eccentricity, Figure 8a-b. Maximum rotational resistance appears to correspond with the shallowest depth of rotation. Though Monopile 2 rotated more than Monopile 1 its deep depth of rotation indicates its behavior was more translational than rotational resulting in decreased moment resistance. It is also interesting that Monopile 3 had a deeper depth of rotation than Monopile 1. This indicates that small differences in initial orientation of the monopile could have a large impact on rotational resistance. Monopile 1 had an initial tilt of 4.63° while Monopile 3 had an initial tilt of only 2.15°. The initial tilt may reduced the depth of rotation.

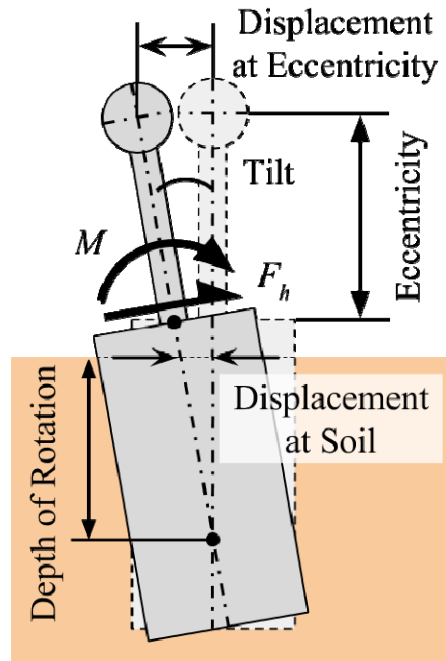


FIG. 5. Monopile Loading and Reactions

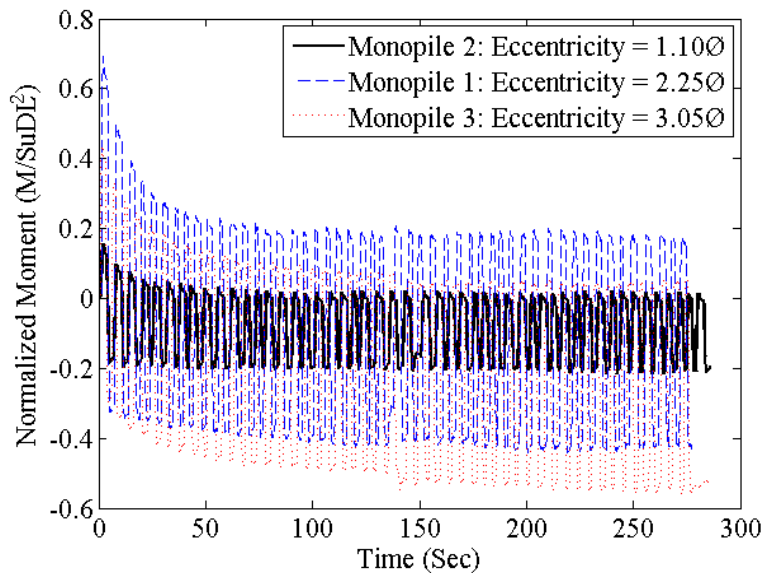


FIG. 6. Reactive Moment All Monopiles, Test 2, Displacement 2.5% Ø

Monopile tilt appears to stabilize quickly and remains constant after a few cycles, Figures 7a. It also appears to increase incrementally for both a decrease of load eccentricity and an increase in displacement magnitude. Though load, moment, and tilt behaviors are fairly stable, displacement at the soil surface appears to drift; with Monopile 1 and 3 drifting in opposite directions, Figures 7b.

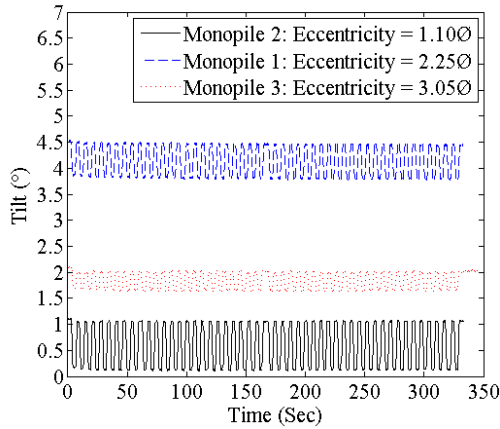


FIG. 7a. Tilt All Monopiles, Test 2, Displacement = 2.5% Ø

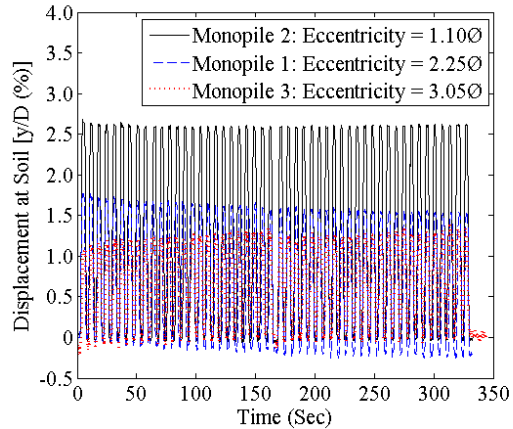


FIG. 7b. Displacement at Soil Surface All Monopiles, Test 2, Displacement = 2.5% Ø

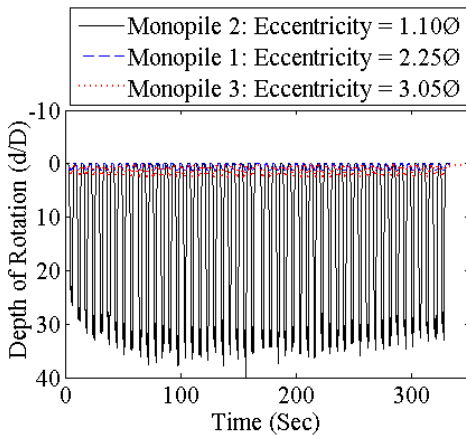


FIG. 8a. Depth of Rotation All Monopiles, Test 2, Displacement 2.5% Ø

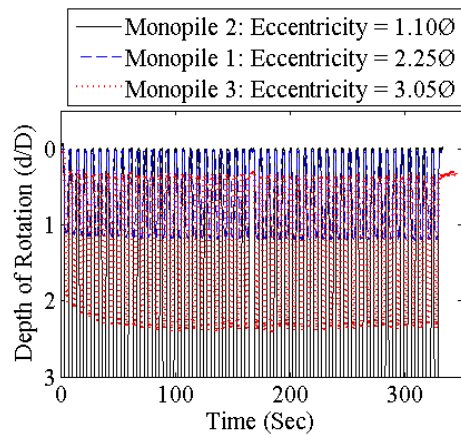


FIG. 8b. Depth of Rotation All Monopiles, Test 2, Displacement 2.5% Ø (Zoomed)

CONCLUSIONS

The initial results from these geotechnical centrifuge experiments provide some insights into the rotational behavior of squat monopiles in soft clay:

1. Monopiles with vertical gravity loads settle significantly under cyclic loading. This may be the result of combined vertical-horizontal-moment loading causing vertical plastic deformation
2. Moment resistance appears dependent on depth of rotation not, specifically, load eccentricity. Initial tilt could have a large impact on depth of rotation and therefore rotational resistance. The pile with the shallowest depth of rotation and highest resistance, had the most initial tilt and not the largest eccentricity.
3. Monopile tilt stabilizes quickly under displacement controlled loading
4. Monopiles appear to translate horizontally under displacement control loading

ACKNOWLEDGMENTS

The authors would like to acknowledge the assistance provided by the Center for Earthquake Engineering Simulations at Rensselaer Polytechnic Institute. This project was funded by National Science Foundation, Award Number: 1041604.

REFERENCES

- Andersen, K. H., and Lauritzsen, R. (1988). "Bearing capacity for foundations with cyclic loads." *J. of Geotech. Eng., ASCE*, 114(5), 540–555.
- Beemer, R. D. (2016). "Experimental studies of squat gravity caissons and piles for offshore applications." PhD Dissertation, Texas A&M University.
- Beemer, R. D., Aubeny, C. P., and Biscontin, G. (2016). "Centrifuge model 2D gravity relative to the rotational reference frame." In Preparation.
- Beemer, R. D., Murali, M., Biscontin, G., and Aubeny, C. P. (2015). "Theory on measuring orientation with MEMS accelerometers in a centrifuge." IFCEE, ASCE, San Antonio.
- Dejong, J. T., Yafrate, N., Degroot, D. J., Low, H. E., and Randolph, M. F. (2012). "Recommended practice for full-flow penetrometer testing and analysis." *Geotech. Test. J., ASTM International*, 33(2), 1-13.
- Elgamal, A., Dobry, R., and Van Laak, P. (1991). "Design, construction and operation of 100 g-ton centrifuge at RPI." *Centrifuge 91*, Boulder, CO, 27–34.
- Garnier, J., Gaudin, C., Springman, S. M., Culligan, P. J., Goodings, D. J., Konig, D., Kutter, B. L., Phillips, R., Randolph, M. F., and Thorel, L. (2007). "Catalogue of scaling laws and similitude questions in geotechnical centrifuge modelling." *Int. J. of Phys. Modell. in Geotech., ICE*, 7(3), 1-23.
- Grajales, F., Beemer, R. D., Murali, M., Aubeny, C. P., and Biscontin, G. (2015). "Response of short monopiles for offshore wind turbine foundations: virgin and post cyclic capacity." *GeoQuebec*, Canadian Geotechnical Society, Quebec City.
- Lau, B. H. (2015). "Cyclic behaviour of monopile foundations for offshore wind farms." PhD Diss., University of Cambridge.
- MEMSIC. (n.d.). CXL-GP series general purpose accelerometer. San Jose, CA.
- Murali, M. (2015). "Characterization of soft clay and the response of soil-foundation system for offshore applications." PhD Diss., Texas A&M University.
- Poulos, H. G., and Davis, E. H. (1991). *Elastic Solutions for Soil and Rock Mechanics*. Centre for Geotechnical Research, University of Sydney, Sydney.
- Randolph, M. F. (1981). "The response of flexible piles to lateral loading." *Geotechnique, ICE*, 31(2), 247–259.
- Silicon Design Inc. (2013). Model 2012. Kirkland, WA.
- Tessari, A. (2012). "Centrifuge modeling of the effects of natural hazards on pile-founded concrete floodwalls." PhD Diss., Rensselaer Polytechnique Institute.
- Ubilla, J., Abdoun, T., and Zimmie, T. (2006). "Application of in-flight robot in centrifuge modeling of laterally loaded stiff pile foundations." 6th ICPMG, Hong Kong, 259–264.
- Zhang, C., White, D., and Randolph, M. F. (2011). "Centrifuge modeling of the cyclic lateral response of a rigid pile in soft clay." *J. Geotech. and Geoenviron. Eng., ASCE*, 137(7), 717–729.

Shear Behavior of Methane Hydrate Bearing Sands during Gas Production

Masayuki Hyodo¹; Shintaro Kajiyama²; and Koji Nakashima²

¹Professor, Dept. of Civil and Environmental Engineering, Ube 755-8611, Japan.

²Post Graduate Student, Dept. of Civil and Environmental Engineering, Ube 755-8611, Japan.

Abstract: A series of mechanical tests were performed on methane hydrate bearing sediments with various host sands by using temperature controlled high stress triaxial shear testing apparatus. A high pressure and low temperature plane strain testing apparatus was also developed for visualizing the deformation of methane hydrate bearing sand due to methane hydrate production. Using this testing apparatus, plane strain compression and methane hydrate dissociation by depressurization tests were performed with the measurement of localized deformation.

INTRODUCTION

Methane hydrate (MH) is a solid compound in which a large amount of methane is trapped within a crystalline structure of water, forming a solid similar to ice. Recently there has been much research into MH in the deep seabed as a developable material. Worldwide, MH is believed to exist in various forms, such as massive structures within muddy layers or at the surface of deep seabeds, or embedded within the pores of sandy layers (Waite, et al. 2009). In Japan, an MH rich layer was found in the Nankai Trough and production tests was performed in March 2013 (Japan Oil, Gas and Metals National Corporation, 2013). MH in the deep sea bed can exist at certain water pressure and temperature conditions. It exists in the pore space of the sandy sediments, bonding their particles. The MH rich layer is located around 100m-300m from the seabed, in deep seas with depths of over 1000m. Currently, the method proposed for abstracting methane in the Nankai Trough is by drilling a rig into the MH-rich layer, and heating, depressurising, or inserting hydrate inhibitors, causing the MH to become dissociated into methane and water after which the gas could be collected (Yamamoto, 2009). Among them the depressurisation method is going to be introduced as the most suitable production method. Using these methods, the solid MH existing in the pores within the soil is transformed into gas for collection; in the process, complex physical events, such as changes in the soil structure and thermal conductivity, pore fluid and gas migration, and other complicated phenomena need to be considered. It is predicted that a combination of such phenomena could cause consolidation and shear deformation of the ground due to changes in the effective stress and decrease in soil particle strength. Therefore, it is important to investigate the mechanical properties of MH-bearing

sediments, for safe and economical exploitation. A series of mechanical tests were performed on MH bearing sediments with various host sands by the authors using temperature controlled high stress triaxial shear testing apparatus. A high pressure and low temperature plane strain testing apparatus was also developed for visualizing the deformation of methane hydrate bearing sand due to methane hydrate production. Using this testing apparatus, plane strain compression and methane hydrate dissociation by depressurization tests were performed with the measurement of localized deformation.

MATERIALS USED IN EXPERIMENTS

Grain size distribution curves for samples from Nankai Trough and the simulation materials prepared in this study are shown in FIG.1. The sediments in Nankai Trough's seabed soil constitute turbidite and show stratified layers with wide grain distribution curves, with contents ranging from sand to clay. The grain size distribution for the MH rich layer in Nankai Trough is shown in grey; it is mostly sand with fines content. In order to simulate the grain size distribution and minerals of this layer, silica sand, kaolin and mica were mixed and four kinds of simulated sands T_a , T_b , T_c , T_d were prepared as host sands. The fines content increases in order of T_b , T_a , T_c , T_d and the mean particle size decreases in order of T_a , T_b , T_c , T_d .

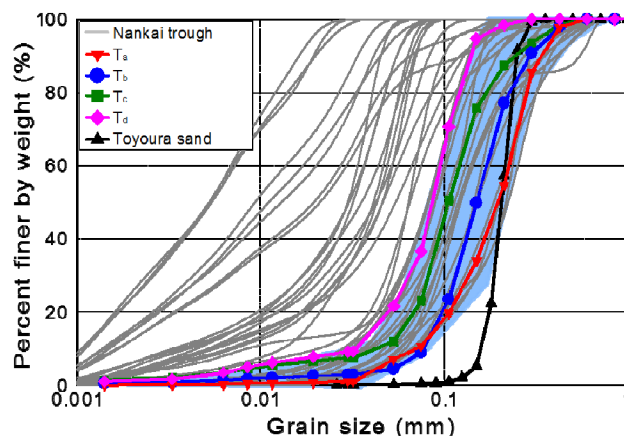


FIG.1. Grain size distribution curves (Nankai trough and artificial samples)

TEMPERATURE-CONTROLLED HIGH STRESS TRIAXIAL TESTS

The temperature-controlled high pressure triaxial testing apparatus was developed such that the back pressure and confining pressure could be controlled under various temperature and high pressure conditions in order to examine the mechanical behaviour of MH-bearing sand specimens under deep seabed stress and temperature conditions (Hyodo, et al., 2007, 2008, 2013). The maximum permissible load was 200kN. To remove the influence of piston friction, a cylindrical-shaped loading cell that was not affected by temperature and pressure was set up in the cell. The cell pressure could be increased up to 30MPa. To reproduce back pressure associated with this high pressure condition, a syringe pump was installed. By using incompressible solution in the cylinder, the measurement of volume change of the specimen was enabled by

calculating the amount of penetration of the piston in the cylinder. To measure the volume change of partially saturated soil during dissociation, an inner cell was installed, with a mechanism similar to the syringe pump for back pressure. Temperature was controlled by a system which circulated the cell fluid from a low temperature water tank set up outside allowing the temperature to be adjusted from -35°C to $+50^{\circ}\text{C}$.

Based on visual observation of the undisturbed core samples obtained from the Nankai Trough, it is believed that MH in-situ is buried within the pores between grains of the sand. Based on this, MH-bearing sand was artificially produced using the grain size distribution curve of the undisturbed core sample (Suzuki, 2009). First, the amount of water for the target MH saturation was mixed with sand whose volume corresponded to a target density. The moist soil was placed in 15 layers in a mould measuring 30 mm in diameter and 60 mm high, with each layer compacted by a tamper 40 times. In order for the specimen to stand by itself, the mould containing the sand was placed in a freezer. The frozen specimen was then removed from the mould and placed on the pedestal, and the membrane was installed. Because the specimens in the tests were subjected to low temperature and high pressure, rubber membranes conventionally used in triaxial tests were avoided; instead, silicon-type membranes were used because of their flexibility under low temperature/high pressure conditions and butyl rubber was used in long term tests, such as MH dissociation because silicone is to some degree permeable to methane gas.

For the simulation material, MH was formed in these host sands with 50%, 30% and 0% degree of MH saturation. From the results of density tests on natural cores from Nankai Trough, the porosities of the simulation materials were set as $n=40\%$ and 45% (Hyodo, et al. 2014). In this paper, only the results of $n=45\%$ are presented. After forming the specimen, it was subjected to a series of processes under specific temperatures and pressures. First of all, the frozen specimen was thawed to room temperature inside the triaxial cell. Then, the back pressure was gradually increased to 4MPa while methane was injected into the specimen by filling the pores of the specimen with methane. At this time, the gas pressure was increased over a period of time so that the specimen's moisture content would not become non-uniform as a result of the pressurized injection. Next, the temperature in the triaxial cell was lowered to 1°C where the MH was stable, and the specimen environment was kept under constant temperature and pressure conditions for 24hours. By keeping the gas pressure constant in the connection between the specimen and the syringe pump and by observing the amount of gas flowing at various times, the transformation of water within the pores into hydrate was judged to be complete if there was no marked change in the amount of gas, as indicated in the figure. After the hydrate was generated, water under constant pressure was allowed to infiltrate the specimen. Then, the pore water pressure was applied and the temperature was adjusted to the prescribed test condition. While keeping the pressure constant, consolidation was carried out until the specified effective stress was reached and shearing was conducted with a strain rate of $0.1\%/min$. After shearing, the temperature in the specimen was increased and MH dissociated; the amount of gas was measured using the gas mass flow meter. The amount of gas measured was then converted into MH saturation, (assuming the density of MH was 0.912 mg/m^3).

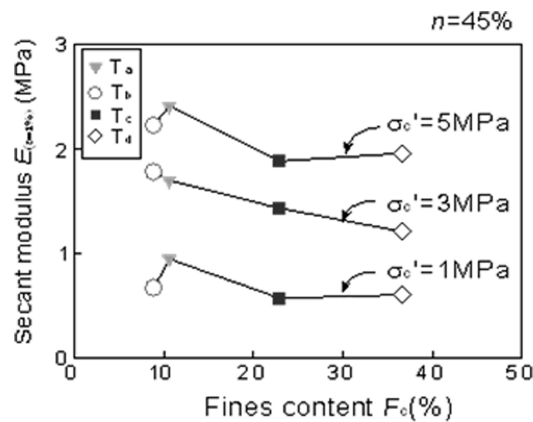


FIG. 2. Relationship between secant modulus and fines content.

FIG. 2 shows the variation of the secant modulus at 1% axial strain against fines content for each material with each confining stress. It can be seen that there is a trend for the secant modulus to decrease with increasing fines content at all confining stresses. However, this is not true for T_a and T_b , due to the effect of their mean particle size. FIG.3(a)-(c) show the shear testing results for MH bearing sands by using T_a , T_b and T_c as host sands. Tests were performed at a porosity of $n = 45\%$ with effective confining stress of 1MPa at various degrees of MH saturation. From the figures it can be observed that initial stiffness and peak residual strengths increased as the degree of MH saturation increased. Corresponding volumetric strain increases and behaves in a more dilative manner with increasing degrees of MH saturation. In FIG.4, the difference between the peak strength of MH bearing sand and the strengths of the host sands, at an axial strain corresponding to the peak value of MH bearing sand, are normalized by effective confining stress and then plotted against the degree of MH saturation. It can be observed that the strength increased rapidly when the degree of MH saturation passed 30%, and the rate of increase decreases in order of T_a , T_b and T_c . It is therefore obvious that the grain size distribution affects the cementation effect of MH.

SHEAR CHARACTERISTICS OF MH- BEARING SANDS BY HIGH-STRESS PLANE STRAIN SHEAR TESTING

An overview of the testing equipment (Yoneda, et al. 2011, 2013) is shown in FIG.5. This apparatus can control temperatures and pressures equivalent to an MH reservoir in deep seabed. Additionally, observation windows are installed in front of and behind the specimen in order to allow the local deformation of the specimen during shear tests to be measured. The specimen is a cuboid with 80mm width, 60mm thickness and 160mm height. A 5mm x 5mm mesh was drawn on the membrane in front of the observation window. The observation was performed using a digital camera(g), which took pictures according to a timer controlled by a remote system. An LED(h) was installed to brighten the pressure cell(i), which allowed the specimen(e) to be observed. Local deformation analysis was performed by observing the cross-points of the mesh during shear tests and using this data in PIV analysis. Thermocouples(k,l) were installed at 60mm and 30mm from the bottom of the specimen in order to measure the variation of

the temperature during the dissociation of MH. T_c and Toyoura sand were the materials used for comparison. Specimens were prepared with water contents equivalent to given

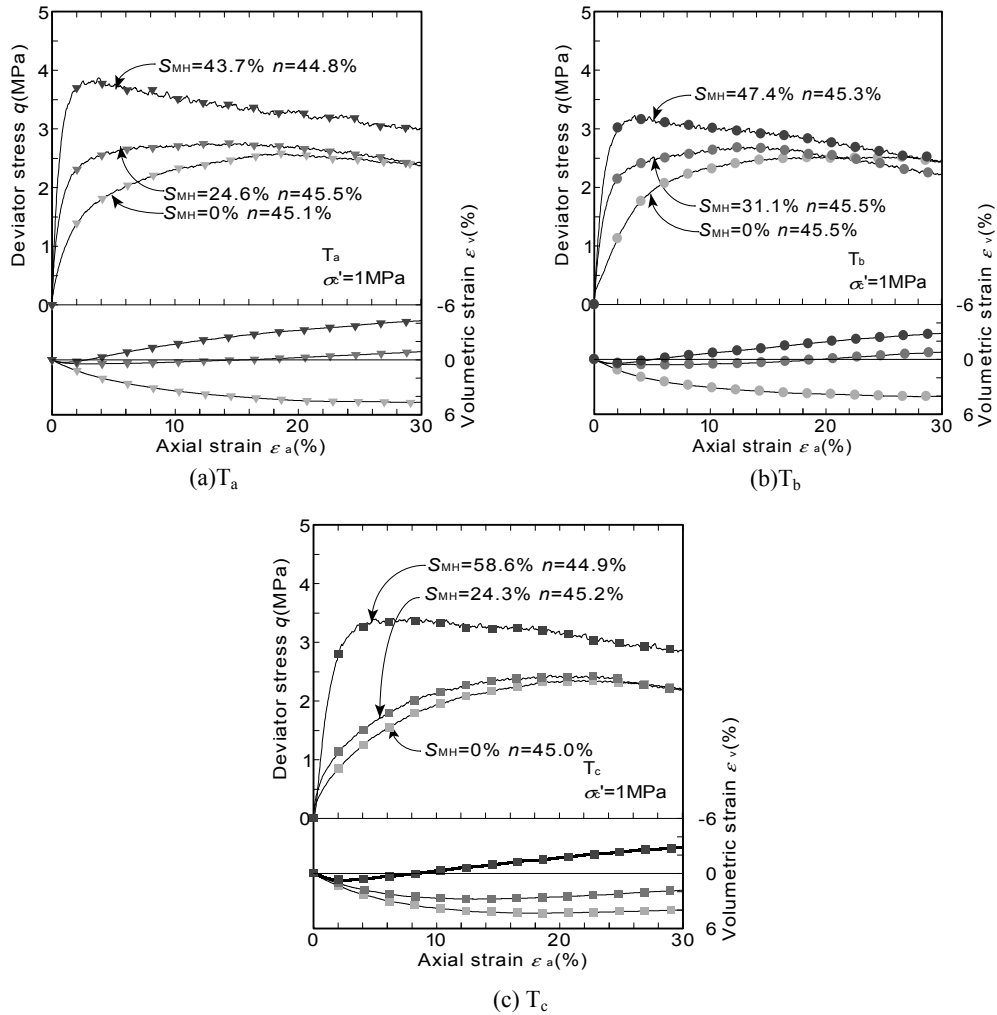


FIG. 3. Variation of deviator stress and volumetric strain against axial strain for methane hydrate bearing sands.

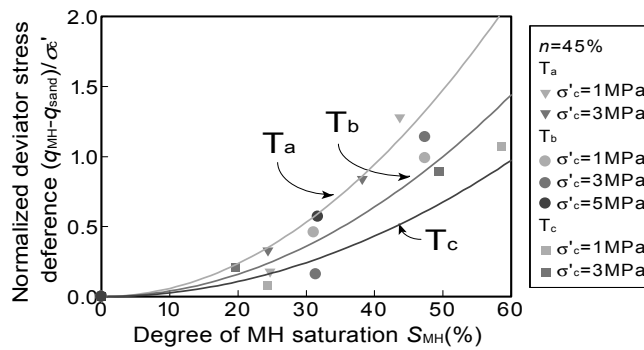


FIG. 4. Variation of normalized deviator stress difference against degree of MH saturation for T_a , T_b , T_c .

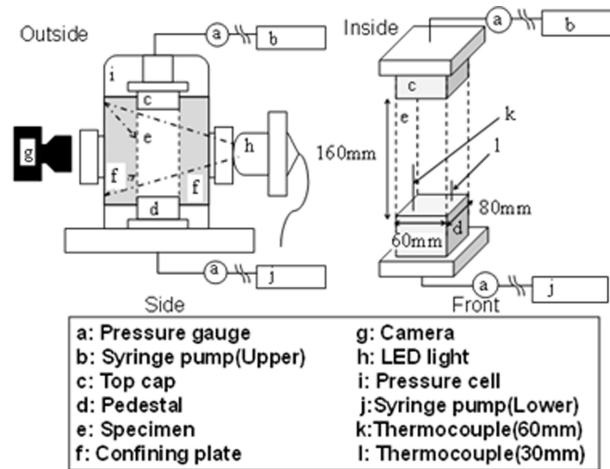


FIG. 5. Schematic overview of the high pressure plane strain testing apparatus.

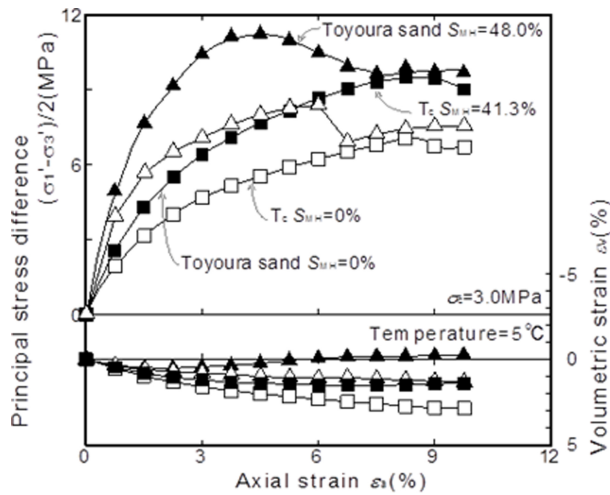


FIG. 6. Variation of principal stress difference and volumetric strain against axial strain for methane hydrate bearing sands.

degrees of MH saturation and tamped in 12 layers to give a porosity of $n = 45\%$. Formation of MH was performed using the same method as in the triaxial compression tests. The specimens were saturated by filling the pore water and consolidated at given effective confining stress and then subjected to shear tests under drained conditions. The speed of shear was $0.1\%/min$. Also, in order to understand the behavior during MH production, MH was dissociated by decreasing pore water pressure by $7MPa$ under constant cell pressure and observing the behavior. After finishing MH dissociation, the pore water pressure again rises and the behavior was also investigated. The rate of depressurization during dissociation of MH and re-pressurization was $0.5MPa/min$.

FIG.6 shows the shear test results for Tc and Toyoura sand with and without MH. A marked increase in the strength and stiffness due to the cementation of MH are observed in both specimens. The increments of strength and initial stiffness for Tc are lower than those of Toyoura sand. The corresponding volumetric strain exhibits a dilative manner for MH bearing Toyoura sand, whilst that of Tc shows a contractive manner during shear. FIG.7 shows the results of the PIV analysis during shear for the

specimens. The upper part of the figure shows volumetric strain and the bottom part shows shear strain contour for specimens at 10% axial strain. On the left hand side there is Tc without MH, then Tc with MH and then Toyoura sand without and with MH. Clearer shear bands can be observed in Toyoura sand than in Tc, so the effect of fines on local deformation can be observed in this figure. The shear band for Toyoura sand with MH is clearer than that of Toyoura sand without MH, but there are no clear differences observed between Tc with and without MH.

Next, in order to simulate the production of MH, pore water pressure was decreased whilst keeping constant initial shear stress, MH was dissociated and the deformation behavior of loss of cementation was investigated. Specimens which had cell pressure 10MPa, pore water pressure 7MPa and consolidated at effective stress 3MPa had their pore water pressure decreased by 7MPa. Stress and temperature conditions were set outside of the MH stability state line and MH was dissociated. FIG.8 and FIG.9 show effective stress paths applied to the experiments. In these figures, only the results for Toyoura sand are shown. Failure envelopes for Toyoura sand with and without MH are shown by broken and solid line, respectively. The dissociation tests were performed in two cases. In Case 1, after the specimens were isotropically consolidated, depressurization was conducted at a rate of 0.5MPa/min. Then, re-pressurization was performed at the same speed after finishing MH dissociation. These pore water pressure histories correspond to real production of MH in recovering pore water pressure after production. In Case 2, after specimens were isotropically consolidated, initial shear stress was applied at an amount greater than the host sand but less than MH bearing sand. Depressurization is then conducted in the same way as Case 1 and at the same speed. After finishing MH dissociation, pore water pressure was increased at the same rate. This test was done to simulate the element in the vicinity of the production well, where the stress condition is close to failure. In FIG.9, the specimen failed during re-pressurization when the stress path reached the failure line of the host sand. In FIG.10, the relationship between the temperature and pore water pressure during the

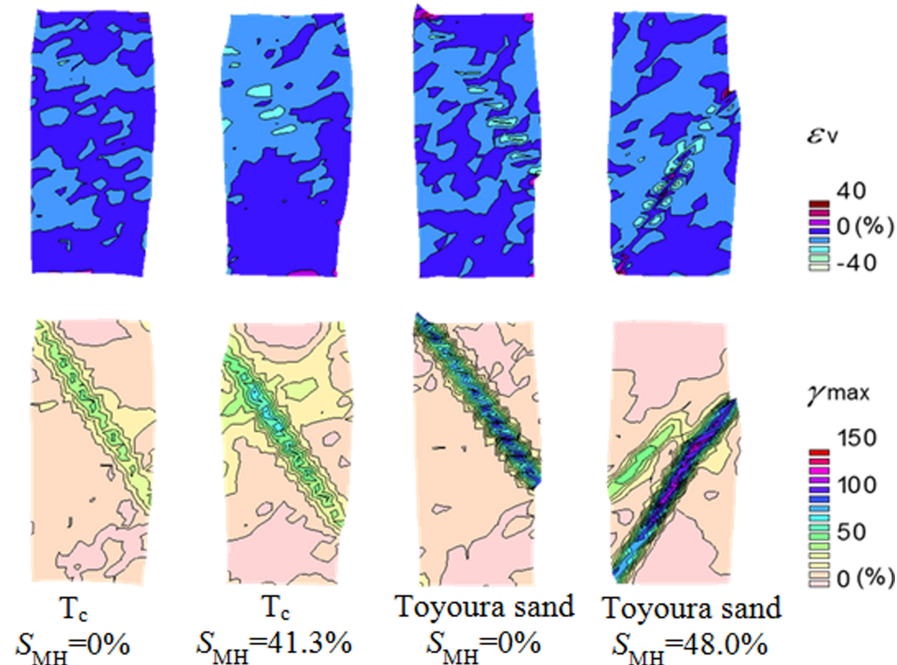


FIG. 7. Volumetric strain and maximum shearing strain contours at axial strain $\epsilon_a = 10\%$ by PIV analysis.

depressurization process is shown. As can be seen, temperature decreased suddenly when the pore pressure was decreased to the value of the state boundary curve. This is due to the temperature absorption phenomena of MH during dissociation. Also, at a pressure of 3MPa dissociation and reformation repeats, and when dissociation is complete the temperature of the specimen rises to room temperature. FIG.11 shows the relationship between the effective stress ratio and active strain during dissociation tests of MH for Case 2. Point (a) corresponds to the point before dissociation, where initial shear stress has been applied. Point (b) corresponds to the point where pore water pressure was decreased from 10MPa to 3MPa. Point (c) corresponds to the point where MH is dissociated. Point (d) corresponds to the point where the specimen failed due to an increase in pore water pressure (re-pressurization).

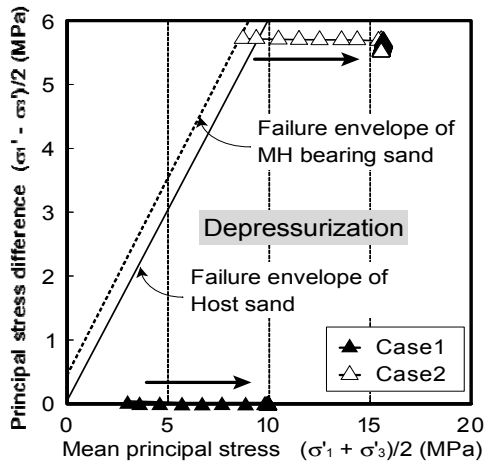


FIG. 8. Stress path in depressurization test.

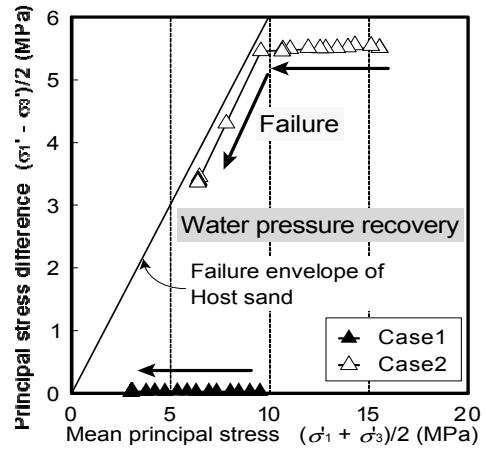


FIG. 9. Stress path in repressurization test.

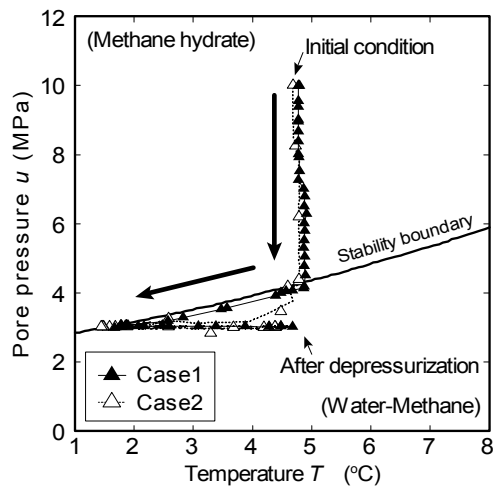


FIG. 10. Temperature and pore pressure path in depressurization test.

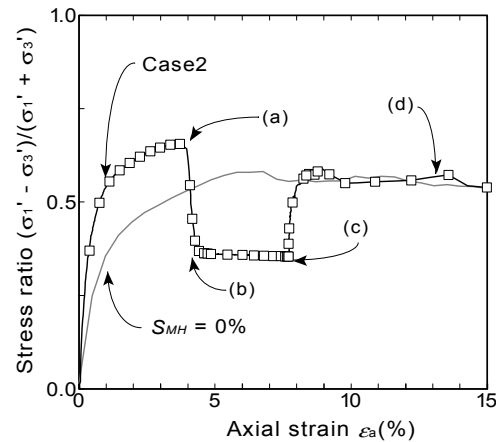


FIG. 11. Relationship between stress ratio and axial strain (Case2).

CONCLUSIONS

The research was done in order to understand the fundamental mechanical and dissociation properties on MH bearing sands. The following conclusions were drawn:

- (1) The strength increased rapidly when the degree of MH saturation passed 30%, and the rate of increase decreases in order of Ta, Tb and Tc. It is therefore obvious that the grain size distribution affects the cementation effect of MH.
- (2) In Triaxial shear tests on host sands, initial stiffness and strength decreased with increasing fines content and there was a strong trend for contraction of volumetric strain.
- (3) For all specimens, the initial stiffness and peak strength of those containing MH increased due to MH's cementation force, and volumetric strain behaved in a more dilative manner. However, both initial stiffness and strength decreased with increasing fines content of host sands.
- (4) In plane strain shear tests, Tc and Toyoura sand as host sands with and without MH were compared. Due to the existence of MH, initial stiffness and strength increased in both materials, however the tendency was more apparent in Toyoura sand compared with Tc.
- (5) The local deformations occurred more clearly in Toyoura sand, compared with fine material. It also appeared more clearly when the specimen contained MH.
- (6) During depressurization, marked deformation was not observed, because of an increase of effective stress. However, after depressurization, repressurization caused the specimen to fail in the case of high initial shear stress conditions.

ACKNOWLEDGMENTS

The present work was done as the activity of Research Consortium for Methane Hydrate Resources in Japan (MH21 Research Consortium) by the Ministry of Economy and Industry and the part of the work was supported by KAKENHI 25249065 by the Ministry of Education and Science in Japan. The authors would like to express their sincere thanks to their supports.

REFERENCES

- Hyodo, M., Nakata, Y., Yoshimoto, N. and Yoneda, J. (2007). Mechanical behavior of methane hydrate-supported sand, *Proc. of Int. Symp. on Geotechnical Engineering, Ground Improvement and Geosynthetics for Human security and Environmental Preservation*, pp.195-208.
- Hyodo, M., Nakata, Y., Yoshimoto, N. and Yoneda, J. (2008). Shear strength of methane hydrate bearing sand and its deformation during dissociation of methane hydrate, *Proc. of 4th Int.Symp. on Deformation Characteristics of Geomaterials*, pp.549-556.
- Hyodo, M., Yoneda, J., Yoshimoto, N., Nakata, Y. (2013):Mechanical and dissociation properties of methane hydrate-bearing sand in deep seabed, *Soils and Foundations*, 53(2), 299-314, <http://dx.doi.org/10.1016/j.sandf.2013.02.010> .
- Hyodo, M., Kajiyama S., Yoshimoto, N., Nakata, Y.(2014):Triaxial behaviour of methane hydrate bearing sand , *Proceedings of 10th Int. ISOPE Ocean Mining & Gas Hydrate Symposium OMS-2013*, Szczecin, Poland, 126-134.
- Japan Oil, Gas and Metals National Corporation (2013). Gas Production from Methane Hydrate Layers Confirmed. *News Release*, 12.03.13, pp. 1e3. <https://www.jogmec.go.jp/english/news/release/release0110.html>.
- Suzuki, K., Ebinuma, T., Narita, H. (2009). Features of methane hydrate- bearing sandy-sediments of the forearc basin along the Nankai trough: effect on methane hydrate-accumulating mechanism in turbidite. *Journal of Geography* 118 (5), 899–912 (in Japanese).
- Waite, W. F., Santamarina, J. C., Cortes, D. D., Dugan, B. Espinoza, D. N., Germaine, J., Jang, J., Jung, J. W., Kneafsey, T. J., Shin, H., Soga, K., Winters, W. J., and Yun, T.-S. (2009). Physical properties of hydrate-bearing sediments, *Reviews of Geophysics*, 47, RG4003.
- Yamamoto, K. (2009). Production techniques for methane hydrate resources and field test programs. *Journal of Geography*, Vol.118, No. 5, 913-934. Japan
- Yoneda, J. and Nakata, Y. (2011). Deformation of deep seabed during dissociation of methane hydrate. *Proc. The 14th Asian Regional Conference on Soil Mechanics and Geotechnical Engineering*. ISSMGE. Paper ID290. China.
- Yoneda, J., Hyodo, M., Nakata, Y., Yoshimoto, Orense, R. (2011). Deformation of seabed due to exploitation of methane hydrate reservoir, *Frontiers in Offshore Geotechnics II*, pp. 245-250, doi: 10.1201/b10132-18.
- Yoneda, J., Hyodo, M., Yoshimoto, N., Nakata, N., Kato, A. (2013a): Development of high-pressure low-temperature plane strain testing apparatus for methane hydrate-bearing sand, *Soils and Foundations*, 53(5), 774-783, <http://dx.doi.org/10.1016/j.sandf.2013.08.014>.

Suction Caissons in Soft Clay for Tidal Current Turbine Applications

Jeff F. Wallace, A.M.ASCE¹; and Cassandra J. Rutherford, Ph.D., A.M.ASCE²

¹Graduate Research Assistant, Dept. of Civil and Environmental Engineering, Univ. of Illinois at Urbana-Champaign, 205 North Mathews Ave., Urbana, IL 61801.

²Assistant Professor, Dept. of Civil and Environmental Engineering, Univ. of Illinois at Urbana-Champaign, 205 North Mathews Ave., Urbana, IL 61801.

Abstract: The exploration into the use of offshore renewable energy resources has been driven by increases in oil and gas prices and the drive to reduce oil dependence. One such offshore renewable energy resource is the tidal current captured through the use of a tidal current turbine. As the tidal current turbine is still in the development and prototyping phase, optimizing the entire system's efficiency and reliability (including the foundation) is key to its successful implementation. Harnessing the tidal current requires turbine blades to interact with the flow of water, unlike the vast majority of offshore energy structures that attempt to minimize this interaction. Standard operating loads on the foundations of tidal current turbines are a result of the rotating turbine blades, fluctuations in tidal current speed and direction, wave loading, turbulence, and vibrations. Suction caisson foundations provide a viable foundation option for tidal current turbines in soft marine clays as they are "green" in that they can be removed at the end of their design life and are able to provide both compressive and uplift resistance in response to the significant horizontal loading when in the tetrapod configuration. The behavior of suction caissons in soft clay in the tetrapod configuration with an aspect ratio of 1 is investigated under monotonic and cyclic vertical loading applicable to tidal current turbine design.

INTRODUCTION

Tidal energy converters (TEC) are mechanical systems that convert the kinetic energy from tidal currents into electric energy. This study will assume that the TEC is configured as a horizontal axis turbine where the rotor axis is oriented parallel to the seabed similar to an offshore wind turbine. As of May 2015, 56% of the TECs in development have been given this classification by the European Marine Energy Centre (2015). While Starling and Scott (2009) and EMEC (2015) have suggested multiple methods of fixing a TEC to the seabed, there are currently no engineering standards or codes for TEC foundation design. This is primarily due to TEC technology being primarily in the development and prototyping phase.

A TEC is designed to interact with horizontal environmental loads unlike oil and natural gas structures that attempt to minimize this interaction resulting in a significant component of the overall loading being oriented laterally. The suction caisson foundation resembles an overturned bucket and is installed based on a combination of self-weight embedment and negative pressures generated through suction applied by a pump. This installation method does not require the mobilization of pile driving equipment or large cranes and promotes the “green” nature of the foundation by allowing removal at the end of the design life by reversing the suction process. By having a sealed top cap after installation, the suction caisson provides greater uplift resistance compared to shallow foundations with the same embedment to diameter ratio. When configured in the tetrapod configuration, the foundations provide resistance to the lateral loading through a compression/uplift mechanism on opposing foundations that will alternate depending on current direction (which can change by approximately 180° due to the ebb/flood of tides).

While the size of a suction caisson foundation for a horizontal axis turbine TEC will be dependent on site specific loads and soil conditions, a previous study by Maynard et al. (2013) has indicated suction caisson diameters of 3.5 m for a tetrapod supported TEC to be founded in very soft to soft marine clay. Due to the high cost of testing full-scale suction caissons, a series of experiments conducted on 1-g model scale foundations are typically used to predict the behavior of full size foundations. Initial small scale 1-g model tests are being conducted prior to centrifuge testing to provide insight into failure mechanisms and foundation behavior in response to cyclic loading. Kelly et al. (2006) has shown that the use of proper nondimensional units to interpret laboratory model scale tests allow for their comparison to field scale tests. The load response of suction installed foundations and anchors in clay have been investigated at the 1-g model scale for various energy applications (Steesen-Bach 1992, Rao et al. 1997, El-Gharbawy and Olson 1998, Luke et al. 2005, Coffman et al. 2006, Kelly et al. 2006, Villalobos et al. 2010, Wang et al. 2012, Li and Wang 2013, Chen et al. 2015, among others) however, these studies have not focused on suction caisson foundations used in a tetrapod configuration for tidal current turbine applications. Decreasing the cost of the foundation system can be an important part of making tidal power a viable source of energy. However, it will require a better understanding of the soil-foundation response to the possible loading conditions and tools to model the influence of the soil and foundation on the whole system. While the focus of the tests will be for TEC applications, it is important to note that the results can also be applied to other offshore energy applications with multiple foundation configurations.

EXPERIMENTAL SET-UP

Foundation Models

The suction caisson foundation model was fabricated from 6061-T6 Aluminum at a scale of 1:25. The diameter of the suction caisson was 152 mm and the skirt length was 152 mm resulting in an aspect ratio, $AR = L/D$, of 1. The wall thickness to diameter ratio was 48. The model was loaded via a rod attached to the center of the top

plate. Horizontally and vertically oriented load cells were positioned along the rod to measure the respectively oriented loads. A locking ball and socket joint was located between the suction caisson and the locking collar that attaches the rod to the loading apparatus. The top cap contained a threaded opening for venting during installation that could be closed during loading and a second opening that allowed for the installation of a miniature pore water pressure sensor.

Testbed Preparation

The clay used for the testbeds was Edgar Plastic Kaolin (or EPK Clay) manufactured by Edgar Minerals, Inc. The reported composition by weight was 98% Kaolinite and 2% Crystalline Silica. Geotechnical properties of the kaolin are given in Table 1. Each model suction caisson test was conducted in its own testbed prepared and consolidated in the same manner as follows. The kaolin slurry was prepared at a water content 1.7 times the liquid limit using a saltwater pore fluid with a NaCl concentration of 35 g/L. The slurry was then allowed to hydrate for a minimum of 7 days in sealed containers placed in a humidity chamber and was regularly agitated to minimize sedimentation. After the hydration period, the slurry was poured into a cylindrical PVC container with a diameter of 600 mm to a height of 610 mm and allowed to consolidate via surcharge with doubly drained conditions provided by geotextiles, sand layers, and drainage valves. The effective vertical stress at the mid depth of the test bed was 4.5 kPa. The surcharge including drainage layers and surficial water was removed from the top of the testbed after 57 days (end of primary consolidation) resulting in a kaolin testbed with a final thickness of approximately 495 mm with a linearly increasing undrained shear strength profile as measured by the laboratory vane shear as shown in Figure 1. Geotechnical properties of a typical testbed consolidated in this manner are shown in Table 1 and Figure 1 while deformation versus the square root of time plots are shown in Figure 2.

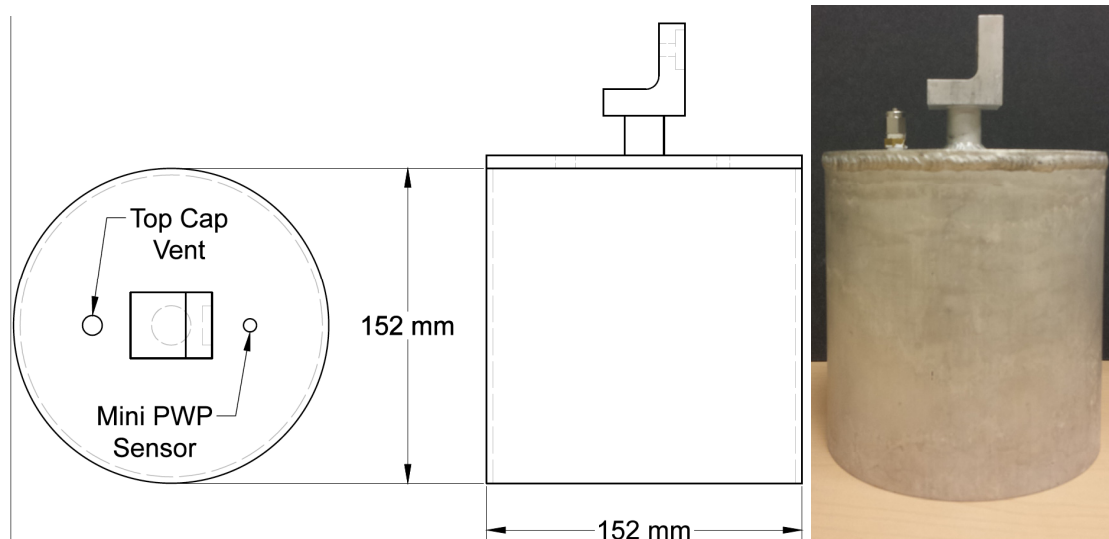


FIG. 1. Schematic and image of the suction caisson model foundation shown up to the perpendicular connection for the horizontal load cell.

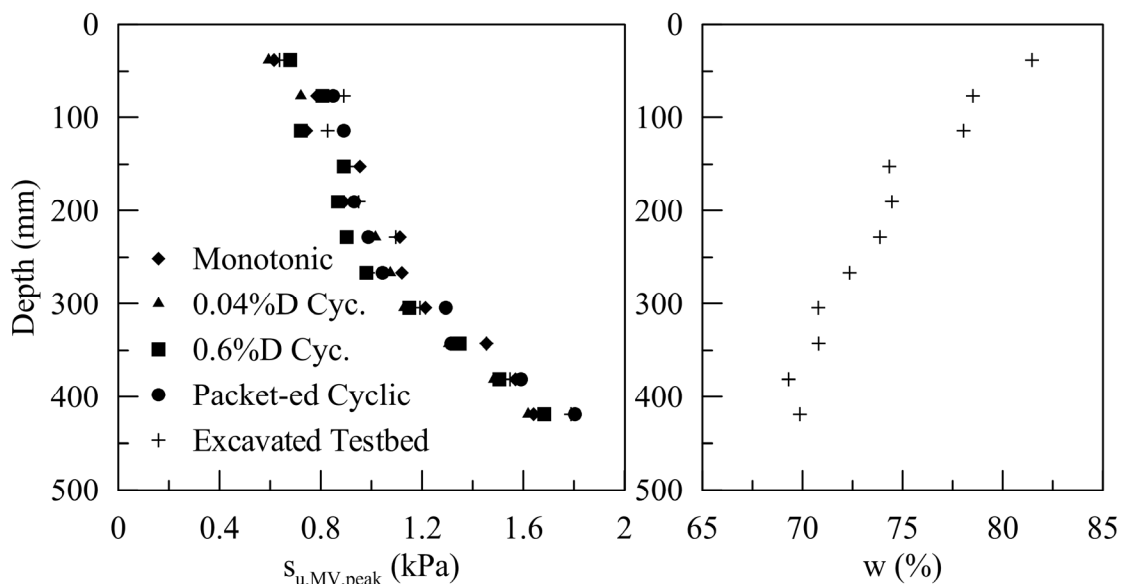


FIG. 2. Undrained shear strength as measured by the miniature vane shear for the four kaolin testbeds utilized in testing and an additional testbed from which water contents were determined with depth.

TABLE 1. EPK Clay and Testbed Properties

<i>Parameter</i>	<i>Value</i>	<i>Parameter</i>	<i>Value</i>
Composition ^a - Kaolinite (%)	98	Compression Index, C _c	0.59
Composition ^a - Crystalline Silica (%)	2	Swelling Index, C _s	0.022
Specific Gravity, G _s	2.64	C _a /C _c	0.016
Liquid Limit, LL (%)	58	Permeability Change Index, C _k	0.99
Plasticity Index, PI (%)	27	Coeff. of Consol. c _v (m ² /yr)	0.92
% < 2μ	68	Void Ratio ^b , e	1.94
Activity, A	0.4	Permeability ^b , (m/s)	2.91*10 ⁻⁹
avg. s _u at surface (kPa)	0.439	Sat. unit weight ^b , γ _{sat} (kN/m ³)	15.3
avg. s _u increase with depth (kPa/m)	2.89		

^aSpecified by the manufacturer

^bAt the mid height of the testbed

Loading Apparatus

The loading apparatus allowed for two-axis (vertical and horizontal) motion of the model foundation in the testbed. This was accomplished through the use of two screw driven linear slides each with a 305 mm range. A 90° mounting bracket was used to attach the vertical slide to the horizontal slide which was in turn attached to a loading frame that was fixed to the platform carrying the testbed containers. Two integrated programmable servo motors were attached to the linear slides and controlled the displacements applied to the model foundation. The loading frame also held the data acquisition hardware which transferred information from the available sensors to a desktop computer for processing.

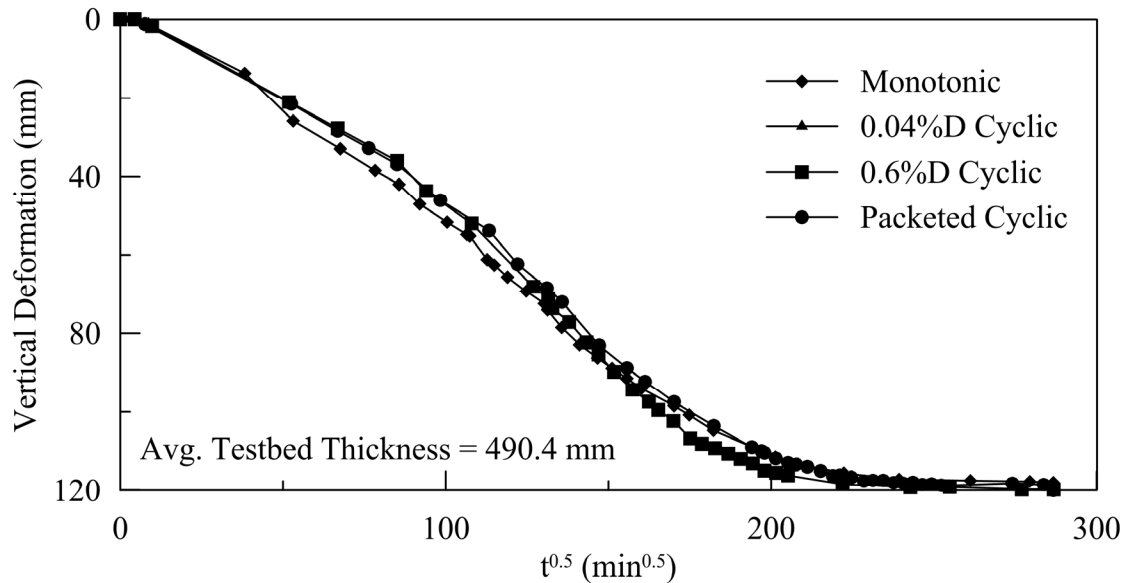


FIG. 3. Vertical deformation versus the square root of time for the four testbeds utilized in testing.

Testing Program

The suction caisson models were installed by jacking at a constant velocity of 0.075 mm/s with the top cap vent open. The installation was terminated when a marked increase was observed in the vertical load cell reading indicating that the bottom of the top cap had made contact with the testbed. A period of 20 minutes was included between the installation and the first loading phase to allow for positioning of the linear displacement transducers, closing of the top cap vent, and reconfiguration of the servo motors.

For the monotonic test, the suction caisson model was first loaded in compression at a constant velocity of 0.025 mm/s with the top cap vent closed. The compression phase was stopped after a displacement of approximately 14% of the diameter. After the compression loading phase, the direction of the linear slides was reversed to load the suction caissons in uplift. The uplift was conducted in two phases, the first was performed at the same constant velocity of 0.025 mm/s as the compression loading phase until the suction caisson was at the location at the end of installation. The second was performed at a constant velocity of 0.15 mm/s. Both uplift loading phases were conducted with the top cap vent closed.

Three displacement controlled cyclic tests were conducted on the suction caisson model. While foundations in the field are typically subjected to load controlled cycles, displacement control was utilized to allow for future non-dimensional comparison with model tests to be conducted on displacement controlled centrifuge equipment. For the first and second cyclic tests, the foundation was oscillated vertically in a sinusoidal pattern with amplitudes of 0.04% and 0.6% of the diameter respectively over the course of 24 hours (approximately 17280 cycles) with a period of 5 seconds

and a constant mean displacement. The third cyclic test was conducted in 100 cycle packets with increasing amplitudes. The amplitudes of the sinusoidal displacements were 0.005%, 0.01%, 0.05%, 0.25%, 1.25%, and 3.5% of the diameter while the period was 5 seconds. A wait time of 20 minutes was included between each pack of cycles. For all cycles, the mean reference elevation of the cycle was the elevation of the soil to top cap interface at the end of installation. A period of 5 seconds corresponds to the average wave period at multiple locations across the USA (NOAA 2015) where tidal “hot spots” have been identified by the Georgia Tech Research Corporation (2011) and also falls near or within the range of blade rotation rates of prototype tidal current turbines (Cornelius and Smith 2009, Verdant Power 2010, Andritz Hydro Hammerfest 2012, Marine Current Turbines 2013). After the cyclic loading phases, the 0.6%D 24 hour test and packeted cyclic test were followed by a monotonic compression and uplift phase to removal with the top cap vent closed at a velocity of 0.025 mm/s while the 0.04%D 24 hour test was followed only by an uplift phase.

EXPERIMENTAL RESULTS

The vertical load versus penetration depth curves of the four tests are shown in Figure 3. The penetration depth is measured from the tip of the suction caisson walls to the original soil surface. Due to the displacement of the clay by the walls into the cavity of the model suction caisson, the penetration depth at the end of installation will be slightly lower than the skirt length of 152 mm. Installation of the model suction caissons required the application of 31, 28, 30, and 27 N for the monotonic test, 0.04%D 24 hour cyclic test, 0.6%D 24 hour cyclic test, and the packeted cyclic test respectively. The installation process for all tests resulted in a shallow gap approximately 2 mm at the soil surface and no more than 5 mm deep around the top of the caisson due to the finite thickness of the model caisson walls.

The load displacement curve of the monotonic test as shown in Figure 3a exhibited strain softening behavior in compression with a peak load of 229 N occurring after a displacement of 2.1% of the diameter. At a displacement of 14% of the diameter, the load had leveled off at 179 N. When the suction caisson model was loaded in uplift, the load showed a less stiff response than in compression with a peak load of -151 N occurring after an upward displacement of 15% of the diameter. After this point, the load decreased with increasing upward displacement with a drastic decrease occurring when the plug of clay in the suction caisson model detached from the remainder of the clay testbed. During the compressive phase of loading, the testbed surface did not show marked deformation. During the uplift phase, a scarp developed in the soil surface around the suction caisson akin to a reverse bearing capacity failure.

The vertical load vs. depth of the 0.04%D 24 hour cyclic test (approximately 17280 cycles) is shown in Figure 3b while the cyclic loading vs. time is shown in Figure 4a. Upon cycling, peak loads of 99 N (compression) and -77 N (uplift) were observed during the first cycle. The mean load of the cyclic loading began in the compression range and as cycling continued the mean load shifted to the uplift range after

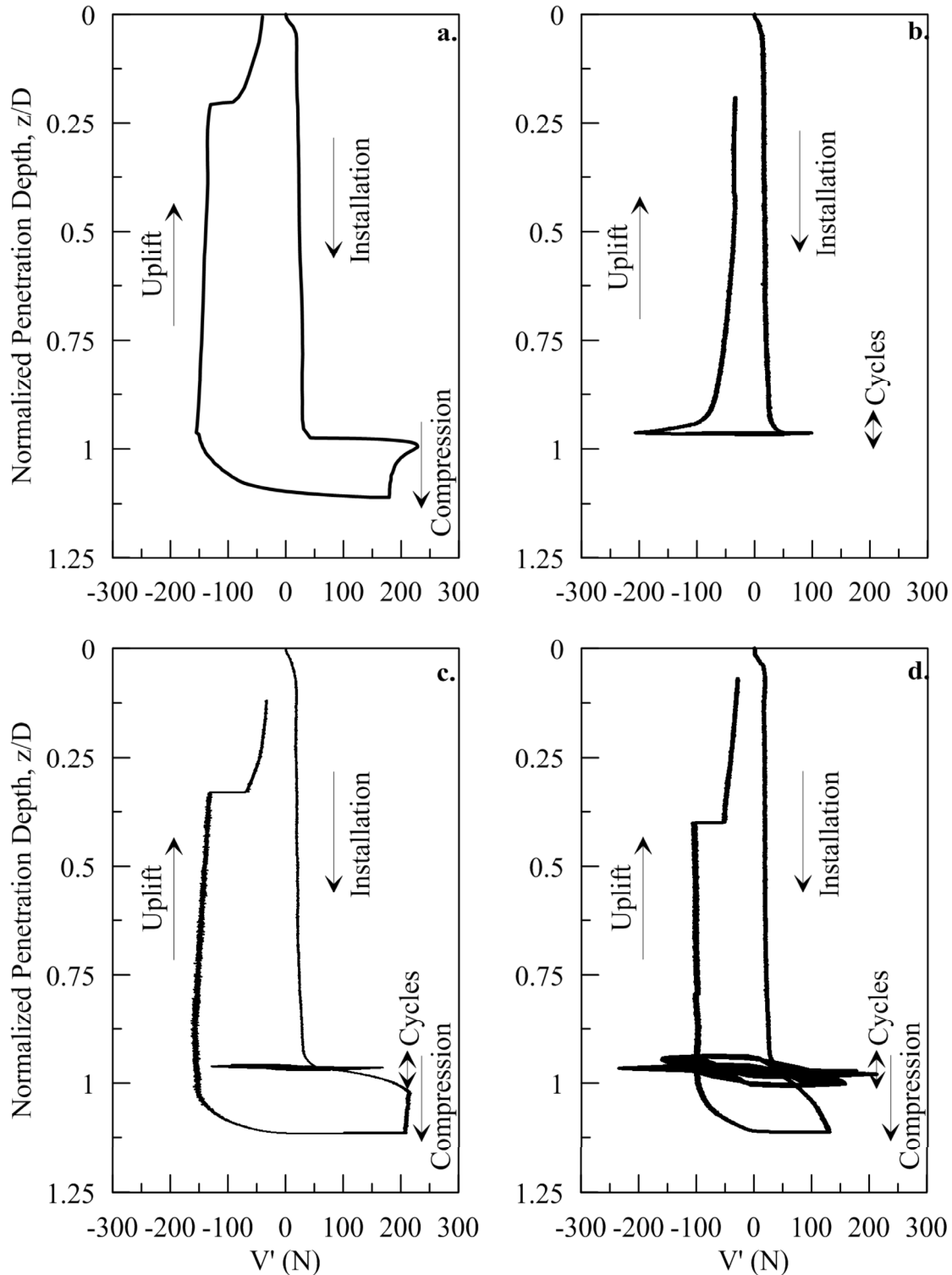


FIG. 4. Vertical load vs. top cap position for the following tests (a.) monotonic, (b.) 0.04%D 24 hour cyclic, (c.) 0.6%D 24 hour cyclic, and (d.) packeted cyclic. Penetration depth measured as the distance between the skirt tips and the original soil surface.

approximately 170 cycles. While the mean load deviated towards a higher uplift load during the first 1950 cycles the cyclic load amplitude had little variation with maximum compression and tension loads of 55 N and -118 N respectively. After 1950 cycles, the maximum compression load of each individual cycle fluctuated between 49 N and 61 N while the maximum uplift load of each individual cycle fluctuated between -110 N and -129 N. The maximum compression and uplift load of the final cycle were 49N and -110 N respectively. The post-cycling vertical monotonic uplift loading resulted in a peak load of -207 N after a displacement of 3.0% of the diameter. Unlike the other three tests, the uplift load decreased dramatically after the peak load was observed indicating that the plug had detached and only the adhesion along the model suction caisson wall was providing the resistance. A scarp did not develop during the uplift loading due to the early detachment of the plug.

The vertical load vs. depth of the 0.6%D 24 hour cyclic test (approximately 17280 cycles) is shown in Figure 3c while the cyclic loading vs. time is shown in Figure 4b. Upon cycling, maximum compression and uplift loads of 169 N and -129 N were observed during the first cycle. The mean load of the cyclic loading began in the compression range and as cycling continued the mean load shifted to the uplift range after approximately 950 cycles. The maximum compression and uplift load of each cycle decreased with the increasing number of cycles to 63 N and -67 N respectively after approximately 2000 cycles. After this point the maximum compression and uplift loads began to increase slightly to 80 N and -91 N respectively at the end of cyclic loading. The post-cycling vertical monotonic compression loading resulted in a peak load of 218 N after a displacement of 5.7% of the diameter. The load vs. displacement curve did not show the same pronounced strain softening behavior of the monotonic vertical test and was stopped at a displacement of 19% of the diameter at a load of 207 N. The peak load during the post-cycling vertical monotonic uplift loading of -159 N was mobilized after a displacement of 22% of the diameter.. The uplift load decreased until the plug detached where a drastic drop in the vertical load was observed. During cycling, the kaolin in contact with the caisson adhered to the surface of the caisson and displaced along with the caisson and filled the gap left after installation. A reverse bearing capacity wedge formed over the course of the cycling. During the post cyclic monotonic loading phases, this wedge moved upwards during compression and downwards during uplift.

The vertical load vs. depth of the packeted cyclic test is shown in Figure 3d while the cyclic loading vs. time is shown in Figure 4c. The amplitudes of the sinusoidal displacement of the 100 cycle packets were 0.005%, 0.01%, 0.05%, 0.25%, 1.25%, and 3.5% of the diameter. The 0.005% and 0.01% packet exhibited shifts in the mean cyclic load with insignificant changes in cyclic load amplitude. In the 0.05% packet, the peak loads on the compressive phase of the sinusoid cycles showed slight degradation while the peak loads on the uplift phase remained relatively constant. The 0.25%, 1.25%, and 3.5% packets all showed significant peak load degradation on the compressive phase of the sinusoid cycles. The 1.25% and 3.5% packets also showed significant peak load degradation on the uplift phase of the sinusoid cycles, however, this degradation was not as prominent in the 0.25% packet. The mean load of the

cycles shifted towards the uplift phase with increasing number of cycles. The post-cycling vertical monotonic compression loading resulted in a peak load of 131 N after a displacement of 14% of the diameter that coincides with where the compression was terminated and transitioned to uplift. The peak load during the post-cycling vertical monotonic uplift loading of -101 N was mobilized after a displacement of 28% of the diameter and remained constant until the plug detached where a drastic drop in the vertical load was observed. After the start of the 1.25% packet, the kaolin in contact with the caisson began to adhere to the surface of the caisson and displaced along with the caisson and filled the gap left after installation. By the 1.25% packet, a circular crack in the soil surface formed around the model suction caisson in the form of a (reverse) bearing capacity failure. During the post cyclic monotonic loading phases, slight upward deformations were observed along the crack during compression and the crack developed into a scarp during uplift.

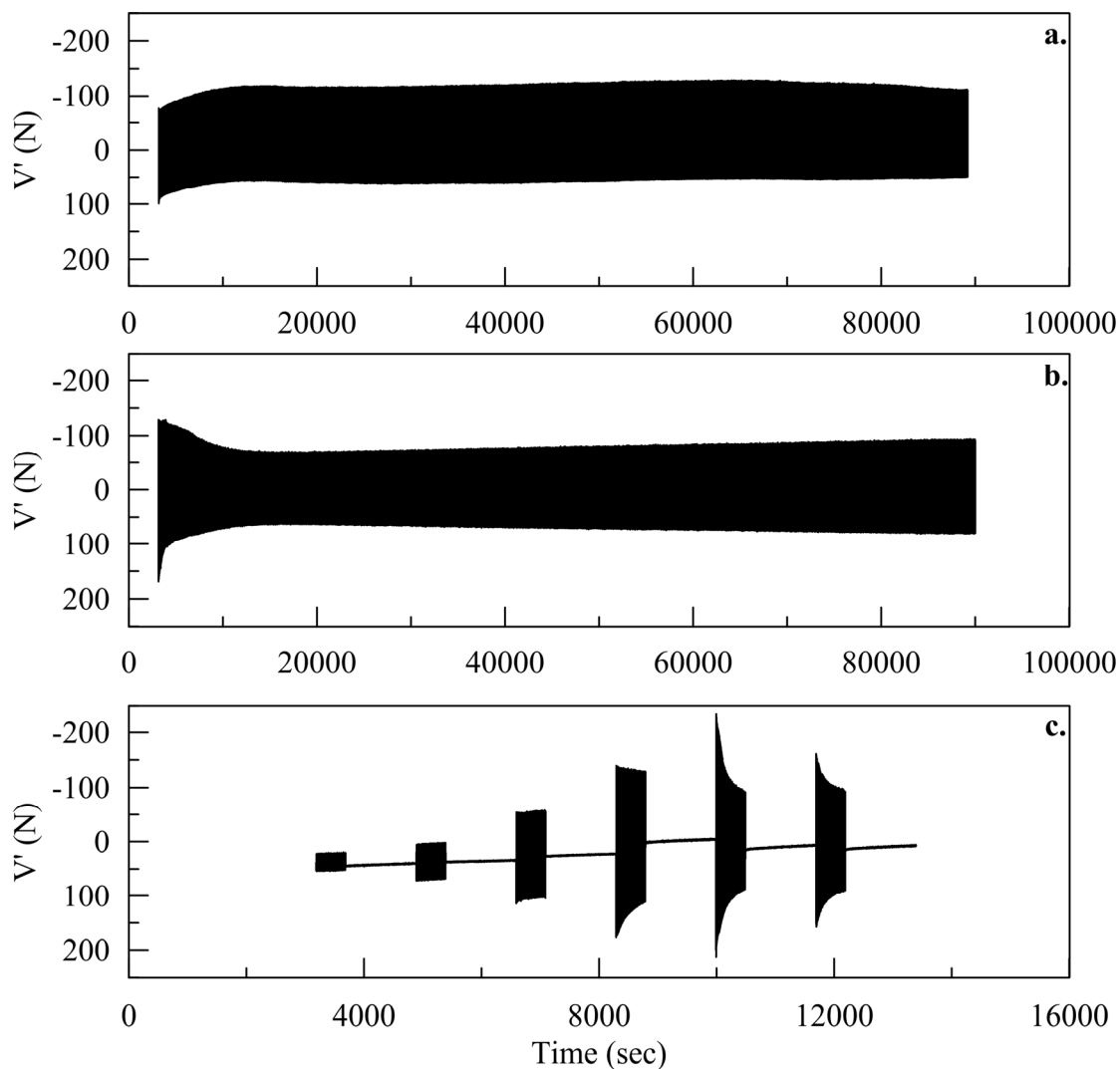


FIG. 5. Vertical load with time for the cyclic phases of loading for a. the 0.04%D 24 hr cyclic test, b. the 0.6%D 24 hr cyclic test, and c. the packeted cyclic test. The period of the cycles was 5 seconds.

CONCLUSIONS

Using the monotonic vertical test as a baseline, the following observations can be made about the effects of cycling: 1) The cycling reduces the peak load capacity of the foundation for any subsequent monotonic loading in both compression and uplift and the magnitude of the reduction increases with increasing cyclic amplitudes. A drastic decrease in the magnitude of the peak monotonic load is observed when the amplitude of the cycles is greater than the displacement required to mobilize the peak load during solely monotonic testing. 2) Any strain softening behavior observed during monotonic loading is not observed after cycling and larger vertical displacements are required to mobilize the peak capacity in compression. 3) The peak capacity in uplift is mobilized at the same order of magnitude when preceded by monotonic compressive loading. 4) The plug detachment from the soil bed occurs sooner for the cyclic tests than for the monotonic test with no previous cyclic loading. This is likely due to a progressive development of the reverse bearing capacity failure surface during cycling and the remolding of the kaolin along this surface with cycling. In the monotonic uplift phase of the 0.04%D 24 hour cyclic test the plug detachment occurred at much lower displacements compared to monotonic uplift loading preceded by monotonic compression while the peak monotonic load is significantly greater. This is likely due to significantly reduced remolding of the clay along the bearing capacity plane forcing failure to occur at the plug rather than along the larger failure plane. 5) At cyclic amplitudes of less than 0.05% of the diameter, the strength degradation with cycling is limited and for cyclic amplitudes of 0.25% of the diameter and higher the soil strength degradation is significant. This indicates that the capacity of the suction caisson foundation for a horizontal axis turbine TEC will be limited by a serviceability constraint that minimizes vertical deformation so that the turbine remains in its optimal position in the water column.

REFERENCES

- Andritz Hydro Hammerfest (2012). "ANDRITZ HYDRO Hammerfest – Renewable energy from tidal currents." Andritz Hydro Hammerfest, Hammerfest, Norway.
- Chen, C.H., Gilbert, R.B., Gerkus, H., Saleh, A.A. and Finn, L. (2015). "Laterally loaded suction caissons with aspect ratio of one." *Frontiers in Offshore Geotechnics III*, Oslo, Norway: 227-232.
- Coffman R.A., El-Sherbiny R.M., Rauch A.F. and Olson R.E. (2004). "Measured horizontal capacity of suction caissons." *Proc. Offshore Technology Conf.*, Houston, TX: 1-10.
- Cornelius, T. and Smith, M. (2009). "Presentation to Offshore Engineering Society – Tidal Stream Energy." Atlantis Resources Ltd., Singapore.
- El-Gharbawy, S. and Olson, R. (1998). "Laboratory modelling of suction caisson foundations." *Proc. 10th Int. Conf. on Offshore and Polar Engineering*, Montreal, Canada, Vol. 1: 531–536.
- European Marine Energy Centre (2015). "European Marine Energy Centre – Tidal Developers." European Marine Energy Centre (EMEC) Ltd., Stromness, Orkney, United Kingdom. Accessed May 2015.

- Georgia Tech Research Corporation (2011). "Assessment of energy Production Potential from Tidal Streams in the United States – Final Project Report." Georgia Tech Research Corporation, Atlanta, GA.
- Kelly, R.B., Houslyby, G.T. and Byrne, B.W. (2006). "A comparison of field and laboratory tests of caisson foundations in sand and clay." *Geotechnique*, 56 (9): 617-626.
- Li, S. and Wang, J. (2013). "Analysis of Suction Anchors Bearing Capacity in Soft Clay." *Proc. 23rd Int. Conf. on Offshore and Polar Engineering*, Anchorage, Alaska, Vol. 1: 495-500.
- Luke, A.M., Rauch, A.F., Olson, R.E. and Mecham, E.C. (2005). "Components of suction caisson capacity measured in axial pullout tests" *Ocean Engineering*, 32: 878-898.
- Marine Current Turbines (2013). "SeaGen-S 2MW." Marine Current Turbines Ltd., Camberley, Surrey, United Kingdom.
- Maynard, M.L., Schneider, J.A., McEntee, J., and Newberg, E. (2013). "Suction caissons for cross-flow tidal power system." *Geotechnical Engineering*, 166 (GE2):99-110.
- National Oceanic and Atmospheric Administration (2015). "National Oceanic and Atmospheric Administration's National Data Buoy Center." National Oceanic and Atmospheric Administration, Washington D.C., USA. Accessed June 2015.
- Rao, S.N., Ravi, R. and Ganapathy, C. (1997). "Pullout behavior of model suction anchors in soft marine clays," *Proc. 7th Int. Conf. on Offshore and Polar Engineering*, Honolulu, Hawaii: Vol. 1: 740-744.
- Starling, M. and Scott, A. (2009). "Foundations and Mooring for Tidal Stream Systems." Produced on behalf of The Carbon Trust. *BMT Cordah*, Report No. L.CAR.002W.
- Steensen-Bach, J.O. (1992). "Recent model tests with suction piles in clay and sand." *Proc. Offshore Technology Conf.*, Houston, TX: 323-330.
- Verdant Power (2010). "Pilot License Application Roosevelt Island Tidal Energy Project: FERC No. 12611." Verdant Power, LLC, New York, NY.
- Villalobos, F.A., Byrne, B.W. and Houslyby, G.T. (2010). "Model testing of suction caissons in clay subjected to vertical loading." *Applied Ocean Research*, 32: 414-424.
- Wang, J.H., Liu, J.L. and Yang, Y. (2012). "Model Tests on Failure Modes and Bearing Capacities of Suction Anchors with Taut Mooring System." *Proc. 22nd Int. Conf. on Offshore and Polar Engineering*, Rhodes, Greece, Vol 1: 658-666.

Towards the Anchoring of Marine Hydrokinetic Energy Devices: Three-Dimensional Discrete Element Method Simulations of Interface Shear

Nan Zhang, S.M.ASCE¹; and T. Matthew Evans, A.M.ASCE²

¹Research Assistant, School of Civil and Construction Engineering, Oregon State Univ., Corvallis, OR.

²Associate Professor, School of Civil and Construction Engineering, Oregon State Univ., Corvallis, OR. E-mail: matt.evans@oregonstate.edu

Abstract:

Interfaces between soils and structures are common in engineering practice. Physical experiments and numerical analyses have been used to explore interface shear behavior. A numerical model based on the discrete element method (DEM) is presented to simulate the three-dimensional granular-continuum interface shear behavior between soil and (e.g.) an anchor for a marine hydrokinetic (MHK) energy device when the anchor is subjected to a constant axial load and embedded into sandy marine sediments. These MHK devices rely upon seafloor anchors and compliant mooring systems to maintain their station, but without retarding the motion being converted to electricity. The capacity of these anchors is a significant design parameter for the entire MHK system. Anchor self-weight and soil-anchor interface shear forces provide holding capacity for the MHK device. Numerous factors will influence the pullout capacity of an anchor, including anchor type and seabed properties – and particularly, how those two components interact to manifest as interface friction. This interface friction is difficult to measure in-situ and thus, robust numerical models are necessary for system simulation and design. The effects of anchor friction are considered. Anchor surface roughness and asperity angle are defined as functions of mean grain size, consistent with prior definitions of counterface roughness from the literature. Fabric evolution at the sediment-anchor interface is investigated and the micromechanics of strain softening are discussed, though not quantified.

INTRODUCTION

Soil-structure interaction in geotechnical engineering has been an area of active research since the 19th century and has evolved significantly over the past 150 years (Kausel, 2010). Previous soil-structure interaction studies have been based on numerical simulations (e.g., Jensen et al. 1999; Jensen, Edil et al. 2001; Jensen, Plesha et al. 2001; Dove et al. 2006; Wang, 2006; Wang, Dove, and Gutierrez, 2007a, 2007b; Wang, Gutierrez, and Dove, 2007) and/or physical experiments (e.g., Uesugi and Kishida 1986a, 1986b, 1988; Hu and Pu 2004;). The majority of the previous

research has employed either the finite element method or the boundary element method for simulating soil-structure response (e.g., Cheng 1989; Kuppusamy et al. 1992; Hall and Oliveto 2003). These methods consider the soil medium as a continuum, which can have drawbacks, particularly when robust simulation of post-peak softening is required.

The discrete element method (DEM) allows for the simulation of soils as a collection of individual particles and is increasingly being applied to a wide array of problems that involve granular materials in contact with a geostructure (e.g., Kress and Evans 2010; Evans and Kress 2011). DEM models predict the emergent behavior of particulate assemblies based on simulation of independent particle behaviors; they have been successfully applied to the study of shear bands in sand, including free-field granular-granular shearing (Jacobsen et al. 2007; Evans and Frost 2010; Zhao and Evans 2011; Frost et al. 2012) and also granular-continuum interface shearing (Hall and Oliveto 2003; Dove et al. 2006; Wang, Gutierrez, and Dove 2007; Wang, Dove, and Gutierrez 2007b; Kress and Evans 2010; Evans and Kress 2011; Wang and Jiang 2011). Previous researchers have modeled the shear banding behaviors of particulate assemblies and the influence of particle or continuum counterface properties on shearing response. Overall, simulated material response from DEM simulations have been shown to be consistent with results from physical experiments for a variety of loading conditions (Zhao and Evans 2009; Evans and Frost 2010).

In marine systems, the interaction between seabed sands and offshore anchors is one specific example of soil-structure interaction. The basic analysis principles for these systems are generally consistent with those for soil-structure interactions for onshore applications, such as those discussed previously. In the case of marine hydrokinetic (MHK) energy generators, however, these anchors serve not only to keep the devices on station, but also as the reaction force necessary for energy generation. The holding capacity of the anchors must bear the tensile force from ocean waves transmitted by mooring lines. For a catenary mooring system, the mooring line has an inclination angle with the seabed and will apply both vertical and horizontal forces to the anchor. The properties of the seabed and the anchor combine to determine the holding capacity and allowable reaction force for a given anchor design. Much of the previous work on offshore anchors has focused on FEM analyses and/or limit equilibrium solutions (Lieng et al. 2000; O'Loughlin et al. 2013; O'Beirne et al. 2015). However, both of these approaches neglect much of the fundamental physics occurring at the anchor-soil interface, and thus, may be unsuitable for simulating the anchor-soil interface softening that occurs for MHK systems. This work uses DEM simulations (*PFC^{3D} v4.0*) to evaluate the effects of soil properties and anchor surface roughness on holding capacity.

MARINE SEDIMENTS

Marine sediments include sands, gravels, clays and organic sediments. In oceanography, they can also be classified into terrigenous, biogenous, hydrogenous and cosmogenous, with hydrogenous and cosmogenous sediments together only making up approximately 2% of the total sediment mass. Terrigenous (~45%) and biogenous (~55%) sediments make up the remainder of the sea floor sediments. Even

though biogenous sediments make up a very large percent of the total sediment, they tend to dominate beginning at depths near 5 km (Huneke and Mulder 2011). Terrigenous sediments derive largely from the erosion of rocks on land and consist primarily of sands, clayey sands, and gravels. Sands and gravels are classified as the discrete solid, macroscopic particles which are all discrete granular materials (Duran 1999). These materials are appropriate for the modeling scheme deployed herein.

DEM SIMULATIONS

Prior DEM studies of particle-counterface frictional behavior have been restricted to two dimensions (e.g., Jensen et al. 1999; Dove et al. 2006; Wang et al. 2007; Kress and Evans 2010), but important three-dimensional effects are expected to contribute to system behavior as well. The current work is focused on the three-dimensional DEM simulation of axisymmetric interface shear.

The geometry of the DEM model of the interface shear test is shown in Figure 1. The central region of the shaft passing through the cylindrical particulate assembly generates frictional resistance at two spatial scales. At the smaller of the two scales, there is sliding resistance due to Coulombic friction between a particle and the continuum counterface. At the larger scale, the shaft has a “zig-zag” texture that is approximately on the same scale as the particle size. We will refer to the smaller-scale effect as *friction* and the larger-scale effect as *roughness*; clearly, both contribute to ultimate shear resistance. The rough shaft section is modeled as alternating conical frusta with user-defined geometry (Figure 2). The asperity angle (θ), tip-tip distance (h) and asperity peak (R) are all defined as functions of median particle size d_{50} . The portion of the shaft outside of the rough central region has neither roughness nor friction and, thus does not contribute to the shear resistance of the shaft.

An assembly of polydisperse spheres is generated to fill the model volume between the shaft and the outer wall at a specified porosity. Mass scaling (e.g., Belheine et al. 2009; Evans and Valdes 2011) was employed to decrease simulation time; as such, the mean particle diameter is $d_{50} = 0.4$ m and other model dimensions are scaled accordingly. Specifically, model height (H), diameter (D), and shaft diameter (D_s) may be expressed in terms of d_{50} as $H/d_{50} = 45$, $D/d_{50} = 30$, and $D_s/d_{50} = 3$, respectively.

Previous research (Uesugi and Kishida 1988; Frost et al. 2004; Wang et al. 2007b), has found that shear band thickness in interface shear tests is approximately 8-10 median particle diameters. Thus, the set radial distance between the shaft and the assembly boundary for the simulations in this study was set as $(D-D_s)/2d_{50}=13.5$. In addition to the annular distance between the shaft and the assembly outer cylinder, Wang et al. (2007b) found that the friction between the particles and the walls is also significantly important. In this study, the friction between the particles and the shaft is treated as a user-defined variable and the outer wall friction is set to zero.

A numerical servo-control mechanism is used to consolidate the specimen such that it is in numerical equilibrium at a specified isotropic stress state with a tolerance of 1% by adjusting the positions of both the cylinder and the platens. This as-consolidated void ratio can be adjusted by varying the particles' and walls' friction

coefficients during consolidation, with a higher friction value resulting in a looser specimen. After consolidation, particle friction can be adjusted to assess the effects of particle friction on pullout resistance. Once the specimen is consolidated and equilibrated, the shaft is translated axially at a constant velocity while specimen volume remains constant, implying rapid (i.e., undrained) shear. To monitor system response during shearing, the particle assembly is divided into four subzones, as shown in Figure 3. System behavior and state (e.g., coordination number, porosity, sliding friction and stress) in each subzone are monitored for further analysis. Normal and tangential forces are generated at contact points using a linear contact model. In the tangential direction, the model is linear elastic-perfectly plastic and the failure force, T_f , is given as $T_f = \mu \cdot N$ where μ is the particle friction coefficient and N is the normal contact force. The interface shearing force is obtained by measuring the out-of-balance normal and shear forces opposite to the direction of shaft motion on all of the shaft walls and summing them. Material and model properties are summarized in Table 1. The simulations discussed herein consist of approximately 15,000 particles and require approximately 48 hours to complete on an Intel Xeon E5-2660 v3 processor running Windows Server 2012.

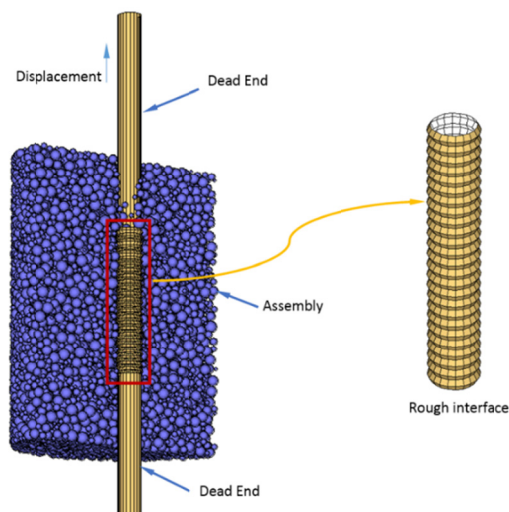


FIG. 1. Geometry of the DEM model (particle assembly shown in section with half of particles removed to reveal continuum counterface). Note that the “dead ends” are frictionless and do not contribute to interface shearing resistance.

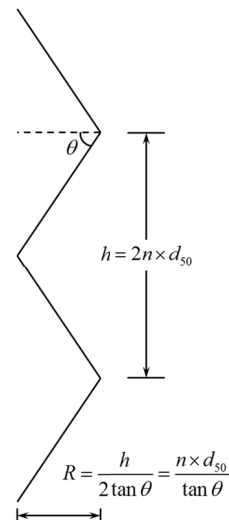


FIG. 2. Shaft surface geometry. The tip-tip sawtooth length, h , is defined by a scale factor, n , the mean particle diameter, d_{50} , and an asperity angle, θ . The tip-trough relief (amplitude), R , is calculated from user defined variables.

Example simulation results are presented in Figure 4. This shows the change in lateral and axial effective stresses during shaft displacement as well as the interface shearing force on the shaft. The initial confining stress was 100 kPa and the shaft friction coefficient for this simulation was 0.31. It can be seen that the stresses on the external walls change rapidly at the onset of shearing (both start at 100 ± 1 kPa), but quickly reach some critical value and remain relatively constant thereafter. This is an

indication that (1) the model domain is sufficiently large; and (2) the use of dead ends prevents the accumulation of boundary stresses at the ends of the cylindrical specimen. This simulation was used as a baseline for a parametric analysis, described subsequently.

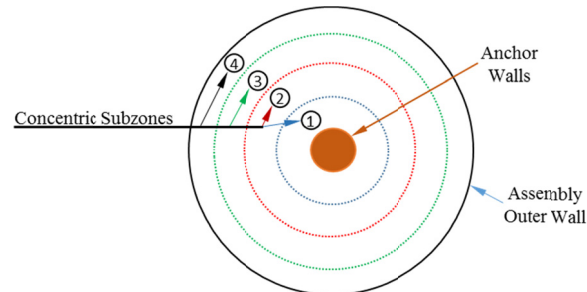


FIG. 3. Subzones of the region between the shaft and model boundary

Table 1. Material and model properties.

	Parameters	Value
Particles	Maximum diameter, d_{max} [m]	0.75
	Minimum diameter, d_{min} [m]	0.05
	Normal stiffness, k_n [N/m]	2×10^6
	Shear stiffness, k_s [N/m]	1×10^6
	Friction coefficient, μ []	0.31
	Density, ρ_s [kg/m ³]	2650
Model	Height, H [d ₅₀]	45
	Diameter, D [d ₅₀]	30
	Wall stiffness, k_w [N/m]	2×10^7
	Initial porosity []	0.426
Shaft walls	Normal stiffness, k_{sn} [N/m]	2×10^8
	Shear stiffness, k_{ss} [N/m]	2×10^8
	Tip-tip distance, h [d ₅₀]	0.5
	Asperity angle, θ [°]	75

PARAMETRIC ANALYSIS

Five simulations are performed to investigate the particle-shaft interface shear behaviors under constant velocity with varying friction coefficients of shaft. To prevent the effects from varying initial fabric on the results of the parametric simulations, a single initial assembly of approximately 25,000 particles is generated for all five cases. From this generated assembly, five separate shear tests are performed, each with a different shaft friction, which are user-defined as 0.11, 0.21, 0.31, 0.41, and 0.51.

Note that the particle friction coefficient (Table 1) is 0.31, so shaft frictions larger than this value should produce the same results as a shaft friction of 0.31 because individual contact sliding failure will occur when the tangential force is greater than

the product of the normal force and the minimum friction coefficient of the two contacting entities. To assess the effects on increasing shaft friction then, it is necessary to set the friction coefficient of all shaft-particle contacts to the shaft friction if $\mu_{shaft} > \mu_{particle}$. This allows higher friction values at the interface without affecting the bulk response of the particulate mass.

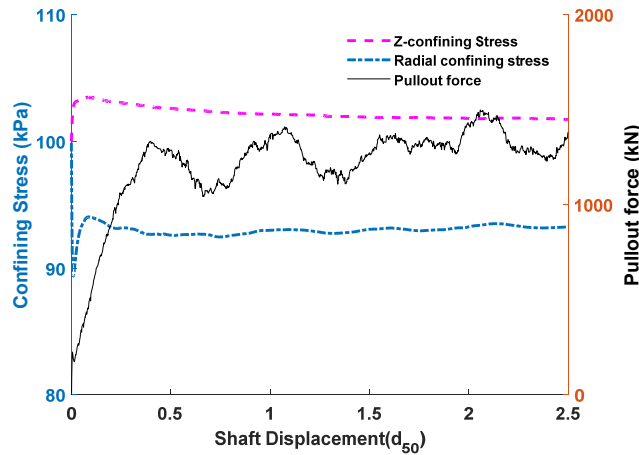


FIG. 4. Results from the baseline interface shear simulation.

RESULTS AND DISCUSSION

Shear resistance as a function of shaft friction is considered below. From the simulations, shaft pullout forces are shown to generally increase with increasing shaft friction coefficient. Since the shaft geometry is also rough (as opposed to simply frictional), the pullout forces during the displacement show oscillations as particles roll and slide over the shaft protrusions. In Figure 5, maximum pullout force for friction coefficients $\mu = 0.41$ and $\mu = 0.51$ are quite similar, implying that increasing the interface strength will require increasing the roughness, not the friction. Specifically, it is necessary to require particles to rotate and translate rather than simply slide along the shaft.

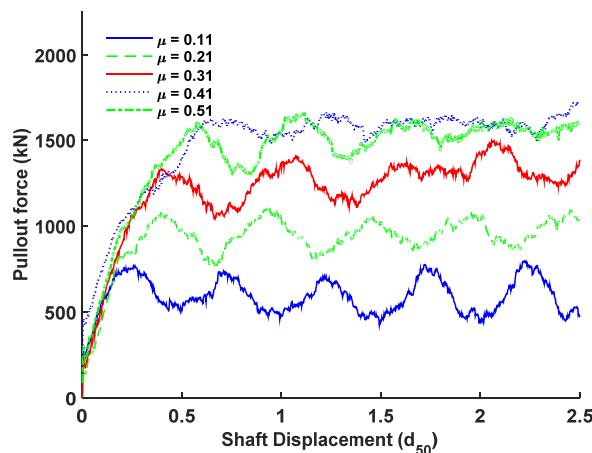


FIG. 5. Pullout force of the shaft with different shaft friction coefficients

From the pullout force, it is possible to calculate the interface friction angle for each value of shaft friction coefficient. These values are presented in Figure 6. For a shaft friction coefficient of 0.11, the peak interface friction angle is 10°, increasing to a value of 20° for a shaft friction coefficient of 0.51. The evolution of interface friction angle with shaft friction follows the bilinear trend observed by Uesugi and Kishida (1986a) in interface shear tests of sand against steel surfaces of varying roughness.

The fraction of sliding contacts within Zone 1 for different shaft friction coefficients is shown in Figure 7. Overall, the response shows a rise to an initial peak at a deformation that corresponds to full mobilization of frictional stress (Figure 5) followed by a decrease to oscillations about a constant value as displacement progresses. The increase in the number of sliding contacts with increasing shaft friction indicates that greater particle rearrangement occurs during shear when the frictional resistance between the particles and the shaft is higher. Uesugi and Kishida (1988) found that the major component of the interface movement is slippage of particles along the surface for smooth surface while particle slippage, rolling and vertical movement are the major components of rough surfaces.

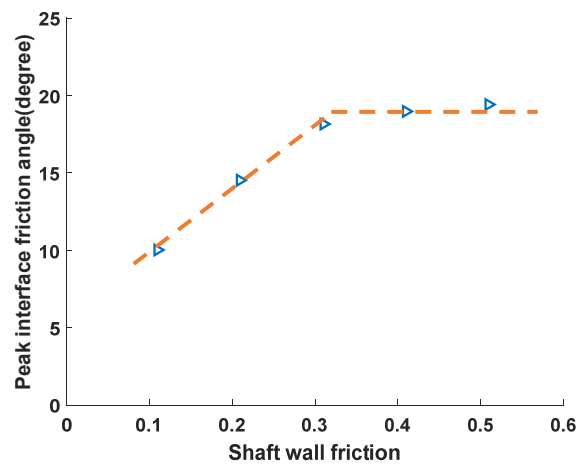


FIG. 6. Peak interface friction angle for different shaft friction coefficients

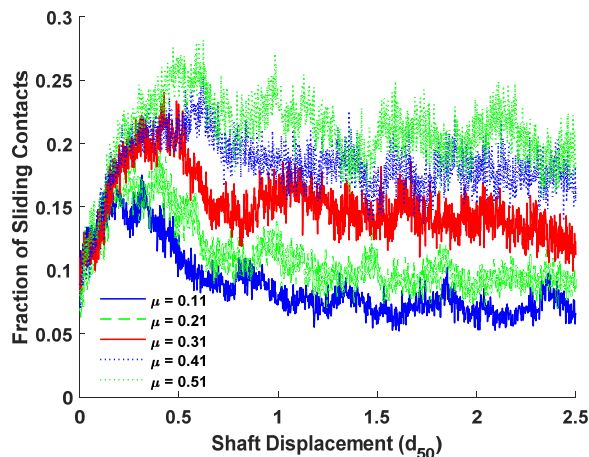


FIG. 7. Fraction of all ball contacts in Zone 1 that are in shear failure

The peak fractions of sliding contacts within Zone 1 for different shaft frictions are shown in Figure 8. Peak sliding fractions steadily increase with the increase of shaft wall friction coefficients. However, the interface friction strength does not continuously increase (Figure 6). This shows clearly that failure moves away from the interface into the bulk soil without increasing the measurable interface shear strength. Thus, interface shear strength cannot be continuously increased by just increasing the counterface friction coefficient. Soil types, microscale soil properties are significantly important for the interface shear strength as well.

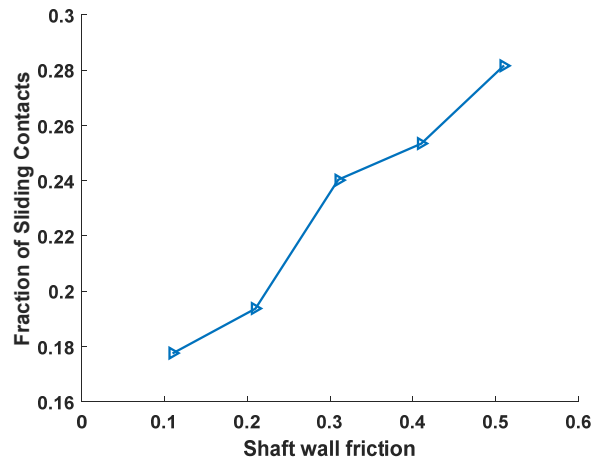


FIG 8. Peak fraction of all Zone 1 contacts for different shaft friction coefficients

ACKNOWLEDGMENTS

This material is based upon work supported by the Department of Energy under Award Number DE-FG36-08GO18179. This report was prepared as an account of work sponsored by an agency of the United States Government. Neither the United States Government nor any agency thereof, nor any of their employees, makes any warranty, expressed or implied, or assumes any legal liability or responsibility for the accuracy, completeness, or usefulness of any information, apparatus, product, or process disclosed, or represents that its use would not infringe privately owned rights. The views and opinions of the authors expressed herein do not necessarily state or reflect those of the United States Government or any agency thereof.

REFERENCES

- Belheine N., Plassiard J. P., Donze F. V., Darve F. and Seridi A. (2009). "Numerical simulation of drained triaxial test using 3D discrete element modeling." *Computers and Geotechnics*, 36(1-2), 320-331.
- Cheng, Y. M. (1989). Finite element analysis of soil-structure interaction problems, with application to basement construction problems. Ph.D. Dissertation, University of Hong Kong.

- Dove, J., Bents, D., Wang, J., and Gao, B. (2006). Particle-scale surface interactions of non-dilative interface systems. *Geotextiles and Geomembranes*, 24(3), 156–168.
- Duran, J. (1999). *Sands, Powders, and Grains: An Introduction to the Physics of Granular Materials*. New York: Springer.
- Evans, T.M., and J.D. Frost. (2010). “Multiscale Investigation of Shear Bands in Sand: Physical and Numerical Experiments,” *International Journal for Numerical and Analytical Methods in Geomechanics*, 34(15), pp. 1634-1650.
- Evans, T.M. and J.G. Kress. (2011). “Discrete simulations of particulate-structure interactions,” ASCE GeoFrontiers 2011, *Geotechnical Special Publication No. 211: Advances in Geotechnical Engineering*, Dallas, TX, pp. 4252-4262.
- Evans, T.M. and Valdes J.R. (2011). “The microstructure of particulate mixtures in one -dimensional compression: numerical studies.” *Granular Matter*, 13, 657-669.
- Frost, J.D., G.L. Hebel, T.M. Evans, and J.T. DeJong. (2004). “Interface Behavior of Granular Soils,” *Proceedings of the 9th ASCE Aerospace Division International Conference on Engineering, Construction, and Operations in Challenging Environments*, Houston, TX, USA, pp. 65-72.
- Frost, J.D., T.M. Evans, Y. Lu, and X. Zhao. (2012). “Selected observations from 3-D experimental and numerical studies of shear banding in biaxial shear tests,” ASCE Geo-Congress 2012, *Geotechnical Special Publication No. 225: State of the Art and Practice in Geotechnical Engineering*, Oakland, CA, pp. 1116-1125.
- Hall, W.S., and Oliveto, G. (2003). *Boundary Element Methods for Soil-Structure Interaction*. Springer Science and Business Media.
- Hu, L., and Pu, J. (2004). Testing and modeling of soil-structure interface. *Journal of Geotechnical and Geoenvironmental Engineering*, 130(8), 851 – 860.
- Hunke, H., and Mulder, T. (2011). *Deep-Sea Sediments. Developments in Sedimentology* (Vol. 63). New York: Elsevier.
- Jacobson, D.E., J.R. Valdes, and T.M. Evans. (2007). “A numerical view into direct shear specimen size effects,” *ASTM Geotechnical Testing Journal*, 30(6), pp. 512-516.
- Jensen, R. P., Bosscher, P. J., Plesha, M. E., and Edil, T. B. (1999). DEM Simulation of Granular Media-Structure Interface: Effects of Surface Roughness and Particle Shape. *International Journal of Geomechanics*, 23, 531–547.
- Jensen, R. P., Edil, T. B., Bosscher, P. J., Plesha, M. E., and Kahla, N. B. (2001). Effect of Particle Shape on Interface Behavior of DEM-Simulated Granular Materials. *International Journal of Geomechanics*, 1(1), 1–19.
- Jensen, R. P., Plesha, M. E., Edil, T. B., Bosscher, P. J., and Kahla, N. B. (2001). DEM Simulation of Particle Damage in Granular Media — Structure Interfaces. *International Journal of Geomechanics*, 1(1), 21–39.
- Kausel, E. (2010). Early history of soil–structure interaction. *Soil Dynamics and Earthquake Engineering*, 30(9), 822–832.
- Kress, J.G. and T.M. Evans. (2010). “Analysis of pile behavior in granular soils using DEM,” *Proceedings of the 35th Annual Deep Foundations Institute Annual Conference*, Hollywood, CA, October 12-15.

- Kuppusamy, T., Zarco, M.A., & Ebeling, R.M. (1992). *Solution of soil-structure interaction problems by coupled boundary element-finite element method*, Report No. TR-ITL-92-3, Virginia Polytechnic Institute and State University, Department of Civil and Environmental Engineering, Blacksburg, VA.
- Lieng, J.T., Kavli, A., and Tjelta, T.I. (2000). Deep penetrating anchor: further development, optimization and capacity clarification. Presented at the *10th International Offshore and Polar Engineering Conference*, International Society of Offshore and Polar Engineers.
- O’Beirne, C., O’Loughlin, C.D., Wang, D., and Gaudin, C. (2015). Capacity of dynamically installed anchors as assessed through field testing and three-dimensional large-deformation finite element analyses. *Canadian Geotechnical Journal*, 52(5), 548–562. <http://doi.org/10.1139/cgj-2014-0209>
- O’Loughlin, C., Richardson, M.D., Randolph, M.F., and Gaudin, C. (2013). Penetration of dynamically installed anchors in clay. *Géotechnique*, 63(11), 909–919.
- Uesugi, M., and Kishida, H. (1986a). Frictional Resistance at Yield between Dry Sand and Mild Steel. *Soils and Foundations*, 26(4), 139–149.
- Uesugi, M., and Kishida, H. (1986b). Influential factors of friction between steel and dry sands. *Soils and Foundations*, 26(2), 33–46.
- Uesugi, M., and Kishida, H. (1988). Behavior of sand particles in sand-steel friction. *Soils and Foundations*, 28(1), 107–118.
- Wang, J. (2006). *Micromechanics of granular media: A fundamental study of interphase systems*. Virginia Tech, Blacksburg, VA.
- Wang, J., Dove, J. E., and Gutierrez, M. S. (2007a). Anisotropy-based failure criterion for interphase systems. *Journal of Geotechnical and Geoenvironmental Engineering*, 133(5), 599–608.
- Wang, J., Dove, J. E., and Gutierrez, M. S. (2007b). Discrete-continuum analysis of shear banding in the direct shear test. *Géotechnique*, 57(6), 513–526.
- Wang, J., Gutierrez, M. S., and Dove, J. E. (2007). Numerical studies of shear banding in interface shear tests using a new strain calculation method. *International Journal for Numerical and Analytical Methods in Geomechanics*, 31(12), 1349–1366.
- Wang, J., and Jiang, M. (2011). Unified soil behavior of interface shear test and direct shear test under the influence of lower moving boundaries. *Granular Matter*, 13(5), 631–641.
- Zhao, X. and T.M. Evans. (2009). “Discrete Simulations of Laboratory Loading Conditions,” *International Journal of Geomechanics*, 9(4), pp. 169-178.
- Zhao, X. and T.M. Evans. (2011). “Numerical Analysis of Critical State Behaviors of Granular Soils Under Different Loading Conditions,” *Granular Matter*, 13(6), pp. 751-764.

Airport Apron Heated Pavement System Operations: Analysis of Energy Consumption, Greenhouse Gas Emissions, and Operating Costs

Weibin Shen¹; Kasthurirangan Gopalakrishnan²; Sunghwan Kim³; and Halil Ceylan⁴

¹Graduate Student, Dept. of Civil, Construction and Environmental Engineering, Iowa State Univ., 24 Town Engineering Bldg., Ames, IA 50011-3232. E-mail:

wshen@iastate.edu

²Research Associate Professor, Dept. of Civil, Construction and Environmental Engineering, Iowa State Univ., 354 Town Engineering Bldg., Ames, IA 50011-3232.

E-mail: rangan@iastate.edu

³Research Scientist, Institute for Transportation, Iowa State Univ., Ames, IA 50011-3232. E-mail: sunghwan@iastate.edu

⁴Professor, Director, Program for Sustainable Pavement Engineering and Research (PROSPER), Dept. of Civil, Construction and Environmental Engineering, Iowa State Univ., 406 Town Engineering Bldg., Ames, IA 50011-3232. E-mail:

hceylan@iastate.edu

Abstract: The primary goal of this study is to employ the life cycle assessment (LCA) methodology to evaluate and compare energy consumptions, GHG emissions, and costs from the operations of three different hydronic heated pavement systems (HHPS): hydronic heated pavement system using geothermal heat pump (HHPS-G), hydronic heated pavement system using electric water heater (HHPS-E), and hydronic heated pavement system using natural gas boiler (HHPS-NG). The system boundaries where the analysis is carried out are defined and established. The consequences of the inventory analysis and impact assessment of both systems are conducted and discussed to provide some actionable insights to the system operators. The LCA results indicate that the operation of HHPS-G for apron snow removal might have the least energy consumption, GHG emissions, and operating costs. Also, the potential sustainability benefits of HHPS-NG is expected to increase as the efficiency of water boiler improves.

INTRODUCTION

Traditional snow removal system usually applies snow removal machines, like snow plow and snow bloom combinations, snow blowers, and deicing chemical sprayers to achieve airfield surface cleaning missions. These mechanical equipment are usually designed for large areas, like runway, in order to increase snow removal efficiency. However, it makes the equipment difficult to operate in a narrow space like the airport apron. Although smaller snow removal machines are used instead to remove snow from apron areas, they are not as efficient as the big equipment used in runway, and more labors and time are required for traditional apron snow removal

application. According to all these reasons, using traditional methods to remove snow from apron areas could cause airline delay problems and high operation costs. Because airport apron is the area where aircraft are parked, unloaded or loaded, refueled, or boarded (FAA 2008), many human activities are involved in this area. Also potential risks, like airport crew safety issues, might happen during traditional snow removal applications. In order to prevent airline delay problem and airport crew accident happening during snow removal application, hydronic heated pavement systems (HHPS) are being studied as the alternative strategy to traditional snow removal system applied in apron areas. Previous study suggested that HHPS could provide sustainable benefits when used for apron snow removal applications (Shen et al. 2015).

HHPS utilizes natural gas boiler or electric water heater to warm up and circulate hot water through embedded pipes in the pavement in order to heat up the pavement and melt the ice. An alternative approach called geothermal heated pavement system is using geothermal energy instead for heating. To achieve the heating function, ground source heat pump (GSHP) is utilized to replace boiler or heater. GSHP can supply space heating by accessing heat in the soil (Kreith and Goswami 2001). It is applied in regions that do not have access to high temperature geothermal resources. GSHP takes the heat absorbed in the land from solar energy through the use of a ground heat exchanger. Ground heat exchanger has three types of systems, direct exchange geothermal system, closed loop geothermal system and open loop geothermal system. Considering the relatively lower efficiency, longer and larger pipe requirements and high construction fee of closed loop systems, this paper focuses on direct exchange based geothermal heated pavement system. The direct exchange system uses a single loop to circulate fluid in contact with the ground to extract or dissipate heat directly.

The overall goal of this study is to understand and compare the energy consumptions, Greenhouse Gas (GHG) emissions, and costs of the operations of three alternative hydronic heated pavement systems: geothermal heated pavement system or hydronic heated pavement system using geothermal heat pump (HHPS-G), hydronic heated pavement systems using electric water heater (HHPS-E), and hydronic heated pavement systems using natural gas boiler (HHPS-NG) for different snow rate conditions. The life cycle assessment (LCA) and technical economic analysis (TEA) methods were employed in this study.

ANALYSIS METHODOLOGY

Operation Boundary

The system boundary of HHPS-G operation to prevent ice/snow accumulation on apron surface were identified and illustrated in FIG. 1(a). Energy production stage and system operation stage are included in this study. Energy production stage describes the life cycle of power plant producing electricity which is used for supplying geothermal heat pump and circulating pump operations. A “cradle-to-gate” assessment of energy production facility (power plant) is applied to estimate the GHG emissions from energy production phase. Among the various power plant types, electricity power plant using natural gas is considered in this study.

The system boundaries of HHPS-E and HHPS-NG are identified and illustrated in FIG. 1 (b) and (c), respectively. Similar to the system boundary of HHPS-G, HHPS-E and HHPS-NG system boundaries both include energy production stage and heated pavement system operation stage. Electricity power plant using natural gas is analyzed for energy production stage in HHPS-E and HHPS-NG as well. For HHPS-E, energy production stage represents that life cycle phase of power plant which generates electricity (by using natural gas) for water heater to warm up solution and circulating pump operation. Different from HHPS-G and HHPS-E, HHPS-NG energy production stage includes life cycle phase of electricity generation and life cycle phase of natural gas production and combustion. Electricity is used to supply circulating pump operation, and natural gas is combusted in natural gas boiler for solution heating as FIG. 1 (c) describes.

Snow Removal System Models

In order to understand the behaviors of both heated pavement systems under different weather conditions, five different snow rates, which were 12.7 mm/h, 19.1 mm/h, 25.4 mm/h, 38.1 mm/h, and 50.8 mm/h, at an ambient temperature of -6.7°C and wind speed of 16.1 km per hour were analyzed in this study.

The airport heated pavement systems in this study are applied in the MD-87 aircraft (short to medium range airliner) gate area, which is about $1,765\text{ m}^2$ (Robert et al. 2010). Both the heated pavement designs were based on Viega Snow Melting System Installation Manual (Viega 2015). The following pipe line design was used for both geothermal and hydronic heated pavement systems: 19-mm cross-linked polyethylene (PEX) pipe, whose circuit length is 122 m, and a total of 71 circuits are required. A 40% by volume of propylene glycol solution is used as a heated medium in both systems to prevent pipe line frozen, and it is circulated in a flow rate of $1.9\text{ m}^3/\text{h}$. The total flow rate of the system is $134\text{ m}^3/\text{h}$ and the pressure drop is about 38 m of head, and a glandless circulating pump with 60% to 80% efficiency (Wilo 2009) can be used to circulate fluid in the systems. In this study, circulating pumps with a 70%-efficiency rating were analyzed for both heated pavement systems.

The models for three approaches are demonstrated in FIG. 2. The heating energy of geothermal heated pavement system is extracted from the ground by applying geothermal heat pumps whose power is supported by electricity. Based on geothermal heat pumps key product criteria, the coefficient of performance (COP) of an efficient direct geo-exchange heat pumps is 3.6 (Energy Star 2012). However, geothermal heat pump coefficient of performance is highly dependent on the sufficiency of geothermal energy of the location. It has been reported that COP can be as low as 2.4 (The Canadian Renewable Energy Network 2002). In this study, a low and high COP of ground source heat pump were analyzed to understand the behavior of HHPS-G under different geothermal situations.

Electric water heater for heating in HHPS-E and natural gas boiler for heating in HHPS-NG are analyzed, respectively. Typical water heaters in the U.S. are electric resistance or atmospheric natural gas tank water heaters. Electric water heaters typically have efficiency of about 90%, while natural gas boiler will be rated about

60% (American Council for an Energy-Efficient Economy 2012). A heat exchanger is required in the HHPS-E and HHPS-NG, because propylene glycol is used as antifreeze to prevent heat transfer medium freezing, and propylene glycol solution cannot be directly heated by the furnace. 40% by volume of propylene glycol solution extracts heat through the heat exchanger and it is circulated under the concrete slab surface by the circulating pump to heat the pavement surface.

As shown in FIG. 2, electricity and natural gas are two main energies used to operate the system in melting snow. Based on U.S. Energy Information Administration (EIA), the 2014 Iowa commercial electricity price is 0.1 \$/kWh (EIA 2014a) and natural gas price is about 0.0167\$/kWh (EIA 2014b). The operating costs of different systems could be obtained by multiplying the energy consumption with unit price.

Analysis Equations

In order to understand the heat (q_o) required for melting snow by using a heated pavement system, the following Equation (1) can be applied (ASHRAE 2003) (the units are modified to SI units):

$$q_o = q_s + q_m + A_r(q_e + q_h) \quad (1)$$

in which, q_s = sensible heat transferred to the snow ($\text{MJ}/\text{h}\cdot\text{m}^2$), q_m = heat of fusion ($\text{MJ}/\text{h}\cdot\text{m}^2$), A_r = ratio of snow-free area to total area (dimensionless), q_e = heat of evaporation ($\text{MJ}/\text{h}\cdot\text{m}^2$), q_h = heat transfer by convection and radiation ($\text{MJ}/\text{h}\cdot\text{m}^2$). The detailed equations for these parameters are available in ASHRAE (2003).

To calculate the energy consumption (kW) for circulating pump, the following equation was applied:

$$P = \frac{Q \times H \times \rho \times g}{3.6 \times 10^6 n} \quad (2)$$

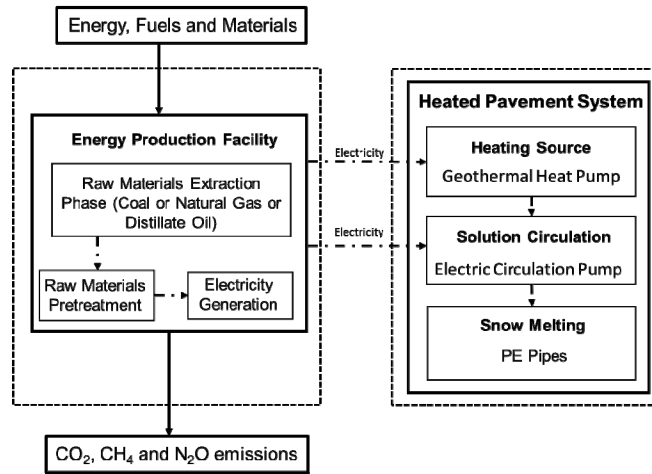
in which, P = energy consumption (kW) for circulating pump, Q = flow rate (m^3/h), H = total head (m), ρ = density of heated solution ($1,000 \text{ kg}/\text{m}^3$ of water and $1,034 \text{ kg}/\text{m}^3$ of 40% propylene glycol), g = Gravity ($9.81 \text{ m}/\text{s}^2$), n = pump efficiency (%).

Energy consumption (E) (in kWh) of geothermal heat pump in HHPS-G is calculated using the equation shown below:

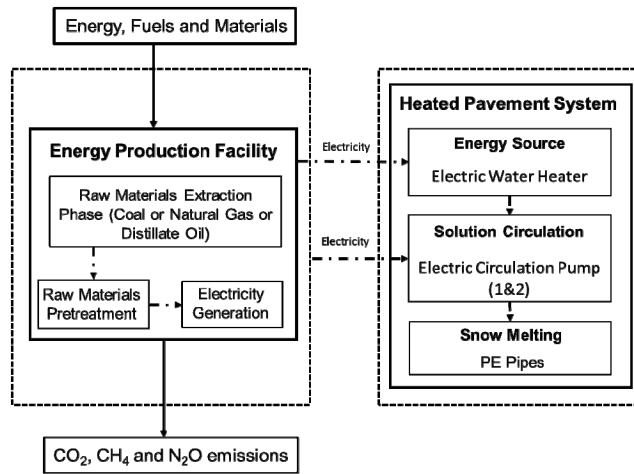
$$E = \frac{q_o}{COP} \quad (3)$$

where E = energy consumption (kW) of geothermal heat pump in HHPS-G, q_o = heat required to melt snow (kW), COP = coefficient of performance.

(a)



(b)



(c)

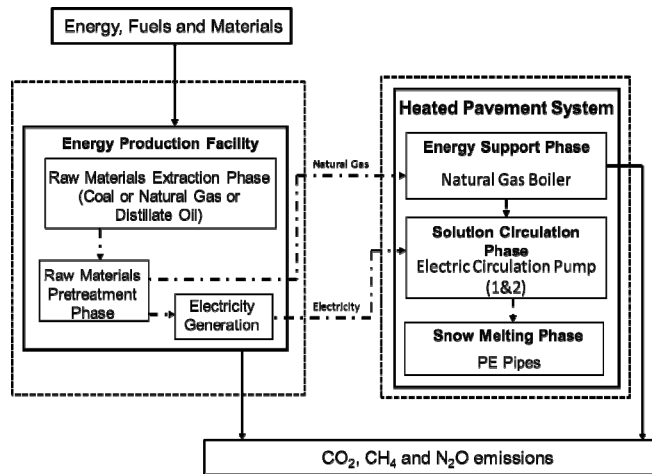


FIG. 1. System boundary of HHPSs: (a) HHP-G, (b) HHPS-E, (c) HHPS-NG.

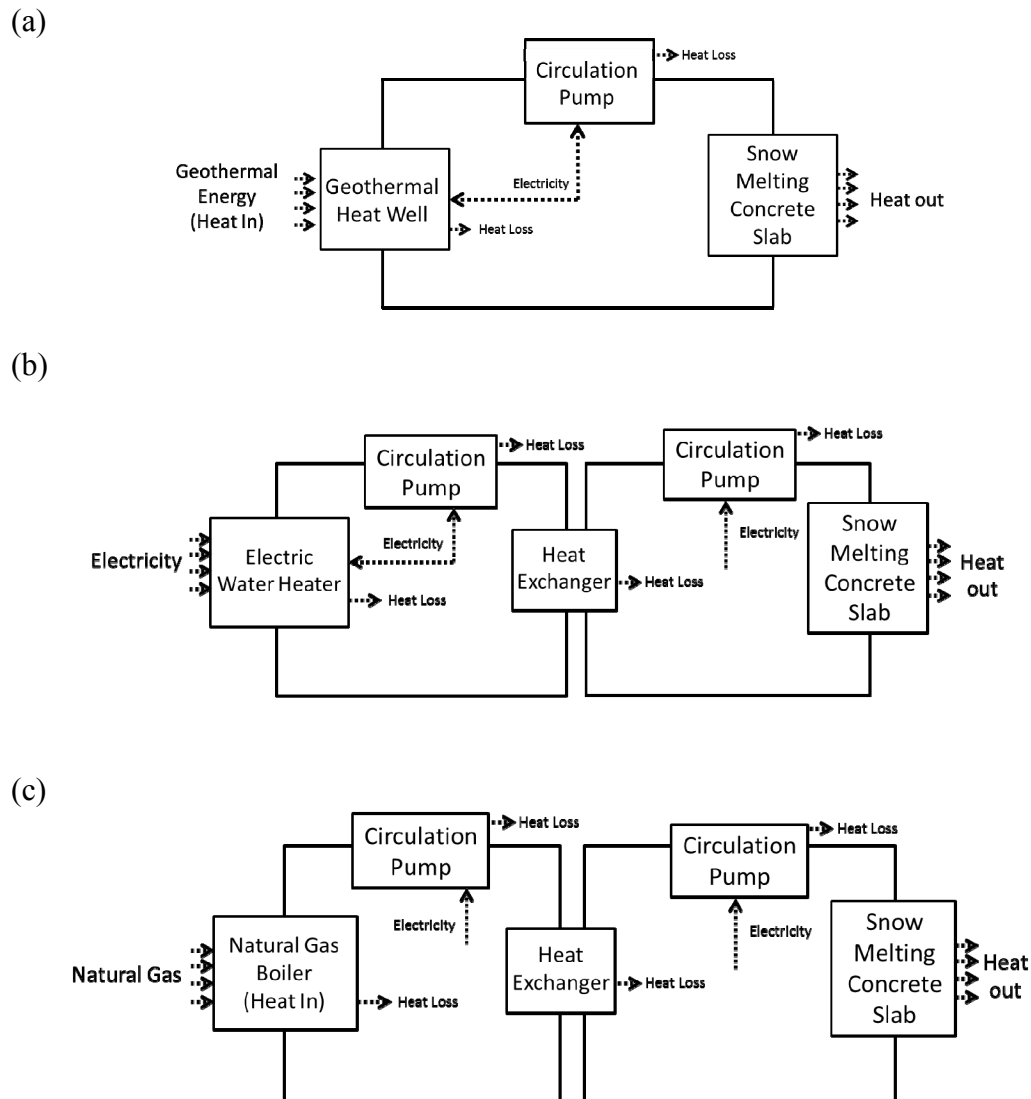


FIG. 2. Airport gate area snow removal system models: (a) HHPS-G, (b) HHPS-E, (c) HHPS-NG.

ANALYSIS RESULTS

Total Energy Consumption of System Operation

The calculated heat energy requirements for snow melting under different snow rates by using Equations (1) are $1.83 \text{ MJ/h}\cdot\text{m}^2$, $2.04 \text{ MJ/h}\cdot\text{m}^2$, $2.35 \text{ MJ/h}\cdot\text{m}^2$, $2.84 \text{ MJ/h}\cdot\text{m}^2$, and $3.42 \text{ MJ/h}\cdot\text{m}^2$, respectively, as considering 20% back and edge heat losses (ASHRAE 2003). Applying values of circulating solution flow rate and total head drop, $134 \text{ m}^3/\text{h}$ and 38 m of head, energy consumption for a circulating pump is about 14.17 kW by using Equation (2). Based on the assumptions and energy balance under the system boundaries, total energy consumptions of operating different heated pavement systems for different snow rate conditions are shown in Table 1.

Table 1 demonstrates that HHPS-G requires about 4 to 5 times less energy than HHPS-E and 6 to 8 times less than HHPS-NG under different snow rate conditions as applied in the same area of apron. More energy is required for geothermal heat pump operation in HHPS-G under low COP condition. Geothermal heat pump COP is highly related to soil conditions and the heat pump appliance, so ground-heating conditions should be evaluated before applying HHPS-G. HHPS-E has lower Energy consumption than HHPS-NG since electric water heater in HHPS-E has a higher efficiency for water heating than natural gas boiler in HHPS-NG.

Table 1. Total Energy Consumption of HHPSs

Snow removal System	Snow Rate (mm/h)	Total Energy Consumption (kWh/h)	
		Coefficient of Performance (COP)	
		Minimum ¹	Maximum ²
HHPS-G	50.8	717	486
	38.1	599	407
	25.4	501	342
	19.1	438	300
	12.7	393	270
HHPS-E	50.8	2,709	
	38.1	2,256	
	25.4	1,880	
	19.1	1,638	
	12.7	1,465	
HHPS-NG	50.8	4,040	
	38.1	3,360	
	25.4	2,796	
	19.1	2,434	
	12.7	2,175	

Note. ¹Minimum COP = 2.4, ²Maximum COP = 3.6

Greenhouse Gas Emission from System Operation

Energy source used for operating HHPS-G is electricity and GHG emissions from the system are released from the power generation facility. Thus, the sum of the GHG releases from the energy production phase has been calculated as the total GHG emissions from HHPS-G life cycle, which is shown in FIG. 1(a).

Heating source of HHPS-E is supplied by electric water heater. For HHPS-E operation life cycle phase, electricity is used for circulating heated water and anti-freeze solution (see FIG. 2(b)). Similar to the GHG emissions from HHPS-G life cycle, there is no GHG directly released from system operation. Thus, the sum of the GHG releases from the energy production phase has been calculated as the total GHG emissions from HHPS with electric water heater. HHPS-NG uses natural gas boiler for heating. For HHPS-NG operation life cycle phase (see FIG. 2(c)), GHG releases from both the natural gas based electricity power plant and the natural gas combustion inside boiler system. So, GHG is released from both energy production phase and operation phase of HHPS-NG operation life cycle phase.

In energy production stage for three HHPS types, natural gas based electricity power plant life cycle phases include natural gas extraction, natural gas pretreatment and transportation, and grid electricity production (NETL 2000). The GHG emissions of electricity power plant using natural gas was estimated to 0.42 kgCO₂eq/kWh (Shen et al. 2015). Natural gas combustion emission factor is 0.181 kgCO₂eq/kWh (EIA 2013) and natural gas facility has an emission factor of 0.004 kgCO₂eq/kWh for natural gas production (NETL 2000). So the total emission factor of natural gas boiler operation in HHPS-NG is 0.185 kgCO₂eq/kWh. Based on different weather conditions, the GHG emissions of HHPS-G, HHPS-E and HHPS -NG airport gate area snow removal applications are shown in Table 2.

Table 2. GHG Emissions from HHPSs

Snow removal System	Snow Rate (mm/h)	GHG Emissions (kgCO ₂ /h)	
		Coefficient of Performance (COP)	
		Minimum ¹	Maximum ²
HHPS-G	50.8	303	205
	38.1	253	172
	25.4	211	144
	19.1	185	127
	12.7	166	114
HHPS-E	50.8	1,140	
	38.1	949	
	25.4	790	
	19.1	688	
	12.7	615	
HHPS-NG	50.8	757	
	38.1	631	
	25.4	526	
	19.1	459	
	12.7	411	

Note. ¹Minimum COP = 2.4, ²Maximim COP = 3.6

Table 2 demonstrates that as the snow rate increases, more GHG is released from the operation of heated pavement system. HHPS-G has lower GHG emissions than HHPS-E and HHPS-NG in this study. Between HHPS-E and HHPS-NG, HHPS-NG has much lower GHG emissions.

Operating Cost

The 2014 Iowa commercial electricity price is 0.1 \$/kWh (EIA 2014a) and natural gas price is about 0.0167\$/kWh (EIA 2014b). By using given price information, operating cost of HHPS-G, HHPS-E, and HHPS-NG are estimated and presented in Table 3. HHPS-G has a lower operation cost than HHPS-E and a comparable operation cost to HHPS-NG.

Table 3. Operating Costs of HHPSs

Snow removal System	Snow Rate (mm/h)	Operating Cost (\$/h)	
		Coefficient of Performance (COP)	
		Minimum ¹	Maximum ²
HHPS-G	50.8	75	51
	38.1	63	43
	25.4	53	36
	19.1	46	31
	12.7	41	28
HHPS-E	50.8	283	
	38.1	236	
	25.4	196	
	19.1	171	
	12.7	153	
HHPS-NG	50.8	67	
	38.1	56	
	25.4	47	
	19.1	40	
	12.7	36	

Note. ¹Minimum COP = 2.4, ²Maximum COP = 3.6

CONCLUSIONS

The operations of three alternative heated pavement systems in airport apron have been analyzed to evaluate the sustainability of such systems. As the analyses for different snow removal system operations demonstrate, several different factors such as snow rates and system efficiencies could affect the sustainability of system operations, and these factors vary among the three types of system operations. While the snow rate is higher or the system efficiencies is lower, the heated pavement systems require more energy which causes more Greenhouse Gas (GHG) emissions and higher operating costs. Among the three alternative heated pavement systems evaluated, hydronic heated pavement system using geothermal heat pump (HHPS-G) results in lesser energy consumption, fewer GHG emissions, and lower or comparable operation costs under the same snow rate conditions.

ACKNOWLEDGEMENTS

This paper was prepared from a study conducted at Iowa State University under the Federal Aviation Administration (FAA) Air Transportation Center of Excellence Cooperative Agreement 12-C-GA-ISU for the Partnership to Enhance General Aviation Safety, Accessibility and Sustainability (PEGASAS). The authors would like to thank the current project FAA Technical Monitor, Mr. Benjamin J. Mahaffay, and the former project FAA Technical Monitors, Mr. Jeffrey Gagnon, Dr. Charles A. Ishee, and Mr. Donald Barbagallo for their invaluable guidance on this study. Although the FAA has sponsored this project, it neither endorses nor rejects the findings of this research. The presentation of this information is in the interest of invoking comments by the technical community on the results and conclusions of the research.

REFERENCES

- American Council for an Energy-Efficient Economy. (2012). “Water heating.” <<http://www.aceee.org/consumer/water-heating>> (Jan 14, 2015).
- American Society of Heating, Refrigerating and Air-Conditioning Research (ASHRAE). (2003). “HVAC applications – chapter 50. Snow melting and freeze protection.” *ASHRAE Handbook*, Atlanta, GA, pp. 50.1 – 50.20.
- Energy Information Administration (EIA). (2013). “Carbon dioxide emissions coefficients.” <http://www.eia.gov/environment/emissions/co2_vol_mass.cfm> (Feb. 20, 2015).
- Energy Information Administration (EIA). (2014a). “Table 5.6.A. average retail price of electricity to ultimate customers by end-use sector.” <http://www.eia.gov/electricity/monthly/epm_table_grapher.cfm?t=epmt_5_6_a> (Nov. 2, 2014).
- Energy Information Administration (EIA). (2014b). “Natural gas prices.” <http://www.eia.gov/dnav/ng/ng_pri_sum_dcu_nus_m.htm> (Nov. 2, 2014).
- Energy Star. (2012). “Geothermal heat pumps key product criteria.” <https://www.energystar.gov/index.cfm?c=geo_heat.pr_crit_geo_heat_pumps> (Jan. 14, 2015).
- Federal Aviation Administration (FAA). (2008). *Airport winter safety and operations*, Publication FAA 150/5200-30C, Washington, DC.
- Kreith, F. and Goswami, D. Y. (2001). *Energy management and conservation handbook*, CRC Press, Boca Raton, FL.
- National Energy Technology Laboratory (NETL). (2000). *Life cycle analysis: natural gas combined cycle (NGCC) power plant*, Publication DOE/NETL-403/110509, Pittsburgh, PA.
- Robert, H., Francis, M., Villiam, S., and Seth, Y. (2010). *Planning and design of airport*, McGraw Hill Professional, NY.
- Shen, W., Gopalakrishnan, K., Kim, S., and Ceylan, H. (2015). “Assessment of greenhouse gas emissions from geothermal heated airport pavement system.” *International Journal of Pavement Research and Technology*, 8(4), 233 - 242.
- The Canadian Renewable Energy Network. (2002). “Commercial earth energy systems: a buyer’s guide.” <<http://publications.gc.ca/collections/Collection/M92-251-2002E.pdf>> (Nov. 20, 2014).
- Viega. 2015. “S-no-Ice[®] snow melting system installation manual, IM-SNO-01/05.” <http://www.viega.us/xbcr/en-us/Viega_S-no-ice_Snow_Melting_System.pdf> (Feb. 25, 2015).
- Wilco. 2009. “Circulating pumps.” <http://www.majo.rs/page_files/page_97/A1-Glandless%20Pumps%20-%202009.pdf> (Feb. 25, 2015).

Characterization of Cement Treated Base Course Using Reclaimed Asphalt Pavement, Aggregate By-Products, and Macro-Synthetic Fibers

Jeffrey R. LaHucik, S.M.ASCE¹; Scott R. Schmidt, S.M.ASCE²; Erol Tutumluer, M.ASCE³; and Jeffery R. Roesler, M.ASCE⁴

¹Graduate Research Assistant. E-mail: lahucik2@illinois.edu

²Graduate Research Assistant. E-mail: schmid61@illinois.edu

³Professor (corresponding author). E-mail: tutumlue@illinois.edu

⁴Professor. E-mail: jroesler@illinois.edu

Dept. of Civil and Environmental Engineering, Univ. of Illinois at Urbana-Champaign, 205 North Mathews Ave., Urbana, IL 61801.

Abstract: This study addresses the feasibility of using coarse fractionated reclaimed asphalt pavement (FRAP), quarry by-products (QB), and macro-synthetic fibers in a cement-stabilized base course application that can be used for inverted pavements or simply as a stronger, more durable base course. The addition of macro-synthetic fibers is studied to add flexural ductility and resistance to crack propagation to the stabilized base course. The use of recycled and by-product aggregates that would otherwise be stockpiled, could improve the durability and permanence of the base course, and reduce surface course thicknesses. Laboratory characterization includes testing flexural toughness and fracture properties. Study results have confirmed more than sufficient mechanical properties are achieved relative to other stabilized base courses. Furthermore, the addition of fibers clearly increases the flexural capacity and fracture properties of the cement treated FRAP and quarry by-product base course mixes. While current pavement design procedures do not account for fracture properties or the effects of fibers (especially in cement stabilized base courses), it is clear that these parameters show trends that conventional strength testing (compressive and flexural) does not and therefore, they should be accounted for in design.

INTRODUCTION

The increasing emphasis within the construction industry on sustainability is leading to increasing use of recycled aggregates in pavement layers. The use of reclaimed asphalt pavement (RAP) is becoming increasingly popular with asphalt producers due to the ability to offset a fraction of virgin asphalt binder with that from the RAP aggregates. In order to maximize the amount of asphalt binder replacement,

asphalt producers almost exclusively use the fine fraction (i.e. passing the 4.75 mm or No. 4 sieve). Therefore, large stockpiles of the coarse fraction of RAP (FRAP) are created. While the use of RAP as an aggregate source is a sustainable practice, this then requires virgin aggregate producers to supply aggregates with reduced fines contents (to offset the fines contents from the RAP). Quarry byproducts (QB), the finer portion (generally passing the 4.75 mm sieve) of mined aggregates, currently comprise 8% of mined aggregates with few applications for their use (Hou et al. 2015). The use of RAP or QB in pavement layers has previously been studied by many researchers (Garg and Thompson, 1996; Taha et al. 2002; Puppala et al. 2008; Puppala et al. 2012; Rezende et al. 2014; Mwumvaneza et al. 2015), however, the use of either of these recycled/marginal materials in cement-treated foundation layers has been somewhat limited, especially the use of QB.

While cement treated foundation layers increase strength, stiffness, and reduce rutting potential, relative to unbound aggregates, they also increase the brittleness of the material. This increased brittleness leads to shrinkage cracking, fatigue cracking from mechanical loading, and potentially other cracking from environmental distresses (i.e. freezing and thawing). It is well known that reflective cracking of hot mix asphalt (HMA) is a common issue when paved on top of a cement treated layer (Mushota et al. 2014). The use of fibers in cement treated layers has been shown to maintain tighter crack widths (Grilli et al. 2012); fibers have also been shown to reduce cracking severity of concrete pavements (Roesler et al. 2012). By maintaining tighter crack widths and reducing the severity of cracking, fiber-reinforced cement treated layers have the potential to reduce the severity of reflective cracking. In addition to reducing cracking severity, fibers have also been shown to increase the fatigue life of cement treated layers as well as concrete pavements (Johnston and Zemp, 1991; Matsumoto and Li, 1999; Cervantes and Roesler, 2009; Sobhan and Krizek, 1999).

This paper investigates the effects of cement content (2–4% by volume) and the use of macro-synthetic fibers (0.4% by volume) on the mechanical properties of a cement treated base course constructed with recycled FRAP and quarry byproducts. Laboratory characterization efforts include testing for strength (compressive, split tensile, and flexural), drying shrinkage, fracture, and flexural toughness properties. Statistical differences in mechanical properties amongst the different mix designs are presented. The addition of fibers is highlighted to increase the flexural capacity, split tensile strength, and fracture properties of the cement treated FRAP and QB base course mixes.

MATERIALS AND MIXTURE DESIGN

Three aggregate sources were utilized in this study: quarry byproducts (QB), coarse fractionated reclaimed asphalt pavement (FRAP), and a dolomitic limestone (coarse and intermediate size fractions). Extensive materials characterization of the QB and FRAP can be found in Mwumvaneza et al. (2015) and Brand and Roesler (2015). The coarse and intermediate size fractions dolomite were used to replace the FRAP for a control mixture. The fiber used in this study was an embossed polymer fiber with a length of 50 mm, elastic modulus of 7 GPa, and tensile strength of 550 MPa. This

synthetic fiber was chosen based on its length (50 mm), which has been shown to be the optimal length with regards to mechanical properties of cement treated layers (Sobhan and Mashnad, 2001).

It is well known that the density of cement treated layers has a large influence on mechanical properties (Xuan et al. 2012); therefore, aggregate packing tests were conducted, according to ASTM C29 (1997), to determine the blend of aggregates that yielded the maximum density. It was found that 70% QB and 30% FRAP yielded the maximum attainable packing density. For the control mixtures with dolomite, coarse and intermediate size fractions of the dolomite were blended to yield a gradation equivalent to that of the FRAP. Using these aggregate blends, six mixtures were designed to address the three variables of this study: virgin vs. FRAP aggregate, cement content (2, 3, 4% by volume), and fiber content (0% and 0.4% by volume). The naming convention for the mixtures consists of three characters; the first character is the cement content (% by volume), the second character indicates recycled or virgin coarse aggregate (R for FRAP and V for virgin dolomite), and the third character represents the presence of fibers (F for 0.4% and N for no fiber or 0%). For example, mix 2RF represents a mixture with 2% cement, recycled coarse aggregate (i.e. FRAP), and fibers (0.4% volume dosage).

Modified Proctor type compaction testing (ASTM D1557, 2012) was performed to determine the moisture-density relationship for each mixture. The maximum dry density (MDD) and optimum moisture content (OMC) of each mixture were used to determine the final mixture proportions as given in Table 1. Further details of the mixture design procedure as well as strength and elastic modulus test results of these mixtures can be found in LaHucik et al. (2016).

Table 1. Mixture Proportions

	2RF	3RF	4RF	4RN	4VF	4VN
Fibers (kg/m³)	3.64	3.64	3.64	-	3.64	-
Cement (kg/m³)	62.9	94.3	125.8	125.8	125.8	125.8
FRAP (kg/m³)	647.9	648.5	638.4	647.3	-	-
Coarse Dolomite (kg/m³)	-	-	-	-	471.7	474.0
Intermediate Dolomite (kg/m³)	-	-	-	-	202.3	203.5
QB (kg/m³)	1,577.0	1,578.2	1,554.4	1,575.2	1,565.1	1,574.0
Water (kg/m³)	151.9	148.3	152.5	147.1	154.9	148.3

1 kg/m³ = 1.686 lb/yd³; (-) means Not Applicable.

FLEXURAL PERFORMANCE TESTING

Flexural performance testing, according to ASTM C1609 (2010), was performed at an age of 14 days on 150 x 150 x 525 mm beam specimens. The beams were tested in four point (third-point) bending using a closed-loop servo-hydraulic load frame along with unlimited travel rollers to reduce friction between the beam and the rollers. The test setup for flexural performance testing is shown in Figure 1. The deflection rates suggested by ASTM C1609 (2010) have been shown to cause premature failure (Banthia and Islam, 2013) and thus modified (slower) deflection rates suggested by

Banthia and Islam (2013) were used. Using a linear variable differential transformer (LVDT) to measure vertical deflection, the tests were run in deflection control up to a net deflection of 3 mm which corresponds to $L/150$ where L represents the span length (450 mm).

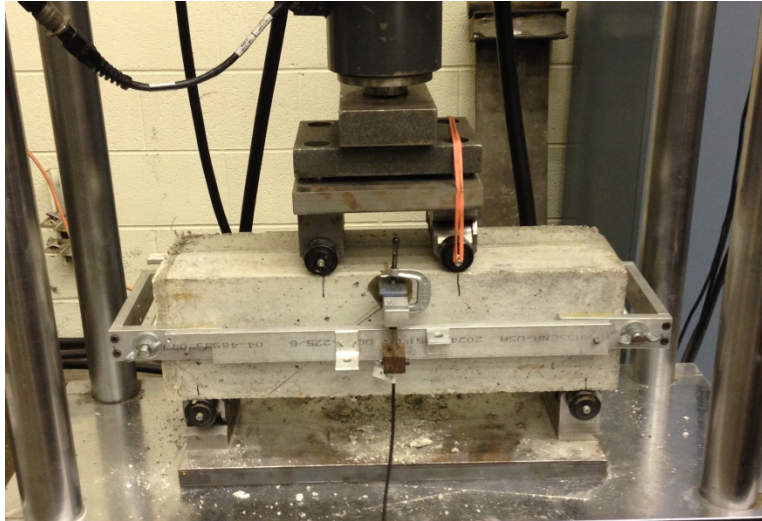


FIG. 1. Flexural Performance Test Setup

The reported properties from the flexural performance testing are peak flexural strength (MOR , MPa), residual flexural strengths corresponding to loads at deflections of $L/600$ and $L/150$ (F_{600} and F_{150} , MPa), respectively, flexural toughness (T_{150} , N-m), and equivalent flexural strength ratio ($R_{T,150}$, %). The peak flexural strength or modulus of rupture, MOR , is computed using Equation 1:

$$MOR = \frac{P \cdot L}{b \cdot d^2} \quad (1)$$

where P represents the peak load (N), L represents the span length (mm), b represents the width of the beam (mm), and d represents the depth of the beam (mm). Residual flexural strengths, F_{600} and F_{150} , are also calculated using Equation 1 by replacing the peak load with the load corresponding to deflections of $L/600$ and $L/150$, respectively. Flexural toughness is calculated by integrating the area under the load-deflection curve up to a deflection of 3 mm. The equivalent flexural strength ratio takes into account flexural toughness and is calculated using Equation 2.

$$R_{T,150} = \frac{150 \cdot T_{150}}{MOR \cdot b \cdot d^2} \cdot 100\% \quad (2)$$

Figure 2 shows load-deflection curves for each mix containing fibers; mixes without fibers are not shown since deflection was not measured due to catastrophic failure of the specimens upon reaching their peak loads which would have caused damage to the LVDT. From Figure 2, the inclusion of fibers produces a quasi-brittle response

with measurable flexural toughness. Note that virgin and FRAP mixtures yield similar load-deflection curves.

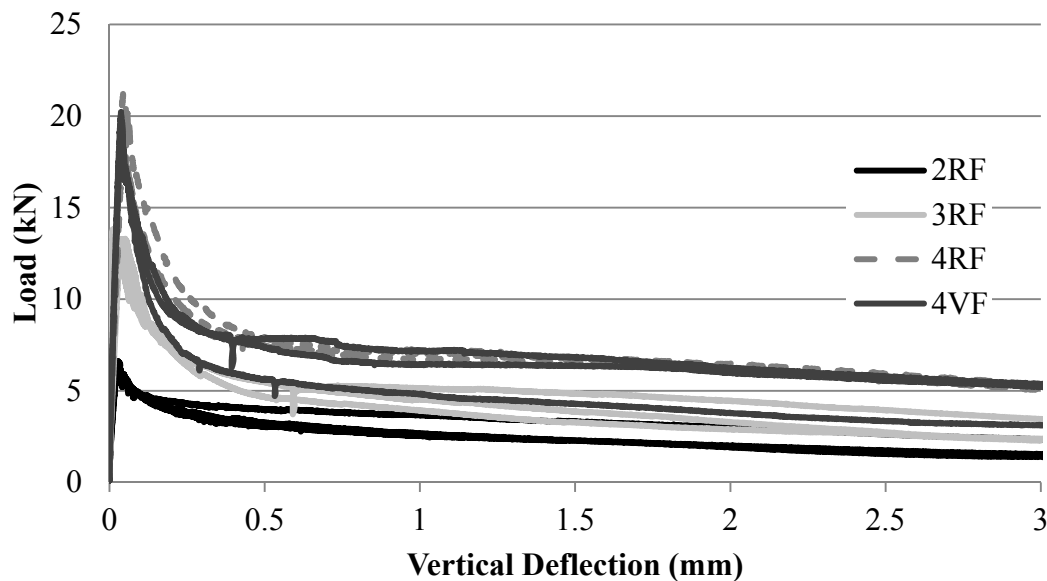


FIG. 2. Load vs. Deflection Curves for the Fiber-Reinforced Mixtures

Results, along with coefficients of variation (COV), from flexural performance testing are presented in Table 2 with the values given as averages of the three beam specimens tested. Increasing cement content led to significantly greater values of peak flexural strength, residual flexural strength, and flexural toughness. And, cement content did not have a statistically significant effect on equivalent flexural strength ratio. As expected, the inclusion of fibers did not have a significant effect on the peak flexural strength. Virgin and FRAP mixtures yielded similar peak and residual strengths, toughness values, and equivalent flexural strength ratios. The peak flexural strengths of the 4% cement mixtures were similar to those from Greene et al. (2011) for lean concrete bases.

Table 2. Flexural Performance Testing Results (COV, %)

	<i>MOR</i> , MPa	<i>F</i> ₆₀₀ , MPa	<i>F</i> ₁₅₀ , MPa	<i>T</i> ₁₅₀ , N-m	<i>R</i> _{<i>T</i>,150} , %
2RF	0.75 (4.0)	0.35 (13.9)	0.20 (22.0)	8.5 (15.5)	43.7 (18.4)
3RF	1.75 (1.8)	0.60 (8.2)	0.35 (19.8)	13.5 (11.0)	32.5 (11.6)
4RF	2.40 (1.7)	0.85 (0.8)	0.60 (1.9)	21.5 (1.2)	34.3 (2.0)
4RN	2.45 (5.8)	N/A	N/A	N/A	N/A
4VF	2.30 (1.2)	0.75 (15.3)	0.55 (23.1)	19.0 (16.1)	31.7 (17.8)
4VN	2.85 (4.8)	N/A	N/A	N/A	N/A

1 MPa = 145 psi; 1 N-m = 8.85 lb-in. N/A signifies not applicable.

Since all layers in a pavement structure experience tensile stresses as a result of loading and/or environmental conditions (Huang, 2004), flexural strength is a key

parameter for the design of rigid (i.e. concrete) pavements and cement-treated layers. It has been shown in this study and in the literature that the flexural strength is not statistically increased by the inclusion of fibers, therefore suggesting that the use of fibers is not beneficial. However, it has been shown that the inclusion of fibers in concrete and cement-treated layers has led to improved fatigue life (Johnston and Zemp, 1991; Matsumoto and Li, 1999; Cervantes and Roesler, 2009; Sobhan and Krizek, 1999) as well as improved slab capacities for concrete pavements (Roesler et al, 2004). Therefore, the use of an adjusted flexural strength (effective modulus of rupture, MOR') has been suggested to account for the increase in fatigue life with the inclusion of fibers (Bordelon and Roesler, 2009; Altoubat et al, 2008). The effective modulus of rupture (MOR' , MPa) takes into account the equivalent flexural strength ratio, which also accounts for the flexural toughness, and is calculated using Equation 3 as follows:

$$MOR' = MOR \cdot \left(1 + \frac{R_{T,150}}{100}\right) \quad (3)$$

For the pavement design example given by Altoubat et al. (2008), a concrete thickness reduction of 17% was observed when using a fiber type/dosage that yielded an equivalent flexural strength ratio of 30%; all of the fiber-reinforced mixtures presented in this study yielded equivalent flexural strength ratios greater than 30%. Therefore, the inclusion of fibers in this cement-treated layer will either: (1) reduce required thickness for a design fatigue/service life, or (2) increase the fatigue/service life for a similar thickness to a non-fiber mixture.

FRACTURE TESTING

Fracture testing was performed at an age of 28 days according to the procedure set forth by Amirkhani et al. (2014) for the disk-shaped compact tension (DCT) geometry. Specimens were fabricated from a 150 x 300 mm cylinder which was compacted according to ASTM C1435 (2008). Due to insufficient strength to withstand the saw-cutting and coring required for DCT specimen preparation, mix 2RF was not tested. In general, specimens were loaded at a crack-mouth opening displacement (CMOD) rate of 0.06 mm/min until the specimen reached a peak load after which the specimen was unloaded. Upon unloading to the original seating load, the specimen was reloaded at the initial CMOD rate until failure. For specimens without fibers (i.e. 4RN and 4VN), failure was defined as reaching a load of 0.1 kN or breaking of the specimen whereas specimens containing fibers (i.e. 3RF, 4RF, and 4VF) were unable to reach this load within the constraints of the test setup. The clip gauge used to measure CMOD has a maximum opening of 6.35 mm; therefore the test was stopped at a CMOD of 5 mm for specimens with fibers. The test setup for DCT fracture testing is shown in Figure 3. The fracture properties reported are: critical stress intensity factor (K_{IC}), critical crack tip opening displacement ($CTOD_C$), initial fracture energy (G_f), and total fracture energy (G_F). Figures 4 and 5 show the load-CMOD curves from the fiber and non-fiber mixtures, respectively. Fracture testing results, which represent an average of four or five specimens, are shown in Table 3 along with their coefficients of variation (COV).



FIG. 3. DCT Fracture Test Setup

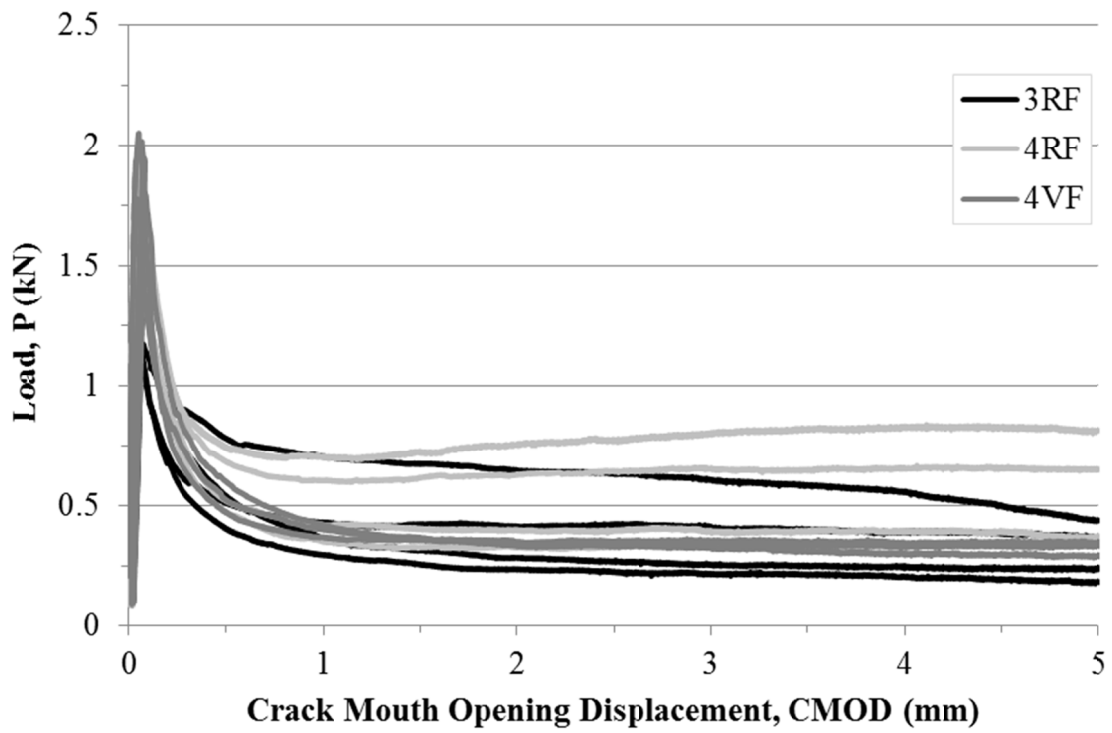


FIG. 4. Load vs. CMOD Curves for Fiber-Reinforced Mixtures

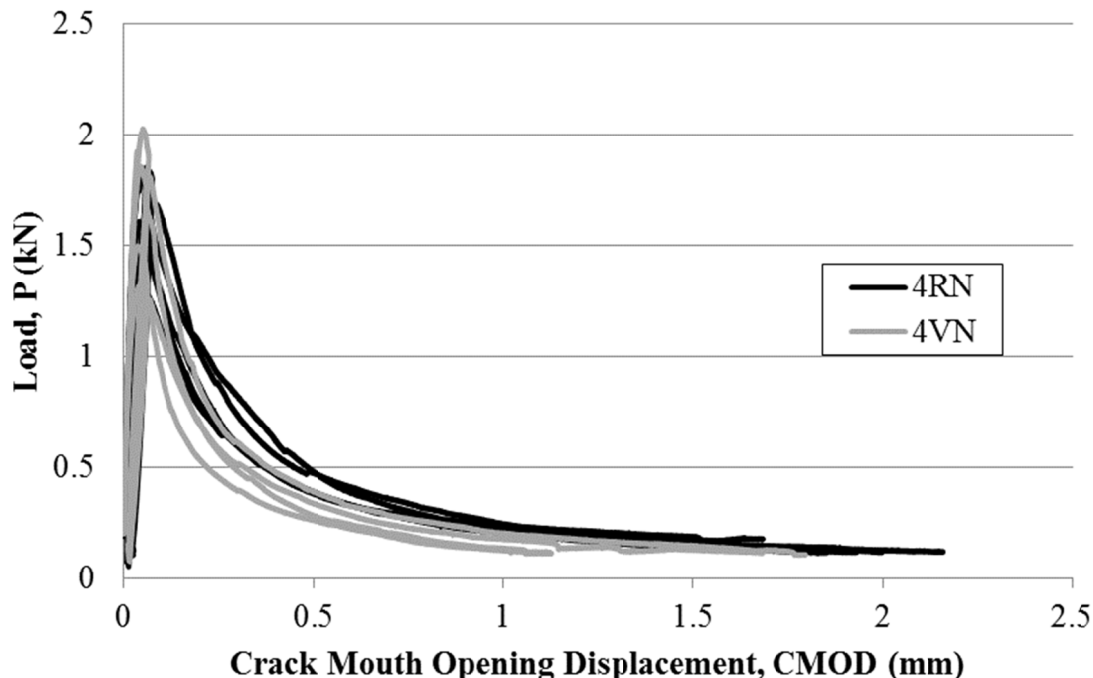


FIG. 5. Load vs. CMOD Curves for Non-Fiber Mixtures

Table 3. DCT Fracture Testing Results (COV, %).

	K_{IC} , MPa-m ^{1/2}	$CTOD_C$ (mm)	G_f (N/m)	G_F (N/m)*
3RF	0.581 (12.1)	0.0145 (16.1)	17.5 (21.3)	515.5 (38.0)
4RF	0.813 (10.6)	0.0159 (16.8)	25.2 (17.9)	698.4 (33.1)
4RN	0.752 (13.9)	0.0147 (17.3)	22.9 (23.2)	178.5 (12.5)
4VF	0.965 (13.8)	0.0195 (20.6)	34.1 (25.3)	522.8 (3.9)
4VN	0.847 (12.3)	0.0189 (12.6)	28.4 (18.7)	131.6 (23.8)

*Total fracture energy for fiber mixes represents fracture energy up to a CMOD of 5 mm.

From Figures 4 and 5 it can be seen that the two non-fiber mixes yielded similar load-CMOD plots while mix 4RF showed a better post-peak load response than mix 4VF. Figure 4 indicates that none of the fiber mixes have reached a load of 0.1 kN even after 5 mm of CMOD. The critical stress intensity factor (K_{IC}), which is a measure of a material's initial cracking resistance, for each of the mixes containing 4% cement was statistically greater (confidence limit of 95%) than that of the mix containing 3% cement. Hou et al. (2011) showed the opposite trend for K_{IC} (i.e. increasing cement content reduced K_{IC}) of cement treated aggregate at cement contents greater than 4% and a testing age of 60 days. Virgin and FRAP mixes yielded statistically similar values of K_{IC} which has also been shown by Brand and Roesler (2015) for concrete containing FRAP. Increasing cement content from 3% to

4% did not result in a statistical increase in total fracture energy (G_F). As shown by Brand and Roesler (2015), the virgin and FRAP mixtures did not yield statistically different values of G_F . The inclusion of fibers did not produce statistically different values of K_{IC} , G_f , or $CTOD_C$ which has been shown by Roesler et al. (2007). The inclusion of fibers yielded statistically greater values of G_F compared to non-fiber mixes which is supported by fiber-reinforced concrete literature (Harris et al., 1972; Cha et al., 1997; Roesler et al., 2007).

CONCLUSIONS

This study characterized the fracture and flexural performance properties of lightly cemented foundation layers (cement contents of 2, 3, and 4% by volume) containing macro-synthetic fibers (volume dosage of 0.4%). The aggregate blend consisted of 70% quarry byproducts (QB) and either 30% coarse fractionated reclaimed asphalt pavement (FRAP) or 30% virgin coarse aggregate. Flexural performance testing showed that the inclusion of fibers resulted in a quasi-brittle response with measurable flexural toughness and significantly greater fracture energy than non-fiber mixtures. Virgin and FRAP mixtures yielded similar flexural and fracture properties. In general, fracture and flexural performance properties improved as cement content increased. Regardless of cement content and aggregate type (i.e. FRAP vs. virgin), all fiber-reinforced mixtures in this study yielded equivalent flexural strength ratios greater than 30%. The inclusion of fibers yields residual shear capacity which will maintain load transfer across joints or cracks as well as improved fatigue resistance. These results show that use of macro-synthetic fibers with recycled and by-product aggregates (FRAP and QB, respectively) for lightly cement treated layers not only increases the fatigue life, but will also maintain tighter cracks which can reduce reflective cracking of overlying pavement layers.

ACKNOWLEDGEMENTS

The authors would like to thank W.R. Grace and Co. for supplying the fibers, Hanson Materials Services for supplying the quarry byproducts, as well as the Illinois Tollway Authority for supplying the fractionated reclaimed asphalt pavement. The authors would also like to thank Mr. Don Marrow for his assistance with the flexural performance testing. The contents of this paper reflect the views of the authors, who are responsible for the facts and the accuracy of the data presented herein. This paper does not constitute a standard, specification, or regulation.

REFERENCES

- Altoubat, S., J. Roesler, D. Lange, and K.A. Rieder. (2006). "Simplified method for concrete pavement design with discrete structural fibers." *Construction and Building Materials* 22, Elsevier Ltd.: 384-393.
- Amirkhanian, A., D. Spring, J. Roesler, and G. Paulino. (2014). "Forward and Inverse Analysis of Concrete Fracture using the Disk-Shaped Compact Tension Test." *Journal of Testing and Evaluation, ASTM*. Accepted for publication.

- Banthia, N. and S. Islam. (2013). "Loading Rate Concerns in ASTM C1609." *Journal of Testing and Evaluation* 41(6), ASTM. West Conshohocken, PA: 1-5.
- Bordelon, A. and J. Roesler. (2009). "Fiber-Reinforced Concrete Pavement Design and Material Requirements." *8th International Conference on the Bearing Capacity of Roads, Railways, and Airfield*
- Brand, A. and J. Roesler. (2015). "Ternary Concrete with Fractionated Reclaimed Asphalt Pavement." *ACI Materials Journal* 112-1 Jan.-Feb. 2015. Title No. 112-M17.
- Cervantes, V. and J. Roesler. (2009). "Performance of Concrete Pavements with Optimized Slab Geometry." *Illinois Center for Transportation Research Report*. ICT-09-053.
- Cha, Y.H., K.S. Kim, and D.J. Kim. (1998). "Evaluation of the Fracture Toughness and Strength of Fiber Reinforced Brittle Matrix Composites." *KSME International Journal*, 12-3: 370-379.
- Garg, N., and M. Thompson. (1996) "Lincoln Avenue Reclaimed Asphalt Pavement Base Project." *Transportation Research Record: Journal of the Transportation Research Board*, No 1547, Transportation Research Board of the National Academies, Washington, D.C.: 89-95.
- Green, J., A. Nazef, and B. Choubane. (2011). "Thirty-Year Performance Evaluation of Two-Layer Concrete Pavement System." *Transportation Research Record: Journal of the Transportation Research Board* No. 2226, Transportation Research Board of the National Academies, Washington D.C.: 21-29.
- Grilli, A., M. Bocci, and A.M. Tarantino. (2013). "Experimental Investigation on Fiber-Reinforced Cement-Treated Materials Using Reclaimed Asphalt." *Construction and Building Materials* 38: 491-496.
- Harris, B., J. Varlow, and C. Ellis. (1972). "The Fracture Behavior of Fiber Reinforced Concrete." *Cement and Concrete Research*, Vol. 2, Pergamon Press: 447-461.
- Huang, Y. (2004). "Pavement Analysis and Design." *Pearson Prentice Hall*, 2nd ed., Upper Saddle River, NJ.
- Hou, W., V. Mwumvaneza, H. Ozer, and E. Tutumluer. (2015). "Sustainable Practices of Aggregate Production in the U.S. Using a Life-Cycle Inventory Assessment Approach." *Airfield and Highway Pavements 2015*, ASCE 2015: 813-824.
- Hou, X., P. Zhang, and M. Zhang. (2011). "Study on Fracture Toughness of Cement Treated Aggregate." *Advanced Materials Research*, Vol. 280. Trans Tech Publications, Switzerland: 76-79.
- Johnston, C. and R. Zemp. (1991). "Flexural Fatigue Performance of Steel Fiber Reinforced Concrete-Influence of Fiber Content, Aspect Ratio, and Type." *ACI Materials Journal*, Vol. 88, Title No. 88-M44. American Concrete Institute: 374-383.
- LaHucik, J., S. Schmidt, S., E. Tutumluer, E., and J.R. Roesler. (2016). "Cement Treated Bases Containing Reclaimed Asphalt Pavement, Quarry Byproducts, and Fibers," Submitted for presentation and publication at the 95th Annual Meeting of the Transportation Research Board, Washington, D.C., January 2016.
- Lanzoni, L, A. Nobili, and A. Tarantino. (2012). "Performance Evaluation of a Polypropylene-Base Draw-Wired Fibre for Concrete Structures." *Construction and Building Materials* 28. Elsevier: 798-806.

- Matsumoto, T. and V. Li. (1999). "Fatigue Life Analysis of Fiber Reinforced Concrete with a Fracture Mechanics Based Model." *Cement & Concrete Composites* 21. Elsevier: 249-261.
- Mushota, C., M. Mwale, G. Mutembo, M. Muya, and L. Walubita. (2014). "Reflective Cracking on Cement Treated Base (CTB) Pavements in Zambia: An Analytical Study." *Application of Nanotechnology in Pavements, Geological Disasters, and Foundation Settlement Control Technology*. ASCE: 62-69.
- Mwumvaneza, V., W. Hou, H. Ozer, E. Tutumluer, I. Al-Qadi, and S. Beshears. (2015). "Characterization and Stabilization of Quarry Byproducts for Sustainable Pavement Applications." *Transportation Research Board 94th Annual Meeting 15-4464*, Transportation Research Board, Washington, D.C.: 17.
- Puppala, Anand J., S. Saride, and R. Williammee. (2012). "Sustainable Reuse of Limestone Quarry Fines and RAP in Pavement Base/Subbase Layers." *Journal of Materials in Civil Engineering* 24(4), ASCE 2012: 418-29.
- Rezende, L., L. Silveira, W. Araújo, and M. Luz. (2014). "Reuse of Fine Quarry Wastes in Pavement: Case Study in Brazil." *Journal of Materials in Civil Engineering*, 26(8). ASCE 2014: Case Study.
- Roesler, J., V. Cervantes, and A. Amirkhanian. (2011). "Accelerated Performance Testing of Concrete Pavement with Short Slabs." *International Journal of Pavement Engineering*, 13:6, 494-507.
- Roesler, J, D. Lange, S. Altoubat, K. Rieder, and G. Ulreich. (2004). "Fracture of Plain and Fiber-Reinforced Concrete Slabs under Monotonic Loading." *Journal of Materials in Civil Engineering, Sept/Oct.* ASCE: 452-460.
- Roesler, J., G. Paulino, C. Gaedicke, A. Bordelon, and K. Park. (2007). "Fracture Behavior of Functionally Graded Concrete Materials for Rigid Pavements." *Transportation Research Record: Journal of the Transportation Research Board No. 2037*, Transportation Research Board of the National Academies, Washington D.C.: 40-49.
- Puppala, A.J., S. Saride, S.K. Sirigiripet, and R. Williammee. (2008). "Evaluation of Cemented Quarry Fines as a Pavement Base Material." *ASCE Geotechnical Special Publication 177, Geo-Congress*, New Orleans, Louisiana: 312-319.
- Sobhan, K. and R. Krizek. (1999). "Fatigue Behavior of Fiber-Reinforced Recycled Aggregate Base Course." *Journal of Materials in Civil Engineering, May, 11:2.* ASCE:124-130.
- Taha, R., A. Al-Harthy, K. Al-Shamsi, and M. Al-Zubeidi. (2002). "Cement Stabilization of Reclaimed Asphalt Pavement Aggregate for Road Bases and Subbases." *Journal of Materials in Civil Engineering* 14(3), ASCE 2002: 239-245.
- Xuan, D., L. Houben, A. Molenaar, and Z. Shui. (2012). "Mechanical Properties of Cement-Treated Aggregate Material – A Review." *Materials and Design* 33. Elsevier: 496-502.

Demonstrating the Worth of Recycled Aggregates—A Case Study from Qatar

J. Murray Reid¹; Khaled E. Hassan²; Okan Sirin³; and Ramzi A. Taha⁴

¹Technical Manager, TRL Limited, Crowthorne House, Wokingham, RG40 3GA, U.K. E-mail: jreid@trl.co.uk

²Regional Director, TRL Ltd-QSTP-B, Qatar Science and Technology Park, P.O. Box 210529, Doha, Qatar. E-mail: khassan@trl.co.uk

³Associate Professor, Dept. of Civil and Architectural Engineering, Qatar Univ., P.O. Box 2713, Doha, Qatar. E-mail: okansirin@qu.edu.qa

⁴Chair and Professor, Dept. of Civil and Architectural Engineering, Qatar Univ., P.O. Box 2713, Doha, Qatar. E-mail: ramzitaha@qu.edu.qa

Abstract: Recycled aggregates are widely used in unbound applications in many countries. However, in some areas the materials available may not meet all the requirements of the local specifications. This is the case in Qatar, where large quantities of excavation waste are available. The excavation waste described in this paper is a weak limestone and did not meet the requirements for sand equivalent and liquid limit/plasticity index in the Qatar construction specifications. It did meet requirements for mechanical properties, durability and grading. A trial road was constructed to demonstrate the suitability of the recycled aggregates as unbound subbase. The road consisted of three sections: (1) recycled aggregates made from excavation waste; (2) recycled aggregates made from clean crushed concrete; and (3) excavation waste mixed with 20% dune sand. Two layers of subbase were placed in each section, and the stiffness was measured with a lightweight deflectometer on top of each layer. The compacted trial sections gave satisfactory stiffness but did not achieve 100% of the laboratory dry density, as required by the Qatar construction specifications. A trafficking trial was carried out on the top layer of subbase, and the resulting rut depths were measured. In each section, the measured rut depths were less than 10 mm, compared to a limiting value of 30 mm, and the trafficked surface of the subbase showed no signs of damage. An asphalt layer was then placed and the road has been subjected to repeated load coming from heavy trucks for over one year and is showing no signs of deterioration. The site trial demonstrated the suitability of the locally available materials, thus contributing to sustainable construction.

INTRODUCTION

The use of recycled aggregates contributes to the sustainability of construction by reducing the use of primary aggregates and avoiding the disposal of waste materials

to landfill. By far the largest source material for recycled aggregates is construction, demolition and excavation waste. Recycled aggregates can contribute significantly to the aggregate supply of nations; in the UK, 29% of the aggregate supply in 2014 was from recycled and secondary aggregates (Mineral Products Association 2015).

The use of recycled aggregates is generally conditional on them performing as well as primary aggregates. This is measured by compliance with the local construction specifications. Additional requirements are often included in specifications for recycled aggregates, such as restrictions on the content of contaminants like wood, paper, plastic, clay, metal and plasterboard.

Quality control is important for recycled aggregates as the nature of the raw material may raise concerns about the presence of contaminants in the product. In developed countries, specifications have generally evolved to enable maximum use to be made of the locally available aggregates. However, in countries where rapid development is taking place, standards and specifications may have been imported from other countries with different climates and materials. In such cases, recycled aggregates may not meet all the requirements of the developing country's specification. Site trials can then be carried out to establish whether the recycled aggregates can meet the performance requirements of the application. The paper describes an example of this situation from Qatar.

CONSTRUCTION IN QATAR

The State of Qatar is a peninsula on the south shore of the Arabian Gulf. It lies between latitudes 24° and 27°N and longitudes 50° and 52°E and has a hot desert climate. Qatar has abundant reserves of oil and gas and has been undergoing rapid development over the last twenty years. This includes many infrastructure projects, including a metro system and the stadiums and infrastructure for the 2022 World Cup.

The construction program requires a supply of aggregates, but Qatar does not possess any sources of hard rock aggregates. The peninsula is underlain by geologically young, relatively weak limestone with bands of clay and gypsum (West 2013). The strata consist of interlayered hard and soft bands of limestone (Fourniadis 2010) with solution cavities and collapsed strata in places. Aggregate for concrete and asphalt is imported by ship from the United Arab Emirates, some 700 km to the east.

The redevelopment of Qatar has also generated vast quantities of construction, demolition and excavation waste. Most of this is taken to a landfill site outside the capital, Doha. On arrival it is separated into excavation waste (EW) and construction and demolition waste (CDW). Because soft materials are not stripped out of buildings prior to demolition, the CDW contains variable amounts of wood, paper, plastic, plasterboard, metal, tires and other contaminants. The site has expanded greatly in recent years and now covers an area of about 8 km². It is estimated that about 10 Mt of EW and CDW are brought to the site each year (MDPS 2014). The total amount of material is approximately 60 to 80 Mt.

Recycled aggregates were produced from the EW and CDW on a small scale up to 2012. However, since 2013 a large-scale recycled aggregate plant has been operating at the site by a Contractor, Lafarge Qatar Quarry Company. Production is dominantly from the relatively clean EW, with some production from clean concrete but not from the mixed CDW.

The government of Qatar is seeking to develop the economy without damaging the environment (General Secretariat for Development and Planning 2008 & 2011). As part of this initiative, the government wants to increase the use of recycled aggregates and limit the dumping of EW and CDW. However, the use of recycled aggregates in hot desert areas such as Qatar has been limited (Walker 2012) due to concerns about the quality of the material and high contents of sulfates, chlorides and lightweight contaminants. The government funded a study by the UK Transport Research Laboratory (TRL), Qatar Standards and Qatar University into the use of recycled and secondary aggregates under the National Priorities Research Programme (NPRP) funded by the Qatar National Research Fund (QNRF) at the Qatar Foundation. The project ran from 2012 to 2015 and the results are presented in Hassan et al (2015).

QATAR UNIVERSITY WORK ON DEMOLITION AND EXCAVATION WASTES

A study conducted by Sirin et al. (2013) investigated the use of EW and reclaimed asphalt pavement (RAP) materials collected from road and building construction projects around Doha. Samples were taken from two EW (EW-1 and EW-2) and one RAP stockpiles. These samples of EW were similar to the material sent to landfill. The three samples were subjected to a wide range of tests including particle size distribution, density, bulk specific gravity, water absorption, Los Angeles abrasion, Sand Equivalent, Liquid Limit, Plasticity Index, standard Proctor compaction, and soaked California Bearing Ratio (CBR).

The two EW samples did not meet the Liquid Limit and Plasticity Index requirements according to the Qatar Construction Specifications (QCS) (2010). The Sand Equivalent value for EW-1 (23%) was also below the requirement established by QCS 2014 ($\geq 25\%$). However, EW-2 and RAP had acceptable Sand Equivalent values of 29% and 96%, respectively. All three materials failed the Los Angeles abrasion requirement of a maximum value of 40%. Furthermore, all three materials did not meet the minimum CBR requirement of 70% specified in QCS (2010) for road base and sub-base materials. Based on these laboratory results, EW and RAP did not seem to be suitable for use in road base and sub-base construction in Qatar.

QUALITY OF RECYCLED AGGREGATES – LABORATORY TESTS

Samples of recycled aggregate produced from EW and CDW were obtained at the start of the QNRF project in 2012. The samples were tested for compliance with the Qatar Construction Specifications (QCS) (2010) for unbound subbase. The results were encouraging, showing compliance with most parameters in the QCS. The crushing and screening involved in aggregate production removed the weaker material which did not comply with the QCS requirements.

As further tests were carried out over the course of the project, it was found that the Liquid Limit, Plasticity Index and Sand Equivalent Value of the EW and CDW aggregates often did not comply with the QCS requirements. Most of the other parameters, including CBR, Los Angeles abrasion value and magnesium sulphate

soundness, did comply with the QCS, with only occasional results not complying. A summary of the results of a number of tests carried out between 2012 and 2014 on recycled aggregates derived from EW and crushed concrete (CC) is given in Table 1. Properties that sometimes do not comply with the QCS requirements are shown in grey shading. The results are compared to the limiting values in the 5th edition of the QCS, which was published in 2014. Recycled aggregates produced from EW are shown in Figure 1(a).

Local limestone is widely used as subbase in Qatar. The limestone does not comply with the QCS requirements for Liquid Limit, Plasticity Index and Sand Equivalent, but it can be mixed with 20% of dune sand to reduce the plasticity. Results for EW, which is basically local limestone, mixed with 20% dune sand are also shown in Table 1. The dune sand is shown in front of EW in Figure 1(b).

The EW failed the Sand Equivalent test even when 20% dune sand was added. Limestone from most of the quarries in Qatar also failed this test (Salim Kutty, personal communication, January 30, 2014). The Sand Equivalent test was developed as a field test to give a rapid assessment of the harmful fines content of a soil. However, these properties are determined more accurately by particle size distribution and plasticity index, which are also required under the QCS. It is therefore unnecessary to also include a limit for Sand Equivalent.

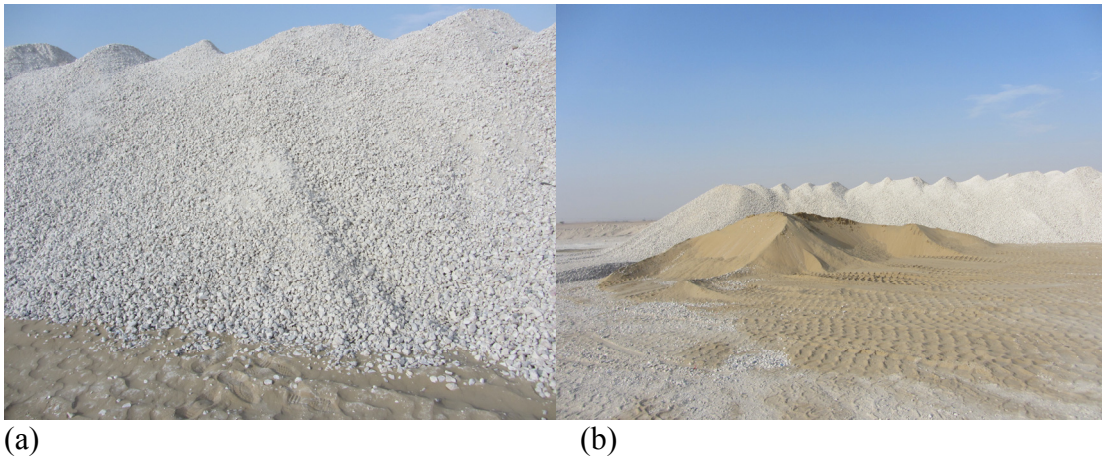


FIG. 1. (a) 0/50mm Recycled aggregates from EW; (b) Dune sand for mixing with 0/50mm EW to form subbase

All the materials gave Liquid Limit values higher than the QCS maximum value. The results of Liquid Limit, Plastic Limit and Plasticity Index showed considerable variation between samples. This reflects variation in the clay content in the original limestone, which is exacerbated when limestone from different sources is mixed in excavation waste. There was also considerable variation between different testing laboratories on samples of the same material, raising further doubts about the reliability of the results.

The concern with high values of Liquid Limit and Plasticity Index is that the material will lose strength if exposed to water. However, all the materials except a few samples of CC gave soaked CBR values well in excess of the limiting value, with swell values well below the limiting value (Table 1). The materials should therefore be capable of forming a satisfactory subbase provided they are above the water table.

Table 1. Laboratory Test Results on Recycled Aggregates

Property	QCS 2014 Subbase Limiting Values	Crushed Concrete (CC)	Excavation Waste (EW)	EW + 20% Dune Sand
Flakiness Index (%)	35% max	11 - 24	14 - 28	12 - 31
Elongation Index (%)	40% max	19 - 30	23 - 40	26 - 32
Sand Equivalent (%)	25% min	31 - 58	10 - 23	11 - 28
Liquid Limit (%)	25% max	Non-plastic to 45	37 - 60	Non-plastic to 29
Plasticity Index (%)	6% max	Non-plastic	2 - 25	Non-plastic
Los Angeles Abrasion Value (%)	40% max	30 - 35	26 - 32	24 - 32
Magnesium Sulphate Soundness (%)	20% max	2 - 5	14 - 19	7 - 16
Soaked CBR (%)	70% min	52 - 134	121 - 265	112 - 266
Swell in soaked CBR (%)	1% max	0.02 - 0.17	0.01 - 0.16	0.02 - 0.13
Maximum dry density (Mg/m ³)	2.05 Mg/m ³ min	1.98 - 2.09	2.18 - 2.20	2.19 - 2.31

In Qatar, subbase will generally be placed in dry conditions and will be covered by impermeable asphalt layers, which will prevent ingress of rainwater. TRL Overseas Road Note 31 (TRL 1993) recommends that for granular subbases in arid and semi-arid climates, the Liquid Limit should be less than 55% and the Plasticity Index less than 20%. All the materials tested to date meet these requirements. It should therefore be possible to use the materials successfully in unbound applications such as subbase.

Because of the extent of the deposits at the landfill site and the variability of the materials, the tests summarized in Table 1 can only provide a snapshot of the properties. However, the process of crushing and screening involved in the production of the recycled aggregates breaks down most of the weaker material, resulting in aggregate with broadly predictable properties. The contractor estimates that only about half the feedstock is processed into aggregate. The rest breaks down to dust and is screened out. The products are tested for compliance with the QCS before sale.

As the materials did not comply with all aspects of the QCS, it was necessary to demonstrate that they could deliver satisfactory performance if they were to be accepted for use in construction. A field trial was therefore carried out.

FIELD TRIAL

A trial road was constructed in October 2014 on the access road to the landfill site and aggregate recycling plant outside Doha to determine whether recycled aggregates could be used successfully as unbound subbase. The trial consisted of three sections each of 120 m length, comprising recycled aggregates produced from EW and CC

plus a section of EW with 20% dune sand, mimicking the use of local limestone mixed with dune sand. The materials were obtained from the nearby aggregate recycling plant.

A cross-section of the trial road is shown in Figure 2. The existing access road was removed and two layers of unbound subbase were placed, with the first layer acting as a regulating layer to even out minor undulations in the subgrade. The second layer was 150 mm thick throughout. An 80 mm layer of asphalt was subsequently placed on top of the unbound subbase layers.

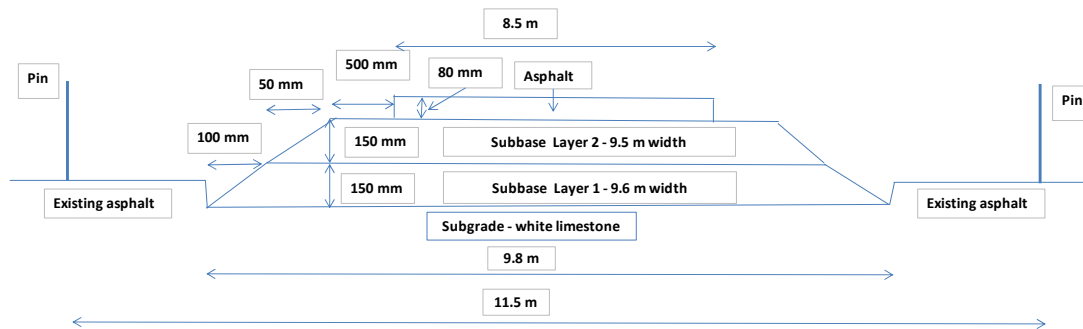


FIG. 2. Cross-section of trial road

The grading of the materials used in the trial is shown in Figure 3. All three materials met the grading limits for unbound subbase in the QCS. The effect of adding dune sand can be seen in the higher sand fraction of the EW+DS material. However the fines content of all materials was well within the QCS limits.

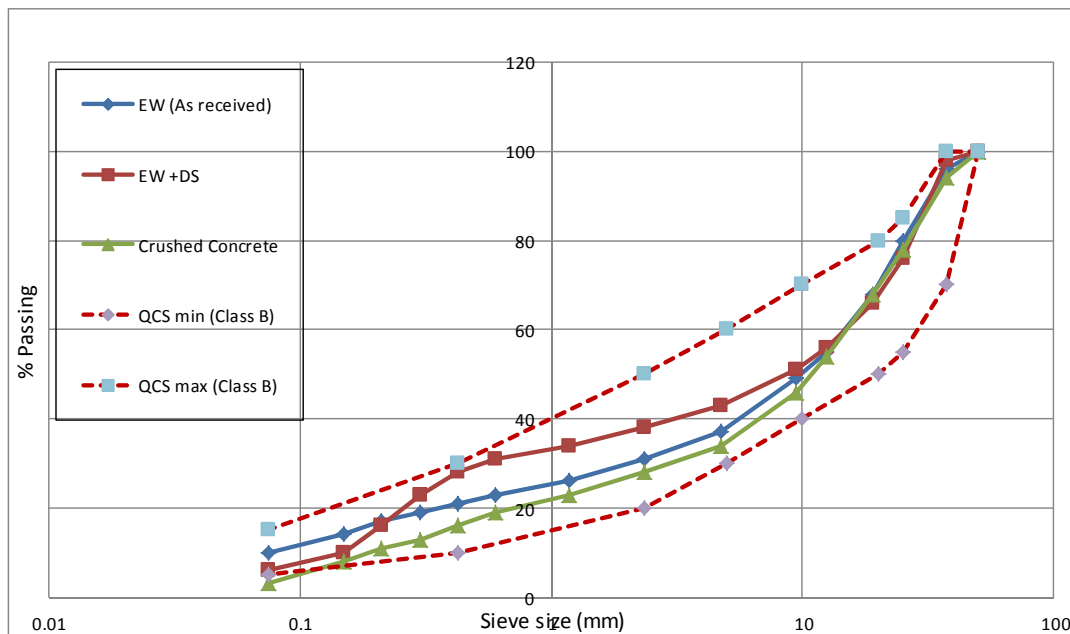


FIG. 3. Grading of recycled aggregates used in the trial road

The properties of the materials used in the trial are shown in Table 2. None of the materials met all the requirements for Sand Equivalent, Liquid Limit and Plasticity

Index; CC fails the Liquid Limit, EW+DS fails the Sand Equivalent and EW fails all three. However all three materials comfortably met the requirements for Los Angeles abrasion value, soaked CBR and swell. The values for maximum dry density in Tables 1 and 2 have been corrected for oversize material in accordance with ASTM D4718 (ASTM, 2007), so can be compared directly with in-situ test results.

Table 2. Laboratory Test Results on Aggregates used in Trial Road

Property	QCS 2014 Subbase Limiting Values	Crushed Concrete (CC)	Excavation Waste (EW)	EW + 20% Dune Sand
Flakiness Index (%)	35% max	10	16	13
Sand Equivalent (%)	25% min	34	13	17
Liquid Limit (%)	25% max	47	47	25
Plasticity Index (%)	6% max	NP	21	NP
Los Angeles Abrasion Value (%)	40% max	30	31	30
Soaked CBR (%)	70% min	145	190	260
Swell in soaked CBR (%)	1% max	0.17	0.16	0.13
Maximum dry density (Mg/m ³)	2.05 Mg/m ³ min	2.09	2.18	2.33

The in-situ density of the subbase layers was determined by the sand replacement method according to BS 1377-9:1990 (British Standards Institution 1990). The foundation surface modulus was measured on the surface of layers 1 and 2 of the subbase with a lightweight deflectometer (Figure 4(a)). The stiffness was measured because the subbase was too coarse-grained to be suitable for in-situ measurement of CBR (British Standards Institution 1990).

The in-situ density tests indicated relative compaction was less than 100%, and for some tests it was less than 95%. The QCS requires dry density to be at least 100% of the laboratory values. However, the material had been thoroughly compacted by suitable compaction plant and visually appeared well compacted.

The dry density depends on the moisture content. The trial road was constructed during the second half of October 2014, when the temperature was well above 30°C. The aggregates were mixed with water to bring them to the required moisture content immediately before placing as shown on Figure 4(b), but dried out rapidly after compaction. As a result, the moisture content, and hence the dry density, varied over time as shown in Table 3. The table shows the average as-placed moisture content taken from samples from the paver, the average moisture content in the sand replacement tests generally taken the day after compaction and the optimum moisture content from laboratory tests.

The moisture content of all the materials was above optimum moisture content when placed but below it by the time the in-situ density tests were carried out. The high initial moisture content may be the reason for the relative compaction being less than 100%. The amount of water added is down to the skill and experience of the

workforce. Lack of familiarity with recycled aggregates may be the cause of the failure to achieve 100% of the maximum dry density. Greater experience with recycled aggregates should result in less over-addition of water. However, given the method used for adjusting moisture content, some deviation from the optimum is almost inevitable.



FIG. 4. (a) Lightweight deflectometer testing on EW+DS; (b) Adding water to CC prior to compaction

Table 3. Variation in Moisture Content of Subbase in Field Trial

Material	As-placed moisture content (%)	Moisture content from in-situ density test (%)	Optimum moisture content from laboratory tests (%)
EW	9.6	5.8	7.1
CC	11.4	7.3	9.0
EW+DS	5.8	4.7	5.0

The subbase was laid in two layers, layer 1 and layer 2. Lightweight deflectometer tests were undertaken on both layers. The results, presented in Table 4, showed an increase in dynamic deflection modulus from layer 1 to layer 2. In layer 1 the EW had higher modulus than CC and EW+DS, but in layer 2 there was no significant difference between the three materials. Comparison of the results with UK guidance for pavement design (Highways Agency et al. 2009) indicates that all three materials in layer 2 would be a Class 2 foundation, suitable for traffic levels up to 80 million standard axles (msa). The lightweight deflection test gives the foundation surface modulus. This is a function of the stiffness and thickness of the overall foundation, not just layer 2. The tests indicate that a foundation consisting of recycled aggregates can give satisfactory performance even under very high traffic loading.

The deflectometer tests give a good indication of the potential of the materials. To further assess the performance of the subbase, a trafficking trial was carried out using the procedure set out in the 800 Series of the UK Specification for Highway Works (Highways Agency et al., 2008). The subbase was subjected to 1000 equivalent

standard axles (ESAL) using a five axle lorry with a loaded weight of 41.4 tonnes. The load on each axle was measured at the weighbridge of the aggregate recycling plant and the ESAL were calculated using the method in TRL Overseas Road Note 40 (TRL, 2004). This gave an ESAL of 5.74, which equated to 175 passes of a loaded lorry to give 1000 ESAL. The trial in progress is shown in Figure 5(a) and the surface of the subbase after completion of the trial in Figure 5(b). The average and maximum rut depths in each material and overall are shown in Table 5. Rut depth averaged less than 10 mm in each section, well within the limiting value of 30 mm in the UK Specification for Highway Works, with the EW+DS giving the best performance. The measured rut depths confirm the visual impression that the materials experienced very little deformation.

Table 4. Lightweight Deflectometer Results from Field Trial

Layer	Material	Average dynamic deflection modulus Evd (MN/mm ²)	Minimum dynamic deflection modulus Evd (MN/mm ²)
Subbase layer 1	EW	82	71
	CC	62	43
	EW+DS	66	39
Subbase layer 2	EW	107	70
	CC	109	88
	EW+DS	105	90
Class 1 Foundation (UK guidance)		40	25
Class 2 Foundation (UK guidance)		80	50



FIG. 5. (a) Trafficking trial in progress; (b) Surface after trial

The trial results suggest that the key aggregate parameters for assessing performance are grading, Los Angeles abrasion value and soaked CBR. The index properties such as Sand Equivalent, Liquid Limit and Plasticity Index appear to be less significant, so long as the materials are above the water table. This supports relaxing the limiting values for Liquid Limit and Plasticity Index to those suggested in TRL Overseas Road Note 31 (TRL 1993) for arid and semi-arid areas and to remove the requirement for Sand Equivalent.

Table 5. Rut Depths Recorded in Trafficking Trial

Material	Average rut depth after 1000 ESAL (mm)	Maximum rut depth after 1000 ESAL (mm)
EW	7.5	11.0
CC	7.4	11.0
EW+DS	0.4	6.0
Overall average	4.8	11.0

The trial was very successful and clearly demonstrated that recycled aggregates produced from EW and CC can perform well as unbound subbase. Asphalt was placed and the road was opened to traffic in late November 2014. Its condition has been monitored visually, and as of December 2015, there were no signs of deterioration. The number of loaded lorries arriving at the site each day was estimated to be about 2,000. Assuming that they were all loaded to the same extent as the lorry used in the trial, with an ESAL of 5.74, and that the site operates 5 days a week for 46 weeks per year, this gives an estimated traffic load of about 2.6 msa over one year.

QATAR CONSTRUCTION SPECIFICATIONS

The use of aggregates in construction in Qatar is governed by the Qatar Construction Specifications. The 4th edition of the QCS (2010) included very limited provision for the use of recycled aggregates. However, a 5th edition was published in 2014. This includes more provisions for recycled aggregates in a range of applications, including unbound pavement materials, asphalt and concrete. The trafficking trial came too late to affect the revision of the QCS, so the 5th edition retains the limiting values for Sand Equivalent, Liquid Limit and Plasticity Index. It also retains the in-situ CBR test on subbase, which is not practical because of the coarse grading, and the requirement for in-situ dry density to be at least 100% of the laboratory dry density, which may not be achievable because of the need to mix water with the fill immediately before placing.

The first edition of the QCS was launched in 2000 as experimental voluntary standards and it has developed rapidly in successive editions to cover a broad range of construction activities. Through these editions it has developed into a comprehensive document that is tailored to the specific circumstances of construction in Qatar. Increasingly, it also reflects the regional situation of rapid development in the neighboring Gulf Cooperation Council (GCC) states and the wider Middle East and North Africa (MENA) region. This trend will continue as further experience is gained in the use of recycled aggregates on actual construction projects, and will feed into future editions of the QCS and wider regional specifications.

CONCLUSIONS

Sustainability in construction requires making the best use of materials available locally. Specifications should enable this to occur. However, in areas of rapid development, specifications and standards from other countries may be used without

taking account of the local circumstances. In such cases, local materials may not meet all the specification requirements. Field trials can be used to demonstrate that the locally available materials can be used successfully. The use of recycled aggregates derived from EW and CC in Qatar illustrates this point. Until recently such materials were not permitted under the QCS and were landfilled while high quality aggregates were imported. However, work has now been carried out on recycled aggregates.

Laboratory testing demonstrated that the recycled aggregates complied with most parameters in the QCS but often failed the requirements for Sand Equivalent, Liquid Limit and Plasticity Index. A trial road was constructed to demonstrate the performance of the recycled aggregates as unbound subbase, with sections of EW, CC and EW+DS. In-situ density tests showed that the recycled aggregates in many cases did not achieve the QCS requirement of 100% of the maximum dry density obtained in laboratory tests. Despite the failure to achieve the specified levels of density, the recycled aggregate subbase gave excellent performance when subjected to a trafficking trial, with minimal development of rutting after being subjected to loading of 1000 ESALs. The road has been monitored visually since being opened to traffic and is showing no signs of deterioration after twelve months in service. Recycled aggregates should thus be permitted in subbase and other applications provided they are placed above the water table.

The QCS has developed considerably since it was first launched in 2000, and is increasingly reflecting construction in Qatar rather than other countries. This process will continue as more experience is gained with recycled aggregates. A further set of trials on a range of construction projects is proposed, and the results from these will feed into future updates of the QCS. This in turn will feed into wider regional construction specifications in the Gulf and the wider MENA region, enabling greater use of recycled aggregates and improving the sustainability of construction.

ACKNOWLEDGMENTS

This work was made possible by the NPRP award [NPRP 4-188-2-061] from the Qatar National Research Fund (a member of Qatar Foundation). The statements made herein are solely the responsibility of the authors.

REFERENCES

- American Society for Test Methods (2007). Standard Practice for Correction of Unit Weight and Water Content for Soils Containing Oversize Particles. ASTM D4178-87.
- British Standards Institution (1990). "Methods of test for soils for civil engineering purposes. Part 9 in-situ tests." *BS 1377-9:1990*. British Standards Institution, London, UK.
- Fourniadis, I. (2010). "Geotechnical Characterization of the Simsim Limestone (Doha, Qatar)." In *GeoShanghai International Conference 2010*, 273-278. ASCE Geotechnical Special Publication No. 204.
- General Secretariat for Development and Planning (2008). "Qatar National Vision 2030." Ministry of Development, Planning and Statistics, Doha, Qatar.

- General Secretariat for Development and Planning (2011). “Qatar National Development Strategy 2011-2016.” Ministry of Development, Planning and Statistics, Doha, Qatar.
- Hassan K.E., Reid J.M. and Al-Kuwari M.S. (2015). “Use of recycled and secondary aggregates in Qatar – Guidance document.” *TRL Published Project Report PPR736*. TRL Limited, Crowthorne, UK.
- <<http://www.trl.co.uk/reports-publications/results/?search=PPR736>> (09/12/2015)
- Highways Agency, Transport Scotland, Welsh Assembly Government and Northern Ireland Roads Service (2008). “Specification for Highway Works”. *Manual of Contract Documents for Highway Works Volume 1 (MCHW1)*. Highways Agency, London, UK.
- <<http://www.standardsforhighways.co.uk/ha/standards/mchw/vol1/index.htm>> (09/12/2015)
- Highways Agency, Transport Scotland, Welsh Assembly Government and Northern Ireland Roads Service (2009). “Design guidance for road pavement foundations (Draft HD25).” *Interim Advice Note 73/06 Revision 1 (2009)*. Highways Agency, London, UK.
- <<http://www.standardsforhighways.co.uk/ha/standards/ians/pdfs/ian73rev1.pdf>> (09/12/2015).
- Mineral Products Association (2015). “The mineral products industry at a glance – key facts.” 2015 Edition. Mineral Products Association, London UK. <http://www.mineralproducts.org/documents/Mineral_Products_Industry_at_a_Glance_2015.pdf> (09/12/2015).
- MDPS (2014). Ministry of Development Planning and Statistics. <[Generation of solid waste by type \(2008 - 2013\)](#)> (09/12/2015)
- Qatar Construction Specification (QCS) (5th edition, 2014). “Qatar National Construction Standards”. Laboratories and Standardization Affairs – Ministry of Environment, Qatar Standards, Doha, Qatar.
- Sirin O., Taha R., Qunnaby R., Alkhamis K., Naser M., Younis M and Shihadeh A. (2013). Evaluation of demolition wastes for use in road bases and sub-bases construction in Qatar. Creative Construction Conference, July 6-9 2013, Budapest, Hungary.
- TRL (Transport Research Laboratory) (1993). “A guide to the structural design of bitumen-surfaced roads in tropical and sub-tropical countries.” *TRL Overseas Road Note 31*. Transport Research Laboratory, Crowthorne, UK.
- TRL (Transport Research Laboratory) (2004). Axle load surveys and traffic counts for traffic loading. *TRL Overseas Road Note 40*. Transport Research Laboratory, Crowthorne, UK.
- Walker, M.J. (ed.) (2012). “Hot deserts: Engineering Geology and Geomorphology.” *Geological Society Engineering Geology Special Publication No. 25*. The Geological Society, London, UK.
- West, I. (2013). “Qatar – Sabkha, Salt Lakes and Other Desert Environments.” <<http://www.southampton.ac.uk/~imw/Qatar-Sabkhas.htm>> (09/12/2015).

Durability Studies on Fly Ash Stabilized Reclaimed Asphalt Pavement Materials

Deepti Avirneni, S.M.ASCE¹; and Sireesh Saride, M.ASCE²

¹Research Scholar, Indian Institute of Technology Hyderabad; Assistant Professor, VNRVJIET, Hyderabad, India. E-mail: deepthcivil@gmail.com

²Associate Professor, Dept. of Civil Engineering, Indian Institute of Technology, Hyderabad, India. E-mail: sireesh@iith.ac.in

Abstract: Reclaimed asphalt pavement (RAP) has predominantly been on the global research focus because of its cost effectiveness as well as sustainability. Lack of proper design guidelines being main reasons, a limited amount of research findings are put into practice. In addition, age hardening of the asphalt coating present over the RAP, affects its long term performance. To confidently use the RAP in flexible pavements, it is essential to evaluate the durability and long term performance of RAP mixes besides for their strength and stiffness properties. The current study aims at evaluating the durability and long term performance of the selected RAP-VA mixes with alkali activated fly ash as a stabilizer. The mixes were selected based on the target unconfined compressive strengths (UCS) specified by the Indian Roads Congress (IRC) guidelines. The RAP-VA mixes were subjected to alternate wet - dry cycles and the weight loss after 12 cycles was measured. The weight loss is found to be within the permissible limits of 14% by weight. Retained UC strength after 12 cycles, for each mix, were also evaluated to know the effect of moisture variation on the strength and was observed that the strength loss was very minimal.

Keywords: Reclaimed asphalt pavements, Durability, Wet-dry cycles, Compressive strength.

INTRODUCTION

Construction activity is on its high due to rapid urbanization and population explosion. Pavement industry is facing severe shortage of virgin materials and hence there is a definite need for sustainable pavement solutions. As a consequence, various secondary materials have made their way into pavement construction. Reclaimed asphalt pavement (RAP) materials being one of the viable alternatives, its production and usage have been remarkably increased all over the world. RAP material is obtained by milling the existing distressed pavements which have reached the end of their design life or had severe premature failures. Apart from conserving natural

resources, usage of RAP not only reduces carbon footprint, but also is cost effective (Saride et al, 2015a). In spite of these advantages, the utilization of RAP is still not up to its potential in many of the countries including India. Most of the existing codes of practice limit the usage of RAP in pavements to about 20 to 30%, depending on the layer in which it is used. Recent research findings proved that RAP dosages can be further increased (more than 50%) when stabilized with additives like cement, fly ash, lime or any other cementitious admixtures (Puppala et al., 2011; Saride et al., 2014; Saride et al., 2015b).

The behavior of RAP is expected to differ from that of virgin aggregates because of the stress history that it has been subjected to and the presence of aged asphalt coating over it. Also, when subjected to seasonal variations, the binder coating over the RAP mixes tends to strip off, thereby altering the strength of the mix. Hence it is necessary to assess the long term strength and durability of treated/untreated RAP before using it in pavement layers, especially when the pavements are subjected to frequent oscillating climatic conditions which lead to moisture fluctuations within the layer. To assess the performance of RAP in semi-arid countries like India, it is appropriate to expose the specimens to various cycles of wetting and drying processes as suggested in existing literature. The present study aims at evaluating the long term strength and durability characteristics of fly ash treated RAP-VA mixes activated with Sodium Hydroxide (NaOH). Fly ash is used as a stabilizer in the present study in view of its abundant availability across the world and its disposal being a serious environmental concern. However, other pozzolanic alternatives like lime, cement, and other slags, etc. can also be used subject to their availability and reactivity.

BACKGROUND

In view of the scarcity of virgin materials and increased infrastructure demands, use of secondary materials in pavements has gained research importance in the recent years all over the world. As a consequence, research has been extended to characterize RAP materials for their use in base/sub base layers of flexible pavements (Arulrajah, 2013). Many studies were also taken up to examine the performance of RAP treated with cementitious additives like cement, fly ash, lime etc. Taha et al. (2002) conducted a series of experiments on high amount of RAP (70 - 100%) in RAP:VA blends. The study revealed that RAP even in higher amounts could potentially perform as a structural component in pavements. The performance was much more superior when the mixes were stabilized with cement. Potturi (2006), conducted studies on the resilient behavior of cement and cement fiber treated RAP mixes without blending with any virgin material. The investigation confirmed the enhancement of resilient modulus when treated with both cement and cement fibers. Saride et al. (2010) conducted various laboratory and field studies on 100% RAP mixes blended with cement-treated limestone quarry fines (CQF). The test results demonstrated that RAP can be effectively used as pavement base material. Saride et al. (2015b) investigated the performance of fly ash treatment on RAP - VA blends containing high amounts of RAP (greater than 50%). The study proved that the mixes can be successfully used in Indian low volume roads (traffic less than 2 million standard axles, msa) with a 50% reduction in base layer thickness.

As evident from the above studies, usage of high amounts of RAP in pavement layers is effective in terms of strength, stiffness and economy. However, assessing their long term performance is essential, failing in, which may necessitate frequent maintenance and thereby incurring huge maintenance costs. Also, the demand for high performance pavements with relatively larger service periods and traffic has been increasing day by day. In this regard, it is essential to evaluate the long term performance and durability of treated RAP. The necessity is more pronounced when the high percentages of RAP (greater than 50%) are desired in the mix. Very limited investigations have been taken up on durability aspects of the RAP. Gurthrie et al. (2007) studied the durability aspects of cement treated RAP mixes by assessing final dielectric value using tube suction test. The dielectric value is a measure of the free, or unbound, water within the sample. It is this unbound water that is thought to be directly related to the strength of the material and its ability to withstand repeated freeze-thaw cycling. The cement treatment resulted in allowable dielectric value (less than 10) because the cement treatment minimizes the moisture ingress into the pavements. Ganne (2009) performed durability studies on untreated and cement treated RAP mixes and reported the weight loss for each mix. The durability was found to be satisfactory and the weight, volume and strength loss were found to be minimal. However, the long term strength and durability of RAP when stabilized with other additives is yet to be confirmed. Hence there is a wide research scope in assessing the long term performance of treated RAP mixes for their use in base / subbase layers of flexible pavements which provides a motivation for the current study.

METHODOLOGY

The present study is a consequential investigation conducted by the authors (Saride et al. 2015b) for the utilization of RAP in base/sub base layers of flexible pavements for the low volume roads (LVR). From this study, 80RAP+20VA stabilized with 40% fly ash and 60RAP+40VA stabilized with 10 – 40% fly ash was found to meet the design requirements specified for LVRs by ministry of rural development, MoRD (1.7 MPa). However, these mixes cannot be employed for the state highways (SH) and national highways (NH) which carry heavy traffic (greater than 2 million standard axels). The reason for low strength of RAP mixes, event after the stabilization with fly ash may be because of low reactivity of the fly ash used. The lime (CaO) reactivity of Neyveli fly ash is very low among all the Indian fly ashes (Sridharan et al. 2001). Hence, in the present study it is proposed to activate the un-used lime, silica and alumina contents present in the fly ash with NaOH in view of its capability to accelerate and improve the pozzolanic reaction between the fly ash and the aggregates. The following best performing mixes as shown in Table 1, were considered for activation with 2% and 4% NaOH. The laboratory grade sodium hydroxide pellets with 98.9% purity was used in the study.

Table 1. Mix Proportions and their Nomenclature

RAP	VA	Fly ash	NaOH	Nomenclature
80	20	30	2	80R:20V+30F+2N
60	40	20	2	60R:40V+20F+2N
60	40	30	2	60R:40V+30F+2N
80	20	30	4	80R:20V+30F+4N
60	40	20	4	60R:40V+20F+4N
60	40	30	4	60R:40V+30F+4N

MATERIALS USED

Reclaimed Asphalt Pavement (RAP) Material and Virgin Aggregates (VA)

The RAP used in the study was collected from a pavement stretch located on NH-5 in the state of Andhra Pradesh where the existing pavement is proposed for reconstruction. In-plant cold recycling was adopted to carry out the milling process. The RAP collected from the project site was transported and stockpiled at IITH laboratory. Grain size distribution studies were performed in accordance with ASTM C136 (ASTM 2006). The gradation curve was presented in Figure 1. The RAP falls under A-1-a, described as non-plastic sandy gravel as per the American Association of State Highway and Transportation Officials (AASHTO). However, the gradation of the RAP is not meeting the gradation limits proposed by Ministry of road transportation and highways (MoRTH) for cemented bases. Hence, RAP was segregated into bins to obtain the average base gradation proposed for treated bases by MoRTH. Graded virgin aggregates were collected from a quarry near IIT Hyderabad.

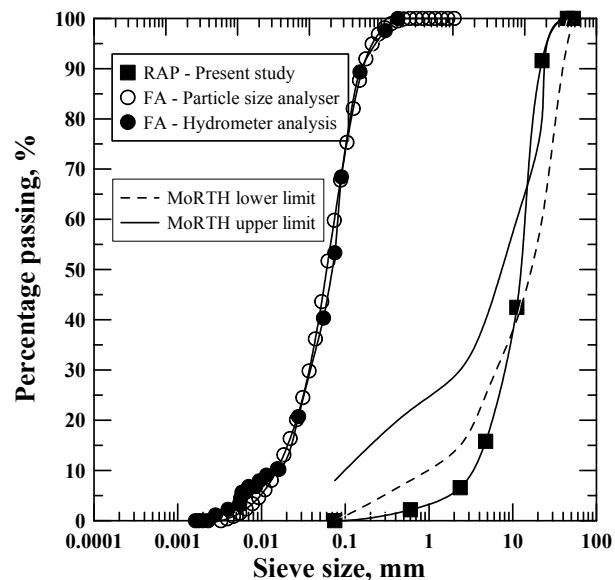


FIG. 1. Gradation curve of RAP and fly ash.

Fly ash (FA) and Sodium Hydroxide (NaOH)

Fly ash (FA) collected from Neyveli Lignite Corporation (NLC), Tamilnadu was used in the present study. Chemical composition of fly ash was found out using X-Ray Florescence (XRF) method and is presented in Table 2. Based on the CaO content (< 20%) present, the fly ash can be classified as class “F” as per ASTM C 618 (ASTM 2012). To determine the particle size distribution of fly ash, hydrometer analysis and particle size analyzer were used. The gradation curves of fly ash determined from both the methods are presented in Figure 1. A close match between both the test results was observed. It is also easy and quick to obtain the gradation from particle size analyzer, making it convenient to verify the repeatability of gradation for different fly ash samples.

Table 2. Chemical Composition of Fly Ash

Chemical Compound	Quantity (%)
Silicon Dioxide (SiO ₂)	40.63
Calcium Oxide (CaO)	11.93
Iron Oxide (Fe ₂ O ₃)	9.61
Aluminum Oxide (Al ₂ O ₃)	32.34
Magnesium Oxide (MgO)	1.85

Fly ash is classified as sandy silt (SM) according to the unified soil classification system (USCS). Compaction characteristics were determined by the standard proctor compaction method. The Maximum Dry Density (MDD) and Optimum Moisture Content (OMC) were found to be 1.37 g/cc and 27% respectively. The gradation and compaction characteristics of RAP:VA mixes were maintained as reported in previous studies by Saride et al. (2015b). However, the NaOH pellets of required weight are dissolved in the calculated OMC prior to the mixing.

TESTS CONDUCTED

Unconfined Compressive Strength (UCS)

Specimens of size 100 mm diameter and 200 mm height were prepared at their respective OMC and MDD with NaOH, using modified compactive effort as discussed by the authors (Saride et al. 2015b). The samples were cured in a humidity chamber under controlled moisture (70% relative humidity) and temperature (25⁰ C) for 1, 7, 28, 56 and 112 days. The UCS tests were then conducted in accordance with ASTM D 1633 (ASTM 2000).

Durability studies

Durability studies intend to understand the long term performance of treated RAP materials when subjected to severe moisture variations that are likely expected during their service period. To simulate and accelerate this phenomenon in the laboratory, IS: 4332 (part IV) – 1968 has given a procedure in which the sample is subjected to

alternate wet-dry cycles. At the end of 28 day storage in moist room, the specimens are immersed in potable water for a duration of 5 hours at room temperature. The samples are then removed and oven dried at 70⁰C for 42 hours. After removing from the oven, the specimens are given two strokes all around the area with a wire brush and are weighed. The above procedure constitutes one cycle of wetting and drying. The procedure is continued for 12 such cycles and the weight of each specimen is recorded after every cycle. The weight loss experienced by the specimen after each cycle is evaluated. UCS tests were carried out on these samples to determine the retained strength after 12 cycles.

RESULTS AND DISCUSSIONS

Unconfined Compressive Strength (UCS)

As compared to the UC strengths observed by Saride et al. (2015b) on the same mixes without activation, the results presented in the study have shown the clear influence of alkali (NaOH) activation on fly ash with RAP-VA mixes. The UCS value increased when the activator dosage increased from 2% to 4% for all the mixes as presented in Figures 2 and 3. This may be due to the dissolution of nonreactive silica and alumina present in the fly ash making it available for the pozzolanic reactions. In addition, at a given activator dosage, 30% fly ash was found to be superior in terms of strength in view of its increased pozzolanic reactivity. As VA content increased from 20 to 40%, there is an obvious increase in the UCS in view of its high reaction potential with fly ash. The UCS gradually increased up to 56 days and then almost remained constant. This may be considered as a sign of termination of pozzolanic reactions. It can also be observed that the UCS of all the mixes satisfied the minimum strength criteria (4.5 MPa) for high volume roads as specified by IRC: 37- 2012 after 28 days of curing.

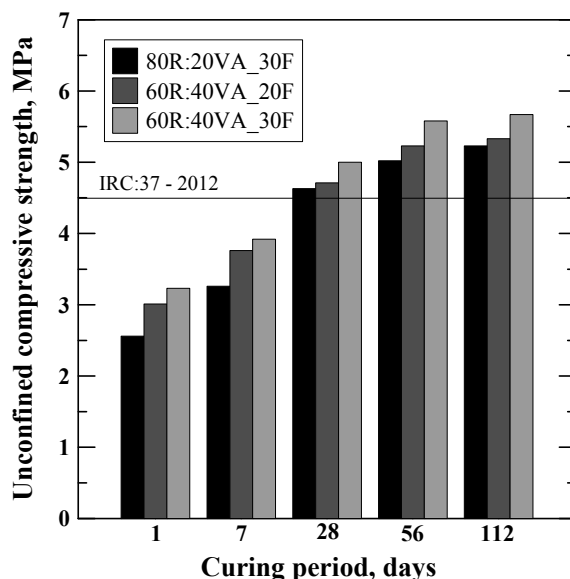


FIG. 2. Variation of UCS with curing period for mixes with 2% activation.

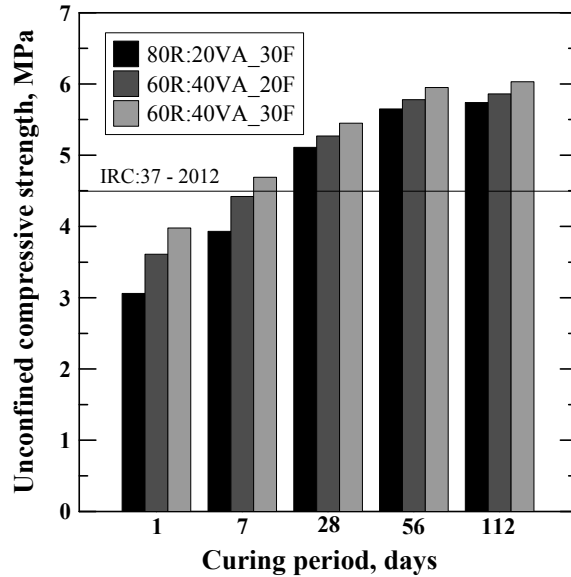


FIG. 3. Variation of UCS with curing period for mixes with 4% activation.

Durability

The weight loss of all the mixes considered in this study for continuous wet-dry cycles are presented in Figure 4. The weight loss of all the mixes is observed to be well within the permissible limit (less than 14%) as specified in IRC: 37-2012 for a cemented base material. As shown in Figure 4, at higher RAP contents (80%) and lower activator contents (2% NaOH), the weight loss, though within the limits, is observed to be relatively higher probably because of the hindered pozzolanic activity due to the high aged bitumen content present in the mix.

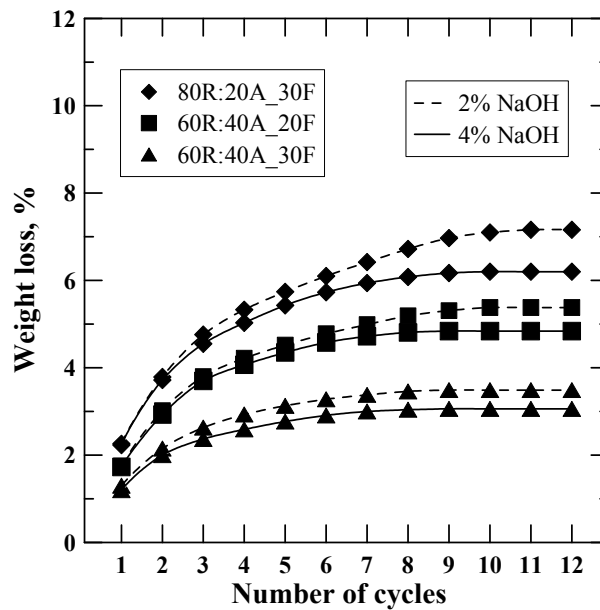


FIG. 4. Weight loss of different mixes subjected to wet-dry cycles.

To understand the strengths of the design mixes after the complete wet-dry cycles, UCS tests were conducted on the same specimens subjected to the durability studies. The strength loss due to continuous wet-dry cycles on all the mixes can be seen in Figure 5. It can be observed that the strength loss in each selected design mix after complete wet-dry cycles was very minimal. The mixes: 60R:40A_30F+2NaOH; 60R:40A_20F+4NaOH and 60R:40A_30F+4NaOH have also exhibited a minimum required strength of 4.5 MPa, reveals that these mixes are highly stable and qualify the requirements of high volume roads even after the aggressive wet/dry cycles. However, the mixes need not qualify for the minimum permissible strength requirements as per the specifications after the durability studies. As long as the 28 days UC strength meets or exceeds 4.5 MPa and the weight loss is less than 14% after 12 wet-dry cycles, the mix is qualified as a cemented base for flexible pavements. Hence, the remaining mixes can still be conveniently used for as cemented bases for flexible pavements.

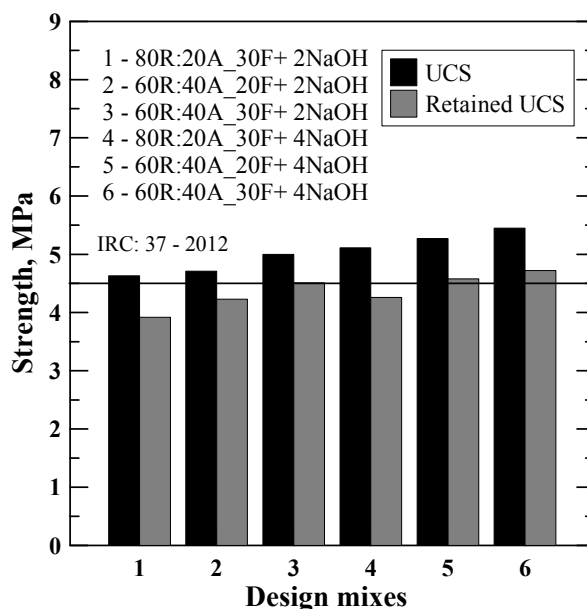


FIG. 5. Variation of UCS and retained strength after 12 wet-dry cycles for different mixes.

CONCLUSIONS

Eight design mixes were selected and tested for UCS and were subjected to wet-dry cycles. Their weight loss and strength loss were recorded. The following conclusions were drawn from the study:

1. Alkali activation of fly ash stabilized RAP-VA mixes by NaOH proved to be a potential technique to improve their strength. All the mixes at 28 days curing were observed to satisfy the minimum strength criteria (4.5 MPa) specified for high volume roads by IRC for their use in base/ subbase layers of flexible pavements.

2. It is evident from the UCS results that at higher RAP contents, there is a notable decrease in the strength because of the inferior pozzolanic reactivity of RAP in comparison with that of VA.
3. Irrespective of the mix proportion, the UCS is observed to gradually increase with curing period till 56 days. Beyond that, the increase is marginal which denoting the deceleration/end of pozzolanic reaction.
4. The weight loss after 12 wet-dry cycles obtained from durability tests on all the mixes was found to be less than 14% as specified in IRC. After the durability studies, based on the retained strength the design mixes 60R:40A_30F+2NaOH; 60R:40A_20F+4NaOH and 60R:40A_30F+4NaOH are found to be highly stable.

REFERENCES

- Arulrajah, A., Piratheepan, J., Disfani, M. M. and Bo, M. W. (2013). “Resilient moduli response of recycled construction and demolition materials in pavement subbase applications.” *J. Mater. Civ. Engrg.*, Vol. 25(10): 1920–1928.
- ASTM (2006). “Standard test method for sieve analysis of fine and coarse aggregate.” *ASTM C 136-06*, West Conshohocken, PA.
- ASTM (2012). “Standard specification for coal fly ash and raw or calcined natural pozzolan for use in concrete.” *ASTM C 618-12a*, West Conshohocken, PA.
- ASTM (2000). “Standard test method for compressive strength of molded soil-cement cylinders.” *ASTM D1633-00*, West Conshohocken, PA.
- Ganne, V.K. (2009). “Long-term durability studies on chemically treated reclaimed asphalt pavement materials.” *Master thesis*, University of Texas, Arlington.
- Guthrie, W.S., Brown, A.V. and Eggett, D.L. (2007). “Cement stabilization of aggregate base material blended with reclaimed asphalt pavement.” *Transportation Research Record No. 2026*, Transportation Research Board, Washington, DC, 47-53.
- Indian Roads Congress. (2012). “Guidelines for the design of flexible pavements.” *IRC-37*, New Delhi, India, 12–18.
- Indian Standard Code (1968). “Wetting and drying, and freezing and thawing tests for compacted soil-cement mixtures.” *IS: 4332 (part IV)*, New Delhi, India, 4-8.
- Potturi, A.K. (2006). “Evaluation of resilient modulus of cement and cement-fiber treated reclaimed asphalt pavement (RAP) aggregates using repeated load triaxial test.” *Master’s thesis*, University of Texas, Arlington.
- Puppala, A.J., Hoyos, L.R. and Potturi, A.K. (2011). “Resilient moduli response of moderately cement-treated reclaimed asphalt pavement aggregates.” *J. Mater. Civ. Engrg.*, Vol. 23(7): 990-998.
- Saride, S., Puppala, A. J. and Williammee, R. (2010). “Assessing recycled/secondary materials as pavement bases.” Special issue on sustainability in ground improvement projects, *Proceedings of ICE*, Ground Improvement, Vol. 163(1): 3-12.
- Saride, S., Avirneni, D., Someswar, R. T., Javvadi, S.C.P. and Dayakar, R. (2014). “Evaluation of fly ash treated reclaimed asphalt pavement for design of sustainable pavement bases - an Indian perspective.” *Geo Congress 2014*, Atlanta, USA, GSP 234: 3676-3685.

- Saride, S., Avirneni, D., Javvadi, S.C.P., Puppala, A.J. and Hoyos L.R. (2015a). "Evaluation of fly-ash-treated reclaimed asphalt pavement for base/sub-base application." *Indian Geotechnical Journal*, Vol. 45 (4): 401 – 411.
- Saride, S., Avirneni, D. and Javvadi, S.C.P. (2015b). "Utilization of reclaimed asphalt pavements in Indian low-volume roads." *J. Mater. Civ. Engrg.*, Vol. 28(2): 10.1061/(ASCE)MT.1943-5533.0001374, 04015107.
- Sridharan, A., Pandian, N.S. and Srinivas, S. (2001). "Compaction behavior of Indian coal ashes," Technical report of task force on characterization of fly ash submitted to Technology Mission-Fly Ash Disposal and Utilization, *Department of Science and Technology*, Govt. of India.
- Taha, R., Al-Harthy, A., Al-Shamsi, K. and Al-Zubeidi, M. (2002). "Cement stabilization of reclaimed asphalt pavement aggregate for road bases and sub bases," *J. Mater. Civ. Engrg.*, 14(3): 239-245.

Energy Harvesting from Pavement via PVDF: Hybrid Piezo-Pyroelectric Effects

Jie Hu¹ and Junliang Tao, A.M.ASCE²

¹Graduate Research Assistant, Dept. of Civil Engineering, Univ. of Akron ASEC 427F, Akron, OH 44325-3905.

²Assistant Professor, Dept. of Civil Engineering, Univ. of Akron ASEC 210, Akron, OH 44325-3905.

Abstract: In the U.S., there are over 4 million miles (6 million km) of roadways and more than 250 million registered vehicles. The energy lost in the pavement system due to traffic-induced vibration and deformation is enormous. If effectively harvested, such energy can serve as an alternative sustainable energy source that can be easily integrated to the transportation system. To harness the mechanical energy from a pavement, the common approach is to utilize a piezoelectric module, which generates electricity when strained. The mostly commonly used piezoelectric material is ceramic PZT, which is fragile and is not resistant to damage from vehicles and adverse weather. In this paper, the potential of PVDF, which is a piezoelectric polymer material, is investigated as a potential energy harvester integrated in pavement systems. The uniqueness of this study lies in that the electrical response of PVDF under coupled mechanical and thermal stimulations are studied. It is well known that most piezoelectric materials are also pyroelectric materials, which convert temperature change into electricity. However, the potential of PVDF as a hybrid piezo-pyroelectric energy harvester has been seldom studied. Through series of well controlled experiments, it is found that there exists interesting coupling phenomenon between piezoelectric and pyroelectric effects of PVDF: the voltage generated by simultaneous mechanical and thermal stimulations is the sum of voltages generated by separate stimulations. In addition, an estimation of power generation through piezoelectric and pyroelectric effect is conducted. Finally, the overall effects of temperature on hybrid piezo-pyroelectric energy harvesting are discussed.

Keywords: Energy harvesting, Pavement, Piezoelectric, Pyroelectric, Hybrid.

INTRODUCTION

With economic development, fossil energy sources such as coal, natural gas and petroleum have been used largely. However, because of excessive consumption, those energy sources will deplete in the future. Sustainable energy is an ideal replacement. Traditional sustainable energy such as wind energy, solar energy, geothermal energy and hydraulic energy have been developed for decades or even thousands of years.

However, these four forms of energy are greatly subjected to weather and location. A novel sustainable energy harvesting from pavement system is proposed in this study. In U.S., there are over 4 million miles (6 million km) of roadways and more than 250 million registered vehicles. The energy lost in the pavement system due to traffic-induced vibration and deformation is enormous and, if effectively harvested, can serve as an alternative sustainable energy source that can be easily integrated to the transportation system. By embedding energy harvesters in pavement structure, electricity can be generated when vehicles pass by.

In the proposed energy harvester system, piezoelectric material is utilized, which converts mechanical deformation into electricity. Piezoelectricity was discovered in 1880 by Jacques and Pierre Curie (Ueberschlag, 2001). Piezoelectric materials can be found in nature, such as quartz and bones. Synthesized piezoelectric materials, such as Lead zirconate titanate (PZT) and Polyvinylidene fluoride (PVDF), are more commonly used for engineering applications. PZT is an inorganic ceramic material and fragile in nature, although it has a large piezoelectric coefficient. On the other hand, PVDF is a flexible and durable polymer material but with a much smaller piezoelectric coefficient. As a pilot study, Virginia Tech proposed a pavement energy harvesting system consisting of a metal box and stacks of PZT discs (Xiong et al. 2012). The design is thought to be bulky and would adversely affect the pavement system due to mechanical mismatch between the pavement and the metals. The durability of the system was found to be questionable due to the fragile nature of the ceramics. Furthermore, the potential pyroelectric effect is not considered. Zhao et al. proposed a cymbal shape PZT based energy harvester and analyzed its coupling with asphalt pavement structure with a finite element model. (Zhao et al., 2010). PVDF based energy harvesters are also investigated, which converts ambient vibration into electricity (Chen, 2014). However the energy efficiency of piezoelectric energy harvester is fairly low, which limits its broad application.

It is also well known that most piezoelectric materials are also pyroelectric materials, which convert temperature change into electricity. The pyroelectric properties of PZT/PVDF composites are studied recently. Dietze et al. added PZT in PVDF-TrFE to make PZT-PVDF-TrFE composite. This increased both the dielectric constant and pyroelectric constant (ρ). But high content of PZT decreases its dielectric constant and ρ . PZT in PZT/PVDF-HFP composite contributed to both its pyroelectric and piezoelectric constants. And in high temperature condition, pyroelectric constant of PZT/PVDF-HFP composite increased greatly (Malmonge et al., 2003). However, the potential of using PVDF composites as a hybrid piezo-pyroelectric energy harvester has been seldom studied.

The ultimate goal of the present study is to develop a highly efficient pavement energy harvesting system utilizing the hybrid piezo-pyroelectric effects of PVDF composites. As the first step, this paper discusses the effects of temperature variation on the power generation using pure PVDF samples. A series of experiments on electricity generation from the pure piezoelectric effect, pure pyroelectric effect and the hybrid piezo-pyroelectric effect are conducted. Based on the test results, theoretical models are developed to predict the power generation through the hybrid piezo-pyroelectric energy harvesting system. A case study is presented to illustrate the effects of temperature variation on energy harvesting from pavement.

Piezoelectric and pyroelectric effect

PVDF is a piezoelectric material since the mechanical stress/deformation of material will change the directions of the electric dipoles and the net effect is accumulation of charges on the surface electrodes. The direct piezoelectric effect can be described with Eq.1. In Eq. 1, σ is the mechanical stress; D and E are the electric displacement and electric field, respectively; ϵ^σ is the dielectric permittivity in a constant stress status; and d is the piezoelectric coefficient.

$$D = \epsilon^\sigma E + d\sigma \quad (1)$$

Eq. 1 considers the full coupling effect between the mechanical and electrical fields. When the inverse piezoelectric effect and the effect of the generated electric field (E) is neglected, the second equation in Eq. 1 can be simplified to Eq. 2, which can be utilized to calculate the charges (integration of D on electrode areas) induced by the stress field (σ).

$$D = d * \sigma \quad (2)$$

PVDF is also a pyroelectric material that exhibits a spontaneous polarization (P_s) in the absence of an applied electric field. Pyroelectric materials produce electricity from temperature fluctuations (dT/dt) and are analogous to piezoelectric harvesters, which convert mechanical oscillations ($d\sigma/dt$) to electric energy. Eq. 3 defines the generated pyroelectric current (i_p) under temperature change (dT/dt):

$$i_p = \frac{dQ_T}{dt} = \rho A \frac{dT}{dt} \quad (3)$$

where Q_T is the pyroelectric charge, A is the surface area of the material, and ρ is the pyroelectric coefficient.

For pavement energy harvesting applications, the harvester will be subject to both mechanical stimuli (i.e., traffic induced deformation and vibrations), as well as thermal stimuli (i.e., transient temperature changes). Therefore, it is interesting to study the coupled piezoelectric and pyroelectric effects and investigate how the temperature changes affect the piezoelectric effects and vice versa.

LABORATORY EXPERIMENTS ON THE HYBRID PIEZO-PYROELECTRIC EFFECTS

Three series of experiments were conducted to study the coupling between piezoelectric and pyroelectric effects:

- 1) To study the pure piezoelectric effect, the temperature conditions were kept as constant when mechanical loading was applied with a weight of 31.7g. The loading tests were conducted at different temperature conditions such as 35 °C, 40 °C and etc. These temperature conditions were controlled by a hot plate as shown in Figure 1b. The piezoelectric effect induced voltage at different temperature conditions is shown in Figure 2a.
- 2) To study the pure pyroelectric effect, the temperature of the PVDF sample was first heated to 60°C and then it was allowed to cool down freely to the room temperature of 30°C (Figure 2b). No mechanical loading was applied. The pyroelectric effect induced voltage is shown in Figure 2c.

- 3) To study the coupled piezo-pyroelectric effect, the temperature of the PVDF sample was first heated to 60°C. The same mechanical loading was repetitively applied as in Step 1, while the temperature gradually went down. The generated voltage at the instances when the mechanical loading was applied is shown in Figure 2d.

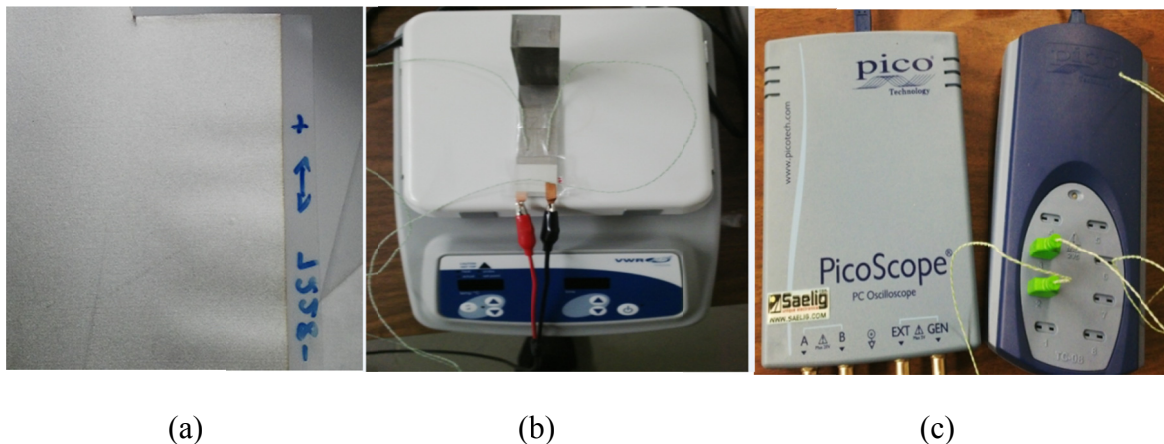


FIG. 1 (a) PVDF film, (b) Hot plate and PVDF film, (c) Picoscope and thermocouple

The PVDF sample measured as 1in by 1in for the experiments is cut from commercially available PVDF film (Measurement Specialties, Product 1-1004346-0). The piezoelectric coefficient, pyroelectric coefficient and the dielectric constant of the PVDF film is shown in Table 2. Care was taken to remove the electrodes on the edges to prevent short condition. An aluminum beam was used as a heat conductor to avoid heating the sample directly. The PVDF film was bounded to one end of the aluminum beam and an electrical insulation layer was added between the sample and the beam. The other end of the beam was fixed on a hot plate (VWR, 97042-690). The two electrodes of the PVDF sample was leaded to a PC Oscilloscope (PICO[®] Technology, Model 3204B) for voltage measurement. In addition, two thermocouples (PICO TC Probe, SE000) are bonded on the top and bottom surfaces of the PVDF sample for temperature measurement. The thermal signal was logged with a thermocouple data logger (TC-08, PICO[®] technology).

The output voltage of the PVDF film under different mechanical and thermal loadings is summarized in Figure 2. Figure 2a shows that the piezoelectric voltage under a same mechanical loading changes linearly with temperature. With decreasing temperature (Figure 2b), the transient pyroelectric voltage also decreases (Figure 2c). The slope of the voltage-temperature curve is the pyroelectric coefficient. The curve can be fitted using either a polynomial or linear curve (as shown in Figure 2c), which means that although the pyroelectric coefficient of PVDF increases slightly with temperature, it can be assumed as a constant in this temperature range. Figure 2d illustrates that the hybrid piezo-pyroelectric effect is close to the algebra sum of the pure piezoelectric effect and the pure pyroelectric effect. Therefore, the total charges induced by the hybrid effect can be expressed as Eq. 4.

$$Q = Q_T + Q_M \tag{4}$$

where Q , Q_T and Q_M is the total charges induced by the hybrid effect, the pure pyroelectric effect and the pure piezoelectric effect, respectively.

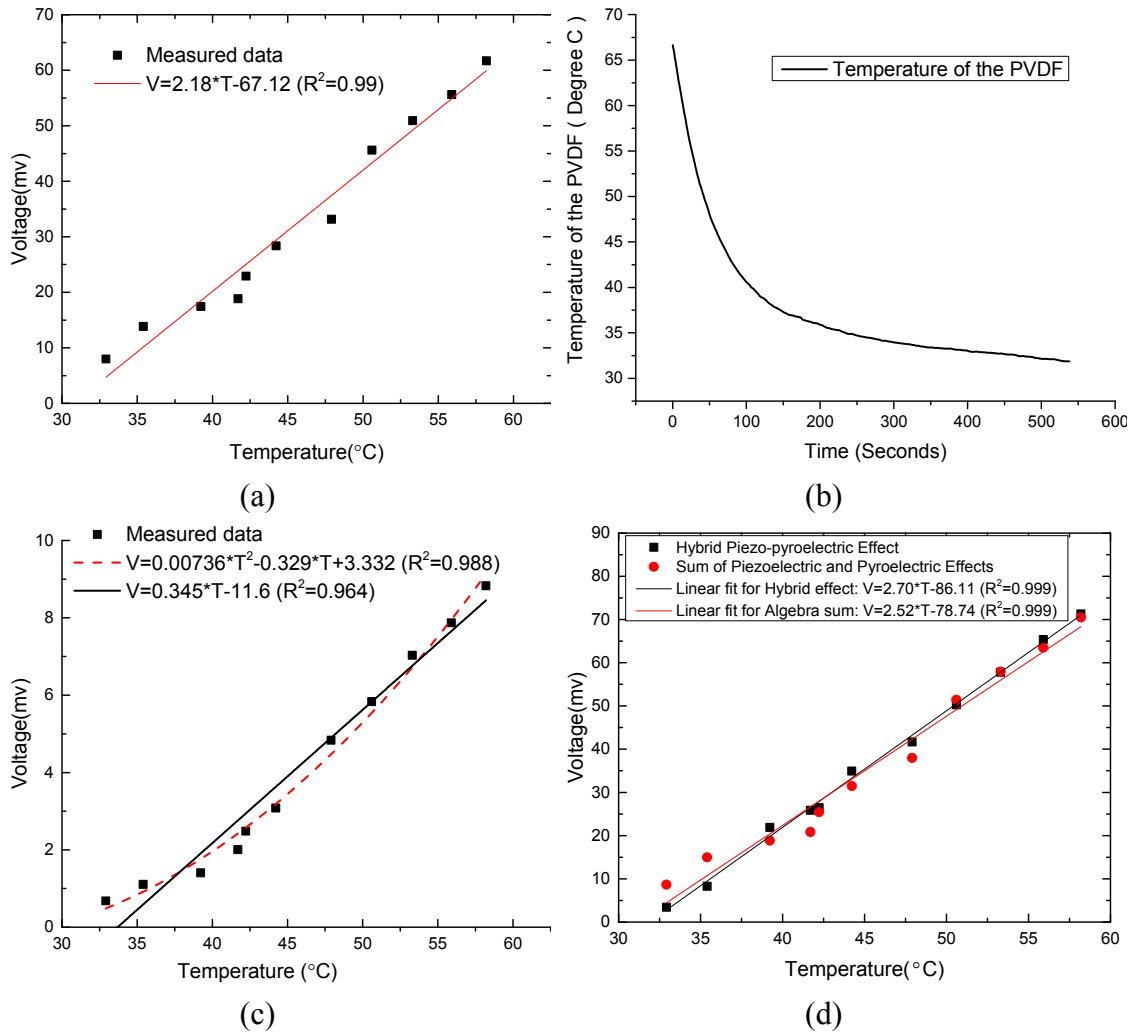


FIG. 2. Experimental results: (a) pure piezoelectric effect; (b) temperature profile; (c) pure pyroelectric effect; and (d) hybrid piezo-pyroelectric effect.

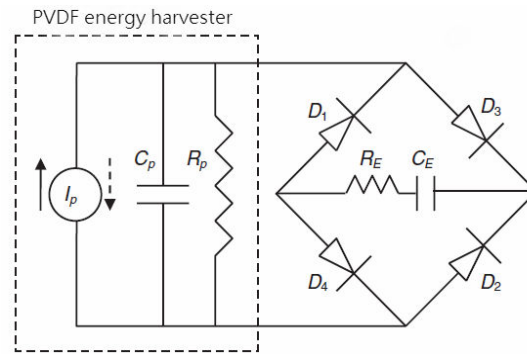


FIG. 3. Standard circuit for energy harvesting (Batra et al., 2011). C_p and R_p is the capacitance and resistance of clamped PVDF harvester, C_E and R_E is external capacitance and resistance, respectively. D_1, D_2, D_3 and D_4 are diodes, which are used to rectify current direction.

MODELING OF THE HARVESTED ENERGY CONSIDERING THE HYBRID PIEZO-PYROELECTRIC EFFECTS

Harvesting circuit

The PVDF energy harvester can be modeled as a current source with internal impedance (internal capacitance C_p and internal resistance R_p) and the energy will be storage in an external capacitor C_E and will be consumed by the external loading R_E (Figure 3). Since the harvester will experience both cooling and heating processes, the direction of I_p will change. Therefore, a full bridge with four diodes rectifier is used to ensure that the charges will flow to C_E in the same direction. The capacitance of

PVDF harvester can be calculated using the parallel plate theory, $C_p = \frac{\epsilon_0 \epsilon_r A_{PVDF}}{h}$,

where ϵ_0 is the permittivity of vacuum, ϵ_r is permittivity of PVDF, A_{PVDF} is the electrode area and h is the thickness of PVDF. The internal resistance is typically very large and it can be assumed that no internal leakage will occur. To further simplify the modeling, it is assumed the diodes are ideal and no dissipation of energy occurs due to rectification. The external capacitance is usually large enough so that most of the charges will be harvested. In the following, the charge, voltage and energy stored in C_E is modeled.

Pyroelectric effect induced charge, voltage and energy

Soedjatmiko et al. verified that pavement temperature varies with time and depth (Soedjatmiko, 1999). During a day, it typically reaches the lowest in the middle night and highest after noon. At a certain depth below the pavement (1.5m in Ohio), the temperature remains as a constant (15°C in Ohio). At the pavement surface, the temperature is the highest in the summer but lowest in the winter. At current stage, we simply assume that the PVDF film is embedded just beneath the wearing layer and its temperature is assumed to be approximately the pavement surface temperature.

The pyroelectric effect induced charges can be calculated using Eq. 5.

$$Q_T = \rho \Delta T A_{PVDF} \quad (5)$$

where ΔT is the temperature change and A_{PVDF} is the surface area of the harvester. Assuming that during one cycle of cooling or heating process, pyroelectric effect induced charge is Q_T . In a random n^{th} cycle, the charge will be distributed between the internal and external capacitors (Eq. 6) (Cuadras et al., 2010).

$$\Delta Q + Q_P(n-1) + Q_E(n-1) = Q_P(n) + Q_E(n) \quad (6)$$

where ΔQ is the charge induced in the n^{th} cycle; Q_P and Q_E are the charges stored in external capacitor (C_E) and internal capacitor (C_P), respectively, typically, $C_E \gg C_P$.

$$Q_P(n) = V(n) C_P$$

$$Q_E(n) = V(n) C_E \quad (7)$$

$$Q_P(n-1) = \pm V(n-1) C_P$$

$$Q_E(n-1) = V(n-1) C_E$$

where V is the voltage across C_E . It should be noted that the sign of in third equation in Eq. 6 depends on the signs of temperature change ΔT . That is, if both the n^{th} and $n-1^{th}$ cycles are cooling or heating process, the current generated will be in the same direction; however, if the n^{th} cycle is cooling (heating) but the $n-1^{th}$ cycle is heating (cooling), then the current generated in these two cycles will be opposite and a negative sign will be used.

By substituting Eq. 7 in Eq. 6, we can get (Batra et al., 2011, Cuadras et al., 2010):

$$V_n = \frac{Q}{C_E + C_P} + \left(\frac{C_E \pm C_P}{C_E + C_P} \right) V_{n-1} = \frac{\rho A_{PVDF} \Delta T}{C_E + C_P} + \left(\frac{C_E \pm C_P}{C_E + C_P} \right) V_{n-1} \quad (8)$$

Assume $V_1=0$ and with $C_E \gg C_P$, Eq. 8 reduces to

$$V_n = \frac{\rho A_{PVDF} \sum |\Delta T|}{C_E + C_P} = \frac{Q_n}{C_E + C_P} \quad (9)$$

where Q_n is the accumulated charges on C_E after n^{th} thermal cycle.

The energy stored in CE is thus,

$$E_n = \frac{1}{2} C_E \left(\frac{\rho A_{PVDF} \sum |\Delta T|}{C_E + C_P} \right)^2 \quad (10)$$

Piezoelectric effect induced charge, voltage and energy

Considering lane changing of vehicles, the PVDF harvester is designed to cover the full lane width. The width of the harvester can be determined considering the length of the contact patches of the tires. The tire contact area can be assumed as a circular

shape with a radius which can be determined using $r = \sqrt{\frac{F_{wheel}}{\pi p_{tire}}}$ (Huang, 1993), where

F_{wheel} is axial wheel load of vehicle, p_{tire} is tire pressure, r is contact radius. It is assumed that the width of the PVDF harvester is $2r$.

Assume that the harvester is embedded at the depth of z and the stress at this depth can be expressed as (Huang, 1993)

$$\sigma_z = p_{cont} \left[1 - \frac{z^3}{(r^2 + z^2)^{1.5}} \right] \quad (11)$$

where σ_z is the stress at the depth of z , p_{cont} is the contact pressure, which can be assumed to be equal to p_{tire} .

Therefore, the piezoelectric effect induced charge when a single tire passes the harvester is, $Q_M = d_{33} \sigma_z A_{cont}$.

Assume that all the vehicles are two-axle vehicles and the traffic volume is N /day, the charges induced by the vehicles in a single day will be,

$$Q_{M_day} = 4Nd_{33}\sigma_z A_{cont} \quad (12)$$

Substituting Eq. 9 and 12 to Eq. 4, the total charges induced by the hybrid piezoelectric effect in a day is,

$$Q_{day} = Q_{T_day} + Q_{M_day} = \rho A_{PVDF} \sum_{day} |\Delta T| + 4Nd_{33}\sigma_z A_{cont} \quad (13)$$

Similar to Eq. 9 and 10, the voltage and energy can be calculated.

CASE STUDY AND DISCUSSION

A typical pavement section in Wooster, Ohio is selected for the case study. This section is selected because both the air temperature and traffic data are available. The traffic data is summarized in Table 1 and the temperature record in 2014 is shown in Figure 4a. The harvester is designed to have a length of 3.7m and width of 24cm. Other parameters used in the calculations are summarized in Table 2.

Table 1. Parameters of truck and car

	Car	Truck	Reference
Wheel load (KN)	4.79	25	(Tao et al., 2014)
Tire pressure (Kpa)	220	550	(Highway and Officials, 1993)
Contact radius (cm)	8.25	12.0	(Huang, 1993)
Traffic Volume (per day)	26,290	4,000	Traffic Survey report of ODOT

Table 2. Parameters of circuit components

Parameter	Value	Reference
C_E	$10^{-3}F$	/
A	$0.888 m^2$	/
ρ	$30\mu C/m^2K$	Measurement Specialties, Inc.
d_{33}	$33nC/N$	Measurement Specialties, Inc.
h	$28\mu m$	Measurement Specialties, Inc.
ϵ_r	12.5	Measurement Specialties, Inc.
ϵ_0	$8.82 nF/m$	/
C_P	$3.50\mu F$	/

Note: ‘/’ means the references are not available.

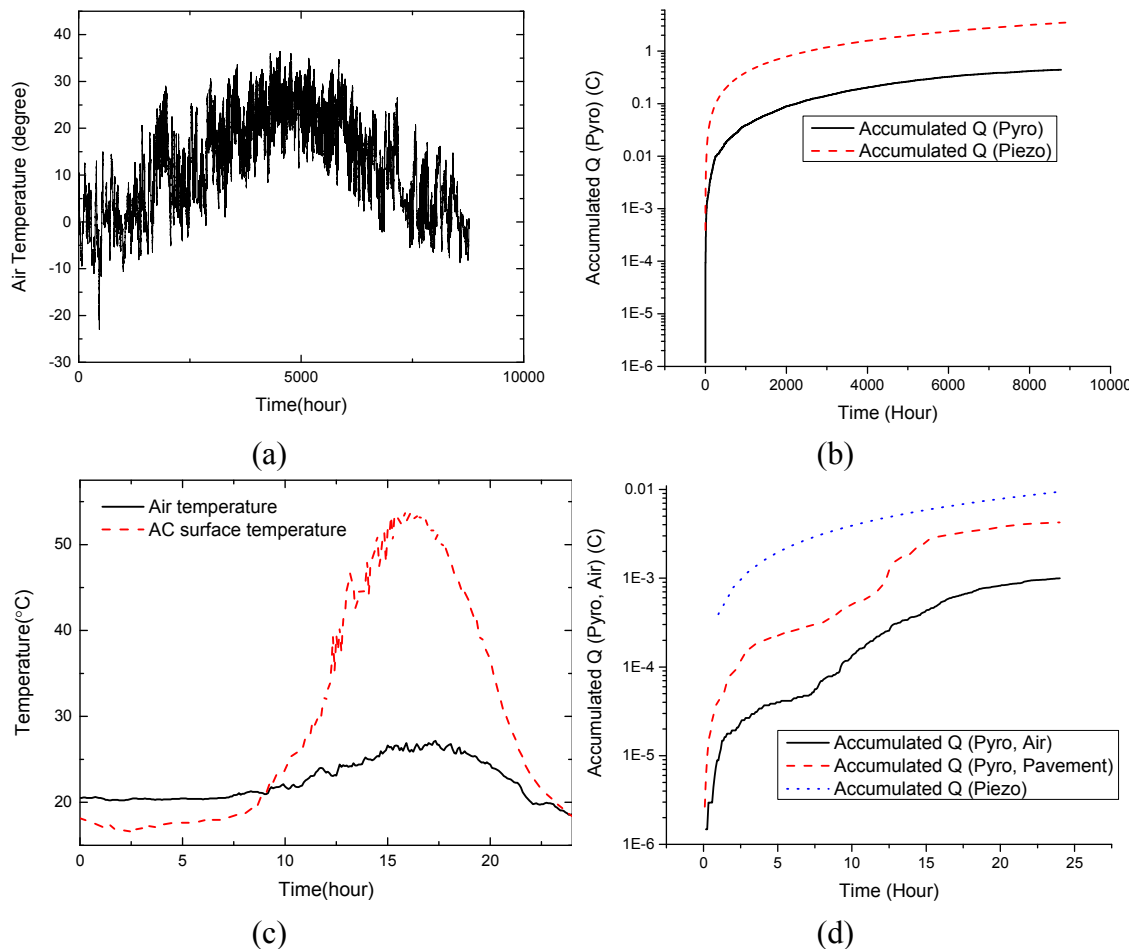


FIG. 4. (a) Temperature record in Wooster OH in 2014; (b) Comparison of piezoelectric and pyroelectric charges accumulated in one year; (c) Comparison of air temperature and pavement temperature in a summer day in Cleveland OH. And (d) Comparison of pyroelectric charges calculated using air and pavement temperature

Based on Eq. 1 and the available weather and traffic data, the accumulated charge due to the pyroelectric and piezoelectric effects during one year is plotted in Figure 4b. It is clear that the piezoelectric charge is significantly larger than the pyroelectric charge. But it should be noted that the temperature we used is the air temperature, which is different from the pavement surface temperature. However, the data for the latter is not available in present. Figure 4c shows the differences between the air temperature and asphalt concrete pavement surface temperature in a typical summer day in Cleveland, OH. It can be concluded that during the daytime, the pavement surface is significantly higher than the air temperature while during the late night, the pavement surface can be cooler than the air. Figure 4d illustrated the differences between the pyroelectric charges calculated using both the air and pavement surface temperature. It can be concluded that if the pavement surface temperature is used, the pyroelectric charge becomes closer to the piezoelectric charges. This means that the pyroelectric effect cannot be neglected when using PVDF as a pavement energy harvester.

CONCLUSION AND FUTURE WORK

In this paper, the concept of energy harvesting from pavement with hybrid piezo-pyroelectric effects is discussed. Laboratory experiments were conducted to study the hybrid effect and it is found that the hybrid effect is equivalent to the algebraic sum of the individual piezoelectric and pyroelectric effect and no coupling effect (mutual-strengthening or mutual weakening) is detected. Analytical models are developed to estimate the charge, voltage and energy harvested considering the weather and traffic data. With such models, case studies are conducted to illustrate the feasibility of the concept. It is concluded that pyroelectric effect cannot be neglected when modeling the energy harvesting capacity of ferroelectric materials when used in pavement systems. It is also found that other materials such as PZT and PVDF nanocomposites can generate more energy than pure PVDF materials. While PZT is fragile and may not be used directly in pavement system, PVDF-TrFE/CNT nanocomposites are viable alternative materials, which can better harness both the thermal and mechanical energy wasted in pavement systems. Ongoing efforts include synthesizing new materials which will future enhance the piezoelectric and pyroelectric conversion efficiency of ferroelectric materials and optimizing the geometry and distribution of the energy harvester. Experiments are also being conducted to further validate the analytical model developed in this paper.

REFERENCE

- BATRA, A. K., BHATTACHARJEE, S., CHILVERY, A. K., AGGARWAL, M. D_m EDWARDS, M. E. & BHALLA, A. 2011. Simulation of energy harvesting from roads via pyroelectricity. *Journal of Photonics for Energy*, 1, 014001-014001-12.
- CHEN, K.-S. Design, Analysis, and Experimental Studies of a Novel PVDF-Based Piezoelectric Energy Harvester With Beating Mechanisms. ASME 2014 International Mechanical Engineering Congress and Exposition, 2014. American Society of Mechanical Engineers, V04BT04A046-V04BT04A046.

- CUADRAS, A., GASULLA, M. & FERRARI, V. 2010. Thermal energy harvesting through pyroelectricity. *Sensors and Actuators A: Physical*, 158, 132-139.
- HIGHWAY, A. A. O. S. & OFFICIALS, T. 1993. *AASHTO Guide for Design of Pavement Structures, 1993*, AASHTO.
- HUANG, Y. H. 1993. *Pavement analysis and design*.
- MALMONGE, L. F., MALMONGE, J. A. & SAKAMOTO, W. K. 2003. Study of pyroelectric activity of PZT/PVDF-HFP composite. *Materials Research*, 6, 469-473.
- SOEDJATMIKO, E. 1999. *Characterization of asphalt layer modulus for Indonesian temperature condition*. MSc thesis, Institut Teknologi Bandung.
- TAO, Y., NIU, Y. & LING, J. 2014. Harvesting energy from asphalt pavement by piezoelectric generator. *Journal of Wuhan University of Technology-Mater. Sci. Ed.*, 29, 933-937.
- UEBERSCHLAG, P. 2001. PVDF piezoelectric polymer. *Sensor review*, 21, 118-126.
- ZHAO, H., YU, J. & LING, J. 2010. Finite element analysis of Cymbal piezoelectric transducers for harvesting energy from asphalt pavement. *Journal of the Ceramic Society of Japan*, 118, 909-915.

Evaluating the Performance of Cementitious Treated/Stabilized Very Weak and Wet Subgrade Soils for Sustainable Pavement

Allam Ardah¹; Murad Abu-Farsakh, A.M.ASCE²; and Qiming Chen, A.M.ASCE³

¹Graduate Research Assistant, Dept. of Civil and Environmental Engineering, Louisiana State Univ., Baton Rouge, LA 70808. E-mail: aardah2@tigers.lsu.edu

²Research Professor, Louisiana Transportation Research Center, Louisiana State Univ., 4101 Gourrier Ave., Baton Rouge, LA 70808. E-mail: cefars@lsu.edu

³Research Associate, Louisiana Transportation Research Center, Louisiana State Univ., 4101 Gourrier Ave., Baton Rouge, LA 70808. E-mail: qchen1@tigers.lsu.edu

Abstract: To evaluate the effect of high moisture content on the performance of subgrade soil and examine the appropriate ways to improve the engineering properties of very wet and weak subgrade soil through using cementitious materials (cement, lime, and/or fly ash), five different soils that represent range of subgrade soil in Louisiana (based on plasticity indices) were collected and considered in this research study. In order to simulate the field conditions for the pavement construction over very weak subgrade layer to create working platform (a target 7-day UCS of 345 kPa) and/or subbase layer (a target 7-day UCS of 690 kPa), the soil/stabilizers were mixed at three different moisture contents in the wet side of optimum moisture content. The repeated load triaxial (RLT) tests were performed on the laboratory molded treated/stabilized specimens in order to evaluate their resilient modulus and to study their deformation behavior under cyclic loading. A good relation was observed between the water/stabilizer ratio and the resilient modulus/permanent deformation. The soil specimens compacted at low water/stabilizer ratio showed better performance than those compacted at high water/stabilizer ratio having identical unconfined compressive strength (UCS). The test results also showed that the permanent deformation is somehow negligible (permanent strain < 0.09%) that might be ignored in the pavement design.

INTRODUCTION

Subgrade is the lowest supporting layer in the pavement structure underlying the base layer. Generally, the subgrade consists of locally available soil deposits that sometimes might be very soft and/or very wet that do not have enough strength/stiffness to support the pavement's traffic loading. The replacement of such soil with better quality of borrow soil fill is not always a good option due to the associated extra cost of excavation and hauling of the materials. Soil stabilization with lime and/or cement was introduced during the 1940s for creating strong subbase when mixed with granular materials. A decade later, stabilization of subgrade became popular with few forerunners (e.g., Reinhold 1955, Handy 1958, Lund and Ramsey 1959, and Jones 1966). Despite the fact that soil stabilization has been known for more than 60 years, very little is known about their capabilities to redistribute the stresses under traffic loading conditions.

A well-engineered and constructed cementitiously treated/stabilized subgrade layer usually requires achieving a threshold compressive strength that is capable of providing a strong and durable support to the construction loading and pavement structures. This treated/stabilized layer

can be incorporated into the structural design of pavements through increasing the modulus of composite subgrade layer or by considering it as a separate subbase layer.

Resilient modulus (M_r) and Unconfined Compressive Strength (UCS) are the essential values of stabilized subgrade in the new Mechanistic Empirical Pavement Design Guide (MEPDG) (NCHRP 2004) when designing flexible pavement. However, only limited studies have specified these parameters (e.g., Abu Farsakh et al. 2015, Tastan et al. 2011, Solanki et al. 2010, Lin et al. 2009, Mohammad and Saadah 2008). Resilient modulus is defined as the ratio of repeated axial deviatoric stress (σ_d) to the recoverable axial strain.

The overall stabilization/treated process in the presence of water can be summarized into four different processes: cation exchange, flocculation and agglomeration, cementitious hydration, and pozzolanic reaction (Prusinski and Bhattacharja 1999, Mallela et al. 2004). Portland cement and lime are both calcium-based products; however, their differences may include important properties such as strength, time dependency on strength development, curing, and durability and performance of the treatment (Prusinski and Bhattacharja 1999). All four aforementioned processes will occur in cement treated/stabilized soils, whereas in case of lime treated/stabilized soils cementitious hydration will be absent. Among them, the hydration of cement is the most important contributor to the improvement of engineering properties of soil (Pendola et al. 1969). Cement hydration is relatively fast and causes immediate strength gain in soil. The cation exchange and the flocculation-agglomeration process also take place immediately after mixing of the soil and cement, resulting in reduction of soil plasticity. The lime generated during hydration of the cement helps increasing the binding between soil particles through pozzolanic reactions. Fly ash stabilization of the soil is similar to cement; however the strength provided is less than the cement.

Many factors have been identified in the literature to affect the stiffness (such as resilient modulus) of cement treated/stabilized soil. Among these factors: state of stress, percent of cement, curing time, curing temperature, moisture content, and soil properties (e.g., Achampong et al. 1997; Mohammad and Saadeh 2008, Little and Nair 2009, Solanki et al. 2010). The resilient modulus can be calculated using the stress state that can be determined from structural analysis of the trial design (after properly accounting for overburden pressure) (ARA 2004). A deviatoric stress of 6 psi is adequate to determine the resilient modulus value in case of the absence of the capability to perform structural analysis for design purposes (Little 2000).

In many cases, the subgrade soils in Louisiana have in situ moisture content that is much higher than the optimum value. This research study focuses on evaluating the behavior of cement treated/stabilized very weak subgrade soils having moisture contents well above the optimum moisture contents in order to cope with the in-situ worst scenario of pavement construction in Louisiana. Two levels of target strengths were selected here to represent the construction of a working table [minimum 7-day strength of 345 kPa (50 psi)] (treated soils) and the construction of a subbase layer [minimum 7-day strength of 690 kPa (100 psi)] (stabilized soils), as recommended by a previous study for Louisiana soils (Gautreau et al. 2009). The performance behavior of the laboratory molded cement soil specimens were observed using repeated load triaxial (RLT) tests in the form of resilient modulus tests and permanent deformation tests.

MATERIAL PROPERTIES AND TEST PROGRAM

Material Properties

Four types of subgrade soils with different plasticity were selected for inclusion in this study. A series of physical property tests were carried out to characterize these soils. These include liquid limit, plastic limit, grain size distribution, and Standard Proctor compaction tests. The results of these tests are presented in Table 1.

Table 1. Properties of soils used in the study

Soil #	Sand (% by mass)	Silt (% by mass)	Clay (% by mass)	LL (%)	PL (%)	PI (%)	AASHTO Classification	USCS Classification	MDD* (kg/m ³)	OMC* (%)
I	23	38	39	30	19	11	A-6	CL	112	17
II	27	32	41	40	19	21	A-6	CL	95	24
III	24	25	51	46	18	28	A-7	CL	100	22
IV	4	44	52	88	35	53	A-7-6	CH	78	35

Note: LL: liquid limit, PL: plastic limit, PI: plastic index, MDD: maximum dry density, OMC: optimum moisture content.

Sample Preparation and Testing Facility

A mold having 142 mm (5.6 in) in height and 71 mm (2.8 in) in diameter was used to prepare 84 resilient modulus specimens and 48 single stage permanent deformation specimens. The specimens were compacted in five layers with nine blows per layer to achieve uniform density. The selected numbers of layers and the number of blows were selected to be consistent with the AASHTO T-307 for resilient modulus, and to achieve the same energy used in the Standard Proctor test (600 kN-m/m³). The molded specimens were placed in airtight plastic wrappers, and kept in a 100% relative humidity room for 7 and 28 days in accordance with ASTM standard procedure prior to testing.

Material Testing System (MTS 810) with a closed loop and servo hydraulic system was used to carry out all the resilient modulus and permanent deformation tests. The applied loads were measured using a load cell. The axial deformation was measured using two Linearly Variable Differential Transducers (LVDTs). The confining pressure was achieved through the use of pressurized air, which was measured using a pressure sensor.

Testing program

RLT tests were performed to determine the resilient modulus (M_r) and the single-stage permanent deformation characteristics of treated/stabilized specimens. Resilient modulus tests were performed in accordance with the AASHTO procedure T307 standard method (AASHTO 2003). According to the test, the specimens were first conditioned by applying 1,000 load cycles to remove the irregularities on the top and bottom surfaces of the test sample and also to suppress most of the initial stage of permanent deformation. After conditioning, a series of steps consisting of applying 100 cycles with a haversine shaped load pulse at different levels of confining and deviatoric stresses. The load pulse used in this study had a 0.1-s load duration and 0.9-s rest period.

For single-state permanent deformation test, the samples were first conditioned by applying a cyclic stress of 15.5 kPa and a confining stress of 41.4 kPa for 1,000 cycles. Once the conditioning phase was completed, the confining pressure was set as 13.8 kPa. A cyclic stress of

37.2 kPa was then applied to the specimen for 10,000 cycles. The loading conditions were selected based on the results of previous tests conducted by Mohammad and Hearth (2005) on subgrade soils in Louisiana. The permanent deformation tests were performed on laboratory molded samples that were cured for 7 days as well as 28 days prior to testing.

TEST RESULTS AND ANALYSIS

Unconfined Compressive Strength

A series of UCS tests were conducted on untreated soils at different moisture contents. A typical variation of the average of three UCS tests of the untreated soil with moisture contents is presented in Figure 1a. This chart is important in selecting the moisture contents for sample preparation for later UCS and RLT tests on treated/stabilized subgrade soils in this study. The set of three moisture contents to produce soil strength of 172 kPa (25 psi) or less (to represent very weak wet soils) for the four untreated subgrade soils were chosen for treatment/stabilization as summarized in Table 2.

Table 2. Summary of selected working moisture contents

Soil #	Soil Name	MC1	MC2	MC3
I	Low PI	20%	23%	26%
II	Medium PI	26%	28%	30%
III	High PI	24%	28%	32%
IV	Heavy clay	38%	42%	46%

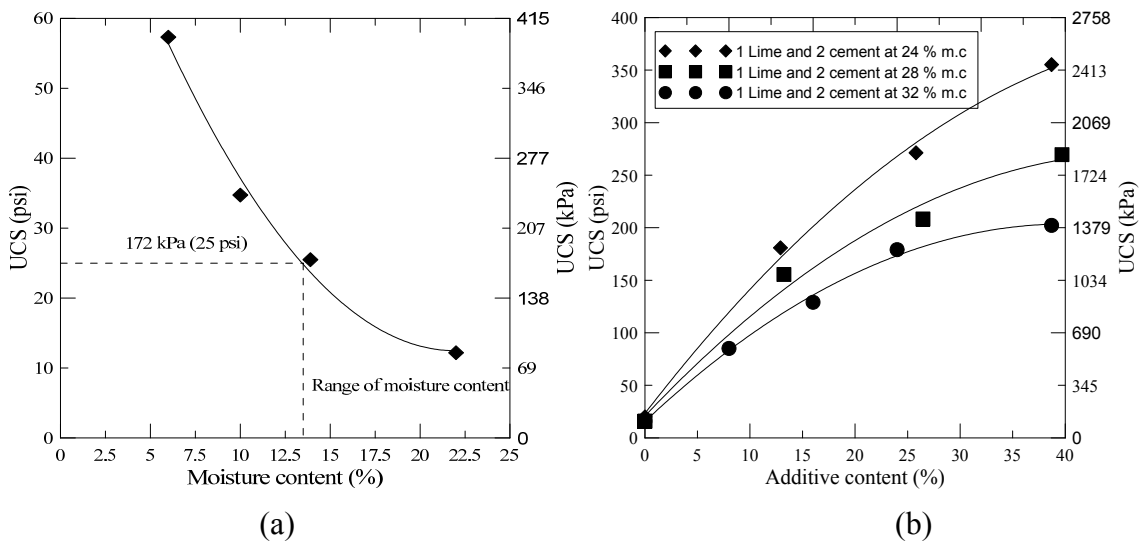


FIG. 1. Variation of UCS with moisture content and additive content for soil II

Preliminary selection of soil stabilizers are made based on basic soil index properties such as plasticity index (PI) and soil gradation characteristics. The UCS tests were then conducted on treated/stabilized soils to evaluate the suitability of the selected stabilizer for particular soil and to determine the percentage of stabilizer needed to achieve the target 7-day strength values of 345 kPa (50 psi) for working table application and 690 kPa (100 psi) for stabilization of subbase.

Figure 1b presents a typical variation of UCS values at different combination of stabilizer and water contents. Based on these results, the final additive contents were selected for this study and are presented in Table 3.

Table 3. Selected additive contents for different soils

Soil #	MC1		MC2		MC3	
	50 psi	100 psi	50 psi	100 psi	50 psi	100 psi
I	5%L+10%F	3%C	6%L+11%F	5%C	7%L+15%F	8%C
II	6%L+8%F	5%C	7%L+10%F	6%C	10%L+14%F	9%C
III	7%L+10%F	4%L+3%C	11%L+15%F	5%L+3.5%C	3%L+2%C	6%L+4%C
IV	2%L+2%C	5%L+3.5%C	3%L+2%C	6%L+4%C	3%L+3%C	7%L+5%C

Note: L: Lime, C: Cement, and F: Fly ash

Resilient Modulus Test

Extensive resilient modulus tests were performed in the laboratory using the MTS machine on the treated/stabilized soil specimens prepared at three different moisture contents (to simulate the range in-situ moisture content of soft soils) as presented in Table 2 and stabilizer contents according to Table 3. The average value of the resilient modulus for the last 10 cycles of each stress sequence was first calculated. Regression analyses were then carried out to fit the data of each test to the generalized constitutive model given in the following model recommended by the AASHTO 2002 - MEPDG to determine the k_1 to k_3 coefficients for the different tested samples. Since the untreated soils at the selected moisture contents were too weak for testing, only the results of treated/stabilized soil samples were included in the analysis part.

$$M_R = k_1 p_a \left(\frac{\theta}{p_a} \right)^{k_2} \left(1 + \frac{\tau_{oct}}{p_a} \right)^{k_3}$$

where θ is bulk stress = $\sigma_1 + \sigma_2 + \sigma_3$; τ_{oct} is octahedral shear stress = $[(\sigma_1 - \sigma_2)^2 + (\sigma_2 - \sigma_3)^2 + (\sigma_3 - \sigma_1)^2]^{1/2}/3$; σ_1 , σ_2 , σ_3 are major, intermediate, and minor principal stresses, respectively; p_a is atmospheric pressure; and k_1 , k_2 , k_3 are model constants.

A typical example on the variation of the resilient modulus with stress conditions obtained from the laboratory tests for treated/stabilized soil II at MC2 and UCS of 345 kPa (50 psi) and 690 kPa (100 psi) specimens is presented in Figure 2. The resilient modulus values of treated/stabilized soils increase with the increase in confining pressure. This is mainly due to the decrease in dilatational properties and the increase in stiffness from increasing confining pressure. The resilient moduli of treated/stabilized soils shows mixed behavior with the increase of deviatoric/cyclic stress, such that it remains constant, increases, or decreases with increasing the deviatoric/cyclic stress, as indicated in Figure 2.

Table 4 presents the average model constants (k_1 , k_2 , and k_3) obtained for the different soils for the AASHTO 2002 M_r model (ARA 2004). Here the averages represent three specimens. These values can be used for pavement design and analysis provided the state of stress is known from layered elastic analysis, finite element analysis, etc. The k_2 coefficient describes the stiffening (higher modulus) of the material with increasing bulk stress. Table 4 shows that all the k_2 coefficients are less than 1. This indicates that the effect of bulk stress decreases with

increasing magnitude. Table 4 also shows that the magnitude of regression coefficients k_1 , k_2 , and k_3 is largely dependent on the soil type and water/stabilizer ratio. This suggests that the specimens with similar UCS but with different water/additive ratios have different resilient characteristics. As such, the use of direct correlation between UCS and M_r for cementitiously treated/stabilized soils can be misleading and should be carefully used in pavement design.

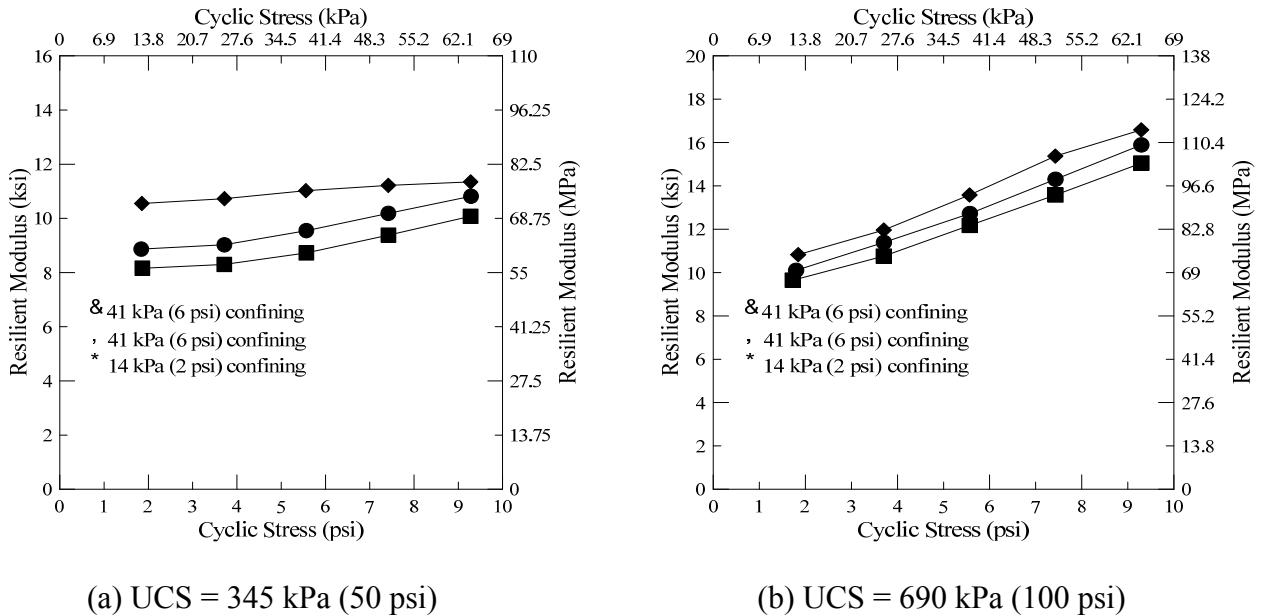


FIG. 2. Resilient modulus of treated soil II specimens [MC = MC2]

The effects of various combinations of water to stabilizer ratios on the resilient modulus for the four different soil types were observed after 7 days of curing. In the case of treated /stabilized soil samples with similar UCS, the test results showed a general trend of slight decrease in the resilient modulus with the increase in the water/additive ratio (Figure 3). One explanation for this behavior may be partially due to the increase in capillary pressure (suction) as saturation decreases; hence the material stiffens as the capillary pressure increases. It should be noted here that an increase in resilient modulus for the tested specimens in this study is also associated with an increase in the cement content. This means that the viability of more calcium ions (divalent) to exchange with monovalent cations present on clay particles during cation exchange processes, hence reduce the thickness of diffused double layer, increased the contact between the clay particles, and thus stiffened the material.

Permanent Deformation

Repeated load triaxial tests were performed to evaluate the permanent deformation behavior of different treated/stabilized subgrade soil specimens. Figure 4 presents the typical curves of the average permanent strain versus the number of cycles obtained for the different RLT cases. The permanent deformation curve has two distinct stages. In the first stage (post-compaction stage), the material accumulates a significant amount of permanent deformation. This is most probably due to extra compaction and initial particle bonding breakage induced particle re-arrangement. During the second stage (secondary stage), the material accumulates permanent strain at a much lower rate and even in some cases the permanent deformation approaches a constant value. The

permanent strains observed for all treated soil specimens after 10,000 cycles of loading are summarized in Table 5. The table shows that the permanent deformation is negligible (permanent strain < 0.09% at 100 psi UCS target value) that could be ignored in pavement design. The effect of water/stabilizer ratio on permanent deformation behavior is presented in Figure 5. The behavior of treated soil specimens (except soil III) clearly demonstrated that the permanent strain increases with the increase in the water/additive ratio. This may be due to the decrease in capillary pressure (suction) with the increase in water/cement ratio, as discussed earlier. It should be noted here that the decrease in water/cement ratio for the tested specimens in this study is associated with an increase in the cement content, i.e., permanent deformation also decreases with the increase in cement content regardless of the moisture content.

Table 4. Model constants for different soils

Soil #	Model Constants	7 days					
		50 psi target (7-day UCS)			100 psi target (7-day UCS)		
		MC1	MC2	MC3	MC1	MC2	MC3
I	k1	527.82	513.56	586.07	466.14	574.46	728.41
	k2	0.41	0.51	0.38	0.16	0.27	0.11
	k3	-0.17	-0.93	-0.35	1.72	1.57	1.77
II	k1	763.73	627.76	655.00	626.02	628.51	701.96
	k2	0.28	0.29	0.07	0.19	0.16	0.21
	k3	-0.48	0.10	2.02	1.95	1.74	1.64
III	k1	673.76	527.26	736.36	1267.51	1479.45	960.05
	k2	0.34	0.37	0.25	0.71	0.57	0.43
	k3	-0.68	-0.25	0.24	-1.20	-1.68	0.65
IV	k1	757.83	643.40	707.91	706.91	687.28	543.39
	k2	0.44	0.45	0.51	0.58	0.29	0.19
	k3	-1.46	-1.14	-1.14	-0.49	0.37	1.46
		28 days					
I	k1	-	472.56	-	-	355.38	-
	k2	-	0.59	-	-	0.58	-
	k3	-	-1.43	-	-	-1.43	-
II	k1	-	641.64	-	-	483.54	-
	k2	-	0.29	-	-	0.30	-
	k3	-	0.92	-	-	0.91	-
III	k1	-	593.65	-	-	447.75	-
	k2	-	0.15	-	-	0.15	-
	k3	-	1.23	-	-	1.23	-
IV	k1	-	503.75	-	-	377.18	-
	k2	-	0.18	-	-	0.17	-
	k3	-	0.78	-	-	0.80	-

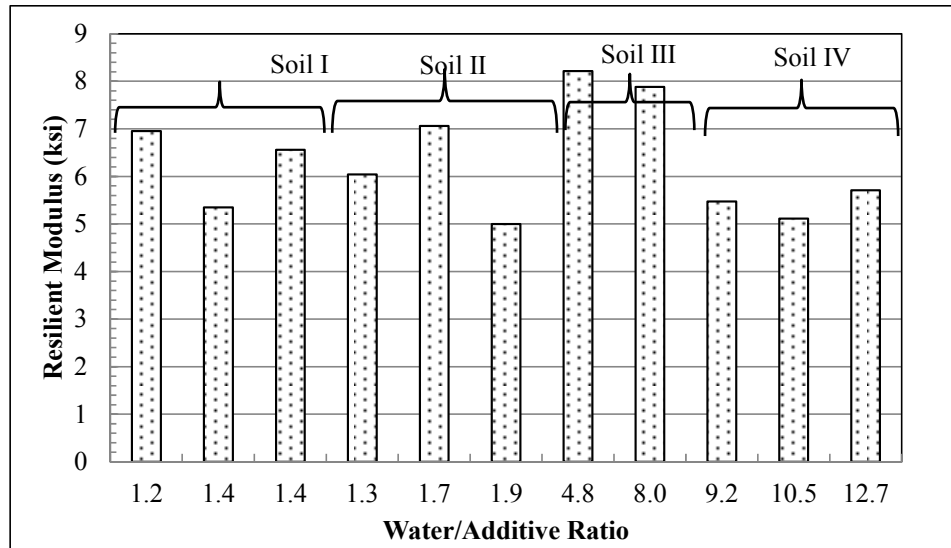
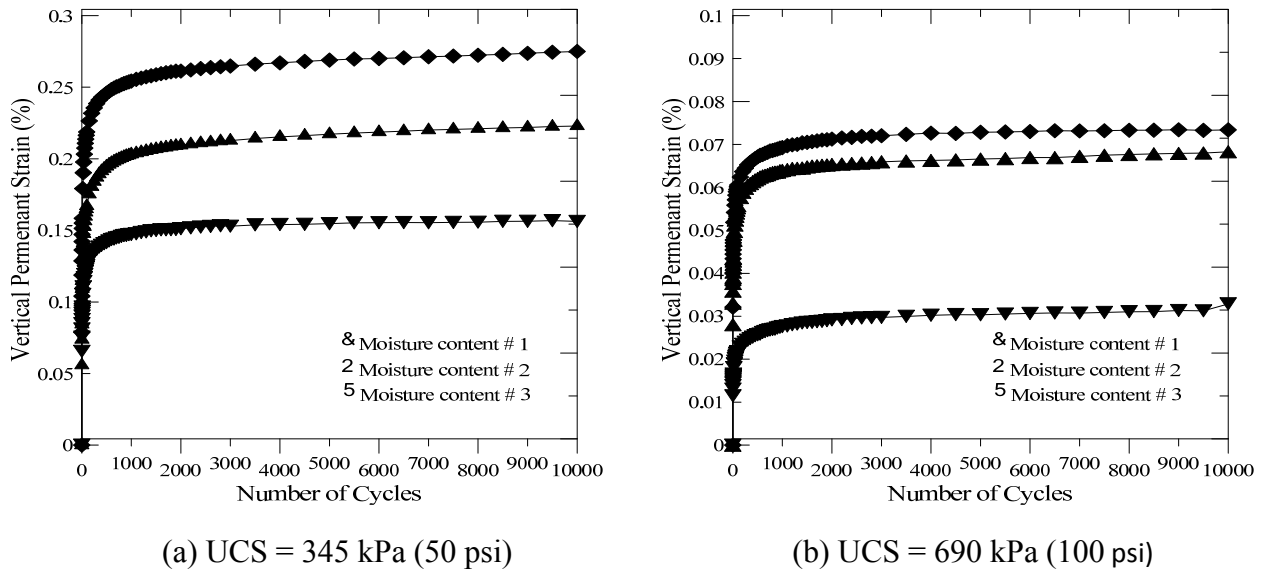


FIG. 3. Resilient modulus of treated soils at different water/additive ratio



(a) UCS = 345 kPa (50 psi)

(b) UCS = 690 kPa (100 psi)

FIG. 4. Permanent deformation of treated soil II specimens

Table 5. Vertical permanent strain of specimens at the 10,000th cycle

Soil #	28 days					
	50 psi target			100 psi target		
	MC1	MC2	MC3	MC1	MC2	MC3
I	0.66%	1.23%	1.60%	0.09%	0.06%	0.03%
II	0.16%	0.22%	0.27%	0.07%	0.07%	0.03%
III	0.15%	0.18%	0.22%	0.07%	0.08%	0.11%
IV	0.26%	0.31%	0.37%	0.06%	0.02%	0.09%

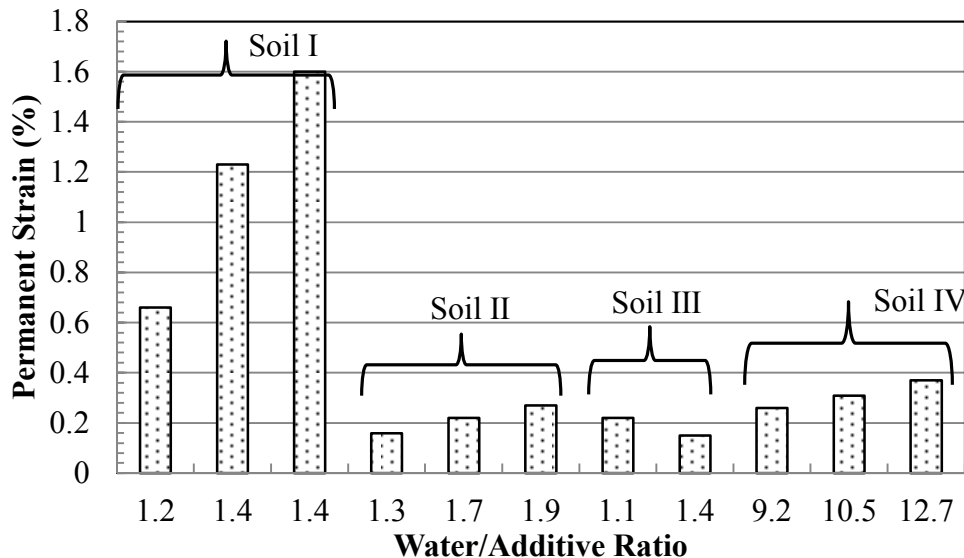


FIG 5. Permanent deformation of treated soils for UCS = 50 psi

SUMMARY AND CONCLUSIONS

The performance-related properties [e.g., the resilient modulus and permanent deformation] of very weak and wet subgrade soils were evaluated in this study. Four different soil types were selected and considered in this study. Three different moisture contents were selected at the wet side of optimum that produce an untreated soil strength value of 172 kPa (25 psi) or less. All the soils were treated with different combinations of lime and fly ash (or cement) to achieve a target 7-day strength target values of 345 kPa (50 psi) to create a working platform and 690 kPa (100 psi) to stabilize the subgrade for subbase application. Based on the results of this study, the following conclusions can be drawn:

- The proper selection of additives and water/additive ratio for very weak and wet subgrade can substantially improve their performance in terms of resilient modulus and permanent deformation for use as working platform table and subbase layer.
- The lime/fly ash combinations were found to achieve the strength target value of 345 kPa (50 psi) but much less than the 690 kPa (100 psi) target value based on the upper practical additive's percentage limit "per volume" of 30%. The cement was then selected to replace the fly ash to achieve the 690 kPa (100 psi) target value.
- The resilient modulus and permanent deformations were found to be related to water/additive ratio, such that the resilient modulus slightly increases and the permanent deformation decreases with the decrease in water/additive ratio.
- The resilient modulus of treated/stabilized soils shows a mixed behavior with the increase of deviatoric/cyclic stress, such that it remains constant, increases, or decreases with the increasing deviatoric/cyclic stress. Furthermore, as expected, the confining pressure has a positive effect on resilient modulus as an increase in the resilient modulus was observed with the increase in confining stress.
- For treated/stabilized subgrade soils, the permanent deformation is somehow negligible (permanent strain < 0.09% at 100 psi UCS target value) that could be ignored in the pavement design.

REFERENCES

- AASHTO T307-99, 2003. *Standard method of test for determining the resilient modulus of soils and aggregates*. American Association of State Highway and Transportation Officials (AASHTO), Washington, D.C.
- Abu-Farsakh M., Dhakal S. and Chen Q., 2015. "Laboratory Characterization of Cementitiously Treated/Stabilized Very Weak Subgrade Soil under Cyclic Loading," *Soils and Foundations Journal*, Volume 55, Issue 3, pp. 504-516.
- Achampong, F., Usman, M., and Kagawa, T., 1997. "Evaluation of resilient modulus for lime- and cement-stabilized synthetic cohesive soils." *Transportation Research Record, Journal of Transportation Research Board 1589*, pp. 70-75.
- ARA, Inc., ERES Consultants Division, 2004. "Guide for mechanistic-empirical design of new and rehabilitated pavement structures." <http://www.trb.org/mepdg/guide.htm>.
- Gautreau, G., Zhang, Z., Wu, Z., Mohammad, L.N., and King, B., 2009. *Accelerated Loading Evaluation of Subbase Layers in Pavement Performance*. Report No. 468, Louisiana Transportation Research Center, Baton Rouge, LA124 p.
- Handy, R. L. 1958. "Cementation of soil minerals with Portland cement or alkalis." *Highway Research Board Bulletin 198*, HRB, Washington, D.C., 55-64.
- Jones, R. 1966. "Measurement of elastic and strength properties of cemented materials in road bases." *Highw. Res. Rec.*, 128, 101-111.
- Lin LM, Tastan O, Benson CH, Edil T.B., 2009. Field Evaluation of Fly Ash Stabilized Subgrade in US 12 Highway. International Foundation Congress and Equipment Expo. ASCE. pp. 385-392.
- Little, D.N., 2000. *Evaluation of Structural Properties of Lime Stabilized Soils and Aggregates, Volume 3: Mixture Design and Testing Protocol for Lime Stabilized Soils*, (<http://www.lime.org/soil3.pdf>), National Lime Association, Arlington, VA, 16 pp
- Little, D.N., and Nair, S., 2009. *Recommended Practice for Stabilization of Subgrade Soils and Base Materials*, National Cooperative Highway research Program Web-Only Document 144, Transportation Research Board, National Research Council, Washington, DC, 57 pp.
- Lund, O. L., and Ramsey, W. J. 1959. "Experimental lime stabilization in Nebraska." *Highway Research Board Bulletin 231*, HRB, Washington, D.C., 24-59.
- Mallela, J., Von Quintus, H., and Smith, K.L., 2004. *Consideration of Lime-Stabilized Layers in Mechanistic-Empirical Pavement Design*. Report prepared for the National Lime Association, pp. 36.
- Mohammad L, Saadeh S. 2008. Performance Evaluation of Stabilized Base and Subbase Material. Geo Congress, ASCE. pp 1073-1080.
- Mohammad, L.N., and Herath, A., 2005. "Accerlated loading evaluation of a sub-base layer on pavement performance, Volume III: resilient and permanent deformation properties of untreated and treated unbound pavement materials," Interim Report, Louisiana Transportation Research Center.
- Mohammad, L.N., and Saadeh, S., 2008. "Performance evaluation of stabilized base and subgase material," *GeoCongress 2008: Geosustainability and Geohazard Mitigation*, pp 1073-1080.
- Pendola, H.J., Kennedy, T.W., and Hudson, W.R., 1969. "Evaluation of factors affecting the tensile properties of cement-treated materials." Report No. 98-3, Texas Highway Department, Austin, TX.
- Prusinski, J.R; and Bhattacharja, S., 1999. "Effectiveness of Portland cement and lime in stabilizing clay soils." *Transportation Research Record: Journal of Transportation Research Board 1652*, National Research Council, Washington, DC, pp. 1-13.
- Reinhold, F. 1955. "Elastic behavior of soil-cement mixes." *Highway Research Board Bulletin 108*, HRB, Washington, D.C., 128-137.
- Solanki, P., Zaman, M.M., and Dean, J., 2010. "Resilient modulus of clay subgrades stabilized with lime, class C fly ash, and cement kiln dust for pavement design." *Transportation Research Record: Journal of Transportation Research Board 2186*, National Research Council, Washington, DC, pp. 101-110.
- Tastan E.O., Edil T.B., Benson C.H., Aydilek A.H., 2011. Stabilization of Organic Soils with Fly Ash. *Journal of Geotechnical and Geoenvironmental Engineering*, ASCE. pp. 819-833.

Feasibility of the Discrete Element Method to Simulate RAP Asphalt Mixtures' Fracture Behavior

Enad M. Mahmoud, M.ASCE, P.E.¹; Shadi M. Saadeh, M.ASCE²; and Roberto R. Yanez³

¹Assistant Professor, Dept. of Civil Engineering, Univ. of Texas – Rio Grande Valley, 1201 W. University Dr., Edinburg, TX 78539. E-mail: enad.mahmoud@utrgv.edu

²Associate Professor, Dept. of Civil Engineering and Construction Engineering Management, California State Univ., Long Beach, 1250 Bellflower Blvd., Long Beach, CA 90840. E-mail: shadi.saadeh@csulb.edu

³Undergraduate Research Assistant, Dept. of Civil Engineering, Univ. of Texas – Rio Grande Valley, 1201 W. University Dr., Edinburg, TX 78539. E-mail: roberto.yanez01@utrgv.edu

Abstract: Fracture of asphalt mixtures was modeled using a heterogeneous 2D-discrete element method (H2DEM). A bilinear cohesive zone model was used to model crack initiation and propagation. Image processing techniques were used to transfer planar images of semi-circular bending (SCB) samples to a two-phase H2DEM model: mastic and coarse aggregates. The sensitivity of the model to the cohesive zone model parameters, coarse aggregate properties, and bond strength was studied to facilitate the calibration process. Experimental data for semi-circular samples with three notch depths of 25.4, 31.8, and 38.0 mm were used. The model calibration had a very good agreement with the experimental results and the model successfully predicted the SCB testing results. The main focus of this paper was to investigate the capability of H2DEM to simulate fracture in asphalt mixtures including RAP, to this end two mixes were included, a control mix and a RAP mix. The results indicated that H2DEM has the capability to capture the stiffening effect of RAP inclusion in asphalt mixes, by adjusting the bilinear cohesive zone model parameters.

INTRODUCTION

Recent advances in numerical modeling have shown a new insight in investigating fracture behavior of the asphalt concrete i.e., mechanism of crack initiation and crack propagation. Numerical methods such as finite element method (FEM) and discrete element method (DEM) have been applied rigorously to analyze the fracture behavior of the asphalt concrete. Several research studies successfully utilized DEM to characterize asphalt mixes, such as, You and Buttlar (2004): prediction of asphalt concrete mixtures modulus; You and Buttlar, (2005): Hollow cylinder tensile test

simulations; Abbas et al. (2005): asphalt mastic stiffness; by Abbas et al. (2007): asphalt mixture response under sinusoidal loading; Mahmoud et al. (2010-a,b, and c): influence of aggregate properties and internal structure on fracture in asphalt mixes; Dai and You (2007), Liu et al. (2009), You et al. (2011), Liu and You, (2011-a&b), Collop et al. (2007), Wu et al. (2011), Cai et al. (2013), and Cai et al. (2014): viscoelastic DEM modeling of asphalt mixtures. DEM fracture model focused on laboratory testing designed to measure fracture properties of asphalt mixtures, namely disk-shaped compact tension test geometry and the single edge notch beam was developed by Professor Buttlar research group at the University of Illinois Urbana-Champaign, the model was in 2D and utilized hexagonal packing scheme and bilinear cohesive zone modeling to account for damage. The model was also expanded to include time-dependent Burger contact model (Kim et al., 2008; Kim and Buttlar 2009-a&b, Kim et al. 2009-a&b).

Kim et al (2008) illustrated the potential efficacy of DEM for studying the crack behavior in asphalt concrete by directly considering the contribution of materials heterogeneity. DEM successfully modeled fracture of single edge notched beam. Kim et al (2008) verified the DEM approach by comparing the bulk response to analytical solution for uniaxial compression and cantilever beams, and simulated the compact disk fracture test with a DEM fracture model and reported that the model results matched well the experimental results. In another study by Kim et al (2009), heterogenous fracture behavior in asphalt materials were investigated with different nominal maximum aggregate size, aggregate types, progressive crack and stress distributions ahead of the crack tip at low temperatures and results showed that the discrete element fracture modeling approach appears to have significant potential to aid in understanding the fracture behavior in asphalt concrete. Mahmoud et al (2010-a) studied the combined effect of aggregate gradation, shape, stiffness and strength on hot mix asphalt (HMA) resistance to fracture successfully by coupling the DEM with image processing techniques. In another studies by Mahmoud et al (2010-b & c), DEM modeling of asphalt mixes was used to find the influence of the actual particle shape on the distribution of internal forces and possible fracture within the aggregate structure. The results showed that mathematical derivation of probability of aggregate fracture and the DEM simulation results compare very well. The literature search clearly indicates that discrete element fracture modeling approach appears to have significant potential for aiding in understanding of fracture behavior in asphalt concrete.

OBJECTIVES AND SCOPE

This paper focuses on investigating the feasibility of using DEM to simulate fracture in RAP asphalt mixes. The Semi-Circular Bending (SCB) test was modeled in DEM coupled with cohesive zone model to capture fracture behavior. The following tasks were performed to achieve this objective:

1. Homogenous DEM simulations are conducted to understand the effect of stiffness and contact bond strength parameters.
2. Image processing techniques are used to transfer the aggregate internal structure into DEM.

- Heterogeneous DEM model was calibrated and its applicability to RAP asphalt mixes was studied.

DISCRETE ELEMENT METHOD

The discrete element method was introduced by the Cundall (1971) to study interaction among assemblies of particles, the method was then extended to study rock mechanics, soils, granular materials, asphalt mixes, etc. The work described in this study uses commercially available discrete element software: particle flow code (PFC). The DEM concept is simple in principle; it is based on successively solving the law of motion (Newton's second law) and the force-displacement law for each element. A bond is installed at the contacts between the discrete elements to simulate a continuum solid, the bond has a limiting strength, once the forces at the contact exceed the specified strength, the bond breaks, progressive breakage of bonds in the assembly represent the fracture behavior: crack initiation and propagation (PFC2D, 2009).

PFC^{2D} provides several standard contact models, and it also allows user defined contact models. In this study, a bilinear cohesive zone model was introduced into DEM by user-defined contact model called displacement-softening model. Previous research studies (Kim et al., 2008; Kim and Buttlar 2009-a&b, Kim et al. 2009-a&b) have showed that cohesive zone model (CZM) was the most promising material separation model for studying fracture of asphalt mixtures. The typical bilinear cohesive zone model is shown in figure 1.

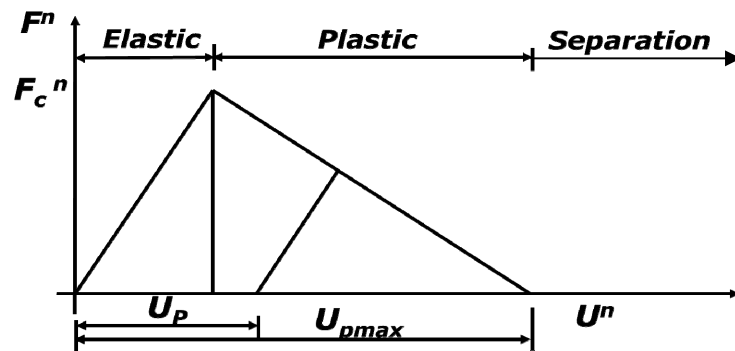


FIG. 1. A typical bilinear cohesive zone model

The contact bond softens, if the contact force (F) is larger than the contact strength (F_{max}), i.e. $F > F_{max}$

where $F = \sqrt{(F^n)^2 + (F^s)^2}$, $F^n =$ normal force, $F^s =$ shear force,

$F_{max} = \left(1 - \frac{2 \cdot \alpha}{\pi}\right) \cdot F^n + \frac{2 \cdot \alpha}{\pi} \cdot F^s$ and α is angle between the direction of contact force

and the line segment connecting center of the particles. When the softening of contact bond takes place, the increment of contact displacement, ΔU^k ($k = n, s$) can be decomposed into elastic and plastic contact displacement increments

$$\Delta U^k = \Delta U_e^k + \Delta U_p^k$$

The force increment, ΔF^k is a function of the increment of the elastic displacement only.

$$\Delta F^k = K^k \cdot \Delta U_e^k$$

where

$$\Delta U_e^k = \Delta U^k - \Delta U_p^k$$

and the contact strength in softening model is function of the accumulated plastic displacement.

$$F_c^k \cdot \left(\frac{U_p}{U_{pmax}} \right) = F_c^k \cdot \left(1 - \frac{U_p}{U_{pmax}} \right)$$

where $U_p = \sum |\Delta U_p|$, U_{pmax} is the accumulated plastic deformation at which the bond strength is zero, and F_c^k is the bond strength (tensile-k=n and shear-k=s).

Kim et al (2008) successfully verified the DEM based cohesive zone model by simulating a double cantilever beam. And the numerical results are found to be in agreement with the analytical solutions. They reported that CZM approach in DEM yields a reasonable result for fracture properties of asphalt concrete.

HOMOGENOUS MODEL ANALYSIS

A homogenous 2D DEM model was created for the SCB test geometry. Figure 2 illustrates a schematic of the test and the DEM model. The model followed the exact dimensions and loading rate from the lab experiment (Hakimelahi et al, 2013). The purpose of the homogenous model was to understand the effect of the bilinear cohesive zone model parameters on the SCB test results. A control homogenous sample was created with the following properties: density of 2650 kg/m³, normal stiffness (Kn) and shear stiffness (Ks) of 1x10⁶ N/m, normal and shear strength equal to 80 N, and U_{pmax} equal to 128 mm.

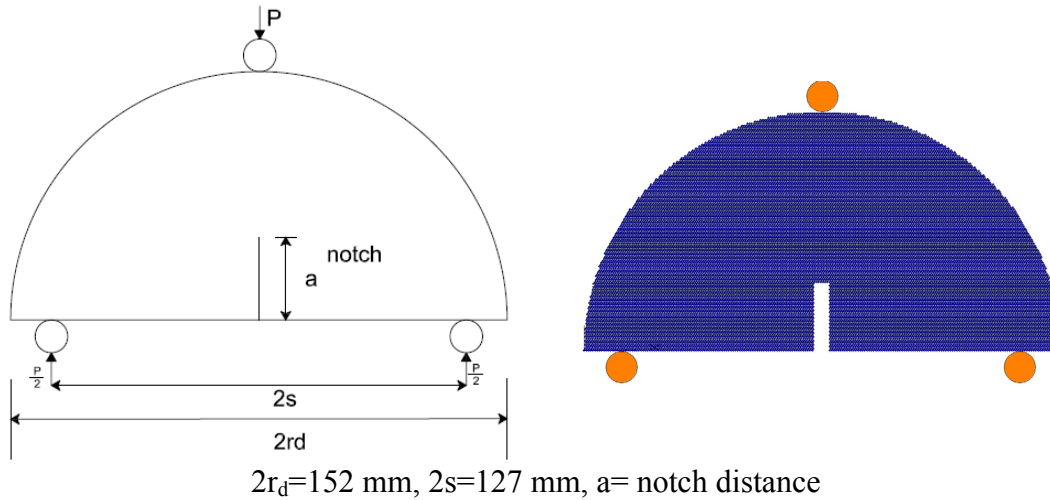
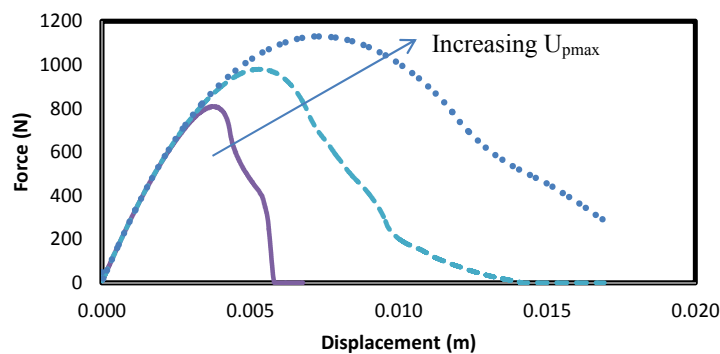
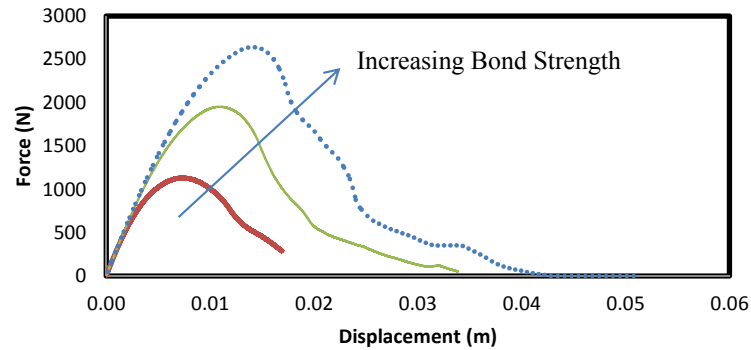


FIG. 2. SCB schematic and DEM homogenous model

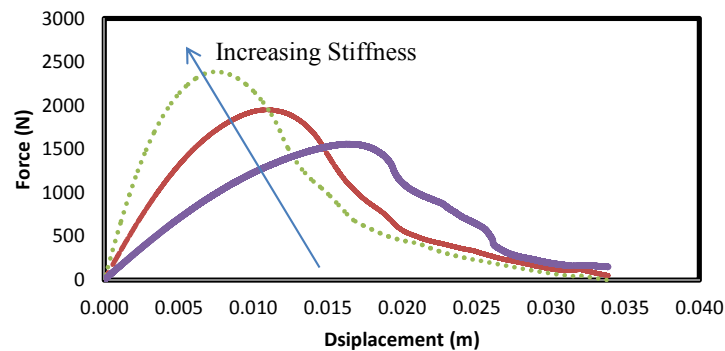
Figure 3 illustrates the effect of each of the cohesive zone model parameters on the force-displacement curves of the SCB test. Figure 3-a illustrates the effect of the U_{pmax} parameter, in this case the stiffness and strength values were held fixed, increasing the U_{pmax} value resulted in an overall increase of the SCB maximum load and its associated displacement, which will result in higher fracture energy. Increasing the bond strength (while keeping U_{pmax} and stiffness constant) resulted in an increase in the maximum force and a shift in the associated displacement, however, comparing Figure 3-a and Figure 3-b clearly indicates that the bond strength had a greater effect on the maximum load while the U_{pmax} had a moderate effect on both maximum load and the displacement. Finally, the effect of the stiffness is shown in figure 3-c, the parametric analysis clearly indicated increase in the maximum load with a reduction in the associated displacement, which indicates reduction in the material ductility.



(a)



(b)



(c)

FIG. 3. Cohesive zone model parameters effect on SCB test results: a) U_{pmax} , b) bond strength, and c) stiffness

HETEROGENEOUS MODEL ANALYSIS

A heterogeneous 2-D DEM (H2DEM) model was developed by importing 2D images of asphalt mixture SCB laboratory samples to DEM. Image processing technique and MATLAB code were used to achieve this. Image-Pro analyzer 7.0 was used to process the digital images and separate the aggregate particles from the asphalt mastic. The processed images were then imported to the DEM model using a user defined MATLAB code. The code was used to process the images and identify the location of every pixel within the aggregate and mastic phases, which was then mapped into the DEM model and the two groups of materials were identified. Three types of contacts are identified in this model: aggregate-to-aggregate, mastic-to-mastic, and aggregate-to-mastic (interface). Linear elastic properties were assigned to the aggregate-to-aggregate contact, while the bilinear cohesive zone model was assigned to the mastic-to-mastic and aggregate-to-mastic contacts. Figure 4 shows an example of a H2DEM of asphalt SCB sample and the contacts within the sample.

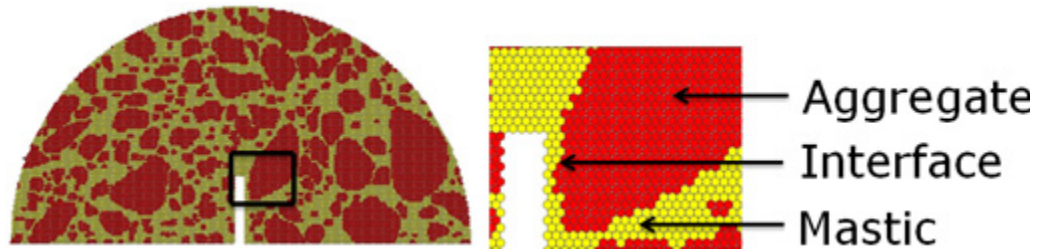


FIG. 4. H2DEM of asphalt SCB sample and types of contacts

Although the main objective of this study is to investigate the use of H2DEM to model RAP asphalt mixes behavior rather than obtain simulation results to fit laboratory data, it was still necessary to provide initial calibration for the model parameters, to have realistic load-displacement curves. This was achieved by utilizing laboratory testing data, specifics of the laboratory prepared samples can be found in published paper (Hakimelahi et al, 2013). Figure 5, shows one example of the model simulation results compared to laboratory sample with 25.4 mm notch size. The model also successfully predicted testing results of different notch sizes (31.75 and 38.1 mm). Figure 6, depict the H2DEM sample after loading, the figure clearly shows the ability of the model to capture the crack initiation and propagation within the sample. Crack propagation within both mastic-to-mastic and the interface contacts was observed. Further analysis of the interface and aggregate properties, among other parameters, and its effect on the simulation results were also studied but it's not the focus of this study, and is not included in this paper.

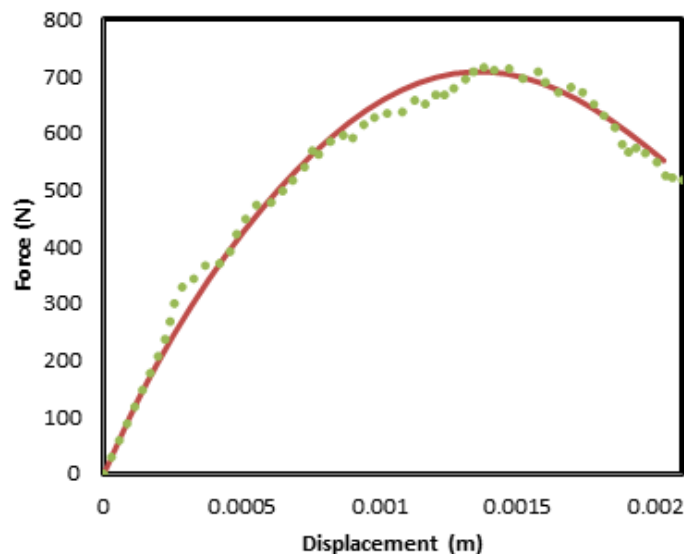


FIG. 5. H2DEM calibration (solid line: laboratory sample, dotted line: simulation)

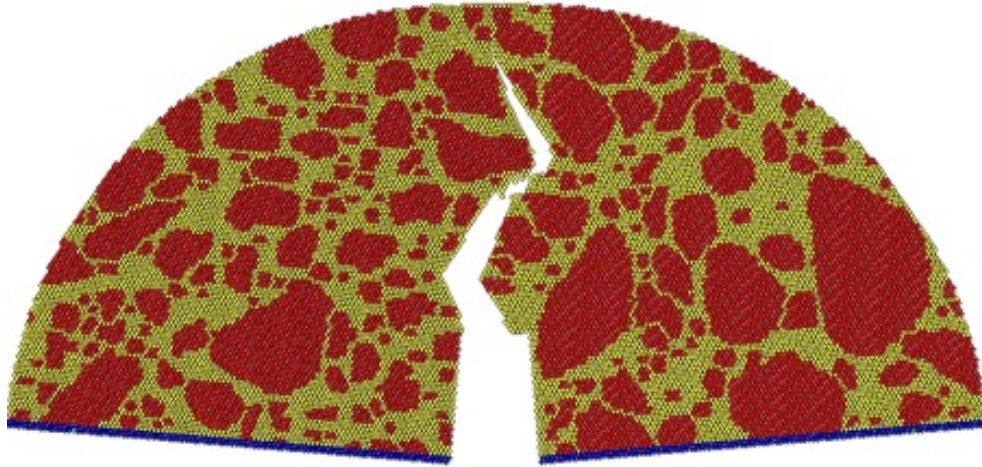


FIG. 6. H2DEM sample crack propagation

Figure 7 illustrates laboratory testing results of a control and RAP asphalt mixes SCB sample with 25.4 notch. The figure indicates the effect of adding RAP to the asphalt mixture, which is an increase in the maximum load with a reduction in the displacement associated with it, resulting in a higher stiffness but less ductility in the materials behavior. Mixture information including binder type, NMA, and gradation of these mixes can be found in Hakimelahi et al. (2013).

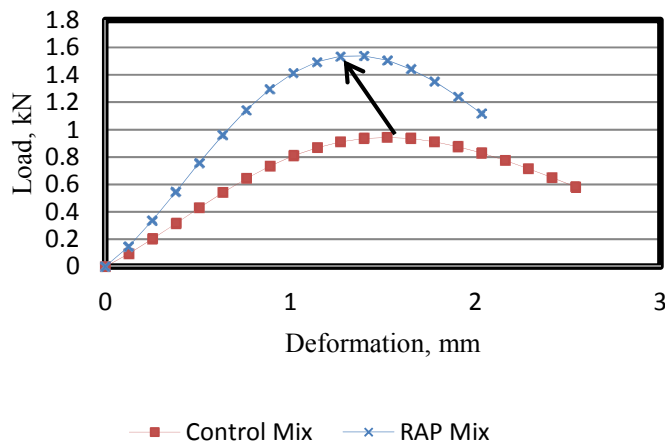


FIG. 7. SCB Laboratory test results for 25.4 mm notch

The heterogeneous model ability to capture the effect of RAP asphalt mixes was investigated by changing the stiffness of the cohesive zone model. Based on the results of the homogenous model, it was anticipated that an increase in the stiffness will capture the effect of inclusion of RAP in asphalt mixtures. Figure 8 illustrates this concept. In this figure, the solid line represents the H2DEM SCB model

simulation results which match the results of laboratory control asphalt mix. The parameters for this matched case were kept constant except for the softening model stiffness which was doubled, the simulation results of this case is presented by the dashed line in figure 8. Compared to figure 7, it's clear that the H2DEM SCB model is capable of capturing the effect of RAP on asphalt mixes fracture behavior, the model had the same exact trend as compared to the laboratory test results. It is important to emphasize that the objective of this paper was to study the model capabilities rather than to match and reproduce experimental results.

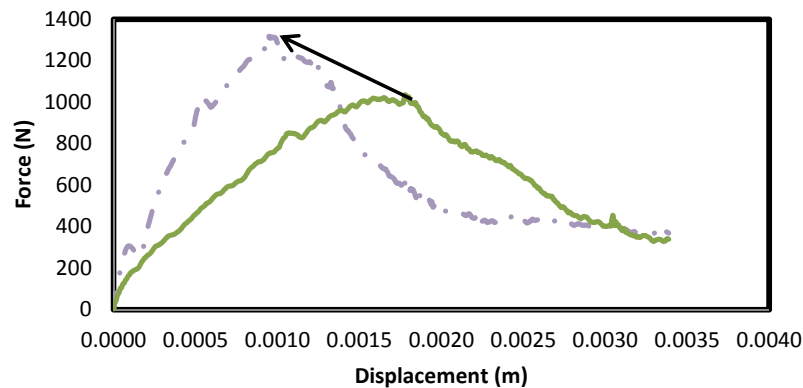


FIG. 8. H2DEM SCB model: (solid line: asphalt mix, dotted line: RAP asphalt mix)

CONCLUSIONS

Simulations of SCB, a laboratory fracture test, using homogeneous and heterogeneous models were performed. Experimental results were used to develop and calibrate the heterogeneous model H2DEM of the SCB test for asphalt mixtures. Based on the results of this study the following conclusions were drawn:

1. The DEM model successfully simulated the SCB test process including the crack initiation and propagation.
2. The model successfully predicted the 31.8 and 38.0 mm notch depth SCB test using calibrated results of the 25.4 mm notch.
3. Homogenous model results indicated that the cohesive zone model parameters have significant effect on the overall behavior of the test, the load-displacement curve key characteristics such as: maximum load, displacement at maximum load, and fracture energy, are all affected by the model properties.
4. Heterogeneous model results indicated crack propagation through different phases of asphalt mixtures such as within mastic and at the mastic-aggregate interface. Furthermore H2DEM is capable of capturing the RAP effect on asphalt mixture properties measured in the SCB test.

ACKNOWLEDGMENTS

The authors would like to thank the United States Department of Transportation, the California Department of Transportation and METRANS for their interest and provision of grant support to make this study possible.

REFERENCES

- Abbas, A., Masad, E., Papagiannakis, T., and Harman, T. (2007). "Micromechanical modeling of the viscoelastic behavior of asphalt mixtures using the discrete-element method." *International Journal of Geomechanics ASCE*, 7(2), 131-139.
- Cai, W., McDowell, G., and Airey, G. (2013). "Discrete element modelling of uniaxial constant strain rate tests on asphalt mixtures" *Granular Matter*, 15(2), 163-174.
- Cai, W., McDowell, G., and Airey, G. (2014) "Discrete element visco-elastic modelling of a realistic graded asphalt mixture" *Soils and Foundations*, 54(1), 12-22.
- Collop, A., McDowell, G., and Lee, Y. (2007), On the use of discrete element modelling to simulate the viscoelastic deformation behaviour of an idealized asphalt mixture. *Geomechanics and Geoengineering* Vol. 2, Iss. 2.
- Cundall, P. A. (1971). "A computer model for simulating progressive large scale movements in blocky rock systems." *Proc., Symposium of the International Society of Rock Mechanics, Nancy, France, Vol. 1, Paper No. II-8.*
- Dai, Q., and You, Z. (2007). "Prediction of creep stiffness of asphalt mixture with micromechanical finite-element and discrete-element models." *Journal of Engineering Mechanics ASCE*, 133 (2), 163-173.
- Hakimelahi, H., Saadeh, S., Harvey, J., (2013) "Comparison of Fracture Properties of Four Point Beam and Semi Circular Bending of Asphalt Concrete." *Journal of Road Materials and Pavement Design*, V 14, Supplement 2, pp 252 - 265.
- Kim, H., and Buttlar, W., (2009-a). "Discrete fracture modeling of asphalt concrete." *International Journal of Solids and Structures*, Vol. 46, No. 13, 2593-2604.
- Kim, H., and Buttlar, W., (2009-b). "Multi-scale fracture modeling of asphalt composite structures." *Composites Science and Technology*, Vol. 69, No. 15-16, 2716-2723.
- Kim, H., Wagoner, M. P., and Buttlar, W. (2008). "Simulation of fracture behavior in asphalt concrete using a heterogeneous cohesive zone discrete element model." *Journal of Materials in Civil Engineering ASCE*, 20(8), 552-563.
- Kim, H., Wagoner, M., and Buttlar, W. (2009-a) "Micromechanical fracture modeling of asphalt concrete using a single-edge notched beam test." *Materials and Structures*, Vol. 42, NO. 5, 677-689.
- Kim, H., Wagoner, M., and Buttlar, W. (2009-b) "Rate-dependent fracture modeling of asphalt concrete using the discrete element method." *Canadian Journal of Civil Engineering*, (36), 320-330.

- Liu, Y., and You, Z. (2011). "Accelerated Discrete-Element Modeling of Asphalt-Based Materials with the Frequency-Temperature Superposition Principle." *Journal of Engineering Mechanics*, 137(5), 355-365.
- Liu, Y., and You, Z. (2011). "Discrete-Element Modeling: Impacts of Aggregate Sphericity, Orientation, and Angularity on Creep Stiffness of Idealized Asphalt Mixtures." *Journal of Engineering Mechanics*, 137(4), 294-303.
- Liu, Y., Dai, Q., and You, Z. (2009). "Viscoelastic Model for Discrete Element Simulation of Asphalt Mixtures." *J. Eng. Mech.*, 135(4), 324-333.
- Mahmoud, E., and Masad, E. (2010). "A Probabilistic Model for Predicting Resistance of Aggregates in Asphalt Mixes to Fracture," *International Journal of Road Materials and Pavements Design (IJ-RMPD)* Vol. 11 No. 2, pp 335-360.
- Mahmoud, E., Masad, E., and Nazarian, S. (2010) "Discrete Element Analysis of the Influence of Aggregate Properties and Internal Structure on Fracture in Asphalt Mixtures," *Journal of Materials in Civil Engineering*, (ASCE) Vol. 22 No. 1, pp 10-20.
- Mahmoud, E., Masad, E., Nazarian, S., and Abdallah, I. (2010) "Modeling and Experimental Evaluation of Influence of Aggregate Blending on Asphalt Mixture Strength," *Journal of Transportation Research Board*, (TRB) Vol. 2180, pp 48-57.
- Particle Flow Code in 2-Dimensions (PFC2D) Manual (2009), Version 4.0, Itasca Consulting Group, Minneapolis, MN.
- Wu, J., Collop, A., and McDowell, G. (2011). "Discrete Element Modeling of Constant Strain Rate Compression Tests on Idealized Asphalt Mixture." *J. Mater. Civ. Eng.* 23, SPECIAL ISSUE: Multiscale and Micromechanical Modeling of Asphalt Mixes, 2-11
- You, Z., and Buttlar, W. G. (2004). "Discrete element modeling to predict the modulus of asphalt concrete mixtures." *Journal of Materials in Civil Engineering* ASCE, 16(2), 140-146.
- You, Z., and Buttlar, W. G. (2005). "Application of discrete element modeling techniques to predict the complex modulus of asphalt—aggregate hollow cylinders subjected to internal pressure." *Transportation Research Record* 1929, Transportation Research Board, Washington, DC; pp 218–226.
- You, Z., Liu, Y., and Dai, Q. (2011). "Three-Dimensional Microstructural-Based Discrete Element Viscoelastic Modeling of Creep Compliance Tests for Asphalt Mixtures." *J. Mater. Civ. Eng.* 23, SPECIAL ISSUE: Multiscale and Micromechanical Modeling of Asphalt Mixes, 79–87.

Feasibility Study on Harvesting Energy from Roadway Infrastructure

H. Roshani, S.M.ASCE¹; S. Dessouky, M.ASCE²; A. T. Papagiannakis, F.ASCE³;
A. Montoya⁴; and J. Helffrich⁵

¹Graduate Research Assistant, CEE Dept., Univ. of Texas at San Antonio, One UTSA Circle, San Antonio, TX 78249.

²Associate Professor, CEE Dept., Univ. of Texas at San Antonio, One UTSA Circle, San Antonio, TX 78249.

³Professor, CEE Dept., Univ. of Texas at San Antonio, One UTSA Circle, San Antonio, TX 78249.

⁴Assistant Professor, CEE Dept., Univ. of Texas at San Antonio, One UTSA Circle, San Antonio, TX 78249.

⁵Scientist, Southwest Research Institute, 6220 Culebra Rd., San Antonio, TX 78238.

Abstract: This paper presents preliminary results of the evaluation of several prototype systems for harvesting energy from the action of traffic on roadways. These systems utilize piezoelectric elements that respond to traffic-induced compressive stresses, and are referred to as HiSEC (highway sensing and energy conversion) modules. The evaluation of the HiSEC prototypes involves laboratory testing of their power output as a function of stress, finite element (FE) simulation of their mechanical behavior and economic analysis of the value of the power being generated. The results available to date suggest that this technology shows promise in powering equipment independently of the power grid.

INTRODUCTION

In recent years, there has been increasing interest in energy harvesting through transduction. Three technologies have been used for this purpose, namely electromagnetic, electrostatic and piezoelectric⁰. Piezoelectric transduction appears to be the most promising, given its widest power density versus voltage envelop, as shown in Fig. 1.

A number of recent studies explored the use of piezoelectric transduction for harvesting energy from roadways, e.g., Xiong (2014), Kim et al. (2015), Zhao et al. (2014). Work by Xiong (2014) at Virginia Tech produced a piezoelectric harvesting system consisting of multiple cylindrical piezoelectric elements that are compressed by the action of traffic tires (Fig. 2). Under a traffic volume of 4,000 vehicle per day (167 vehicles/hour), this system generated voltage ranging from 400 to 700V and electric currents ranging from 0.2 to 0.35 mA. The corresponding power output was obtained by multiplying voltage by current, yielding a power range between 0.08 and 2.1 Watts per system.

Work by Kim et al. (2015) at Georgia Southern University involved laboratory testing using an Asphalt Pavement Analyzer (APA). Two piezoelectric materials were tested one

manufactured by *Noliac* and the other by *Kinetic*. APA wheel loads at three levels were applied, namely 50, 100 and 200 lbs. The maximum resulting voltages for the *Noliac* were 5, 5, and 15 Volts, respectively, while for the *Kinetic* were 5, 10 and 20 Volts, respectively. Assuming a traffic level of 600 vehicles/hour at a speed of 45 mph, such a system could produce up to 2.67 mW of power.

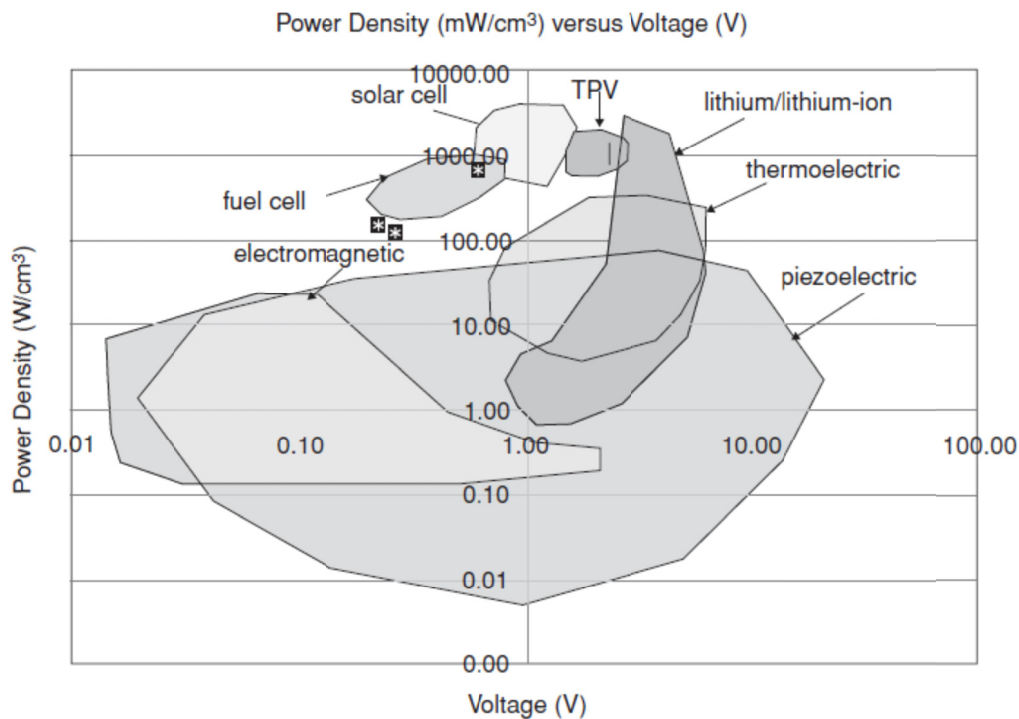


FIG 1. Power Density versus Voltage for various Energy Harvesting Technologies (Cook-Chenault et al., 2008).



FIG. 2. Piezoelectric Energy Harvesting System Developed By Xiong (2014).

Zhao et al. (2014) at Tongji University studied power generation from several types of piezoelectric sensor configurations. These included multiple lead zirconate titanate (i.e., PZT) prismatic elements referred to as “piles” with circular, square or hexagonal cross sections, as well as commercially available cymbal-shaped and bridge-shaped elements (Fig. 3). They

performed FE analysis to study the effect of the shape of the PZT piles in producing electric power output, concluding that the circular cross section piles were preferable. Power generators involving multiple piles were analyzed. Stress analysis combined with theoretical calculations established that generators with 8-16 piles each can be used to harvest significant amounts of electrical power under heavy traffic.

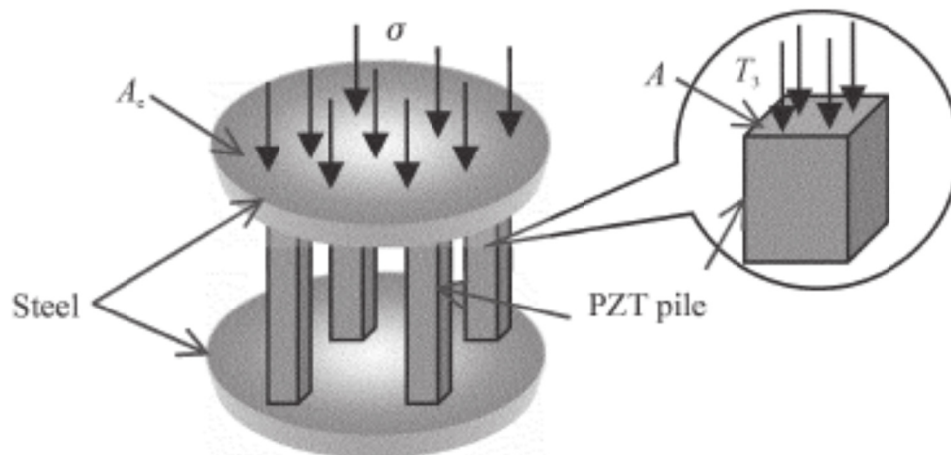


FIG. 3. Schematic of PZT Pile Generator (Zhao et al., 2014).

A report was recently completed on behalf of the California Energy Commission (CEC) to independently evaluate the feasibility of piezoelectric technology in harvesting energy from roadways and establish if this technology warrants further study (Hill et al., 2013). It evaluated some of the pilot systems developed by Universities, as well as commercially available harvesting systems. Three commercially available systems were evaluated in terms of their vendor output claims, namely, *Treenvolt* (www.treenvolt.com), *Genziko* (www.genziko.com) and *Innowattech* (Edel-Ajulay 2010). The first two of these three vendors appear to continue development of this technology. The *Treenvolt* harvesters, marketed in the USA under the *POWERLeap* name, consist of recycled butyl-propylene membranes sandwiching sheets of harvesting devices are embedded under the top layer of asphalt concrete and are activated in compression. The vendor claims that 1.0 km length of roadway equipped with 6,000 *Treenvolt* harvesters and carrying 600 vehicles per hour can generate approximately 720 kW of power. *Genziko* claims that under the same traffic level, their vibration-activated harvesters have the potential to generate a considerably higher 13,600 kW of power, an amount that was considered “optimistic” by the CEC report. *Innowattech* claims that their harvesters can generate 200 kW under similar traffic levels, assuming that harvesters are placed under both wheel paths. The CEC study observed that there are considerable differences in the energy output claims made by different vendors, especially with respect to the assumptions made for the number of sensors involved and the traffic level. It was recommended adopting a standardized way of reporting power or energy output by piezo unit surface area, referred to as power or energy density (i.e., W/unit area or Wh/unit area, respectively). In evaluating the cost effectiveness of these systems, the CEC report recommended using the “levelized” cost of energy (LCOE) produced by the various harvesting systems varies. The LCOE is defined as the average total life-cycle cost to construct, operate and maintain a power-generating system divided by its total energy output

over its service life. This report concludes by recommending further field testing of this technology.

OBJECTIVE

The objective of this paper is to further explore the application of piezoelectric technologies for harvesting energy from the action of traffic using the roadways. It provides a brief overview of piezoelectricity fundamentals, a review of the pertinent literature and a preview of our efforts to develop and test several prototypes for harvesting energy. The most promising prototype will be refined and integrated into a series of modules laid down in the wheel path of roadways for harvesting energy. They are referred to as the HiSEC (Highway Sensing and Energy Conversion) modules.

PRINCIPLES OF ENERGY FROM PIEZOELECTRIC TRANSDUCTION

Piezoelectric materials generate electricity when subjected to stress or vibration. They are crystalline ceramics (e.g., lead zirconate titanate, abbreviated as PZT) or polymers (e.g., polyvinyl fluoride abbreviated as PVF) heated above their Curie temperature and subjected to a magnetic field to orient their electric dipoles in the same direction. Stress/strain parallel to the poling direction of a piezoelectric material generates an electrical charge. Conversely, an electric charge generates stress/strain across a piezoelectric material. For simplicity the physics governing piezoelectric power generation are explained below in uniaxial terms (i.e., strain/stress in a single direction only). A complete treatment of the subject can be found in the literature (Ertuk and Inman 2011).

Consider the piezoelectric element of dimensions a , b and c shown in Fig. 4 and assume that the direction of polarization is vertical. A force F , parallel to the polarization direction will generate an electrical charge Q (Coulombs) given by:

$$Q = Fd_{33} \quad (1)$$

Where, d_{33} is the piezoelectric charge constant (Coulombs/N). This mode of loading is referred to as 3-3 loading.

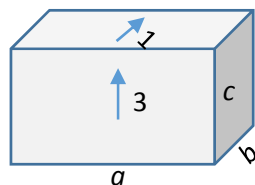


FIG. 4. Schematic of a Piezoelectric Element

Equ. 1 can be normalized with respect to the area $A = ab$ as follows:

$$D = \frac{Q}{A} = \sigma d_{33} \quad (2)$$

Where σ is normal stress (Pa) and D is the charge density (Coulombs/m²), which is related to the electric field E (Volts/m) through:

$$D = \epsilon_0 \epsilon_r E \quad (3)$$

With ϵ_0 and ϵ_r the dielectric constant of the air (8.85×10^{-12} Farad/m) and the relative (dimensionless) dielectric constant of the piezoelectric material, respectively. Equating Equ. 2 and 3 gives:

$$\epsilon_0 \epsilon_r E = \sigma d_{33} \quad (4)$$

Which reduces to:

$$E = \sigma g_{33} \quad (5)$$

Where g_{33} is the piezoelectric constant of the material (Volts/m/Pa) related to the earlier defined constants through:

$$g_{33} = \frac{d_{33}}{\epsilon_0 \epsilon_r} \quad (6)$$

The V (Volts) produced from the piezoelectric element of thickness c (Fig. 4) is given by:

$$V = c \frac{F}{ab} g_{33} \quad (7)$$

The corresponding electrical power P generated over a time period t is:

$$P = \frac{VQ}{t} \quad (8)$$

Which allows computing the energy output by substituting Equ. 1 and 7 into Equ. 8 as:

$$Pt = F d_{33} c \frac{F}{ab} g_{33} = d_{33} g_{33} \left(\frac{F}{ab}\right)^2 abc \quad (9)$$

Which integrated over time gives the energy output W_{33} of the piezoelectric sensor as:

$$W_{33} = \frac{1}{2} \int_0^t d_{33} g_{33} \left(\frac{F}{ab}\right)^2 abc d\xi \quad (10)$$

Noting that $\frac{F}{ab}$ represents engineering stress, allows expressing Equ. 10 as follows:

$$W_{33} = \frac{1}{2} d_{33} g_{33} Y^2 abc \int_0^t \epsilon_{33}^2 d\xi \quad (11)$$

Where Y is the Young's modulus and ϵ_{33} is the normal strain in direction 3 and abc is the volume of the element. Equ. 11 suggests that the relationship between the strain applied and the amount of electrical energy being generated is non-linear. A similar expression can be derived for a force applied perpendicularly to the direction of polarization (i.e., parallel to direction 1 as shown in Fig. 4). This is referred as 3-1 loading mode and is denoted by subscripts 31 as opposed to 33.

DEVELOPING THE HISEC PROTOTYPES

In developing prototypes for the proposed HiSEC module, various configurations of boxes containing selected number of PZT elements of various shapes were considered. The number of PZT elements included represents a trade-off since the fewer the elements, the higher the stress applied, while the higher the number of elements the higher is the combined power output of the module. The analysis involved FE modeling of the stress distribution inside the boxes, laboratory testing of the power output under load, durability testing under repeated loading and economic feasibility analysis.

Finite Element Analysis

The various configurations of the HiSEC prototypes were analyzed using the FE model Abaqus®. Key considerations in the development of the prototypes was the stiffness of the box plates, the number of PZT elements included and the way they are arranged to ensure mechanical stability under load. An example of the FE mesh used to analyze Prototype II is shown in Fig. 5. The FE analysis explored the stresses in the PZT elements, the effect of the stiffness of the box and the effect of the stiffness of the surrounding asphalt concrete pavement.

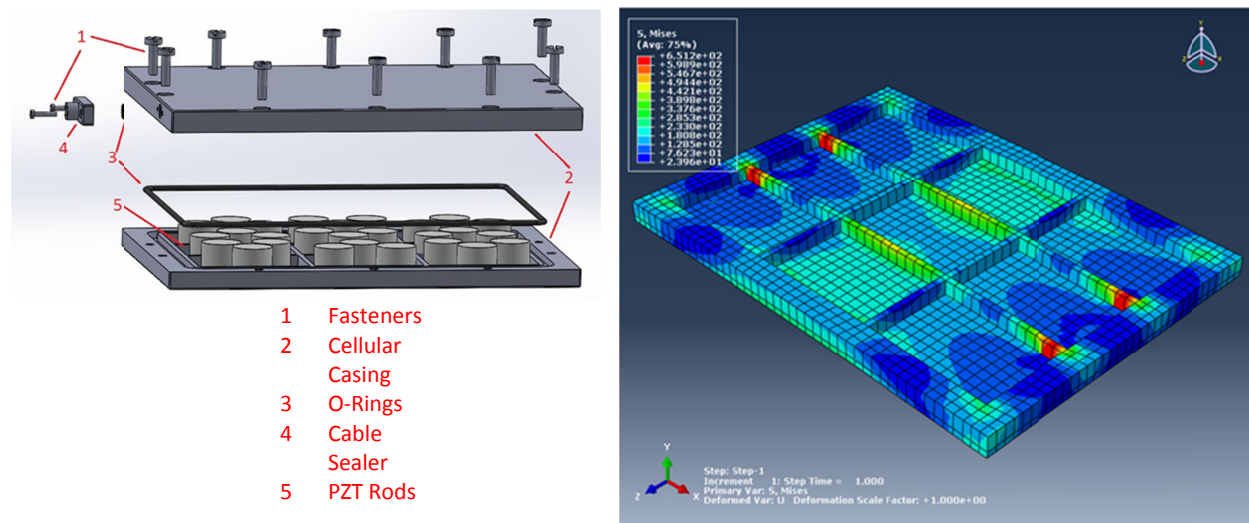


FIG. 5. Prototype II; CAD Drawing and Part of the FE Analysis Mesh.

This analysis revealed that the stiffness of the upper side of the box had a marginal effect on the uniformity of the stress distribution in the PZT elements. Furthermore, it determined that for the number and cross section size of the PZT elements considered, the stresses under a moving truck tire are well within the compressive strength range of the PZT elements, which is in the order of 900 MPa₀ (Ewart and McLaughlin (1999)). In addition, buckling of the elements was not an issue for the prototypes analyzed so far under the truck tire service loads anticipated (max dual tire load of 10,000 lbs or 44.4 kN). Additional stress analysis was conducted to ensure that the boundaries of the box do not cause unduly high strains in the asphalt concrete layer that encapsulates them. A depth of 5 cm was selected for installing the HiSEC modules, to allow

typical asphalt pavement rehabilitation involving milling of the top 5 cm and overlaying. In addition, statistical analysis was conducted with respect to the width of the HiSEC unit and its optimum lateral placement in the driving lane. It was estimated that a module width of 0.45 m will suffice to fully support the dimensions of standard dual truck tires, which is approximately 0.5 m. The center of the HiSEC module should be located to maximize the probability of truck tires been located on it. Work by Timm and Priest (2005) suggests that this should be about 0.80 m from the edge stripe marking the right hand-side of the driving lane.

Laboratory Testing of Power Output

The HiSEC prototype elements were tested in the laboratory using a UTM® system. Testing was carried by applying a sinusoidal compressive load at a frequency of 10 Hz with a peak-to-peak magnitude ranging from 0.5 to 3.5 kN. Electric power output in the form of Watts Root Mean Square (RMS) was measured directly using a METRAhit® Watt-meter. In doing so, external resistance (R_L) was added through a resistance substitution box to match the internal resistance (R_S) of each prototype as a function of the loading frequency f applied, using:

$$R_S = \frac{1}{2\pi cf} \quad (12)$$

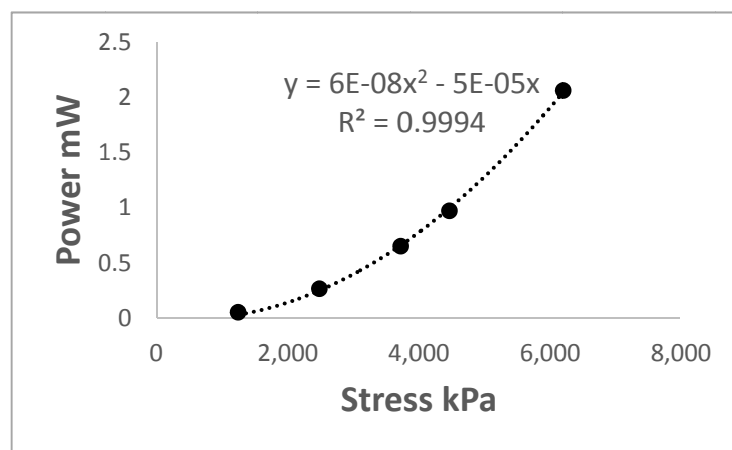
Where, c is the capacitance of each prototype module.

Three of the prototypes tested already are described next, namely prototypes 0, I and IV shown in Figs. 6(a) and 7(a), and 8(a), respectively:

- Prototype 0 is made of 8 PZT elements, each with a diameter of 8mm and a thickness of 8mm. They were sandwiched between two plates of copper of 150mm diameter and were loaded through two half sections of a 150mm diameter asphalt concrete core.
- Prototype I is made of 3 layers connected in series each consisting of 25 PZT prismatic elements of rectangular cross section measuring 3.5mm by 3.5mm. Each layer is 11.7 mm tall and the volume between the PZT elements is filled with epoxy.
- Prototype IV consists of a stack of six cylindrical PZT-5A elements, each with a diameter 44.5 mm and a thickness of 6 mm, resulting in a cylindrical element of 36 mm in height. This element is enclosed into a commercially available electrical box.



(a)



(b)

FIG. 6 Prototype 0: Configuration (a) and RMS Power Output for 8 PZT Units (b)

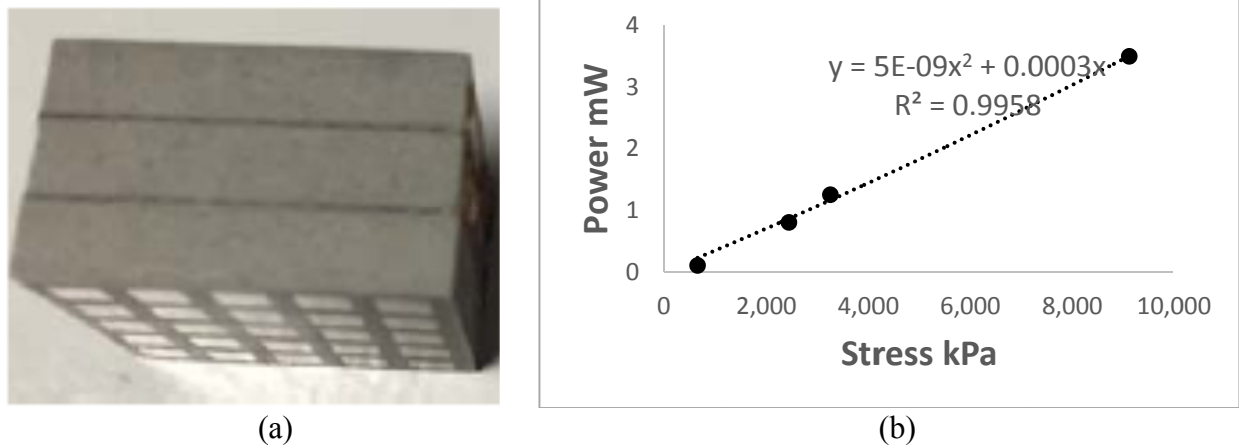


FIG. 7 Prototype I: Configuration (a) and RMS Power Output for 25 PZT Units (b)

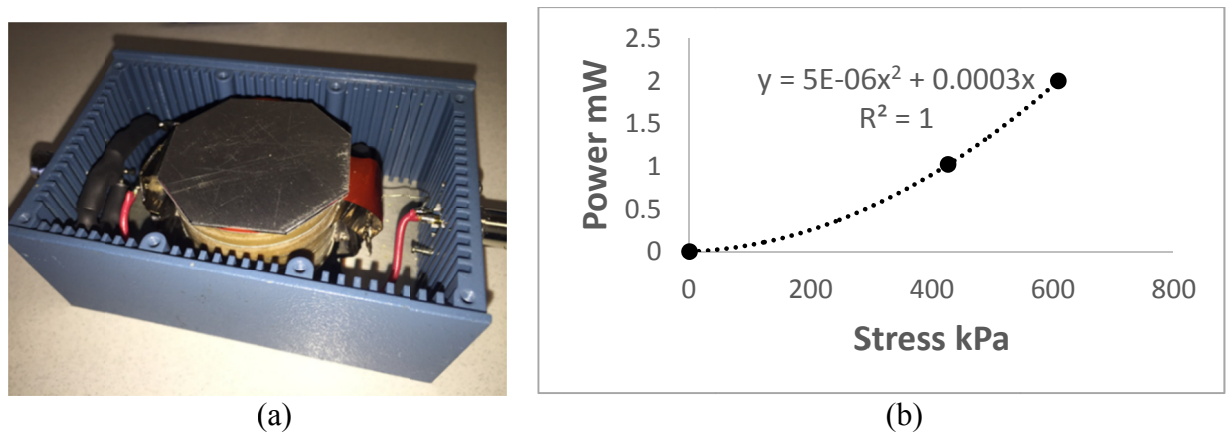


FIG. 8 Prototype IV: Configuration (a) and RMS Power Output for a Single Unit (b)

The laboratory results of the four other prototypes considered had not been completed at the time this paper was prepared. The laboratory results available are plotted for Prototypes 0, I and IV in terms of RMS power (mW) versus the vertical stress applied (kPa) (Figs., 6(b), 7(b) and 7(b), respectively). These relationships agree with the non-linear form of the energy versus stress/strain suggested by Equ.11. Following this laboratory testing, these prototypes will be subjected to durability testing by embedding them into asphalt concrete samples and subjecting them to repetitive loading from an Asphalt Pavement Analyzer (APA).

Economic Considerations

The capability of electric power production from these devices was studied using the laboratory obtained curves of power versus stress level highlighted above, i.e., Figs. 6(b), 7(b) and 8(b). For the power production calculations, it was assumed that each HiSEC module measured 0.09 m^2 (i.e., 1 foot x 1 foot) and was fitted with the same number of PZT elements used in the laboratory testing that is, 8, 25 and 1, respectively. It is noted that a much higher number of PZT elements can be included per square foot. As mentioned earlier, however, the

number of PZT elements will affect the stress applied as well as the combined amount of power being generated.

The traffic volume and composition were considered as variables to the power production analysis. The traffic input assumed for the results presented next is summarized in Table 1 and reflects a moderately busy Interstate highway in the USA. Table 2 shows the calculation steps for the electric power and energy production from the car tires and truck tires expected to pass over a HiSEC module. In doing so, it was assumed that all axles are loaded to the limit and that the entire load of half the axle in each wheel path is applied to the harvesting module (i.e., all car half-axles applies 1,500 lbs and each truck half-axles applies 10,000 lbs).

Table 2 suggests that Prototype IV is the best amongst those tested to-date. Under the traffic conditions specified, each Prototype IV module can produce up to 241 Watt-hrs per year. This level of energy is low. Its monetary value, at typical commercial rates of about \$0.20-\$0.30/kWatt-hour, is negligible, where the electric power grid is available roadside. Hence, energy harvesting may be economically feasible only at locations where access to the power grid is not readily available (i.e., typical cost of overhead power lines is in the order of \$285,000/mile). On the other hand, the HiSEC modules are particularly attractive for self-contained LED traffic lighting and traffic sensing (e.g., traffic volume counting, axle weighing and so on). In effect, a direct HiSEC application would be a low-cost and self-contained weigh-in-motion system. Additional data can be collected, such as strain cycles, temperature and so on.

Table 1. Traffic Assumptions

Traffic Property	Value
Input	
Traffic speed (80 km/hr) m/sec	22.2
Average Annual Daily Traffic (AADT)	30,000
No lanes	4
AADT/Direction	15,000
Percent Trucks in traffic stream	25
Percent trucks in right Lane	75
Calculated	
Number of cars in right lane/day	5,625
Number of Trucks in right lane/day	2,813
Number of car axles in right lane/day	11,250
Number of truck axles in right lane/day	14,063

SUMMARY

This paper presented preliminary results of the evaluation of several prototype systems for harvesting energy from the action of traffic on roadways. Prototypes were mechanically analyzed using FE, were tested in the laboratory to establish their electric energy generation potential as a function of stress level and were evaluated for their financial viability. The results available to

date suggest that this technology shows promise in powering warning lights, instrumentation and sensors independently of the power grid.

Table 2. Energy Output for Prototypes I and IV under the Traffic described in Table 1

Output	Prototype 0	Prototype I	Prototype IV
Power			
mWatts/module/car tire pass	1.76	34.26	93.16
mWatts/module/truck tire pass	12.63	1,560	4,098
Energy			
Watt-hours/module/year from cars	0.08	1.58	4.30
Watt-hours/module/year from trucks	0.73	90.08	236.65
Total Watt-hours/module/year	0.81	91.66	240.95

ACKNOWLEDGEMENT

Funding for this study was provided by the Texas Department of Transportation

REFERENCES

- Cook-Chennault, K.A., N. Thambi and A.M., Sastry, (2008). Powering MEMS portable devices-a review of non-regenerative and regenerative power supply systems with emphasis on piezoelectric harvesting systems. *Smart Materials and Structures*, Vol. 17, pp. 1-33.
- Xiong, H. (2014). "Piezoelectric Energy Harvesting for Public Roadways". Dissertation, Virginia Polytechnic Institute and State University, Blacksburg. Virginia
- Kim, S., J Shen and M. Ahad, (2015). "Piezoelectric-Based Energy Harvesting Technology for Roadway Sustainability." *International Journal of Applied Science and Technology*, Vol. 5(1), pp. 20-25.
- Zhao, H., Y. Tao, Y. Niu and J. Ling (2014). Harvesting Energy from Asphalt Pavement by Piezoelectric Generator, *Journal of Wuhan University of Technology*, Vol. 29(5), pp. 933-937.
- Hill, D., A. Agrawal, N. Tong, (2013). "Assessment of Piezoelectric Materials for Roadway Energy Harvesting." Final Report CSC-500-2013-007, DNV KEMA Energy and Sustainability Inc. www.treevolt.com, accessed 1-5-2016.
- www.genziko.com/technology/road-power-generation/ accessed 1-5-2016.
- Edel-Ajulay, J. (2010) "Innowattech; Harvesting Energy and Data." *Presentation to the 1st International Symposium the Highway to Innovation*, Tel Aviv, Israel.
- Ertuk, A. and D. J. Inman (2011). "Piezoelectric Energy Harvesting" John Wiley and Sons Ltd., Hoboken, NJ.
- Ewart, L.M., E. A McLaughlin and K. D. Gittings (1999). "Investigation of the Compressive Material Properties of PZT, NUWC-NPT." Technical Report, Naval Undersea Warfare Center Division, Newport RI.
- Timm, D. H. and A. L. Priest (2005) "Wheel Wander at the NCAT Test Track" NCAT Report No. 05-02, Auburn, Alabama

Geothermal Energy for Bridge Deck and Pavement Deicing - A Brief Review

Xinbao Yu¹; Nan Zhang²; Asheesh Pradhan²; and Anand J. Puppala³

¹Assistant Professor, Dept. of Civil Engineering, Univ. of Texas at Arlington, TX 76019. E-mail: xinbao@uta.edu

²Research Associate, Dept. of Civil Engineering, Univ. of Texas at Arlington, TX 76019.

³Professor, Dept. of Civil Engineering, Univ. of Texas at Arlington, TX 76019.

Abstract: Geothermal energy is characterized as renewable, sustainable, clean (i.e. zero carbon emission) and directly used energy, which has been widely used in many engineering applications, such as ground source heat pumps (GSHP), geothermal energy piles (GEP), and soil borehole thermal energy storage (BTES). This paper presents a literature study of geothermal energy for deicing approach pavement slabs and bridge decks. The background with respect to the related applications of geothermal energy was firstly introduced. The working principle and design criteria of geothermal system were then presented for future field applications where the soil thermal conductivity is a key parameter that can be studied by our newly developed thermo-time domain reflectometry (TDR) probe. Several case studies in Europe and Asia were also reviewed to further demonstrate the feasibility and applicability of this innovative technology. The long term cost-benefit was finally analyzed, and some recommendations for field implementation were also provided.

INTRODUCTION

Ice and snow on pavement slabs and bridge decks always cause serious driving conditions to motorists both in safety and ability to accelerate and climb grades. They are also responsible for the traffic jam and accidents each year because the movement of cold air above and below bridge decks leads to icing on the pavement surface of this kind of elevated structures. Hence, deicing pavement slabs and bridge decks is very essential under certain weather conditions in winter. Commonly used deicing methods include plowing, salting, and sanding, or the use of heat from various sources to melt ice and snow for maintenance. However, the relatively high cost for sand, salt, fuel, repairs and labors limits the development of these methods.

Geothermal energy is considered as a new heating source for deicing in order to keep all the roads and bridges clean and safe in winter. Firstly, it is harmless and free as well as climate neutral energy. Secondly, geothermal energy is much easier to be obtained everywhere than any other heating sources. The most important is that it is independent from the weather above ground over 24 hours per day even the whole

year in most areas. Even in summer, the pavement slabs and bridge decks equipped with geothermal system can benefit from the heat collection process which can reduce their temperature and thus reduce the intensity of ruts, resulting in a longer lifespan (Pomerantz and Akbari, 1998; Qin, 2015). There are also some techniques that harvest heat from the pavement in summer and store it in the ground for winter pavement deicing (Van Bijsterveld et al., 2000, 2001 and 2002). Consequently, the exploration and utilization of geothermal energy for deicing pavement slabs and bridge decks is a promising and cost-effective approach.

GEOHERMAL DEICING HISTORY

As early as in 1970s, Bienert (1974) demonstrated the technical feasibility of using earth heat in combination with heat pipes for deicing and removing snow/ice from pavement surfaces (in the Baltimore/Washington climate) in the test performed at the Fairbank Highway Research Station (located at McLean, Virginia) during two winters. Ferrara (1975) described the efforts of using heat pipes to prevent the preferential freezing of highway pavement slabs and bridge decks. Griffin (1982) attempted to explore a kind of new system with non-fossil fuel heat sources for deicing roadway structures in Colorado and focus on the conceptual designs, life expectancy, performance and cost estimates for all the potential systems.

In 1990s, Wadivkar (1994) built a test setup of an active ground source heat pump system to prevent the ice formation on a concrete slab of a bridge deck. Cress (1995) designed a hydronic bridge/pavement deck heating system and applied it into the real test. His system was installed in the deck of 367 m long and 3.7 m wide viaduct in Lincoln, Nebraska, and monitored for 12 months after installation. It was demonstrated that the heating system can remove ice and snow from the slab and deck surfaces and eliminate the possibility of frosting and preferential icing for several days following a storm event. Chiasson (1999) proposed a modeling approach to design a hydronic snow/ice melting system for bridge deck deicing on an interstate highway in Oklahoma. The typical construction of a hydronic snow-melting system and the heat transfer mechanism in a hydronically-heated bridge deck are shown in Figure 1 and 2. The heat source was provided by a vertical borehole, closed-loop ground-source heat pump system to meet the heating requirement. The advantage of his design using modeling approach had been demonstrated successfully through numerical simulation. A system with 16 heat pumps of nominal 30-ton capacity and 250 boreholes, each 250 ft deep, was finally selected.

In recent years, Balbay (2010) experimentally investigated the use of ground-source heat pump (GSHP) system to meet the heating requirement for snow/ice melting process. Considering the effect of borehole depth on system working efficiency, the system studied in this work for snow/ice melting consists of ground borehole heat exchangers with three different depths (30, 60 and 90 m), a water-to-water heat pump and heating pipes buried under the bridge-slab (BS) and pavement-slab (PS). Figure 3 shows the photographs of initial and intermediate snow melting process on slabs.

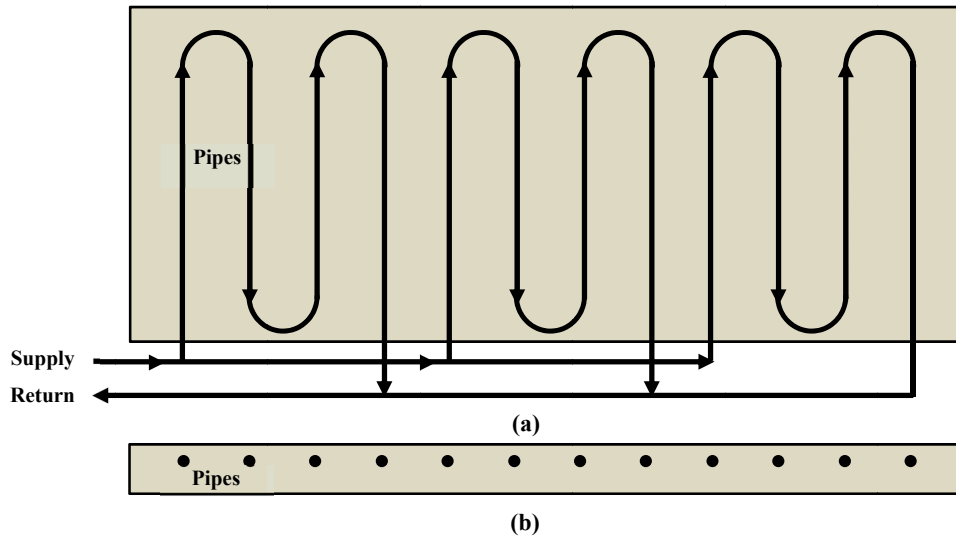


FIG. 1. Typical pavement section of a hydronic snow-melting system, (a) plan view, (b) cross section view.

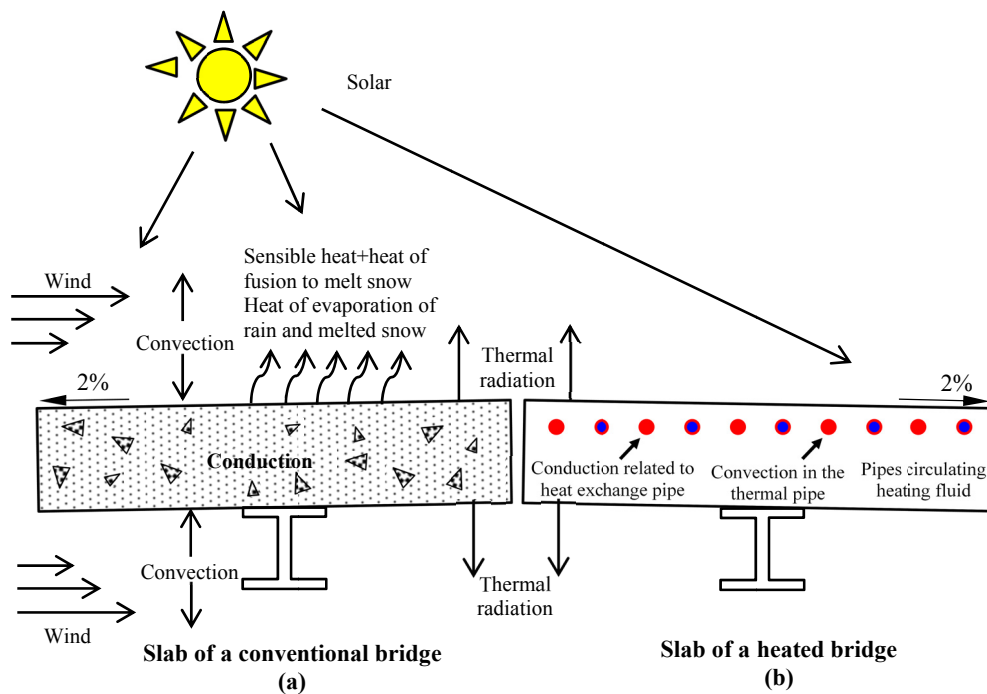


FIG. 2. Heat transfer mechanisms: (a) conventional bridge; (b) heated bridge.

Olgun and Bowers (2013) presented the operational principles of geothermal heating system for deicing the pavement slabs and bridge decks (as shown Figure 4). He also related these principles to the design parameters of bridge deck deicing systems. A series of parametric studies were performed to investigate the bridge deck heating process. The parameters need to be analyze consist of tube spacing, inlet fluid temperatures, flow rates, wind speeds, ambient temperatures and thicknesses of concrete cover over the circulation tubes.



FIG. 3. Photographs of initial and intermediate snow melting process on slabs: (a) initial state ($t=0$), (b) intermediate state ($t=30$ min) (Balbay and Esen, 2010).

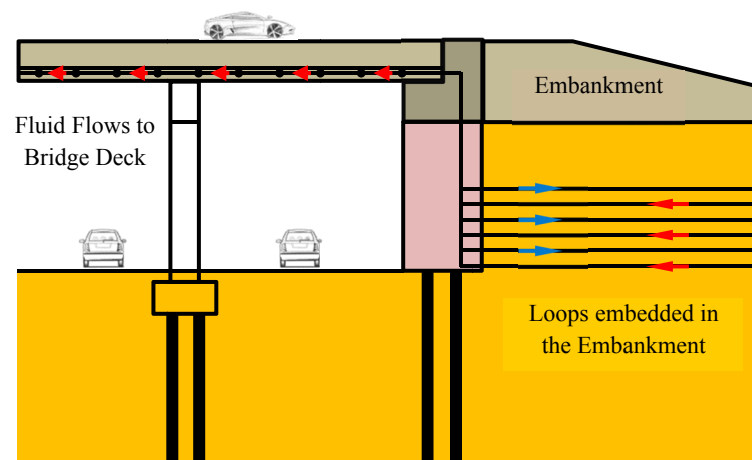


FIG. 4. Conceptual schematic of ground-source heated bridge deck (after Olgun and Bowers, 2013).

In terms of numerical simulation of geothermal systems for deicing pavement slabs and bridge decks, Sass (1992) presented a description and sensitivity testing of a physical model based on the balance of surface energy through fluxes of radiation, sensible heat, latent heat and heat conduction through the ground, which is used for predicting road surface temperature distribution according to the recorded data from a single road station in Denmark. Shao (1993 and 1995) developed a prediction model, which is used operationally in Europe. It is also designed for predicting road surface temperatures and conditions. The predicted surface temperature values were verified against observations. Liu (2005) studied the long performance of heated bridge deck anti-icing systems under certain weather conditions through numerical simulation based on finite difference method (FDM). In the system, the hydronic tubing and a ground-coupled heat pump system with vertical borehole heat exchangers was regarded as heat source. Balbay (2013) developed a 3D finite element method (FEM) to simulate heating process and obtain the temperature distribution of bridge decks and pavement slabs heated by vertical ground-source heat pump to deice snow/ice during cold period. The meshed model and typical temperature distribution of pavement slab (30 meters) are shown in Figure 5, respectively. Xiao (2013)

developed a 2D finite element model used to assess the power demands to heat a typical bridge decks. The performance of the model was also validated using a case study for a bridge in Rhode Island where the temperatures of the twelve bridge decks was monitored for about one year.

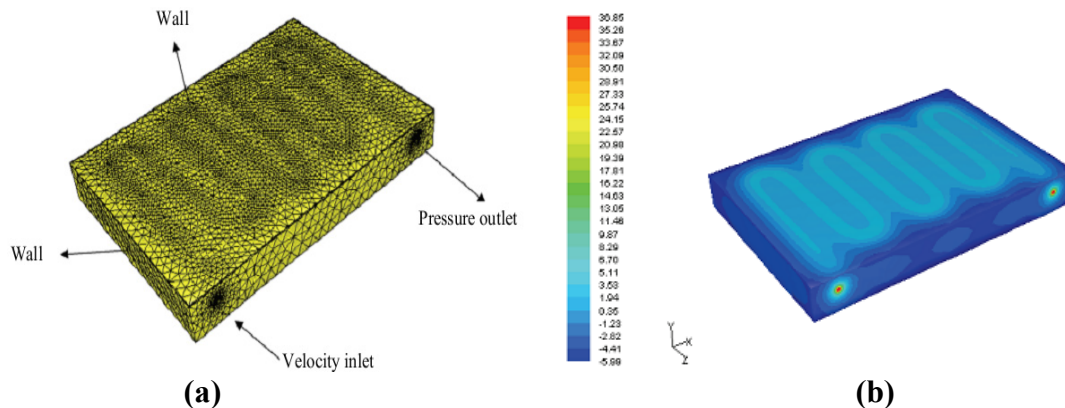


FIG. 5. (a) FEM mesh of a bridge deck; (b) Temperature distributions of the bridge deck (Balbay and Esen, 2013).

DESIGN OF GEOTHERMAL HEATING SYSTEM

A geothermal heating system for deicing pavement slabs and bridge decks consists of two parts: (1) ground-loop heat exchanger (GLHE) system; (2) hydronically-heated pavement slabs and bridge decks. Design of the entire system is divided into four phases (Chiasson and Spitler, 2000): (1) establish the required heat flux to the bridge surface; (2) estimate the bridge heating loads; (3) estimate the energy available for thermal recharge of the ground in summer; (4) design GLHE system including the number, spacing, diameter and depth of the boreholes according to user manual of GLHEPro 4.1. The design chart of ground-source heat pump bridge deck deicing system is shown in Figure 6.

The purpose of estimating the required heat flux is to ensure the average temperature of the pavement slabs and bridge decks higher than the freezing point under icy or snowy weather conditions. The heat flux needed for efficiently operation of the system is affected by many factors: (1) environmental heat transfer mechanisms as shown in Figure 2; (2) the material properties of the pavement slabs and bridge decks, such as thickness, area and orientation; (3) the material properties of embedded hydronic tube, such as the diameter, spacing and burial depth; (4) the properties of the circulating fluid, such as the flow rate and inlet temperature; (5) thermal properties of concrete and soils underground, such as thermal conductivity, diffusivity and heat capacity. In addition, the common way to determine the heat flux is to use the heat pump model coupled with slab model by inputting design weather conditions (i.e. air temperature, wind speed and snowfall rate) and varying design parameters (i.e. number of heat pumps, flow rate and inlet temperature).

The above design of heat flux only considers the maximum potential output of the system; however, the actual energy use varies along with the seasons. It is therefore necessary to estimate the required heating load based on selected weather conditions in order to design a more reliable and cost-effective system.

Thermal recharge of the ground in summer is a reversed process of the thermal discharge in winter for deicing, which will reduce the number or the size of boreholes and therefore the cost of the GLHE. In summer, the pavement slabs and bridge decks are considered as solar energy collector, and the temperature of them are supposed to be greater than air. The potential thermal recharge rate of the ground can be estimated using the numerical slab or bridge deck model on the basis of temperature difference between slabs or decks and the air.

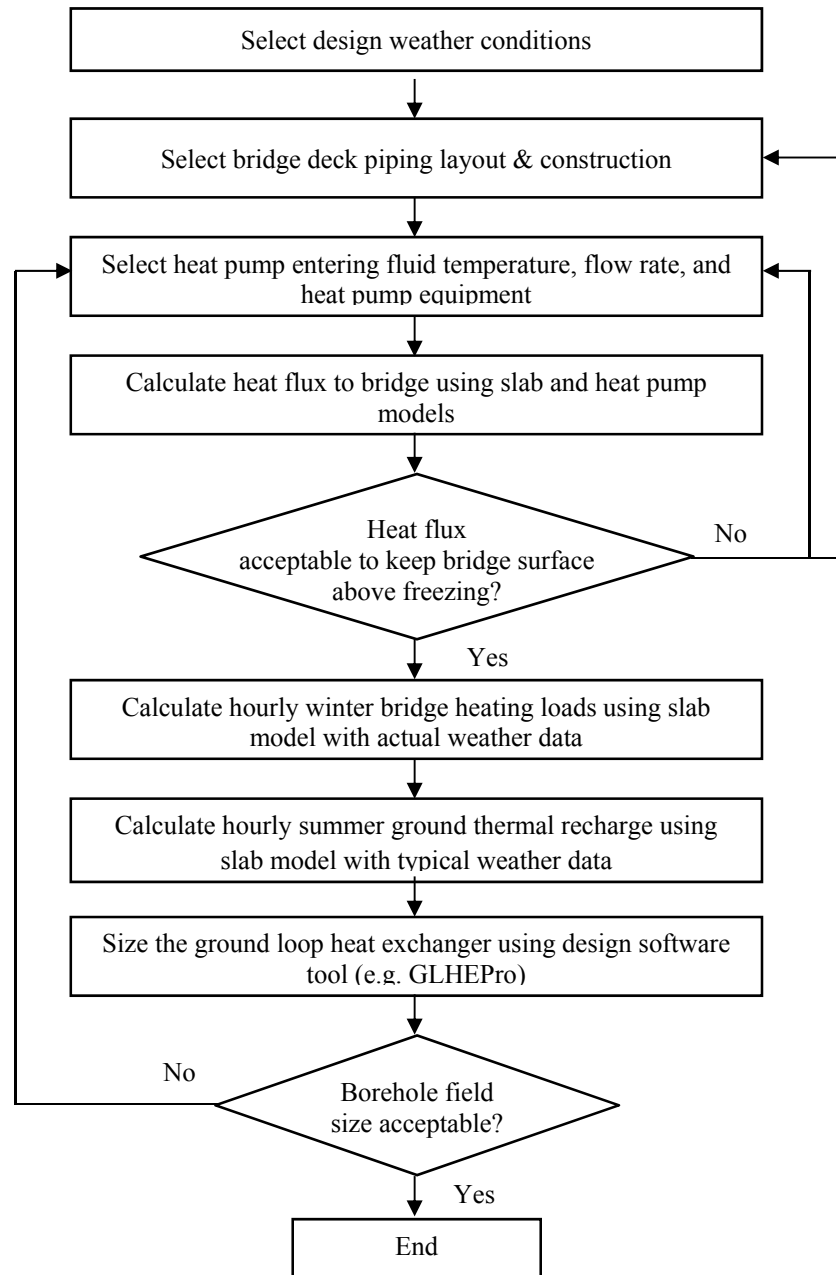


FIG. 6. Design chart of ground-source heat pump bridge deck deicing system (Chiasson and Spitler, 2000)

GLHE can be designed using GLHEPro 4.1 software developed by Spitler (1996). The input parameters include the heating loads, the thermal recharge rate, the thermal properties of the ground, and the geometry of the boreholes, physical and thermal properties of the heat carrier fluid and information of the selected heat pumps. Design of the entire system can be obtained after several iterations as shown in Figure 6.

CASE STUDIES

This section will introduce several full-scale field case studies found in Europe and Asia regarding the use of geothermal energy for deicing pavement slabs and bridge decks.

SERSO: Bridge heating in Switzerland

SERSO system was invented and designed in the early 1990. It is working continuously until today. The function of this system is to guarantee a passable road conditions on the bridge decks as well as the same surface conditions on other normal roads. In summer, the heat from solar radiation is collected and stored in a rock storage volume, and it is reused to control the surface temperature of pavement slabs and bridge decks to avoid formation of snow and ice in winter. Typical road surface temperature controlled by the SERSO system is shown in Figure 7 (a) (Eugster 2007). The photo of SERSO system in operation is shown in Figure 7 (b).

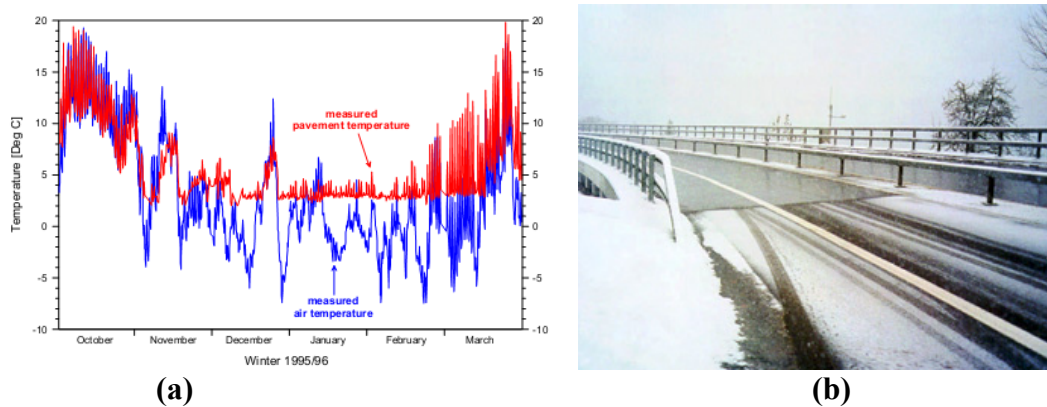


FIG. 7. (a) Monitored operation temperature; (b) photo of the bridge deck with the SERSO system in operation during snow (Eugster, 2007).

Japan: Sidewalk heating in Aomori City

Two sidewalk heating systems were constructed to melt snow on sidewalks in Aomori City in Japan in 2002. The city has more than 300 thousand people and is known as the snowiest city in Japan. It was reported that the annual snowfall sometimes exceeds 10 m. Consequently, it is essential to deice snow/ice on road surface. The design heat output of the system is 170 W/m^2 . The annual operation time was around 500 hours during the first two years. The total heat output of a unit was roughly 35 MWh. And the operating costs of this sidewalk heating system are given with 6 Euros/ m^2 /year for the electricity consumption only. A schematic plain view of

the site is shown in Figure 9 (a). The sidewalk heating system in operation is shown in Figure 9 (b).

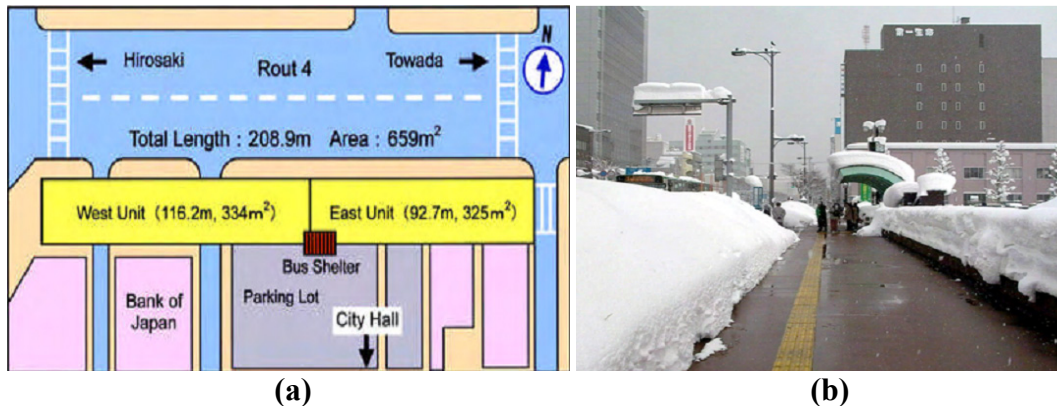


FIG. 9. (a) The schematic plain view of the site; (b) The sidewalk heating in operation (Eugster, 2007)

Germany: Geothermal train platform heating

The first geothermal heating system in Germany went into operation in 2005 and applied into a platform of a train stop in the Harz region. This project used exactly the same idea as the SERSO system as described previously. The platform is 200 m in length. The underground heat storage is tapped with 9 borehole heat exchangers with a length of 200 m each. The project is actually working as shown in Figure 10.



FIG. 10. The Harz platform heating in operation (Eugster, 2007).

COST-BENEFIT ANALYSIS

This section discusses the comparative cost-benefit analysis of traditional chemical methods and the innovative thermal heating technology. The applicability and cost of various chemical methods depends on several factors, including eutectic temperature, availability of raw materials, and process methods. Zhang et al. (2009) presented the cost of various chemical methods as shown in Table 1 and the estimated cost of thermal heating technology as shown in Table 2. It is evident that the cost of thermal heating method is much higher than that of chemical methods. However, the chemical

methods will cause some detrimental effects on the environment. For example, chloride tends to accumulate and change natural chemical balance, repress the growth of roadside vegetation at high concentration. In addition, some organic matter in chemicals will also pollute air and water if large amount is used.

Table 3 shows the estimated annual cost of typical deicing operations on the Knik Arm Bridge. It is indicated that the total cost of chemical method is substantially less than that of thermal method. Although the cost of equipment and installation of thermal method is much higher than that of chemical method, it has a great potential to save cost for long term operation because of the lower cost of labor compared with chemical method. More importantly, the impact of thermal method on natural environment is also reduced considerably.

Table 1. Cost of deicing chemicals and their temperature range and application rate (Johnson, 1992; Cryotech, 1995; Yehia and Tuan, 1998; Zhang et al., 2009)

Deicing Chemicals	Temperature Range	Application Rate	Approximate Cost in Volume	Approximate Cost in Area
Sodium Chloride (NaCl)	-10°C to 1°C (14°F to 34°F)	13 to 68 g/m ² (170 to 890 lb/12 ft lane-mile)	\$29/m ³ (\$26/ton)	\$0.0003/m ²
Calcium Chloride (CaCl ₂)	-25°C (-13°F)	Use along with sodium chloride in U.S.	\$294/m ³ (\$267/ton)	\$0.03/m ²
Salt mixed with calcium chloride (NaCl and CaCl ₂)	-17°C to 0°C (0°F to 32°F)	21-50 l/m ³ salt (5 to 12 gal/ton)	\$108/m ³ (\$98/ton)	\$0.01/m ²
Magnesium chloride (MgCl ₂)	-15°C (5°F)	8 to 11 g/m ² (100 to 150 lb/12 ft lane-mile)	Not available	\$0.0002/m ²
Calcium magnesium acetate (CMA)	-5°C to 0°C (23°F to 32°F)	15 to 39 g/m ² (200 to 500 lb/12 ft lane-mile)	\$738/m ³ (\$670/ton)	\$0.004/m ²
Potassium acetate (KAc)	50% to 35% Concentration solution freezes at -60°C to -30°C (-76°F to -22°F)	0.9 to 9.1 gal/1000 ft ²	Not available	Not available

Table 2. Cost estimates of various thermal heating systems (Xie et al., 1996; Yehia and Tuan, 1998; Spitler and Ramamoorthy, 2000; Zhang et al., 2009)

Heating	Approximate Capital Cost	Power Consumption	Operating Cost
Infrared Heat Lamp	\$96/m ² (\$8.9/ft ²)	75 W/m ² (7 W/ft ²)	Not available
Electric Heating Cable	\$54/m ² (\$5/ft ²)	323-430 W/m ² (30-40 W/ft ²)	\$4.8/m ² (\$0.45/ft ²)
Hot Water	\$161/m ² (\$15/ft ²)	473 W/m ² (44 W/ft ²)	\$250/Storm, 3-inch snow
Heated Gas	\$378/m ² (\$35/ft ²)	Not available	\$2.1/m ² (\$0.2/ft ²)
Conductive Concrete Overlay	\$48/m ² (\$4.5/ft ²)	516 W/m ² (48 W/ft ²)	\$5.4/m ² (\$0.5/ft ²)

Table 3. Estimated annual cost of typical deicing operations on the Knik Arm Bridge (Zhang et al. 2009)

Cost		Chemical Method		Thermal method
		Calcium chloride	Potassium acetate	
NPC	Equipment	20	20	300
	Installation	5	5	400
	Lifecycle	2	2	30
	Utility incentive payment	0	0	0
COO	Materials	60	120	100
	Labor	60	60	2
Total cost=NPC+COO		147	207	832

NOTES: NPC is the net participants cost; COO is the operation cost.

SUMMARY AND CONCLUSIONS

Use of geothermal energy for deicing pavement slabs and bridge decks is an innovative, feasible and environment-friendly technology to increase traffic and public safety. The development of exploitation and utilization of geothermal energy was reviewed and summarized based on the previous related experimental and numerical studies. The design of geothermal heating system, including ground-loop heat exchanger (GLHE) system and hydronically-heated pavement slabs and bridge decks, was then presented in four steps. Several case studies in Europe and Asia were also introduced to further demonstrate the feasibility and applicability of this new technology. Comparing with the traditional deicing methods, i.e. chemical methods, the advantages of the long term operation cost-benefit of the geothermal methods was analyzed and corroborated.

ACKNOWLEDGMENTS

The authors appreciate the financial support of this research from Texas Department of Transportation.

REFERENCES

- Balbay, A. and Esen, M. (2010). "Experimental investigation of using ground source heat pump system for snow melting on pavements and bridge decks." *Scientific Research and Essays*. 5(24): 3955-3966.
- Balbay, A. and Esen, M. (2013). "Temperature distribution in slab and bridge deck heated by using vertical GSHP system." *Acta Scientiarum Technology*. 35(4): 677-685.
- Bienert, W. B., Pravda, M. F., Suelau, H. H. and Wolf, D. A. (1974). "Snow and ice removal from pavements using stored earth energy." *NASA STI/Recon Technical Report N, 75: 27581*.
- Chiasson, A. (1999). "Advances in Modeling of Ground-Source Heat Pump Systems." M.S. Thesis, School of Mechanical and Aerospace Engineering, Oklahoma State University.
- Chiasson, A. and Spitler, J. D. (2000). "A modeling approach to design of a ground source heat pump bridge deck heating system." *Proceedings of 5th International Symposium on Snow Removal and Ice Control Technology, Roanoke, V.A. September 5-8*.
- Cress, M. D. (1995). "Heated bridge deck construction and operation in Lincoln, Nebraska." *Symposium on Extending the Life span of Structures, San Francisco. International Association for Bridges and Structural Engineering*, pp. 449-454.
- Cryotech, (1995). "Importance of product concentration for potassium acetate runway deicers." [cited 2007 February 6]; Available from: <URL http://www.cryotech.com/technical_bulletins/E36/9-15-95.php>.
- Eugster, W. J. (2007). "Road and bridge heating using geothermal energy: overview and Examples." *Proceedings European Geothermal Congress*.
- Ferrara, A. A. and Haslett, R. (1975). "Prevention of preferential bridge icing using heat pipes." *Washington, D.C.-Federal Highway Administration, FHWARD-75-111*.
- GLHEPro 4.1 Users' Guide. (2014). School of Mechanical and Aerospace Engineering, Oklahoma State University.
- Griffin, R. G. (1982). "Highway bridge deicing using passive heat sources: Final report." Colorado Department of Highways.
- Johnson, K. L. (1992). "Environmentally safe liquid runway deicer." [cited 2007 February 6]; Available from: <URL <http://www.p2pays.org/ref/12/11425.pdf>>.
- Liu, X. (2005). "Development and experimental validation of simulation of hydronic snow melting systems for bridges." Ph.D. Dissertation, Oklahoma State University.
- Olgun, C. G. and Bowers, G. A. "Numerical modeling of ground source bridge deck deicing." *International Workshop on Geomechanics and Energy—The Ground as Energy Source and Storage, Lausanne, Switzerland, 26-28*.

- Pomerantz, M., and Akbari, H. (1998). Cooler paving materials for heat island mitigation. *In Proceedings of the 1998 ACEEE summer study on energy efficiency in buildings*, Vol. 9, p. 135.
- Qin, Y. (2015). "A review on the development of cool pavements to mitigate urban heat island effect." *Renewable and Sustainable Energy Reviews*, Vol. 52: 445-459.
- Sass, B. H. (1992). "A numerical model for prediction of road temperature and ice." *Journal of Applied Meteorology*, Vol. 31: 1499-1506.
- Shao, J., Thornes, J. E. and Lister, P. J. (1993). "Description and verification of a road ice prediction model." *Transportation Research Record*, Vol. 1387: 216-222.
- Shao, J. and Lister, P. J. (1995). "The Prediction of Road Surface State and Simulation of the Shading Effect." *Boundary Layer Meteorology*, Vol. 73: 411-419.
- Spitler, J. D., Marshall, C., Delahoussaye, R. and Manicham, M. (1996). "Users Guide of GLHEPRO." School of Mechanical and Aerospace Engineering, Oklahoma State University, Stillwater, OK.
- Spitler, J. D. and Ramamoorthy, M. (2000). "Bridge deck deicing using geothermal heat pumps." *Proceedings of the Fourth International Heat Pumps in Cold Climates Conference, in Alymer, Quebec*.
- Van Bijsterveld, W. T., Houben, L. J. M, Scarpas, A, Modenaar, A. (2000) Controlling temperature in asphalt pavements. *Proceedings of 3DFEM 2000 Finite Element Modeling of Pavement Structures*. University of West Virginia 2000. p. 413-31.
- Van Bijsterveld, W., Houben, L., Scarpas, A., Molenaar, A. (2001) Using pavement as solar collector: effect on pavement temperature and structural response. *Transportation Research Record: Journal of the Transportation Research Board*. Vol. 1778:140-148.
- Van Bijsterveld, W. T., De Bondt, A. H. (2002) Structural aspects of asphalt pavement heating and cooling systems. *In Proceedings of 3rd international symposium on 3d finite element modeling, Design & Research*. Amsterdam, Netherlands.
- Wadivkar, O. (1994). "An experimental and numerical study of the thermal performance of a bridge deck de-icing system." Bachelor thesis, South Gujarat University, India.
- Xiao, S. G., Suleiman, M. T., Natio, C. J. and Neti, S. (2013). "Use of geothermal deep foundations for bridge deicing." *Transportation Research Record: Journal of the Transportation Research Board*, pp. 56-65.
- Xie, P., Gu, P. and Beadon, J. J. (1996). "Electrical percolation phenomena in cement composites containing conductive fibers." *Journal of Materials Science*. 31(15): 4093-4097.
- Yehia, S. and Tuan, C. Y. (1998). "Bridge deck deicing." *In Transportation Conference Proceedings*.
- Zhang, J., Das, D. K. and Peterson, R. (2009). "Selection of effective and efficient snow removal and ice control technologies for cold-region bridges." *Journal of Civil, Environmental and Architectural Engineering*. 3(1): 1-14.

Gradation Effects on the Strength Properties of Cement and Fly Ash Stabilized Quarry By-Products

Issam Qamhia¹; Joshua Cheung¹; Wenting Hou¹;
Vincent Mwumvaneza¹; Hasan Ozer²; and Erol Tutumluer, M.ASCE³

¹Graduate Research Assistants.

²Research Assistant Professor. E-mail: hozer2@illinois.edu

³Professor (corresponding author). E-mail: tutumlue@illinois.edu

Dept. of Civil and Environmental Engineering, Univ. of Illinois at Urbana-Champaign, 205 North Mathews Ave., Urbana, IL 61801.

Abstract: Crushing of aggregates at quarries produce large amounts of waste by-product materials that, if not utilized, pile up or end up in landfills. Current research at the Illinois Center for Transportation has focused on the sustainable applications of by-product materials in transportation infrastructure. Samples of quarry by-products (QB) were collected from several stone quarries in the State of Illinois and characterized for their engineering properties. Due to their low strengths and potential high fines contents, stabilization of QB was necessary for pavement use. Accordingly, the QB samples were stabilized with both 2% Type I portland cement and 10% class 'C' fly ash and tested for the 7-day unconfined compressive strengths. Initially, the unstabilized and stabilized QB specimens from two different crushing stages were tested for their unconfined compressive strengths. Then, the QB samples were sieved, size separated, and the gradations were engineered to match certain gradation curves that are power exponents of the ratio of the sieve size to the maximum particle size. This paper presents findings for the different QB gradations established as a factorial based on the Fuller curve for optimum packing and maximum density. For both stabilizers, the effects of gradation on the unconfined compressive strengths of QB were evaluated. Gradations that produce optimum packing and higher compressive strength are recommended to be utilized in pavement construction to achieve optimal field performance.

INTRODUCTION

With the high production rate of aggregate in the U.S., multiple aggregate quarry processes such as blasting, crushing and screening of aggregates produce large amounts of by-product mineral fine materials, commonly known as quarry waste or

quarry dust. Depending on the type of rock quarried, quarry by-products can be up to 25% of the total aggregate produced. Quarry by-products (QB) are typically less than 6 mm (¼ in.) in size and consist of coarse, medium and fine sand particles, and a clay/silt fraction, which is less than No. 200 sieve (0.075 mm) in size. Since unconfined compressive strength for QB materials is quite low, chemical stabilizers are often used to improve the engineering properties of QB materials.

The stabilization of QB with Portland cement develops relatively high rigidity with a small amount of cement compared with granular soil-cement stabilization. This also has an advantage of reducing shrinkage cracking due the low amount of cement. Several studies suggested pavement applications for QB stabilized with cement. Kumar and Hudson (1992) proposed using QB as base course material additive, flowable fill, under-slab granular fill, and in cement-stabilized subbase and base layer. A study by the International Center of Aggregate Research (ICAR) investigated the effects of using high fines content in aggregate pavement layers and reported that aggregate systems with high fines benefited considerably from low percentages (1-2%) of cement stabilization (Ashtiani & Little, 2007). The study found that the stabilized systems with high fines content had equivalent or better performance than untreated systems with standard fines content; given a proper design for fines content, cement content and moisture levels.

Other researchers have also reported that quarry fines stabilized with cement are economical and can produce adequate strength and modulus properties (compressive strength, modulus of elasticity, and tensile strength characteristics) required for subbase applications (Kumar & Hudson, 1992; Kalcheff & Machemehl Jr, 1980; Puppala, Saride, Sirigiripet, & Williammee, 2008). Puppala et al. (2008) showed that untreated QB material used as subbase material on expansive subgrade exhibits moderate swelling, low strength and low modulus, while the strength and resilient modulus of cement-treated quarry fines (CQF) are similar to those of sandy material with very few fines. Similar results were reported by Tutumluer et al. (2015) and Mwumvaneza et al. (2015), who reported increases in compressive strength up to 30 times for cement and class C fly ash-treated QB compared to untreated QB. A recent Iowa DOT study also focused on road construction utilizing admixture stabilized limestone fines and found that stabilized fines could perform satisfactorily as a structural layer in road construction through visual observations (Rupnow et al., 2010). Laboratory compaction, unconfined compression, freezing and thawing, and wet-dry durability test results showed that cement kiln dust (CKD) was not an acceptable stabilizer due to poor durability performance; however, class C fly ash and CKD mixtures were determined to be appropriate.

Studies have also been performed to characterize the impacts of gradation and packing on stabilized material properties. Cunningham et al. (2013) studied the effects of varying gradation on the mechanical properties and performance of an aggregate base course. They developed five different gradations based on North Carolina Department of Transportation (NCDOT) typical specifications and found that the maximum dry density, optimum moisture content (OMC), and Atterberg limits were not significantly affected by the changes in gradation, but mixtures with high amount of fines (passing the No. 200 sieve) above 8-12% changed the mechanical responses of the material. Ghabchi et al. (2013) also performed a similar

study by preparing several gradations of different aggregate types in the upper and lower limits of the specification. They found that the gradations at the upper limit provided higher densities and OMC than the gradations prepared at the lower limit of specification. They also found that these mixes had higher stability due to better packing, as the resilient modulus was also higher.

Studies on the effect of packing and gradation on the engineering properties of QB and quarry fines are rare in literature. Galetakis et al. (2012) used an optimization packing density model to maximize the density of mixtures of stone sludge, lime stone dust and quarry sand, and found that mixtures with 52% limestone dust and 48% quarry sand had slightly higher compressive strength and density compared to other sample proportions. Regarding gradation quantification methods, the Talbot equation or Fuller curve were the earliest to describe a maximum density curve for a given maximum aggregate size (Talbot & Frank, 1923; Fuller & Thompson, 1906). Fuller and Thompson originally proposed the Fuller curve equation in 1907 with an exponent of 0.5 for proportioning concrete (Fuller & Thompson, 1906). The exponent was then modified to 0.45 by the Federal Highway Administration (FHWA) in 1962, following the work of Nijboer in Netherlands (Nijboer, 1948) that showed the 0.45 exponent would result in the minimum voids and the maximum packing for the aggregates in asphalt mixtures (Goode & Lufsey, 1962).

The Talbot equation works best for well graded gradations, and for other gradations such as open graded, the Rosin–Rammler distribution function described by Djamarani and Clark (1997) gives better fits. Most recently, Xiao et al. (2012) proposed an optimum gravel-to-sand ratio of around 1.5 to achieve the minimum possible porosity, and the highest shear strength for unbound aggregates sampled and tested in Minnesota. Another common method to characterize aggregate gradations is given by the Baily method (Vavrik et al. 2002) to optimize packing of aggregate-based infrastructures, such as hot-mix asphalt.

This paper presents findings from a laboratory study at the University of Illinois to determine the effects of packing on the engineering properties of chemically stabilized quarry by-products (QB). The results are part of a more comprehensive study that investigated the index and engineering properties of QB collected from four different quarries in Illinois at different crushing stages.

OBJECTIVE AND SCOPE

The main objective of this paper is to investigate the effect of gradation on the unconfined compressive strength of cement and class ‘C’ fly ash stabilized quarry byproducts. The byproducts of a sample quarry in Illinois were size separated and engineered to match certain gradation curves that are power exponents of the ratio of the sieve size to the maximum particle size. The byproducts were stabilized with 2% cement or 10% class ‘C’ fly ash, moisture cured and tested for the 7-day compressive strength. The effects of packing and varying the gradations of QB on the strength properties of cement and fly ash stabilized samples are determined using different power values for the Fuller power gradation curve.

LABORATORY TESTS

Laboratory Characterization of the Untreated QB

The material used in this study was a quarry byproduct collected from a Quarry in central Illinois in December 2014. Because only two main crushing/screening stages were utilized on site for this quarry, the collected material was sampled from two different crushing stages: primary and tertiary. The grain size distributions of the two crusher stages was determined as per ASTM D422 method and are presented in Figure 1. Based on the grain size distributions, the primary crusher stage is classified by the Unified Soil Classification System (USCS) as a well-graded sand with silt (SW-SM) and the tertiary crusher stage is classified as silty sand (SM). Atterberg limit tests were performed in accordance with the ASTM D4318-10 method. QB samples from the primary and tertiary crushing stages were found to be essentially non-plastic, indicating that the shrink swell potential and moisture affinity is low for this QB.

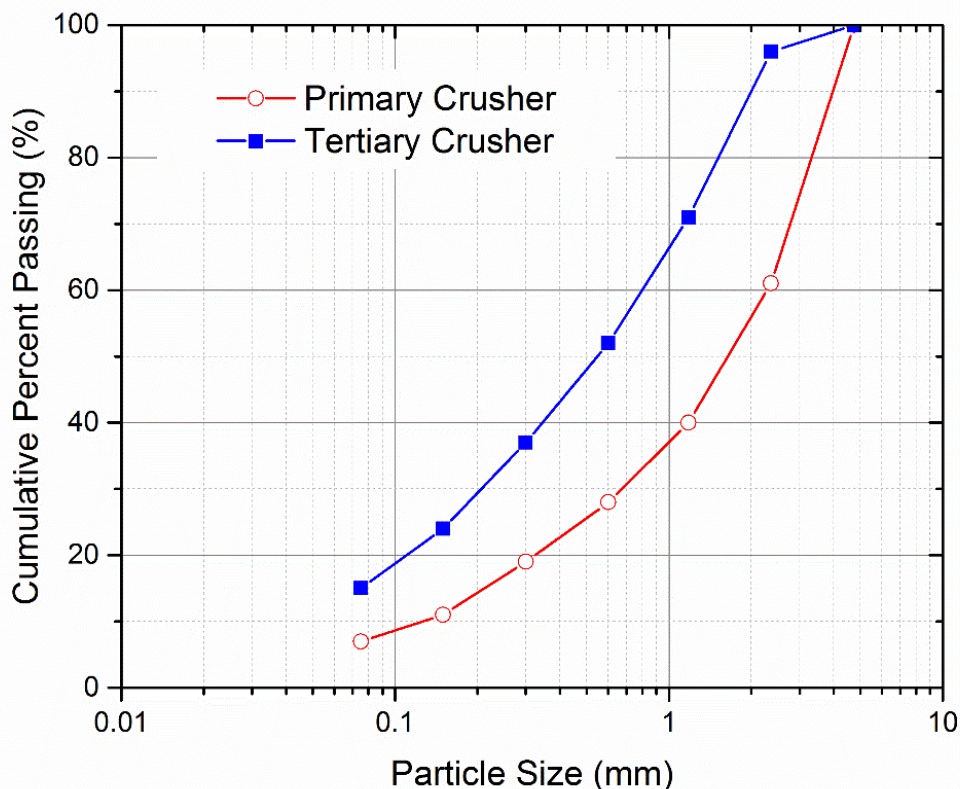


FIG. 1. Gradation Curves for QB from the Primary and Tertiary Crushers

The shape properties of the quarry byproducts were quantified using the Enhanced-University of Illinois Aggregate Image Analyzer (E-UIAIA). The imaging based shape indices of interest are the Angularity Index (AI), Flat and Elongated (F&E) ratio, and Surface Texture Index (STI); which are among the reliable indices to quantify morphological properties of aggregates. A total of 52 and 45 particles were

scanned from the primary and tertiary crusher stages, respectively. The scanned particles were randomly selected from the particles retained on sieve No. 8 (2.38 mm / 0.0937 in). The two crusher stages were found to have similar shape properties (see Table 1) and thus were mixed together to perform the packing study. Aggregates scanned from the tertiary crusher stage had a wider distribution and a higher Coefficient of Variation (COV) for the F&E ratio and STI. Note that the shape properties from different crushing stages might vary depending on the crushing equipment and rock mineralogy. QB collected from another quarry in Illinois showed more significant differences in shape properties at the different crushing stages, especially for F&E ratio and STI (Tutumluer et al., 2015).

Table 1. Particle Shape Properties for QB from Primary and Tertiary Crushers (Tutumluer et al., 2015)

Crusher Stage Property	Primary		Tertiary	
	Average	COV (%)	Average	COV (%)
Angularity Index (AI)	472.5	18.8	466.8	18.9
Flat & Elongated (F&E) ratio	2.2	23.1	2.1	35.7
Surface Texture Index (STI)	3.1	25.1	3.1	38.5

Laboratory Test Procedure for the Chemically-treated QB

The chemical stabilizers used for this study are Type I Portland cement and the self-cementing class C fly ash. The compressive strength of the QB material is quite low (less than 70 kPa or 10 psi according to Tutumluer et al., 2015), and stabilization was required to improve the strength to meet the requirements for various highway construction applications. The rationale behind the selection of stabilizers is to maximize strength gain with the lowest cost and environmental impact. To achieve these objectives, 2% (of the dry weight of the QB) Type I Portland cement and 10% class C fly ash were selected for stabilization.

Moisture-Density Relationships

The optimum moisture content and the maximum dry density for the QB from the tertiary and primary crusher stages were determined using the standard Proctor drop hammer compaction as per ASTM D698. As stated above, byproducts from the two crushing stages were mixed together to conduct the gradation effect study. Therefore, the average OMC and maximum dry density values of the two crushing stages were used for the preparation and compaction of the unconfined compressive strength specimens. The values for the OMC and maximum dry density for the two crusher stages were not significantly different for the same stabilizer material, and therefore used as the average values in this study. The results for OMC and maximum dry density (γ_{dmax}) are given in Table 2.

TABLE 2. Moisture-Density Test Results per ASTM D698

Material	Sample	$\gamma_{d\ max}$ kN/m ³ (pcf)	Optimum moisture content, OMC, w_{opt} (%)
QB + 2% cement	Primary	20.6 (131.2)	9.4
	Tertiary	20.9 (133.0)	9.1
Average (Cement)		20.7 (132.1)	9.2
QB + 10% Class C fly ash	Primary	21.0 (133.9)	8.2
	Tertiary	20.9 (133.1)	7.8
Average (Fly ash)		21.0 (133.5)	8.0

Engineered Gradations

The main objective of this study is to determine the effect of gradation and packing on the unconfined strength properties of cement and fly-ash stabilized QB. For this purpose, five different gradation curves were generated by varying the ‘n’ value in the Talbot equation below.

$$p_i = \left(\frac{D_i}{D_{max}} \right)^n \quad (1)$$

where p_i is the percentage passing the i^{th} sieve, D_i is the i^{th} sieve size in mm (in.), D_{max} is the maximum sieve size and is taken to be the No. 4 sieve for sampled QB, and ‘n’ is power exponent of the curve; also known as the shape factor. The shape factor (n) values considered were 0.3, 0.4, 0.45, 0.5, and 0.6 to obtain five different gradation curves. The 0.45 exponent was found to result in the minimum voids and the maximum packing for the aggregates in asphalt mixtures (Goode & Lufsey, 1962). The proposed gradation curves used in this study are shown in Figure 2.

Gradation or packing is reported to have a significant impact on the mechanical properties of soils such as shear strength. A uniform particle distribution is usually desired to increase the packing and minimize excessive deformation. To adequately study the effect of packing on the strength of stabilized QB, samples were engineered for the corresponding gradations. The material from the primary and tertiary crusher stages were equally and uniformly mixed and then size separated on a stack of sieves that included No. 4 (4.76 mm /0.187 in), No.8 (2.38 mm /0.0937 in), No. 16 (1.19 mm/0.0469 in), No. 30 (0.595 mm/0.0234 in), No. 50 (0.297 mm/0.0117 in), No. 100 (0.149 mm/0.0059 in) and No. 200 (0.076 mm/0.0029 in) sieves. A dry sieving procedure was used as per ASTM D422 method, and the material was oven-dried overnight at a temperature of 110 °C (230 °F) before sieving.

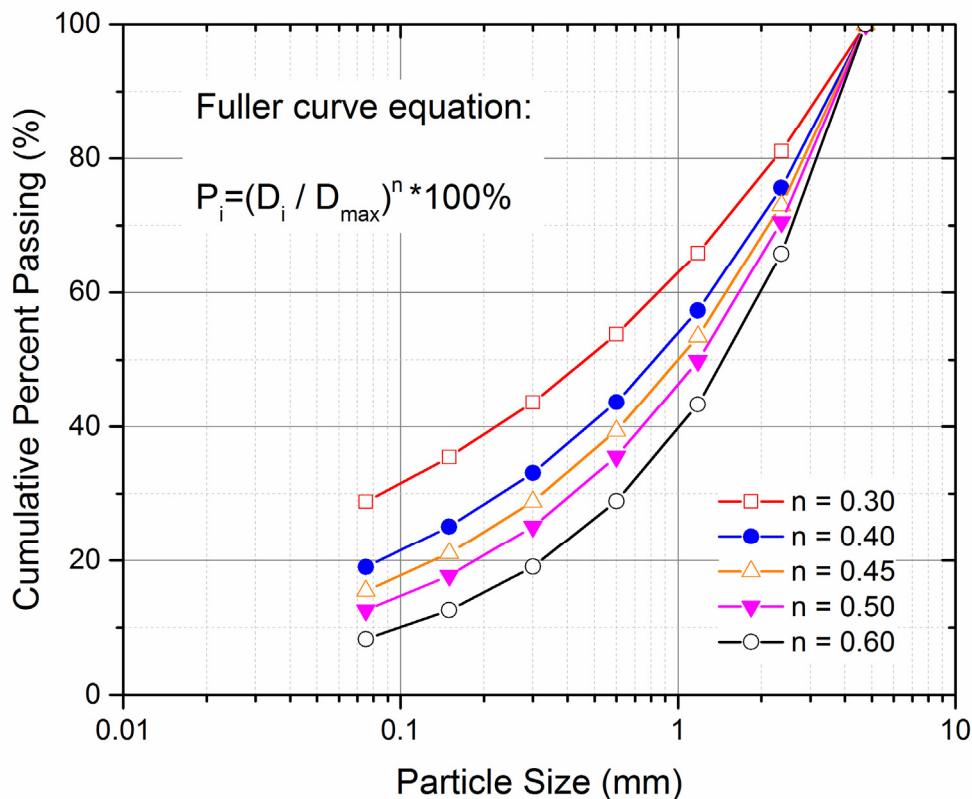


FIG. 2. Fuller (or Talbot) Power Curve Gradations Considered for the Power Exponent $n = 0.3, 0.4, 0.45, 0.5,$ and 0.6

Unconfined Compressive Strength (UCS)

Sample preparation was carried out according to the recommendations and procedure outlined in ASTM D1632: "Standard Practice for Making and Curing Soil-Cement Compression and Flexure Test Specimens in the Laboratory." Two sets of samples were prepared for the different gradations; one set with 2% cement and the other with 10% class C fly ash by dry weight of the aggregate. The samples were prepared in batches of 10 each; with each batch having one sample stabilized with cement and the other with fly ash for the same gradation curve. A total of 3 batches were prepared, or a total number of 30 samples. Each of the three batches studied the same gradation curves outlined in Figure 2. Samples were compacted into a 71 mm (2.8 in) in diameter and 142 mm (5.6 in) tall cylinder in 3 equal lifts using the standard Proctor hammer for compaction. All samples were then cured unsealed in a moisture-controlled room at 100% relative humidity and at room temperature for 7 days.

Stabilized QB Samples were tested for the 7-day compressive strengths using the recommendations and procedure outlined in ASTM D1633: "Standard Test Methods for Compressive Strength of Molded Soil-Cement Cylinders." Prior to testing, samples were completely soaked in water for 4 hours, surface-dried and capped at the ends using a sulfuric compound, then tested for compressive strength on a Forney loading frame at a rate of 18-49 kN/minute (4000-11000 lb./minute).

TEST RESULTS AND DISCUSSION

Results for average unconfined compressive strength for 2% cement-treated and 10% class C fly ash-treated QB materials are presented in Figure 3 for the different values of the exponent or shape factor 'n' in the Talbot equation. On the basis of the UCS measurements, both 2% cement and 10% Class C fly ash are found to be effective stabilizers that can be used with the aggregate QB for strength improvement. The untreated UCF values for the primary and tertiary crusher stages of the tested QB materials were 34.5 and 20.0 kPa (5.0 and 2.9 psi), respectively. The compressive strength samples for the untreated QB were prepared and tested in the same manner described above for the treated samples in an earlier stage of the study (Tutumluer et al., 2015). On the other hand, the strengths of the treated samples were in the order of 1,000 to 1,500 kPa (145 to 217 psi) for the cement and fly ash-treated samples, respectively, indicating a significant increase in strength. The UCS values for the cement-treated QB range from 1157 to 1482 kPa (167.8 to 214.9 psi), indicating a 28% increase in UCS when gradation is shifting from $n=0.3$ to $n=0.45$ curves. For the fly ash samples, the UCS range is 941-1176 psi (136.4 to 170.5 psi) when gradation is shifting from $n=0.3$ to $n=0.45$ curves. This again indicates a 25% increase in strength for the best packing achieved with $n=0.45$.

For both the cement and class C fly ash treated QB samples, the unconfined compressive strength was the lowest for the 0.3 power curve (the highest fines content), and increased steadily up to the 0.45 power curve. The UCS values decreased from $n=0.45$ to $n=0.6$. Accordingly, the strength is the highest for the 0.45 power curve due to optimum packing that maximizes the solid density for this gradation, leading to the best aggregate interlock and shear strength properties. Note that, the strength drop for the higher 'n' values of 0.5 and 0.6 is not as significant as that for the finer gradations ($n = 0.3$ and 0.4). An explanation can be that the coarser gradations having more of the larger sized particles would have a higher load capacity, acting as the primary structure, and thus can take more load compared to the finer gradations, which may have more of the secondary structure with smaller particles and less of the interconnected larger primary-sized particles. Further investigation into the sieve size separator of the primary and secondary structures in a typical QB gradation would be quite beneficial. Such a study would identify an optimum packing gradation ratio similar to the established Gravel-to-Sand ratio explained by Xiao et al. (2012) for the 25-mm (1-in.) top sized pavement base course unbound aggregate materials.

Note that from the UCS test results some certain trends were observed from one batch to another, as indicated by the standard deviations given in Figure 3. However, for each tested batch, samples consistently showed the highest UCS for the $n=0.45$ curve, followed by the $n=0.5$ curve, and the lowest UCS for the $n=0.3$ curve for both cement- and class C fly ash-treated QB. A possible reason for the lower strengths for the fly ash-stabilized batch that was prepared the last is that Class C fly ash has a shelf life that depends on storage conditions, and the effectiveness of fly ash decreases with time as it hydrates in damp conditions. Furthermore, for the fly-ash treated QB samples, as pozzolanic reactions start, clay sized particles are expected to be more reactive with fly ash, leading to higher strengths after 28 days of curing.

Generally, for stabilized QB materials, gradation has been shown to be a dominating factor affecting maximum dry density and strength. Other factors might include particle shape and angularity, the uniformity of distribution of the stabilizers within the soil as well as the effectiveness of the stabilizer.

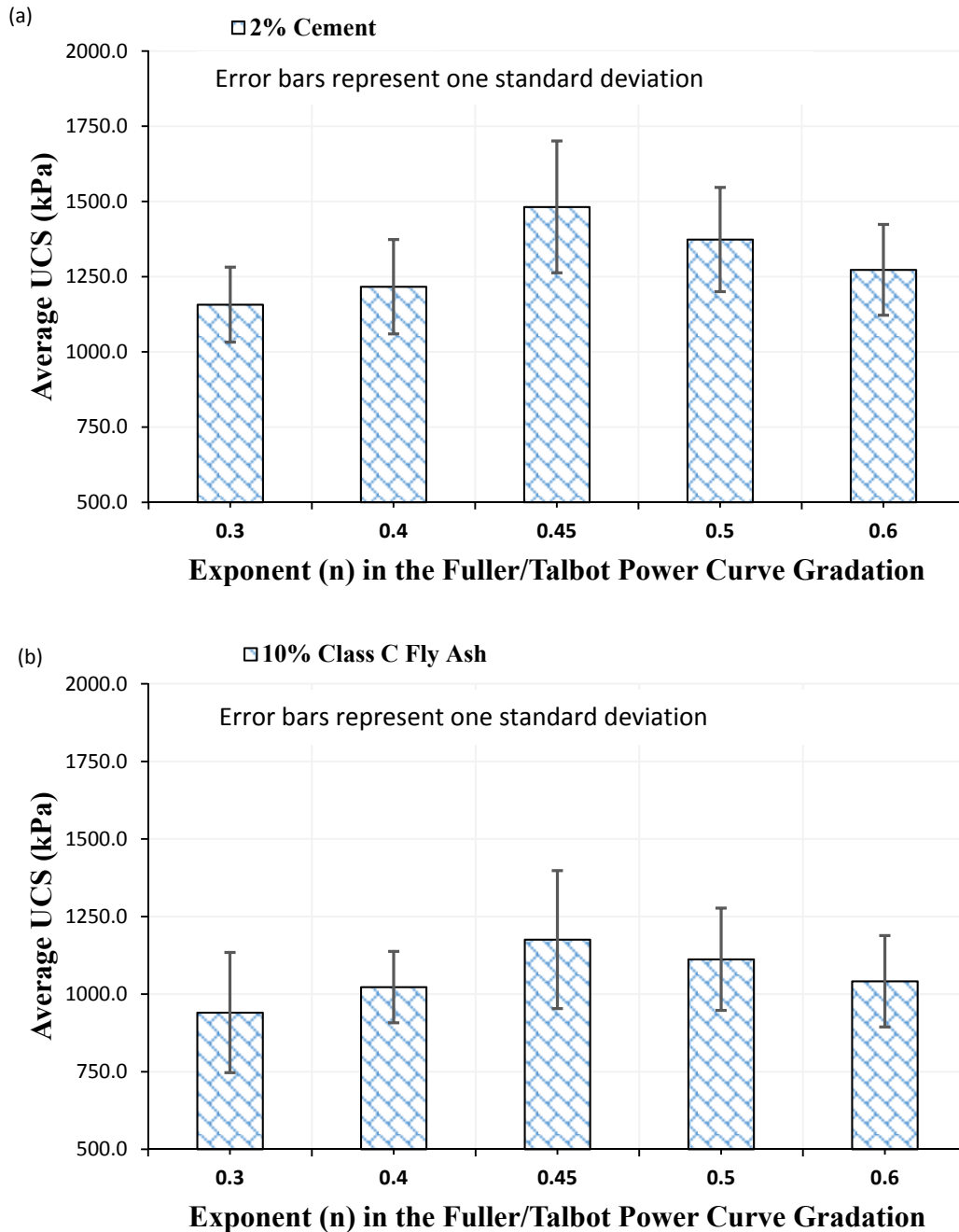


FIG. 3. Average Unconfined Compressive Strengths for (a) 2% Cement-Treated and (b) 10% Class C Fly Ash-Treated QB Materials

SUMMARY AND CONCLUSIONS

The main objective of this study was to investigate the effect of gradation and packing on the strength of quarry byproducts (QB) stabilized with the chemical admixtures: 2% Portland cement and 10% class C fly ash by the dry weight of QB aggregate. The QB obtained from the primary and tertiary crusher stages from a quarry in central Illinois were size separated into different sizes and then blended together to achieve certain engineered gradations generated by varying the exponent 'n' value in the Talbot equation to 0.3, 0.4, 0.45, 0.5 and 0.6. For each gradation studied, three replicate samples were tested for the 7-day unconfined compressive strength (UCS) with each type of stabilizer. Cement showed consistently higher UCS than class C fly ash for the same gradation curve, and both stabilizers showed consistent trends for the effect of gradation and packing, with the UCS peaking for the 0.45 power curves, and the lowest UCS occurring for the finer gradations, or smaller 'n' values. Gradation with 'n' value of 0.45 that produced optimum packing and the highest UCS values for both cement-treated and class C fly ash-treated QB are recommended to be utilized in pavement construction to achieve optimal field performance.

ACKNOWLEDGEMENTS

The support for this study was provided by the Illinois Department of Transportation (IDOT) as part of the recent ICT R27-125 research project. The authors would like to acknowledge Sheila Beshears from IDOT and others members of the R27-125 Technical Review Panel for their useful advice at different stages of this research. Special thanks go to Illinois Center for Transportation (ICT) research engineers James Meister and Dr. Aaron Coenen. The contents of this paper reflect the views of the authors who are responsible for the facts and the accuracy of the data presented herein. This paper does not constitute a standard, specification, or regulation.

REFERENCES

- Ashtiani, R. S., and Little, D. N. (2007). "Acceptability Criteria for High Fines Content Aggregate Pavement Layers." Rep. No. ICAR/401131, *International Center for Aggregates Research (ICAR)*. Texas Transportation Institute, Austin, TX, 1-100.
- Cunningham, C. N., Evans, T. M., and Tayebali, A. A. (2013). "Gradation Effects on the Mechanical Response of Crushed Stone Aggregate." *The International Journal of Pavement Engineering*, Vol. 14(3): 231-241.
- Djamarani, K. M., and Clark, I. M. (1997). "Characterization of Particle Size Based on Fine and Coarse Fractions." *Powder Technology*, Vol. 93(2): 101-108.
- Fuller, W. B., and Thompson, S. E. (1907). "The laws of proportioning concrete." *Transactions of the American Society of Civil Engineers*, Vol. 57(2): 67-143.

- Galetakis, M., Alevizos, G., and Leventakis, K. (2012). "Evaluation of fine limestone quarry by-products, for the production of building elements—An experimental approach." *Construction and Building Materials*, Vol. 1(26): 122-130.
- Ghabchi, R., Zaman, M., Khoury, N., Kazmee, H., and Solanki, P. (2013). "Effect of gradation and source properties on stability and drainability of aggregate bases: a laboratory and field study." *The International Journal of Pavement Engineering*, Vol. 14(3): 274-290.
- Goode, J. F., and Lufsey, L. A. (1962). "A new graphical chart for evaluating aggregate gradation." Monograph Accession No. 00217546: 13-26
- Kalcheff, I. V., and Machemehl Jr, C. A. (1980). "Use of crushed stone screening in highway construction (ABRIDGMENT)." Washington D.C.: *Transportation Research Record* 741. Monograph Accession No. 01411567: 40-42
- Kumar, D. S., and Hudson, W. R. (1992). "Use of Quarry Fines for Engineering and Environmental Applications." Special Report. *National Stone Association, Center for Transportation Research*, The University of Texas-Austin, Austin, TX.
- Mwumvaneza, V., Hou, W., Ozer, H., Tutumluer, E., Al-Qadi, I. L., & Beshears, S. (2015). "Characterization and Stabilization of Quarry By-products for sustainable Pavement Applications." *Transportation Research Record*, 15-4464:1-9
- Nijboer, L. W. (1948). "Plasticity as a Factor in the Design of Dense Bituminous Road Carpets." New York, NY: *Elsevier Pub. Co.*
- Puppala, A., Saride, S., Sirigiripet, S., Williammee, R., and Dronamraju, V. (2008). "Evaluation of Cemented Quarry Fines as a Pavement Base Material." *GeoCongress 2008: Geotechnics of waste management and remediation*, 9-12.
- Rupnow, T., Schaefer, V., and White, D. (2010). "Investigation of the Use of Limestone Screenings in Roadway Construction." *Transportation Research Record: Journal of the Transportation Research Board*, 2167: 53-60.
- Talbot, A., and Frank, E. (1923). "The strength of concrete-its relation to the cement, aggregates and water". Monograph No. 137, *Illinois Univ Eng Exp Sta Bulletin*.
- Tutumluer, E., Ozer, H., Hou, W., and Mwumvaneza, V. (2015). "Sustainable Aggregates Production: Green Applications for Aggregate By-Products." *Illinois Center for Transportation*. Report No FHWA-ICT-15-012. Rantoul, IL
- Vavrik, W., Pine, W., and Carpenter, S. (2002). "Aggregate Blending for Asphalt Mix Design: Bailey Method." *Transportation Research Record: Journal of the Transportation Research Board*, 1789: 146-153.
- Xiao, Y., Tutumluer, E., Qian, Y., and Siekmeier, J. (2012). "Gradation effects influencing mechanical properties of aggregate base-granular subbase materials in Minnesota." *Transportation Research Record: Journal of the Transportation Research Board*, 2267: 14-26.

Ground Granulated Blast Furnace Slag (GGBS) and Rice Husk Ash (RHA) Uses in the Production of Geopolymer Concrete

Sundeep Inti, M.ASCE¹; Megha Sharma, M.ASCE¹; and Dr.Vivek Tandon, P.E., M.ASCE²

¹Graduate Student, Dept. of Civil Engineering, The Univ. of Texas at El Paso, El Paso, TX 79902.

²Associate Professor, Dept. of Civil Engineering, The Univ. of Texas at El Paso, El Paso, TX 79902.

E-mail: vivek@utep.edu

Abstract: Research for complete OPC free concrete is still evolving and there is a need for developing alternative binding agents which are environmentally friendly. One such alternative is identified to be Geopolymer which often consists of fly ash, sodium silicate, and sodium or potassium hydroxide (NaOH or KOH). Since, many coal based power plants in US have been retiring due to thrust towards cleaner energy production and this may lead to scarcity of flyash in future. Hence the objective of this study is to incorporate other Pozzolanic materials in geopolymer concrete. In line with objective two Pozzolanic materials granulated blast furnace slag (GGBS) and rice husk ash (RHA) were used to replace flyash in Geopolymer concrete. Tests are performed on compressive strength of geopolymer concrete by varying percentages of RHA and GGBS. Results indicated that complete replacement of flyash in geopolymer concrete with RHA and GGBS is not feasible. As geopolymerization needs specific amount alumina, RHA & GGBS have minimal amount which is adversely affecting the strength. Nevertheless GGBS up to 50% can be used as replacement of flyash to attain compressive strength around 2000 psi and 5-10% of RHA can be used to achieve similar strength. In addition micro-characterization of geopolymers was performed using Scanning electron microscope and X-ray diffraction. These techniques helped in understanding the characteristics of binder formation around the sand particles which is affecting the strength.

INTRODUCTION

Portland cement concrete (PCC) is considered as the second most used material after water and most used man made material (Hajek et al. 2013). According to Hajek et al (2013) the production of concrete in the industrialized countries, 1.5-3.0 tonnes of concrete is produced per year and is still increasing. Portland cement is key component in concrete. According to United States Environmental Protection Agency (US EPA) 3.4 percent of Worlds greenhouse gases is generated from production of Portland cement. The production of cement releases CO₂ in two different phases: (1) calcium carbonate decomposes to lime and carbon dioxide when heated, and (2) due to burning of fuel needed for production of cement. Although, the cement industry has increased energy efficiency, the amount of CO₂ emitted during production is still roughly 900 grams per kg (1.98 lb. per 2.2 lb.) of cement produced. In order to reduce the burden on the environment, some percentage of cement in PCC is replaced with

Flyash for past few decades, which reduces the environment impacts to certain extent. The demand for PCC is increasing due to urbanization of world population; therefore, there is a need for developing alternative binding materials which are more environmental friendly. Geopolymer cement is one such material proposed to replace Ordinary Portland Cement (OPC).

Geopolymer cement is a polymer produced by combining materials rich in silica and alumina (like fly ash) with sodium or potassium silicate and sodium/potassium hydroxide. Fly ash plays a key role in geopolymer cement, as it is rich in silica and alumina. Fly ash used in construction industry mostly is a byproduct from coal based power plants. The burning of coal, generates approximately twenty to thirty tons of CO₂ per ton of fly ash generated. Burning of coal is the chief cause of smog, acid rain, and toxic air pollution (“Coal Power: Air Pollution” 2015). Many coal based power plants in US have been retiring due to thrust towards cleaner energy production and this may lead to scarcity of flyash in future.

Geopolymer concrete may be a possible replacement for PCC, but scarcity of fly ash in the future, may jeopardize the progress of geopolymer. Hence, there is need to use alternate materials in producing geopolymer.

OBJECTIVE

The objective of this study is to incorporate other Pozzolanic materials in geopolymer concrete. In line with objective two Pozzolanic materials, Ground Granulated Blast Furnace Slag (GGBS) and Rice Husk Ash (RHA) were used to replace flyash in Geopolymer concrete.

METHODOLOGY

The feasibility of replacing fly ash with other pozzolanic materials like GGBS and RHA is verified in this study. Compressive strength of geopolymer mortar is used to monitor the feasibility of replacing fly ash. Tests were performed by replacing fly ash with various percentages of GGBS or RHA in geopolymer mortar. In addition to compressive strength the geopolymer mortar with GGBS, RHA, and Fly ash are characterized by using Scanning Electron Microscope (SEM) and X-Ray powder Diffraction (XRD). The following section explains the material properties and mix design employed in this study.

MATERIALS AND MIX DESIGN

Geopolymer

In 1994, Davidovits proposed 'Geopolymer' binder that comprises of high amount of silicon (Si) and aluminum (Al) and can be created through chemical reaction in the presence of alkaline liquid. The chemical reaction under alkaline condition on Si, Al minerals produces three dimensional polymeric chain and ring structure consisting of Si-O-Al-O bonds. During chemical reaction, dissolution of Si and Al atoms occurs, from source material, by action of hydroxide ions and then dissolute ions forms into

monomers' by either transportation or orientation or condensation of ions. These monomers are then poly condensed/polymerized into polymeric structures. However, the chemical reactions overlap with each other and it is difficult to differentiate them (A. Palomoa 1999). Water is released while Geopolymer is formed. The release of water, during geo-polymerization, allows formation of discontinuous nano pores in matrix, which enhances the performance of Geopolymer. Although, water has no role in chemical reaction but it influences the strength as well as the workability of the mixture (Rangan 2005).

The behavior of mortar prepared with Geopolymer is dependent on ingredients and curing regime (temperature as well as duration). The Geopolymer mortar or concrete can be produced from base materials that have high amounts of Si and Al in amorphous form such as Metakaolin or Calcined Kaolin (Davidovits 1999), low calcium ASTM Class F fly ash (Palomoa et al. 1999) , (Hardjito et al. 2005) and granulated blast furnace slag (Cheng and Chiu 2003) etc., alkaline solution to dissolve the Si and Al atoms in the base material, and additional water for workability and aggregates.

Alkaline solution plays a vital role in chemical reaction and most commonly used alkaline solution is a mixture of sodium hydroxide (NaOH) or potassium hydroxide (KOH) and sodium silicate or potassium silicate (Palomoa et al. 1999, Hardjito et al. 2005, Davidovits 1999, Cheng and Chiu 2003). According to Hardjito et al and Nuruddin et al, alkaline liquid plays a key role in the polymerization process and reaction rate is enhanced when alkaline liquid contains soluble silicate either in the form of sodium or potassium silicate. Sodium hydroxide is more effective in dissolving minerals than potassium hydroxide. The following sections explain the various constituents in Geopolymer.

Fly Ash

The ratio of Si to Al in base material plays an important role and Davidovits (Davidovits J 1999) proposed that if Si to Al ratio is 2 to 3, it can be used for preparation of low CO₂ cements, concrete, etc. The silica content normally varies from 50-60% and alumina content varies from 20 to 30% for a typical Class F fly ash. The chemical composition of Fly ash used in this study is shown in Table 1.

Ground Granulated Blast Furnace Slag (GGBS)

GGBS is a byproduct from manufacturing of iron and steel-making. Blast furnace slag is formed in the processes of iron manufacture from iron ore, combustion residue of coke, and fluxes such as limestone or serpentine and other materials. If the molten slag is rapidly chilled by immersion in water, a vitreous Ca–Al–Mg silicate fine grain glass is formed with a highly cementitious in nature. Due to presence of SiO₂ and Al₂O₃ in GGBS it can be used in geopolymer as a base material (Yunsheng et al. 2007). A typical chemical composition of GGBS is shown in Table 1. The GGBS was finely crushed in the laboratory for this study as the available GGBS was in larger size (around 20mm).

Rice Husk Ash (RHA)

Rice husk is an agricultural residue abundantly available in rice producing countries. Burning rice husk at 500-800° C temperature results in the formation of silica. The silica content in RHA is around 90-95%. A typical chemical composition of RHA is shown in Table 1. In this study rice husk ash is prepared by burning rice husk at 600° C for four hours.

Alkaline Solution

Alkaline solution for Geopolymer is a combination of sodium silicate/potassium silicate and sodium hydroxide/potassium hydroxide. There are no fixed guidelines for the proportion of sodium silicate/potassium silicate to sodium hydroxide/potassium hydroxide. Ratios of 0.4 & 2.5 were used by Hardjito and Rangan (Hardjito et al. 2005) , 2.5 by Reddy et al , Nuruddin et al , Lloyd and Rangan, and Anuradha et al. Research conducted by Hardjito and Rangan (Hardjito et al. 2005) suggests that higher ratio of sodium silicate solution-to-sodium hydroxide solution by mass, results in higher compressive strength of Geopolymer concrete.

Sodium hydroxide is effective in dissolving the minerals within fly ash. The important parameter to be considered is molarity of NaOH. Many researchers worked at higher molarity such as 8M to 16M (Hardjito et al. 2005), 8M to 14M (Reddy et al. 2012, Nuruddin at al. 2011), 8M & 14M (Llyod and Rangan 2010), 16M (Anuradha et al. 2012). Hardjito and Rangan (Hardjito et al. 2005) concluded that high molar sodium hydroxide results in higher compressive strength of fly ash based Geopolymer concrete, but decrease in workability with increase in molarity was also observed by (Nuruddin at al. 2011). According to Caustic Soda Manual (Industries 2008), in every 100 pounds of pure NaOH 77.48 pounds of Na₂O is present. NaOH normally available in market is 98-99% pure which typically consists of 76-76.7% Na₂O.

Sodium silicate is the common name for a compound sodium metasilicate, (Na₂SiO₃), also known as “waterglass or liquid glass.” Sodium silicate is characterized by SiO₂/Na₂O. Most of the researchers have used a ratio of 2.0 in their research which gives SiO₂ 29.4%, Na₂O 14.7% and 55.9% of H₂O and Palomo et al. (Palomoa et al. 1999) suggested a higher ratio of 3 for geopolymer.

If proportion of Sodium Silicate to Sodium hydroxide is considered as 2.5 and high molar sodium hydroxide (8M-16M) is used than molar ratio of SiO₂/Na₂O in alkaline solution will be in the range of 1.33 to 1.070. Davidovits (Davidovits 2013) stated that published literature on alkali activated Geopolymer based on fly ashes comprised molar ratio of SiO₂/Na₂O was below 1.20 with an average of 1.0 and most of them propose to use pure NaOH of 8M to 12M without considering safety. A higher ratio of SiO₂/Na₂O is recommended.

In this study sodium silicate with $\text{SiO}_2/\text{Na}_2\text{O}$ ratio of 1.65 with 4M sodium hydroxide. A lower ratio of $\text{SiO}_2/\text{Na}_2\text{O}$ and higher molar sodium hydroxide generates higher compressive strength, but hazardous to work.

Water

Even though water has no role in chemical reaction as mentioned, but it has effect on fresh and hardened Geopolymer concrete (Hardjito et al. 2005). From various proposed mix designs, molar ratio of $\text{H}_2\text{O}/\text{Na}_2\text{O}$ should be in range of 10.0 to 14.0 (Hardjito et al. 2005). If molar ratio is lower than 10, the produced concrete or mortar is stiffer while molar ratio higher than 14.0 cause's segregation. In this study a molar ratio of 14.3 is chosen considering the workability of mortar when produced in large quantities. 20 percentage to weight of alkaline solution is additional added to increase the $\text{H}_2\text{O}/\text{Na}_2\text{O}$ to 14.3.

Curing

The temperature and duration of curing plays vital role on strength gain of Geopolymer concrete. In a study conducted by Hardjito and Rangan (Hardjito et al. 2005), concrete was cured at 30°C, 45°C, 60°C, 75°C and 90°C for 24 hours. After 24 hours, the specimens were kept at room temperature for 28 days prior to testing. Other studies have suggested curing the specimens at 60°C for 24 hours [Hardjito et al. 2005, Nuruddin et al. 2011, Jaarsveld et al. 1997] or 24-48 hours (Anuradha et al. 2012). Typically, curing at high temperature is specified. In this study all the samples were cured at 60°C for three days. The curing was kept constant as the study was focused on the impact of various materials on geopolymer. However, the impact of curing temperature was addressed previously by authors for the same design mix with fly ash only (Inti et al. 2014)

Table 1. Chemical composition of Fly ash, GGBS, and RHA

SNo	Chemical Tests	Flyash	GGBS ¹	RHA ²
1	Silicon Dioxide (SiO_2)	60.8	27-38	94.95
2	Aluminum Oxide (Al_2O_3)	23.57	7-12	0.39
3	Iron Oxide (Fe_2O_3)	6.16	0.2-1.6	0.26
4	Calcium Oxide (Cao)	4.41	34-43	0.54
5	Magnesium Oxide (MgO)	1.10	7-15	0.90
6	Sulfur Trioxide (SO_3)	0.41	-	-
7	Sodium Oxide (Na_2O)	0.93	-	0.25
8	Potassium (K_2O)	1.14	-	0.94
9	Manganese Oxide (MnO)	-	0.15-0.76	0.16
10	Sulfur	-	1.0-1.9	-

¹ Blast Furnace Slag - Material Description - User Guidelines for Waste and Byproduct Materials in Pavement Construction

² Della et al. 2002

FIG. 1 displays the SEM images of the various pozzolanic materials used in this study. Fly ash particles were more spherical in shapes and RHA has fiber like structures. The exact shape for GGBS particles were not evident in the assessment. The GGBS used for this study was finely crushed in the laboratory using mechanical strength, whereas Fly ash and RHA were produced through burning which might affected the shape of particles. XRD analysis was performed on this materials. FIG. 2 shows the XRD images for the three materials, as mentioned earlier the presence of silica (SiO_2) and alumina (Al_2O_3) is required for geopolymer, the focus of XRD was to identify the compounds of silica and alumina. It is evident from XRD that the fly ash and GGBS have silica and alumina, whereas no alumina was identified in RHA. XRD analysis supports the chemical composition of these materials as shown in Table 1.

Mix Design

- In this study 2 inch (50 mm) cubes were used for testing the compressive strength of geopolymer. The ratio of Fly ash: Sand used is 1:2.75 which is as per the ASTM C109/C109M – 12 for preparing hydraulic cement mortar cubes. Alkaline solution is prepared by mixing sodium silicate with sodium hydroxide and a ratio (sodium silicate/sodium hydroxide) of 2.45 was used for preparing mortar.
- Although ASTM standard suggests having a water cement ratio of 0.485, alkaline solution to fly ash ratio of 0.5 was used in this study because workability reduced significantly at lower ratios.

Geopolymer with 100 percent flyash was used as a baseline for comparison. Fly ash was replaced with various percentages of GGBS (10 to 100%) and RHA (5-20%). The samples were cured for 3 days at 60°C.

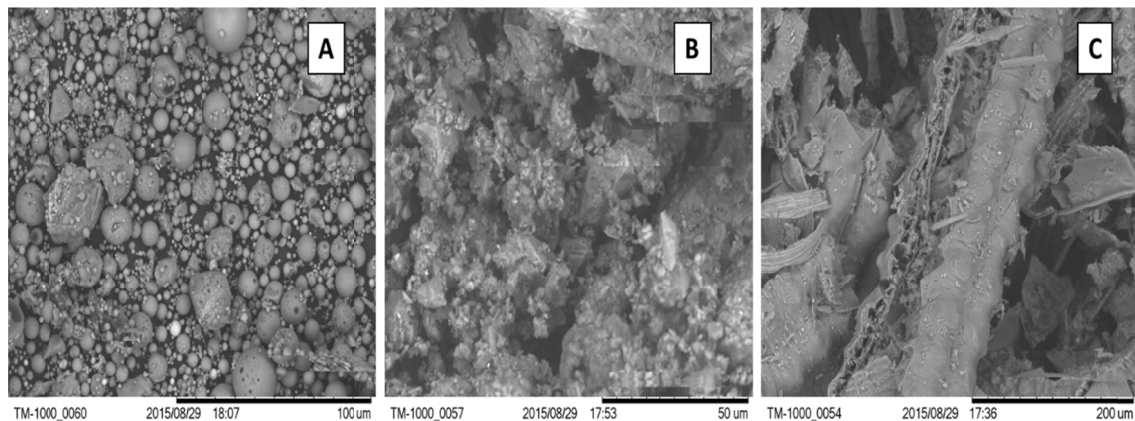


FIG. 1. SEM images of A) Fly ash, B) GGBS, and C) RHA.

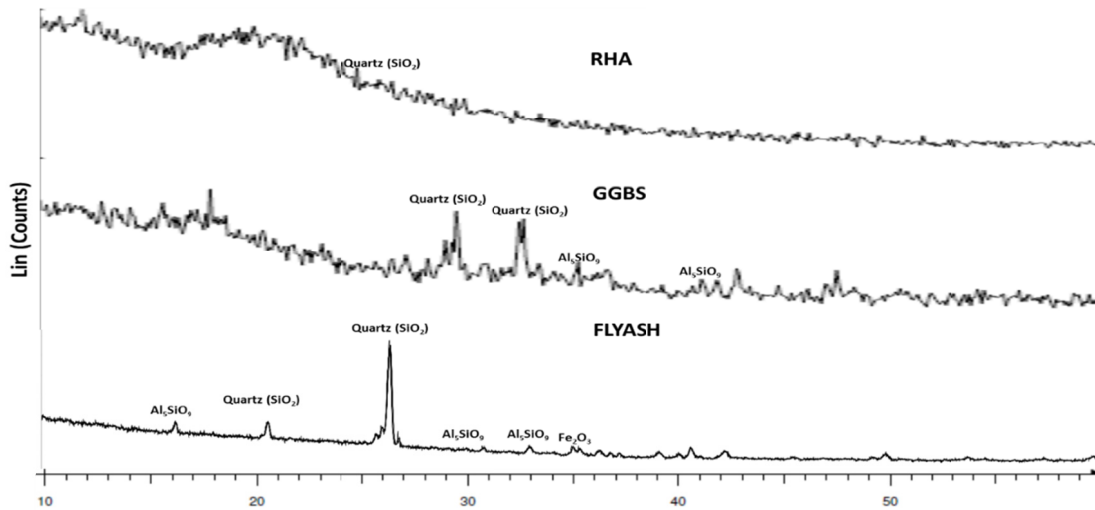


FIG. 2. XRD images of Flyash, GGBS, and RHA

RESULTS

The compressive strength of geopolymer mortar was reduced with increasing percentage of GGBS and was evident from the results FIG. 3. Similarly, the compressive strength dropped with increase of RHA in geopolymer and the results were displayed in the FIG. 4.

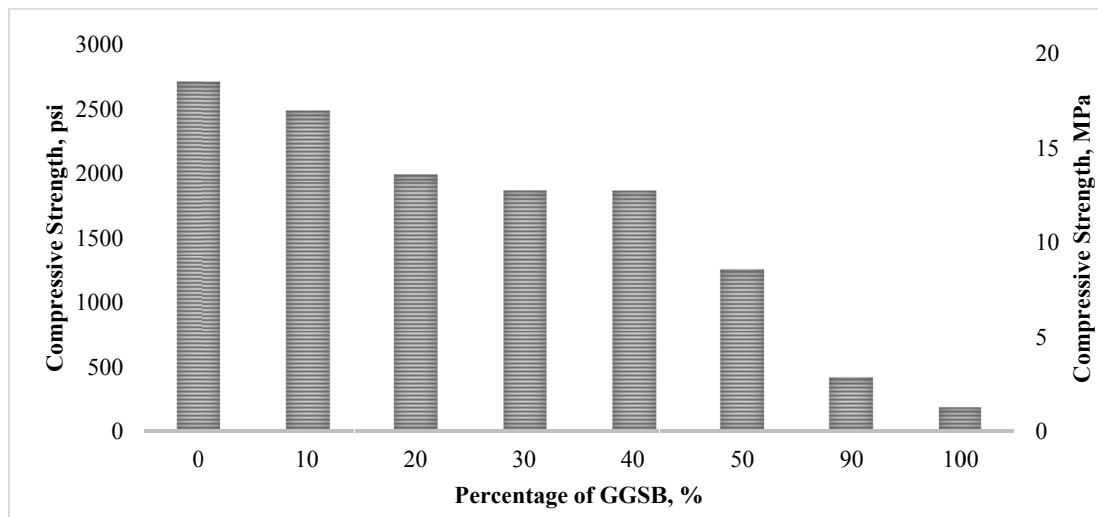


FIG. 3. Compressive strength of geopolymer mortar with various percentages of GGBS.

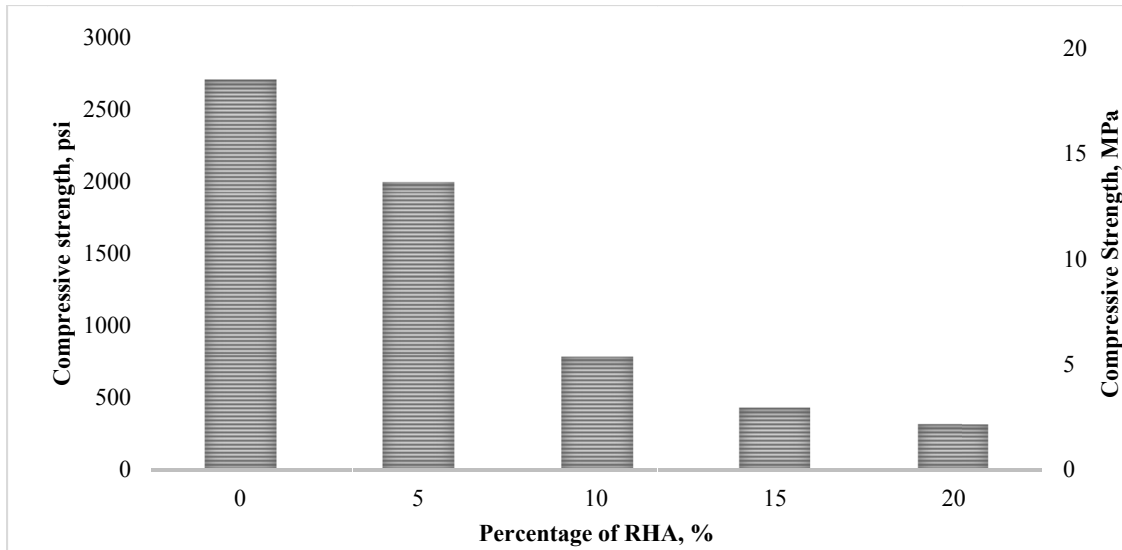


FIG. 4. Compressive strength of geopolymer mortar with various percentages of RHA.

DISCUSSIONS

Usage of GGBS in Geopolymer yielded better results compared to RHA. XRD and SEM analysis were performed on geopolymer mortar for further analysis. FIG. 5 shows the XRD analysis with three geopolymers mortars made with 1) 40 % GGBS and 60% fly ash, 2) 10% RHA and 90 % fly ash, and 3) 100 % flyash. It was observed that geopolymer with only flyash has more compounds of alumina and silica compared with other geopolymers.

Similarly, SEM analysis was performed on the above geopolymer mortars and FIG. 6 shows the bonds formed between sand particles and geopolymer. Strong bonds were observed when complete flyash was used, and weak bonds were observed with increasing percentage of RHA in the mix. GGBS has relatively stronger bonds compared with RHA. With the increase of GGBS percentage (above 40%) the bond between sand particles and geopolymer was observed weak.

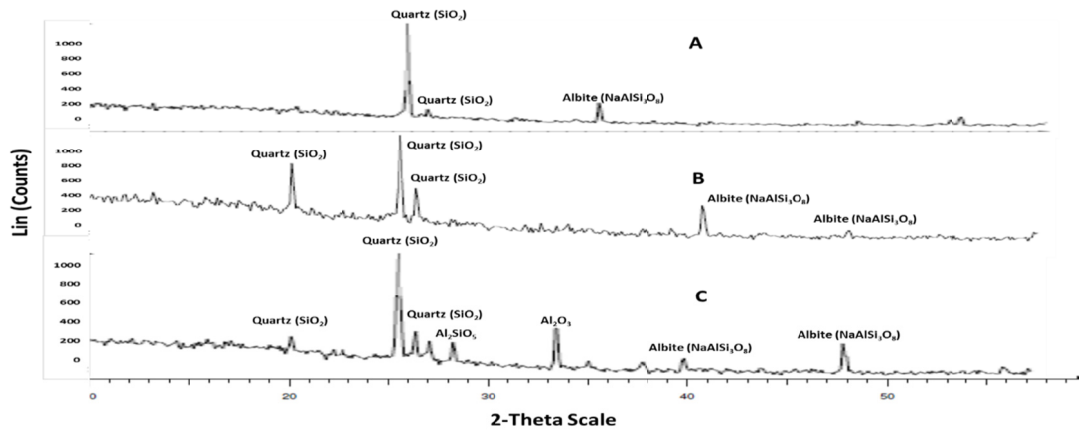


FIG. 5. XRD of geopolymer A) with 40 % GGBS, B) with 10% RHA, C) Complete Flyash

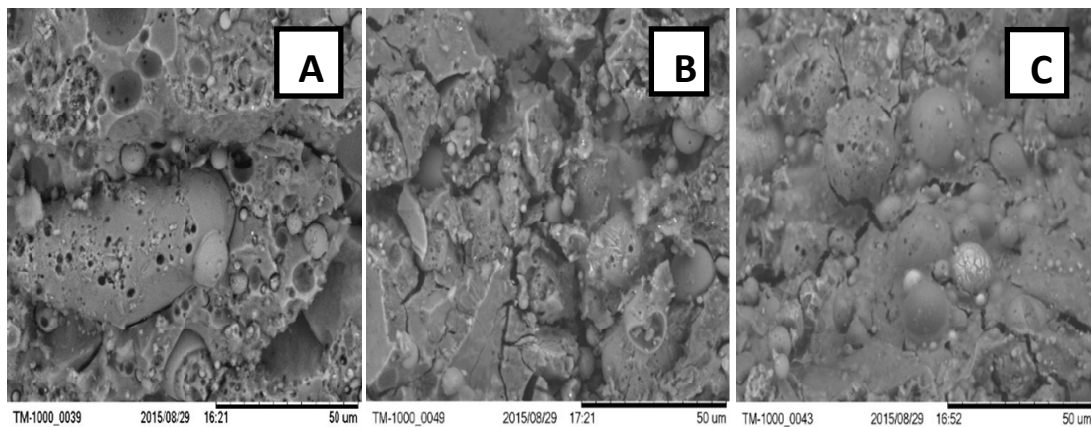


FIG. 6. SEM images of geopolymer A) Complete Flyash , B) with 40 % GGBS, C) with 10% RHA.

The possible reason for lower strength of geopolymer mortar with RHA and higher proportions of GGBS might be the higher ratio of SiO_2 (silica) and Al_2O_3 (alumina). The approximate ratios of SiO_2 and Al_2O_3 in the mixes were estimated and displayed in Table 2. By comparing the compressive strengths of mortars in FIG. 3, FIG. 4 and Table 2, it is evident that there is drastic drop in compressive strength if the ratio of $\text{SiO}_2/\text{Al}_2\text{O}_3$ is greater than 2.76. The findings of this study are line with findings of Davidovits (Davidovits J 1999) who proposed that if SiO_2 to Al_2O_3 ratio is 2 to 3, it can be used for preparation of low CO_2 cements, concrete, etc.

Table 2. Chemical composition of Flyash, GGBS, and RHA

% Flyash	% GGBS	Ratio of SiO₂/Al₂O₃
100	0	2.58
90	10	2.62
80	20	2.66
70	30	2.70
60	40	2.76
50	50	2.82
40	60	2.90
30	70	2.99
20	80	3.10
10	90	3.24
0	100	3.42
% Flyash	% RHA	Ratio of SiO₂/Al₂O₃
100	0	2.58
95	5	2.79
90	10	3.02
85	15	3.28
80	20	3.57

CONCLUSIONS

- The results of the study indicates that GGBS and RHA use in the production of geopolymer mortar or concrete depends on the ratio of SiO₂ to Al₂O₃. Higher proportion of Al₂O₃ is desired in order to completely replace fly ash in geopolymer.
- The results of this study are based on a single fly ash, GGBS, and RHA. Results needed to be validated by using materials from different sources.
- Further study is recommended by changing the proportions of SiO₂/Na₂O and molarity of NaOH of alkaline solutions to study their impact on properties of Geopolymers made with different base materials.

ACKNOWLEDGEMENT

The authors like to gratefully acknowledge financial support for this project received from the Civil Engineering Department (UTEP), Center for Advanced Infrastructure and Transportation Rutgers, and U.S. Department of Transportation/Research and Innovative Technology Administration. This project was conducted in labs of Biomolecule Analysis Core Facility and the Center for Transportation Infrastructure Systems at The University of Texas at El Paso.

REFERENCES

- Anuradha, R., Sreevidya, V., Venkatasubramani, R., & Rangan, B. V. (2012). "Modified guidelines for geopolymer concrete mix design using Indian standard". *Asian Journal of Civil Engineering (Building and Housing)*, 13(3), 353-364.
- Cheng, T. W., and Chiu, J. P. (2003). "Fire-resistant geopolymer produced by granulated blast furnace slag". *Minerals Engineering*, 16(3), 205-210.
- "Coal Power: Air Pollution." 2015. Union of Concerned Scientists. Accessed August 15. http://www.ucsusa.org/clean_energy/coalvswind/c02c.html.
- Davitovits, J. (2013). [www.Geopolymer.org](http://www.geopolymer.org)
<http://www.geopolymer.org/category/library/technical-papers>. (June 15, 2013)
- Davidovits, J. (1999). "Chemistry of geopolymeric systems, terminology." *In Geopolymer*, 99, 9-40.
- Davidovits, J. (1994). "Properties of geopolymer cements". *In First international conference on alkaline cements and concrete*, 1, 131-149.
- Della, V. P., Kühn, I., and Hotza, D. (2002). "Rice husk ash as an alternate source for active silica production." *Materials Letters*, 57(4), 818-821.
- Hajek, P., Ctislav, F., Buhr, J. B., and Ivana, L. 2013. "Integrated Life Cycle Assessment of Concrete Structures". *Lausanne, Switzerland: fédération internationale du béton*
- Hardjito D., and B. Vijaya Rangan. (2005). "Low-Calcium Fly Ash-Based Geopolymer Concrete: Reinforced Beams and Columns." *Curtin University of Technology. Perth, Australia.* http://espace.library.curtin.edu.au/cgi-bin/espace/pdf?file=/2008/11/13/file_6/19466.
- Industries PPG. (2008). "NaOH Caustic Soda Manual". Canada: PPG Industries INC.
- Inti, S., Hernandez, M. G., Tandon, V., and Tarquin, A. J. (2014). "Influence of Low Molarity Sodium Hydroxide and Curing on Mechanical Properties of Geopolymer". *In Transportation Research Board 93rd Annual Meeting (No. 14-4703)*.
- Lloyd, N. A., and Rangan, B. V. (2010). "Geopolymer concrete with fly ash." *In Second international conference on sustainable construction materials and technologies*, 3, 1493-1504.
- Nuruddin, M. F., Demie, S., Ahmed, M. F., and Shafiq, N. (2011). "Effect of superplasticizer and NaOH molarity on workability, compressive strength and microstructure properties of self-compacting geopolymer concrete". *World Academy of Science, Engineering and Technology*, 5(3), 1378-1385.

- Palomo, A., Grutzeck, M. W., and Blanco, M. T. (1999). "Alkali-activated fly ashes: a cement for the future." *Cement and concrete research*, 29(8), 1323-1329.
- Reddy, D. V., Edouard, J. B., and Sobhan, K. (2012). "Durability of fly ash-based geopolymer structural concrete in the marine environment." *Journal of Materials in Civil Engineering*, 25(6), 781-787.
- Yunsheng, Z., Wei, S., Qianli, C., and Lin, C. (2007). "Synthesis and heavy metal immobilization behaviors of slag based geopolymer". *Journal of hazardous materials*, 143(1), 206-213.

Heat Exchangers for Pavement Surface De-Icing

Soji Pallathu Abraham¹; Sherif L. Abdelaziz, A.M.ASCE²; and Jon Longtin³

¹Master Student, Dept. of Mechanical Engineering, Stony Brook Univ.

²Assistant Professor, Dept. of Civil Engineering, Stony Brook Univ., 116 Heavy Engineering, Stony Brook, NY 11794-2323.

³Professor, Dept. of Mechanical Engineering, Stony Brook Univ., 159 Light Engineering, Stony Brook, NY 11794-2300.

Abstract: The goal of this paper is to investigate the potential use of pavement heat exchangers buried in the aggregate base layer to de-ice the pavement surface. Icy pavement forms a major roadway hazard with the annual fatalities due to loss of vehicle control on icy pavements exceeding those from natural disasters. Various efforts to use innovative techniques have been reported in the literature for deicing of bridge decks with very little dealing with de-icing of pavements. Heated pavement using geothermal energy is reported in the Netherlands. In their system, the pavement loops were buried in the asphalt layer which created several construction and operational concerns limiting the widespread of the technology. This study considers burying the loops in the base layer beneath the asphalt and it intends to investigate the feasibility of that technique. Finite element models were performed for New York City and it is shown that burying pavement loops in the base layer is a viable technique to de-ice pavements.

INTRODUCTION

Pavement plays a vital role in the performance of the national transportation system as vehicles and trucks travel on the pavement surface. Thus, the conditions of the pavement surface have a great impact on the traffic flow, smooth riding, and safety of passengers. One of the critical pavement surface condition occurs during cold weather as ice accumulates on the surface of the pavement. Icy pavements reduce the highway capacity by up to one-third due to slow moving traffic, lane closures due to snow accumulations and/or accidents. Additionally, icy pavements represent a safety hazard due to reduced tire-pavement traction, which causes loss of vehicle control. In fact, the annual fatalities due to accidents on icy pavements (U.S. Department of Transportation 2015) exceed four-times the fatalities due to natural hazards (NOAA 2015). Therefore, the state and local highway agencies utilize various de-icing and anti-icing chemicals to reduce the negative impacts of icy pavement surfaces. In addition to wearing the pavement surface, these chemicals contaminate groundwater aquifers; highway de-icing chemicals are the main reason for the dramatic increase of the salt percentage (Jackson and Jobbagy, 2005, Kaushal et al., 2005) in New England groundwater aquifers. Thus, there is a desperate need to use sustainable techniques to de-ice pavements.

Several techniques are available to ensure that ice does not form in pavements. Permeable pavements, for instance, allow the surface water to drain faster thereby preventing the ability to form ice in winter (Qin, 2015). Since the high porosity of these pavements rely on having more voids in the pavement, the lifetime of these pavements under heavy traffic has yet to be assessed. Further, in addition to relatively high initial costs, permeable pavements lose their ability to drain water quickly over time as fine particles fill the porous structure. Heat Pipe is another technique for heating the bridge decks, (Minsk, 1999) that was first introduced in 1963 (Kumagai and Nohara, 1988). This technique use tubes filled with a fluid that vaporizes at the heat source and condenses at the sink giving out the heat obtained from the source side of the tube (Dunn et al., 1976, Ivanovskii et al., 1982). Another technique used to heat the pavements is by passing an electric current through conductors that are pre-installed in the pavement structure. As electricity flows in the conductor, it encounters certain resistance which heats the conductor and the surrounding pavement layers. Although these techniques are feasible in keeping pavement ice-free, the high energy costs needed for external heating constrained the practical implementations of such techniques (Havens et al., 1978, Hoppe, 2001).

To minimize the use of costly heating system, Netherlands proposed to use the shallow geothermal energy to heat pavements (de Bondt, 2003). The Dutch technology is implemented by circulating a geothermal fluid through loops pre-installed in the asphalt layer and geothermal heat exchangers on the sides of the roadway. A full scale implementation of the Dutch system showed that this technique is capable of keeping the pavement surface ice-free throughout the winter (Spitler and Ramamoorthy, 2000). However, the Dutch technique required expensive crack-resistant asphalt and three-dimensional polypropylene geo-grid to be used in order to prevent asphalt cracks due to severe stress concentrations around the pavement loops (de Bondt et al., 2006). Another concern with the Dutch system is the fact that special construction approaches should be followed to limit the asphalt temperature during paving to the maximum allowed for the loops (de Bondt et al., 2006).

Aiming to overcome the challenges associated with the Dutch heated pavement technology, this study aims to investigate the potential of burying the pavement loops in the base aggregate base layer beneath the asphalt layer. Burying the loops in the base layer makes it possible to use asphalt mixes conforming to the local and national standard specifications, i.e. no need for high crack resistant asphalt. Further, the proposed technology does not require any construction constraints with respect to the asphalt temperature during paving.

CONTROLLING PHYSICAL PHENOMENON

In order to approximate the temperature distribution in the pavement, it is assumed that heat conduction controls heat transfer from the pavement surface to greater depths. In other words, convection due to groundwater flow is ignored. Thus, the temperature at any point in the pavement can be approximated using the heat conduction equation shown in Eq. (1).

$$\rho C_p \frac{\partial T}{\partial t} - \frac{\partial q}{\partial z} = 0 \quad (1)$$

where ρ is the density in kg/m^3 , C_p is the specific heat capacity in $\text{J}/(\text{kgK})$, and k is the thermal conductivity in $\text{W}/(\text{mK})$ of the pavement layers, T is the temperature in K , t is the time in s , and z and q are the depth and the heat flux at the point of concern, respectively.

The pavement temperature for the proposed self-heated pavement technique depends on two physical phenomena: (1) the amount of heat penetrating the pavement as a result of thermal interaction of the pavement surface with the ambient; this phenomena can be considered using the surface energy balance relations at the pavement surface, and (2) the amount of heat injected to the pavement by the embedded loops.

Surface Energy Balance at Pavement Surface

The heat flux penetrating the pavement surface (G) can be approximated by setting the depth equals to zero in the conduction heat flux equation as shown in Eq. (2).

$$G = -k \cdot \left. \frac{\partial T}{\partial z} \right|_{z=0} \quad (2)$$

According to the surface energy balance concept, the conductive heat flux can be approximated as shown in Eq. (3). In this equation, the conductive heat flux is approximated as the difference between the solar radiation at the pavement surface ($I_{surface}$) and the summation of (1) the convective heat between the wind and the pavement surface (H), (2) the long-wave emission of the short wave radiations (L), and (3) the latent heat used to evaporate water from the pavement surface (E). The evaporation heat (E) can be ignored since pavements are typically impermeable and do not have water to evaporate.

$$G = I_{surface} - (H + L + E) \quad (3)$$

A portion of the solar radiation that reaches the Earth's surface is reflected back into the sky ($I_{surface}$). This reflected radiation is proportional to the reflection coefficient, known as the albedo (ϕ), which is a measure of reflectivity of the surface, and the solar radiation in the sky (I_{sky}) as per Eq. (4).

$$I_{surface} = (1 - \phi) \cdot I_{sky} \quad (4)$$

The heat convection is related to the heat transfer coefficient (h_c), the pavement surface temperature (T_s), and the air temperature (T_a) and it can be approximated as given in Eq. (5).

$$H = h_c \cdot (T_s - T_a) \quad (5)$$

The heat transfer coefficient can be approximated as a function of the wind speed (v) and is given by the empirical formula shown in Eq. (6) (Bentz, 2000).

$$h_c = \begin{cases} 5.6 + 4 \cdot v & \text{for } v < 5 \text{ m/s} \\ 7.2 \cdot v^{0.78} & \text{for } v \geq 5 \text{ m/s} \end{cases} \quad (6)$$

The long-wave emission is related to the irradiative coefficient (h_r), the sky temperature (T_{sky}), and the pavement surface temperature as shown in Eq. (7).

$$L = h_r \cdot (T_s - T_{sky}) \quad (7)$$

The irradiative coefficient and the sky temperature can be approximated using Eq. (8) and Eq. (9), respectively.

$$h_r = \varepsilon \cdot \sigma \cdot (T_s^2 + T_{sky}^2) \cdot (T_s + T_{sky}) \quad (8)$$

$$T_{sky} = \varepsilon_{sky}^{0.25} \cdot T_d \quad (9)$$

where ε is the surface emissivity, σ is the Stefan-Boltzmann constant ($\sigma = 5.67 \text{ e}^{-8} \text{ W/m}^2 \cdot \text{K}^4$), ε_{sky} is the sky emissivity given by Eq. (10), T_d is the dew point approximated by Eq. (11).

$$\varepsilon_{sky} = 0.574 + 0.0044T_d \quad (10)$$

$$T_d = \frac{b_0 \cdot \gamma}{a_0 - \gamma}, \quad a_0 = 17.3, \quad \text{and } b_0 = 237.7 \quad (11)$$

where g is a factor related to the ambient air temperature (T_a) and the relative humidity (RH) as shown in Eq. (12).

$$\gamma = \frac{a_0 \cdot T_a}{b_0 + T_a} + \ln\left(\frac{RH}{100}\right) \quad (12)$$

Heat from pavement loops

The amount of heat supplied to the pavement from the fluid in the loops that are installed in the base layer can be calculated if the fluid density (ρ_f), heat capacity ($C_{p,f}$), flowrate (V) and the temperature change (ΔT) between the inlet and the outlet points of the loop is known. This heat is given by the Eq. (13).

$$q_{loop} = \rho_f \cdot C_{p,f} \cdot V \cdot \Delta T \quad (13)$$

This heat is reduced as it moves through the thickness of the pipe walls. The reduced heat at the external surface of the loops can be approximated by accounting for the thermal resistance of the internal film and the wall as given in Eq. (14).

$$q_{wall} = h_{eff} \cdot (T_{ext} - T) \quad (14)$$

The effective heat transfer coefficient (h_{eff}) is approximated as given by Eq. (15).

$$h_{eff} = \frac{2\pi}{\frac{2}{d_{in}h_{int}} + \frac{\ln(d_{out}/d_{in})}{k_p}} \quad (15)$$

where d_{in} and d_{out} are the inner and outer diameters of the loop, k_p is the thermal conductivity of the loop, and h_{int} is the heat transfer coefficient between the flowing fluid inside the loops and the internal wall of the loop, which can be approximated using Eq. (16).

$$h_{int} = N_u \cdot \frac{k_f}{d_{in}} \quad (16)$$

Where N_u is Nusselt number (Gnielinski, 1976), and k_f is fluid thermal conductivity.

NUMERICAL MODELING APPROACH

The two phenomena addressed previously were incorporated in numerical models performed using COMSOL Multiphysics finite element package (COMSOL, 2014) to approximate the temperature of the pavement provided with the proposed loops. The models were initially validated against temperatures measured in pavement section without loops, in Davis, CA. Qin and Hiller (2014) provided the intensity of the solar radiation, wind speed, relative humidity, and ambient temperature over a 10-days period extending from July 1st to July 11th, 2012. The pavement temperature at 12.7, 38.1, and 63.5 mm in the asphalt layer were recorded over the test period. Figure 1 presents a comparison between pavement temperatures measured at 38.1 mm in the field and those approximated using the adopted numerical modeling technique. As can be seen from this figure, the pavement temperatures approximated using the finite element models are in good agreement with the measured temperatures; the relative error between these two sets of data is approximated to be about 7.5% which is considered acceptable since the field data were manually digitized. Similar results were found for the temperatures at 12.7 and 63.5 mm.

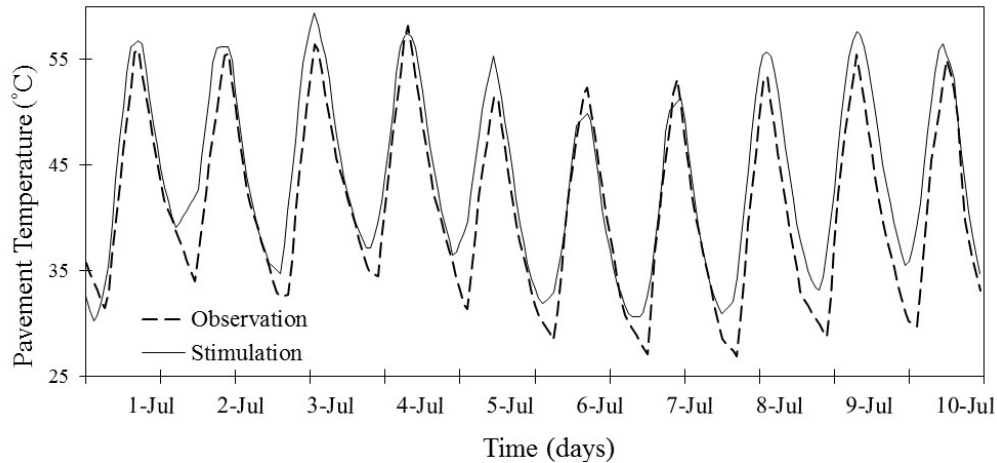


FIG. 1. Numerical Modeling Validation for Pavement Temperatures.

Model Description

The pavement section used in this study consists of 125 mm asphalt layer overlying a 300 mm aggregate base layer underlined with a 6 m subgrade layer. Pavement loops were embedded 75 mm below the bottom of the asphalt in the aggregate base layer. The inner and outer diameters of the pavement loops are 25 and 28 mm, respectively. Pavement loops were placed at 230 mm center to center spacing. The initial temperature was assumed to be 15 °C. The properties of various materials used in the model are given in Table 1.

Table 1. Thermal Properties of Various Materials.

Thermal Property	Pipe	Water	Asphalt	Base	Subgrade
Density (kg/m^3)	960	1000	2350	2000	1750
Thermal Conductivity ($\text{W/m}\cdot\text{K}$)	0.39	0.594	1.80	2.0	2.0
Specific Heat Capacity ($\text{J/kg}\cdot\text{K}$)	2300	4187	900	800	1500

The typical meteorological year (TMY) weather data for New York City is used as inputs for the model. The TMY database provides the most critical hourly weather data over the last 30 years (Wilcox and Marion, 2008). Figure 2 presents the variation of ambient air temperature, relative humidity, solar intensity, and wind velocity over the TMY for New York City.

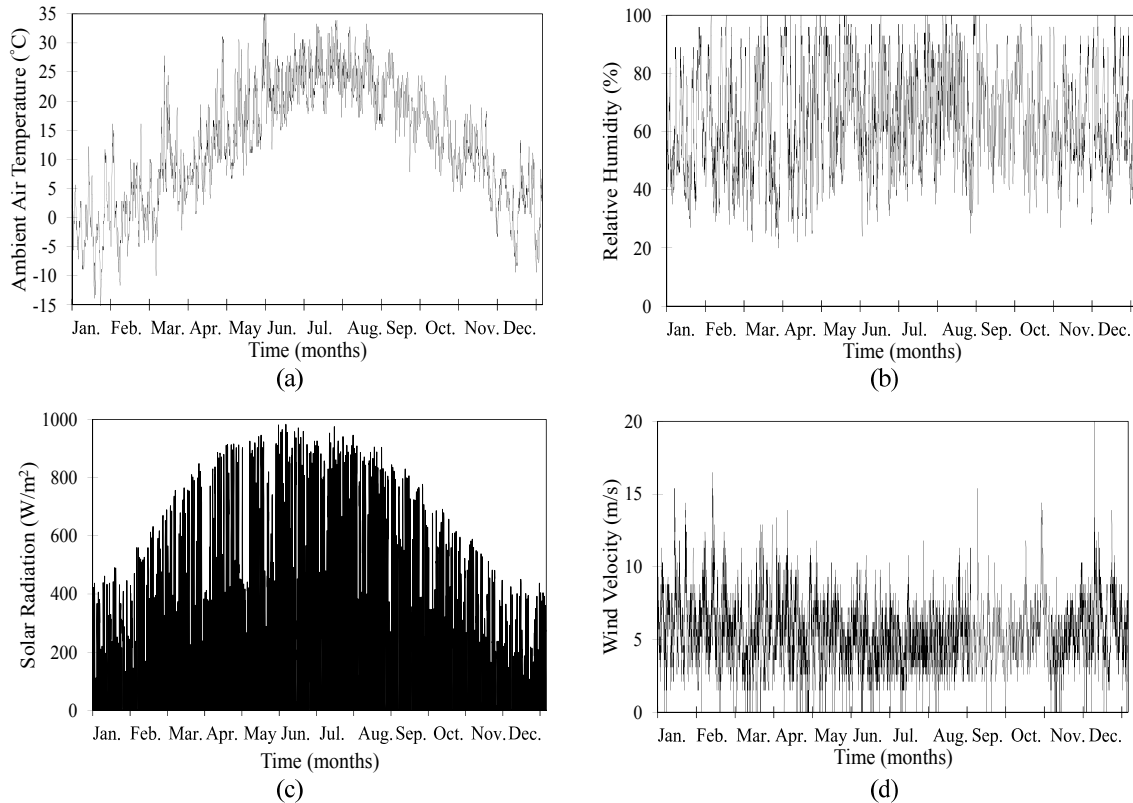


FIG. 2. TMY Weather Data for New York City, USA.

Hierarchical discretization was utilized to build the finite element mesh for the selected pavement section; the fluid domain was initially discretized using quadrilateral elements followed by the pipe walls which were also discretized using quadrilateral elements. Finally, pavement and soil layers were discretized using triangular finite elements.

RESULTS AND DISCUSSIONS

Initial analysis for the pavement section without loops was performed in order to determine the period of time over which the temperature of the pavement fall below freezing. According to this model, it was found that for the considered pavement, freezing occurs between November and March, with the minimum pavement surface temperature at the end of January as shown in Figure 3.

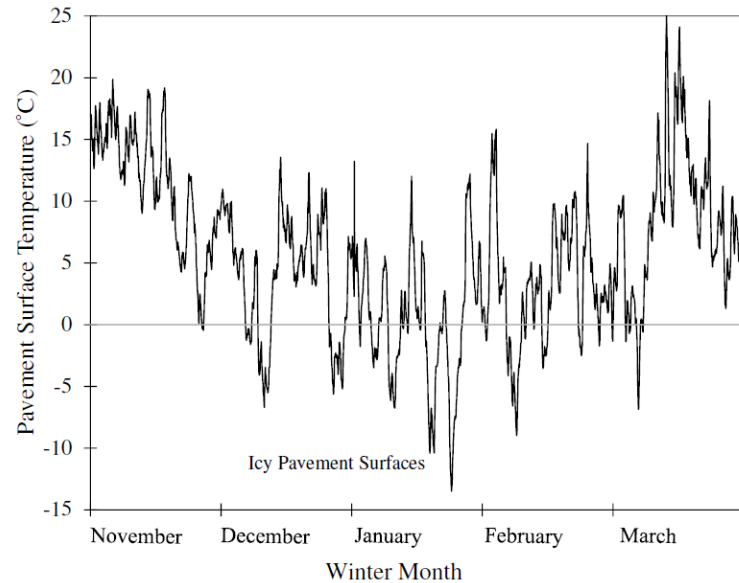


FIG. 3. Surface Temperature for Traditional Pavements (i.e. without loops) over Winter Months in New York City.

Proposed Self-Heated Pavements

The main goal of this study is to investigate the ability of the proposed self-heated pavement technology to maintain the pavement surface temperature above freezing under various weather conditions. In order to assess the feasibility of the proposed system, the amount of heat flux that has to be injected from the loops to the pavement structure to ensure an ice-free pavement surface needs to be approximated. The analysis of the model was carried out by incrementally increasing the amount of heat flux from the pavement loops (q_{loop}). It is found that the heat flux in the pavement loops that ensures an ice-free pavement surface is about 170 Watts per linear meter of the loop as shown in Figure 4. Additionally, it is also noted that the maximum pavement temperature raised above acceptable range for pavement temperature. The main cause of this undesired pavement temperature increase is due to applying the loop heat flux continually even when the temperature of conventional pavement was above freezing. The numerical models reported in this study will be revised to mimic the response of an actual system in which the loop heat flux varies in accordance to the pavement surface temperature. In reality, the amount of heat flux that has to be added to the pavement surface from the loops is achieved by varying the rate of fluid flow inside the loops.

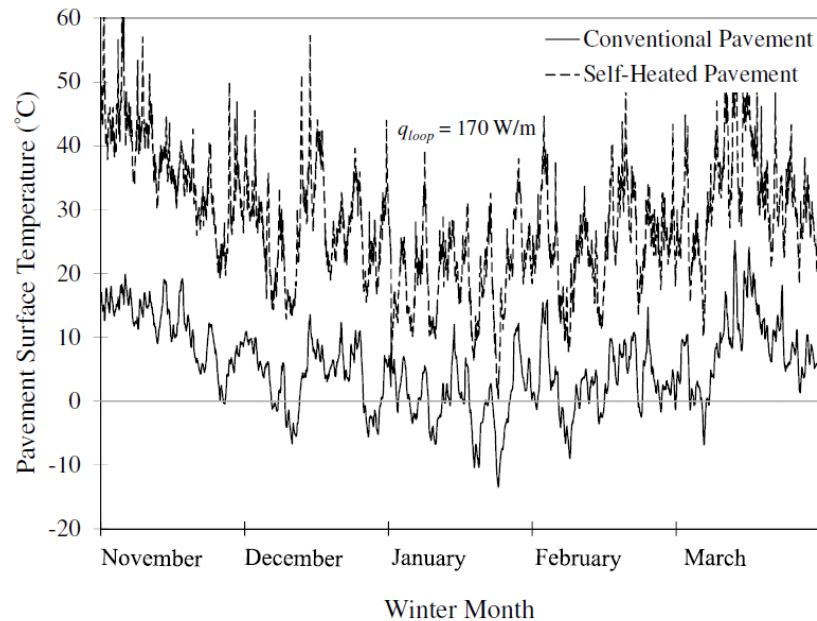


FIG. 4. Comparison between the Surface Temperature for Conventional Pavements and the Proposed Self-Heated Pavements over Winter Months in New York City.

Freezing Hours versus Loop Heat Flux

While a heat flux of 170 W/m has to be applied in the pavement loops to ensure that the pavement surface temperature never falls below freezing for New York City, a lower loop heat fluxes increases the number of hours over which the temperature of the pavement surface falls below freezing compared to the number of freezing hours for conventional pavements. As shown in Figure 5, the total annual number of hours over which the surface temperature of conventional pavements fall below freezing is 750 hours representing 8.5% of the total annual hours, i.e. over one full month. As the heat flux from the loops increases, the minimum annual pavement temperature increases while the annual number of hours for pavement freezing reduces. For instance, only 44 hours of pavement surface freezing are expected annually, i.e. 0.5% of total annual hours, when pavement loops inject 75 W/m. It should be noticed that these 44 hours are not continuous and were observed to occur during early morning hours when low traffic volumes are expected. Further, the impact of the moving vehicles is expected to reduce these number of hours which is a factor not accounted for in the numerical models reported in this study.

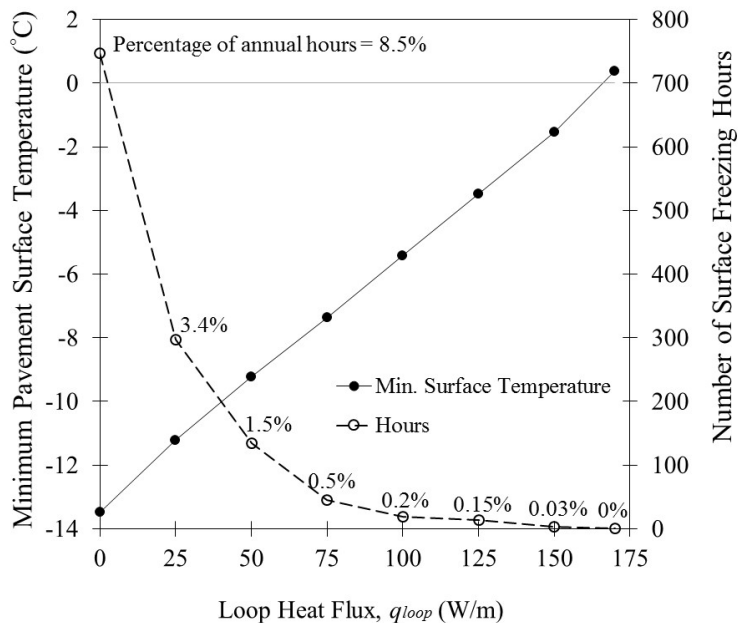


FIG. 5. Effect of Loop Heat Flux on Minimum Pavement Surface Temperature and the Annual Number of Freezing Hours.

CONCLUSIONS

Based on the numerical models reported in this study, it can be inferred that burying loops in the aggregate base layer of pavements allows to maintain the pavement surface temperature above freezing. For New York City, it is estimated that a heat flux of 170 Watts per linear meter (heat flux per unit depth) has to be injected to the pavement to keep its temperature ice-free at all times. However, injecting 75 W/m is sufficient to reduce number of pavement freezing hours to less than two-days annually. Finally, from the supply and demand energy perspective, the thermal demand needed to maintain the pavement surface ice-free at all times is approximated to be about 700 W/m² corresponding to 170 Watts per linear meter of the pavement loop. Innovative systems to supply this required thermal demands need to be considered for economic systems.

ACKNOWLEDGMENT

The work performed in this study is supported by University Transportation Research Center for Region 2 (UTRC 2). The authors appreciate UTRC-2 for their support.

REFERENCES

- Bentz, D.P. (2000). "A computer model to predict the surface temperature and time of wetness of concrete pavements and bridge decks." National Institute of standards and technology, Vol. 6551.
- de Bondt, A.H. (2003). "Generation of energy via asphalt pavement surfaces.", *Asphaltica Padova* 2003.
- de Bondt, A.H. and Jansen, R. (2006). "Generation and saving of energy via asphalt pavement surfaces," OIB aktuell, Nov 13, 2006.
- Gnielinski, V. (1976). "New equations for heat and mass transfer in turbulent pipe and channel flow." *International Journal of Chemical Engineering* Vol. 16: 359-368.
- Havens, J., Azevedo, W., and Rahal, A. (1978). "Heating bridge decks by electrical resistance," Proceedings of the 2nd International Symposium on Snow Removal and Ice Control Research, Special Report 185, Hanover, 159-168, 15-19 May 1978.
- Hoppe, E.J. (2001). "Evaluation of Virginia's first heated bridge." *Transportation Research Record* Vol. 1741: 199-206.
- Ivanovskii, M.N., Sorokin, V.P., and Yagodka, I.V. (1982). "The physical principles of heat pipes." Translated by R. Berman. New York: Oxford University Press.
- Jackson, R.B. and Jobbagy, E.G. (2005). "From Icy roads to salty streams." Proc Natl Acad Sci, USA. Vol. 102(41): 14487-14488.
- Kaushal, S.S., Groffman, P.M., Likens, G.E., Belt, K.T., Stack, W.P., Kelly, V.R., Band, L.E., and Fisher, G.T. (2005). "Increased salinization of fresh water in the northeastern United States." Proc Natl Acad Sci, USA. Vol. 102(38): 13517-20.
- Kumagai, M. and Nohara, I. (1988). "Studies on a practical use of snow melting system by using the heat of ground water through pipes." National Research Center for Disaster Prevention, Japan, Report No. 41: 285-309.
- Minsk, L.D. (1999), "Heated bridge technology: Report on ISTEA Sec. 6005 program." Publication FHWA-RD-99-158, FHWA, US Department of Transportation.
- NOAA 2015, Office of Climate, Water, and Weather Services. *Natural Hazard Statistics*. Available from: <<http://www.nws.noaa.gov/om/hazstats.shtml>> [July 20, 2015]
- Ozudogru, T.Y., Olgun, C.G., and Senol, A. (2014). "3D numerical modelling of vertical geothermal heat exchangers." *Geothermics* Vol. 51: 312-324.
- Qin, Y. and Hiller, J.E. (2014). "Understanding pavement-surface energy balance and its implications on cool pavement development." *Energy and Buildings* Vol. 85: 389-399.
- Qin Y. (2015). "A review on the development of cool pavements to mitigate urban heat island effect." *Renewable and Sustainable Energy Reviews* Vol. 52: 445-59.
- Spitler, J.D. and Ramamoorthy, M. (2000). "Bridge deck deicing using geothermal heat pumps." In proceedings of the 4th International Heat Pumps in Cold Climates Conference. 2000. Aylmer, Quebec.
- U.S. Department of Transportation, Federal Highway Administration 2015. *How do weather events impact roads*. Available from: <http://www.ops.fhwa.dot.gov/weather/q1_roadimpact.htm>. [July 20, 2015]
- Wilcox, S. and Marion, W. (2008). "Users Manual for TMY3 Data Sets, N.R.E.L." NREL/TP-581-431556. National Renewable Energy Laboratory: Golden, Colorado 50 p.

Laboratory Evaluation of Mixtures Incorporating GTR and RAP

Md. Tanvir Iqbal¹; Munir D. Nazzal²; Sang Soo Kim³; Ala Abbas⁴; Md. Tanvir Quasema⁵; and Walaa Mogawer⁶

¹Graduate Student, Civil Engineering Dept., Ohio Univ., Athens, OH.

²Associate Professor, Civil Engineering Dept., Ohio Univ., Athens, OH 45701 (corresponding author).
E-mail: nazzal@ohio.edu

³Associate Professor, Civil Engineering Dept., Ohio Univ., Athens, OH.

⁴Associate Professor, Civil Engineering Dept., Univ. of Akron, Akron, OH.

⁵Graduate Student, Civil Engineering Dept., Univ. of Akron, Akron, OH.

⁶Professor, Civil Engineering Dept., Univ. of Massachusetts, Fall River, MA.

Abstract

This paper presents the results of a study that was conducted to evaluate the performance of ground tire rubber (GTR) modified asphalt mixtures containing reclaimed asphalt pavement (RAP) materials and compare them to that of a typical styrene-butadiene-styrene (SBS) polymer modified asphalt mixture. Two types of GTR materials that were produced using the ambient and cryogenic methods were considered. Different laboratory tests were conducted on the prepared GTR and polymer modified mixtures to evaluate their resistance to low temperature cracking, fatigue cracking, and rutting. The results of the laboratory tests showed that mixtures prepared using the GTR modified binders had similar low temperature cracking resistance to the polymer modified mixture. In addition, the GTR mixtures had higher indirect tensile strength, but lower toughness index values than the polymer modified mixture. While the ambient GTR mixture had slightly better rutting performance than the polymer modified mixture; the cryogenic GTR mixture exhibited similar rutting resistance. In general, all GTR mixtures with RAP exhibited good resistance to low temperature cracking, fatigue cracking, and rutting.

INTRODUCTION

Recently, there has been a growing interest to reduce the CO₂ emissions. One way that can be used to achieve that is to increase the use of recycled materials. In 2009, 161 million tons of waste materials were generated in the United States. About 82 million tons of the generated waste materials were recycled resulting in CO₂ emission reduction equivalent to taking 33 million passenger vehicles of the road

(Keep America Beautiful, Inc, 2015). Therefore, the use of recycling waste materials in construction of civil engineering structure is the demand of the century.

One of the recycled materials that has been used in asphalt mixture is reclaimed asphalt pavement (RAP) material. RAP is a useful alternative to virgin materials because it reduces the need to use virgin aggregate, which is a scarce commodity in some areas of the United States. It also reduces the amount of costly new asphalt binder required in the production of asphalt paving mixtures. Because of its' valuable re-usable aggregates and asphalt binder, RAP has already become one of the most widely used recycled materials in the United States.

Another type of the recycled materials that can be used in asphalt mixtures is Ground tire rubber (GTR), also known as crumb rubber. In 2003, approximately 290 million scrap tires were generated in the United States (EPA, 2014). The number of scrap tires has increased steadily from 1993 when 233 million scrap tires were generated. On the contrary, the available disposal space has declined. In 2003 approximately 80% of the scrap tires generated were utilized in some market such as tire derived fuel, civil engineering applications and rubber modified asphalt. The remaining 20% scrap tires were disposed in landfills. Many states have established legislation imposing restrictions on the disposal of scrap tires. It is important to decrease this burden on environment by utilizing these scrap tires in some constructive way.

GTR has been incorporated in asphalt mixtures using two different processes, namely the dry process and the wet process (Heitzman, 1992). In the wet process, the GTR is blended with the asphalt binder before being mixed with the aggregate. In the dry process, GTR is added to the aggregate before being mixed with the asphalt binder, while in the wet process, GTR is blended with the asphalt binder before being mixed with the aggregate. The latter is expected to provide better blending between the GTR particles and the asphalt binder, resulting in better performance for the GTR asphalt mixtures (Myhre and MacKillop, 2002).

In the United States, the wet process has been achieved using two main methods (Hicks 2009). The first method involves adding graded GTR particles to the asphalt binder and agitating the blend in a specialized unit at elevated temperatures to promote chemical and physical bonding between the two materials. The agitation is required due to the relatively large size and amount of GTR used in this method. The second method involves adding finer GTR particles to the asphalt binder at a refinery or at an asphalt binder storage/distribution terminal before being transported to an asphalt mix plant. The GTR obtained using this method is commonly referred to as pre-blended GTR or terminal blend GTR. The main advantage of this method is that it eliminates the need for the specialized blending equipment at the job site, resulting in lower production costs.

During the past decade several studies have been conducted to evaluate the behavior and performance of GTR asphalt binders and mixtures produced using terminal blend wet process. Different factors were found to affect the performance of GTR modified asphalt binders. The influence of the GTR on binder properties was found to depend on the interaction between the rubber particles and the asphalt binder which influenced by the rubber particle size, production method (type), and surface

area (Abdelrahman, 1999). There are two main types of GTR based on the production method, namely ambient and cryogenic. For the ambient GTR, the scrap tire is processed at or above room temperature. Ambient processing typically provides irregularly shaped, torn particles with relatively large surface areas to improve the interaction with the asphalt binder (Attia, 2009). On the other hand, for cryogenic GTR liquid nitrogen is used to freeze the scrap tire typically to a temperature between -87 to -198 °C until it becomes brittle, and then uses a hammer mill to shatter the frozen rubber into smooth particles.

Shen et al. (2009) studied the effect of the particle size and surface area of GTR on the high temperature properties of GTR modified asphalt binders. Two base binders (PG 64-22 and PG 52-28) and two types of GTR (ambient and cryogenic) with three different sizes were considered. The binders were mixed with GTR at a mixing temperature of 176°C for 15, 30 and 45 minutes using a high shear mixer at 700 rpm. The results of this study showed that the larger the GTR particle size is, the more improvement in the elastic properties of the GTR modified binder. In addition, the stiffness of the GTR modified binder increased with the rubber particle size and decreased with its surface area. However, the effect of the particle size was more dominant than the surface area. For the same particle size, the ambient GTR modified asphalt binder was stiffer than the cryogenic GTR modified binder.

Willis et al. (2012) studied the effect of the GTR loading rate as well as the rubber particle size, surface area, and production method on the performance grade of GTR modified binders. Based on the binder test results, it was concluded that the GTR loading rate, and particle size had the most influence on increasing the high and low-temperature grade of the modified binder. In addition, the surface area had significant effect on the high temperature properties only. However, the GTR processing method had little to no influence on the modified binders due to relatively higher surface area of the cryogenic GTR materials used in their study. GTR with larger particle sizes showed greater indication of rubber separation.

Baumgardner (2015) evaluated the properties of an asphalt binder modified using several types of GTR and compared them to those obtained for a polymer modified asphalt binder. The results of his study showed that modification with 10% GTR is comparable to modification with approximately 3% of a styrene-butadiene-styrene (SBS) polymer. Baumgardner (2015) also examined the resistance of GTR and polymer modified dense graded mixtures to rutting as well as to fatigue and low temperature cracking. The GTR and polymer modified mixtures had similar good rutting performance but poor resistance to fatigue cracking. Furthermore, the results of Bending Beam Rheometer (BBR) tests that were conducted on the considered mixtures indicated that the use of GTR modifications had adverse effects on the low temperature cracking performance. However, the author indicated that the GTR modification of some asphalt binders may improve the low temperature performance.

In summary, there has been several research studies that evaluated the effects of GTR materials on the high temperature properties of asphalt binders, but few studies were conducted to examine their effects on low temperature properties of binder and the overall mixture performance. In addition, limited research work was reported on mixtures containing GTR modified binders and RAP materials. This study evaluates the laboratory performance of mixtures incorporating RAP and GTR

and examines the effect of GTR properties on the performance of GTR modified binders and mixtures. To this end, two different types of GTR materials were used to prepare GTR modified binders. Laboratory tests were conducted on the GTR modified binders and a typical styrene-butadiene-styrene (SBS) polymer modified binder and on mixtures prepared using these binders and RAP.

LABORATORY TESTING PROGRAM

Materials

The laboratory testing program included two GTR materials that were produced using the ambient and cryogenic methods. Both GTR materials were passing sieve number 30. The study also included a polymer modified asphalt binders meeting the specifications for PG 76-22 typically used in construction of pavements, which was obtained from an asphalt contractor in Ohio. The GTR binders were prepared by heating a neat asphalt binder meeting specification of PG 64-22 to a temperature of 190°C (375 °F) and adding 10% GTR by weight. The GTR and the binder were then blended using a high shear mixer at 3600 RPM for 50 minutes. A heating mantle was used to ensure that the binder's temperature remained constant at 190 °C (375 °F) during mixing.

Binder Performance Grade Testing

Dynamic shear rheometer (DSR) test was conducted on the GTR and polymer modified binders to determine their high temperature performance grade in accordance with AASHTO M320. The DSR test was conducted using a 2-mm gap to accommodate the presence of the GTR particles in the asphalt binder. Table 1 presents the continuous high temperature obtained based on the DSR test results. The GTR and polymer modified binders had a continuous high temperature grade greater than 76 °C.

Bending Beam Rheometer (BBR) test was also performed according to AASHTO Standard Specification T313 at two temperatures to determine the continuous low temperature grade of the considered binders. Table 1 presents the obtained continuous low temperature grade. It is noted that the GTR binders had a continuous low temperature grade less than that of the polymer modified binder.

Table 1. Continuous Grading for Evaluated Binders

Continuous Grading	64-22	76-22M	Ambient GTR	Cryogenic GTR
High Temperature (°C)	65.3	81.0	78.0	80.5
Low Temperature (°C)	-24.7	-25.4	-29.0	-29.6

Mixtures Design

To select the aggregate gradation of the mixture to be evaluated in this study, the gradations of aggregates of dense graded polymer modified mixtures previously

used in Ohio was selected. Based on that, the selected asphalt mixture had a 3/8 inch (9.5 mm) nominal maximum aggregate size (NMAS) and was designed to meet ODOT specification for Item 441 for medium traffic surface mixtures. It is noted that three aggregate types (47% limestone #8, 16% natural sand, 17% manufactured sand and 20% RAP) were blended to produce the required gradation. It is noted that 20% RAP was used, as it is the maximum percentage of RAP material typically used in surface mixtures in Ohio. Mix design was performed using the SBS polymer modified binder specification for PG 76-22M to determine the optimum asphalt content for the selected aggregate gradation. Verification of the mix design with the GTR binders was also performed using the same aggregate gradation and a target air void of 3.5%. Table 2 compares the obtained optimum binder content for the different GTR binders. The ambient GTR mixture required slightly higher (0.1%) asphalt binder content than the polymer modified mixture. This may be attributed to the percent of the base PG 64-22 binder replaced by the GTR material in GTR binders.

Table 2. Volumetric Properties of Evaluated Mixtures

Property	PG 76-22M	Ambient GTR	Cryogenic GTR
Design air Void (%)	3.5	3.5	3.5
Total Asphalt Binder Content (%)	6.2	6.3	6.2
Virgin Asphalt Binder Content (%)	5.7	5.8	5.7
VMA	16.7	16.7	16.4

Mixtures Testing

A laboratory testing program was performed to evaluate the performance of the control SBS polymer modified asphalt mixture and the GTR modified mixtures with respect to low temperature cracking, fatigue cracking, and permanent deformation (or rutting). All tested samples were compacted to target air void of $7 \pm 0.5\%$.

Asphalt Concrete Cracking Device (ACCD) test was also performed on the samples to evaluate their low temperature cracking resistance. To perform ACCD test, 2.3 inch (60 mm) diameter inner core of the prepared 6 inch (150 mm) samples was cored out. A 0.88 inch (22.4 mm) long-notch was then introduced at the outer surface of the sample to control the location of the crack. The test sample and the ACCD ring were heated for 60 minutes at 65°C and the tapered end of the heated ACCD ring slid through the center hole of the heated test sample. The sample with the ACCD ring fitted inside was placed in the environmental chamber. As the temperature decreases, the contraction of the asphalt mix specimen is restrained by the ACCD ring, developing tensile stress within the test specimen and compressive stress within the ACCD ring. Four samples are typically tested at the same time. The temperature and strain of each ACCD ring are continuously recorded until failure.

The temperature corresponding to the maximum slope of the ACCD strain-temperature curve is considered as the onset on thermal cracking. As the temperature is lowered, the rate of the strain increase per unit temperature ($d\varepsilon/dT$) decreases due to additional crack development and crack propagation. The ACCD cracking temperature is arbitrarily defined as the temperature where the slope of strain-temperature curve equals to 80% of the maximum slope after the onset of cracking.

The ACCD was performed on short-term and long-term aged specimens. The short-term aged samples were prepared by placing the loose asphalt mixture in an air draft oven at the compaction temperature for 4 hours prior to compaction. Long term aging of compacted mix was performed according AASHTO R3 30 procedure after the compacted samples were cut. AASHTO R 30 involves placing compacted asphalt mixtures in an oven at 85°C for 5 days to simulate the long term aging that takes place in the field.

The indirect tensile strength (IDT) and strain test was also conducted to evaluate propensity of the asphalt mixtures to fatigue cracking. The test was performed in accordance with AASHTO T245 at 25 °C. A deformation rate of 2 in/min was used. The load as well as the vertical and lateral deformations were continuously recorded and the indirect tensile strength was computed. In addition, the toughness index (TI), which is a parameter that describes the toughening characteristics in the post-peak region was also calculated using Equation 1.

$$TI = \frac{A_{3\%-P}}{(3\% - \varepsilon_p) * \text{Stress}_{\text{peak}}} \quad (1)$$

Where:

$A_{3\%-p}$: is the area under stress-strain curve between the peak lateral strain and a lateral strain value of 3%

ε_p : is the lateral strain at peak stress in %

$\text{Stress}_{\text{peak}}$: maximum stress value obtained.

The asphalt pavement analyzer (APA) test was also conducted according to AASHTO TP 63 to examine the permanent deformation (rutting) resistance of the GTR and polymer modified mixtures. APA tests were conducted at a temperature of 120°F (49°C). The samples were conditioned for a minimum of 12 hours at the test temperature prior to loading. During the test, rut depth measurements were obtained at 5, 500, 1000, and 8000 cycles. The total permanent deformation (or rutting) was calculated as the difference between the rut depth readings at the 8000th cycle and the 5th cycle.

RESULTS

ACCD Test Results

Figure 1 presents the average ACCD cracking temperature for the short-term and long-term aged samples tested in this study. For the short-term aged samples, the GTR modified mixes had similar cracking temperature to that of the polymer modified mixture. The long-term aging reduced the cracking temperature of all mixes. However, the GTR mixtures still had similar low temperature cracking resistance to that of the polymer modified mixture.

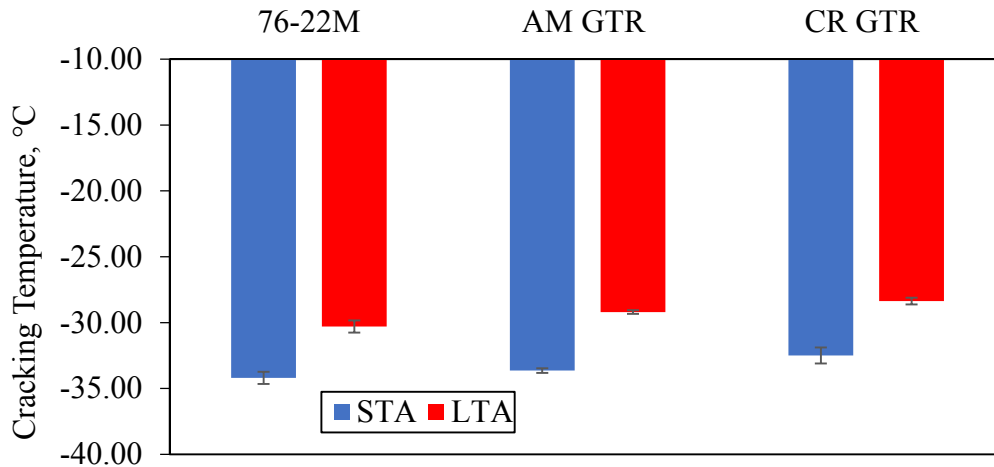


FIG. 1. Cracking temperature obtained from ACCD test.

Indirect Tensile Strength (IDT) Test Results

Figure 2 shows the mean and standard deviation of the ITS values for the considered mixtures at 25°C. Higher ITS values are desirable as they correspond to a strong and durable mixture. In general, GTR mixtures had slightly higher ITS values than the polymer modified 76-22M mixture; however, mixes with ambient GTR modified binder had the highest the ITS value.

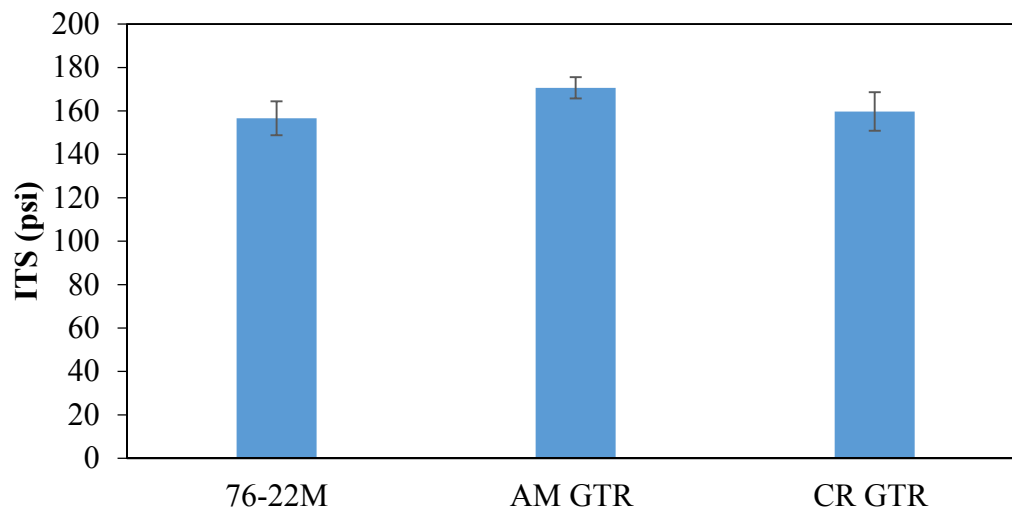


FIG. 2. Results of indirect tensile strength test.

Figure 3 shows the average and standard deviation of the TI values of the evaluated mixtures. The TI value represents the amount of energy absorbed by the mixture under tensile strain; lower TI value indicates more brittle behavior of the mixture. It is noted that the PG 76-22M polymer modified mixture had higher TI values than the GTR modified mixtures.

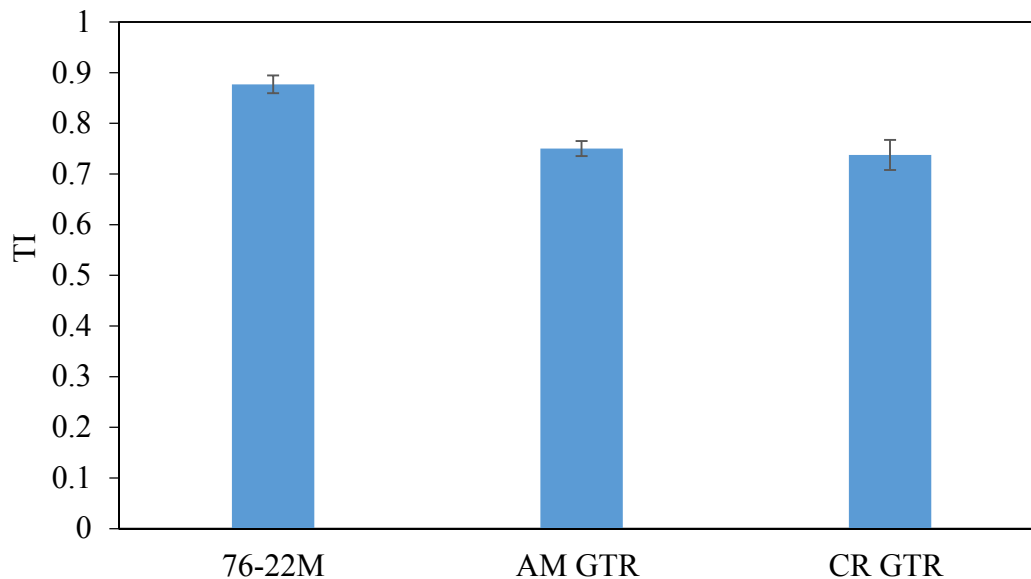


FIG. 3. Toughness index values of indirect tensile strength test.

APA Test Results

Figure 4 presents the APA test results for the GTR and polymer modified mixtures. While the ambient GTR mixture had slightly lower rutting than the polymer modified mixture, the cryogenic GTR mixture exhibited similar rutting resistance. It is noted that the mixture with cryogenic GTR had slightly higher rut depth than that with ambient GTR. However, the GTR and polymer modified mixtures have rut values less than 5 mm, which is the maximum allowable values specified by the Ohio Department of Transportation (DOT) as well as other DOTs.

CONCLUSIONS

This paper presented the results of a laboratory study that was conducted to evaluate the performance of asphalt mixtures containing RAP material and prepared using different types of GTR modified asphalt binders. Based on the results of this paper, the following conclusions can be drawn:

- The cryogenic and ambient GTR modified binders had a continuous high temperature grade greater than 76 °C. Furthermore, the GTR binders had a continuous low temperature grade colder than that of the polymer modified binder considered in this study.

- Mixtures prepared with cryogenic and ambient GTR modified binders had similar resistance to low temperature cracking as that of the PG 76-22M polymer modified binder as indicated by the ACCD test results.
- The GTR and polymer modified mixes showed good rutting performance in the APA test. While the ambient GTR mixture had slightly lower rutting than the polymer modified mixture, the cryogenic GTR mixture exhibited similar rutting resistance.
- The GTR mixes had slightly higher indirect tensile strength values than that prepared using PG 76-22M polymer modified binder. However, the mixture with 76-22M polymer modified binder had higher TI value than those with GTR modified binders.
- In general, the ambient GTR resulted in slightly better resistance to rutting and low temperature cracking as compared to the cryogenic GTR. However, all GTR mixtures exhibited good performance similar to that of the polymer modified mixture.

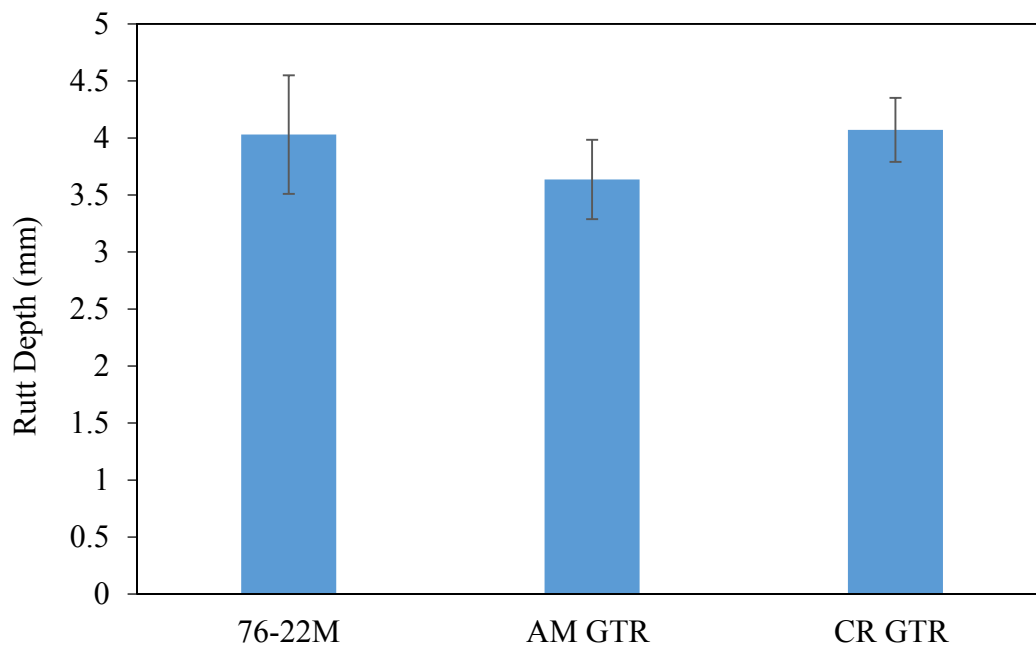


FIG. 4. APA test results.

REFERENCES

- Abdelrahman, M. Carpenter S. (1999). "The mechanism of the interaction of asphalt cement with crumb rubber modifier (CRM)." *Transport Research Record*, No. 1661, 106–13.
- Abdelrahman, M. A. (1996). "Engineering characterization of the interaction of asphalt with crumb rubber modifier (CRM)." *Ph.D. thesis*. University of Illinois at Urbana-Champaign.

- Attia, M. and Abdelrahman, M. (2009). "Enhancing the performance of crumb rubber-modified binders through varying the interaction conditions." *International Journal of Pavement Engineering*. Volume 10, no. 6: 423-434.
- Baumgardner, G. (2015). "Characterization and implementation of ground tire rubber as post-consumer polymers for asphalt concrete." *PhD Thesis*, Mississippi State University.
- Heitzman, M. (1992). "State of the Practice – Design and Construction of Asphalt Paving Materials with Crumb Rubber Modifier." *Research Report No. FHWA-SA-92-022*, Federal Highway Administration, Washington, D.C.
- Hicks, R.G., D. Cheng, and T. Duffy. (2010). "Evaluation of Terminal Blend Rubberized Asphalt in Paving Applications," *Report No CP2C-2010-102TM*, California Pavement Preservation Center, 2010. Available at http://www.paramountasphalt.com/blog/Paramount_Asphalt_News/post/Evaluation_of_Terminal_Blend_Rubberized_Asphalt_in_Paving_Applications/. Accessed on August 27, 2015.
- Myhre, M., and MacKillop, D.A. (2002). "Rubber Recycling." *Rubber Chemistry and Technology*. Vol. 75, No. 3, pp. 429-474. <http://dx.doi.org/10.5254/1.3547678>
- Shen, J., Amirkhania, S., Xiao, F. and Tang, B (2009). "Influence of surface area and size of crumb rubber on high temperature properties of crumb rubber modified binders." *Construction and Building Materials*, Volume 23, No. 1, 304-310.
- USEPA (2014). "Scrap Tires." *United States Environmental Protection Agency*, Washington, D.C. Available at <http://www.epa.gov/wastes/conservation/materials/tires/basic.htm>. Accessed on March 19, 2014.
- Willis, R., Clayton, P., Turner, P., Rodezno, C. and Mitchell, T. (2012). "Effect of Ground Tire Rubber Particle Size and Grinding Method on Asphalt Binder Properties." *NCAT Report: 12-09*, National Center for Asphalt Technology, Auburn, Al.
- "Recycling Facts & Stats." *Recycling Facts & Statistics*. Accessed August 29, 2015. http://www.kab.org/site/PageServer?pagename=recycling_facts_and_stats.

Performance of Aggregate Subgrade Layers in Low-Volume Roads Constructed with Unconventional Recycled Aggregates

Hasan Kazmee¹; Erol Tutumluer, M.ASCE²; and Debakanta Mishra³

¹Graduate Research Assistant. E-mail: kazmee2@illinois.edu

²Professor, Paul F. Kent Endowed Faculty Scholar. E-mail: tutumlue@illinois.edu
(corresponding author)

Dept. of Civil and Environmental Engineering, Univ. of Illinois at Urbana-Champaign, 205 North Mathews Ave., Urbana, IL 61801.

³Assistant Professor. E-mail: debmishra@boisestate.edu, Dept. of Civil Engineering, Boise State Univ., 1910 University Dr., ERB 3137, Boise, Idaho 83725.

Abstract

With transportation sector accounting for approximately 27% of total greenhouse gas emissions, transportation agencies all over United States have made sincere efforts to reduce such carbon footprint by incorporating more recycled materials in design mixes. In Illinois, recycled materials commonly include large sized unconventional aggregates used to stabilize weak subgrade soils that are abundantly found in wet of optimum conditions and prone to frost effects. To facilitate increased use of such “aggregate subgrade” materials, IDOT has recently introduced new gradation bands. However, performance of such recycled aggregate subgrade materials within the bounds of current design framework is largely unknown. To this end, a full scale accelerated pavement test study was undertaken to study six different aggregate subgrade materials involving construction of twelve full scale flexible pavement sections over weak engineered subgrade. Results of accelerated pavement testing on six test sections and performance of three different aggregate subgrade materials are highlighted in this paper including data from quality control tests such as nuclear density gauge, GeoGauge for composite layer modulus, and lightweight and falling weight deflectometers. Current pavement design framework was adequate when designing with two out of three aggregate subgrade materials that constituted different proportions of recycled materials. One noteworthy finding was that as-constructed hot mix asphalt thickness variation was found to be quite large due to reclaimed asphalt pavement subbase sinkage observed during paving operations.

INTRODUCTION

Adequate subgrade stability is essential for maintaining a stable working platform for pavement construction and longer service life. Illinois Department of Transportation (IDOT) requires an existing subgrade to have a minimum Immediate Bearing Value

(IBV) (also known as unsoaked CBR) of 6% for placement and construction of pavement layers (Bureau of Bridges and Structures 2005). IDOT *Subgrade Stability Manual (SSM)* also dictates that rutting under construction traffic must be limited to 12.7 mm (1/2 in.). Conversely, typical Illinois soils do not meet such ideal conditions due to excessive resilient deformation tendency along with low permeability and high suction potential. Moreover, periodic freeze-thaw actions in the Midwest adversely influence subgrade stability required for long term pavement serviceability.

To this end, IDOT frequently uses a layer of large size granular materials, often referred to as ‘aggregate subgrade’ for improved subgrade stability. The principal goal for inclusion of such layer is to provide a stable working platform for pavement construction where the existing very weak soil can be rapidly and conveniently improved. In addition, these large size granular materials can be effectively used for mitigating frost action. As a sustainable construction practice, IDOT Bureau of Design and Environment has recently introduced certain gradation bands, i.e. CS01, CS02 and RR01, under the special provision titled as ‘Section 303’ to allow the use of large size virgin and recycled materials for such improved subgrade applications (Division of Highways 2013).

Due to dimension specific requirements, engineering properties and performance of such large aggregates cannot properly be characterized using standard laboratory tests (Kazmee et al. 2015b). Moreover, current IDOT mechanistic based pavement design procedures do not acknowledge any structural contribution from the aggregate subgrade layer (Heckel 2009). Henceforth, performance trends of these materials are largely unknown. Though past experience in Illinois and other states have often been satisfactory for use of such large size aggregates from virgin sources; there is almost little to no information related to large size recycled materials used for weak subgrade stabilization (Mathis 1991; Uhlmeier et al. 2003).

In light of the above issues, a full scale pavement test study was undertaken at the University of Illinois to investigate the field performance of low volume asphalt pavements constructed with six different aggregate subgrade materials. Three different recycled materials were selected alongside three different virgin aggregates for construction so that the effect of material composition and source properties could clearly be identified. Totally, twelve full scale test sections were constructed and monitored for surface rut accumulation under accelerated pavement testing. Considering the limited space, this paper has scope to summarize six of these test sections that utilized the selected recycled aggregate subgrade materials.

DESIGN AND CONSTRUCTION OF FULL SCALE TEST SECTIONS

Table 1 summarizes the design thicknesses of constructed test sections. The existing subgrade was tilled up to a depth of 30.5 cm (12 in.) and compacted to a controlled strength of CBR = 1% and 3%, respectively. Engineering the subgrade strength was intended to simulate weak soil condition. Details of this procedure can be found elsewhere (Kazmee et al. 2015a). Note that the finished subgrade was sealed with an asphalt binder coating to prevent moisture evaporation. The thickness of aggregate subgrade layer was determined in accordance with the IDOT subgrade stability manual. Four of the test sections were constructed with two different recycled large rocks over CBR = 1% subgrade; meanwhile, the remaining two sections were built

with typical dense graded reclaimed asphalt pavement (RAP) over CBR = 3% subgrade.

For conventional flexible pavements, IDOT requires a minimum of 20.3-cm (8-in.) thick granular layer surfaced with 7.6-cm (3-in.) thick hot mix asphalt (HMA) layer. Since, the objective of this study to investigate performance trends of low volume roads, the design thicknesses for granular subbase and hot mix asphalt (HMA) were selected to be 15.2 cm (6 in.) and 10.2 cm (4 in.), respectively. The thickness of the granular subbase was intentionally scaled down so that the material effect of various aggregate subgrade compositions can be determined. Individual sections were designated with two different alphabetical letters where the first letter identifies the subbase material type and the second one represents the aggregate subgrade type. All of the designed test sections were 4.6 m (15 ft) long and 2.7 m (9 ft) wide.

Table 1. Design thicknesses of full scale test sections and selected materials

Section Designation		Z-W	Y-W	Z-X	Y-X	Z-Y	Y-Y
Thickness (cm)	HMA	10.2	10.2	10.2	10.2	10.2	10.2
	SB*	15.2	15.2	15.2	15.2	15.2	15.2
	AS**	53.3	53.3	53.3	53.3	22.9	22.9
AS Material Type		W		X		Y	
Subgrade CBR (%)		1				3	

*SB = Subbase, AS** = Aggregate Subgrade;

†Odd numbered section: Dolomite (Type Z) subbase, Even numbered section: RAP (Type Y) subbase.

†Type W = Crushed concrete aggregates;

Type X = Blended recycled aggregates;

Type Y = Reclaimed asphalt pavement (RAP) aggregates.

Each aggregate subgrade type had two different subbase materials namely Type Z and Type Y in consecutive sections. Type Z consisted of dense graded dolomite crushed stones; whereas, Type Y comprised of 100% reclaimed asphalt pavement (RAP) materials screened to 25.4 mm (1 in.) top size. Type W aggregates originated from concrete demolition waste; whereas, Type X aggregates had 60%-40% blend of large size recycled concrete and RAP. The HMA layer was designed to be constructed in thin lifts (5.1 cm or 2 in.) of binder and surface courses. The surface course was finer than the binder course having a 9.5 mm (3/8 in.) nominal maximum aggregate size. A PG 64-22 asphalt binder was used in both of the HMA lifts.

Aggregate Materials Used

Figure 1(a) shows the particle size distributions of selected aggregate types. Both Type W and Type X aggregate subgrade materials were selected to replicate CS01 gradation band. However, the blended recycled aggregates (Type X) were well-graded compared to the Type W recycled concrete aggregates. Sieve analyses results indicated that the crushed dolomite had approximately 10% materials passing the No. 200 sieve (0.075 mm), which is significantly higher than that of the remaining aggregate types.

Proper aggregate interlock is essential for improved granular layer performance. Apart from gradation, previous studies reported that aggregate shape properties can also greatly influence granular layer performance (Tutumluer et al. 2000; Tutumluer and Pan 2008). Accordingly, aggregate morphological properties like angularity, surface texture and flat-elongated ratio were also assessed with state of the art field imaging technique and Enhanced University of Illinois Aggregate Image Analyzer (E-UIAIA) (Moaveni et al. 2013). The related results are summarized in Figure 1(b) through 1(d).

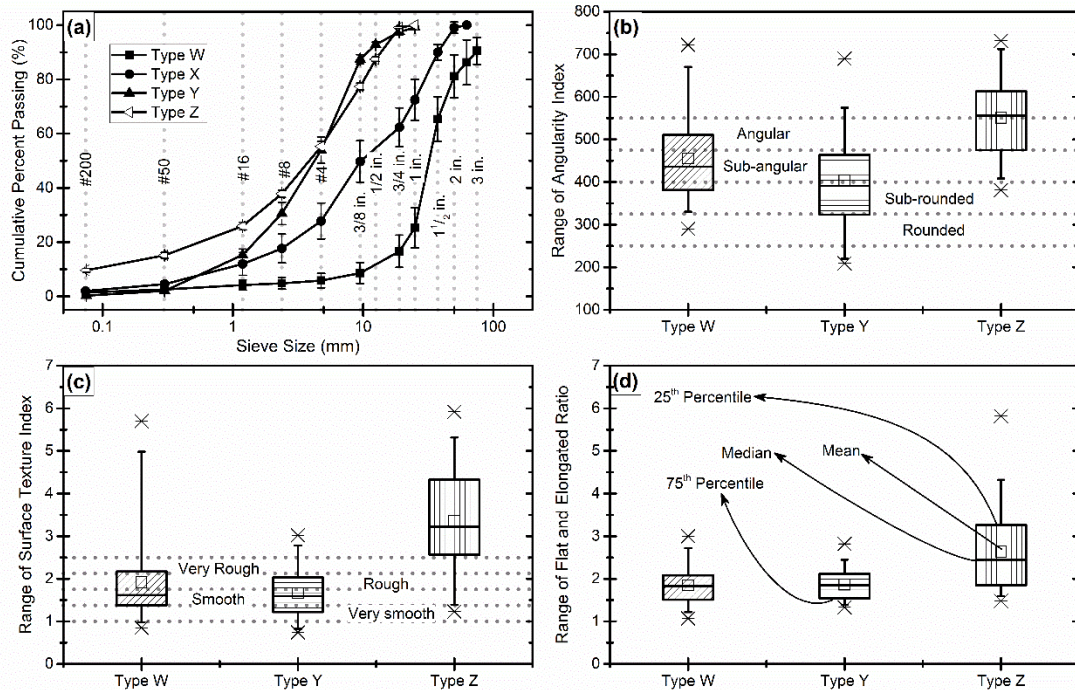


FIG. 1. (a) Particle size distributions, (b) Angularity Index, (c) Surface Texture (ST) index and (d) Flat and Elongated (F&E) ratio imaging based shape properties of selected materials

The dotted lines in Figure 1(b) and (c) identify the aggregate imaging based shape classifications established earlier (Kwon 2007). From image analyses, Type Z virgin dolomite was significantly angular and rougher compared to the recycled aggregate subgrade materials. Similarly, the dolomite crushed stone exhibited higher flat and elongated ratios. The 75th percentile of angularity index fell into the angular category for Type Z aggregates whereas those of the recycled aggregate types were found to be in the subrounded category. The 25th and 75th percentiles of surface texture index for the recycled concrete aggregates (RCA) and RAP were found to be varying in between rough and smooth categories. However, Type W recycled concrete aggregates showed the largest variations in both angularity and surface texture indices among the three aggregate types.

In Place Density Assessment

During placement and compaction, a nuclear density gauge was used to determine the level of compaction achieved in the field. Figure 2 shows the nuclear gauge measured densities and moisture contents along with the target laboratory standard compaction densities identified by dashed lines. Note that the moisture contents obtained in RAP sections were corrected for hydrogen bound materials according to the IDOT procedure (Bureau of Materials and Physical Research 2015). Reported densities in aggregate subgrade was compared with the maximum dry density of Type Y RAP. Section Y-X was reported to have the lowest density owing to large voids present in the aggregate matrix.

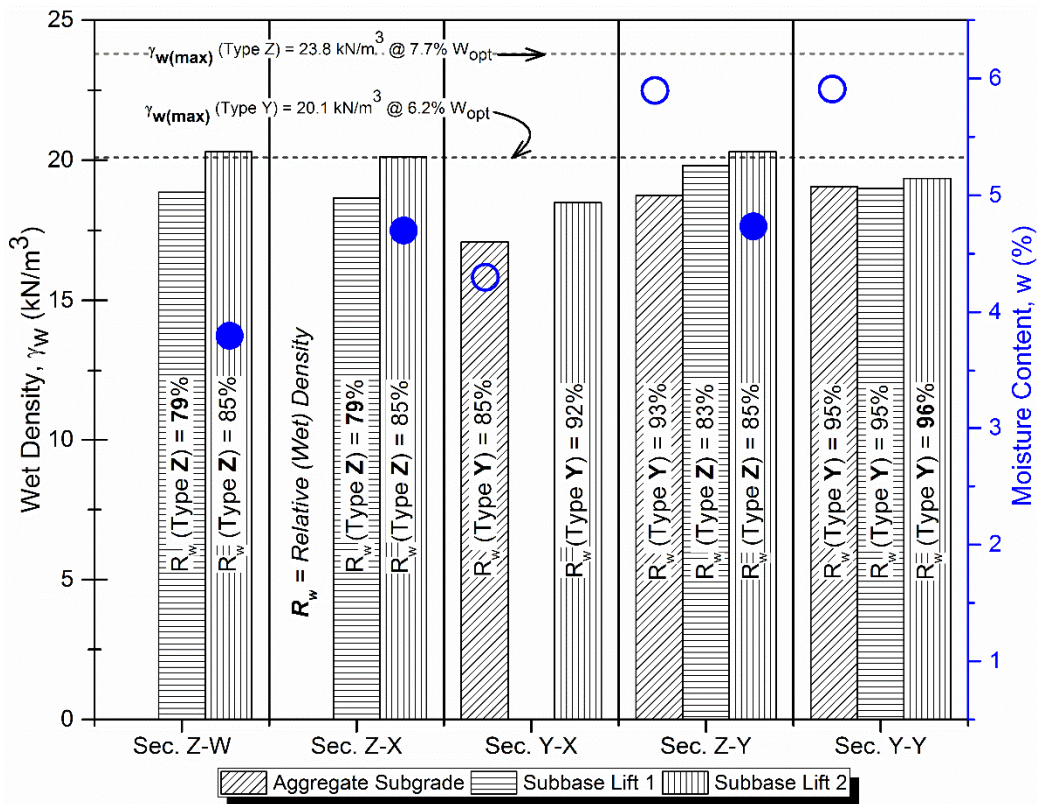


FIG. 2. Achieved densities of granular layers by the nuclear gauge

Subbase aggregates were placed and compacted in two 7.6-cm (3-in.) thick lifts. Since relative compaction achieved in the first lift was not satisfactory with conventional 6-12 roller passes; additionally 6 vibratory roller passes were applied on the second lift of the aggregate subbase layer. Sections Z-W and Z-X showed significant improvement in achieved densities compared to the other sections. Moreover, the dolomite (Type Z) subbase layers exhibited higher nuclear gauge densities than those for Type Y RAP aggregates. Conversely, relative compaction with respect to corresponding maximum dry density was found to be higher in Type Y RAP subbase sections. Note that, Type Y RAP showed a minimal peak in moisture-density relationship for the standard compactive effort (Kazmee and

Tutumluer 2015). As a result, achieving 95% of maximum dry density was easier in the case of RAP layers. On the other hand, maximum dry density of Type Z dolomite was almost equal to the density of Portland cement concrete. Moisture contents determined from both nuclear gauge and oven drying procedure revealed that the in place moisture distribution was on the dry side of optimum for dolomite crushed stones. These two factors might have contributed to the low level of relative compaction in Type Z subbase sections. Despite an increase in the compactive effort, the relative density reported for the second lift of Section Y-Y was similar to that of the first lift. Similar trends were also observed in other test sections that are not discussed in this paper for brevity. Thus, the density of Type Y RAP was found to be insensitive to the increase in compaction energy.

In Place Modulus Evaluation

Compacted granular layer stiffness was evaluated using a lightweight deflectometer (LWD) and soil stiffness gauge (GeoGauge). Figure 3 shows the composite surface modulus values recorded for aggregate subgrade and subbase layers. The dotted lines represent corresponding English units at an interval of 34.5 MPa (5 ksi).

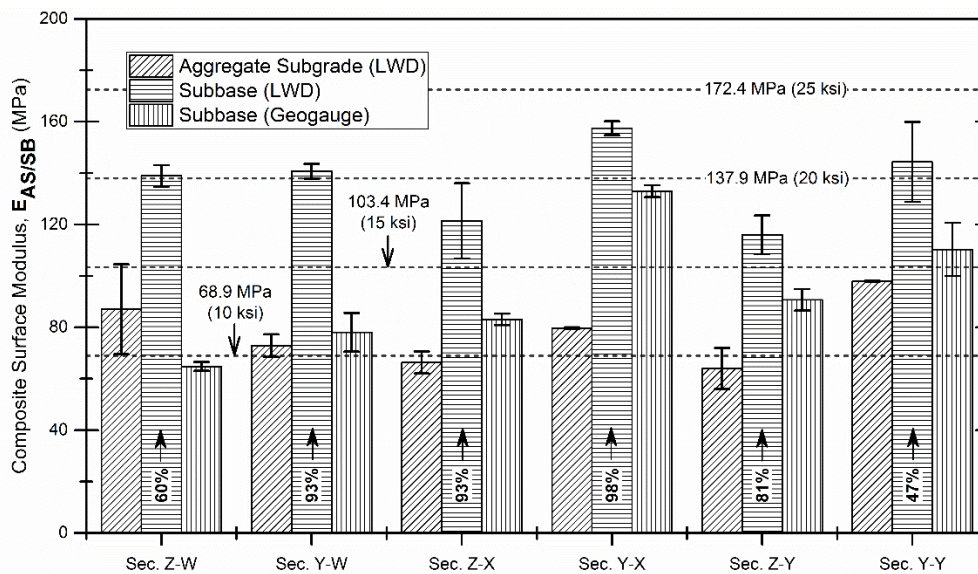


FIG. 3. Composite moduli of constructed aggregate subgrade and subbase layers

Test results indicated that inclusion of dense graded subbase led to an increase in composite modulus values of aggregate subgrade and subbase layers. Note that the large size recycled aggregates with large voids were susceptible to particle movement and reorientation upon due to moving wheel load. That’s why, addition of well graded base course size materials helped to confine these large rocks and fill up the voids. As a result, composite stiffness increased significantly in the cases of Type W and X aggregate subgrade sections. Owing to dense packing and the highest achieved relative compaction, Section Y-Y exhibited the highest surface modulus among all the sections.

Further, comparing the virgin dolomite and RAP subbase sections on the same aggregate subgrade revealed that the RAP subbase sections exhibited higher modulus values compared to their virgin counterpart. Both LWD and GeoGauge measurements reported the highest stiffness in RAP subbase of Section Y-X. This observation agrees with the laboratory resilient modulus test results previously reported by several researchers (Bennert and Maher 2005; Dong and Huang 2014; Wu 2011).

RUTTING PERFORMANCE

Upon completion of construction, rut accumulations of the test sections were evaluated through accelerated pavement testing. A super single tire exerting 44.5 kN (10 kip) of load was pulled uni-directionally at a constant speed of 8 km/h (5 mph) using the Accelerated Transportation Loading ASsembly (ATLAS). Periodic rutting measurements up to 40,000 passes were conducted at a distance of 1.5 m (5 ft) from each transverse edge with an automated laser profiler. Over a span of 810 mm, the laser profiler recorded data at an interval of 2 mm. Rutting failure criterion was selected to be 12.7 mm (1/2 in.) in compliance with IDOT guidelines. Figure 4 presents the accumulated rut depth in different test sections with increasing number of passes.

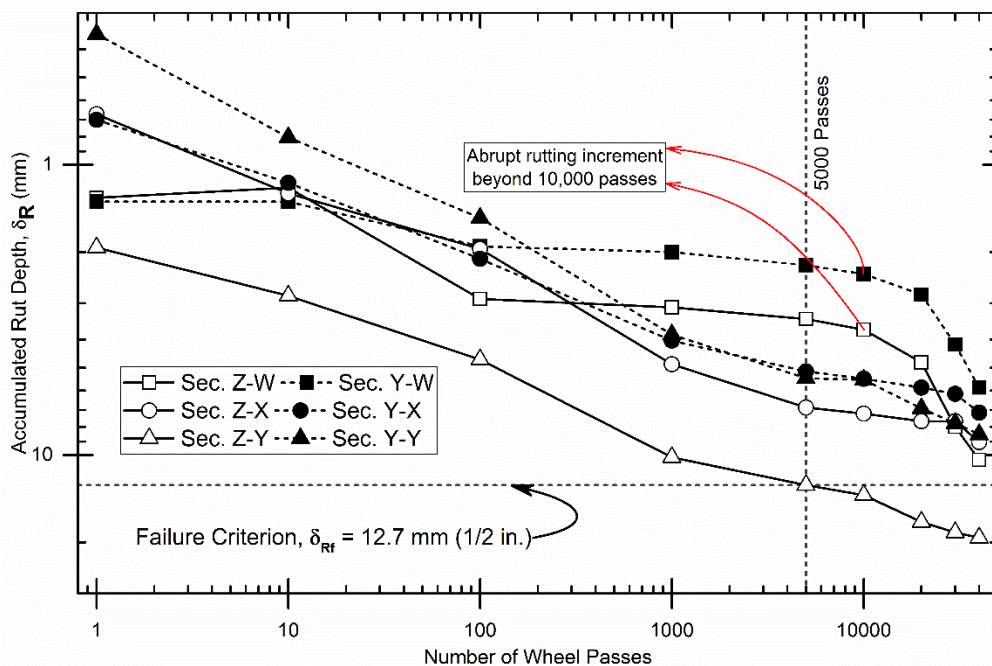


FIG. 4. Surface rut accumulations with traffic in flexible pavement test sections

Rutting trends observed in Figure 4 reveal that sections with Type Y RAP subbase outperformed corresponding Type Z subbase sections. Moreover, Section Z-Y and Y-Y exhibited the highest discrepancy in rutting accumulation compared to the remaining four sections. In accordance with the previous laboratory studies, the RAP materials were found to produce increased rutting despite having higher resilient moduli (Bennert and Maher 2005; Wu 2011). Superior performance of Type Y RAP

subbase sections, however, contradicts with the previously established laboratory permanent deformation trends. Among the six different test sections, only Section Y-X failed at 5,000 passes; whereas the other sections ended up with similar magnitude of rutting at the end of 40,000 passes. Contrary to other sections, Sections Z-W and Y-W exhibited more gradual increases in permanent deformation followed by an abrupt increase in rutting after 10,000 passes. To identify the contributing factors of observed rutting behavior, forensic investigation was conducted by assessment of relative density on cored HMA samples, thickness measurements and trenching. The following section briefly discusses the major findings from pavement forensic investigation.

FORENSIC EVALUATIONS OF FLEXIBLE PAVEMENTS

Figure 5(a) shows the extracted hot mix asphalt (HMA) cores at three different locations of transverse measurement lines in Section Z-Y and Y-Y. The thin black line aligned with the HMA samples identifies the target HMA thickness. Overall HMA thickness in Section Y-Y was significantly higher than that of Section Z-Y. The lowest HMA thickness in Section Z-Y was recorded to be 8.6 cm (3.4 in.). On the other hand, the largest recorded thickness in Section Y-Y was approximately 69% greater than the lowest recorded thickness of Section Z-Y. Similar to the preceding observation, HMA thickness over RAP subbase were also greater than those of dolomite subbase sections for other aggregate subgrade types. Such large variations in HMA thickness resulted in relatively poor rutting performance of HMA sections with dolomite (Type Z) subbase. Note that bottom surface of HMA layer in each section was examined for probable traces of interface bonding between the HMA layer and underlying RAP granular subbase. However, no such interface bonding was noticed in any of the sections.

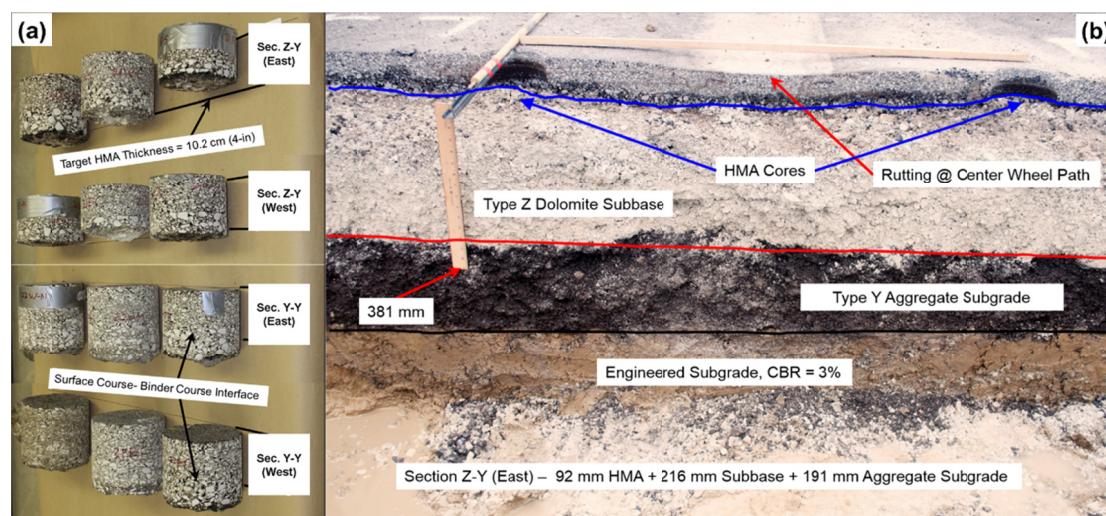


FIG. 5. (a) HMA cores extracted from Sections Y-Y and Z-Y, respectively; (b) Excavated trench in Section Z-Y

For further investigation, the test sections were trenched so that any discrepancy in granular foundation support or overall pavement thickness could be determined. Figure 5(b) shows the excavated trench in Section Z-Y. According to the figure, primary mode of rutting was observed through the densification of bound HMA layer. Neither the granular layer nor the subgrade exhibited any depression near the wheel path. However, as constructed layer thicknesses were substantially different from the design thicknesses. Type Z subbase thickness was found to be almost equal to that of Type Y RAP aggregate subgrade. Bulk specific gravity tests were also conducted on the cored samples to determine achieved degree of HMA compaction with respect to the reported theoretical maximum specific gravity. Figure 6 displays the relative compaction of surface and binder courses alongside nuclear gauge readings.

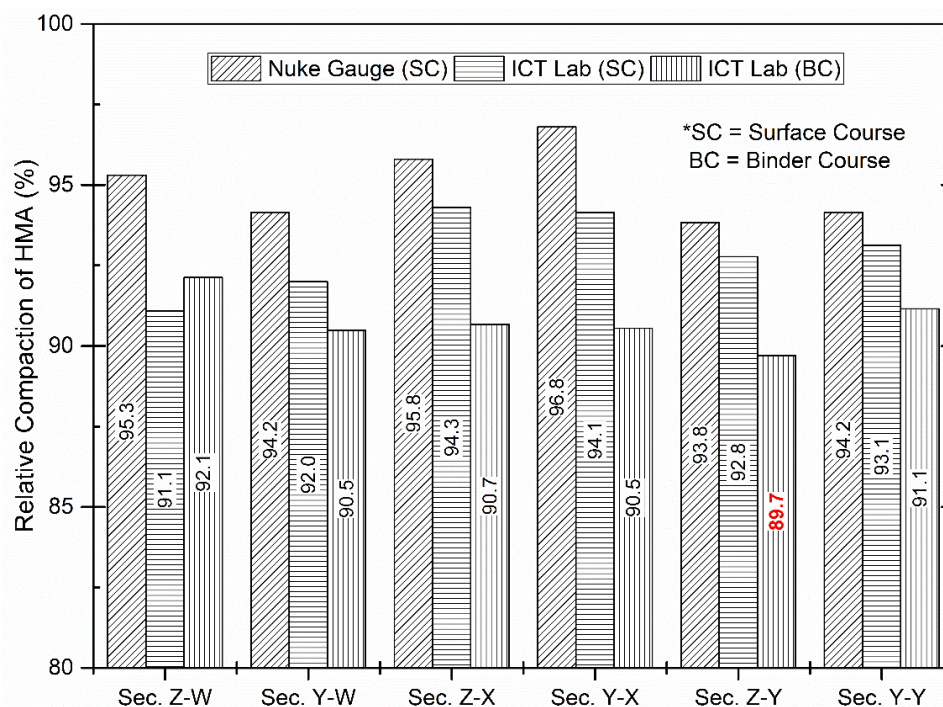


FIG. 6. Relative compaction of HMA layer in constructed test sections

Nuclear gauge densities of HMA surface course were consistently higher than the laboratory measured values. Also, relative densities in the binder course was significantly lower than those of the surface course. The highest magnitude of relative compaction was found to be 97% in the surface course for Section Y-X; whereas, the lowest degree of compaction was recorded in case of binder course for Section Z-Y. Henceforth, low relative compaction might also be responsible for premature failure of the corresponding test section. However, the influence of density on rutting performance could not be clearly established by comparing the rutting behavior of other sections. Despite having similar HMA thickness and compaction densities in binder layer, Section Y-X exhibited considerably higher permanent deformation than Section Y-W up to 20,000 passes. This indicates that the granular material composition might also be contributing to the differences in rutting behavior.

Considering the above discussion, as constructed layer thicknesses were plotted in terms of elevation in Figure 7 to have a better insight to the rutting trends. The horizontal dotted lines in Figure 7 pinpoint the engineered subgrade interface. According to the figure, pavement surface elevation varied over a wide range and such disparity originated from the aggregate subgrade interface. Note that the total pavement thickness in Type W aggregate subgrade sections (Sections Z-W and Y-W) was in close proximity to the design thickness. However, as the percentage of RAP materials increased in the subsequent sections, pavement surface elevation along with total thickness also started to fluctuate substantially. In a similar way, the variation in binder layer thickness between the successive dolomite and RAP subbase sections increased significantly as the percentage of RAP in aggregate subgrade blends reached from 0% to 100%.

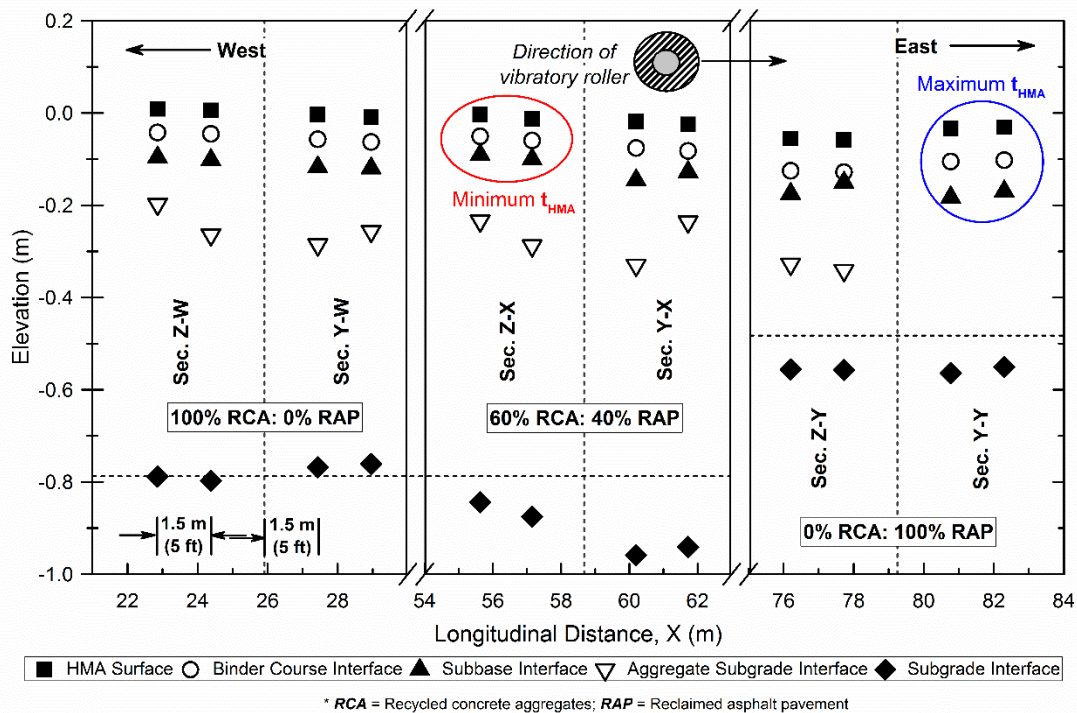


FIG. 7. Longitudinal profiles of HMA test sections at the center of wheel path

Rutting trends and as-constructed layer thicknesses presented in the above discussions narrow things down to four critical factors namely: (i) quality of granular foundation, (ii) HMA thickness, (iii) relative density of HMA layer, and (iv) percentage of RAP in the aggregate blend. The quality of granular foundation became evident from the rutting trends observed in Sections Z-W and Y-W. These two sections accrued less permanent deformation in spite of having less aggregate cover thickness. However, for the same reason, as the traffic exceeded certain critical number of load repetitions, a sharp increase in rutting was observed in those two sections.

Even though the RAP subbase sections accumulated lower permanent deformation, the rutting potential of RAP can still be corroborated. Despite having the lowest HMA thickness, Section Z-X did not fail prematurely; whereas, Section Z-Y which

had somewhat higher HMA and unbound granular layer thickness, reached the failure limit at only 5,000 passes. Similarly, Section Y-Y did not exhibit the lowest rutting accumulation in spite of the thickest HMA layer. Upon closer examination of surface elevation, it can be argued that test sections containing RAP materials accumulated excessive deformation along the direction of compaction during paving operation. Note that surface elevation in Section Y-Y increased because of the proximity to another section containing 100% virgin aggregate subbase and aggregate subgrade.

CONCLUSIONS

The primary objective of this study was to evaluate the adequacy of three different recycled materials as large size aggregate subgrade materials for improved subgrade applications in conventional flexible pavements. Accordingly, six full scale test sections were constructed and tested for rutting accumulation under accelerated condition. Results from the associated quality control and traffic tests were presented in this paper along with forensic investigation findings to identify pavement rutting mechanisms linked with the use of large size recycled aggregate subgrade foundations. In light of these analyses, the following conclusions can be drawn:

- i. The 100% recycled concrete aggregates (Type W: RCA) and 60%-40% blend of RCA and reclaimed asphalt pavement aggregates (Type X: RAP) surpassed the dense graded Type Y RAP aggregates in terms of rutting performance.
- ii. Granular layers containing certain percentage of RAP were prone to sinkage into the soft subgrade during paving operation which cautiously highlighted the increased rutting potential of RAP.
- iii. Despite measure lower density and surface modulus characteristics, Type Z virgin dolomite subbase sections did not exhibit any sinkage tendency in comparison to RAP. As a consequence, to maintain same elevation during asphalt paving between two consecutive sections with dissimilar strength and density, the dolomite subbase sections ended up with lower HMA thicknesses.
- iv. Use of RAP in improved subgrade applications required higher HMA surface course thickness. Hence, the use of RAP alone as aggregate subgrade and subbase may be cautioned in future sustainable construction practices considering the tendency of RAP layer sinkage on soft subgrade.

ACKNOWLEDGEMENTS

The support for this study was provided by the Illinois Department of Transportation (IDOT) as part of the recent ICT R27-124 research project. The authors would like to acknowledge Sheila Beshears from IDOT and others members of the R27-124 Technical Review Panel for their useful advice at different stages of this research. Special thanks go to Illinois Center for Transportation (ICT) research engineers James Meister and Dr. Aaron Coenen, and John Hart and Dr. Maziar Moaveni for characterizing aggregate shape properties. The contents of this paper reflect the views of the authors who are responsible for the facts and the accuracy of the data presented herein. This paper does not constitute a standard, specification, or regulation.

REFERENCES

- Bennert, T., and Maher, A. (2005). "The Development of a Performance Specification for Granular Base and Subbase Material." *Rep. No. FHWA-NJ-2005-003*, New Jersey Department of Transportation Bureau of Research and Technology, New Jersey.
- Bureau of Bridges and Structures. (2005). *Subgrade Stability Manual*. Illinois Department of Transportation, Springfield, IL.
- Bureau of Materials and Physical Research. (2015). *Manual of test procedures for materials*. Illinois Department of Transportation, Springfield, IL.
- Division of Highways. (2013). "Section 303: Special Provision for Aggregate Subgrade Improvement." *Bureau of Design and Environment (BDE) Manual*, Illinois Department of Transportation, Springfield, IL, .
- Dong, Q., and Huang, B. (2014). "Laboratory evaluation on resilient modulus and rate dependencies of RAP used as unbound base material." *Journal of Materials in Civil Engineering*, 26(2), 379-383.
- Heckel, G. (2009). *Aggregate Subgrade Thickness Determination*. Illinois Department of Transportation, Bureau of Materials and Physical Research, .
- Kazmee, H., Mishra, D., and Tutumluer, E. (2015a). "Sustainable alternatives in low volume road base course applications evaluated through accelerated pavement testing." *Proceedings of The 2015 International Foundations Congress and Equipment Exposition*, American Society of Civil Engineers, San Antonio, TX, 409-418.
- Kazmee, H., and Tutumluer, E. (2015). "Evaluation of aggregate subgrade materials used as pavement subgrade/granular subbase." *Rep. No. FHWA-ICT-15-013*, Illinois Department of Transportation, Springfield, IL.
- Kazmee, H., Tutumluer, E., and Mishra, D. (2015b). "Performance evaluations of pavement working platforms constructed with large-sized unconventional aggregates." *Proceedings of Airfield and Highway Pavements Conference*, American Society of Civil Engineers, Miami, FL, 849-860.
- Kwon, J. (2007). "Development of a mechanistic model for geogrid reinforced flexible pavements". Doctor of Philosophy in Civil Engineering. University of Illinois, Urbana, IL.
- Mathis, D. (1991). "Rock Cap: A True Free Draining Base." *Proceedings of 42nd Annual Road Builders' Clinic*, Coeur D'Alene, ID, 153-156.
- Moaveni, M., Wang, S., Hart, J., Tutumluer, E., and Ahuja, N. (2013). "Evaluation of aggregate size and shape by means of segmentation techniques and aggregate image processing algorithms." *Transportation Research Record: Journal of the Transportation Research Board*, (2335), 50-59.
- Tutumluer, E., and Pan, T. (2008). "Aggregate morphology affecting strength and permanent deformation behavior of unbound aggregate materials." *Journal of Materials in Civil Engineering*, 20(9), 617-627.
- Tutumluer, E., Rao, C., and Stefanski, J. A. (2000). "Video image analysis of aggregates." *Rep. No. FHWA-IL-UI-278*, Illinois Department of Transportation, Springfield, IL.
- Uhlmeier, J., Pierce, L., Lovejoy, J., Gribner, M., Mahoney, J., and Olson, G. (2003). "Design and construction of rock cap roadways: Case study in Northeast Washington State." *Transportation Research Record: Journal of the Transportation Research Board*, (1821), 39-46.
- Wu, M. (2011). "Evaluation of high percentage recycled asphalt pavement as base course materials". Master of Science in Civil Engineering. Washington State University, Pullman, WA.

Rejuvenators for Asphalt Binders Using Oil Extracted from Spent Coffee Grounds

Rita Jalkh¹; Mohamad Abiad²; and Ghassan R. Chehab³

¹Graduate Student, Dept. of Nutrition and Food Sciences, American Univ. of Beirut Riad El-Solh, Beirut 1107 2020, Lebanon. E-mail: rmj31@aub.edu.lb

²Assistant Professor, Dept. of Nutrition and Food Sciences, American Univ. of Beirut Riad El-Solh, Beirut 1107 2020, Lebanon. E-mail: ma192@aub.edu.lb

³Associate Professor, Dept. of Civil and Environmental Engineering, American Univ. of Beirut Riad El-Solh, Beirut 1107 2020, Lebanon. E-mail: gc06@aub.edu.lb

Abstract: Interest in recycling and reuse of various waste materials has been growing over the years especially with increasing environmental awareness and public health concerns. This paper explores the opportunity to recycle spent coffee grounds (SCG) as a modifier for reclaimed asphalt binders. In the scope of the study, oil extracted from SCG is incorporated at various percentages in PG 58-XX virgin and laboratory aged PG 76-XX asphalt binders. The rheological properties of the blends are characterized using dynamic shear and multiple stress creep and recovery following ASTM and AASHTO standards. Accordingly, it is observed that blending the extracted oil with asphalt restores the binder's linear behavior and increases the softening of the blend thus altering the high temperature PG grade. Moreover, the rejuvenated aged asphalt exhibits higher strain recovery at low stress levels as compared to the control un-aged binder. This, in fact, lowers its susceptibility to permanent damage when used in asphalt concrete mixtures.

INTRODUCTION

Green energy is gaining interest due to growing environmental awareness and limited crude reserves. This pushed for sustainable asphalt production and paving practices to reduce both carbon emissions and the need for landfill area whilst increasing cost effectiveness. Consequently, recent studies have focused on incorporating recycled materials, such as reclaimed asphalt pavements (RAP), in asphalt mixes. Researchers have emphasized the benefit of using RAP in different proportions (Daniel, Chehab et al. 2009, Ayyala, Chehab et al. 2011), rather than

continuously dumping old pavements deteriorated by oxidative aging and consequent cracking. Moreover, using RAP serves as an environmentally friendly solution since asphalt waste was found to be a threatening source of toxic leachates - mainly polycyclic aromatic hydrocarbons (PAHs), organic compounds and heavy metals Townsend (1998) - which could potentially pollute soil and water tables.

On the other hand, alternative binders are being produced from biomasses (Wen, Bhusal et al. 2013) which constitute one of the largest sources of energy worldwide. It supplies about 10 % of primary energy globally (Kucuk Mm 1997, Kaltschmitt M 2007, MF 2010). An additional benefit is by utilizing biomass residues such as waste cooking oil (Zhang, Dubé et al. 2003, Shi and Bao 2008), and spent coffee ground (SCG) (Kondamudi, Mohapatra et al. 2008). The latter is a solid waste that remains after coffee is brewed which poses some environmental concerns due to its high oxygen demand during decomposition and the discharge of organic matter residues and contaminants as caffeine, tannins and polyphenol (Mussatto, Machado et al. 2011, Vardon, Moser et al. 2013). The United States Department of Agriculture (USDA) reported more than six billion kilograms of coffee being exported worldwide (USDA June 2015). Moreover, studies on spent coffee ground reported high percentages of oil mostly lipid constituting around 15% by dry weight (Kondamudi, Mohapatra et al. 2008, Mussatto, Machado et al. 2011). Other studies explored the antioxidant effect of spent coffee ground on the rheology and aging of asphalt properties, especially for the hardening effect caused by oxidative aging, but were found to serve as a solvent rather than an antioxidant (Zofka and Yut 2012), with no change in temperature susceptibility being recorded.

It is known that hardening, difficult workability, deterioration and loss of oils of asphalt and RAP over time results from oxidative aging. This requires their modification using rejuvenators to restore desirable properties and improve their performance (Chen, Chen et al. 2015). As such, since it was demonstrated that large amounts of oil can be potentially used from spent coffee ground, it is then of interest to explore the rejuvenating effects of this oil on the rheology and physical properties of aged asphalt, while at the same time evading the problematic disposal of both asphalt and SCG waste. Therefore, the main purpose of this study is to decrease the environmental impact related to construction and food wastes by providing an innovative solution and new potential uses for the recycling of oxidized binders and SCG.

OBJECTIVES

This paper explores the use of oil extracted from spent coffee grounds as a rejuvenator for asphalt binders in an attempt to promote sustainability and recycling. The main objectives of this study are:

- Minimizing environmental impact of a problematic food waste, spent coffee grounds (SCG) by providing an innovative solution for its recycling, and
- Producing binder rejuvenators from SCG for use in enhancing the performance of recycled asphalt binder from reclaimed pavements (RAP), thus allowing its effective incorporation in new asphalt-aggregate mixtures.

Succeeding in the above-stated objectives fosters sustainable development through minimizing the environmental and social impacts of improper handling of waste, relieving pressure on landfills and incineration plants, decreasing illegal dumping, and limiting the mining of natural resources.

SCOPE

In order to investigate the feasibility and effectiveness of rejuvenation and amelioration of the physical properties of recycled asphalt binders, two types of binders (un-aged PG58-XX and aged PG76-XX) were mixed under laboratory conditions with various percentages of extracted oil from the food industry waste.

The scope of this study covers the following tasks:

- Collection and extraction of oil from SCG,
- Evaluating the softening effect of the oil on asphalt binders by mixing various percentages of oil with un-aged PG58-XX binder and test for changes in its physical properties, including linearity, high temperature performance grading and creep behavior;
- Laboratory aging of the PG58-XX binder to produce a higher temperature grade binder, specifically, PG 76-XX;
- Repetition of the aforementioned suite of tests on the aged PG76-XX binder to investigate the rejuvenating effectiveness of the oil.

MATERIALS AND METHODS

Materials

Various samples of SCG were collected from selected coffee shops in Beirut, Lebanon pertaining to four different international chains. The asphalt binder used was unmodified Pen 60/70 asphalt which met the PG 58-XX high temperature grade based on results from Dynamic Shear Rheometer (DSR) testing conducted according to ASTM-D7175-08.

Methods

The experimental design followed in this study, along with the tested parameters, is presented in Fig. 1.

Un-aged PG58-XX binder

For the experiments conducted on un-aged PG 58-XX binder, oil was extracted from SCG and mixed in 5%, 7% and 10% w/w with the binder and tested for linearity, performance grading and recovery using the Linearity check test, Complex Shear Modulus test and Multiple Stress Creep Recovery check; respectively.

Aged PG 76-XX binder

Based on the results for the un-aged PG 58-XX binder, SCG oil was mixed with aged PG 76-XX binder at 1%, 5%, 10%, 12% and 15% w/w as per Fig. 1. The same rheological tests were conducted as for the un-aged binder.

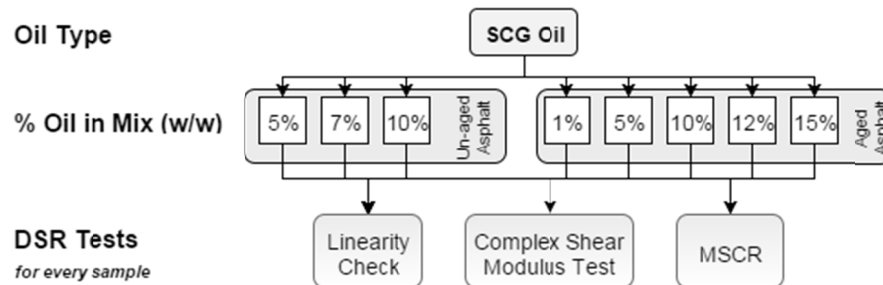


FIG. 1. Experimental program conducted to study the effect of mixing oils on the rheological properties of un-aged and aged asphalt binder.

Oil Collection from Spent Coffee Grounds (SCG)

Spent coffee grounds were collected from various coffee shops and dried at 105°C for three hours prior to oil extraction which was done using hexane as a solvent in a reflux extractor. The extraction was conducted for a period of three hours. Consequently, the oil/solvent mixture was separated using a rotary evaporator operating at 335 mbar and 55 °C for 1.5 hours. The oil content in both SCG and defatted SCG were measured using ANKOM fat extractor model XT-10 (Ankom Technology, Macedon, NY, USA). An average of 14% oil content was obtained similar to previously reported values (S.Caetano, Silvaac et al. 2012).

Binder Aging and Oil Mixing

Following ASTM D1754/D1754M – 09, thin layers of un-aged PG 58-XX binder were poured in plates and aged in a Thin Film Oven (TFO) for 24 hours at 165°C in order to increase the grade to PG 76-XX. Although unquantifiable, the aim of this aging was to surpass short term aging and increase the PG grade of the binder by two grades in order for it to become somehow comparable to field samples regarded as long term aged. Oil was then incorporated in the un-aged and aged binders following the experimental design described in Fig 1. Blending of oil and asphalt binders was done using a warring mixer (IKA Eurostar 40, 79219 Staufen, Germany).

Characterization of Rejuvenated Asphalt Binder

All rheological measurements – Linearity, Complex Shear Moduli and Multiple Stress Creep Recovery of rejuvenated asphalt blends were performed using a Discovery Series Hybrid Rheometer – DHR (TA-Instruments, New Castle, DE, USA) equipped with 25mm upper heated parallel plates. Tests were conducted in duplicates as the standard error did not exceed 5% between replicates.

Rejuvenated Asphalt Binder Linear Viscoelastic Range Verification

In order to conduct the rheological measurements in the linear viscoelastic range, a linearity check was first performed on all rejuvenated-asphalt blends at 58°C with 10 rad/s angular frequency, strain values ranging from 2% to 16% at 2% increment according to ASTM D7175 – 08.

Measurement of Complex Shear Modulus

After confirming the rejuvenated asphalt's linear visco-elastic behavior, oscillatory tests were conducted in order to determine the dynamic shear modulus ($|G^*|$) and the phase angle (δ) in order to analyze the rutting factor and performance grade ($|G^*|/\sin\delta$) (ASTM D7175 – 08). The tests were conducted at 52, 58, 64, 70, 76 and 82°C with 12% strain and angular frequency ranging from 0.1 to 100 rad/sec. To meet a specific performance grade, the value of $|G^*|/\sin\delta$ at the high temperature of the grade should exceed 1 for unaged samples and 2.2 after 5 hours of aging.

Multiple Stress Creep Recovery (MSCR) Test

The MSCR tests were conducted following ASTM-D7405 at temperatures same as the binder's high grade temperatures, determined from the oscillation tests. Ten cycles with stress levels of 100 Pa and 3200 Pa were applied with a creep time of 1 second and a recovery time of 9 seconds.

RESULTS AND DISCUSSION

Rheological Measurement

In this following section, the rheological properties of the various binder samples are presented. It is worth noting that the aged binder beyond using the adopted aging method lost its visco-elastic properties, which can be observed in Fig 2. However; upon addition of the rejuvenated oil, those properties have been regained as seen in Fig 2.

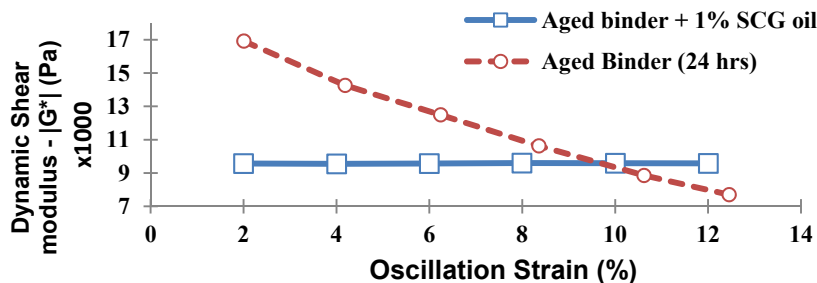


FIG. 2. Loss in linear behavior in binder aged for 24 hours followed by the restoration of linear behavior by the addition of 1% SCG oil.

Effect on Performance Grade

The oscillatory tests conducted on the control unaged binder classified it as potentially having a high PG of 64-XX; however, after aging the sample for 5 hours the values of $|G^*|/\sin\delta$ were less than 2.2 at 64°C. Consequently, the unaged binder used in this study was classified as PG 58-XX.

The oscillatory tests conducted on the rejuvenated binder blends under the same testing conditions resulted in decreased values of $|G^*|/\sin\delta$ in comparison to the control unaged binder which may be correlated to potential fatigue cracking under field conditions as demonstrated by (Daniel and Chehab 2008). The tests further illustrate that blending SCG oil has a significant effect on softening the asphalt. SCG oil at 5% and 7% w/w reduced the high performance grade of the control binder from PG 58-XX to PG 52-XX, whereas the blend containing 10% SCG oil reduced the PG even lower. The reduction in $|G^*|/\sin\delta$ of SCG oil blends at 52°C are presented in Fig. 3. As the oil percentage in the rejuvenated asphalt increases, the degree of softening increases, thus increasing susceptibility to permanent deformation but decreasing susceptibility to fatigue cracking.

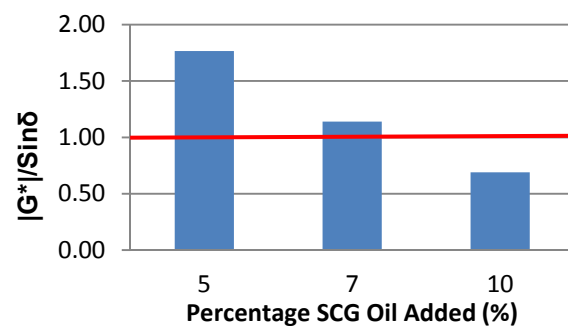


FIG. 3. Values of $|G^*|/\sin\delta$ for SCG blends at 52°C

Effect on Stiffness and Elasticity

In comparison to the unmodified binder, mixing SCG oil at any percentage decreases the stiffness of the rejuvenated asphalt blends by decreasing the values of the dynamic shear modulus ($|G^*|$) to values lower than 6,342 Pa. This was further elaborated when statistical analysis using SPSS showed the significant decrease in stiffness caused by the increased percentage of added oil, reflected by the values of ($|G^*|$), but not on the elastic behavior (phase angle, δ). This is when the blends were seen to soften and thus become more prone to deformation, as reflected by the decreased ratio of $|G^*|/\sin\delta$. This was also demonstrated by Wen *et al* (Wen, Bhusal et al. 2013) using waste cooking oil-based bio-asphalt which also decreased the resistance of conventional binder to permanent deformation.

The oscillatory tests conducted on the aged control binder concluded its high performance grade as PG 76-XX. Oscillatory tests conducted on asphalt blends using SCG oil under the same testing conditions resulted in decreased values of $|G^*|/\sin\delta$ in comparison to the aged control binder, confirming that mixing SCG oil

softened the asphalt. SCG oil in 1, 5, 10, 12 and 15% w/w blends also reduced the high performance grade of the control binder from PG 76-XX to PG 70-XX, 64-XX, 58-XX and 52-XX respectively as shown in Table 1. It is thus noticed that 10% SCG oil is required to bring back the PG of the aged asphalt to the initial PG of the control. Fig.4 represents the changes in $|G^*|/\sin\delta$ with increased percentage of SCG oil at a constant temperature. This model representation could be used to interpolate the quantity of required SCG oil to reach a certain preferred PG.

Table 1. Effect of mixing SCG oil on the PG of aged PG 58-XX binder

% SCG oil in aged binder blend(w/w)	Performance Grade
0 (control)	76
1 %	70
5 %	64
10 %	58*
12 %	52
15%	52

* 10% SCG oil required to bring back the aged binder to its initial PG

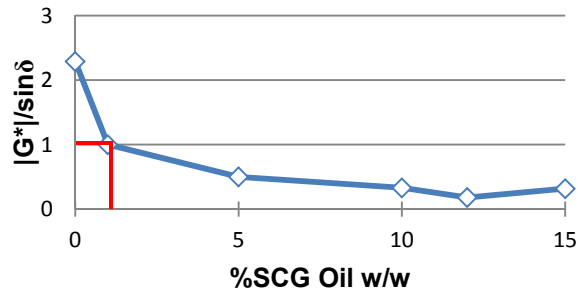


FIG. 4. A model representation of the percentage of SCG oil required to reach PG 70-XX, starting from PG 76-XX.

Multiple Stress Creep Recovery (MSCR)

MSCR tests were conducted for PG 58-XX samples at temperatures where $|G^*|/\sin\delta$ exhibited values larger than 1. MSCR is a relatively new method that helps evaluate the elastic behavior of binders. During an MSCR test, a binder gets subjected to a low and high stress levels (0.1 kPa and 3.2 kPa) by applying 10 loading and unloading stresses at each level. A creep load is applied for one second, followed by a nine second release which will allow the sample to relax and recover; during which the recovered and unrecovered strains will be measured. An MSCR measures the Non-Recoverable Creep Compliance (J_{nr}), which represents the amount of residual strain remaining in the sample after the repeated cycles of creep and recovery are applied. J_{nr} can be considered as an indicator of permanent deformation.

In comparison to the control unaged PG 58-XX binder, both blends with 5% and 7% w/w SCG oil had lower values of J_{nr} thus higher recovery at 0.1 and 3.2 kPa as seen in Fig 5.a. and 5.b. The reported lower values of J_{nr} could be due to the different temperatures undertaken. On the other hand, oil percentage was found to have significant effect on J_{nr} values where the 7% w/w blend (Fig. 5.b), having the same PG 52-XX as the 5% w/w blend (Fig. 5.a), is noticed to have a higher level of J_{nr} thus higher damage due to the binder’s increased softening caused by the oil. Similarly to the un-aged samples, all blends with aged binder resulted in lower values of J_{nr} in comparison to the control thus higher recovery and consequently lower susceptibility to permanent deformation, as seen in Fig 6.

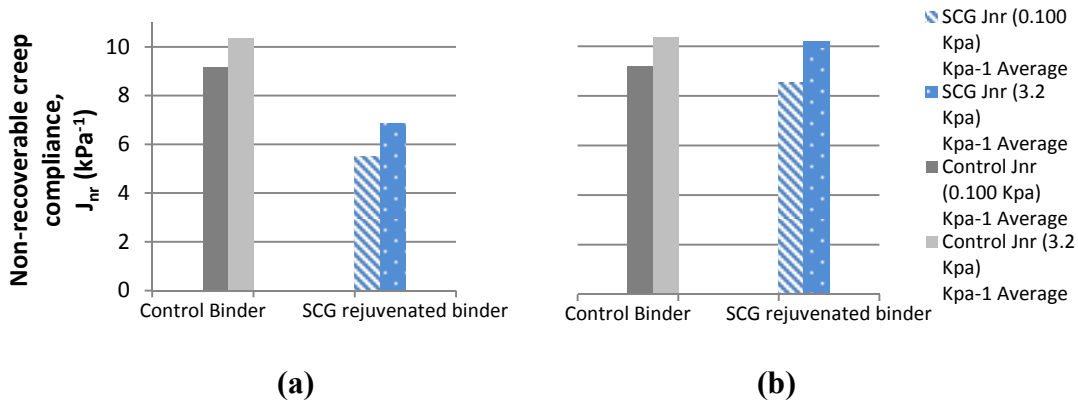


FIG. 5. (a) J_{nr} results for blends of un-aged PG 58-XX binder with 5% SCG oil (b) J_{nr} results for blends of un-aged PG 58-XX binder with 7% SCG oil.

Likewise, values of J_{nr} were noticed to increase with the increase in oil percentage reflecting the decrease in recovery of the samples, hence the higher susceptibility to permanent damage caused by the increased softening of the blends. Similar results were obtained by (Wen, Bhusal et al. 2013) when waste cooking oil bio-asphalt was used. The following results were concluded after the values of J_{nr} at 0.1kPa were observed to increase from 0.32kPa to 6.8kPa in the 12% w/w blend upon the increase in oil percentage. J_{nr} values at 3.2kPa followed a similar trend to that of 0.1kPa; knowing that J_{nr} at 3.2kPa is always higher than that at 0.1kPa because the higher level of stress leads to more damage in the blend. Finally, it is imperative to mention that the blend containing 10% SCG oil, having the same PG 58-XX as the control binder, has a higher level of recovery and therefore is less damaged and holds better physical characteristics than the control, as lower susceptibility to permanent deformation.

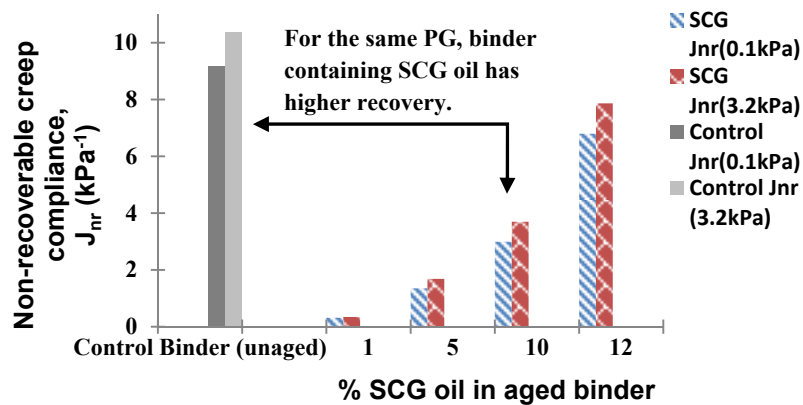


FIG. 6. J_{nr} values of the control un-aged binder in comparison to the 1, 5, 10 and 12% asphalt/SCG oil blends

CONCLUSION, RECOMMENDATION AND FUTURE WORK

Global studies highlighted the importance of recycling and the use of renewable energy in order to decrease environmental impacts. Decreasing crude oil reserves and technical difficulties in modifying asphalt properties additionally draw attention to further needs. For that reason, oil from Spent Coffee Grounds (SCG), a food waste, was introduced to un-aged PG 58-XX and aged PG 76-XX asphalt binder to change their physical properties. The blending was studied to assess the feasibility of using SCG oil to modify and enhance recycled asphalt binder. The use of SCG oil in asphalt binder was found to:

- Restore linear behavior which was lost upon the aging process.
- Increasingly soften the asphalt with increasing quantities of oil thus decreasing its PG, with 10% oil required to return the binder to its initial PG. This characteristic could be possibly used in order to modify and customize new or recycled asphalt to a PG that suits specific needs and preferences related to geographical location or other technical reasons.
- MSCR tests showed that all binder blends had lower values of non-recoverable creep compliance (J_{nr}), even for the same PG as the control, thus lower susceptibility to permanent deformation as compared to un-aged asphalt with an increasing J_{nr} with increased percentage of SCG oil.

Future studies will include the exploration of oxidized SCG oil in aged asphalt binder in order to better comprehend the behavior. This will help conclude a model for best matching oxidation levels with oil quantities incorporated in either new or recycled asphalt for customization of the physical properties and PG according to need.

ACKNOWLEDGMENTS

This study was funded by the University Research Board (URB) at the American University of Beirut (AUB). The authors would like to thank all the coffee shops in Beirut who provided us with the required wastes to conduct this study. The authors would also like to thank the Department of Civil and Environmental Engineering and the Central Research Science Laboratory at AUB for allowing the use of their facilities and equipment which made this research possible. Special thanks to Ms. Dima Al Hassanieh and Mr. Hussein Kassem for their technical assistance in laboratory experiments.

REFERENCES

- Ayyala, D., G. R. Chehab and J. Daniel (2011). "Sensitivity of the MEPDG Level 2 and 3 Inputs using Statistical Analysis Techniques for New England States." International Review of Civil Engineering (IRECE) **2**(1).
- Chen, J.-S., S.-F. Chen, M.-C. Liao and S. W. Huang (2015). "Laboratory Evaluation of Asphalt Blends of Recycling Agents Mixed with Aged Binders." Journal of Materials in Civil Engineering **27**(4): 04014143.

- Daniel, J. S. and G. R. Chehab (2008). Use of RAP Mixtures in Mechanistic Empirical Pavement Design Guide. Transportation Research Board 87th Annual Meeting, Washington DC, Transportation Research Board Business Office.
- Daniel, J. S., G. R. Chehab and D. Ayyala (2009). "Sensitivity of RAP Binder Grade on Performance Predictions in the MEPDG." Journal of the Association of Asphalt Paving Technologists **78**: 325-376.
- Kaltschmitt M, S. W., Wiese A (2007). Renewable energy: technology, economics and environment, Springer.
- Kondamudi, N., S. K. Mohapatra and M. Misra (2008). "Spent Coffee Grounds as a Versatile Source of Green Energy." Journal of Agricultural and Food Chemistry **56**(24): 11757-11760.
- Kucuk Mm, D. A. (1997). "Biomass conversion processes " Energy Convers Manage **38**(2): 151-165.
- MF, D. (2010). "Microalgae as a feedstock for biodiesel." Energy Educ Sci Technol **25**: 31-43.
- Mussatto, S., E. S. Machado, S. Martins and J. Teixeira (2011). "Production, Composition, and Application of Coffee and Its Industrial Residues." Food and Bioprocess Technology **4**(5): 661-672.
- S.Caetano, N., V. F. M. Silvaac and T. M. Matab (2012). "Valorization of Coffee Grounds for Biodiesel Production." The Italian Association of Chemical Engineering **26**: 268-272.
- Shi, H. and Z. Bao (2008). "Direct preparation of biodiesel from rapeseed oil leached by two-phase solvent extraction." Bioresour Technol **99**(18): 9025-9028.
- Townsend, T. G. (1998). Leaching Characteristics of Asphalt Road Waste. State University System of Florida, Florida Center for Solid Hazardous Waste Management
- USDA (June 2015). Coffee: World Markets and Trade. Foreign Agricultural Service.
- Vardon, D. R., B. R. Moser, W. Zheng, K. Witkin, R. L. Evangelista, T. J. Strathmann, K. Rajagopalan and B. K. Sharma (2013). "Complete Utilization of Spent Coffee Grounds To Produce Biodiesel, Bio-Oil, and Biochar." ACS Sustainable Chemistry & Engineering **1**(10): 1286-1294.

Wen, H., S. Bhusal and B. Wen (2013). "Laboratory Evaluation of Waste Cooking Oil-Based Bioasphalt as an Alternative Binder for Hot Mix Asphalt." Journal of Materials in Civil Engineering **25**(10): 1432-1437.

Zhang, Y., M. A. Dubé, D. D. McLean and M. Kates (2003). "Biodiesel production from waste cooking oil: 2. Economic assessment and sensitivity analysis." Bioresource Technology **90**(3): 229-240.

Zofka, A. and I. Yut (2012). Investigation of Rheology and Aging Properties of Asphalt Binder Modified with Waste Coffee Grounds. Alternative Binders for Sustainable Asphalt Pavements. Washington DC, Transportation Research Board of the National Academies: 61-72.

Resilient Modulus of a Blended Mixture of Recycled Asphalt Pavement and Natural Aggregate as Road Pavement Base Material

Prabir K. Kolay, M.ASCE¹; and Pralendra Singh²

¹Associate Professor; ²Former Graduate Student, Dept. of Civil and Environmental Engineering, Southern Illinois Univ. Carbondale, 1230 Lincoln Dr., MC 6603, Carbondale 62901, IL.

Abstract: The present paper characterizes recycled asphalt pavement (RAP) samples from old parking lot and determines their suitability as road pavement materials. Virgin aggregates or natural coarse aggregate (NCA), recycled asphalt pavement (RAP) aggregates, and several blended mixtures with 20 to 80% replacement of virgin aggregate by weight with RAP were prepared and tested for resilient modulus (M_r) and California bearing ratio (CBR) test. The resilient modulus value for 100% RAP was found to be higher than that of 100% NCA. The resilient modulus (M_r) of the RAP sample blended with NCA mixtures increases with the increase of RAP percentage and with the increase in the confining pressure. Also with the increase in the deviator stress there was decrease in the resilient modulus of the blended samples. The results of CBR value for the blended mixture decreases with the increase in the percentage of the recycled asphalt pavement aggregates. Based on the test results, RAP can be used for granular base material for road pavement.

INTRODUCTION

According to USGS (2009) it has been predicted that more than 2.5 billion tons of coarse aggregates are expected to be consumed annually by the year 2020 for construction purposes. The raw material i.e., coarse aggregate used for concrete or pavement is becoming costly, depleting day by day, and its production uses a lot of energy. Hence, the use of recycled aggregate provides the perfect solution for this problem. The use of recycled aggregate can be cheaper than the virgin or natural aggregates; can replace the natural aggregate to some percentage on the road pavement or partial replacement in concrete which can reduce the depletion of natural aggregate resources. It also helps to reduce and save the landfill cost; and the energy consumed for preparing the recycled aggregate is less than the natural aggregate and also beneficial in sustainability view point.

Recycled aggregate can be used in many ways e.g., as fill material in embankments, shoulder concrete, porous granular fills, gabion baskets, riprap for the protection of banks, as a granular aggregate base or as trench backfill (CMRA, 2010). It can also be used as a sub-base, base, and subgrade layers in the road pavements. Usually, two major types of recycled aggregates are used for different purposes i.e., recycled concrete aggregate (RCA) and reclaimed or recycled asphalt pavement (RAP).

Reclaimed or recycled asphalt pavements are the products of the demolished asphalt pavement when the condition of a pavement becomes severely deteriorated or when it needs to be rehabilitated and reconstruction of the pavement may become an economic and feasible solution. The demolished asphalt pavements are collected from the demolition site to the crusher and the RAP is formed. RAP production is also made on-site. In United States more than 90% of roads and highways are constructed with hot mix asphalt (FHWA, 2011). According to the National Asphalt Pavement Association (NAPA, 2009), asphalt pavement is the most recycled material used in U.S. and highway construction industry annually produces more than 100 million ton of RAP that is recycled into new pavements. RAP has been used as base, sub-base, and subgrade material in pavement construction in recent years but the inadequate strength and stiffness characteristics limit their use in the pavement (Mulheron and O'Mahony, 1990; Maher et al., 1997; Rana, 2004). The characteristics of the RAP is influenced by the asphalt content, temperature, moisture content, dry density, and age of the RAP. Han et al. (2012) mentioned that the limitations of RAP is it's creep behavior under a sustained load due to the presence of the asphalt binder when RAP use as a base material. RAP shows low water absorption properties due to asphalt coating on it which prevents the water from reaching the individual particles of the materials (Guthrie et al., 2007; FHWA, 2008). Bennert et al. (2000) found that the RAP is stiffer than the dense-graded aggregate base course but RAP has the greatest amount of permanent strain, in comparison to RCA and NCA; which might be due to the breakdown of asphalt binder under loading.

One of the key parameter for the pavement design system is resilient modulus (M_r). It is a measure of material stiffness under repeated loading and is an important criterion in mechanistic design of flexible pavement (AUSTROADS, 2012). Resilient modulus is the knowledge of pavement layer materials which allows the determination of how the pavement system will respond to traffic loading (Buchanan, 2007). The resilient response of granular material is important factor for the load carrying capacity of the pavement and the permanent strain response which characterizes the long-term performance of the pavement (Bozyurt et al., 2012). While modulus of elasticity is stress divided by strain for a slowly applied static load; resilient modulus, M_r is described as the ratio of rapidly applied deviator stress (σ_d) to "recoverable" or "resilient" strain (ϵ_r), as those experienced by pavements.

$$\text{Resilient modulus, } M_r = \frac{\sigma_d}{\epsilon_r}$$

Costa et al. (2014) have studied the resilient moduli of an unbound sub-base material on the specimen of RAP and virgin aggregate. They found that with the increase of RAP content from 15% to 40%, there was an increment of the resilient modulus by approximately 15%. This result was in consistent with the result found by Kim et al. (2007). There was not much change in the resilient modulus value with change in the relative compaction within the ranges of RAP content from 15% to 40% tested. One of their major finding was that with an increase of relative density, particularly at higher bulk stress, the resilient modulus decreases slightly; opposing the statement that the resilient modulus increases as the strength and stiffness of specimen increases with an increase in relative density.

Camargo et al. (2013) have evaluated the mechanical properties of a full-depth reclaimed pavement material (RPM) stabilized with high carbon/high calcium fly ash, and compared these with properties of a conventional crushed aggregate. The RPM had the higher resilient modulus (M_r) than the traditional base course of crushed aggregate, at the same time, showed the higher plastic strain than crushed aggregate, indicating the higher potential of rutting. California Bearing Ratio (CBR) of the RPM was higher than crushed aggregates due to the stabilizer.

The present study focuses on laboratory testing of virgin aggregate or natural coarse aggregate (NCA) from Anna Quarry, Anna, Illinois and the recycled asphalt pavement (RAP) from an old parking lot. The characterization of recycled aggregates was performed to ascertain their suitability for the use in the pavement base. Different index property tests were conducted to characterize the materials (i.e., NCA, and RAP) which involved the determination of the particle size distribution, specific gravity and absorption, California Bearing Ratio (CBR) and resilient modulus (M_r) values in order to ascertain whether the materials are suitable to use as pavement materials or not.

MATERIALS AND METHODS

Natural Coarse Aggregate (NCA)

The virgin aggregates or natural coarse aggregate (NCA) were the crushed limestone rocks obtained from Anna Quarries, Southern Illinois. It was free from any foreign materials. The range of the particle sizes of the aggregates was from 4.0 mm to 19 mm.

The Recycled Asphalt Pavement (RAP)

The reclaimed or recycled asphalt pavement (RAP) sample was obtained from the old school parking lot asphalt pavement in Marion, Illinois. The asphalt road pavement demolished was full depth reclamation. The range of the sizes of the RAP was from 0 to 25 mm. As the RAP being recycled from the full-depth reclamation, it had lots of finer particles. Besides that, there were foreign materials like leaves, grasses, woods, plastics, papers etc. which were screened off while preparing the specimen.

Aggregate Testing and Characterization

Different index properties (i.e., particle size distribution, specific gravity and absorption) were carried out for the characterization of NCA and RAP sample. The gradation analysis of the samples was determined as per ASTM C33-03 (2003) and AASHTO T27-06 (2007) standard. AASHTO T85-91 (2004) standard test method has been used to determine the specific gravity and absorption of the aggregate samples. The CBR test was conducted to determine the potential strength or bearing capacity of materials as per ASTM D 1883-07 (2007) and AASHTO T193-99 (2003) standard. The CBR test was carried out on all aggregates separately, and on various blended mixtures with different ratios of RAP and NCA (% RAP:NCA); 0:100, 20:80, 40:60, 60:40, 80:20. The resilient modulus (M_r) test was conducted using AASHTO T307-99 (2007) standard on the aggregate samples to check the stiffness of the materials and to ensure whether materials can be used in the pavement construction or not. The resilient modulus equipment used in this research was manufactured by GeoComp, USA. For the resilient modulus test the sample size of 152.4 mm in diameter and 304.8 mm in height has been used. For this study K- θ model (Hicks and Monismith, 1971) was used to estimate resilient modulus (M_r) values. Due to different specific gravity of the RAP and NCA samples, for the blended mixtures had different density. Hence, the average density was used to conduct the CBR test for the blended mixtures. The average densities (in kN/m^3) of the blended mixtures with different ratios of RAP and NCA (% RAP: NCA); 0:100, 20:80, 40:60, 60:40, 80:20 were 15.37, 15.65, 15.98, 18.95, 15.49 and 15.30, respectively. The density is quite low because the resilient modulus test has been conducted using these densities for a particular mix.

Particle Size Distribution

Particle size distribution or gradation analysis was carried out on natural coarse aggregate (NCA) and recycled asphalt aggregate (RAP) samples presented in Fig. 1. From Fig. 1, it can be observed that the NCA is uniformly graded and RAP is well-graded. The RAP sample had much finer particles than NCA sample since it was collected from fully reclaimed asphalt pavement. The RAP sample didn't fall into the criteria completely for the base gradation according to the AASHTO D 2940 granular base.

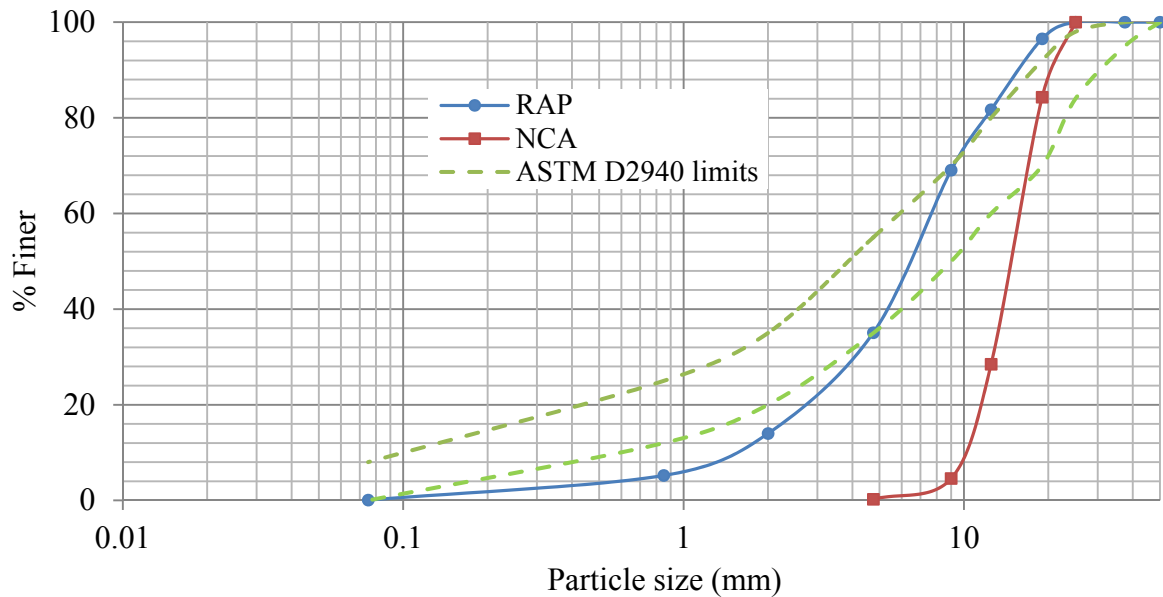


FIG. 1. Gradation of natural coarse aggregate (NCA) and reclaimed asphalt pavement (RAP) aggregates.

Specific Gravity and Absorption

The results of specific gravity and absorption are presented in Table 1.

Table 1. Specific gravity and absorption of NCA and RAP sample

Particle size		Property	NCA	RAP	IDOT specification
Passing	Retained				
25.0 mm	4.75 mm	Bulk SG (Dry)	2.85	2.48	2.54 - 2.60
		Bulk SG (SSD)	2.86	2.51	
		Apparent SG (ASG)	2.88	2.55	
		Absorption (%)	0.46	0.94	

From Table 1 it can be observed that, the bulk specific gravity of dry NCA was 2.85 and bulk specific gravity in SSD (Saturated Surface Dry) condition was 2.86 which denote that NCA doesn't have much pore on it to absorb water which is indicator of the good aggregate. The apparent specific gravity of NCA was 2.88. The bulk specific gravity (dry) of the RAP was 2.48 and for the SSD condition it is 2.51. The apparent specific gravity of the RAP was 2.55. It is very similar to the results reported by Han et al. (2012) but it is lesser than the values obtained by

Xiao and Amirkhanian (2009). The absorption of NCA sample was found to be 0.46% which falls in the range (i.e., 0.4% - 2.0%) obtained by Cross and Mgonella (2005). The absorption of the RAP was 0.94% which was close to the NCA sample. The reason for lower absorption value of RAP sample may be due to asphalt coating around the aggregate. The increase in asphalt coating may increase the water drainage during compaction, while reducing the absorption capacity of the material (Attia and Abdelrahman, 2010).

RESULTS AND DISCUSSION

California Bearing Ratio (CBR)

The CBR test was carried out on both aggregates (i.e., RAP & NCA) separately, and on various blended mixtures with different ratios of RAP and NCA (i.e., % RAP:NCA); 0:100, 20:80, 40:60, 60:40, 80:20) and the results are presented in Figure 2.

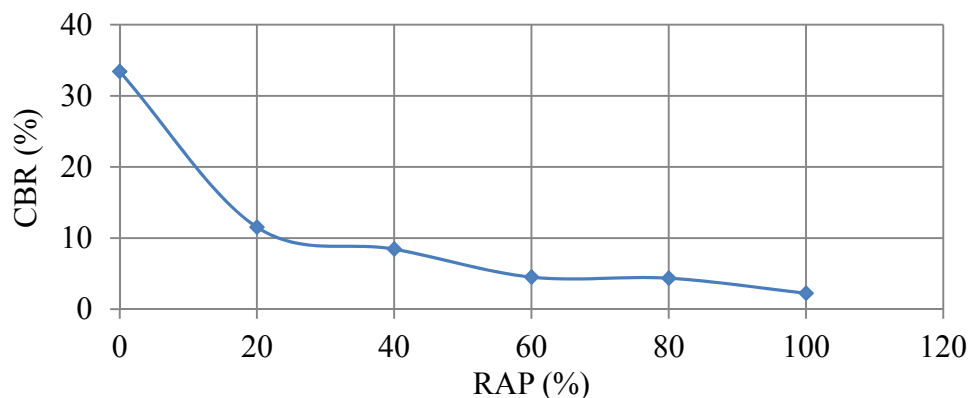


FIG. 2. CBR value of different percentages of NCA and RAP mixtures.

The CBR value of NCA is higher than that of pure RAP when tested separately. The CBR values for the blended mixtures seem to decrease as the percentage of RAP increases. It shows that the bearing capacity of the blended mixtures decreases as the percent of recycled aggregate increases. The CBR value obtained for the NCA, and RAP were 33.42%, and 2.24%, respectively. Stolle et al. (2005) reported that CBR values of different virgin aggregate ranges from 30% to 162% for different types of virgin aggregate. Han et al. (2012) reported that the CBR value of RAP as 6.8% and 9.3% for two different types of RAP. The CBR values for the Crushed aggregate and recycled pavement materials were 133% and 19%, respectively (Camargo et al., 2013). In the present study, the results obtained for CBR tests were very low as compared to the average CBR values reported by other researcher due to less compacting effort applied during the test. The density for the CBR test has been maintained the same as resilient modulus test density.

Resilient Modulus

The resilient modulus test of both aggregate samples were conducted separately, and was tested on various blended mixtures with different ratios of RAP & NCA (% RAP:NCA); 0:100, 20:80, 40:60, 60:40, 80:20. The sample size for the resilient modulus test was 152.4 mm diameter and 304.8 mm length. The resilient modulus values for 100% NCA and 100% RAP sample with various confining stresses and mean deviator stress are presented in Table 2.

From Table 2 it can be noticed that the resilient modulus for 100% NCA was obtained as 220.21 MPa at lower confining pressure (13.79 kPa) and deviator stress (68.95 kPa) and 307.00 MPa for higher confining pressure (41.37 kPa) and deviator stress (27.58 kPa). Pure RAP (i.e., 100%) sample had the resilient modulus value 299.06 MPa at lower confining pressure (13.79 kPa) and deviator stress (68.95 kPa) and 388.75 MPa for higher confining pressure (41.37 kPa) and deviator stress (27.58 kPa).

Table 2. Resilient modulus of 100% NCA and 100% RAP

Confining Stress, (kPa)	Mean Deviator Stress, (kPa)	Bulk Stress, (kPa)	Mean Resilient Modulus (M_r), (MPa)	
			100% NCA	100% RAP
41.37	27.58	151.68	307.00	388.75
	41.37	165.47	264.08	363.45
	55.16	179.26	245.44	345.34
	68.95	193.05	255.47	350.69
27.58	27.58	110.32	271.54	344.50
	41.37	124.11	244.83	331.97
	55.16	137.90	234.51	324.64
	68.95	151.68	238.63	310.78
13.79	27.58	68.95	252.13	322.99
	41.37	82.74	210.16	313.56
	55.16	96.53	188.72	301.94
	68.95	110.32	220.21	299.06

Bozyurt et al. (2012) have reported the resilient modulus values for various RCA and RAP samples from different places were; for RAP it was from 180 MPa to 266 MPa, and for Class 5 Aggregate it was 152 MPa. Costa et al. (2012) found that for RAP and virgin aggregate blend mixtures from 15 to 40% and the resilient modulus was found to be 120 MPa to 513 MPa. They also concluded that there was increase in resilient modulus with the increase in the RAP content by approximately 15%. Camargo et al. (2013) found the resilient modulus of 220 MPa for the crushed aggregate and 257 MPa for the RPM (Reclaimed Pavement Material) sample.

Effect of Confining Pressure and Deviator Stress

It has been observed that there is an increase in the resilient modulus value with the increase in confining pressure. There was 23.05% increase in the resilient modulus of the NCA when the confining pressure was increased from 13.79 kPa to 41.37 kPa. For 100% RAP there was an increase of 15.82% when the confining pressure was increased from 13.79 kPa to 41.37 kPa. Monismith et al. (1967) stated that resilient modulus may increase up to 500% for a change in confining pressure from 20 to 200 kPa. Smith and Nair (1973) reported that there was 50% increase in the resilient modulus when there was increase in the sum of principal stresses, θ ; from 70 to 140 kPa. Hicks (1970) reported that the resilient modulus is practically unaffected by the magnitude of the deviator stress applied, provided excessive plastic deformation is not generated. From Table 2 it can be observed that with the increase in the confining pressure, there was an

increase in the resilient modulus of the recycled asphalt aggregates and for blended mixtures with NCA and with the increase in the deviator stress there was decrease in the resilient modulus of the samples.

Comparison of Resilient Modulus of different proportion of RAP and NCA

From Table 2 and Fig. 3, it can be noticed that for the confining pressure 13.79 kPa and deviator stress of 27.58 kPa, the resilient modulus for the 100% RAP was 322.99 MPa which is higher than the resilient modulus of the NCA i.e., 252.13 MPa and for blended mixtures there was a decrease in the resilient modulus values than that of the 100% RAP except in the case of 80% of RAP and 20% of NCA blended mixtures; which was almost equal to 100% RAP. It was found that there was an increase in the resilient modulus of the RAP blended mixtures when there was increase in the percentage of the RAP content. From Table 2, for the confining pressure 41.37 kPa and deviator stress of 68.95 kPa, the resilient modulus for the 100% RAP was 350.69 MPa which is higher than the resilient modulus of the NCA i.e., 255.47 MPa and in blended mixtures (shown in Fig. 4) there was decrease in the resilient modulus than that of the 100% RAP. It was found that there was increase in the resilient modulus of the RAP blended mixtures when there was increase in the percentage of the RAP content. The increase in the resilient modulus (M_r) with the increase in the percentage of RAP may be due to the RAP and NCA blended mixture the density increases; also the bitumen present in the RAP played the role of binder and as the percentage of RAP increases the bitumen content was also increases. The density of blended mixture of RAP and NCA was increasing from 100% NCA to 60% RAP: 40% NCA mixture then it decreases when the percentage of RAP was increases.

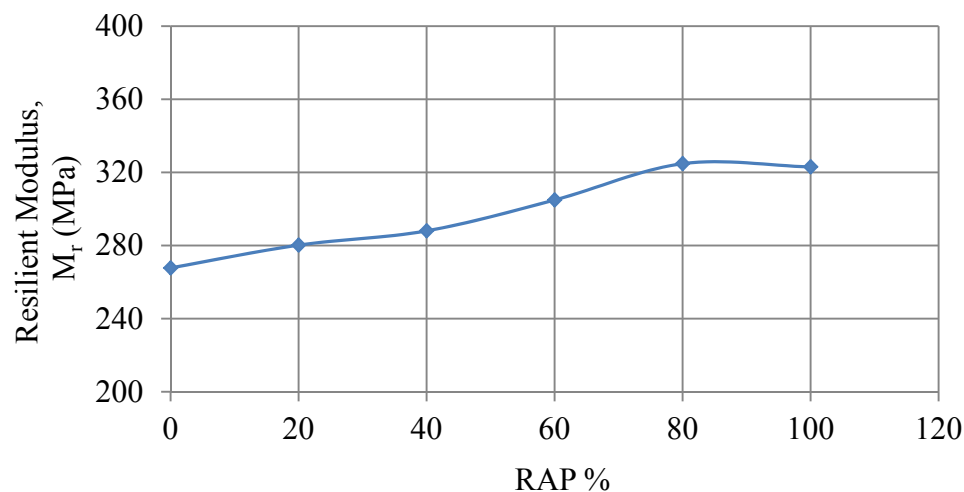


FIG. 3. Resilient modulus of different percent of blended mixtures of RAP and NCA for confining pressure of 13.79 kPa and deviator stress of 27.58 kPa.

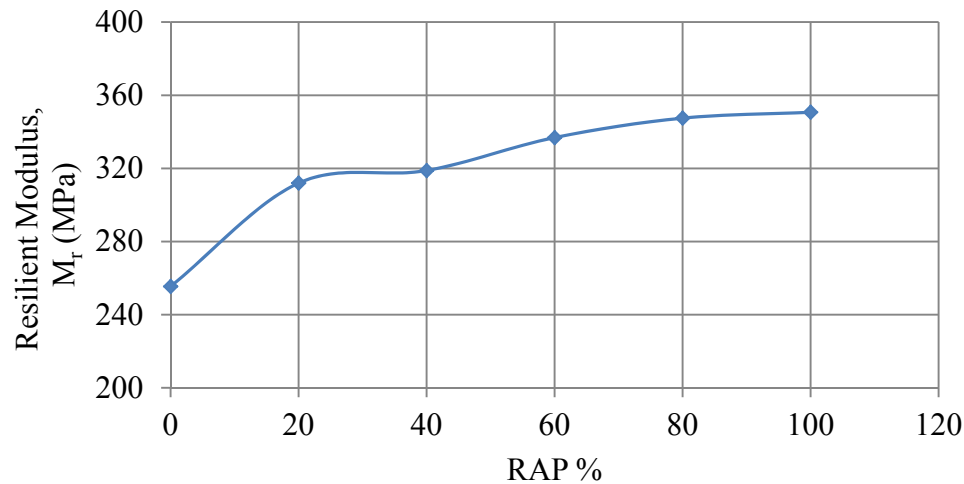


FIG. 4. Resilient modulus of different percent of blended mixtures of RAP and NCA for confining pressure of 41.37 kPa and deviator stress of 68.95 kPa.

The resilient modulus of the 100% RAP and NCA and their blended mixtures were compared in the Figure 4 for the confining pressure 41.37 kPa and deviator stress 68.95 kPa. From Fig. 4 it can be observed that at 41.37 kPa the resilient modulus, M_r of RAP sample was around 37% higher than that of NCA. Whereas for different blended mixtures, M_r value increases with the increase in the RAP percentage.

CONCLUSIONS

The following conclusions can be drawn as per the natural and recycled asphalt pavement aggregate used and tested in this study.

- The gradation of the recycled aggregates (i.e., RAP) used in this research did not meet the criteria fully for the base gradation according to the AASHTO D2940 granular base.
- NCA has specific gravity higher than that of IDOT specification and the absorption of the NCA was lower than expected values. The specific gravity of the RAP was lower than IDOT specification but it was similar to results obtained by Han et al. (2012) and absorption of RAP was lower than IDOT specification.
- The increase on the percent of RAP resulted into the decrease in the CBR value. The CBR values for all the aggregates and its blended mixtures are quite low as compared to other researches since the sample was compacted and tested as per the compaction density achieved in the resilient modulus test.
- The resilient modulus (M_r) values for pure (i.e., 100%) RAP was higher than the 100% NCA for different confining pressure and deviator stresses. But, the resilient modulus of the blended mixtures of RAP and NCA had a tendency of increasing resilient modulus values with increase in percent of RAP.

Based on the results from the present study, it can be concluded that RAP can be used for granular base for road pavement works.

REFERENCES

- AASHTO T193-99 (2003). Standard Method of Test for the California Bearing Ratio.
- AASHTO T27-06 (2007). Standard Method of Test for Sieve Analysis of Fine and Coarse Aggregates.
- AASHTO T307-99 (2007). Standard Method of Test for Determining the Resilient Modulus of Soils and Aggregate Materials. Washington, DC, American Association of State Highway and Transportation Officials.
- AASHTO T 84-09 (2009). Standard Method of Test for Specific Gravity and Absorption of Fine Aggregate.
- AASHTO T85-91 (2004). Standard Method of Test for Specific Gravity and Absorption of Coarse Aggregate.
- ASTM D2940 (2003). Graded Aggregate Material for Bases or Subbases for Highways or Airports.
- ASTM D1883-07 (2007). Standard Test Method for CBR (California Bearing Ratio) of Laboratory-Compacted Soils, ASTM International, West Conshohocken, PA.
- ASTM C33-03 (2003). Standard Specification for Concrete Aggregates, ASTM International, West Conshohocken, PA.
- Attia, M., and Abdelrahman, M. (2010). "Modeling the Effect of Moisture on Resilient Modulus of Untreated Reclaimed Asphalt Pavement." *Transportation Research Record: Journal of the Transportation Research Board*, No. 1981, 30-40.
- AUSTROADS (2012). "Guide to Pavement Technology Part 2: Pavement Structural Design." *ARRB group Ltd., AGPT02-12*, Melbourne, Australia.
- Bennert, T., Papp, Jr. W. J., Maher, A. and Gucunski, N. (2000). "Utilization of Construction and Demolition Debris Under Traffic-Type Loading in Base and Subbase Applications." *Journal of the Transportation Research Board*, No. 1714, Transportation Research Board of the National Academies, Washington, D.C., pp. 33- 39.
- Bozyurt, O., Tinjum, J. M., Son, Y. H., Edil, T. B., and Benson, C. H. (2012). "Resilient Modulus of Recycled Asphalt Pavement and Recycled Concrete Aggregate." *Geo-Congress 2012*, USA.
- Buchanan, S. (2007). Resilient Modulus: What, why, and How? Retrieved from <http://www.vulcaninnovations.com/public/pdf/2-Resilient-Modulus-Buchanan.pdf> accessed on September 02, 2014.
- Camargo, F. F., Wen, H., Edil, T., and Son, Y. H. (2013). "Comparative Assessment of Crushed Aggregates and Bound/Unbound Recycled Asphalt Pavement as Base Materials." *International Journal of Pavement Engineering*, 14(3), 223-230.
- CMRA (2010). Construction Materials Recycling Association, Concrete Materials Website; <http://www.ConcreteRecycling.org>, accessed on January 7, 2013.
- Costa, J. M., Aaron S. B., and Snyder, R. L. (2014). "Resilient Moduli of a Naturally aged RAP and Aggregate Blend." In *ASCE Geo-Congress 2014, Geo-characterization and Modeling for Sustainability*, 3025-3034.
- Cross, S. A., and Mgonella, M. K. (2005). "Evaluation of Test Methods for Determination of Aggregate Specific Gravity." *The Oklahoma Department of Transportation, FHWA-OK-05-02, ODOT Item No.2169, OSU: AA-5-81504*. College of Engineering Architecture and Technology Stillwater, Oklahoma.

- FHWA (2008). "User Guidelines for Byproducts and Secondary Use Materials in Pavement Construction." *FHWA Report FHWA-RD-97-148*, FHA, McLean, Virginia.
- FHWA (2010). "Reclaiming Roads." *FHWA-HRT-10-001*. Retrieved from <http://www.fhwa.dot.gov>.
- FHWA (2011). "Reclaimed Asphalt Pavement in Asphalt Mixtures: State of the Practice." *Publication FHWA-HRT-11-021*. FHWA, U.S. Department of Transportation.
- Guthrie, W. S., Cooley, D., and Eggett, D. L. (2007). "Effects of Reclaimed Asphalt Pavement on Mechanical Properties of Base Materials." *Transportation Research Record*, No. 2006, 44-52.
- Han, J., Acharya, B., Thakur, J. K., and Parsons, R. (2012). "Onsite Use of Recycled Asphalt Pavement Materials and Geo-cells to Reconstruct Pavements Damaged by Heavy Trucks." *A cooperative Research Project Sponsored by the U.S. Department of Transportation Research and Innovative Technology Administration*. Report # MATC-KU: 462.
- Hicks, R. G. (1970). "Factors Influencing the Resilient Properties of Granular Materials." PhD Dissertation, University of California, Berkeley, USA.
- Hicks, R. G., and Monismith, C.L. (1971), "Factors Influencing the Resilient Response of Granular Materials." *Highway Research Record 345*, Highway Research Board, Washington D.C., 32 – 44.
- Kim, W., Labuz, J. F. and Dai, S. (2007). "Resilient Modulus of Base Course Containing Recycled Asphalt Pavement." *Transportation Research Records: Journal of the Transportation Research Board*, 27 – 37.
- Maher, M. H., Gucunski, N., and Papp, W. J. Jr., (1997). "Recycled Asphalt Pavement as a Base and Subbase Material." *ASTM Special Technical Publication*, 1275, 42-53.
- Monismith, C. L., Seed, H. B., Mitry, F. G., and Chan, C. K. (1967). "Prediction of Pavement Deflections from Laboratory Tests." *Proc., 2nd Int. Conf. Struct. Des. of Asphalt Pavements*, 109-140.
- Mulheron, M., and O'Mahony, M. M., (1990). "Properties and Performance of Recycled Aggregates." *Highway Transportation*, 37(2), 35-37.
- NAPA (2009). "How to Increase RAP Usage and Ensure Pavement Performance." *National Asphalt Pavement Association*.
- Rana, A. S. M. A., (2004). "Evaluation of Recycled Material Performance in Highway Application and Optimization of Their Use." *PhD dissertation, Texas Tech University*, Lubbock TX, 170.
- Smith, W. S., and Nair, K. (1973). "Development of Procedures for Characterization of Untreated Granular Base Coarse and Asphalt-Treated Base Course Materials." *Rep. No. FHWA-RD-74-61*, Federal Highway Administration, Washington, D.C.
- Stolle, D. F. E., Guo, P., and Liu, Y. (2005). "Unbound Resilient Modulus Testing of Typical Base, Subbase Materials in Ontario." *Ministry of Transportation, Provincial Highways Management Division Report, Highway Infrastructure Innovation Funding Program*. Department of Civil Engineering, McMaster University, 84 p.
- USGS (2009). "2007 Minerals Yearbook-Cement (Advance Release), Washington, DC." *U.S. Geological Survey*, September; <http://minerals.usgs.gov/minerals/pubs/commodity/zinc/myb1-2009-zinc.pdf>, accessed on May 14, 2012.
- Xiao, F., and Amirhanian, S. N. (2009). "Effects of Binders on Resilient Modulus of Rubberized Mixtures Containing RAP Using Artificial Neural Network Approach." *Journal of Testing and Evaluation*, 37(2), 129-138.

Sustainability Evaluation of Geosynthetic Stabilized Soft Subgrade Soil in Unpaved Test Sections

Murad Abu-Farsakh, A.M.ASCE¹; Shadi Hanandeh²; Xiaochao Tang, A.M.ASCE³; and Qiming Chen, A.M.ASCE⁴

¹Research Professor, Louisiana Transportation Research Center, Louisiana State Univ., 4101 Gourrier Ave., Baton Rouge, LA 70808. E-mail: cefars@lsu.edu

²Graduate Research Assistant, Dept. of Civil and Environmental Engineering, Louisiana State Univ., Baton Rouge, LA 70808. E-mail: shanan1@tigers.lsu.edu

³Assistant Professor, Dept. of Civil Engineering, Widener Univ., Chester, PA 19013. E-mail: xtang@widener.edu

⁴Research Associate, Louisiana Transportation Research Center, Louisiana State Univ., 4101 Gourrier Ave., Baton Rouge, LA 70808. E-mail: qchen1@tigers.lsu.edu

Abstract: This paper presents the findings from an ongoing research study aimed to evaluate two recently developed geosynthetic products, a triaxial geogrid and a high-strength woven geotextile for reinforcing/stabilizing sustainable roads constructed over soft subgrade soil. A total of six full-scale test lane sections were constructed, among which two sections were reinforced by one and two layers of triaxial geogrids, respectively; while high strength geotextile was used to reinforce two of the other sections with different aggregate layer thicknesses. The rest of the two sections were left as control sections, of which one section was constructed over 30-cm thick sand embankment representing the common practice in Southern Louisiana. The unpaved test sections were subjected to a full-scale moving wheel load applied by the accelerated loading facility (ALF). A variety of instrumentations were used to measure the load-associated and the environment-associated pavement responses and performance. Results of the full-scale testing on the unpaved test sections demonstrate the benefits of geosynthetic reinforcement/stabilization in reducing the permanent deformation in the pavement structure. The test sections' resilient behavior did not seem to be influenced by the presence of geosynthetics. It was also found that, instead of the soft soil subgrade, the aggregate layer is the primary contributor to the total permanent deformation/surface rutting of the unpaved sections under the testing conditions in this study. Geosynthetics were mobilized and generally exhibited a strain around 0.2%.

INTRODUCTION

The aging highway infrastructure, growing demands for roads' usage, and the constrained funding for repair and maintenance have made the federal and state transportation agencies search for alternative and cost-effective roadway design, construction, and materials. As an unconventional construction material, geosynthetics have been used in roadways in the US since 1970's and have seen a steady growth. As of 2001, the geosynthetic market in the US was estimated to be \$1.1 billion, among

which the geosynthetic used for reinforcement applications in roadways is worth about \$200 million per year (Perkins et al. 2005).

Over the decades, numerous studies have shown that geosynthetics provide benefits in roadway structures by either extending the roads' service life or reducing structural layer thickness, especially the aggregate base layer, with equivalent performance (Haas 1984; Barksdale et al. 1989; Al-Qadi 1994; Abu-Farsakh et al. 2004; Tang et al. 2008; Abu-Farsakh et al. 2012). Along with the release of the Mechanistic-Empirical Pavement Design Guide (MEPDG) by AASHTO (2008), the recent research on applications of geosynthetic reinforcements in pavements has been focused on quantifying the effects and benefits of geosynthetics and incorporating them into the Mechanistic-Empirical (ME) analysis and design (Kwon et al. 2005; Nazzal et al. 2010; Perkins et al. 2011).

Aimed to evaluate two recently emerged geosynthetic products, a triaxial geogrid and a high-strength woven geotextile, a full-scale accelerated testing was conducted on a total of six unpaved road sections. Each section was instrumented by a variety of sensors to measure critical responses and performance and environmental factors that may affect the performance. The response and performance measurements are intended to be used to calibrate or develop ME models that account for effects of geosynthetics. Presented in this paper are some preliminary results of the full-scale accelerated testing.

EXPERIMENTAL INVESTIGATION

Test Section and Instrumentation

A total of six test sections were constructed over natural soil foundations at an outdoor site located at the Pavement Research Facility (PRF) of Louisiana Department of Transportation and Development (LA DOTD) in Port Allen, LA. Each test section is 24 m (80ft) long and 4 m (13 ft) wide. Figure 1 shows the cross sections of the six test sections. Section 1 and Section 4 were control sections without geosynthetic reinforcements, of which Section 1 was constructed over sand embankments as a common practice in Southern Louisiana. Section 2 and Section 3 were reinforced by the triaxial geogrid, GG placed at the base-subgrade interface. An additional layer of geogrid, GG was installed at the upper one-third of the base in Section 2. The high strength geotextiles, GT were used to reinforce Section 5 and Section 6 with different base thicknesses.

The natural subgrade soil in the study is classified as heavy clay (CL) per Unified Soil Classification System (USCS) or A-7-6 according to the American Association of State Highway and Transportation (AASHTO) classification system. The soil has a PI of 55% with 96.6% passing the #200 sieve. The optimum moisture content is 29.5% at a maximum dry density of 1305 kg/m³. The aggregate used for base course construction is a crushed limestone, which had 1.56% passing No. 200 opening sieve, an effective particle size (D_{10}) of 0.382 mm, a mean particle size (D_{50}) of 3.126 mm, a uniformity coefficient (C_u) of 37, and a coefficient of curvature (C_c) of 3. This crushed limestone is classified as GW and A-1-a according to the USCS and the AASHTO classification systems, respectively. A modified Proctor test of the aggregate yields an optimum moisture content of 9.4% and maximum dry density of 2066 kg/m³. The resilient modulus of the crushed limestone specimen, prepared at the optimum moisture content, ranges from 75 MPa to 316 MPa, depending on the deviatoric and confining stresses.

Two recently emerged geosynthetic products, a triaxial geogrid and a high-strength woven geotextile, are selected for this study and are herein designated as GG and GT. The triaxial geogrid was made by means of punching and drawing polypropylene (PP) sheets. The geotextile was made from high-tenacity polypropylene filaments that are formed into weaves. Table 1 lists the physical and mechanical properties of the geosynthetic materials reported by the manufactures.

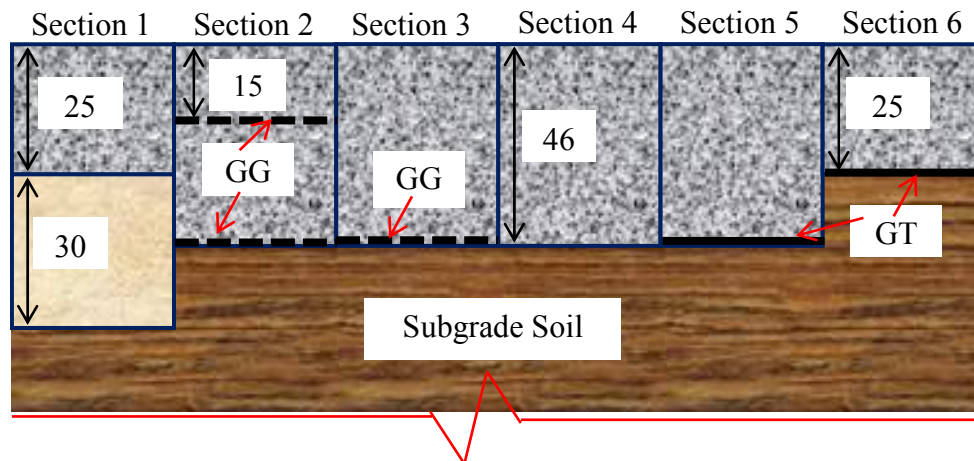


FIG. 1. Cross sections of the six test sections, units in cm.

Table 1. Physical and mechanical properties of geosynthetics used in this study

Index Property	GG	GT	
		MD*	XMD*
Polymer Type	Polypropylene	Polypropylene	
Aperture Size (mm)	40×40×40	N/A	N/A
Ultimate Tensile Strength (kN/m)	7.5	7	26.26
Junction Strength (kN/m)	375	N/A	N/A

* MD: machine direction; XMD: cross-machine direction.

The test sections were instrumented by a variety of sensors to measure load- and environment-associated pavement responses and performance. In general, for each test section, two earth pressure cells (Geokon 3500) were installed at the top of the subgrade to measure the total vertical stresses while piezometers (Geokon 3400) were installed next to the pressure cells to measure possible excess pore water pressure. Potentiometers were installed at the mid-height of the base course layer to measure compressive strains. The use of the potentiometer measurements for estimating the aggregate layer deformation is based on the assumption that the compressive strain of the aggregate layer is uniformly distributed and represented by the mid-height compressive strain. Spring-loaded LVDTs (RDP DCTH2000A) were customized and attached to a 1.0 m (3 ft) long steel rod that was driven into the soil subgrade. A thin yet rigid disk with diameter of 5 cm (2 in) was attached onto the contact tip of the spring-loaded LVDT to provide sufficient contact area with the soil. The LVDT measured the total deformation of the subgrade, since the end of each LVDT was fixed

with respect to the far depth of the subgrade. The geosynthetics were instrumented with foil strain gauges installed in pairs on opposite side of the geosynthetic. Other instruments include thermocouples and time-domain reflectometers (TDR) for monitoring moisture contents. Only a part of the instrumentation measurements will be presented in this paper due to the constraint of space.

As-Constructed Condition of the Test Sections

The nuclear density gauge, light falling weight deflectometer (LFWD), Geogauge, and dynamic cone penetrometer (DCP) were used to measure the density and stiffness/modulus of natural subgrade and as-constructed base layer. For the subgrade layer, the dry densities varied from 1,044 to 1,192 kg/m³, with moisture contents ranging from 44 to 52%. The corresponding LFWD moduli, geogauge moduli, and DCP index (DCPI) were in the range of 3.5 to 6 MPa, 20 to 25 MPa, and 150 to 200 mm/blow, respectively. For the base course layer, the target degree of compaction during construction was 95%. The dry densities varied from 1,925 to 2,065 kg/m³, with moisture contents ranging from 6 to 10%. The corresponding LFWD moduli, geogauge moduli, and DCPI were in the range of 50 to 70 MPa, 140 to 230 MPa, and 7.5 to 9.5 mm/blow, respectively. No surface sealing was applied on top of the aggregate surface.

Vane shear testing was conducted at various depths of the subgrade to investigate the in-situ undrained shear strength of the native subgrade (Table 2). Results of the vane shear testing showed that the subgrade of Section 6 had overall the highest undrained shear strength, while Section 1 had the lowest at all three depths. This is basically due to the higher elevation of the subgrade in Section 6 compared to other sections (as described in Figure 1), and thus above the water table of 0.3 m below the Section 6 subgrade level.

TABLE 2 Subgrade in-situ undrained shear strength (kPa) from vane shear tests

Test Section	30.5 cm (12 in)		61.0 cm (24 in)		91.4 cm (36 in)	
	below surface		below surface		below surface	
	Avg.	Stdv.	Avg.	Stdv.	Avg.	Stdv.
1	46.0	21.4	72.8	19.6	79.2	23.9
2	52.8	10.3	73.8	9.0	86.4	12.6
3	55.2	16.6	76.6	16.6	91.4	15.7
4	57.0	11.6	76.6	12.0	88.8	18.6
5	56.2	12.5	81.0	15.8	90.6	20.9
6	66.5	7.9	80.6	25.4	96.3	11.4

Full-Scale Accelerated Testing

A full-scale accelerated load facility (ALF) was utilized to apply cyclic moving traffic loads. ALF is a testing device that applies unidirectional trafficking to the test sections with a nominal speed of 16.8 km/h (10.5 mph) or 350 passes per hour. ALF has a due-tire axle consisting of two Michelin XZE-model truck tires and applies a 43.4-kN (9,750-lb) axle load, approximately representing half of the standard axle load, the

80-kN (18-kip) single-axle load. ALF has the capacity of applying a normally-distributed wander covering a transverse distance of 76 cm (30 in) to simulate live traffic pattern. The wheel path generated by ALF is about 12 m (40 ft).

A total of 2000 passes were applied to the sections with geosynthetic reinforcements while only 400 passes were applied to the two control sections. Using a wireless laser profilometer, the transverse surface profile of the test sections were measured at select intervals of load repetitions at 8 different locations along the wheel path. The pavement responses to the moving loads of ALF were also recorded. Static measurements were taken without the ALF surcharge load to monitor the accumulation of the permanent deformation of the base and the subgrade. The static measurements were averaged into one value at each interval while the dynamic measurements were processed and peak responses were extracted.

Upon the completion of the accelerated testing, the in-situ strength and stiffness of the sections were tested by several different devices, including a light-weight deflectometer (LWD), a Geogauge, and a dynamic cone penetrometer (DCP). For each section, the in-situ tests on the base layer were conducted along locations outside and inside the wheel path to represent the respective site conditions before and after the traffic loading.

RESULTS AND ANALYSIS

Resilient Responses to Moving Wheel Load

The pavement resilient responses to moving traffic load are of great importance since they can be used to calibrate and verify the mechanistic models for ME analysis and design. Figure 2 (a) shows the vertical stresses at the top of the subgrade in Section 5 and Section 6 measured by the pressure cell. The base layer of Section 5 is 21 cm (8 in) thicker than that of Section 6 (Figure 1). As a result, the peak value (54.4 kPa) of the vertical stresses in Section 5 is much less than the peak value (86.5 kPa) in Section 6. Additionally, the duration of the stress pulse in Section 5 is greater than that of Section 6. Figure 2 (b) illustrate the elastic vertical displacement at the top of the subgrade in Section 6.

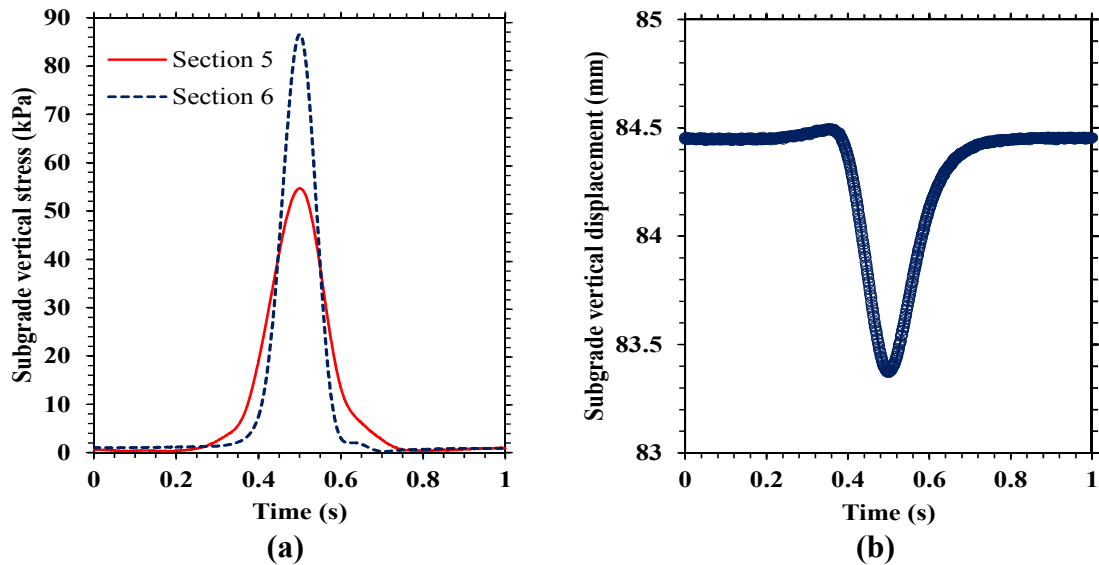


FIG. 2. Resilient responses of subgrade under moving traffic load: (a) vertical stress in Section 5 and Section 6; (b) vertical displacement in Section 6.

Total Permanent Deformation-Surface Rutting

Figure 3 presents the accumulation of the total permanent deformation along with the number of wheel passes. The accumulation of the total permanent deformation was calculated by subtracting the baseline measurement from the subsequent maximum values of profile measurements. The total permanent deformation for each section shown in Figure 3 is the average of the measurements taken at the eight different locations along the wheel path in each section. It can be seen that the change of profiles occurs at a faster rate at the initial stage of the traffic loading due to the densification of the unbound materials under the wheel load.

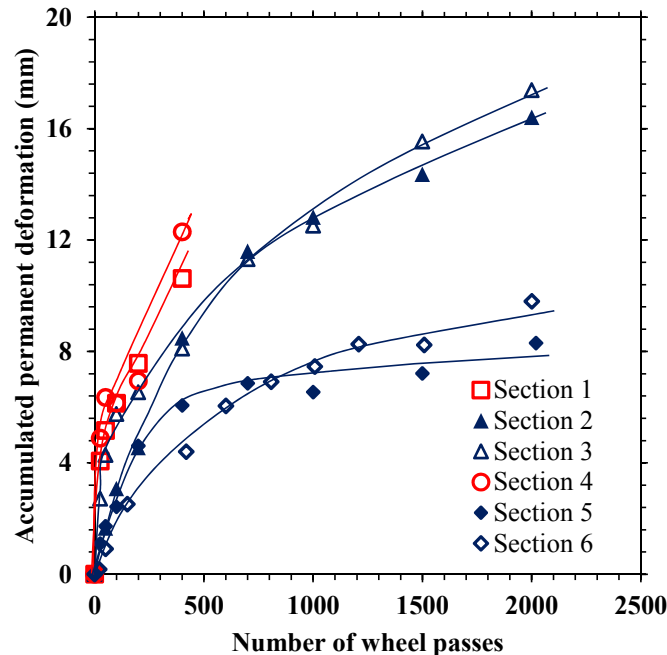


FIG. 3. Accumulated surface permanent deformation.

The control sections, Section 1 and Section 4, exhibited significantly greater total permanent deformation than reinforced sections at the same number of wheel load applications, indicating the benefits of geosynthetics in reducing permanent deformation in pavement structures. Compared to the test sections (Sections 2 and 3) reinforced with the triaxial geogrids (GG), the test sections (Sections 5 and 6) with the high-strength geotextile, GT overall showed less permanent deformations. Since Section 5 has a thicker base layer than Section 6, Section 5 showed less deformation than that of Section 6 and had a much smaller rate of deformation accumulation after about 500 wheel passes. In comparing Section 5 to the control section (Section 4), it is noted that the inclusion of the high-strength geotextile in Section 5 at the base-subgrade interface reduced almost half of the permanent deformation after 400 wheel passes.

Between Sections 2 and 3, Section 2 reinforced with two layers of geogrids showed less permanent deformation at the end of the testing. It is worth pointing out that there is less deformation at the early stage of the traffic in Section 2, which is most likely due to the mobilization of the geogrid installed at the upper one-third of the base course in Section 2. The two control sections, Section 1 and Section 4 showed similar performance in terms of total permanent deformation.

In addition to the presence of geosynthetics or geosynthetic types, there are many factors affecting the performance of resisting surface rutting among the six sections. The change of the subgrade soil and base aggregate moisture content due to rainfall throughout the testing may significantly affect the pavement's condition, and thus its performance. Variations in construction such as material placing and degree of compaction may also affect the pavement performance. Further analysis of the in-situ tests will help to determine whether the variations in site conditions contributed to the differences in the performance of the six sections.

Permanent Deformation in Subgrade

The subgrade was instrumented to measure both permanent and elastic deformations of the subgrade at select intervals of the ALF traffic. As previously mentioned, the LVDTs were mounted in a steel rod, which had one end relatively fixed to the great depth of the soil foundation. Therefore, the permanent deformation measured by LVDTs represented the overall deformation of the entire subgrade layer. Some of the LVDTs were damaged due to the construction or moisture intrusion. Figure 4 shows the accumulation of subgrade permanent deformation along with the number of wheel passes for Section 4 and Section 6. As can be seen in Figure 4, the control section (Section 4) has a significantly less deformation than Section 6 reinforced by the high-strength geotextile. This is likely due to that the base course layer of Section 4 is 21 cm (8 in) thicker than that of Section 6, suggesting that 21 cm (8 in) base layer provides more protection to the subgrade than the high-strength geotextile does.

The total pavement permanent deformation or surface rutting, measured by using the laser profilometer at various intervals of traffic load applications, consists of permanent deformation in the base layer and the subgrade permanent deformation. By comparing Figures 3 and 4, it is noted that the majority of the total permanent deformation is attributed to the permanent deformation in the base course layer. Additionally, the development of the subgrade permanent deformation became stable after certain number of wheel passes while the total permanent deformation still increased dramatically, especially for Section 4. Load-induced permanent deformation is usually a result of material densification, shear-related deformation, or a combination of both, and occurs in any layer of the pavement system. Measurements of base course layer deformation would shed light on the relative layer contributions to the total permanent deformation.

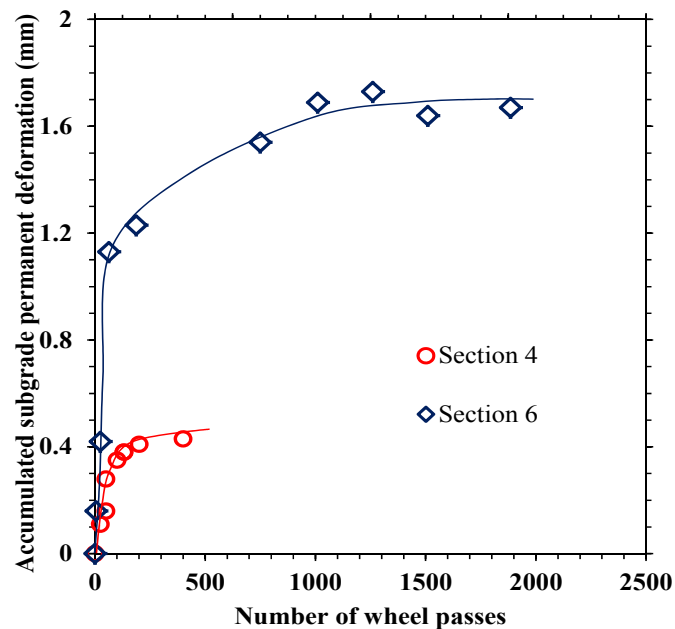


FIG. 4. Accumulated subgrade permanent deformation.

SUMMARY AND CONCLUSIONS

As geosynthetics have been used in roadway structures for a long history and proven to be beneficial in improving the roadways' performance, recent research has been focused on incorporating the benefits and effects of geosynthetics into ME design and analysis. A full-scale accelerated testing was carried out to test two geosynthetic products, a triaxial geogrid and a high-strength woven geotextile. A total of six test sections were constructed and extensively instrumented to measure critical responses and performance.

Instrumentation measurements demonstrate the resilient responses to the moving traffic load, which can be used for mechanistic modeling. Results of the full-scale accelerated testing showed the benefits of both the geosynthetic products in significantly reducing the permanent deformation. Although other factors such as the variations of site conditions may affect the pavement performance, preliminary analysis suggests that the high-strength geotextile may be more effective in reducing the permanent deformation under the specific conditions of this study. Between the two sections reinforced by geogrids, the section with an additional layer of geogrid at the upper one-third of the base layer showed less deformation at the early stage of the traffic loading probably due to the early mobilization of the upper geogrid. It was also found that the majority of the permanent deformation was due to the aggregate base layer.

ACKNOWLEDGMENTS

The authors acknowledge and appreciate the financial support provided by the Louisiana Department of Transportation and Development (LA DOTD), Tensar International., and TenCate. The authors also wish to thank the personnel at Pavement Research Facility of Louisiana Transportation Research Center (LTRC) and graduate students at LTRC who helped with installing instruments and in-situ testing.

REFERENCES

- AASHTO. Mechanistic-Empirical Pavement Design Guide, Interim Edition: A Manual of Practice. AASHTO, Washington, D.C., 2008.
- Abu-Farsakh, M. Y., Nazzal, M. D., and Mohammad, L. N. (2004). "Effect of Reinforcement on Resilient and Permanent Deformations of Base Course Material." *Transportation Research Record 2004*, Transportation Research Board of the National Academies, Washington, D. C. pp. 120-131.
- Abu-Farsakh, M. Y., Souci, G., Voyiadjis, G. Z., and Chen, Q. (2012). "Evaluation of Factors Affecting the Performance of Geogrid-Reinforced Granular Base Material Using Repeated Load Triaxial Tests." *Journal of Materials in Civil Engineering*, 24(1): 72-83.
- Al-Qadi, I.L, Brandon, T.L., Valentine, R.J., Lacina, B.A., and Smith, T.E. (1994). "Laboratory Evaluation of Geosynthetic-Reinforced Pavement Sections." *Transportation Research Record 1439*, Transportation Research Board, National Research Council, Washington D.C., 25-31.

- Barksdale, R.D., Brown, S. F., and Chan, F. (1989). "Potential Benefits of Geosynthetics in Flexible Pavement Systems." *National Cooperative Highway Research Program Report No. 315*, Transportation Research Board, National Research Council, Washington D.C.
- Haas, R. (1984). "Structural Behaviour of Tensar Reinforced Pavements and Some Field Applications." *Proceedings of the Conference on Polymer Grid Reinforcement in Civil Engineering*, Thomas Telford Publishing, London, 166-170.
- Kwon, J., Tutumluer, E., and Kim, M. (2005). "Development of a Mechanistic Model for Geosynthetic-Reinforced Flexible Pavements." *Geosynthetics International*, 12(6): 310-320.
- Nazzal, M., Abu-Farsakh, M. Y., and Mohammad, L. (2010). "Implementation of a Critical State Two-Surface Model to Evaluate the Response of Geosynthetic Reinforced Pavements." *International Journal of Geomechanics*, 10(5): 202-212.
- Perkins, S. W., Bowders, J. J., Christopher, B. R., and Berg, R. R. (2005). "Geosynthetic Reinforcement for Pavement Systems: US Perspectives." GSP 141, International Perspectives on Soil Reinforcement Applications, *Proceedings of Geo-Frontiers Congress 2005*, Austin, Texas, US, January 24-26, 2005, pp. 1-13.
- Perkins, S. W., Christopher, B. R., Lacina, B. A., and Klompmaker, J. (2011). "Mechanistic-Empirical Modeling of Geosynthetic-Reinforced Unpaved Roads." *International Journal of Geomechanics*, 12(4): 370-380.
- Tang, X., Chehab, G.R., and Palomino, A.M. (2008). "Evaluation of Geogrids for Stabilizing Weak Pavement Subgrade." *International Journal of Pavement Engineering*, Vol. 9 (5), 413-429.

The Effect of Rejuvenators on RAP Mixtures: A Study Based on Multiple Scale Laboratory Test Results

H. F. Haghshenas¹; H. Nabizadeh²; and Y.-R. Kim³

¹Graduate Research Assistant, Dept. of Civil Engineering, Univ. of Nebraska, 362D Whittier Research Center, Lincoln, NE 68583. E-mail:

h.haghshenas@huskers.unl.edu

²Graduate Research Assistant, Dept. of Civil Engineering, Univ. of Nebraska, 362D Whittier Research Center, Lincoln, NE 68583. E-mail:

hesam.nabizadeh@huskers.unl.edu

³Associate Professor, Dept. of Civil Engineering, Univ. of Nebraska, 362N Whittier Research Center, Lincoln, Nebraska 68583. E-mail: ykim3@unl.edu

Abstract:

Utilizing the reclaimed asphalt pavement (RAP) materials for production of asphalt mixtures are environmentally friendly and economical. One necessary step towards arriving at an efficient use of these materials is the understanding of undesired inherent characteristics of RAP such as aged (stiff) asphalt binder and inconsistent aggregate properties. Previous studies on the rejuvenating agents have reported a fairly high improvement in the engineering properties of asphalt mixtures with the high contents of RAP. The paper presents the effects of various rejuvenators on the engineering characteristics of the asphalt mixtures containing high percentage RAP (65%) with two different scales of mixture: asphalt concrete (AC) and fine aggregate matrix (FAM). Resulting experimental tests of viscoelastic stiffness and cracking behavior of asphaltic materials in both AC and FAM scales were compared.

Keywords: Reclaimed asphalt pavement, Rejuvenator, Hot mix asphalt, Multi-scale laboratory tests.

INTRODUCTION

The use of reclaimed asphalt pavement (RAP) materials in producing asphalt mixtures offers great benefits by reducing costs for producers and highway agencies and the environmental impact associated with the extraction, transportation, and processing of natural materials. Although the use of RAP materials in asphalt mixtures can be favorable, the implementation of such mixtures is complex due to the undesired inherent characteristics of RAP such as aged (stiff) asphalt binder and inconsistent aggregate properties. In order to overcome these problematic issues, many efforts have been made during recent years (Zaumanis et al. 2015; Yu et al, 2014; Mogawer et al. 2013; Hajj et al. 2013; Al-Qadi et al. 2012)

Probably the main significant concern of the state transportation agencies in using asphalt mixtures with a high RAP is that the resulted mixtures are stiff with a poor workability which makes them hard to compact in the field and ultimately leads to premature field failure (Mogawer et al. 2012). In order to moderate the stiffness of RAP-blended mixtures, a softer binder or rejuvenator can be used. Rejuvenating agents can improve the engineering properties (e.g. cracking resistance) of asphalt mixtures containing high contents of RAP (Zhou et al, 2014). Generally, a rejuvenator is an asphalt additive used for softening the stiffness of the oxidized asphalt mixtures. The rejuvenators typically consist of a high proportion of maltenes which balance the chemical composition of aged binder and losses the maltenes during construction and service (Terrel and Epps, 1989). According to Carpenter and Wolosick (1980), the softening mechanisms of a typical rejuvenator can be considered as:

- Formation a very low viscose layer around the asphalt-coated aggregate which is a highly aged binder layer.
- Penetration of the rejuvenator into the aged binder layer where the amount of raw rejuvenator diminishes.
- Disappearance of rejuvenator and the continual penetration which decreases the viscosity of the inner layer and gradually increases the viscosity of the outer layer.
- After a certain time, reaching to equilibrium conditions in the majority of the recycled binder film.

Several recent study (Im and Zhou, 2014; Zaumanis et al. 2013; Hajj et al. 2013; Hill et al. 2013; Elseifi et al. 2011) have evaluated the effect of rejuvenators on the engineering properties and performance characteristics of mixtures and/or binders. Shen et al. (2007) have reported that the rejuvenator dosage can significantly affect the properties of asphalt binders and mixtures. Furthermore, Mogawer et al. (2013) reported that rejuvenators can mitigate the stiffness of the resulting binder and improve cracking resistance of the mixtures.

Although the experimental determination of the linear viscoelastic stiffness and fracture characteristics of asphalt concrete (AC) mixtures can be performed, it is generally time consuming and expensive to reach statistically repeatable results. Thus, cheaper, faster and repeatable alternative methods are pursued to efficiently predict the linear viscoelastic stiffness and fracture characteristics of asphalt mixtures. AC can be considered a mixture with coarse aggregates and fine aggregate matrix (FAM). FAM consists of fine aggregates (i.e., aggregates passing sieve No. 16), entrained air voids, and binder. Im et al. (2015) investigated deformation characteristics of AC

mixture and its corresponding FAM phase. They performed a simple creep-recovery test at various stress levels for AC and FAM, and they concluded that viscoelastic and viscoplastic deformation of AC mixtures can be predicted from FAM testing. In another research study, Karki et al. (2015) tried to predict dynamic modulus of AC mixtures using a computational micromechanics modeling approach. They carried out dynamic modulus test on AC mixtures and its corresponding FAM phase, and they point out that FAM phase can anticipate viscoelastic characteristics of AC mixtures. Moreover, many studies (Branco, 2008; Kim et al. 2003a,b; Kim et al. 2002; Marasteanu et al. 2000) demonstrated that FAM plays a significant role on performance characteristics (i.e. viscoelastic behavior, fatigue cracking, permanent deformation, etc.) of asphalt concrete mixtures and it can predict entire mixture behavior. In addition, fabricating and testing FAM specimens are not time-consuming nor costly compared to fabrication and testing of AC specimens.

RESEARCH OBJECTIVES AND SCOPE

The main objective of this study is to identify the effects of various rejuvenators on the mechanical characteristics of the asphalt mixtures containing recycled materials with two different scales of mixture, namely asphalt concrete (AC) and fine aggregate matrix (FAM). Resulting experimental tests of viscoelastic stiffness and cracking behavior of asphaltic materials in both AC and FAM scales are compared. Four mixtures were prepared for the comparative evaluation of the rejuvenators to the mechanical characteristics of AC and FAM (Table 1).

Table 1. Mixtures studied.

Mixture ID	Compositions
C	virgin aggregates (35%) + RAP (65%) + virgin binder (PG 64-34)
CR1	virgin aggregates (35%) + RAP (65%) + virgin binder (PG 64-34) + Rejuvenator 1
CR2	virgin aggregates (35%) + RAP (65%) + virgin binder (PG 64-34) + Rejuvenator 2
CR3	virgin aggregates (35%) + RAP (65%) + virgin binder (PG 64-34) + Rejuvenator 3

MATERIALS

Rejuvenators

Three different rejuvenators, based on different technologies (i.e., petroleum, green, and agriculture) were chosen in this study. Table 2 summarizes the information on the rejuvenators used in this study.

Table 2. Rejuvenators used.

Additives	Description
Rejuvenator 1 (Petroleum Technology)	❖ dosage: 9% of RAP binder ❖ Added to virgin binder
Rejuvenator 2 (Green Technology)	❖ dosage: 0.65% of RAP material ❖ Added to batch
Rejuvenator 3 (Agriculture Technology)	❖ dosage: 5% of virgin binder ❖ Added to virgin binder

Aggregates and Binder

Three different aggregates, limestone, 2A gravel, and 3ACR gravel, were blended as virgin aggregates with a single source of RAP for the production of five mixtures. The nominal maximum aggregate size (NMAS) of the final aggregate blend was 12.5 mm. Table 3 summarizes the basic information on the mixtures including percent of each aggregate source, its aggregate gradation, and the combined gradation of the blend.

A virgin asphalt binder, Superpave performance graded binder PG 64-34, was used for all four mixtures. The percentage of remaining binder in the RAP material was 5.4%. With the combined aggregate blend, virgin binder and RAP, a Superpave volumetric design of the AC mixture was conducted and resulted in binder content of 5.2% by weight of the total aggregate to yield air voids between 2.0 to 4.0% and dust-binder ratio of 0.7 to 1.7%. In order to achieve the dust-binder ratio criterion, all virgin aggregates were washed before mixing. In Table 4 the mixing and compaction temperatures together with the heating and curing time are listed.

After completing the volumetric design of the asphalt concrete mixture, the next step was to pursue a mix design to produce the FAM phase. FAM is defined here as a separate phase composed of an asphalt binder, fine aggregates passing sieve No. 16 (mesh size of 1.18 mm), and air voids. Based on this definition, the FAM gradation was obtained from the original mixture gradation by excluding the aggregates larger than 1.18 mm (i.e., retained on sieve No. 16).

Table 3. Mixture information.

Material	% Agg.	Aggregate Gradation (% Passing on Each Sieve)								
		19mm	12.5mm	9.5mm	#4	#8	#16	#30	#50	#200
RC 1	11	100	50	45	43	30	20	2.7	2.5	2.1
3 A Cr. Gravel	17	100	100	100	98	80	39.5	24.2	14.6	5.9
2A Gravel	7	100	100	100	95	6.8	2.5	0	0	0
RAP	65	100	95.8	91.3	75	54.1	38.9	28.7	19.9	8.6
Combined		100	91.8	88.3	76.8	52.5	34.3	23.1	15.7	6.8

Table 4. Mixing/compaction temperatures and heating/curing time.

	Time in the oven (hours)	Oven temperature (F)
Virgin Aggregate	24	320
Virgin Binder	2	320
RAP	2	320
Curing	2	275
Compaction	-	275

SAMPLE FABRICATION

Semicircular Bend (SCB) AC Specimens

The cylindrical sample (diameter of 150 mm and length of 170 mm) was compacted with a Superpave gyratory compactor. After removing two slices (with 10 mm thickness) from the top and bottom of the compacted AC mixture sample, the cylinder was cut into three disks of 50 mm tall. Then, each disk was cut into two identical halves. Finally, a vertical notch (15 mm long) was made with a saw machine. SCB specimen fabrication process is illustrated in Fig. 1.

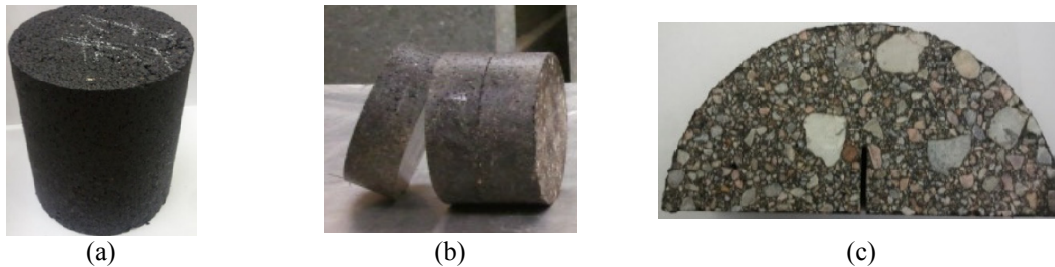


FIG. 1. SCB specimen fabrication process: (a) compacting, (b) slicing, and (c) notching.

FAM Specimens

FAM specimens were fabricated by using a cylindrical mold as shown in Fig. 2. The height and diameter of each specimen are 50 mm and 12 mm, respectively. 12 grams of FAM mixture were used to produce each FAM specimen based on previous studies (Kim et al. 2003b,c; Kim et al. 2002).



Fig 2. (a) Cylindrical mold to make FAM specimens, (b) FAM specimens.

TEST METHODS

Semicircular Bending (SCB) Test of AC

Three SCB specimens were prepared for each mixture. Prior to testing, individual SCB specimens were placed inside the environmental chamber of a mechanical testing machine for temperature equilibrium (25°C). Then, the specimens were subjected to a simple three-point bending configuration with monotonic displacement rate (i.e., 5mm/min.) applied to the top centerline of the SCB specimens. Reaction force at the loading point was monitored by the data acquisition system installed in the mechanical testing machine. The results of SCB tests are presented by plotting the reaction forces at the point of the load application versus displacements.

Strain Sweep and Time Sweep Tests of FAM

Two different types of tests were performed to determine stiffness and cracking characteristics of FAM mixtures: strain sweep test and time sweep test. Strain sweep tests were performed at 25°C to determine strain levels that satisfy the homogeneity principle of linear viscoelasticity and corresponding linear viscoelastic stiffness of each FAM mixture. To evaluate fatigue cracking potential of each mixture, time sweep tests were then carried out at testing temperature of 25°C with strains greater than the level of strain satisfying linear viscoelasticity. The strains are considered large enough to cause nonlinear behavior (such as fatigue damage) (Kim et al. 2006, Kim et al. 2003 a, b, c; Kim et al. 2002).

RESULTS AND DISCUSSION

Fig 3. presents SCB test results of all four mixtures by plotting the reaction forces versus vertical displacements. The characteristic of asphalt mixtures (i.e. stiffness and fracture behavior) can then be estimated using the SCB test results. The upward slope (i.e. the slope up to peak) of SCB load-displacement curve represents the stiffness of mixtures. To characterize fracture behavior of mixtures, researchers have proposed different indicators (Wu et al. 2005; Zegeye et al. 2012; Al-Qadi et al. 2015). One of

the common indicators is fracture energy quantified by an area under the load-displacement curve; however, using fracture energy can be sometimes deceptive, in particular to distinguish fracture resistance of different types of asphalt concrete mixtures. As a result, Al-Qadi et al. (2015) proposed the flexibility index (FI) to distinguish cracking resistance of mixtures by combining the fracture energy with downward slope (i.e., the post-peak slope) as written below:

$$FI = A \times \text{fracture energy} / \text{downward slope (m2)}$$

where A is the calibration coefficient for unit conversions

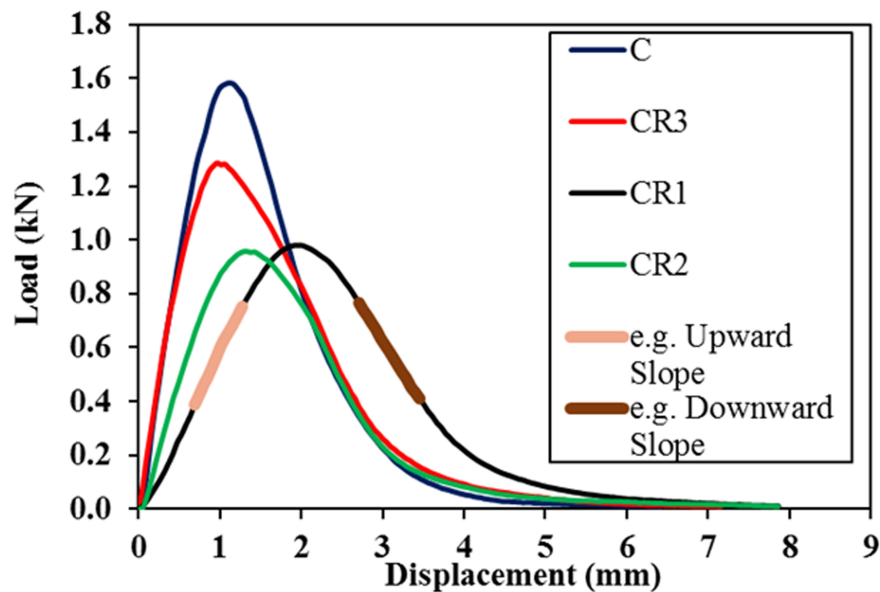


Fig. 3. SCB test results.

The fracture energy, FI and corresponding two slopes (upward and downward) from the SCB load-displacement curves are given in Table 5. As can be seen in Fig. 3 and Table 5, the upward slope decreased with the addition of rejuvenators into the control mixture, which indicates that the rejuvenators can make the high-RAP control mixture soft. This finding is in a good agreement with many other studies including Zhou et al. (2014) and Al-Qadi et al. (2012).

As mentioned before, using only fracture energy to characterize fracture behavior of mixtures can be sometimes misleading. For instance, a comparison made between fracture energy of mixtures (i.e., C, CR1 and CR2) shown in Table 5, does not provide clear distinction on fracture behavior of those mixtures since the fracture energies are very similar. However, the post-peak and FI vividly indicate that the high-RAP mixture becomes somewhat more compliant due to the addition of softening agents (i.e., rejuvenators). The increase of mixture ductility may improve cracking resistance of the control mixture, which was also presented in other studies (Zhou et al. 2014; Im and Zhou, 2014).

Table 5. Several indicators obtained from the SCB fracture test.

Mixture ID	Upward Slope (m1)	Downward Slope (m2)	Fracture Energy (J/m ²)	Flexibility Index
CR1	0.623	-0.480	851	18
CR3	1.453	-0.605	865	13.5
CR2	0.891	-0.613	685	11
C	1.815	-1.063	926	9

Fig. 4. shows the results of FAM strain sweep. Regarding the level of strain within LVE behavior, based on a study by Marasteanu and Anderson (2000) which claims that LVE region holds until 10% drop in the initial value of dynamic shear modulus, the results depict that the linear viscoelastic region held until around 0.01% strain. The control mixture had the stiffest behavior, and rejuvenators decreased stiffness of the control mixture. Additionally, the petroleum tech rejuvenated mixture showed the softest behavior between rejuvenated mixtures, and the green tech and the agriculture tech rejuvenated mixtures displayed similar behavior.

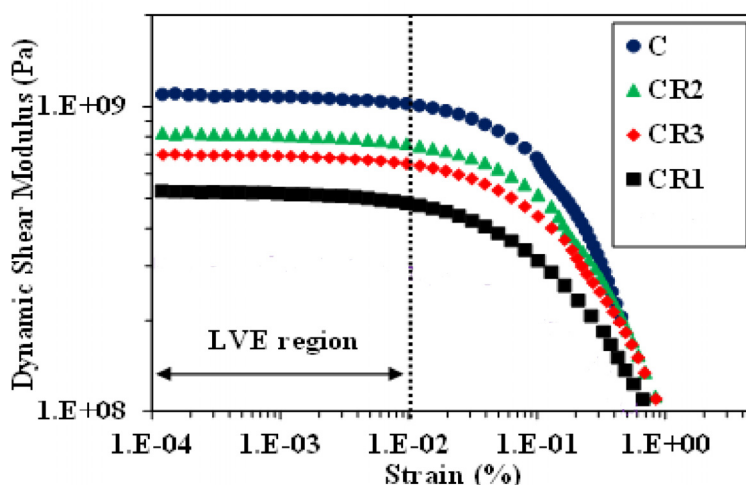


Fig.4. FAM strain sweep test results at 25°C.

Fig. 5 shows FAM time sweep test results plotted on a log-log scale of the strain level versus the fatigue life for all mixtures. In this study, the number of loading cycles at maximum phase angle (or the number of loading cycles at the transition point) was considered as the fatigue life of the mixture (Kim et al. 2006). The results noticeably illustrated that rejuvenators increased the fatigue life of mixtures, and the petroleum tech rejuvenated mixture showed greater fatigue resistance than the two other rejuvenated mixtures. These results strongly implied that rejuvenators made mixtures softer and capable of accumulating more fatigue damage before failure because of the slow rate of stiffness reduction. Furthermore, the results displayed that the control mixture had less fatigue resistance than the other mixtures especially at lower strain levels, and green and agriculture tech rejuvenated mixtures showed shorter fatigue lives than the petroleum tech rejuvenated mixture, especially at higher strain levels.

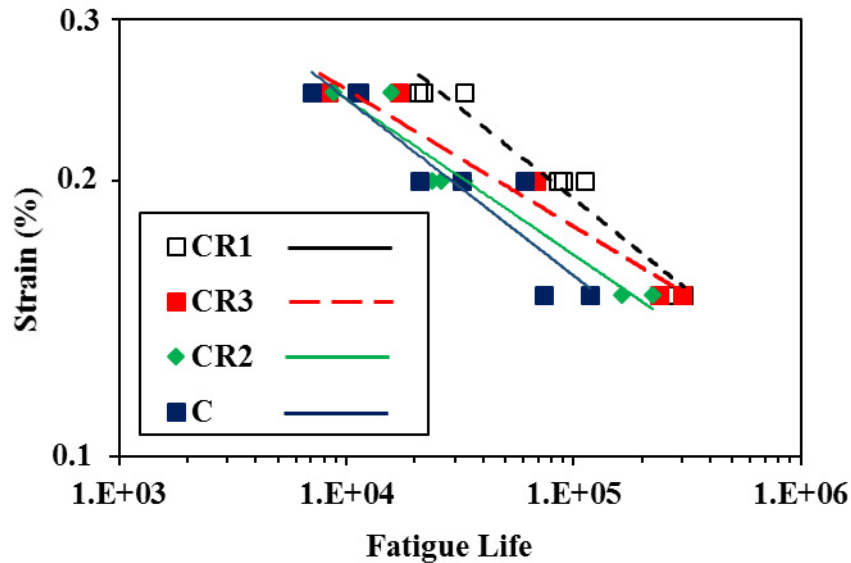


Fig. 5. FAM time sweep test results at 25°C.

The aforementioned discussions imply that FAM test results generally agree well with the AC SCB test results. In case of stiffness, the results of AC mixtures show that the petroleum tech rejuvenated mixture is softest, and the control mixture is the stiffest and mixtures treated by agriculture tech and green tech rejuvenators behaved similarly. The same trend was also observed in FAM mixtures which indicate that control mixture and the petroleum tech rejuvenated mixture showed the stiffest and the softest behavior, respectively. In case of fatigue fracture and cracking behavior, among the different SCB test indicators, the post-peak slope and FI showed a good correlation with the FAM fatigue test results. This implies that the post-peak slope and FI in the SCB fracture test represent the mixture's rate of damage which is particularly related to cracking.

CONCLUSIONS

This paper presented experimental results of mixtures containing high RAP by adding three different types of rejuvenators in two different length scales: AC and FAM. Test results from the two length scales demonstrated that rejuvenators made high-RAP mixtures softer and more compliant (ductile), which decreased viscoelastic stiffness and improved fatigue resistance of high-RAP mixtures. Experimental results of the two length scales generally showed a good agreement. This indicates that there is a linkage between the AC and FAM. Although more studies and investigations with many other cases need to be carried out to reach any definite conclusions, FAM scale tests seem a good alternative for predicting asphalt concrete mixture behavior, which may bring significant savings in experimental tests and costs.

ACKNOWLEDGMENTS

The authors acknowledge the Nebraska Department of Roads for the financial support for this study.

REFERENCES

- Al-Qadi, I., Aurangzeb, Q., Carpenter, S., Pine, W., Trepanier, J. (2012). "Impact of High RAP Contents on Structural and Performance Properties of Asphalt Mixtures" *University of Illinois at Urbana-Champaign*, Report No.FHWA-ICT-12-002.
- Al-Qadi, I., Lippert, D., Ozer, H., Thompson, M. (2015). "ICT Engineering for Performance and Sustainability of Future Paving Asphalt Materials" *Illinois Center for Transportation*, web: <http://ict.illinois.edu/>.
- Al-Qadi, I. L., Ozer, H., Lambros, J., El-Khatib, A., Singhvi, P., Khan, T., Rivera-Perez, J., and Doll, B. (2015). Testing Protocols to Ensure Performance of High Asphalt Binder Replacement Mixes Using RAP and RAS, *Research Report: FHWA-ICT-15-017*, Illinois Center for Transportation/Illinois Department of Transportation.
- Branco, V.T.F.C. (2008). "A unified method for the analysis of nonlinear viscoelasticity and fatigue cracking of asphalt mixtures using the dynamic mechanical analyzer." Ph.D Dissertation, Texas A&M University.
- Carpenter, S., Wolosick, J. (1980). "Modifier Influence in the Characterization of Hot-Mix Recycled Material." *Transportation Research Record*, 777: 15-22.
- Elseifi, M. A., Mohammad L. N., Cooper S. B. (2011). "Laboratory Evaluation of Asphalt Mixtures Containing Sustainable Technologies." *Journal of the Association of Asphalt Paving Technologists*, 80: 227-254.
- Hajj, E. Y., Souliman, M. I., Alavi, M. Z., Salazar, L. G. L. (2013). "Influence of Hydrogreen Bio-Asphalt on Viscoelastic Properties of Reclaimed Asphalt Mixtures." *Transportation Research Board CD-ROM*.
- Hill, B., Oldham, D., Behnia, B., Fini, E. H., Buttlar, W. G, Reis, H. (2013). "Low Temperature Performance Characterization of Bio-Modified Asphalt Mixtures Containing Reclaimed Asphalt Pavement." *Transportation Research Board CD-ROM*.
- Im, S., Zhou, F. (2014) "Field Performance of RAS Test sections and Laboratory Investigation of Impact of Rejuvenators on Engineering Properties of RAP/RAS Mixes" *Texas Department of Transportation*, Report No. FHWA/TX-14/0-6614-3.
- Im, S., You, T., Ban, H., & Kim, Y. R. (2015). "Multiscale testing-analysis of asphaltic materials considering viscoelastic and viscoplastic deformation." *International Journal of Pavement Engineering*, 1-15.
- Karki, P., Kim, Y.R., and Little, D.N. (2015). "Dynamic Modulus Prediction of Asphalt Concrete Mixtures through Computational Micromechanics." *Transportation Research Board 94th Annual Meeting*, No. 15-1934.
- Kim, Y.R., Little, D.N., and Lytton, R.L. (2002). "Use of dynamic mechanical analysis (DMA) to evaluate the fatigue and healing potential of asphalt binders in sand asphalt mixtures (with discussion and closure)." *Journal of the Association of Asphalt Paving Technologists*, 71: 176-206.
- Kim, Y.R., Little, D.N., and Song, I. (2003). "Mechanistic evaluation of mineral fillers on fatigue resistance and fundamental material characteristics." *Transportation Research Board, Washington*, 1832, DOI 10.3141/1832-01.

- Kim, Y.R., Little, D.N., and Lytton, R.L. (2003). "Fatigue and healing characterization of asphalt mixtures." *Journal of Materials in Civil Engineering*, 15 (1): 75-83.
- Kim, Y. R., Song, I. N. J. U. N., & Little, D. N. (2003). "Use of Dynamic Mechanical Analysis to Predict Damage in Asphalt Mastic." *In International Center for Aggregates Research 11th Annual Symposium: Aggregates-Asphalt Concrete, Bases and Fines*.
- Kim, Y., Lee, H. J., Little, D. N., & Kim, Y. R. (2006). "A Simple Testing Method to Evaluate Fatigue Fracture and Damage Performance of Asphalt Mixtures (With Discussion)." *Journal of the Association of Asphalt Paving Technologists*, 75.
- Marasteanu, M.O and Anderson, D.A. (2000). "Establishing linear viscoelastic conditions for asphalt binders." *Journal of the Transportation Research Board*, 1728 (1): 1-6.
- Mogawer, W., Bennert, T., Daniel, J. S., Bonaquist, R., Austerman, A., Booshehrian, A. (2012). "Performance Characteristics of Plant-Produced High RAP Mixtures." *Journal of the Association of Asphalt Paving Technologists*, Vol. 81: 403-439.
- Mogawer W., Booshehrian, A., Vahidi S., and Austerman A. A. (2013). "Evaluating the Effect of Rejuvenators on the Degree of Blending and Performance of High RAP, RAS, RAP/RAS Mixtures." *Road Materials and Pavement Design*, 14(2): 193-213.
- Shen, J., Amirkhani, S., Tang, B. (2007). "Effects of Rejuvenator on Performance-based Properties of Rejuvenated Asphalt Binder and Mixtures." *Construction and Building Materials*, 21: 958-964.
- Terrel, R., Epps, J. (1989). "Using Additives and Modifiers in Hot-Mix Asphalt." *Quality Improvement Series (QIP 114 A)*, NAPA, Lanham, MD.
- Wu, Z., Mohammad, L. N., Wang, L. B., and Mull, M. A. (2005). "Fracture resistance characterization of superpave mixtures using the semi-circular bending test." *Journal of ASTM International*, 2(3): 1-15.
- Yu, X., Zaumanis, M., Santos, S., Poulidakos, L. (2014) "Rheological, microscopic, and chemical characterization of the rejuvenating effect on asphalt binders" *Journal of Fuel*, 135: 162–171.
- Zaumanis, M., Mallick, R. B., Frank, R. (2015). "Evaluation of different recycling agents for restoring aged asphalt binder and performance of 100 % recycled asphalt" *Journal of Materials and Structures*, Vol. 48 (8): 2475-2488.
- Zaumanis, M., Mallick, R. B, Frank, R. (2013). "Evaluation of Rejuvenator's Effectiveness with Conventional Mix Testing For 100% RAP Mixtures." *Transportation Research Board CD-ROM*.
- Zegeye, E., Le, J-L., Turos, M., and Marasteanu, M. (2012). "Investigation of size effect in asphalt mixture fracture testing at low temperature" *Road Materials and Pavement Design*, 13(1): 88-101.
- Zhou, F., Estakhri, C., Scullion, T. (2014). "Literature Review: Performance of RAP/RAS Mixes and New Direction" *Texas Department of Transportation*, Report No. FHWA/TX-13/0-6738-1.

Variability Associated with the Resilient Modulus of Reclaimed Asphalt Pavements

Pranav R. T. Peddinti, S.M.ASCE¹; Sireesh Saride, M.ASCE²; and
B. Munwar Basha, M.ASCE³

¹Research Scholar, Dept. of Civil Engineering, Indian Institute of Technology Hyderabad, Kandi, Sangareddy, 502285 Telangana, India.

E-mail: ce14resch11005@iith.ac.in

²Associate Professor, Dept. of Civil Engineering, Indian Institute of Technology Hyderabad, Kandi, Sangareddy, 502285 Telangana, India. E-mail: sireesh@iith.ac.in

³Assistant Professor, Dept. of Civil Engineering, Indian Institute of Technology Hyderabad, Kandi, Sangareddy, 502285 Telangana, India. E-mail: basha@iith.ac.in

Abstract: Research on reclaimed asphalt pavement (RAP) material has been on its high all over the world since last three decades. Sustainability, cost effectiveness and eco-friendliness of RAP make it a potential secondary alternative in pavement applications. Often, to meet the strength and stiffness requirements, RAP is blended with virgin aggregates (VA) at various proportions. The resilient modulus (M_r) of base material plays a major role in deciding the pavement thickness. A considerable amount of variability in the M_r values of RAP is observed from laboratory and field studies all over the world. In view of the increased usage of RAP, there is a definite need to understand the statistical variability associated with the M_r of RAP. In this paper, the variability associated with M_r is quantified statistically. Based on the compilation of M_r values from several published studies, the average values of mean, standard deviation, coefficient of variation (COV), and the best fit probability density functions for M_r are computed. The appropriate distributions for RAP and VA mixes are discussed. The outcome of the study will be useful to quantify the performance of the flexible pavements using reliability based design optimization (RBDO) framework which is based on the probability theory.

INTRODUCTION

In view of the population explosion, trade and industrial development, 21st century have experienced a never before demand for sustainable infrastructure facilities in terms of roads and buildings. This sudden increase in demand led to a drastic scarcity of natural construction resources. Therefore, research towards utilization of secondary or recycled products gained importance all over the world. Most of the reclaimed

asphalt pavement (RAP) materials do not often meet the minimum requirements for use in base courses (Arulrajah et al., 2013). In case of flexible pavements, RAP materials proportioned with virgin aggregates (VA) gained a lot of prominence because of their vast production and promising research implications in terms of strength, stiffness and durability. RAP can be used in hot mix asphalt (HMA) and base/subbase layers by proper blending with virgin granular materials and/or cementitious additives/admixtures as evident from the recent studies (Taha et al. 2002; Guthrie et al. 2007; Saride et al. 2010; Puppala et al. 2011; Arulrajah et al. 2013; Saride et al. 2015).

In spite of having a good knowledge about the behavior of RAP in controlled conditions, the confidence level in utilizing RAP as a base material is still low in many countries. Many of the existing codes of practice does not discuss stringent guidelines for the use of RAP in flexible pavements and some of them restrict their dosage to smaller quantities (less than 30%). The main reason could be the variability exhibited by these materials. When observed from the recent literature, the results of certain parameters such as strength and stiffness do not follow a common trend. Even if the trend is similar, the results had a lot of variation from project to project, investigator to investigator, and place to place. In general, all granular materials used in base/subbase layer exhibit high level of aleatory/inherent uncertainty. This uncertainty is more profound when secondary granular materials like RAP are employed. There is a definite need to understand and quantify the variability exhibited by the RAP in terms of its strength and stiffness which will be useful to bring out a globally accepted procedure for use of RAP materials in flexible pavements. As a first step to achieve this goal, the current study aims at quantifying the variability in resilient modulus (M_r) obtained from various studies as reported in Table 1 on RAP and VA mixes performed all over the world. The resilient modulus being an important parameter which accounts for the overall stiffness and recoverable strains of the pavement system, it is appropriate to quantify its variability/uncertainty.

UNCERTAINTY IN FLEXIBLE PAVEMENTS

Uncertainties in any structural system could arise from many factors like lack of knowledge, inaccuracy in the data, variability in materials, degree of belief, likelihood of certain events, etc. The uncertainty in the complete life cycle of a pavement arises from variability in traffic, climate, and materials (Xiao 2012). The uncertainty in traffic can be reduced by conducting actual/timely traffic counts and also by incorporating appropriate traffic increment factors. Similarly, calibrating the design for respective local climatic conditions can eliminate the uncertainty from climate. However, when it comes to materials, the uncertainty is irreducible/aleatory which can only be assessed or quantified but cannot be eliminated. The aleatory uncertainty in any system is generally quantified by plotting the frequency distribution or density function for the data under study.

The distribution of probability mass over a finite sample space is known as the probability density function (PDF). The uncertainty analysis uses the PDF of a particular distribution. It has been a general practice to use normal and lognormal

distributions to analyze geotechnical properties of granular materials in pavements. Timm et al. (2000) presented a study to develop *PerRoad* software and reported that the modulus of granular base materials vary lognormal with a coefficient of variation (COV) of 40%. The use of these distributions is skeptical when secondary materials like RAP are used. The use of generalized distributions may result in misinterpretation of pavement reliability, thereby leading to improper pavement design. In case of variability associated with RAP materials, developing the PDF can be achieved by analyzing the available laboratory or field data relevant to the property under uncertainty analysis. The larger the data set available, the higher will be the accuracy in density function. However, before applying these stochastic/probabilistic methods to the pavements, it is very important to understand the factors that cause this variability in RAP materials failing in which may result in misinterpretation of data and thereby erratic quantification of variability. In addition to the natural factors like temperature, material factors like gradation/ fines content, aggregate type and shape, moisture content, and compacted density influence the resilient behavior of granular materials (Lekarp 2000). In case of RAP materials, in addition to these general factors, asphalt content also has a major impact on the engineering performance. As asphalt is thermo-sensitive, variation in temperature also dramatically changes its viscosity, thereby altering the stiffness.

OBJECTIVES OF THE STUDY

In view of the importance of resilient behavior of RAP in flexible pavements, the present study aims at the following objectives:

- To perform statistical analysis on the collected resilient modulus data from various studies to quantify its variability by verifying the goodness of conventionally used PDFs for RAP and VA mixes.
- To identify the best fit PDF for the data under consideration based on percentile (P-P) plots.

DATA PERTAINING TO RESILIENT MODULUS OF RAP

Resilient modulus data are collected from various published studies wherein RAP is tested for its use in base/subbase applications. The M_r data along with the characteristics of RAP is presented in Table 1. The range of M_r is selected such that they fall between 100 to 700 MPa to meet the general range of M_r for pavement base/subbase applications. To account for the similar test conditions, the M_r calculated at confining pressures of 34.5 or 68.9 kPa (5 or 10 psi) or cyclic stress, ranging from 137.9 – 208 kPa (20 – 30 psi) were considered in the present study. As observed in Table 1, the asphalt content in RAP falls within 3 to 7 percent by weight of the mix as reported by Chesner et al. 1998 for most of the old pavements.

Table 1. Resilient Modulus Reported for Various RAP and VA Mixes

Source / Characteristics of RAP	R A P (%)	⁺⁺ M _r	Source/ Characteristics of RAP	R A P (%)	⁺⁺ M _r
Macgregor et al. (1997) * Gradation : A-1-a fines : < 5 % ** D10 : 0.61 mm	10 30 50 100	114 142 153 198	Attia et al. (2010) Max. size: < 12.5 mm fines : < 2% D10: 0.3 mm (approx.) *** AC: 3.6 – 4 %	50 100	414 482
Maher et al (1997) fines : < 1 % D10 : 1.6 mm (approx.)	100	260	Saride et al. (2010) Gradation: SP (USCS) D10: 0.3 mm AC: 4.0 %	100	280
Bennett et al. (2000) Gradation : A-1-a D10 : 1.19 mm fines : 0.4 %	25 50 75 100	159 178 188 263	Kim and Labuz (2007) Gradation: A-1-a D10 : 0.15 – 0.60 mm AC : 2.3 – 6 %	25 50 75	220 260 350
Bahia et al. (2000) Gradation : A-1-a D10 : 0.425 mm fines : 2.5 %	50	235	FHWA (2011) Gradation: A-1-a fines: < 10% D10: 0.60 mm	25 50 75	163 158 189
Cosentino et al. (2003) Gradation : A-1-a D10 : 0.43 mm fines: < 1%; AC : 6.04 %	60 80 100	143 211 231	Tolbert (2014) Gradation: A-1-a D10: 0.60 mm	25 50 75 100	620 592 641 406
Puppala et al. (2011) Gradation : A-1-a D10: 0.3 mm; fines: <1%	100	275	Costa et al. (2014) Gradation: A-1-a fines: <15%; AC: 6.5%	15 20 40	250 340 350
Bennett et al (2005) D10 : 0.516 mm fines : 0.1 %	25 50 75 100	193 220 213 267	Edil et al (2012) Gradation: A-1-a, A-1-b D10: 0.30 – 1.0 mm fines: 0.5 – 2.5 % AC: 4.7 – 7.1 %	100	180 184 173 198 197 209 266
Locander (2009) Gradation : A-1-a AC : 4.65 – 6.20 % D10 : 0.6 – 1mm	100	235	Dong and Huang (2014) D10: 0.3 mm AC: 2%	100	280

⁺⁺ M_r in MPa; * Gradation as per AASHTO; ** D10: Effective particle size;
*** AC: Asphalt content by weight of mix.

HISTOGRAMS, PDF, AND P-P PLOTS

The histogram statistics for M_r is shown in Table 2. In the current study, PDF's are plotted for the magnitudes of M_r using a trial and error method so that the best fit can be chosen from the various distribution functions available. The shape, scale, and location parameters are computed using trial and error method such that the skewness of the observed M_r value match with the PDF of that particular distribution. It is essential to understand the shape, scale and location parameters of these PDFs to arrive at the exact distribution corresponding to M_r . There can be many types of PDFs among which a few fits better to the observed data frequency. The goodness of fit depends on the characteristics of the distribution and variability associated with the data under consideration. The PDF giving a close fit is supposed to yield a better prediction.

From the analysis, Burr distribution was found suitable for RAP-VA mixes. The Burr distribution is a continuous probability distribution for non-negative random variables. It was first discussed by Burr (1942) as a two-parameter family and later an additional scale parameter for the same distribution was introduced by Tadikamalla (1980). To compare the Burr distribution with conventional distributions, analysis is also done using normal and lognormal distributions. The PDF and cumulative distribution function (CDF) values corresponding to normal, lognormal, and Burr distributions are computed using equations provided in Table 3. Table 5 presents the PDF values for normal, lognormal and Burr distributions. For a better visual comparison of PDFs, the frequency density functions are superimposed on the histogram charts. Figures 1, 3 and 5 show the histograms with superimposed PDFs of normal, lognormal and Burr type distributions respectively.

Table 2. Histogram Data for the RAP and VA Mixes

Bin Centers	Bin Centers	Bin Centers	Bin Centers	Bin Centers
152.5	14	14	31.82	0.33
237.5	19	33	75.00	0.44
322.5	5	38	86.37	0.12
407.5	2	40	90.91	0.05
492.5	1	41	93.19	0.023
577.5	1	42	95.45	0.023
662.5	2	44	100.00	0.047

Figures 2, 4 and 6 show the percentile-percentile (P-P) plots comparing the observed cumulative distribution of M_r with the expected cumulative distribution. The reference line represents the theoretical distribution of M_r depending on the shape and scale parameters of each distribution. The statistical data for the M_r as shown in Table 4 depicted additional variability (COV 47.15%) in RAP – VA mixes as compared to virgin aggregates (COV 30 – 40%).

Table 3. PDF and CDF Functions

Distribution/ Fit Parameters	PDF	CDF
<p>Normal σ = Scale parameter μ = Location parameter</p>	$f(M_r) = \frac{1}{\sigma \sqrt{2\pi}} \exp\left\{-\frac{1}{2}\left(\frac{M_r - \mu}{\sigma}\right)^2\right\}$	$f(M_r) = \Phi\left(\frac{M_r - \mu}{\sigma}\right)$
<p>Lognormal σ = Scale parameter μ = Location parameter</p>	$f(M_r) = \frac{1}{M_r \sigma \sqrt{2\pi}} \exp\left\{-\frac{1}{2}\left(\frac{\ln M_r - \mu}{\sigma}\right)^2\right\}$	$f(M_r) = \Phi\left(\frac{\ln(M_r) - \mu}{\sigma}\right)$
<p>Burr k = Shape parameter α = Shape parameter β = Scale parameter γ = Location parameter</p>	$f(M_r) = \frac{\alpha k \left(\frac{M_r - \gamma}{\beta}\right)^{\alpha-1}}{\beta \left[1 + \left(\frac{M_r - \gamma}{\beta}\right)^\alpha\right]^{(k+1)}}$	$f(M_r) = 1 - \left[1 + \left(\frac{M_r - \gamma}{\beta}\right)^\alpha\right]^{-k}$

It can be observed from Figures 2 and 4 that the percentiles fall close to reference line in the lower range and deviates thereafter. It indicates that the normal and lognormal distributions are not the best fit PDFs for M_r . However, most of the previous studies on resilient modulus of granular materials assumed the probability distribution to be the normal or lognormal. It may be concluded that the assumption of normal or lognormal distributions may lead to a considerable error in the reliability based designs, especially when secondary materials like RAP are used in pavements. It can be observed from Figure 6 that the percentiles are aligned to the reference line over the entire range, which indicates the zero skewness and unimodal nature of the Burr distribution. Hence, the Burr distribution appears to be reasonably good for the resilient modulus of RAP and VA mixes.

Table 4. Statistical Data for M_r

Statistical Parameter	Value
sample size	44.00
mean (μ)	262.32
variance (σ^2)	15317.00
standard deviation (σ)	123.67
coefficient of variation (COV)	47.15 %

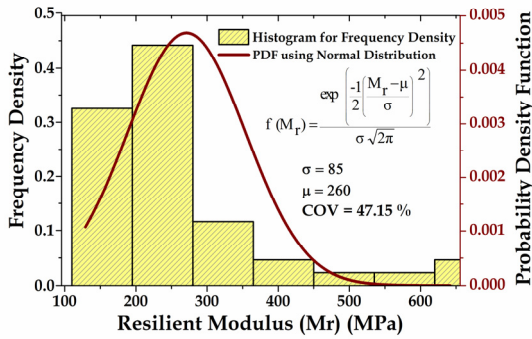


FIG. 1. PDF of Normal distribution

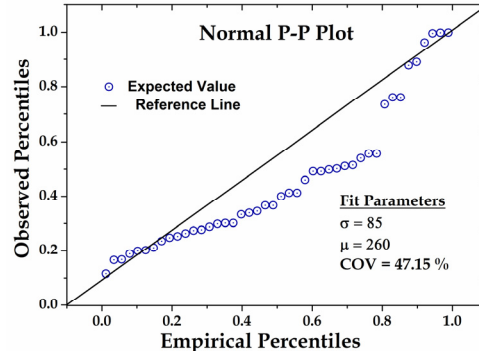


FIG. 2. P-P plot for Normal distribution

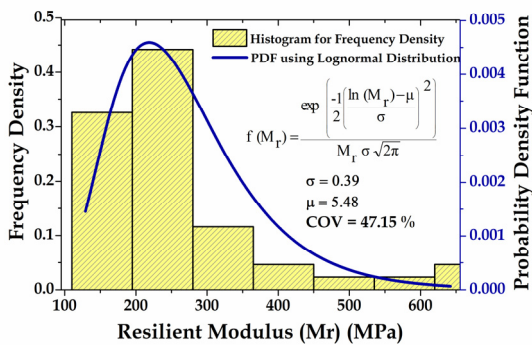


FIG. 3. PDF of Lognormal distribution

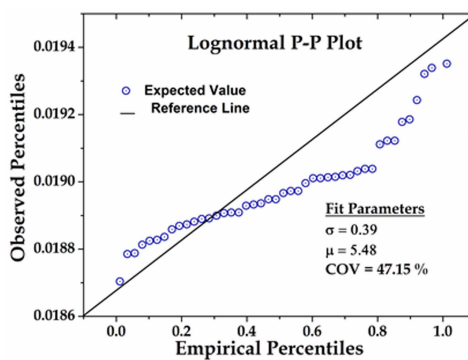


FIG. 4. P-P plot for Lognormal distribution

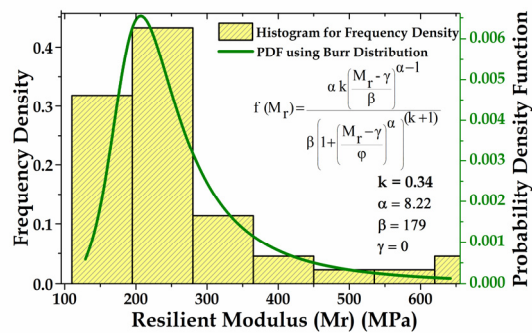


FIG. 5. PDF of Burr distribution

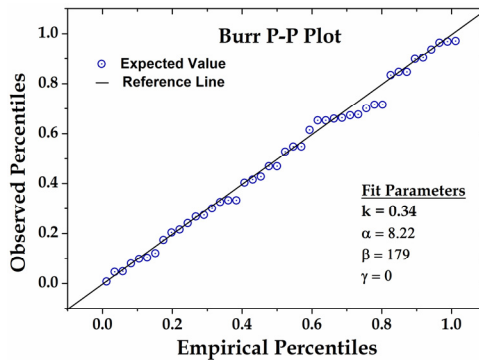


FIG. 6. P-P plot for Burr distribution

This information is useful to further quantify the performance of the flexible pavements using Reliability Based Design Optimization (RBDO) framework which is based on the probability theory. It is also an affirmative opinion of the authors that a detailed statistical analysis is utmost required to obtain an accurate PDF for a given data set to accurately predict the reliability of the data.

Table 5. Normal, Lognormal, and Burr PDF values of M_r

M_r (MPa)	Normal PDF	Lognor- mal PDF	Burr PDF	M_r (MPa)	Normal PDF	Lognor- mal PDF	Burr PDF
114	0.00107	0.00146	0.00058	231	0.00443	0.00441	0.00508
142	0.00179	0.00292	0.00243	235	0.00449	0.00435	0.00485
143	0.00182	0.00297	0.00254	235	0.00449	0.00435	0.00485
153	0.00212	0.0034	0.00363	250	0.00466	0.00407	0.00404
158	0.00228	0.00365	0.00421	260	0.00469	0.00385	0.00356
159	0.00231	0.00369	0.00432	260	0.00469	0.00385	0.00356
163	0.00244	0.00384	0.00477	262	0.00469	0.00380	0.00347
173	0.00278	0.00416	0.00574	263	0.00469	0.00378	0.00343
178	0.00294	0.0043	0.00611	266	0.00468	0.00371	0.00331
180	0.00301	0.00433	0.00622	267	0.00468	0.00369	0.00326
184	0.00314	0.00441	0.00641	275	0.00462	0.00350	0.00294
188	0.00328	0.00448	0.00653	280	0.00456	0.00338	0.00276
189	0.00331	0.00449	0.00655	280	0.00456	0.00338	0.00276
193	0.0034	0.00454	0.00659	340	0.00301	0.00202	0.00136
197	0.00357	0.00457	0.00657	350	0.00268	0.00183	0.00122
198	0.00360	0.00458	0.00655	350	0.00268	0.00182	0.00122
198	0.00360	0.00458	0.00655	406	0.00107	0.00101	0.0007
209	0.0039	0.00460	0.00623	414	0.00091	0.00093	0.00065
211	0.00397	0.00459	0.00614	482	0.00015	0.00043	0.00036
213	0.00403	0.00458	0.00605	592	2.3E-06	0.00012	0.00017
220	0.00420	0.00454	0.00570	620	5.9E-07	8.5E-05	0.00014
220	0.00420	0.00454	0.00570	641	2.0E-07	6.7E-05	0.00012

CONCLUSIONS

Based on the statistical analysis, the following conclusions can be drawn from the current study.

1. Generalizing and limiting the distributions to normal and lognormal fits does not hold good when secondary granular materials are used in the flexible pavements.
2. It may be noted from the study that the assumption of inappropriate distribution may lead to considerable error in the reliability based designs due to either under/over prediction of values of probability density function.
3. The statistical analysis of resilient modulus data indicates that RAP mixes comparatively exhibit higher variability as compared to natural aggregates.
4. The Burr distribution was found to be a reasonably good model for such mixes as proven by the P-P plot (normality test) assessments.
5. Using an appropriate distribution for uncertainty analysis is expected to improve the overall reliability, thereby making the design procedures more robust and accurate.

REFERENCES

- Arulrajah, A., Piratheepan, J., Disfani, M.M. and Bo, M.W. (2013). "Resilient moduli response of recycled construction and demolition materials in pavement subbase applications." *J. Mater. Civ. Engrg.*, 25 (10): 1920 – 1928.
- Attia, M.I.E. (2010). "Characterization of the structural behavior of reclaimed asphalt pavement as pavement base layer." *Master's Thesis*, North Dakota State University, ND.
- Bahia, H.U., Bosscher, P.J., Christensen, J. and Yu Hu. (2000). "Layer coefficients for new and reprocessed asphalt mixes." *Report No. WI/SPR-04-00*. Wisconsin department of transportation, WI.
- Bennett, T. and Maher, A. (2005). "The development of performance specification for granular base and subbase material." *FHWA – NJ – 2005-03*, Rutgers University, NJ.
- Bennett, T., Papp, W.J., Maher, A. and Gucunski, N. (2000). "Utilization of construction and demolition debris under traffic-type loading in base and subbase applications." *Transportation Research Record*, No. 1714: 33-39.
- Burr, Irving W. (1942). "Cumulative frequency functions." *The Annals of Mathematical Statistics*, Vol. 13(2): 215 – 232.
- Chesner W. H., Collins R. J. and MacKay, M. H. (1998). "User Guidelines for Waste and By-Product Materials in Pavement Construction." *Federal Highway Administration*, Report no. FHWA-RD-97-148.
- Cosentino, P.J., Kalajian, E.H., Shieh C.S., Mathurin W.J.K., Gomez, F.A., Cleary E.D. and Treerattakoon. A. (2003). "Developing specifications for using recycled asphalt pavement as base, subbase, or general fill materials." Phase II. *Final Report, FDOT*. FL/DOT/RMC/06650-7754 BC 819, Florida Department of Transportation, FL.
- Costa, J., Bradshaw, A. and Snyder, R. (2014). "Resilient moduli of a naturally aged RAP and aggregate blend." *Geo-Characterization and Modeling for Sustainability (GSP 234)*, ASCE, Reston/VA: 3025-3034.
- Dong, Q. and Huang, B. (2014). "Laboratory evaluation on resilient modulus and rate dependencies of RAP used as unbound base material." *J. Mater. Civ. Engrg.*, Vol. 26(2): 379–383.
- Edil, T. B., Tinjum, J. A. and Benson, C. H. (2012). "Recycled unbound materials." Minnesota Department of Transportation, Report No. MN/RC 2012-35, <http://www.dot.state.mn.us/research/TS/2012/201235.pdf>.
- Federal Highway Administration. (2011). "Quality base material produced using full depth reclamation on existing asphalt pavement structure." *FHWA*, Report No. FHWA-HIF-12-015. Washington, D.C.
- Guthrie, W.S., Brown, A.V. and Eggett, D.L. (2007). "Cement stabilization of aggregate base material blended with reclaimed asphalt pavement." *Transportation Research Record*, 2026, Transportation Research Board, Washington, D.C., 47-53.
- Kim, W. and Labuz, J.F. (2007). "Resilient modulus and strength of base course with recycled bituminous material." Report No. MN/RC-2007-05, Minnesota department of transportation, MN.

- Lekarp, F., Isacsson, U. and Dawson, A. (2000). "State of the art. I: Resilient response of unbound aggregates." *J. Transp. Engg.*, ASCE, Vol. 126 (1): 66–75.
- Li, P. and Liu, J. (2010). "Characterization of asphalt treated base course material." *Report No. INE/AUTC-11.02*, Alaska University Transportation Center, AL.
- Locander, R. (2009). "Analysis of reclaimed asphalt pavement as a base course material." *Report No. CDOT-2009-5*, Colorado department of transportation, CO.
- Macgregor, J.A.C., Highter, W.H. and Groot, D.D.J. (1997). "Structural numbers of reclaimed asphalt pavement base and subbase course mixes." *Transportation Research Record*, 1687, Transportation Research Board, Washington, D.C., 22-28.
- Maher, M. H., Gucunski, N. and Papp Jr. W. J. (1997). "Recycled Asphalt Pavement as a Base and Subbase Material." *ASTM Special Technical Publication*, Vol. 1275: 42-53.
- Puppala, A.J., Hoyos, L.R. and Potturi, A.K. (2011). "Resilient moduli response of moderately cement-treated reclaimed asphalt pavement aggregates." *J. Mater. Civ. Engrg.*, Vol. 23(7): 990-998.
- Saride, S., Avirneni, D. and Javvadi, S. (2015). "Utilization of reclaimed asphalt pavements in Indian low-volume roads." *J. Mater. Civ. Engrg.*, DOI: 10.1061/(ASCE)MT.1943-55330001374, 0401510.
- Saride, S., Puppala, A.J. and Williammee, R. (2010). "Assessing recycled/secondary materials as pavement bases." Special issue on sustainability in ground improvement projects, Proceedings of ICE, *Ground Improvement*, Vol. 163: 3-12.
- Tadikamalla, P. R. (1980). "A look at the Burr and related distributions." *International Statistical Review*, Vol. 48 (3): 337–344.
- Taha, R., Al-Harthy, A., Al-Shamsi, K. and Al-Zubeidi, M. (2002). "Cement stabilization of reclaimed asphalt pavement aggregate for road bases and sub bases," *J. Mater. Civ. Engrg.*, Vol. 14(3): 239–245.
- Timm, D.H., Newcomb, D.E. and Galambos, T.V. (2000). "Incorporation of reliability into Mechanistic-Empirical pavement design." *J. Transportation Research Board*, No. 1730, Washington, D.C., 73-80.
- Tolbert, J.C. (2014). "Effect of high percentages of reclaimed asphalt pavement on mechanical properties of cement-treated base material." *Master's Thesis*, Department of Civil and Environmental Engineering, Brigham Young University.
- Xiao, X.D. (2012). "Risk analysis and reliability improvement of mechanistic-empirical pavement design." *Doctoral Thesis*, Department of Civil Engineering, University of Arkansas, Fayetteville, AR.